frontiers

RESEARCH TOPICS

INFERIOR COLLICULUS MICROCIRCUITS

Topic Editors
Manuel S. Malmierca and
Eric Daniel Young

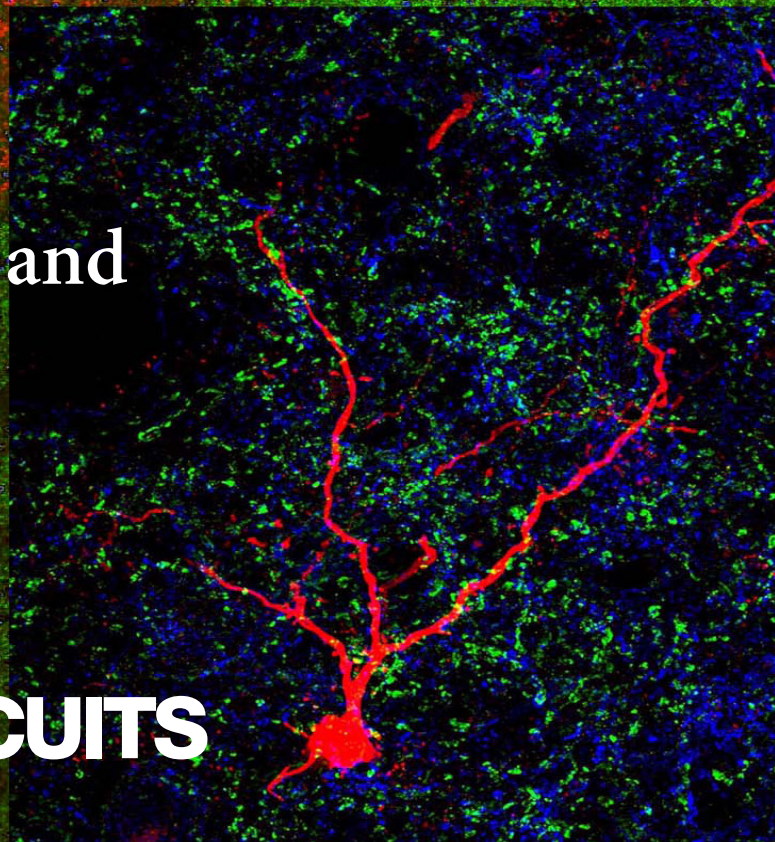

frontiers in
NEURAL CIRCUITS

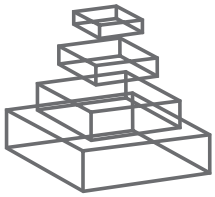

frontiers

ISSN 1664-8714
ISBN 978-2-88919-385-1
DOI 10.3389/978-2-88919-385-1

ABOUT FRONTIERS

Frontiers is more than just an open-access publisher of scholarly articles: it is a pioneering approach to the world of academia, radically improving the way scholarly research is managed. The grand vision of Frontiers is a world where all people have an equal opportunity to seek, share and generate knowledge. Frontiers provides immediate and permanent online open access to all its publications, but this alone is not enough to realize our grand goals.

FRONTIERS JOURNAL SERIES

The Frontiers Journal Series is a multi-tier and interdisciplinary set of open-access, online journals, promising a paradigm shift from the current review, selection and dissemination processes in academic publishing.
All Frontiers journals are driven by researchers for researchers; therefore, they constitute a service to the scholarly community. At the same time, the Frontiers Journal Series operates on a revolutionary invention, the tiered publishing system, initially addressing specific communities of scholars, and gradually climbing up to broader public understanding, thus serving the interests of the lay society, too.

DEDICATION TO QUALITY

Each Frontiers article is a landmark of the highest quality, thanks to genuinely collaborative interactions between authors and review editors, who include some of the world's best academicians. Research must be certified by peers before entering a stream of knowledge that may eventually reach the public - and shape society; therefore, Frontiers only applies the most rigorous and unbiased reviews.
Frontiers revolutionizes research publishing by freely delivering the most outstanding research, evaluated with no bias from both the academic and social point of view.
By applying the most advanced information technologies, Frontiers is catapulting scholarly publishing into a new generation.

WHAT ARE FRONTIERS RESEARCH TOPICS?

Frontiers Research Topics are very popular trademarks of the Frontiers Journals Series: they are collections of at least ten articles, all centered on a particular subject. With their unique mix of varied contributions from Original Research to Review Articles, Frontiers Research Topics unify the most influential researchers, the latest key findings and historical advances in a hot research area!
Find out more on how to host your own Frontiers Research Topic or contribute to one as an author by contacting the Frontiers Editorial Office: researchtopics@frontiersin.org

INFERIOR COLLICULUS MICROCIRCUITS

Topic Editors:
Manuel S. Malmierca, University of Salamanca, Spain
Eric Daniel Young, Johns Hopkins University, USA

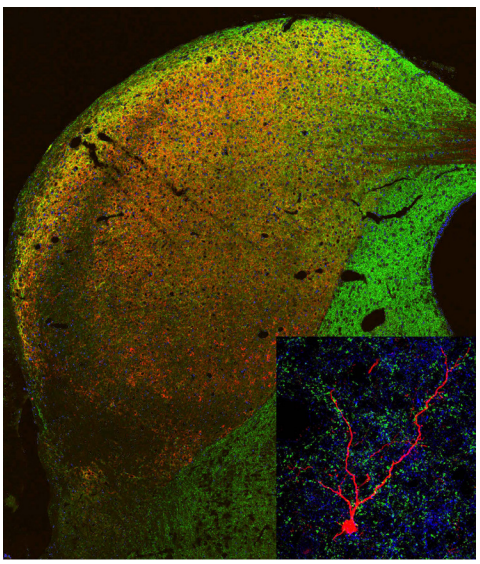

Figure provided by Doug Oliver and Tetsufumi Ito.
Background: An image of a coronal IC section of a Japanese house bat (Pipistrellus abramus) immunostained for VGLUT2 (green) and GAD67 (red). Inset: A rat IC neuron filled with tetramethylrhodamine-cadaverine (red) by juxtacellular recording-labeling technique. The section was immunostained for VGLUT1/2 (green) and GAD67 (blue). The image was reconstructed from 151 z-stack optical slices.

Table of Contents

frontiers in
NEURAL CIRCUITS

EDITORIAL
published: 09 October 2014
doi: 10.3389/fncir.2014.00113

Inferior colliculus microcircuits

Manuel S. Malmierca[1,2] and Eric D. Young[3]*

[1] *Auditory Neurophysiology Unit, Laboratory for the Neurobiology of Hearing, Institute of Neuroscience of Castilla y León, University of Salamanca, Salamanca, Spain*
[2] *Department of Cell Biology and Pathology, Faculty of Medicine, University of Salamanca, Salamanca, Spain*
[3] *Neural Encoding Laboratory, Biomedical Engineering, Johns Hopkins University, Baltimore, MD, USA*
**Correspondence: eyoung@bme.jhu.edu*

Edited and reviewed by:
Catherine Carr, University of Maryland, USA

Keywords: inferior colliculus, neural pathways, internal circuitry, inhibitory circuits, ion channel models, representation of sound, sonar

A unique aspect of the auditory system is the inferior colliculus (IC). This large midbrain structure serves as an obligatory synaptic station in both the ascending and descending auditory pathways. It has no equivalent in other sensory systems and it meets several unique needs of the auditory system. Most important, of course, is unifying the representation of sound in the two ears, which allows sound localization and other spatial calculations such as demasking and the analysis of complex auditory scenes. In addition, the IC is a major target for non-auditory inputs to the auditory system, including connections from other sensory systems and from neuromodulatory systems like the locus coeruleus. The IC also distributes auditory information in cortico-cortical loops and in connections to the superior colliculus.

There is much to be learned about the IC. The goal of this special topic is to bring together papers, both reviews and original research, on a wide range of aspects of the IC's organization and function. These include the internal and external connections of the IC, the molecular determinants of its response properties, and the nature of sound encoding in the IC. In this e-book, 31 contributions are organized into these three broad categories.

The first 12 chapters address the morphological and functional organization of the IC. They include descriptions of the connections of the IC to other parts of the brain, both ascending and descending projections, as well as the organization of internal microcircuits within the IC itself. In most brainstem auditory centers, the neurons have a diverse array of morphological and molecular structure which correlates strongly with connectivity and functional role (inhibition vs. excitation for example). By contrast, it has been difficult to define such internal circuitry in the IC. The papers in this section describe a variety of approaches, anatomical, molecular, and physiological to this question and contribute to our emerging understanding of IC's internal and external organization.

The next 6 chapters describe analyses of the molecular characteristics of IC neurons in relationship to function. These include papers on the role of ion channels in generating responses of IC neurons and on the effects of mutations, aging, and damage to the auditory system. Such insults change the expression of genes and produce a variety of functional consequences for the representation of sound.

The final 13 chapters describe the encoding of sound in the IC, especially in its ascending pathways. These include analyses of responses to sound, convergence of auditory and other inputs in the IC, and analyses of emergent properties like stimulus-specific adaptation. The bat auditory system has long provided fertile ground for auditory research, because of the relatively well-defined computations needed for sonar processing. Almost half of the chapters on sound encoding deal with the bat IC, especially the role of inhibition in determining response selectivity, delay tuning, and duration tuning.

The study of the IC is too large a topic to produce a satisfactory overall view in a collection of papers of the size of this one. However, these papers do represent the main trends in current research on the IC and make clear some of the most important outstanding problems. It is hoped that they will inspire and guide the next steps in working out this critical part of the auditory system.

Conflict of Interest Statement: The authors declare that the research was conducted in the absence of any commercial or financial relationships that could be construed as a potential conflict of interest.

Received: 23 September 2013; accepted: 28 August 2014; published online: 09 October 2014.
Citation: Malmierca MS and Young ED (2014) Inferior colliculus microcircuits. Front. Neural Circuits ***8****:113. doi: 10.3389/fncir.2014.00113*
This article was submitted to the journal Frontiers in Neural Circuits.

frontiers in
NEURAL CIRCUITS

ORIGINAL RESEARCH ARTICLE
published: 06 March 2013
doi: 10.3389/fncir.2013.00029

Patterns of convergence in the central nucleus of the inferior colliculus of the Mongolian gerbil: organization of inputs from the superior olivary complex in the low frequency representation

Nell B. Cant*

Department of Neurobiology, Duke University Medical Center, Durham, NC, USA

Edited by:
Manuel S. Malmierca, University of Salamanca, Spain

Reviewed by:
Douglas L. Oliver, University of Connecticut Health Center, USA
Victoria M. Bajo Lorenzana, University of Oxford, UK

****Correspondence:***
Nell B. Cant, Department of Neurobiology, Duke University Medical Center, Research Drive, PO Box 3209, Durham, NC 27710, USA.
e-mail: nellcant@neuro.duke.edu

Projections to the inferior colliculus (IC) from the lateral and medial superior olivary nuclei (LSO and MSO) were studied in the gerbil (*Meriones unguiculatus*) with neuroanatomical tract-tracing methods. The terminal fields of projecting axons were labeled via anterograde transport of biotinylated dextran amine (BDA) and were localized on series of horizontal sections through the IC. In addition, to make the results easier to visualize in three dimensions and to facilitate comparisons among cases, the data were also reconstructed into the transverse plane. The results show that the terminal fields from the low frequency parts of the LSO and MSO are concentrated in a dorsal, lateral, and rostral area that is referred to as the "pars lateralis" of the central nucleus by analogy with the cat. This region also receives substantial input from both the contralateral and ipsilateral cochlear nuclei (Cant and Benson, 2008) and presumably plays a major role in processing binaural, low frequency information. The basic pattern of organization in the gerbil IC is similar to that of other rodents, although the low frequency part of the central nucleus in gerbils appears to be relatively greater than in the rat, consistent with differences in the audiograms of the two species.

Keywords: auditory pathways, binaural, hearing, neuroanatomy

INTRODUCTION

The inferior colliculus (IC) receives input from most of the auditory nuclei in the brainstem, as well as from a number of areas in the forebrain, including the auditory cortex (reviewed, e.g., in Casseday et al., 2002; Malmierca, 2005). In the cat, in which these projections have been studied in the most detail, it has been established that the terminal fields formed by the multiple inputs are not distributed homogeneously throughout the nucleus (e.g., Roth et al., 1978; Brunso-Bechtold et al., 1981; Kudo, 1981; Henkel and Spangler, 1983; Oliver, 1984, 1987; Shneiderman and Henkel, 1987; Shneiderman et al., 1988; Oliver et al., 1997; Loftus et al., 2004, 2010). The apparent partial or complete segregation of terminal fields formed by different sources of input supports the concept of synaptic domains in which specific neuronal populations in the IC form synaptic connections with only a subset of the total inputs to the IC (Oliver and Huerta, 1992; Oliver, 2000, 2005).

The purpose of the present study is to describe the distribution of terminal fields formed by inputs from the lateral and medial superior olivary nuclei (LSO and MSO) in the IC of the gerbil, a rodent commonly used in auditory research. Although the intrinsic organization of the IC of the rodent appears grossly similar to that in the cat, there are important differences (e.g., rat: Faye-Lund and Osen, 1985; Loftus et al., 2008). As rodents become more and more common in studies of the central auditory system, it is important to compare and contrast the details of the termination patterns in their IC with those established in the cat. Similar to results in the cat, differential termination of inputs from some of the major afferent sources to the IC have been reported in rodents (e.g., projections from the cochlear nucleus: Oliver et al., 1999; Malmierca et al., 2005; Cant and Benson, 2008; projections from the superior olivary complex: Fathke and Gabriele, 2009; Saldaña et al., 2009; projections from the nuclei of the lateral lemniscus: Gabriele et al., 2000; commissural projections: Malmierca et al., 2009; projections from the auditory cortex: Saldaña et al., 1996; Bajo and Moore, 2005), but there are no detailed published descriptions of the terminal distribution of the inputs from the LSO and MSO, two brainstem nuclei that extract binaural cues important for sound localization and other perceptual processes. In this paper, terminal fields formed in the gerbil IC by projections from the LSO and MSO are described and related to patterns of intrinsic organization. The results are consistent with the conclusion that the gerbil IC is organized according to the common plan proposed by Loftus et al. (2008). The extent to which the gerbil IC *appears* different from that of the cat or rat may be explained by a differential representation of specific frequency ranges in each species.

MATERIALS AND METHODS

ANIMALS AND TRACER INJECTIONS

Animals

This paper contains a description of the axonal termination patterns in the inferior colliculi of seven cases taken from a large collection with tracer injections in either the IC itself or in nuclei of the SOC. In all cases, female gerbils (*Meriones unguiculatus)* were obtained from Charles River Laboratories at approximately 8 weeks of age. They were housed in the Duke University Medical Center animal facilities until use. All procedures using these animals were approved by the Duke University Institutional Animal Care and Use Committee and were in accordance with NIH guidelines. The animals were deeply anesthetized for all surgical procedures and for the terminal perfusion.

Tracer injections in the IC or SOC and histological procedures

Three cases chosen from those described by Cant and Benson (2006) are used here to describe the intrinsic organization of the gerbil IC. The procedures for the surgery, injections, perfusions, and post-perfusion histological procedures were reported in detail in that paper. Very briefly, for the injections, gerbils were anesthetized with Nembutal (i.p., 50–70 mg/kg). A small hole was made in the skull and 10% biotinylated dextran amine (BDA) in 0.9% saline was injected iontophoretically through a glass pipette inserted into the IC. After survival periods of 5–11 days, the animals were given an overdose of Nembutal. When respiration ceased, they were perfused through the heart with a 4% paraformaldehyde fixative. Sections through the brain were cut at 40 μm and processed in 2 alternating series. One set of every other section was processed for visualization of BDA, and the second set was processed for cytochrome oxidase (CO) histochemistry. The procedures for injection of BDA into either the LSO or MSO in another four cases were exactly the same except for the location of the injection sites.

ACQUISITION AND MANIPULATION OF IMAGES

Digital photography

Digital images of all BDA- and CO-reacted sections were collected with a Zeiss Axiocam HRc camera attached to a Zeiss Axioscope 2 and controlled by Zeiss Axiovision software. The BDA sections were magnified through a 10× Plan-Apochromat objective, passed through a camera adapter with a magnification factor of 0.63×, and photographed at a resolution setting of 2600 × 2060 pixels (high resolution). The CO sections were magnified through either a 2.5× Plan-Neofluar or a 5× Plan-Apochromat objective, passed through the same adapter, and photographed at a resolution setting of 1300 × 1030 pixels (low resolution). All subsequent processing of these images was done in Photoshop CS4 running on Apple Macintosh computers.

Procedures for relating the sections from the experimental brains to a standard atlas

In a previous report (Cant and Benson, 2005), we described an atlas of the gerbil IC in which we established a coordinate system relating sections in the horizontal, transverse, and sagittal planes, referred to here as "the atlas." In the present study, the atlas coordinates were transferred to the experimental cases through a series of systematic steps. First, images of the sections reacted for CO histochemistry were paired with sections from comparable levels of the atlas and were oriented and resized to give the best possible fit. The IC is a surface structure, and distortions of its superficial conformation often occur during histological procedures. Internal structural relationships appear to be much less affected by distortion. Therefore, landmarks such as differences in levels of CO activity within the IC, the border formed by the fibers of the commissure of the IC, the obvious boundary of the periaqueductal gray layer, the orientation of the midline, and the caudal boundaries of layers of the superior colliculus carried more weight in the matching process than did the exact contour of the surface. The procedure was constrained in two ways: (1) The spacing of sections was maintained in the experimental series. That is, once level H120 (for example) was established, levels H40 and H200 had to be represented by the CO sections immediately ventral and dorsal to it, respectively. (2) Once the best percent change in size was established for a given case, all sections had to be resized by the same amount, and resizing was always uniform. Through this procedure, the atlas coordinates for the appropriate plane were transferred to each CO-reacted section.

In a second series of steps, each experimental BDA-reacted section was re-sized and oriented to match its adjacent CO-reacted section (by convention, for a horizontal series, the CO section ventral to it and for a transverse series, the CO section rostral to it). Again, resizing was uniform, and the same percent change was used for every section in a given case. After the CO and BDA sections were matched, the coordinate grid of the atlas could be superimposed onto the BDA sections. (A brief summary of the procedure is illustrated in Cant and Benson, 2008). The final step was to group the BDA-reacted sections into a stack in which they were automatically lined up based on the atlas coordinates that had been applied to each one. These image stacks were used for the procedures described below.

Reconstructions from the horizontal to the transverse plane based on "Photoshop drawings"

Six of the seven cases described here were cut in the horizontal plane, which is a relatively unfamiliar plane for most readers. Both to make the results easier to visualize in three dimensions and also to facilitate comparisons across cases, the horizontally sectioned colliculi were reconstructed into the more commonly portrayed transverse plane. Although the reconstructions could be accomplished using the original digital images, the results are easier to compare and represent on the printed page if the original images are converted to black and white. Photoshop offers a way to do this that results in an image that superficially resembles a drawing made at the microscope but that is fast enough to make it practical to "draw" all of the sections through each IC. To make the drawings, the original color digital images were converted to grayscale and the stamp filter (under the sketch filter menu) was applied to each image. (Smoothness was always set to 1, but the light/dark balance was adjusted from case to case depending on the exposure and background staining in that case.) The stamp filter finds edges in the image and strokes them (O'Quinn, 2001),

producing a black and white image that, especially at low magnification, looks similar to a drawing made by hand. (Note that this procedure works well only on very high resolution images; this is the reason that the digital images of the BDA sections were made at a resolution higher than that needed for routine visualization.) To complete the drawing, the surface contour of each section was traced by hand (i.e., by mouse) and applied to the filtered image. The images obtained in this way will be referred to as "Photoshop drawings."

To make the reconstructions from the horizontal plane to the transverse plane, a "slice" 80 μm thick (one interval on the atlas grid) was selected at a given transverse level on each horizontal image in the image stack. The set of slices was copied to a file containing the chosen transverse atlas section, and each slice was positioned at the appropriate horizontal level. This procedure was repeated for each transverse level in the atlas (see Results). (Although not illustrated here, sections cut in the transverse plane could be reconstructed into the horizontal plane using the same procedure.) Because all of the cases are referenced to the same atlas coordinates, comparisons among cases are facilitated.

RESULTS

NOTE ON NOMENCLATURE

In order to avoid excessive and potentially confusing use of terminology based on relative position (i.e., lateral, rostral, etc.), I have employed nomenclature used in descriptions of the IC of other species but not applied previously to the gerbil. First, I will refer to a portion of the dorsolateral and rostral central nucleus as the *pars lateralis*. This designation is adopted from the classic description of the cat IC (Morest and Oliver, 1984; Oliver and Morest, 1984). (This region probably also corresponds to the part of the rat IC referred to as the "lemniscal zone" by Faye-Lund and Osen, 1985). Second, nomenclature introduced for the rat and guinea pig (e.g., Saldaña and Merchán, 1992, 2005; Malmierca et al., 1995) will be employed to refer to the axonal plexuses labeled when BDA is injected into the IC itself.

PATTERNS FORMED BY COMMISSURAL CONNECTIONS IN THE GERBIL IC

To provide a context for the description of the results of tracer injections in the SOC, the labeling patterns seen after tracer injections in the IC itself are presented for three cases (**Figures 1**–**4**). As in the rat (Saldaña and Merchán, 1992, 2005) and guinea pig (Malmierca et al., 1995), injection of an anterograde tracer into one IC gives rise to a characteristic pattern of labeling that reveals the topographic organization on both sides of the auditory midbrain.

Case 460 (Figures 1A–E, 2)

The center of the BDA injection site in this case (**Figure 1C**) was judged to be located in the "middle frequency" portion of the IC on the basis of the location of the labeled cells in the contralateral cochlear nucleus (Cant and Benson, 2006). In both inferior colliculi, labeled axon terminals are densely concentrated in two plexuses as described in other species. In the contralateral IC (where the pattern is not partially obscured by the injection site itself), the external (or lateral) plexus (**Figures 1B,C**, green arrows), lies just beneath the lateral surface and part of the caudal surface. The main (or medial) plexus (**Figures 1A–C**, red arrows) is most dense rostrally but extends caudally, where it appears to meet the caudal extension of the lateral plexus (**Figures 1B,C**, thin black arrows). The sparsely labeled rostrolateral area that lies between the two plexuses in this case is the pars lateralis of the central nucleus (**Figures 1A–C**, blue arrows). Where visible, the same pattern is evident on the ipsilateral side, with an external plexus (**Figures 1A–C**, open green arrows) and a main plexus (**Figures 1A,B**, open red arrows). As on the contralateral side, the ipsilateral pars lateralis (**Figures 1B,C**, open blue arrows) is relatively sparsely labeled even though it is quite close to the center of the injection site.

Reconstructions of the IC of case 460 into the transverse plane (**Figure 2**) make it easier to appreciate that the pattern in the gerbil is similar to that in other rodents. At middle levels through the IC, the main plexus (e.g., **Figures 2C–E**, red arrows) lies at an angle of approximately 45 degrees (with respect to the horizontal) in a location compatible with a presumed frequency representation in the middle range; rostrally, the main plexus assumes a more vertical orientation (**Figures 2F,G**, red arrows). The external plexus (**Figures 2C–G**, green arrows) lies lateral and caudal to the central nucleus of the IC and follows the curve of its external surface. In sections from about 25 to 50% of the caudal-to-rostral extent of the IC, a connection between the main and external plexuses is evident ventrally (**Figures 2C–E**, black arrows), but in more rostral sections (**Figures 2F,G**), the plexuses do not appear connected. In the most caudal sections, the two plexuses also appear connected (**Figures 1A–B**), but, in these sections, it is difficult to distinguish the rostral plexus from the caudal extension of the lateral plexus in the transverse plane. The dorsolateral and rostral part of the IC lying between the two main plexuses is relatively unlabeled in this case (**Figures 2D–G**, blue asterisks); it is this part of the IC that is referred to here as the pars lateralis.

Case 462 (Figures 1F–J, 3)

The injection site in this case was located at approximately the same dorsal-to-ventral and rostral-to-caudal level as that in 460 but was situated slightly more laterally (compare **Figure 1H** to **Figure 1C**). Based on the distribution of labeled cells in the cochlear nucleus, the injection site was judged to be centered in the low frequency representation of the IC (Cant and Benson, 2006).

In the contralateral IC, the external plexus (**Figures 1F–H**, green arrows) and main plexus (**Figures 1G,H**, red arrows) are both shifted in position compared to those in case 460 (dorsally and dorsolaterally, respectively). An apparent connection between the two plexuses (**Figures 1G,H**, thin black arrows) is shifted laterally and rostrally and lies in the pars lateralis of the central nucleus (**Figure 1H**, blue arrow). The pattern on the ipsilateral side is hidden by the injection site except in the most dorsal and ventral sections, where it can be seen that the pars lateralis is filled with labeled axons and terminals (**Figures 1F,I**, open blue arrows).

In the reconstruction of case 462 (**Figure 3**), the external (**Figures 3D–F**, green arrows) and main (**Figures 3D–G**, red

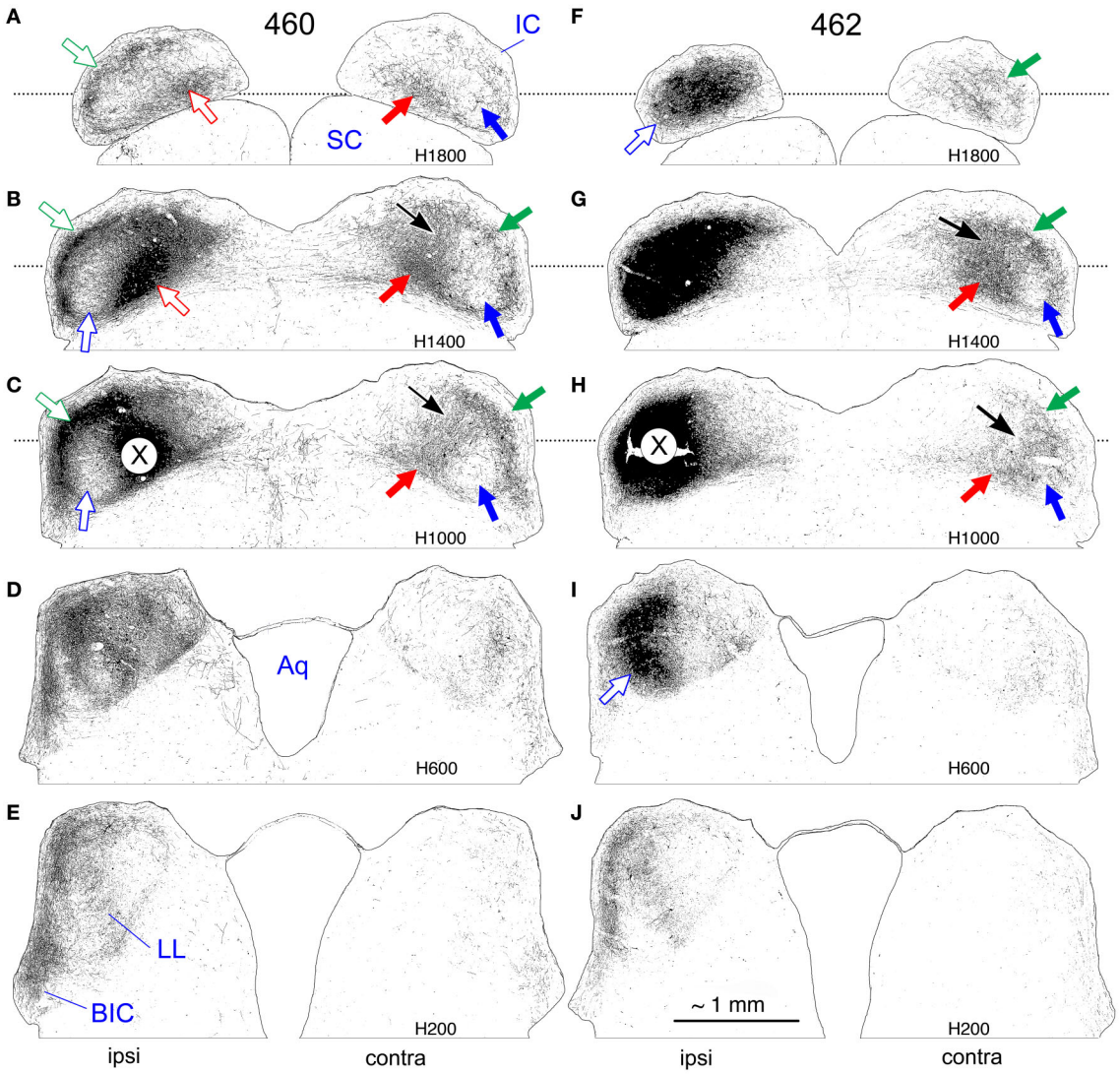

FIGURE 1 | Photoshop drawings of five evenly-spaced horizontal sections from cases 460 (A–E) and 462 (F–J). The more dorsal sections are located at the top **(A,F)** and the more ventral sections are located at the bottom **(E,J)**. The caudal aspect of the IC is oriented toward the top. The corresponding atlas levels (H1800-H200) are indicated on each section. The dotted lines behind the top three rows indicate the approximate location of transverse level 960 (T960) of the IC atlas. The approximate locations of the injection sites in each case are indicated by the large X **(C,H)** on the right IC (located more precisely in Cant and Benson, 2006). Abbreviations: Aq, cerebral aqueduct; BIC, brachium of the inferior colliculus; contra, contralateral; IC, inferior colliculus; ipsi, ipsilateral; LL, lateral lemniscus; SC, superior colliculus. Arrows are referenced in the text. Scale bar (panel **J**) indicates approximately 1 mm and applies to all panels.

arrows) plexuses on the contralateral side appear less obviously separate compared to case 460 (**Figure 2**); they are located more dorsally and are closer together. A connection between them lies in the pars lateralis (**Figures 3C–F**, black arrows), and, as for case 460, two distinct plexuses are difficult to distinguish in more caudal sections. Rostrally, the main plexus, while oriented vertically, does not extend quite so far ventrally as in case 460 (compare **Figure 3G** to **Figure 2G**).

Case 430 (Figure 4)

The center of the injection site in this case was located on a medial-to-lateral and a dorsal-to-ventral line with that of case 462 (**Figure 1H**) but was located rostral to it (illustrated in Cant and Benson, 2006). Based on the location of labeled cells in the cochlear nucleus (as well as in the MSO and LSO), the injection was centered in the part of the IC that represents the lowest frequencies processed in the gerbil IC. In contrast to the pattern in cases 460 and 462, two laminar plexuses are not clearly distinguishable in the contralateral IC. Rather, throughout most of the IC, an elongated plexus occupies pars lateralis, extending along part of its dorsal to ventral extent (**Figures 4C–H**, dark blue arrows). At rostral levels, the plexus reaches almost to the ventral boundary of the central nucleus (**Figures 4G,H**, dark blue arrows). Although a distinct lateral plexus cannot be identified at

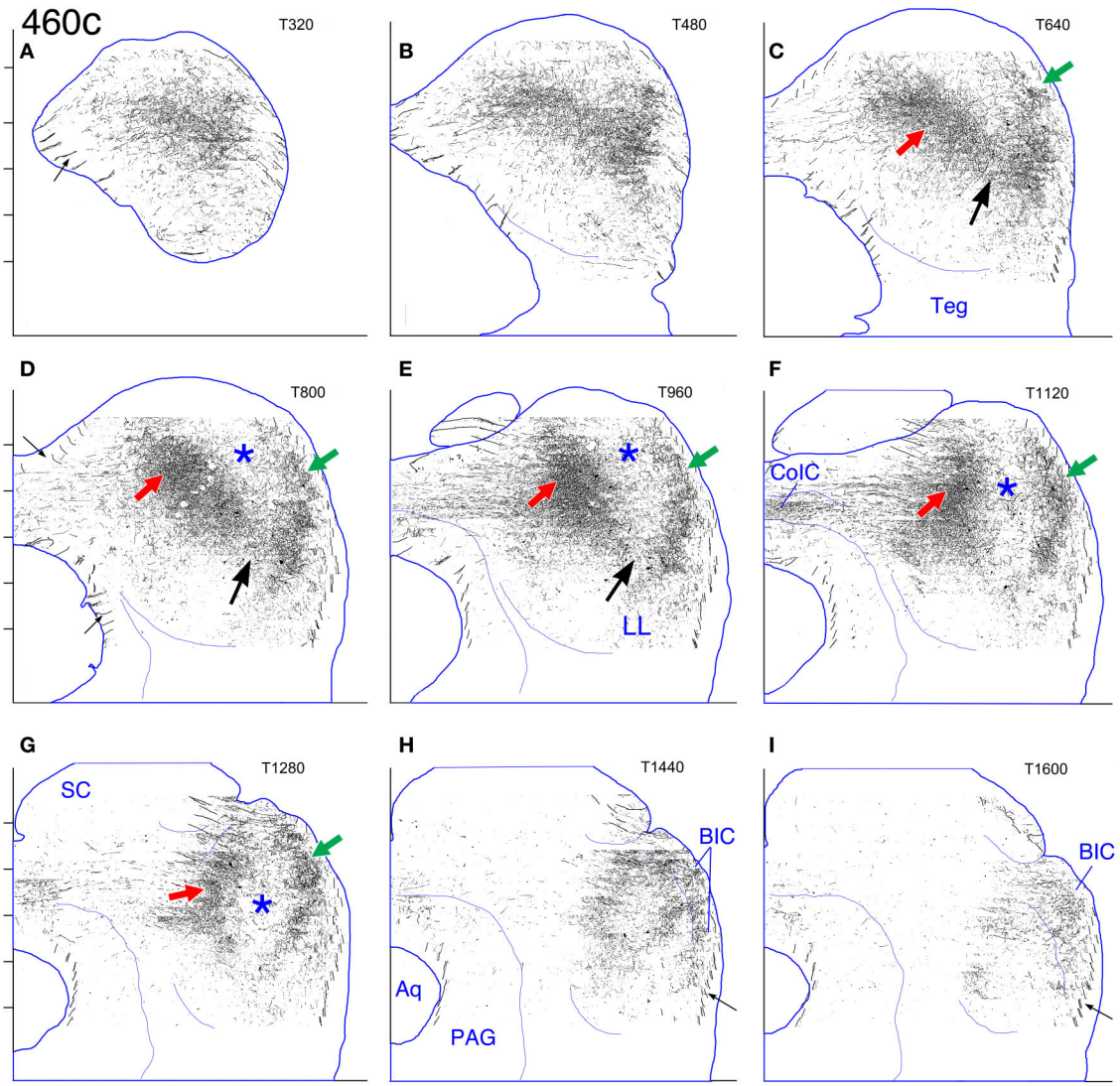

FIGURE 2 | Case 460c. (A–I) Reconstruction of the contralateral (left) IC after a BDA injection in the right IC. In this and also in **Figures 3**, **6**, and **9–14**, nine evenly-spaced reconstructions of the IC are located on the corresponding atlas sections from caudal (panel **A**) to rostral (panel **I**). The dorsal direction is toward the top of each panel; the lateral direction is to the right; the midline is indicated by the line at the left of each panel. The transverse levels (T320, T480, etc.) indicated in the upper right of each panel refer to the atlas (see text). The outline of the *atlas section* at each level is drawn in blue. The short horizontal marks to the left of the ordinate for panels **(A,D,** and **G)** are 400 μm apart and indicate the levels of the horizontal sections shown in **Figure 1** (i.e., from dorsal to ventral, H1800 to H200). For reasons of clarity, given the low magnification of the figures, all filled pixels *outside* the blue outlines were erased. (A little information in the reconstructions is lost because of this procedure since the contour lines [e.g., **(A,D,I)**, small arrows] for some of the stacked layers lie outside the blue outlines.) Regardless of whether the reconstructed IC was from the left or right side of the brain, all cases were plotted on atlas sections representing the right IC. (For those cases in which the left IC is reconstructed, as in this figure, the images were reflected about the midline.) Abbreviations: Aq, cerebral aqueduct; BIC, brachium of the inferior colliculus; CoIC, commissure of the inferior colliculus; PAG, periaqueductal gray matter; SC, superior colliculus; Teg, subcollicular tegmentum. Large arrows and asterisks are referenced in the text.

any level, a main plexus appears in the rostral IC (**Figures 4F,G**, red arrows), occupying a location comparable to that occupied by the main plexus in case 462 (compare **Figure 4F** to **Figure 3F**, red arrows). The density of terminal labeling within the plexus of labeled axons in pars lateralis is not uniform. Particularly obvious is a dense accumulation of terminals at some levels that appears to almost bisect the elongated axonal plexus (**Figures 4D,E,G**, light blue arrows).

PROJECTIONS INTO THE IC FROM THE LATERAL AND MEDIAL SUPERIOR OLIVARY NUCLEI

One case with a BDA injection in the MSO and three cases with injections in the LSO are presented in **Figures 5–14**. Two of the LSO injections were located in the lateral limb. (Both are included here in order to emphasize the consistency of the results.) The third LSO injection was centered in the middle of the nucleus. These four cases illustrate the pattern of olivary

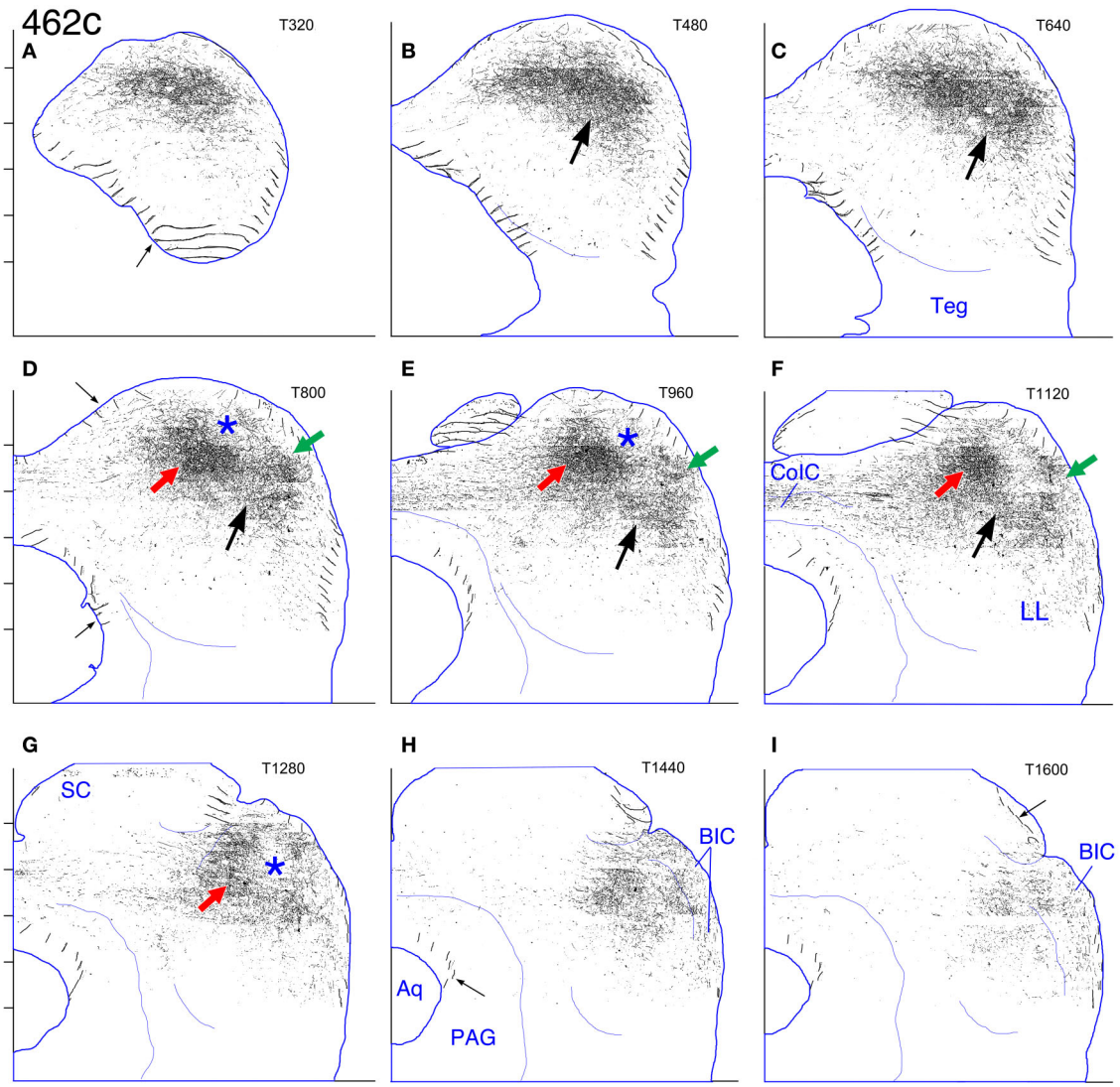

FIGURE 3 | Case 462c. (A–I) Reconstruction of the contralateral (left) IC after BDA injection in the right IC. Details as for **Figure 2**.

projections from the dorsal MSO and the lateral and middle parts of both the ipsilateral and contralateral LSO (i.e., the parts of these olivary nuclei that represent low and, to some extent, middle frequencies).

Case 644 (Figures 5, 6, 7A,B)

In the horizontal plane, the injection site in this case (**Figure 5K**) appears quite small, although it appeared to be elongated in the dorsal to ventral dimension (along the track of the injection pipette, not shown) and was visible in approximately the dorsal 50% of the MSO. Retrogradely labeled cells in the cochlear nucleus were confined to the most rostral part of the anteroventral cochlear nucleus (i.e., the spherical cell area) on both sides and were most numerous ventrally, although labeled cells were present in approximately the lower ¾ of the dorsal-to-ventral extent of the nucleus. In horizontal sections through the dorsal half of the ipsilateral IC, a labeled plexus of axons is located in pars lateralis of the central nucleus (**Figures 5A,B,F,H**, blue arrows). (A *very* few axon terminals were labeled in comparable sections through the contralateral IC in this case. Their position mirrored that of the most rostrally located axons on the ipsilateral side.) In the most dorsal sections through the ipsilateral IC, the plexus of labeled terminals extends caudomedially in an elongated strip (**Figure 5A**, blue arrow). In transverse reconstructions (**Figure 6**), the plexus of labeled axons and terminals has the appearance of an elongated column (**Figures 6B–H**, bounded dorsally and ventrally by dark blue arrows) that extends from a dorsal position caudally (**Figure 6B**) to a relatively ventral position rostrally (**Figure 6H**). Comparison of the appearance of the plexus in horizontal and transverse sections suggests the shape of a long, bent cylinder stretching from the rostroventral boundary of the IC to its dorsocaudal pole.

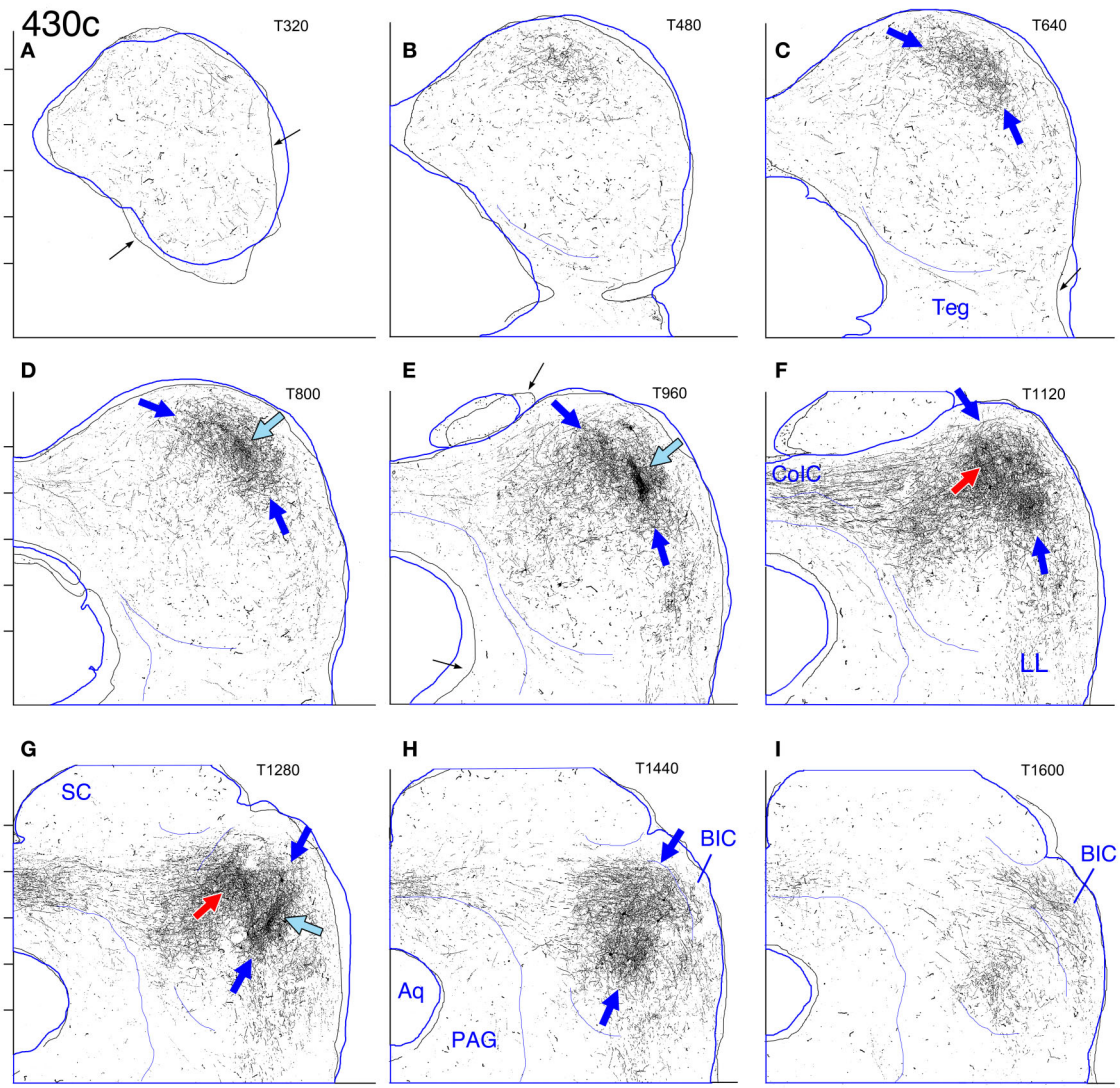

FIGURE 4 | Case 430c. (A–I) Photoshop drawings of transverse sections through the contralateral (left) IC after a BDA injection in the right IC. Nine evenly-spaced sections were matched to transverse atlas sections. As in the other figures, the outlines of the atlas sections are shown in blue; the outlines of the sections from case 430 are indicated by the black outlines (e.g., small black arrows on panels **A,C,** and **E**). Other details as for **Figure 2**.

The plexus of labeled axons appears patchy, containing areas with relatively dense accumulations of terminals (**Figure 6E**, light blue arrow; **Figures 7A,B**, black arrows) as well as areas of relatively sparse terminal labeling (**Figures 5B,E**, black arrows; **Figure 7A**, open arrow). At some transverse levels, a thin "line" of densely clustered terminals appears to run through the center of the plexus (e.g, **Figure 6E**, light blue arrow).

Cases 618 and 652 (Figures 7C–F, 8A–F, and K–M, 9–12)

These two cases are considered together because the location of the injection sites and the patterns of labeling are very similar. In case 618, the injection site was mostly confined to the lateral limb of the LSO (**Figure 8L**). Ventrally, however, the injection extended slightly into the rostral part of the lateral nucleus of the trapezoid body (LNTB) and the trapezoid body fibers that run around and through it. Retrogradely labeled cells in the ipsilateral medial nucleus of the trapezoid body (MNTB) were lined up on the lateral boundary along its entire caudal-to-rostral extent (e.g., **Figure 8L**). In the cochlear nuclei, labeled cells were concentrated in the spherical bushy cell area on both sides and were especially numerous rostrolaterally and ventrally. In addition, on the ipsilateral side only, scattered multipolar cells were distributed throughout the ventral cochlear nucleus. A very few small cells were labeled in the ipsilateral dorsal cochlear nucleus. The injection site in case 652 (**Figure 8M**) was located in almost exactly the same part of the LSO as that in case 618, but did not appear to extend into the LNTB. The locations of labeled cells in the ipsilateral MNTB (e.g., **Figure 8M**) and in the ipsilateral

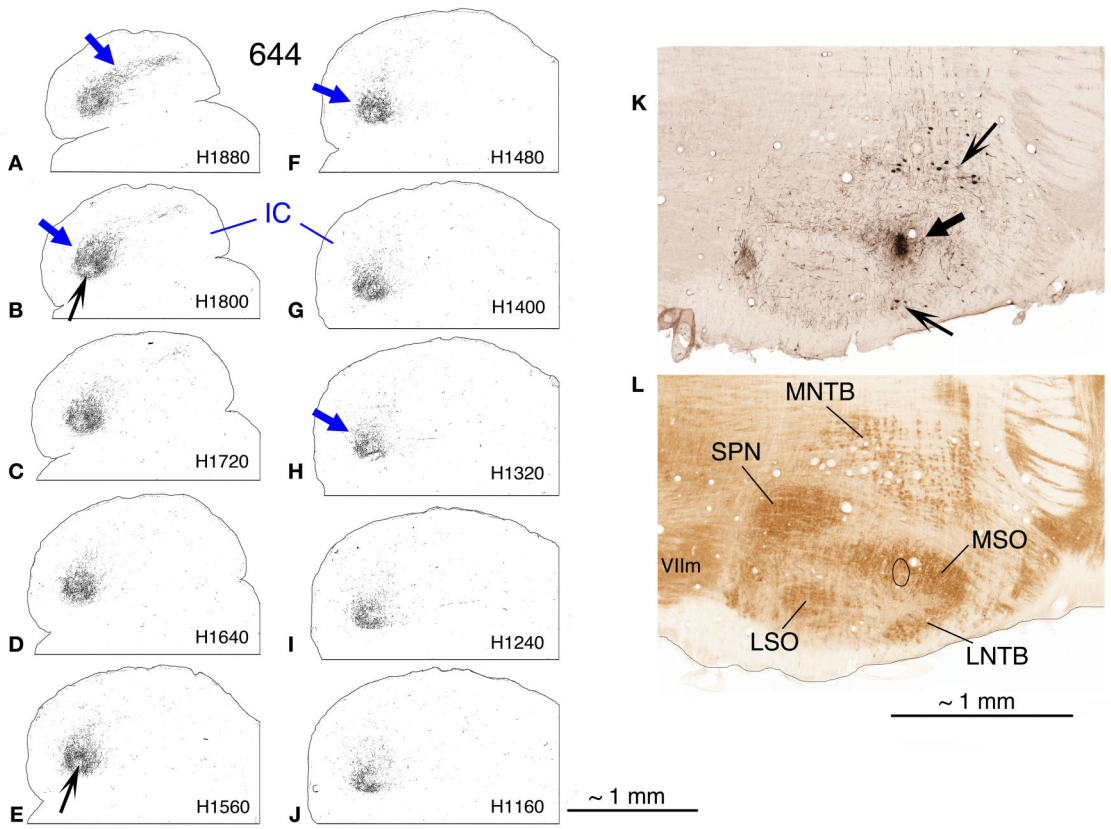

FIGURE 5 | Case 644, BDA injection in right MSO. (A–J) Photoshop drawings of evenly-spaced horizontal sections through the top half of the right (ipsilateral) IC. The most dorsal section is illustrated in panel **(A)**; the most ventral, in panel **(J)**. The caudal aspect of the IC is oriented toward the top of each section; the lateral direction is toward the left, and the midline is at the right. Corresponding atlas levels are indicated on each section **(K,L)**. Horizontal sections through the right superior olivary complex. A BDA-reacted section through the MSO is shown in panel **(K)**. The large arrow indicates the injection site; the smaller arrows indicate labeled cells in the MNTB (upper arrow) and LNTB (lower arrow). The ventrally adjacent CO-reacted section is shown in panel **(L)**. Abbreviations: LNTB, lateral nucleus of the trapezoid body; LSO, lateral superior olivary nucleus; MNTB, medial nucleus of the trapezoid body; MSO, medial superior olivary nucleus; SPN, superior paraolivary nucleus; VIIm, motor nucleus of the seventh nerve. Scale bar next to panel **(J)** applies to panels **(A–J)**; scale bar in panel **(L)** applies to panels **(K)** and **(L)**.

and contralateral ventral cochlear nuclei followed the same pattern as in case 618, although the number of labeled cells was greater. One potential complication in case 652 (and in case 631, presented below) is that the injection pipette passed through the IC itself on the way to the LSO. Its track can be seen as a small spot of decreased cytochrome oxdase activity on sections through the IC (cf. Cant and Benson, 2006). No anterograde labeling of either cells or axons appeared to be associated with this track.

The terminal plexus in the *contralateral* IC in both cases (618: **Figures 8A–C** and **9**; 652: **Figures 8D–F** and **11**) occupies pars lateralis of the central nucleus. The location of the plexus is similar to that seen after the MSO injection (case 644, **Figures 5A–J**, **6**) except that the dorsal-to-ventral position of the plexus in case 618 appears to be shifted slightly ventrally relative to that in case 644, and that in 652 appears to be shifted slightly ventrally relative to that in 618. In the most dorsal sections, the labeled plexus extends across the width of the IC (**Figures 8A,D**, blue arrows). The labeled plexus in the *ipsilateral* IC in these cases (618: **Figures 8A–C** and **10**; 652: **Figures 8D–F** and **12**) is in a location similar to that on the contralateral side but is less extensive, being almost absent at caudal levels (compare **Figures 9A–C** to **Figures 10A–C** and **Figures 11A–C** to **Figures 12A–C**).

On both the ipsilateral and contralateral sides, the appearance of the terminal plexus is patchy. Small areas containing dense tangles of axon terminals (e.g., **Figures 7C,D,F**, black arrows; **Figures 9E,G**; **10F**; **11D,G**; **12F**, light blue arrows) are interspersed among areas of relatively sparser terminations (e.g., **Figures 7C,E**, open arrows). At some levels an ipsilateral dense patch appears to occupy a position comparable to the location of a relatively empty space on the contralateral side (e.g., **Figure 7C** compared to **Figure 7D** and **Figure 7E** compared to **Figure 7F**; similar comparisons can be made of **Figures 8B** and **8E**, thin black arrows).

On the contralateral side in case 652 (and to a lesser extent on the ipsilateral side) there is sparse but definite terminal labeling in the ventral (i.e., high frequency) part of the IC (**Figures 11**, **12**). Caudally, the ventral axons appear to form interrupted stacks

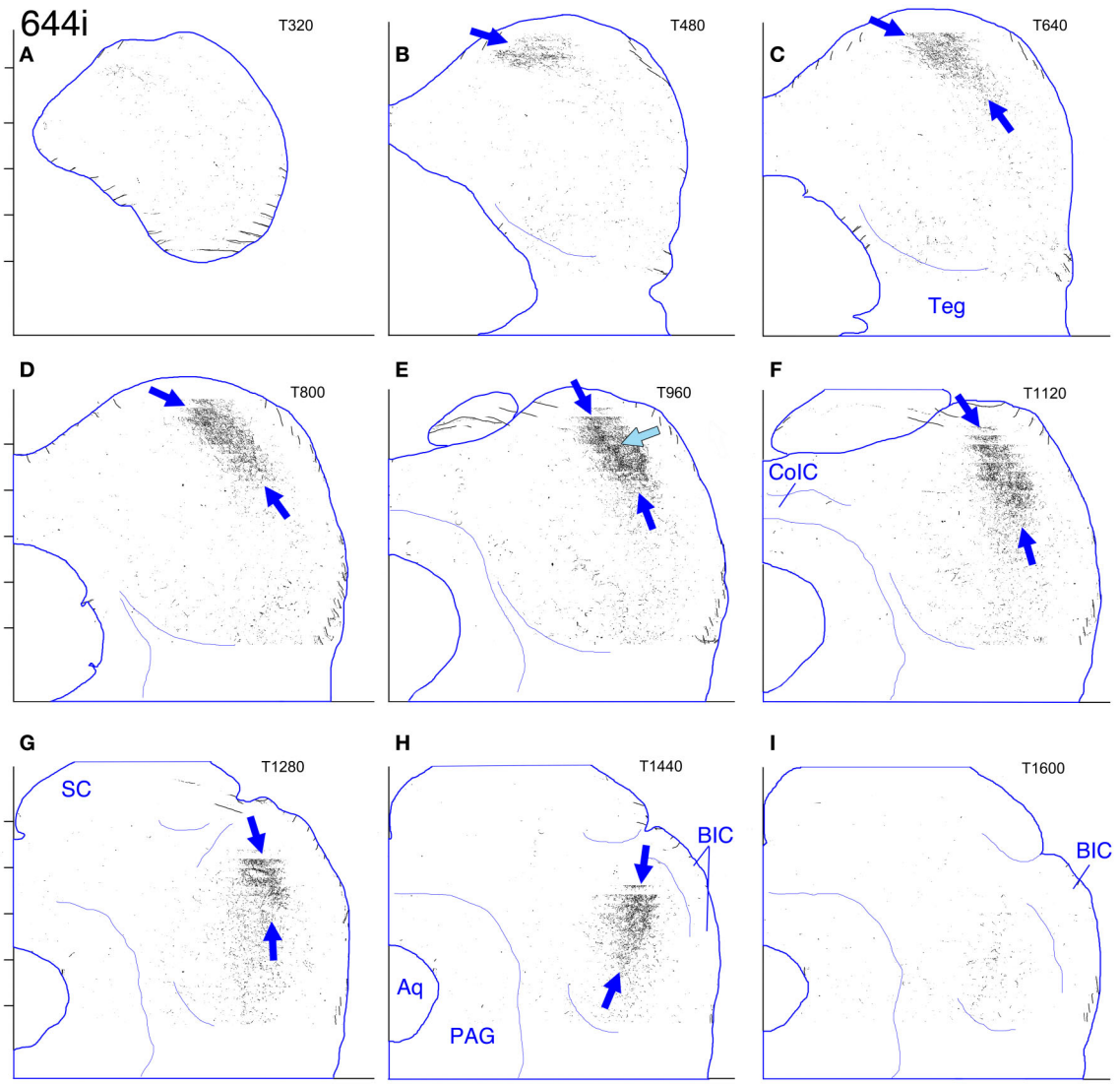

FIGURE 6 | Case 644i. (A–I) Reconstruction of the ipsilateral (right) IC after a BDA injection in the dorsal half of the right MSO. In this and also in **Figures 9–12**, the main plexus of labeled axon terminals is indicated by the blue arrows positioned at its dorsal and ventral extremes. Details as for **Figure 2**.

(**Figures 11C** and **12C**, thin magenta arrows), reminiscent of the banding of LSO axons described by others (see "Discussion"). Banding of inputs is less obvious in the more densely labeled dorsolateral terminal field, although there is sometimes a hint of it (e.g., **Figure 7D**, thin arrows; **Figure 8E**, ipsi, thin blue arrows). In case 618, which otherwise exhibits almost the same labeling pattern as that in case 652, axons in the ventral IC are not labeled (with the exception of one tiny tuft on the ipsilateral side at atlas level T640, **Figure 10C**, magenta arrow).

Case 631 (Figures 8G–J,N, 13, 14)

The apparent injection site in this case (**Figure 8N**) was considerably smaller than those in cases 618 and 652. (It was more comparable in size to that in case 644). It appeared to be mostly confined to the middle of the LSO. In the transverse plane, the LSO in the gerbil has the shape of a baby duck; the injection site was located approximately at the duck's neck. According to maps of the adult gerbil LSO constructed by Sanes et al. (1989), the frequency representation in this part of the IC would be around 3–6 kHz. Ventrally, the injection site appeared to encroach slightly on the lateral part of the LSO. As noted above, the pipette in this case passed through the IC on its way to the LSO, but no labeled axons or terminals were visible around the location of the track. Retrogradely labeled cells in the MNTB (e.g., **Figure 8N**) stretched along its caudal-to-rostral (and dorsal-to-ventral) extent and the sheet of cells was centered at about 30–35% of its lateral-to-medial extent. As with cases 618 and 652, labeled cells were plentiful in the spherical bushy cell area in the anteroventral cochlear nucleus on both sides but were shifted dorsomedially with respect to those cases. In addition, scattered cells (most likely, multipolar cells) were located throughout the ipsilateral ventral cochlear nucleus.

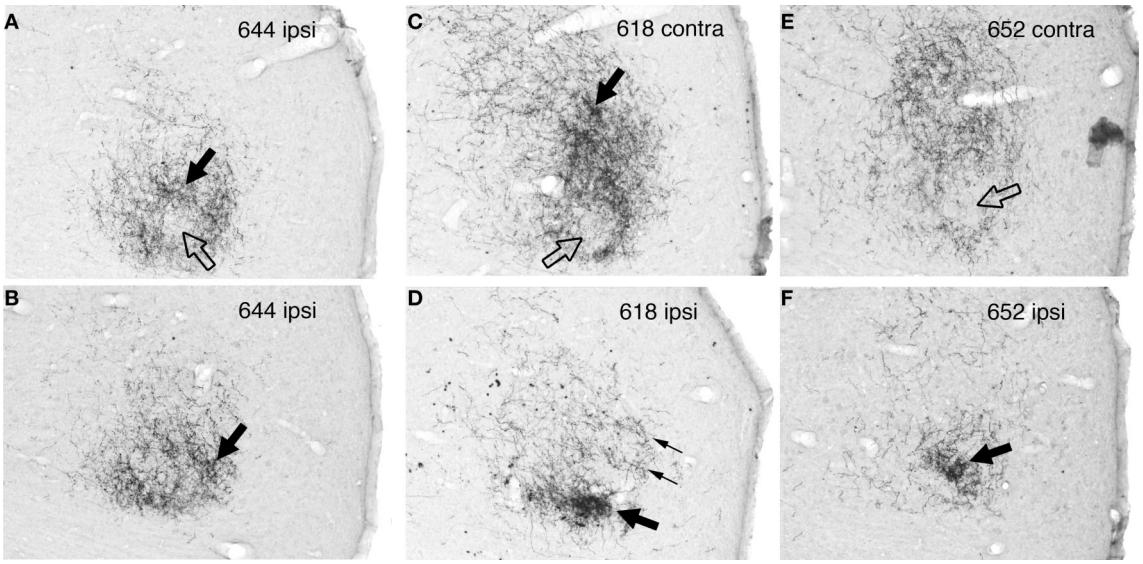

FIGURE 7 | Digital photographs of the rostrolateral IC in BDA-reacted sections from case 644 (MSO injection) and cases 618 and 652 (LSO injections). (A) Case 644, ipsilateral IC at level H1720 (also illustrated in **Figure 5M**). **(B)** Case 644, ipsilateral IC at level H1400 (also illustrated in **Figure 5Q**). **(C)** Case 618, contralateral IC at level H1400 (also illustrated in **Figure 8B**). **(D)** Case 618, ipsilateral IC at level H1400 (also illustrated in **Figure 8B**). **(E)** Case 652, contralateral IC at level H1240. **(F)** Case 652, ipsilateral IC at level H1240. On all panels, the filled black arrows indicate regions of relatively dense terminal labeling, and open arrows indicate areas of relatively sparse labeling. In panel **(D)**, thin arrows point to a hint of banding (also indicated on **Figure 8B**). In all cases, the lateral boundary of the IC is to the right and the rostral boundary is toward the bottom. (Images of the ipsilateral IC were reflected about the midline to facilitate comparisons.) The brightness and contrast of the images were manipulated using the levels function in Adobe Photoshop.

In the IC on both sides, a labeled terminal plexus lies in the ventral part of pars lateralis (**Figures 8I–J**, blue arrows; **Figures 13C–G**, black arrows; **Figures 14E,F**, black arrows) and also extends out into the territory of the main intrinsic plexus described above (**Figures 12E–G**, red arrows), where it forms a truncated layer with a ventrolateral to dorsomedial tilt. The axonal plexus in the ipsilateral IC is less widely distributed than that on the contralateral side, especially at caudal levels (compare **Figures 13B–D** [contralateral] to **Figures 14B–D** [ipsilateral]). The extension of the plexus outside pars lateralis also appears to be truncated compared to that on the contralateral side. For example, the same point with respect to the atlas coordinates is indicated by the red arrows in **Figures 13E,F** (contralateral side) and the open red arrows in **Figures 14E,F** (ipsilateral side). In general, the labeled plexus in case 631 appears to be less patchy than those in cases 644, 618, and 652.

On both the ipsilateral and contralateral sides in case 631, in addition to the heavily labeled plexus located in the middle of the IC, a less dense axonal plexus occupies the same position in the pars lateralis seen for the plexuses in cases 644, 618, and 652 (**Figure 8G**, thin blue arrow; **Figures 13E–F**, **14E–F**, blue arrows). The presence of this lightly labeled plexus is most likely accounted for by the fact that the injection site, although mainly located in the middle of the LSO, probably also encroached on the lateral LSO.

Comparisons among cases

Because all of the cases presented here were mapped onto a common set of coordinates, direct comparisons of labeling patterns can be made at different levels through the IC. As examples, a few of the possible comparisons at one transverse level are presented in **Figures 15A–C**. These particular comparisons were chosen to support the interpretation of the results developed in the Discussion; they are representative of the results generally. **Figure 15A** illustrates the region in which there was overlap of the terminal plexuses in cases 460 and 462 (injections in contralateral IC) at transverse level T960 (**Figures 2E** and **3E**, respectively). The black fill in this panel represents *only* those filled pixels which were common to both of the cases. The important point is that there is considerable overlap in the region of the main terminal plexus (red arrow) and in the region of the lateral terminal plexus (green arrow) but that very little overlap is evident between these two plexuses (that is, in the pars lateralis, blue arrows). Reference to **Figures 2D,E** and **3D,E** (black arrows) confirms that labeled axon terminals were located in pars lateralis in both of these cases at this level; however, those in case 462 were located more dorsally than those in case 460 with the result that there was very little overlap. In **Figure 15B**, the labeled terminal plexuses at level T960 from both sides in cases 618 and 652 (injections in lateral LSO) are superimposed. The shape and general location of the pixels from the four ICs combined (blue arrows) looks very similar to those in each individual IC (i.e., **Figures 9–12**, T960, blue arrows). **Figure 15C** illustrates the plexuses labeled in case 644 (MSO injection, blue pixels) and case 631 (middle LSO injection, red pixels). As for cases 618 and 652 (**Figure 15B**), the labeled axons in case 644 and most of those in case 631 lie in pars lateralis (blue arrows), but in case 631, a small extension into the central part of the central nucleus is also present (red arrow). An important

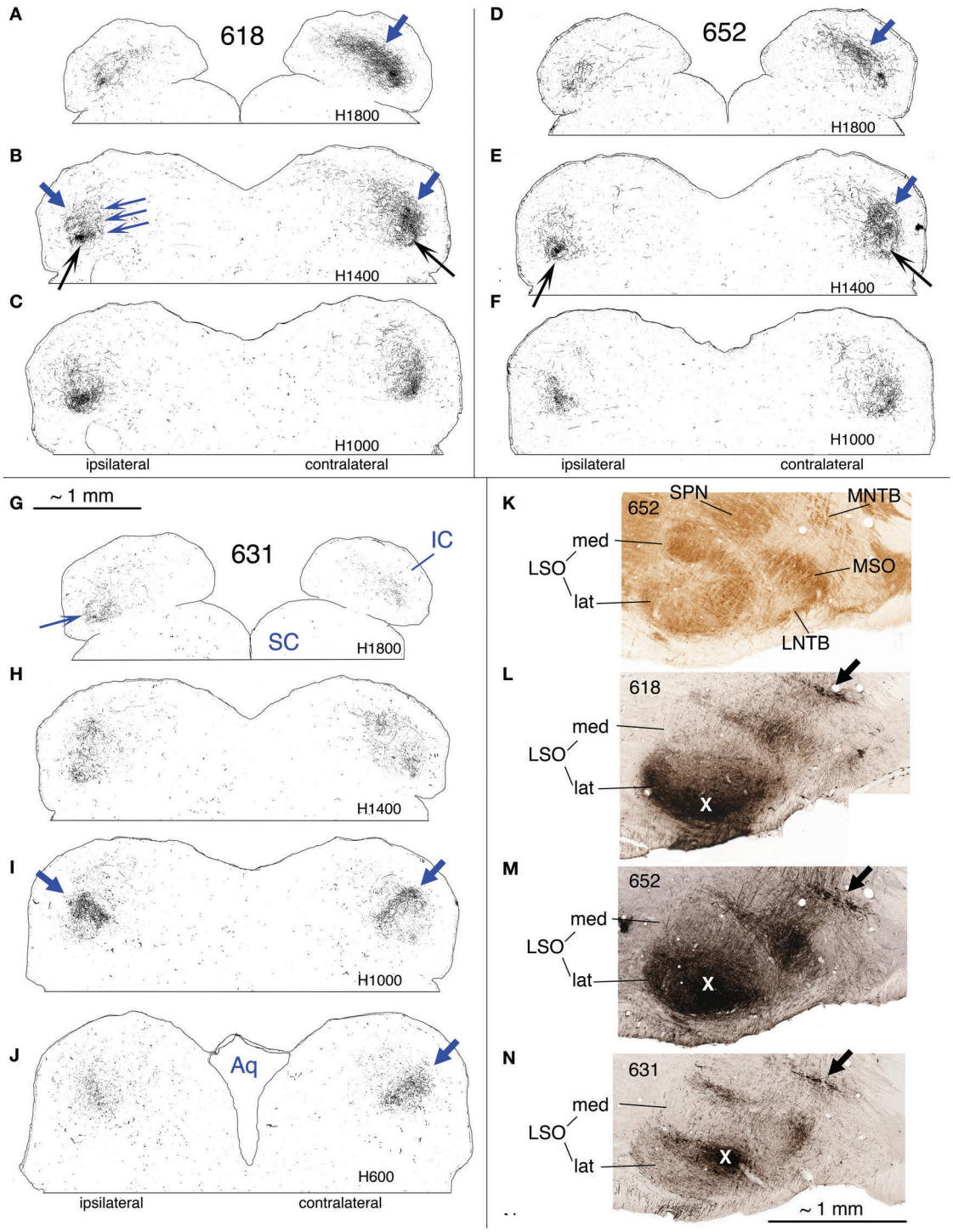

FIGURE 8 | (A–J) Photoshop drawings of evenly spaced sections through part of the IC in 3 cases with BDA injections in the right LSO. **(A–C)** Case 652. **(D–F)** Case 618. **(G–J)** Case 631. Scale bar above panel **(G)** applies to panels **(A–J)**. Other details as for **Figure 1**. **(K–N)** Digital images of horizontal sections through the right superior olivary complex that illustrate the locations of the injection sites in the three cases **(K)**. CO-reacted section from case 652. (The section is ventrally adjacent to that illustrated in panel **(M)**. The sections illustrated in panels **(L)** and **(N)** were located at an equivalent level.) Abbreviations: LNTB, lateral nucleus of the trapezoid body; LSO lat, lateral limb of the lateral superior olivary nucleus; LSO med, medial limb of the lateral superior olivary nucleus; MNTB, medial nucleus of the trapezoid body; MSO, medial superior olivary nucleus; SPN, superior paraolivary nucleus. **(L)** BDA-reacted section through the injection site in case 618. **(M)** BDA-reacted section through the injection site in case 652. **(N)** BDA-reacted section through the injection site in case 631. In panels **(L–N)**, the white "X" indicates the approximate location of the center of the injection site in the LSO. The black arrows indicate rows of labeled cell bodies in the MNTB. Scale bar in panel **(N)** applies to panels **(K–N)**.

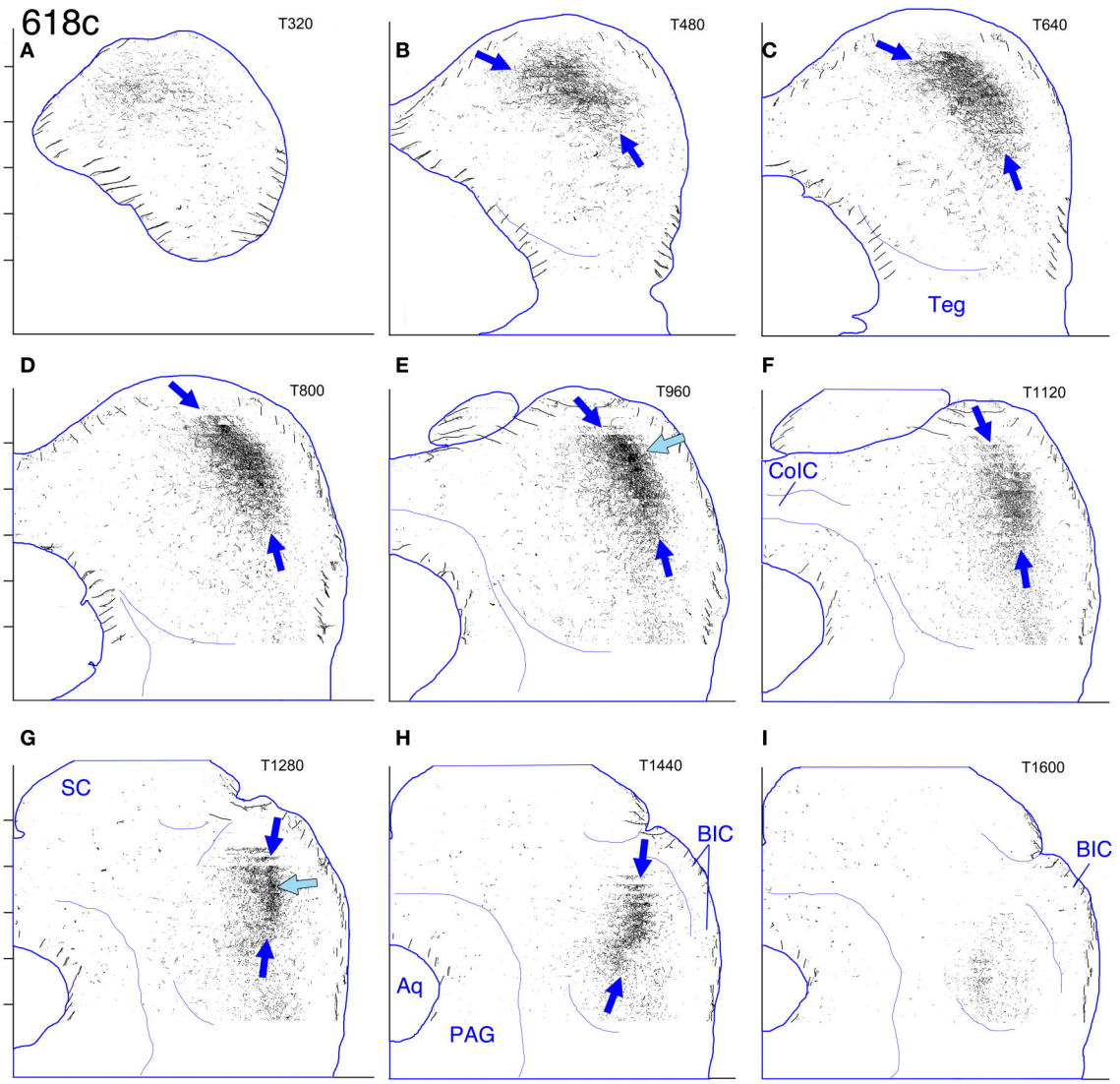

FIGURE 9 | Case 618c. (A–I) Reconstruction of the contralateral (left) IC after BDA injection into the right lateral LSO. The sections have been reflected about the midline.

point is that the plexus in case 631 lies *ventral* to that in case 644 (and also to those in cases 618 and 652, compare **Figure 15C** to **Figure 15B**). **Figure 15D** illustrates the cytochrome-oxidase stained atlas section at level T960. The part of the IC with the highest CO activity is highlighted in black. As described previously (Cant and Benson, 2005), this region of highest metabolic capacity forms a crescent-shaped swath through the IC at middle levels (as in this figure). The blue arrows indicate the dorsal and ventral extent of the part of this crescent that I have referred to as pars lateralis of the central nucleus.

DISCUSSION

The results provide new information about the organization of the part of the IC that receives inputs from the LSO and MSO in the gerbil. The discussion of the results is divided into three parts. First, interpretation of the injection sites is examined. Second, a working model of the basic organization of the gerbil IC is presented and compared to the more well-established models for the rat and cat. Finally, I discuss the organization of one subdivision of the central nucleus of the IC—the pars lateralis—in these three species.

INTERPRETATION OF THE INJECTION SITES

BDA is an excellent anterograde tracer, but interpretation of results is complicated by the fact that it can be transported to terminal fields arising from axonal branches of neurons located outside the injection site that send a separate branch into the site (so-called "false anterograde" or "collateral" label; Chen and Aston-Jones, 1998; see Discussion in Saldaña et al., 2009). Because of this, the more that is known about the branching and

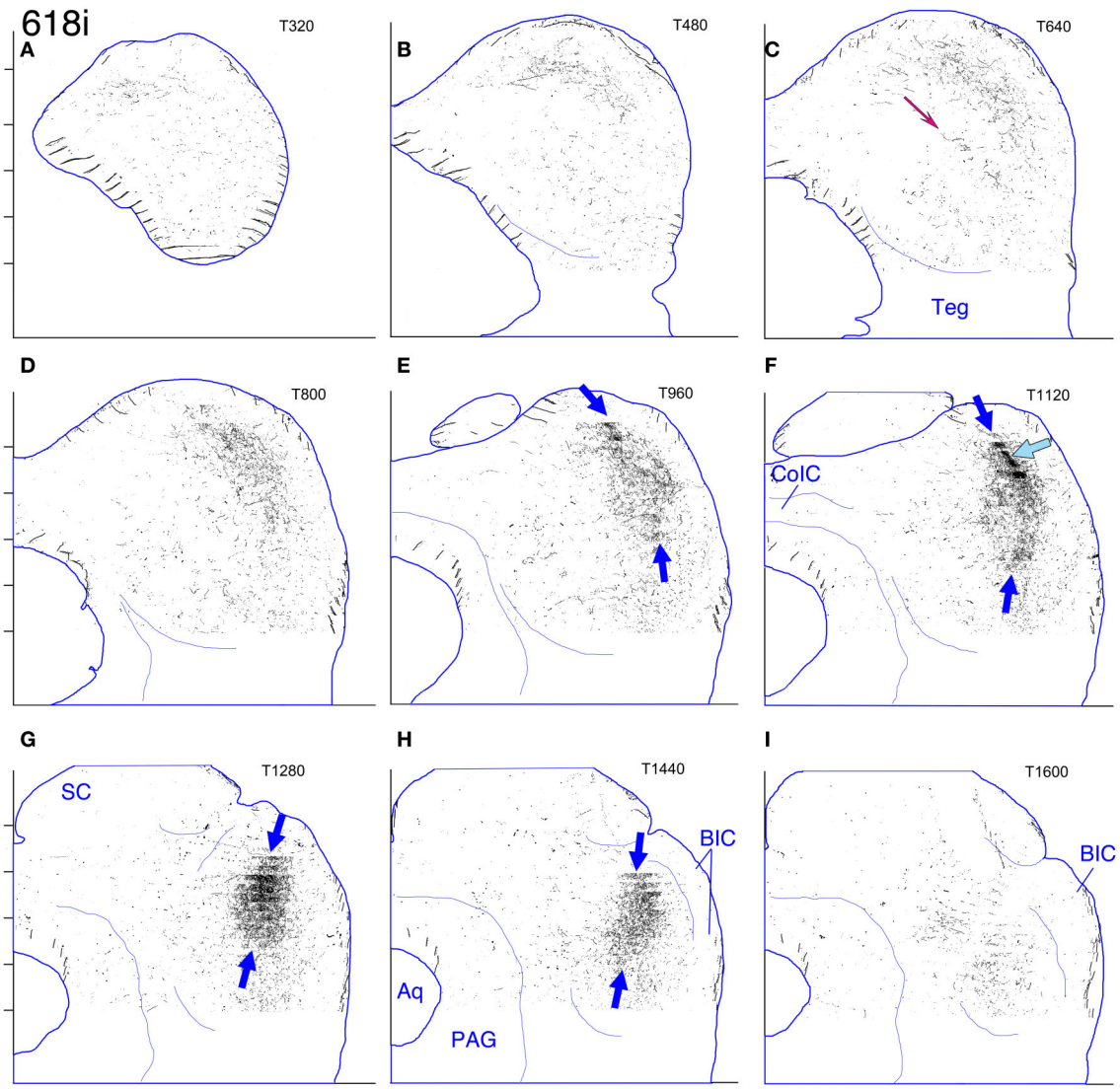

FIGURE 10 | Case 618i. (A–I) Reconstruction of the ipsilateral (right) IC after BDA injection into the right lateral LSO.

projection patterns of the labeled neurons, the more convincing the interpretation of the origin of any particular terminal field can be.

The injection sites for the three cases with BDA in the IC itself (**Figures 1–4**) were previously discussed in Cant and Benson (2006). The arguments presented in that paper did not depend on a precise definition of the effective uptake area in each case (the center of the site being the most important consideration), nor does it make much difference for the arguments presented here. The sources of labeling after an injection into one IC have been discussed in detail elsewhere (e.g., Saldaña and Merchán, 1992; Malmierca et al., 2009). What is important for the purposes of the present study is the shape and arrangement of the terminal plexuses that are labeled, regardless of the source of the neurons that give rise to them.

On the other hand, it is critically important to consider the possible sources of terminals in the cases with injection sites in the MSO or LSO. In all of these cases, spherical bushy cells were labeled in the ventral cochlear nucleus on both sides, principal cells were labeled in the ipsilateral MNTB, and cells were labeled in the ipsilateral LNTB, all well-known sources of input to the MSO and LSO (reviewed by Schofield, 2005). Neither the bushy cells nor the MNTB principal cells project to the IC (Cant and Benson, 2003; Schofield, 2005). The LNTB, however, does project bilaterally to the IC (Schofield and Cant, 1992; Schofield, 2005), and it is not known whether the LNTB cells that project to the MSO or LSO also project to the IC. Therefore, the LNTB must be considered as a potential source of some of the terminals labeled in all of the SOC-injection cases, especially in case 618 in which the injection site probably included a portion of

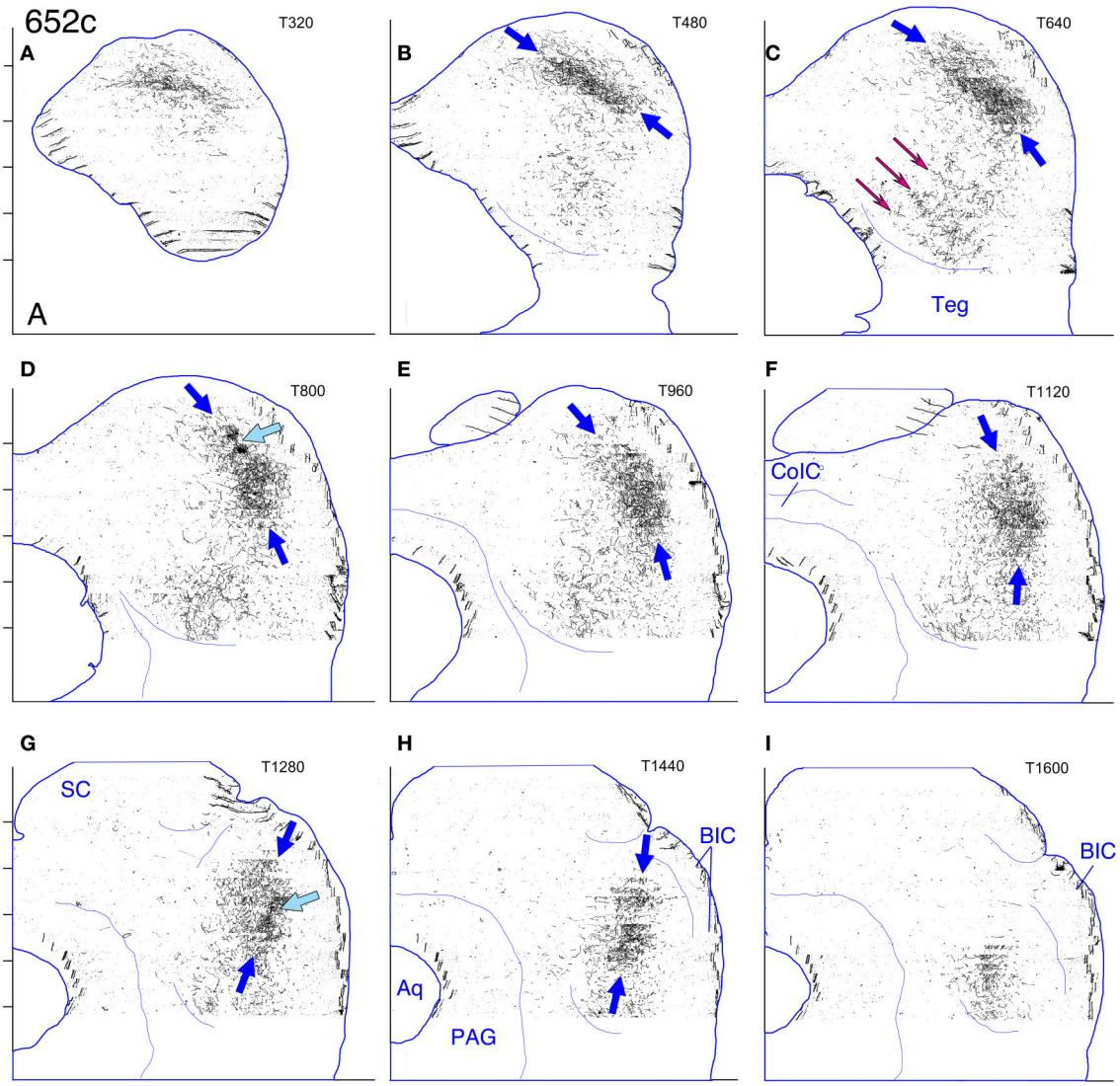

FIGURE 11 | Case 652c. (A–I) Reconstruction of the contralateral (left) IC after BDA injection into the right lateral LSO. The sections have been reflected about the midline.

the LNTB. Although it seems most likely that terminals contributed by the LNTB would be substantially fewer than those contributed by the MSO or LSO (where the injection sites are centered), to my knowledge, this has not been demonstrated experimentally.

In the ipsilateral cochlear nuclei in the cases with injection sites in the LSO, multipolar cells are also labeled. A projection to the LSO from multipolar cells is well-documented (e.g., Doucet and Ryugo, 2003), and it appears to arise partly or exclusively from the "planar" multipolar cells (or "T-stellate" cells; see Oertel et al., 2011). Planar multipolar cells also project to the IC (reviewed in Cant and Benson, 2003; Oertel et al., 2011), and although it is not known whether the same neurons give rise to both projections, it is possible that they do and that some of the anterogradely labeled axons in the cases described here arise from the ventral cochlear nucleus rather than from the LSO. However, it seems highly unlikely that LSO-projecting multipolar cells are a major source of the labeled plexuses in the IC for several reasons. First, cells in the cochlear nucleus labeled after IC injections (e.g., Cant and Benson, 2006) are much more numerous and, in general, more densely packed than those in the LSO injection cases described here, in which they are sparsely distributed. Second, in IC injection cases (e.g., those described in Cant and Benson, 2006), in which multipolar cells are labeled in the VCN, there is only sparse terminal labeling (if any) in the LSO on either side, even in cases with very large numbers of labeled multipolar cells in the VCN. This is evidence (albeit negative) that the multipolar cells that project to the IC do not also project to the LSO. Finally, Doucet and Ryugo (2003) noted that the main (or perhaps only) projections from multipolar cells to the LSO were to its middle

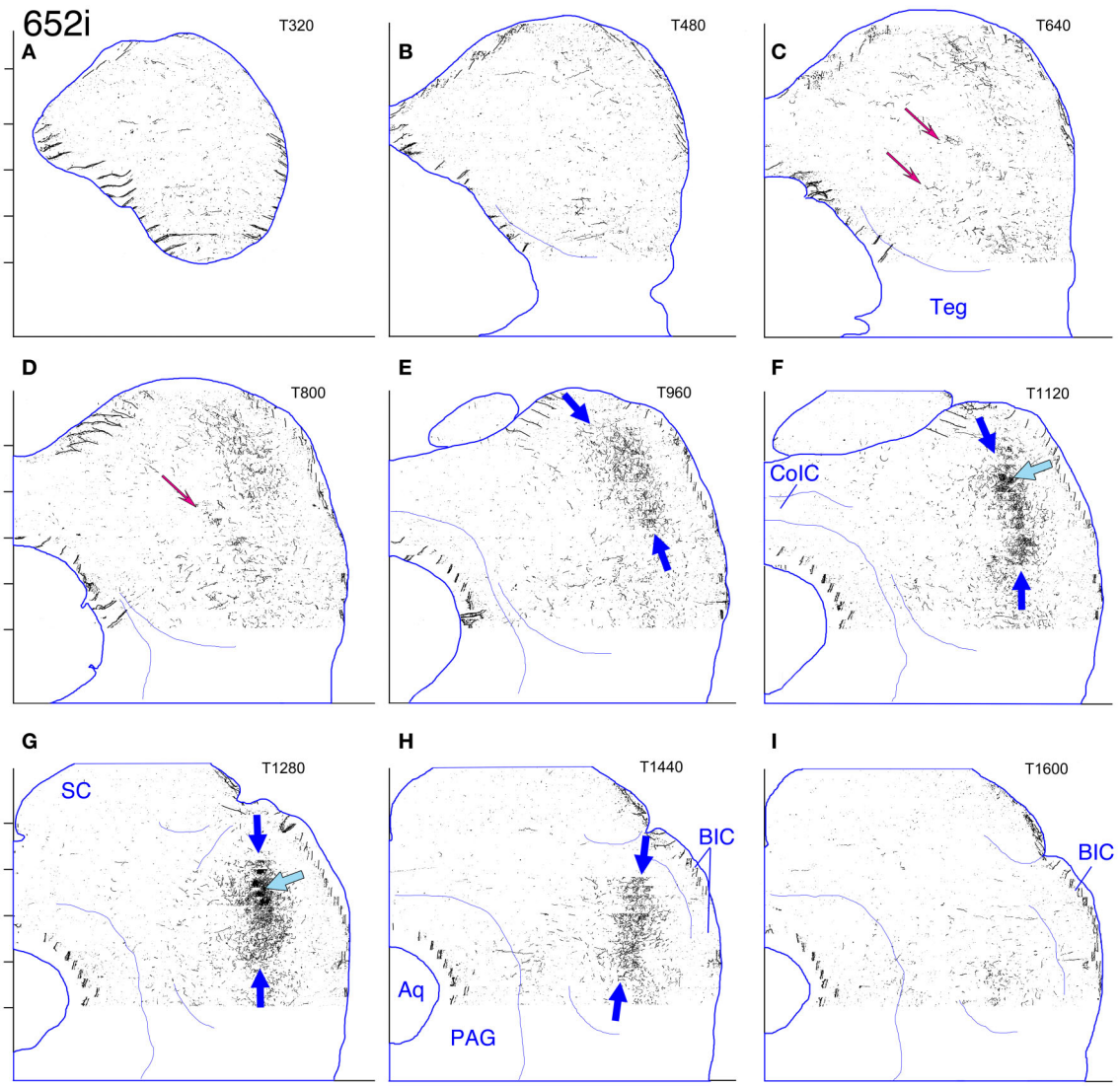

FIGURE 12 | Case 652i. (A–I) Reconstruction of the ipsilateral (right) IC after BDA injection into the right lateral LSO.

and high frequency parts; they did not see terminations in the lateral (low frequency) limb of the LSO. Thus, injections in the part of the LSO described in the present paper may be less likely to include any terminations from multipolar cells that do happen to project to both the IC and LSO. In summary, both the LNTB and VCN could be sources of some of the terminal labeling described in the LSO injection cases described in this report, but they are not likely to account for a substantial proportion of that labeling.

One mystery that I do not have a good solution for is the source of the relatively sparse terminations in the *ventral* IC in case 652. The injection sites in the LSO in cases 652 and 618 appear very similar, but only case 652 exhibits this labeling in the part of the IC that represents high frequencies. Although present on both sides, the ventral labeling is most prominent on the ipsilateral side, which would seem to rule out the VCN as a source since, in the gerbil, the ipsilateral projections from the VCN terminate almost exclusively in the dorsal and rostral IC (Nordeen et al., 1983; Cant and Benson, 2008). One possibility is that they are from the LSO itself. The banded pattern certainly fits with this possibility (see later Discussion), but the axons that leave the high frequency part of the LSO do not pass through the low frequency part (where the injection is; unpublished observations).

COMPARISON OF THE IC IN GERBIL TO THE IC IN RAT AND CAT

Loftus et al. (2008) argued that superficial differences in the appearance of the IC among species may be the result of a difference in the proportion of collicular space devoted to a particular functional region rather than to a fundamental difference in the basic plan of organization. In the gerbil, a large proportion of the IC appears to be devoted to frequencies below about 3 kHz (e.g., Ryan et al., 1982; Harris et al., 1997), and the representation

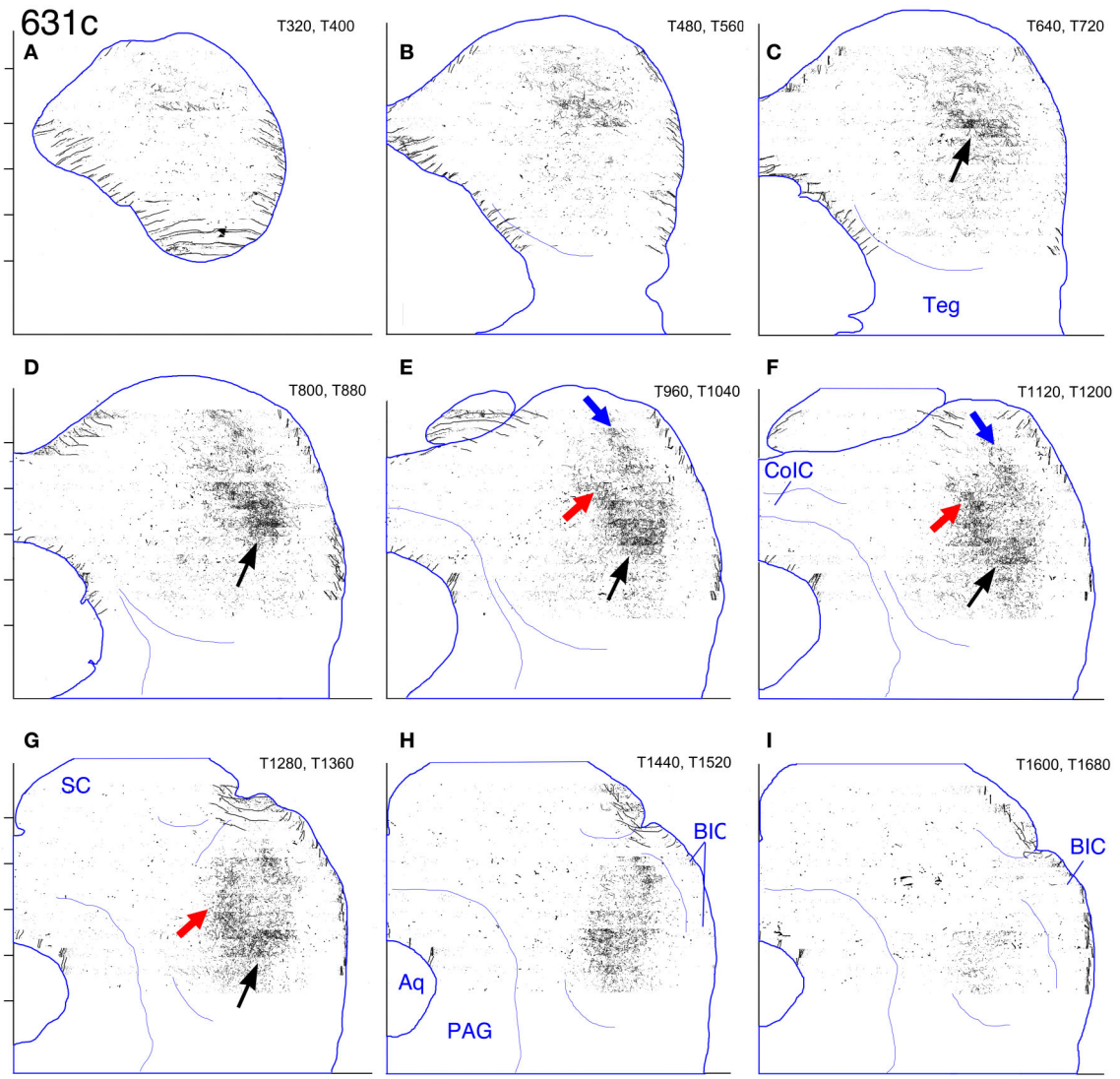

FIGURE 13 | Case 631c. (A–I) Reconstruction of the contralateral (left) IC after BDA injection into the right middle LSO. The sections have been reflected about the midline. In this and also in **Figure 14**, the black and red arrows indicate the most heavily labeled axon plexus (referenced further in the text). The blue arrows indicate a more lightly labeled (and more dorsolaterally located) plexus. For this case only, each panel in the figures represents an overlay of the labeled elements from two transverse sections as indicated in the upper right corner of each. Other details as in **Figure 2**.

of middle and higher frequencies is consequently relatively compressed. Allowing for this difference, the basic plan of the gerbil IC appears to be like that of the cat and rat. To emphasize important commonalities, I have used the nomenclature developed in the rat and cat for the model presented below.

The present results, in combination with those previously reported (Cant and Benson, 2006, 2007, 2008), form the basis for the working model of the organization of the gerbil IC presented in **Figure 15**, panels **E–G**. Schematic representations at caudal (T640), middle (T960), and rostral (T1280) levels (**Figures 15E–G**, respectively) illustrate the general appearance of the subdivisions. The central nucleus (which is roughly defined according to Cant and Benson, 2005, 2006) is itself divided into two parts: a relatively dorsolateral and rostral part referred to as pars lateralis (**Figures 15E–G**, blue fill) and a relatively ventromedial and caudal part (bounded by a dotted line) that itself can probably be further subdivided (see below). Surrounding these two parts of the central nucleus are a dorsal cortex, a rostral cortex, an external cortex, (or lateral nucleus) and a ventrolateral nucleus. I have not attempted to illustrate boundaries between these surrounding (or shell) regions; their more precise delineation is a goal of continuing studies.

With the caveat that the relative volume devoted to different frequency ranges is markedly different, the auditory midbrain in rats and gerbils appears to be organized in much the same way. Faye-Lund and Osen (1985) provided a detailed and systematic description of the rat IC. With several modifications proposed by others and one new modification suggested below,

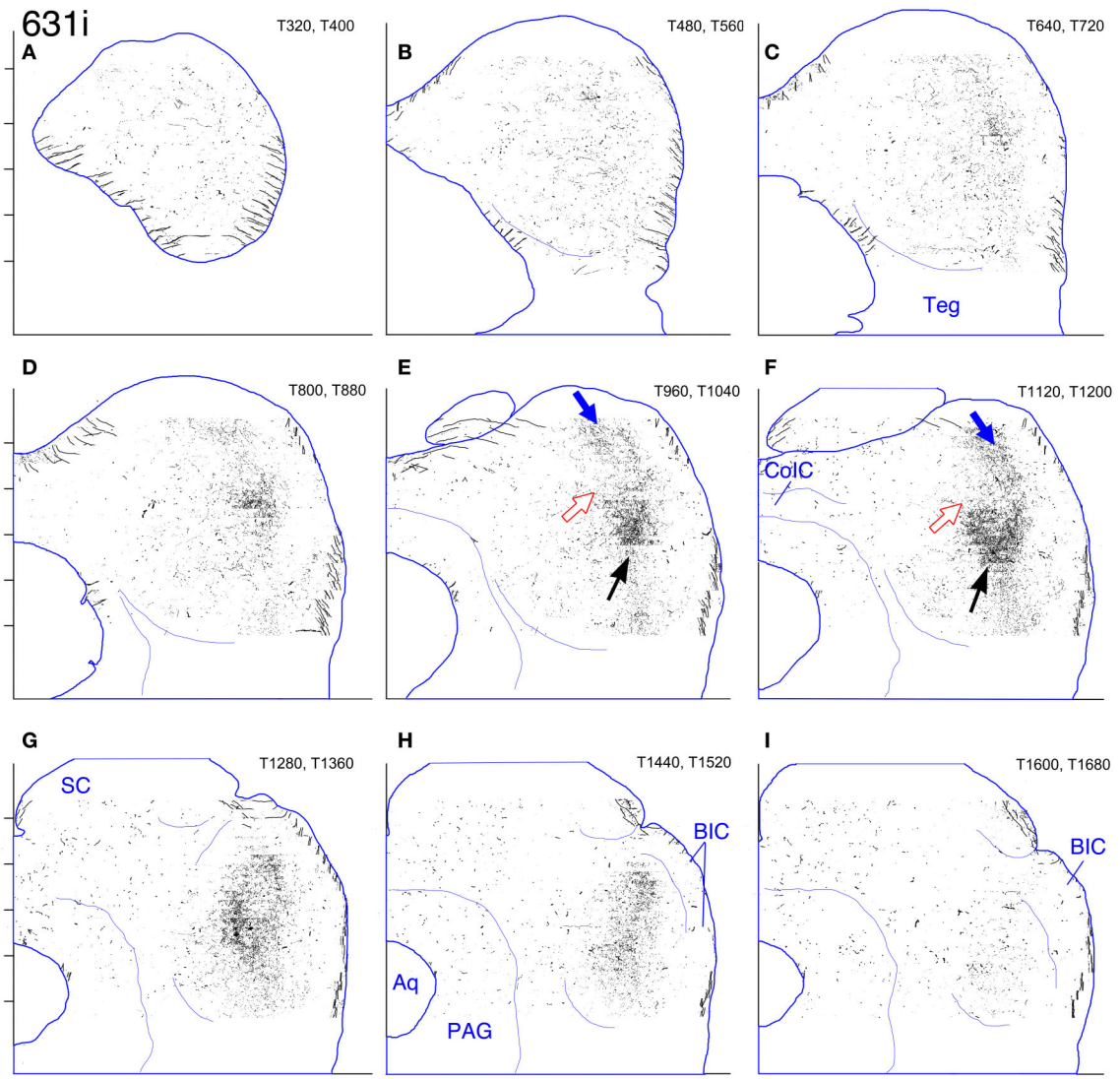

FIGURE 14 | Case 631i. (A–I) Reconstruction of the ipsilateral (right) IC after BDA injection into the right middle LSO.

their parcellation applies to the gerbil as well. First, a rostral and medial part of the IC that was included in the external cortex of Faye-Lund and Osen (1985) is now recognized as a separate subdivision and is referred to as the rostral cortex (e.g., Saldaña and Merchán, 2005; Malmierca et al., 2011). This designation is also appropriate for the gerbil. A second modification of the original scheme for the rat is based on comparisons to the cat. Loftus et al. (2008) noted that the external cortex along the lateral surface of the rat IC is considerably thicker and more obviously laminar in the rat compared to the cat. Their explanation for the difference seems to apply to the gerbil as well. That is, with a relative expansion of the low frequency representation in the cat compared to that in the rat, the prominent third layer characteristic of the rat external cortex (which they renamed the ventrolateral nucleus) becomes displaced ventrally, where it forms a smaller ventrolateral nucleus that is considered to be equivalent to the larger and more extensive version in the rat. A ventrolateral nucleus can also be identified in the gerbil (Cant and Benson, 2008).

I suggest one further modification to the rat scheme that involves the delineation of the central nucleus. In the gerbil, the central nucleus, if defined as the part of the IC with the highest relative CO activity (Cant and Benson, 2005, 2006), extends almost all the way to the rostral and dorsal boundaries of the IC. Unlike the location of the central nucleus as defined in the rat, it is not confined to either the medial 2/3 or the caudal 2/3 of the IC and, in the lateral part of the IC, is not flattened in the frontal plane. I suggest that the apparent difference between the rat and gerbil can be reconciled by reconsidering the identification of the rostrolateral area that Faye-Lund and Osen (1985) called the "lemniscal field" (and that they labeled LL, "like the lemniscus itself"). Although "lemniscal field" may be an apt description (this part of the IC is relatively heavily myelinated

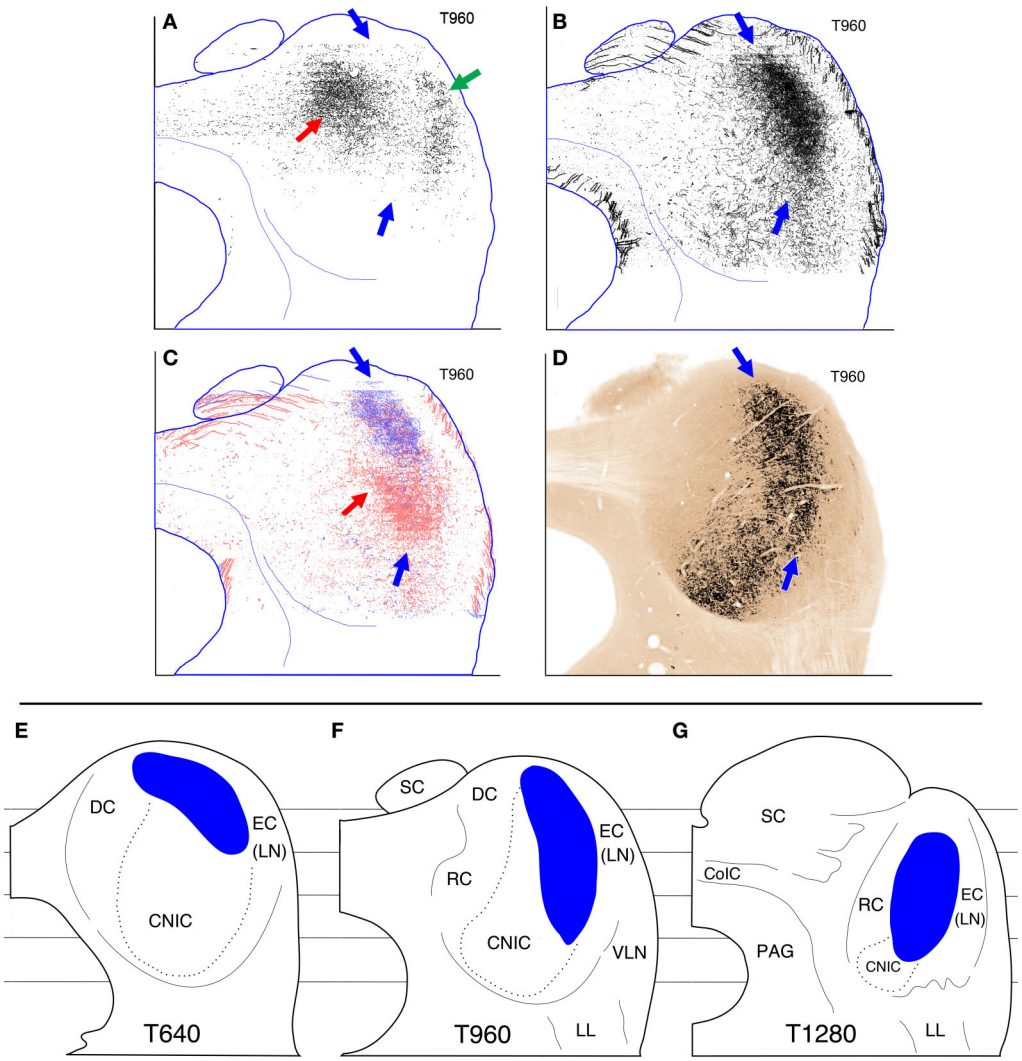

FIGURE 15 | (A–C) Comparisons of anterograde labeling patterns at one transverse atlas level (T960). **(A)** Overlap between the labeled plexuses in cases 460 and 462 (IC injections, **Figures 2E** and **3E**). The black fill indicates the pixels that were filled at this atlas level in *both* cases. There was substantial overlap in the main plexus (red arrow) and the lateral plexus (green arrow) but very little overlap in pars lateralis (dorsal and ventral extent indicated by blue arrows). **(B)** Overlay of the reconstructions at level T960 from the ipsilateral and contralateral IC in cases 618 and 652 (injections in lateral limb of LSO, **Figures 9**–**12**, panel **E**). Most of the labeled terminals and axons in these 4 ICs overlap in pars lateralis (blue arrows). **(C)** Overlay of the reconstructions at level T960 from the ipsilateral MSO in case 644 (from **Figure 6E**, blue pixels) and the contralateral LSO in case 631 (injection in middle LSO; from **Figure 12E**, red pixels). Most of the labeled terminals from both cases lie in pars lateralis, but some terminals in case 631 also extend into a more medial part of the central nucleus (red arrow) **(D)**. Cytochrome oxidase-reacted section at atlas level T960. The part of the IC with the highest CO activity is highlighted in black (see Cant and Benson, 2005, 2006). The blue arrows indicate the approximate dorsal and ventral boundaries of the CO-dense area identified as pars lateralis **(E–G)**. Schematic drawings of the gerbil IC at three transverse levels: **(E)** T640, **(F)** T960, **(G)** T1280. The blue fill indicates the approximate spatial extent of the pars lateralis of the central nucleus in the gerbil as described in the text. The dotted outline indicates the approximate boundaries of the rest of the central nucleus. For each drawing, dorsal is toward the top and lateral is toward the right. The lines behind the outlines of the sections indicate, from top (dorsal) to bottom (ventral), the levels of horizontal atlas sections H1800, H1400, H1000, H600, and H200. Abbreviations: CNIC, central nucleus of the inferior colliculus; ColC, commissure of the inferior colliculus; DC, dorsal cortex; EC, external cortex; LL, lateral lemniscus; LN, lateral nucleus; PAG, periaqueductal gray matter; RC, rostral cortex; SC, superior colliculus; VLN, ventrolateral nucleus.

and axons arising from the lemniscus do extend into this part of the central nucleus—*as well as into other parts*), the choice of the label "LL" implies that the area represents a dorsal continuation of the fiber bundle itself (although it is clear from their figures that this is not the case). In fact, the dorsolateral IC (the "lemniscal field") is filled with neurons and terminals. In contrast to the lateral lemniscus itself, which, like all fiber bundles, exhibits relatively low CO activity, this part of the IC exhibits CO activity as high or higher than any other part of the structure (e.g., gerbil: Gonzalez-Lima and Jones, 1994; Cant and Benson, 2005; rat: Loftus et al., 2008; mouse: Gonzalez-Lima and Cada, 1994).

A good agreement between the appearance of the central nucleus in gerbils and rats is achieved if the rat's lemniscal field is incorporated into its central nucleus. A direct comparison can be made between **Figure 1** in the present report and the schematic diagram in **Figure 11** of Faye-Lund and Osen (1985). The blue arrows in **Figure 1** (panels **A–C** and **G,H**) point to the rostral part of the central nucleus in the gerbil; the same relative location is labeled "LL" on the middle panels in Faye-Lund and Osen's **Figure 11**, column 3. This is the part of the central nucleus in the gerbil that represents low frequencies (Ryan et al., 1982; Brückner and Rübsamen, 1995; Cant and Benson, 2008). The low frequency representation is considerably smaller in the rat (Ryan et al., 1988), but the relative location in the dorsolateral and rostral IC appears to be consistent with the location of the lemniscal field. In contrast to my interpretation as stated here, Gonzalez-Lima and Jones (1994) in their survey of CO activity patterns in the auditory nuclei of the gerbil apparently *excluded* the dorsal and rostral part of the central nucleus as we have defined it and instead, following Faye-Lund and Osen (1985) labeled that region the "lateral lemniscal field" (their **Figure 10**). Thus, although there is agreement about the correspondence between the lemniscal field in the rat and a part of the gerbil IC that has high CO activity, I have concluded that both should be considered a part of the central nucleus, whereas Gonzalez-Lima and Cada did not. My rationale for considering this to be a part of the central nucleus is that the dorsal and rostral part of the IC is where the lowest frequencies are represented and, as shown in this paper, it is also the terminal zone of the projections from the low frequency parts of the MSO and LSO. If this part of the IC is excluded from the central nucleus, then the central nucleus would not include a part of the structure involved in low-frequency, binaural processing. Further justification for this interpretation is based on comparisons to the cat as discussed in the next section.

Oliver and Morest (1984), in their studies of the cat, were the first to identify subdivisions in the central nucleus of the IC. They defined three main parts based on the arrangement of the fibrodendritic laminae characteristic of the central nucleus in Golgi preparations. Their pars lateralis occupies the lateral and dorsal part of the central nucleus and extends to its rostral boundary where the fibrodendritic laminae assume a curved shape. This is the same relative position occupied by the part of the gerbil central nucleus that I have identified as pars lateralis (**Figure 15**); the curved arrangement of the laminae is reflected in a curved arrangement of inputs from the ventral parts of the cochlear nuclei (i.e., the fibers representing low frequencies; Cant and Benson, 2008). This part of the central nucleus exhibits high levels of CO activity in both the gerbil (**Figure 15D**; also Cant and Benson, 2005, 2007) and the cat (Loftus et al., 2008).

The rat central nucleus was not subdivided explicitly by Faye-Lund and Osen (1985), but my conclusion, as discussed above, is that they did actually define a lateral subdivision, that is, the area they called the "lemniscal zone." I suggest that this small zone is, in fact, analogous to the proportionately much larger pars lateralis in the cat and gerbil. In addition to the similar shape and position in the IC, several other observations support this interpretation. First, similar to the pattern in the gerbil, the dorsolateral and rostral IC in the rat exhibits relatively high CO activity (unpublished observations; a similar region of high metabolic capacity is seen in the dorsolateral IC of the mouse, Gonzalez-Lima and Cada, 1994; Willott, 2001). Also in common with the cat and gerbil, the extreme dorsolateral part of the rat IC represents the lowest frequencies processed by the rat (e.g., Ryan et al., 1988), and is the target of projections from the MSO (Saldaña et al., 2009).

The central nucleus of the IC is usually modeled as a stack of layers representing successively higher frequencies from the top (dorsal) to the bottom (ventral) of the stack (e.g., Merzenich and Reid, 1974). In this sense, the pars lateralis could be taken to represent the top layer(s) in the stack. In the caudal IC (e.g., as schematized in **Figure 15E**), this description may fit, but moving to middle and rostral levels (**Figures 15F,G**), this interpretation does not seem appropriate because the pars lateralis, taken as a whole, does not have the shape of a disk-shaped layer at the top of a stack. Rather it takes on the shape of a long bent cylinder that extends upward from the rostroventral boundary of the IC, curving caudally and dorsally and finally extending medially just beneath the dorsal surface of the IC. The same shape is seen in the part of the central nucleus of the cat that is activated by a 500 Hz tone (2-deoxyglucose studies, Brown et al., 1997, their **Figure 5A**). and, to some extent, in the more dorsal (low frequency) laminar plexus reconstructed in three dimensions in the guinea pig (Malmierca et al., 1995). This apparent divergence from the more orderly stacks that characterize most of the central nucleus could be the reason why Merzenich and Reid (1974) observed that the "series of stacked disks" in the cat appear to be "simultaneously toppling rostrally and laterally."

PARS LATERALIS OF THE CENTRAL NUCLEUS IS A MAJOR TARGET OF LOW-FREQUENCY, BINAURAL INPUTS

Oliver and Morest (1984) raised the possibility that each subdivision of the central nucleus plays a different functional role in auditory processing. The unique neuroanatomical organization of pars lateralis suggests that it is primarily involved in integrating binaural inputs from the superior olivary complex and the cochlear nuclei. Further, the pars lateralis may project to a part of the ventral division of the medial geniculate nucleus separate from the projections of other parts of the central nucleus (Cant and Benson, 2007).

Input from the superior olivary complex

Henkel and Spangler (1983) demonstrated that the axons arising from the MSO in the cat terminate in only a part of the central nucleus, and they suggested that the terminal field might be restricted mainly to the pars lateralis. Their results were corroborated by Oliver et al. (1995), who further demonstrated that up to 36% of the excitatory terminals (i.e., terminals with round synaptic vesicles) in pars lateralis originate in the MSO. Indeed, several studies in the cat include cases in which a large majority (up to greater than 90%) of labeled cells are located in the MSO after small injections of a retrograde tracer in the lateral central nucleus (Roth et al., 1978; Brunso-Bechtold et al., 1981; Aitkin and Schuck, 1985; Loftus et al., 2010). In our studies in the gerbil, labeled cells in the MSO were always accompanied by labeled

cells in the LSO and cochlear nuclei (Cant and Benson, 2007), but our injections were not as small as those in the studies cited above. The results of the small injections are consistent with the view that the IC laminae are made up of a mosaic of anatomically (and, therefore, functionally) distinct areas (e.g., Oliver and Huerta, 1992; Loftus et al., 2010). (The larger injections most likely include a number of the small areas and so could mask any specificity of connections).

In the cat, terminations from the MSO, even from its ventralmost part, do not extend all the way into the ventral part of the central nucleus (Henkel and Spangler, 1983). The results of our retrograde tracing experiments suggest that the same is true for the gerbil, as the MSO never contained more than a few labeled cells (if any) when the injections were in the ventral IC (Cant and Benson, 2006). In the cat, cells in the ventral MSO may terminate in pars centralis of the central nucleus (suggested on the basis of the patterns illustrated by Henkel and Spangler, 1983, their **Figure 11** and by Loftus et al., 2004, their case 56). The pars centralis appears to be proportionately much smaller in the gerbil than in the cat, and it is difficult to come to a conclusion about its input from the MSO in the gerbil. The MSO in the gerbil appears to be heavily biased toward the lower frequency range (i.e., below about 3 kHz) based on patterns of 2-deoxyglucose uptake during tonal stimulation (Ryan et al., 1982), and it is possible that terminations from the MSO in the gerbil are confined entirely to the pars lateralis.

Both our retrograde results (Cant and Benson, 2006) and the anterograde results presented here suggest that the inputs from the ipsilateral and contralateral LSOs overlap extensively with the inputs from the MSO in the pars lateralis as a whole, but that at a local level, the inputs from these sources are not distributed homogeneously. In the two cases with tracer injections in the lateral limb of the LSO (cases 618 and 652), the ipsilateral and contralateral inputs appear to form complementary terminal fields at some (but not all) levels. This is compatible with the findings of Loftus et al. (2004, 2010) in the cat that the inputs from the ipsilateral MSO and LSO appear to overlap locally in parts of the central nucleus that do not receive input from the contrateral LSO. (It is not known whether the excitatory and inhibitory projections from the ipsilateral LSO [e.g., Saint Marie et al., 1989] are distributed differentially.) Like the MSO, both LSOs contribute a significant number of the excitatory inputs to the parts of the central nucleus in which they terminate. Oliver et al. (1995; Oliver, 2000) estimated that the contralateral LSO contributes up to 18% of the excitatory terminals in some parts of the central nucleus and that the ipsilateral LSO can contribute up to 26% of the excitatory terminals. However, given the results of Loftus et al. (2010; also the present results), it is not likely that both LSOs contribute a maximum number of synapses to a given patch of neuropil. The ipsilateral LSO also sends inhibitory projections to pars lateralis of the central nucleus, where it can account for up to 26% of the terminals with pleomorphic vesicles (Oliver et al., 1995). Additional inhibitory input to the dorsolateral central nucleus arises in the periolivary nuclei as well as in the nuclei of the lateral lemniscus (e.g., Whitley and Henkel, 1984; Saint Marie and Baker, 1990; Bajo et al., 1999). In the gerbil, this part of the central nucleus appears to be a major target of the dorsal nuclei of the lateral lemniscus (Cant and Benson, 2006).

Input from the cochlear nuclei

In addition to the dense terminal plexuses formed by the inputs from the superior olivary complex, the lateral part of the central nucleus also receives substantial inputs from both the ipsilateral and contralateral cochlear nuclei. In fact, the pars lateralis is the main, if not the only, target of the ipsilateral cochlear nucleus in both cats (Oliver, 1987) and gerbils (Nordeen et al., 1983; Moore and Kitzes, 1985; Cant and Benson, 2006, 2008). In the gerbil, the inputs arise from both the ventral and dorsal cochlear nuclei (Nordeen et al., 1983; Cant and Benson, 2006, 2008). In the cat, only the ventral cochlear nucleus appears to contribute substantially to the projection (Oliver, 1987). The difference could be related to the relatively compressed low frequency representation in the cat dorsal cochlear nucleus (Spirou et al., 1993), especially when compared to that of the gerbil (Hancock and Voigt, 2001).

Like the inputs from the superior olivary complex, the inputs from the cochlear nuclei are not distributed homogeneously throughout their terminal zone, and the patchy inputs from the ipsilateral and contralateral sides may not fully overlap (Cant and Benson, 2008). The inputs from the cochlear nuclei form their densest terminations in the same part of the central nucleus that receives the inputs from the superior olivary complex (based on comparing the plots in Moore and Kitzes [1985] with those in Cant and Benson [2008] with those in the present results). Although the projections from the ipsilateral dorsal and ventral cochlear nuclei arise from a relatively small number of neurons (e.g., Nordeen et al., 1983), they form a relatively dense terminal field in the pars lateralis (Cant and Benson, 2008). Oliver (1984, 1985, 1987, 2000) found that the ipsilateral anteroventral cochlear nucleus can account for up to 18% of the excitatory terminals in the pars lateralis, whereas the contralateral anteroventral cochlear nucleus can account for up to 13% and the contralateral DCN, for up to 11%. Presumably, there is an additional contribution from the posteroventral cochlear nucleus, which also projects to pars lateralis (Cant and Benson, 2007, 2008).

Directions for further study: synaptic organization within pars lateralis

A major goal of neuroanatomy is to discover how specific populations of neurons are interconnected. The more precisely specific cell types can be defined in terms of their synaptic organization and projection patterns, the more useful the anatomical data will be for interpreting the results of physiological studies. For this reason, it is important not only to understand the circuitry but also to understand how the components are organized within the three-dimensional space of the structure under consideration. In the cochlear nuclei, tremendous progress has been made in correlating structure and function (reviewed, e.g., by Romand and Avan, 1997), in large part because of the physical segregation within the nucleus of many of the main cell types. In the central nucleus of the IC, progress is being made in identifying anatomically distinct cell types (e.g., Ito and Oliver, 2012), but these cell types are less obviously segregated within the structure.

However, in many instances, the terminal fields formed by axons projecting from various sources into the central nucleus do appear to be partially or completely segregated from each other in some parts of the central nucleus and to converge in various combinations in others. Thus, precise mapping of the terminal fields of the inputs from the different sources can serve to constrain hypotheses about the circuitry in each region. The inputs to the gerbil IC from the LSO and MSO appear to intersect with each other and with the inputs from the cochlear nucleus (Cant and Benson, 2008) in a complex way with the potential for segregation of some of the inputs and overlap of others within the confines of this one subdivision. The pars lateralis is the part of the central nucleus in the cat that contains neurons sensitive to interaural delays (Semple and Aitkin, 1979), and the connections (as discussed above) suggest that the same would be true for the gerbil. Thus, the convergence in pars lateralis from most of the main sources of ascending excitatory input to the IC combined with a non-homogeneous distribution of the terminations suggests the potential for a number of different types of processing units within this one subdivision devoted to binaural integration. The pars lateralis gives rise to projections to at least two different regions within the ventral division of the medial geniculate nucleus (Cant and Benson, 2007), and it is quite possible that the projections arise from different cell populations with different complements of synaptic inputs.

A particularly important concept for guiding studies of the organization of the IC at the level of individual circuits is the concept of the "synaptic domain," first articulated by Oliver and Huerta (1992). The central idea is that embedded within the frequency band laminae characteristic of the central nucleus is some number of functional modules, potentially definable on the basis of unique sources and arrangements of inputs and outputs. This is an attractive idea and evidence for it has been discussed in some detail by Oliver and colleagues (e.g., Oliver, 2000, 2005; Loftus et al., 2010). Given the wealth of possibilities for interactions among ascending sources within the pars lateralis, it seems like a particularly interesting part of the IC for continuing studies based on the hypothesis of synaptic domains.

ACKNOWLEDGMENTS

The research was supported by a grant from the National Institute on Deafness and Other Communication Disorders, DC00135. Much of this work was done in collaboration with Dr. Christina G. Benson; the studies would not have been accomplished without her participation.

REFERENCES

Aitkin, L. M., and Schuck, D. (1985). Low frequency neurons in the lateral central nucleus of the cat inferior colliculus receive their input predominantly from the medial superior olive. *Hear. Res.* 17, 87–93.

Bajo, V. M., Merchán, M. A., Malmierca, M. S., Nodal, F. R., and Bjaalie, J. G. (1999). Topographic organization of the dorsal nucleus of the lateral lemniscus in the cat. *J. Comp. Neurol.* 407, 349–366.

Bajo, V. M., and Moore, D. R. (2005). Descending projections from the auditory cortex to the inferior colliculus in the gerbil, *Meriones unguiculatus*. *J. Comp. Neurol.* 486, 101–116.

Brown, M., Webster, W. R., and Martin, R. L. (1997). The three-dimensional frequency organization of the inferior colliculus of the cat: a 2-deoxyglucose study. *Hear. Res.* 104, 57–72.

Brückner, S., and Rübsamen, R. (1995). Binaural response characteristics in isofrequency sheets of the gerbil inferior colliculus. *Hear. Res.* 86, 1–14.

Brunso-Bechtold, J. K., Thompson, G. C., and Masterton, R. B. (1981). HRP study of the organization of auditory afferents ascending to central nucleus of inferior colliculus in cat. *J. Comp. Neurol.* 197, 705–722.

Cant, N. B., and Benson, C. G. (2003). Parallel auditory pathways: projection patterns of the different neuronal populations in the dorsal and ventral cochlear nuclei. *Brain Res. Bull.* 60, 457–474.

Cant, N. B., and Benson, C. G. (2005). An atlas of the inferior colliculus of the gerbil in three dimensions. *Hear. Res.* 206, 12–27.

Cant, N. B., and Benson, C. G. (2006). Organization of the inferior colliculus of the gerbil (*Meriones unguiculatus*): differences in distribution of projections from the cochlear nucleus and the superior olivary complex. *J. Comp. Neurol.* 495, 511–528.

Cant, N. B., and Benson, C. G. (2007). Multiple topographically organized projections connect the central nucleus of the inferior colliculus to the ventral division of the medial geniculate nucleus in the gerbil, *Meriones unguiculatus*. *J. Comp. Neurol.* 503, 432–453.

Cant, N. B., and Benson, C. G. (2008). Organization of the inferior colliculus of the gerbil (*Meriones unguiculatus*): projections from the cochlear nucleus. *Neuroscience* 154, 206–217.

Casseday, J. H., Fremouw, T., and Covey, E. (2002). "The inferior colliculus: a hub for the central auditory system," in *Integrative Functions in the Mammalian Auditory System*, eds D. Oertel, R. R. Fay, and A. N. Popper (New York, NY: Springer), 238–318.

Chen, S., and Aston-Jones, G. (1998). Axonal collateral-collateral transport of tract tracers in brain neurons: false anterograde labeling and useful tool. *Neuroscience* 82, 1151–1163.

Doucet, J. R., and Ryugo, D. K. (2003). Axonal pathways to the lateral superior olive labeled with biotinylated dextran amine injections in the dorsal cochlear nucleus of rats. *J. Comp. Neurol.* 461, 452–465.

Fathke, R. L., and Gabriele, M. L. (2009). Patterning of multiple layered projections to the auditory midbrain prior to experience. *Hear. Res.* 249, 36–43.

Faye-Lund, H., and Osen, K. K. (1985). Anatomy of the inferior colliculus in rat. *Anat. Embryol.* 171, 1–20.

Gabriele, M. L., Brunso-Bechtold, J. K., and Henkel, C. K. (2000). Development of afferent patterns in the inferior colliculus of the rat: projection from the dorsal nucleus of the lateral lemniscus. *J. Comp. Neurol.* 416, 368–382.

Gonzalez-Lima, F., and Cada, A. (1994). Cytochrome oxidase activity in the auditory system of the mouse: a qualitative and quantitative histochemical study. *Neuroscience* 63, 559–578.

Gonzalez-Lima, F., and Jones, D. (1994). Quantitative mapping of cytochrome oxidase activity in the central auditory system of the gerbil: a study with calibrated activity standards and metal-intensified histochemistry. *Brain Res.* 660, 34–49.

Hancock, K. E., and Voigt, H. F. (2001). Intracellularly labeled fusiform cells in dorsal cochlear nucleus of the gerbil. II. Comparison of physiology and anatomy. *J. Neurophysiol.* 87, 2520–2530.

Harris, D. M., Shannon, R. V., Snyder, R., and Carney, E. (1997). Multiunit mapping of acoustic stimuli in gerbil inferior colliculus. *Hear. Res.* 108, 145–156.

Henkel, C. K., and Spangler, K. M. (1983). Organization of the efferent projections of the medial superior olivary nucleus in the cat as revealed by HRP and autoradiographic tracing methods. *J. Comp. Neurol.* 221, 416–428.

Ito, T., and Oliver, D. L. (2012). The basic circuit of the IC: tectothalamic neurons with different patterns of synaptic organization send different messages to the thalamus. *Front. Neural Circuits* 6:48. doi: 10.3389/fncir.2012.00048

Kudo, M. (1981). Projections of the nuclei of the lateral lemniscus in the cat: an autoradiographic study. *Brain Res.* 221, 57–69.

Loftus, W. C., Bishop, D. C., and Oliver, D. L. (2010). Differential patterns of inputs create functional zones in central nucleus of inferior colliculus. *J. Neurosci.* 30, 13396–13408.

Loftus, W. C., Bishop, D. C., Saint Marie, R. L., and Oliver, D. L. (2004). Organization of binaural excitatory and inhibitory inputs to the inferior colliculus from the superior olive. *J. Comp. Neurol.* 472, 330–344.

Loftus, W. C., Malmierca, M. S., Bishop, D. C., and Oliver, D. L. (2008). The

cytoarchitecture of the inferior colliculus revisited: a common organization of the lateral cortex in rat and cat. *Neuroscience* 154, 196–205.

Malmierca, M. S. (2005). The inferior colliculus: a center for convergence of ascending and descending auditory information. *Neuroembryol. Aging* 3, 215–229.

Malmierca, M. S., Blackstad, T. W., and Osen, K. K. (2011). Computer-assisted 3-D reconstructions of Golgi-impregnated neurons in the cortical regions of the inferior colliculus of rat. *Hear. Res.* 274, 13–26.

Malmierca, M. S., Hernández, O., Antunes, F. M., and Rees, A. (2009). Divergent and point-to-point connections in the commissural pathway between the inferior colliculi. *J. Comp. Neurol.* 514, 226–239.

Malmierca, M. S., Rees, A., Le Beau, F. E. N., and Bjaalie, J. G. (1995). Laminar organization of frequency-defined local axons within and between the inferior colliculi of the guinea pig. *J. Comp. Neurol.* 357, 124–144.

Malmierca, M. S., Saint Marie, R. L., Merchán, M. A., and Oliver, D. L. (2005). Laminar inputs from dorsal cochlear nucleus and ventral cochlear nucleus to the central nucleus of the inferior colliculus: two patterns of convergence. *Neuroscience* 136, 883–894.

Merzenich, M. M., and Reid, M. D. (1974). Representation of the cochlea within the inferior colliculus of the cat. *Brain Res.* 77, 397–415.

Moore, D. R., and Kitzes, L. M. (1985). Projections from the cochlear nucleus to the inferior colliculus in normal and neonatally cochlea-ablated gerbils. *J. Comp. Neurol.* 240, 180–195.

Morest, D. K., and Oliver, D. L. (1984). The neuronal architecture of the inferior colliculus in the cat: defining the functional anatomy of the auditory midbrain. *J. Comp. Neurol.* 222, 209–236.

Nordeen, K. W., Killackey, H. P., and Kitzes, L. M. (1983). Ascending auditory projections to the inferior colliculus in the adult gerbil, *Meriones unguiculatus*. *J. Comp. Neurol.* 214, 131–143.

Oertel, D., Wright, S., Cao, X.-J., Ferragamo, M., and Bal, R. (2011). The multiple functions of T stellate/multipolar/chopper cells in the ventral cochlear nucleus. *Hear. Res.* 276, 61–69.

Oliver, D. L. (1984). Dorsal cochlear nucleus projections to the inferior colliculus in the cat: a light and electron microscope study. *J. Comp. Neurol.* 224, 155–172.

Oliver, D. L. (1985). Quantitative analyses of axonal endings in the central nucleus of the inferior colliculus and distribution of ^{3}H-labeling after injections in the dorsal cochlear nucleus. *J. Comp. Neurol.* 237, 343–359.

Oliver, D. L. (1987). Projections to the inferior colliculus from the anteroventral cochlear nucleus in the cat: possible substrates for binaural interaction. *J. Comp. Neurol.* 264, 24–46.

Oliver, D. L. (2000). Ascending efferent projections of the superior olivary complex. *Microsc. Res. Tech.* 51, 355–363.

Oliver, D. L. (2005). "Neuronal organization in the inferior colliculus," in *The Inferior Colliculus,* eds J. A. Winer and C. E. Schreiner (New York, NY: Springer), 69–114.

Oliver, D. L., Beckius, G. E., Bishop, D. C., and Kuwada, S. (1997). Simultaneous anterograde labeling of axonal layers from lateral superior olive and dorsal cochlear nucleus in the inferior colliculus of cat. *J. Comp. Neurol.* 382, 215–229.

Oliver, D. L., Beckius, G. E., and Shneiderman, A. (1995). Axonal projections from the lateral and medial superior olive to the inferior colliculus of the cat: a study using electron microscopic autoradiography. *J. Comp. Neurol.* 360, 17–32.

Oliver, D. L., and Huerta, M. F. (1992). "Inferior and superior colliculi," in *Springer Handbook of Auditory Research, Vol. 1: The Mammalian Auditory Pathway: Neuroanatomy,* eds D. B. Webster, A. N. Popper, and R. R. Fay (New York, NY: Springer-Verlag), 168–221.

Oliver, D. L., and Morest, D. K. (1984). The central nucleus of the inferior colliculus in the cat. *J. Comp. Neurol.* 222, 237–264.

Oliver, D. L., Ostapoff, E.-M., and Beckius, G. E. (1999). Direct innervation of identified tectothalamic neurons in the inferior colliculus by axons from the cochlear nucleus. *Neuroscience* 93, 643–658.

O'Quinn, D. (2001). *Photoshop 6 Shop Manual*. Indianapolis, IN: New Riders.

Romand, R., and Avan, P. (1997). "Anatomical and functional aspects of the cochlear nucleus," in *The Central Auditory System,* eds G. Ehret and R. Romand (New York, NY: Oxford University Press), 97–191.

Roth, G. L., Aitkin, L. M., Andersen, R. A., and Merzenich, M. M. (1978). Some features of the spatial organization of the central nucleus of the inferior colliculus of the cat. *J. Comp. Neurol.* 182, 661–680.

Ryan, A. F., Furlow, Z., Woolf, N. K., and Keithley, E. M. (1988). The spatial representation of frequency in the rat dorsal cochlear nucleus and inferior colliculus. *Hear. Res.* 36, 181–190.

Ryan, A. F., Woolf, N. K., and Sharp, F. R. (1982). Tonotopic organization in the central auditory pathway of the Mongolian gerbil: a 2-deoxyglucose study. *J. Comp. Neurol.* 207, 369–380.

Saint Marie, R. L., and Baker, R. A. (1990). Neurotransmitter-specific uptake and retrograde transport of [H^{3}]glycine from the inferior colliculus by ipsilateral projections of the superior olivary complex and nuclei of the lateral lemniscus. *Brain Res.* 524, 244–251.

Saint Marie, R. L., Ostapoff, E.-M., Morest, D. K., and Wenthold, R. J. (1989). Glycine-immunoreactive projection of the cat lateral superior olive: possible role in midbrain ear dominance. *J. Comp. Neurol.* 279, 382–396.

Saldaña, E., Aparicio, M.-A., Fuentes-Santamaría, V., and Berrebi, A. S. (2009). Connections of the superior paraolivary nucleus of the rat: projections to the inferior colliculus. *Neuroscience* 163, 372–387.

Saldaña, E., Feliciano, M., and Mugnaini, E. (1996). Distribution of descending projections from primary auditory cortex to inferior colliculus mimics the topography of intracollicular projections. *J. Comp. Neurol.* 371, 15–40.

Saldaña, E., and Merchán, M. A. (1992). Intrinsic and commissural connections of the rat inferior colliculus. *J. Comp. Neurol.* 319, 417–437.

Saldaña, E., and Merchán, M. A. (2005). "Intrinsic and commissural connections of the rat inferior colliculus," in *The Inferior Colliculus,* eds J. A. Winer and C. E. Schreiner (New York, NY: Springer), 155–181.

Sanes, D. H., Merickel, M., and Rubel, E. W. (1989). Evidence for an alteration of the tonotopic map in the gerbil cochlea during development. *J. Comp. Neurol.* 279, 436–444.

Schofield, B. R. (2005). "Superior olivary complex and lateral lemniscal connections of the auditory midbrain," in *The Inferior Colliculus,* eds J. A. Winer and C. E. Schreiner (New York, NY: Springer), 132–154.

Schofield, B. R., and Cant, N. B. (1992). Organization of the superior olivary complex in the guinea pig: II. Patterns of projection from the perioliveary nuclei to the inferior colliculus. *J. Comp. Neurol.* 317, 438–455.

Semple, M. N., and Aitkin, L. M. (1979). Representation of sound frequency and laterality by units in central nucleus of cat inferior colliculus. *J. Neurophysiol.* 42, 1626–1639.

Shneiderman, A., and Henkel, C. K. (1987). Banding of lateral superior olivary nucleus afferents in the inferior colliculus: a possible substrate for sensory integration. *J. Comp. Neurol.* 266, 519–534.

Shneiderman, A., Oliver, D. L., and Henkel, C. K. (1988). Connections of the dorsal nucleus of the lateral lemniscus: an inhibitory parallel pathway in the ascending auditory system? *J. Comp. Neurol.* 276, 188–208.

Spirou, G. A., May, B. J., Wright, D. D., and Ryugo, D. K. (1993). Frequency organization of the dorsal cochlear nucleus in cats. *J. Comp. Neurol.* 329, 36–52.

Whitley, J. M., and Henkel, C. K. (1984). Topographical organization of the inferior collicular projection and other connections of the ventral nucleus of the lateral lemniscus in the cat. *J. Comp. Neurol.* 229, 257–270.

Willott, J. F. (2001). "Focus: diversity of the mouse central auditory system," in *Handbook of Mouse Auditory Research. From Behavior to Molecular Biology,* ed J. F. Willott (Boca Raton, FL: CRC Press), 239–242.

Conflict of Interest Statement: The author declares that the research was conducted in the absence of any commercial or financial relationships that could be construed as a potential conflict of interest.

Received: 14 October 2012; accepted: 07 February 2013; published online: 06 March 2013.

Citation: Cant NB (2013) Patterns of convergence in the central nucleus of the inferior colliculus of the Mongolian gerbil: organization of inputs from the superior olivary complex in the low frequency representation. Front. Neural Circuits 7:29. doi: 10.3389/fncir.2013.00029

frontiers in
NEURAL CIRCUITS

REVIEW ARTICLE
published: 11 July 2012
doi: 10.3389/fncir.2012.00045

The representation of sound localization cues in the barn owl's inferior colliculus

Martin Singheiser*[1,2]*, Yoram Gutfreund*[3] *and Hermann Wagner*[2]

[1] *Department of Biology, RWTH Aachen University, Aachen, Germany*
[2] *Department of Zoology and Animal Physiology, Institute for Biology II, RWTH Aachen University, Aachen, Germany*
[3] *Department of Physiology and Biophysics, The Ruth and Bruce Rappaport Faculty of Medicine, Technion, Haifa, Israel*

Edited by:
Manuel S. Malmierca, University of Salamanca, Spain

Reviewed by:
Andrew J. King, University of Oxford, UK
Gestur B. Christianson, University College London, UK

****Correspondence:***
Hermann Wagner, Department of Zoology and Animal Physiology, Institute for Biology II, RWTH Aachen University, Mies-van-der-Rohe Strasse 15, 52056 Aachen, Germany.
e-mail: wagner@bio2.rwth-aachen.de

The barn owl is a well-known model system for studying auditory processing and sound localization. This article reviews the morphological and functional organization, as well as the role of the underlying microcircuits, of the barn owl's inferior colliculus (IC). We focus on the processing of frequency and interaural time (ITD) and level differences (ILD). We first summarize the morphology of the sub-nuclei belonging to the IC and their differentiation by antero- and retrograde labeling and by staining with various antibodies. We then focus on the response properties of neurons in the three major sub-nuclei of IC [core of the central nucleus of the IC (ICCc), lateral shell of the central nucleus of the IC (ICCls), and the external nucleus of the IC (ICX)]. ICCc projects to ICCls, which in turn sends its information to ICX. The responses of neurons in ICCc are sensitive to changes in ITD but not to changes in ILD. The distribution of ITD sensitivity with frequency in ICCc can only partly be explained by optimal coding. We continue with the tuning properties of ICCls neurons, the first station in the midbrain where the ITD and ILD pathways merge after they have split at the level of the cochlear nucleus. The ICCc and ICCls share similar ITD and frequency tuning. By contrast, ICCls shows sigmoidal ILD tuning which is absent in ICCc. Both ICCc and ICCls project to the forebrain, and ICCls also projects to ICX, where space-specific neurons are found. Space-specific neurons exhibit side peak suppression in ITD tuning, bell-shaped ILD tuning, and are broadly tuned to frequency. These neurons respond only to restricted positions of auditory space and form a map of two-dimensional auditory space. Finally, we briefly review major IC features, including multiplication-like computations, correlates of echo suppression, plasticity, and adaptation.

Keywords: sound localization, central nucleus of the inferior colliculus, auditory, plasticity, adaptation, interaural time difference, interaural level difference, frequency tuning

INTRODUCTION

The barn owl (*Tyto alba*) is a nocturnal hunter. These birds are able to approach distant targets under dim illumination and in complete darkness with high accuracy and precision (Payne, 1962, 1971; Konishi, 1973a,b; Hausmann et al., 2008; Singheiser et al., 2010b). They mainly use auditory information for prey capture, and are established as a well-known model system for the study of sound localization. The hearing range of barn owls covers frequencies from 0.2 to 12 kHz. This is rather narrow compared with mammals but broad in comparison with other birds. The lowest thresholds are found between 4 and 8 kHz (Konishi, 1973b; Dyson et al., 1998).

The outstanding auditory capabilities of these animals are mediated by morphological as well as neuronal specializations. For example, the facial ruff functions as a sound collector and amplifier guiding the incoming sound to the ear openings (Payne, 1971; Coles and Guppy, 1988). The facial ruff also enhances the directionality of the ears (Von Campenhausen and Wagner, 2006; Hausmann et al., 2009, 2010). This enhanced directionality improves the representation of the main behavioral cues involved in sound localization: interaural time differences (ITDs) and interaural level differences (ILDs). ITDs change almost exclusively with azimuth. The asymmetrically arranged ears of the barn owl cause ILDs in the high frequency range to change along an axis that is inclined toward the horizontal plane (Moiseff, 1989a,b; Von Campenhausen and Wagner, 2006). The importance of ITDs and ILDs for sound localization was demonstrated in behavioral studies with virtual auditory stimuli replayed to the owls via headphones (Moiseff and Konishi, 1981; Saberi et al., 1998; Egnor, 2001; Poganiatz and Wagner, 2001; Poganiatz et al., 2001; Hausmann et al., 2009, 2010).

The inferior colliculus (IC) is a central processing unit through which almost all auditory information must pass before it can reach the more central nuclei in both mammals and birds (Caird, 1991; Covey and Carr, 2005). The correct anatomical term for the avian homolog of the IC is mesencephalicus lateralis dorsolis (MLd). In line with the owl literature since the study of Knudsen (1983), we shall use the term IC. Much more is known about the mammalian IC than the avian IC. On the other hand the barn owl IC shows some specializations that make it interesting for comparative studies on the anatomy and function of the auditory system. This review concentrates on the morphology

and physiology of the barn owl IC. While reviews on specialized issues are available (Wagner, 2004; Takahashi, 2010; Ashida and Carr, 2011), a comprehensive overview over the different aspect of computations in barn owl IC is missing. We shall introduce the auditory pathway and then describe the different sub-nuclei of the IC before we turn to the physiological response characteristics and the relevant computational steps in each sub-nucleus of IC.

THE AUDITORY PATHWAY

The auditory pathway of the barn owl corresponds to the general pathway found in birds. However, the nuclei are enlarged in size (Kubke et al., 2004; Guitiérez-Ibáñez et al., 2011). This holds especially for the IC. The IC is a major relay and processing station for acoustic information and two distinct projections emerge from its central nucleus (Arthur, 2005).

The sounds arriving at the two ears are first decomposed into frequency components at the basilar papilla of the cochlea (Köppl et al., 1993). This frequency decomposition creates narrow bandpass filters. The fibers of the 8th nerve receive input from auditory hair cells and send their axons to the cochlear nucleus. In birds, the cochlear nucleus consists of two parts: the laterally positioned nucleus angularis (NA) and the medially lying nucleus magnocellularis (NM) (see **Figure 1** for a scheme of the auditory pathway). Each auditory nerve fiber bifurcates into two main collaterals, one of which terminates in NA and the other in NM (Carr and Boudreau, 1991). Both the hair cells and the fibers of the 8th nerve are narrowly tuned to frequency. While the 8th nerve fibers carry information about both the timing and level of the stimulus, information about these two cues splits at the synapses between the 8th nerve fibers and the cells in the cochlear nuclei, so that the neurons of NA carry precise information about stimulus level while cells of NM carry precise information about stimulus timing (Sullivan and Konishi, 1984). In other words, the NA is the starting point of the so called intensity pathway, processing information to compute, and represent ILD, while NM is the first nucleus in the time pathway, processing information to compute and represent ITD (Moiseff and Konishi, 1983). Iso-ITD lines and iso-ILD lines do not run parallel, but are inclined to each other in three-dimensional space. Such a spatial outlay is equivalent to independence in mathematics. The two non-overlapping pathways guarantee independent processing. The information converges in the IC (Adolphs, 1993a), where the construction of a two-dimensional map of auditory space starts (Takahashi et al., 1984).

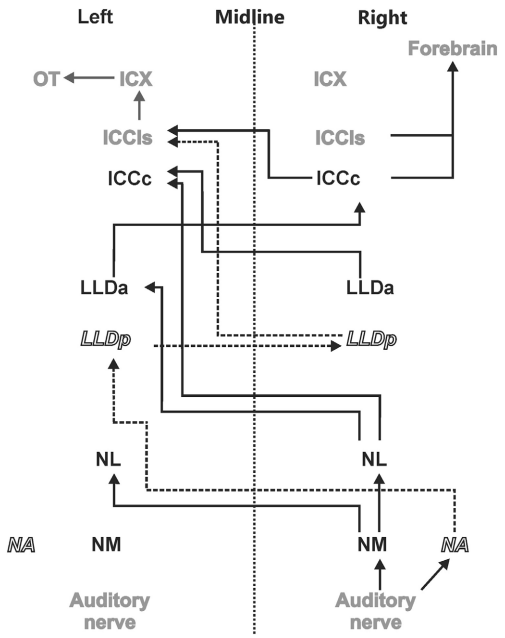

FIGURE 1 | Auditory pathway. The afferent auditory pathway is schematically illustrated starting from the auditory nerve upstream to the optic tectum (OT) where the auditory and visual maps merge. Nuclei mentioned in black transmit only ITD information (black solid lines) whereas nuclei indicated in white underlie processing of ILDs and their precursors only (dashed lines and italics). Nuclei shown in gray are involved in the processing of both ITD and ILD information.

Information about stimulus level is encoded in the spike rates of NA neurons that exhibit a large dynamic range (Sullivan and Konishi, 1984; Köppl and Yates, 1999). Information from NA reaches the contralateral dorsal lateral lemniscal nucleus pars posterior (LLDp, previously referred to as VLVp, **Figure 1**). Binaural interactions occur in LLDp and as a consequence, the response of the neurons varies with ILD. Timing information in NM is preserved by locking the temporal occurrence of action potentials to the stimulus phase (Sullivan and Konishi, 1984; Köppl, 1997b). Phase-locking in the barn owl occurs up to frequencies of about 9 kHz (Köppl, 1997a) or at least one octave higher than in other laboratory animals. NM projects to both ipsi- and contralateral nucleus laminaris (NL) (Takahashi and Konishi, 1988a,b). NL is, therefore, the first site in the auditory pathway where input from both hemispheres converges. The axons originating in NM form delay lines and contact arrays of coincidence detector neurons in NL (Carr and Konishi, 1988, 1990). The organization of NL is very similar to what was originally proposed by Jeffress (1948). Coincidence detector neurons fire maximally when information from both sides arrives simultaneously within a short time window. Because the delay lines compensate individual interaural delays in a space-dependent manner, information is converted from a time code into a place code in NL. Laminaris neurons project to both, the contralateral LLDa (previously referred to as VLVa) (Takahashi and Konishi, 1988b) and the core of the central nucleus of the IC (ICCc) (Moiseff and Konishi, 1983). Neurons in the ICCc project contralaterally to the lateral shell of the central nucleus of the IC (ICCls) (Takahashi et al., 1989), where the time and the intensity pathways converge (Adolphs, 1993b). From ICCls, information is sent ipsilaterally to the external nucleus of the IC (ICX), where so called space-specific neurons represent the location of a sound source (Knudsen and Konishi, 1978a) by their combined sensitivities to ITD and ILD. Space-specific neurons in the ICX are arranged in a topographic manner to create a two-dimensional map of auditory space.

From ICX the information is projected to the optic tectum (OT) where the auditory map merges with the visual map from the retina to create a multisensory map of space (Knudsen and Knudsen, 1983). This midbrain pathway (ICC-ICX-OT) is the pathway that subserves precise sound localization (Cohen and

Knudsen, 1999; Vonderschen and Wagner, 2009; Singheiser et al., 2010b). An additional pathway, the forebrain pathway, also originates in the ICC. ICC neurons project to the thalamic nucleus ovoidalis (NO) (Proctor and Konishi, 1997; Cohen and Knudsen, 1998; Arthur, 2005). Upstream of NO, information is further propagated to Field L (Cohen et al., 1998) and to the auditory arcopallium (AAr) (Cohen and Knudsen, 1995, 1998). In these nuclei, neurons show a broader frequency tuning than in ICX. Specifically frequencies below 3 kHz, which are missing in the midbrain pathway, are represented (Pérez and Peña, 2006; Pérez et al., 2009; Vonderschen and Wagner, 2009). No map of auditory space could be found in the forebrain (Cohen and Knudsen, 1995, 1996). ITD tuning curves are differently shaped and represent auditory space coarsely (Vonderschen and Wagner, 2009, 2012). Therefore, the forebrain pathway seems to be involved in coarse rather than precise sound localization.

THE MORPHOLOGY OF THE INFERIOR COLLICULUS

The IC and its subdivisions were originally described by Knudsen (1983). This author distinguished a central nucleus (ICC), an external nucleus (ICX), and a superficial (ICS) nucleus on the basis of their cyto- and myeloarchitecture as well as the connectivity and physiological response properties. By using different stainings (Nissl, Golgi, fiber, and myelin stains), Knudsen (1983) further subdivided the ICC into a dorsal and a ventral part, ICCd, and ICCv, respectively. However, no evidence for functional relevance of the latter differentiation has been found so far. Knudsen (1983) also noted that auditory information ascending from the lateral lemniscal nuclei exclusively enters the ICC, and not ICX or ICS.

In a different approach Takahashi and Konishi (1988a) used anterograde (tritiated [^{3}H]-proline) and retrograde [horseradish peroxidase (HRP)] labeling to uncover the projections of lower brainstem nuclei like NM, NL, and NA to the IC. Labeling of the rostral part of ICC was observed after injections of [^{3}H]-proline into NL. The horizontal level of labeled fibers depended on the injection site along the tonotopic axis of NL: when proline was injected in low best frequency regions of NL, the staining occurred in dorsal regions of ICC whereas proline injections in high frequency regions resulted in more ventral staining in ICC giving a hint of a tonotopy of frequencies that is maintained from NL to ICC (see Takahashi and Konishi, 1988a; their Figure 8). In contrast to the tonotopy, no evidence for topography could be found in ICC, when proline was injected at different dorso-ventral positions at similar antero-posterior positions of NL: the labeling in ICC was indistinguishable from each other. In retrospect it seems that these injections might have been too large, because it is now known that NL contains a map of ITD in its dorso-ventral extent (Sullivan and Konishi, 1986) that is reflected in an equivalent map in the antero-posterior direction in ICC (Wagner et al., 1987).

When Takahashi and Konishi (1988a) analyzed the labeling in ICC produced by injections of proline, they observed that the terminal field of NL in ICC forms a vertical "core" restricted to the rostral 40% of the ICC. Their core-region involved both the laminated as well as the non-laminated parts of ICC that were previously described by Knudsen (1983). Injecting the retrogradely transported HRP into the ICC resulted in labeled somata predominantly in NL. The sub-nucleus of the ICC that receives NL input was termed the ICCc.

When proline was injected into the NA of the owls, it was anterogradely transported to the contralateral ICC as well as to other brainstem nuclei like the contralateral LLDp (VLVp). [^{3}H]-proline labeling in ICC was present throughout the nucleus. While caudally the whole nucleus was labeled, from about 0.4 of the total length of IC in reference to the caudal pole, the labeled field split in two regions. Takahashi and Konishi termed this region the "shell" of the ICC (for further details see Takahashi and Konishi, 1988a, their Figure 13). Nowadays, the shell of the ICC is further divided into a medial shell (ICCms) and a lateral shell (ICCls) (Takahashi et al., 1989; Wagner et al., 2003). Takahashi and Konishi (1988a) demonstrated that the terminal fields of NA and NL seem to be largely non-overlapping, supporting the hypothesis that ITD (via NL to ICCc) and ILD (via LLDp to ICCls) were processed in parallel non-overlapping pathways.

A further study on the anatomy of the IC subdivisions and neighboring structures was carried out by Wagner et al. (2003). These authors used antibodies directed against several substances (e.g., tyrosine hydroxylase, γ-amino butyric acid $(GABA)_{A\beta}$, dopamine- and cyclic AMP regulated phosphor protein (DARPP-32), calretinin and calbindin) as well as somata staining with cresyl violet and fiber staining using the Gallyas procedure. Wagner et al. (2003) discriminated eight different structures belonging to the three IC subdivisions (ICC, ICX and ICS) as well as the neighboring OT. The periventricular tectal layers 15a and 15b could be well stained with all antibodies used in the study. All antibodies tested in the study sufficiently marked the boundary between the tectal layer 15a and the ICX. The DARPP-32 antibody caused much more darkly labeled somata in ICX than in ICCls. In addition Rodriguez-Contreras et al. (2005) demonstrated exclusive expression of calcium/calmodulin-dependent protein kinase II in ICX. Antibodies against calbindin and calretinin clearly marked the neurons of ICCc (**Figure 2**). None of the antibodies was sufficient to delineate the border between ICCls and ICCms.

THE CORE OF THE CENTRAL NUCLEUS OF THE INFERIOR COLLICULUS (ICCc)

TUNING PROPERTIES OF ICCc NEURONS

ITD tuning is observed across the entire dorso-ventral extent of ICCc (Wagner et al., 1987, 2002, 2007; Takahashi et al., 1989; Wagner and von Campenhausen, 2002; Bremen et al., 2007). The responses of the neurons in ICCc are phase ambiguous within the physiological range of ITDs (**Figure 3A**). This response pattern occurs to stimulation with both broadband noise as well as with pure tones. The heights of the peaks in the ITD tuning curve are all comparable. Thus, it is impossible to discriminate a main peak from the side peaks when information about only a single neuron is available (for a possible discrimination in the case of many neurons tuned to different frequencies, see below). Since all peaks have similar heights, side peak suppression does not occur in these neurons. The distance between the ITD peaks corresponds to about 1/best or characteristic frequency (BF/CF) for noise/pure tone stimulation (Wagner et al., 1987, 2002, 2007; Wagner, 1990; Fujita and Konishi, 1991). Due to this cyclic tuning with similar

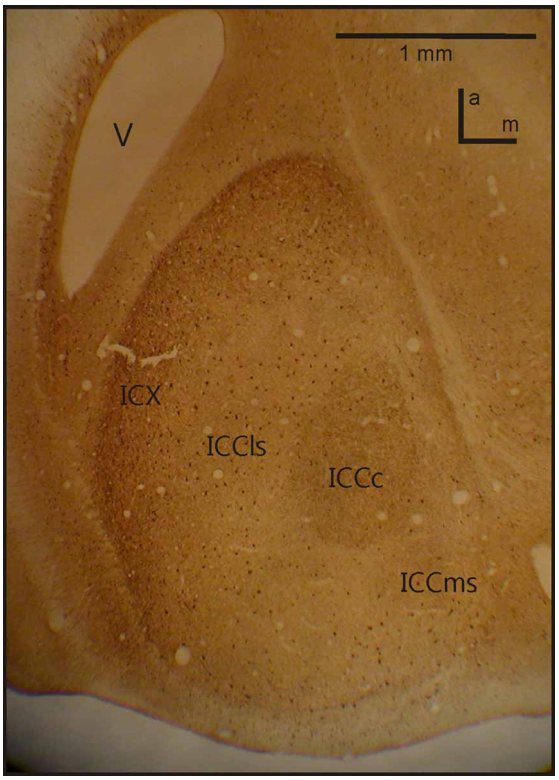

FIGURE 2 | IC anatomy. A horizontal section through IC with the four important sub-nuclei. Photograph from a staining with Calbindin. *V*, ventricle; *a*, anterior; *m*, medial.

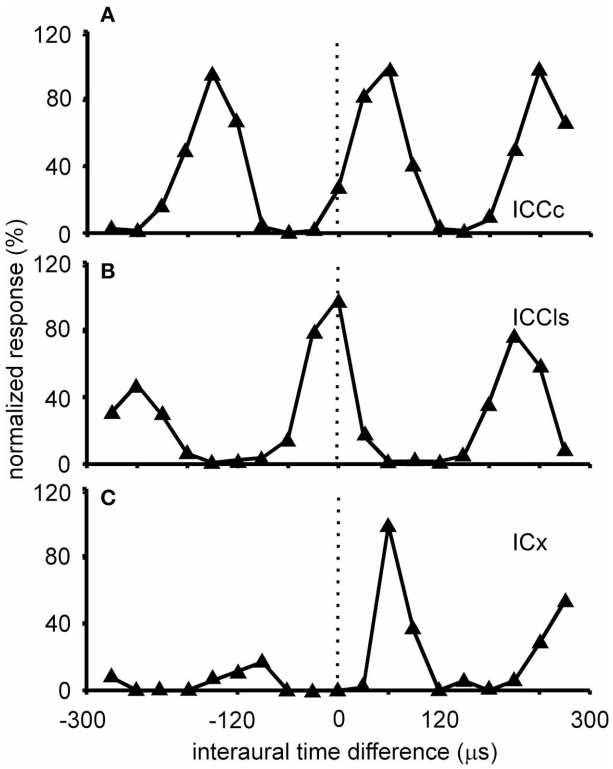

FIGURE 3 | ITD tuning. Shown are examples of the variations of the normalized responses with ITD of neurons located in different sub-nuclei of the IC. The stimulus for collecting these tuning curves was broadband noise. ITD tuning is periodic in the ICCc with the distance of the peaks reflecting the best frequency of the neuron **(A)**. All peaks have a similar height. A similar tuning is observed in the cells of the ICCls **(B)**. By contrast in the responses of the cells of the ICX one peak, the main peak, is clearly dominant compared to the other peaks, the side peaks **(C)**.

heights of the ITD peaks, ICCc neurons represent the phase difference between sounds arriving at the left and right ears. Since these phase differences correspond to more than one ITD, ICCc neurons show phase-ambiguity to ITD stimulation and cannot signal the azimuthal position of the sound source unambiguously. Note that this holds, although the mechanism underlying the detection of the phase difference is based on delays (Wagner, 2004; Ashida and Carr, 2011). The core of the ICC is tonotopically organized, with low frequencies represented in the dorsal region of the nucleus and high frequencies ventrally (Wagner et al., 1987, 2002, 2007; Takahashi et al., 1989). When electrode penetrations are made perpendicular to iso-frequency laminae in ICCc, recorded neurons share one common best ITD, the so called array-specific ITD. The array-specific ITD corresponds to the slope of the regression line in phase-frequency plots and represents ipsilateral locations in ICCc (Wagner et al., 1987, 2007). The array-specific ITD also corresponds to the main peak in the ITD tuning curve in most cases. Furthermore, array-specific ITDs are mapped and represent the entire auditory space of the barn owl (Wagner et al., 1987, 2007; Takahashi et al., 1989).

ITD coding in the IC of mammals differs from that observed in the IC of the barn owl (McAlpine et al., 2001; Wagner et al., 2002, 2007; Harper and McAlpine, 2004). In small mammals, the steepest slopes of many ITD curves cross 0 μs ITD, while this is not the case in the barn owl. Harper and McAlpine (2004) proposed a model of optimal ITD representation. According to this model, the representation of ITD depends on frequency. The representation above a frequency whose period is smaller than twice the physiological ITD range (about 2–2.5 kHz in the barn owl) is map-like. The experimental data collected from the high frequency region in the barn owl's IC are in agreement with this theory. By contrast, certain interaural phase differences are preferred for lower frequencies in the model. For example, the model did not produce any data points from −0.5 to −0.25 and +0.25 to 0.5 mean interaural phase difference in the low-frequency range. The data from ICCc in the low-frequency region show a distribution with a preference for 0 mean interaural phase difference (**Figure 4**). The similarity with the theoretical prediction is limited, if the plot shown in **Figure 4** is compared with the corresponding plot (Figure 2D) in the paper by Harper and McAlpine (2004). A two-dimensional cross-correlation between the model data and the experimental data revealed that not more than 20% of the data can be explained by the theory. This low explanatory power of the model seems to be mainly due to the existence of experimental data points from −0.5 to −0.25 and from 0.25 to 0.5 mean interaural phase difference which are absent in the model data. Additionally, best ITDs were observed that not only

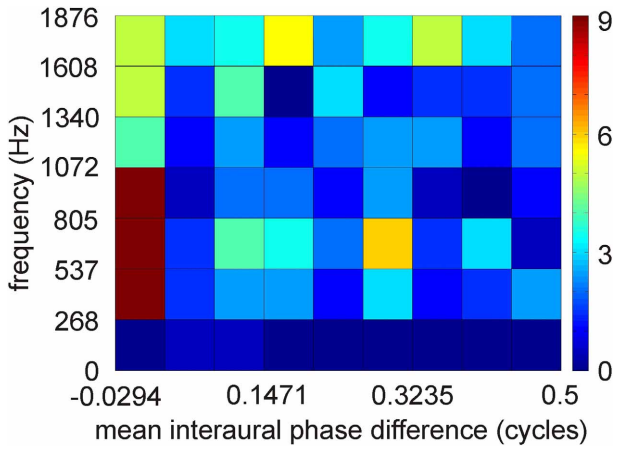

FIGURE 4 | Distribution of interaural phase difference in low-best frequency neurons of ICCc. Distribution of 251 data points. Interaural phase differences were calculated from interaural time differences by first restricting the mean interaural phase differences to a range from −0.5 to 0.5 cycles by phase wrapping and then take the absolute value. A binwidth of 0.0625 and of 268 Hz was chosen to make the data comparable to the model data of Harper and McAlpine (2004).

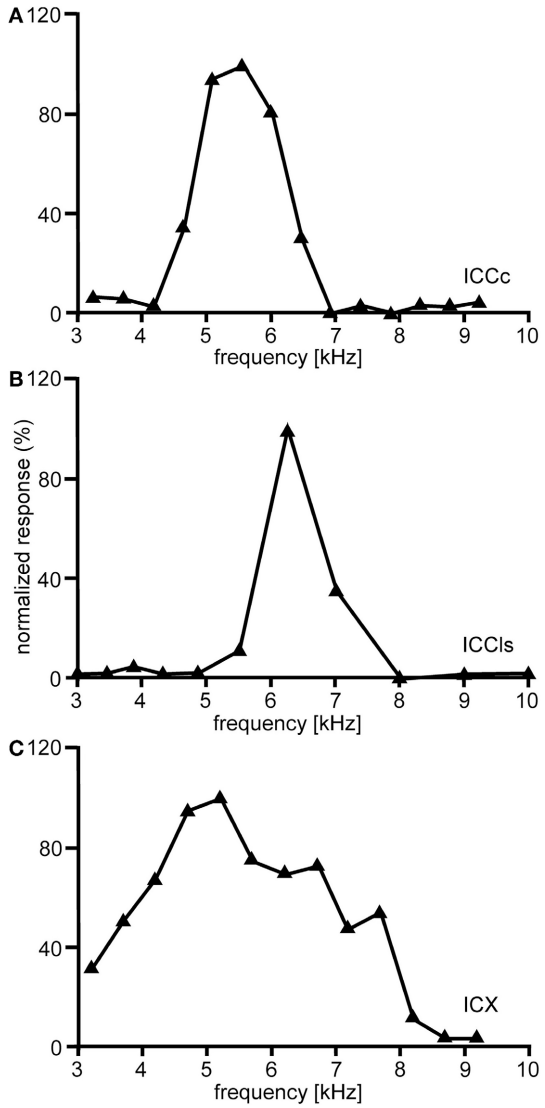

FIGURE 5 | Frequency tuning. Shown are examples of the variations of the normalized responses with frequency of neurons located in different nuclei of the IC. In ICCc frequency tuning is narrow **(A)**. A similar tuning is observed in the cells of ICCls **(B)**. By contrast frequency tuning of the cells of the ICX is broader than in ICC **(C)**.

lie outside the physiological ITD range (Wagner et al., 2002, 2007; Singheiser et al., 2010a) but also outside the so called π-limit (Wagner et al., 2007). The functional significance of the ITDs outside the physiological ITD range in the barn owl remains elusive. Neither the model of slope coding (McAlpine et al., 2001; Brand et al., 2002; Hancock and Delgutte, 2004; Harper and McAlpine, 2004; Siveke et al., 2006; Wagner et al., 2007) nor the stereausis model (Singheiser et al., 2010a) could account for these peaks.

The entire frequency spectrum of the barn owl's hearing range (0.2–12 kHz, Wagner et al., 2002, 2007) is represented in ICCc. Iso-intensity frequency tuning curves (hereafter referred as to frequency tuning curves) are typically symmetric and narrowly tuned ($Q_{10\,dB}$ = 1–14; Knudsen, 1984), single peaked with steep slopes on both the low- and high frequency flanks of the peak (**Figure 5A**). Frequency tuning widths measured at half-height of the frequency tuning curves are positively correlated with BF for both binaural (Wagner et al., 2002) and monaural stimulation. Nonetheless, the quality factor of frequency tunings (ratio of tuning width to BF) decreases with BF (Wagner et al., 2002). Generally, frequency tuning widths are on average one octave for neurons having BFs <1 kHz and about 1/3 octave for neurons having higher frequencies (Wagner et al., 2002). Moreover, no significant differences between BFs in the ipsi- and contralateral inputs of ICCc have been observed, at least for neurons in the low-frequency range (Singheiser et al., 2010a).

Further tuning characteristics of ICCc neurons will be mentioned briefly in the following. ILD tuning curves in ICCc are flat (**Figure 6A**), while rate-vs.-level functions (RLF) in ICCc are primary-like (Wagner et al., 2002; Bremen et al., 2007). Input to both the ipsi- and the contralateral ear excites ICCc neurons (EE property). Responses to ipsi- and contralateral stimulation do not differ in threshold, slope, dynamic range, or saturation level (Wagner et al., 2002).

CONNECTIVITY OF ICCc AND FURTHER PHYSIOLOGICAL PROPERTIES

The ICCc receives its inputs directly from the contralateral NL (Takahashi and Konishi, 1988a) and indirectly from the ipsilateral NL via the contralateral LLDa (Adolphs, 1993a). Whereas NL neurons require averaging of responses derived from multiple presentations for each ITD to arrive at a veridical representation (Christianson and Peña, 2006; Fischer and Konishi, 2008), in the ICCc a single presentation of ITD is sufficient for a reliable ITD response, showing a profound noise reduction in the ascending auditory pathway (Christianson and Peña, 2006). Phase-locking

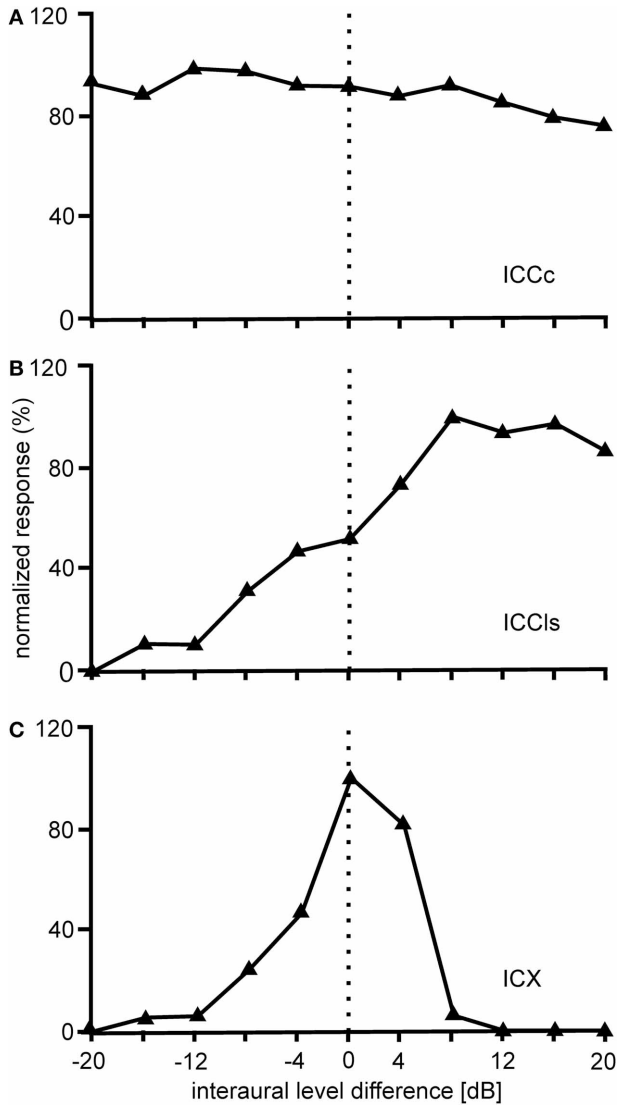

FIGURE 6 | ILD tuning. Shown are examples of the variations of the normalized responses with ILD of neurons located in different nuclei of the IC. The responses of ICCc cells do not vary with the interaural level difference (ILD) **(A)**. The ILD tuning of the cells in ICCls is sigmoidal **(B)**, while the ILD tuning in ICX is bell-shaped **(C)**.

is also dramatically reduced in the projection from NL to ICCc. This loss of fine temporal information in the ongoing spike train is replaced by envelope coding of the signal, preserving the temporal information of the ITD pathway in the temporally integrated responses (Christianson and Peña, 2007).

The ICCc has two ascending projections: one reaches the contralateral ICCls, endowing it with ITDs from the contralateral hemifield, as first shown by both retrograde (HRP) and anterograde (tritiated proline) labeling of neurons in ICCls and ICCc, respectively (Takahashi et al., 1989). As mentioned above, this projection is the beginning of the midbrain pathway that continues via ICX to the OT. The second projection goes upstream via the thalamic NO to higher order nuclei (Cohen et al., 1998; Arthur, 2005) and is the beginning of the forebrain pathway.

THE LATERAL SHELL OF THE CENTRAL NUCLEUS OF THE INFERIOR COLLICULUS (ICCLs)

TUNING PROPERTIES OF ICCLs NEURONS

Responses of ICCls neurons to varying ITDs are generally comparable to those recorded in ICCc: when stimulated either with pure tones or broadband noise, neurons in ICCls show a cyclic tuning, where the side peaks are almost as high as the main peak. Sidepeak suppression with broadband stimulation is absent or very weak (Gold and Knudsen, 2000) (**Figure 3B**). Thus, the responses are phase ambiguous. This phase-ambiguity occurs irrespective of stimulus bandwidth, due to the narrow frequency tuning curves in ICCls. Furthermore, the distance between the peaks is again characterized by integer multiples of the best frequency (Wagner et al., 1987, 2007; Wagner, 1990; Fujita and Konishi, 1991; Bremen et al., 2007). In contrast to ICCc, however, where the array-specific ITD represents ipsilateral locations, array-specific ITDs in ICCls represent locations in contralateral space (Wagner et al., 1987, 2007; Takahashi et al., 1989).

The frequency tuning of the neurons in ICCls is similar to that seen in ICCc (compare **Figure 5A** with **Figure 5B**). Frequency-tuning width is narrow to intermediate (Takahashi and Konishi, 1986; Wagner et al., 1987, 2007). The width of frequency tuning curves varies both with best frequency (Wagner et al., 2002) and with the location within ICCls (Mazer, 1998). Neurons located more laterally have wider tuning than neurons located more medially. A clear tonotopy covering the entire frequency range of the barn owl is found in the dorso-ventral extension of ICCls. However, a smaller proportion of neurons in ICCls than in ICCc have best frequencies below 2.5 kHz (31.1% in ICCc and 17.4% in ICCls) and frequencies below 0.8 kHz were extremely rare (Wagner et al., 2007). As a consequence of missing very low best frequencies, the ITD range in ICCls is narrower than that in ICCc (750 μs vs. 1500 μs, respectively; Wagner et al., 2007).

The ICCls is the first station in IC where ILD information is present. ILDs from the contralateral LLDp are added (Takahashi and Konishi, 1988b; Takahashi and Keller, 1992; Adolphs, 1993b) to the ITD information ascending from the time pathway (**Figure 6B**). Data from Adolphs (1993a) suggested the presence of a bilateral ILD projection from LLDp to ICCls. Using pharmacological manipulations to increase or decrease the neural activity of LLDp, Adolphs (1993a) demonstrated that LLDp provides direct functional GABAergic inhibition to ICCls neurons. Tuning curves to varying ILDs in ICCls show a sigmoidal or open peaked characteristic favoring contralateral-ear louder ILDs (Adolphs, 1993a; Bremen et al., 2007). Monaural responses show an EI pattern: excitation to contralateral stimulation and inhibition to ipsilateral stimulation (Adolphs, 1993a; Wagner et al., 2002).

Auditory responses in the ICCls are mediated by a family of excitatory amino acid receptors of which the most prominent are NMDA and non-NMDA glutamate receptors. By applying the NMDA receptor antagonist 2-amino-5-phosphonovaleric acid (AP5) as well as the non-NMDA receptor antagonist 6-cyano-5-nitroquinoxaline-2,3-dione (CNQX), responses in ICCls could be altered: while AP5 reduced the stimulus-evoked responses significantly in only less than 50% of the recording sites, CNQX application strongly reduced responses in most ICCls sites

(Feldman and Knudsen, 1994). Thus, non-NMDA currents seem to mediate most auditory responses in ICCls.

OUTPUT PROJECTIONS OF ICCLs

The ICCls has two output targets (**Figure 1**). One projection parallels the thalamic output of ICCc neurons to NO and higher brain centers (Cohen et al., 1998; Arthur, 2005). The second projection reaches the ipsilateral ICX and serves to eliminate phase ambiguities and to compute the spatially restricted receptive fields of auditory neurons in ICX (Wagner et al., 1987).

THE EXTERNAL NUCLEUS OF THE INFERIOR COLLICULUS (ICX)

The responses of ICX neurons to pure-tone ITD stimulation are similar to those of the neurons in ICC, in that all response peaks have a similar height (Takahashi and Konishi, 1986; Fujita and Konishi, 1991; Wagner, 1993). However, when broadband noise is used as stimulus, the ITD tuning curve, although still cyclic, is characterized by a dominant main peak and smaller side peaks (Takahashi et al., 1984; Takahashi and Konishi, 1986; Wagner, 1990, 1993; Fujita and Konishi, 1991) (**Figure 3C**). In other words, strong sidepeak suppression is typically observed in these neurons when they are stimulated with broadband noise. In the ICX, ILD-tuning curves are generally bell shaped (Takahashi et al., 1984) (**Figure 6C**), and the values of the best ILDs span the range from about −15 to +15 dB. Frequency tuning is broader in ICX than in ICC (compare **Figure 5C** with **Figures 5A**,**B**) with $Q_{10\,dB}$ values of frequency tuning in ICX lying between 1 and 4 (Knudsen, 1984). Unlike in ICC, in the ICX there is almost no representation of best frequencies below 2.5 kHz (Knudsen and Konishi, 1978a; Mazer, 1998; Wagner et al., 2007). Monaural stimulation or binaurally uncorrelated stimulation elicits only weak responses in ICX neurons (Takahashi et al., 1984, 1989; Albeck and Konishi, 1995).

THE COMPUTATION OF AUDITORY SPACE—ELIMINATION OF PHASE AMBIGUITIES

To unambiguously represent the position of a sound source in the horizontal plane, phase ambiguities have to be eliminated. Both electrophysiological recordings in the barn owl's ICX (Mazer, 1998) and OT (Saberi et al., 1998) and behavioral experiments using head turning movements (Saberi et al., 1999) have demonstrated that the a signal bandwidth of at least 3 kHz is needed for an unambiguous signaling of the position of a sound source in azimuth. To do so, convergence of neurons tuned to different BFs onto a single neuron or a small cluster of neurons is required. This converging projection is realized at the synapses between ICCls and ICX: narrowly tuned ICCls neurons that respond to different BFs in a column of an array-specific ITD project onto single neurons located in ICX which consequently become broadly tuned to frequencies but signal the same best ITD (Takahashi and Konishi, 1986; Wagner et al., 1987). This frequency convergence enhances the response to the "true" position of the sound source compared with the responses to phase equivalent positions in a bandwidth-dependent manner; the broader the tuning, the higher sidepeak suppression (Mazer, 1998). However, this frequency convergence is not the only mechanism underlying sidepeak suppression. Peña and Konishi (2000) recorded intracellularly from space-specific neurons in ICX and found that the difference between the main and the side peaks is smaller in postsynaptic potentials than in spike counts. This finding led to the conclusion that ICX neurons themselves enhance side peak suppression when converting membrane potentials into spikes. A third factor in side peak suppression is GABAergic inhibition that acts on the side peaks and thus enhances the main side peak ratio (Fujita and Konishi, 1991; Albeck, 1997; Mori, 1997; Peña and Konishi, 2000, 2002). When GABAergic inhibition was blocked by the antagonist bicuculine methiodide, ICX neurons no longer signaled only the main ITD but also responded to its phase-equivalents (Fujita and Konishi, 1991).

SPACE-SPECIFIC NEURONS AND THE MAP OF AUDITORY SPACE

The existence of a physiological map of auditory space in IC was first demonstrated by Knudsen and Konishi (1978a). Using a combination of free field stimulation with moveable speakers and extracellular recordings in the barn owl's IC, these authors were able to demonstrate that neurons in the lateral region of the IC, today known as the ICX, responded only when the sound was within a well circumscribed region of auditory space. This spatial receptive field was later found to be defined by a best ITD and best ILD determining the horizontal and elevational position of the receptive field, respectively. The level of the stimulus had little effect on the location of a receptive field. These neurons were termed space-specific neurons. When Knudsen and Konishi (1978a) plotted the receptive fields of space-specific neurons on a globe it turned out that the receptive fields of neighboring units overlapped. Furthermore, when plotting the receptive fields of neurons sequentially recorded along a dorso-ventral penetration of the electrode the fields shifted in elevation from high to low. Elevational positions covered the vertical space spanning from +20° to −90°. Moreover, the receptive fields of space-specific neurons in the ICX shifted from frontal space in the rostral parts of ICX to far contralateral space in the caudal portions of the ICX. Thus, azimuthal space was mapped along the rostrocaudal axis of ICX while elevational space was mapped along the dorso-ventral axis. The frontal azimuthal space between ±20° was overrepresented (Knudsen and Konishi, 1978a,b). While the initial study was based on only one animal and only 19 neurons, many subsequent studies have confirmed the original finding (Wagner et al., 1987; Brainard and Knudsen, 1993; Hyde and Knudsen, 2000; DeBello et al., 2001; Bergan et al., 2005). In a further experimental study on the tuning characteristics in ICX, Takahashi et al. (1984) demonstrated the independence of timing and intensity cues to create space-specific neurons. When NA was silenced with lidocaine, ILD tuning curves of space-specific neurons in ICX were shifted, whereas ITD tuning curves remained stable. When NM was temporally knocked out, ITD tuning curves changed while ILD tuning curves remained unaltered. Furthermore, the best ITD was independent of the ILD of a stimulus (Takahashi et al., 1984; see **Figure 7** for an example). The same effect was found for ILD tuning curves recorded with different ITDs. In a third study on the organization of space-specific neurons and the encoding of auditory space in the barn owl's ICX, Knudsen and Konishi (1978c), again using free-field

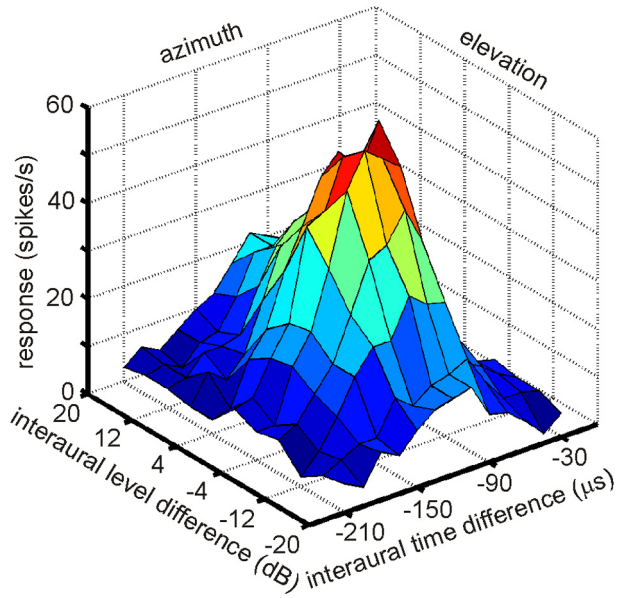

FIGURE 7 | A multiplicative receptive field of an ICX neuron. The response of this cell depends on ITD, which correlates with azimuth and on ILD, which correlates with elevation. Note that the responses in the two orthogonal directions, azimuth and elevation, are independent, because the shape of the curve of one parameter remains constant as the other parameter is changed. Only the height of the peak changes.

stimulation and extracellular recordings, reported "two functionally antagonistic areas": whereas the center of the receptive field was excitatory, the surround was inhibitory. The inhibitory surround of the receptive field was strongly dependent on the location of inhibition. The inhibitory surround was stronger for the azimuthal than the elevational direction which well matched the higher resolution of space-specific neurons in the horizontal plane.

The relevance of space-specific neurons for precise sound localization was demonstrated by small lesions in the auditory space map (Wagner, 1993). Head movements of three owls were recorded before and after lesioning. Whereas the head turns were precise before the lesions were made, head turns were not related to stimulus position after the lesions. The failures in precise head turns could be predicted by the azimuthal position of the lesion site in the space map.

More than 20 years after the first experiments by Knudsen and Konishi (1978a); Peña and Konishi (2001, 2002) as well as Fischer and colleagues (Fischer et al., 2007, 2009) investigated the computations underlying the creation of spatial receptive fields with intracellular recordings and mathematical models. Peña and Konishi (2001) asked how post-synaptic potentials of neurons carrying both ITD and ILD information interact to produce sub- and suprathreshold responses to certain combinations of ITD and ILD. They observed that some ITD-ILD combinations elicited suprathreshold depolarizing postsynaptic potentials whereas other combinations caused hyperpolarization. Such observations are in accordance with the reports of Knudsen and Konishi (1978c) of an excitatory center and an inhibitory surround of space-specific neurons. By careful analysis of the subthreshold responses, Peña and Konishi (2001) confirmed that the inputs of ITD and ILD onto an ICX neuron are independent of each other, consistent with the data of Takahashi et al. (1984). This independence is also obvious from the response profile shown in **Figure 7** in which the shape of ILD tuning is independent of the ITD and vice versa. Peña and Konishi (2001) also demonstrated that a multiplicative model for ITD/ILD integration fitted the postsynaptic potential data better than an additive model. Spiking thresholds changed gradually with ongoing stimulus presentation so that the thresholds for the first spikes were lower than those for later spikes. As a consequence, thresholding can sharpen the tuning over time, as had also been suggested by Wagner (1990). While these studies demonstrated that multiplicative processes take place in the integration of ITD and ILD information, they did not resolve where in the auditory pathway this is happens. Fischer and coworkers (2007) recorded extracellularly in ICCls. The majority of the responses (61%) were well described by the multiplicative model, suggesting that ICCls is the first nucleus where multiplicative responses occur. Under natural conditions, ILDs change in a frequency-specific manner, especially for high frequencies, while ITDs are largely frequency-independent (Coles and Guppy, 1988; Keller et al., 1998; Hausmann et al., 2010). Fischer et al. (2009) developed a model, which included natural listening conditions. These authors proposed that multiplication between ITD- and ILD-dependent signals only occurs within frequency channels, and that frequency integration is based on a linear-threshold mechanism. This mechanism allows the system to represent multiple sound sources with natural sound localization cues. The authors concluded that non-linear responses in the owl's IC can be generated by a combination of cellular and network mechanisms.

Bala et al. (2003) investigated the relationship between the barn owl's sound-localization acuity and the neuronal activity rates of space-specific neurons. The pupillary dilation response served as a criterion for behavioral acuity. The pupillary dilation response is a common response in all vertebrates elicited by events that deviate from the common input stream. The response to an auditory stimulus from a given location was habituated, before the stimulus changed location, resulting in an increase of the pupillary dilation response. The threshold value of the spatial change of a sound source that caused the pupillary dilation response to change was about 3°. The change of activity of the space-specific neurons reflected this threshold, leading to the conclusion that behavioral discrimination performance of the barn owl is realized by a change in the activity of a population of space-specific neurons in ICX.

SOUND LOCALIZATION IN ECHOIC ENVIRONMENTS—A POSSIBLE ROLE OF SPACE-SPECIFIC NEURONS

Under natural conditions, sounds directly arriving from a single source are generally followed by successive echoes from different locations in space. The system's ability to localize the leading but not the lagging sound is due to the so called precedence effect, meaning the leading sound dominates later arriving reflections of the sounds (for a review see Blauert, 1997). The Takahashi lab (Takahashi and Keller, 1994; Keller and Takahashi, 1996a,b, 2005;

Spitzer et al., 2003, 2004; Spitzer and Takahashi, 2006; Nelson and Takahashi, 2008, 2010) has investigated the precedence effect and the underlying mechanisms for precise sound localization in simulated echoic environments in the barn owl by using both behavioral paradigms and electrophysiological recordings. When identical sounds are presented simultaneously from two different positions in space, owls perceive a single sound source in the middle. This behavior is due to "summing localization" (Takahashi and Keller, 1994; Keller and Takahashi, 1996a). Under natural conditions the direct sound leads the echo by a few milliseconds. The leading sound dominates the perception responsible for precise sound localization; this effect is also known as localization dominance. As the delay between lead and lag increases, the lag can be more easily localized. The echo-threshold is defined as the minimal delay required for the perception of a lagging sound. Several studies in barn owls have shown that they turn their head toward leading sound source if the interval between lead and lag is shorter than 10 ms. When the delay between lead and lag increases, the number of head saccades to the lag increase (Keller and Takahashi, 1996b; Spitzer and Takahashi, 2006; Nelson and Takahashi, 2008), accompanied by a reduced ability to signal changes in the locations of simulated echoes (Spitzer et al., 2003). The neural basis for this behavior was found in the responses of the space-specific neurons of the ICX (Keller and Takahashi, 1996b; Spitzer et al., 2004; Nelson and Takahashi, 2008). Not only does the temporal segregation between two stimuli influence localization dominance, but also differences in frequency spectrum, amplitude modulations, and ILDs between the sound and its echoes play a role (Takahashi and Keller, 1994; Keller and Takahashi, 1996a, 2005; Nelson and Takahashi, 2008, 2010).

PLASTICITY IN THE BARN OWL'S INFERIOR COLLICULUS

Several studies have demonstrated that early auditory experience during sensitive periods of maturation has profound effects on the tuning properties of neurons to binaural stimuli like ITD and ILD. Manipulation of spatial cues was achieved by plugging one ear (Mogdans and Knudsen, 1992, 1993, 1994a,b), by implanting a passive filtering device in the ear canal (Gold and Knudsen, 1999, 2000; Miller and Knudsen, 2001, 2003) or by raising barn owls in broadband masking noise (Efrati and Gutfreund, 2011). After about two months of manipulation, the responses to ITD and ILD were recorded in different nuclei of the auditory pathway (ICC, ICX, OT, and NO) and compared to units recorded in control animals. All of the above manipulations induced large changes in the tuning to binaural cues in higher order nuclei [OT (Mogdans and Knudsen, 1992; Gold and Knudsen, 1999; Efrati and Gutfreund, 2011), ICX (Gold and Knudsen, 2000, 2001), NO (Miller and Knudsen, 2003)]. Noise rearing resulted in broader ILD and ITD tuning curves and atypical asymmetrical ILD tuning curves in the OT. Monaural ear-devices or earplugs resulted in frequency-specific changes in the patterns of binaural cues. Changes were in all cases in the adaptive direction, i.e., in the direction that compensates for the distorted spatial cues. For example, monaural occlusion led to shifts of the receptive field of space-specific neurons depending on the side of the earplug: when the left ear was plugged, receptive fields were shifted left- and downward (Knudsen and Konishi, 1980). Thus, space-specific neurons are shaped by experience allowing frequency specific compensation for individual differences as well as unexpected changes in the mapping between auditory cues and space.

In contrast to the large-scale changes of tuning curves found in the ICX, NO, and OT, ICC tuning curves were rather insensitive to the manipulations mentioned above. This suggested that the connections between the ICCls and the ICX are the site of experience-dependent plasticity. The ICCls-ICX projection is the pathway where information across frequency channels converges to create space-specific neurons. This connection is highly topographic in normal owls resulting in a mapped organization of ITDs in the ICX, which is further topographically relayed to the OT (Feldman and Knudsen, 1997; Knudsen and Knudsen, 1983).

The importance of the ICCls-ICX projections in experience-dependent plasticity has been best demonstrated by raising young barn owls with displacing prisms, which shift the visual field horizontally either to the left or to the right (Knudsen, 2002). Barn owls cannot move their eyes by more than a few degrees from their resting positions. Therefore, prisms produce a chronic discrepancy between visual and auditory spatial information. The immediate effect of prisms is an optical displacement of visual space but no effect on auditory space. As a result a mismatch occurs between the internal representation of auditory and visual space. Experience with the prism spectacles over a period of about two months, leads to a horizontal shift in auditory spatial tuning in the OT that realigns auditory receptive fields with the optically displaced visual receptive fields (Knudsen and Brainard, 1991). This is achieved by a systematic shift of ITD tuning curves.

In prism-reared owls, the auditory space map in the ICX was shifted as well as the tectal map (Brainard and Knudsen, 1993). In contrast, the representation of ITD in the ICCls remained normal (Brainard and Knudsen, 1993). This again pointed to the connection between the ICCls and the ICX as the site of plasticity. Indeed, changes in the anatomy of the axonal projections from the ICCls to the ICX have been observed (Feldman and Knudsen, 1997; DeBello et al., 2001). In prism reared owls the projection is asymmetrically broader than normal. Thus, as a result of prism experience, axons projecting from the ICCls are systematically shifted in the direction that supports the shift of the ITD tuning curves in the ICX (**Figure 8**).

Pharmacological experiments in prism-reared owls also demonstrated that the ICX is a site of plasticity. Excitatory transmission in the ICX is glutamatergic and relies heavily on NMDA receptor currents (Feldman and Knudsen, 1994). Blocking NMDA-receptors in the ICX selectively by focal application of the NMDA receptor blocker AP5 caused a reduction of about 50% of the normal auditory response. However, in owls that have been exposed to prisms, newly learned responses were far more sensitive to NMDA receptor blockade (Feldman et al., 1996). These data indicated that newly functional synapses in the ICX, supporting shifted responses, are richer in NMDA-receptors. On the other hand, in prism reared owls, responses to normal ITDs were far more suppressed by GABAergic inhibition in the ICX than newly learned responses (Zheng and Knudsen, 1999).

The plasticity of the auditory map in the ICX that is induced by the prism experience is an example of supervised learning, where

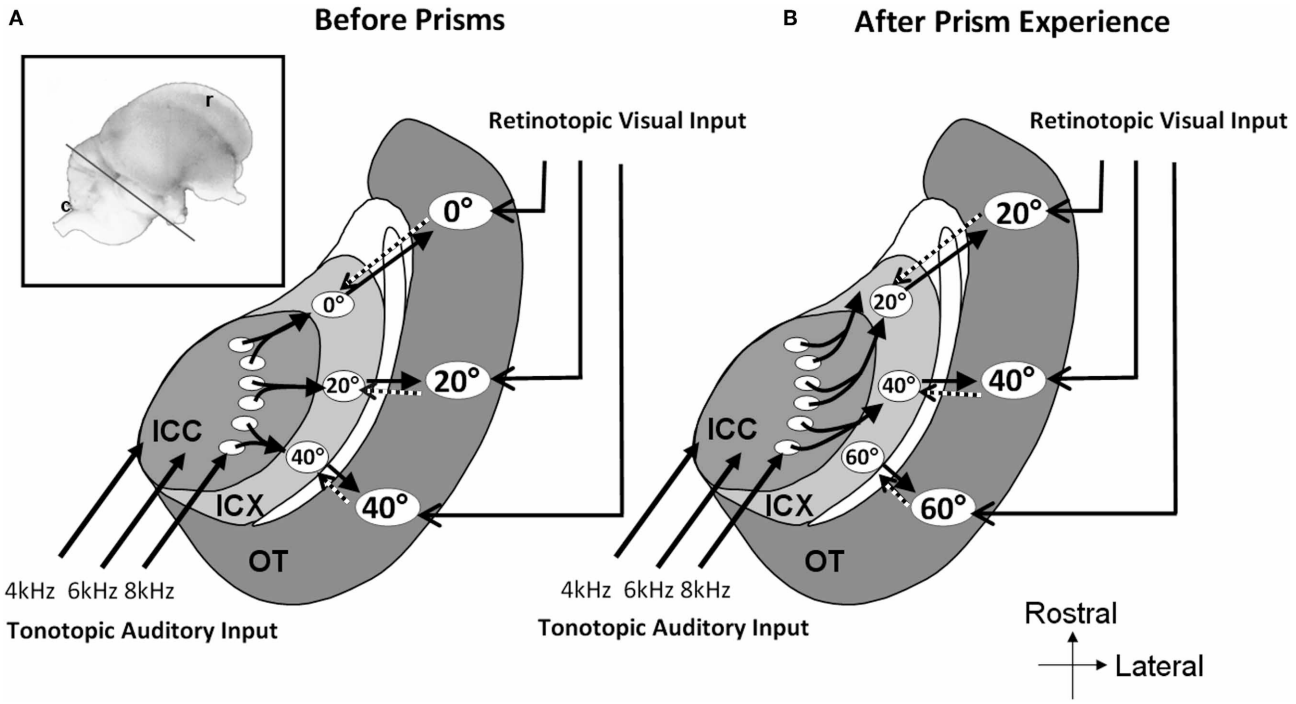

FIGURE 8 | Schematic representation of the mid-brain auditory localization pathway in normal and in prism-reared owls. The inset shows a lateral view of the barn owl's brain. The line marks the approximate plane of the section through the tectal lobe illustrated schematically in **A** and **B**. **(A)** Information flows from the central nucleus of the inferior colliculus (ICC) to the external nucleus of the inferior colliculus (ICX) and from there to the optic tectum (OT). A map of auditory space is created in ICX. This map joins the visual retinotopic map arriving from the retina and forebrain in OT. Topographic connections from the OT to the ICX presumably carry spatial visual information to instruct auditory plasticity in the ICX (dotted arrows). The circled numbers in the ICX and OT represent the azimuthal positions in space to which the neurons are tuned to. **(B)** Following a period of several weeks of prism adaptation the axonal connections between the ICC and the ICX grow in an abnormal pattern. Connections are shifted to the rostral direction in one side of the brain and to the caudal direction in the other side of the brain. This pattern of axonal re-growth shifts the auditory maps in the ICX and the OT to align with the shifted visual map.

a visually based instructive signal guides the plasticity (Gutfreund and Knudsen, 2004). The source of the instructive signal to the ICX is the OT (Hyde and Knudsen, 2002). The signal is presumably carried by feedback topographic connections from the OT to the ICX (Hyde and Knudsen, 2000; Luksch et al., 2000). Indeed, the activity of neurons in the ICX can be modulated by visual stimuli (Gutfreund et al., 2002; Bergan and Knudsen, 2009). The visual inputs to the ICX are however strongly gated by GABAergic inhibition in the OT (Gutfreund et al., 2002) and can only be elicited by salient visual stimuli (Bergan and Knudsen, 2009). Visual responses in the ICX are retinotopic and spatially restricted. This makes them ideally suited to provide a template for guiding auditory space representation to match visual space representation through Hebbian learning (Hyde and Knudsen, 2001; Gutfreund et al., 2002; Gutfreund and Knudsen, 2004; Witten et al., 2008). In addition, the highly gated nature of these visual inputs in the ICX is presumably necessary to prevent maladaptive overflow of visual information in the ICX.

The experience-dependent-plasticity in the ICX, as in many other systems, dominates the sensitive period at an early age (Knudsen and Knudsen, 1986; Knudsen, 1998). Prisms that were mounted in owls older than 200 days of age induced very little shifts in the ITD tuning curves of ICX neurons (Knudsen, 1998). More recent experiments, however, have shown that prism experience can modify the auditory space map in the ICX in adult owls. Linkenhoker and Knudsen (2002) demonstrated that incremental training, i.e., using small optical displacements and gradually stepping out, is a powerful strategy to elicit plasticity in adult ICX. A second strategy was to provide a richer sensory environment by allowing the prisms mounted owls to hunt live mice (Bergan et al., 2005). Plasticity was five times greater in the hunting owls compared to the control group that was fed with dead mice. Therefore, plasticity can be induced during adulthood as well, but to a smaller extent and it requires a richer and more rigorous sensory experience than in young owls. Analysis of the anatomical changes in the IC that accompany adult plasticity showed that the changes are similar to those accompanying plasticity in young owls suggesting that in the IC the same basic mechanisms of plasticity take place in adults as well as young owls (Linkenhoker et al., 2005).

CORRELATES OF RESPONSE ADAPTATION IN THE BARN OWL'S INFERIOR COLLICULUS

Two studies have investigated response adaptation in IC neurons. Gutfreund and Knudsen (2006) investigated same- and

across frequency adaptation using a double stimulus paradigm in IC neurons. Whereas same-frequency stimulation resulted in relatively strong adaptation of the second stimulus (probe) in reference to the first stimulus (masker), across-frequency adaptation could not be observed in ICCls. Singheiser et al. (2012) investigated response adaptation in ICC with a slightly different double-stimulus paradigm (**Figure 9**). Singheiser et al. (2012) found weaker response adaptation than Gutfreund and Knudsen (2006) that might be due to monaural stimulation versus binaural stimulation, respectively. The former authors determined the increase in the stimulus level of the probe that was necessary to overcome response adaptation. They found a value of <7 dB that depended on the overall stimulus level of the first stimulus (**Figure 9A**). Furthermore, by varying the interstimulus interval between first and second stimulus, recovery from adaptation could well be described by a double exponential fit with a fast (1.5 ms) and a slow component of 800 ms (**Figure 9B**). Wagner (1991) also found very short time constants (about 2 ms) when barn owls were tested to detect brief appearances of ITDs. Recovery functions of Gutfreund and Knudsen (2006) yielded time scales of about 100 ms intermediate between the two components obtained by Singheiser et al. (2012).

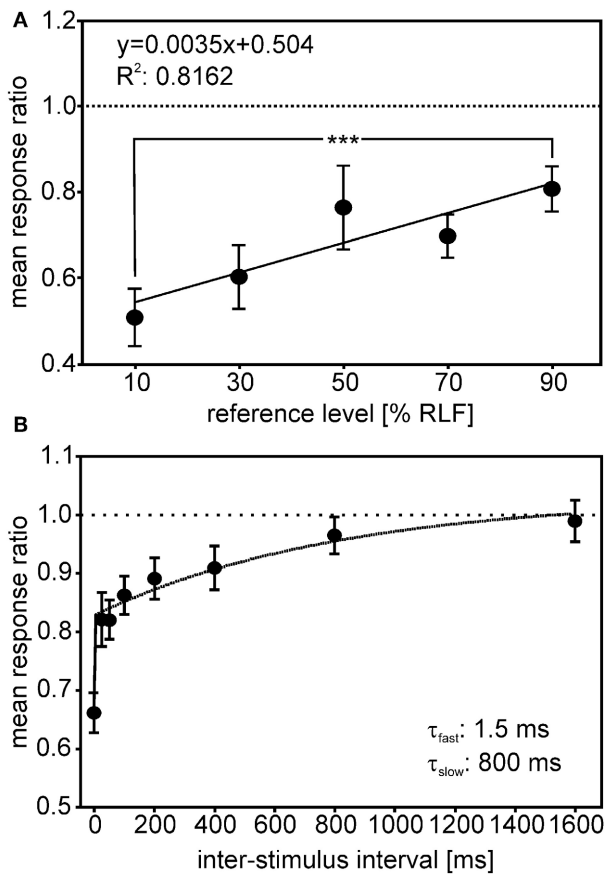

FIGURE 9 | Adaptation in ICC. The response ratio, defined as the quotient of the unit's response rate to a given probe (second stimulus), divided by the response rate of a particular reference-stimulus (first stimulus), is plotted. **(A)** The mean response ratios as a function of the relative reference-stimulus level. Probe and reference stimulus had the same level. The reference level refers to the dynamic range as determined from the rate-level function (RLF). The responses ratios decreased with decreasing reference level and differed significantly between 90 and 10% reference-stimulus level (Mann–Whitney test, $P < 0.0001$). **(B)** Responses ratios as a function of the interstimulus interval (ISI) tested. Response ratios were significantly reduced compared with unity for ISIs up to 400 ms (one-sample *t*-tests, all $P < 0.05$; significance levels are indicated as follows: $P < 0.05$: *; $P < 0.01$: **; $P < 0.001$: ***). The recovery function could be fitted well ($R^2 = 0.982$) by a double exponential with a short time constant of 1.25 ms and a long time constant of 800 ms (see inset in **B**).

Reches and Gutfreund (2008) investigated stimulus-specific adaptation in the auditory pathways of the owl by recording sequences of different stimuli (ITD, ILD, sound level, and frequency) in the ICX, the OT and the arcopallium gaze fields (AGF) in the forebrain. In an stimulus-specific adaptation paradigm, a standard stimulus is presented frequently in comparison to a deviant stimulus. The standard and the deviant stimulus are chosen from tuning curves such that they evoke the same response if they are presented at the same rate. It is tested whether neurons show higher response rates to the deviant than to the standard stimulus. By this context-dependent stimulation neurons involved in novelty-detection can be found. Neurons in ICX showed stimulus-specific adaptation only to frequency but not to the other cues, neurons recorded in OT displayed strong stimulus-specific adaptation to all four types of stimuli. The same was observed for neurons in AGF that were tested with the frequency and ITD cues. Reches and Gutfreund (2008) hypothesized that stimulus-specific adaptation is computed at least twice in the brain, once for frequency, at the level of the IC or below, and once for other auditory features at higher order nuclei. SSA to the frequency of the sound was also reported in the mammalian IC, mostly in broadly tuned units (Malmierca et al., 2009).

OUTLOOK

The barn owl IC has numerous adaptions linked to neural coding of sound location. In the past four decades many of the underlying morphological and functional specializations have been discovered. In this context, work on the barn owl's IC has often served as role model for studies in other systems. This holds specifically for the map of auditory space, and the role of the IC in plasticity, noise reduction, cross-frequency integration, and multiplicative interactions between orthogonal cues. On the other hand, research on owl IC has profited from both morphological and physiological progress made in studies with other birds and mammals. This include, for example, questions on the functional properties of ICS, the role of envelope, and carrier in responses to ITDs, as well as the function of adaptation in these neurons.

Interestingly, one of the hallmarks of processing in the barn owl's IC, the map of auditory space in ICX, has still not been clearly shown in mammalian IC. Early work by Binns et al. (1992) and Aitkin et al. (1985) suggested that the mammalian IC may contain a map. The significance of these findings remains unclear, however, because no one has followed up these findings. Also, potential homologies between the avian ICX and the mammalian ICX remain unresolved. For example, ICX in mammals contains somatosensory information (Aitkin et al., 1981), which has not been reported for barn owl ICX so far. The clearest evidence for

a map in the mammalian IC comes from the work of Schnupp and King (1997), which revealed a map of sound azimuth in the nucleus of the brachium of the IC. Since this nucleus projects topographically to the superior colliculus (King et al., 1998) and in turn receives information from the superior colliculus, the nucleus of the brachium of the IC has many functions analog to the owl ICX. In the pigeon a map of auditory space has been observed in ICX (Lewald, 1988). A map of ITD was found in chicken NL (Köppl and Carr, 2008). These maps are, however, not as sophisticated as the map in the barn owl. For example, the maps in the pigeon and the chicken are maps of azimuth and not of two-dimensional space as in the barn owl. Moreover, in other owl species such as the burrowing owl and the great-horned owl that are not as much adapted to live and hunt in the dark as the barn owl and do not exhibit ear asymmetry the elevational restrictions of receptive fields are less strict than in the barn owl or missing at all (Volman and Konishi, 1990). In this respect, the evolutionary pressure arising from hunting in the dark has shaped IC morphology and physiology in the barn owl.

Another interesting feature of barn owl IC is the existence of a lateral and a medial shell. Many regions have been detected anatomically in chicken IC (Puelles et al., 1994; Wang and Karten, 2010). However, it is not clear which, if any, corresponds to ICCls. To find out more about this, both morphological tracing studies and physiological characterization of these structures will be necessary. The same holds for ICCms. On the other hand, while the barn owl clearly has a superficial subnucleus, the physiological properties of the cells in this structure have not yet been studied.

For barn owl research itself, several challenging questions remain: one is whether the functional arrays that have been identified by subsequent recordings at many positions in dorsoventral penetrations indeed act in concert. Testing this would require the use of new techniques like multichannel-electrodes recordings. A second question relates to microcircuits: most cells have been quantified morphologically and by extracellular recordings, but intracellular characterizations of IC response properties are largely missing (for exceptions see Peña and Konishi, 2001, 2002) as is the precise synaptic interaction in all of the sub-nuclei. Here, working with slices might bring progress.

This brief review of the current knowledge about the barn owl IC was intended to summarize what is known about this structure, to point out its remarkable adaptation to a specific task, sound localization, and to mention briefly remaining issues. Much more work will be necessary to arrive at a broader and deeper understanding of the barn owl IC as is, for example, available for the mammalian IC.

REFERENCES

Adolphs, R. (1993a). Acetylcholinesterase staining differentiates functionally distinct auditory pathways in the barn owl. *J. Comp. Neurol.* 329, 365–377.

Adolphs, R. (1993b). Bilateral inhibition generates neuronal responses tuned to interaural level differences in the auditory brainstem of the barn owl. *J. Neurosci.* 13, 3647–3668.

Aitkin, L. M., Kenyon, C. E., and Philpott, P. (1981). The representation of the auditory and somatosensory systems in the external nucleus of the cat inferior colliculus. *J. Comp. Neurol.* 196, 25–40.

Aitkin, L. M., Pettigrew, J. D., Calford, M. B., Philips, S. C., and Wise, L. Z. (1985). Representation of stimulus azimuth by low-frequency neurons in inferior colliculus of the cat. *J. Neurophysiol.* 53, 43–59.

Albeck, Y. (1997). Inhibition sensitive to interaural time difference in the barn owl's inferior colliculus. *Hear. Res.* 109, 102–108.

Albeck, Y., and Konishi, M. (1995). Responses of neurons in the auditory pathway of the barn owl to partially correlated binaural signals. *J. Neurophysiol.* 74, 1689–1700.

Arthur, B. J. (2005). Distribution within the barn owl's inferior colliculus of neurons projecting to the optic tectum and thalamus. *J. Comp. Neurol.* 492, 110–121.

Ashida, G., and Carr, C. E. (2011). Sound localization: Jeffress and beyond. *Curr. Opin. Neurobiol.* 21, 745–751.

Bala, A. D. S., Spitzer, M. W., and Takahashi, T. T. (2003). Prediction of auditory spatial acuity from neural images on the owl's auditory space map. *Nature* 424, 771–774.

Bergan, J. F., and Knudsen, E. I. (2009). Visual modulation of auditory responses in the owl inferior colliculus. *J. Neurophysiol.* 101, 2924–2933.

Bergan, J. F., Ro, P., Ro, D., and Knudsen, E. I. (2005). Hunting increased adaptive auditory map plasticity in adult barn owls. *J. Neurosci.* 25, 9816–9820.

Binns, K. E., Grant, S., Withington, D. J., and Keating, M. J. (1992). A topographic representation of auditory space in the external nucleus of the inferior colliculus of the guinea pig. *Brain Res.* 589, 231–242.

Blauert, J. (1997). *Spatial Hearing. The Psychophysics of Human Sound Localization.* Cambridge, MA: The MIT Press.

Brainard, M. S., and Knudsen, E. I. (1993). Experience-dependent plasticity in the inferior colliculus: a site for visual calibration of the neural representation of auditory space in the barn owl. *J. Neurosci.* 13, 4589–4608.

Brand, A., Behrend, O., Marquardt, T., McAlpine, D., and Grothe, B. (2002). Precise inhibition is essential for microsecond interaural time difference coding. *Nature* 417, 543–547.

Bremen, P., Poganiatz, I., von Campenhausen, M., and Wagner, H. (2007). Sensitivity to interaural time difference and representation of azimuth in central nucleus of inferior colliculus of the barn owl. *J. Comp. Physiol. A Neuroethol. Sens. Neural Behav. Physiol.* 193, 99–112.

Caird, D. (1991). "Processing in the colliculi," in *Neurobiology of Hearing. The Central Auditory System,* eds R. A. Altschuler, R. P. Bobbin, B. M. Clopton, and D. W. Hoffman (New York, NY: Raven Press), 253–292.

Carr, C. E., and Boudreau, R. (1991). Central projections of auditory nerve fibers in the barn owl. *J. Comp. Neurol.* 314, 306–318.

Carr, C. E., and Konishi, M. (1988). Axonal delay lines for time measurement in the owl's brainstem. *Proc. Natl. Acad. Sci. U.S.A.* 85, 8311–8315.

Carr, C. E., and Konishi, M. (1990). A circuit for detection of interaural time differences in the brainstem of the barn owl. *J. Neurosci.* 10, 3227–3246.

Christianson, G. B., and Peña, J. L. (2006). Noise reduction of coincidence detector output by the inferior colliculus of the barn owl. *J. Neurosci.* 26, 5948–5954.

Christianson, G. B., and Peña, J. L. (2007). Preservation of spectrotemporal tuning between the nucleus laminaris and the inferior colliculus of the barn owl. *J. Neurophysiol.* 97, 3544–3553.

Cohen, Y. E., and Knudsen, E. I. (1995). Binaural tuning of auditory units in the forebrain archistriatal gaze fields of the barn owl: local organization but no space map. *J. Neurosci.* 15, 5152–5168.

Cohen, Y. E., and Knudsen, E. I. (1996). Representation of frequency in the primary auditory field of the barn owl forebrain. *J. Neurophysiol.* 76, 3682–3692.

Cohen, Y. E., and Knudsen, E. I. (1998). Representation of binaural spatial cues in field L of the barn owl forebrain. *J. Neurophysiol.* 79, 879–890.

Cohen, Y. E., and Knudsen, E. I. (1999). Maps versus clusters: different representations of auditory space in the midbrain and the forebrain. *Trends Neurosci.* 22, 128–135.

Cohen, Y. E., Miller, G. L., and Knudsen, E. I. (1998). Forebrain pathway for auditory space processing in the barn owl. *J. Neurophysiol.* 79, 891–902.

Coles, R. B., and Guppy, A. (1988). Directional hearing in the barn owl (*Tyto alba*). *J. Comp. Physiol. A* 163, 117–133.

Covey, E., and Carr, C. E. (2005). "The auditory midbrain in bats and birds," in *The Inferior Colliculus,*

eds C. Schreiner and J. A. Winer (New York, NY: Springer), 493–536.
DeBello, W. M., Feldman, D. E., and Knudsen, E. I. (2001). Adaptive axonal remodeling in the midbrain auditory space map. *J. Neurosci.* 21, 3161–3174.
Dyson, M. L., Klump, G. M., and Gauger, B. (1998). Absolute hearing thresholds and critical masking ratios in the barn owl: a comparison with other owls. *J. Comp. Physiol. A* 182, 695–702.
Efrati, A., and Gutfreund, Y. (2011). Early life exposure to noise alters the representation of auditory localization cues in the auditory space map of the barn owl. *J. Neurophysiol.* 105, 2522–2535.
Egnor, R. (2001). Effects of binaural decorrelation on neural and behavioral processing of interaural level differences in the barn owl (*Tyto alba*). *J. Comp. Physiol. A* 187, 589–595.
Feldman, D. E., Brainard, M. S., and Knudsen, E. I. (1996). Newly learned auditory responses mediated by NMDA receptors in the owl inferior colliculus. *Science* 271, 525–528.
Feldman, D. E., and Knudsen, E. I. (1994). NMDA and non-NMDA glutamate receptors in auditory transmission in the barn owl inferior colliculus. *J. Neurosci.* 14, 5939–5958.
Feldman, D. E., and Knudsen, E. I. (1997). An anatomical basis for visual calibration of the auditory space map in the barn owl's midbrain. *J. Neurosci.* 17, 6820–6837.
Fischer, B. J., Anderson, C. H., and Peña, J. L. (2009). Multiplicative auditory spatial receptive fields created by a hierarchy of population codes. *PLoS ONE* 4:e8015. doi: 10.1371/journal.pone.0008015
Fischer, B. J., and Konishi, M. (2008). Variability reduction in interaural time difference tuning in the barn owl. *J. Neurophysiol.* 100, 708–715.
Fischer, B. J., Peña, J. L., and Konishi, M. (2007). Emergence of multiplicative auditory responses in the midbrain of the barn owl. *J. Neurophysiol.* 98, 1181–1193.
Fujita, I., and Konishi, M. (1991). The role of GABAergic inhibition in processing of interaural time difference in the owl's auditory system. *J. Neurosci.* 11, 722–739.
Gold, J. I., and Knudsen, E. I. (1999). Hearing impairment induces frequency-specific adjustments in auditory spatial tuning in the optic tectum of young owls. *J. Neurophysiol.* 82, 2197–2209.
Gold, J. I., and Knudsen, E. I. (2000). Adaptive adjustment of connectivity in the inferior colliculus revealed by focal pharmacological inactivation. *J. Neurophysiol.* 85, 1575–1584.
Gold, J. I., and Knudsen, E. I. (2001). Adaptive adjustment of connectivity in the inferior colliculus revealed by focal pharmacological inactivation. *J. Neurophysiol.* 85, 1575–1584.
Guitiérez-Ibáñez, C., Iwaniuk, A. N., and Wylie, D. R. (2011). Relative size of auditory pathways in symmetrically and asymmetrically eared owls. *Brain Behav. Evol.* 78, 286–301.
Gutfreund, Y., and Knudsen, E. I. (2004). "Visual instruction of the auditory space map in the midbrain," in *The Handbook of Multisensory Processes*, eds G. Calvert, G. C. Spence, and B. E. Stein (Cambridge, MA: The MIT press), 613–624.
Gutfreund, Y., and Knudsen, E. I. (2006). Adaptation in the auditory space map of the barn owl. *J. Neurophysiol.* 86, 813–825.
Gutfreund, Y., Zheng, W., and Knudsen, E. I. (2002). Gated visual input to the central auditory system. *Science* 297, 1556–1559.
Hancock, K. E., and Delgutte, B. (2004). A physiologically based model of interaural time difference discrimination. *J. Neurosci.* 24, 7110–7117.
Harper, N. S., and McAlpine, D. (2004). Optimal neural population coding of an auditory spatial cue. *Nature* 430, 682–686.
Hausmann, L., Plachta, D. T. T., Singheiser, M., Brill, S., and Wagner, H. (2008). In-flight corrections in free-flying barn owls (*Tyto alba*) during sound localization tasks. *J. Exp. Biol.* 211, 2976–2988.
Hausmann, L., von Campenhausen, M., Endler, F., Singheiser, M., and Wagner, H. (2009). Improvements of sound localization abilities by the facial ruff of the barn owl (*Tyto alba*) as demonstrated by virtual ruff removal. *PLoS ONE* 4:e7721. doi: 10.1371/journal.pone.0007721
Hausmann, L., von Campenhausen, M., and Wagner, H. (2010). Properties of low-frequency head-related transfer functions in the barn owl (*Tyto alba*). *J. Comp. Physiol. A Neuroethol. Sens. Neural Behav. Physiol.* 196, 601–612.
Hyde, P. S., and Knudsen, E. I. (2000). Topographic projection from the optic tectum to the auditory space map in the inferior colliculus of the barn owl. *J. Comp. Neurol.* 421, 146–160.
Hyde, P. S., and Knudsen, E. I. (2001). A topographic instructive signal guides the adjustment of the auditory space map in the optic tectum. *J. Neurosci.* 21, 8586–8593.
Hyde, P. S., and Knudsen, E. I. (2002). The optic tectum controls visually guided adaptive plasticity in the owl's auditory space map. *Nature* 415, 73–76.
Jeffress, L. A. (1948). A place theory of sound localization. *J. Comp. Physiol. Psychol.* 41, 35–39.
Keller, C. H., Hartung, K., and Takahashi, T. T. (1998). Head-related transfer functions of the barn owl: measurement and neural responses. *Hear. Res.* 118, 13–34.
Keller, C. H., and Takahashi, T. T. (1996a). Binaural cross-correlation predicts the responses of neurons in the owl's auditory space map under conditions simulating summing localization. *J. Neurosci.* 16, 4300–4309.
Keller, C. H., and Takahashi, T. T. (1996b). Responses to simulated echoes by neurons in the barn owl's auditory space map. *J. Comp. Physiol. A* 178, 499–512.
Keller, C. H., and Takahashi, T. T. (2005). Localization and identification of concurrent sounds in the owl's auditory space map. *J. Neurosci.* 25, 10446–10461.
King, A. J., Jiang, Z. D., and Moore, D. R. (1998). Auditory brainstem projections to the ferret superior colliculus: anatomical contribution to the neural coding of sound azimuth. *J. Comp. Neurol.* 390, 342–365.
Knudsen, E. I. (1983). Subdivisions of the inferior colliculus in the barn owl (*Tyto alba*). *J. Comp. Neurol.* 218, 174–186.
Knudsen, E. I. (1984). Auditory properties of space-tuned units in the owl's optic tectum. *J. Neurophysiol.* 52, 709–723.
Knudsen, E. I. (1998). Capacity for plasticity in the adult owl auditory system expanded by juvenile experience. *Science* 279, 1531–1533.
Knudsen, E. I. (2002). Instructed learning in the auditory localization pathway of the barn owl. *Nature* 417, 322–328.
Knudsen, E. I., and Brainard, M. S. (1991). Visual instruction of the neural map of auditory space in the developing optic tectum. *Science* 253, 85–87.
Knudsen, E. I., and Knudsen, P. (1983). Space-mapped auditory projections from the inferior colliculus to the optic tectum in the barn owl (*Tyto alba*). *J. Comp. Neurol.* 218, 187–196.
Knudsen, E. I., and Knudsen, P. (1986). The sensitive period for auditory localization in barn owls is limited by age, not by experience. *J. Neurosci.* 6, 1918–1924.
Knudsen, E. I., and Konishi, M. (1978a). A neural map of auditory space in the owl. *Science* 200, 795–797.
Knudsen, E. I., and Konishi, M. (1978b). Space and frequency are represented separately in auditory midbrain of the owl. *J. Neurophysiol.* 41, 870–884.
Knudsen, E. I., and Konishi, M. (1978c). Center-surround organization of auditory receptive fields in the owl. *Science* 202, 778–780.
Knudsen, E. I., and Konishi, M. (1980). Monaural occlusion shifts receptive-field locations of auditory midbrain units in the owl. *J. Neurophysiol.* 44, 687–695.
Konishi, M. (1973a). How the owl tracks its prey. *Am. Sci.* 61, 414–424.
Konishi, M. (1973b). Locatable and nonlocatable acoustic signals for barn owls. *Am. Nat.* 107, 775–785.
Kubke, M. F., Masoglia, D. P., and Carr, C. E. (2004). Bigger brains or bigger nuclei? Regulating the size of auditory structures in birds. *Brain Behav. Evol.* 63, 169–180.
Köppl, C. (1997a). Frequency tuning and spontaneous activity in the auditory nerve and cochlear nucleus magnocellularis of the barn owl *Tyto alba*. *J. Neurophysiol.* 77, 354–377.
Köppl, C. (1997b). Phase locking to high frequencies in the auditory nerve and cochlear nucleus magnocellularis of the barn owl *Tyto alba*. *J. Neurosci.* 17, 3312–3321.
Köppl, C., and Carr, C. E. (2008). Maps of interaural time difference in the chicken's brainstem nucleus laminaris. *Biol. Cybern.* 98, 541–559.
Köppl, C., Gleich, O., and Manley, G. A. (1993). An auditory fovea in the barn owl cochlea. *J. Comp. Physiol. A* 171, 695–704.
Köppl, C., and Yates, G. (1999). Coding of sound pressure level in the barn owl's auditory nerve. *J. Neurosci.* 19, 9674–9686.
Lewald, J. (1988). Neuronal coding of azimuthal sound direction in the auditory midbrain of the pigeon. *Naturwissenschaften* 75, 470–472.
Linkenhoker, B. A., and Knudsen, E. I. (2002). Incremental training increases the plasticity of the auditory space map in adult barn owls. *Nature* 419, 293–296.
Linkenhoker, B. A., von der Ohe, C. G., and Knudsen, E. I. (2005). Anatomical traces of juvenile learning in the auditory system of adult barn owls. *Nat. Neurosci.* 8, 93–98.
Luksch, H., Gauger, B., and Wagner, H. (2000). A candidate pathway for a visual instructional signal to

the barn owl's auditory system. *J. Neurosci.* 20, RC70–RC74.

Malmierca, M. S., Cristaudo, S., Perez-Gonzalez, D., and Covey, E. (2009). Stimulus-specific adaptation in the inferior colliculus of the anesthetized rat. *J. Neurosci.* 29, 5483–5493.

Mazer, J. A. (1998). How the owl resolves auditory coding ambiguity. *Proc. Natl. Acad. Sci. U.S.A.* 95, 10932–10937.

McAlpine, D., Jiang, D., and Palmer, A. R. (2001). A neural code for low-frequency sound localization in mammals. *Nat. Neurosci.* 4, 396–401.

Miller, G. L., and Knudsen, E. I. (2001). Early auditory experience induces frequency-specific, adaptive plasticity in the forebrain gaze fields of the barn owl. *J. Neurophysiol.* 85, 2184–2190.

Miller, G. L., and Knudsen, E. I. (2003). Adaptive plasticity in the auditory thalamus of juvenile barn owls. *J. Neurosci.* 23, 1059–1065.

Mogdans, J., and Knudsen, E. I. (1992). Adaptive adjustment of unit tuning to sound localization cues in response to monaural occlusion in developing owl optic tectum. *J. Neurosci.* 12, 3473–3484.

Mogdans, J., and Knudsen, E. I. (1993). Early monaural occlusion alters the neural map of interaural level differences in the inferior colliculus of the barn owl. *Brain Res.* 619, 29–38.

Mogdans, J., and Knudsen, E. I. (1994a). Representation of interaural level difference in the VLVp, the first site of binaural comparison in the barn owl's auditory system. *Hear. Res.* 74, 148–164.

Mogdans, J., and Knudsen, E. I. (1994b). Site of auditory plasticity in the brain stem (VLVp) of the owl revealed by early monaural occlusion. *J. Neurophysiol.* 72, 2875–2891.

Moiseff, A. (1989a). Binaural disparity cues available to the barn owl for sound localization. *J. Comp. Physiol. A* 164, 629–636.

Moiseff, A. (1989b). Bi-coordinate sound localization by the barn owl. *J. Comp. Physiol. A* 164, 637–644.

Moiseff, A., and Konishi, M. (1981). Neuronal and behavioral sensitivity to binaural time differences in the owl. *J. Neurosci.* 1, 40–48.

Moiseff, A., and Konishi, M. (1983). Binaural characteristics of units in the owl's brainstem auditory pathway: precursors of restricted spatial receptive fields. *J. Neurosci.* 3, 2553–2562.

Mori, K. (1997). Across-frequency nonlinear inhibition by GABA in processing of interaural time difference. *Hear. Res.* 111, 22–30.

Nelson, B. S., and Takahashi, T. T. (2008). Independence of echo-threshold and echo-delay in the barn owl. *PLoS ONE* 3:e3598. doi: 10.1371/journal.pone.0003598

Nelson, B. S., and Takahashi, T. T. (2010). Spatial hearing in echoic environments: the role of envelope in owls. *Neuron* 67, 643–655.

Payne, R. S. (1962). How the barn owl locates prey by hearing. *Living Bird* 151–159.

Payne, R. S. (1971). Acoustic location of prey by barn owls (*Tyto alba*). *J. Exp. Biol.* 54, 535–573.

Peña, J. L., and Konishi, M. (2000). Cellular mechanisms for resolving phase ambiguity in the owl's inferior colliculus. *Proc. Natl. Acad. Sci. U.S.A.* 97, 11787–11792.

Peña, J. L., and Konishi, M. (2001). Auditory spatial receptive fields created by multiplication. *Science* 292, 249–252.

Peña, J. L., and Konishi, M. (2002). From postsynaptic potentials to spikes in the genesis of auditory spatial receptive fields. *J. Neurosci.* 22, 5652–5658.

Poganiatz, I., Nelken, I., and Wagner, H. (2001). Sound-localization experiments with barn owls in virtual space: influence of interaural time difference on head-turning behavior. *J. Assoc. Res. Otolaryngol.* 2, 1–21.

Poganiatz, I., and Wagner, H. (2001). Sound-localization experiments with barn owls in virtual space: influence of broadband interaural level difference on head-turning behavior. *J. Comp. Physiol. A* 187, 225–233.

Proctor, L., and Konishi, M. (1997). Representation of sound localization cues in the auditory thalamus of the barn owl. *Proc. Natl. Acad. Sci. U.S.A.* 94, 10421–10425.

Puelles, L., Robles, C., Martínez-de-la-Torre, M., and Martínez, S. (1994). New subdivision schema for the avian torus semicircularis: neurochemical maps in the chick. *J. Comp. Neurol.* 340, 98–125.

Pérez, M. L., and Peña, J. L. (2006). Comparison of midbrain and thalamic space-specific neurons in barn owls. *J. Neurophysiol.* 95, 783–790.

Pérez, M. L., Shanbhag, S. J., and Peña, J. L. (2009). Auditory spatial tuning in the crossroads of the midbrain and the forebrain. *J. Neurophysiol.* 102, 1472–1482.

Reches, A., and Gutfreund, Y. (2008). Stimulus-specific adaptation in the gaze control system of the barn owl. *J. Neurosci.* 28, 1523–1533.

Rodriguez-Contreras, A., Liu, X. B., and DeBello, W. M. (2005). Axodendritic contacts onto calcium/calmodulin-dependent protein kinase type II-expressing neurons in the barn owl auditory space map. *J. Neurosci.* 25, 5611–6622.

Saberi, K., Farahbod, H., and Konishi, M. (1998). How do owls localize interaurally phase-ambiguous signals. *Proc. Natl. Acad. Sci. U.S.A.* 95, 6465–6468.

Saberi, K., Takahashi, Y., Farahbod, H., and Konishi, M. (1999). Neural bases of an auditory illusion and its elimination in owls. *Nat. Neurosci.* 2, 656–659.

Schnupp, J. W., and King, A. J. (1997). Coding for auditory space in the nucleus of the brachium of the inferior colliculus in the ferret. *J. Neurophysiol.* 78, 2717–2731.

Singheiser, M., Ferger, R., von Campenhausen, M., and Wagner, H. (2012). Adaptation in the auditory midbrain of the barn owl (*Tyto alba*) induced by tonal double stimulation. *Eur. J. Neurosci.* 35, 445–456.

Singheiser, M., Fischer, B. J., and Wagner, H. (2010a). Estimated cochlear delays in low best-frequency neurons in the barn owl cannot explain coding of interaural time difference. *J. Neurophysiol.* 104, 1946–1954.

Singheiser, M., Plachta, D. T. T., Brill, S., Bremen, P., van der Willigen, R. F., and Wagner, H. (2010b). Target-approaching behavior of barn owls (*Tyto alba*): influence of sound frequency. *J. Comp. Physiol. A Neuroethol. Sens. Neural Behav. Physiol.* 196, 227–240.

Siveke, I., Pecka, M., Seidl, A. H., Baudoux, S., and Grothe, B. (2006). Binaural response properties of low-frequency neurons in the gerbil dorsal nucleus of the lateral lemniscus. *J. Neurophysiol.* 96, 1425–1440.

Spitzer, M. W., Bala, A. D., and Takahashi, T. T. (2003). Auditory spatial discrimination by barn owls in simulated echoic conditions. *J. Acoust. Soc. Am.* 113, 1631–1645.

Spitzer, M. W., Bala, A. D., and Takahashi, T. T. (2004). A neuronal correlate of the precedence effect is associated with spatial selectivity in the barn owl's auditory midbrain. *J. Neurophysiol.* 92, 2051–2070.

Spitzer, M. W., and Takahashi, T. T. (2006). Sound localization by barn owls in a simulated echoic environment. *J. Neurophysiol.* 95, 3571–3584.

Sullivan, W. E., and Konishi, M. (1984). Segregation of stimulus phase and intensity coding in the cochlear nucleus of the barn owl. *J. Neurosci.* 4, 1787–1799.

Sullivan, W. E., and Konishi, M. (1986). Neural map of interaural phase difference in the owl's brainstem. *Proc. Nat. Acam. Sci. U.S.A.* 83, 8400–8404.

Takahashi, T. T. (2010). How the owl tracks its prey – II. *J. Exp. Biol.* 213, 3399–3408.

Takahashi, T. T., and Keller, C. H. (1992). Commissural connections mediate inhibition for the computation of interaural level difference in the barn owl. *J. Comp. Physiol. A* 170, 161–169.

Takahashi, T. T., and Keller, C. H. (1994). Representation of multiple sound sources in the owl's auditory space map. *J. Neurosci.* 14, 4780–4793.

Takahashi, T. T., and Konishi, M. (1986). Selectivity for interaural time difference in the owl's midbrain. *J. Neurosci.* 6, 3413–3422.

Takahashi, T. T., and Konishi, M. (1988a). Projections of the cochlear nuclei and nucleus laminaris to the inferior colliculus of the barn owl. *J. Comp. Neurol.* 274, 190–211.

Takahashi, T. T., and Konishi, M. (1988b). Projections of nucleus angularis and nucleus laminaris to the lateral lemniscal nuclear complex of the barn owl. *J. Comp. Neurol.* 274, 212–238.

Takahashi, T. T., Moiseff, A., and Konishi, M. (1984). Time and intensity cues are processed independently in the auditory system of the barn owl. *J. Neurosci.* 4, 1781–1786.

Takahashi, T. T., Wagner, H., and Konishi, M. (1989). Role of commissural projections in the representation of bilateral auditory space in the barn owl's inferior colliculus. *J. Comp. Neurol.* 281, 545–554.

Volman, S. F., and Konishi, M. (1990). Comparative physiology of sound localization in four species of owls. *Brain Behav. Evol.* 36, 196–215.

Von Campenhausen, M., and Wagner, H. (2006). Influence of the facial ruff on the sound-receiving characteristics of the barn owl's ears. *J. Comp. Physiol. A Neuroethol. Sens. Neural Behav. Physiol.* 192, 1073–1082.

Vonderschen, K., and Wagner, H. (2009). Tuning to interaural time difference and frequency differs between the auditory arcopallium and the external nucleus of the inferior colliculus. *J. Neurophysiol.* 101, 2348–2361.

Vonderschen, K., and Wagner, H. (2012). Transformation from a pure time delay to a mixed time

and phase delay representation in the auditory forebrain pathway. *J. Neurosci.* 32, 5911–5923.

Wagner, H. (1990). Receptive fields of neurons in the owl's auditory brainstem change dynamically. *Eur. J. Neurosci.* 2, 949–959.

Wagner, H. (1991). A temporal window for lateralization of interaural time difference by barn owls. *J. Comp. Physiol. A* 169, 281–289.

Wagner, H. (1993). Sound-localization deficits induced by lesions in the barn owl's auditory space map. *J. Neurosci.* 13, 371–386.

Wagner, H. (2004). A comparison of neural computations underlying stereo vision and sound localization. *J. Physiol. Paris* 98, 135–145.

Wagner, H., Asadollahi, A., Bremen, P., Endler, F., Vonderschen, K., and von Campenhausen, M. (2007). Distribution of interaural time difference in the barn owl's inferior colliculus in the low- and high-frequency ranges. *J. Neurosci.* 27, 4191–4200.

Wagner, H., Güntürkün, O., and Nieder, B. (2003). Anatomical markers for the subdivisions of the barn owl's inferior collicular complex and adjacent peri- and subventricular structures. *J. Comp. Neurol.* 465, 145–159.

Wagner, H., Mazer, J., and von Campenhausen, M. (2002). Response properties of neurons in the core of the central nucleus of the inferior colliculus of the barn owl. *Eur. J. Neurosci.* 15, 1343–1352.

Wagner, H., Takahashi, T. T., and Konishi, M. (1987). Representation of interaural time difference in the central nucleus of the barn owl's inferior colliculus. *J. Neurosci.* 7, 3105–3116.

Wagner, H., and von Campenhausen, M. (2002). Distribution of auditory motion-direction sensitive neurons in the barn owl's midbrain. *J. Comp. Physiol. A Neuroethol. Sens. Neural Behav. Physiol.* 188, 705–713.

Wang, Y., and Karten, H. J. (2010). Three subdivisions of the auditory midbrain in chicks (*Gallus gallus*) identified by their afferent and commissural projections. *J. Comp. Neurol.* 518, 1199–1219.

Witten, I. B., Knudsen, E. I., and Sompolinsky, H. (2008). A Hebbian learning rule mediates asymmetric plasticity in aligning sensory representations. *J. Neurophysiol.* 100, 1067–1079.

Zheng, W., and Knudsen, E. I. (1999). Functional selection of adaptive auditory space map by $GABA_A$-mediated inhibition. *Science* 284, 962–965.

Conflict of Interest Statement: The authors declare that the research was conducted in the absence of any commercial or financial relationships that could be construed as a potential conflict of interest.

Received: 04 April 2012; accepted: 21 June 2012; published online: 11 July 2012.

Citation: Singheiser M, Gutfreund Y and Wagner H (2012) The representation of sound localization cues in the barn owl's inferior colliculus. Front. Neural Circuits ***6****:45. doi: 10.3389/fncir.2012.00045*

frontiers in
NEURAL CIRCUITS

REVIEW ARTICLE
published: 26 July 2012
doi: 10.3389/fncir.2012.00048

The basic circuit of the IC: tectothalamic neurons with different patterns of synaptic organization send different messages to the thalamus

***Tetsufumi Ito*[1,2]* and *Douglas L. Oliver*[3]**

[1] *Department of Anatomy, Faculty of Medical Sciences, University of Fukui, Eiheiji, Japan*
[2] *Research and Education Program for Life Science, University of Fukui, Fukui, Japan*
[3] *Department of Neuroscience, University of Connecticut Health Center, Farmington, CT, USA*

Edited by:
Manuel S. Malmierca, University of Salamanca, Spain

Reviewed by:
Nell B. Cant, Duke University, USA
Edward L. Bartlett, Purdue University, USA

***Correspondence:**
Tetsufumi Ito, Department of Anatomy, Faculty of Medical Sciences, University of Fukui, 23-3 Matsuoka-Shimoaizuki, Eiheiji, Fukui 910-1193, Japan.
e-mail: itot@u-fukui.ac.jp

The inferior colliculus (IC) in the midbrain of the auditory system uses a unique basic circuit to organize the inputs from virtually all of the lower auditory brainstem and transmit this information to the medial geniculate body (MGB) in the thalamus. Here, we review the basic circuit of the IC, the neuronal types, the organization of their inputs and outputs. We specifically discuss the large GABAergic (LG) neurons and how they differ from the small GABAergic (SG) and the more numerous glutamatergic neurons. The somata and dendrites of LG neurons are identified by axosomatic glutamatergic synapses that are lacking in the other cell types and exclusively contain the glutamate transporter VGLUT2. Although LG neurons are most numerous in the central nucleus of the IC (ICC), an analysis of their distribution suggests that they are not specifically associated with one set of ascending inputs. The inputs to ICC may be organized into functional zones with different subsets of brainstem inputs, but each zone may contain the same three neuron types. However, the sources of VGLUT2 axosomatic terminals on the LG neuron are not known. Neurons in the dorsal cochlear nucleus, superior olivary complex, intermediate nucleus of the lateral lemniscus, and IC itself that express the gene for VGLUT2 only are the likely origin of the dense VGLUT2 axosomatic terminals on LG tectothalamic neurons. The IC is unique since LG neurons are GABAergic tectothalamic neurons in addition to the numerous glutamatergic tectothalamic neurons. SG neurons evidently target other auditory structures. The basic circuit of the IC and the LG neurons in particular, has implications for the transmission of information about sound through the midbrain to the MGB.

Keywords: GABA, glutamate, local circuit, inferior colliculus

INTRODUCTION

The inferior colliculus (IC) is a hub of the auditory nervous system. It receives inputs from virtually all brainstem auditory nuclei and the auditory cortex, and it sends axons to the medial geniculate body (MGB). The basic neural circuit of the IC is defined by the different types of neurons, their inputs and their outputs, and they are the topic of our review.

A basic circuit for the IC should be composed of common components. Within each subdivisions of the IC, i.e., central nucleus (ICC), and the dorsal and lateral cortices (DC and LC), there may be common cellular components. However, the neuron types may be distributed in unequal proportions within each subdivision. Likewise, the inputs from specific afferent pathways may not terminate uniformly (Oliver et al., 2003; Cant and Benson, 2006; Loftus et al., 2010). There may be, however, patterns of input common to all of IC. Finally, the outputs of IC may come from neurons with different dendritic morphology, i.e., disc-shaped or stellate, but the differences in the dendritic morphology may not predict the pattern of projection (Oliver, 1984; Oliver et al., 1991). There may be other aspects of neurons that are better correlated with their axon targeting. These would be the components of the basic IC circuit.

NEURON TYPES IN THE IC

Neurons in the IC have been defined on the basis of dendritic morphology, neurotransmitter synthesis, and synaptic organization. Morphologically, two basic types of IC neurons have been identified in Golgi preparations. Disc-shaped (flat) neurons extend their dendrites parallel to the fibrodendritic laminae, while stellate (less flat) cells have spherical or elliptical dendritic fields that often cross the borders of fibrodendritic laminae (Oliver and Morest, 1984; Malmierca et al., 1993). This morphology may be important to shaping the inputs of the IC neuron and relevant to the frequency bandwidth of the response to sound. There are subtypes of neurons of different somatic and perikaryal size (see also Paloff et al., 1989). Paloff also has divided IC neurons into spiny and non-spiny varieties (Paloff et al., 1992), but there has

been little subsequent study of spine morphology or function in the IC.

The IC contains GABAegic and non-GABAergic neurons (Roberts and Ribak, 1987; Oliver et al., 1994; Merchan et al., 2005). Roughly 20–25% of the IC neurons are GABAergic (Oliver et al., 1994; Merchan et al., 2005). The remaining 75% are glutamatergic based on their expression of one of the vesicular glutamate transporters (VGLUT), specifically VGLUT2 (Ito et al., 2011). Disc-shaped and stellate cells can be GABAegic or non-GABAergic (Oliver et al., 1994). Thus, the dendritic morphology does not predict the neurotransmitter synthesis of the neuron. As we will see below, it also fails to predict the axonal target of the neuron. Therefore, a single morphological or neurochemical signature is insufficient to identify the neuron type in the IC. However, recent findings on the synaptic organization of GABAegic and non-GABAergic neurons appear to better distinguish different neuronal types that also can be identified with specific outputs, and this may clarify the neural circuit in which they are embedded.

IDENTIFICATION OF AXOSOMATIC INPUTS ON LARGE GABAergic NEURONS

Excitatory axosomatic inputs are seen on only a subpopulation of neurons, and this distinguishes them from other neuronal types in the IC. Glutamate, the main excitatory neurotransmitter in CNS, is loaded into synaptic vesicles by VGLUT (Takamori et al., 2000). Because these proteins are presynaptic, they are excellent markers for glutamatergic presynaptic axonal terminals. Three subtypes of VGLUT have been found (VGLUT1, VGLUT2, and VGLUT3) (Takamori, 2006). Of these, only VGLUT1 and VGLUT2 were found axonal terminals of the adult rat IC (Altschuler et al., 2008; Ito et al., 2009). Both VGLUT1 and VGLUT2 terminals are abundant throughout the neuropil of the IC and contact many dendrites. However, Altschuler and colleagues discovered that only VGLUT2-immunopositive terminals made dense contacts on the somata and proximal dendrites of a subpopulation of large IC neurons, while VGLUT1-positive terminals were only seen in the neuropil on dendrites (Altschuler et al., 2008).

The VGLUT2 axosomatic terminals are seen only on large GABAergic (LG) neurons, and they are absent on other cell types. Only neurons that were immunopositive for GAD67, a synthetic enzyme for GABA and a marker for GABAergic neurons, had VGLUT2 axosomatic endings (98.9% ± 0.34; mean ± S.D., $N = 3$; **Figure 1**). All LG neurons (diameter >16.5 μm) received VGLUT2 axosomatic endings, but small GABAegic (SG) neurons (diameter <10.7 μm) did not. The two types of GABAergic neurons overlapped at intermediate sizes. Nevertheless for simplicity, we will use the term LG to refer to GABAergic neurons with VGLUT2 axosomatic terminals and the term SG to refer to GABAergic neurons lacking those endings.

Samples of IC GABAergic neurons were collected with stereological methods (Ito et al., 2009), and the total population of LG and SG neurons was estimated (**Table 1**). There were 32,495 ± 4607 (mean ± S.D., $N = 4$) LG neurons in the IC out of 56,490 ± 7424 total GABAergic neurons. Thus, the ratio of LG to all GABAergic cells is 57.5% ± 1.5[1]. Since the IC is estimated to have 373,600 neurons (Kulesza et al., 2002), roughly 10% of IC neurons are the LG type. These results suggest that LG neurons are the largest group of GABAegic IC neurons and represent a substantial amount of the entire population of IC neurons.

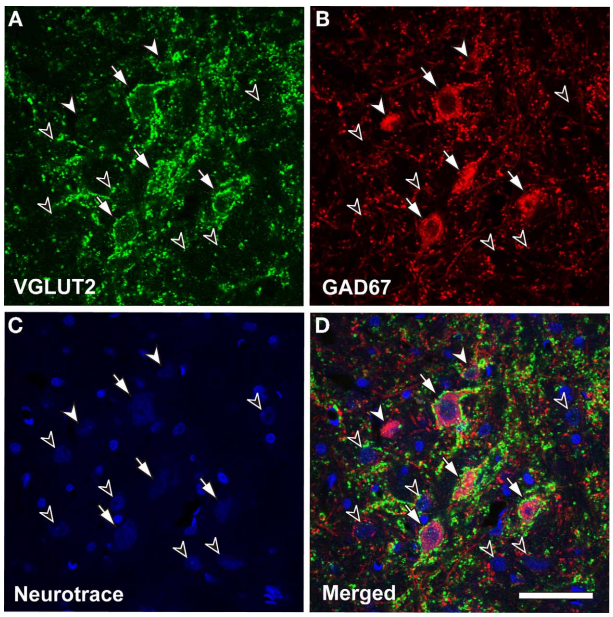

FIGURE 1 | Glutamatergic axosomatic terminals on large GABAegic (LG) neurons. VGLUT2-immunopositive terminals (**A**, green) make dense axodendritic and axosomatic contacts (**A**–**D**, arrows) on GAD67-immunopositive (**B**, red) LG neurons. Smaller GAD67-positive neurons (**A**–**D**, SG, white arrowheads) and GAD67-negative cells (**A**–**D**, black arrowheads) do not receive VGLUT2 axosomatic terminals. Neurotrace Nissl Stain (blue) is shown in **C**. Bar: 50 μm.

Table 1 | Stereological estimates of GABAergic neurons in the IC (mean ± S.D., $N = 4$).

Estimated number of all GABAergic neurons	56,490 ± 7424
Estimated number of LG neurons	32,495 ± 4607
Estimated number of SG neurons	23,995 ± 3032
Estimated number of IC neurons (Kulesza et al., 2002)	373,600

DISTRIBUTION OF LG NEURONS

LG neurons are found in all subdivisions of the IC, but the ratio of LG neurons to SG neurons differs between subnuclei. The proportion of LG to total GABAergic cells is higher in the ICC (73.2% ± 6.0*), lower in the cortices (DC: 51.4% ± 7.3*, LC: 47.7% ± 15.3*), and lowest (about 20%; calculated from non-stereological samples; Figure 5B of Ito et al., 2009) in the GABA modules (Chernock et al., 2004) of the LC. This suggests that LG neurons are more important for the ICC functions than cortical functions.

[1]The ratio is slightly different from our previous result, which was obtained from montage of whole IC image (Figure 5B of Ito et al., 2009) but was not stereological. The new ratio was calculated from stereological samples (Figure 4 of Ito et al., 2009).

The density of each class of GABAergic neuron in the IC was calculated for each subdivision (Figure 5B of Ito et al., 2009) (**Table 2**). LG neurons have the highest density in the ICC; however, there was no significant difference in the density in most other subdivisions. The exception was layer 1 of the LC that has significantly fewer LG neurons than the ICC ($P = 0.0012$, Tukey's multiple comparison test). In contrast, the density of SG neurons was especially high in the GABA modules but very low in layer 1 of the LC. In the other subdivisions, there was no significant difference in the density of SG neurons. Thus, there is little difference in the density of LG and SG neurons for most IC subdivisions. The exceptions are LC layer 1 and the GABA modules that may have a local circuit that differs from most of the IC. Indeed, LC layer 1 and the GABA modules have GABAergic neurons that are distinguished by their phasic responses to current injection (Ono et al., 2005), and both receive strong corticofugal input (Chernock et al., 2004; Winer, 2005). Since the other subdivisions, i.e., ICC, DC, and layer 2&3 of LC, have a similar density of LG and SG neurons, they are likely to share a common local circuit with minor differences.

In the ICC, where LG cells are most numerous, the distribution of LG and SG neurons should not be clustered if the types of GABAergic neurons are not associated with specific inputs (see below). To assess the randomness of the distribution, we calculated Ripley's *L* function (Ripley, 1976) from the distribution of the two classes of GABAergic neurons in the ICC (Figure 5B of Ito et al., 2009, **Figure 2A**). The *L* function gives the mean number of neurons separated by a distance smaller than *h* per density standardized with *h*. If the neurons form clusters, the *L* function will be larger than the confidence limits, but the L function is smaller than the confidence limits when the cell bodies are homogeneously distributed. Within the confidence limits, the distribution of the cell bodies cannot be distinguished from a random distribution. When *h* is one or two times the diameter of the cell body, it suggests a local deviation of the distribution, but a larger *h* (several hundred micrometers) implies a global deviation in the distribution.

The distributions of both LG and SG neurons were estimated along the rostrocaudal axis of ICC. They were distributed randomly in the central part but less so in the rostral and caudal parts. In the central ICC, the distribution fell within the 95% confidence limits (left part of **Figures 2B,C**): we counted the number of times the *L* function exceeded the confidence limits at 10 evenly spaced points of *h* and found significant differences in only 0–3 points on average (**Table 3**). Even at the points where significance was detected, the difference between *L* functions and the confidence limit was very small (left part of **Figures 2B,C**). Therefore, we conclude that LG and SG GABAergic neurons are distributed randomly in the central ICC.

In contrast, in the rostral and caudal part of the ICC, *L* functions of LG neurons were significantly larger than the 95%

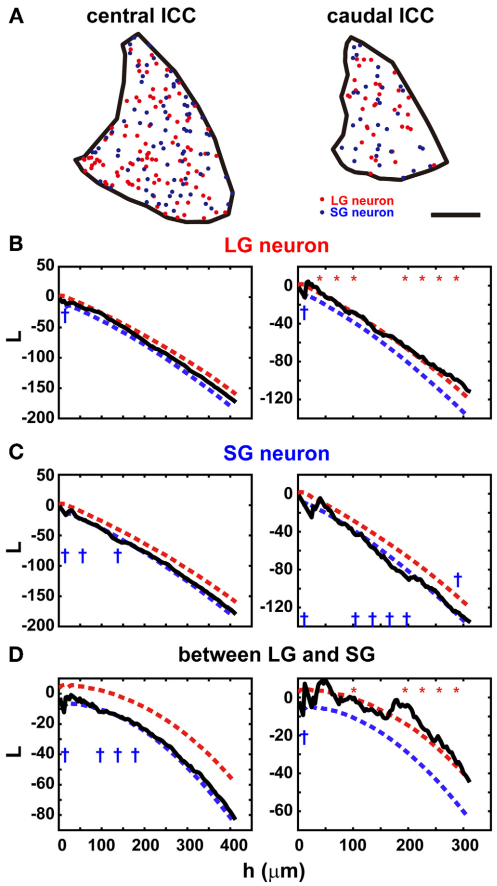

FIGURE 2 | Distribution in the ICC of two classes of GABAergic neurons. (A) Location of the cell bodies of LG neurons (red) and SG neurons (blue) in the ICC (black border). Left: center of the ICC. Right: caudal ICC. Note the sparse and clustered distribution in the caudal ICC. Scale bar: 400 μm. **(B)** The *L* function of LG neurons in the central ICC (left) and caudal ICC (right). Red and blue dotted lines are upper and lower limits of the 95% confidence interval, respectively. In the central ICC, the function falls primarily within the confidence limits, while in the caudal ICC, the function is slightly larger than the confidence interval. At 10 points of *h* evenly spaced, asterisks and daggers are shown if the function is larger or smaller than the confidence interval, respectively. **(C)** The *L* function of SG neurons in the central ICC (left) and caudal ICC (right). In the central ICC, the function falls within the confidence limits in the larger values of *h*. When *h* is smaller, the function falls below the confidence limit. In the caudal ICC, the *L* function is significant for larger values of *h*. **(D)** reciprocal *L* functions for two classes of GABAergic neurons in the central ICC (left) and caudal ICC (right). In the central ICC, the function is significant for only the smaller *h*. In the caudal ICC, the function is significantly at larger values of *h*.

Table 2 | Density of two classes of GABAergic neuron in IC subdivisions.

Subdivision	Density (counts/ mm^2)	
	LG	SG
Whole IC	29.5 ± 6.9	42.7 ± 8.8
ICC	54.5 ± 8.2^{A}	50.6 ± 13.8^{BH}
DC	30.9 ± 5.5	50.8 ± 12^{CG}
LC layer 1	0.5 ± 0.8^{A}	10.0 ± 6.1^{DFGH}
LC layer 2&3	33.3 ± 9.7	62.4 ± 4.3^{EF}
GABA modules	41.3 ± 32.3	164.5 ± 5.7^{BCDE}

$^{A}P = 0.012$; $^{BCDEF}P < 0.001$; $^{GH}P = 0.002$, Tukey's multiple comparison test.

Table 3 | Mean number of points detecting significance in *L* functions.

	Rostral and caudal ICC (6 sections)		Central ICC (8 sections)	
	Larger	Smaller	Larger	Smaller
LG neuron	6.3	2.7	1.4	1.1
SG neuron	2.2	3.5	0.3	2.9
Between LG and SG	4.0	2.8	0.8	2.3

For each L function, 10 points of h are examined for significance.

confidence interval (right part of **Figure 2B**; 5/6 sections, $N = 3$) over a large range of h values, and this suggests a clustered distribution for LG neurons. For SG neurons, the L functions were smaller than the 95% confidence interval in three of six sections over a wide range of h values. This suggests a more uniform distribution for SG cells. Although there is a possible clustering of LG neurons in the rostral and caudal ICC, fewer LG neurons are found in these regions (32.2% ± 4.9 of all GABAegic neurons) than in the central ICC. Therefore, the majority of LG neurons did not make clusters, and this implies that LG neurons are randomly distributed and available equally to all inputs to the ICC.

The two classes of neurons appear to be distributed independently of each other in the ICC (**Figure 2D**). In the rostral and caudal ICC, L functions were significantly larger than the confidence interval over a large range of h values (4/6 sections). This implies the two classes of GABAergic neurons tend to cluster together. In contrast, in the central ICC the L functions were usually within the confidence levels (left part of **Figure 2D**). Thus, in the central ICC where the cells are most numerous, the LG and SG neurons are independently distributed.

INPUTS TO THE IC

It is clear that the major subdivisions of IC receive different inputs. A basic circuit for the IC should be composed of common components (Oliver, 2005). Within the subdivisions of the IC, there may be further regional subdivisions, e.g., functional zones, in which axons from a subset of afferent sources dominantly the input (Oliver et al., 2003; Cant and Benson, 2006; Loftus et al., 2010). The detailed organization of the inputs to the IC is beyond the scope of this review. However, the concept of a basic circuit suggests that within each subdivision or functional zone, there may be some common cell types with a common pattern of synaptic input. This is the aspect of inputs we wish to consider.

ORIGINS OF EXCITATORY INPUTS TO THE IC

It appears that all IC neurons receive axodendritic synapses from glutamatergic sources. These may come from a variety of sources depending on the subdivision of IC or functional zone (see above). Only the LG neuron has axosomatic glutamatergic synapses. What is the source of these inputs? As noted above, there appears to be different types of glutamatergic input. Only VGLUT1 and VGLUT2 are present in the adult IC, but there are three patterns of VGLUT expression in axonal terminals: VGLUT1 only, VGLUT2 only, and a colocalization of both (Ito et al., 2009). Any of these patterns may be seen in axodendritic terminals, but the axosomatic terminals on LG neurons were only positive for VGLUT2 (97.1% ± 1.8). In order to identify the origin of the VGLUT2 axosomatic endings, the expression of VGLUT1 and VGLUT2 mRNA in neurons that project to the IC was used since the VGLUT proteins are seldom seen in the cell body of neurons.

In situ hybridization for VGLUT1 and VGLUT2 was performed in the auditory brainstem of the rat and mouse (Ito et al., 2011). Gene expression for these transporters was found in most brainstem centers including in the IC, the intermediate nucleus of the lateral lemniscus (INLL), the dorsal and ventral cochlear nuclei (DCN and VCN), and the superior olivary complex (SOC) including the lateral superior olive (LSO), medial superior olive (MSO), rostral periolivary (RPO), dorsal periolivary (DPO), lateroventral periolivary (LVPO), and ventromedial periolivary nuclei (VMPO) (**Figure 3**). Neurons expressing genes for VGLUT were absent or very sparse in the dorsal and ventral

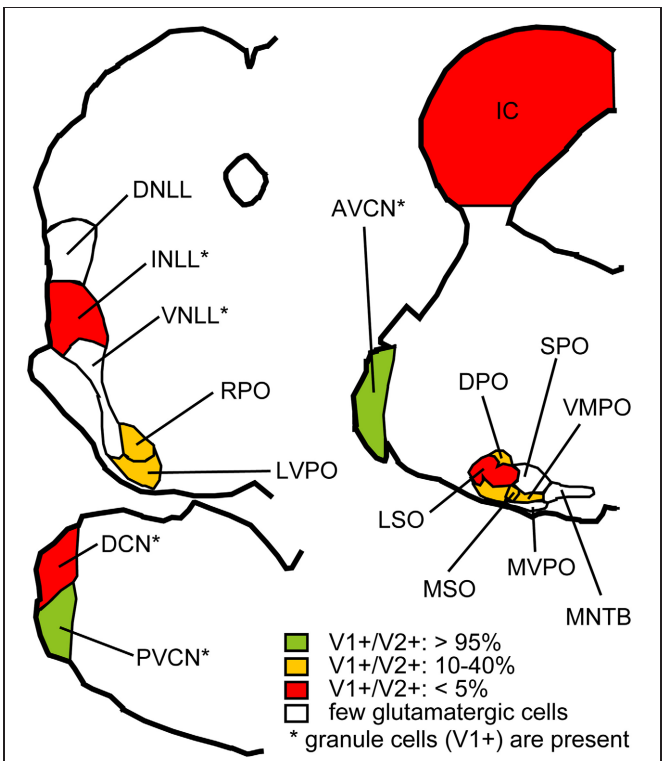

FIGURE 3 | Summary of VGLUT mRNA expression in the rat auditory brainstem. Red: Nuclei where less than 5% of glutamatergic neurons express both VGLUT1 and VGLUT2 and other glutamatergic neurons express VGLUT2 only. Green: Nuclei where more than 95% of glutamatergic neurons express both VGLUT1 and VGLUT2. Orange: Nuclei where 10–40% of glutamatergic neurons express both VGLUT1 and VGLUT2, and other glutamatergic neurons express VGLUT2 only. White: Nuclei with almost no glutamatergic neurons. Note that granule cells, expressing VGLUT1 only, are found in nuclei with asterisks, and excluded from analysis. Abbreviations: DNLL, dorsal nucleus of the lateral lemniscus; AVCN, anteroventral cochlear nucleus; PVCN, posteroventral cochlear nucleus; MVPO, medioventral periolivary nucleus; SPO, superior paraolivary nucleus; MNTB, medeial nucleus of the trapezoid body. For other abbreviations, see text. Modified from Ito et al. (2011).

nuclei of the lateral lemniscus (DNLL and VNLL), medial nucleus of the trapezoid body (MNTB), superior paraolivary nucleus, (SPO), and medioventral periolivary nucleus (MVPO).

Expression of VGLUT2 alone was the most common pattern, and a smaller number co-expressed VGLUT1 (**Figure 3**). Only a few cells expressed VGLUT1 alone, and these were confined to the granule cells in the cochlear nuclei, granule cells in the nuclei of the lateral lemniscus, and neurons in DPO and VMPO. The incidence of colocalization of VGLUT2 and VGLUT1 differed among nuclei. VGLUT2 was never colocalized in the IC. In the DCN, INLL, and LSO, co-expression of VGLUT1 and VGLUT2 was rare and in fewer than 5% of the glutamatergic neurons (**Figure 3**, red). In the DPO, LVPO, and MSO, more neurons co-expressed VGLUT1 (10–25%), and 30–40% of neurons in the RPO and VMPO co-expressed VGLUT1 (**Figure 3**, yellow). In the VCN, the vast majority of glutamatergic neurons (95%) expressed both VGLUT1 and VGLUT2 (**Figure 3**, green). Auditory cortex is also likely to be a source of VGLUT1 terminals since most cortical pyramidal neurons express only VGLUT1 (Fremeau et al., 2001; Herzog et al., 2001). Neurons with only VGLUT1 expression can be excluded from consideration as a source of the VGLUT2 axosomatic terminals on LG neurons.

PUTATIVE SOURCES OF EXCITATORY AXOSOMATIC INPUTS ON LG NEURONS

To test whether specific VGLUT-expressing cells project to the IC, we performed *in situ* hybridization for VGLUT1 and VGLUT2 combined with retrograde tracing (Ito and Oliver, 2010). After an injection of Fluorogold (FG), a fluorescent retrograde tracer, into the IC, retrogradely labeled neurons were found throughout the auditory pathways and cortex. Four patterns of VGLUT gene expression in FG-positive cells were found; (1) VGLUT1 only, (2) VGLUT2 only (For example, fusiform cells of the DCN; **Figure 4**), (3) co-expressed VGLUT1&2, and (4) no VGLUT expression. FG-positive cells expressing VGLUT1 alone were found only in the auditory cortex. Nuclei that had a substantial number of FG-positive cells expressing VGLUT are shown in **Figure 5**[2]. The most likely sources of the VGLUT2 axosomatic terminals on LG neurons (**Figure 5**, red) were the ipsilateral INLL, the contralateral LSO, the contralateral DCN, and the IC, since other nuclei have fewer neurons that express VGLUT2 only. These sources may also produce the numerous VGLUT2-positive terminals on dendrites in the IC.

OUTPUTS OF THE IC

TECTOTHALAMIC INHIBITORY NEURONS

One of the main outputs of the IC is the auditory thalamus, the MGB. Both disc-shaped and stellate cells project to the MGB (Oliver, 1984; Oliver et al., 1991). Some of the tectothalamic neurons are GABAergic (Winer et al., 1996). GABA-immunopositive neurons were labeled were found in all subdivisions of the IC after retrograde tracing from the MGB. In cats, GABAegic neurons comprised 20% ± 9 of the tectothalamic neurons in the ICC (mean ± S.D., $N = 5$, Winer et al., 1996) and a slightly higher

[2]For the scope of this review, we ignored FG-positive cells not expressing VGLUT from the original data of Ito and Oliver (2010).

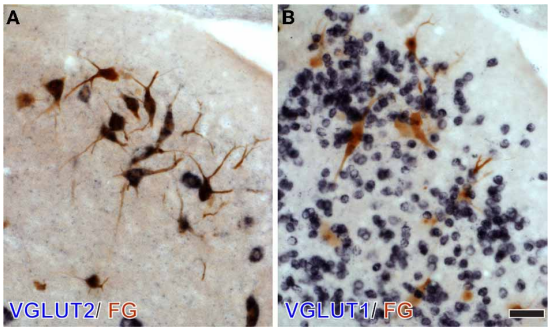

FIGURE 4 | DCN neurons projecting to the IC express VGLUT2 but not VGLUT1. After an injection of Fluorogold (FG) into the IC, large DCN neurons, presumably fusiform and giant cells, show immunoreactivity for FG (brown). Their cell bodies are positive for VGLUT2 mRNA (dark blue in **A**), and negative for VGLUT1 mRNA **(B)** Note that numerous granule cells express VGLUT1 only. Bar: 40 μm.

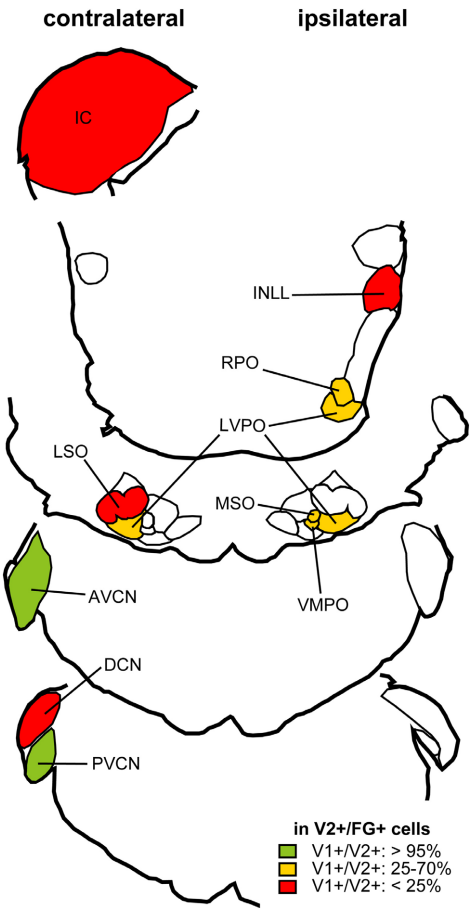

FIGURE 5 | Summary of distribution of retrogradely labeled glutamatergic cells after an injection of FG into the IC. Percentage of neurons positive for FG and VGLUT2 that co-localize VGLUT1 calculated from three cases. Nuclei that have more than 10 mean cell count of cells positive for both FG and VGLUT2 are shown. Red: Brainstem regions where fewer than 25% of cells express VGLUT1. Green: Nuclei where more than 95% cells express VGLUT1. Orange: Nuclei where 25–70% of retrogradely labeled cells co-expressed VGLUT1. Modified from Ito and Oliver (2010).

proportion in the cortices (LC: 20% ± 13, DC: 28% ± 12). In rats, the percentage was slightly higher (around 40% in the ICC and LC) except for the DC (20%, Peruzzi et al., 1997). These results suggest that a substantial amount of GABAergic tectothalamic neurons are found in all IC subdivisions and are the one of the output components of the IC's basic circuit.

LG NEURONS WITH AXOSOMATIC ENDINGS ARE TECTOTHALAMIC CELLS

GABAergic axons in the brachium of the IC have a larger diameter than non-GABAergic axons (Saint Marie et al., 1997). Semithin cross sections of the brachium of the IC immunostained for GABA revealed that GABAergic fibers had larger diameters than non GABAergic axons, and the largest axons (diameter $>4\,\mu m$) were exclusively GABA-immunopositive. The LG neurons are the most likely source for these LG axons. To determine whether LG neurons project to MGB, neurons in the IC were studied after retrograde labeling from the MGB (Ito et al., 2009). After injecting FG into the MGB, both LG and SG tectothalamic cells were identified by immunohistochemistry for GAD67, VGLUT2, and FG. The majority of the GABAergic tectothalamic neurons were LG neurons, and they encircled by VGLUT2-positive axosomatic endings (81.8% ± 12.4, 68.3% ± 7.6, and 75.1% ± 13.3 in ICC, DC, and LC, respectively). There were significantly fewer LG neurons in the GABA modules of the LC (40.3% ± 18.4) when compared to other subdivisions. Since the incidence of LG neurons was different between subdivisions, a "preference ratio" was calculated. The percentage of tectothalamic LG neurons to all tectothalamic GABAergic cells was divided by the percentage of LG neurons to all GABAergic neurons. In all subdivisions, the ratio was larger than 1.5 (1.56 in ICC, 1.87 in DC, 1.97 in LC, and 2.13 in GABA modules) and indicates that the LG neurons is the predominant GABAergic cell type in the projection from the IC to the MGB.

Although the majority of tectothalamic inhibitory neurons are the LG type, 20–30% of inhibitory projection was made by SG neurons. This suggests that there should be more variability in the IPSPs in the MGB. However, in brain slice experiments, the IPSPs had relatively uniform short latencies (Peruzzi et al., 1997) to suggest that inhibitory tectothalamic inputs to MGB are mainly LG inputs. Since relatively large injections of FG were made in the MGB, neurons sending axons to structures adjacent to the ventral division of the MGB could have been labeled. It is possible that some SG neurons project to non-lemniscal auditory thalamic nuclei or non-auditory nuclei in the neighborhood of the MGB such as the suprageniculate nucleus and posterior intralaminar nucleus.

TARGETS OF TECTOTHALAMIC INHIBITORY CELLS

Not all MGB neurons receive inhibitory inputs from the IC. Bartlett and Smith (2002) recorded responses of MGB neurons during stimulation of the brachium of the IC. MGB neurons that received a smaller amplitude and longer latency excitatory input were the recipient of tectothalamic inhibitory projections, while neurons with larger amplitude and shorter latency excitatory inputs were not. The former neurons are likely to be innervated by small axon terminals, and the latter are likely to be innervated by large terminals. This data suggests the presence of at least two types of tectothalamic excitatory neurons. One of these excitatory tectothalamic excitatory neurons may share the same target MGB neurons with the inhibitory tectothalamic neuron.

A second study mapped the origin of the inputs from the IC onto a single MGB neuron (Lee and Sherman, 2010). Not all MGB neurons received the tectothalamic inhibitory input. Inhibitory and excitatory tectothalamic neurons that share the same postsynaptic MGB neuronwere always topographically segregated. This suggests a large degree of tectothalamic convergence. Both studies demonstrated that both tufted and stellate neuron types in the MGB may receive the tectothalamic inhibitory input, while only tufted neurons sometimes lack the tectothalamic inhibitory input (Bartlett et al., 2000; Lee and Sherman, 2010).

BASIC CIRCUIT OF THE IC

Since LG neurons are found in all IC subdivisions and distributed randomly in the ICC (**Figure 2**), they are not likely to be embedded in specific pathways, and they may have a common function in the ICC and other parts of the IC. Accordingly, the basic circuit of the IC must contain at least three types of neurons that project from the IC to the MGB, the two types of glutamatergic neurons which make large and small EPSPs on the MGB cells and the LG neuron (**Figure 6**). SG neurons are less likely to project to MGB and may have other targets like the contralateral IC. With two types of glutamatergic input and one type of GABAergic input, the information transmitted by this circuit to the MGB will depend on how and when these different inputs are activated.

Since LG neurons are the largest IC neurons, they might be expected to be sluggish and have a longer latency than smaller IC cells. For example, they might have greater membrane capacitance to overcome before they fire. It is possible that the dense VGLUT2 axosomatic terminals may help the LG neurons overcome this capacitance and fire more quickly despite their large size. A recent *in vivo* study investigated the properties of visually identified neurons of different size in the dorsal IC cortex of mouse (Geis and Borst, 2011). The largest cells had a low input resistance. When responses were evoked by sound, the largest cells had short latency excitatory synaptic responses, and they fired action potentials with a short latency. The sound evoked excitatory input was often followed by longer latency inhibitory postsynaptic potentials. These data are consistent with the LG neuron as a source of short latency inhibitory input to the MGB.

Since an LG neuron is also likely to have an axon with a large diameter in the brachium of the IC (Saint Marie et al., 1997), its IPSP actually may arrive at the MGB before the EPSP from the glutamatergic IC neuron assuming these two IC neurons fire simultaneously. This was the finding after electrical stimulation of the brachium of the IC (Peruzzi et al., 1997). Therefore, the relative timing of action potentials in LG neurons and glutamatergic tectothalamic IC neurons will determine the signals arriving at the MGB.

If LG neurons are driven more by local glutamatergic IC sources than ascending afferent sources, the IPSPs produced by LG neurons may reach the MGB simultaneously or later than the EPSPs from glutamatergic IC neurons. A local or recurrent excitation of the LG neuron might erase the 2 ms lead time of the

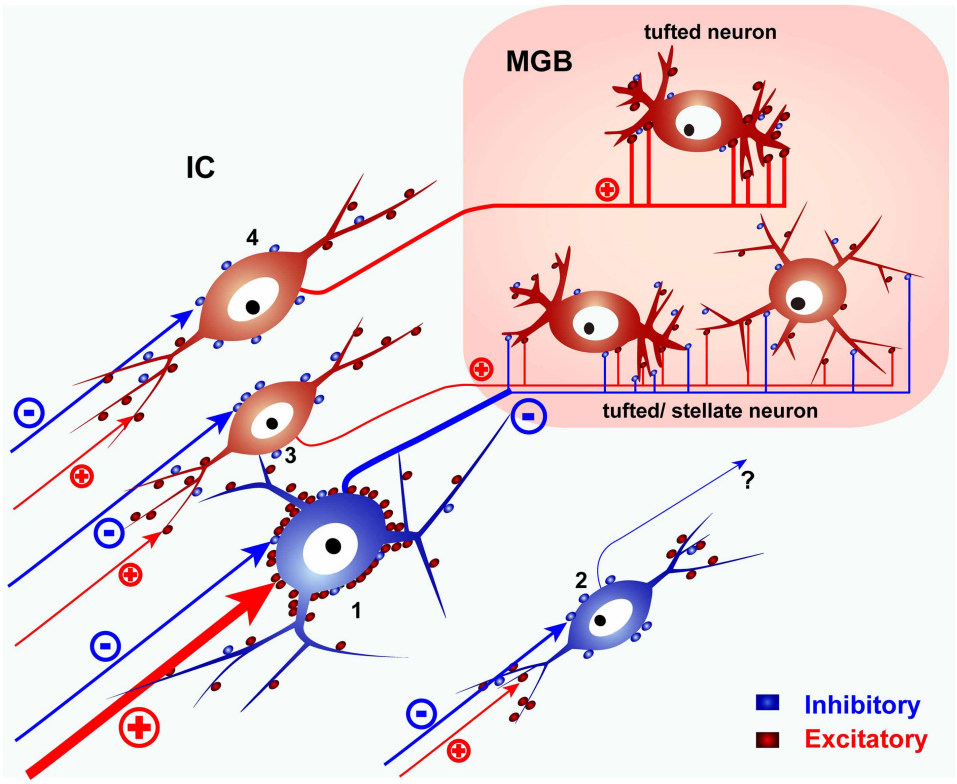

FIGURE 6 | A schematic diagram of the basic IC circuit. LG neurons (1) receive strong excitatory inputs on their somata, send their axons to the MGB, and presumably inhibit tufted or stellate neurons in the MGB. SG neurons (2) do not target MGB. Glutamatergic neurons (3, 4) project to the MGB but lack the dense VGLUT2 axosomatic inputs. Glutamatergic neurons with small terminals (3) co-innervate tufted or stellate neurons with LG neurons. Other tufted neurons are innervated by glutamatergic neurons with large terminals (4) and do not receive inputs from LG neurons. SG and glutamatergic neurons receive most of their excitatory inputs on their dendrites. Red puncta indicate excitatory glutamatergic terminals. Blue puncta indicate inhibitory (GABAergic and glycinergic) terminals. Modified from Ito et al. (2009).

IPSP over the EPSP after BIC shock (Peruzzi et al., 1997). In that case, the MGB neuron will receive almost simultaneous excitatory and inhibitory inputs, comparable to the triad synapses formed by glutamatergic inputs from IC and local GABAergic dendrites in the cat (Morest, 1971, 1975). In that synaptic arrangement, excitation is followed by very short latency inhibition.

Since rodents lack local GABAergic neurons in the MGB (Ito et al., 2011), one may suspect that the LG neurons are a compensatory mechanism in the rodent. However, LG neurons have been observed in Japanese macaque, marmoset, and rabbit where GABAergic neurons are present in the MGB (unpublished observations, Ito and Takada, 2011). Thus, the LG tectothalamic neurons in the IC may not be a rodent specialization but rather a fundamental neuron type in the IC. That may differentiate its role from that of the MGB triad synapse. LG neurons may receive more convergent input than the MGB triad. The LG neurons are the largest neurons in the IC, and they are likely to have a stellate dendritic field that promotes additional convergence especially in the DC and LC (Oliver et al., 1994). Additional convergence may be seen in the MGB (Lee and Sherman, 2010). In contrast, the triad synapse may have less convergence since the same IC afferent drives both excitatory afferent and the dendro-dendritic GABAergic synapse.

If axosomatic terminals on LG neurons arise from multiple sources, the arrival of the IPSP on the MGB neurons may be variable and context dependant. Both faster and slower EPSPs will be possible. We do not know yet how many VGLUT2 axosomatic terminals must be active to fire a LG neuron. Calyx- or endbulb-type synapses have not been found in the IC, so the VGLUT2 axosomatic synapses are not from a single axon. This suggests that a highly synchronized excitatory input to the LG neuron is not as likely as a more asynchronous event. In the latter case, some acoustic stimuli may activate the excitatory inputs on a LG neuron more than other stimuli. Thus, the selective firing of excitatory inputs to the LG neuron might filter the inhibition received by the auditory thalamus.

MATERIALS AND METHODS

STATISTICAL ANALYSIS

Distribution of GABAergic cells

Data obtained from three Long–Evans rats in the previous study (Ito et al., 2009) were used. Twenty-μm-thick IC coronal sections were collected, and every 24th section was immunostained for GAD67 and VGLUT2, and then counterstained with Neurotrace 510 (Invitrogen, Grand Island, NY). Photomicrographs of the whole IC were taken by a laser scanning confocal microscope, and

montage images of the whole IC were made from four IC sections at interval of 480 μm.

L function

To measure both local and global dispersion of GABAergic neurons in the ICC, we counted the number of neurons located within a distance of h from other neurons. Ripley's K function (Ripley, 1976) is calculated as:

$$K = \frac{\sum_{i \neq j} I(d_{ij} < h)}{n\lambda}$$

where I is the number of neurons, d_{ij} is the distance between i th and j th neurons in a set of n neurons, and λ is the density of neurons. For data analysis, the function is standardized with h in a following manner:

$$L = \sqrt{K/\pi} - h$$

Monte-Carlo simulation

To test whether the obtained L functions show random, uniform, or concentrated distribution, a 95% confidence interval of given ICC region was calculated by Monte-Carlo simulation in the following manner. First, neurons were randomly re-distributed, and the L function was calculated. The process was repeated 10,000 times, and the distribution of the L function of random distribution was obtained. If the original L function was outside of the 95% confidence interval at given h, the distribution is not likely to be random at the range h. If the L function is smaller than the confidence interval, neurons are more uniformly distributed. If it is larger, they are more concentrated. At 10 points of h evenly separated, significant difference between L function and the confidence interval was examined, and mean counts of significance were calculated (**Table 3**). The L functions and confidence intervals were calculated with custom-made scripts on MATLAB Statistics Toolbox (version: R14; Mathworks, Natick, MA).

Stereological estimate of GABAergic cells

Data obtained from four Long Evans rats in the previous study (Ito et al., 2009) were used. Twenty-μm-thick IC coronal sections were collected, and every 12th section was immunostained for GAD67 and VGLUT2, and counterstained with Neurotrace 510. IC sections were divided into a 500 × 500 μm grid, with a 57.1 × 57.1 × 20 μm box in the center as a sampling frame. If nucleoli of GAD67-positive cells were found inside the box, images of the cells were taken, and categorized as LG or SG by the presence or absence of dense axosomatic VGLUT2-positive endings. After acquiring stereological samples, low-magnification montage images of the IC were taken to locate the sampling frames and to measure the size of the IC. The density of GABAergic neurons was calculated by dividing the total number of GABAergic neurons by number of the sampling frames and volume of a sampling frame. Total volume of the IC was estimated by linear interpolation of the volume of every 12th section. Estimated number of GABAergic neurons was calculated by multiplying the density with total volume of the IC.

ACKNOWLEDGMENTS

The authors acknowledge constructive criticisms by reviewers. This work was supported by National Institutes of Health Grant R01 DC00189 (Douglas L. Oliver), and grants from Uehara Memorial Foundation (Tetsufumi Ito), The Ichiro Kanehara Foundation (Tetsufumi Ito), Ministry of Education, Science, and Culture of Japan (Grant number: 22700365 for Tetsufumi Ito), and Research and Education Program for Life Science of University of Fukui (Tetsufumi Ito).

REFERENCES

Altschuler, R. A., Tong, L., Holt, A. G., and Oliver, D. L. (2008). Immunolocalization of vesicular glutamate transporters 1 and 2 in the rat inferior colliculus. *Neuroscience* 154, 226–232.

Bartlett, E. L., and Smith, P. H. (2002). Effects of paired-pulse and repetitive stimulation on neurons in the rat medial geniculate body. *Neuroscience* 113, 957–974.

Bartlett, E. L., Stark, J. M., Guillery, R. W., and Smith, P. H. (2000). Comparison of the fine structure of cortical and collicular terminals in the rat medial geniculate body. *Neuroscience* 100, 811–828.

Cant, N. B., and Benson, C. G. (2006). Organization of the inferior colliculus of the gerbil (*Meriones unguiculatus*): differences in distribution of projections from the cochlear nuclei and the superior olivary complex. *J. Comp. Neurol.* 495, 511–528.

Chernock, M. L., Larue, D. T., and Winer, J. A. (2004). A periodic network of neurochemical modules in the inferior colliculus. *Hear. Res.* 188, 12–20.

Fremeau, R. T. Jr., Troyer, M. D., Pahner, I., Nygaard, G. O., Tran, C. H., Reimer, R. J., Bellocchio, E. E., Fortin, D., Storm-Mathisen, J., and Edwards, R. H. (2001). The expression of vesicular glutamate transporters defines two classes of excitatory synapse. *Neuron* 31, 247–260.

Geis, H.-R., and Borst, G. G. (2011). Synaptic inputs to large tectothalamic projection neurons of the mouse inferior colliculus. *2011 Neuroscience Meeting 479.409/KK429.*

Herzog, E., Bellenchi, G. C., Gras, C., Bernard, V., Ravassard, P., Bedet, C., Gasnier, B., Giros, B., and El Mestikawy, S. (2001). The existence of a second vesicular glutamate transporter specifies subpopulations of glutamatergic neurons. *J. Neurosci.* 21, RC181.

Ito, T., and Oliver, D. L. (2010). Origins of glutamatergic terminals in the inferior colliculus identified by retrograde transport and expression of VGLUT1 and VGLUT2 genes. *Front. Neuroanat.* 4:135. doi: 10.3389/fnana.2010.00135

Ito, T., and Takada, M. (2011). Distribution of glutamatergic, GABAergic, and glycinergic neurons in the auditory brainstem of Japanese macaque (*Macaca fuscata*). *The 34th Annual Meeting of the Japan Neuroscience Society P2-j11*, (Yokohama, Japan).

Ito, T., Bishop, D. C., and Oliver, D. L. (2009). Two classes of GABAergic neurons in the inferior colliculus. *J. Neurosci.* 29, 13860–13869.

Ito, T., Bishop, D. C., and Oliver, D. L. (2011). Expression of glutamate and inhibitory amino acid vesicular transporters in the rodent auditory brainstem. *J. Comp. Neurol.* 519, 316–340.

Kulesza, R. J., Vinuela, A., Saldana, E., and Berrebi, A. S. (2002). Unbiased stereological estimates of neuron number in subcortical auditory nuclei of the rat. *Hear. Res.* 168, 12–24.

Lee, C. C., and Sherman, S. M. (2010). Topography and physiology of ascending streams in the auditory tectothalamic pathway. *Proc. Natl. Acad. Sci. U.S.A.* 107, 372–377.

Loftus, W. C., Bishop, D. C., and Oliver, D. L. (2010). Differential patterns of inputs create functional zones in central nucleus of inferior colliculus. *J. Neurosci.* 30, 13396–13408.

Malmierca, M. S., Blackstad, T. W., Osen, K. K., Karagulle, T., and Molowny, R. L. (1993). The central nucleus of the inferior colliculus in rat: a Golgi and computer reconstruction study of neuronal and laminar structure. *J. Comp. Neurol.* 333, 1–27.

Merchan, M., Aguilar, L. A., Lopez-Poveda, E. A., and Malmierca, M. S. (2005). The inferior colliculus of the rat: quantitative immunocytochemical study of GABA

and glycine. *Neuroscience* 136, 907–925.

Morest, D. K. (1971). Dendrodendritic synapses of cells that have axons: the fine structure of the Golgi type II cell in the medial geniculate body of the cat. *Z. Anat. Entwicklungsgesch.* 133, 216–246.

Morest, D. K. (1975). Synaptic relationships of Golgi type II cells in the medial geniculate body of the cat. *J. Comp. Neurol.* 162, 157–193.

Oliver, D. L. (1984). Neuron types in the central nucleus of the inferior colliculus that project to the medial geniculate body. *Neuroscience* 11, 409–424.

Oliver, D. L. (2005). "Neuronal organization in the inferior colliculus. Chapter 2," in *The Inferior Colliculus,* eds J. A. Winer and C. E. Schreiner (New York, NY: Springer), 69–114.

Oliver, D. L., Beckius, G. E., Bishop, D. C., Loftus, W. C., and Batra, R. (2003). Topography of interaural temporal disparity coding in projections of medial superior olive to inferior colliculus. *J. Neurosci.* 23, 7438–7449.

Oliver, D. L., Kuwada, S., Yin, T. C., Haberly, L. B., and Henkel, C. K. (1991). Dendritic and axonal morphology of HRP-injected neurons in the inferior colliculus of the cat. *J. Comp. Neurol.* 303, 75–100.

Oliver, D. L., and Morest, D. K. (1984). The central nucleus of the inferior colliculus in the cat. *J. Comp. Neurol.* 222, 237–264.

Oliver, D. L., Winer, J. A., Beckius, G. E., and Saint Marie, R. L. (1994). Morphology of GABAergic neurons in the inferior colliculus of the cat. *J. Comp. Neurol.* 340, 27–42.

Ono, M., Yanagawa, Y., and Koyano, K. (2005). GABAergic neurons in inferior colliculus of the GAD67-GFP knock-in mouse: electrophysiological and morphological properties. *Neurosci. Res.* 51, 475–492.

Paloff, A. M., Usunoff, K. G., and Hinova-Palova, D. V. (1992). Ultrastructure of Golgi-impregnated and gold-toned neurons in the central nucleus of the inferior colliculus in the cat. *J. Hirnforsch.* 33, 361–407.

Paloff, A. M., Usunoff, K. G., Hinova-Palova, D. V., and Ivanov, D. P. (1989). The fine structure of the inferior colliculus in the cat. I. Neuronal perikarya in the central nucleus. *J. Hirnforsch.* 30, 69–90.

Peruzzi, D., Bartlett, E., Smith, P. H., and Oliver, D. L. (1997). A monosynaptic GABAergic input from the inferior colliculus to the medial geniculate body in rat. *J. Neurosci.* 17, 3766–3777.

Ripley, B. D. (1976). The second-order analysis of stationary point processes. *J. Appl. Prob.* 13, 255–266.

Roberts, R. C., and Ribak, C. E. (1987). GABAergic neurons and axonal terminals in the brainstem auditory nuclei of the gerbil. *J. Comp. Neurol.* 258, 267–280.

Saint Marie, R. L., Stanforth, D. A., and Jubelier, E. M. (1997). Substrate for rapid feedforward inhibition of the auditory forebrain. *Brain Res.* 765, 173–176.

Takamori, S. (2006). VGLUTs: 'exciting' times for glutamatergic research? *Neurosci. Res.* 55, 343–351.

Takamori, S., Rhee, J. S., Rosenmund, C., and Jahn, R. (2000). Identification of a vesicular glutamate transporter that defines a glutamatergic phenotype in neurons. *Nature* 407, 189–194.

Winer, J. (2005). "Three systems of descending projections to the inferior colliculus," in *The Inferior Colliculus,* eds J. Winer and C. E. Schreiner (New York, NY: Springer), 231–247.

Winer, J. A., Saint Marie, R. L., Larue, D. T., and Oliver, D. L. (1996). GABAergic feedforward projections from the inferior colliculus to the medial geniculate body. *Proc. Natl. Acad. Sci. U.S.A.* 93, 8005–8010.

Conflict of Interest Statement: The authors declare that the research was conducted in the absence of any commercial or financial relationships that could be construed as a potential conflict of interest.

Received: 29 March 2012; accepted: 08 July 2012; published online: 26 July 2012. Citation: Ito T and Oliver DL (2012) The basic circuit of the IC: tectothalamic neurons with different patterns of synaptic organization send different messages to the thalamus. Front. Neural Circuits 6:48. doi: 10.3389/fncir.2012.00048

frontiers in
NEURAL CIRCUITS

ORIGINAL RESEARCH ARTICLE
published: 26 November 2012
doi: 10.3389/fncir.2012.00092

The level and distribution of the $GABA_BR1$ and $GABA_BR2$ receptor subunits in the rat's inferior colliculus

Lena Jamal, Aziz N. Khan, Sehrish Butt, Chirag R. Patel and Huiming Zhang*

Department of Biological Sciences, University of Windsor, Windsor, ON, Canada

Edited by:
Manuel S. Malmierca, University of Salamanca, Spain

Reviewed by:
Laura M. Hurley, Indiana University, USA
Richard Altschuler, University of Michigan, USA

***Correspondence:**
Huiming Zhang, Department of Biological Sciences, University of Windsor, Windsor, ON N9B 3P4, Canada.
e-mail: hzhang@uwindsor.ca

The type B γ-aminobutyric acid receptor ($GABA_B$ receptor) is an important neurotransmitter receptor in the midbrain auditory structure, the inferior colliculus (IC). A functional $GABA_B$ receptor is a heterodimer consisting of two subunits, $GABA_BR1$ and $GABA_BR2$. Western blotting and immunohistochemical experiments were conducted to examine the expression of the two subunits over the IC including its central nucleus, dorsal cortex, and external cortex (ICc, ICd, and ICx). Results revealed that the two subunits existed in both cell bodies and the neuropil throughout the IC. The two subunits had similar regional distributions over the IC. The combined level of cell body and neuropil labeling was higher in the ICd than the other two subdivisions. Labeling in the ICc and ICx was stronger in the dorsal than the ventral regions. In spite of regional differences, no defined boundaries were formed between different areas. For both subunits, the regional distribution of immunoreactivity in the neuropil was parallel to that of combined immunoreactivity in the neuropil and cell bodies. The density of labeled cell bodies tended to be higher but sizes of cell bodies tended to be smaller in the ICd than in the other subdivisions. No systematic regional changes were found in the level of cell body immunoreactivity, except that $GABA_BR2$-immunoreactive cell bodies in the ICd had slightly higher optic density (OD) than in other regions. Elongated cell bodies existed throughout the IC. Many labeled cell bodies along the outline of the IC were oriented in parallel to the outline. No strong tendency of orientation was found in labeled cell bodies in ICc. Regional distributions of the subunits in ICc correlated well with inputs to this subdivision. Our finding regarding the contrast in the level of neuropil immunoreactivity among different subdivisions is consistent with the fact that the $GABA_B$ receptor has different pre- and postsynaptic functions in different IC regions.

Keywords: hearing, auditory system, auditory midbrain, GABA, $GABA_B$ receptor, $GABA_BR1$ subunit, $GABA_BR2$ subunit, inhibition

INTRODUCTION

γ-aminobutyric acid (GABA) is an important inhibitory neurotransmitter in the central nervous system (Enna and Möhler, 2007). This neurotransmitter exists at a high level in the midbrain auditory structure, the inferior colliculus (IC) (Roberts and Ribak, 1987; Merchán et al., 2005). Neurons in the IC receive GABAergic projections from extrinsic sources as well as local inhibitory interneurons (Adams and Mugnaini, 1984; Helfert et al., 1989; Li and Kelly, 1992; Vater et al., 1992; Shneiderman et al., 1993; Merchán et al., 1994; González-Hernández et al., 1996; Zhang et al., 1998; Kulesza and Berrebi, 2000; Riquelme et al., 2001; Saldaña et al., 2009). GABAergic receptors in the IC include the metabotropic $GABA_B$ receptor as well as the ionotropic $GABA_A$ receptor (Glendenning and Baker, 1988; Marianowski et al., 2000; LeBeau et al., 2001; Shiraishi et al., 2001; Zhang and Kelly, 2003; Malmierca and Merchán, 2004; Kelly and Caspary, 2005; Hilbig et al., 2007; Caspary et al., 2008; Jamal et al., 2011).

The $GABA_B$ receptor contributes to sound-driven responses in the IC (Faingold et al., 1989; Szczepaniak and Møller, 1995, 1996; Vaughn et al., 1996; Burger and Pollak, 1998). These contributions are dependent on the pre- and/or postsynaptic functions of the receptor (Zhang and Wu, 2000; Ma et al., 2002; Sun et al., 2006; Sun and Wu, 2009). Activation of presynaptic $GABA_B$ receptors reduces the release of neurotransmitters including glutamate and GABA (Ma et al., 2002; Sun et al., 2006). This reduction is a result of decreased calcium influx (Mintz and Bean, 1993; Filippov et al., 2000; Kornau, 2006; Ulrich and Bettler, 2007). Activation of postsynaptic $GABA_B$ receptors leads to prolonged membrane hyperpolarization (Sun and Wu, 2009). This membrane-voltage change is due to an increase in the opening probability of potassium channels (Luscher et al., 1997; Ulrich and Bettler, 2007). The receptor also contributes to long-term enhancement of excitatory neural responses in the IC (Zhang and Wu, 2000).

A functional $GABA_B$ receptor is a heterodimer consisting of two subunits, $GABA_BR1$ and $GABA_BR2$ (Huang, 2006). Both of these subunits are made in the endoplasmic reticulum. Due to a retention signal, the $GABA_BR1$ subunit remains within the endoplasmic reticulum after it is made. Binding by the $GABA_BR2$

subunit masks the retention signal, allowing the two subunits to form a heterodimer and to traffic toward the plasma membrane (Pin et al., 2004; Pooler and McIlhinney, 2007).

The GABA$_B$ receptor is not homogeneously expressed in the IC. Receptor autoradiographic studies have revealed that functional GABA$_B$ receptors are more abundant in the dorsomedial than the ventral region of the structure (Milbrandt et al., 1994; Fubara et al., 1996; Hilbig et al., 2007). Our recent immunohistochemical study on the GABA$_B$R2 subunit revealed a similar distribution in the rat's IC (Jamal et al., 2011).

It has yet to be determined whether the GABA$_B$R1 subunit has a similar distribution in the IC. Also, it is important to find how the level of the GABA$_B$ receptor in the IC is dependent on the density of cell bodies expressing the receptor and the abundance of the receptor in the neuropil. Furthermore, it is important to examine the morphological features of cells expressing the receptor. Addressing these questions can provide an insight into the role of the receptor in auditory processing. Therefore, we conducted Western blotting and immunohistochemical experiments to examine the expression of the GABA$_B$R1 and GABA$_B$R2 subunits in the IC.

EXPERIMENTAL PROCEDURES

ANIMAL PREPARATION

Experiments were conducted using 11 male adult Wistar albino rats (*Rattus norvegicus*). These rats had a body weight of 250–400 g and were obtained from Charles River Canada Inc., St. Constant, Quebec. The animals were housed in the University of Windsor animal care facility for at least a week before experiments were conducted. The noise level in the animal facility was 55–60 dB SPL. All experimental procedures were approved by the University of Windsor Animal Care Committee and were in accordance with the guidelines of the Canadian Council on Animal Care.

WESTERN BLOTTING

For each experiment, an animal was euthanized by an overdose of sodium pentobarbital (120 mg/kg, i.p.). The brain was extracted and sliced in the coronal plane into 240 μm thick sections using a VT1000S vibratome (Leica Microsystems, Heidelberg, Germany). Tissues of the central nucleus, the dorsal cortex, and the external cortex of the IC (ICc, ICd, and ICx) were collected from the resulting brain slices using a scalpel blade and an SZX7 stereoscope (Olympus, Tokyo, Japan). The IC was subdivided based on a standard rat brain atlas (Paxinos and Watson, 2007) and current anatomical results on this structure (Malmierca et al., 1993, 1995, 2011; Oliver, 2005; Loftus et al., 2008). The lateral and the rostral cortices of the IC as suggested by recent publications (Loftus et al., 2008; Malmierca et al., 2011) were combined into an external cortex in the present study.

For Western blotting analysis, a sample of a subdivision of the IC was formed by combining tissue from all the different slices with the subdivision. The entire cerebellum and a part of the liver were also collected and used as controls. Thus, a set of five samples was formed for Western blotting analyses for each independent case (i.e., each individual animal). During slicing and tissue collection, the brain was submerged in artificial cerebrospinal fluid containing (in mM): 126 NaCl, 3 KCl, 1.4 KH_2PO_4, 26 $NaHCO_3$, 4 glucose, 1.3 $MgSO_4$, and 1.4 $CaCl_2$.

Tissue in each sample was homogenized manually in homogenization buffer (0.32 M sucrose in 5 mM Tris, pH 7.4) containing protease inhibitors (3 μM aprotinin, 10 μM phenylmethyl sulfonyl fluoride, 1 μM leupeptin, and 3 μM pepstatin). Lysate was cleared at 3400 g for 20 min at 4°C. The protein concentration of the supernatant was measured using a Bradford assay (Sigma-Aldrich, Oakville, ON) and quantified using a Biomate5 spectrophotometer (Thermo Scientific, Surrey, United Kingdom).

Thirty micrograms of protein from each sample were added to 4X sample buffer and subjected to electrophoresis on a 10% sodium dodecyl sulphate-polyacrylamide gel (SDS-PAGE) for 2 h at 125 V. Proteins were transferred from the gel to a polyvinylidene fluoride (PVDF)-Plus 0.45 μm membrane (Osmonics Inc., Minnetonka, MN) for 2 h at 30 V. The membrane was blocked at room temperature for 1 h in Tris-Buffered Saline Tween (TBST, 50 mM Tris/HCl, 153 mM NaCl, 0.05% Tween-20, pH 7.6) containing 1% skim milk. The membrane was then incubated in a primary antibody (see section "Antibodies and Control Experiments") overnight at 4°C. Following three TBST washes (10 min each), the membrane was incubated in a secondary antibody (see section "Antibodies and Control Experiments") for 1 h at room temperature. Following another three TBST washes (10 min each), the membrane was developed with an ECL kit (Pierce, Rockford, IL). Images were acquired using an HD2 gel imaging system and AlphaEase digital analysis software (Alpha Innotech, San Leandro, CA).

IMMUNOHISTOCHEMISTRY

A rat was euthanized by an overdose of sodium pentobarbital (120 mg/kg, i.p.) and transcardially perfused with Tyrode's solution followed by 4% paraformaldehyde in 0.1 M PB. The brain was extracted and cryoprotected in a sucrose gradient (10, 20, and 30% in 0.1 M PB) at 4°C. The brain was then sectioned into 30 μm slices in the coronal plane using a CM1050 S cryostat (Leica Microsystems, Heidelberg, Germany) and thaw-mounted onto SuperFrost Plus glass slides (Fisher Scientific, Pittsburg, PA). Every fourth section over the entire rostrocaudal extent of the IC was collected to form a set of tissue samples. Out of the four sets of samples, one or two were used for the present study (see section "Results"). The other sets were used for purposes not related to this study. For an immunoreaction, each step was conducted with all the sections in a set placed in a single container (keeper), so that the same experimental conditions were applied to the entire set of sections.

Prior to an immunoreaction, sections were warmed to room temperature. They were then incubated overnight at room temperature in a primary antibody (see section "Antibodies and Control Experiments") in 0.1 M PBS with 0.05% Triton X-100 and 5% normal donkey serum (Jackson ImmunoResearch Laboratories, 017-000-121). Following three thorough washes with 0.1 M PBS (10 min each), the sections were incubated in a secondary antibody (see section "Antibodies and Control Experiments") in 0.1 M PBS containing 2% normal donkey serum at room temperature for 2 h. After three additional

washes (10 min each) in 0.1 M PBS, sections were incubated in ExtrAvidin®-peroxidase (Sigma E2886, 1:400) in 0.1 M PBS for 1.5 h at room temperature. The sections were then rinsed three times (10 min each) and incubated in 0.05% 3, 3-Diaminobenzidine tetrahydrochloride (DAB) in 0.1 M PB with 0.04% $NiSO_4$ and 0.1% glucose oxidase at room temperature for 15–30 min. The DAB reaction was terminated by a wash with 0.1 M PBS. The tissues were then dehydrated with an ethanol gradient (60, 70, 95, 100, and 100%) and cleared twice with Histosol (10 min each). The slides were mounted with Permount (Fisher Scientific, SP-500) and coverslipped. Sections were examined using a *CTR 6500* microscope (Leica Microsystems, Heidelberg, Germany) and photomicrographic images were taken using a DFC 380 FX digital camera (Leica Microsystems, Heidelberg, Germany).

ANTIBODIES AND CONTROL EXPERIMENTS

The primary antibody for probing the GABA$_B$R1 subunit in both Western blotting and immunohistochemical experiments was rabbit polyclonal GABA$_B$R1 antiserum (Santa Cruz Biotechnology R-300, 1:3000 for Western blotting and 1:1000 for immunohistochemistry). The primary antibody for probing the GABA$_B$R2 subunit in Western blotting and immunohistochemical experiments was guinea-pig polyclonal GABA$_B$R2 antiserum (Chemicon AB5394, 1:3000 for Western blotting and 1:1000 for immunohistochemistry). Primary antibodies for probing Actin and α-Tubulin in Western blotting experiments were mouse monoclonal anti-Actin antiserum (Chemicon MAB1501, 1:1000) and mouse monoclonal anti-α-Tubulin antiserum (Chemicon 05-829, 1:1000), respectively.

Secondary antibodies used in Western blotting experiments were horseradish peroxidase (HRP)-conjugated Goat anti-rabbit IgG (Santa Cruz Biotechnology SC-2004, 1:6000), HRP-conjugated goat anti-guinea pig IgG (Chemicon AQ108, 1:6000), and HRP-conjugated goat anti-mouse IgG (Chemicon 12-349, 1:10000). Secondary antibodies used in immunohistochemistry experiments were biotinylated donkey anti-rabbit IgG (Jackson ImmunoResearch Laboratories 711-005-152, 1:400) and biotinylated donkey anti-guinea pig IgG (Jackson ImmunoResearch Laboratories 706-065-148, 1:400).

The effectiveness and specificity of the antibody against the GABA$_B$R2 subunit had been verified by our previous Western blotting and immunohistochemical experiments (Jamal et al., 2011) and were confirmed by control experiments in the present study. In agreement with previous findings (Charles et al., 2001; Benke et al., 2002; Panzanelli et al., 2004), our Western blotting experiments using the antibody against the GABA$_B$R1 subunit and cerebellar tissue revealed two bands at 100 and 130 kDa, respectively, (**Figure 1A**). These bands were absent in the lane for liver tissue. Further experiments using antibodies against Actin and α-Tubulin revealed that loading was even, and that α-Tubulin can serve as a selective loading control for neural tissue. Immunohistochemical experiments using cerebellar tissue revealed labeling by the antibody against the GABA$_B$R1 subunit in the molecular layer, Purkinje cell layer, and granule cell layer (**Figure 2A**). Immunoreactivity was absent in white matter. No labeling was found in the

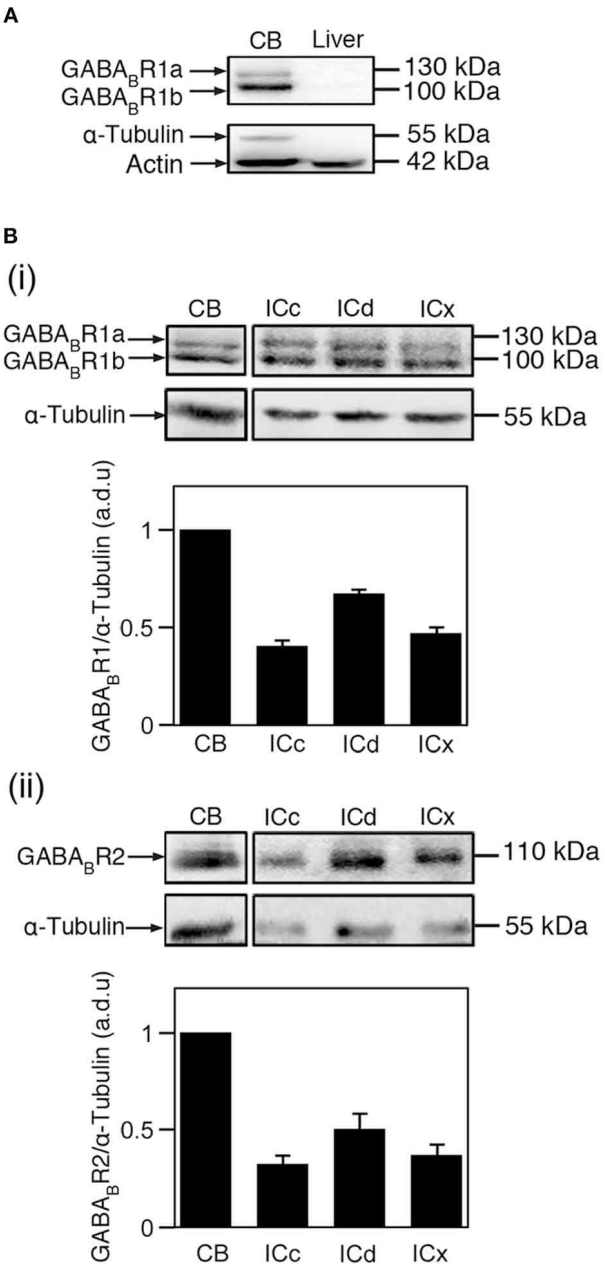

FIGURE 1 | Immunoreactivity to antibodies against the GABA$_B$R1 and GABA$_B$R2 subunits as revealed by Western blots. (A) Western blots obtained by using the antibody against the GABA$_B$R1 subunit and tissues from the cerebellum and the liver (top panel). Actin was used as a general loading control (lower band of the lower panel) and α-Tubulin was used as a brain tissue-specific loading control (upper band of the lower panel). Two bands with molecular weights of 100 and 130 kDa are revealed in the blot for cerebellar tissue. **(B)** Western blots showing GABA$_B$R1 **(i)** and GABA$_B$R2 **(ii)** immunoreactivities in the cerebellum, ICc, ICd, and ICx. In **(i)** and **(ii)**, blots reflecting α-Tubulin immunoreactivity are shown below the blots reflecting the GABA$_B$R1 and GABA$_B$R2 immunoreactivities. The ratio between the OD of a GABA$_B$R1 or GABA$_B$R2 band and the OD of an α-Tubulin band was obtained for each of the four neural structures in each animal. The ratio from the cerebellum was used for normalization. Group results based on ratios from four animals are shown in bar charts in **B(i)** and **B(ii)**. Error bars indicate standard errors.

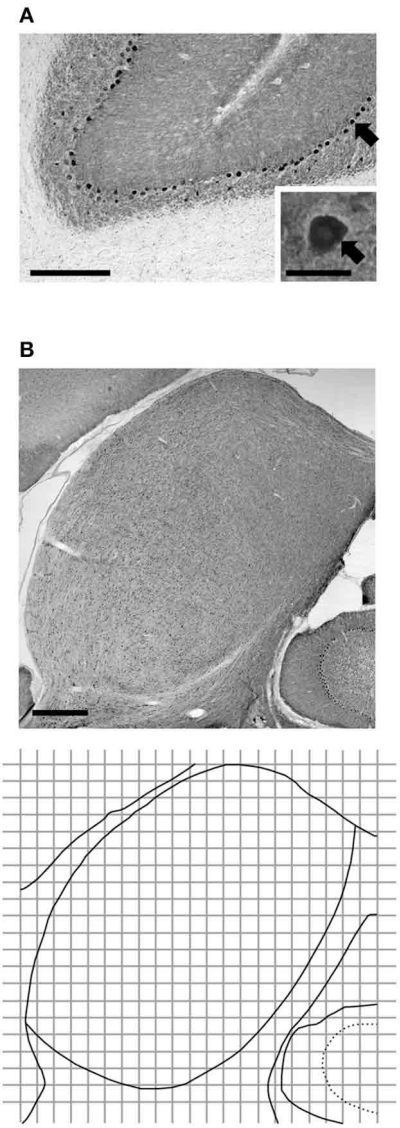

FIGURE 2 | Immunoreactivity to the antibody against the GABA$_B$R1 subunit in the cerebellum (A) and the IC (B) as revealed by immunohistochemistry. The cerebellar section shows molecular, Purkinje cell, and granule cell layers, and white matter. Inset in **(A)** shows a labeled somata of a Purkinje cell, as well as adjacent areas in the molecular and granule layers. Arrow points toward the labeled Purkinje cell. The diagram in the bottom panel of **(B)** is the outline of the section shown in the top panel of **(B)** along with a grid used in the measurement of cell body and neuropil immunoreactivity. The grid was also used in the measurement of morphological features of immunoreactive cells. Each grid box has 150 × 150 μm dimensions. Scale bars in **(A)** and **(B)**: 500 μm in low magnification image; 25 μm in the inset.

cerebellum and the IC when the primary antibody was replaced by 0.1 M PBS (data not shown). These immunochemical results are consistent with previous findings (Ige et al., 2000; Charles et al., 2001). Thus, our control experiments indicated that the antibody against the GABA$_B$R1 subunit was effective and specific.

DATA ANALYSIS

Analyses of western blotting results

For each case, levels of the GABA$_B$R1 subunit, the GABA$_B$R2 subunit, Actin, and α-Tubulin were evaluated by using gel images probed by respective primary antibodies. For each gel image, an optic density (OD) value was measured for each of the four bands corresponding to the ICc, ICd, ICx, and cerebellum. For each structure, the OD value for a receptor subunit (i.e., either the GABA$_B$R1 or GABA$_B$R2 subunit) was normalized against the OD value for α-Tubulin. A ratio was obtained between the normalized OD value of a collicular subdivision and the normalized OD value of the cerebellum. The ratios from all the cases studied were then used to obtain a mean and a standard error to reflect the level of a receptor subunit in a collicular subdivision in reference to that in the cerebellum.

Analyses of immunohistochemical images

Digital photomicrographic images were taken for each section probed by an antibody against the GABA$_B$R1 or the GABA$_B$R2 subunit. A grid with 150 × 150 μm squares (named as grid boxes elsewhere in the text) and an arbitrary origin was placed over the area of the IC (bottom panel of **Figure 2B**). The origin was used as a reference point for superimposing the outline of the IC and a contour showing the regional distribution of OD or cell body morphological characteristic in the IC (see below). Images were taken for all the grid boxes or alternating grid boxes in the IC using a 63X oil immersion objective at a focal plane 10 μm below the top surface of the tissue. These images were used to examine the number of GABA$_B$R1- or GABA$_B$R2-immunoreactive (GABA$_B$R1-IR or GABA$_B$R2-IR) cell bodies as well as the level of immunoreactivity and morphological features of these cell bodies. The images were also used to evaluate the neuropil level of subunit expression as well as the overall level (i.e., combined cell body and neuropil level) of expression. Images for each set of tissue samples were taken in multiple sessions. At the beginning of each imaging session, a predetermined area of a cerebellar section was examined and the mean OD of this area was measured (see below for measurement of OD) to ensure that illumination conditions of the microscope were consistent across different imaging sessions.

To assess the overall level of immunoreactivity in an area (e.g., an 150 × 150 μm grid box), a gray level was measured at each pixel within the area. In such a measurement, white and black colors corresponded to pixel values of 0 and 255, respectively. The mean and the standard deviation of all the pixel gray levels in the box were obtained to indicate the OD of this area. To assess the level of neuropil labeling within a grid box, five small square areas with 10 × 10 μm dimensions were randomly picked within the grid box. These squares were devoid of any cell bodies or parts of cell bodies. A gray level was measured at each pixel in these five areas and the mean and standard deviation of all the pixel gray levels were obtained to represent the OD of the neuropil in the grid box.

A normalized OD value was calculated for an area of interest by using the mean OD from the molecular layer of the cerebellum and the mean OD from an area with the lightest

labeling in the entire set of section (typically white matter of the cerebellum):

$$Normalized\ OD = (OD_{aud} - OD_l) / (OD_{cm} - OD_l)$$

where OD_{aud} is the mean OD value of an area of interest (i.e., a grid box, five 10 × 10 μm squares, or a cell body). OD_{cm} and OD_l are the mean OD values of the cerebellar molecular layer and the area with the lightest labeling, respectively.

Immunoreactive cell bodies were counted in each grid box. An immunoreactive cell body had an identifiable nucleus and a mean OD value higher than a threshold OD level for the grid box. This threshold level equaled the mean neuropil OD plus one standard deviation of the neuropil OD in the grid box. Only cell bodies with a major axis (i.e., longest axis) longer than 6 μm were counted.

For each labeled cell body, the level of labeling and the size of the cell body were examined. A cell body was outlined manually and the level of labeling in the cell body was obtained by calculating the mean OD within the outlined area. The perimeter, occupied area, length of the major axis, and orientation of the major axis were also measured for the cell body. The area occupied by a cell (a) and the length of the major axis (l) were used to calculate an elongation index (EI) to describe the shape of an immunoreactive cell body:

$$EI = 1 - \frac{a}{\frac{\pi}{4} l^2}$$

An EI value is within the range between 0 and 1. An elongated cell body results in a large EI value, while a perfect circular cell body results in an EI value of 0.

Measurements of OD values and cell body morphological features from all grid boxes were combined to calculate mean values or to create histograms for the three subdivisions. For this purpose, a grid box divided by a border between two subdivisions was assigned to the subdivision that covered a larger part of the grid box.

Image J software (U.S. National Institute of Health, Bethesda, MD) was used in the counting and analyses of immunoreactive neurons, and the measurements of OD values. DeltaGraph software (RedRock software, Salt Lake City, UT) was used for plotting contours, histograms, and vector charts to show regional distributions of immunoreactivity and morphological features of immunoreactive cell bodies. For the purpose of illustration, brightness and contrast of photomicrographic images was adjusted using Photoshop CS4 Extended software (Adobe Systems, San Jose, CA). Outlines of neural structures in photomicrographic images were traced using Illustrator (Adobe Systems, San Jose, CA). Areas outside the IC in a contour plot made using DeltaGraph were cropped using Illustrator.

RESULTS

LEVELS OF THE GABA$_B$R1 AND GABA$_B$R2 SUBUNITS IN THE IC: WESTERN BLOTTING

Western blotting experiments were conducted using four rats. In three of the four animals, both the GABA$_B$R1 and the GABA$_B$R2 subunits were probed. In the fourth animal, only the GABA$_B$R2 subunit was probed. As shown in **Figure 1B**, both the GABA$_B$R1 and GABA$_B$R2 subunits were expressed at a higher level in the ICd than in the other two collicular subdivisions. This area difference was confirmed by all the other cases examined in this study (2 and 3 cases for the GABA$_B$R1 and GABA$_B$R2 subunits, respectively). The GABA$_B$R1/α-Tubulin ratio in the ICc and ICx were about 65 and 70% of that in the ICd, respectively. The GABA$_B$R2/α-Tubulin ratio in the ICc and ICx were about 55 and 75% of that in the ICd, respectively.

LOCALIZATION OF THE GABA$_B$R1 AND GABA$_B$R2 SUBUNITS: IMMUNOHISTOCHEMISTRY

Immunohistochemical experiments were conducted using a total of seven rats. In one of these rats, both the GABA$_B$R1 and the GABA$_B$R2 subunits were probed. In three rats the GABA$_B$R1 subunit was probed, while in another three rats the GABA$_B$R2 subunit was probed. Regional and cellular distributions of immunoreactivity were examined in each of these cases. For each subunit, OD values were measured in four cases to evaluate the distribution of neuropil and overall (combined cell body and neuropil) immunoreactivities over the entire IC. In three of the four cases OD values were measured in alternating grid boxes in each section, while in one of the four cases OD values were measured in all the grid boxes in each section. Comparisons made in the cases in which ODs were measured for all the grid boxes (one for each subunit) revealed that contours showing distributions of neuropil and overall immunoreactivity based on measurements from all the grid boxes were similar to those based on measurements from alternating boxes. Therefore, results presented in the following section will be based on measurements from alternating grid boxes for all cases in order to keep consistency. The level of cell body immunoreactivity, the density of labeled cell bodies, and the size and orientation of labeled cell body were examined in two cases for each subunit.

The GABA$_B$R1 and GABA$_B$R2 subunits were found throughout the entire IC (**Figures 2B** and **3**). For a section from the middle portion of the rostrocaudal extent of the IC [**Figures 3A(ii)**,**B(ii)**], the overall level of expression was higher in the dorsomedial region (i.e., the ICd) than the ventrolateral region of the IC (i.e., the ventral parts of the ICx and ICc). The dorsal parts of the ICc and ICx also had relatively high level of expression. The reduction in the level of immunoreactivity from dorsomedial to the ventrolateral part of the IC was gradual. No defined boundaries were found among the three subdivisions. In the rostral part of the IC, an area defined as the rostral cortex of the IC by recent publications (Loftus et al., 2008; Malmierca et al., 2011), the level of immnoreactivity was higher in the medial than in the lateral region [**Figures 3A(i)**,**B(i)**]. Stronger labeling in the medial than the lateral region of the IC was also observed in the caudal part of the IC [**Figures 3A(iii)**,**B(iii)**]. Across the rostrocaudal extent of the IC, the level of labeling appeared to be higher in the caudal than the rostral part. This rostrocaudal difference is more apparent for GABA$_B$R2 immunoreactivity than GABA$_B$R1 immunoreactivity.

Over the area of the IC in a section, a mean OD value was obtained for each of the alternating grid boxes to reflect

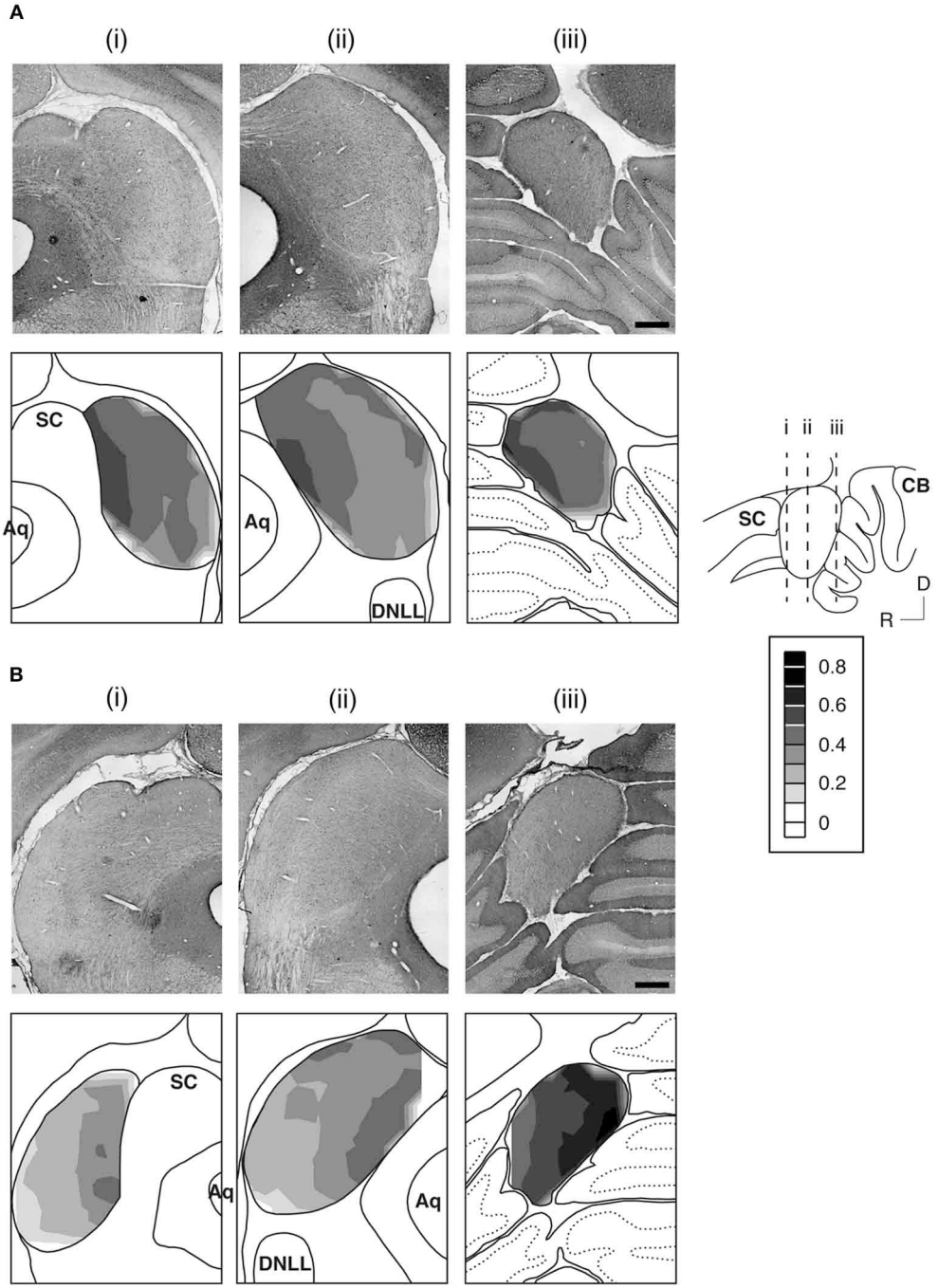

FIGURE 3 | An example showing immunoreactivity to antibodies against the GABA$_B$R1 subunit (A) and the GABA$_B$R2 subunit (B) at different rostrocaudaul locations of the IC. The rostrocaudal locations of the sections shown in **(A)** and **(B)** are indicated in a sagittal diagram in the inset. Below each photomicrograph in **(A)** and **(B)** is a diagram of the section with a contour plot showing the distribution of a combined level of cell body and neuropil immunoreactivity over the area of the IC. For making a contour, a normalized OD was obtained for each of the alternating grid boxes over the area of the IC. Results in **(A)** and **(B)** are from a single animal. Scale bars in **(A)** and **(B)**: 500 μm.

the combined level of cell body and neuropil labeling in the boxes. A contour plot was created by using the mean OD values from these grid boxes. Contour plots for sections shown in **Figure 3** indicate that the GABA$_B$R1 and GABA$_B$R2 subunits displayed similar distributions of a combined level of cell body and neuropil immunoreactivity. For both subunits, a high level of immunoreactivity was observed in the medial/dorsomedial part of the IC. Measurements of OD values in three additional

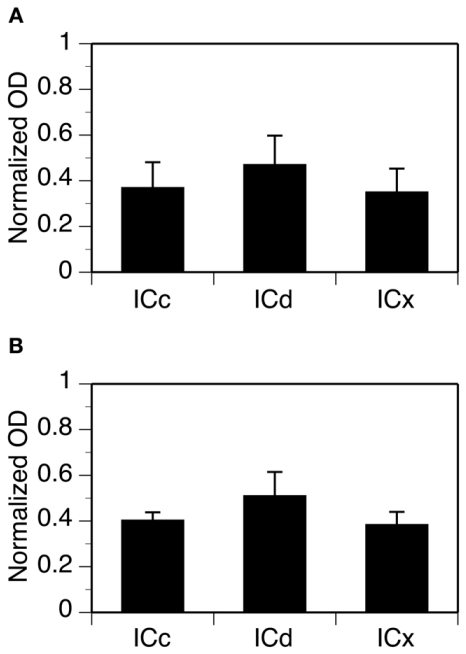

FIGURE 4 | Group results from immunohistochemical experiments showing overall (cell body and neuropil combined) levels of GABA$_B$R1 and GABA$_B$R2 immunoreactivity (A and B) in three subdivisions of the IC. For each section in an animal, a normalized OD was obtained for each of the alternating grid boxes. A mean normalized OD value was obtained for each collicular subdivision of an animal. Each bar in a bar chart represents a grand mean value for four animals for a subdivision. Error bars indicate standard errors.

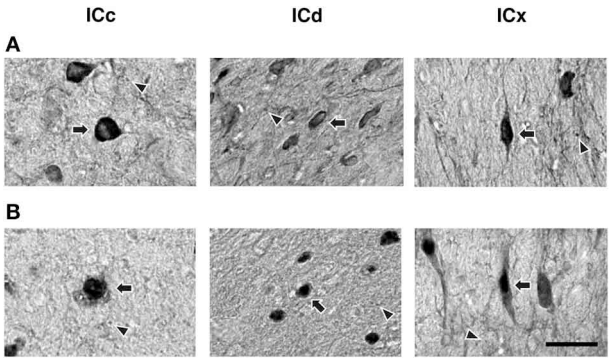

FIGURE 5 | High magnification photomicrographs showing GABA$_B$R1 and GABA$_B$R2 immunoreactivity (A and B) in the ICc, ICd, and ICx. Arrows point toward labeled cell bodies while arrowheads point toward labeled puncta in the neuropil. Scale bars: 25 μm.

cases for each subunit supported findings from the case shown in **Figure 3**.

For each case, OD values from alternating grid boxes in an entire set of sections were combined to generate three mean OD values to reflect overall levels of GABA$_B$R1 or GABA$_B$R2 immunoreactivity in the ICc, ICd, and ICx. Group results from four cases for each subunit confirmed that the overall levels of GABA$_B$R1 and GABA$_B$R2 immunoreactivity were higher in the ICd than in the ICc and the ICx (**Figure 4**). For both subunits, levels of immunoreactivity in the ICc and ICx were about 75% of that in the ICd.

Higher magnification images revealed that labeling of cell bodies in the IC by an antibody against the GABA$_B$R1 or GABA$_B$R2 subunit was either punctate or diffused (**Figure 5**). Punctate labeling was observed in the neuropil of the IC. Cell bodies immunoreactive to the GABA$_B$R1 antibody typically had strong labeling on or close to the cell membrane, while those immunoreactive to the GABA$_B$R2 antibody typically had strong labeling throughout the cell body including areas in and close to the nucleus.

Distributions of GABA$_B$R1-IR and GABA$_B$R2-IR cell bodies in the IC were quantitatively examined in two cases for each subunit. For each case, the density of immunoreactive cell bodies was examined in an entire set of tissue sections. In each section, immunoreactive cell bodies were counted in all the alternating grid boxes. As shown by an example in **Figure 6**, labeled cell bodies were densely packed in the dorsomedial region of the IC in sections from the mid portion of the rostrocaudal extent of the structure [**Figure 6A(ii)** top and bottom panels]. Cell packing density was low in the ventral region. In the rostral part of the IC, the density of labeled cells appeared to be slightly higher in the dorsal or dorsolateral than the other regions [**Figure 6A(i)** top and bottom panels]. In sections close to the caudal pole of the IC, density of labeled cells was higher in the dorsal than the ventral region [**Figure 6A(iii)** top and bottom panels]. The overall density of labeled cell bodies was reduced at the caudal pole, with the dorsal-ventral contrast still observed (data not shown). Densities of labeled cell bodies in all of the alternating grid boxes in the entire set of sections were summarized in histograms shown in **Figure 6B**. Distributions of the density of immunoreactive cell bodies peaked at higher values in the ICd than in the ICc and ICx for the GABA$_B$R1 subunit (**Figure 6B** left panel). The mean number of labeled cells/grid box supported that GABA$_B$R1-IR cells were more densely packed in the ICd than in the ICc and ICx (**Table 1**). For the GABA$_B$R2 subunit, the difference in the distribution of density of immunoreactive cell bodies among the three subdivisions was smaller than for the GABA$_B$R1 subunit (**Figure 6B** right panel). However, the ICd still had the highest average density of labeled cells among the three collicular subdivisions (**Table 1**). The relatively small difference was likely partially related to the fact that few GABA$_B$R2-IR cells were found in the caudal pole of the ICd. The area difference in the packing density of immunoreactive cells was confirmed by quantitative analysis of results from a second case for each subunit.

The level of cell body immunoreactivity was examined in two cases for each subunit. For each case, ODs of immunoreactive cell bodies were measured using an entire set of tissue sections and measurements were conducted in each of the alternating grid boxes in each section. Results shown in **Figure 7A** revealed a normal distribution of cell body OD in each of the three collicular subdivisions. For the GABA$_B$R1 subunit, the distributions of OD peaked at a value about one fourth lower than the mean OD of the cerebellar molecular layer (**Figure 7A** left panel). For the

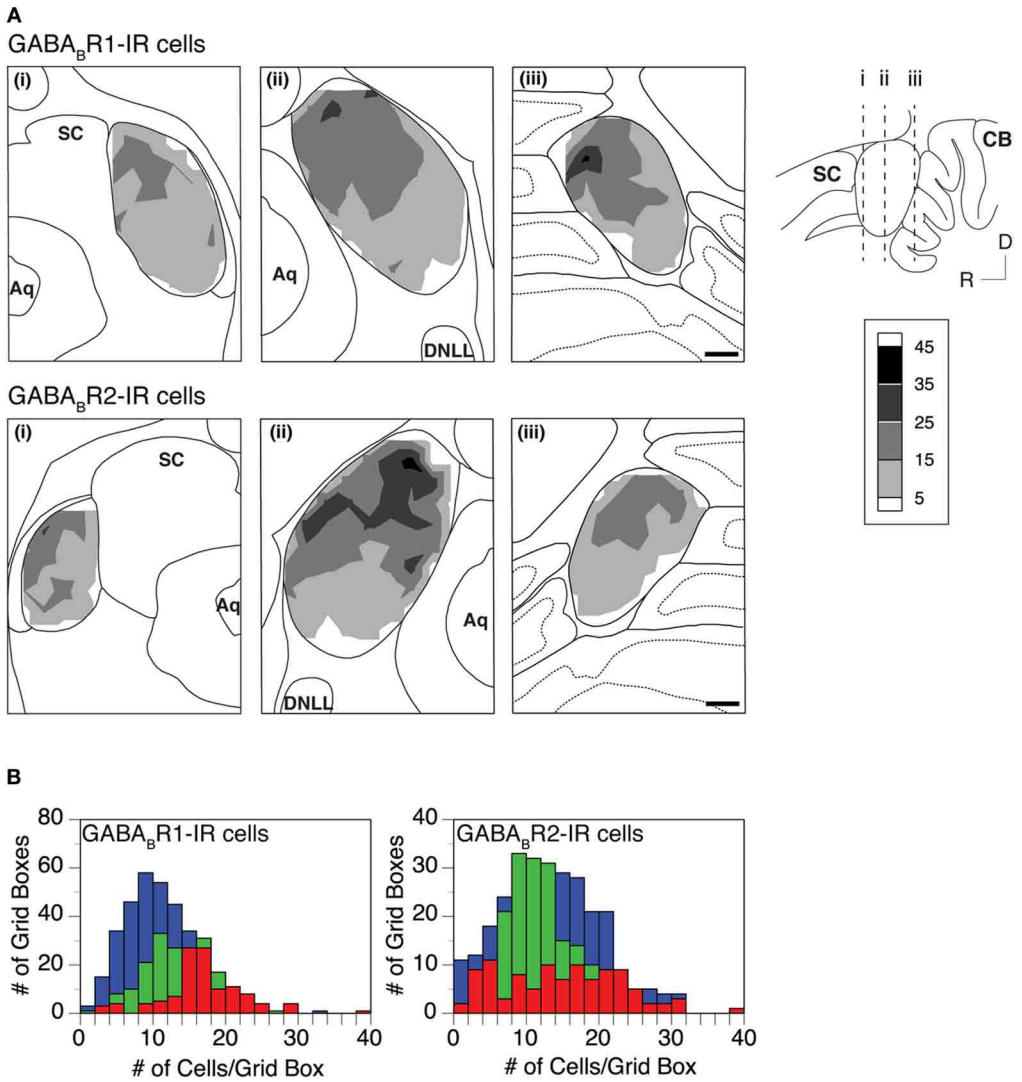

FIGURE 6 | (A) Densities of GABA$_B$R1-IR and GABA$_B$R2-IR cells (top and bottom rows) in the IC. Analyses were conducted on two animals for each subunit. Results in the two rows are from two different animals. In each row, contour plots in three panels show densities of labeled cells in three coronal sections at different rostrocaudal locations as indicated in the inset. A density of labeled cells represents the total number of immunoreactive cells in a 150 × 150 μm grid box. Each contour is made by using densities of cells in alternating grid boxes over the area of the IC. **(B)** Histograms showing distributions of GABA$_B$R1-IR cells (left panel, results from the same animal as in the top row in **A**) and GABA$_B$R2-IR cells (right panel, results from the same animal as in the bottom row in **A**) in the ICc (green), ICd (red), and ICx (blue). Scale bars in **(B)**: 500 μm.

Table 1 | Summary of results from two animals for GABA$_B$R1-IR and GABA$_B$R2-IR cell bodies, respectively.

	GABA$_B$R1-IR cells mean ± SD			GABA$_B$R2-IR cells mean ± SD		
	ICc	**ICd**	**ICx**	**ICc**	**ICd**	**ICx**
Total number of neurons examined	2538	1879	3476	2038	1380	3508
Number of cells/grid box	13.4 ± 5.0	16.3 ± 5.7	10.4 ± 4.9	12.0 ± 5.1	14.5 ± 8.2	12.9 ± 6.8
Normalized optic density	0.77 ± 0.12	0.76 ± 0.12	0.76 ± 0.13	0.98 ± 0.17	1.06 ± 0.16	0.98 ± 0.17
Area of cell body (μm^2)	67.0 ± 34.6	58.0 ± 26.5	63.4 ± 35.2	69.1 ± 45.9	53.8 ± 27.8	66.7 ± 42.0
Perimeter of cell body (μm)	32.3 ± 11.1	30.3 ± 9.6	31.9 ± 12.0	32.4 ± 12.3	28.7 ± 9.4	32.4 ± 12.1
Major axis of cell body (μm)	11.5 ± 4.1	11.0 ± 3.7	11.6 ± 4.5	11.4 ± 5.0	10.3 ± 3.5	11.7 ± 4.5

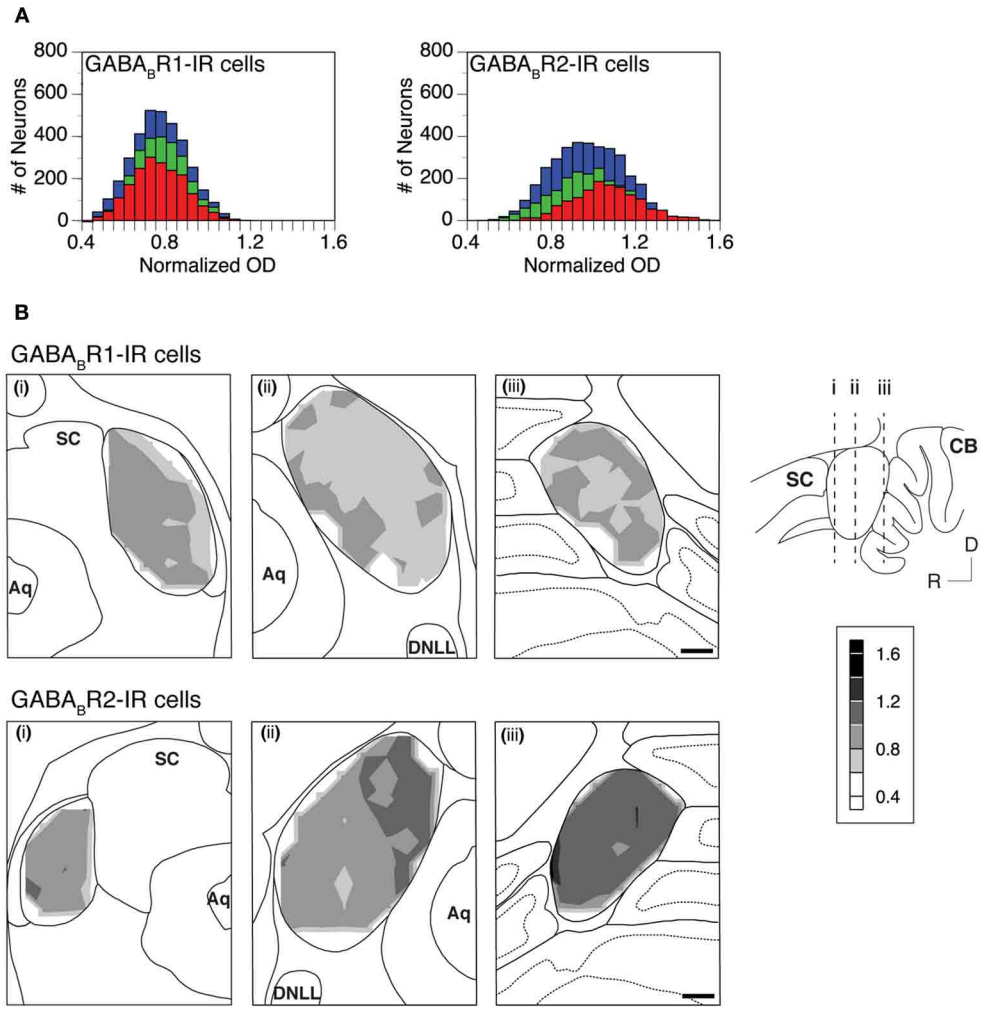

FIGURE 7 | (A) Histograms showing distributions of the normalized OD for individual GABA$_B$R1-IR cell bodies (left panel) and GABA$_B$R2-IR cell bodies (right panel) in the ICc (green), ICd (red), and ICx (blue). Analyses were conducted on two animals for each subunit. Results in the left and right panels are from two different animals. **(B)** Regional distribution of the mean normalized OD of GABA$_B$R1-IR cells (top panels) and GABA$_B$R2-IR cells (bottom panels) over the area of the IC in three coronal sections at different rostrocaudal locations as indicated in the inset. The mean normalized OD represents the mean of the normalized ODs of all the labeled cells in a 150 × 150 μm grid box. A contour is made by using the mean normalized OD values from alternating grid boxes over the area of the IC. Scale bars in **(B)**: 500 μm.

GABA$_B$R2 subunit, the distributions of the cell body OD in the ICc and ICx peaked at a level slightly lower than the mean OD of the cerebellar molecular layer (**Figure 7A** right panel). In contrast, the distribution in the ICd peaked at a value slightly higher than the mean OD of the cerebellar molecular layer. The similarity in the level of cell body GABA$_B$R1 immunoreactivity among the three subdivisions and the small difference in the cell body GABA$_B$R2 immunoreactivity between the ICd and ICc/ICx were also reflected by mean OD values shown in **Table 1**.

A mean value was obtained for the OD values of all the immunoreactive cell bodies in each of the alternating grid boxes in a section. These mean OD values were used to create a contour to show the regional distribution of cell body immunoreactivity. Contour plots in **Figure 7B** revealed small variations in the mean OD over the IC. These variations resulted in a patchy pattern over the IC for GABA$_B$R1 immunoreactivity (**Figure 7B** top panels). For GABA$_B$R2 immunoreactivity, OD values were slightly higher in sections from the caudal part of the IC and the dorsomedial region of the IC in sections from the mid rostrocaudal extent of the structure (**Figure 7B** bottom mid and right panels). Relatively high OD values in these regions were in agreement with the fact that individual GABA$_B$R2-IR cell body ODs had a distribution that peaked at a higher value in the ICd than in other collicular subdivisions (**Figure 7A** right panel). The regional distribution of cell body OD shown in **Figure 7** was verified by one additional case for each subunit.

The area, perimeter, and major axis of an immunoreactive cell body were measured over the IC in two cases for each subunit. For each case, measurements were made in alternating grid

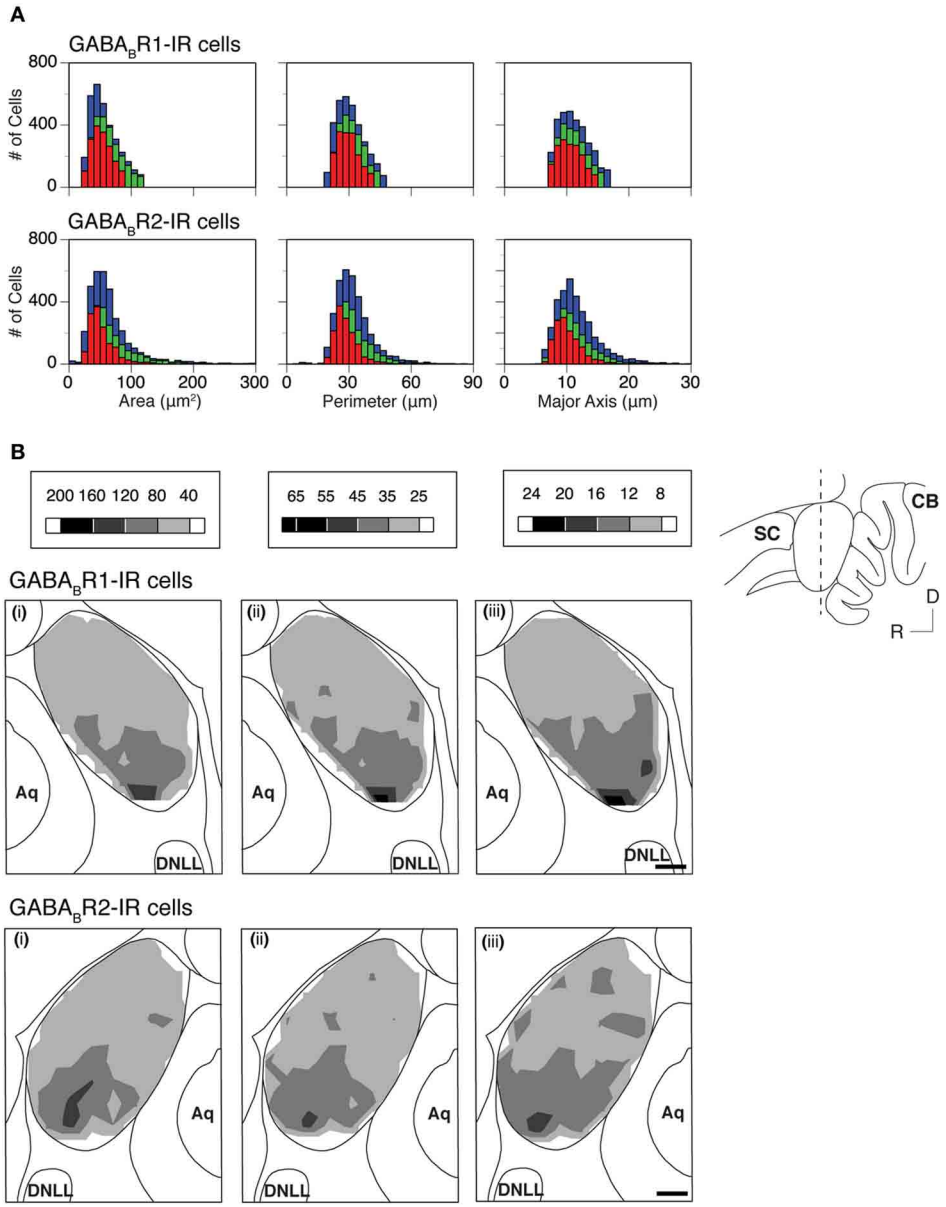

FIGURE 8 | (A) Histograms showing distributions of the area (left panels), perimeter (middle panels), and major axis (right panels) for individual GABA$_B$R1-IR cell bodies (top panels) and GABA$_B$R2-IR cell bodies (bottom panels) in the ICc (green), ICd (red), and ICx (blue). Analyses were conducted on two animals for each subunit. Results in the top and bottom panels are from two different animals. **(B)** Regional distributions of the mean area **(i)**, mean perimeter **(ii)**, and mean major axis **(iii)** of GABA$_B$R1-IR cells (top row) and GABA$_B$R2-IR cells (bottom row) over the IC in a coronal section as indicated in the inset. A mean area, a mean perimeter, and a mean major axis were obtained by using the corresponding parameters from all the labeled cells in a 150 × 150 μm grid box. A contour is made by using the mean values from all the alternating grid boxes over the area of the IC. Results in the top panels of **(B)** are from the same animal as in the top panels of **(A)** while results in the bottom panels of **(B)** are from the same animal as in the bottom panels of **(A)**. Scale bars in **(B)**: 500 μm.

boxes in each section. Histograms were made to show distributions of cell body area, perimeter, and major axis in the ICc, ICd, and ICx. Results from the two cases shown in **Figure 8A** indicated that GABA$_B$R1-IR and GABA$_B$R2-IR cell bodies tended to have smaller sizes in the ICd than in the ICc and ICx. For both cases, grand mean values for cell body size parameters in the three subdivisions supported that immunoreactive cell bodies tended to have smaller sizes in the ICd (**Table 1**).

Mean area, perimeter, and longest axis were obtained for all immunoreactive cell bodies in a grid box for the two cases shown in **Figure 8A**. Contour plots based on these mean values revealed that at the mid portion of the rostrocaudal extent of the IC,

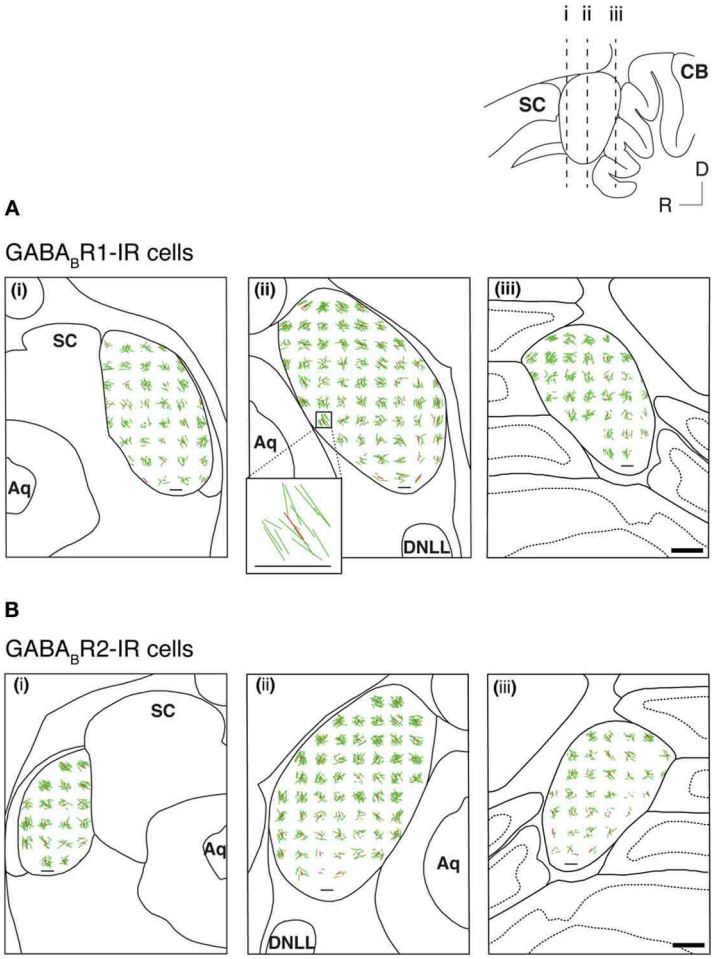

FIGURE 9 | Vector plots reflecting shapes and orientations of GABA$_B$R1-IR cell bodies (A) and GABA$_B$R2-IR cell bodies (B) over the IC in three coronal sections at different rostrocaudal levels as indicated in the inset. Analyses were conducted on two animals for each subunit. Results in **(A)** and **(B)** are from two different animals. In each section, shapes and orientations of labeled cell bodies were measured in alternating 150 × 150 μm grid boxes. Each green line is a vector representing results from one individual neuron, with the length indicating the elongation index (EI) and the orientation indicating the orientation of the major axis of the neuron. Each red line indicates the mean of individual vectors in a grid box. Inset shows individual vectors and the mean vector in a grid box located at the ventromedial region of the IC in a section from the middle rostrocaudal level of the IC of the case shown in **(A)**. A small horizontal black line in the area of IC in each panel and the horizontal line at the bottom of the inset indicate an EI value of 1. Scale bar (thick horizontal line) in **A(iii)** and **B(iii)**: 500 μm.

immunoreactive cell bodies tended to be smaller in the dorsomedial region (ICd) than in the ventral region (ventral ICc and ICx) (**Figure 8B**). In rostral and caudal part of the IC, neurons in the dorsal region also tended to have relatively small cell body sizes. However regional differences seemed smaller (data not shown). The area differences in cell body size as shown in **Figure 8** were verified by one additional case for each subunit.

Many GABA$_B$R1-IR and GABA$_B$R2-IR neurons in the IC display elongated cell bodies (see **Figure 5** for examples). The elongated shape of a cell body was quantitatively described by using an EI (see section "Experimental Procedures" for details). For each section, an EI was calculated for each of the cell bodies in all the alternating grid boxes over the area of the IC. A vector plot was made by using EI values and angles of the major axes of all these cell bodies. **Figure 9** displays results from two cases respectively for the GABA$_B$R1 and GABA$_B$R2 subunits. For sections obtained from the mid portion of the rostrocaudal extent of the IC [**Figures 9A(ii)**,**B(ii)**], vectors close to the outline of the IC had a tendency of orientation parallel to the outline. In contrast, vectors in the ICc region did not show a strong tendency of orientation. A mean vector was calculated for each grid box by using the EIs and the angles of major axes of individual neurons. Mean vectors in grid boxes along the outline of the IC were larger and had a tendency to follow the outline. In contrast, mean vectors in the ICc region were small and did not show a tendency of orientation. These results are consistent with observations from individual neurons. In the rostral and caudal parts of the IC, no strong tendency of orientation was found, although many neurons in these parts display elongated shapes [**Figures 9A(i)**,**(iii)**,**B(i)**,**(iii)**].

Neurons immunoreactive to the GABA$_B$R1 and GABA$_B$R2 antibodies were found among fibers in the commissure of the inferior colliculus (CIC) and the brachium of the inferior colliculus (BIC) (**Figure 10**). In the CIC, immunoreactive cell bodies existed over the entire lateral-medial extent. These cell bodies had elongated shapes (as indicated by arrows), which were oriented in parallel with the commissural fibers. The level of labeling of these cell bodies was similar to that of cell bodies in the ICd. Immunoreactive cell bodies in the BIC also had elongated shapes. These cells tended to have a vertical orientation and the level of labeling of these cells was similar to that of cell bodies in the ICx.

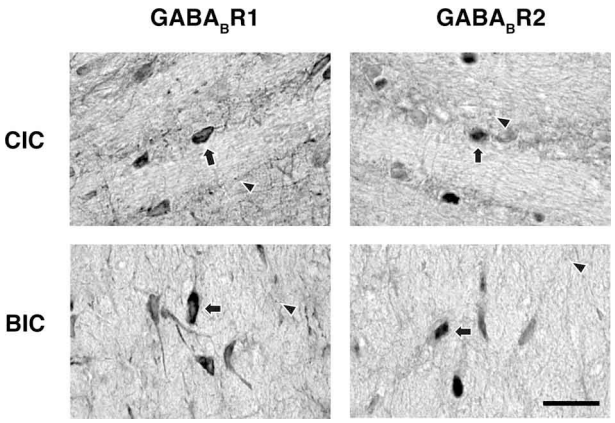

FIGURE 10 | Photomicrographs showing GABA$_B$R1 and GABA$_B$R2 immunoreactivity in the CIC and BIC regions. Arrows point toward labeled cell bodies while arrowheads point toward labeled puncta in the neuropil. Scale bars: 25 μm.

Neuropil OD values were measured in four cases for each subunit. In each case, measurements were conducted in alternating grid boxes in each section (see "Experimental Procedures") and a contour plot was made for the section. Results indicated that immunoreactivity for both the GABA$_B$R1 and the GABA$_B$R2 subunits was higher in the medial/dorsomedial part than the ventrolateral part of the structure (**Figures 11A**,**B**). For each case, OD values from alternating grid boxes over the area of IC in the entire set of sections were combined and three grand mean values were obtained for the three collicular subdivisions. Group results (four cases for each subunit) indicated that the ICd had a higher level of neuropil labeling than the ICc and ICx (**Figure 12**).

DISCUSSION

TECHNICAL CONSIDERATIONS

Sections at 30 μm thickness were used in our immunohistochemical experiments. Strengths of immunoreaction might not have been even at different depths of a section. In an effort to minimize this effect, all photomicroscopic images were taken when the focal plane was at a depth of 10 μm below the tissue surface. In spite of this effort, differences might have existed in immunopenetration between sections treated with antibodies against the GABA$_B$R1 and GABA$_B$R2 subunits, respectively. These differences might

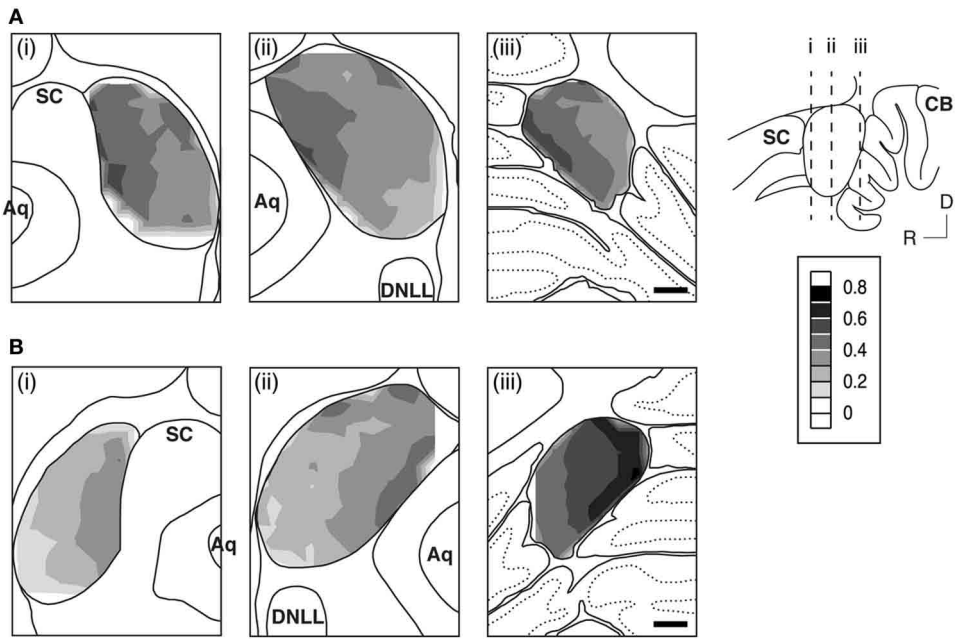

FIGURE 11 | An example showing regional distributions of the level of neuropil immunoreactivity to antibodies against the GABA$_B$R1 (A) and the GABA$_B$R2 (B) subunits over the IC in sections from different rostrocaudaul locations of the IC indicated in the inset. For making a contour, normalized OD values were obtained for the neuropil in each of the alternating grid boxes over the area of the IC. Results in **(A)** and **(B)** and those in **Figure 3** are from the same animal. Scale bars in **(A)** and **(B)**: 500 μm.

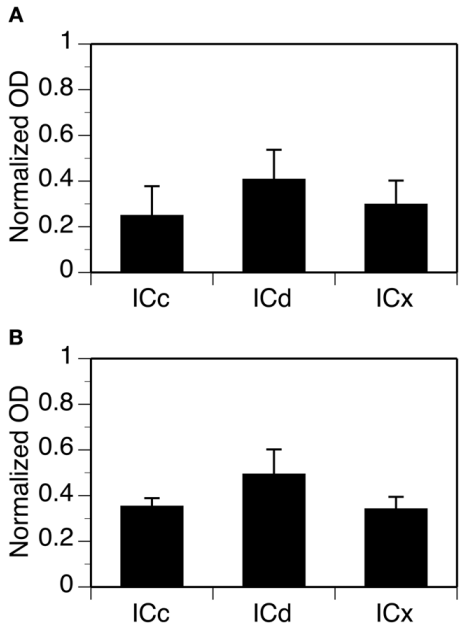

FIGURE 12 | Group results showing levels of GABA$_B$R1 (A) and GABA$_B$R2 (B) immunoreactivity in the neuropil in three subdivisions of the IC. For each section in an animal, normalized OD was obtained for each of the alternating grid boxes. A mean normalized OD value was obtained for each collicular subdivision. Each bar in a bar chart represents a grand mean value for four animals for a subdivision. Error bars indicate standard errors.

have, to some extent, introduced disparities between the two subunits in the distribution of immunoreactivity.

The relatively thick tissue section might have also affected measurements of OD values. Although measured OD values were mainly determined by photons from the focal plane, contributions from off-focal planes should not be completely ignored. Photons from off-focal planes would not necessarily affect the evaluation of the distribution of the overall level of immunoractivity. It might have, to some extent, smeared distributions of neuropil and cell body immunoreactivity, as measurements of cell body labeling in the focal plane could be affected by neuropil in the off-focal planes and vice versa. Even with this possible effect, a difference between the neuropil and cell bodies in the area distribution of immunoreactivity was evident (Compare **Figures 7** and **11**).

LEVEL AND DISTRIBUTION OF THE GABA$_B$R1 AND GABA$_B$R2 SUBUNITS OVER THE IC

Our immunohistochemical and Western blotting experiments reveal that the combined level of cell body and neuropil expression is higher in the ICd than in the ICc and ICx for both GABA$_B$R1 and GABA$_B$R2 subunits. Results based on the two techniques revealed that for both subunits, the combined level of expression in the ICc and ICx was about two thirds of that in the ICd.

Results from the present study support our previous qualitative observation regarding the distribution of the GABA$_B$R2 subunit in the IC (Jamal et al., 2011). The results also support findings from receptor autoradiographical studies indicating that functional GABA$_B$ receptors are expressed at a higher level in the dorsomedial region of the IC and a lower level in the ventral region of the structure (Big brown bat: Fubara et al., 1996; Rhesus monkey: Hilbig et al., 2007; Rat: Bowery et al., 1987; Milbrandt et al., 1994). Results from the rhesus monkey revealed that the receptor had a higher level in the rostral than the caudal part of the ICd (Hilbig et al., 2007). This difference was not observed in the present study.

A question arises as to whether the area differences in the level of combined cell body and neuropil level of immunoreactivity are mainly dependent on the immunoreactivity in cell bodies, the neuropil, or both. For each of the two subunits, the neuropil OD value was higher in the ICd than the other regions of the IC while the cell body OD had very small regional differences over the IC. A relatively high neuropil OD value in the ICd certainly contributed to the high overall level of labeling in this region as the brain tissue in the IC was predominately occupied by the neuropil. The contribution of immunoreactive cell bodies to the overall level of labeling cannot be compared by only using cell body OD values. Results shown in **Figures 6** and **8** suggest that the combined area of cell bodies in a grid box in the ICd was almost equal to or slightly larger than that in the ICc and ICx. Along with distribution of cell body OD over the IC, the slightly larger combined cell body area in the ICd likely resulted in a slightly larger contribution of cell bodies to the overall level of labeling in the ICd.

Regional dependences in the level of GABA$_B$R1 and GABA$_B$R2 did not result in clear boundaries within the IC. Contour plots based on cell body, neuropil, and combined cell body and neuropil OD values had shapes different from the borders between different collicular subdivisions (Paxinos and Watson, 2007; Loftus et al., 2008; Malmierca et al., 2011). Differences in the level of GABA$_B$R1 and GABA$_B$R2 immunoreactivity also existed among different regions within a collicular subdivision. The differences were especially apparent in the ICc and ICx. Within each of these two subdivisions, levels of immunoreactivity were higher in the dorsal than the ventral region. Therefore, it is not appropriate to use the level of expression of the GABA$_B$ receptor to define borders of IC subdivisions.

The GABA$_B$R1 and GABA$_B$R2 subunits had similar regional distributions over the IC. This similarity is consistent with findings from many other brain structures (White et al., 1998; Kuner et al., 1999; Ige et al., 2000; Charles et al., 2001; López-Bendito et al., 2002; Kulik et al., 2003; Panzanelli et al., 2004; Marshall and Foord, 2010). It supports that a functional GABA$_B$ receptor is a heterodimer consisting of both subunits.

In spite of the similarity in regional distribution, differences were observed between the two subunits in cellular/subcellular distribution. For example, a GABA$_B$R2-IR neuron typically had strong labeling throughout the cell body. In contrast, a GABA$_B$R1-IR neuron typically had stronger labeling on and close to the cell membrane than the rest of the cell body. Similar differences were found by previous studies in other brain structures (Charles et al., 2001; Panzanelli et al., 2004). In the present study, both subunits were visualized using DAB reaction product. Therefore, cellular/subcellular distributions of labeling cannot be

directly used to localize functional GABA$_B$ receptors in individual IC neurons. Colocalization of the two subunits and distribution of functional GABA$_B$ receptors can be studied only by conducting double labeling experiments involving two different fluorophores for visualizing two subunits respectively. As shown by previous studies, GABA$_B$R1 and GABA$_B$R2 subunits are made separately in the endoplasmic reticulum before trafficking to the cell membrane to form functional receptors (Pin et al., 2004; Restituito et al., 2005; Pooler and McIlhinney, 2007) or to the cell nucleus to regulate gene expression (Gonchar et al., 2001). Immunoreactivity against a subunit observed in the present study not only reflected the subunit molecules in functional receptors but also those available for making functional receptors. The disparity between the cellular/subcellular distributions of GABA$_B$R1 and GABA$_B$R2 immunoreactivity very likely indicates that a difference exists between the two subunits in the distribution of available molecules for making functional receptors.

For both the GABA$_B$R1 and the GABA$_B$R2 subunits, labeled puncta were found on cell bodies as well as in the neuropil. In addition, diffused cytoplasmic labeling was found in cell bodies. While labeled puncta on cell bodies likely indicated the sites where post- and/or presynaptic GABA$_B$ receptors were located, those in the neuropil could be either associated with bouton synapses or cross-sections of small dendrites or axons. An ultrastructural examination has to be conducted to determine whether the puncta in the neuropil represent functional GABA$_B$ receptors. Diffused labeling in cell bodies likely reflected the subunits available for making functional receptors, although the possibility that it was directly associated with functional receptors could not be ruled out.

Previous anatomical studies have found that neurons in the IC have specific orientation and thickness of dendritic arbors (Oliver and Morest, 1984; Faye-Lund and Osen, 1985; Malmierca et al., 1995, 2011; Oliver, 2005). Disc-shaped (or flat) and stellate (or less-flat) cells are the two major cell types in the ICc. About 80% of the neurons in the ICc are disc shaped. Dendritic fields of disc-shaped cells are oriented with similar directions and fibrodendritic laminae are formed among these dendritic fields. Labeling of cell bodies along with proximal and secondary dendrites using HRP has revealed that most of the cell bodies of ICc neurons with disc-shaped dentritic fields have fusiform or oval shapes (Oliver, 1984). For these neurons, cell bodies have the same orientations as the dendritic fields, which are highly oriented in a ventrolateral to dorsomedial direction. With Nissl staining, although dendritic fields are not visible, a similarity in orientation among cell bodies is still evident (Oliver, 1984). In the present study, no strong tendency was observed in the orientations of immunoreactive cell bodies in the ICc. Further examinations are needed to find whether this lack of similar orientations indicates that most GABA$_B$ receptor-immunoreactive cell bodies are outside fibrodendritic laminae in the ICc. Dendritic fields of neurons in the ICx and ICd are less oriented (Malmierca, 1991; Oliver et al., 1991; Malmierca et al., 2011). In the mid portion of the rostrocaudal extent of the IC, neurons in the deep layer of the ICx have dendritic fields perpendicular to the surface of the structure (Malmierca et al., 2011). Neurons located in the ICd bordering the ICc appear to have elongated dendritic fields and are oriented at an obtuse angle with the fibrodendritic laminae of the ICc (Malmierca et al., 2011). Our immunohistochemical results indicate that cell bodies in these regions tend to orient along the surface of the structure, suggesting that orientations of cell bodies and dendritic fields can be different in the ICd and ICx.

EXPRESSION OF GABA$_B$ RECEPTOR SUBUNITS AND SYNAPTIC INPUTS

The existence of the GABA$_B$R1 and GABA$_B$R2 subunits in the ICc is in agreement with inputs to this subdivision. Inputs to the ICc are predominantly from brainstem structures (see Cant, 2005; Schofield, 2005 for review). Some of these projections are GABAergic (Saint Marie et al., 1989; Saint Marie and Baker, 1990; Li and Kelly, 1992; Shneiderman et al., 1993; Oliver et al., 1994; Riquelme et al., 2001). Within the ICc, levels of immunoreactivity against the two subunits were relatively high in the dorsal than the ventral region. This difference is likely due to the differences in the input to these two regions. While the dorsal region of the ICc receives inhibitory projections predominantly from the dorsal nucleus of the lateral lemniscus, the ventral part of the ICc receives inhibitory projections predominantly from the superior olivary complex (Malmierca and Merchán, 2004). It has been shown that the dorsal nucleus of the lateral lemniscus is a major source of GABAergic projections (Shneiderman et al., 1988; Zhang et al., 1998; Chen et al., 1999). In contrast, the superior olivary complex is a major source of glycinergic projections, although GABAergic projections are also provided by this structure (Saint Marie et al., 1989; Saint Marie and Baker, 1990; Kulesza and Berrebi, 2000; Saldaña et al., 2009).

Cell bodies and the neuropil in the ICd and the dorsal part of the ICx are heavily labeled by antibodies against the two GABA$_B$ receptor subunits. This observation is in contrast to the extrinsic inputs to these two collicular subdivisions. Major auditory inputs to these two subdivisions are from the auditory cortex (AC) and the medial geniculate nucleus (MGN) (Kuwabara and Zook, 2000; Winer, 2006). Projections from the AC are likely glutamatergic (Feliciano and Potashner, 1995). Projections from the MGN are also likely excitatory, as less than 1% of neurons in the rat's MGN are GABAergic (Winer and Larue, 1996). Therefore, GABA$_B$ receptors in the ICd and ICx cannot be associated with direct inputs from the two forebrain structures. Possible sources of projections for activating GABA$_B$ receptors in the ICd and ICx include local interneurons driven by descending inputs from the AC or the MG as well as neurons in the ICc. *In vivo* neurophysiological experiments revealed that electrical stimulation of the AC results in a delayed and long-lasting inhibitory effect on responses to sounds in the IC (Syka and Popelár, 1984; Torterolo et al., 1998; Bledsoe et al., 2003). These results support the existence of local GABAergic interneurons innervated by cortico-collicular projections.

The existence of GABA$_B$R1 and GABA$_B$R2 subunits in cell bodies and the neuropil in the CIC region is interesting. It is well known that the left and right inferior colliculi are connected by the CIC (Malmierca et al., 2009b). Some of the CIC fibers are GABAergic (Hernández et al., 2006). Therefore, the possibility exists that some GABA$_B$ receptors in the IC are associated with CIC inputs. *In vitro* physiological recordings have indicated that

inhibitory postsynaptic potentials elicited in IC neurons by stimulation of CIC fibers can be completely blocked by bicuculline, an antagonist for the GABA$_A$ receptor (Smith, 1992; Moore et al., 1998). It is therefore unlikely that commissural stimulation can directly activate postsynaptic GABA$_B$ receptors. Inhibitory postsynaptic potentials elicited by stimulation of CIC display paired-pulse inhibition that can be suppressed by an antagonist of the GABA$_B$ receptor (Li et al., 1999). This finding suggests that stimulation of CIC can lead to the activation of presynaptic GABA$_B$ receptors that regulate the release of inhibitory neurotransmitters. However, it is still unknown whether these GABA$_B$ receptors are directly activated by CIC fibers or indirectly through local interneurons. Further research is needed for finding the relationship between GABA$_B$ receptors and CIC projections.

AREA DIFFERENCES IN RECEPTOR EXPRESSION AND SYNAPTIC FUNCTIONS

As revealed by the present study, area differences exist in the level and cellular distribution of the GABA$_B$ receptor in the IC. While the level of cell body immunoreactivity was very similar in different collicular subdivisions, the level of neuropil immunoreactivity was higher in the ICd than in the other collicular subdivisions. Concomitantly, area differences exist in the synaptic function of the receptor in the IC. In the ICc, GABA$_B$ receptors only exist at presynaptic sites and are responsible for the regulation of the release of glutamate and GABA (Hosomi et al., 1997; Lo et al., 1998; Ma et al., 2002; Sun et al., 2006). In the ICd, GABA$_B$ receptors exist at both pre- and postsynaptic sites, with postsynaptic GABA$_B$ receptors involved in the mediation of inhibitory postsynaptic potentials and presynaptic GABA$_B$ receptors involved in the regulation of release of glutamate and GABA (Sun and Wu, 2009). Similar to results from other neural structures including the hippocampus and substantia nigra pars compact (Isaacson et al., 1993; Kulik et al., 2003; Saitoh et al., 2004), inhibitory postsynaptic currents mediated by GABA$_B$ receptors in the ICd can only be evoked by electrical pulses presented at a high repetition rate (Sun and Wu, 2009). In many brain structures, inhibitory postsynaptic potentials mediated by GABA$_B$ receptor at a high rate of stimulation are elicited as a result of spillover of GABA from the synaptic cleft as postsynaptic GABA$_B$ receptors exist mainly at extrasynaptic sites of the cell membrane (Ige et al., 2000; Gonchar et al., 2001; Kulik et al., 2002, 2003). Our results regarding higher neuropil levels of the GABA$_B$R1 and GABA$_B$R2 in the ICd than ICc likely suggest that the postsynaptic function of the GABA$_B$ receptor in the ICd is associated with axodendritic synapses in the neuropil. The presynaptic function of the GABA$_B$ receptor in the IC may be associated with axosomatic synapses, although the contribution of axodendritic synapses to the presynaptic function of GABA$_B$ receptors in the ICd cannot be ruled out. Moreover, it's very possible that spillover of GABA from the synaptic cleft can activate the postsynaptic GABA$_B$ receptors in the neuropil in the ICd. Further experiments have yet to be conducted to confirm these suggestions.

AUDITORY FUNCTIONS OF THE GABA$_B$ RECEPTOR

Previous *in vivo* neurophysiological studies have shown that responses elicited by tone bursts and amplitude modulated tones in the IC can be changed by local application of agonists or antagonists of the GABA$_B$ receptor (Faingold et al., 1989; Szczepaniak and Møller, 1995, 1996; Vaughn et al., 1996; Burger and Pollak, 1998). These results indicate that the GABA$_B$ receptor is involved in auditory processing in this structure. It has yet to be determined what specific aspects of auditory processing are dependent on the GABA$_B$ receptor.

As the GABA$_B$ receptor has multiple pre- and postsynaptic functions including the mediation of inhibitory postsynaptic potentials and regulation of the release of glutamate and GABA, the receptor likely plays an important role in many aspects of auditory processing in the IC. However, it is unlikely that these functions are related to the processing of fine temporal structures of sounds. The reason is that the time course of the activation of the receptor is relatively slow, as this activation results in changes in the opening probability of ion channels through involving a guanine nucleotide-binding protein and multiple intracellular signaling steps (Chalifoux and Carter, 2011). In the IC, the duration of the inhibitory postsynaptic current mediated by the GABA$_B$ receptor lasts for over 800 ms (Sun and Wu, 2009).

The pre- and postsynaptic functions of the GABA$_B$ receptor along with the slow time course of activation suggests that the receptor is important for regulating the overall neural sensitivity to sounds as well as for setting the gain of signal processing in auditory neurons. Long-lasting inhibition mediated by the GABA$_B$ receptor can counteract with long-lasting excitation mediated by the NMDA receptor. This counteraction can help maintain a balance between excitation and inhibition in neural processing (Morrisett et al., 1991; Sun and Wu, 2009).

The GABA$_B$ receptor is important for plastic changes of neural sensitivity to stimuli in the IC. *In vitro* neurophysiological recordings in the ICc have revealed that presynaptic GABA$_B$ receptors contribute to long-term potentiation in the structure (Zhang and Wu, 2000). Studies in other auditory structures as well as non-auditory structures have shown that GABA$_B$ receptors also contribute to other forms of plastic changes of neural responses. For example, postsynaptic GABA$_B$ receptors in the lateral superior olive are important for long-term depression of inhibitory transmission (Kotak et al., 2001; Chang et al., 2003). Presynaptic GABA$_B$ receptors are important for short-term depression of glutamatergic transmission in avian auditory brainstem neurons (Brenowitz et al., 1998) and frequency-dependent depression of excitatory potentials in perirhinal cortex (Ziakopoulos et al., 2000). It has yet to be determined whether GABA$_B$ receptors in the rat's IC can also cause these types of plastic changes in synaptic responses. In response to sounds, neurons in the IC display a type of short-term plastic change termed stimulus-specific adaptation (SSA) (Pérez-González et al., 2005, 2012; Malmierca et al., 2009a; Lumani and Zhang, 2010; Patel et al., 2012). These neurons reduce their sensitivity to sounds over repetitive presentations and increase the sensitivity when novel sounds are presented in the acoustic environment. Among the three subdivisions of the IC, the ICd and ICx have more neurons showing high-degree of SSA. In the ICd, the generation of SSA is likely dependent on inhibitory events that are slightly delayed but long lasting compared with excitatory events (Patel et al., 2012).

The relatively slow time course of activation of the GABA$_B$ receptor makes it an ideal candidate for mediating these long-lasting inhibitory events. The coincidence between strong SSA in the ICd and a high level of the GABA$_B$ receptor in this collicular subdivision supports the involvement of the receptor in the generation of SSA. *In vivo* neuropharmacological experiments have yet to be conducted to verify this possibility.

The level of sensitivity to sounds and the gain of signal processing in auditory neurons are important for many other aspects of hearing. Age-related hearing loss, tinnitus, and audiogenic seizures can all be related to an abnormal level of sensitivity and gain in the IC (Caspary et al., 1995; Faingold, 2002; Wang et al., 2011). With its pre- and postsynaptic functions in regulating the sensitivity and gain in auditory neurons, the GABA$_B$ receptor has to maintain a normal level of expression in the IC for preventing these hearing problems from occurring.

ACKNOWLEDGMENTS

This research is supported by a grant from the Natural Science and Engineering Research Council of Canada to Huiming Zhang We thank Dr. Lisa Porter for kindly providing a facility for conducting Western blotting experiments. We thank Dr. Barbara Zielinski for assistance in immunohistochemical experiments. We also thank Cory Ochs for providing assistance in the collection of tissue for Western blotting and immunohistochemical experiments.

REFERENCES

Adams, J. C., and Mugnaini, E. (1984). Dorsal nucleus of the lateral lemniscus: a nucleus of GABAergic projection neurons. *Brain Res. Bull.* 13, 585–590.

Benke, D., Michel, C., and Mohler, H. (2002). Structure of GABA$_B$ receptors in rat retina. *J. Recept. Signal Transduct. Res.* 22, 253–266.

Bledsoe, S. C., Shore, S. E., and Guitton, M. J. (2003). Spatial representation of corticofugal input in the inferior colliculus: a multicontact silicon probe approach. *Exp. Brain Res.* 153, 530–542.

Bowery, N. G., Hudson, A. L., and Price, G. W. (1987). GABA$_A$ and GABA$_B$ receptor site distribution in the rat central nervous system. *Neuroscience* 20, 365–383.

Brenowitz, S., David, J., Trusell, L. (1998). Enhancement of synaptic efficacy by presynaptic GABA$_B$ receptors. *Neuron* 20, 135–141.

Burger, R. M., and Pollak, G. D. (1998). Analysis of the role of inhibition in shaping responses to sinusoidally amplitude-modulated signals in the inferior colliculus. *J. Neurophysiol.* 80, 1686–1701.

Cant, N. B. (2005). "Projections from the cochlear nucleus complex to the inferior colliculus," in *The Inferior Colliculus,* eds J. A. Winer and C. E. Schreiner (New York, NY: Springer), 115–132.

Caspary, D. M., Ling, L., Turner, J. G., and Hughes, L. F. (2008). Inhibitory neurotransmission, plasticity and aging in the mammalian central auditory system. *J. Exp. Biol.* 211, 1781–1791.

Caspary, D. M., Milbrandt, J. C., and Helfert, R. H. (1995). Central auditory aging: GABAchanges in the inferior colliculus. *Exp. Gerontol.* 30, 349–360.

Chalifoux, J. R., and Carter, A. G. (2011). GABA$_B$ receptor modulation of synaptic function. *Curr. Opin. Neurobiol.* 21, 339–344.

Chang, E. H., Kotak, V. C., Sanes, D. H. (2003). Long-term depression of synaptic inhibition is expressed postsynaptically in the developing auditory system. *J. Neurophysiol.* 90, 1479–1488.

Charles, K. J., Evans, M. L., Robbins, M. J., Calver, A. R., Leslie, R. A., and Pangalos, M. N. (2001). Comparative immunohistochemical localisation of GABA$_{B1a}$, GABA$_{B1b}$ and GABA$_{B2}$ subunits in rat brain, spinal cord, and dorsal root ganglion. *Neuroscience* 106, 447–467.

Chen, L., Kelly, J. B., and Wu, S. H. (1999). The commissure of probst as a source of GABAergic inhibition. *Hear. Res.* 138, 106–114.

Enna, S. J., and Möhler, H. (2007). *The GABA Receptors, 3rd Edn*. Totowa, NJ: Humana Press.

Faingold, C. L. (2002). Role of GABA abnormalities in the inferior colliculus pathophysiology-audiogenic seizures. *Hear. Res.* 168, 223–237.

Faingold, C. L., Gehlbach, G., and Caspary, D. M. (1989). On the role of GABA as an inhibitory neurotransmitter in inferior colliculus neurons: iontophoretic studies. *Brain Res.* 500, 302–312.

Faye-Lund, H., and Osen, K. K. (1985). Anatomy of the inferior colliculus in rat. *Anat. Embryol.* 171, 1–20.

Feliciano, M., and Potashner, S. J. (1995). Evidence for a glutamatergic pathway from the guinea pig auditory cortex to the inferior colliculus. *J. Neurochem.* 65, 1348–1357.

Filippov, A. K., Couve, A., Pangalos, M. N., Walsh, F. S., Brown, D. A., and Moss, S. J. (2000). Heteromeric assembly of GABA$_B$R1 and GABA$_B$R2 receptor subunits inhibits Ca^{2+} current in sympathetic neurons. *J. Neurosci.* 20, 2867–2874.

Fubara, B. M., Casseday, J. H., Covey, E., and Schwartz-Bloom, R. D. (1996). Distribution of GABA$_A$, GABA$_B$, and glycine receptors in the central auditory system of the big brown bat, *Eptesicus fuscus*. *J. Comp. Neurol.* 369, 83–92.

Glendenning, K. K., and Baker, B. N. (1988). Neuroanatomical distribution of receptors for three potential inhibitory neurotransmitters in the brainstem auditory nuclei of the cat. *J. Comp. Neurol.* 275, 288–308.

Gonchar, Y., Pang, L., Malitscherk, B., Bettler, B., and Burkhalter, A. (2001). Subcellular localization of GABA$_B$ receptor subunits in rat visual cortex. *J. Comp. Neurol.* 431, 182–197.

González-Hernández, T., Montolán-Sarmiento, B., González-González, B., and Pérez-González, H. (1996). Sources of GABAergic input to the inferior colliculus of the rat. *J. Comp. Neurol.* 372, 309–326.

Helfert, R. H., Bonneau, J. M., Wenthold, R. J., and Altschuler, R. A. (1989). GABA and glycine immunoreactivity in the guinea pig superior olivary complex. *Brain Res.* 501, 269–286.

Hernández, O., Rees, A., and Malmierca, M. S. (2006). A GABAergic component in the commissure of the inferior colliculus in rat. *Neuroreport* 17, 1611–1614.

Hilbig, H., Nowack, S., Boeckler, K., Bidmon, H. J., and Zilles, K. (2007). Characterization of neuronal subsets surrounded by perineuronal nets in the rhesus auditory brainstem. *J. Anat.* 210, 507–517.

Hosomi, H., Mori, M., Amatsu, M., and Okada, Y. (1997). GABA-activated con- ductance in cultured rat inferior colliculus neurons. *J. Neurophysiol.* 77, 994–1002.

Huang, Z. J. (2006). GABAB receptor isoforms caught in action at the scene. *Neuron* 50, 521–524.

Ige, A. O., Bolam, J. P., Billinton, A., White, J. H., Marshall, F. H., and Emson, P. C. (2000). Cellular and subcellular localisation of GABA(B1) and GABA(B2) receptor proteins in the rat cerebellum. *Mol. Brain Res.* 83, 72–80.

Isaacson, J. S., Solis, J. M., and Nicoll, R. A. (1993). Local and diffuse synaptic actions of GABA in the hippocampus. *Neuron* 10, 165–175.

Jamal, L., Zhang, H., Finlayson, P. G., Porter, L. A., and Zhang, H. (2011). The level and distribution of the GABABR2 receptor subunit in the rat's central auditory system. *Neuroscience* 181, 243–256.

Kelly, J. B., and Caspary, D. M. (2005). "Pharmacology of the inferior colliculus," in *The Inferior Colliculus*, eds J. A. Winer and C. E. Schreiner (New York, NY: Springer), 248–281.

Kornau, H. C. (2006). GABA(B) receptors and synaptic modulation. *Cell Tissue Res.* 326, 517–533.

Kotak, V. C., DiMattina, C., and Sanes, D. H. (2001). GABA$_B$ and Trk receptor signaling mediates long-lasting inhibitory synaptic depression. *J. Neurophysiol.* 86, 536–540.

Kulesza, R. J. Jr., and Berrebi, A. S. (2000). Superior paraolivary nucleus of the rat is a GABAergic nucleus. *J. Assoc. Res. Otolaryngol.* 1, 255–269.

Kulik, A., Nakadate, K., Nyiri, G., Notomi, T., Malitschek, B., Bettler, B., et al. (2002). Distinct localization of GABA(B) receptors relative to synaptic sites in the rat cerebellum and ventrobasal thalamus. *Eur. J. Neurosci.* 15, 291–307.

Kulik, A., Vida, I., Luján, R., Haas, C. A., López-Bendito, G., Shigemoto, R., et al. (2003). Subcellular localization of metabotropic GABA(B) receptor subunits GABA(B1a/b) and GABA(B2) in the rat hippocampus. *J. Neurosci.* 23, 11026–11035.

Kuner, R., Kohr, G., Grunewald, S., Eisenhardt, G., Bach, A., and Kornau, H. C. (1999). Role of heteromer formation in GABA$_B$ receptor function. *Science* 283, 74–77.

Kuwabara, N., and Zook, J. M. (2000). Geniculo-collicular descending projections in the gerbil. *Brain Res.* 878, 79–87.

LeBeau, F. E. N., Malmierca, M. S., and Rees, A. (2001). Iontophoresis *in vivo* demonstrates a key role for GABA$_A$ and glycinergic inhibition in shaping frequency response areas in the inferior colliculus of guinea pig. *J. Neurosci.* 21, 7303–7312.

Li, L., and Kelly, J. B. (1992). Inhibitory influence of the dorsal nucleus of the lateral lemniscus on binaural responses in the rat's inferior colliculus. *J. Neurosci.* 12, 4530–4539.

Li, Y., Evans, M. S., and Faingold, C. L. (1999). Synaptic response patterns of neurons in the cortex of rat inferior colliculus. *Hear. Res.* 137, 15–28.

Lo, Y.-J., Rao, S. C., and Sanes, D. H. (1998). Modulation of calcium by inhibitory systems in the developing auditory midbrain. *Neuroscience* 83, 1075–1084.

Loftus, W. C., Malmierca, M. S., Bishop, D. C., and Oliver, D. L. (2008). The cytoarchitecture of the inferior colliculus revisited: a common organization of the lateral cortex in rat and cat. *Neuroscience* 154, 196–205.

López-Bendito, G., Shigemoto, R., Kulik, A., Paulsen, O., Fairén, A., and Luján, R. (2002). Expression and distribution of metabotropic GABA receptor subtypes GABA$_B$R1 and GABA$_B$R2 during rat neocortical development. *Eur. J. Neurosci.* 15, 1766–1778.

Lumani, A., and Zhang, H. (2010). Responses of neurons in the rat's dorsal cortex of the inferior colliculus to monaural tone bursts. *Brain Res.* 1351, 115–129.

Luscher, C., Jan, L. Y., Stoffel, M., Malenka, R. C., and Nicoll, R. A. (1997). G protein-coupled inwardly rectifying K channels (GIRKs) mediate postsynaptic but not presynaptic transmitter actions in hippocampal neurons. *Neuron* 19, 687–695.

Ma, C. L., Kelly, J. B., and Wu, S. H. (2002). Presynaptic modulation of GABAergic inhibition by GABA$_B$ receptors in the rat's inferior colliculus. *Neuroscience* 114, 207–215.

Malmierca, M. S. (1991). *Computer-Assisted 3D Reconstructions of Golgi-Impregnated Cells in the Rat Inferior Colliculus.* Ph.D. thesis, University of Salamanca and University of Oslo.

Malmierca, M. S., Blackstad, T. W., and Osen, K. K. (2011). Computer-assisted 3-D reconstructions of Golgi-impregnated neurons in the cortical regions of the inferior colliculus of rat. *Hear. Res.* 274, 13–26.

Malmierca, M. S., Blackstad, T. W., Osen, K. K., Karagülle, T., and Molowny, R. L. (1993). The central nucleus of the inferior colliculus in rat: a golgi and computer reconstruction study of neuronal and laminar structure. *J. Comp. Neurol.* 333, 1–27.

Malmierca, M. S., Cristaudo, S., Pérez-González, D., and Covey, E. (2009a). Stimulus- specific adaptation in the inferior colliculus of the anesthetized rat. *J. Neurosci.* 29, 5483–5493.

Malmierca, M. S., Hernández, O., Antunes, F. M., and Rees, A. (2009b). Divergent and point-to-point connections in the commissural pathway between the inferior colliculi. *J. Comp. Neurol.* 514, 226–239.

Malmierca, M. S., and Merchán, M. A. (2004). "Auditory system," in *The Rat Nervous System, 3rd Edn,* ed G. Paxinos (San Diego, CA: Academic Press), 997–1082.

Malmierca, M. S., Seip, K. L., and Osen, K. K. (1995). Morphological classification and identification of neurons in the inferior colliculus: a multivariate analysis. *Anat. Embryol. (Berl.)* 191, 343–350.

Marianowski, R., Liao, W. H., Van Den Abbeele, T., Fillit, P., Herman, P., Frachet, B., et al. (2000). Expression of NMDA AMPA and GABA(A) receptor subunit mRNAs in the rat auditory brainstem: I. Influence of early auditory deprivation. *Hear. Res.* 150, 1–11.

Marshall, F. H., and Foord, S. M. (2010). Heterodimerization of the GABAB receptor-implications for GPCR signaling and drug discovery. *Adv. Pharmacol.* 58, 63–91.

Merchán, M., Aguilar, L. A., Lopez-Poveda, E. A., and Malmierca, M. S. (2005). The inferior colliculus of the rat: quantitative immunocytochemical study of GABA and glycine. *Neuroscience* 136, 907–925.

Merchán, M., Saldaña, E., and Plaza, I. (1994). Dorsal nucleus of the lateral lemniscus in the rat: concentric organization and tonotopic projection to the inferior colliculus. *J. Comp. Neurol.* 342, 259–278.

Milbrandt, J. C., Albin, R. L., and Caspary, D. M. (1994). Age-related decrease in GABA$_B$ receptor binding in the Fischer 344 rat inferior colliculus. *Neurobiol. Aging* 15, 699–703.

Mintz, I. M., and Bean, B. P. (1993). GABA$_B$ receptor inhibition of P-type Ca^{2+} channels in central neurons. *Neuron* 10, 889–898.

Moore, D. R., Kotak, V. C., and Sanes, D. H. (1998). Commissural and lemniscal synaptic input to the gerbil inferior colliculus. *J. Neurophysiol.* 80, 2229–2236.

Morrisett, R. A., Mott, D. D., Lewis, D. V., Swartzwelder, H. S., and Wilson, W. A. (1991). GABA$_B$-receptor-mediated inhibition of the N-methyl-D-aspartate component of synaptic transmission in the rat hippocampus. *J. Neurosci.* 11, 203–209.

Oliver, D. L. (1984). Neuron types in the central nucleus of the inferior colliculus that project to the medial geniculate body. *Neuroscience* 11, 409–424.

Oliver, D. L. (2005). "Neuronal organization in the inferior colliculus," in *The Inferior Colliculus,* eds J. A. Winer and C. E. Schreiner (New York, NY: Springer), 69–114.

Oliver, D. L., Kuwada, S., Yin, T. C., Haberly, L. B., and Henkel, C. K. (1991). Dendritic and axonal morphology of HRP-injected neurons in the inferior colliculus of the cat. *J. Comp. Neurol.* 303, 75–100.

Oliver, D. L., and Morest, D. K. (1984). The central nucleus of the inferior colliculus in the cat. *J. Comp. Neurol.* 222, 237–264.

Oliver, D. L., Winer, J. A., Beckius, G. E., and Saint Marie, R. L. (1994). Mophology of GABAergic neurons in the inferior colliculus of the cat. *J. Comp. Neurol.* 340, 27–42.

Panzanelli, P., López-Bendito, G., Luján, R., and Sassoé-Pognetto, M. (2004). Localization and developmental expression of GABAB receptors in the rat olfactory bulb. *J. Neurocytol.* 33, 87–99.

Patel, C. R., Redhead, C., Cervi, A. L., and Zhang, H. (2012). Neural sensitivity to novel sounds in the rat's dorsal cortex of the inferior colliculus as revealed by evoked local field potentials. *Hear. Res.* 286, 41–54.

Paxinos, G., and Watson, C. (2007). *The Rat Brain in Stereotaxic Coordinates, 6th Edn.* Amsterdam: Academic Press.

Pérez-González, D., Hernández, O., Covey, E., and Malmierca, M. S. (2012). GABA(A)-mediated inhibition modulates stimulus-specific adaptation in the inferior colliculus. *PLoS ONE* 7:e34297. doi: 10.1371/journal.pone.0034297

Pérez-González, D., Malmierca, M. S., and Covey, E. (2005). Novelty detector neurons in the mammalian auditory midbrain. *Eur. J. Neurosci.* 22, 2879–2885.

Pin, J. P., Kniazeff, J., Binet, V., Liu, J., Maurel, D., Galvez, T., et al. (2004). Activation mechanism of the heterodimeric GABAB receptor. *Biochem. Pharmacol.* 68, 1565–1572.

Pooler, A. M., and McIlhinney, R. A. (2007). Lateral diffusion of the GABA$_B$ receptor is regulated by the GABAB2 C terminus. *J. Biol. Chem.* 282, 25349–25356.

Restituito, S., Couve, A., Bawagan, H., Jourdain, S., Pangalos, M. N., Calver, A. R., et al. (2005). Multiple motifs regulate the trafficking of GABA(B) receptors at distinct checkpoints within the secretory pathway. *Mol. Cell. Neurosci.* 28, 747–756.

Riquelme, R., Saldaña, E., Osen, K. K., Ottersen, O. P., and Merchán, M. A. (2001). Colocalization of GABA and glycine in the ventral nucleus of the lateral lemniscus in rat: an in situ hybridization and semiquantitative immunocytochemical study. *J. Comp. Neurol.* 432, 409–424.

Roberts, R. C., and Ribak, C. E. (1987). An electron microscopic study of GABAergic neurons and terminals in the central nucleus of the inferior colliculus of the rat. *J. Neurocytol.* 16, 333–345.

Saldaña, E., Aparicio, M. A., Fuentes-Santamaría, V., and Berrebi, A. S. (2009). Connections of the superior paraolivary nucleus of the rat: projections to the inferior colliculus. *Neuroscience* 163, 372–387.

Saint Marie, R. L., and Baker, R. A. (1990). Neurotransmitter-specific uptake and retrograde transport of [3H] glycine from the inferior colliculus by ipsilateral projections of the superior olivary complex and nuclei of the lateral lemniscus. *Brain Res.* 524, 244–253.

Saint Marie, R. L., Ostapoff, E.-M., Morest, D. K., and Wenthold, R. J. (1989). Glycine-immunoreactive projection of the cat lateral superior olive: possible role in midbrain ear dominance. *J. Comp. Neurol.* 279, 382–396.

Saitoh, K., Isa, T., and Takakusaki, K. (2004). Nigra GABAergic inhibition upon mesencephalic dopaminergic cell groups in rats. *Eur. J. Neurosci.* 19, 2399–2409.

Schofield, B. R. (2005). "Superior olivary complex and lateral lemniscal connections of the auditory midbrain," in *The Inferior Colliculus,* eds J. A. Winer and C. E. Schreiner (New York, NY: Springer), 132–154.

Shiraishi, S., Shiraishi, Y., Oliver, D. L., and Altschuler, R. A. (2001). Expression of GABA(A) receptor subunits in the rat central nucleus of the inferior colliculus. *Brain Res. Mol. Brain Res.* 96, 122–132.

Shneiderman, A., Chase, M. B., Rockwood, J. M., Benson, C. G., and Potashner, S. J. (1993). Evidence for a GABAergic projection from the dorsal nucleus of the lateral lemniscus to the inferior colliculus. *J. Neurochem.* 60, 72–82.

Shneiderman, A., Oliver, D. L., and Henkel, C. K. (1988). Connections of the dorsal nucleus of the lateral lemnioscus: an inhibitory parallel pathway in the ascending auditory system? *J. Comp. Neurol.* 276, 188–208.

Smith, P. H. (1992). Anatomy and physiology of multipolar cells in the rat inferior collicular cortex using the *in vitro* brain slice technique. *J. Neurosci.* 12, 3700–3715.

Sun, H., Ma, C. L., Kelly, J. B., and Wu, S. H. (2006). GABA$_B$ receptor-mediated presynaptic inhibition of glutamatergic transmission in the inferior colliculus. *Neurosci. Lett.* 399, 151–156.

Sun, H., and Wu, S. H. (2009). The physiological role of pre- and postsynaptic GABA$_B$ receptors in membrane excitability and synaptic transmission of neurons in the rat's dorsal cortex of the inferior colliculus. *Neuroscience* 160, 198–211.

Syka, J., and Popelár, J. (1984). Inferior colliculus in the rat: neuronal responses to stimulation of the auditory cortex. *Neurosci. Lett.* 51, 235–240.

Szczepaniak, W. S., and Møller, A. R. (1995). Effects of L-baclofen and D-baclofen on the auditory system: a study of click-evoked potentials from the inferior colliculus in the rat. *Ann. Otol. Rhinol. Laryngol.* 104, 399–404.

Szczepaniak, W. S., and Møller, A. R. (1996). Effects of (-)-baclofen, clonazepam, and diazepam on tone exposure-induced hyperexcitability of the inferior colliculus in the rat: possible therapeutic implications for pharmacological management of tinnitus and hyperacusis. *Hear. Res.* 97, 46–53.

Torterolo, P., Zurita, P., Pedemonte, M., and Vellut, R. A. (1998). Auditory cortical efferent actions upon inferior colliculus unitary activity in the guinea pig. *Neurosci. Lett.* 249, 172–176.

Ulrich, D., and Bettler, B. (2007). GABA(B) receptors: synaptic functions and mechanisms of diversity. *Curr. Opin. Neurobiol.* 17, 298–303.

Vater, M., Kössl, M., and Horn, A. K. E. (1992). GAD- and GABA-immunoreactivity in the ascending auditory pathway of horseshoe and mustached bats. *J. Comp. Neurol.* 325, 183–206.

Vaughn, M. D., Pozza, M. F., and Lingenhöhl, K. (1996). Excitatory acoustic responses in the inferior colliculus of the rat are increased by GABA$_B$ receptor blockade. *Neuropharmacology* 35, 1761–1767.

Wang, H., Brozoski, T. J., and Caspary, D. M. (2011). Inhibitory neurotransmission in animal models of tinnitus: maladaptive plasticity. *Hear. Res.* 279, 111–117.

White, J. H., Wise, A., Main, M. J., Green, A., Fraser, N. J., Disney, G. H., et al. (1998). Heterodimerization is required for the formation of a functional GABA$_B$ receptor. *Nature* 396, 679–682.

Winer, J. A. (2006). Decoding the auditory corticofugal systems. *Hear. Res.* 212, 1–8.

Winer, J. A., and Larue, D. T. (1996). Evolution of GABAergic circuitry in the mammalian medial geniculate body. *Proc. Natl. Acad. Sci. U.S.A.* 93, 3083–3087.

Zhang, D. X., Li, L., Kelly, J. B., and Wu, S. H. (1998). GABAergic projections from the lateral lemniscus to the inferior colliculus of the rat. *Hear. Res.* 117, 1–12.

Zhang, H., and Kelly, J. B. (2003). Glutamatergic and GABAergic regulation of neural responses in inferior colliculus to amplitude-modulated sounds. *J. Neurophysiol.* 90, 477–490.

Zhang, Y., and Wu, S. H. (2000). Long-term potentiation in the inferior colliculus studied in rat brain slice. *Hear. Res.* 147, 92–103.

Ziakopoulos, Z., Brown, M. W., Bashir, Z. I. (2000). GABA$_B$ receptors mediate frequency-dependent depression of excitatory potentials in rat perirhinal cortex *in vitro*. *Eur. J. Neurosci.* 12, 803–809.

Conflict of Interest Statement: The authors declare that the research was conducted in the absence of any commercial or financial relationships that could be construed as a potential conflict of interest.

Received: 31 May 2012; accepted: 02 November 2012; published online: 26 November 2012.

Citation: Jamal L, Khan AN, Butt S, Patel CR and Zhang H (2012) The level and distribution of the GABA$_B$R1 and GABA$_B$R2 receptor subunits in the rat's inferior colliculus. Front. Neural Circuits ***6****:92. doi: 10.3389/fncir.2012.00092*

frontiers in
NEURAL CIRCUITS

ORIGINAL RESEARCH ARTICLE
published: 20 March 2013
doi: 10.3389/fncir.2013.00041

Functional architecture of the inferior colliculus revealed with voltage-sensitive dyes

Lakshmi Chandrasekaran, Ying Xiao and Shobhana Sivaramakrishnan*

Department of Anatomy and Neurobiology, Northeast Ohio Medical University, Rootstown, OH, USA

Edited by:
Manuel S. Malmierca, University of Salamanca, Spain

Reviewed by:
Julian Budd, University of Sussex, UK
Alan R. Palmer, Medical Research Council Institute of Hearing Research, UK
Monty Escabi, The University of Connecticut, USA

****Correspondence:***
Shobhana Sivaramakrishnan, Department of Anatomy and Neurobiology, Northeast Ohio Medical University, 4209 State Route 44, Rootstown, OH 44272, USA.
e-mail: ssivaram@neomed.edu

We used optical imaging with voltage-sensitive dyes to investigate the spatio-temporal dynamics of synaptically evoked activity in brain slices of the inferior colliculus (IC). Responses in transverse slices which preserve cross-frequency connections and in modified sagittal slices that preserve connections within frequency laminae were evoked by activating the lateral lemniscal tract. Comparing activity between small and large populations of cells revealed response areas in the central nucleus of the IC that were similar in magnitude but graded temporally. In transverse sections, these response areas are summed to generate a topographic response profile. Activity through the commissure to the contralateral IC required an excitation threshold that was reached when GABAergic inhibition was blocked. Within laminae, module interaction created temporal homeostasis. Diffuse activity evoked by a single lemniscal shock re-organized into distinct spatial and temporal compartments when stimulus trains were used, and generated a directional activity profile within the lamina. Using different stimulus patterns to activate subsets of microcircuits in the central nucleus of the IC, we found that localized responses evoked by low-frequency stimulus trains spread extensively when train frequency was increased, suggesting recruitment of silent microcircuits. Long stimulus trains activated a circuit specific to post-inhibitory rebound neurons. Rebound microcircuits were defined by a focal point of initiation that spread to an annular ring that oscillated between inhibition and excitation. We propose that much of the computing power of the IC is derived from local circuits, some of which are cell-type specific. These circuits organize activity within and across frequency laminae, and are critical in determining the stimulus-selectivity of auditory coding.

Keywords: laminar organization, population coding, microcircuits, local circuits, post-inhibitory rebound

INTRODUCTION

The inferior colliculus (IC) is the first major computational opportunity in the central auditory system, and provides information about the identity and location of a sound source. Extensive input convergence from most ascending and descending auditory areas (Oliver, 1984; Glendenning et al., 1992; Winer et al., 1998) gives the IC a critical position in auditory coding. In addition to external inputs, local circuitry within each colliculus (Oliver et al., 1991), commissural connections between colliculi (Aitkin and Phillips, 1984) and morphological and physiological cell-type heterogeneity (Oliver and Morest, 1984; Faye-Lund and Osen, 1985; Herrera et al., 1988; Paloff et al., 1992; Malmierca et al., 1993; Sivaramakrishnan and Oliver, 2001) generates a complex functional architecture that produces the broad range of responses to complex sounds that characterizes the IC (Irvine, 1992). In the same neuron, for instance, sounds can evoke excitatory and inhibitory synaptic potentials, and the timing and interactions of postsynaptic responses can be altered by varying the frequency or inter-aural properties of the sound (Nelson and Erulkar, 1963). The timing of synaptic and spike responses to free-field acoustic stimulation varies between neurons (Covey et al., 1996), and supra-threshold response properties are altered by inhibition (Kuwada et al., 1997). Understanding the basis of this extensive computing power is important for normal auditory processing and for pathological conditions where response constraints are compromised.

The anatomical architecture of the IC, with fibro-dendritic frequency laminae, cross-frequency projections, and bilateral tonotopic connectivity, provides a framework for complex acoustic processing. Laminae serve as modules of sound frequency, with rows of input axons making *en passant* synapses on neurons with aligned dendritic fields (Malmierca et al., 1993). Despite their narrow frequency range (Schreiner and Langner, 1997), however, laminae do not appear to be physiologically uniform, and exhibit systematic shifts in response characteristics such as onset latency (Langner et al., 1987) and threshold (Stiebler and Ehret, 1985). In addition to intra-laminar connections, inter-laminar connections within the same colliculus (Oliver et al., 1991) represent a major avenue for interactions between neurons tuned to different frequencies. Binaural processing also relies on commissural connectivity between the two colliculi, a major inhibitory source. Commissural fibers bilaterally connect laminae of the same best frequency (Saldaña and Merchan, 1992; Malmierca et al., 1995), and neurons activated by both lemniscal and commissural pathways (Moore et al., 1998) are distributed throughout the central nucleus (Adams, 1980; Aitkin and Phillips, 1984; Gonzalez-Hernandez et al., 1996). While the broad spectrum of functional

architecture is well characterized, less is known about local interactions that create the functional fine structure and dynamical hierarchies that give the IC its computing power.

Determining functional connectivity patterns in the IC benefits from measuring responses simultaneously in distributed neuronal populations within and across laminae. While intrinsic optical signals (Higgins et al., 2010; Middleton et al., 2011) and calcium-sensitive dyes (Grienberger et al., 2012; Kubota et al., 2012) have been used to measure population activity in the auditory system, dyes that change their activity with membrane voltage measure the point of origin of responses and their propagation and have demonstrated the dimensions and functional organization of neural circuitry in the CNS (Blasdel and Salama, 1986; Horikawa et al., 1996; Huang et al., 2010). Voltage-sensitive dyes (VSDs) are membrane-bound molecules that change either their fluorescence or absorption (depending on the VSD used) on the same time scale as membrane voltage changes (<10 μs) (Loew et al., 1985), and responses are linear in the physiological range (Ross et al., 1977), allowing real-time measurements of activity. Here, we describe the use of VSD imaging to examine the functional architecture of the IC in brain slices, and demonstrate its viability in exploring activity in real-time within and across laminae. We further demonstrate that stimuli patterned to uniquely activate physiologically distinct cell types (Sivaramakrishnan and Oliver, 2001) reveal domains of microcircuits that are cell-type specific.

MATERIALS AND METHODS

PREPARATION OF LAMINAR AND TRANSVERSE SLICES

Long-Evans rats (P18–30) or CBA/Ca mice (P18–28) were used in experiments. Procedures were in accord with the regulations of the Institutional Animal Care and Use Committee at the Northeast Ohio Medical University and guidelines of the National Institutes of Health. Techniques for making transverse and laminar brain slices through the IC have been previously described (Sivaramakrishnan et al., 2004; Sivaramakrishnan and Oliver, 2006) and will be briefly outlined here. To obtain brain slices, animals were anesthetized with isoflurane and then decapitated. A block containing the IC was removed from the brain with two transverse cuts. For transverse slices, the block was glued to the cutting stage of a vibratome (Dosaka, Japan) with the superior colliculus facing down and slices made parallel to the surface of the brain block (**Figure 1A**). For laminar slices, two additional cuts were made in the brain block, one parallel to the lateral lemniscus in the parasagittal plane and a second at 45° to the sagittal plane, parallel to the ICC laminae. The cut surface was aligned on a vibratome stage with the lemniscus and IC in the same plane (**Figure 1B**). With this orientation, the first 80–100 μm of tissue, consisting mainly of the external cortex of the IC, was discarded. Slices were 150 μm thick in both the transverse and laminar planes. Slices were made in oxygenated (95% O_2/5% CO_2) artificial cerebrospinal fluid (ACSF) (in mM: 120 NaCl, 3 KCl, 2 $CaCl_2$, 1.3 $MgSO_4$, 1 NaH_2PO_4, 20 $NaHCO_3$, 25 glucose, pH 7.4) and cut, stored and recorded from at 35°C. For recordings, slices were transferred to a temperature-regulated recording chamber and superfused with ACSF at 2 ml/min. Antagonists of the AMPA receptor (NBQX; 10 μM), the $GABA_A$ receptor (SR95531; 20 μM), and tetrodotoxin (TTX; 1 μM), a blocker of voltage-gated sodium channels, were bath applied at the same flow rates as ACSF. Chemicals were obtained from Sigma-Aldrich. Data are reported from 102 slices (72 rat IC, 30 mouse IC) from 33 rats and 21 mice.

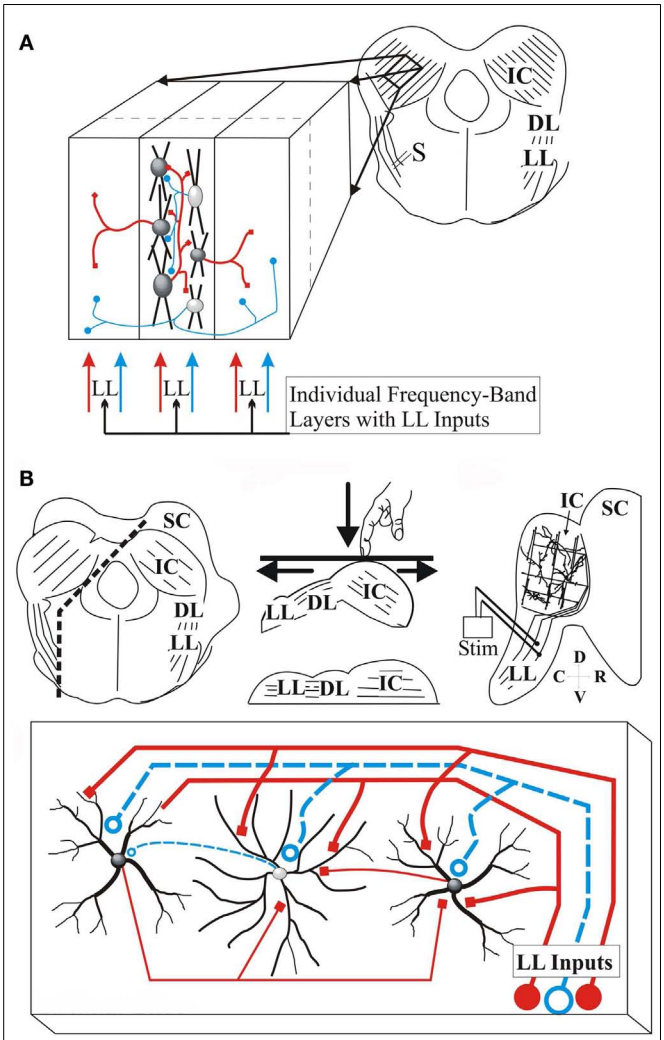

FIGURE 1 | Transverse and laminar slice planes of the IC. (A) Schematic of the transverse IC slice. Right, slice plane with parallel arrangement of laminae; IC, inferior colliculus; LL, lateral lemniscus; DL, dorsal nucleus of the lateral lemniscus; S, Lemniscal stimulating electrode; Left, Expanded region of the slice illustrates laminar and cross-laminar arrangement with lemniscal input; Center section, arrangement of cells within a lamina with intra-laminar connections; Left and right sections, neighboring laminae receive inter-laminar connections; Red, excitatory; blue, inhibitory. **(B)** Schematic of laminar IC slice plane. Top, Transverse brain slab with additional cuts to generate a laminar slab; Left panel, Direction of the two cuts (dashed lines) made in the transverse brain slab; the lower cut parallel to LL afferents and the upper cut parallel to the laminae; middle panel, orientation of the brain slab on the surface of the vibratome cutting plate. The slab is pushed down so that the bottom surface straightens out, generating a single plane containing LL afferents and the IC. Right panel, the laminar slice; Only one side of the IC is present. SC, superior colliculus; Stim, LL stimulating electrode; Bottom, The laminar slice plane contains LL input fibers synapsing on rows of disk-shaped neurons, and local circuitry; Red, excitatory; blue, inhibitory (Reprinted and adapted with permission from Springer).

ELECTRICAL STIMULATION OF THE LATERAL LEMNISCAL TRACT

The lateral lemniscal (LL) nerve bundle was stimulated with an extracellular concentric bipolar electrode made from tungsten/platinum wire, with an active diameter of 100 μm. In both the transverse and laminar slices, the stimulus electrode was placed on the LL tract before it entered the IC (**Figure 1**). The location of the LL stimulus electrode allowed stimulation of LL fibers of passage from lower brainstem nuclei as well as those from the dorsal nucleus of the LL. Stimulation was performed with a multi-channel stimulator (AMPI) through a constant current isolation unit (WPI A365). The biphasic stimulus currents used created negligible net DC current flow between pulses and prevented build-up of current on the LL tract during stimulus trains. Stimulus parameters were modified as needed to evoke specific response patterns. For "minimal" stimulus paradigms, stimulus currents and durations were kept low (<0.3 mA; 0.1–0.3 ms); in other experiments, stimulus currents or durations were increased as necessary.

MEASUREMENT OF VOLTAGE-SENSITIVE DYE SIGNALS IN IC BRAIN SLICES

Slices were incorporated with the oxonol VSD NK3630 (first synthesized by R. Hildesheim and A. Grinvald as RH482; available from Nippon Kankoh-Shikiso Kenkyusho Co., Ltd., Japan; See Momose-Sato et al., 1999 for molecular structure) dissolved in ACSF to a final concentration of 5–10 μg/ml. A staining period of 90–120 min produced even staining in the slice. After staining, slices were washed in dye-free ACSF for at least 30 min. before experiments. The slice was trans-illuminated by light from a 100 W tungsten-halogen bulb passing through a 705 nm (BW 15 nm) filter to measure peak absorbance or a 640 nm (BW 15 nm) filter (Chroma) as a control. The slice was exposed to the 705 nm wavelength only during recording, for a maximum of 2 s/trial and <50 trials per slice. With this level of exposure, photodynamic damage and dye bleaching were minimal. Images were collected with a 464-element photodiode array of optical detectors and eight additional analog channels (WuTech instruments; www.wutech.com). Frame rates with this array are ∼1600 frames/s (inter-frame interval of ∼0.614 ms). The diode array was mounted on an Olympus microscope fitted with 5× (dry, NA 0.1) and 20× (water immersion, NA 0.95) objective lenses. The optical signal from each detector was individually amplified 200 times, low-pass filtered at 333 Hz, and then multiplexed and digitized with 12 bit at 1600 samples/s/channel. Data were collected and analyzed using NeuroPlex software (RedShirtImaging, Fairfield, CT, USA) and Origin (OriginLab) and displayed as traces for numerical analysis and pseudocolor images for still time-lapse and real-time activity patterns. A digital camera fitted on to a second port was used to photograph the slice, on which VSD images were superimposed. Field potentials, measured with a tungsten electrode, were passed through a differential amplifier (A-M Systems) and fed into an auxiliary (BNC) channel of the data-acquisition interface board. In the recordings reported in this study, the field electrode was used only as an indicator of the stimulus current and did not provide any direct information about cellular activity. To minimize visual obstruction within the ICC, the field electrode was placed in the dorsal or external cortices in transverse slices and at the rostral or caudal edges of laminar slices.

Responses in the IC were evoked by activating afferent input through stimulation of the LL nerve tract with an extracellular bipolar electrode placed on the tract before it entered the IC (**Figure 2Ai**). With a 5× objective, one side of the IC is visible, extending sometimes to the beginning of the commissural region depending on the age of the animal and the species (mouse or rat) (**Figure 2Aii**). The field electrode, *f*, was placed in the dorsal or external cortices. NK3630 preferentially incorporates into neuronal membranes, with little glial contamination (Konnerth et al., 1987). We confirmed glial insensitivity in the IC by recording responses before and after blocking glial transporter currents with DL-threo-β-aspartic acid (Kojima et al., 1999) and detected no measureable change in the absorbance signal [$n = 6$ slices; average over different regions of the IC central nucleus; $t(5) = 1.31$; $p = 0.23$].

To assess the uniformity of dye penetration in the slice and to control for changes in signal magnitude with bleaching, the relative light intensity (RLI; the background absorbance in the slice) was measured before an experiment and between recordings. The RLI is generally 0.01–0.001 of the illumination intensity (the light intensity that the tissue receives), and is about 10^7 photons/ms/detector (Lippert et al., 2007). A fairly uniform RLI suggested adequate dye penetration through the slice (**Figure 2B**, compare response magnitudes of red, blue, and yellow pixels). The RLI was either subtracted from the VSD signal or the VSD signal measured as a ratio (VSD/RLI); we did not notice significant differences in the net change in the stimulus-evoked signal between these methods.

Before analysis, pixels at the edge of the diode array, those covering regions beyond the IC, and pixels covered by the field electrode (**Figure 2C**) are blanked, limiting analysis of the VSD signal to the IC or smaller regions within it. Activity may be summed or averaged over several pixels (**Figure 2C**, e.g., red pixels) or measured in single pixels (**Figure 2C**, e.g., blue and yellow pixels) and plotted as traces (**Figure 2D**). We perform several controls to detect artifactual changes in the VSD signal. Uneven fluid movement over the slice during bath perfusion, which produces varying path lengths for light transmitted to the objective, is minimized by turning off perfusion for 30 s before LL stimulation and, in addition, switching absorbance filters between the 705 nm (BW15 nm) filter used with NK3630 (**Figure 2D**, top traces) to a 640 nm (BW15 nm) filter, which filters out the NK3630 signal (**Figure 2D**, bottom traces). A second potential source of artifact is phototoxicity. NK3630 has been reported to have almost no toxicity at the concentrations we used (Xu et al., 2010), however, we tested for toxicity by comparing the field potential and VSD signals before and after turning on the transmitted light and placing the 705 nm filter in the light path. Repeated trials showed no change in either recording, confirming a lack of toxicity in IC slices ($n = 4$ slices; $p = 0.2$). A third source of artifact, which arises from direct transmission of the electrical current from the LL stimulus electrode, is minimized by placing the stimulus electrode well away from the IC (as in **Figure 2Ai**) and using stimulus currents <5 mA. VSD signals in the central nucleus of the IC often consist of an initially rapid response followed by a slower one (**Figure 2E**, left column, single and double asterisks). To

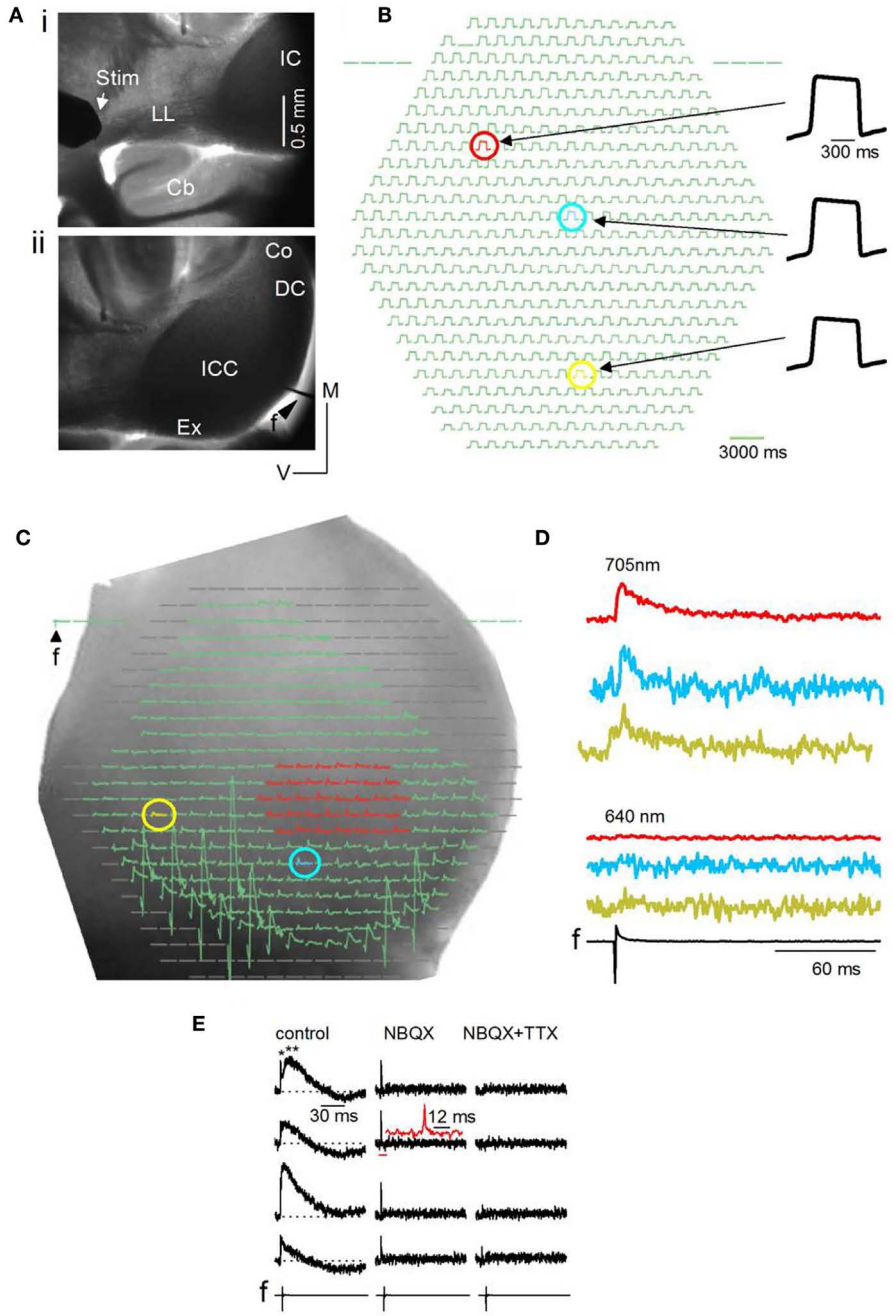

FIGURE 2 | General methods and artifactual considerations for the use of VSDs in IC brain slices. (A) Image plane of one side of the inferior colliculus (IC) (mouse, P23) viewed through a 5× objective. Transverse slice, 150 μm thick. (i) Furthest possible placement of the stimulating electrode (Stim) on the lateral lemniscal (LL) tract. Cb, cerebellum. (ii) Field electrode (*f*) at the dorsal edge of the slice. ICC, central nucleus; Ex, external cortex; DC, dorsal cortex; Co, commissure. **(B)** Resting light intensity (RLI) for a small area of the ICC; 20× objective. The RLI is the light absorbed by the VSD in the un-stimulated state. The red, blue, and yellow pixels show slight differences in maximum signal amplitude. **(C)** Diode array coverage of one side of the IC (rat) in a transverse slice. 5× objective. *f*, field electrode input. Blanked pixels outside the edge of the slice or the region of interest are omitted before analysis. Regions of interest for analysis are color-coded. Red, a group of multiple pixels over which responses are averaged; blue and yellow, different single pixels. The RLI has been subtracted before displaying this image. **(D)** VSD responses evoked by a single LL shock displayed as traces. Traces correspond to the red area and individual yellow and blue pixels selected in **(C)**. Absorbance measured through a 705 nm filter (top) and a 640 nm filter (bottom). *f*, field recording. **(E)** VSD signals evoked by a single LL shock are shown at different detectors covering the IC central nucleus. Left panel, normal ACSF; middle panel, 10 μM NBQX (an antagonist of glutamatergic AMPA receptors); right panel, 10 μM NBQX + 1 μM TTX. LL shock strength 3 mA. Left panel, top trace, single and double asterisks point to the first fast and second slower components; Inset, second trace from top, expanded region corresponds to the horizontal red bar; The 12 ms scale bar is associated with the inset.

control for stimulus current-related artifacts that may give rise to the rapid signal, in addition to switching filters between 705 and 640 nm, we apply the glutamate AMPA receptor blocker NBQX followed by the sodium channel blocker TTX. The slow response is abolished by NBQX, leaving a rapid response with the shape of a spike (**Figure 2E**, middle column; inset, second trace from top), that is abolished by the further addition of TTX (**Figure 2E**, right column), suggesting a sodium spike. Thus, provided camera frame rates are fast enough, the ability of NK3630 to distinguish between spikes and synaptic potentials in IC slices, even at low magnifications (5×), makes it a viable means of measuring fine temporal structure within activity patterns.

DATA-ACQUISITION AND ANALYSIS

The strength (current magnitude × duration) and frequency of LL stimulation were critically varying parameters in these experiments. For minimal stimulation experiments, stimulus strength was carefully adjusted, first, to obtain responses throughout the central nucleus of the IC and second, to prevent spikes in single pixels. This adjustment was made for every slice. The optimal current strength was a 0.1–0.3 ms, 0.1–0.3 mA pulse(s). Data were analyzed only if the single-pixel signal to noise ratio, averaged over the entire ICC within the field of view, was >3. For other experiments, stimulus strengths were altered as needed. Stimulus train frequencies were also adjusted, again in each slice, to generate the responses needed. For example, rebound circuits described in **Figure 14** were isolated by stimulating the LL with 20–40 Hz trains >400 ms long, using shock strengths <0.2 mA. This stimulus pattern allowed for the gradual build-up of a net hyperpolarizing response that was required to generate rebound spiking. Stimulus parameters were adjusted for each slice by examining the responses in all the pixels covering the ICC; stimulus currents were within a 0.1 mA range across different slices.

In minimal stimulation experiments, responses summed over multiple pixels were compared to responses in single pixels. Multiple pixels in each area were clustered, and the number of pixels and the region of slice they covered were kept constant between slices. We used several slices to obtain an optimum estimate of the number of pixels that would adequately represent high, middle, and low frequency regions within slices. For transverse slices, we found that 16 pixels were optimum within one slice as well as for the sample of slices used for data analysis. The selection of this number of pixels and the area they covered were determined using four main criteria: (1) the extent of coverage of each frequency region in the slice, (2) the consistency of the number of pixels covered by each frequency region in different slices, (3) no overlap between frequency regions, and (4) no loss of pixels at the edge of the slice. In the 26 transverse slices from which data are reported in **Figures 4–6**, data were analyzed using the same 4 × 4 arrangement of the 16 pixels within each topographic region in every slice. In 5 of the 26 transverse slices, one pixel in the ventral ICC (in each of three slices), and two pixels in the dorsal ICC (one in each slice) did not take up the dye and therefore did not contribute to the data. In these slices, data was analyzed from 15 pixels in the regions missing the single pixel and 16 pixels in the regions with no loss of dye. The loss of data from one pixel did not affect results significantly. In laminar slices, we used 38 pixels to define each region in both the ventral-dorsal and rostral-caudal directions. The selection of this number of pixels allowed adjacent regions of interest to be separated by two rows of pixels. To control for deterministic bias, we performed multi-pixel analysis by choosing other arrangements of clustered pixels within each region of interest, one example of which is demonstrated in **Figure 4B**. These could include as many as 40 pixels or as few as six pixels within each cluster. As long as the number of pixels was kept the same between regions, the results did not vary from the 16 pixel (transverse) or 38 pixel (laminar) clusters used in this study. Further, although we used clusters of pixels, results did not differ if random pixels were selected in an area, as long as the number of pixels between slice regions was the same. The equivalence of data obtained from different multi-pixel configurations was only possible with minimal stimulation experiments designed to evoke sub-threshold responses in individual pixels. Single-pixel analysis was performed on individual pixels, and as an average of the 16 or 38 single pixels within the same cluster used for multi-pixel analysis. For both multi- and single pixel analyses, responses within a slice were first averaged from multiple trials, and then further averaged over the sample of transverse or laminar slices.

The placement of the field electrode, which was used to record the stimulus artifact, and the position of the stimulating electrode on the LL tract varied between slices, thus all multi-pixel latencies were measured with respect to the average value of the multi-pixel onset latency in the ventral ICC. This average was determined over the same set of multiple pixels used for multi-pixel analyses. Latencies of onsets of the different peaks in different topographic regions were measured from the multi-pixel onset latency within that region. Because the amplitude of the VSD signal has arbitrary units, peak amplitudes were compared by combining multi- and single-pixel responses into one data set, and expressing all peak heights as a ratio of the peak height of the multi-pixel response in the ventral ICC. Response durations were compared using absolute values measured at half the maximum response amplitude.

Results are expressed as mean ± SEM. SD, when used, is indicated in the text. Significance was determined using Student's t-test or ANOVA where pertinent; $p < 0.05$ with the Bonferroni correction factor applied. p and $F(df1, df2)$ values are indicated in the text. Trials were repeated several times (4–10 trials) on a single slice, and the average of that data taken as the data for that particular slice. This was done for each slice in our sample. The averaged data from each slice was further averaged across all the slices. Means and SEs were calculated, significance determined, and ANOVA was performed on data both within a slice and on the pooled data from the sample.

RESULTS

We describe the use of VSD imaging in transverse and laminar slice planes to examine spatio-temporal patterns of lemniscally evoked activity across and within frequency regions.

ACTIVITY IN THE INTER-LAMINAR PLANE OF THE IC

Transverse planes of the IC preserve inter-laminar connections and minimize connections within a lamina, which are limited mainly to the dorso-ventral extent of that lamina within the slice

(Oliver et al., 1991). Commissural fibers are intact in this slice plane, connecting laminae of the same best frequency in the two colliculi (Saldaña and Merchan, 1992; Malmierca et al., 1995). Recordings in the gerbil IC show that most neurons are activated by both lemniscal and commissural pathways (Moore et al., 1998). Commissurally derived inhibition is primarily GABAergic, whereas lemniscal afferents provide both GABA and glycinergic inputs (Moore et al., 1998) with monosynaptic and polysynaptic components (Wagner, 1996; Moore et al., 1998). The transverse slice plane has been used extensively for recordings from single neurons in the central nucleus of the IC (ICC) in response to direct current injection, and lemniscal and commissural synaptic input (Moore et al., 1998; Peruzzi et al., 2000; Sivaramakrishnan and Oliver, 2001; Sivaramakrishnan et al., 2004). Incoming LL axons can be stimulated in this slice plane, with placement of the stimulus electrode allowing activation of afferent input from the dorsal nucleus of the LL and from lower brainstem centers (**Figure 1A**).

Synaptically evoked activity within the ipsilateral colliculus

We first briefly describe qualitative features of VSD responses in different regions of the IC in transverse slices ($n = 86$ slices). Slices were oriented to allow visualization, through the 5× objective, of the ICC, the external cortex and the region toward, but not including, the commissure (**Figure 3A**). We evoked synaptic activity by stimulating LL afferents, and recorded changes in VSD absorbance within the ipsilateral IC. In most regions of the ICC, low stimulus currents (<0.2 mA) evoked net depolarizing responses (**Figure 3A**, e.g., light blue, yellow, dark blue pixels; **Figure 3B**). Onset latencies and response characteristics within the ICC are described in detail in **Figures 4–13**. Outside the ICC, responses in the external cortex were predominantly depolarizing (**Figure 3A**, red pixel) and prolonged (**Figure 3B**), with durations of 278 ± 92 ms and average onset latencies delayed by 0.35 ± 0.05 ms compared to those in the ventral ICC (see Materials and Methods). In the commissural region, responses were less frequent (**Figure 3A**, pink pixel; **Figure 3B**); average response onsets lagged by 4.22 ± 0.07 ms from the ventral ICC.

Hyperpolarizing (**Figure 3A**, arrowheads; **Figure 3C**) or mixed de- and hyperpolarizing (**Figure 3A**; asterisks; **Figure 3C**) responses were less frequent than net depolarizing responses. When the net response in a pixel was hyperpolarizing, latencies of the hyperpolarizing peak were rapid (7.8 ± 2.4 ms; 108 events/18 slices) compared to latencies of hyperpolarizing responses that followed a depolarization (34 ± 12 ms; 94 events/27 slices) (**Figure 2C**; e.g., top and bottom traces). Because the VSD signal measures the summed response of cells within the pixel, a net depolarizing or hyperpolarizing response suggests the direction of the predominant response within that pixel. Thus, with low LL stimulus strengths, we were able to isolate pixels containing groups of cells with a dominance of either depolarization or hyperpolarization. Of the total number of pixels covering the ICC, 78% were depolarizing, 8% were hyperpolarizing, and 14% had mixed de- and hyperpolarizing responses ($n = 8030$ pixels; 32 transverse slices).

A predominantly de- or hyperpolarizing response in any given pixel suggests the direction of the largest response within the population of neurons represented by the pixel. A net depolarizing response within a single pixel is expected from the relatively larger amplitude of excitatory postsynaptic potentials compared with inhibitory synaptic potentials in the ICC (Sivaramakrishnan et al., 2004; Sivaramakrishnan and Oliver, 2006). Pixels with predominantly hyperpolarizing or mixed de- and hyperpolarizing responses were surprising, and suggested small regions where inhibitory strength was unusually large. The area of tissue covered by a single pixel depends on the magnification of the objective lens used. With a 5× objective, each photodetector receives light from ~17,660 μm^2 of tissue (150 μm × 150 μm) (J. Y. Wu, personal communication). In a 150 μm thick slice, with a 5× objective, each photodetector (pixel) would record responses from 26,50,000 μm^3; assuming a total IC volume of 3.8 mm^3 (Brückner and Rubsamen, 1995) and a cell count of 3,73,600 (Kulesza

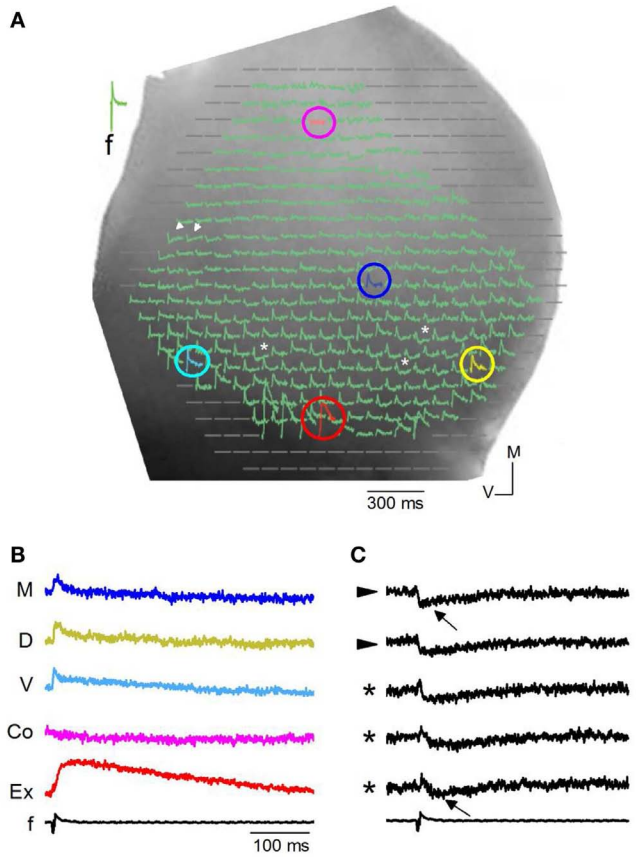

FIGURE 3 | Responses in a transverse slice evoked by minimal LL stimulation. (A) Image of one side of a rat IC seen through a 5× objective with diode array superimposed. Colored circles, pixels with depolarizing responses. Pink, commissure; dark blue, medial ICC; yellow, dorsal ICC; red, external cortex; light blue, ventral ICC. White arrowheads, pixels with hyperpolarizing responses; asterisks, pixels with mixed de- and hyperpolarizing responses. **(B)** Traces of depolarizing VSD responses corresponding to the color-coded pixels in **(A)**. M, medial ICC; D, dorsal ICC; V, ventral ICC; Co, just lateral to the commissural region; Ex, External cortex; *f*, field recording. **(C)** Traces of hyperpolarizing and mixed de- and hyperpolarizing VSD responses corresponding respectively to the arrowheads and asterisks in **(A)**. Arrows, peak hyperpolarization.

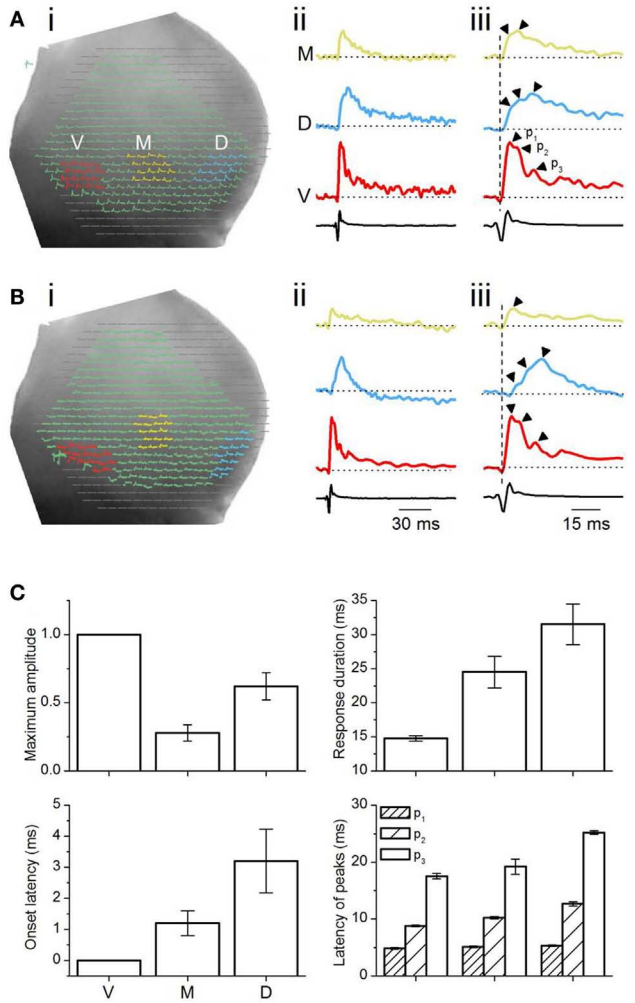

FIGURE 4 | Analysis of multi-pixel responses in the transverse plane. **(A,B)** (i) Two slices illustrating different sets of 16 pixels chosen in the ventral (red), medial (yellow), and dorsal (light blue) regions of the ICC. (ii) Responses summed over the 16 pixels in each area. M, medial ICC; D, dorsal ICC; V, ventral ICC. (iii) Expanded illustrations of the traces in (ii). Arrowheads by each trace: peaks in the response. p_1, p_2, p_3, peak 1, peak 2, peak 3; Dotted vertical line, time of response onset in the ventral ICC. Scale bars apply to traces in **(A,B)**. **(C)** Multi-pixel measures of maximum amplitudes, duration of response, onset latency, and times of subsequent peaks. Maximum amplitudes were measured as a fraction of the maximum amplitude in the ventral ICC. Response durations are absolute values, measured at half-maximum amplitude. Onset latencies were measured with respect to the onset of the response in the ventral ICC, which was set to zero. The latencies of peaks were measured with respect to the onset latency in each region. Each point is the average of three to four trials from each slice, further averaged over 26 slices, with the exception of p_3 in the medial ICC (average of 14 slices). Error bars are SEM.

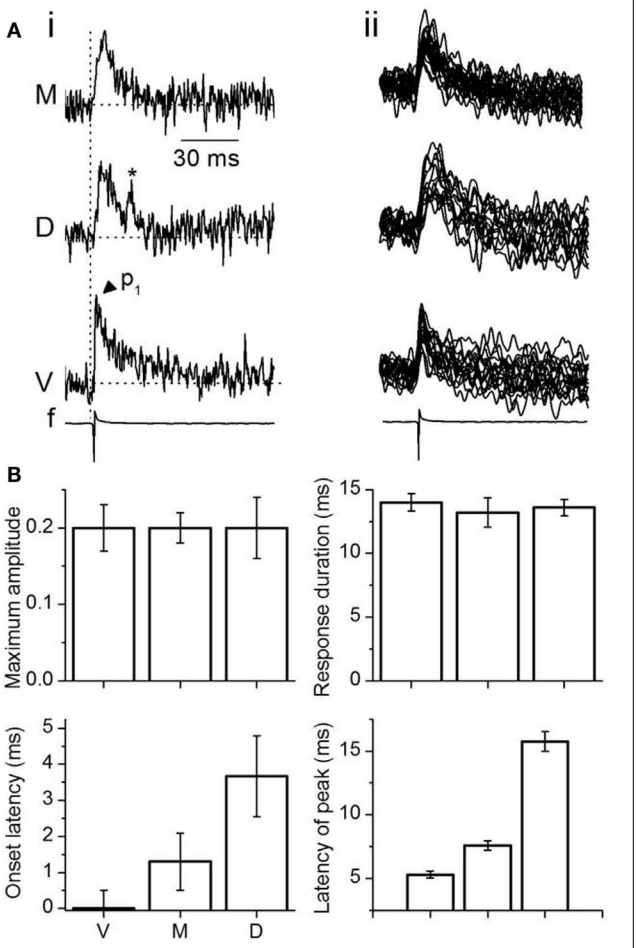

FIGURE 5 | Analysis of single-pixel responses in the transverse plane. **(A)** (i) LL-evoked responses in single pixels from different ICC regions. M, medial; D, dorsal; V, ventral ICC; *f*, field recording. Vertical dotted line, time of response onset in the ventral ICC; p_1, single-peak; Asterisk, spontaneous event. (ii) Superimposed traces from 16 single pixels in each region illustrated for the same slice as (i). The 16 pixels picked are the same ones used for multi-pixel analysis. **(B)** Single-pixel measures of maximum amplitudes, duration of response, onset latency, and time of single-peak. Maximum amplitudes are depicted as fractions of the maximum amplitude of the multi-pixel response in the ventral ICC. Response durations were absolute values, measured at half-maximum amplitude. Onset latencies were measured with respect to the onset of the multi-pixel peak response in the ventral ICC, which was set to zero. Peak time of responses in individual pixels was measured with respect to the average single-pixel onset latency in each region. Averages are from the 16 pixels used for multi-pixel analysis in each region of the slice. Each point is the average of three to four trials from each slice, further averaged over 26 slices. Error bars are SEM.

et al., 2002), a single pixel (at 5×) represents ∼260 soma, in addition to neuropil. With the 5× objective, these neuronal groups are separated by 150 μm, the inter-pixel distance. Because the VSD signal is proportional to membrane surface area (Xu and Loew, 2003), response variations between pixels could reflect variations in somatic, dendritic, and axonal contributions to the signal.

Response properties within frequency regions of the IC

We used VSDs to understand the relationship between responses within the broader topographical regions of the ICC (Merzenich and Reid, 1974; Glendenning et al., 1992; Loftus et al., 2004) and those due to the fine structure of localized afferent inputs within each region (Oliver et al., 2003). In the transverse slice, topographic regions were broadly defined as ventral, medial, and dorsal

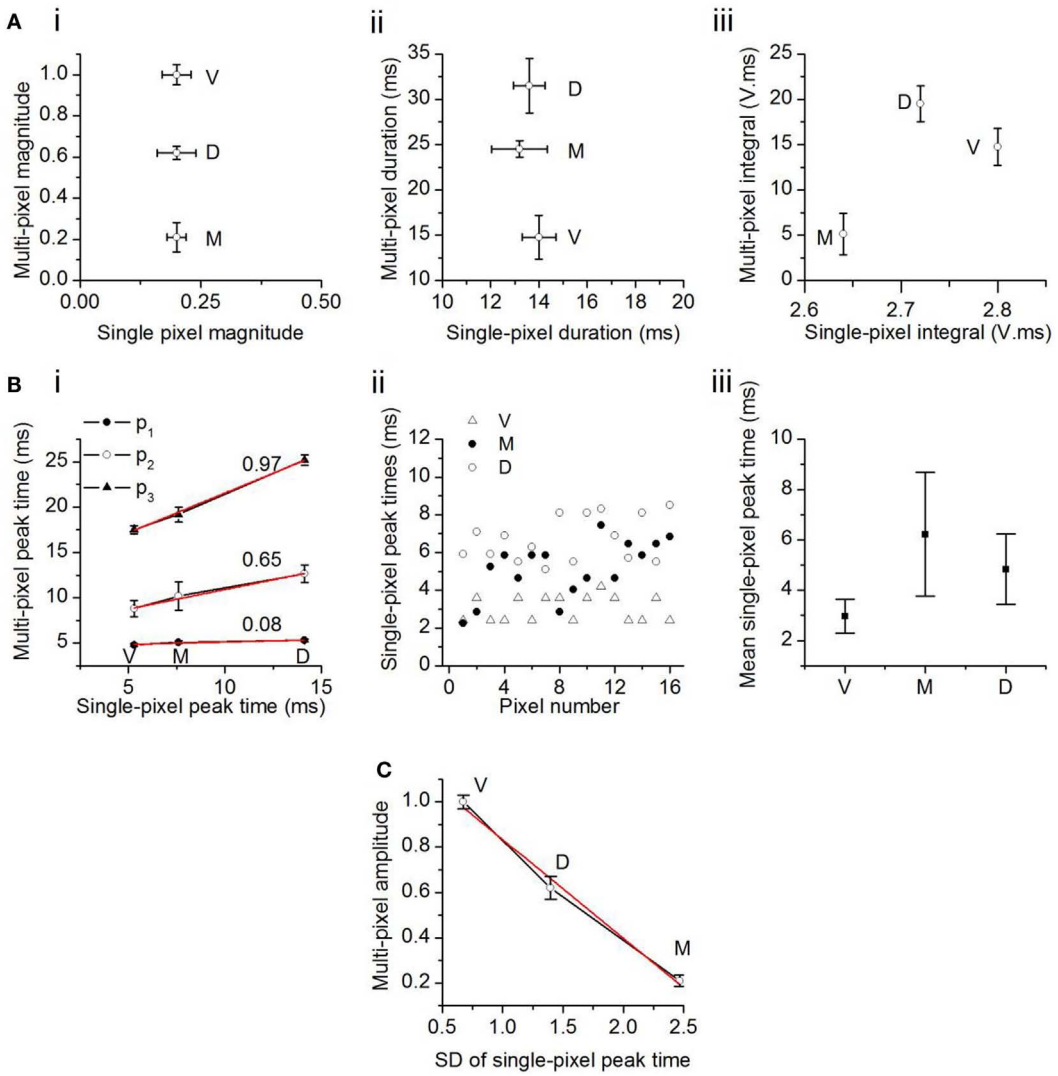

FIGURE 6 | Comparison between multi- and single-pixel responses in the transverse plane. (A) Multi-pixel measures as functions of the same measures in single-pixel responses. (i) Response magnitude; (ii) duration; (iii) integral of magnitude and duration. The component V in the unit of integral, V. ms, is a fraction of the maximum response in the ventral ICC, and is unitless. Twenty-two slices; mean and SEM. **(B)** (i) Times of onset of the first, second, and third multi-pixel peaks as a function of the single pixel peak time. Linear fits (r^2: p_3, 0.998; p_2, 0.985; p_1, 0.949) with slopes as indicated. V, ventral; M, medial; D, dorsal ICC. (ii) Distribution of single pixel peak times in the ventral, medial, and dorsal regions in one slice. Pixels chosen are the same 16 pixels used for multi-pixel analysis in that slice. (iii) Mean single-pixel peak time in the ventral, medial, and dorsal ICC. Values are mean and SD of data from 14 transverse slices. **(C)** Maximum amplitude of the multi-pixel response plotted as a function of the SD of the scatter in single pixel peak times. Data from 14 transverse slices. Error bars are SEM. Red line, linear fit, $r^2 = 0.987$.

areas (**Figure 4Ai**). To determine whether responses in broad topographic regions were scaled responses of smaller areas within each region, we stimulated LL afferents with very low currents (<0.2 mA, 0.1–0.2 ms) to prevent spikes from being generated in single pixels (as in **Figure 2E**, for example) or the complex oscillations that occur at high activity levels (unpublished observations). We then summed responses contained within a 4×4 area covering 16 diodes within each topographic region. The summed multi-pixel response within each region was then compared to the average response of the same 16 single pixels used for summation (see Materials and Methods). This method of analysis treats each broad topographic region as a single compartment, and does not attempt to examine gradients within each region. We first separately describe multi- and single pixel response characteristics, and then compare them. Data are reported from 26 transverse slices (416 pixels in each topographic region).

Summed multi-pixel depolarizations were complex, with multiple peaks and varying magnitudes (**Figure 4Aii**). Maximum response amplitudes were largest in the ventral ICC, declining in the dorsal and further in the medial ICC. Responses in the ventral

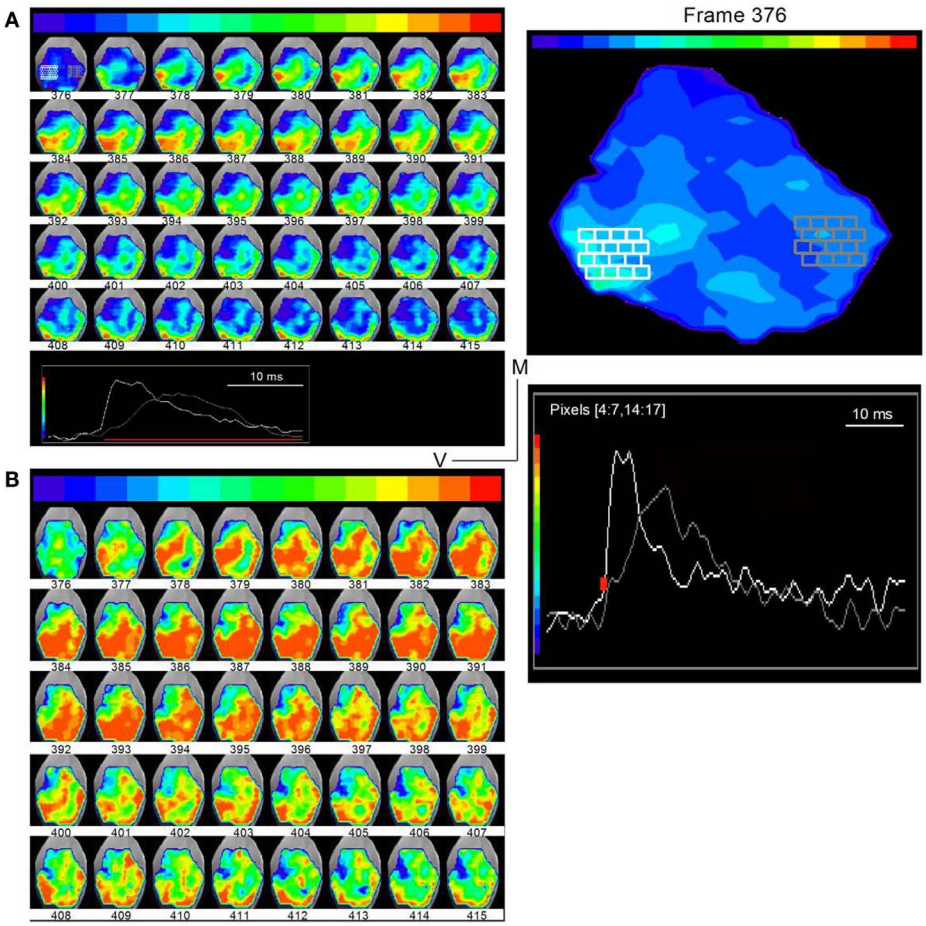

FIGURE 7 | Direction of lemniscal and cross-laminar propagation. Time lapse images of responses in a transverse slice superimposed on a photograph of the IC (rat, P21) taken through a digital camera on a second port of the microscope. Frame numbers are indicated below each frame. Frames are 0.6 ms apart. **(A)** Low-gain images show primarily the direction of lemniscal propagation. Inset at bottom: white and gray traces are the summed responses in the corresponding white and gray pixelated areas in the first image (frame 376). Right panel, Expanded image of the first frame, 376, with inset traces of averaged responses in white and gray pixelated areas. The areas picked are used to illustrate different regions of the slice. The region displayed between frames 376 and 415 occur during the region of the response depicted by the red line in the inset. **(B)** High-gain images of the same time-lapse series show activity in directions that would correspond to cross-frequency connections. The frame sequence is the same as in **(A)**.

and dorsal ICC exhibited at least three clear peaks; multiple peaks were less obvious in the medial ICC, where response magnitudes were lower (**Figure 4Aiii**, arrowheads). To control for an arbitrary effect of pixel location on response profiles, we compared responses in other 16-pixel regions within the ventral, medial, and dorsal ICC. **Figure 4B** shows one example of response patterns evoked by 16 pixels that were not in a 4×4 grid (**Figure 4Bi**). Response profiles exhibited the same directional decrease in peak height [ventral to dorsal to medial] (**Figure 4Bii**) to those in the 4×4 grid, as well as the presence of multiple peaks (**Figure 4Biii**). Additional peaks were observed in several slices with either the 4×4 grid or other patterns of clustered pixels (e.g., **Figure 4Biii**; the response in the ventral ICC has a fourth peak), but did not occur consistently. These results suggested that minimal LL afferent input evoked distinct responses in topographically distinct areas of the ICC.

To quantify differences in the responses between the topographic regions, we used two measures of response magnitude – the maximum response amplitude and the response duration; and two temporal measures – onset latency and the latencies of multiple peaks (**Figure 4C**). Multi-pixel amplitudes declined from the ventral to dorsal to medial ICC in a 1:0.6:0.3 ratio [$F(2, 75) = 7.93$; $p < 0.05$]. Response durations, which increased from the ventral to medial to dorsal ICC, were also significantly different between the frequency regions [$F(2, 75) = 3.8$; $p < 0.05$], with a ∼15 ms range between the ventral and dorsal ICC. Onset latencies increased systematically from the ventral to medial to dorsal regions, with a ventral-dorsal delay of ∼3.5 ms, suggesting that differences in arrival times of LL inputs in different regions of the ICC was the primary contributor to onset latency. Onset latencies were longer in slices where pixel clusters in the dorsal ICC were chosen at the edge of the slice (8.8 ± 1.6 ms; $n = 16$ slices).

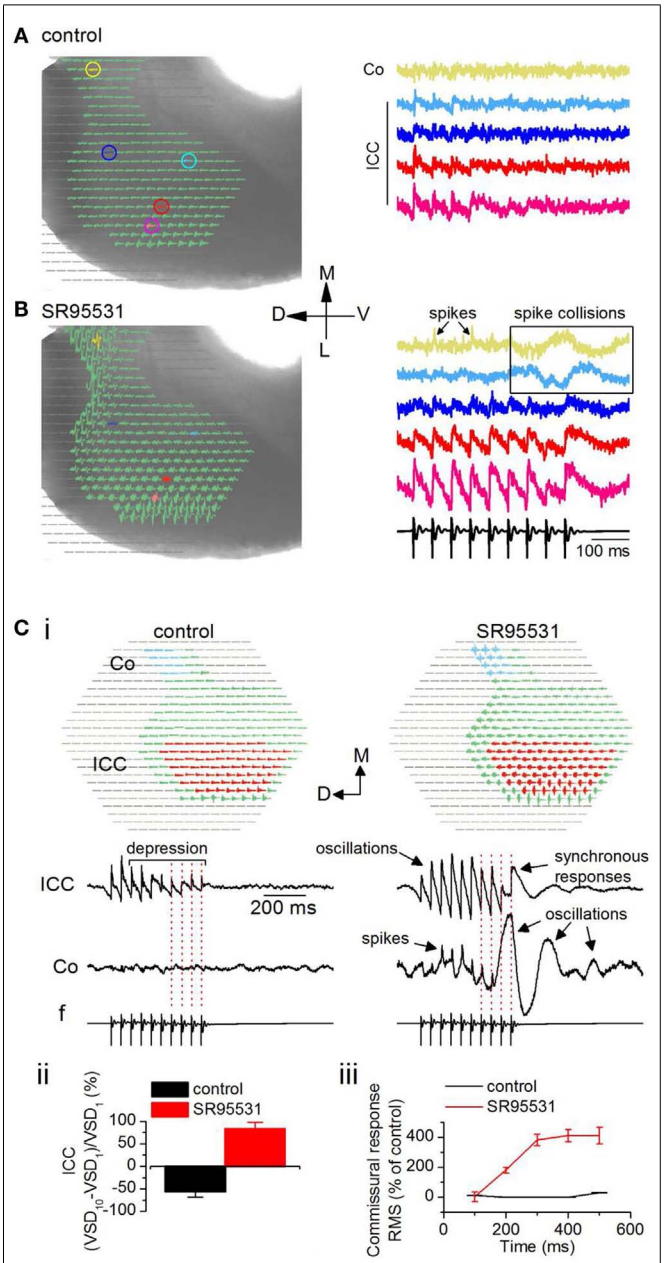

FIGURE 8 | Loss of inhibition promotes inter-collicular connectivity. Responses in a transverse IC slice (mouse, P18). **(A)** Normal ACSF. **(B)** SR95531 (an antagonist of $GABA_A$ receptors; 20 μM). **(A,B)** Left panels, Diodes chosen to be displayed include the commissural region (yellow) through the lateral region of the ICC. Pixels at the lateral edge of the slice in the region of the external cortex have been omitted from the display. Right panels, Traces corresponding to the colored pixels in left panels. Traces are averages of eight trials in control and six in SR95531. Boxed region highlights non-linear activity profiles in the commissure. Co, commissure; ICC, IC central nucleus. **(C)** Effect of SR95531 on time-dependent changes in commissural activity during a 20 Hz stimulus train. (i) Left panel, control; right panel, SR95531. Top, regions in the ICC and the commissural area (Co) over which responses are averaged. Bottom, Averaged responses illustrated as traces. *f*, field recording. Vertical dotted lines are aligned to the shocks in the field recording. (ii) Depression/facilitation index for responses in the ICC in control and SR95531. VSD_1, VSD_{10}, responses to the first and

(*Continued*)

FIGURE 8 | Continued
10th shocks in the stimulus train. (iii) Root mean square (RMS) of the response integral in the commissural region plotted as a function of sequential 100 ms time windows during the response. The 100 ms data point is the integral of the response between 0 and 100 ms; the 200 ms data point is the integral of the response between 100 and 200 ms, and so on. Data in (ii) and (iii), 19 slices, mean and SEM.

The latencies of the three response peaks exhibited a complex profile. The first peak occurred at approximately the same time in different ICC regions [~1.1 ms range; $F(2, 75) = 1.37$; $p = 0.08$], suggesting that the initial rise of the summed multi-pixel depolarization was due to either spikes or summation of synaptic responses with little temporal jitter. The frame rate of the VSD camera, ~1600 Hz (0.614 ms/point), is too slow to record the complete waveform of single sodium-dependent spikes. The presence of a spike-like rapid rise time in the depolarizing waveform seen with multi-pixel measurements is more likely to imply summation, with a slight temporal staggering, of dendritic and somatic synaptic responses with some spike inclusion over the area covered by the photodetectors. The latencies of the second and third peaks, which were greatly delayed compared to the first peak, were clearly graded, with a ventral-dorsal gradient of ~4 and ~8 ms respectively, suggesting that synaptic responses formed the primary components of these later peaks.

We next examined responses in the same 16 single pixels used for multi-pixel analysis in each topographic region. In stark contrast to multi-pixel responses, the average single pixel response magnitude and duration did not vary topographically. In all three frequency regions, single pixel responses exhibited a single depolarizing peak (**Figures 5Ai,ii**); an occasional second peak that did not occur consistently between trials suggested spontaneous activity (**Figure 5Ai**, asterisk). The magnitude of depolarizations in the ventral, dorsal, and medial regions were the same fractional component [0.2:0.2:0.2; $F(2, 75) = 0.42$; $p = 0.2$] of the multi-pixel response in the ventral ICC. Response durations (measured at half-peak height) did not differ significantly between topographic regions and were within a narrow ~1.5 ms range [$F(2, 75) = 1.08$; $p = 0.1$]. The similarity in response durations and peak amplitudes between individual pixels suggested that, within small discrete populations of soma, with their accompanying axonal and dendritic processes and LL inputs, the strength of the response (amplitude and duration) was "homogeneous" within a greater part of the ICC, provided the shock strength delivered to the LL was low. These data therefore suggested the presence of response areas of constant magnitude (amplitude and duration) of depolarization, separated by ≤150 μm (the inter-pixel distance at 5×).

Single pixel onset latencies increased systematically from the ventral to medial to dorsal ICC, as they did with multi-pixel measures, providing supporting evidence for their origin from LL afferent input. In contrast to the unchanged response magnitudes and durations, the range of latencies of the peak response was very large between the ventral and dorsal ICC [~12 ms; 5.2–17.1 ms between the ventral and dorsal ICC; $F(2, 75) = 10.6$; $p < 0.05$] (**Figure 5B**, bottom right panel). These long latencies suggested the predominance of synaptic responses over spikes, which would

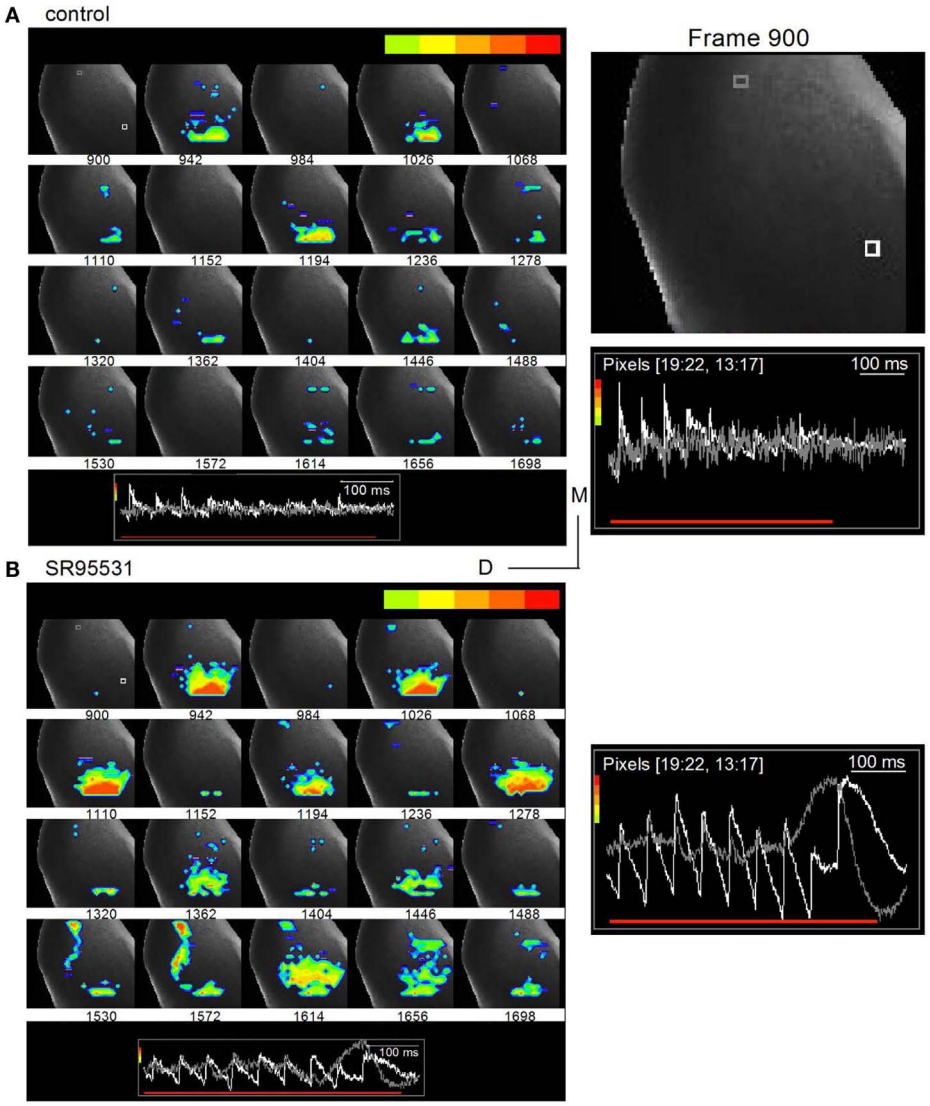

FIGURE 9 | Commissural propagation in the presence of $GABA_A$ antagonists. Time lapse images of the response during a 20 Hz train superimposed on an image of the IC. The color bar at the top of each panel shows the range of responses illustrated is restricted to the peak response regions to isolate commissural propagation from the more diffuse spread of activity in the ICC. **(A)** Normal ACSF. Right panel, Expanded image of the first frame, 900, with inset traces of responses in single white and gray pixels. White pixel, ICC; gray pixel, commissure. Frames are 25 ms apart. **(B)** 20 μm SR95531. Insets, traces correspond to the white and gray pixels highlighted in the first frame (frame 900) in the top panel. The gray pixel is in the commissural region. Right panel, Expanded image of inset traces of responses in the white and gray pixels. Pixelated areas in frame 900 [**(A)**, right panel] also applies to **(B)**. Frame intervals are the same as in **(A)**. Directional scale bar applies to both images.

be expected from the low LL shock strengths used, which were adjusted to keep single pixel responses sub-threshold.

To examine how single pixel responses translated into the topographical differences in multi-pixel responses, we plotted multi-pixel response measures as a function of the corresponding single pixel measures. Differences in maximum response magnitudes and durations within each broad topographic region (multi-pixel measures) did not follow the same trend as the corresponding single pixel values. First, although single pixel magnitudes did not vary between topographic regions, multi-pixel response magnitudes decreased from the ventral to dorsal to medial ICC (**Figure 6Ai**). Second, the average single pixel response duration also did not vary between topographic regions, however, multi-pixel response durations decreased from the dorsal to medial to ventral ICC (**Figure 6Aii**). Thus, the two individual features of multi-pixel response magnitudes, peak amplitude, and duration, had different topographic gradients, although the corresponding single-pixel parameters did not vary topographically. The product of the multi-pixel response amplitude and duration exhibited a slight dependence on the single-pixel product; it decreased from the ventral to medial [$t(21) = 3.13$; $p < 0.05$], and dorsal to medial [$t(21) = 3.65$; $p < 0.05$], ICC, but

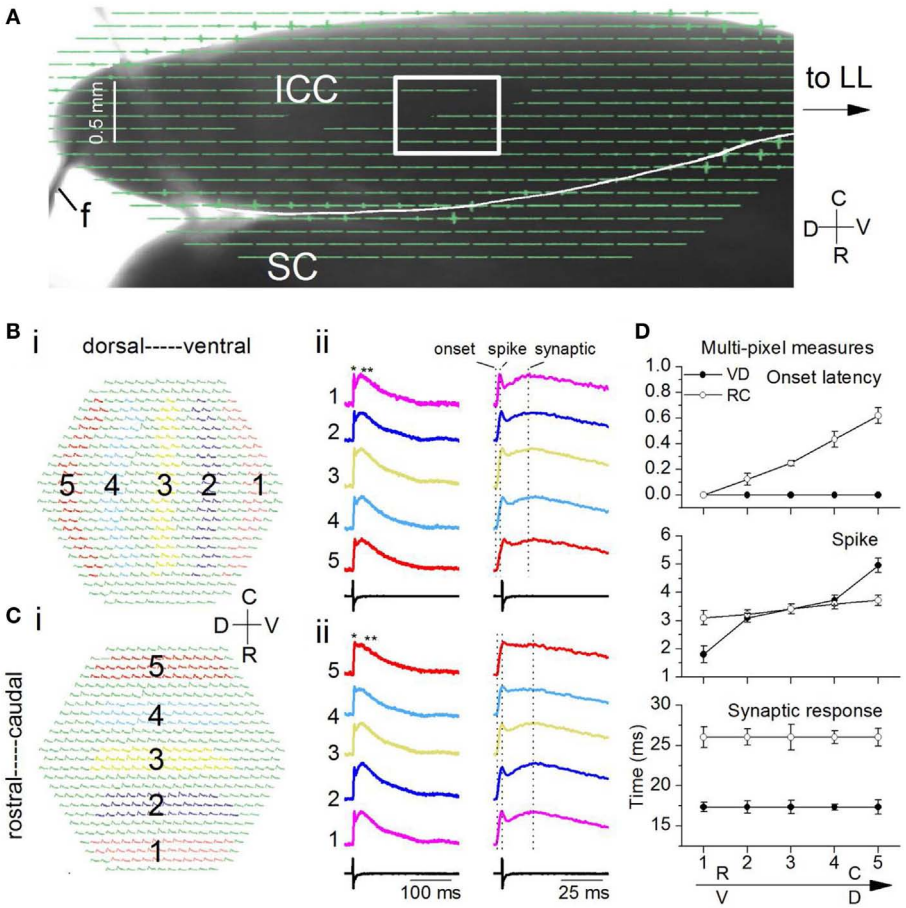

FIGURE 10 | Spatio-temporal activity patterns within a frequency lamina. (A) Image of the laminar slice (mouse IC; P19) seen through the diode array with a 5× objective. The LL is out of the field of view. *f*, field electrode. Light gray line across the dorsal edge of the slice is a string from the slice anchor. Box, region of the ICC analyzed with a 20× objective. SC, superior colliculus. **(B,C)** Responses to a single LL shock. Average of 10 trials. **(B)** (i) Areas chosen in the ventral (1) and moving incrementally toward the dorsal (5) region of the ICC. The same number of pixels are chosen in each area. (ii) Left columns, Traces corresponding to the color-coded areas in the ventral-dorsal and rostral-caudal directions; single asterisk, spike; double asterisk, synaptic response; Right columns, expanded traces to show onset latencies and peak times (vertical dotted lines). **(C)** (i) Areas in the rostral (1) toward the caudal (5) region. (ii) Left and right columns are as in **(B)**. **(D)** Response times along the ventral-dorsal (V-D) and rostral-caudal (R-C) directions. Top, onset; middle, first peak/spike; bottom, second peak/synaptic response. Times were measured with respect to onset in the ventral or rostral ICC (area 1). Each point is the average of 3–10 trials in each of 14 slices. Error bars are SEM.

the gradient between the ventral and dorsal ICC was not significant [**Figure 6Aiii**; $t(21) = 1.76$; $p = 0.09$]. Taken together, these data suggested that the average response magnitude within single pixels, which was uniform across topographic regions, did not completely account for the broader topographic gradient of response magnitude.

We examined the possibility that temporal summation of single pixel responses gave rise to the topographical (multi-pixel) gradient in response amplitudes. The latencies of the first, second, and third multi-pixel peaks varied linearly with the average latency of the single pixel peak within each topographic region (**Figure 6Bi**). However, as multi-pixel peak latency increased (i.e., from p_1 to p_3), the topographical differential between single- and multi-pixel peak times also increased. The ventral to medial to dorsal differential increased seven times between p_1 and p_2 (an increase in slope from 0.08 to 0.65) and 0.5 times between p_2 and p_3 (an increase in slope from 0.65 to 0.97). The increase in slope suggested an increased scatter in the times at which responses in single pixels reached their peaks. **Figure 6Bii** illustrates peak scatter within the group of 16 single pixels in each topographic region in one transverse slice; peak times exhibited the greatest scatter in the medial ICC, and the least scatter in the ventral ICC. Population analysis of the 16-pixel groups in different slices confirmed an increasing gradient of peak scatter in single pixel peak latencies from the ventral to dorsal to medial ICC [14 slices, mean and SD; $F(2, 39) = 8.58$; $p < 0.05$] (**Figure 6Biii**). The direction of this gradient was similar to the topographical gradient of response magnitudes (compare **Figure 4C**, top left panel). The relationship between multi-peak response magnitudes and the standard deviation of single-peak latencies was linear, with a slope of −0.43 (**Figure 6C**; $n = 14$ slices). These results suggested that temporal summation of single pixel responses, which

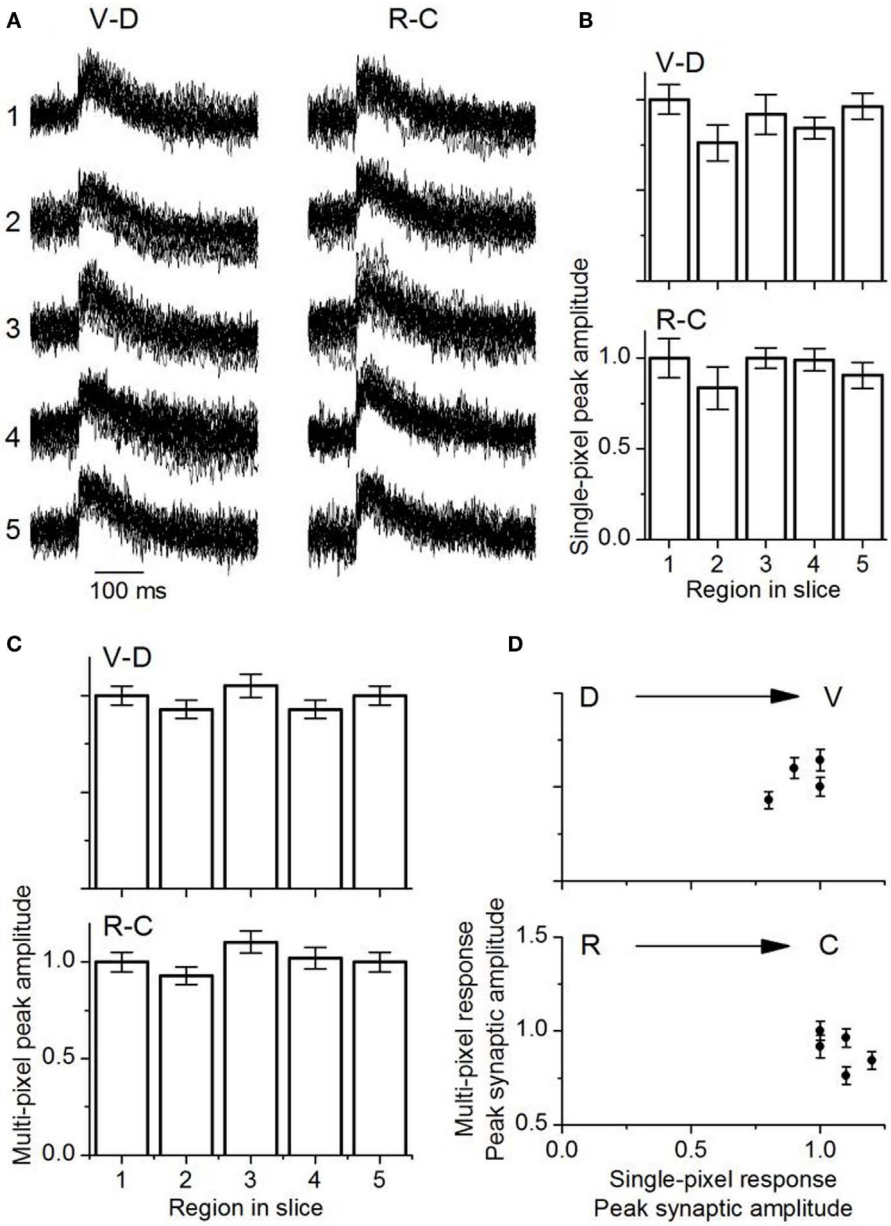

FIGURE 11 | Comparison of multi-pixel and single-pixel responses in the laminar plane. (A) Overlapped traces from 16 single pixels in the ventral-dorsal (V-D) and rostro-caudal (R-C) directions for a single slice. Rat IC (P26). The numbers one to five correspond to the respective areas in each region as highlighted in **Figure 10**. The 16 single pixels displayed in each region are the same ones used for multi-pixel analysis. **(B)** Mean single-peak amplitudes in each direction as indicated (18 slices; SEM.). **(C)** Mean multi-pixel peak amplitudes in each direction as indicated (18 slices; SEM.). **(D)** Multi-pixel peak amplitudes as a function of the average single pixel peak amplitude in the dorso-ventral and rostro-caudal directions. The second and fourth data points in the dorso-ventral plot overlap. Averages of 18 slices. Error bars are SEM.

would become more efficient as the scatter of peak times decreased, is likely to contribute strongly to the topographical gradient in response magnitudes.

The comparison between multi- and single pixel response characteristics thus suggests the presence of unitary areas of response magnitude in the ICC that sum temporally to create a graded response magnitude that decreases from the ventral to dorsal to medial ICC.

To examine the spread of activity within and across frequency regions in the transverse slice, we plotted time-lapse images during the response to a single LL shock under low- and high-gain to visualize different spatial features (**Figure 7**; frame intervals are one frame; 0.6 ms apart). Regions in the ventral and dorsal areas (**Figure 7A**, white and gray pixels, frame 376; traces, inset at bottom; expanded in the right panel) were chosen to illustrate examples of responses. At low-gain, activity was observed

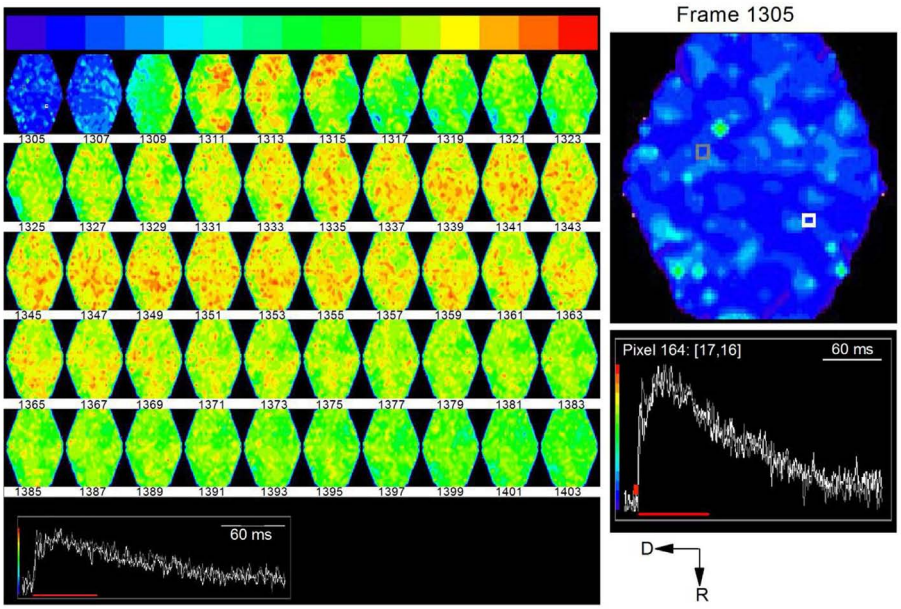

FIGURE 12 | Time lapse series of the response to a single lemniscal shock in a laminar slice. Images are 1.22 ms apart. A noticeable response begins in the ventral region of the ICC in frame 1309 (top row: third frame) and propagates dorsally. Inset, white and gray traces correspond to white and gray pixels in the first frame (1305). Red line, region of the response covered by frames 1305–1403. To utilize the full range of colors, the baseline that precedes the response has been set to blue and the peak of the response to red. Right panel, Expanded image of the first frame, 1305, with inset traces of corresponding to the white and gray pixels.

primarily in three segregated bands. A band that began initially in the ventral region (frame 378), propagated into the central ICC within ∼2.4 ms (frame 382). The origin of this ventral band, close to the entry of LL fibers, its propagation perpendicular to the direction of the frequency laminae, and the short propagation time, suggested primary propagation along lemniscal input tracts. A second narrower band of activity, first appearing in the dorso-lateral region (frame 379) and propagating dorso-medially, reached its maximum spatial extent in ∼3 ms (frame 384) and is likely to reflect propagation along the low frequency laminar region of the IC. A third band of activity, in the region of the external cortex, which began with the initial spread of lemniscal inputs in the ventral IC (frame 393), remained after both the ventral and dorsal band had declined (up to frame 415), reflecting prolonged responses in the external cortex (Movie S1 in Supplementary Material).

Images analyzed at higher gains revealed possible cross-laminar propagation (**Figure 7B**). In addition to the three primary regions of activity seen in the low-gain images, now clearer at slightly earlier times (frame 378), activity in a direction perpendicular to or angled to the main three bands was clear during the later part of the response (e.g., frames 401–415). In frame 401, for example, this "cross-laminar" movement began at the medial end of the dorsal band and, in successive frames, propagated ventrally and then back into the dorsal band. This pattern of movement from the dorsal or ventral laminae into the central portion of the ICC, and the consequent formation of additional activity bands was a consistent finding in all transverse slices ($n = 56$) in which either a strong dorsal or strong ventral band was present, suggesting that the relatively weaker strength of these additional bands did not necessarily arise from cut connections in any particular slice. The precise positions of bands and their widths varied between slices, sometimes occurring more medially or more laterally, and orientation angles differed slightly, which would be expected from variations in the slice plane, the number of intact connections, and the currents used to activate LL fibers.

Propagation of activity across the commissure

Cross-talk between the two inferior colliculi through the commissure regulates the balance of excitation and inhibition in the IC (Moore et al., 1998; Ingham and McAlpine, 2005; Malmierca et al., 2009). Here we use VSDs to show that blocking $GABA_A$-mediated inhibition following activation of ipsilateral LL inputs causes excitation to propagate through the commissure to the contralateral IC, suggesting that functional ipsilateral-contralateral (excitatory) connectivity requires an excitation threshold.

To record the effects of $GABA_A$ antagonists on commissural propagation, we first set a low level of baseline excitation in normal ACSF to prevent the onset of depolarization block in the presence of $GABA_A$ antagonists, both in brain slices and *in vivo*, when normal excitation levels are already high (Sivaramakrishnan et al., 2004). Excitation was kept low by stimulating the LL with low-frequency shock trains, and adjusting the current strength to generate weak depolarizing responses that further depressed during the train. With a 20 Hz train (0.2 mA shock strength), for example, depolarizing potentials were restricted to the ICC, with little or no commissural activity (**Figure 8A**, left panel). Response magnitudes, illustrated in individual pixels, did not differ greatly

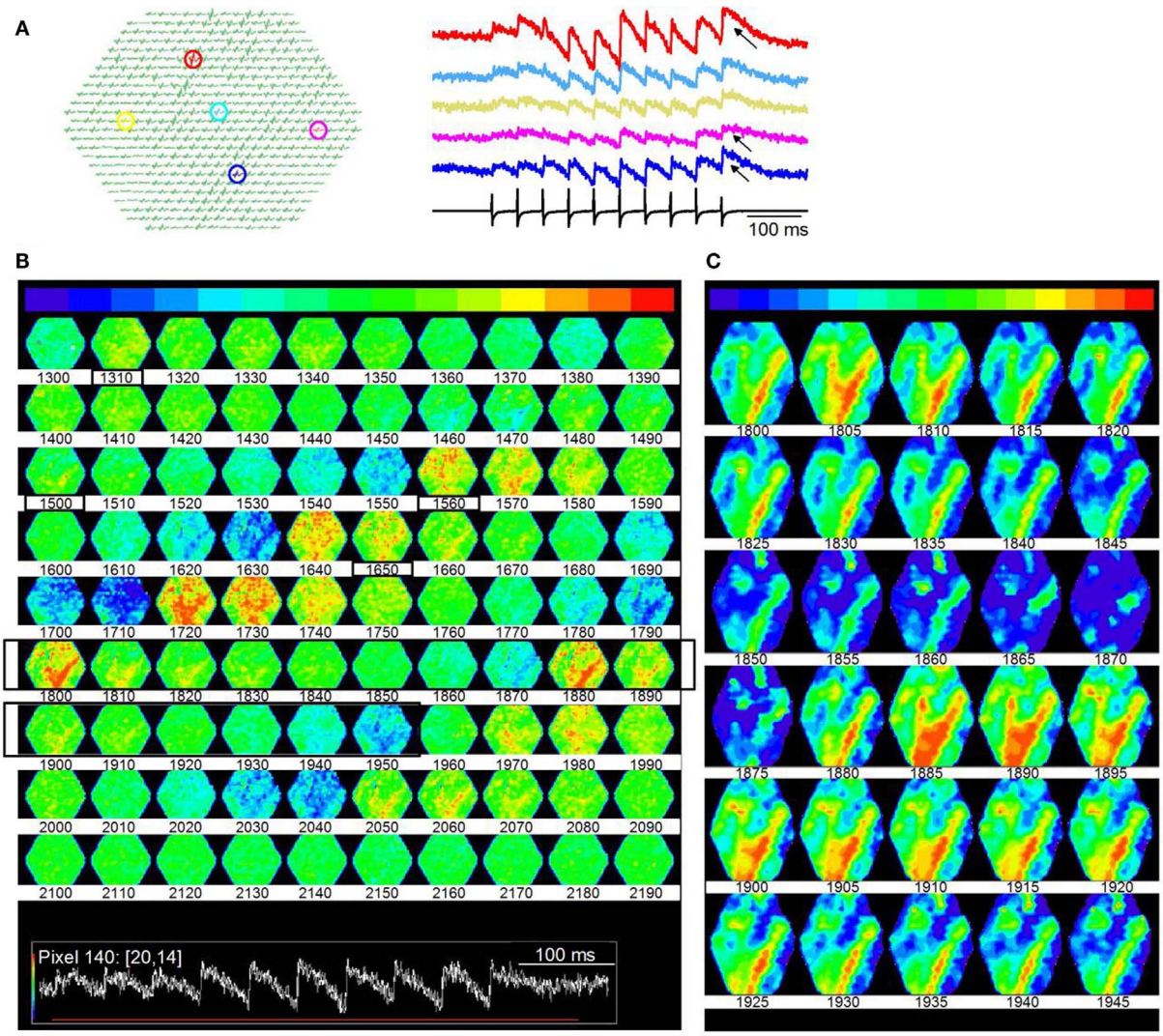

FIGURE 13 | Microdomains of activity within an ICC lamina. **(A)** Responses to a 20 Hz LL stimulus train. Shock strength is the same as in **Figure 10**. Same slice as **Figure 10**. Left panel, highlighted pixels (arrows); Right panel, corresponding traces; Arrows, regions of accumulating depolarization. **(B)** Time lapse images of responses during the train. Images are 10 frames apart (6 ms inter-frame interval). Frame numbers, Row 1, 1300–1390; Row 2, 1400–1490; Row 3, 1500–1590; Row 4, 1600–1690; Row 5, 1700–1790; Row 6, 1800–1890; Row 7, 1900–1990; Row 8, 2000–2090; Row 9, 2100–2190. Black boxed region, frames 1800–1850 that are illustrated in **(C)**. Inset: Red line, region of the response covered by frames 1300–2190. **(C)** Expansion of black boxed region (frames 1800–1845) in **(B)**. Frames are 3 ms apart. The baseline color in **(C)** has been changed from green to blue to extend the minimum to maximum color scale.

in different regions of the ICC (e.g., **Figure 8A**, right panel, pink and red traces), however they declined toward the commissure (e.g., **Figure 8A**, right panel, light blue and yellow traces). In the presence of the $GABA_A$ antagonist SR95531 (20 μM), activity during the train increased in the ICC and depolarizing responses were now observed in the commissural region (**Figure 8B**, left panel). In the ICC, responses to the individual shocks in the stimulus train increased in amplitude, they no longer depressed and were oscillatory (**Figure 8B**, right panel, pink and red traces). Spikes now occurred in the commissural region with non-linearities suggestive of spike collisions (Huang et al., 2010) (**Figure 8B**, right panel, yellow and blue traces; boxed region).

To quantify the effects of SR95531 on ICC and commissural activity, we averaged responses separately over a large part of the respective regions (**Figure 8Ci**, top panels, red and blue pixels). In control conditions, the 20 Hz LL stimulus train evoked a depressing but stimulus-locked response in the ICC (**Figure 8Ci**, bottom left panel; red dotted lines on traces), with no measureable activity through the commissure. In SR95531, responses in the ICC remained stimulus-locked (**Figure 8Ci**, bottom right panel; red dotted lines on traces), however, they exhibited oscillations, and prolonged responses that arise from synchronization (SS, unpublished observations). In addition, responses facilitated. The facilitation/depression index (Sivaramakrishnan et al.,

1991) of the responses to the first and last pulses in the train $[(VSD_{10} - VSD_1)/VSD_1]$ showed a 53% depression at the last pulse of the train compared to the response to the first pulse in control conditions (**Figure 8Cii**). In SR95531, the loss of depression did not result in a return to steady excitation (a depression/facilitation index of zero), but instead facilitated by almost 85% compared to the first pulse in the train, a 30% increase in response amplitude compared to the control [19 slices; $t(18) = 3.84$; $p < 0.05$].

The commissural region showed clear evidence of spikes in SR95531, suggesting a high incidence of synchronous firing in commissural axons (**Figure 8Ci**, bottom right panel). Importantly, however, whereas responses were stimulus-locked during the early part of the train, large oscillations caused temporal smearing toward the end of the train (**Figure 8Ci**, bottom right panel; red dotted lines on traces). Responses outlasted the stimulus by several hundreds of milliseconds (300–950 ms across 12 slices) and exhibited different degrees of oscillatory behavior. The change from spikes and stimulus-locked responses during the early part of the stimulus train, toward a greater prevalence of oscillations and decreased incidence of stimulus locking toward the later part of the train suggested a time-dependent increase in activity in the commissure. In control conditions, commissural activity did not change during the early part of the train [**Figure 8Ciii**; 200 and 400 ms time points; $t(18) = 0.98$; $p = 0.3$], but increased slightly toward the end of the train [50% increase; $t(18) = 3.61$; $p < 0.05$; 19 slices]. In SR95531, a steep increase during the earlier part of the stimulus saturated at ∼400% of the control toward the later part of the train ($n = 19$ slices).

Although the incidence of commissural propagation in the absence of $GABA_A$ antagonists was rare with low frequency LL stimulus trains, very high-frequency (>80 Hz) trains did evoke prolonged commissural excitation (14 slices, data not illustrated), suggesting that propagation of excitation through the commissure to the contralateral IC requires an excitation threshold in the ipsilateral ICC. Reducing inhibition is one way of reaching this threshold, and may involve neuronal circuitry.

Time-lapse images illustrated oscillatory response patterns during the latter part of the train that coincided with commissural propagation. To prevent the normal spread of activity within the IC from masking the direction of commissural propagation, we filtered out low excitation levels and restricted analysis to the region of peak depolarization, which was scaled to be within the light green-red color range (**Figure 9A**, inset traces; frame intervals are 42 frames; 25 ms apart). In normal ACSF, the depressing peak excitation during the train is illustrated in the nine frames that correlate with each shock in the train (**Figure 9A**; frames 942, 1026, 1110, 1194, 1278, 1362, 1446, 1530, 1614). With this analysis window, the strongest excitation was restricted to the ventral ICC where the lemniscal afferents enter; there was little spread into the central ICC and no evidence of commissural activity. In the presence of SR95531, the strongest activity remained temporally locked to each shock in the train, occurring approximately at the same frame times as the control. Activity remained restricted mainly to the ventral region of the ICC, although there was a greater spread at some times during the train (**Figure 9B**, right panel; e.g., frames 942, 1278), and less depression. The main features of interest, however, are frames 1530–1614, which correlate with the region of non-linear responses in traces from the commissural region (**Figure 8B**, boxed region). Activity in some of these frames did not coincide with a shock in the train (**Figure 9B**; e.g., commissural propagation in frame 1572 occurred between the eighth and ninth shock of the train), a contrast to the clear 1–1 stimulus-response correlation in normal conditions (**Figure 9A**; frame 1572, during which there was no LL shock, did not show a response) (Movies S2 and S3 in Supplementary Material).

ACTIVITY IN THE INTRA-LAMINAR PLANE OF THE ICC

To examine connections within a lamina, we previously developed a laminar slice plane of the ICC that preserves intra-laminar connections and minimizes inter-laminar circuitry (Sivaramakrishnan and Oliver, 2006; **Figure 1B**). By limiting the thickness of the slice to 100–150 μm, the extent of laminar spread (Schreiner and Langner, 1997), the number of laminar planes is theoretically restricted to a single "sheet," with highly reduced circuitry that contains a laminar module with its fibro-dendritic arrangement of input lemniscal fibers traversing the central nucleus parallel to and synapsing in the dendritic fields of disk-shaped neurons (Oliver, 2000; Malmierca et al., 2005). The laminar slice plane contains only one colliculus, primarily the ICC, and intact LL afferents. Whole-cell recordings from neurons in this slice plane demonstrate an extensive stimulus-dependent polysynaptic influence on response properties (Sivaramakrishnan and Oliver, 2006), suggesting that local interactions within a lamina increase with afferent recruitment.

As with the transverse slice, stimulating electrodes were placed on the LL before it entered the IC, and a field electrode, *f*, recorded the stimulus (**Figure 10A**). To increase spatial resolution, we used a 20× objective instead of the 5× used with the transverse slice. Each pixel would cover responses from ∼65 neurons (compared to ∼260 neurons with the 5× objective), with a pixel separation of 37 μm. With the 20× objective, we isolated a small portion of the lamina for image acquisition and analysis (**Figure 10A**; boxed area). We illustrate responses within the boxed region following activation of the LL with a single shock (**Figures 10–12**) and a 20 Hz train of 10 shocks at the same current strength as the single shock (**Figure 13**). Single shock results are reported from 18 laminar slices and train results from four additional (22) slices.

Responses to a single shock

Responses evoked by a single LL shock were dispersed within a lamina. We measured the spatial response profile by summing responses over multiple pixels within circumscribed areas progressively (1–5) in either the ventral to dorsal (VD) (**Figure 10Bi**) or rostral to caudal (RC) (**Figure 10Ci**) directions. Each of these multi-pixel areas was treated as single compartment. In both the VD and RC directions, depolarizations were widespread and generally contained an initial spike followed by a slower synaptic response (**Figures 10Bii,Cii**, single and double asterisks). We did not observe the complex multi-peaked responses seen in transverse IC slices under similar stimulus conditions. To compare differences in propagation between the VD and RC directions, we used measures of the latency of response onset and the peaks of the spike and synaptic responses, measured from the onset. We measured

all times with respect to the onset latency at either the ventral or the rostral end of the portion of the ICC in the image field.

Two key differences in peak times between the VD and RC directions suggested both temporal inhomogeneities as well as homeostasis within the lamina. First, onset latencies were identical along the VD axis [$F(4, 65) = 0.8$; $p = 0.9$], but increased along the RC axis with a range of ∼0.65 ms [**Figure 10D**, top; $F(4, 65) = 15.7$; $p < 0.001$; $n = 14$ slices], suggesting an axis-dependent functional orientation of LL axon path length. Second, the gradient of spike peak times was larger in the VD direction [**Figure 10D**, middle panel; RC gradient 0.6 ms; VD gradient 3.1 ms; $t(13) = 4.22$; $p < 0.05$], however, the time to peak of the synaptic response showed no gradient in either direction [**Figure 10D**, bottom; VD, $t(13) = 1.28$; $p = 0.2$; RC, $t(13) = 1.14$; $p = 0.27$]. Although a gradient in synaptic latency was absent along either axis, absolute latencies were axis-dependent, being longer by ∼6 ms in the RC direction [**Figure 10D**, bottom panel; $t(13) = 5.51$; $p < 0.05$]. A gradient in the latency of the spike but not the synaptic response suggested that secondary local interactions within the lamina counteracted the temporal gradient caused by afferent input, and exerted homeostatic control of synaptic peak latency. Homeostasis could occur through differences in membrane time constants (Sivaramakrishnan and Oliver, 2006) or synapse location on dendrites.

Single pixel responses consisted mainly of synaptic activity, with no detectable evidence of the spike observed in the multi-pixel summed responses (**Figure 11A**), which was expected from the low LL stimulus shock strength which was adjusted to keep single pixel responses sub-threshold. The presence of spikes in multi-pixel responses could arise from summating local interactions between single-pixel response areas. Responses in single pixels had similar maximum amplitudes along both axes [**Figure 11B**; VD, $F(4, 85) = 1.55$; $p = < 0.05$; RC, $F(4, 85) = 2.05$; $p < 0.05$]. These response areas were 37 μm apart (the inter-pixel distance with the 20×), closer than the 150 μm separation in the transverse slice.

Multi-pixel responses, measured over each of the broad areas (1–5) and normalized to responses in either the ventral or rostral regions respectively, also had uniform response amplitudes without significant gradients in either the VD or RC directions [**Figure 11C**; VD, $F(4, 85) = 0.8$; $p < 0.05$; RC, $F(4, 85) = 1.01$; $p < 0.05$]. A comparison of multi- and single pixel measures of maximum synaptic response magnitude indicated that the transfer function between single- and multi-pixel magnitudes was also not graded in either the VD or RC direction, with no scaling of response magnitude [**Figure 11D**; VD, $F(4, 85) = 1.3$; $p < 0.05$; RC, $F(4, 85) = 1.26$; $p < 0.05$; $n = 18$ slices].

Time-lapse images of responses to the single shock showed a wave of activity that began at the ventral end and propagated dorsally and rostrally (**Figure 12**, e.g., frames 1307, 1309; frame intervals are two frames; 1.2 ms apart). This initial wave corresponded to the first peak of the depolarizing response caused by LL axonal spikes. The secondary activity that followed this initial wave was widely distributed in the region of the ICC being imaged. This second phase corresponded temporally to the slower phase of the depolarizing response, resulting mainly from synaptic potentials and probable cellular spiking. The directional nature of LL afferent input and its restricted spatial spread, followed by the distributed nature of the synaptic response, suggests widespread effects within a lamina from a low level of afferent input (Movie S4 in Supplementary Material).

Responses to a shock train

In contrast to the dispersed activity evoked by a single LL shock, stimulus trains re-organized activity in the lamina into distinct spatial domains, suggesting that local circuitry within a lamina creates spatio-temporal response compartments. Shock strengths of each stimulus in the LL train (20 Hz stimulus frequency) were delivered at the same current strength as the single shock described in **Figure 10**. Each shock in the train evoked a depolarization (**Figure 13A**). Unlike the uniformity of response amplitudes observed with the single shock, responses in different regions of the ICC varied in amplitude and the degree of accumulating depolarization (**Figure 13A**, right panel, arrows) during the train. Distributed responses, similar to those evoked by single shocks did occur during the train, but only to the first few stimulus pulses (∼120 ms from train onset) (**Figure 13B**; frames 1310–1500; boxed frame numbers rows 1 and 3; frame intervals are 10 frames; 6 ms apart). Corresponding to the region of accumulating depolarization, response magnitudes increased greatly (e.g., **Figure 13B**, frames 1560–1650; boxed frames numbers rows 3 and 4), and organized this region of the ICC into bands of high activity (**Figure 13B**, frames 1800–2070; rows 6–8).

We plotted time-lapse images of banded activity (**Figure 13B**; Frames 1800–1950; rows 6, 7; black boxed regions) with greater temporal resolution (**Figure 13C**; 3 ms between frames). In this particular slice, the banded region began ∼300 ms (frame 1800) after the onset of the train (frame 300), when depolarization began to accumulate (as in **Figure 13A**, traces). The pattern consisted of the primary band and secondary orthogonal bands running oblique to either the dorsal-ventral or rostral-caudal axes. In other laminar slices where similar minimal stimulation was used ($n = 22$), bands were oriented differently, slightly deviating from the angles described in this figure, which is expected if a particular band depends on the subset of lemniscal afferents activated. 5/22 slices exhibited a single band oblique to the dorso-ventral axis, 7/22 slices displayed two distinct bands, parallel to the rostro-caudal axis, and 10/22 slices displayed two bands, one of which was parallel to the rostral-caudal axis, the other at an oblique angle to the dorso-ventral axis. The bands remained consistently strong once activated, also suggesting prolonged depolarizing responses. In single ICC neurons, accumulating depolarization results from synaptic summation and changes in intrinsic ion channel activity (Sivaramakrishnan and Oliver, 2006); the spatial information obtained from VSD images suggests that accumulating depolarization recruits a subset of the lamina into regions of high activity.

STIMULUS-AND CELL TYPE-SPECIFIC MICROCIRCUITS IN THE ICC

Whole-cell patch recordings of LL-evoked responses in single ICC neurons suggest that the amplitude and duration of synaptic potentials, the frequency of spiking and the ability to follow their inputs is determined by the relative numbers and frequency of afferent axons activated, which can be varied by changing the strength and frequency of electrical shocks applied to the LL

(Sivaramakrishnan et al., 2004). We now use VSD imaging to highlight the importance of stimulus parameters in determining the specificity of functionally active circuits in the ICC. We illustrate the stimulus-circuit dependence using two LL stimulus paradigms: (1) low- and high-frequency trains that produce different spatio-temporal profiles (**Figure 14A**), and (2) a long train at very low input strength that isolates a cell-type specific local circuit (**Figure 14B**).

With a low frequency, 10 Hz train, responses were locked to each stimulus (**Figure 14Ai**, frames 846, 1010, 1172; frame intervals are 18 frames; 11 ms apart), were of equal magnitude, decayed rapidly, and were confined to the ventral region of the ICC. This response can be explained as a relatively simple recruitment of a small, localized, population of cells close to the region of LL entry in the ICC. In the same slice, when the train frequency was increased to 40 Hz, the activity profile indicated a spatial recruitment of other regions in the ICC and, in addition, a temporal component to the recruitment. Stimulus-response locking occurred during the first several stimuli, with spatially restricted, rapidly decaying responses (**Figure 14Aii**, frames 870–1150; frame intervals are 40 frames; 24 ms apart), however, ∼300 ms after the train onset, responses spread from the LL entry point, laterally, medially, and dorsally (frames 1310–1590). Thus afferent input frequency may be a factor in the recruitment of previously silent microcircuits in the ICC (Movie S5 in Supplementary Material).

The second stimulus pattern, which is especially interesting in its ability to isolate a circuit that is specific for a certain physiologically defined cell-type is a long, low frequency train that results in a gradual build-up of inhibition followed by post-inhibitory rebound firing. Intrinsic rebound neurons comprise almost 50% of the physiologically defined cell-types in the ICC (Sivaramakrishnan and Oliver, 2001), and rebound spikes, whether generated intrinsically or through lemniscal stimulation, can be abolished by $NiCl_2$, an antagonist of T-type calcium channels (SS unpublished observations). VSD imaging shows that rebound neurons form characteristic microcircuits, defined by a focal point of initiation that then spreads to an annular ring that oscillates between inhibition and excitation. The current strength of the stimulus pulses in the train is adjusted so that little or no depolarizing activity occurs during the train, and the predominant response is the rebound motif, consisting of a hyperpolarization followed by a rebound depolarization, that occurs at the end of the train. 400 ms-2 s long trains were found to be most efficient at evoking a single rebound motif at the end of the train.

In the slice illustrated in **Figure 14B**, the time lapse images span the region just preceding and covering the rebound activity (bottom, inset, red line). Frame intervals are 12 frames (7.2 ms) apart. The 1500 ms long train evoked minimal depolarization, apparent as a small, localized region of activity in the ventral ICC (frame 2112), just preceding the onset of the rebound motif. Inhibition that preceded the rebound depolarization was observed in the ventral ICC spreading toward the lateral edge (frame 2160), increasing in strength and area in the succeeding frames. A focal point of depolarization then began (frame 2198), increased in strength and spatial spread, and covered most of the area that was previously inhibitory (frames 2224–2280). Within this region that was now excitatory, an annular ring developed (frames 2244–2280), which corresponded to the excitatory region of the rebound motif, and was followed by a gradual fading of response in the succeeding frames. (Movie S6 in Supplementary Material). Rebound motifs occurred in different areas of the slice; the sequence of inhibition, focal excitation, and annular ring of depolarization was characteristic (32 slices). The observation that the same or similar area switches between excitation and inhibition, as well as the loss of the pattern in the presence of $NiCl_2$ (data not shown), suggests that the rebound motif occurs in cells with an intrinsic rebound firing pattern.

These results suggest the activation of local circuits in the ICC from interactions between synaptic and intrinsic membrane parameters. The spatial and temporal spread of activity that occurs when LL activation switches from a low to a high-frequency train suggests the recruitment of large cell populations that create a network through which activity propagates out into the greater part of the ICC. The establishment of these local networks, which require a change in synaptic strength, is likely to include cells that differ intrinsically. On the other hand, local circuits involving post-inhibitory rebound cells form a loop of alternating excitation and inhibition, restricted to the same spatial region. Within this region, cells interconnect to form these alternating patterns, thus the network arises when activity propagates recurrently between these interconnected cells. There is little spread of activity beyond this region of alternating excitation and inhibition, however, suggesting that rebound firing recruits regions of the ICC into closed-loop local circuits.

DISCUSSION

We describe optical techniques using VSDs to measure activity within and across frequency laminae and to isolate stimulus- and cell-type-specific circuitry in the IC. The central nucleus of the IC appears to operate from a base of functional units that are homogenous in response magnitude, but graded in response time. As input parameters change, these units interact to create a global activity pattern that is directionally sensitive, topographically from high to low to middle frequencies, or along the rostro-caudal or dorso-ventral axes within frequency laminae. Our results suggest the presence of an intrinsic spatial activity profile in the central nucleus created by local interactions between small populations of temporally graded, equal magnitude, response areas.

FOCAL VERSUS GLOBAL ACTIVITY AND THE CONCEPT OF INDEPENDENT RESPONSE AREAS IN THE ICC

The comparison of VSD responses in single pixels with those in a broader area covered by multiple pixels attempts to address the general question of whether responses in small subsets of ICC neurons scale to produce responses in larger populations. The concept of synaptic domains, consisting of clustered inputs with similar functionality (Loftus et al., 2010) residing within the broader topographical frequency mosaic of the ICC, the gradation of timing information along the medial-lateral (Schreiner and Langner, 1988; Langner et al., 2002), and of spectro-temporal features along the dorso-ventral axes (Rodriguez et al., 2010) and the postulated functionally segregated units for sound frequency (Semple and Aitkin, 1979), all strongly indicate the existence of a response transfer function from sub-domains of neurons into a larger

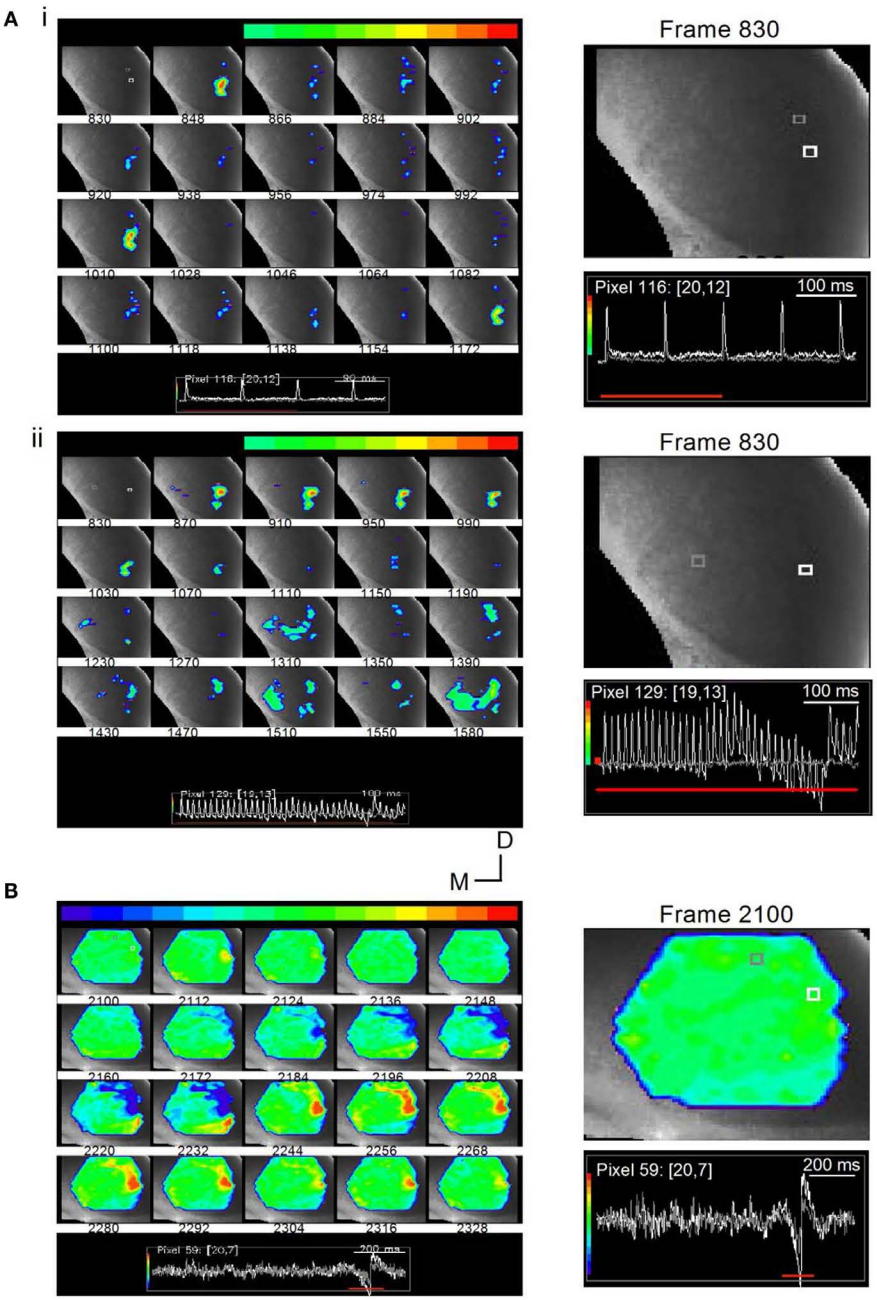

FIGURE 14 | Stimulus-specific microcircuits in the ICC. (A) Time lapse images of responses in a transverse IC slice (mouse; P20) to changing LL stimulus frequencies. (i) Responses to a 10 Hz train are localized to the ventral ICC where LL axons enter. Frames are 12 ms apart. Inset: White and gray traces correspond to the similarly colored pixels in the first frame 830. The pixels chosen are close together to illustrate the spatially restricted nature of the response. While the response at the white pixel is large, there is no response at the gray pixel. Responses in frames 848, 1010, and 1172 correspond to the times of each of the three shocks (100 ms apart). Right panel, Expanded image of the first frame, 830, with inset traces of responses in white and gray pixels; Red line, response area (three of the four shocks) covered by frames 830-1172. (ii) Responses to a 40 Hz train spread and exhibit accumulating non-linearities. Shock current strength is the same as in (i). Frames are 25 ms apart (the same separation as the interpulse interval). The 1–1 stimulus-response coupling as well as the spatially restricted response seen in the early frames (870–1070) is lost during the later part of the train (frames 1310–1590). Inset: Color range is chosen to highlight the depolarizing response. Instances of hyperpolarization, e.g., activity below baseline seen toward the end of the train, are therefore omitted from the total response; Right panel, Expanded image of the first frame, 830, with inset traces of responses in white and gray pixels. **(B)** Time lapse images of responses in a transverse IC slice (rat; P25) to a 1-s long train at 40 Hz. Shock strength 0.15 mA. Frames are 7.2 ms apart. Response region (frames 2100-2328) corresponds to the inhibitory and excitatory motifs of the rebound region only (inset, red line). Color scale is adjusted so that the baseline is set to green to allow for inhibitory responses to appear toward the blue regions. Frame 2112 shows a small localized depolarizing response. This frame precedes the onset of inhibition (frame 2148) by 22 ms. Directional scale bar applies to **(A,B)**. Right panel, Expanded image of the first frame, 2100, with inset traces of responses in white and gray pixels.

topographical organization. Our VSD data suggests that, under conditions of very low afferent activation, small groups of neurons, together with their inputs, form spatially constricted response areas with uniform magnitude but temporal spread. A differential in the temporal summation of these response areas results in a gradient of response magnitude between the broader topographic regions of the ICC, introducing topographic-dependent gain control.

Population coding in the auditory midbrain has compared single neuron responses with responses pooled from multiple neurons by using average firing rates or spike trains as the measure of activity (Fitzpatrick et al., 1997; Schneider and Woolley, 2010). Since changes in firing rate can arise from changes in either or both the magnitude and timing of the sub-threshold response to inputs, we designed our stimulus paradigms so that responses occurred throughout the ICC and, in individual pixels, were primarily sub-threshold. Together with the use of the low-power objective through which much of the ICC was visible, this stimulus paradigm allowed us to simultaneously measure activity in both large and small neuronal populations evoked by small, "baseline" stimuli that would evoke responses in a greater portion of the ICC.

The uniformity, throughout the ICC, of sub-threshold response magnitude within the small neuronal population represented by a single pixel suggests that, without significant non-linearity in neuronal responses, synaptic strength is constant throughout the ICC. The single-peaked, small duration, depolarizing responses in individual pixels are similar to those obtained with whole-cell patch recordings from single ICC neurons in brain slices using similar minimal LL stimulation (Sivaramakrishnan and Oliver, 2006), thus at these low stimulus levels, the lack of activation of postsynaptic voltage-dependent currents prevents the diversity of ICC intrinsic properties (Sivaramakrishnan and Oliver, 2001) from affecting response patterns. Thus, in the probable absence of active conductances, sub-threshold response magnitudes in the ICC appear as functionally defined response areas.

In contrast to the uniformity in sub-threshold response magnitude across topographic regions, a clear temporal gradient existed between single pixels. This gradient included a slight gradient in onset latency, but predominantly, a gradient in the time of occurrence of the peak depolarization. Thus between each functional module, responses vary either in onset or rise time, and produce a systematically graded effect on the timing of the peak response in the ventral to dorsal, and lateral to medial directions. In the transverse slice, a micro-temporal gradient within a module could occur in the 150 μm rostral-caudal or in the 150 μm $\times$ 150 μm dorso-ventral and lateral-medial directions covered by each pixel. This gradient could arise intrinsically through differences in membrane time constants (Sivaramakrishnan and Oliver, 2006), or extrinsically, from different brainstem sources (Schofield, 1991; Gabriele et al., 2000; Saldaña et al., 2009) through lemniscal axons with variable path lengths and diameters. Afferent LL weighting might become more important at higher recruitment levels and create greater variations in single pixel responses within and across topographic regions.

Global activity, in areas selected in transverse ICC sections to analogously represent the topographic distribution of frequency regions, exhibited a gradient in both response magnitude and timing. In contrast to the predominantly sub-threshold activity in single pixels, the summed activity in multiple pixels clearly demonstrated the presence of spikes followed by synaptic responses. In VSD signals, for spikes to become visible as a component distinct from synaptic responses, there must be sufficient synchrony. If the predominance of spikes was due to an increased directional ratio, along a topographic axis, of lemniscal or ICC neuronal axons to soma, then spikes should have become increasingly visible in single pixels in either the ventral-dorsal or lateral-medial directions. Because this did not occur, we conclude that the increased prevalence of spikes in these global regions resulted from the temporal summation of sub-threshold synaptic potentials between neighboring single pixels, suggesting that local circuits exist between functional units, and their activity increases neuronal output. A similar local circuit effect on sub-threshold summation is likely to underlie the increased response amplitude; multiple peaks with varying latencies and the changing response magnitude with direction are likely to result from the temporal gradient between individual pixels. Gain control in the ICC is integral to auditory coding (Palombi and Caspary, 1996; Ingham and McAlpine, 2005). Our VSD data suggests that, under minimal stimulus conditions, gain control occurs through *temporal* enhancement via local circuits, within an effective radius $\geq$150 μm, the inter-pixel distance. We cannot, however, rule out additional changes in gain within the smaller spatial units imaged by single pixels.

CIRCUITRY WITHIN AND ACROSS FREQUENCY LAMINAE

A comparison of LL-driven activity between the transverse and laminar slice planes suggests an intriguing functional organization of frequency domains. In transverse slices, bands of strong activity appear to occur roughly in the direction of lemniscal input (Saldaña et al., 2009), and might indicate fibro-dendritic laminae. The width or dorso-ventral extents of these bands suggests several overlapping laminae which are not resolvable with low-power objectives. However, we were able to distinguish at least three main regions of lemniscal propagation in the ventral and dorsal ICC and in the external cortex and to measure the time taken by activity to propagate into these regions. The $\sim$2.5 ms time taken by lemniscal input to reach the dorsal and middle regions of the ICC is a rough estimate of the maximum contribution of travel time in the ICC to the onset latency to sound, which is $\sim$10–20 ms for most ICC neurons in the unanesthetized mammal (Kuwada et al., 1997; Sivaramakrishnan et al., 2004). A second interesting aspect of the initial strong activity pattern is the response in the external cortex that lasted long after the response in the ICC had declined, suggesting slow processing, a characteristic that may enhance integration of the different sensory inputs to this region (Robards, 1979; Zhou and Shore, 2006). In contrast to the strong activity in the direction of laminae, the cross-laminar connections appeared to be much weaker, and delayed. Thus cross-laminar movement might be a secondary, rather than a direct, consequence of lemniscal input, with boosting by local circuits.

Inhibitory postsynaptic potentials in the ICC evoked by commissural activation show paired-pulse facilitation (Vale and Sanes, 2000), suggesting that the GABergic inhibitory component of commissural connectivity (Hernandez et al., 2006) exerts a non-linear effect on ICC excitation. VSD imaging shows that

commissural connectivity is more easily established when $GABA_A$ receptors are blocked, providing supporting evidence for the damping effect of the commissure on ICC excitability. The change from a normally depressing to a facilitating excitation in the ICC in the absence of GABAergic activity is likely to result from the loss of facilitating inhibitory synaptic potentials and may contribute to the gain control exerted by inhibition in the ICC (Palombi and Caspary, 1996; Sivaramakrishnan et al., 2004; Ingham and McAlpine, 2005). The shape of spikes in the commissural region, suggestive of collisions, indicates bidirectional activity in the commissural bundle caused by spikes moving in opposite directions in different commissural axons. The gradual change from spikes to collisions and oscillations in the commissure is time-dependent, thus propagation through the commissure contributes to a temporal regulation of the excitatory-inhibitory balance in the ICC. Since the whole slice was bathed in $GABA_A$ antagonists, we did not establish whether the increased excitation that triggered commissural propagation was localized to specific ICC regions or arose from the contralateral ICC from similar or dissimilar frequency bands (Malmierca et al., 2009).

Voltage-sensitive dye images of activity within frequency laminae illustrate a complex functional architecture, where directional homeostasis, the maintenance, along the dorso-ventral or rostro-caudal axes, of synaptic latency in spite of a changing input onset latency, appears to be created through a stimulus-dependent recruitment of local circuits. Within a particular direction, homeostasis was maintained in the temporal response of ICC neurons to LL inputs; irrespective of a gradient in lemniscal input times, a gradient in cellular response times did not develop in either direction. Along the rostral-caudal axis, the latencies of response onset and the peak of the first spike both varied, which is expected from the direction of LL afferent input (Saldaña et al., 2009), and their gradients were similar, however, the latency of the synaptic peak showed no gradient at all. Along the ventral-dorsal axis, there was no change in response onset, a larger gradient in first spike latencies compared to the rostral-caudal direction, and yet, no gradient in synaptic peak times. These results suggest an intrinsic regulation of synaptic response gradients within a lamina. The longer absolute synaptic response times in the rostral-caudal direction, cannot be explained by the small range in response onsets or first spike latencies, but could be due to differences in cell diameters, synapse clustering, or input strength. We caution that the homeostatic control of synaptic response time occurs when the entire LL afferent tract is activated by a single shock and future studies in the brain slice will benefit from single LL axon stimulation to isolate specific spatially segregated inputs. In spite of this drawback, however, our results demonstrate that a gradient in input arrival times does not necessarily translate into a gradient in cellular response times between groups of cells spaced 37 μm apart.

Re-orientation of activity within a lamina triggered by LL stimulus trains suggests that intra-laminar connections recruit sub-sets of ICC neurons into spatial patterns of activity. Much of this recruitment is due to the accumulation of depolarization during the train. Plateau or accumulating depolarizations recorded in single ICC neurons in a laminar slice result from polysynaptic inputs suggestive of local circuit activation (Sivaramakrishnan and Oliver, 2006), and VSD images indicate that intra-laminar circuitry creates spatial orientation within laminae. Taken together with the single shock data, these results indicate that the anatomical and physiological axes within ICC frequency laminae (Lim and Anderson, 2007) arise from a local circuit-driven enhancement or suppression of specific sets of input domains.

MICRODOMAINS OF LOCAL CIRCUITS IN THE ICC

A major advantage of using VSD imaging in the ICC is the ability to image different components of circuitry and therefore design stimuli to activate specific regions of the ICC in a relatively controlled way. We have used two stimulus paradigms to illustrate how responses propagate from a point of origin and reveal functional architecture in the ICC. Low frequency stimulus trains, for example, produce localized responses, a one-to-one stimulus-response relationship and consistency in spatial dimension. The highest activity levels in local circuitry activated by this type of stimulus-response coupling is restricted to near neighbors of ICC neurons, with its spatial extent determined by the stimulus current and the number of LL axons activated. The greater part of the ICC, which remains mainly silent, is recruited into activity by changing the frequency of the stimulus. Localization of the response at the beginning, and its spread only during the latter part of the train, suggest the requirement for a build-up in depolarization before activity can spread into other ICC regions, reinforcing the concept of local circuit activation. The long stimulus train at low current strength that activates circuits involving post-inhibitory rebound cells also has a point of origin from which it propagates. This circuit differs from those activated by the low- and high-frequency trains described above in that it oscillates between inhibitory and excitatory activity. The presence of a clear rebound motif within the single pixel implies that most of the cells within that pixel are post-inhibitory rebound neurons, suggesting that these neurons might be grouping together. This grouping is likely to provide a sufficiently strong point source that begins the propagation into an annular ring of excitatory-inhibitory oscillation.

CONCLUSION

Voltage-sensitive dye imaging is a viable tool to correlate activity in small groups of cells with those in larger populations in slices of the IC. The ability to distinguish between spikes and synaptic potentials provides a way of separately analyzing the fast and slow components of a response in any given region. Since spikes do contribute to the total signal, however, there is some smearing of temporal components. VSD imaging of IC activity benefits from multiple approaches to both acquire and analyze optical data. A comparison between single- and multi-pixel summated responses suggests the presence of unitary activity domains and non-linear processes that create spatio-temporal activity profiles. Activity within and across frequency laminae, which appears to have different strengths and a dynamic spatial and temporal spread, can be revealed by using specific stimulus patterns, windowing responses, and varying the image gain to measure activity at the peak and closer to sub-threshold regions of the response. Stimulus patterns

derived from knowledge of the electrophysiological behavior of identified cell-types are an especially important tool to establish the presence of cell-type specific microcircuitry in the ICC.

ACKNOWLEDGMENTS

We thank Jian-young Wu for extensive help with setting up the VSD system, Srdjan Antic for continued discussions on VSD imaging, Douglas Oliver for discussions on IC anatomy, and reviewers for critical comments on the manuscript. This work was supported by National Institutes of Health, National Institutes of Deafness, and Other Communication Disorders R01-DC008120.

SUPPLEMENTARY MATERIAL

The Supplementary Material for this article can be found online at http://www.frontiersin.org/Neural_Circuits/10.3389/fncir.2013.00041/abstract

Movie S1 | VSD recording of activity in a transverse slice of the IC in response to a single LL shock. Movie corresponds to **Figure 7**.

Movie S2 | VSD recording of activity in normal ACSF. Movie corresponds to **Figure 9A**.

Movie S3 | VSD recording of activity in SR95531. Movie corresponds to **Figure 9B**.

Movie S4 | VSD recording of activity in a laminar slice in response to a single LL shock. Movie corresponds to **Figure 10**.

Movie S5 | VSD recording of activity in a transverse IC slice evoked by an LL stimulus train. Movie corresponds to **Figure 13C**.

Movie S6 | VSD recording of activity in a transverse IC slice to a stimulus that evoked a circuit involving post-inhibitory rebound neurons. Movie corresponds to **Figure 14B**.

REFERENCES

Adams, J. C. (1980). Crossed and descending projections to the inferior colliculus. *Neurosci. Lett.* 19, 1–5.

Aitkin, L. M., and Phillips, S. C. (1984). The interconnections of the inferior colliculi through their commissure. *J. Comp. Neurol.* 228, 210–216.

Blasdel, G. G., and Salama, G. (1986). Voltage-sensitive dyes reveal a modular organization in monkey striate cortex. *Nature* 321, 579–585.

Bruckner, S., and Rubsamen, R. (1995). Binaural response characteristics in isofrequency sheets of the gerbil inferior colliculus. *Hear. Res.* 86, 1–14.

Covey, E., Kauer, J. A., and Casseday, J. H. (1996). Whole-cell patch-clamp recording reveals subthreshold sound-evoked postsynaptic currents in the inferior colliculus of awake bats. *J. Neurosci.* 16, 3009–3018.

Faye-Lund, H., and Osen, K. K. (1985). Anatomy of the inferior colliculus in rat. *Anat. Embryol.* 171, 1–20.

Fitzpatrick, D. C., Batra, R., Stanford, T. R., and Kuwada, S. (1997). A neuronal population code for sound localization. *Nature* 388, 871–874.

Gabriele, M. L., Brunso-Bechtold, J. K., and Henkel, C. K. (2000). Development of afferent patterns in the inferior colliculus of the rat: projection from the dorsal nucleus of the lateral lemniscus. *J. Comp. Neurol.* 416, 368–382.

Glendenning, K. K., Baker, B. N., Hutson, K. A., and Masterton, R. B. (1992). Acoustic chiasm V: inhibition and excitation in the ipsilateral and contralateral projections of LSO. *J. Comp. Neurol.* 319, 100–122.

Gonzalez-Hernandez, T., Mantolan-Sarmiento, B., Gonzalez-Gonzalez, B., and Perez-Gonzalez, H. (1996). Sources of GABAergic input to the inferior colliculus of the rat. *J. Comp. Neurol.* 372, 309–326.

Grienberger, C., Adelsberger, H., Stroh, A., Milos, R. I., Garaschuk, O., Schierloh, A., et al. (2012). Sound-evoked network calcium transients in mouse auditory cortex in vivo. *J. Physiol. (Lond.)* 590, 899–918.

Hernandez, O., Rees, A., and Malmierca, M. S. (2006). A GABAergic component in the commissure of the inferior colliculus in rat. *Neuroreport* 17, 1611–1614.

Herrera, M., Correa, J., Sanchez del Campo, F., and Ruiz, A. (1988). Stellate cells and their axonal patterns in the central nucleus of the inferior colliculus of the cat (*Felis domesticus*). *J. Hirnforsch.* 29, 393–402.

Higgins, N. C., Storace, D. A., Escabi, M. A., and Read, H. L. (2010). Specialization of binaural responses in ventral auditory cortices. *J. Neurosci.* 30, 14522–14532.

Horikawa, J., Hosokawa, Y., Kubota, M., Nasu, M., and Taniguchi, I. (1996). Optical imaging of spatiotemporal patterns of glutamatergic excitation and GABAergic inhibition in the guinea-pig auditory cortex in vivo. *J. Physiol. (Lond.)* 497(Pt 3), 629–638.

Huang, X., Xu, W., Liang, J., Takagaki, K., Gao, X., and Wu, J. Y. (2010). Spiral wave dynamics in neocortex. *Neuron* 68, 978–990.

Ingham, N. J., and McAlpine, D. (2005). GABAergic inhibition controls neural gain in inferior colliculus neurons sensitive to interaural time differences. *J. Neurosci.* 25, 6187–6198.

Irvine, D. R. F. (1992). "Physiology of the auditory brainstem," in *The Mammalian Auditory Pathway: Neurophysiology*, 1st Edn, eds A. N. Popper and R. R. Fay (New York: Springer-Verlag), 153–231.

Kojima, S., Nakamura, T., Nidaira, T., Nakamura, K., Ooashi, N., Ito, E., et al. (1999). Optical detection of synaptically induced glutamate transport in hippocampal slices. *J. Neurosci.* 19, 2580–2588.

Konnerth, A., Obaid, A. L., and Salzberg, B. M. (1987). Optical recording of electrical activity from parallel fibres and other cell types in skate cerebellar slices in vitro. *J. Physiol. (Lond.)* 393, 681–702.

Kubota, M., Miyamoto, A., Hosokawa, Y., Sugimoto, S., and Horikawa, J. (2012). Spatiotemporal dynamics of neural activity related to auditory induction in the core and belt fields of guinea-pig auditory cortex. *Neuroreport* 23, 474–478

Kulesza, R. J., Vinuela, A., Saldana, E., and Berrebi, A. S. (2002). Unbiased stereological estimates of neuron number in subcortical auditory nuclei of the rat. *Hear. Res.* 168, 12–24.

Kuwada, S., Batra, R., Yin, T. C., Oliver, D. L., Haberly, L. B., and Stanford, T. R. (1997). Intracellular recordings in response to monaural and binaural stimulation of neurons in the inferior colliculus of the cat. *J. Neurosci.* 17, 7565–7581.

Langner, G., Albert, M., and Briede, T. (2002). Temporal and spatial coding of periodicity information in the inferior colliculus of awake chinchilla (*Chinchilla laniger*). *Hear. Res.* 168, 110–130.

Langner, G., Schreiner, C., and Merzenich, M. M. (1987). Covariation of latency and temporal resolution in the inferior colliculus of the cat. *Hear. Res.* 31, 197–201.

Lim, H. H., and Anderson, D. J. (2007). Spatially distinct functional output regions within the central nucleus of the inferior colliculus: implications for an auditory midbrain implant. *J. Neurosci.* 27, 8733–8743.

Lippert, M. T., Takagaki, K., Xu, W., Huang, X., and Wu, J. Y. (2007). Methods for voltage-sensitive dye imaging of rat cortical activity with high signal-to-noise ratio. *J. Neurophysiol.* 98, 502–512.

Loew, L. M., Cohen, L. B., Salzberg, B. M., Obaid, A. L., and Bezanilla, F. (1985). Charge-shift probes of membrane potential. Characterization of aminostyrylpyridinium dyes on the squid giant axon. *Biophys. J.* 47, 71–77.

Loftus, W. C., Bishop, D. C., and Oliver, D. L. (2010). Differential patterns of inputs create functional zones in central nucleus of inferior colliculus. *J. Neurosci.* 30, 13396–13408.

Loftus, W. C., Bishop, D. C., Saint Marie, R. L., and Oliver, D. L. (2004). Organization of binaural excitatory and inhibitory inputs to the inferior colliculus from the superior olive. *J. Comp. Neurol.* 472, 330–344.

Malmierca, M. S., Blackstad, T. W., Osen, K. K., Karagulle, T., and Molowny, R. L. (1993). The central nucleus of the inferior colliculus in rat: a Golgi and computer reconstruction study of neuronal and laminar structure. *J. Comp. Neurol.* 333, 1–27.

Malmierca, M. S., Hernandez, O., Antunes, F. M., and Rees, A. (2009). Divergent and point-to-point connections in the commissural pathway between the inferior colliculi. *J. Comp. Neurol.* 514, 226–239.

Malmierca, M. S., Rees, A., Le Beau, F. E., and Bjaalie, J. G. (1995). Laminar organization of frequency-defined local axons within and between the inferior colliculi of the guinea pig. *J. Comp. Neurol.* 357, 124–144.

Malmierca, M. S., Saint Marie, R. L., Merchan, M. A., and Oliver, D. L. (2005). Laminar inputs from dorsal cochlear nucleus and ventral cochlear nucleus to the central nucleus of the inferior colliculus: two patterns of convergence. *Neuroscience* 136, 883–894.

Merzenich, M. M., and Reid, M. D. (1974). Representation of the cochlea within the inferior colliculus of the cat. *Brain Res.* 77, 397–415.

Middleton, J. W., Kiritani, T., Pedersen, C., Turner, J. G., Shepherd, G. M., and Tzounopoulos, T. (2011). Mice with behavioral evidence of tinnitus exhibit dorsal cochlear nucleus hyperactivity because of decreased GABAergic inhibition. *Proc. Natl. Acad. Sci. U.S.A.* 108, 7601–7606.

Momose-Sato, Y., Sato, K., Arai, Y., Yazawa, I., Mochida, H., and Kamino, K. (1999). Evaluation of voltage-sensitive dyes for long-term recording of neural activity in the hippocampus. *J. Membr. Biol.* 172, 145–157.

Moore, D. R., Kotak, V. C., and Sanes, D. H. (1998). Commissural and lemniscal synaptic input to the gerbil inferior colliculus. *J. Neurophysiol.* 80, 2229–2236.

Nelson, P. G., and Erulkar, S. D. (1963). Synaptic mechanisms of excitation and inhibition in the central auditory pathway. *J. Neurophysiol.* 26, 908–923.

Oliver, D. L. (1984). Dorsal cochlear nucleus projections to the inferior colliculus in the cat: a light and electron microscopic study. *J. Comp. Neurol.* 224, 155–172.

Oliver, D. L. (2000). Ascending efferent projections of the superior olivary complex. *Microsc. Res. Tech.* 51, 355–363.

Oliver, D. L., Beckius, G. E., Bishop, D. C., Loftus, W. C., and Batra, R. (2003). Topography of interaural temporal disparity coding in projections of medial superior olive to inferior colliculus. *J. Neurosci.* 23, 7438–7449.

Oliver, D. L., Kuwada, S., Yin, T. C., Haberly, L. B., and Henkel, C. K. (1991). Dendritic and axonal morphology of HRP-injected neurons in the inferior colliculus of the cat. *J. Comp. Neurol.* 303, 75–100.

Oliver, D. L., and Morest, D. K. (1984). The central nucleus of the inferior colliculus in the cat. *J. Comp. Neurol.* 222, 237–264.

Paloff, A. M., Usunoff, K. G., and Hinova-Palova, D. V. (1992). Ultrastructure of Golgi-impregnated and gold-toned neurons in the central nucleus of the inferior colliculus in the cat. *J. Hirnforsch.* 33, 361–407.

Palombi, P. S., and Caspary, D. M. (1996). GABA inputs control discharge rate primarily within frequency receptive fields of inferior colliculus neurons. *J. Neurophysiol.* 75, 2211–2219.

Peruzzi, D., Sivaramakrishnan, S., and Oliver, D. L. (2000). Identification of cell types in brain slices of the inferior colliculus. *Neuroscience* 101, 403–416.

Robards, M. J. (1979). Somatic neurons in the brainstem and neocortex projecting to the external nucleus of the inferior colliculus: an anatomical study in the opossum. *J. Comp. Neurol.* 184, 547–565.

Rodriguez, F. A., Read, H. L., and Escabi, M. A. (2010). Spectral and temporal modulation tradeoff in the inferior colliculus. *J. Neurophysiol.* 103, 887–903.

Ross, W. N., Salzberg, B. M., Cohen, L. B., Grinvald, A., Davila, H. V., Waggoner, A. S., et al. (1977). Changes in absorption, fluorescence, dichroism, and Birefringence in stained giant axons: optical measurement of membrane potential. *J. Membr. Biol.* 33, 141–183.

Saldaña, E., Aparicio, M. A., Fuentes-Santamaria, V., and Berrebi, A. S. (2009). Connections of the superior paraolivary nucleus of the rat: projections to the inferior colliculus. *Neuroscience* 163, 372–387.

Saldaña, E., and Merchan, M. A. (1992). Intrinsic and commissural connections of the rat inferior colliculus. *J. Comp. Neurol.* 319, 417–437.

Schneider, D. M., and Woolley, S. M. (2010). Discrimination of communication vocalizations by single neurons and groups of neurons in the auditory midbrain. *J. Neurophysiol.* 103, 3248–3265.

Schofield, B. R. (1991). Superior paraolivary nucleus in the pigmented guinea pig: separate classes of neurons project to the inferior colliculus and the cochlear nucleus. *J. Comp. Neurol.* 312, 68–76.

Schreiner, C. E., and Langner, G. (1988). Periodicity coding in the inferior colliculus of the cat. II. Topographical organization. *J. Neurophysiol.* 60, 1823–1840.

Schreiner, C. E., and Langner, G. (1997). Laminar fine structure of frequency organization in auditory midbrain. *Nature* 388, 383–386.

Semple, M. N., and Aitkin, L. M. (1979). Representation of sound frequency and laterality by units in central nucleus of cat inferior colliculus. *J. Neurophysiol.* 42, 1626–1639.

Sivaramakrishnan, S., Brodwick, M. S., and Bittner, G. D. (1991). Presynaptic facilitation at the crayfish neuromuscular junction. Role of calcium-activated potassium conductance. *J. Gen. Physiol.* 98, 1181–1196.

Sivaramakrishnan, S., and Oliver, D. L. (2001). Distinct K currents result in physiologically distinct cell types in the inferior colliculus of the rat. *J. Neurosci.* 21, 2861–2877.

Sivaramakrishnan, S., and Oliver, D. L. (2006). Neuronal responses to lemniscal stimulation in laminar brain slices of the inferior colliculus. *J. Assoc. Res. Otolaryngol.* 7, 1–14.

Sivaramakrishnan, S., Sterbing-D'Angelo, S. J., Filipovic, B., D'Angelo, W. R., Oliver, D. L., and Kuwada, S. (2004). GABA(A) synapses shape neuronal responses to sound intensity in the inferior colliculus. *J. Neurosci.* 24, 5031–5043.

Stiebler, I., and Ehret, G. (1985). Inferior colliculus of the house mouse. I. A quantitative study of tonotopic organization, frequency representation, and tone-threshold distribution. *J. Comp. Neurol.* 238, 65–76.

Vale, C., and Sanes, D. H. (2000). Afferent regulation of inhibitory synaptic transmission in the developing auditory midbrain. *J. Neurosci.* 20, 1912–1921.

Wagner, T. (1996). Lemniscal input to identified neurons of the central nucleus of mouse inferior colliculus: an intracellular brain slice study. *Eur. J. Neurosci.* 8, 1231–1239.

Winer, J. A., Larue, D. T., Diehl, J. J., and Hefti, B. J. (1998). Auditory cortical projections to the cat inferior colliculus. *J. Comp. Neurol.* 400, 147–174.

Xu, C., and Loew, L. M. (2003). The effect of asymmetric surface potentials on the intramembrane electric field measured with voltage-sensitive dyes. *Biophys. J.* 84, 2768–2780.

Xu, X., Olivas, N. D., Levi, R., Ikrar, T., and Nenadic, Z. (2010). High precision and fast functional mapping of cortical circuitry through a novel combination of voltage sensitive dye imaging and laser scanning photostimulation. *J. Neurophysiol.* 103, 2301–2312.

Zhou, J., and Shore, S. (2006). Convergence of spinal trigeminal and cochlear nucleus projections in the inferior colliculus of the guinea pig. *J. Comp. Neurol.* 495, 100–112.

Conflict of Interest Statement: The authors declare that the research was conducted in the absence of any commercial or financial relationships that could be construed as a potential conflict of interest.

Received: 08 October 2012; accepted: 28 February 2013; published online: 20 March 2013.

Citation: Chandrasekaran L, Xiao Y and Sivaramakrishnan S (2013) Functional architecture of the inferior colliculus revealed with voltage-sensitive dyes. Front. Neural Circuits ***7****:41. doi: 10.3389/fncir.2013.00041*

frontiers in
NEURAL CIRCUITS

ORIGINAL RESEARCH ARTICLE
published: 20 August 2012
doi: 10.3389/fncir.2012.00055

Morphological and physiological characteristics of laminar cells in the central nucleus of the inferior colliculus

Mark N. Wallace*, Trevor M. Shackleton and Alan R. Palmer

MRC Institute of Hearing Research, Medical Research Council, Nottingham, UK

Edited by:
Manuel S. Malmierca, University of Salamanca, Spain

Reviewed by:
Edward Lee Bartlett, Purdue University, USA
Philip Smith, University of Wisconsin Medical School, USA

****Correspondence:***
Mark N. Wallace, MRC Institute of Hearing Research, University Park, Nottingham NG7 2RD, UK.
e-mail: markw@ihr.mrc.ac.uk

The central nucleus of the inferior colliculus (IC) is organized into a series of fibro-dendritic laminae, orthogonal to the tonotopic progression. Many neurons have their dendrites confined to one lamina while others have dendrites that cross over a number of laminae. Here, we have used juxtacellular labeling in urethane anesthetized guinea pigs to visualize the cells with biocytin and have analyzed their response properties, in order to try and link their structure and function. Out of a sample of 38 filled cells, 15 had dendrites confined within the fibro-dendritic laminae and in 13 we were also able to reconstruct their local axonal tree. Based on dendritic morphology they were subdivided into flat or less flat; small, medium, or large; elongated or disk-shaped cells. Two of the elongated cells had many dendritic spines while the other cells had few or none. Twelve of the cells had their local axonal tree restricted to the same lamina as their dendrites while one cell had its dendrites in a separate lamina from the axon. The axonal plexus was more extensive (width 0.7–1.4 mm) within the lamina than the dendrites (width generally 0.07–0.53 mm). The intrinsic axons were largely confined to a single lamina within the central nucleus, but at least half the cells also had output axons with two heading for the commissure and five heading into the brachium. We were able to identify similarities in the physiological response profiles of small groups of our filled cells but none appeared to represent a homogeneous morphological cell type. The only common feature of our sample was one of exclusion in that the onset response, a response commonly recorded from IC cells, was never seen in laminar cells, but was in cells with a stellate morphology. Thus cells with laminar dendrites have a wide variety of physiological responses and morphological subtypes, but over 90% have an extensive local axonal tree within their local lamina.

Keywords: inferior colliculus, microcircuits, fibro-dendritic laminae, flat cells, juxtacellular labeling, neuronal reconstruction, intrinsic axon

INTRODUCTION

The inferior colliculus (IC) integrates projections from lower auditory nuclei with descending projections from the thalamus and cortex. Despite this pivotal position in the auditory pathway the intrinsic wiring for the IC has still not been fully described in any species. The central nucleus of the IC (CNIC) is made up of layers of neurons with their dendrites oriented in parallel, forming a series of 10–12 laminae (see Morest, 1964; Rockel and Jones, 1973; Oliver and Morest, 1984; Malmierca et al., 1995). Recent work suggests that pathways from the lower brainstem may remain functionally segregated at the IC (e.g., Davis, 2002) with terminals from different input pathways interleaved, terminating in different sublaminae within the central nucleus (Oliver et al., 1997). Descending projections from the cortex mainly terminate in the dorsal or external cortex of the IC (Coomes et al., 2005), but influence the functional properties of cells in the CNIC (Palmer et al., 2007; Wu and Yan, 2007; Nakamoto et al., 2008, 2010), presumably via intrinsic connections.

Histological studies using Golgi staining have demonstrated a limited number of separable morphological cell classes in the IC. One of the earliest studies (Oliver and Morest, 1984) defined two cell types, some of which ("disk-shaped" cells) have dendrites and probably axons that are flattened in extent so as to remain within one lamina. Other ("stellate") cells have dendrites and axons that cut across two or more laminae and may integrate inputs from different sources. More recently, Malmierca et al. (1993) described two types of cell that contributed to the laminar organization "flat" (F) and "less flat" (LF). However, *in vitro* intracellular recordings in brain slice preparations have demonstrated at least six different cell types in the IC (Peruzzi et al., 2000; Ono et al., 2005), but the discharge patterns did not correspond simply to disk-shaped (flat) or stellate (LF) categories (Oliver et al., 1991). In a landmark study, Oliver et al. (1991) reconstructed the morphology of cells in the IC after filling with HRP. What is very clear from that study is that there is a widespread ramification of local axons within the IC and that the orientation of the soma, dendrites, and axonal fields depend upon the cell type and the position within the whole IC: within the central nucleus there were cells that based on dendrite and axon orientation seemed to correspond to the disk-shaped and stellate distinction. However, we do not know if there are also differences in the way these cell types respond acoustically *in vivo*.

In this study of the intrinsic wiring and responses of IC neurons we used juxtacellular labeling (see Palmer et al., 2003; Arnott et al.,

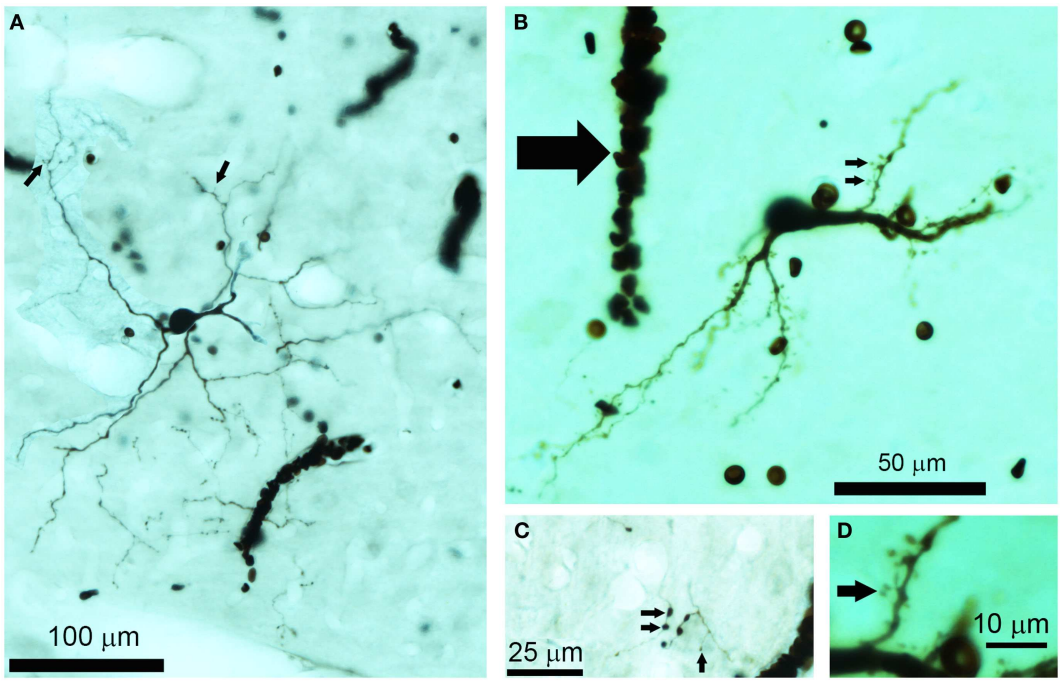

FIGURE 1 | Photomicrographs of biocytin labeled cells and processes in the IC. (A) Photomontage of a large, flat disk cell (1079R) viewed in the horizontal plane. This cell only has a few sparse dendritic spines on its distal dendrites (small arrows). Red blood corpuscles are also stained and partially obscure a few of the processes. **(B)** Flat, medium elongated cell (339L) sectioned in the coronal plane. This has numerous dendritic spines even on its proximal dendrites (small arrows). Near the soma there is an electrode track that filled up with blood during the removal of the electrode (large arrow). **(C)** The disk cell shown in **(A)** had an axon with numerous axonal swellings some of which were quite large (2 μm diameter) as indicated by the pair of small arrows, but nearby there were other small axonal endings (<1 μm) as indicated by the single small arrow. **(D)** A higher power view of the dendritic spines indicated by the lower small arrow in **(B)**. These are only about 20 μm from the soma and have a long thin stalk.

2004) that allowed us to measure physiological response profiles of single cells, to dye fill them, and to recover their morphology. In an attempt to reduce the heterogeneity, we report the physiological characteristics of one group of cells that, superficially at least, have similar morphologies with axons and dendrites restricted to within a single frequency band lamina.

MATERIALS AND METHODS

Experiments were carried out using male and female pigmented guinea pigs ranging from 350 to 884 g. Experiments were performed in accordance with a project license issued under the United Kingdom Animals (Scientific Procedures) Act 1986. All reagents were obtained from Sigma, except where otherwise stated.

ANIMAL PREPARATION

Animals were anesthetized with urethane (0.9 g kg^{-1} i.p., in 20% solution in 0.9% saline) and Hypnorm (0.2 ml i.m., comprising fentanyl citrate 0.315 mg ml^{-1} and fluanisone 10 mg ml^{-1}). Atropine sulfate (0.06 mg kg^{-1} s.c.) was administered at the start of the experiment. Anesthesia was supplemented, on indication, with further doses of Hypnorm (0.2 ml i.m.). A tracheotomy was performed, followed by bilateral exposure of the ear canal by removal of the tragus and adjacent tissue. The animal was mounted in a stereotaxic frame in which the ear bars were replaced with plastic speculae to allow visualization of the tympanic membrane and delivery of sound stimuli. Pressure equalization within the middle ear was achieved by a narrow polythene tube (0.5 mm external diameter) sealed into a small hole in the bulla on each side. The angle of the head was adjusted such that the surface of the skull in the rostro-caudal axis was horizontal at points 5 and 13 mm in front of ear-bar zero (see Rapisarda and Bacchelli, 1977). Craniotomies were performed on both sides, extending 2–3 mm rostral and caudal of the interaural axis, and 3–4 mm lateral from midline. Following removal of the dura, the exposed brain was covered with 1.5% agar.

The animal's temperature was maintained at 38°C throughout the experiment by means of a heating blanket which was thermostatically controlled using a rectal thermistor. The animals were artificially respired with 100% oxygen and the respiratory rate and end-tidal CO_2 was monitored via an infra-red capnometer; heart rate was monitored via a pair of electrodes inserted into the skin to either side of the animal's thorax (both Vetspecs VSM8, Canton, GA, USA).

STIMULATION, RECORDING, AND JUXTACELLULAR LABELING

Experiments were carried out in a sound-attenuated booth. Stimuli were delivered through a sealed acoustic system comprising custom-modified Radio Shack 40-1377 tweeters (M. Ravicz, Eaton Peabody Laboratory, Boston) that coupled to damped 4 mm-diameter probe tubes, which fitted into the speculum. In every experiment, the sound system close to the tympanic membrane was calibrated using a Brüel and Kjaer 4134 microphone fitted

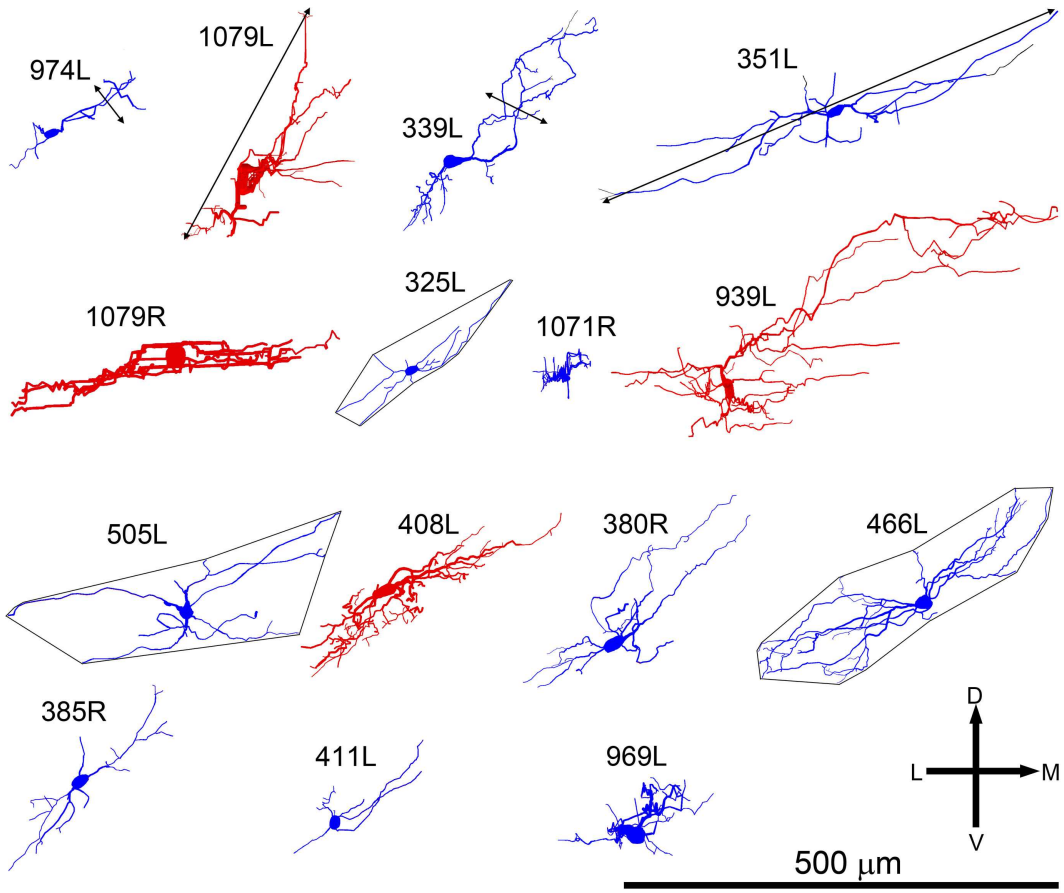

FIGURE 2 | Soma and dendrites of all 15 filled cells viewed in the coronal plane. Most cells were filled on the left (L suffix) but some were filled in the right IC (R suffix) and these have been reversed so that all the cells appear as though they were on the left. All of the cells are flattened and their long axis is oriented approximately in the plane of the fibro-dendritic laminae. They are arranged in tonotopic order with the cell having the lowest CF (300 Hz) located in the top left corner (974L) and the cell with the highest CF (5.1 kHz) near the bottom right corner. Their "flatness" was measured by the thickness of their dendritic tree in or close to the coronal plane as illustrated by the double-headed black arrow for cells 974L and 339L. Their size was taken as the maximum dendritic extent measured in either the coronal or horizontal planes as illustrated by the double-headed arrow for cells 1079L and 351L. The area of the dendritic tree was measured in either the coronal or horizontal plane) by drawing a polygon round the main dendrites as illustrated for cells 325L, 505L, and 466L. They range in size from small, $<20{,}000\,\mu m^2$ to large, $>45{,}000\,\mu m^2$ with just under half (7/15) classed as medium.

with a 1-mm probe tube. The sound system response on each side was flat to within ±10 dB from 100 to 35,000 Hz.

Stimuli used in this study consisted of 50 ms bursts of tones and wideband noise (bandwidth 0.1–50 kHz), which were presented to either or both ears every 200 ms. All stimuli were generated by an array processor (Tucker-Davis Technologies AP2) housed in a computer. The stimuli were output via a waveform reconstruction filter and digital-to-analog converter at rates of at least 100 kHz. The maximum output level was set to approximately 100 dB SPL.

Recordings were made with stereotaxically placed aluminosilicate glass capillary microelectrodes (1.0 mm outer diameter with filament, Clarkes SM100F-10, Harvard Apparatus Ltd., Edenbridge, UK), pulled, filled with 1.5% biocytin in 0.5 M sodium chloride and broken back to give a tip impedance of 15–30 MΩ and advanced by a piezoelectric motor (Burleigh Inchworm, IW-711-00) into the IC through the intact cortex. Extracellular action potentials were amplified (Axoprobe 1A, Axon Instruments, Burlingame, CA, USA), filtered (300–2,000 Hz), and monitored via an oscilloscope and a loudspeaker. Action potentials were discriminated using a level-crossing detector and converted into voltage pulses which were recorded digitally with a resolution of 1 μs (Tucker-Davis Technologies SD1 and ET1).

When a single cell was isolated, using a search stimulus of diotic broadband noise or pure tones of variable level, the cell's characteristic frequency (CF) and minimum threshold for response were determined audio-visually. The cell responses were then characterized physiologically using a battery of stimuli delivered to either or both ears as appropriate. The battery consisted of the following:

1. Frequency response areas measured in pseudo-random order by presenting single tones over a 3 octave by 100 dB range in steps of 1/8 octave and 5 dB.
2. Frequency response areas as above with a CF tone simultaneously presented at 10 dB above threshold. This revealed inhibitory areas in those neurons with low rates of spontaneous activity.

Table 1 | Morphological characteristics of the 15 filled cells.

Cell no.	CF (kHz)	Soma Area (μm^2)	Dendrites Area (μm^2)	Dendritic morphology						Dendrites (μm) min/max diameter	Local axon	Projection
				Shape of tree			Spines	Orientation				
974L	0.297	133	9,777	Flat	Small	Elongated	Sparse	A	M/L	80 × 162	Incomplete	2
1079L	0.669	308	32,383		Medium	Disk	Sparse	A	M/L	125 × 272	Incomplete	2
339L	0.933	185	24,994	Flat	Medium	Elongated	Many	A	Oblique	50 × 364	Laminar	Commissural
351L	0.947	205	48,412		Large	Elongated	Sparse	S	M/L	90 × 574	Laminar	2
1079R	0.983	243	90,371	Flat	Large	Disk	Sparse	S		70 × 395	Laminar	Brachium
325L	0.991	130	7,260	Flat	Small	Elongated	1	S	M/L	20 × 141	Unstained	2
1071R	1.144	62	7,583	Flat	Small	Elongated	Many	S	R/C	75 × 253	Laminar	Intrinsic 2
939L	1.377	214	133,235		Large	Disk	1	A	M/L	135 × 612	Laminar	Brachium
505L	1.469	264	27,568		Medium	Elongated	1	S	M/L	100 × 373	Laminar	2
408L	2.193	193	32,887	Flat	Medium	Disk	Sparse	S		60 × 306	Laminar	Commissural
380R	2.332	213	24,016	Flat	Medium	Elongated	Sparse	A	M/L	45 × 331	Laminar	Brachium 2
466L	3.303	218	34,754		Medium	Elongated	Sparse	S	M/L	100 × 396	Laminar	Brachium
385R	4.497	248	14,350	Flat	Small	Elongated	Sparse	S	M/L	60 × 281	Unstained	2
411L	4.929	118	7,230	Flat	Small	Elongated	1	A	Oblique	60 × 195	Laminar	Intrinsic
969L	5.119	402	37,337		Medium	Elongated	1	S	R/C	100 × 343	Laminar	Brachium

A, asymmetric; S, symmetric; M/L, medio-lateral; R/C, rostocaudal. [1]The staining was too weak to be certain whether spines were present or not. [2]Uncertain on where the cells project to.

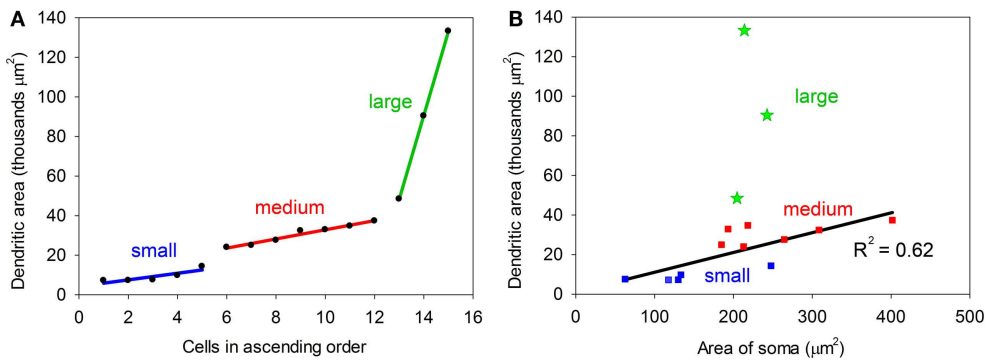

FIGURE 3 | (A) Plot showing the dendritic areas of the 15 labeled cells arranged in ascending order. Regression lines have been plotted for each of the three groups which have been defined by a break in the slope of the plot. **(B)** Plot relating the area of the cell body to the area of the dendritic tree. For the small and medium cells there is a reasonably good correlation ($R^2 = 0.62$), but for the large cells (green) the two values are not correlated.

3. Rate-level functions to 10 repetitions of CF tones presented separately to the left and right ears and to both ears. The tones were presented in pseudo-random order over a 100-dB range in 5 dB steps.
4. Peristimulus time histograms of responses evoked by 150 repetitions of CF tones presented to each ear separately and to both. The tones were delivered at 20 dB above the CF response threshold.
5. Modulation transfer functions from 10 to 1,000 Hz modulation rate (11 logarithmic spaced values) measured using 200 ms of 100% amplitude modulated CF tones presented at 20 dB above threshold to both ears once every 0.8 s for 10 repetitions.
6. Interaural Level Difference (ILD) functions measured by setting the contralateral tone to 20 dB above CF threshold and varying the level of the ipsilateral tone over a range of ±20 dB above and below that level in 2 dB steps for 10 repetitions. In some experiments ILD functions were also obtained by setting the average level to 20 dB above threshold and varying both the contra and ipsilateral levels symmetrically over a ±20 dB range in 2 dB steps.
7. Interaural Time Difference (ITD) functions (only when the CF was below about 1.5 kHz) to 20 repetitions of 20 dB suprathreshold CF tones. The ITD was varied in pseudo-random order over 31 steps of 0.1 of the period of the CF tone.

Following physiological characterization, the cell was labeled with biocytin according to the juxtacellular method of Pinault (1996). Briefly, biocytin was ejected from the recording pipette under physiological control using +3 to +11 nA square wave

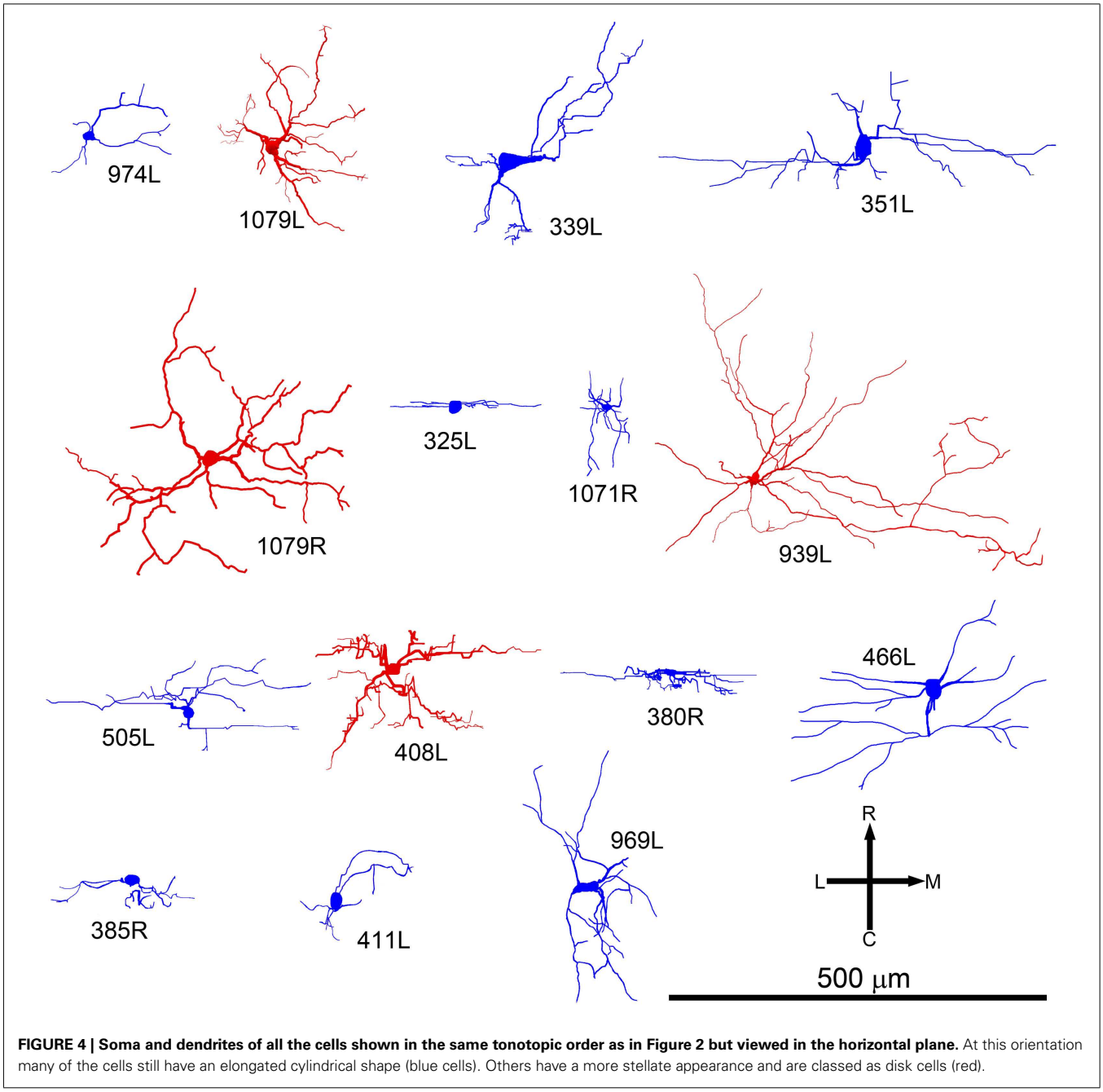

FIGURE 4 | Soma and dendrites of all the cells shown in the same tonotopic order as in Figure 2 but viewed in the horizontal plane. At this orientation many of the cells still have an elongated cylindrical shape (blue cells). Others have a more stellate appearance and are classed as disk cells (red).

current pulses, of 200 ms duration (50% duty cycle), which were applied using the current injection circuit of the microelectrode amplifier. Adequate current injection, appropriately close to the cell, caused action potentials to be evoked robustly during the depolarizing epochs. The current strength was titrated carefully to ensure that the cell remained firing throughout the labeling, but was not damaged by over driving; labeling occurred when current injection-associated firing was maintained for 2–15 min. We gained the impression that the duration of action potential entrainment, preferably using currents in the range +5 to +10 nA, was the most significant factor governing the distance through which a neuron might, subsequently, be traced. In three of the first cells we labeled (325L, 351L, and 385R) the spike was still well-isolated at the end of the current injection and we repeated the frequency response analysis to confirm that the cell's physiological properties were not altered by the 10 or 15-min of driving. However, in seven of the cells we either lost the spike or it faded away during the injection and in two of the cells (505L and 939L) we recorded a burst of spikes that indicated damage associated with an injury potential. Most of the cells which showed a distinctive injury potential were never recovered. Thus, in the later experiments, we carefully backed off from the cell immediately after the end of the injection period to avoid any risk of damage.

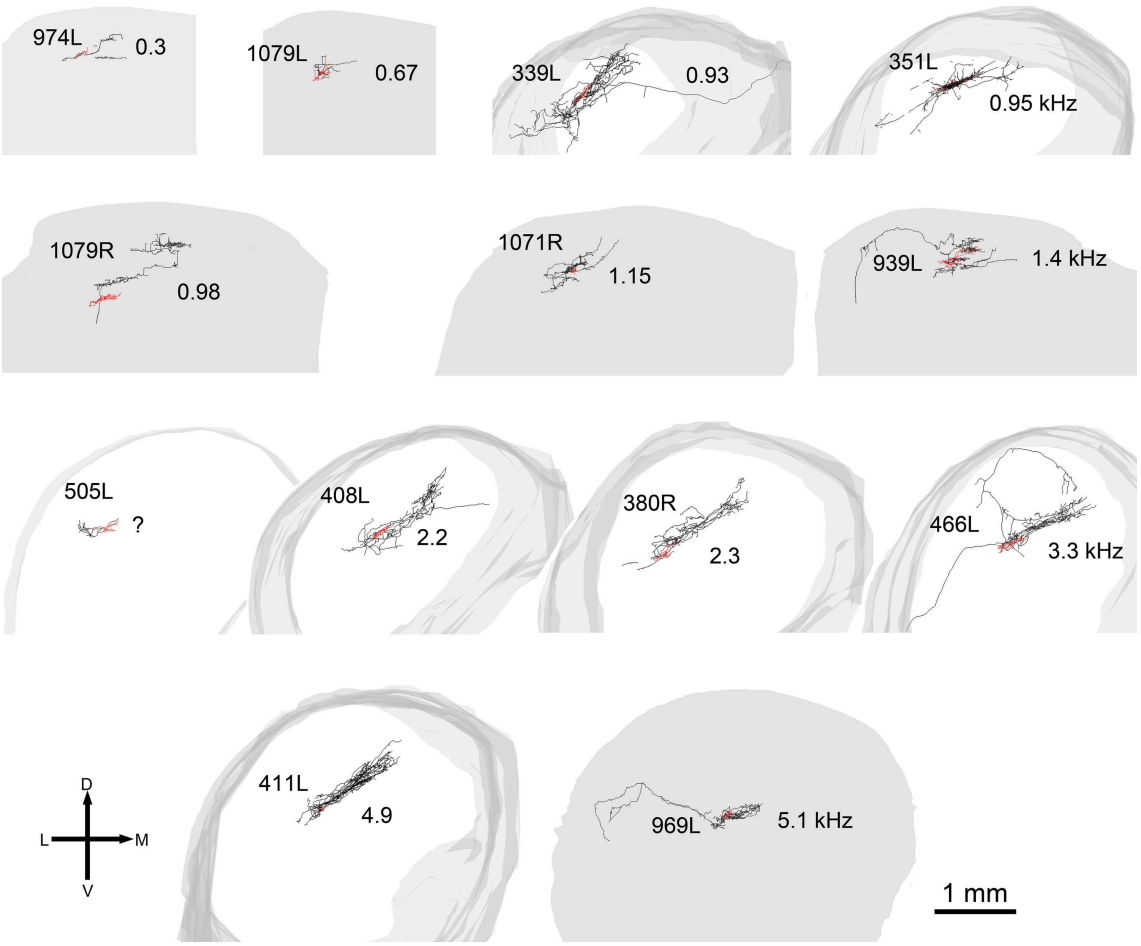

FIGURE 5 | Reconstructions of the axons and dendrites of filled cells viewed in the coronal plane. The axons are black, the dendrites are red, and the shape of the IC is represented in gray. In some cells the axon has been incompletely filled and sections are missing (e.g., 974L) while for two of the cells the axon was not stained and these cells are not shown. The cells are arranged in the same tonotopic order as in **Figure 2** and the CF of the cell (in kHz) is shown to the right of each cell except for 505L where we had two physiological response profiles recorded and could not determine which one corresponded to the filled cell.

HISTOLOGY

Following up to 9 h survival (during which time we undertook recordings from the IC using tungsten-in-glass microelectrodes (Bullock et al., 1988) for a number of different studies) the animal was anesthetized deeply with an overdose of sodium pentobarbitone. The animal was then perfused transcardially with 250 ml 0.1 M phosphate buffer pH 7.4 (PB) followed by 500 ml PB containing 4% paraformaldehyde and 0.5% glutaraldehyde. The brain was removed and stored in the same fixative overnight at 4˚C.

The following day, the brain was embedded in a mixture of gelatine and egg albumin and serial 50 μm coronal or horizontal sections were cut using a vibratome. The freely floating sections were washed twice in PB and were incubated overnight at 4˚C in PB containing 0.3% Triton X-100 and avidin-biotin peroxidase complex (ABC Elite, Vector Laboratories). The sections were washed twice in PB before being incubated for 10 min with 0.05% diaminobenzidine (DAB), 0.005% hydrogen peroxide, 0.0015% nickel ammonium sulfate, and 0.0015% cobalt chloride in PB. After quenching the reaction with excess PB, and washing the sections twice, the sections were mounted on subbed slides.

ANATOMICAL RECONSTRUCTIONS

Three-dimensional reconstructions were undertaken using computer software (Neurolucida, Microbrightfield, Colchester, VT, USA) connected to a microscope (Axioskop2, Carl Zeiss) with a motorized stage. DAB-stained material was traced using a 40× objective lens (NA 0.95) within the traced boundaries of the IC in each section. It was not usually possible to see the electrode tracks except when blood had infiltrated them as in the track shown in **Figure 1B** (thick arrow), which was located 50 μm lateral to the track (not visible) where cell 339L was labeled. The "flatness" of the filled cell was obtained by measuring the short axis of the dendritic tree in or close to the coronal plane as illustrated by the double-headed arrow for cells 974L and 339L in **Figure 2**. The maximum dendritic extent was also measured in either the coronal or horizontal planes (whichever was longer) as illustrated for cells 1079L and 351L in **Figure 2**. The area of the dendritic tree was measured

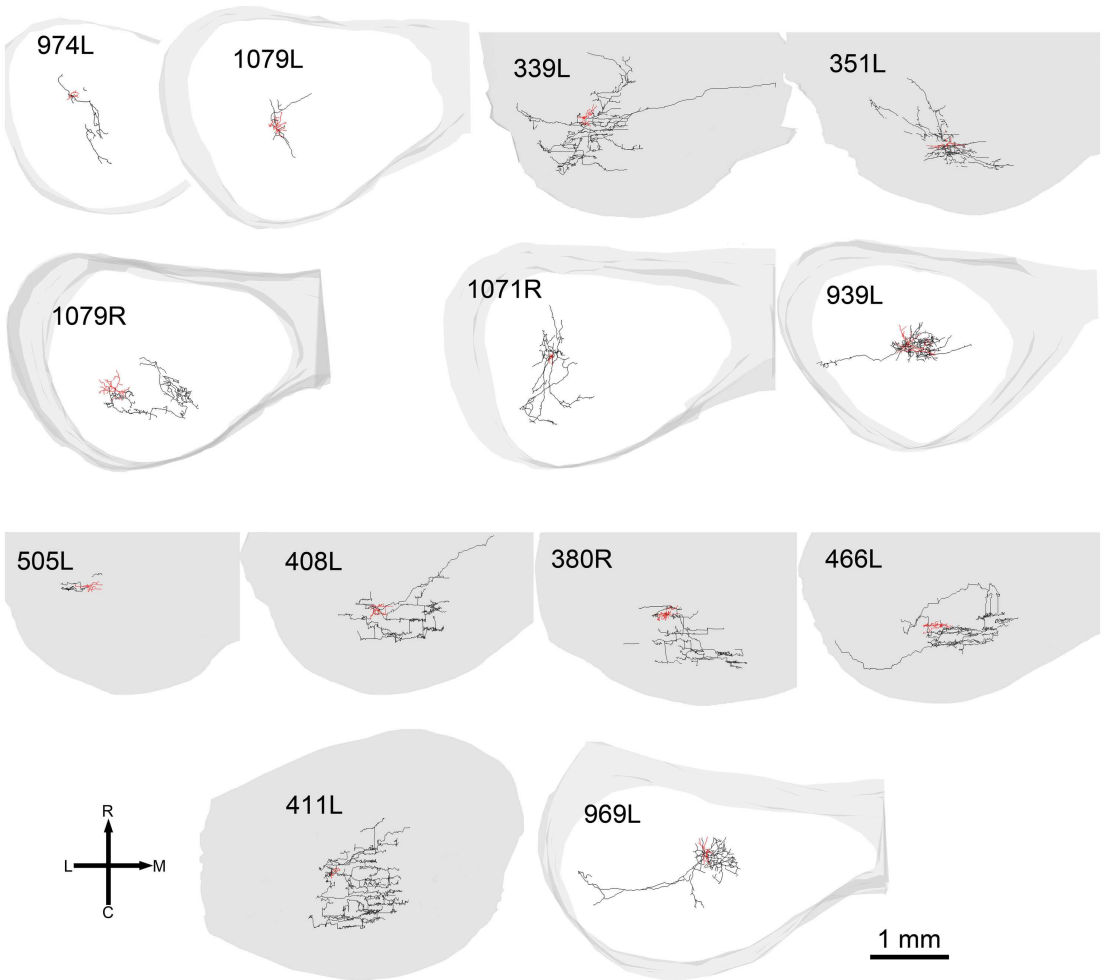

FIGURE 6 | Reconstructions of axons and dendrites of filled cells in the same format and order as in Figure 4 but viewed in the horizontal plane.

in either the coronal or horizontal plane (whichever was larger) by drawing a polygon round the main dendrites as illustrated for cells 325L, 505L, and 466L in **Figure 2**. The borders of the different divisions of the IC are difficult to discern in the guinea pig even when sections have been counterstained for Nissl substance and the borders mainly seem to be gradual transitions rather than having a sharp edge. We therefore estimated cell positions based on comparisons with a standard series of sections stained for nitric oxide synthase (Coote and Rees, 2008). The strength of staining in the dendrites varied between cells, but as we could distinguish dendritic spines in 10/15 cells, even when the staining was relatively weak, we were confident that we were able to follow most of the dendrites to their end.

RESULTS

DENDRITIC MORPHOLOGY OF LAMINAR CELLS

In our study of the IC we filled and recovered 38 individual cells. Some of these were in the external or dorsal cortices and of those in the central nucleus some had dendritic trees that were oriented across the laminae or were big enough to extend over two or more laminae (stellate cells). This left 15 cells which had dendrites oriented along the plane of a lamina in the central nucleus and where the dendrites appeared to be restricted to one lamina. Some of the cells were less flat than others and the thickness (dorsoventral) of the dendritic trees within the lamina varied from 20 to 135 μm. Thus nine of the cells had a flat morphology (dendritic thickness =80 μm viewed in the coronal plane) while six were LF. All were considered to be laminar cells because all their major dendrites were primarily oriented in the plane of their intrinsic axon which we assumed formed part of a single lamina. In practice, all the cells had dendritic trees where the longest dimension within the lamina was at least twice that of the thickness across the lamina and the mean ratio of these two dimensions was 4.7 (range 2–7.4) as shown in column 11 of **Table 1**. These 15 cells form the basis of the current report and examples of the soma and dendrites of two of them are shown in **Figure 1**. Although we defined the laminar cells as a single class, the characteristics of their dendrites meant that the cells could be subdivided on the basis of flatness, dendritic area, orientation, symmetry, and number of spines (**Table 1**).

All the cells had a similar orientation when viewed in the coronal plane (**Figure 2**). In this figure the cells are illustrated as though they were all from the left IC and all have an orientation

running from ventro-lateral to dorso-medial. The exact orientation varies, with the long axis varying between about 10° and 45° to the horizontal. This range of orientations is also found in the fibro-dendritic laminae visualized by the course of stained groups of intrinsic or commissural axons (Malmierca et al., 1995) and there seems no doubt that these 15 filled cells form part of the laminae. The cells were all multipolar with three to seven primary dendrites. Two of the cells had quite dense dendritic spines even on the proximal dendrites whereas the rest had either no spines or they were sparsely located on the distal dendrites (**Figure 1**). Most cells had well-stained dendrites and we were confident that any spines present would have been stained. However, five cells had weakly stained dendrites and the absence of spines may have been due to inadequate staining (see **Table 1**).

Most of the axonal swellings observed were "en passant" although there were some terminal boutons as well. The size of these swellings varied from 1 to 2 μm and varied along the length of an axonal branch (**Figure 1C**) so that small and larger boutons were present close to each other. We made no attempt to plot the distribution of axonal swellings or determine if a particular subtype of laminar cell was associated with a higher proportion of large axonal swellings and so this remains a possibility that may be worth pursuing in future.

One obvious difference is in the extent of the dendritic spread with the maximum area of the dendrites in some cells being less than 20,000 μm^2 (small) and over 45,000 μm^2 in others (large). The medium cells have an intermediate range of values and when dendritic area is plotted in ascending sequence the values seem to fall into three distinct groups (**Figure 3A**). However the small sample size means that these groups are a bit arbitrary and we cannot conclude that there are three discrete groups in any absolute sense. The cross-sectional area of the somata also varied with values ranging from 62 to 402 (μm^2). The area of the soma and the area of the dendritic field were roughly proportional for the small and medium cells as shown in **Figure 3B**. When a regression line is plotted for these two groups the correlation value is reasonably high, $R^2 = 0.62$. By contrast, there is a definite lack of correlation between the area of the soma and the dendritic area for the three large cells as their somata are the same size as the smaller medium cells. This indicates that in histological preparations where only the somata are stained it cannot be assumed that a larger soma automatically means a larger dendritic tree. In other neuronal systems the cell body size is proportional to the length of the axon (Ho et al., 1992) and this may also be true in the IC.

When the cells were viewed in the horizontal plane it was possible to visualize the extent of the dendrites within what we assume was the plane of a single lamina (**Figure 4**). In this orientation there were striking differences in the shape of the dendritic tree with four of the cells having dendrites radiating out in at least four directions (disk cells) while the other 11 cells had their dendrites arranged primarily along a single axis to give an elongated shape. Seven of the elongated cells were oriented in the mediolateral direction, two in the rostro-caudal direction, and two were obliquely oriented (**Table 1**). Some of the disk cells and elongated cells were reasonably symmetric, but others had clear asymmetries with a greater number or length of dendrites oriented in one direction than in the opposite direction.

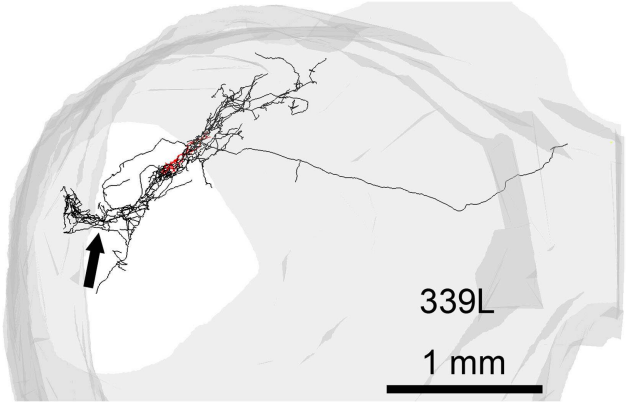

FIGURE 7 | Reconstruction of the axon (black) and dendrites (red) of a single cell (339L) viewed in an oblique plane optimized to show how the branches of the intralaminar intrinsic axon bend round to follow the upward sweep of the lamina at the lateral edge (black arrow).

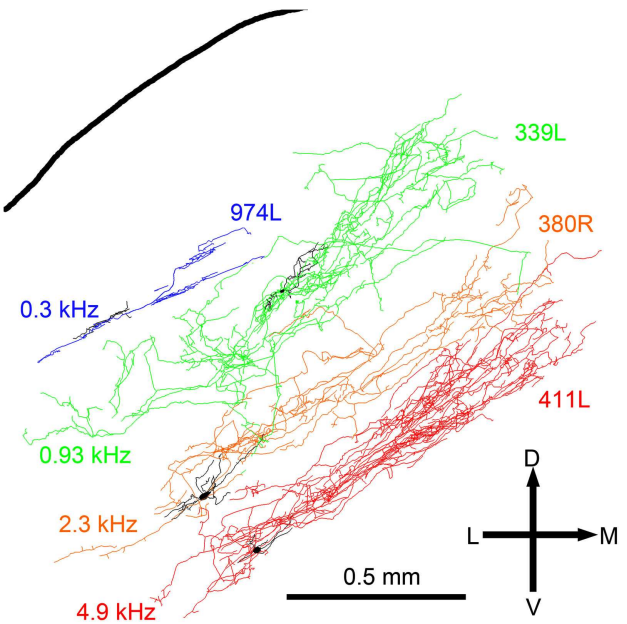

FIGURE 8 | Reconstructions of the intrinsic axons (blue, green, orange, and red respectively) and dendrites (black) of four filled cells superimposed at the appropriate depth below the IC surface and arranged in order of CF (shown to the left).

SPATIAL EXTENT OF INTRINSIC AXONS

In 13 of the cells the labeling was sufficiently good that we were able to reconstruct much of the intrinsic axon (see **Figure 5**, axons in black, dendrites in red). When viewed in the coronal plane, 12 of these cells had intrinsic axonal trees that were more extensive than the dendrites, but confined to the same lamina. Some also appeared to have an extrinsic axon with two cells sending an axon toward the commissure and five separate cells sending an axon toward the brachium. Two cells had relatively small axonal trees that were also

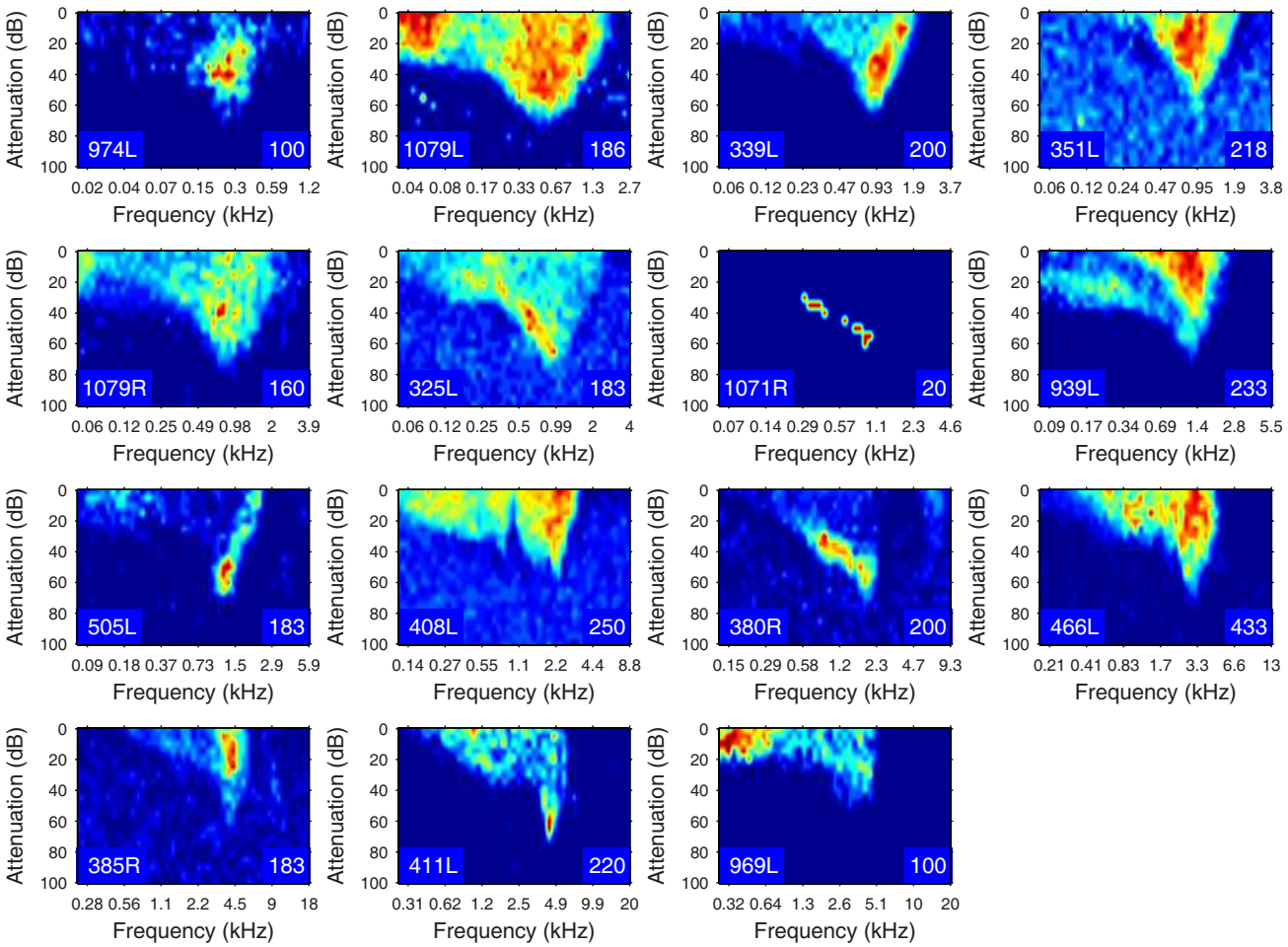

FIGURE 9 | Frequency response areas (see "Materials and Methods") for the 15 filled cells. The topographic arrangement follows the previous figures and is tonotopic. The response areas are normalized on a temperature scale from blue (zero response) to red (maximum response). The number in the bottom right hand corner of each panel for this and the next figure indicates the maximum firing rate to which the plot is scaled (spikes/s).

mainly in the same lamina as the dendrites, but were incompletely stained. However, one cell (1079R) had an intrinsic axon that appeared to be confined to a separate lamina from that in which the dendrites lay. When viewed in the horizontal plane it was possible to see the whole extent of each axon within a lamina (**Figure 6**). There was no apparent correlation between the extent of the intrinsic axonal tree and that of the dendrites. One of the small, flat elongated cells (411L) had one of the biggest axonal extents, while the other small, flat elongated cell (1071R) had a less extensive tree. Similarly, the large disk cell (939L) had one of the smallest axonal trees, while the other large disk cell (1079R) had a more extensive axonal tree. The pattern of the intrinsic axon seemed quite specific both in terms of extent and orientation of the axon terminals. Some cells (e.g., 408L) had axons oriented in the medio-lateral direction, some (e.g., 1071R) in a rostro-caudal direction, and some (e.g., 1079R) in an oblique direction. The axons were always more extensive than the dendrites with the medio-lateral width of the dendrites being 0.07–0.53 mm and the width of the axonal tree being 0.7–1.4 mm. The axonal trees never extended across the whole width of the central nucleus, but they sometimes extended over half the width and this was true in the rostro-caudal direction as well. Cells that were placed in the lateral part of the central nucleus generally had axonal trees that were mainly located medial to the soma. In the case of one laterally placed neuron, that had axonal branches running both medially and laterally (339L), the lateral branches followed the lamina round as it turned in the dorsal direction. This is shown in **Figure 7**, where the reconstruction has been oriented to show how the axon terminals line up in the dorsal extension of the lamina (thick arrow).

The laminar cells included in this report have CFs below 5.2 kHz. Their position within the IC and the orientation of their dendritic and axonal trees follow the tonotopic laminae with low frequencies more dorsally located (**Figure 8**). The four illustrated cells have CFs that just over 1 octave apart and there is almost no overlap in their axonal trees. For the cells with CFs of above 1 kHz the laminar thickness of their axonal tree is about 200 μm. For the low-frequency cells (CFs <1 kHz) the intrinsic axons were less extensive and there may not be such clear laminae.

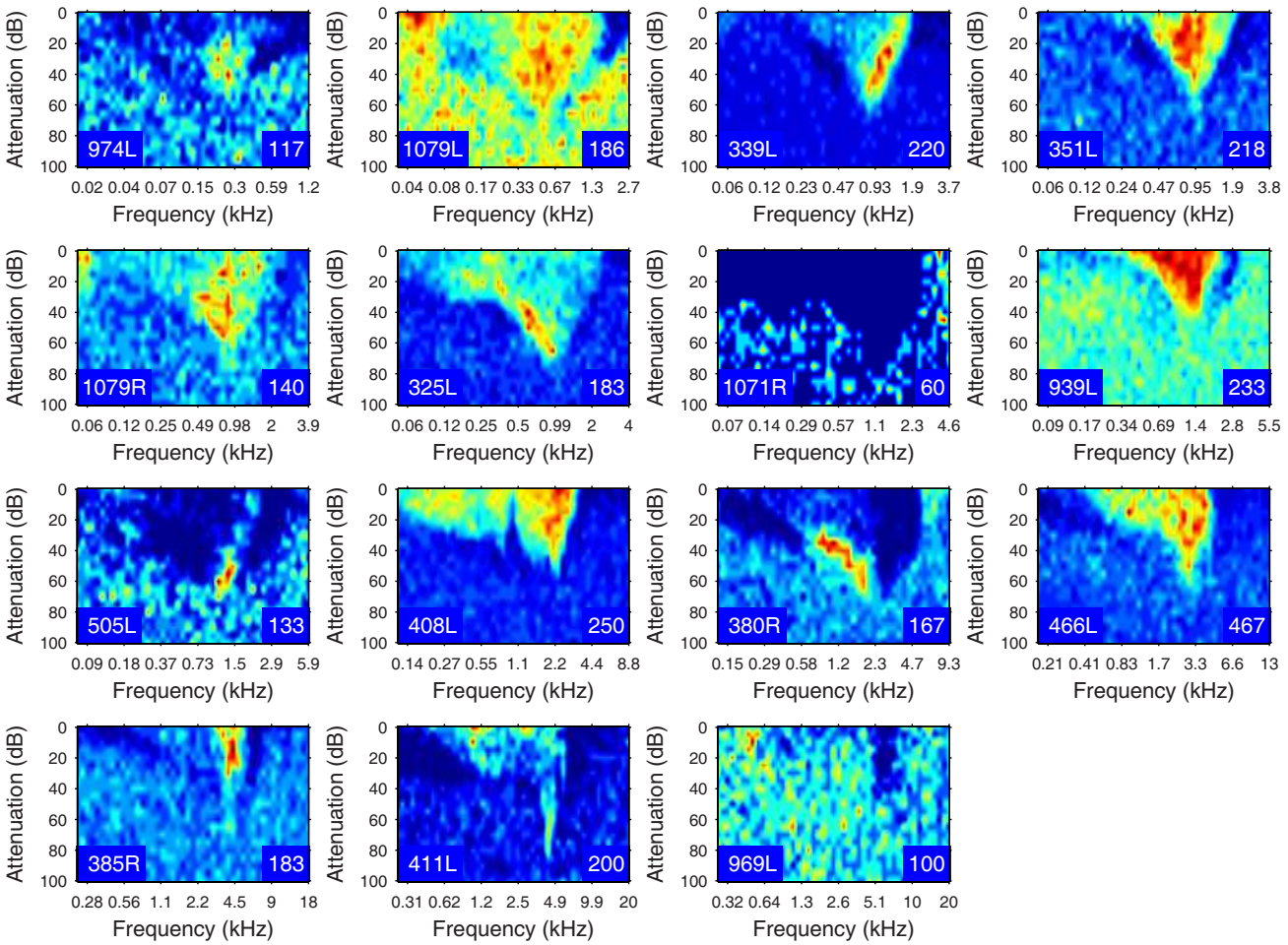

FIGURE 10 | Frequency response areas in the same format as Figure 8, but measured in the presence of a simultaneously presented CF tone at 10 dB above minimum threshold. Units 351L, 325L, and 408L are repeated from **Figure 9** since they had a sufficiently high spontaneous rate to reveal inhibition without the presence of a second tone.

PHYSIOLOGICAL RESPONSES OF LAMINAR CELLS

The heterogeneity of the somatic, dendritic, and axonal morphologies was also evident in the physiological response profiles recorded from each of the cells prior to dye filling. This is illustrated for five elements of the profile in **Figures 9–13** and summarized in **Table 2**. The binaural response properties (interaural time and level difference sensitivities) did not appear to provide additional explanatory leverage in this sample and are not shown here. Each of the physiological figures is arranged in exactly the same tonotopic order as the summary morphological (**Figures 2** and **4**) so responses can be associated with individual cells. **Figures 9** and **10** show respectively the response areas and the inhibitory areas that are revealed by simultaneously presenting a tone at the CF. It is clear that within this relatively small sample we see examples of many of the well-described response area types ("V": 351L; "tilted": 339L, 1071R, 505L, 380R; "O": 974L). It is also clear that many of the cells receive extensive inhibitory input (1071R, 505L, 380R, 411L). When inhibition is evident in the single tone response area at the CF this results in non-monotonic rate-level functions as shown in **Figure 11** (1071R, 505L, 380R, 411L). It is also clear from the rate-level functions that most cells receive binaural inputs, although some are monaurally dominated (**Table 2**). They are generally dominated by the contralateral inputs (red lines), in some instances the ipsilateral response is suppressive, reducing the binaural response below that to the contralateral alone (411L) and in others it is facilitatory (974L, 339L, 385R, 969L). The PSTHs to suprathreshold CF tones (**Figure 12**; **Table 2**) are diverse, but have one thing in common: none of them is a pure onset response. Onset responses were relatively common in our sample, with 16% (6/38) of our filled cells showing pure onset responses, but none of them had a laminar morphology and they will be described elsewhere.

The cell with the lowest CF (974L) shows excellent phase locking to the CF tone, but only when presented to both ears (consistent with the rate-level response). Some of the cells show responses that exceed the duration of the CF tones (50 ms) and two showed a very prominent offset response (1079R and 466L). Latency varied

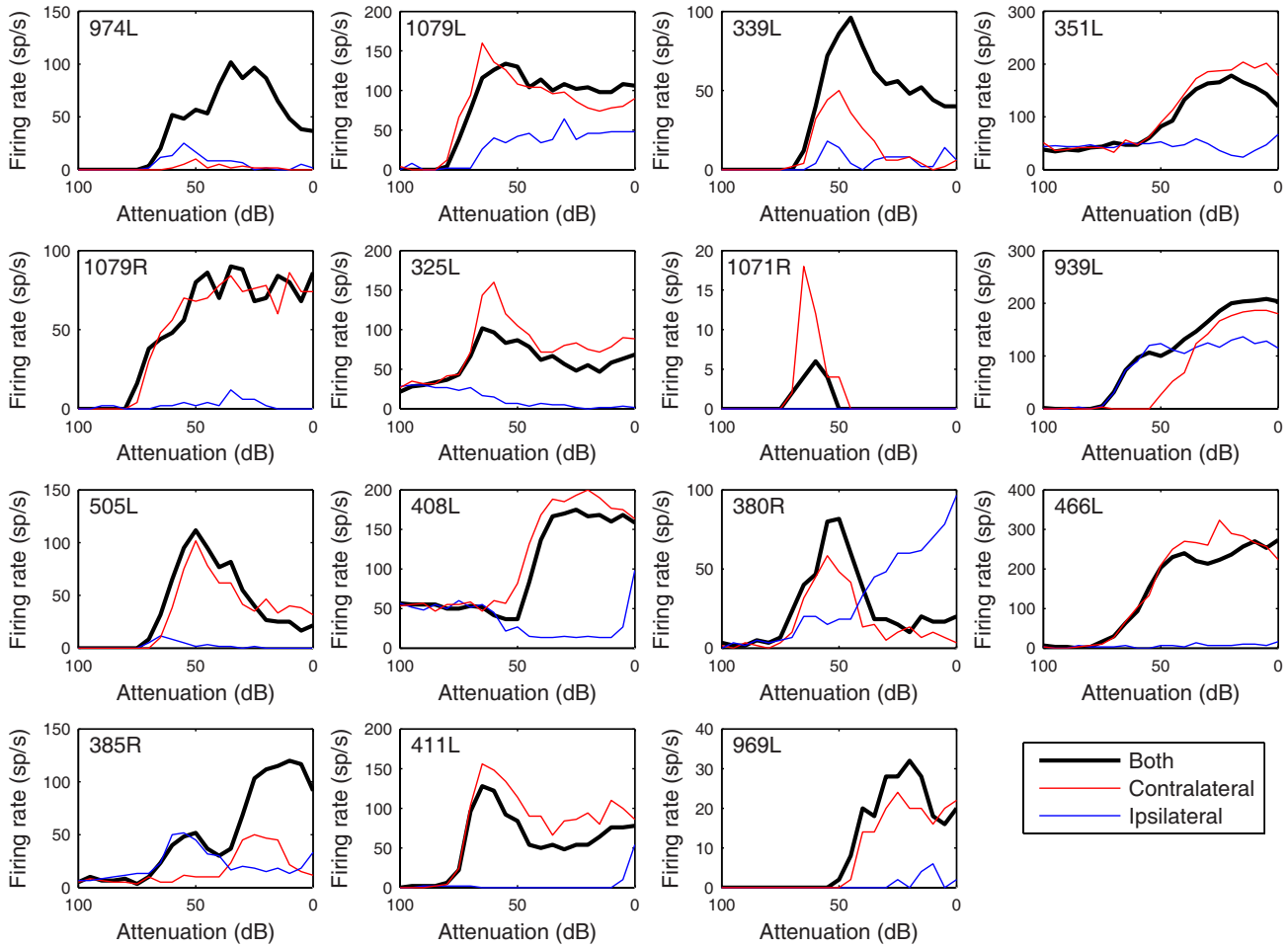

FIGURE 11 | Rate versus level functions in response to 50 ms CF tones arranged in the same order as previous figures. The black curves show responses to binaural presentation, red to contralateral, and blue to ipsilateral.

between 8 (408L) and 25 ms (1071R) for all bar the two cells with strong offset responses (see **Table 2**).

The rate and temporal modulation transfer functions (**Figure 13**) were generally not very informative with two exceptions (1079R and 466L), which were the only cells that showed a relatively narrow bandpass rate response to the modulated stimuli. Note that in this sample of 14 cells none showed a pronounced tuning in their temporal responses (red lines show the vector strengths of period histograms locked to the modulation waveform) even though locking to the modulation was often very good (1079R for example).

Given the diversity of both morphology and physiology it is perhaps unsurprising that correlations between the two were not strong. Two cells from different animals had almost interchangeable response profiles: 1079R and 466L: V-shaped response areas with weak inhibitory input, monotonic contralaterally dominated, monotonic rate-level responses, very prominent offset responses and narrow bandpass average rate modulation transfer functions. Both cells were relatively large multipolar cells, but at least by our subjective criteria 1079R was disk-shaped, while the dendrites of 466L were oriented (see **Figure 4**) and hence we describe it as elongated. Cell 466R was a LF, sparsely spinous, medium elongated cell of which we have two other examples (505L and 969L, see **Table 1**). These latter cells show some similarities in response profile with each other, but not with 466R. The two flat sparsely spinous, medium elongated cells (380R and 385R, see **Table 1**) also share similar physiological response profiles: they have single and two-tone response areas and rate-level functions showing evidence of inhibition, pauser PSTHs, and untuned or broadly tuned responses to modulated stimuli. Two cells that appeared to show chopping at the onset to CF tones (351L, 325L) both had V-shaped response areas with sufficient spontaneous activity that we did not need to measure responses to two tones, had monotonic, contralaterally dominated rate-level functions, and untuned modulation transfer functions. However, one was a large elongated cell (351L) and the other was a flat, small elongated cell (325L). Similarly, for the two cells with on-sustained responses which also shared other response similarities, one was a flat, medium fusiform cell with many spines (339L) while the other was a large disk cell with only a few sparse spines (939L). Finally, the very smallest cells

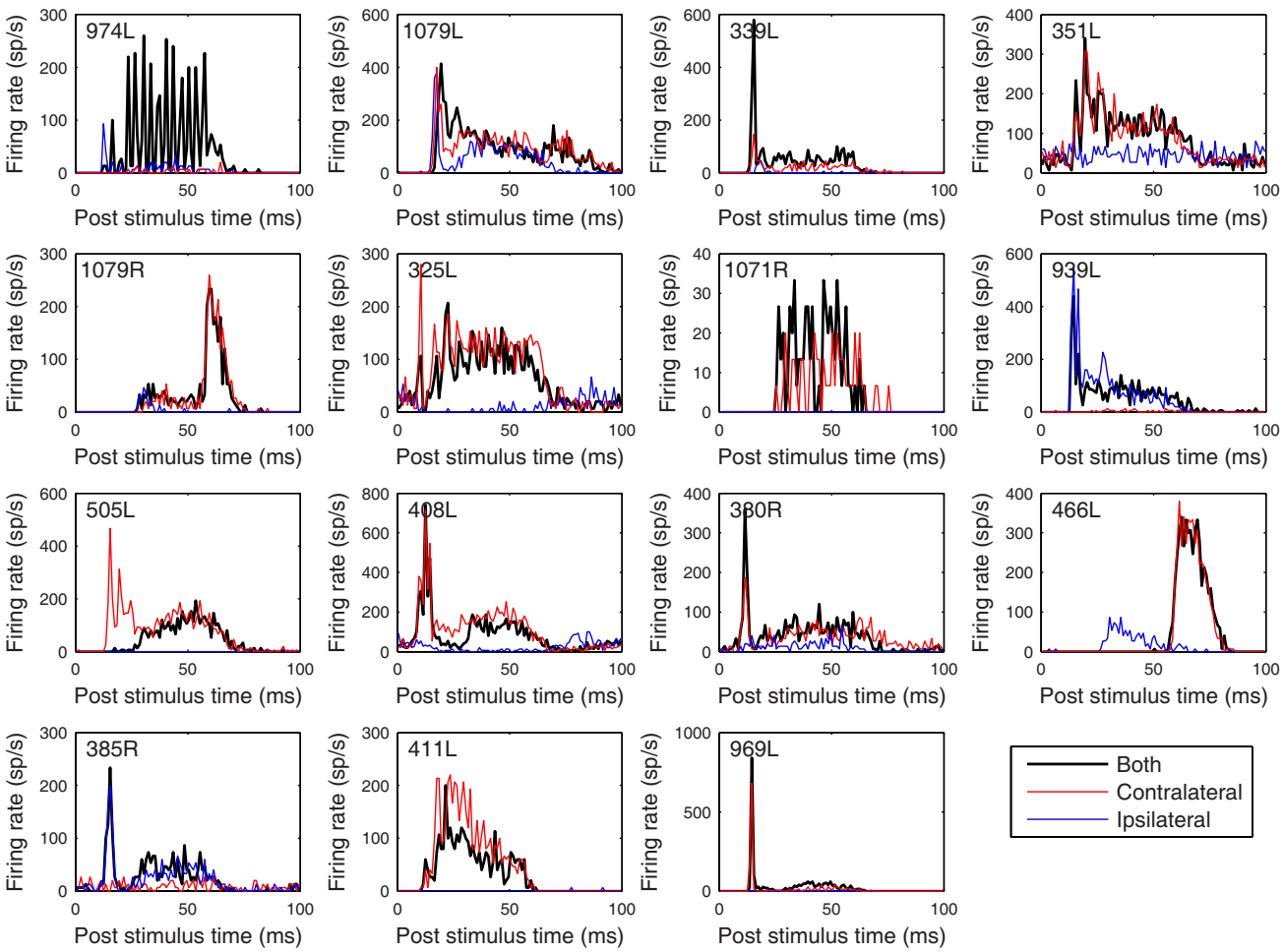

FIGURE 12 | Peristimulus time histograms to 50 ms CF tones. The figure is arranged in the same order as previous figures with the tones presented binaurally (black), contralaterally (red), and ipsilaterally (blue) at 20 dB above minimum threshold. Binwidth is 1 ms.

such as 325L, 1071R, 380R, 411L appeared to be subject to stronger and more widespread inhibitory inputs (see **Figure 10**).

It is clear that there are similarities in the response profiles between small numbers of cells in our sample and some of these seem to relate to small subgroups of the filled cells. However, given the diversity of morphological and physiological subtypes a much larger sample would be needed to be sure that these were real correlations.

DISCUSSION

DEFINITION OF CELL TYPES BASED ON DENDRITIC MORPHOLOGY

The CNIC has been the subject of many morphological studies, but since a common nomenclature has not emerged that can be applied across all mammalian species, we have used descriptive terms taken from a number of studies. We followed the classification used in the cat IC, where cells in the central nucleus were divided into laminar disk cells and translaminar stellate cells (Oliver and Morest, 1984; Oliver et al., 1991). For the present purposes, we have chosen to describe only those cells in our sample that had their dendrites oriented along the axis of a single fibro-dendritic lamina. We excluded the cells which had dendrites primarily oriented across the lamina or appeared to extend beyond a single lamina. Based on a preliminary analysis we have about 10 such translaminar stellate cells in our material, but have not yet reconstructed them and are unable to describe them here. We also labeled about 12 stellate neurons in the dorsal and external cortex and one in the rostral nucleus, but will not be sure of their exact location until after we have reconstructed them.

The width of disk cells in the optimal plane, using the original definition (Oliver and Morest, 1984; Oliver et al., 1991), was no more than 70 μm, but some of our laminar cells clearly had a dendritic width that was almost double this. In their study of the rat IC Malmierca et al. (1993) defined flat cells based on complex criteria and stated that the mean width of their dendrites was 50 μm, while the mean width of the LF cells was 100 μm. However, the term disk cell is a useful descriptor and for this study we have extended the definition to include both the original "flat" and also "LF" laminar cells. We considered all the laminar cells in this study to be disk cells and divided them into flat and LF varieties. Two types of "disk-shaped" cells were also described in the squirrel monkey

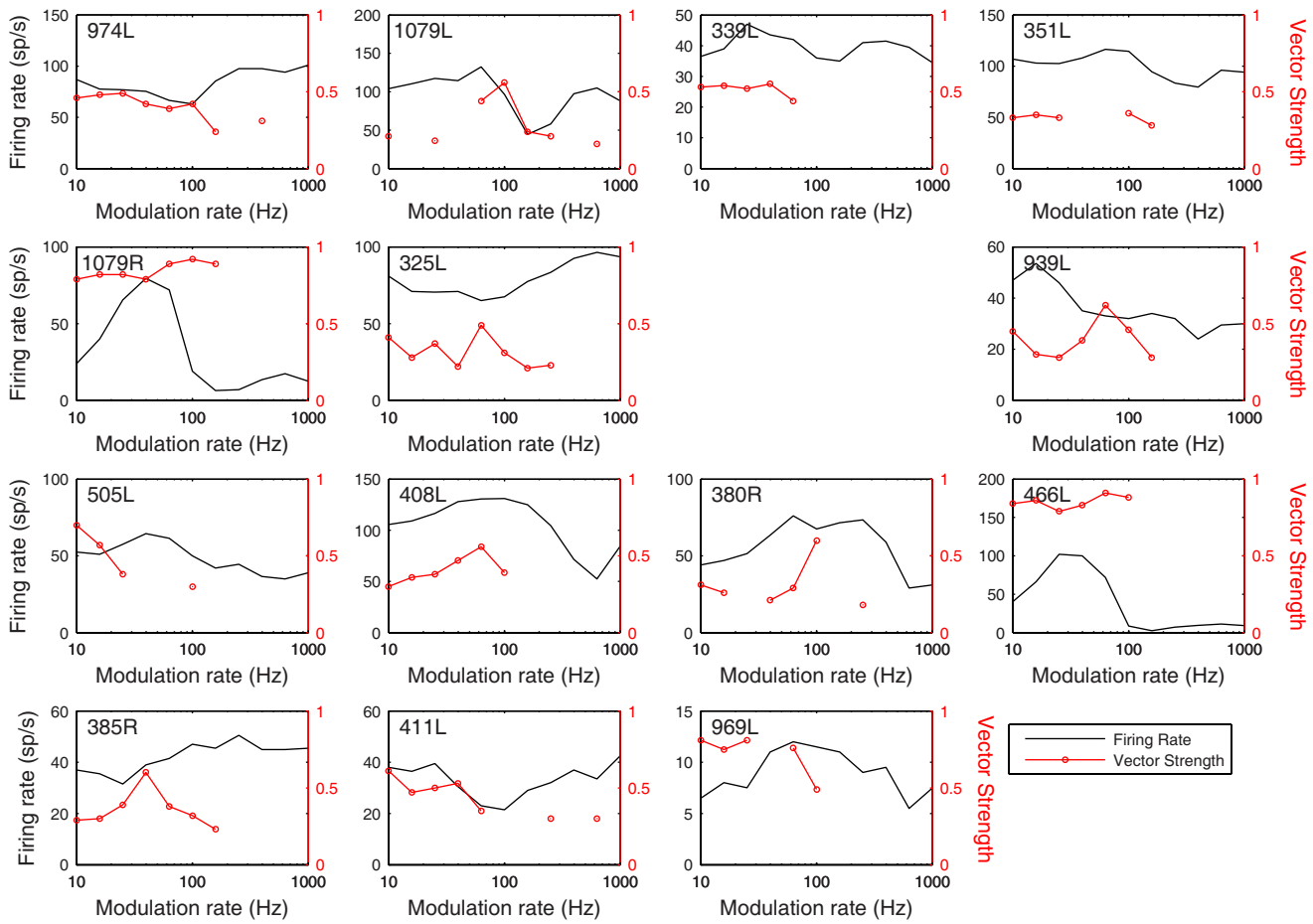

FIGURE 13 | Modulation transfer functions in response to 200 ms, 100% amplitude modulated CF tones arranged in the same order as previous figures. The black lines show the average discharge rate in response to the modulated stimuli. The red curves show the vector strength measured from period histograms locked to the modulation waveform.

by Fitzpatrick (1975), but she also described a type of stellate cell which appeared to be confined to a single lamina. When viewed in the horizontal plane some (4/15) of our disk cells had a clear stellate morphology with multiple dendrites radiating out from the soma. However, the majority were clearly polarized so that most of their dendrites were oriented in one direction. It might have been appropriate to call these fusiform or bitufted cells as has been done previously in the cat central nucleus (Rockel and Jones, 1973), but we chose instead the more neutral term of elongated.

Another feature that has been used in classifying cells in the IC has been the distribution and density of their spines (Gonzalez Hernandez et al., 1986). In the auditory cortex spiny stellate cells are exclusively excitatory, while smooth or sparsely spinous stellates are inhibitory and GABAergic (Wallace and He, 2011). However, it is not clear if there is a similar correlation in the IC. It would be very useful to be able to identify GABAergic neurons based on their morphology, but that does not seem to be possible currently and inhibitory cells have to be identified by the use of immunohistochemical identification of specific markers (Ito et al., 2009) or genetic alteration to link production of a fluorescent protein to that of the synthetic enzyme for GABA (Ono et al., 2005). A high proportion of cells in the IC are GABAergic (about 20% in the cat; Oliver et al., 1994) and a similar proportion may be present in the guinea pig (Thompson et al., 1985). There are at least two morphological types of GABAergic cells in the central nucleus with the larger ones projecting to the thalamus (Peruzzi et al., 1997; Ito et al., 2009), while the smaller ones may be intrinsic. Many of these GABAergic cells are stellate (Oliver et al., 1994), but up to half of them may be laminar cells. In one study of GABAergic cells in the mouse IC (Ono et al., 2005) 17 GABAergic cells in the central nucleus were filled with biocytin to demonstrate their dendrites. Four of these appeared to be laminar cells and some of the laminar cells in our sample may also have been GABAergic. The most likely candidate was cell 1079R which was large, sparsely spinous, had an output axon that entered the brachium and was the only laminar cell to have an intrinsic axon that appeared to terminate in a different lamina. GABAergic laminar cells could provide a local inhibition of nearby cells with the same CF, of the sort that have been demonstrated in the guinea pig (Le Beau et al., 2001), since the axons are generally in the

Table 2 | Physiological characteristics of the 15 filled cells.

Cell no.	CF kHz	RSP	Inhibitory sidebands		Histograms			Binaural response	ITD	ILD	Lat. ms
			Lower	Upper	Contra	Ipsi	Both				
974L	0.297	C	Strong	Strong	Low-sustained	Onset	Phase-locked	ee/F	Strong	Weak	12
1079L	0.669	V	Strong	Strong	Pauser	Pauser	Sustained	EE/s	Weak	Weak	16
339L	0.933	TU	Strong	Strong	Pauser	None	On-sustained	EO/F	Weak	Peak	15
351L	0.947	V	Weak	Weak	Spont.	Chop T	Chop T	EO/m	None	Moderate	15
1079R	0.983	V	Weak	Weak	Sustained+large offset	None	Sustained+large offset	eE/m	Weak	Weak	30
325L	0.991	V	None	None	Chop T	Inhibited	Chop T	EI/i		Strong	10
1071R	1.144	TD/C			Sustained	None	Sustained	EO/m	Strong		25
939L	1.377	V	Weak	Strong	Low-sustained	On-sustained	On-sustained	eE/i	None	Weak	13
505L	1.469	TU	Strong close	Strong	Pauser	None		EO/i		Strong	15
408L	2.193	V	Weak	Weak	On-sustained	Inhibited	Pauser	Ei/i		Weak	8
380R	2.332	TD	Strong	Strong	Pauser	Low-sustained	Pauser	eE/f		Weak	10
466L	3.303	V	Weak far	Strong	Offset	Sustained	Offset	Eo/m		None	58
385R	4.497	N	Strong close	Strong	Spont.	Pauser	Pauser	OE/m		Strong	14
411L	4.929	V	Strong far	Strong	Build-up	None	Build-up	EO/i		Strong	12
969L	5.119	V	Weak	Strong	Pauser	None	Pauser	EO/m		Weak	13

C, closed; V, v-shaped; TD, tilt down; TU, tilt up; N, narrow. Histograms were defined following Le Beau et al. (1996): sustained units fired throughout the stimulus; On-sustained had a clear onset response, but also fired throughout the stimulus; Low-sustained fired at low level throughout the stimulus (relative to other conditions for that cell); Pausers fired strongly at stimulus onset then paused before firing for the rest of the stimulus; Build-ups were like pausers but without the onset component; Chop T fired regularly at the beginning of the response, but became less regular throughout the stimulus; Inhibited showed a decline in firing below spontaneous; Spont fired at the same spontaneous rate throughout the stimulus; None did not fire before or during the stimulus. Binaural responses: three letters show response: contralateral, ipsilateral/binaural: e, weak excitation; E, strong excitation; O, no response; f, weak facilitation; F, strong facilitation; s, summation; i, weak inhibition; I, strong inhibition; m, monaural response only, no binaural interaction (Irvine, 1986).

same lamina as the dendrites. It is not known if the dendrites of all GABAergic neurons in the central nucleus are smooth/sparsely spinous, but there does not seem to be any evidence that they are spiny. In a double labeling study of the connections of GABAergic neurons in the rat IC many cells with commissural axons were labeled, but none of them appeared to have many spines (Zhang et al., 1998), even though some spiny neurons are known to have commissural axons (Gonzalez Hernandez et al., 1986). Two of our filled cells had numerous spines, some of which were present on the proximal dendrites and one of these had a commissural axon. Based on Zhang et al.'s (1998) data and its aspiny nature this would indicate that it was probably excitatory. Others clearly had a lower density of spines that were more restricted to the distal dendrites. Some cells had no discernable spines, but in some of these the dendrites were only relatively weakly stained and thus any spines would probably not have been stained.

SIGNIFICANCE OF THE INTRINSIC AXONS

One of the most striking features of the cells described here was that the intrinsic axons were restricted to a single lamina: in all but one case this was the same lamina as that containing the dendrites. The presence of dense bands of intrinsic axons that form a single lamina has already been shown by small extracellular injections of tracers in the rat (Saldana and Merchan, 1992) and guinea pig (Malmierca et al., 1995), but it was not clear what cell types produced them. A previous intracellular study of cells in the cat (Oliver et al., 1991) had shown some examples of cells with laminar dendrites and axons confined to the same lamina, but the present study is the first to show how extensively individual axons can ramify within a lamina. These intrinsic laminae have similar dimensions to the laminae formed by inputs from other brainstem nuclei such as the cochlear nucleus or nuclei of the lateral lemniscus (Malmierca et al., 2005; Loftus et al., 2010) and are 150–200 μm.

The lack of an identifiable projecting axon in many of the cells in our sample is interesting. Given that we were able to stain the intralaminar axonal plexus of many of these cells extending widely from the cell body into very small axon branches and further that we were able to identify projecting axons in some of our sample, it seems unlikely that we would not have stained a major output axon. Clearly, given the obvious complexity of the axonal trees we might simply have not recognized the projecting axon, or the stain might have faded before the axon exited the lamina. However, one intriguing possibility, in line with other anatomical considerations, is that many of the response types that have been identified could be from neurons intrinsic to the IC and not necessarily represent the information that is passing from the IC to the thalamus.

The high density of intrinsic axons (and presumed synaptic contacts) shown in the present study is reminiscent of the neocortex where even in the input layer IV the density of intrinsic synapses is thought to outnumber the thalamic synapses by almost 10 to 1 (Peters and Payne, 1993). Although we have only studied laminar

cells, the other types of cells in the central nucleus have also been shown to have extensive intrinsic axons (Oliver et al., 1991). As the IC is the largest subcortical auditory nucleus in the rat (Kulesza et al., 2002), and has almost five times as many auditory neurons as in the entire medulla and pons, the synapses derived from intrinsic axons are thought to greatly outnumber those from all other sources to the central nucleus (Saldana and Merchan, 2005). Given the large number of intrinsic synapses it is perhaps surprising how similar the responses of neurons in the central nucleus are to those of their brainstem inputs (McAlpine et al., 1998; Davis et al., 1999; Ramachandran et al., 1999). The extrinsic inputs create at least three functional zones in the central nucleus so that the low-frequency cells (<500 Hz) with a phase-locked response pattern and strong ITD sensitivity, such as cell 974L, almost certainly have their main extrinsic input from the ipsilateral medial superior olive (Loftus et al., 2010). When we measured the latency for the beginning of driven activity in our labeled cells it ranged from 8 to 30 ms (**Table 2**). This is much greater that the range of latencies typically seen among lower brainstem nuclei such as the cochlear nucleus (e.g., Palmer et al., 2003; Arnott et al., 2004) and leaves open the possibility that some IC neurons are partially or even mainly driven by intrinsic connections rather than by a direct extrinsic input alone. The significance of this is not clear, but it may make the individual cellular responses more consistent and reproducible because the form of the sustained response reflects an average of the local population rather than a more variable representation of its extrinsic inputs. The IC also receives a substantial input from the auditory thalamus and cortex, but these are thought to mainly terminate in the external nucleus and dorsal cortex (Winer, 2005).

CORRELATION OF MORPHOLOGY AND PHYSIOLOGICAL RESPONSES

A primary goal of the present study was to look for correlations between cellular morphology and physiological response properties, as has been successfully accomplished previously in the cochlear nucleus (Rhode et al., 1983a,b; Palmer et al., 2003; Arnott et al., 2004). Previous anatomical and physiological studies of the IC have revealed considerable diversity, but have generally summarized their findings in terms of a small number of identifiable classes whether of response type or morphology. Thus, in some studies only a few different frequency response areas have been recognized (e.g., Ramachandran et al., 1999; Davis, 2005), only two major morphological types have been recognized in another (Morest and Oliver, 1984), and only six response types have been described in brain slices (Peruzzi et al., 2000). Given these relatively small numbers it seemed entirely reasonable that one should be able to associate the physiological response profiles with the underlying morphological response types. Certainly, our understanding of the cochlear nucleus wiring pattern was enormously advanced by the pioneering studies correlating structure and function (Rhode et al., 1983a,b). However, early in our analysis it became clear that we, like many others, were seeing considerable diversity in both the physiological response profiles (see for example Irvine, 1986; Le Beau et al., 1996) and in the morphology: despite the fact that nearly all cells had a multipolar shape they clearly did not appear to fall into a small number of homogeneous groups.

Nevertheless, there are some possible correlations that might be drawn between the present data and the six classes of response shown in the slice preparation. A vast majority of the responses in the slice were sustained with pause or build-up temporal response patterns and such patterns are readily seen in the PSTHs in **Figure 12** (505L, 408L, 380R, 385R, 969L), where all of our sample had sustained responses of some kind. Other sustained cells in the slice had offset rebound responses or neither rebound nor build-up. We had two cells with very noticeable rebound PSTH patterns (1079R and 466L) and others with neither rebound nor build-up (1079L, 339L, 351L, 325L, 939L). The rebound cells in the slices were "flat, disk-shaped" cells and in our material we described the cells with rebound as medium sized, one with disk-shaped dendrites and the other quite similar, but with elongated shape. Both cells were wider than the criteria used by us and others to label a cell as "flat."

We have drawn attention to some correlations between small groups of cells with similar morphologies and similar physiological profiles; however, a major drawback in our study and others is that they are relatively under powered given the permutations of morphologies and responses. The use of brain slices from a knock-in mouse allows specific cell types to be targeted and the correlation of dendritic morphology with membrane properties (Ono et al., 2005), but even this approach is limited because it is not possible to trace the axonal output or the physiological inputs. Thus we are still in a position of having to painstakingly piece together an overall picture based on many studies each of which has a very limited set of data.

The IC is the site of termination of numerous projections from the brainstem (Brunso-Bechtold et al., 1981) and receives descending inputs from the cortex (Winer, 2005). It is considered to be a major site of reintegration of information processed at lower levels and some authors have even suggested that it is both the last level of analysis of the acoustical properties of sounds and also the level at which these are beginning to be formed into auditory objects (Nelken, 2008). The widespread ramification of the axons of the cells within the fibro-dendritic laminae detailed here and elsewhere provides a rich neuronal framework for such integration.

ACKNOWLEDGMENTS

We would like to thank Zoe Thompson for histological and Liang-fa Liu for general assistance on this project.

REFERENCES

Arnott, R. H., Wallace, M. N., Shackleton, T. M., and Palmer, A. R. (2004). Onset neurones in the anteroventral cochlear nucleus project to the dorsal cochlear nucleus. *J. Assoc. Res. Otolaryngol.* 5, 153–170.

Brunso-Bechtold, J. K., Thompson, G. C., and Masterton, R. B. (1981). HRP study of the organization of auditory afferents ascending to central nucleus of inferior colliculus in cat. *J. Comp. Neurol.* 197, 705–722.

Bullock, D. C., Palmer, A. R., and Rees, A. (1988). Compact and easy-to-use tungsten-in-glass microelectrode manufacturing workstation. *Med. Biol. Eng. Comput.* 26, 669–672.

Coomes, D. L., Schofield, R. M., and Schofield, B. R. (2005). Unilateral and bilateral projections from cortical cells to the inferior colliculus in guinea pigs. *Brain Res.* 1042, 62–72.

Coote, E. J., and Rees, A. (2008). The distribution of nitric oxide synthase in the inferior colliculus of guinea pig. *Neuroscience* 154, 218–225.

Davis, K. A. (2002). Evidence of a functionally segregated pathway from dorsal cochlear nucleus to inferior colliculus. *J. Neurophysiol.* 87, 1824–1835.

Davis, K. A. (2005). Spectral processing in the inferior colliculus. *Int. Rev. Neurobiol.* 70, 169–205.

Davis, K. A., Ramachandran, R., and May, B. J. (1999). Single-unit responses in the inferior colliculus of decerebrate cats. II. Sensitivity to interaural level differences. *J. Neurophysiol.* 82, 164–175.

Fitzpatrick, K. A. (1975). Cellular architecture and topographic organization of inferior colliculus of squirrel-monkey. *J. Comp. Neurol.* 164, 185–207.

Gonzalez Hernandez, T. H., Meyer, G., and Ferres-Torres, R. (1986). The commissural interconnections of the inferior colliculus in the albino mouse. *Brain Res.* 368, 268–276.

Ho, K. C., Gwozdz, J. T., Hause, L. L., and Antuono, P. G. (1992). Correlation of neuronal cell body size in motor cortex and hippocampus with body height, body-weight, and axonal length. *Int. J. Neurosci.* 65, 147–153.

Irvine, D. R. F. (1986). *The Auditory Brainstem*. Berlin: Springer-Verlag.

Ito, T., Bishop, D. C., and Oliver, D. L. (2009). Two classes of GABAergic neurons in the inferior colliculus. *J. Neurosci.* 29, 13860–13869.

Kulesza, R. J., Vinuela, A., Saldana, E., and Berrebi, A. S. (2002). Unbiased stereological estimates of neuron number in subcortical auditory nuclei of the rat. *Hear. Res.* 168, 12–24.

Le Beau, F. E. N., Malmierca, M. S., and Rees, A. (2001). Iontophoresis in vivo demonstrates a key role for GABA(A) and glycinergic inhibition in shaping frequency response areas in the inferior colliculus of guinea pig. *J. Neurosci.* 21, 7303–7312.

Le Beau, F. E. N., Rees, A., and Malmierca, M. S. (1996). Contribution of GABA- and glycine-mediated inhibition to the monaural temporal response properties of neurons in the inferior colliculus. *J. Neurophysiol.* 75, 902–919.

Loftus, W. C., Bishop, D. C., and Oliver, D. L. (2010). Differential patterns of inputs create functional zones in central nucleus of inferior colliculus. *J. Neurosci.* 30, 13396–13408.

Malmierca, M. S., Blackstad, T. W., Osen, K. K., Karagulle, T., and Molowny, R. L. (1993). The central nucleus of the inferior colliculus in rat – a Golgi and computer reconstruction study of neuronal and laminar structure. *J. Comp. Neurol.* 333, 1–27.

Malmierca, M. S., Rees, A., Le Beau, F. E., and Bjaalie, J. G. (1995). Laminar organization of frequency-defined local axons within and between the inferior colliculi of the guinea-pig. *J. Comp. Neurol.* 357, 124–144.

Malmierca, M. S., Saint Marie, R. L., Merchan, M. A., and Oliver, D. L. (2005). Laminar inputs from dorsal cochlear nucleus and ventral cochlear nucleus to the central nucleus of the inferior colliculus: two patterns of convergence. *Neuroscience* 136, 883–894.

McAlpine, D., Jiang, D., Shackleton, T. M., and Palmer, A. R. (1998). Convergent input from brainstem coincidence detectors onto delay-sensitive neurons in the inferior colliculus. *J. Neurosci.* 18, 6026–6039.

Morest, D. K. (1964). The laminar structure of the inferior colliculus of the cat. *Anat. Rec.* 148, 314.

Morest, D. K., and Oliver, D. L. (1984). The neuronal architecture of the inferior colliculus in the cat: defining the functional anatomy of the auditory midbrain. *J. Comp. Neurol.* 222, 209–236.

Nakamoto, K. T., Jones, S. J., and Palmer, A. R. (2008). Descending projections from auditory cortex modulate sensitivity in the midbrain to cues for spatial position. *J. Neurophysiol.* 99, 2347–2356.

Nakamoto, K. T., Shackleton, T. M., and Palmer, A. R. (2010). Responses in the inferior colliculus of the guinea pig to concurrent harmonic series and the effect of inactivation of descending controls. *J. Neurophysiol.* 103, 2050–2061.

Nelken, I. (2008). Processing of complex sounds in the auditory system. *Curr. Opin. Neurobiol.* 18, 413–417.

Oliver, D. L., Beckius, G. E., Bishop, D. C., and Kuwada, S. (1997). Simultaneous anterograde labeling of axonal layers from lateral superior olive and dorsal cochlear nucleus in the inferior colliculus of cat. *J. Comp. Neurol.* 382, 215–229.

Oliver, D. L., Kuwada, S., Yin, T. C. T., Haberly, L. B., and Henkel, C. K. (1991). Dendritic and axonal morphology of HRP-injected neurons in the inferior colliculus of the cat. *J. Comp. Neurol.* 303, 75–100.

Oliver, D. L., and Morest, D. K. (1984). The central nucleus of the inferior colliculus in the cat. *J. Comp. Neurol.* 222, 237–264.

Oliver, D. L., Winer, J. A., Beckius, G. E., and Saint Marie, R. L. (1994). Morphology of GABAergic neurons in the inferior colliculus of the cat. *J. Comp. Neurol.* 340, 27–42.

Ono, M., Yanagawa, Y., and Koyano, K. (2005). GABAergic neurons in inferior colliculus of the GAD67-GFP knock-in mouse: electrophysiological and morphological properties. *Neurosci. Res.* 51, 475–492.

Palmer, A. R., Hall, D. A., Sumner, C., Barrett, D. J., Jones, S., Nakamoto, K., and Moore, D. R. (2007). Some investigations into non-passive listening. *Hear. Res.* 229, 148–157.

Palmer, A. R., Wallace, M. N., Arnott, R. H., and Shackleton, T. M. (2003). Morphology of physiologically characterised ventral cochlear nucleus stellate cells. *Exp. Brain Res.* 153, 418–426.

Peruzzi, D., Bartlett, E., Smith, P. H., and Oliver, D. L. (1997). A monosynaptic GABAergic input from the inferior colliculus to the medial geniculate body in rat. *J. Neurosci.* 17, 3766–3777.

Peruzzi, D., Sivaramakrishnan, S., and Oliver, D. L. (2000). Identification of cell types in brain slices of the inferior colliculus. *Neuroscience* 101, 403–416.

Peters, A., and Payne, B. R. (1993). Numerical relationships between geniculocortical afferents and pyramidal cell modules in cat primary visual cortex. *Cereb. Cortex* 3, 69–78.

Pinault, D. (1996). A novel single-cell staining procedure performed in vivo under electrophysiological control: morpho-functional features of juxtacellularly labelled thalamic cells and other central neurons with biocytin or Neurobiotin. *J. Neurosci. Methods* 65, 113–136.

Ramachandran, R., Davis, K. A., and May, B. J. (1999). Single-unit responses in the inferior colliculus of decerebrate cats I. Classification based on frequency response maps. *J. Neurophysiol.* 82, 152–163.

Rapisarda, C., and Bacchelli, B. (1977). The brain of the guinea pig in stereotaxic coordinates. *Arch. Sci. Biol. (Bologna)* 61, 1–37.

Rhode, W. S., Oertel, D., and Smith, P. H. (1983a). Physiological response properties of cells labeled intracellularly with horseradish peroxidase in cat ventral cochlear nucleus. *J. Comp. Neurol.* 213, 448–463.

Rhode, W. S., Smith, P. H., and Oertel, D. (1983b). Physiological response properties of cells labeled intracellularly with horseradish peroxidase in cat dorsal cochlear nucleus. *J. Comp. Neurol.* 213, 426–447.

Rockel, A. J., and Jones, E. G. (1973). The neuronal organization of the inferior colliculus of the adult cat. I. The central nucleus. *J. Comp. Neurol.* 147, 11–60.

Saldana, E., and Merchan, M. A. (1992). Intrinsic and commissural connections of the rat inferior colliculus. *J. Comp. Neurol.* 319, 417–437.

Saldana, E., and Merchan, M. A. (2005). "Intrinsic and commissural connections of the inferior colliculus," in *The Inferior Colliculus*, eds J. A. Winer and C. E. Schreiner (New York: Springer), 155–181.

Thompson, G. C., Cortez, A. M., and Lam, D. M.-K. (1985). Localization of GABA immunoreactivity in the auditory brainstem of guinea pigs. *Brain Res.* 339, 119–122.

Wallace, M. N., and He, J. F. (2011). "Intrinsic connections of the auditory cortex," in *The Auditory Cortex*, eds J. A. Winer and C. E. Schreiner (New York: Springer), 133–147.

Winer, J. A. (2005). "Three systems of descending projections to the inferior colliculus," in *The Inferior Colliculus*, eds J. A. Winer and C. E. Schreiner (New York: Springer), 231–247.

Wu, Y., and Yan, J. (2007). Modulation of the receptive fields of midbrain neurons elicited by thalamic electrical stimulation through corticofugal feedback. *J. Neurosci.* 27, 10651–10658.

Zhang, D. X., Li, L., Kelly, J. B., and We, S. H. (1998). GABAergic projections from the lateral lemniscus to the inferior colliculus of the rat. *Hear. Res.* 117, 1–12.

Conflict of Interest Statement: The authors declare that the research was conducted in the absence of any commercial or financial relationships that could be construed as a potential conflict of interest.

Received: 01 June 2012; accepted: 30 July 2012; published online: 20 August 2012.
Citation: Wallace MN, Shackleton TM and Palmer AR (2012) Morphological and physiological characteristics of laminar cells in the central nucleus of the inferior colliculus. Front. Neural Circuits ***6****:55. doi: 10.3389/fncir.2012.00055*

frontiers in
NEURAL CIRCUITS

ORIGINAL RESEARCH ARTICLE
published: 27 September 2012
doi: 10.3389/fncir.2012.00062

Spectrotemporal sound preferences of neighboring inferior colliculus neurons: implications for local circuitry and processing

Chen Chen[1], Francisco C. Rodriguez[2,3], Heather L. Read[2,4] and Monty A. Escabí[1,2,4]*

[1] Department of Electrical and Computer Engineering, University of Connecticut, Storrs, CT, USA
[2] Department of Biomedical Engineering, University of Connecticut, Storrs, CT, USA
[3] Vicerrectoría Estudios de Postgrado, Universidad Don Bosco, San Salvador, El Salvador
[4] Department of Psychology, University of Connecticut, Storrs, CT, USA

Edited by:
Eric D. Young, Johns Hopkins University, USA

Reviewed by:
Hubert Lim, University of Minnesota, USA
Sean Slee, University of Washington, USA
Bertrand Delgutte, Massachusetts Eye and Ear Infirmary, USA

***Correspondence:**
Monty A. Escabí, Department of Electrical and Computer Engineering, University of Connecticut, 371 Fairfield Road, Unit 2157, Storrs, CT 06269-1157, USA.
e-mail: escabi@engr.uconn.edu

How do local circuits in the inferior colliculus (IC) process and transform spectral and temporal sound information? Using a four-tetrode array we examined the functional properties of the IC and metrics of its micro circuitry by recording neural activity from neighboring single neurons in the cat. Spectral and temporal response preferences were compared for neurons found on the same and adjacent tetrodes (ATs), as well as across distant recording sites. We found that neighboring neurons had similar preferences while neurons recorded across distant sites were less similar. Best frequency (BF) was the most correlated parameter between neighboring neurons and BF differences exhibited unique clustering at ∼0.3 octave intervals, indicative of the frequency band lamina. Other spectral and temporal parameters of the receptive fields were more similar for neighboring neurons than for those at distant sites and the receptive field similarity was larger for neurons with small differences in BF. Furthermore, correlated firing was stronger for neighboring neuron pairs and increased with proximity and decreasing BF difference. Thus, although response selectivities are quite diverse in the IC, spectral, and temporal preference within a local microcircuit are functionally quite similar. This suggests a scheme where local circuits are organized into zones that are specialized for processing distinct spectrotemporal cues.

Keywords: spectrotemporal receptive field, laminar organization, receptive field transformation, correlated activity

INTRODUCTION

Three organization principles for brainstem input to the central nucleus of inferior colliculus (ICC) are the basis of the "synaptic domain hypothesis" that predicts a division of ICC into synaptic and functional domains with unique sound processing capability (Oliver, 2000; Loftus et al., 2010). First, tonotopically organized inputs from the brainstem project onto banded anatomical lamina with spatially restricted dendritic arbors and common best frequency (BF), that in the cat can extend across a $\sim 3.5 \times 3.5\,mm^2$ area (Morest and Oliver, 1984; Oliver and Morest, 1984; Serviere et al., 1984; Malmierca et al., 1993; Brown et al., 1997; Schreiner and Langner, 1997). Second, there is considerable convergence of different brainstem nuclei as well as different neuronal cell types onto a given frequency lamina that could allow for genesis of novel sound response properties (Adams, 1979; Oliver, 2000; Malmierca et al., 2005; Loftus et al., 2010). Third, brainstem projections are not uniformly distributed throughout all frequency laminae or even within a single frequency lamina (Oliver, 2000; Malmierca et al., 2005; Cant and Benson, 2008). These three anatomic patterns of pathway input to the ICC suggest a division of ICC into domains that process distinct sound features.

Though there is considerable evidence for anatomic domains, there is some debate regarding the structure of response property domains within ICC and how to demonstrate them. Frequency selectivity for single neurons shifts in spatial register with anatomically defined frequency laminae within the ICC (Schreiner and Langner, 1997; Malmierca et al., 2008). These BF response domains that we will refer to as, "frequency-band laminae," can be resolved with micrometer precision along the dorso-ventral axis of ICC using single and multi-unit recording methodologies (Schreiner and Langner, 1997; Malmierca et al., 2008). Though it is clear that best frequencies are highly organized within and across laminae, how other response properties are locally organized within this laminar structure is less clear. Response property gradients for temporal modulations and spectral resolution have been shown to exist along the laminar dimension of the ICC (Schreiner and Langner, 1988; Ehret et al., 2003). Thus, it might be expected that neural response properties other than best frequencies should cluster within a local neighborhood so that neighboring neurons encode similar acoustic features. However, a recent study addressed this question and found that the tone-response properties of neighboring neurons were quite diverse (Seshagiri and Delgutte, 2007).

We examine how spectrotemporal response properties are organized and the degree of precisely correlated firing within a local ICC neighborhood. We used tetrode arrays to record and isolate neighboring single neurons and compared the spectrotemporal receptive preferences of each neuron pair. We demonstrate that neurons are highly organized within a local neighborhood where the receptive field similarities depend on both proximity and BF match. Furthermore, although correlated firing between neighboring neurons was generally low, it was more prevalent than expected by chance and the strength of correlated firing between neighboring neurons increased with local proximity. Thus, ICC is organized into distinct zones or neighborhoods with common spectrotemporal preferences that can effectively signal similar messages to the thalamus.

MATERIALS AND METHODS

EXPERIMENT PROCEDURE AND ACOUSTIC STIMULI

Animals were handled according to approved procedures by the University of Connecticut Animal Care and Use Committee and in accordance with National Institutes of Health and the American Veterinary Medical Association guidelines. Adult cats ($N = 7$) were initially anesthetized with a mixture of Ketamine (10 mg/Kg) and Acepromazine (0.28 mg/Kg I.M.) and were subsequently maintained in a surgical state with either sodium pentobarbital (30 mg/Kg, $N = 2$) or isoflurane gas mixture (3–4%, $N = 5$). The pinnae were retracted and the animal was placed in a stereotaxic assembly with hollow earbars. The Inferior Colliculus (IC) was exposed by removing the overlying cortical tissue and the bony tentorium. Following surgery, the animal was maintained in an areflexive state of by continuous infusion of Ketamine (2 mg/kg·h) and Diazepam (3 mg/kg·h), in a lactated ringers solution (4 mg/kg·h). Physiologic data (heart rate, temperature, breathing rate, and reflexes) was monitored to control the infusion rate. All neural recordings were performed over a period of 24–72 h.

Sounds were delivered in a sound-shielded chamber (IAC, Bronx, NY) via hollow ear-bars (Kopf Instruments, Tujunga, CA). The system was calibrated (flat spectrum between 200 Hz and 40 kHz, ±3 dB) with a Finite Impulse Response (FIR) inverse Filter (Implemented on a TDT® RX6 Multifunction Processor, Alchua, Fl). Sounds were delivered with a RME DIGI 9652 (Haimhausen, Germany) through dynamic speaker drivers (Beyer DT770). Dynamic Moving Ripple (DMR) sound was delivered dichotically in five experiments and monaurally to the contralateral ear in two experiments (Escabí and Schreiner, 2002). The DMR is a time-varying broadband sound (1–48 kHz; 96 kHz sampling rate; 100 spectral components/octave) that contains spectral (0–4 cycles/octave) and temporal (0–500 Hz) modulations that have been shown to efficiently activate ICC neurons and are prominent features in natural sounds (Rodriguez et al., 2010a). A 10-min sequence of the DMR was presented twice (Trial A and Trial B, 20 min in total) at fixed intensity (80 dB SPL, 65 dB spectrum level per 1/3 octave).

ELECTROPHYSIOLOGY

We used tetrode arrays (NeuroNexus Technologies, Ann Arbor, MI) to record neural activity from neighboring neurons in the ICC. The dorsal aspect of the exposed IC is shown from one experiment along with the penetration locations (white and red dots; **Figure 1A**). At each penetration location, a four-tetrode array was inserted (**Figure 1B**) and sound evoked neural activity was recorded. The tetrode array consists of four tetrodes (4×4 electrodes; two shanks with two tetrodes on each shank; impedance 1.5–3.5 MΩ at 1 kHz) with an inter-tetrode separation of 150 μm. This configuration is ideal for recording from neighboring neurons within and across adjacent frequency band laminae, which have a reported separation of ∼150 μm in the cat (Rockel and Jones, 1973; Oliver and Morest, 1984).

The probes were first positioned on the surface of the IC with the assistance of a stereotaxic frame (Kopf Instruments, Tujunga, CA) at an angle of ∼30° relative to the sagittal plane (∼ orthogonal to the laminar orientation) (Merzenich and Reid, 1974; Semple and Aitkin, 1979; Schreiner and Langner, 1997). Electrodes were inserted into the IC with a LSS 6000 Inchiworm (Burleigh EXFO; Vanier, Quebec). Efforts were made to sample different regions of ICC by moving the electrode along the mediolateral and rostral-caudal axis. **Figure 1A** shows a picture of the IC exposure from one of the experiments with the recording positions (white circles). At each penetration location we advanced the probe depth and recorded only from locations that followed a clear tonotopic gradient (Merzenich and Reid, 1974; Semple and Aitkin, 1979) and which exhibited well-isolated single units (sorted offline, see below). The probes were advanced until the end of the probe was reached (3 mm total length).

Neural responses were digitized and recorded with a RX5 Pentusa Base station (TDT®, Alchua, Fl) followed by offline analysis in MATLAB (Mathworks Inc., Natick, MA). The continuous neural traces were digitally band-pass filtered (300–5000 Hz) and the cross-channel covariance was computed across tetrode channels. Vectors consisting of the instantaneous channel voltages across the tetrode array that exceeded a hyperellipsoidal threshold of $f = 5$ (Rebrik et al., 1999) were used to detect candidate action potentials. This method takes into account across-channel correlations between the voltage waveforms of each channel and requires that the normalized voltage variance exceeds 25 units: $V^T C^{-1} V > f^2$, where V is the vector of voltages, C is the covariance matrix, and f is the normalized threshold level. Spike waveforms were aligned and sorted using peak voltage values and first principle components with an automated clustering software (KlustaKwik software) (Harris et al., 2000). Sorted units were classified as single units only if the waveform signal-to-noise ratio exceeded 3 (9.5 dB, SNR defined as the peak waveform amplitude normalized by the waveform standard deviation), the inter-spike intervals exceeded 1.2 ms for >99.5% of the spikes, and the distribution of peak waveform amplitudes was unimodal (Hartigan Dip test, $p < 0.05$). These sorting criteria yielded 410 well-isolated single units from 280 tetrode recordings (an average of 1.46 well-isolated units per tetrode). The normalized separation between sorted units was ascertained by computing the Mahalanobis distance between the waveforms of two clustered units:

$$D_{1-2} = \sqrt{\left(\overline{V}_1 - \overline{V}_2\right)^T C_{12}^{-1} \left(\overline{V}_1 - \overline{V}_2\right)},$$

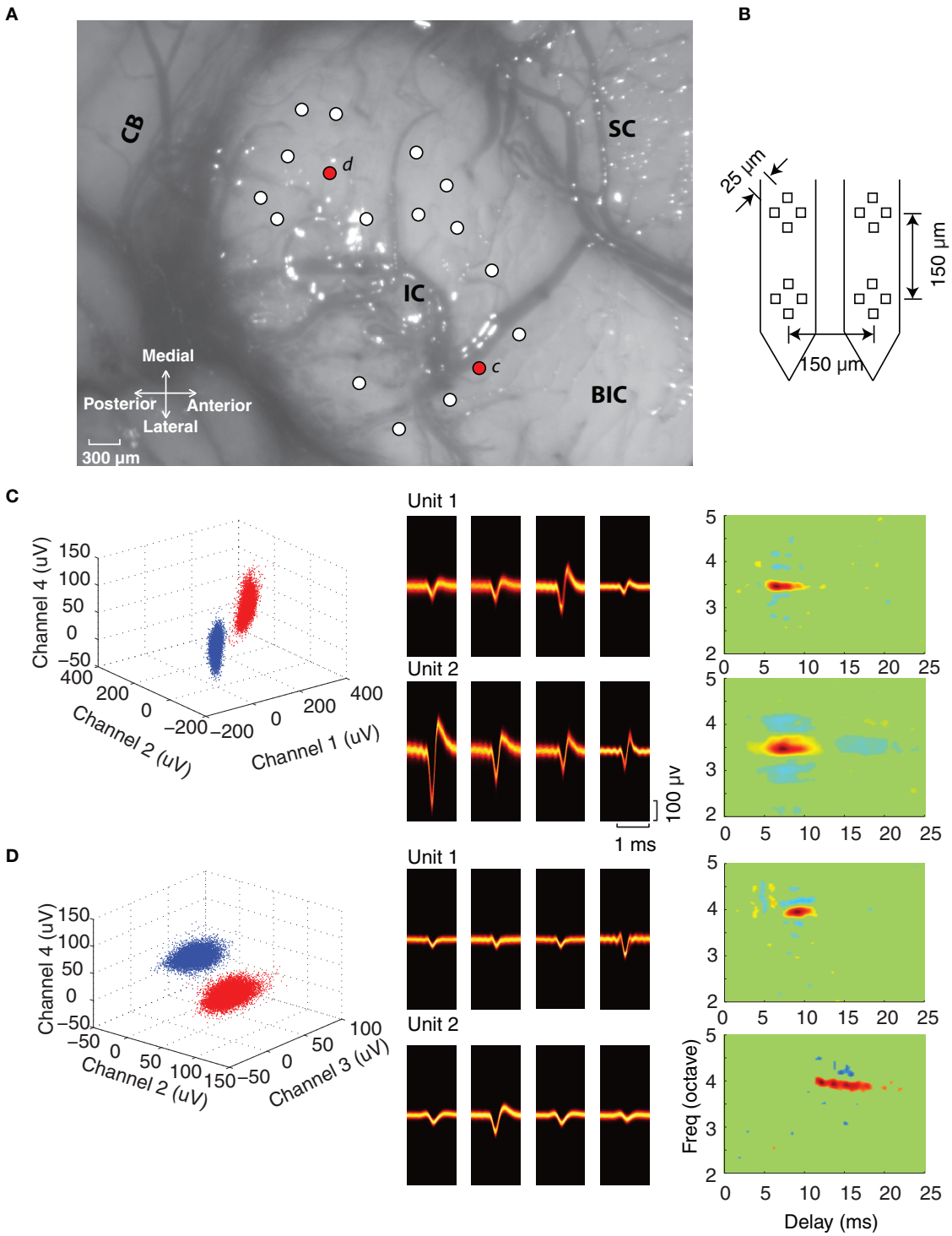

FIGURE 1 | Experiment configuration and single unit isolation. (A) The dorsal–lateral surface of the exposed IC in one experiment along with the surrounding neural structures (SC, superior colliculus; BIC, brachium of the inferior colliculus; CB, cerebellum). Electrode penetrations are marked by circles (white and red) and were orientated an angle of 30° relative to the sagittal plane (roughly orthogonal to the frequency-band lamina). **(B)** Four-tetrode array used for the neural recordings. **(C,D)** Single unit isolation in two tetrode recordings. Each site has two well-isolated units as noted by the peak waveform amplitudes clusters at selected tetrode channels (blue and red clusters, *left*). The spike waveform density plots (*middle*) on each of the tetrode channels are shown for each of the isolated units. The waveform density represents the probability that the action potentials recorded on a given channel follow a particular waveform trajectory (color represents probability; orange is high, black is low), thus highlighting the most likely waveform pattern for each channel. Spectrotemporal receptive fields (STRF) are shown for each of the isolated units on the far *right*.

where $\overline{V}_1$ and $\overline{V}_2$ are the average waveforms for cluster 1 and 2 and $C_{12} = (C_1 + C_2)/2$ is the average covariance matrix of the spike waveform clusters. This quantity is unitless and represents the average separation between two clusters after normalizing by the average cluster spread. Distances between isolated clusters ranged from 2.3 to 22.1 (mean = 7.3) with most pairs above 3 (97%).

The interpretation of the tetrode recordings as they relate to the micro-circuitry of the ICC is critically dependent on the spatial separation between the recorded units. Thus it is desirable to define bounds for the distance between neighboring neurons in order to allow us to make inferences about functional organization. The recording radius of the tetrode array was estimated using the procedure outlined by Mechler and colleagues (Mechler et al., 2011). Briefly, the recording radius is estimated as

$$R = -\Delta s \cdot C_T \cdot \log(n) / \log(A)$$

where $\Delta s = 28.5\,\mu$m is the average separation between the electrode contacts, $C_T = 0.57$ is a correction form factor that takes into account the geometry of the tetrode array (square geometry for the electrode contacts in our case), A is the contact-pair potential attenuation ratio (a number <1) which is defined as the average ratio of measured voltages across all contact pairs ($A = \langle V_i/V_j \rangle = 0.63$) arranged so that $V_i/V_j < 1$, and $n = V_{\max}/V_{\min} = 16.3$ is an approximation of the signal-to-noise ratio where $V_{\max}$ and $V_{\min}$ is the largest and the smallest observed action potential amplitudes, respectively. Using this approach we estimated a recording radius of 97 μm for our recordings.

SPECTRO-TEMPORAL ANALYSIS

Spectrotemporal receptive fields (STRFs) for the contralateral ear of identified ICC single neurons were obtained using spike-triggered averaging. Spectro-temporal parameters were obtained for each STRF according to procedure described previously (Rodriguez et al., 2010b). Briefly, we first determined the STRF power density by computing the STRF power at each time-frequency location, $p(t, x)$ where t is time and $x = \log_2(f/1000)$ is octave frequency (relative to 1000 Hz). The spectral and temporal power marginals were obtained by collapsing $p(t, x)$ along the temporal and spectral dimensions and normalizing for unit area, respectively. Latency and BF were defined as the peak of the temporal and spectral power marginals; integration time and bandwidth were defined as twice the SD of the temporal and spectral power marginals, respectively.

The spectral and temporal modulation parameters of each unit were obtained directly from the ripple transfer function (RTF) by performing a two-dimensional Fourier transform of the STRF and subsequently computing the transfer function magnitude. The characteristic temporal and spectral modulation frequencies (cTMF and cSMF, respectively) were derived by computing the centroids from the modulation power marginal of the RTF (Rodriguez et al., 2010b).

SAMPLE SELECTION AND STATISTICAL ANALYSIS

Following the single unit isolation and the receptive field calculations, neural data was checked for stability. Due to the sound delivery paradigm, which consists of two 10-min repeats of the DMR, it is possible that adaptation or changes in anesthetic state could bias the results. To assure that neural response sensitivities were stable across consecutive trials we required that the STRF similarity index between the two DMR trials exceeded 0.5 (Escabí and Schreiner, 2002). This resulted in a reduction of the sample size from 410 to 344 single units, but assured that the receptive fields were stable across trials (mean SI = 0.71 prior to pruning; mean SI = 0.83 after pruning), thus minimizing any potential biases that could occur from the recording stability. For verification, we performed all of the analysis before and after removal of unstable neurons and the resulting trends and findings of the study were the same.

The neural data was next partitioned into three experimental and two control groups in order to make comparisons between neighboring and distant neuron pairs. The experimental and control groups were selected on the basis of the recording proximity between neighboring neurons and their BF difference. The first experimental group consisted of all neuron pairs that were isolated on the same tetrode (ST). A second group was defined for pairs of neurons that were isolated concurrently on adjacent tetrodes (ATs) but within the same recording site. Based on the estimated recording radius of 100 μm and an inter-tetrode separation of 170 μm, ST pairs are limited to ∼200 μm separation while AT pairs are at most ∼370 μm apart. Although, there is no guarantee that individual ST pairs are actually closer than individual AT pairs, on average ST pairs are closer to one another since the effective volume sampled by a single tetrode is substantially smaller than the effective volume sampled by ATs. Due to the fact that the average distance between ATs is 170 μm and the recording radius of each tetrode is ∼100 μm, it is possible for two ATs to pick up the same unit at the same time. This was indeed the case for some AT pairs (14%) as evidenced by a strong single peak at the center bin of their spike train correlogram (i.e., at zero delay). For such sites, we kept the isolated unit with highest signal-to-noise ratio and discarded the accompanying unit from the AT. Finally, a third experimental group was defined to account for the fact that spectral and temporal response parameters such as bandwidth and latency are strongly correlated with the BF of neurons (Rodriguez et al., 2010b). Pairs from this third experimental group exist on the ST, but are chosen to be matched in BF (within 0.1 octave; same tetrode best frequency matched, STBF). Overall, the experimental groups consisted of 333 AT pairs, 93 ST pairs, and 54 STBF pairs.

Two control groups were defined as references for our statistical comparisons. As a null hypothesis, we require that spectrotemporal properties between neighboring neurons are uncorrelated and do not depend on proximity. The first control group was chosen by selecting neuron pairs from distant recording sites (DS group). Pairs from this control group were chosen at random from different recording sites and thus we expect that receptive field properties will be uncorrelated between selected pairs of neurons. A second control group was defined to account for the fact that certain spectral and temporal parameters are correlated with BF. For instance, latencies and bandwidth are both correlated with BF (Rodriguez et al., 2010b). Since, our intent is to identify response correlations that strictly depend on the

proximity, and neighboring neurons are expected to have similar BFs, such dependencies need to be accounted for. The distant site BF matched (DSBF) control group was defined by selecting DS pairs that were closely matched in frequency (within 0.1 octave). The DSBF control group is thus necessary to account for any residual correlation that arises because two neighboring neurons share a similar BF, irrespective of proximity. Overall, the control groups consisted of 22,178 distant recording site pairs (DS) and 1963 DSBF pairs.

Statistical analysis was carried out on each of the receptive field parameters by comparing the control and experimental groups. For each receptive field parameter (e.g., BW, latency, etc.), the correlation coefficient was computed as a measure of similarity between the receptive field parameter of the selected neuron pairs from each group. Significant differences between temporal and spectral response properties between groups were identified by performing a Fisher z-transform test on the correlation coefficient. Four comparisons were made to characterize the effects of receptive field similarity and the dependence with proximity and BF match. First, DS vs. AT and AT vs. ST groups were compared to determine whether proximity has an effect on receptive field similarity. Next, we determined whether BF match has an effect on the receptive field similarity by comparing the ST vs. STBF groups. Finally, we controlled for the fact that some of the correlation observed as a function of proximity might be due to BF dependence and so we compared the STBF vs. DSBF groups. All tests were performed at a chance level of 0.05 with Bonferroni correction to account for the number of comparisons.

SPIKE TRAIN CROSSCOVARIANCE

The shuffled crosscovariance (SCC) between the spike trains of single units was computed to evaluate the level of stimulus-driven response correlation (neuron 1 vs. neuron 2). The SCC between the spike trains of two neurons is defined as

$$\phi_{12}(\tau) = \frac{\phi_{1A,2B}(\tau) + \phi_{1B,2A}(\tau)}{2}$$

where 1 and 2 designates the neuron, A and B designates the stimulus trial. Here $\phi_{XY}(\tau) = \langle (r_X(t) - \lambda_X) \cdot (r_Y(t+\tau) - \lambda_Y) \rangle$ is the spike train crosscovariance (i.e., crosscorrelation with means removed), $r_X(t)$ and $r_Y(t)$ are the response spike trains (units of spikes/s) sampled at 4 kHz sampling rate (250 μs bin width), and λ_X and λ_Y represent the average spike rates over the entire sound duration. The trial shuffling is performed to isolate stimulus driven correlations. The SCC was normalized as

$$C_{12}(\tau) = \frac{\phi_{12}(\tau)}{\sqrt{\phi_{1A,1B}(0) \cdot \phi_{2A,2B}(0)}}$$

so that $-1 \leq C_{12}(\tau) \leq 1$. The spike train correlation index (CI) is defined as $C_{12} = \max[C_{12}(\tau)]$

Significance testing was performed by considering a random spike train with matched firing rate and interspike intervals as a null hypothesis. To do this, random spike trains were generated by shuffling the interspike intervals from the original spike trains from neuron 1 and 2. This procedure was repeated iteratively and the crosscovariance was computed for each iteration. The crosscovariance samples were used to estimate the mean and SE for the shuffled (null hypothesis) case. A *t*-test was then performed between the measured crosscovariance and the null hypothesis by requiring that the CI exceed chance level of $p < 0.001$ above (positive correlation) or below (negative correlation) the mean.

RECEPTIVE FIELD CROSSCOVARIANCE

A metric of receptive field similarity was defined to characterize the diversity of spectrotemporal features across the neural population. The receptive field crosscovariance (RFCC) function is first obtained by crosscorrelating the STRFs between two units (1 and 2) according to

$$\Phi_{1,2}(\tau, \chi) = \iint \mathrm{STRF}_1(t, x) \cdot \mathrm{STRF}_2(t+\tau, x+\chi)\, dtdx.$$

where τ and χ are temporal and spectral delays, respectively. The normalized RFCC is obtained as (Chen et al., 2012):

$$\overline{C}_{12}(\tau) = \frac{\Phi_{12}(\tau, 0)}{\sigma_1 \cdot \sigma_2}$$

where σ_1^2 and σ_2^2 correspond to the STRF power (i.e., $\sigma_k^2 = \iint \mathrm{STRF}_k(t, x)^2\, dtdx$). The RFCC corresponds to the normalized covariance between the predicted responses of two neurons under the assumption that each of the neurons behaves linearly. Thus the RFCC serves as a linear model prediction for the SCC. Values near one indicate that the receptive fields of the two units and, hence, the predicted spike rate patterns, are identical while values near zero indicate that the receptive fields and predicted spike trains are uncorrelated. Finally, it can be shown that the magnitude of the RFCC sets an upper bound on the magnitude of the spike train crosscovariance:

$$\left|\overline{C}_{12}(\tau)\right| \geq |C_{12}(\tau)|$$

where equality holds for the case of linear processing This upper bound strictly holds under the assumption that neural variability and non-linearities are independent between the two neurons tested. Although, this may not strictly hold, we've demonstrated that the upper bound holds for most neuron pairs tested in the ICC (Chen et al., 2012).

RESULTS

We used tetrode arrays to compare the spectrotemporal response properties of neighboring neurons in the ICC (**Figure 1B**). We asked whether neighboring ICC neurons have similar spectrotemporal preferences and how receptive field properties vary with BF and proximity within a local neighborhood. A concerted effort was made to thoroughly sample the rostral-caudal and medio-lateral dimensions of the ICC (as evident from **Figure 1A**) to assure that neurons with a diverse repertoire of spectral and temporal properties were included in the sample.

The effective size of the recording neighborhood for the tetrode array was estimated with the triangulation method of

Mechler et al. (2011) (see Materials and Methods). We assume that the measured action potential voltage decays as a power-law with distance from the source and that the rate of decay depends on the tetrode geometry, impedance and the electrical characteristics of the surrounding tissues. For our configuration, the tetrode electrodes are arranged in a square with an inter-electrode separation of 25 μm on the sides, so that the average separation between electrodes is 28.5 μm (after considering diagonals). Based on the observed maximum SNR (16.3) and the average inter-electrode attenuation ratio (0.63) we estimated a recording radius of 97 μm. Thus, neuron pairs that are isolated concurrently on a single tetrode are likely to be at most ∼200 μm apart. Neuron comparisons made between isolated neurons in ATs are at most ∼370 μm apart (170 μm average tetrode separation and 2 × 97 μm based on the recording radius).

At each recording location well-defined action potential clusters could be identified. As can be seen for the example recordings (**Figures 1C,D**; also **Figures 2A–F**), the waveform density plots for each isolated unit exhibits a consistent and unique pattern across each of the tetrode channels (middle panels). Furthermore, the peak amplitudes for selected tetrode channels form well-defined clusters (left, blue and red), which is indicative of well-isolated single units. Stringent criteria were applied to identify single units (see Materials and Methods) and in total we had 344 well-isolated single units from 123 recording sites, which resulted in 93 single unit pairs identified on a single tetrode (ST pairs) and 333 single unit pairs identified across ATs (AT pairs).

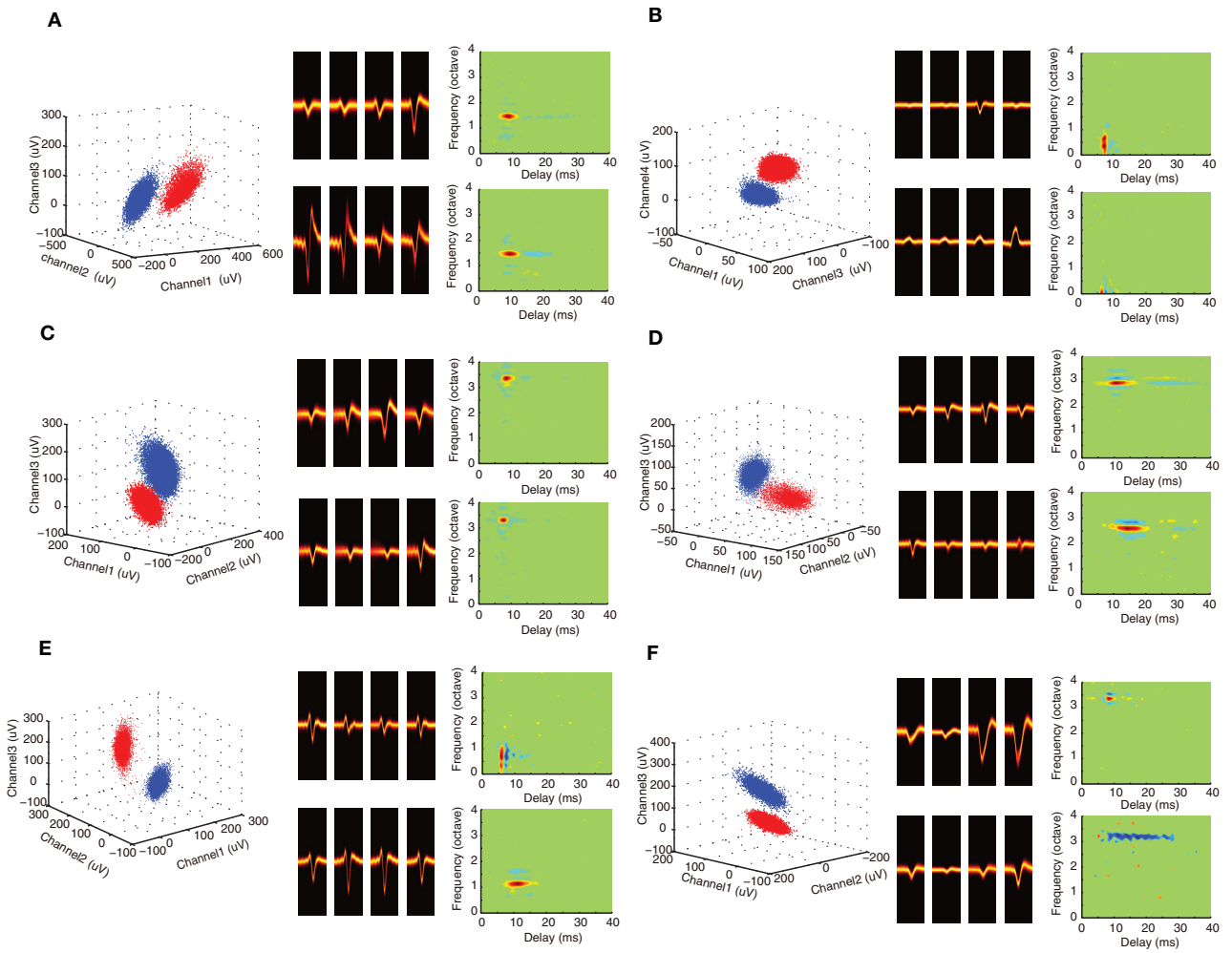

FIGURE 2 | Spectrotemporal selectivity of neighboring single neurons. **(A–F)** Example single unit waveforms and the corresponding STRFs are shown for neighboring neurons. All of the examples follow the same format as **Figures 1C,D**. For each unit, the waveform peak amplitude clusters are shown (*left*, selected tetrode channels) along with the spike waveform density plots for the isolated units (*middle*). STRFs are shown on the *right* two panels for each isolated single unit example. Red colors indicate that the sound tended to be on prior to the occurrence of an action potential (at 0 ms delay) and are thus indicative of excitation. Blue domains indicate that the sound tended to be off and are thus indicative of inhibition or suppression. Green colors indicate that the sound had no effect on the generation of action potentials. As can be seen from the examples, neighboring neurons can have similar STRFs indicative of similar spectral and temporal selectivity (e.g., **A–D**). By comparison, other sites have STRFs that can differ substantially along the temporal and/or spectral dimensions (e.g., **E–F**).

SPECTROTEMPORAL RESPONSE PROPERTIES OF NEIGHBORING NEURONS

DMR sound was delivered while recording neural responses from multiple single neurons. This dynamic stimulus contains spectral and temporal features such as temporal modulations, spectral peaks and notches that are common features in natural sounds and which efficiently drive ICC neurons (Escabí and Schreiner, 2002; Rodriguez et al., 2010a). The DMR is statistically unbiased and contains temporal modulations spanning 0–500 Hz and spectral modulations from 0 to 4 cycles/octave, which allows us to measure STRF of each neuron. The STRF is obtained as the average spectrotemporal envelope preceding all action potentials and it thus represents the spectrotemporal sound pattern that is most likely to evoke an action potential. Alternately, the STRF can be viewed as a spectrotemporal filter function that maps the sound to a neural response pattern. Positive regions in the STRF are thus indicative of excitation while negative regions indicate inhibition or suppression. As can be seen for example neuron pairs (**Figures 1C,D**; **Figures 2A–F**), the STRFs can be highly similar across neighboring neuron pairs (**Figures 2A–D**) or quite different (**Figures 2E–F**). For example, the neighboring neurons in **Figure 1C** have an overlapping excitatory region around 3.5 octave (all frequency measurements are performed relative to 1 kHz). Accordingly, these neurons have similar BFs (3.45 vs. 3.48 octave) and latency (6.5 vs. 7.2 ms). However, other spectral and temporal characteristics can be more varied across neighboring pairs such as the amount and strength of suppression/inhibition (blue STRF domains), which is quite different for these two units. Certain neighboring pairs have largely similar STRFs with similar BF, bandwidth and integration time (e.g., **Figures 2A–D**). However, at other recording sites, the receptive field structure between neighboring neurons can vary substantially (e.g., **Figure 1D**; **Figures 2E–F**). The neighbors shown in **Figure 2E** have similar BFs (0.71 vs. 1.17 octave), however, the latency (6.5 vs. 11.75 ms) and integration time (1.9 vs. 6.5 ms) of unit 2 are substantially longer. Furthermore, the general arrangement of excitation and inhibition are quite different for these neighboring units: unit 1 has an on–off temporal pattern while unit 2 exhibits strong lateral inhibition. For the pair in panel **F**, BFs are similar (3.3 vs. 3.2), however, unit 1 is fast and predominantly excitatory while unit 2 has a long-lasting and predominantly inhibitory structure (3.9 vs. 14.5 ms integration time). Thus for some recording sites the STRF of neighboring neurons can be quite similar while for other sites the receptive field structure can be more varied.

To characterize how much of the receptive field similarity between neighboring neurons is due to the proximity and BF match we grouped the data into five categories in the subsequent sections (see Materials and Methods). AT pairs are obtained from the same recording site but on different tetrodes while ST pairs consist of neurons isolated on the same tetrode. Distant site pairs (DS) serve as a reference control designed to account for the receptive field variability between ICC pairs that is expected by chance. Finally, the ST frequency matched group (STBF) and DS frequency matched control group (DSBF) were designed to control for the fact that certain receptive field parameters can depend strongly on BF (Joris and Yin, 1992; Rodriguez et al., 2010b) irrespective of proximity.

CLUSTERING OF BEST FREQUENCIES BETWEEN NEIGHBORING NEURONS

ST and AT neighboring neurons exhibited similar frequency selectivity and were generally closely matched in BF. The BF difference distribution is shown for AT and ST pairs (**Figure 3**). Although, BF difference could be as large as 3.3 and 4.1 octave for a small subset of ST and AT pairs (>2 octave for 3 and 8%; data not shown), respectively, most pairs were closely matched in BF. For both groups, BF differences were tightly clustered around 0 octave difference as can be seen by the mode near the origin in the distributions (**Figures 3A,B**). A large incidence of pairs had a BF difference <0.1 octave although the proportion of pairs where this was true was higher for the ST group (ST: 58%; AT = 36%). For ST pairs 80% fell within 0.32 octave whereas 80% of the AT pairs fell within 0.55 octaves of each other (**Figure 3C**). Furthermore, the average frequency difference for ST and AT groups was 0.28 and 0.48 octave, respectively. Thus, ST pairs are more closely matched in BF than AT pairs.

Evidence for the laminar organization was evident when we conditioned AT pairs according to the recording geometry. Given the four-pronged geometry of the tetrode array (**Figure 1B**) and the orientation of the electrode penetrations (∼30 relative to sagittal; ∼ orthogonal to the frequency band lamina), it is expected that AT pairs found on tetrodes oriented orthogonal to the frequency band lamina would differ more in BF than pairs recorded from tetrodes oriented along a lamina. As can be seen from the distribution of BF differences, orthogonal AT pairs (**Figure 3E**) exhibit a mode around 0.28 octave BF difference which is not present for the laminar AT pairs (**Figure 3B**). BF differences were bimodally distributed for orthogonal AT pairs (**Figure 3E**; Hartigan Dip test, $p < 0.05$) but not for laminar AT pairs (**Figure 3D**; Hartigan Dip test, $p = 0.33$, NS). This disparity is consistent with the idea that orthogonal AT pairs are more likely to sample neurons from neighboring frequency band lamina which have a reported frequency difference of ∼0.28 octave in the cat (Schreiner and Langner, 1997) and a spatial separation comparable to the AT separation (150 μm) (Rockel and Jones, 1973; Oliver and Morest, 1984).

SPECTRAL RESPONSE PREFERENCES ARE MORE SIMILAR FOR NEIGHBORING NEURONS THAN FOR THOSE AT DISTANT SITES

Spectral and temporal response properties have been shown to vary systematically within and across the frequency-band laminae in the ICC (Schreiner and Langner, 1988; Langner et al., 2002; Ehret et al., 2003; Rodriguez et al., 2010b; Baumann et al., 2011). This and anatomical data predict that response similarity would drop-off with distance between neuron pairs. We tested this prediction by measuring the similarity between spectral response properties for neighboring vs. distant pairs of neurons in each of our experimental (**Figure 4**; AT = gray; ST = black, and STBF = red) and control (**Figure 4**; DS = blue; DSBF = green) groups described above. Scatter plots for spectral STRF parameters of neighboring neurons are shown in **Figures 4A–D** and the resulting statistics for each of the experimental and control groups

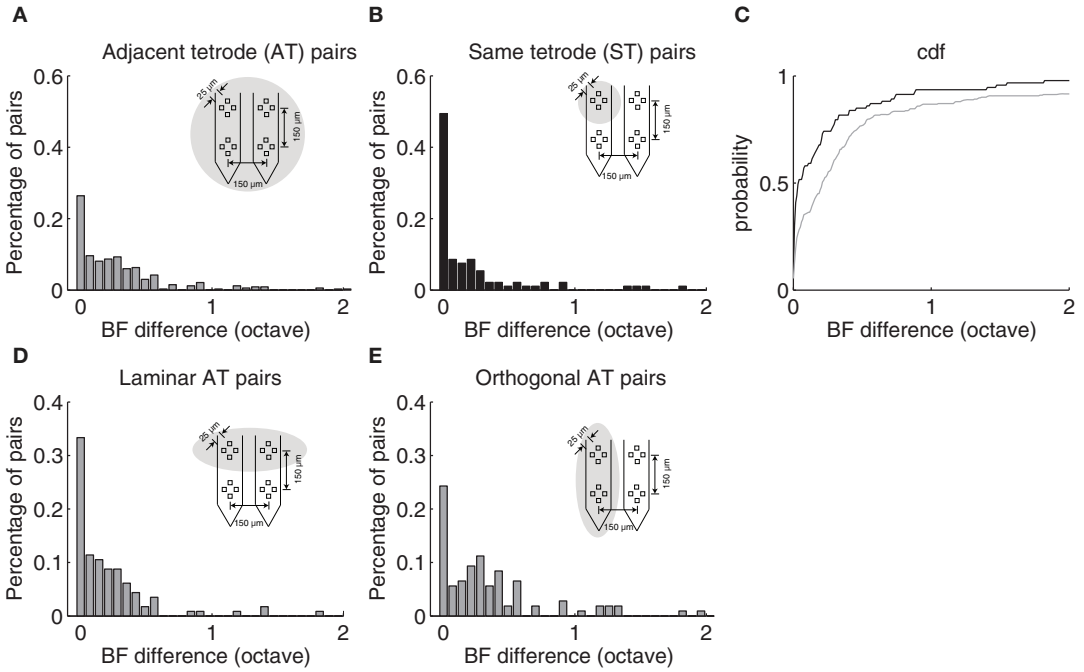

FIGURE 3 | Best frequency differences between neighboring neurons depend on proximity. (A) BF difference distribution for neuron pairs isolated on adjacent tetrodes (AT) with a separation of 150 µm as illustrated in **Figure 1B**. Eighty percent of AT pairs fall within 0.55 octave. **(B)** The distribution of BF differences for neuron pairs isolated on the same tetrode (ST) are largely confined to 0.32 octave (80%). **(C)** BF difference cumulative distribution function for same (*black*) and adjacent (*gray*) tetrode neuron pairs. **(D)** BF difference distribution for neuron pairs isolated on adjacent tetrodes that are along the ICC lamina orientation. **(E)** The distribution for neuron pairs isolated on adjacent tetrodes that are orthogonal to the lamina orientation. A significant mode is observed at ∼0.28 octave consistent with the average BF difference between adjacent laminae.

are shown in **Figures 4E–H**. As expected in the ICC, neuron pairs recorded on the ST had highly correlated BFs while those on ATs (more distant on average) were slightly less so (DS<AT<ST, $p < 0.001$; **Figures 4A,E**). Not surprisingly, randomly selected neuron pairs from different recording sites (DS group) were not correlated on average.

Spectral bandwidth varies systematically within and across the frequency-band laminae (Schreiner and Langner, 1988; Rodriguez et al., 2010b) leading us to test the prediction that bandwidth similarity would drop-off with distance. Spectral bandwidths (in octaves; **Figures 4B,F**) were more correlated for the AT group compared to DSs (**Figure 4F**; **Table 1**). This correlation systematically increased with proximity (DS vs. AT, $p < 0.01$) and BF match (ST vs. STBF, $p = 0.017$) and the resulting correlation is stronger than the BF matched control group (STBF vs. DSBF, $p = 0.002$, **Table 1**). This suggests that, on average, relative bandwidths are more similar between neighboring neurons than for DSs even when BF match is taken into account. We also measured the similarity for absolute bandwidths (in Hz; **Figures 4C,G**; **Table 1**) since relative and absolute bandwidths have distinct trends and organizations within the ICC: absolute bandwidths tend to increase while relative bandwidths tend to decrease with increasing BF (Rodriguez et al., 2010b). As for relative bandwidths, absolute bandwidths exhibit similar trends, however, the correlation for the DSBF control group was substantially higher likely reflecting the fact that absolute bandwidth are strongly correlated with BF. Despite this residual correlation, the ST frequency matched group (STBF) were more correlated on average (STBF vs. DSBF; **Figure 4G**, $p < 0.001$, **Table 1**) indicating that some of the correlation is strictly do to the proximity of neurons. Furthermore, absolute bandwidth correlation increased with decreasing distance (DS<AT<ST, $p < 0.001$).

We also tested whether selectivity for spectral modulations was similar for neighboring neurons. Spectral modulations are common features in natural sounds, consisting of peaks and valleys in the sound spectrum, such as for head related spatial cues (Kulkarni and Colburn, 1998) or formants in speech (Klein et al., 1970; van-Veen and Houtgast, 1985). Given that ICC neurons respond selectively to spectral modulations and their characteristic spectral modulation frequency (cSMF, see Materials and Methods) is inversely related to their BW (Qiu et al., 2003; Rodriguez et al., 2010b), we expect to see similar dependencies between BW and cSMF. As illustrated, there was an increase in the cSMF correlation with our metrics of proximity for pairs of neurons (i.e., DS<AT<ST, $p < 0.01$; **Figures 4D,H**; **Table 1**); though the trend was less pronounced than that associated with BW and BF match did not have a significant effect (**Figure 4H**, ST vs. STBF, $p = 0.31$). However, the correlation for STBF group is much higher than the DSBF ($p < 0.001$). This indicates that spectral modulation preferences are more similar among local neighboring neurons pairs even when BF match is accounted for.

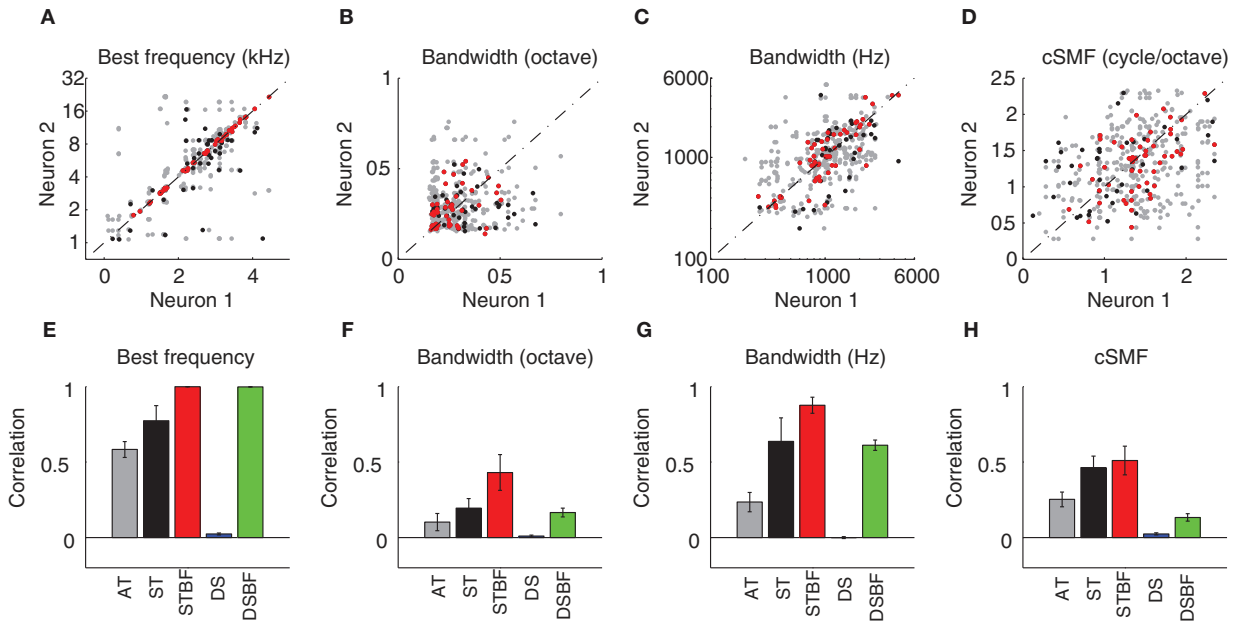

FIGURE 4 | Neighboring ICC neurons share similar spectral preferences. **(A–D)** Scatter plots showing the spectral STRF parameters (**A**, Best Frequency; **B**, Bandwidth in octave; **C**, Bandwidth in Hz; **D**, cSMF) of neighboring single units (neuron 1 and 2). For each of the STRF parameters the data was partitioned into three experimental groups that depend on the spatial proximity and BF match. The experimental groups consist of neuron pairs found on adjacent tetrodes (AT, *gray*; 150 μm tetrode separation), neuron pairs detected on the same tetrode (ST, *black*), and same tetrode pairs that were matched in best frequency (STBF, *red*; <0.1 octave BF difference). **(E–H)** The Pearson correlation coefficient was used to compare the similarity for each of the spectral parameters between neighboring neurons. The measured correlation is shown for each of the experimental groups (AT, ST, and STBF) as well as for two reference controls. The reference controls consist of pairs recorded from distant sites (DS, *blue*) or distant site pairs that where matched in frequency (DSBF; <0.1 octave BF difference). Statistics for the spectral parameter comparisons are provided in **Table 1**. The error bars in **E–H** represent the SE of the correlation coefficient.

Table 1 | Spectral receptive field similarity between neighboring neurons and their dependence on proximity and frequency match.

	DS vs. AT (*df* = 22,509)	AT vs. ST (*df* = 424)	ST vs. STBF (*df* = 145)	DSBF vs. STBF (*df* = 2015)
BW (octave)	$Z = 1.7$ $p = 0.009$	$Z = 0.80$ $p = 0.13$/N.S.	$Z = 1.5$ $p = 0.017$	$Z = 2.1$ $p = 0.002$
BW (Hz)	$Z = 4.3$ $p < 0.001$	$Z = 4.3$ $p < 0.001$	$Z = 3.5$ $p < 0.001$	$Z = 4.6$ $p < 0.001$
cSMF	$Z = 4.2$ $p < 0.001$	$Z = 2.0$ $p = 0.002$	$Z = 0.35$ $p = 0.31$/N.S.	$Z = 3.0$ $p < 0.001$

*Statistics are shown for the receptive field bandwidth (in octave and Hz) and the characteristic spectral modulation frequency (cSMF). The correlation coefficient between the parameters of neurons pairs was estimated for each of the experimental and control groups (data shown in **Figure 4**). Statistics for the comparisons between experimental (AT, ST, and STBF) and control groups (DS and DSBF). Comparisons of the correlation coefficient between groups were made at a chance level of 0.05 and were corrected for the number of comparisons (Bonferroni correction). Non-significant comparisons are noted by N.S.*

TEMPORAL RESPONSE PREFERENCES ARE MORE SIMILAR FOR NEIGHBORING NEURONS THAN FOR THOSE AT DISTANT SITES

Temporal response properties in the ICC vary systematically with position within and across the frequency-band laminae (Schreiner and Langner, 1988; Langner et al., 2002; Middlebrooks and Snyder, 2010; Rodriguez et al., 2010b). Once again, this response organization leads us to hypothesize a drop off in the similarity of temporal response properties between neuron pairs with distance. The first temporal response property we considered, STRF latency, was the most correlated temporal parameter between neighboring neurons (**Figures 5A,D**). STRF latencies were quite varied across our sample and confined mostly between 5 and 15 ms. Correlations for neighboring pairs in a recording site were significantly higher than those from distant recording sites (DS vs. AT, $p < 0.001$, **Table 2**) regardless of whether the pairs had matched BF or not (DSBF vs. STBF, $p < 0.001$, **Table 2**). However, within the radius of the tetrode array there was not a significant relationship between the latencies of neighboring neurons as a function of proximity or BF match (AT vs. ST; ST vs. STBF, **Table 2**, N.S.).

A similar trend was observed for the STRF integration time (IT; **Figures 5B,E**; **Table 2**). The IT represents the time window over which the sound history has a significant effect on the neuron's response (Chen et al., 2012). For most neurons, ITs were confined between 2 and 10 ms implying that temporal features in the DMR of at most 10 ms duration had a direct effect on the neuron's response. Within a local neighborhood, ITs were more similar than for DSs (AT, ST vs. DS, $p < 0.001$; **Figures 5B,E**, **Table 2**), even when BF match is taken into account (STBF vs. DSBF, $p = 0.005$). However, a significant trend was not observed

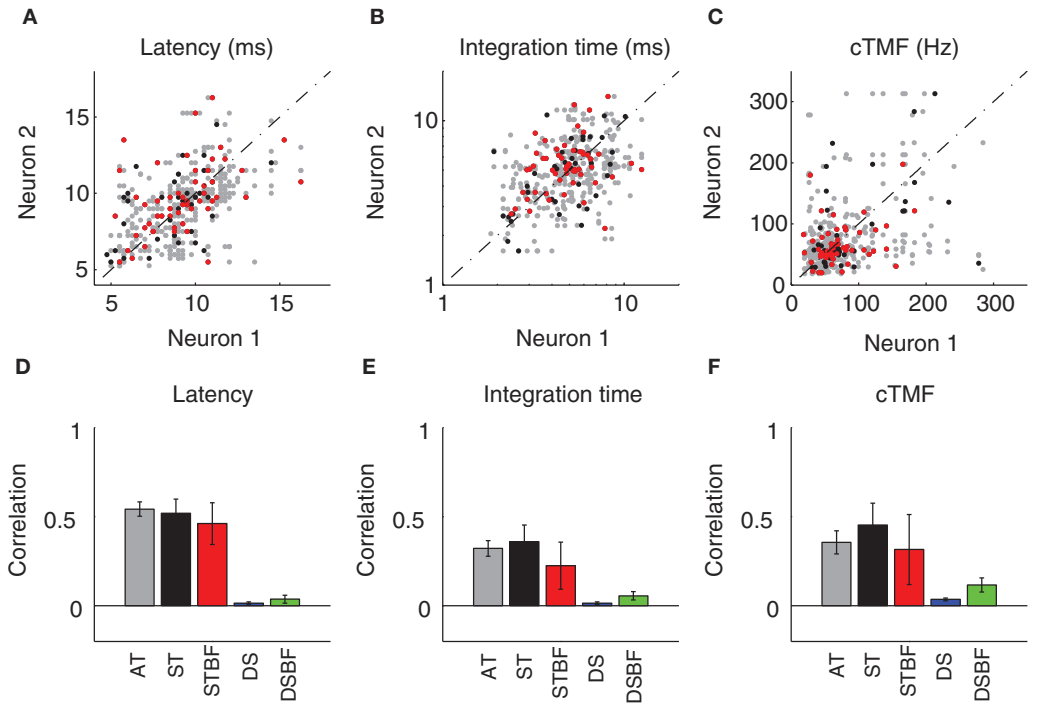

FIGURE 5 | Neighboring ICC neurons share similar temporal preferences. **(A–D)** Scatter plots showing the temporal STRF parameters (**A**, Latency; **B**, Duration; **C**, cTMF) of neighboring single units (neuron 1 and 2). The data was partitioned into three experimental groups as in **Figure 4** (AT, *gray*; ST, *black*; STBF, *red*). The Pearson correlation coefficient was used to compare the similarity for each of the temporal parameters between neighboring neurons. The correlation coefficient is shown for each of the experimental groups as well as for two reference controls (DS, *blue*; DSBF, *green*). Statistics for the temporal parameter comparisons are provided in **Table 2**. The error bars in **D–F** represent the bootstrapped SE of the correlation coefficient.

Table 2 | Temporal receptive field similarity between neighboring neurons and their dependence on proximity and frequency match.

	DS vs. AT (*df* = 22,509)	AT vs. ST (*df* = 424)	ST vs. STBF (*df* = 145)	DSBF vs. STBF (*df* = 2015)
Latency	$Z = 10.7$	$Z = -0.27$	$Z = -0.44$	$Z = 3.3$
	$p < 0.001$	$p = 0.35$/N.S.	$p = 0.27$/N.S.	$p < 0.001$
IT	$Z = 7.1$	$Z = 0.53$	$Z = -0.92$	$Z = 1.8$
	$p < 0.001$	$p = 0.23$/N.S.	$p = 0.10$/N.S.	$p = 0.005$
cTMF	$Z = 6.1$	$Z = 0.98$	$Z = -0.92$	$Z = 1.5$
	$p < 0.001$	$p = 0.08$/N.S.	$p = 0.09$/N.S.	$p = 0.018$/N.S.

*Statistics are shown for the receptive field latency (ms), integration time (ms), and the characteristic temporal modulation frequency (cTMF). Tests for significant differences of the parameter correlation coefficients (**Figure 5**) were performed and are reported between the experimental (AT, ST, and STBF) and control groups (DS and DSBF). All comparisons were made at a chance level of 0.05 and were corrected for the number of comparisons (Bonferroni correction). Non-significant comparisons are noted by N.S.*

with increasing proximity and BF match (AT vs. ST; ST vs. STBF, **Table 2**, N.S.), indicating that the IT similarity amongst neighboring neuron does not vary substantially within a local neighborhood.

Temporal modulation preferences are also organized systematically within and across the frequency-band laminae (Schreiner and Langner, 1988; Rodriguez et al., 2010b). Here, the relationship between temporal modulation preferences and proximity was determined by computing the characteristic temporal modulation frequency (cTMF) of each neuron (see Materials and Methods). As for the other temporal STRF parameters, cTMFs were more similar between neighboring neurons compared to DSs (AT vs. DS, $p < 0.001$; **Figures 5C,F**, **Table 2**). cTMFs have also been shown to vary with BF (Rodriguez et al., 2010b), however, even when BF dependence is taken into account neighboring neurons were still more similar than distant and BF matched sites (STBF vs. DSBF, $p = 0.018$; **Figures 5C,F**, **Table 2**). However, unlike spectral modulation sensitivity where neighboring neurons were more similar as a function of local proximity and BF match in a local neighborhood, we did not observe such effects for cTMFs (AT vs. ST; ST vs. STBF, N.S.; **Figures 5C,F**, **Table 2**).

RECEPTIVE FIELD AND SPIKE TRAIN CORRELATION OF NEIGHBORING NEURONS

The results from the previous analysis demonstrated that spectral and temporal receptive field characteristics are relatively more similar within a local neighborhood. One may thus be led to believe that the transmitted signals to the auditory thalamus from neighboring neurons would be highly correlated, which could indicate a form of redundant information transfer. However, the analysis employed in the previous section strictly examines the preferred sensory features of neighboring neurons and tells us

little about the temporal response pattern for each particular feature. For instance, two neurons may respond to similar sound features on average (as noted by their STRFs). However, the same average STRF can be obtained by summing different (even non-overlapping) subsets of elements so that the individual features that evoke spikes for each neuron can be quite different from one action potential to the other (Escabi et al., 2005). Thus, the temporal patterning of the resulting spike trains to a sound for each neuron could be vastly different even when neurons have similar STRFs (Chen et al., 2012). Thus, it is theoretically possible that, although ICC neurons share similar preferences in a local neighborhood, their temporal responses are uncorrelated so that each neuron conveys independent sensory information to the thalamus.

To examine how sound information is represented by ICC neuron pairs we examined how the receptive field of neighboring neurons contributes to correlated activity. As a measure of receptive field similarity we estimated the RFCC (RFCC; see Materials and Methods) between pairs of neighboring (**Figure 6**; **A** = ST; **B** = AT) and distant neurons (**C** = DSBF; **D** = DS). Example STRFs are show for four pairs of neurons (**Figure 6**) along with the resulting RFCC for each pair. The RFCC represents the stimulus driven correlations that are shaped by the spectral and temporal integration properties of each neuron. Neighboring neurons pairs with similar STRFs have a strong localized peak in the RFCC about zero frequency shift (**Figures 6A,B**; 3rd panel), indicating a high degree of spectral and temporal receptive field alignment. In contrast, the RFCC for a distant pair with frequency

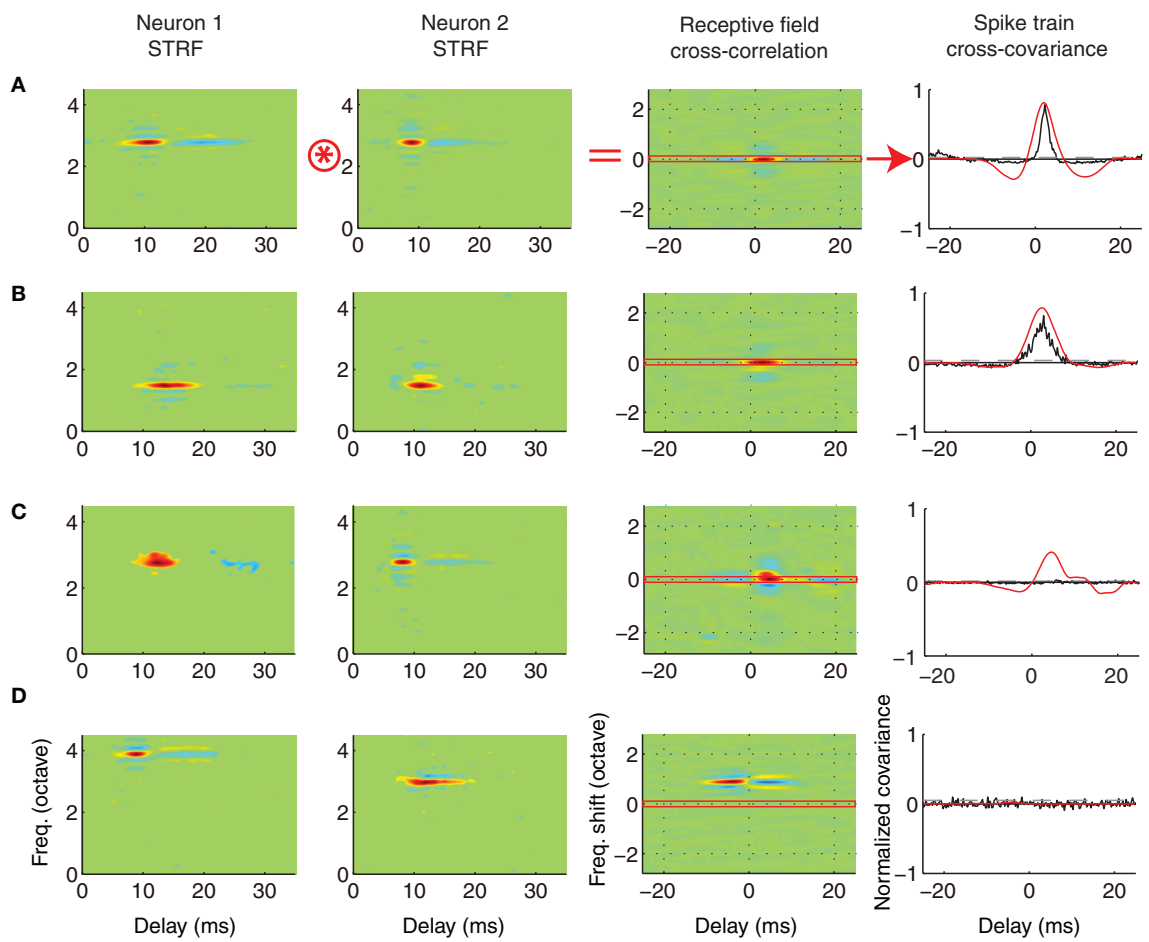

FIGURE 6 | Relationship between the receptive field and spike train crosscovariance of neighboring and distant neurons. The STRFs of four example neuron pairs are shown (**A–D**, *columns 1 and 2*). The examples were chosen from the experimental (**A**, ST; **B**, AT) and control groups (**C**, DS; **D**, DSBF). For each pair, we computed the spike train crosscovariance function (SCC, normalized between -1 and 1, see Materials and Methods) to determine the strength and timing of the temporal correlations between the spike trains of neighboring neurons (*column* 4, *black*). We used the STRFs for each pair to predict the SCC. For each pair of neurons, this is done by performing a two-dimensional cross-correlation between the STRF of each neuron (*column* 3) and subsequently selecting the temporal cross-section about zero frequency shift (red horizontal section, in *column* 3; see Materials and Methods). For instance, the example neuron pairs of **A** and **B** have STRFs with similar structure and thus the RFCC shows a strong positive peak about zero frequency shift. The predicted spike train covariance mirrors the SCC for each pair (column 4, *red*). In **C**, the neurons are highly overlapped in frequency, however, STRFs fail to predict the lack of correlation observed between the neural spike trains. The pair shown in **D** has receptive fields that are temporally delayed (neuron 1 leads neuron 2) and which differ in frequency by 1 octave. Because of the lack of frequency overlap the predicted (*red*) and measured SCC (*black*) are both zero.

mismatched STRFs have a displaced peak at ∼1 octave frequency separation (**Figure 6D**, 3rd panel), indicative of their frequency mismatch.

For each of the neuron pairs we next measured the amount of correlated activity in their neural spike trains by computing the normalized shuffled spike train cross covariance (SCC) (**Figure 6**; right panel, black lines). The RFCC was then used to predict the SCC. This is done by selecting the RFCC cross-section about zero frequency shift (**Figure 6**, right panel, red lines). As illustrated, the SCC is smaller in magnitude than the prediction based on the RFCC (**Figures 6A,B**, right panel) or it can be completely absent, as for the BF matched distant pairs (**Figure 6C**). Thus the RFCC sets an upper bound on the SCC (Chen et al., 2012). Furthermore, when there are strong spike train correlations as for the neighboring pairs of **Figures 6A,B**, the RFCC faithfully predicts the timing of the SCC. If neighboring neurons had a linear stimulus-response relationship the SCC and the prediction based on the RFCC would be identical. The observed reduction in the correlation strength between the neuron's integration process (RFCC) and the output spike train (SCC) could theoretically reflect factors that are specific to each neuron, such as intrinsic response variability ("neural noise") or output non-linearities in the spike generating mechanisms (Chen et al., 2012).

We asked whether receptive field similarity between neuron pairs determine the amount of correlated neural activity in their spike trains and whether these factors depend on proximity and frequency match. Given that the receptive field parameters of neighboring neurons tend to be similar within a local neighborhood, we expect that the RFCC and SCC should follow similar trends. For each pair we computed the receptive field and spike train correlation index (CI, peak of the RFCC and SCC, respectively) and the results were analyzed as a function of proximity and frequency match (**Figure 7**, see **Table 3** for statistics). As can be seen, both the receptive field and spike train CI are larger for neighboring neurons compared to the distant control group (AT vs. DS, **Figures 7A,B**; **Table 3**). Both the receptive field and spike train CI increase with proximity (AT vs. ST, $p < 0.001$; **Figures 7A,B**; **Table 3**) and frequency match (ST vs. STBF, $p < 0.001$; **Figures 7A,B**; **Table 3**). Furthermore, these effects were not simply the result of frequency match between neighboring neurons since the receptive field and spike train CI of distant neurons with matched frequency was significantly lower than for frequency matched neighboring neurons (STBF vs. DSBF, $p < 0.001$; **Figures 7A,B**; **Table 3**).

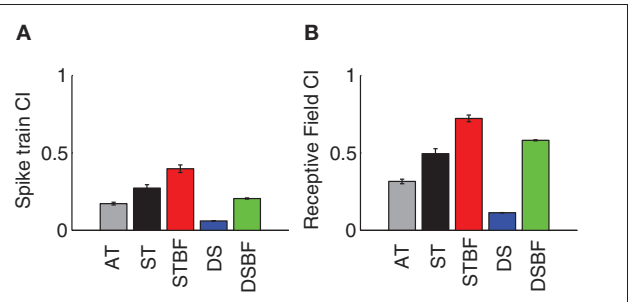

FIGURE 7 | Receptive field and spike train correlation statistics for neighboring ICC neurons. The average absolute spike train CI **(A)** and receptive field CI **(B)** both increases with proximity (AT, *gray* vs. ST, *black*) and BF match (ST, *black* vs. STBF, *red*). All examples are shown for three experimental groups (AT, *gray*; ST, *black*; STBF, *red*) and two control groups (DS, *blue*; DSBF, *green*). The error bars represent the bootstrapped SE.

Table 3 | Response and receptive field correlation between neighboring neurons and their dependence on proximity and frequency match.

	DS vs. AT (*df* = 22,509)	AT vs. ST (*df* = 424)	ST vs. STBF (*df* = 145)	DSBF vs. STBF (*df* = 2015)
RFCI	$T = 20.5$ $p < 0.001$	$T = 6.1$ $p < 0.001$	$T = 4.8$ $p =< 0.001$	$T = 6.6$ $p =< 0.001$
STCI	$T = 23.1$ $p < 0.001$	$T = 4.8$ $p < 0.001$	$T = 3.5$ $p =< 0.001$	$T = 7.8$ $p =< 0.001$

*Statistical comparisons are reported for the receptive field correlation (RFCI) and spike train correlation index (STCI). Test for significant differences were performed between the experimental (AT, ST, and STBF) and control groups (DS and DSBF; data shown in **Figure 7**). All comparisons were made at a chance level of 0.05 and were corrected for the number of comparisons (Bonferroni correction). Non-significant comparisons are noted by N.S.*

DISCUSSION

The synaptic domain hypothesis predicts the brainstem inputs to the ICC cluster into zones with common anatomic input and similar sounds preference (Oliver, 2000; Loftus et al., 2010). Here, we have demonstrated that neurons are highly localized into functional zones with similar spectrotemporal sensitivity, supporting the domain hypothesis organization within the ICC.

RELATIONSHIP BETWEEN MICRO AND GLOBAL ORGANIZATION

Spectral and temporal preferences of neighboring neurons were highly organized within the recording radius of the tetrode array; yet these organizations were subtly different for spectral and temporal preferences. For both spectral and temporal receptive field parameters, correlations between neighboring neurons were substantially larger than for DSs. This was true even when distant recording pairs were compared with matched BF suggesting that the observed correlations are not simply due to frequency dependence of response properties. Spectral properties were the most similar between neighboring neurons and the spectral receptive field similarity increased with proximity and BF match. This suggests that spectral properties are highly localized into zones within a recording radius of at most ∼100 μm. In contrast, no such effects were observed for the temporal receptive field parameters (**Figure 5**). Temporal preferences were similarly correlated for ST (100 μm radius) and AT (185 μm radius) comparisons. This implies that temporal preferences were relatively homogeneous over a larger recording radius implying that the size of the "neighborhood" is more extensive for temporal than for spectral response preferences.

Clustering for BF was observed for AT pairs oriented orthogonal to the anatomical laminar organization (**Figures 3D,E**)

consistent with the hypothesis that frequency organization is discretized within the ICC (Schreiner and Langner, 1997; Malmierca et al., 2008). However, no such clustering was observed for other spectral and temporal response properties (data not shown). All of the correlations for spectral and temporal parameters were not significantly different for orthogonal vs. laminar AT pairs (Fisher z-transform test, all comparisons NS). This supports the hypothesis that adjacent laminae perform similar functions and thus process similar acoustic cues.

Several organizational schemes could lead to the observed response patterns observed here. First, spectral and temporal response properties are topographically ordered within and across the ICC laminae. Temporal properties have been shown to have a gradient organization along the medial and lateral aspect of the IC (Schreiner and Langner, 1988; Langner et al., 2002) while spectral preferences seem to have a concentric organization within a lamina (Schreiner and Langner, 1988; Ehret et al., 2003). Spectral and temporal sensitivities also vary systematically along the dorsoventral extent and are thus highly correlated with the frequency organization (Rodriguez et al., 2010b). Regardless of whether the organization is patchy or continuous, our results support a scheme where local networks of neurons share a common organizing principle as inferred from the local similarities in the sound preferences.

BF DIFFERENCE AND LAMINAR ORGANIZATION

The measured BF differences from neighboring neurons are quantitatively consistent with previously reported frequency-band laminar organization, which is the primary organizing principle within the central nucleus. Adjacent laminae are reported to be ∼150 μm apart in the cat ICC (Rockel and Jones, 1973; Oliver and Morest, 1984) and have reported frequency separation of ∼0.28 octave (Schreiner and Langner, 1997).

Based on our estimated recording radius for ST pairs of 100 and 185 μm for AT pairs, and the measured BF differences we estimate that most of our recordings fall within the bounds of two or three adjacent laminae for ST and AT groups, respectively. The ratio of the estimated recording radius for ST vs. AT pairs is 100/185 = 0.54 is similar to the ratio of the average BF difference for the same groups, 0.28/0.48 = 0.58. Thus the spread of the measured BF distribution increases proportional to the recording radius. For ST comparisons, the estimated recording radius of 100 μm implies that neurons were at most 200 μm apart, which implies that neighboring neurons were either within the same lamina or one lamina apart. The average BF difference of 0.28 octave for ST comparisons fits with this expectation since it matches the average frequency separation between adjacent laminae in the cat (Schreiner and Langner, 1997). Furthermore, 80% of ST pairs fall within 0.32 octave which likewise supports the idea that most neurons are at most one lamina apart while 80% of AT pairs fall within 0.55 octave, which is consistent with the idea that pairs from this group could be up to two laminae apart. Finally, additional support for laminar organization is provided by the fact that BF differences for AT pairs oriented orthogonal to the laminar orientation exhibited a mode at 0.28 octave, comparable to the laminar separation, while AT pairs oriented along a lamina did not.

Although, the vast majority of neighboring neuron pairs were closely aligned in BF, consistent with the laminar separation, a small number of neuron pairs (6% of ST and 13% of AT pairs) were substantially more dispersed (i.e., more than 1 octave). Several factors could account for such large BF disparities. First, the estimated recording radius represents the average radius based on the statistical measurements from the recordings. For any given neuron, the recording radius actually depends on the strength of the source current, which scales proportional to the neuron size (Mechler et al., 2011). Within the ICC, disk shaped cells are the most prominent and have relatively small cell bodies with flattened dendrites that are confined to a single anatomical lamina while stellate cells are less prevalent but they have a substantially larger soma. Thus, it may be expected that disk shaped cells, which are the most abundant, will have a relatively small recording radius and BF differences between these neuron types will be relatively small as for most of our recordings. The recording radius of the more sparsely distributed stellate cells, however, should be substantially larger, which could explain the large BF disparities observed for a small number pairs. This possibility is supported by the fact that pairs with large BF differences (>1 octave) had highly similar temporal properties (delay: $r = 0.75 \pm 0.05$, $p < 0.001$; integration time: $r = 0.47 \pm 0.07$, $p < 0.001$; cTMF: $r = 0.55 \pm 0.1$, $p < 0.001$) but differed vastly in spectral properties (bandwidth: $r = -0.16 \pm 0.13$, N.S.; cSMF, $r = 0.25 \pm 0.1$, N.S.). Secondly, across-lamina integration (Biebel and Langner, 2002) could also potentially account for the large disparities observed. Stellate cells can have extensive collaterals that can cross and integrate across multiple frequency laminae (Oliver et al., 1991). Inputs from distant collaterals could thus potentially shift the BF of a neuron relative to that of its local neighbors.

RECEPTIVE FIELD CORRELATION AND CORRELATED FIRING: IMPLICATIONS FOR DOWNSTREAM SIGNALING

The structure of the sensory information relayed to the thalamus ultimately depends on the spike train output from ICC onto recipient thalamic neurons. The amount, strength, and type of correlated activity between converging ICC neurons can potentially enhance the fidelity of the transmitted message or alternately limit the amount of transmitted information due to a high degree of redundant firing.

Several functional rules were identified for the structure of correlated activity between neighboring ICC neurons. First, the receptive field and spike train correlation between neighboring neurons increases with proximity and BF match (**Figures 7A,B**) so that neighboring neurons have more similar receptive fields and more strongly correlated firing patterns compared to DSs. This supports the idea that neighboring neurons are organized into functional zones that preferentially respond to certain spectrotemporal features.

An intriguing aspect of these finding is the dependence of correlated firing on ∼1/3 octave spectral separation. Significant correlated firing is not found outside this range (Chen et al., 2012) and here we have shown a second dependence on the spatial separation of neighboring neurons. This contrasts with a previous study where correlated activity was pervasive within

the IC for sequentially recorded neurons that could differ vastly in their BF (Chechik et al., 2006). One factor that potentially contributes to this disparity is the fact that the natural sounds used in that study where synthetically shifted in frequency for some neurons to match their BF. Under such conditions neurons with different BFs would be driven with the same sound envelope even if the original natural sound envelopes for each neuron are uncorrelated. This could artificially increase the likelihood of observing correlated firing between neurons. Furthermore, the natural sounds used consisted of a limited subset of slow but transient bird vocalizations with highly restricted spectrotemporal variation. The sharp transients in those sounds presented against silence could potentially drive onset activity in the ICC (Zheng and Escabi, 2008), which could amplify the amount of correlation between neurons. This contrasts with the DMR, which extensively probes the modulation space and, in particular, extends to high modulation frequencies (up to 500 Hz) that IC neurons can selectively respond to. The biased sound repertoire in that study could likewise exacerbate the amount and strength of correlated activity.

Non-linearities in the spike generating mechanisms can impact the amount and strength of correlated activity between neurons. As seen for the data, the receptive field CI on average exceeded the spike train CI, implying that non-linearities may contribute to the low levels of spike train correlation between neurons. Intriguingly, for some neuron pairs spike train correlations are not present even though the receptive field correlations was strong (e.g., **Figure 6C**). Thus, two neurons can respond to similar sound patterns on average even if their spike times are temporally uncorrelated. This may seem surprising, but is consistent with our recent findings demonstrating that non-linearities in the spike generating mechanism can decorrelate neural spike trains between neurons that have similar BF and receptive field preferences (Chen et al., 2012). Thus, differences in the dynamics of the spike generation, intrinsic noise, and adaptive non-linearities can all potentially reduce the amount and strength of spike train correlation. As observed, the spike train CI of nearby neuron pairs with matched BF (STBF) was substantially larger than that of DSs with matched BF (DSBF). Thus, it is possible that neighboring neurons share similar types of non-linearities while more distant neurons have uniquely different non-linear response properties, which would ultimately reduce the strength of correlated activity between distant neurons.

Anesthesia and binaural interactions can also potentially impact the correlation strength. Anesthesia would have a tendency to reduce driven firing rates, which would in turn produce lower correlation values (de la Rocha et al., 2007). However, this is unlikely to affect the observed trends between neighboring and distant neurons. As demonstrated, the RFCC and SCC exhibited similar trends as a function of the proximity and BF match between neurons although the magnitude of the SCC was smaller (**Figures 7A,B**). This is consistent with the fact that RFCC serves as a upper bound for the SCC. Furthermore, we have previously demonstrated that the RFCC can predict various attributes of the SCC including the waveform shape and peak timing (Chen et al., 2012). This indicates that the resulting population trends largely reflect phase-locked stimulus driven correlations, as intended. Binaural interactions can also potentially affect the correlation between neurons since ipsilateral inputs to the ICC can have strong inhibitory influence (Oliver, 2000). Out of five experiments where we delivered sounds dichotically, only 17% of neurons exhibited significant ipsilateral STRFs and these where always weaker than the contralateral STRF. Thus, phase-locked activity originating in the ipsilateral ear is weak and likely contributed little to the SCC. This is consistent with the fact that RFCC derived from the contralateral ear STRF and SCC, which was obtained with sounds delivered dichotically, had similar trends. Furthermore, the general trends for the five experiments where we delivered sounds dichotically were the same for the remaining two experiments where we delivered sounds monaurally (data not shown). This implies that binaural interactions had little effect on the results.

There are several implications of the observed patterns of correlated activity within local IC populations. First, strongly correlated activity is potentially detrimental from a coding efficiency perspective because the neural messages relayed would be highly redundant (Barlow, 2001). However, correlated firing can be beneficial as it may allow for postsynaptic signal transmission via coincidence detection of weak synaptic inputs (Bruno and Sakmann, 2006). For instance, correlated firing between neighboring neurons in the retina has been shown to enhance information transmission in retinal ganglion cell populations (Pillow et al., 2008). Within the IC a fine balance in the amount of correlated firings seems to be achieved since most of the neural activity is uncorrelated except for a small subset of neurons pairs falling within ∼1/3 octave. Strikingly this spectral separation of ∼1/3 octave for correlated firing roughly corresponds to the anatomical laminar distance in cat (Schreiner and Langner, 1997) and mirrors the "critical band" which is the hallmark for perceptual resolution in humans and mammals (Fletcher, 1940; Yost and Shofner, 2009).

COMPARISON TO PREVIOUS STUDIES

A single previous study directly examined the response preferences between neighboring neurons in the IC of cats (Seshagiri and Delgutte, 2007). They found that neighboring single neurons recorded on a single tetrode had similar BF and bandwidths which is similar to our findings. However, many of the remaining response parameters measured in that study including the type of frequency response area and temporal response patterns were uncorrelated between neighboring neurons. This suggests that neighboring neurons are largely heterogenous within an ICC neighborhood, which contrasts our result.

One difference between the studies is that we observe substantially more correlation for temporal response properties based on our metrics. Seshagiri and Delgutte compared the type of PSTH (i.e., onset, sustained, chooper etc.) between adjacent neurons and found that the temporal response pattern to tone-burtsts (measured at CF) where randomly distributed. In our case, we performed detailed analysis by comparing temporal parameters of the STRFs and found significant correlations for all parameters measured (**Figures 5**, **7**). Furthermore, we found that the spike trains to the DMR are correlated between neighboring

neurons and these correlations increased with proximity indicating that the firing pattern of neighboring neurons are similar. Seshagiri and Delgutte also compared the patterns of excitation and inhibition in the frequency response maps of neighboring neurons using the classifications of Ramachandran et al. (1999) and found these to be randomly distributed throught the IC. Although, we did not categorize neurns into specific types based on excitation and inhibition, we note that cSMF and cTMF measurements depend strongly on spectral and temporal inhibitory patterns (Rodriguez et al., 2010b) and both of these parameters where significantly correlated. Finally, Seshagiri and Delgutte did not observe clustering of BF differences whereas we observed clustering for AT recordings (**Figure 3**).

The simplest explanation for the differences between these studies is that they are due to differences in the tetrode recording configuration. Based on our (100 μm) and their reported estimates (125 μm) of the recording radius this is unlikely a factor. One possible explanation is that the spectro-temporal parameters we tested are more in line with the organizing principles of the IC. In particular, all of the metrics employed here are based on phase-locked neural responses to the stimulus envelope while most of the measures reported in the earlier study are based on average firing rates. The types of stimuli employed are distinctly different between the two studies and likely contribute to the differences. The DMR sound employed here dynamically activates the entire sensory epithelium and, because of its broadband structure, concurrently activates excitatory and inhibitory circuits within and outside the IC. By comparison, Seshagiri and Delgutte measured pure-tone response properties that only activate a restricted portion of the sensory network and do not sample sound modulation preferences that have been shown to be organized within the IC. In particular, spectral and temporal resolution and modulation parameters similar to those employed here are systematically ordered within the ICC lamina as well as across the frequency dimension (Schreiner and Langner, 1988; Rodriguez et al., 2010b; Baumann et al., 2011).

Our extensive sampling across the rostral-caudal, mediolateral, and dorso-ventral dimensions may assure that there is sufficient variation in the response properties, which is necessary to observe correlations between neighboring neurons. In our case, electrode penetrations where oriented roughly orthogonal to the frequency lamina (∼30 relative to the sagittal axis) while Seshagiri and Delgutte employed a caudal-to-rostral trajectory where penetration tracks course roughly parallel to the ICC frequency band lamina. As a result, that study focused primarily on low frequency recording locations (mostly 0.5–2 kHz) while our study focus on higher frequencies (97% of neurons within 1–16 kHz), which likely contributes to some of the differences between the studies. Given our extensive sample we defined two controls (DS and DSBF) that set a reference point for defining a baseline level of receptive field and spike train correlation. This scheme enabled us to demonstrate that some of the correlation between neighboring neurons is due to BF match (irrespective of proximity) while the remaining correlation is accounted by the recording proximity (i.e., distant vs. neighboring sites). Finally, the four-tetrode configuration used in this study enabled us to compare neurons found on the ST vs. those found on AT. Using this scheme we demonstrate that even within the small recording radius of the tetrode array (∼185 μm for AT pairs; ∼100 μm for ST pairs) receptive field correlations can further increase with the local proximity of neurons indicating that neuron preferences cluster into relatively small neighborhoods with highly similar response preferences.

ACKNOWLEDGMENTS

This work was supported by the National Institutes of Deafness and Other Communication Disorders (DC006397) and a grant from the University of Connecticut Research Foundation. We would like to thank S. Kuwada and D. L. Oliver for reviewing the manuscript and providing thoughtful feedback. We also acknowledge the reviewers for the numerous valuable suggestions.

REFERENCES

Adams, J. C. (1979). Ascending projections to the inferior colliculus. *J. Comp. Neurol.* 183, 519–538.

Barlow, H. (2001). Redundancy reduction revisited. *Network* 12, 241–253.

Baumann, S., Griffiths, T. D., Sun, L., Petkov, C. I., Thiele, A., and Rees, A. (2011). Orthogonal representation of sound dimensions in the primate midbrain. *Nat. Neurosci.* 14, 423–425.

Biebel, U. W., and Langner, G. (2002). Evidence for interactions across frequency channels in the inferior colliculus of awake chinchilla. *Hear. Res.* 169, 151–168.

Brown, M., Webster, W. R., and Martin, R. L. (1997). The three-dimensional frequency organization of the inferior colliculus of the cat: a 2-deoxyglucose study. *Hear. Res.* 104, 57–72.

Bruno, R. M., and Sakmann, B. (2006). Cortex is driven by weak but synchronously active thalamocortical synapses. *Science* 312, 1622–1627.

Cant, N. B., and Benson, C. G. (2008). Organization of the inferior colliculus of the gerbil (*Meriones unguiculatus*): projections from the cochlear nucleus. *Neuroscience* 154, 206–217.

Chechik, G., Anderson, M. J., Bar-Yosef, O., Young, E. D., Tishby, N., and Nelken, I. (2006). Reduction of information redundancy in the ascending auditory pathway. *Neuron* 51, 359–368.

Chen, C., Read, H. L., and Escabi, M. A. (2012). Precise feature based time-scales and frequency decorrelation lead to a sparse auditory code. *J. Neurosci.* 32, 8454–8468.

de la Rocha, J., Doiron, B., Shea-Brown, E., Josic, K., and Reyes, A. (2007). Correlation between neural spike trains increases with firing rate. *Nature* 448, 802–806.

Ehret, G., Egorova, M., Hage, S. R., and Muller, B. A. (2003). Spatial map of frequency tuning-curve shapes in the mouse inferior colliculus. *Neuroreport* 14, 1365–1369.

Escabi, M. A., Nassiri, R., Miller, L. M., Schreiner, C. E., and Read, H. L. (2005). The contribution of spike threshold to acoustic feature selectivity, spike information content, and information throughput. *J. Neurosci.* 25, 9524–9534.

Escabí, M. A., and Schreiner, C. E. (2002). Nonlinear spectrotemporal sound analysis by neurons in the auditory midbrain. *J. Neurosci.* 22, 4114–4131.

Fletcher, H. (1940). Auditory patterns. *Rev. Mod. Phys.* 12, 47–65.

Harris, K. D., Henze, D. A., Csicsvari, J., Hirase, H., and Buzsaki, G. (2000). Accuracy of tetrode spike separation as determined by simultaneous intracellular and extracellular measurements. *J. Neurophysiol.* 84, 401–414.

Joris, P. X., and Yin, T. C. (1992). Responses to amplitude-modulated tones in the auditory nerve of the cat. *J. Acoust. Soc. Am.* 91, 215–232.

Klein, W., Plomp, R., and Pols, L. C. W. (1970). Vowel spectra, vowel spaces, and vowel identification. *J. Acoust. Soc. Am.* 48, 999–1009.

Kulkarni, A., and Colburn, H. S. (1998). Role of spectral detail in sound-source localization. *Nature* 396, 747–749.

Langner, G., Albert, M., and Briede, T. (2002). Temporal and spatial coding of periodicity information in the inferior colliculus of awake chinchilla (*Chinchilla laniger*). *Hear. Res.* 168, 110–130.

Loftus, W. C., Bishop, D. C., and Oliver, D. L. (2010). Differential patterns of inputs create functional zones in central nucleus of inferior colliculus. *J. Neurosci.* 30, 13396–13408.

Malmierca, M. S., Blackstad, T. W., Osen, K. K., Karagulle, T., and Molowny, R. L. (1993). The central nucleus of the inferior colliculus in rat: a Golgi and computer reconstruction study of neuronal and laminar structure. *J. Comp. Neurol.* 333, 1–27.

Malmierca, M. S., Izquierdo, M. A., Cristaudo, S., Hernandez, O., Perez-Gonzalez, D., Covey, E., and Oliver, D. L. (2008). A discontinuous tonotopic organization in the inferior colliculus of the rat. *J. Neurosci.* 28, 4767–4776.

Malmierca, M. S., Saint Marie, R. L., Merchan, M. A., and Oliver, D. L. (2005). Laminar inputs from dorsal cochlear nucleus and ventral cochlear nucleus to the central nucleus of the inferior colliculus: two patterns of convergence. *Neuroscience* 136, 883–894.

Mechler, F., Victor, J. D., Ohiorhenuan, I., Schmid, A. M., and Hu, Q. (2011). Three-dimensional localization of neurons in cortical tetrode recordings. *J. Neurophysiol.* 106, 828–848.

Merzenich, M. M., and Reid, M. D. (1974). Representation of the cochlea within the inferior colliculus of the cat. *Brain Res.* 77, 397–415.

Middlebrooks, J. C., and Snyder, R. L. (2010). Selective electrical stimulation of the auditory nerve activates a pathway specialized for high temporal acuity. *J. Neurosci.* 30, 1937–1946.

Morest, D. K., and Oliver, D. L. (1984). The neuronal architecture of the inferior colliculus in the cat: defining the functional anatomy of the auditory midbrain. *J. Comp. Neurol.* 222, 209–236.

Oliver, D. L. (2000). Ascending efferent projections of the superior olivary complex. *Microsc. Res. Tech.* 51, 355–363.

Oliver, D. L., Kuwada, S., Yin, T. C., Haberly, L. B., and Henkel, C. K. (1991). Dendritic and axonal morphology of HRP-injected neurons in the inferior colliculus of the cat. *J. Comp. Neurol.* 303, 75–100.

Oliver, D. L., and Morest, D. K. (1984). The central nucleus of the inferior colliculus in the cat. *J. Comp. Neurol.* 222, 237–264.

Pillow, J. W., Shlens, J., Paninski, L., Sher, A., Litke, A. M., Chichilnisky, E. J., and Simoncelli, E. P. (2008). Spatio-temporal correlations and visual signalling in a complete neuronal population. *Nature* 454, 995–999.

Qiu, A., Schreiner, C. E., and Escabi, M. A. (2003). Gabor analysis of auditory midbrain receptive fields: spectro-temporal and binaural composition. *J. Neurophysiol.* 90, 456–476.

Ramachandran, R., Davis, K. A., and May, B. J. (1999). Single-unit responses in the inferior colliculus of decerebrate cats. I. Classification based on frequency response maps. *J. Neurophysiol.* 82, 152–163.

Rebrik, S. P., Wright, B. D., Emondi, A. A., and Miller, K. D. (1999). Cross-channel correlations in tetrode recordings: implications for spike-sorting. *Neurocomputing* 26/27, 1033–1038.

Rockel, A. J., and Jones, E. G. (1973). The neuronal organization of the inferior colliculus of the adult cat. I. The central nucleus. *J. Comp. Neurol.* 147, 11–60.

Rodriguez, F. A., Chen, C., Read, H. L., and Escabi, M. A. (2010a). Neural modulation tuning characteristics scale to efficiently encode natural sound statistics. *J. Neurosci.* 30, 15969–15980.

Rodriguez, F. A., Read, H. L., and Escabi, M. A. (2010b). Spectral and temporal modulation tradeoff in the inferior colliculus. *J. Neurophysiol.* 103, 887–903.

Schreiner, C. E., and Langner, G. (1988). Periodicity coding in the inferior colliculus of the cat. II. Topographical organization. *J. Neurophysiol.* 60, 1823–1840.

Schreiner, C. E., and Langner, G. (1997). Laminar fine structure of frequency organization in auditory midbrain. *Nature* 388, 383–386.

Semple, M. N., and Aitkin, L. M. (1979). Representation of sound frequency and laterality by units in central nucleus of cat inferior colliculus. *J. Neurophysiol.* 42, 1626–1639.

Serviere, J., Webster, W. R., and Calford, M. B. (1984). Isofrequency labelling revealed by a combined [14C]-2-deoxyglucose, electrophysiological, and horseradish peroxidase study of the inferior colliculus of the cat. *J. Comp. Neurol.* 228, 463–477.

Seshagiri, C. V., and Delgutte, B. (2007). Response properties of neighboring neurons in the auditory midbrain for pure-tone stimulation: a tetrode study. *J. Neurophysiol.* 98, 2058–2073.

van-Veen, T. M., and Houtgast, T. (1985). Spectral sharpness and vowel dissimilarity. *J. Acoust. Soc. Am.* 77, 628–634.

Yost, W. A., and Shofner, W. P. (2009). Critical bands and critical ratios in animal psychoacoustics: an example using chinchilla data. *J. Acoust. Soc. Am.* 125, 315–323.

Zheng, Y., and Escabi, M. A. (2008). Distinct roles for onset and sustained activity in the neuronal code for temporal periodicity and acoustic envelope shape. *J. Neurosci.* 28, 14230–14244.

Conflict of Interest Statement: The authors declare that the research was conducted in the absence of any commercial or financial relationships that could be construed as a potential conflict of interest.

Received: 30 April 2012; accepted: 19 August 2012; published online: 27 September 2012.

*Citation: Chen C, Rodriguez FC, Read HL and Escabí MA (2012) Spectrotemporal sound preferences of neighboring inferior colliculus neurons: implications for local circuitry and processing. Front. Neural Circuits **6**:62. doi: 10.3389/fncir.2012.00062*

frontiers in
NEURAL CIRCUITS

REVIEW ARTICLE
published: 19 April 2013
doi: 10.3389/fncir.2013.00068

Neural interactions in unilateral colliculus and between bilateral colliculi modulate auditory signal processing

Hui-Xian Mei*[1,2]*, Liang Cheng*[1] *and Qi-Cai Chen*[1]*

[1] School of Life Sciences and Hubei Key Lab of Genetic Regulation and Integrative Biology, Central China Normal University, Wuhan, China
[2] School of Sport, Hubei University, Wuhan, China

Edited by:
Charles F. Stevens, The Salk Institute for Biological Studies, USA

Reviewed by:
Alex Koulakov, Cold Spring Harbor Laboratory, USA
Ken K. Yung, Hong Kong Baptist University, China

****Correspondence:***
Qi-Cai Chen, School of Life Science, Lab of Neurobiology, Central China Normal University, Luoyu Avenue 152, Wuhan 430079, Hubei, China.
e-mail: qcchen2003@yahoo.com.cn

In the auditory pathway, the inferior colliculus (IC) is a major center for temporal and spectral integration of auditory information. There are widespread neural interactions in unilateral (one) IC and between bilateral (two) ICs that could modulate auditory signal processing such as the amplitude and frequency selectivity of IC neurons. These neural interactions are either inhibitory or excitatory, and are mostly mediated by γ-aminobutyric acid (GABA) and glutamate, respectively. However, the majority of interactions are inhibitory while excitatory interactions are in the minority. Such unbalanced properties between excitatory and inhibitory projections have an important role in the formation of unilateral auditory dominance and sound location, and the neural interaction in one IC and between two ICs provide an adjustable and plastic modulation pattern for auditory signal processing.

Keywords: inferior collicular neurons, excitatory interaction, inhibitory interaction, bilateral collicular interaction, auditory signal processing

INTRODUCTION

In sound reception, auditory signal processing has traditionally been explained by neural interactions of divergent and convergent projections within the ascending auditory system through the interplay between excitation and inhibition (Suga, 1997). Auditory interactions can be found between neurons in one auditory nucleus, bilateral symmetrical auditory structures or nuclei, and even in auditory and non-auditory structures. This implies a neural modulation that plays an important role in maintaining the diversity and accuracy of auditory functions (Mei and Chen, 2010). For example, all sound signals in the range of audible frequency can be perceived by ear, however, we only notice those sounds interested by us and other sound signals that assumed to have no biological significance are filtered by excitatory or inhibitory modulation during transmission upward to different auditory nucleus.

Inferior colliculi (ICs), paired auditory structures, are located between the lower brainstem auditory nuclei and the auditory thalamus in the central auditory pathway. IC receives excitatory and inhibitory inputs from many lower auditory nuclei (Adams, 1979; Adams and Wenthold, 1979; Brunso-Bechtold et al., 1981; Adams and Mugnaini, 1984; Pollak and Casseday, 1989; Covey and Casseday, 1995; Casseday and Covey, 1996), contralateral IC (Malmierca et al., 1995, 2009) and from the primary auditory cortex (AC; Games and Winer, 1988; Herbert et al., 1991; Ojima, 1994; Saldaña et al., 1996; Malmierca and Ryugo, 2011). IC functions as an important relay station, and not only analyzes and integrates sound signals in terms of amplitude, frequency, and time course, etc., from different sources, but also prepares to route these signals to higher level center (Casseday et al., 1994; Jen et al., 1998; Suga et al., 1998; Jen and Zhang, 2000; LeBeau et al., 2001). A number of studies have shown that auditory signal processing and integration in ICs are significantly modulated by the massive descending corticofugal system which adjusts and improves ongoing collicular signal processing in multiple-parametric domains but also reorganizes collicular auditory maps according to the acoustic experience (Jen et al., 1998; Jen and Zhou, 2003; Popelar et al., 2003; Yan et al., 2005; Zhou and Jen, 2007; Ma and Suga, 2008; Suga, 2008; Suga et al., 2010). However, few studies have characterized how neural circuits in or between ICs can affect collicular auditory signal processing and integration. Therefore, in this article, we review recent findings and focus mainly on neural interactions either in one IC or between two ICs.

EFFECT OF INTERACTIONS BETWEEN NEURONS IN ONE IC IN THE AUDITORY SIGNAL PROCESSING

There are extensive intrinsic connections between neurons in one IC such that the IC neurons are likely to be a major source of inputs to other IC cells (Saldaña and Merchán, 1992). Such intercollicular fibers contribute to the formation of the known fibrodendritic laminae in one IC (Herrera et al., 1988, 1989; Oliver and Schneiderman, 1991). How do the neurons inside one auditory center interact with each other? Little is known about this interaction, but immunocytochemical localization demonstrated that one IC contained considerable amounts of glutamic acid, glycine, and glutamate decarboxylase (GAD), an enzyme that catalyzed the decarboxylation of glutamate to γ-aminobutyric acid (GABA), although some of these molecules could have an extrinsic origin (Adams and Wenthold, 1979; Ottersen and Storm-Mathisen, 1984; Vetter and Mugnaini, 1984; Moore and Moore, 1987; Roberts and Ribak, 1987; Caspary et al., 1990; Merchán et al., 2005). The presence of these excitatory and inhibitory transmitters suggests extensive interactions and modulations between neurons in one IC, because excitation and inhibition are the two most important neural interactions that modulate auditory

signal processing by increasing and decreasing responses of auditory neurons. To study the effect of neural interactions on sound amplitude and frequency selectivities of IC neurons, the auditory responses including the rate-intensity function (RIF) and frequency tuning curve (FTC) of each IC neuron in two simultaneously recorded IC neurons (or paired neurons) were examined under two-tone stimulation conditions. A pair of electrodes was used to simultaneously record two IC neurons in the same iso-frequency lamina or different iso-frequency (non-iso-frequency) laminae of the IC (**Figure 1**). A modulating tone with the best frequency (BF) of one of the paired IC neurons was delivered prior to a probe tone. This two-tone stimulating paradigm provided an opportunity to examine how a neuron activated by its BF sound might affect the response of the other neuron in amplitude and frequency domains. In particular, this procedure allows us to study the possible correlation of each pair of neurons in signal processing. For example, when a pair of IC neurons was stimulated by their two BF tones, the response of one IC neuron was either inhibited (two-tone suppression, **Figure 1A**) or facilitated (two-tone facilitation, **Figure 1B**) by the other. It has been reported that the proportion of neurons inhibited by interactions between simultaneously recorded neurons was always higher than that of facilitated neurons (Jen et al., 2002; Wu and Jen, 2008). Thus, the high level of inhibition in IC is basically similar to that in other reports (Vater et al., 1992; Suga, 1995; Fuzessery and Hall, 1996; Zhou and Jen, 2000; Lu and Jen, 2002; Mayko et al., 2012).

Further testing of inhibitory interactions on responses of the paired neurons revealed that the percent two-tone suppression of auditory responses decreased significantly with BF and recording depth differences between paired IC neurons (Jen et al., 2002). This observation is similar to a study in which auditory spatial selectivity of IC neurons was studied under two-tone stimulation conditions (Zhou and Jen, 2000). It was proposed that this phenomenon might be caused by the tonotopic organization of IC neurons, and that inputs from neurons with small BF differences arrive earlier with less attenuation than neurons with large BF differences (Jen et al., 2002). On the other hand, this observation also suggests a gradient of decreasing two-tone suppression along the dorsoventral axis of the IC (Schreiner and Langner, 1997). However, the neural basis underlying this observation remains to be explored.

Because the two-tone stimulation was based on the BFs of two simultaneously recorded neurons, two-tone suppression and facilitation might be thought to be caused by interactions between the two simultaneously recorded neurons activated by their respective BF sounds. Since IC neurons are tonotopically organized, interactions between the IC neurons are actually interactions between frequency laminae or bands. For a pair of IC neurons simultaneously recorded in big brown bat, a sound with the BF of one neuron could modulate the frequency tuning of another neuron by sharpening or broadening it's FTC (Wu et al., 2004). The pairs of neurons involved in frequency band interaction are not only within the same frequency band, but also across different frequency bands. The sharpening degrees of neurons within the same frequency band are higher than those of neurons across frequency bands. It was also found that the strength of frequency band interactions was weaker near the BF but gradually increased with frequency away from the BF of FTC (Wu et al., 2004). Moreover, FTCs of neurons with a BF of 20–30 kHz are most strongly sharpened which is similar to that observed in the chinchilla (Biebel and Langner, 2002).

These data suggest that IC neurons are highly correlated during frequency analysis such that frequency selectivity of the IC neurons is improved through inhibition while the spectrum of frequency sensitivity of other IC neurons is enhanced through excitation.

To further explore the mechanism underlying the effect of two-tone suppression on the responses of two simultaneously recorded neurons, bicuculline (an antagonist of $GABA_A$ receptor) was applied to one of the paired IC neurons in big brown bat to abolish GABAergic inhibition (**Figure 2**). Using a pair of neurons (A and B, for example), when bicuculline was applied to neuron A, it's number of impulses was greatly increased (**Figure 2** Aa vs Aa+bic), and the two-tone suppression was completely removed in neuron A (**Figure 2** Aa+bic vs Aa+bic ⊢ b), but was stronger in neuron B (**Figure 2** Bb ⊢ a vs Bb ⊢ a+bic). Thus, the degree of response inhibition decreased in the bicuculline-applied neuron but increased in the paired neuron, suggesting that GABAergic inhibition directly mediated the inhibitory interactions between two simultaneously recorded or paired IC neurons (Wu and Jen, 2008, 2009). However, for another pair of neurons C and D, the number of impulses greatly increased following bicuculline administration to neuron C (**Figure 2** Cc vs Cc+bic), but the two-tone suppression was only partly abolished in neuron C (**Figure 2** Cc+bic vs Cc+bic⊢ d), and was slightly increased in neuron D (**Figure 2** Dd⊢ a vs Dd⊢ c+bic). A previous study in big brown bat indicated that IC neurons with $GABA_A$ receptors are mostly distributed in the dorsomedial region but are sparsely distributed in the ventrolateral region which is mostly distributed with neurons containing glycine receptors (Fubara et al., 1996). Therefore, the degree of GABA-mediated two-tone suppression would progressively decrease along the dorsoventral axis of the IC. In brief, when an IC neuron is excited, it may inhibit other neighboring neurons to stand out as the best in the neurons through inhibitory interaction. These inhibitory interactions between neurons in one IC improves auditory sensitivity during auditory signal processing.

BILATERAL COLLICULAR INTERACTION IN AUDITORY SIGNAL PROCESSING

Many previous studies have clearly shown the anatomical connections between two ICs through the commissure of IC (CoIC). Injecting retrograde tracer in one IC demonstrated that commissure neurons in the central nucleus of IC (ICc) sent projections or fibers to the central nucleus, dorsal and lateral cortices of opposite IC. The commissural fibers ending in the contralateral IC to the injection point formed a laminar plexus that was symmetrical to the ipsilateral plexus, and interconnected mirror symmetric regions of the ICs representing similar frequency bands (Saldaña and Merchán, 1992; Malmierca et al., 1995). Even in the ICc, retrograde labeling of neurons demonstrated that commissural neurons send a divergent projection to the whole extent of the

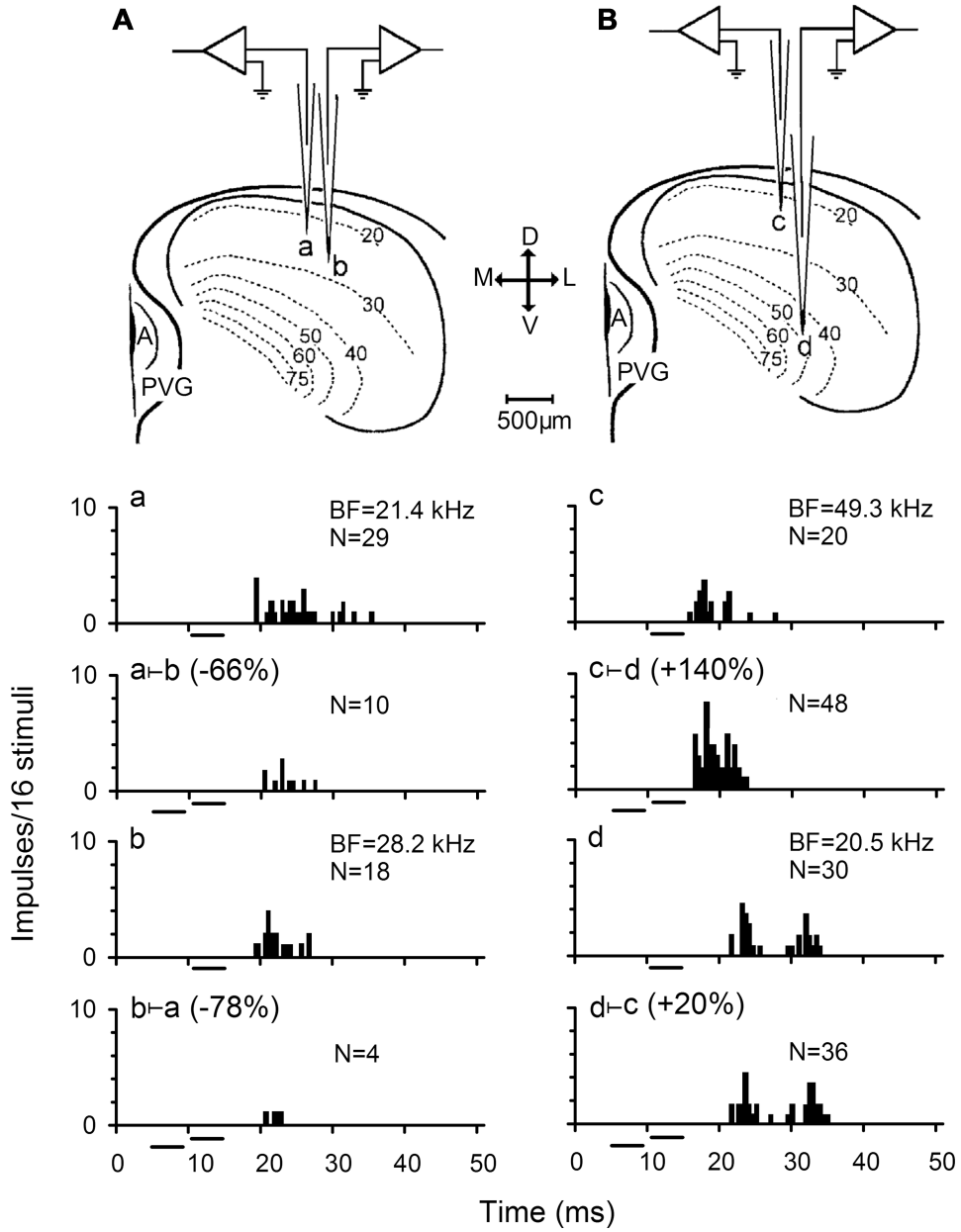

FIGURE 1 | Responses of two pairs of simultaneously recorded IC neurons. (A,B) Sketches showing the experimental arrangement for simultaneous recording two pairs of IC neurons. a and b represent a pair of IC neurons in iso-frequency laminae while c and d are another pair of IC neurons in non-iso-frequency laminae. M, medial; L, lateral; D, dorsal; V, ventral; A, aqueduct; PVG, paraventricular gray. The firing rates of these neurons in response to a 4 ms best frequency (BF) sound at 10 dB above the minimum threshold (MT) was inhibited (Aa vs Aa ⊢ b, Ab vs Ab ⊢ a) and facilitated (Bc vs Bc ⊢ d, Bd vs Bd ⊢ c) to different degrees when the 10 dB BF sound was preceded by a 4 ms sound at the BF and 20 dB above the MT of its counterpart neuron (abbreviated as the counterpart sound). N: number of impulses. All sound stimuli are shown by short horizontal bars. (based on Jen et al., 2002).

contralateral lamina, which resulted in a V-shaped axonal plexus that covered most of the ICc laminae and extended into the dorsal and lateral cortices. However, the density of the labeled commissurally projecting neurons was weighted toward a point that matched the position of the corresponding tracer injection into the contralateral IC, which is consistent with a point-to-point pattern (**Figure 3**). The coexistence of point-to-point and divergent projections suggest that CoIC is likely to be involved in interactions between specific regions of corresponding frequency band laminae as well as in integration across the laminae. (Malmierca et al., 2009).

An immunocytochemistry study in CoIC (Saint Marie, 1996) demonstrated the presence of both excitatory projections mediated by glutamate and inhibitory projections mediated by

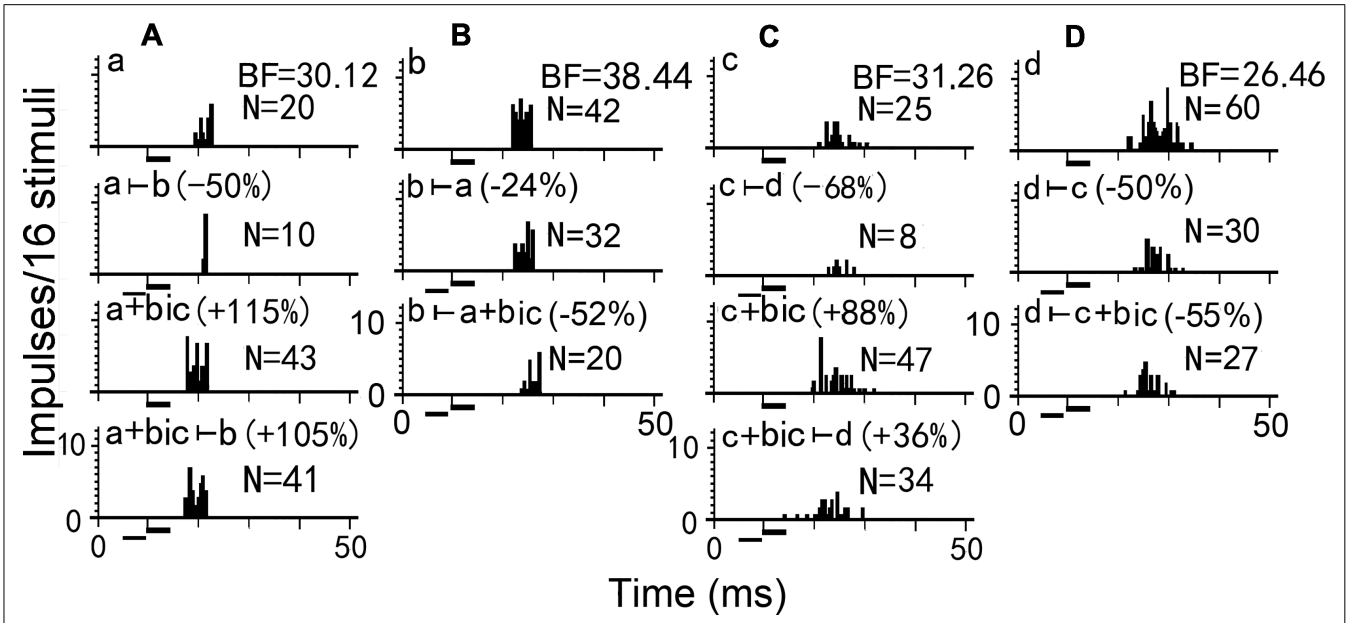

FIGURE 2 | Two-tone suppression on responses of two pairs of simultaneously recorded IC neurons before and during bicuculline (bic) application. Presentation of a counterpart sound decreased the firing rates of each IC neuron in the **(A,B)** pair or **(C,D)** pair (Aa, Bb, Cc, Dd vs Aa ⊢ b, Bb ⊢ a, Cc ⊢ d, Dd ⊢ c). When bicuculline was applied to neurons A and C, the number of impulses increased (Aa vs Aa+bic, Cc vs Cc+bic). The presentation of a counterpart sound during bicuculline application to neurons A and C decreased the number of impulses only slightly in neuron A but substantially in neuron C (Aa+bic vs Aa+bic ⊢ b, Cc+bic vs Cc+bic ⊢ d), however, decreased the number of impulses substantially in neuron B and slightly in neuron D (Bb vs Aa+bic ⊢ b, Cc+bic vs Cc+bic ⊢ d). N: number of impulses. All sound stimuli are shown by short horizontal bars. (Wu and Jen, 2008)

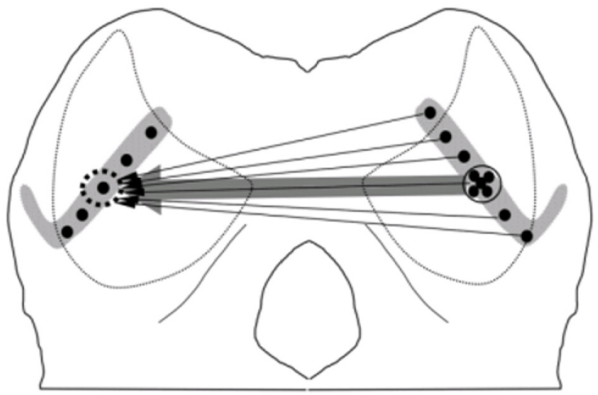

FIGURE 3 | Schematic wiring diagrams of the commissural connections. In the central nucleus of IC (ICc), the retrograde labeling of neurons demonstrated that an injection into one point on the lamina (dotted circle, left IC) retrogradely labeled neurons over the whole extent of the contralateral lamina, consistent with a divergent pattern of connections (thin arrows). The density of the projection is centered on a point matching the position of the tracer injection which is consistent with a point-to-point-weighted wiring pattern (thick arrow; Malmierca et al., 2009).

GABA. Injections of D-[3H] aspartate which is considered a selective marker for glutamatergic synapses, suggested that some glutamatergic endings in the IC originated from the opposite IC in the chinchilla. Studies that combined tract-tracing with horseradish peroxidase (HRP) and immunocytochemical labeling for GABA, found that double labeled neurons were mostly in the contralateral IC following a tracer injection into the ipsilateral IC in rat. These GABAergic CoIC could exert a direct monosynaptic inhibitory influence on their contralateral counterparts (González-Hernández et al., 1996; Hernández et al., 2006).

These anatomical findings are consistent with an electrophysiological study that concentrated on the interactions between two ICs. *In vitro* whole cell recording of IC neurons demonstrated that an excitatory and inhibitory postsynaptic current (EPSC and IPSC) was evoked by direct stimulation of the CoIC. The addition of GABAergic or glycinergic antagonists to CoIC could reduce the IPSC to various degrees, even there was a strong inhibitory input that was almost exclusively GABAergic. Furthermore, ionotropic glutamic receptor antagonists reduced both the EPSC and IPSC. This indicated that much of the inhibitory input appears to be mediated by interneuronal connection (Moore et al., 1998). Inactivation of excitatory CoIC could inhibit recorded IC neurons by direct elimination of the excitation and facilitate recorded neurons by disinhibiting inhibitory synapse of interneurons.

Bilateral collicular interaction between two ICs in auditory signal processing were examined using extracellular recordings *in vivo*. Malmierca et al. (2003, 2005) blocked the transmission of excitatory fibers in CoIC by means of local hydraulic injection of kynurenic acid (KA; a non-specific glutamatergic receptor antagonist) into one IC and observed changes in the frequency response area, number of impulses and monotonicity of neurons located in the corresponding region of the contralateral IC.

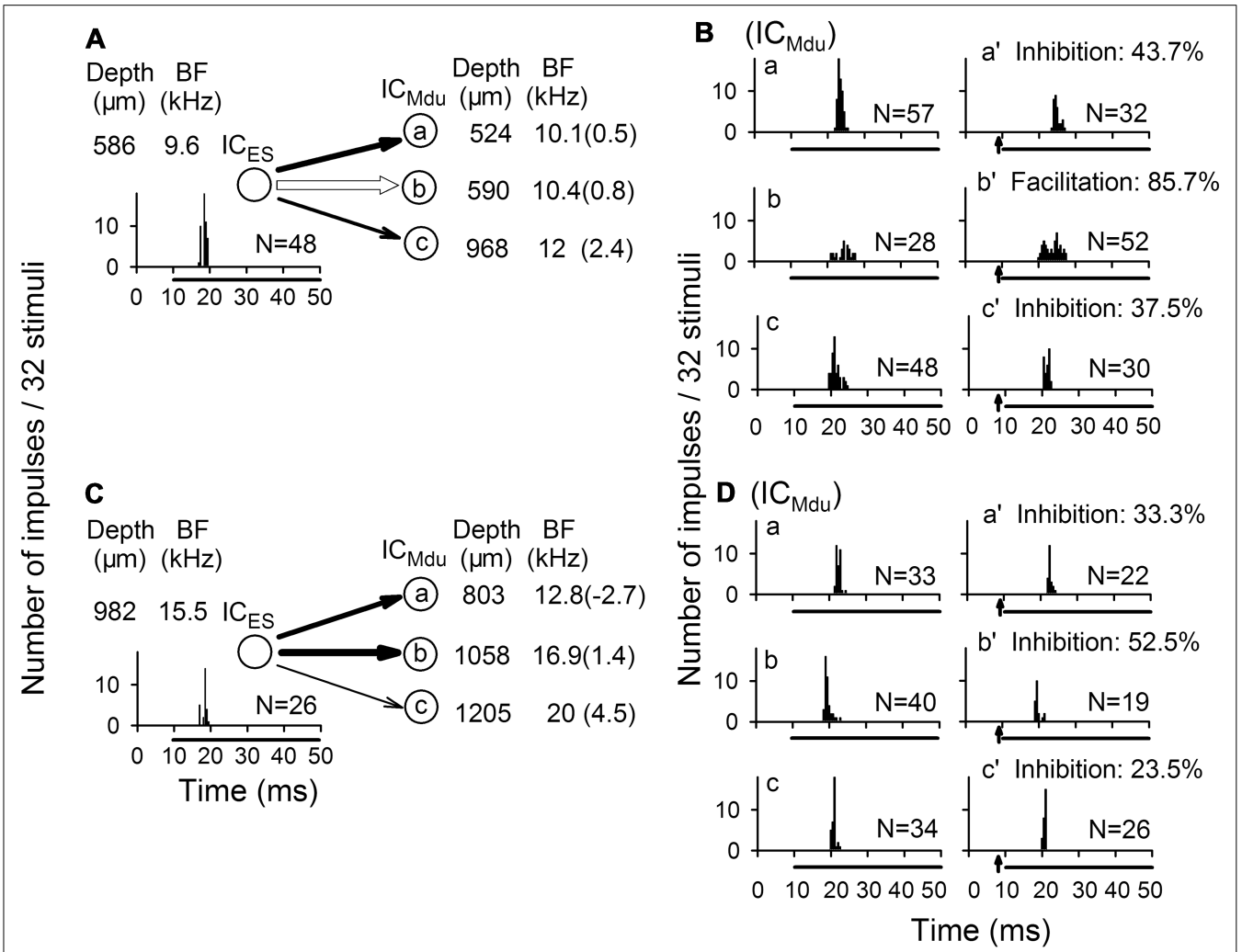

FIGURE 4 | Modulation of response of IC neuron (IC_{Mdu}) during focal electrical stimulation of the contralateral IC neuron (IC_{ES}). (A,B) Focal electrical stimulation of one IC_{ES} neuron produced inhibition of two IC_{Mdu} neurons but produced facilitation of another IC_{Mdu} neuron. **(C,D)** Focal electrical stimulation of another IC_{ES} neuron produced inhibition of all three IC_{Mdu} neurons studied. The BF of all six IC_{Mdu} neurons progressively increased with recording depth, and the percent inhibition was closely correlated with BF difference. N, number of impulses; %, percent inhibition or facilitation; of response of each IC_{Mdu} neuron. Arrow: focal electric stimulation (Mei et al., 2012b).

These studies indicated bilateral collicular interactions in the corresponding frequency laminae between the two ICs that were mediated by CoIC. Consistent with the result of whole cell recording, focal injection of KA in one IC both decreased and increased the number of impulses in the opposite IC neurons. This provided further evidence for an inhibitory influence mediated by inhibitory interneuronal connection.

Moreover, our recent study also demonstrated that focal electrical stimulation of one IC produced widespread inhibition and focused excitation of responses in contralateral IC neurons. The excitatory modulation of bilateral collicular interactions expands the RIFs and FTCs of facilitated IC neurons but decreased the slope of their RIFs and Q_{10} value of their FTCs for wider amplitude and frequency responses to sound stimuli. Conversely, the inhibitory modulation of bilateral collicular interaction sharpens the RIFs and FTCs of inhibited IC neurons but increased the slope of their RIFs and Q_{10} value of their FTCs for sharper sensitivity to sound amplitude and frequency (Mei et al., 2012b; Cheng et al., 2013). It is also suggested that the small proportion of bilateral collicular excitatory interactions between neurons in corresponding frequency laminae and the large proportion of bilateral collicular inhibitory interactions between neurons in different frequency laminae may be involved in the formation of binaural neurons (i.e., excitation–excitation, EE neurons that can be excited by same BF sound stimulation to either ear; excitation–inhibition, EI neurons that are strongly excited by sound stimulation to the contralateral ear and are inhibited by sound stimulation to the ipsilateral ear; Mei et al., 2012a). The possible neural pathway may be described that the excitation from ipsilateral ear can cross to the contralateral IC in a lower auditory nucleus and then to the ipsilateral IC via facilitatory or inhibitory CoIC, respectively. The unbalanced properties between excitatory and inhibitory projections have a very

important role in the formation of unilateral auditory dominance and sound location.

In accordance with the anatomical data of point-to-point and divergent projections between two ICs, focal electrical stimulation of one neuron modulated the responses of three contralateral neurons (**Figures 4A** vs **4B** and **4C** vs **4D**). Each of three contralateral IC neurons was sequentially isolated at a different depth with a progressive increase in BF. The degree of bilateral collicular interaction was dependent upon the BF difference between the electrically stimulated IC neurons and the modulated IC neurons. The percent modulation in the number of impulses was larger for the neuron with a smaller BF difference than for the neuron with a larger BF difference (Mei et al., 2012b).

In addition, after the focal electrical stimulation was delivered for 30 min, a long term shift in an IC neuron's BF was induced which remained for as long as 150 min and decreased with time (Cheng et al., 2013). Therefore the bilateral collicular interaction modulates both auditory signal processing and auditory plasticity of IC neurons that is similar to the corticofugal modulation of IC neurons (Jen et al., 1998; Ma and Suga, 2001; Suga et al., 2002; Yan and Ehret, 2002; Jen and Zhou, 2003; Yan et al., 2005; Zhou and Jen, 2007). Since the BF-dependent modulation of bilateral collicular interaction is not entirely comparable to the egocentric selectivity of corticofugal modulation, further studies are required to determine whether the modulation effect of bilateral collicular interactions might also be mediated through corticofugal feedback loops.

Interestingly, following reciprocal electrical stimulation of pairs of neurons, respectively, in two ICs, we found that the bilateral collicular interaction was either reciprocal or unilateral. However, after HRP deposits were made in CoIC, regions of the IC supplying fibers to the commissure were not the main targets for the terminals of these fibers, which suggested that interconnections of the ICs through their commissure were complementary, rather than reciprocal (Aitkin and Phillips, 1984).

PROSPECTS

Neural interactions are of great interest because of their contribution to sensory information processing, neural functional integration and neural modulation. As for the auditory midbrain, neural interactions were found both in one IC and between two ICs, even in unilateral iso-frequency and non-iso-frequency laminae as well as bilateral corresponding and non-corresponding frequency laminae. Generally, there is a large percentage of inhibitory interactions but a small percentage of excitatory interactions, which is likely because of the presence of many inhibitory interneurons. These excitatory and inhibitory interactions in or between ICs modulate auditory signal processing in amplitude and frequency domains, and provide an adjustable and plastic modulation pattern for the auditory signal processing of ICs. However, many details, such as neural plasticity of the structure and function as well as cellular and synaptic mechanisms of the neural modulation underlying neural interactions in auditory signal processing, remain unclear and require further study. We have sufficient reasons to believe that new knowledge about the various neural interactions will be obtained with successive studies. Thus, the studies of neural interactions in one IC and between two ICs are in the ascendancy.

ACKNOWLEDGMENTS

We thank the anonymous reviewers for commenting on an earlier version of this manuscript. This work was supported by the grants (#31070971, #30970972) from the National Science Foundation of China.

REFERENCES

Adams, J. C. (1979). Ascending projections to the inferior colliculus. *J. Comp. Neurol.* 183, 519–538.

Adams, J. C., and Mugnaini, E. (1984). Dorsal nucleus of the lateral lemniscus: a nucleus of GABAergic projection neurons. *Brain Res. Bull.* 13, 585–590.

Adams, J. C., and Wenthold, R. (1979). Distribution of putative amino acid transmitters, choline acetyltransferase and glutamate decarboxylase in the inferior colliculus. *Neuroscience* 4, 1947–1951.

Aitkin, L. M., and Phillips, S. C. (1984). The interconnections of the inferior colliculi through their commissure. *J. Comp. Neurol.* 228, 210–216.

Biebel, U. W., and Langner, G. (2002). Evidence for interaction across frequency channels in the inferior colliculus of awake chinchilla. *Hear. Res.* 169, 151–168.

Brunso-Bechtold, J. K., Thompson, G. C., and Masterton, R. B. (1981). HRP study of the organization of auditory afferents ascending to central nucleus of inferior colliculus in cat. *J. Comp. Neurol.* 197, 705–722.

Casseday, J. H., and Covey, E. (1996). A neuroethological theory of the operation of the inferior colliculus. *Brain Behav. Evol.* 47, 311–336.

Caspary, D. M., Raza, A., Lawhorn Armour, B. A., Pippin, J., and Americ, S. P. (1990). Immunocytochemical and neurochemical evidence for age-related loss of GABA in the inferior colliculus: implications for neural presbycusis. *J. Neurosci.* 10, 2363–2372.

Casseday, J. H., Ehrlich, D., and Covey, E. (1994). Neural tuning for sound duration: role of inhibitory mechanisms in the inferior colliculus. *Science* 264, 847–850.

Cheng, L., Mei, H. X., Tang, J., Fu, Z. Y., Jen, P. H. S., and Chen, Q. C. (2013). Bilateral collicular interaction: modulation of auditory signal processing in frequency domain. *Neuroscience* 235, 27–39.

Covey, E., and Casseday, J. H. (1995). "The lower brainstem auditory pathways," in *Springer Handbook of Auditory Research Vol. 5, Hearing by Bats*, eds A. N. Popper, and R. R. Fay (New York: Springer), 235–295.

Fubara, B. M., Casseday, J. H., Covey, E., and Schwartz-Bloom, R. D. (1996). Distribution of GABAA, GABAB and glycine receptors in the central auditory system of the big brown bat, *Eptesicus fuscus. J. Comp. Neurol.* 369, 83–92.

Fuzessery, Z. M., and Hall, J. C. (1996). Role of GABA in shaping frequency tuning and creating FM sweep selectivity in the inferior colliculus. *J. Neurophysiol.* 76, 1059–1073.

Games, K. D., and Winer, J. A. (1988). Layer V in rat auditory cortex: projections to the inferior colliculus and contralateral cortex. *Hear. Res.* 34, 1–25.

González-Hernández, T., Mantolán-Sarmiento, B., González-González, B., and Pérez-González, H. (1996). Sources of GABAergic input to the inferior colliculus of the rat, *J. Comp. Neurol.* 372, 309–326.

Herbert, H., Aschoff, A., and Ostwald, J. (1991). Topography of projections from the auditory cortex to the inferior colliculus in the rat. *J. Comp. Neurol.* 304, 103–122.

Hernández, O., Rees, A., and Malmierca, M. S. (2006). A GABAergic component in the commissure of the inferior colliculus in rat. *Neuroreport* 17, 1611–1614.

Herrera, M., Correa, J., Sanchez del Campo, F., and Ruiz, A. (1988). Stellate cells and their axonal patterns in the central nucleus of the inferior colliculus of the cat (*Felis domesticus*). *J. Hirnforsch.* 29, 393–402.

Herrera, M., Shchez del Campo, F., Puchades, A., and Correa, J. (1989). Axonal patterns of discshaped cells in the central nucleus of the cat inferior colliculus. *Z. mikrosk. Anat. Forsch.* 103, 515–525.

Jen, P. H. S., Chen, Q. C., and Sun, X. D. (1998). Corticofugal regulation of auditory sensitivity in the bat inferior

colliculus. *J. Comp. Physiol. A* 183, 683–697.

Jen, P. H. S., Wu, F. J., and Chen, Q. C. (2002). The effect of two-tone stimulation on responses of two simultaneously recorded neurons in the inferior colliculus of the big brown bat, *Eptesicus fuscus. Hear. Res.* 168, 139–149.

Jen, P. H. S., and Zhang, J. P. (2000). The role of GABAergic inhibition on direction-dependent sharpening of frequency tuning in bat inferior collicular neurons. *Brain Res.* 862, 127–137.

Jen, P. H. S., and Zhou, X. M. (2003). Corticofugal modulation of amplitude domain processing in the midbrain of the big brown bat, *Eptesicus fuscus. Hear. Res.* 184, 91–106.

LeBeau, F. E., Malmierca, M. S., and Rees, A. (2001). Iontophoresis in vivo demonstrates a key role for GABAA and glycinergic inhibition in shaping frequency response areas in the inferior colliculus of guinea pig. *J. Neurosci.* 21, 7303–7312.

Lu, Y., and Jen, P. H. S. (2002). Interaction of excitation and inhibition in inferior collicular neurons of the big brown bat, *Eptesicus fuscus. Hear. Res.* 169, 140–150.

Ma, X., and Suga, N. (2001). Plasticity of bat's central auditory system evoked by focal electric stimulation of auditory and/or somatosensory cortices. *J. Neurophysiol.* 85, 1078–1087.

Ma, X., and Suga, N. (2008). Modulation of the paradoxical latency shifts of inferior collicular neurons. *J. Neurophysiol.* 100, 1127–1134.

Malmierca, M. S., Hernández, O., Antunes, F. M., and Rees, A. (2009). Divergent and point-to-point connections in the commissural pathways between the inferior colliculi. *J. Comp. Neurol.* 514, 226–239.

Malmierca, M. S., Hernandez, O., Falconi, A., Lopez-Poveda, E. A., Merchan, M., and Rees, A. (2003). The commissure of the inferior colliculus shapes frequency response areas in rat: an in vivo study using reversible blockade with microinjection of kynurenic acid. *Exp. Brain Res.* 153, 522–529.

Malmierca, M. S., Hernandez, O., and Rees, A. (2005). Intercollicular commissural projections modulate neuronal responses in the inferior colliculus. *Eur. J. Neurosci.* 21, 2701–2710.

Malmierca, M. S., Rees, A., Le Beau, F. E., and Bjaalie, J. G. (1995). Laminar organization of frequency-defined local axons within and between the inferior colliculi of the guinea pig. *J. Comp. Neurol.* 357, 124–144.

Malmierca, M. S., and Ryugo, D. K. (2011). "Descending connections of auditory cortex to the midbrain and brain stem," in *The Auditory Cortex*, eds J. Winer, and C. E. Schreiner (New York: Springer), 189–208.

Malmierca, M. S., Saint Marie, R. L., Merchan, M. A., and Oliver, D. L. (2005). Laminar inputs from dorsal cochlear nucleus and ventral cochlear nucleus to the central nucleus of the inferior colliculus: two patterns of convergence. *Neuroscience* 136, 883–894.

Mayko, Z. M., Roberts, P. D., and Portfors, C. V. (2012). Inhibition shapes selectivity to vocalization in the inferior colliculus of awake mice. *Front. Neural Circuits* 6:73. doi: 10.3389/fncir.2012.00073

Merchán, M., Aguilar, L. A., Lopez-Poveda, E. A., and Malmierca, M. S. (2005). The inferior colliculus of the rat: quantitative immunocytochemical study of GABA and glycine. *Neuroscience* 136, 907–925.

Mei, H. X., and Chen, Q. C. (2010). Neural modulation in inferior colliculus and central auditory plasticity. *Front. Biol.* 5, 123–127.

Mei, H. X., Cheng, L., Tang, J., Fu, Z. Y., Jen, P. H. S., and Chen, Q. C. (2012a). Modulation of amplitude sensitivity by bilateral collicular interaction among different frequency laminae. *Neurosci. Lett.* 517, 13–17.

Mei, H. X., Cheng, L., Tang, J., Fu, Z. Y., Jen, P. H. S., and Chen, Q.-C. (2012b). Bilateral inferior collicular interaction: modulation of auditory signal processing in amplitude domain. *PLoS ONE* 7:e41311. doi: 10.1371/journal.pone.0041311

Moore, D. R., Kotak, V. C., and Sanes, D. H. (1998). Commissural and lemniscal synaptic input to the gerbil inferior colliculus. *J. Neurophysiol.* 80, 2229–2236.

Moore, J. K., and Moore, R. Y. (1987). Glutamic acid decarboxylase-like immunoreactivity in brainstem auditory nuclei of the rat. *J. Comp. Neurol.* 260, 157–174.

Ojima, H. (1994). Terminal morphology and distribution of corticothalamic fibers originating from layers 5 and 6 of cat primary auditory cortex. *Cereb. Cortex* 4, 646–663.

Oliver, D. L., and Schneiderman, A. (1991). "The anatomy of the inferior colliculus: A cellular basis for integration of monaural and binaural information," in *Neurophysiology of Hearing: The central auditory system*, eds R. A. Altschuler, R. P. Bobbin, B. M. Clopton, and D. W. Hoffman (New York: Raven Press), 195–222.

Ottersen, O. P., and Storm-Mathisen, J. (1984). "Neurons containing or accumulating transmitter amino acids," in *Handbook of Chemical Neuroanatomy, Vol. 3, Classical Transmitters and Transmitter Receptors in the CNS*. eds A. Bjorklund, T. Hokfelt, and M.J. Kuhar (Amsterdam: Elsevier), 141–246.

Pollak, G. D., and Casseday, J. H. (eds). (1989). *The Neural Basis of Echolocation in Bats*. Berlin: Springer press.

Popelar, J., Nwabueze-Ogbo, F. C., and Syka, J. (2003). Changes in neuronal activity of the inferior colliculus in rat after temporal inactivation of the auditory cortex. *Physiol. Res.* 52, 615–628.

Roberts, R. C., and Ribak, C. E. (1987). An electron microscopic study of GABAergic neurons and axon terminals in the central nucleus of the inferior colliculus of the rat. *J. Neurocytol.* 16, 333–345.

Saint Marie, R. L. (1996). Glutamatergic connections of the auditory midbrain: selective uptake and axonal transport of D-[3H] aspartate. *J. Comp. Neurol.* 373, 225–270.

Saldaña, E., Feliciano, M., and Mugnaini, E. (1996). Distribution of descending projections from primary auditory neocortex to inferior colliculus mimics the topography of intracollicular projections. *J. Comp. Neurol.* 371, 15–40.

Saldaña, E., and Merchán, M. A. (1992). Intrinsic and commissural connections of the rat inferior colliculus. *J. Comp. Neurol.* 319, 417–437.

Schreiner, C. E., and Langner, G. (1997). Laminar fine structure of frequency organization in auditory midbrain. *Nature* 388, 383–386.

Suga, N. (1995). Sharpening of frequency tuning by inhibition in the central auditory system: tribute to Yasuji Katsuki. *Neurosci. Res.* 21, 287–299.

Suga, N. (1997). "Parallel-hierarchical processing of complex sounds for specialized auditory function," in *Encyclopedia of Acoustics*, ed. M. J. Crocker (New York: Wiley), 1409–1418.

Suga, N. (2008). Role of corticofugal feedback in hearing. *J. Comp. Physiol A* 194,169–183.

Suga, N., Ji, W., Ma, X., Tang, J., Xiao, Z., and Yan, J. (2010). "Corticofugal modulation and beyond for auditory signal processing and plasticity," in *Auditory and Vestibular Efferents*, eds D. K. Ryugo, R. R. Fay, and A. N. Popper, (Berlin: Springer), 313–352.

Suga, N., Xiao, Z., Ma, X., and Ji, W. (2002). Plasticity and corticofugal modulation for hearing in adult animals. *Neuron* 36, 9–18.

Suga, N., Yan, J., and Zhang, Y. F. (1998). "The processing of species-specific complex sounds by the ascending and descending auditory systems," in *Central Auditory Processing and Neural Modeling*, eds P. Poon, and J. Brugge (New York: Plenum Press), 55–70.

Vater, M., Habbicht, H., Kossl, M., and Grothe, B. (1992). The functional role of GABA and glycine in monaural and binaural processing in the inferior colliculus of horseshoe bats. *J. Comp. Physiol. A* 171, 541–553.

Vetter, D. E., and Mugnaini, E. (1984). Immunocytochemical localization of GABAergic elements in the rat inferior colliculus. *Soc. Neurosci. Abstr.* 10, 1148.

Wu, F. J., Chen, Q. C., Jen, P. H. S., and Shen, J. X. (2004). Effect of frequency-band integration on the sharpening frequency tuning of IC neurons in bat, *Eptesicus fuscus. Chin. Sci. Bull.* 49, 1026–1031.

Wu, F. J., and Jen, P. H. S. (2008). GABA-mediated modulation of the discharge pattern and rate-level function of two simultaneously recorded neurons in the inferior colliculus of the big brown bat, *Eptesicus Fuscus. Chin. J. Physiol.* 51, 13–26.

Wu, F. J., and Jen, P. H. S. (2009). Involvement of GABA-mediated inhibition in shaping the frequency selectivity of neurons in the inferior colliculus of the big brown bat, *Eptesicus fuscus. Chin. J. Physiol.* 52, 1–9.

Yan, J., and Ehret, G. (2002). Corticofugal modulation of midbrain sound processing in the house mouse. *Eur. J. Neurosci.* 16, 119–128.

Yan, J., Zhang, Y., and Ehret, G. (2005). Corticofugal shaping of frequency tuning curves in the central nucleus of the inferior colliculus of mice. *J. Neurophysiol.* 93, 71–83.

Zhou, X. M., and Jen, P. H. S. (2000). Neural inhibition sharpens auditory spatial sensitivity of bat inferior collicular neurons. *J. Comp. Physiol. A* 186, 389–398.

Zhou, X. M., and Jen, P. H. S. (2007). Corticofugal modulation of multi-parametric auditory selectivity in the midbrain of the big brown bats. *J. Neurophysiol.* 98, 2509–2516.

Conflict of Interest Statement: The authors declare that the research was conducted in the absence of any commercial or financial relationships that could be construed as a potential conflict of interest.

Received: 01 July 2012; accepted: 30 March 2013; published online: 19 April 2013.

Citation: Mei H-X, Cheng L and Chen Q-C (2013) Neural interactions in unilateral colliculus and between bilateral colliculi modulate auditory signal processing. Front. Neural Circuits **7**:*68. doi: 10.3389/fncir.2013.00068*

frontiers in
NEURAL CIRCUITS

REVIEW ARTICLE
published: 03 January 2013
doi: 10.3389/fncir.2012.00114

Cortical modulation of auditory processing in the midbrain

Victoria M. Bajo* and Andrew J. King*

Department of Physiology, Anatomy and Genetics, University of Oxford, Oxford, UK

Edited by:
Eric D. Young, Johns Hopkins University, USA

Reviewed by:
Alan R. Palmer, Medical Research Council Institute of Hearing Research, UK
Brett R. Schofield, Northeast Ohio Medical University, USA

****Correspondence:***
Victoria M. Bajo and Andrew J. King, Department of Physiology, Anatomy and Genetics, University of Oxford, Sherrington Building, Parks Road, Oxford, OX1 3PT, UK.
e-mail: victoria.bajo@dpag.ox.ac.uk; andrew.king@dpag.ox.ac.uk

In addition to their ascending pathways that originate at the receptor cells, all sensory systems are characterized by extensive descending projections. Although the size of these connections often outweighs those that carry information in the ascending auditory pathway, we still have a relatively poor understanding of the role they play in sensory processing. In the auditory system one of the main corticofugal projections links layer V pyramidal neurons with the inferior colliculus (IC) in the midbrain. All auditory cortical fields contribute to this projection, with the primary areas providing the largest outputs to the IC. In addition to medium and large pyramidal cells in layer V, a variety of cell types in layer VI make a small contribution to the ipsilateral corticocollicular projection. Cortical neurons innervate the three IC subdivisions bilaterally, although the contralateral projection is relatively small. The dorsal and lateral cortices of the IC are the principal targets of corticocollicular axons, but input to the central nucleus has also been described in some studies and is distinctive in its laminar topographic organization. Focal electrical stimulation and inactivation studies have shown that the auditory cortex can modify almost every aspect of the response properties of IC neurons, including their sensitivity to sound frequency, intensity, and location. Along with other descending pathways in the auditory system, the corticocollicular projection appears to continually modulate the processing of acoustical signals at subcortical levels. In particular, there is growing evidence that these circuits play a critical role in the plasticity of neural processing that underlies the effects of learning and experience on auditory perception by enabling changes in cortical response properties to spread to subcortical nuclei.

Keywords: auditory cortex, inferior colliculus, corticofugal, descending projection, plasticity, sound localization

The traditional view of the central auditory pathway begins with the auditory nerve fibers entering and bifurcating in the cochlear nuclei from where information is transmitted successively via other centers in the brainstem, midbrain, and thalamus to the auditory cortex, where further processing gives rise to our perception of the auditory world. According to this hierarchical view of the ascending pathways, the inferior colliculus (IC) in the midbrain is usually regarded as an obligatory relay for the transmission of auditory signals (e.g., Aitkin and Phillips, 1984). When a retrograde tracer injection is placed in the IC, however, more cells are labeled in the auditory cortex than in brainstem centers such as the cochlear nuclei or superior olivary complex (**Figure 1A**). Consequently, processing in the IC must be influenced by cortical outputs. In fact, descending projections connect almost all levels of the auditory pathway, indicating that a bidirectional flow of information takes place.

Even though descending pathways have been characterized in numerous species [reviewed in Winer (2003)], the function of different nuclei still tends to be thought of in terms of the serial processing of auditory signals. Thus, when a particular property, such as contrast gain control (Rabinowitz et al., 2011) or novelty detection (Ulanovsky et al., 2003), is identified in cortical cells, one immediate question is whether that property is genuinely cortical in origin or inherited from the auditory thalamus or midbrain. This issue is, of course, not limited to the auditory system, as all sensory pathways comprise a series of subcortical and cortical centers. But the auditory system stands out in having so many subcortical processing stations, and therefore presents a particular challenge for indentifying how ascending and descending signals interact to determine the response properties of the neurons found there.

In this review, we first discuss the anatomical organization of the descending projections from the auditory cortex to the IC, then look at how cortical inputs influence the response properties of IC neurons, and finally consider what the functions of corticocollicular modulation might be. Rather than viewing it as an independent set of ascending and descending connections, we

Abbreviations: I, II, III, VI, V, VI, cortical layers I–VI; A, anterior; A1, primary auditory cortex; AEG, anterior ectosylvian gyrus; AVCN, anteroventral cochlear nucleus; CN, cochlear nucleus; CNIC, central nucleus of the inferior colliculus; Contra, contralateral; D, dorsal; DC, dorsocaudal field in the guinea pig auditory cortex; DCIC, dorsal cortex of the IC; DCN, dorsal cochlear nucleus; DNLL, dorsal nucleus of the lateral lemniscus; HP, hippocampus; IC, inferior colliculus; ILD, interaural level difference; Ipsi, ipsilateral; IS, injection site; L, lateral; LCIC, lateral cortex of the inferior colliculus; LGN, lateral geniculate nucleus; LSO, lateral superior olive; LV, lateral ventricle; M, medial; MEG, middle ectosylvian gyrus; MGB, medial geniculate body; MSO, medial superior olive; nBIC, nucleus of the brachium of the IC; P, posterior; PEG, posterior ectosylvian gyrus; ps, pial surface; pss, pseudosylvian sulcus; s, section; SC, superior colliculus; SOC, superior olivary complex; SSG, suprasylvian gyrus; sss, suprasylvian sulcus; VNLL, ventral nucleus of the lateral lemniscus; wm, white matter.

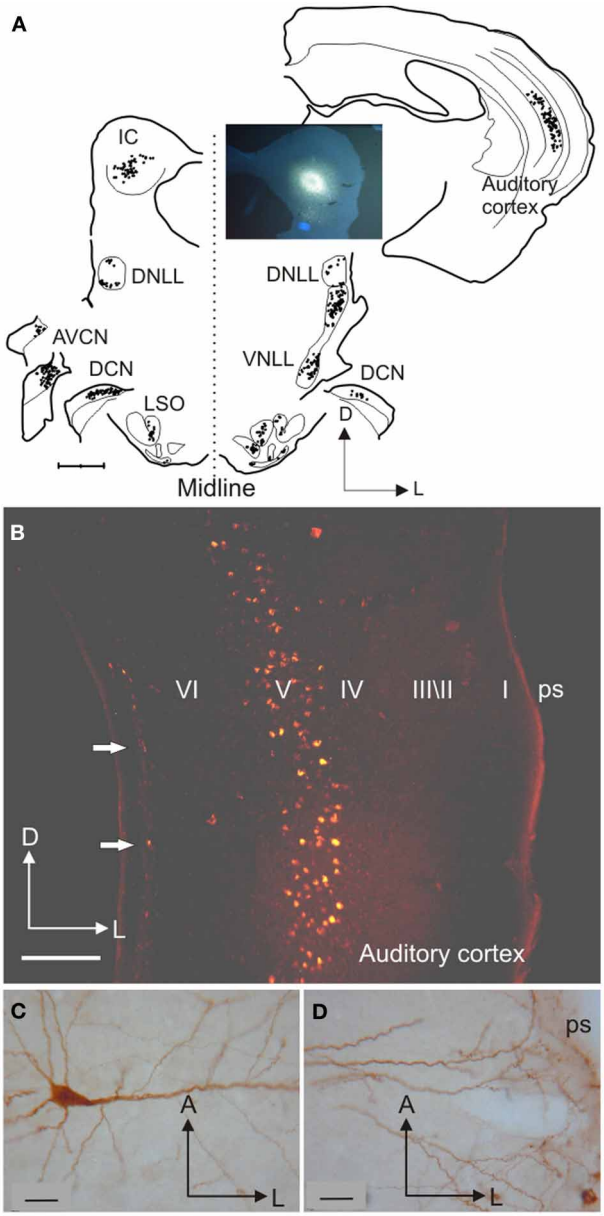

FIGURE 1 | Inputs from different auditory centers converge in the IC. **(A)** A small fluorogold tracer injection in the ventromedial part of the IC central nucleus of the gerbil produces retrograde labeling of neurons in the MSO, periolivary nuclei, VNLL, and A1 on the same side, in the cochlear nuclei and IC on the opposite side, and in the LSO, DCN, and DNLL on both sides. **(B)** Retrogradely labeled cells in the cortex are found mainly in layer V after a rhodamine tracer injection in the IC. **(C)** Large labeled pyramidal cell with the soma located in cortical layer V and **(D)** a tufted dendritic tree ending in layer I. Calibration bars: 1 mm **(A)**, 0.2 mm **(B)**, and 25 μm **(C,D)**. Modified with permission from Bajo and Moore (2005).

suggest that it is more appropriate to consider the auditory system as a series of dynamic loops in which neural coding in the IC and other subcortical nuclei is continually updated by changes in activity at higher levels as much as by the signals received from the brainstem.

CORTICAL CELLS THAT PROJECT TO THE INFERIOR COLLICULUS

Although studies demonstrating that lesions in the temporal lobe of the cerebral cortex result in axon degeneration in the midbrain date back more than 50 years, the first evidence using an anatomical tracing method for a descending projection from the auditory cortex to the IC was provided by Beyerl (1978). After making injections of horseradish peroxidase (HRP) in the central nucleus of the IC (CNIC) in rats, he found that layer V pyramidal cells were retrogradely labeled in the ipsilateral auditory cortex. Beyerl (1978) also reported that small HRP injections resulted in restricted patches of labeled neurons in the cortex, raising the possibility that this projection might be topographically organized in much the same way as the ascending projections to the IC from auditory brainstem structures. No labeling was reported, however, in other cortical layers or in the contralateral cortex, probably due to the short survival times (24–48 h) and the limitations of the tracer used.

In the following decades, corticocollicular projections were described in squirrel monkeys (Winer et al., 2002), cats (Kelly and Wong, 1981; Winer and Prieto, 2001), ferrets (Bajo et al., 2007), guinea pigs (Strutz, 1987; Coomes et al., 2005), rats (Druga and Syka, 1984; Games and Winer, 1988; Herbert et al., 1991), gerbils (Bajo and Moore, 2005), and even in Madagascan tenrecs (Künzle, 1995). The use of modern retrograde tracers has confirmed that projection neurons that target the IC are found in layer V of the auditory cortex layer (**Figures 1A,B** and **2A**) and revealed much about the morphology of these neurons (**Figures 1–3**).

Figure 1C shows a typical example of a large cortiocollicular pyramidal cell with a triangular cell body located in layer V. This neuron has 3–6 primary basal dendrites oriented parallel to the cortical layers, which branch to form a dendritic tree located mainly in the same layer, and a thick apical dendrite running perpendicular to the pial surface up to layer II and beyond, giving-off second-order dendrites along its length. When the IC cortices are included in the injection site in gerbils, the apical dendrites divide into 2–3 thinner dendrites, creating tufted apical endings in layer I (**Figure 1D**), suggesting that two different subpopulations of layer V pyramidal neuron, tufted and untufted, contribute to this projection (Bajo and Moore, 2005). However, these subpopulations have not been observed routinely in other species, such as ferrets (Bajo et al., 2007), possibly due to the incomplete filling of the distal dendritic arborization.

In another approach to examining the morphology of corticocollicular neurons, Games and Winer (1988) compared retrogradely labeled neurons in layer V with Golgi impregnated cells in rat cortex, and concluded that the IC projection neurons correspond to the medium- and large-sized pyramidal cells identified in Golgi-Cox preparations. Pyramidal cells in layer V are glutamatergic (Kaneko et al., 1987) and many of the corticocollicular projection neurons can be labeled using a specific antibody against the non-phosphorylated form of the neurofilament H protein SMI_{32} (Bajo et al., 2010a), although it is not known if every large neuron in layer V that projects to the IC is SMI_{32} positive or vice versa.

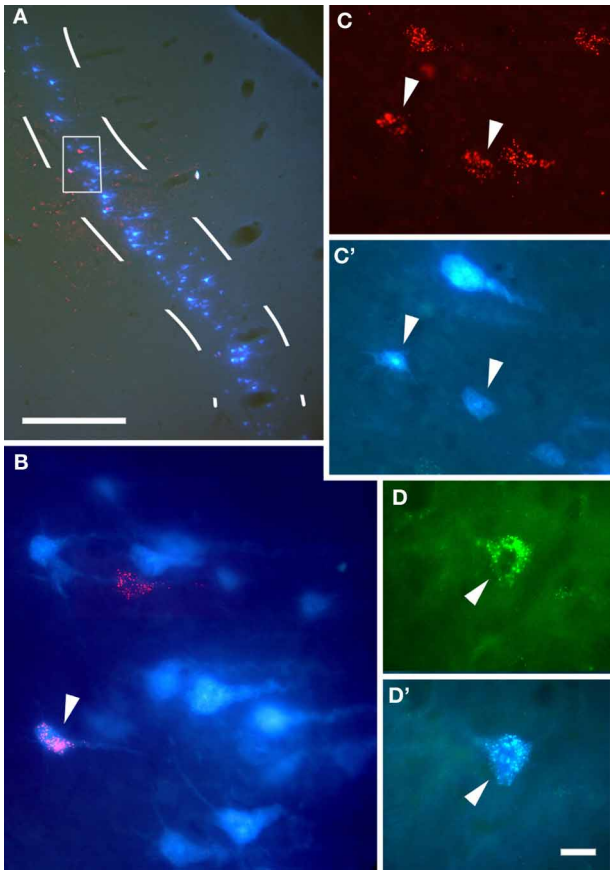

FIGURE 2 | Anatomical tracing experiments in guinea pigs show that cortical cells project to the IC bilaterally. (A) Coronal section at the level of the right auditory cortex showing the overlay of cells labeled retrogradely by injections of Fast Blue in the right IC and rhodamine microbeads in the left IC, with a higher magnification of the area enclosed by the white box in **(B)**. **(C,C')** Double-labeled cortical cells (arrowheads) using the same tracer combination. **(D,D')** A double-labeled cortical cell following an injection of Fast Blue in the ipsilateral IC and fluorescein microbeads in the contralateral IC. Arrowheads indicate double labeled cells. Calibration bars: 0.5 mm **(A)** and 20 μm **(B–D)**. Modified with permission from Coomes et al. (2005).

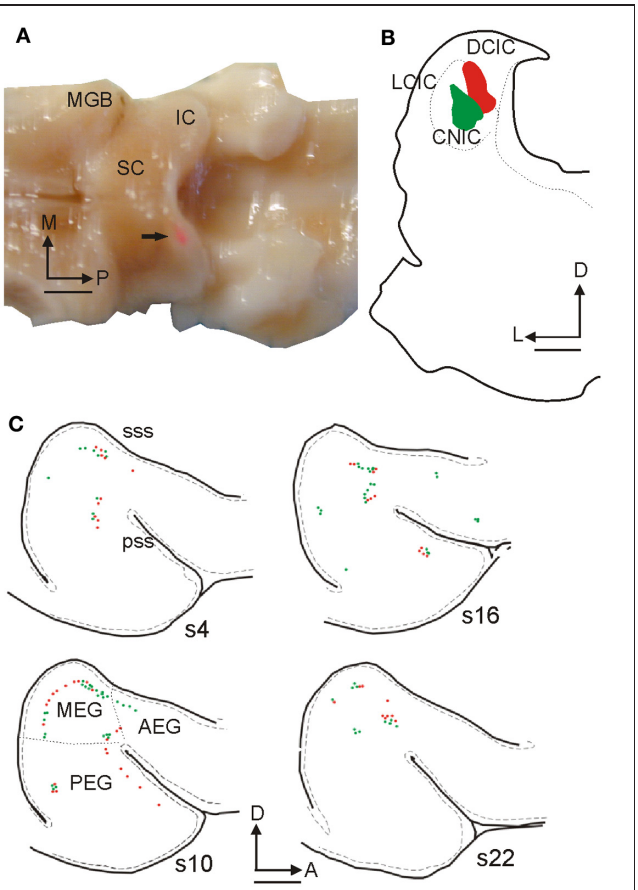

FIGURE 3 | Retrogradely labeled cells in ferret auditory cortex after fluorescent microbead injections in the IC. (A) Dorsal view of the ferret brain where both the cerebral cortices and the cerebellum were removed to visualize the thalamus and midbrain. A rhodamine microbead injection site can be seen in the left IC (arrow). **(B)** Coronal section at the level of the IC from this animal illustrating rhodamine and fluorescein microbead injection sites. **(C)** Drawings of tangential 50 μm sections spaced 300 μm apart from lateral to medial (s22 is the most medial) at the level of the left ectosylvian gyrus where the auditory cortex is located, showing green and red retrogradely labeled cells. Calibration bars: 2 mm **(A,C)** and 1 mm **(B)**. Based on Bajo et al. (2007).

Layer V neurons are not the only cortical cells involved in the projection (Künzle, 1995; Doucet et al., 2003; Bajo and Moore, 2005; Schofield, 2009). When large tracer injections are placed in the IC, layer VI cells can also be labeled in the auditory cortex ipsilateral to the injection site (**Figure 1B**, arrows). Those labeled neurons located close to the border of the layer with the white matter (wm) are smaller than layer V projection neurons, and are not always pyramidal with some having an elongated soma often orientated parallel to the layers (Schofield, 2009). Although layer VI corticocollicular neurons are much less numerous than those found in layer V, they comprise about 10% of the population projecting to the ipsilateral IC and have a similar distribution across different cortical fields independent of the location of the injection site in the IC, except that very few are labeled by injections in the CNIC (Schofield, 2009).

The influence that layer V pyramidal cells exert on IC neurons may be very different from that of layer VI cells. Cortical layer V is both necessary and sufficient to produce synchronous cortical activity (Silva et al., 1991) and morphological evidence suggests that layer V projection neurons might correspond to the intrinsic bursting (IB) cells described by Hefti and Smith (2000) in the auditory cortex. They proposed that IB cells may be well-suited to generate synchronized bursts of activity that match the frequency of cortical oscillations and it has also been hypothesized that bursting cells may be particularly important for information processing (Lisman, 1997). The possibility that regular spiking (RS) neurons in layer V also contribute to the corticocollicular projection, providing less robust but more specific information about sensory stimuli, has also been put forward (Bajo and Moore, 2005) on the basis of morphological similarities between the neurons projecting selectively to the CNIC in the gerbil and the RS cells described in rat auditory cortex (Hefti and Smith, 2000). Less clear is the role played by layer VI

cells that project to the IC due to the morphological variety of the cortical cells involved and the absence of further functional studies.

All auditory cortical fields are thought to participate in the corticocollicular projection (Winer et al., 1998). The primary areas of the auditory cortex most heavily target the IC, whereas non-primary areas project mainly to tegmental areas and the superior colliculus (SC). For example, in the ferret, injections of fluorescent microbeads in the IC (**Figures 3A,B**) label cells that are located mainly in the middle ectosylvian gyrus (MEG, **Figure 3C**), where the primary areas, A1, and the anterior auditory field, AAF, are located. In contrast, when tracer injections are placed in the SC, labeled cells are more prominent in the posterior and anterior regions of the gyrus (Bajo et al., 2010b) where secondary and association cortical areas are located (Bizley et al., 2005).

Neurons projecting to the IC are segregated within A1, with different cortical regions targeting different locations in the dorsomedial region of the IC. In rats, Saldaña et al. (1996) have shown that the location of the terminal fields in the dorsal cortex of the IC (DCIC) and the CNIC changes from dorsolateral to ventromedial as the cortical injection sites are placed more anterior in Te1 (corresponding to A1), and according to the well-described tonotopic arrangement in both structures.

The corticocollicular projection is predominantly ipsilateral, but about 15% of the neurons comprising this pathway terminate in the contralateral IC (Bajo et al., 2010a), and these cells originate only in layer V (Schofield, 2009). Although neurons that project ipsi- or contralaterally are intermingled throughout the auditory cortex, only a small proportion project to both sides (**Figure 2**). After injecting tracers in each IC, Coomes et al. (2005) found a small number of double labeled cells, and these formed a much larger proportion (up to 80%) of the weaker contralateral projection than of the corticollicular neurons on the ipsilateral side (6%) (**Figure 2**, arrows).

SEGREGATION OF THE CORTICOFUGAL INPUT: DO SUBCORTICAL AUDITORY NEURONS RECEIVE A COMMON INPUT?

Given that the corticofugal pathway links the cerebral cortex with many auditory structures, including the medial geniculate body (MGB), IC, superior olivary complex (SOC), cochlear nuclei (CN), sagulum, and the paralemniscal regions [reviewed in Winer (2007); Malmierca and Ryugo (2010)], an important question is whether individual cortical neurons target more than one subcortical region via long-range collaterals or whether these projections are segregated. This will determine whether descending corticofugal influences selectively affect specific subcortical regions or have a more general influence on subcortical processing.

Although not all combinations have been studied, the evidence currently available [reviewed in Lee et al. (2011)] indicates that less than 10% of corticofugal neurons with long-branching axons innervate multiple nuclei. Regarding the corticocollicular cells, no neurons have been found that target both the IC and the MGB (Wong and Kelly, 1981), but neurons projecting to both the IC and either the caudal striatum (Moriizumi and Hattori, 1991), SOC, or CN (Doucet et al., 2003) have been described.

It therefore appears that the auditory cortex modulates thalamic, midbrain, and brainstem neurons via a set of parallel channels that largely originate from different cortical cells. However, there are technical limitations in studying long-range collaterals. With anterograde tracers, it is difficult to follow individual axons for long distances and visualize terminal fields in regions that are far apart. Injecting different combinations of retrograde tracers into corticofugal target structures can be used to visualize double or triple labeled cells bodies in the cortex (Schofield et al., 2007), but this approach tends to underestimate the size of these projections because the injection sites rarely cover the full extent of the structures in question.

Physiological studies combining stimulation of layer V projection neurons with simultaneous recordings from each IC or from the IC and other brainstem nuclei provide an alternative method for investigating the extent to which these pathways are divergent, but this approach has so far been limited to examining corticofugal inputs to individual target nuclei. In addition to the presence of some collateral projections to multiple targets, it is possible that nearby cortical output cells connected by profuse local axonal branching (Lee et al., 2011), and therefore sharing common properties, may modulate auditory and non-auditory neurons located in different thalamic, midbrain, and brainstem regions.

Schofield (2010) has recently proposed that corticofugal projections from layer V form two general patterns with potentially different functions. In most cases, these projections have single subcortical targets, consistent with descending influences operating via independent, parallel projections. The minority of cortical neurons with divergent projections to multiple targets presumably exert more widespread influences on subcortical processing of auditory signals.

TERMINAL FIELDS IN THE INFERIOR COLLICULUS: DIFFERENT IC SUBDIVISIONS

Evidence for the existence of a corticocollicular projection was actually provided using anterograde tracing techniques before the cortical projection neurons had themselves been characterized. In fact, the use of the axon degeneration technique led to the first observation of degenerating fibers in the monkey midbrain after lesions had been made in the temporal cortex (Thompson, 1901). Later Diamond et al. (1969) used the degeneration method of Nauta and Gygax to reveal the presence of this projection in cats and established its key features, which are now known to apply across different species. First, all fields of the auditory cortex send fibers to the IC bilaterally, although more sparsely on the contralateral side. Second, the corticocollicular pathway targets the three IC subdivisions, with CNIC receiving the smallest input. Third, corticocollicular fibers in the CNIC are oriented in parallel laminae.

With these methods, however, it was difficult to demonstrate that the degenerated fibers observed actually terminate in the IC itself, but this was subsequently confirmed using different anterograde neural tracers in a large variety of mammals (tamarin, Luethke et al., 1989; squirrel monkey, Fitzpatrick and Imig, 1978; cat, Andersen et al., 1980; Winer et al., 1998; ferret, Bajo et al., 2007; rat, Coleman and Clerici, 1987; Herrera

et al., 1994; Saldaña et al., 1996; gerbil, Budinger et al., 2000). An example of cortical terminal fields in the IC is shown in **Figure 4**. In this case, a large rhodamine injection was made in ferret A1 (**Figure 4A**), which produced a symmetrical pattern of terminal labeling in each IC. As expected, the ipsilateral IC was most heavily labeled (**Figure 4E**). Cortical axons mainly innervated the dorsomedial region of the IC, with terminal fields more profuse in the DCIC than in the dorsal part of the CNIC. The labeled axons in the CNIC were also thinner and their terminals smaller, with lower bouton density, than those in the DCIC (**Figures 4C,D**). In the lateral cortex (LCIC) of this animal, a network of fibers was observed with many terminals and *en passant* boutons (**Figure 4B**).

The corticocollicular pathway has been described most extensively with anterograde tracers in the cat by Winer et al. (1998), who made tracer injections in each of 12 auditory or auditory-related cortical fields. They defined the corticocollicular pathway as a divergent and convergent system, with individual cortical areas projecting to several IC subdivisions and each IC subdivision receiving convergent inputs from multiple cortical fields. In addition, they stressed the importance of the primary cortical areas in this projection, the fact that corticocollicular axons mainly target IC regions that receive less ascending input, and raised the possibility that at least two parallel cortical systems may exist that target the IC cortices and CNIC independently.

Only two studies have analyzed the corticollicular terminals at an ultrastructural level. Jones and Rockel (1973) examined degenerated boutons in the IC of cats in which cortical lesions had been made, while Saldaña et al. (1996) labeled terminal boutons in the rat IC after making biotinylated dextran amine injections in A1 (**Figure 5**). Labeled boutons in every IC subdivision contained round synaptic vesicles and made asymmetric synaptic contacts (**Figure 5**, arrows), which are generally thought to be features of excitatory synapses (Peters et al., 1991). This is consistent with evidence for the glutamatergic nature of this projection as demonstrated by a decrease in D-aspartate release in the different IC subdivisions following auditory cortex ablation (Feliciano and Potashner, 1995). Corticocollicular fibers synapse mainly on distal dendritic profiles, including dendritic spines, with few contacts on cell bodies or large dendrites (Saldaña et al., 1996).

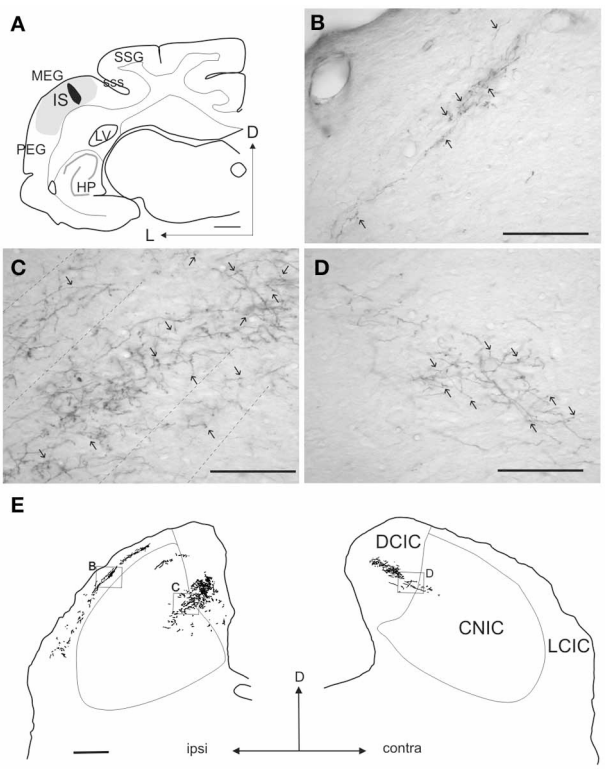

FIGURE 4 | Terminal fields in the IC after a tracer injection in the ferret auditory cortex. (A) Coronal section at the level of the left auditory cortex showing the location of a rhodamine injection site in the center of the MEG where A1 is located. The halo of the injection site is shown in gray while the center is in black. **(B–D)** Examples of anterograde terminal fields in the IC at the locations indicated by the boxes in **(E)**. Calibration bars: 1 mm **(A)**, 100 μm **(B–D)**, 0.5 mm **(E)**. Modified with permission from Bajo et al. (2007).

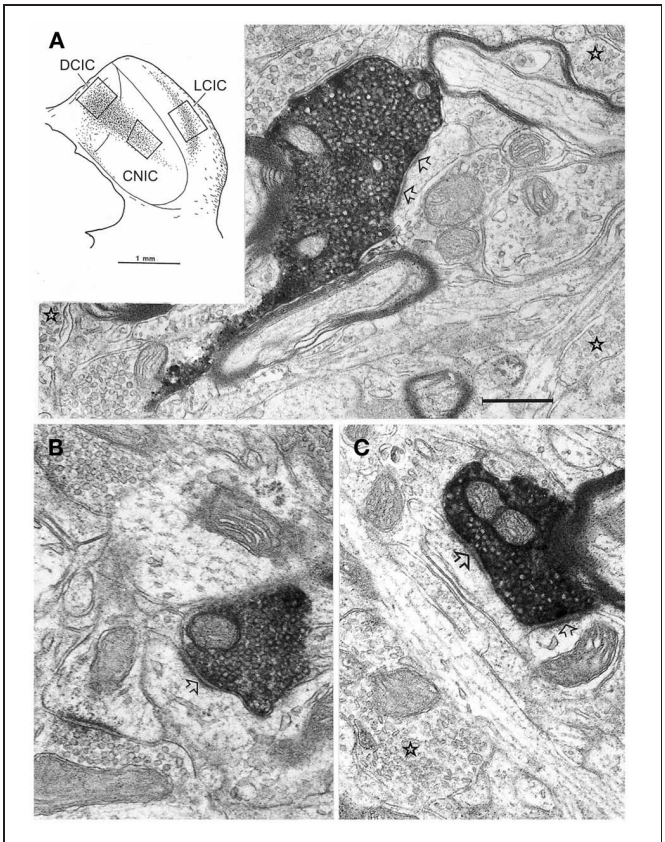

FIGURE 5 | Electron micrographs of labeled endings in the three main subdivisions of the IC after a large injection of biotinylated dextran amine was made in the ipsilateral primary auditory cortex in the rat. Labeled terminals in DCIC **(A)**, CNIC **(B)**, and LCIC **(C)** contain round vesicles and make asymmetric synaptic contacts (arrows). Unlabeled terminals with pleomorphic vesicles are also observed (stars). Inset in panel **(A)** shows the distribution of corticocollicular terminal fields and the areas (the box in each IC subdivision) that were used for electron microscopy. Calibration bar: 0.4 μm. Modified with permission from Saldaña et al. (1996).

Although these morphologic features suggest that corticocollicular axons may be non-driving, electrical stimulation of A1 has been found to evoke short latency (1.0–1.4 ms) excitatory responses and longer latency IPSPs in IC neurons (Massopust and Ordy, 1962; Mitani et al., 1983). This is more consistent with a strong driving input from the cortex, although EPSPs with longer latencies can also be evoked, mainly in the CNIC, suggesting a polysynaptic pathway and/or more diffuse influence. Cortical axons have a direct excitatory effect on ascending colliculogeniculate neurons as well as an indirect inhibitory effect via GABAergic collicular interneurons (Mitani et al., 1983).

TOPOGRAPHIC ORGANIZATION OF CORTICOCOLLICULAR INPUTS

In view of the physiological studies described in the next section, the corticocollicular projection to the CNIC deserves particular attention. The magnitude of this pathway has been a matter of controversy for several years, and it is possible that species differences may exist. On the other hand, variations in the results reported may be more a consequence of differences in the techniques used in these studies and the difficulty in interpreting negative results in tracing experiments.

Anterograde tracing studies have shown that the location of the terminal fields in the CNIC varies topographically with the location of the injection sites in A1 (Saldaña et al., 1996; Bajo et al., 2007). For example, Bajo et al. (2007) found that injecting tracers at two distinct locations in ferret A1, where neurons were tuned to different frequencies, produced two distinct bands of labeling in the CNIC, suggesting that the A1-CNIC projection links neurons in both structures with similar frequency tuning. This has been confirmed physiologically in the guinea pig by positioning multi-site probes along the tonotopic axes of A1 and the CNIC (Lim and Anderson, 2007). After electrically stimulating different locations in the CNIC, these authors recorded antidromic-evoked activity in A1 locations with matching best frequencies (**Figure 6**). By linking neurons with common sound frequency preferences, this topographic projection provides an anatomical substrate for corticofugal modulation of IC neurons with related receptive field properties.

CORTICOFUGAL MODULATION OF AUDITORY PROCESSING IN THE INFERIOR COLLICULUS

Attempts to investigate the role of descending corticofugal projections in auditory processing have utilized two approaches

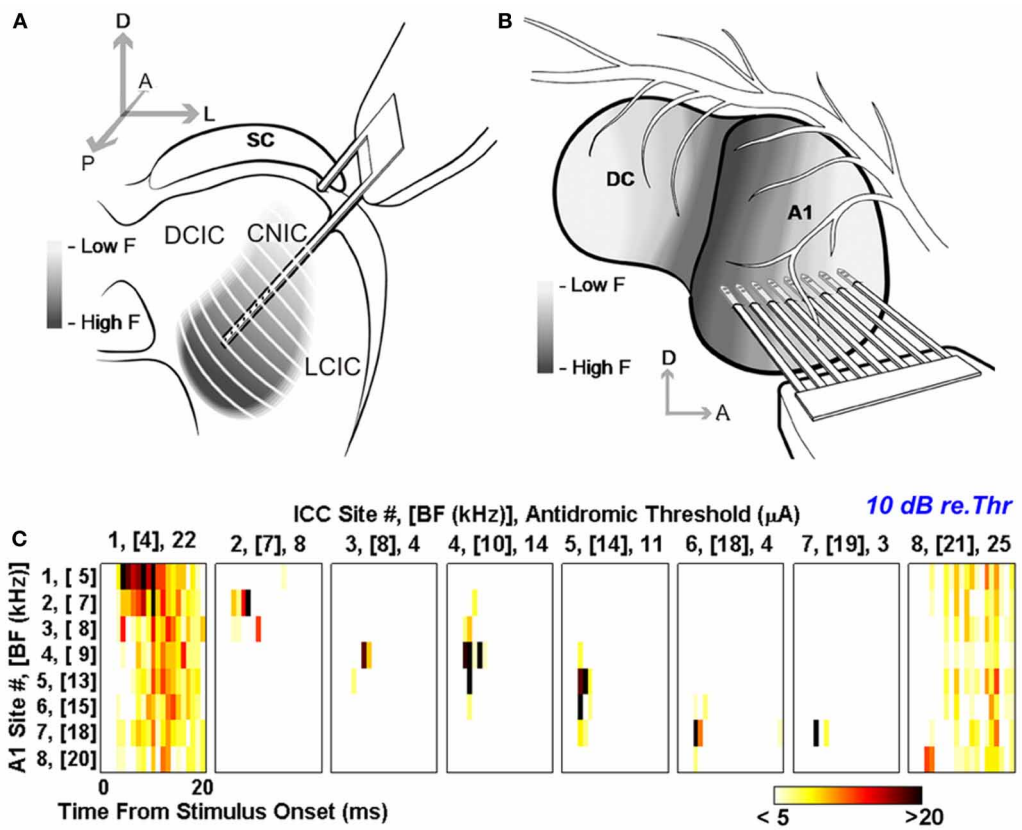

FIGURE 6 | Antidromic activation reveals tonotopically organized projections from A1 to the CNIC in guinea pig. Multi-site probes were positioned along the tonotopic axis of the guinea pig CNIC **(A)** and A1 **(B)**. **(C)** Post-stimulus time histograms (PSTHs) for eight A1 locations with different best frequencies (BF) from low (location 1) to high (location 8). These responses were evoked by antidromic stimulation equivalent to 10 dB above threshold at eight frequency-matched locations in the IC. Color scale corresponds to the total number of spikes across 40 trials where any values ≤5 and ≥20 were set to white and black, respectively. Modified with permission from Lim and Anderson (2007).

[reviewed in Suga (2012)]. First, effects on the response properties of subcortical neurons have been examined following focal electrical stimulation of A1. Second, the complementary approach of inactivating the cortex, either locally or globally, has been used in an attempt to remove the influence of descending projections. In most cases, electrophysiological recordings have been carried out to examine whether such manipulations of cortical activity result in transient changes in the response properties of subcortical neurons. Cortical inactivation has also been used to determine the extent to which the effects on subcortical processing of activating other brain areas, such as the nucleus basalis in the basal forebrain, are mediated via cortical circuits.

These studies have provided considerable evidence that corticofugal inputs make an important contribution to the response properties of neurons at multiple subcortical levels. In the IC, neuronal sensitivity to sound frequency (Ma and Suga, 2001a; Yan et al., 2005), intensity (Yan and Ehret, 2002), duration (Ma and Suga, 2001b), and location (Zhou and Jen, 2005; Nakamoto et al., 2008) changes after manipulating activity in A1 (**Figures 7**, **8**). Thus, the descending system can shape the way midbrain neurons respond to stimulus attributes, such as sound frequency or intensity, which are initially encoded in the cochlea, as well as those that rely on central processing, like sound source location. This suggests that cortical feedback is likely to influence the representation of multiple sound features in the midbrain, implying widespread effects on auditory perception. Recent research also suggests that the auditory cortex modulates collicular processing of simultaneously presented harmonic complexes, suggesting a possible role for descending projections in segregating different sound sources (Nakamoto et al., 2010).

The nature of the changes evoked by focal cortical stimulation or inactivation depends on the similarity between the response properties of the neurons in the cortex and the midbrain (Yan and Suga, 1998; Ma and Suga, 2001b; Yan and Ehret, 2002; Jen and Zhou, 2003; Yan et al., 2005; Zhou and Jen, 2005). For example, if IC neurons are tuned to the same frequency as the cortical neurons recorded at the site of the stimulating electrode, their best frequencies remain the same after the cortex is activated and, in some studies, their frequency tuning is sharpened [reviewed by Suga (2012)]. By contrast, if the neurons are tuned to different frequencies, the best frequencies of the IC neurons are typically shifted toward those of the activated cortical neurons (**Figure 7**). In a similar vein, the magnitude of the changes induced in the minimum thresholds, dynamic ranges and both the sound duration and azimuth tuning of IC neurons varies with how closely their response properties are matched to those of the neurons activated in the cortex (Suga, 2012).

The dependence of these effects on the relative frequency preferences of the neurons is consistent with the topographic nature of the corticocollicular pathway. Modulation of IC response properties appears to involve a combination of cortically evoked facilitation of the responses of IC neurons that have corresponding tuning properties and inhibition in unmatched neurons. Consequently, these descending inputs provide a route by which localized increases in cortical activity can selectively enhance auditory processing in specific regions of the IC. This, in turn, will presumably provide stronger input via the thalamus to that part of cortex, further modulating the representation of potentially important stimuli at higher levels of the auditory system.

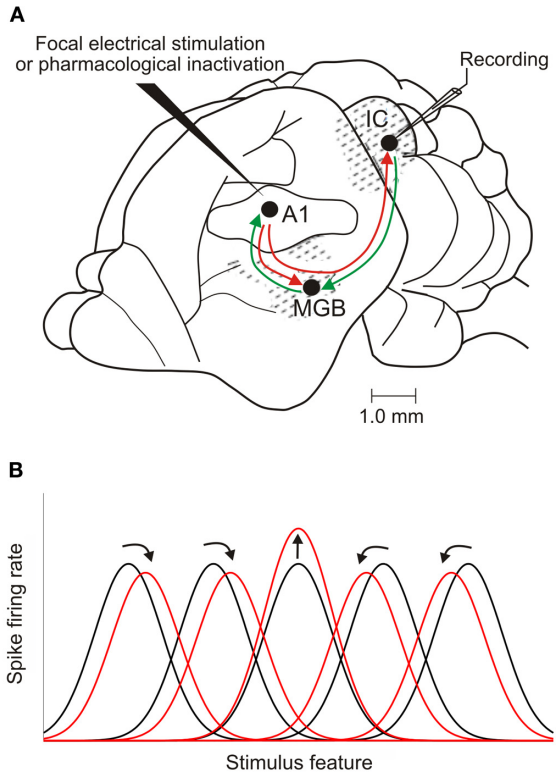

FIGURE 7 | Corticofugal modulation of IC response properties. **(A)** Lateral view of the brain of a mustached bat, one of the species used most in cortical stimulation and inactivation experiments. The auditory cortex has reciprocal ascending and descending connections with the medial geniculate body (MGB) in the thalamus. It also sends a descending projection to the IC, which, in turn, projects to the MGB. **(B)** Focal electrical stimulation in the cortex results in facilitation of the responses of IC neurons that have tuning properties matched to those of cortical neurons at the site of the stimulating electrode. The tuning of unmatched IC neurons may shift toward that of the stimulated cortical neurons (as illustrated here), resulting in an expanded representation of the stimulus feature. Shifts in tuning away from that of the stimulated cortical neurons have also been described, compressing the midbrain representation. Adapted with permission from Suga (2012).

Most studies have focused on the effects of electrically stimulating or inactivating neurons in A1, although Yan and Suga (1996) also examined the influence of descending inputs originating in the frequency modulation-frequency modulation (FM-FM or FF) cortical area of the mustached bat on the sensitivity of IC neurons to biosonar pulse-echo combinations. Similarly, although all subdivisions of the IC receive descending cortical inputs, the recording studies appear to have been restricted mainly to the CNIC. Given that corticocollicular inputs primarily target other regions of the IC, it seems likely that the changes recorded in the response properties of CNIC neurons are mediated, at least in part, via polysynaptic pathways involving the DCIC or LCIC.

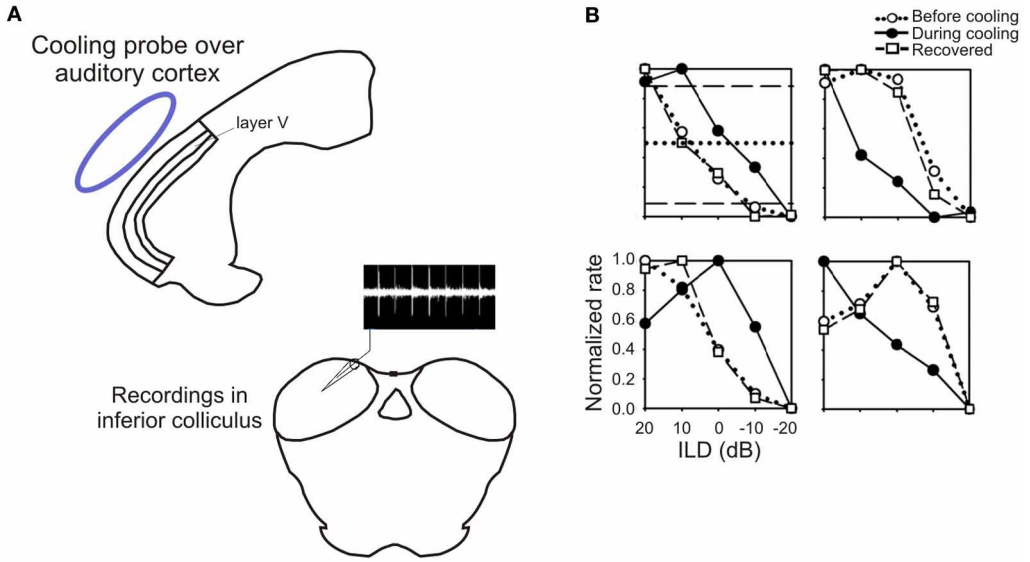

FIGURE 8 | Inactivation of the auditory cortex alters sensitivity to interaural level differences (ILD) in the inferior colliculus. (A) Schematic of the experimental setup, showing a cooling probe (blue) above the auditory cortex and a recording electrode in the ipsilateral IC. **(B)** Examples of rate-ILD functions obtained before, during and after cortical inactivation. Adapted with permission from Nakamoto et al. (2008).

CORTICOFUGAL MODULATION AND AUDITORY PLASTICITY

The changes induced in the response properties of IC neurons following local manipulation of cortical activity have been reported to last for periods ranging from a few seconds to several hours (e.g., Zhang and Suga, 2000; Zhou and Jen, 2005). Corticofugal projections may therefore contribute to the selective processing of sounds that acquire behavioral significance as a result of learning. For example, combining tones of a particular frequency with a mild electric shock causes the best frequencies of A1 neurons to undergo a relatively long-lasting shift toward that value (Bakin and Weinberger, 1990; Weinberger et al., 1993). Training-induced improvements in sound discrimination are also accompanied by plasticity in the response properties of A1 neurons (e.g., Polley et al., 2006; Schnupp et al., 2006). Whether perceptual learning results in comparable changes at subcortical levels as a result of corticofugal feedback is unknown, but the experience-dependent plasticity produced by auditory fear conditioning is seen not only in the cortex, but also subcortically in both the thalamus (Edeline and Weinberger, 1991) and IC (Gao and Suga, 1998). This shift in best frequencies in the IC closely resembles that evoked by cortical electrical stimulation and is abolished by global inactivation of A1, indicating that it is mediated by corticocollicular feedback (Gao and Suga, 1998).

An involvement of the corticofugal system in representational plasticity in the auditory system has also been demonstrated by studies in which behavioral salience is simulated by electrical stimulation of the nucleus basalis, the region of the cholinergic basal forebrain that projects to the neocortex (Casamenti et al., 1986; Rasmusson et al., 1992). The resulting release of acetylcholine facilitates auditory thalamocortical synaptic transmission and increases cortical excitability (Metherate and Ashe, 1993). Stimulus-specific changes in cortical receptive fields are produced by pairing electrical stimulation of the nucleus basalis with sound presentation, which are very similar to those seen after behavioral training (Bakin and Weinberger, 1996; Kilgard and Merzenich, 1998; Yan and Zhang, 2005). Thus, neuronal best frequencies are shifted toward those of the paired stimuli. This pairing paradigm also induces shifts in the best frequencies of IC neurons, which are dependent on activity in the auditory cortex (Zhang et al., 2005), providing further evidence for the role of corticofugal descending connections in experience-dependent plasticity.

Although studies utilizing either electrical stimulation or inactivation of A1 have provided valuable insights into the influence of corticofugal projections on the response properties of neurons in other brain regions, these methods are not particularly selective. Thus, related changes in the auditory responses and tuning properties of neurons have been reported at multiple levels of the auditory pathway, including both the thalamus and cochlear nucleus, as well as neighboring regions of the cortex [reviewed by Suga (2012)]. The extent to which the changes observed in the IC following manipulation of A1 activity represent direct effects of corticocollicular modulation or the indirect involvement of other areas that provide inputs to the IC remains unclear. More importantly, none of the studies considered so far has examined the behavioral consequences of activating or deactivating the corticocollicular projection, and so the function of this descending pathway in auditory processing remains unclear.

To address this question, Bajo et al. (2010a) used a chromophore-targeted neuronal degeneration technique to investigate the behavioral effects in ferrets of selectively eliminating layer V pyramidal cells in the primary auditory cortical areas that project to the IC (**Figure 9**). This involved retrogradely labeling corticocollicular projection neurons by injecting fluorescent

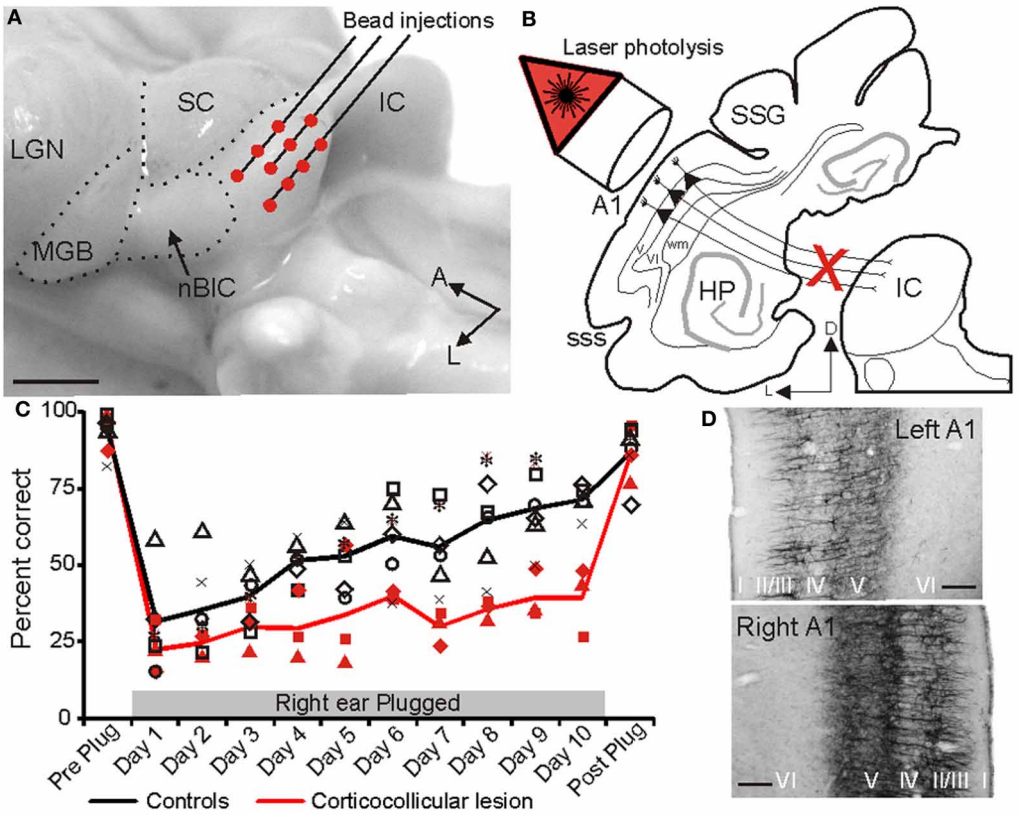

FIGURE 9 | The projection from the auditory cortex to the inferior colliculus is essential for training-induced plasticity of spatial hearing in adult ferrets. (A) Lateral view of the ferret midbrain showing the location and number of injections of fluorescent microspheres conjugated with chlorine e_6 in the left IC. **(B)** Schematic showing the selective ablation of retrogradely labeled layer V corticocollicular neurons by illumination of the ipsilateral auditory cortex with near-infrared light. **(C)** Sound localization accuracy (averaged across 12 speaker locations in the horizontal plane) before the right ear was plugged (Preplug), on each of the 10 days over which an ear plug was worn and following its removal (Post-plug). Data from control animals are shown in black and from the ferrets with corticocollicular lesions in red. The symbols represent different animals and the lines show the mean scores. **(D)** Staining with the SMI_{32} antibody, a marker of layer III and layer V pyramidal cortical neurons, was sparser in the left (lesioned) primary auditory cortex, resulting in a less distinct bilaminar appearance (top) than on the right side (bottom). Calibration bars: 2 mm in **(A)** and 0.1 mm in **(D)**. Modified with permission from Bajo et al. (2010a).

microbeads conjugated with chlorine e_6 in the IC on one side of the brain, and subsequently illuminating the ipsilateral auditory cortex with near-infrared light. This resulted in a loss of about two thirds of the A1 neurons that project to the IC, without affecting those in surrounding cortical areas. As previously discussed, most corticocollicular axons target the ipsilateral IC, so this approach allowed an assessment of the effects of removing descending axons predominantly on one side of the brain only.

Given that cortical electrical stimulation (Zhou and Jen, 2005) or inactivation (Nakamoto et al., 2008; **Figure 8**) alters the spatial response properties of IC neurons, Bajo et al. (2010a) examined the effects of eliminating corticocollicular neurons on auditory localization and its recalibration by experience. Although they observed no change in sound localization accuracy, the training-induced plasticity that normally occurs in adult ferrets after disrupting the available spatial cues by occluding one ear was severely impaired (**Figure 9C**). Thus, while control animals recover their ability to localize sounds accurately despite the continued presence of a plug in one ear, this was not the case in ferrets in which the corticocollicular projection had been largely removed, suggesting that descending pathways are essential for recalibration of the brain's representation of auditory space. This learning deficit was most pronounced in the hemifield contralateral to the lesioned pathway, implying that corticofugal modulation of each IC mediates plasticity in the opposite hemifield.

What information the auditory cortex provides to IC neurons via these descending projections to allow auditory spatial learning to take place is presently unknown. One mechanism for adapting to the presence of an earplug in one ear would be to adjust the sensitivity of auditory neurons to binaural localization cues. Recent studies have shown that the sensitivity of IC neurons to interaural level differences (ILDs; Dahmen et al., 2010) and interaural time differences (ITDs; Maier et al., 2012) can change following short-term adaptation to stimulus statistics, and, as previously illustrated (**Figure 8**), cortical cooling can produce pronounced alterations in collicular firing-rate-ILD

functions. Behavioral evidence, however, suggests that adaptation to a conductive hearing loss in one ear takes place by learning to reweight different localization cues in favor of the monaural spectral localization cues provided by the non-occluded ear rather than by remapping the altered binaural cues (Kacelnik et al., 2006; Kumpik et al., 2010). It has been shown that individual IC neurons can carry information about ILDs, ITDs, and spectral cues using different neural coding strategies (Chase and Young, 2008), suggesting that corticofugal modulation of specific aspects of their spike discharge patterns could change the contribution of each cue to the output of the neurons and therefore to the perception of sound source location.

The corticocollicular projection is, however, unlikely to work is isolation in mediating the experience-dependent plasticity of spatial coding. Thus, behavioral adaptation by adult ferrets to a unilateral earplug is also impaired following midline lesions of the olivocochlear bundle (Irving et al., 2011), which originates in the superior olivary complex where sensitivity to binaural cues is first derived. This suggests that activation of olivocochlear neurons, which are in turn innervated by the IC (Vetter et al., 1993), could produce a frequency-specific adjustment in cochlear output, potentially altering the localization cue sensitivity of neurons at higher levels of the auditory pathway. These findings again highlight the influence of descending pathways at multiple levels of the auditory pathway and the difficulty in isolating the functions of specific projections.

CONCLUDING REMARKS

It is becoming increasingly clear that the descending projections found throughout the auditory pathway can have a considerable impact on stimulus processing. This has been demonstrated most clearly for the projection from the auditory cortex to the IC, which is now known to be part of the circuitry responsible for the plasticity and learning observed in the adult brain. Thus, experience-dependent changes in the receptive field properties of cortical neurons that result from classical conditioning or behavioral training can, in turn, trigger a reorganization of subcortical processing. Furthermore, there is growing evidence from studies in which auditory brainstem responses to complex sounds have been recorded in humans that language (Krishnan et al., 2005), musical experience (Kraus and Chandrasekaran, 2010), and auditory training (Carcagno and Plack, 2011; Song et al., 2012) can all modify subcortical processing. This is again thought to reflect the corticofugal modulation of neural processing at subcortical levels, and the IC in particular, where the relevant stimulus features are represented most precisely. Consequently, the plasticity in neuronal response properties that underlies a change in perceptual skills may actually occur subcortically, which, in turn, will alter the information delivered to the cortex.

Although electrical stimulation and inactivation studies have shown that the auditory cortex can facilitate or inhibit the responses of IC neurons according to how well-matched their response properties are, we still know relatively little about how corticofugal modulatory effects are mediated or the relationship between these signals and other inputs to the IC. Because of its pivotal position within the auditory pathway as a site of convergence of bottom up signals from multiple brainstem areas, descending inputs to the IC are likely to play a particularly important role in auditory processing. Nevertheless, the corticocollicular projection is only one of several descending pathways in the auditory system. If we are to understand the role of these circuits, it will be necessary to make greater use of cutting edge techniques for imaging and selectively manipulating the activity of specific cell types and their projections during behavior.

ACKNOWLEDGMENTS

Our research is supported by the Wellcome Trust through a Principal Research Fellowship (WT07650AIA) to Andrew J. King, and by Action on Hearing Loss and Deafness Research UK.

REFERENCES

Aitkin, L. M., and Phillips, S. C. (1984). Is the inferior colliculus an obligatory relay in the cat auditory system? *Neurosci. Lett.* 44, 259–264.

Andersen, R. A., Snyder, R. L., and Merzenich, M. M. (1980). The topographic organization of corticocollicular projections from physiologically identified loci in the AI, AII, and anterior auditory cortical fields of the cat. *J. Comp. Neurol.* 191, 479–494.

Bajo, V. M., and Moore, D. R. (2005). Descending projections from the auditory cortex to the inferior colliculus in the gerbil, *Meriones unguiculatus*. *J. Comp. Neurol.* 486, 101–116.

Bajo, V. M., Nodal, F. R., Bizley, J. K., Moore, D. R., and King, A. J. (2007). The ferret auditory cortex: descending projections to the inferior colliculus. *Cereb. Cortex* 17, 475–491.

Bajo, V. M., Nodal, F. R., Moore, D. R., and King, A. J. (2010a). The descending corticocollicular pathway mediates learning-induced auditory plasticity. *Nat. Neurosci.* 13, 253–260.

Bajo, V. M., Nodal, F. R., Bizley, J. K., and King, A. J. (2010b). The non-lemniscal auditory cortex in ferrets: convergence of corticotectal inputs in the superior colliculus. *Front. Neuroanat.* 4:18. doi: 10.3389/fnana.2010.00018

Bakin, J. S., and Weinberger, N. M. (1990). Classical conditioning induces CS-specific receptive field plasticity in the auditory cortex of the guinea pig. *Brain Res.* 536, 271–286.

Bakin, J. S., and Weinberger, N. M. (1996). Induction of a physiological memory in the cerebral cortex by stimulation of the nucleus basalis. *Proc. Natl. Acad. Sci. U.S.A.* 93, 11219–11224.

Beyerl, B. D. (1978). Afferent projections to the central nucleus of the inferior colliculus in the rat. *Brain Res.* 145, 209–223.

Bizley, J. K., Nodal, F. R., Nelken, I., and King, A. J. (2005). Functional organization of ferret auditory cortex. *Cereb. Cortex* 15, 1637–1653.

Budinger, E., Heil, P., and Scheich, H. (2000). Functional organization of auditory cortex in the mongolian gerbil (*Meriones unguiculatus*). IV. Connections with anatomically characterized subcortical structures. *Eur. J. Neurosci.* 12, 2452–2474.

Carcagno, S., and Plack, C. J. (2011). Subcortical plasticity following perceptual learning in a pitch discrimination task. *J. Assoc. Res. Otolaryngol.* 12, 89–100.

Casamenti, F., Deffenu, G., Abbamondi, A. L., and Pepeu, G. (1986). Changes in cortical acetylcholine output induced by modulation of the nucleus basalis. *Brain Res. Bull.* 16, 689–695.

Chase, S. M., and Young, E. D. (2008). Cues for sound localization are encoded in multiple aspects of spike trains in the inferior colliculus. *J. Neurophysiol.* 99, 1672–1682.

Coleman, J. R., and Clerici, W. J. (1987). Sources of projections to subdivisions of the inferior colliculus in the rat. *J. Comp. Neurol.* 262, 215–226.

Coomes, D. L., Schofield, R. M., and Schofield, B. R. (2005). Unilateral and bilateral projections from cortical cells to the inferior colliculus in guinea pigs. *Brain Res.* 1042, 62–72.

Dahmen, J. C., Keating, P., Nodal, F. R., Schulz, A. L., and King, A. J. (2010). Adaptation to stimulus statistics in the perception and neural representation of auditory space. *Neuron* 66, 937–948.

Diamond, I. T., Jones, E. G., and Powell, T. P. (1969). The projection of the auditory cortex upon the diencephalon and brain stem in the cat. *Brain Res.* 15, 305–340.

Doucet, J. R., Molavi, D. L., and Ryugo, D. K. (2003). The source of corticocollicular and corticobulbar projections in area Te1 of the rat. *Exp. Brain Res.* 153, 461–466.

Druga, R., and Syka, J. (1984). Ascending and descending projections to the inferior colliculus in the rat. *Physiol. Bohermoslov.* 33, 31–42.

Edeline, J. M., and Weinberger, N. M. (1991). Subcortical adaptive filtering in the auditory system: associative receptive field plasticity in the dorsal medial geniculate body. *Behav. Neurosci.* 105, 154–175.

Feliciano, M., and Potashner, S. J. (1995). Evidence for a glutamatergic pathway from the guinea pig auditory cortex to the inferior colliculus. *J. Neurochem.* 65, 1348–1357.

Fitzpatrick, K. A., and Imig, T. J. (1978). Projections of auditory cortex upon the thalamus and midbrain in the owl monkey. *J. Comp. Neurol.* 177, 537–555.

Games, K. D., and Winer, J. A. (1988). Layer V in rat auditory cortex: projections to the inferior colliculus and contralateral cortex. *Hear. Res.* 34, 1–26.

Gao, E., and Suga, N. (1998). Experience-dependent corticofugal adjustment of midbrain frequency map in bat auditory system. *Proc. Natl. Acad. Sci. U.S.A.* 95, 12663–12670.

Hefti, B. J., and Smith, P. H. (2000). Anatomy, physiology, and synaptic responses of rat layer V auditory cortical cells and effects of $GABA_A$ blockade. *J. Neurophysiol.* 83, 2626–2638.

Herbert, H., Aschoff, A., and Ostwald, J. (1991). Topography of projections from the auditory cortex to the inferior colliculus in the rat. *J. Comp. Neurol.* 304, 103–322.

Herrera, M., Hurtado-García, J. F., Collía, F., and Lanciego, J. (1994). Projections from the primary auditory cortex onto the dorsal cortex of the inferior colliculus in albino rats. *Arch. Ital. Biol.* 132, 147–164.

Irving, S., Moore, D. R., Liberman, M. C., and Sumner, C. J. (2011). Olivocochlear efferent control in sound localization and experience-dependent learning. *J. Neurosci.* 31, 2493–2501.

Jen, P. H., and Zhou, X. (2003). Corticofugal modulation of amplitude domain processing in the midbrain of the big brown bat, *Eptesicus fuscus*. *Hear. Res.* 184, 91–106.

Jones, E. G., and Rockel, A. J. (1973). Observations on complex vesicles, neurofilamentous hyperplasia and increased electron density during terminal degeneration in the inferior colliculus. *J. Comp. Neurol.* 147, 93–118.

Kacelnik, O., Nodal, F. R., Parsons, C. H., and King, A. J. (2006). Training-induced plasticity of auditory localization in adult mammals. *PLoS Biol.* 4:e71. doi: 10.1371/journal.pbio.0040071

Kaneko, T., Urade, Y., Watanabe, Y., and Mizuno, N. (1987). Production, characterization, and immnohistochemical application of monoclonal antibodies to glutaminase purified from rat brain. *J. Neurosci.* 7, 302–309.

Kelly, J. P., and Wong, D. (1981). Laminar connections of the cat's auditory cortex. *Brain Res.* 212, 1–15.

Kilgard, M. P., and Merzenich, M. M. (1998). Cortical map reorganization enabled by nucleus basalis activity. *Science* 279, 1714–1718.

Kraus, N., and Chandrasekaran, B. (2010). Music training for the development of auditory skills. *Nat. Rev. Neurosci.* 11, 599–605.

Krishnan, A., Xu, Y., Gandour, J., and Cariani, P. (2005). Encoding of pitch in the human brainstem is sensitive to language experience. *Brain Res. Cogn. Brain Res.* 25, 161–168.

Kumpik, D. P., Kacelnik, O., and King, A. J. (2010). Adaptive reweighting of auditory localization cues in response to chronic unilateral earplugging in humans. *J. Neurosci.* 30, 4883–4894.

Künzle, H. (1995). Regional and laminar distribution of cortical neurons projecting to either superior or inferior colliculus in the hedgehog tenrec. *Cereb. Cortex* 5, 338–352.

Lee, C. C., Kishan, A. U., and Winer, J. A. (2011). Wiring of divergent networks in the central auditory system. *Front. Neuroanat.* 5:46. doi: 10.3389/fnana.2011.00046

Lim, H. H., and Anderson, D. J. (2007). Antidromic activation reveals tonotopically organized projections from primary auditory cortex to the central nucleus of the inferior colliculus in guinea pig. *J. Neurophysiol.* 97, 1413–1427.

Lisman, J. E. (1997). Bursts as a unit of neural information: making unreliable synapses reliable. *Trends Neurosci.* 20, 38–43.

Luethke, L. E., Krubitzer, L. A., and Kaas, J. H. (1989). Connections of primary auditory cortex in the new world monkey, *Sanguinus*. *J. Comp. Neurol.* 285, 487–513.

Ma, X., and Suga, N. (2001a). Plasticity of bat's central auditory system evoked by focal electric stimulation of auditory and/or somatosensory cortices. *J. Neurophysiol.* 85, 1078–1087.

Ma, X., and Suga, N. (2001b). Corticofugal modulation of duration-tuned neurons in the midbrain auditory nucleus in bats. *Proc. Natl. Acad. Sci. U.S.A.* 98, 14060–14065.

Maier, J. K., Hehrmann, P., Harper, N. S., Klump, G. M., Pressnitzer, D., and McAlpine, D. (2012). Adaptive coding is constrained to midline locations in a spatial listening task. *J. Neurophysiol.* 108, 1856–1868.

Malmierca, M. S., and Ryugo, D. K. (2010). "Descending connections of auditory cortex to the midbrain and brain stem," in *The Auditory Cortex,* eds J. A. Winer and C. E. Schreiner (New York, NY: Springer), 189–207.

Massopust, L. C., and Ordy, J. M. (1962). Auditory organization of the inferior colliculi in the cat. *Exp. Neurol.* 6, 465–477.

Metherate, R., and Ashe, J. H. (1993). Nucleus basalis stimulation facilitates thalamocortical synaptic transmission in the rat auditory cortex. *Synapse* 14, 132–143.

Mitani, A., Shimokouchi, M., and Nomura, S. (1983). Effects of stimulation of the primary auditory cortex upon colliculogeniculate neurons in the inferior colliculus of the cat. *Neurosci. Lett.* 42, 185–189.

Moriizumi, T., and Hattori, T. (1991). Pyramidal cells in rat temporoauditory cortex project to both striatum and inferior colliculus. *Brain Res. Bull.* 27, 141–144.

Nakamoto, K. T., Jones, S. J., and Palmer, A. R. (2008). Descending projections from auditory cortex modulate sensitivity in the midbrain to cues for spatial position. *J. Neurophysiol.* 99, 2347–2356.

Nakamoto, K. T., Shackleton, T. M., and Palmer, A. R. (2010). Responses in the inferior colliculus of the guinea pig to concurrent harmonic series and the effect of inactivation of descending controls. *J. Neurophysiol.* 103, 2050–2061.

Peters, A., Palay, S. L., and Webster, H. D. (1991). *The Fine Structure of the Nervous System: Neurons and Their Supporting Cells, 3rd Edn.* New York, NY: Oxford University Press.

Polley, D. B., Steinberg, E. E., and Merzenich, M. M. (2006). Perceptual learning directs auditory cortical map reorganization through top-down influences. *J. Neurosci.* 26, 4970–4982.

Rabinowitz, N. C., Willmore, B. D., Schnupp, J. W., and King, A. J. (2011). Contrast gain control in auditory cortex. *Neuron* 70, 1178–1191.

Rasmusson, D. D., Clow, K., and Szerb, J. C. (1992). Frequency-dependent increase in cortical acetylcholine release evoked by stimulation of the nucleus basalis magnocellularis in the rat. *Brain Res.* 594, 150–154.

Saldaña, E., Feliciano, M., and Mugnaini, E. (1996). Distribution of descending projections from primary auditory neocortex to inferior colliculus mimics the topography of intracollicular projections. *J. Comp. Neurol.* 371, 15–40.

Schnupp, J. W., Hall, T. M., Kokelaar, R. F., and Ahmed, B. (2006). Plasticity of temporal pattern codes for vocalization stimuli in primary auditory cortex. *J. Neurosci.* 26, 4785–4795.

Schofield, B. R. (2009). Projections to the inferior colliculus from layer VI cells of auditory cortex. *Neuroscience* 159, 246–258.

Schofield, B. R. (2010). "Structural organization of the descending auditory pathway," in *The Oxford Handbook of Auditory Neuroscience: The Auditory Brain*, eds A. Rees and A. R. Palmer (Oxford: Oxford University Press), 43–64.

Schofield, B. R., Schofield, R. M., Sorensen, K. A., and Motts, S. D. (2007). On the use of retrograde tracers for identification of axon collaterals with multiple fluorescent retrograde tracers. *Neuroscience* 146, 773–783.

Silva, L. R., Amitai, Y., and Connors, B. W. (1991). Intrinsic oscillations of neocortex generated by layer 5 pyramidal neurons. *Science* 251, 432–435.

Song, J. H., Skoe, E., Banai, K., and Kraus, N. (2012). Training to improve hearing speech in noise: biological mechanisms. *Cereb. Cortex* 22, 1180–1190.

Strutz, J. (1987). Anatomy of the central auditory pathway. Demonstration with horseradish peroxidase in the guinea pig. *HNO* 35, 407–415.

Suga, N. (2012). Tuning shifts of the auditory system by corticocortical and corticofugal projections and conditioning. *Neurosci. Biobehav. Rev.* 36, 969–988.

Thompson, W. H. (1901). Degenerations resulting from lesions of the cortex of the temporal lobe. *J. Anat. Physiol.* 35, 147–165.

Ulanovsky, N., Las, L., and Nelken, I. (2003). Processing of low-probability sounds by cortical neurons. *Nat. Neurosci.* 6, 391–398.

Vetter, D. E., Saldaña, E., and Mugnaini, E. (1993). Input from the inferior colliculus to medial olivocochlear neurons in the rat: a double label study with PHA-L and cholera toxin. *Hear. Res.* 70, 173–186.

Weinberger, N. M., Javid, R., and Lepan, B. (1993). Long-term retention of learning-induced receptive-field plasticity in the auditory cortex. *Proc. Natl. Acad. Sci. U.S.A.* 90, 2394–2398.

Winer, J. A. (2003). "Three systems of descending projections to the inferior colliculus," in *The Inferior Colliculus,* eds J. A. Winer and C. E. Schreiner (New York, NY: Springer), 231–247.

Winer, J. A. (2007). Decoding the auditory corticofugal systems. *Hear. Res.* 207, 1–9.

Winer, J. A., Chernock, M. L., Larue, D. T., and Cheung, S. W. (2002). Descending projections to the inferior colliculus from the posterior thalamus and the auditory cortex in rat, cat, and monkey. *Hear. Res.* 168, 181–195.

Winer, J. A., Larue, D. T., Diehl, J. J., and Hefti, B. J. (1998). Auditory cortical projections to the cat inferior colliculus. *J. Comp. Neurol.* 400, 147–174.

Winer, J. A., and Prieto, J. J. (2001). Layer V in cat primary auditory cortex (AI): cellular architecture and identification of projection neurons. *J. Comp. Neurol.* 434, 379–412.

Wong, D., and Kelly, J. P. (1981). Differentially projecting cells in individual layers of the auditory cortex: a double-labeling study. *Brain Res.* 230, 362–366.

Yan, J., and Ehret, G. (2002). Corticofugal modulation of midbrain sound processing in the house mouse. *Eur. J. Neurosci.* 16, 119–128.

Yan, W., and Suga, N. (1996). Corticofugal modulation of time-domain processing of biosonar information in bats. *Science* 273, 1100–1103.

Yan, W., and Suga, N. (1998). Corticofugal modulation of the midbrain frequency map in the bat auditory system. *Nat. Neurosci.* 1, 54–58.

Yan, J., and Zhang, Y. (2005). Sound-guided shaping of the receptive field in the mouse auditory cortex by basal forebrain activation. *Eur. J. Neurosci.* 21, 563–576.

Yan, J., Zhang, Y., and Ehret, G. (2005). Corticofugal shaping of frequency tuning curves in the central nucleus of the inferior colliculus of mice. *J. Neurophysiol.* 93, 71–83.

Zhang, Y., Hakes, J. J., Bonfield, S. P., and Yan, J. (2005). Corticofugal feedback for auditory midbrain plasticity elicited by tones and electrical stimulation of basal forebrain in mice. *Eur. J. Neurosci.* 22, 871–879.

Zhang, Y., and Suga, N. (2000). Modulation of responses and frequency tuning of thalamic and collicular neurons by cortical activation in mustached bats. *J. Neurophysiol.* 84, 325–333.

Zhou, X., and Jen, P. H. (2005). Corticofugal modulation of directional sensitivity in the midbrain of the big brown bat, *Eptesicus fuscus*. *Hear. Res.* 203, 201–215.

Conflict of Interest Statement: The authors declare that the research was conducted in the absence of any commercial or financial relationships that could be construed as a potential conflict of interest.

Received: 15 October 2012; accepted: 11 December 2012; published online: 03 January 2013.

Citation: Bajo VM and King AJ (2013) Cortical modulation of auditory processing in the midbrain. Front. Neural Circuits ***6****:114. doi: 10.3389/fncir.2012.00114*

frontiers in
NEURAL CIRCUITS

ORIGINAL RESEARCH ARTICLE
published: 14 December 2012
doi: 10.3389/fncir.2012.00100

Deactivation of the inferior colliculus by cooling demonstrates intercollicular modulation of neuronal activity

Llwyd D. Orton[1], Paul W. F. Poon[1,2] and Adrian Rees[1]*

[1] *Institute of Neuroscience, Faculty of Medical Sciences, Newcastle University, Newcastle upon Tyne, UK*
[2] *Department of Physiology, National Cheng Kung University, Tainan, Taiwan*

Edited by:
Manuel S. Malmierca, University of Salamanca, Spain

Reviewed by:
Stephen G. Lomber, University of Western Ontario, Canada
Mark N. Wallace, Medical Research Council, UK

****Correspondence:***
Adrian Rees, Institute of Neuroscience, Faculty of Medical Sciences, Newcastle University, Newcastle upon Tyne, UK.
e-mail: adrian.rees@ncl.ac.uk

The auditory pathways coursing through the brainstem are organized bilaterally in mirror image about the midline and at several levels the two sides are interconnected. One of the most prominent points of interconnection is the commissure of the inferior colliculus (CoIC). Anatomical studies have revealed that these fibers make reciprocal connections which follow the tonotopic organization of the inferior colliculus (IC), and that the commissure contains both excitatory and, albeit fewer, inhibitory fibers. The role of these connections in sound processing is largely unknown. Here we describe a method to address this question in the anaesthetized guinea pig. We used a cryoloop placed on one IC to produce reversible deactivation while recording electrophysiological responses to sounds in both ICs. We recorded single units, multi-unit clusters and local field potentials (LFPs) before, during and after cooling. The degree and spread of cooling was measured with a thermocouple placed in the IC and other auditory structures. Cooling sufficient to eliminate firing was restricted to the IC contacted by the cryoloop. The temperature of other auditory brainstem structures, including the contralateral IC and the cochlea were minimally affected. Cooling below 20°C reduced or eliminated the firing of action potentials in frequency laminae at depths corresponding to characteristic frequencies up to ~8 kHz. Modulation of neural activity also occurred in the un-cooled IC with changes in single unit firing and LFPs. Components of LFPs signaling lemniscal afferent input to the IC showed little change in amplitude or latency with cooling, whereas the later components, which likely reflect inter- and intra-collicular processing, showed marked changes in form and amplitude. We conclude that the cryoloop is an effective method of selectively deactivating one IC in guinea pig, and demonstrate that auditory processing in the IC is strongly influenced by the other.

Keywords: inferior colliculus, cooling inactivation, auditory pathways, single unit, commissure, guinea pig, auditory processing

INTRODUCTION

Sub-thalamic auditory processing in mammals is mediated by bilaterally organized pathways that originate with the entry of the auditory nerves into the cochlear nuclei and culminate in the inferior colliculi. On each side of the midline, the connections between multiple processing centers in the brainstem give rise to several parallel processing streams that converge in the inferior colliculus (IC) (for review see: Oliver and Huerta, 1992; Malmierca and Hackett, 2010). Although inputs from both left and right ears contribute to the pathway on each side, the representation in each IC is dominated by the information about the contralateral sound field (Jenkins and Masterton, 1982; Aitkin et al., 1984; Kelly and Kavanagh, 1994; Delgutte et al., 1999; Litovsky et al., 2002). An interaction between these two representations is mediated at the subcortical level by the commissure of the inferior colliculus (CoIC), a bundle of fibers that connects the two ICs and which constitutes one of the largest of the many afferent inputs the IC receives (Moore, 1988; Saldaña and Merchán, 1992, 2005).

The anatomical organization of the CoIC is well established, but we know relatively little about its functional properties (Adams, 1980; Coleman and Clerici, 1987; González-Hernández et al., 1991; Saldaña and Merchán, 1992; Malmierca et al., 1995, 2009). One of the problems in addressing this issue is the difficulty in breaking the connection the commissure makes between the ICs. Previous studies have attempted to do so by sectioning the CoIC, or by drug-induced blockade of glutamatergic transmission in one IC by pressure injection, while recording responses in the other (Moore et al., 1974; Malmierca et al., 2003, 2005). The first method is limited by the difficulty of the surgical procedure, uncertainty, prior to histological processing,

Abbreviations: CF, characteristic frequency; CoIC, commissure of the inferior colliculus; DNLL, dorsal nucleus of the lateral lemniscus; EI, excitatory-inhibitory; FRA, frequency response area; IC, inferior colliculus; IQR, interquartile range; ISI, interspike interval; ISIH, interspike interval histogram; LFP, local field potential; PSTH, post stimulus time histogram; SPL, sound pressure level.

that the commissurotomy is complete, and the impossibility of reversal. When applied *in vivo*, the second approach, while informative, yields a low number of tested units. This is primarily because of the difficulty in maintaining contact with a recorded neuron in the face of the mechanical instability caused by the pressure injection, and the time required for recovery from the drug effect (Malmierca et al., 2005). These limitations severely impede the testing of specific hypotheses about the function of the CoIC.

In an attempt to overcome these difficulties, we have tested the feasibility of using cooling-induced deactivation as a means of deactivating one IC in guinea pig. This means of neural deactivation, first developed at the beginning of the twentieth century [see Brooks (1983) for review], has been used extensively in both electrophysiological and behavioral studies, and has the important advantage of rapid onset and recovery (Schiller and Malpeli, 1977; Sherk, 1978; McClurkin and Marrocco, 1984; Girard and Bullier, 1989; Michalski et al., 1993; Payne et al., 1996; Lomber et al., 1999; Lomber and Malhotra, 2008; Girardin and Martin, 2009). It has been applied in several paradigms, including as a means of reversibly switching off the afferent input to a recorded brain region (e.g., Schiller and Malpeli, 1977; Sherk, 1978; McClurkin and Marrocco, 1984; Michalski et al., 1993; Nakamoto et al., 2008; Antunes and Malmierca, 2011).

An important question about the utility of the technique is the extent to which the cooling effect spreads through neural tissue, both from the perspective of ensuring that the tissue targeted for cooling has been fully deactivated, and that the recording site has not been functionally affected by spreading cold. These issues have been addressed in earlier investigations, but as cited above, mostly in the cortex, and mainly in cat and primate. Cooling has been applied to midbrain sites in only a few studies (e.g., Keating and Gooley, 1988; Lomber and Payne, 1996; Lomber et al., 2001, 2007b). In smaller animals such as guinea pig (Villa et al., 1999; Nakamoto et al., 2008; Coomber et al., 2011) and rat (Kayama et al., 1984; Yuan et al., 1986; Diamond et al., 1992; Villa et al., 1999; Antunes and Malmierca, 2011) cooling has only been used to deactivate cortex. Because several factors determine the efficacy of cooling (the geometry of the tissue, the surface area to which the cryoloop is applied, the blood flow in the tissue, and the distance between the sites of cooling and recording) it is not possible to extrapolate the effects of cooling from one brain structure to another.

Here we test the hypothesis that cooling-induced deactivation in guinea pig offers an effective means of deactivating one IC while recording sound-driven electrophysiological activity from the other IC. We discuss the extent to which the observed changes are mediated by commissural input rather than by descending pathways. We conclude that cooling can be used to abolish neuronal spiking in a well-defined part of one IC without deactivating the contralateral IC or neighboring nuclei, thus allowing us to observe the effects of substantially reducing commissural input.

MATERIAL AND METHODS

ANIMALS: MAINTENANCE AND SURGICAL PREPARATION

All experiments were performed under the terms and conditions of a license issued by the UK Home Office under the Animals (Scientific Procedures) Act 1986 and with the approval of the Local Ethical Review Committee of Newcastle University.

Experiments were performed on 15 adult pigmented guinea pigs (*Cavia porcellus*) of either sex, weighing between 595 and 888 g. Additional data gathered in these experiments will be reported separately.

Anesthesia was induced with urethane (1 g/kg as 20% solution, i.p.) and supplemented by Hypnorm (1 ml/kg, i.m., VetaPharma, UK). Atropine (0.05 mg/kg, s.c.) was given following induction of anesthesia to suppress bronchial secretions. Anesthesia was maintained with further doses of Hypnorm (1/3 original dose) on indication of a pedal reflex elicited by a pinch to the hind paw. A tracheotomy was performed and an endotracheal tube inserted to maintain air flow.

Core temperature was monitored via a rectal thermometer and maintained at 38°C by a thermostatically controlled electric blanket (Harvard Apparatus). Animals were allowed to respire spontaneously, but if breathing became labored they were artificially respired with medical air via a modified small animal ventilator (Harvard Apparatus) to maintain the end-tidal CO_2 at 5%.

Animals were placed in a sound attenuating room and the head secured in a stereotaxic frame in which the ear bars were replaced with hollow conical Perspex specula, the apices of which were placed in the auditory meatuses allowing visualization of the tympanic membranes.

A dorsal mid-sagittal incision was made along the length of the skull. The skin was reflected and the tissues overlying the skull were abraded. A small hole was trephined 10.5 mm caudal and 2.5 mm left of bregma. Rongeurs were used to extend the diameter of the craniotomy to 5 mm, centered on the pilot hole. To reveal the left IC, the dura was retracted and the overlying occipital cortex was aspirated with a glass Pasteur pipette attached to a vacuum pump (Matburn). The auditory thalamus and cortex were undamaged by this procedure.

ELECTROPHYSIOLOGICAL RECORDING

Electrical activity was recorded with glass-coated tungsten microelectrodes advanced into either the cooled or uncooled IC (Merrill and Ainsworth, 1972). Extracellular action potentials and local field potentials (LFPs) were amplified (x10,000) and filtered (0.1 Hz to 3 kHz) by a preamplifier (Dam-80; World Precision Instruments). The spike signal was further high-pass filtered (300 Hz) and amplified before being discriminated, converted to logic pulses, and time stamped to an accuracy of 10 μs by dedicated hardware (Tucker Davis Technologies, TDT System 2). As well as recording spike times, in some cases we also collected spike waveforms using a MacLab 4/e recorder (AD Instruments) running Scope software. This allowed us to monitor changes in the size and shape of spikes during the cooling cycles.

LFPs were recorded using the same electrode as the spike activity and extracted by low pass filtering the output of the preamplifier at 1 kHz, to remove spikes, before averaging the response using MacLab.

SOUND STIMULATION

Pure-tone, noise and click stimuli were generated by TDT System 2 hardware under computer control through custom-written

software that allowed the frequency and level of stimuli to be varied in real time.

Stimuli were delivered by a calibrated closed acoustic system consisting of Sony MDR 464 earphones housed in an alloy enclosure and coupled to damped probe tubes (4 mm diameter) that fitted into the ear bars (Rees et al., 1997). The maximum output of the system was flat from 0.1 to 9 kHz (100 ± 5 dB SPL) and then fell with a slope of ∼15 dB per octave. Second and third harmonic components in the signal were ≤60 dB of the fundamental at the highest output level.

On isolation of a single unit, the characteristic frequency (CF) and minimum threshold to contralaterally presented tones was determined audio visually to establish the settings for data collection.

Frequency response areas (FRAs) were derived as described previously to both diotic and contralaterally presented pure tones (Evans, 1979; LeBeau et al., 2001). The response area was constructed by counting the number of spikes elicited in response to 50-ms tone-bursts (5-ms rise/fall time, repetition rate 5/s), which varied in 51 logarithmically spaced frequency steps over an intensity range of 90 dB (in 5 dB steps). The number of spikes produced in response to each stimulus was counted and displayed color coded at the appropriate position in a plot of tone frequency versus attenuation level. Post stimulus time histograms (PSTHs) were constructed from the responses to 75-ms duration tones with a repetition rate of 4/s. LFP responses were recorded in response to transient 10-kHz tone pulses of 1-ms duration and 0.01 ms rise/fall time.

Recording location was determined by the presence of sound driven spiking and a tonotopic progression with electrode depth. All recordings were made within the IC from neurons with response properties that were similar to previous recordings made within the central nucleus (Rees et al., 1997; LeBeau et al., 2001), but we make no claims as to the exact location of individual recordings.

IC COOLING

Cooling of the IC was achieved using a variation of the method described by Lomber et al. (1999). A cryoloop was made by forming a loop from 23 gauge stainless steel tubing. Each end of the tubing was soldered to a 19 gauge needle (**Figure 1**). These needles served as the inlet and outlet for circulating coolant. A peristaltic pump (Gilson Minipuls 2) drew ethanol cooled in a deep freeze to −80°C from a reservoir. The ethanol was pumped through a coil of fluorinated ethylene propylene tubing (Cole-Parmer) inside a vacuum flask (Dilvac) containing ethanol cooled to −80°C before passing through the cryoloop and back into the reservoir. The tip of a type T (copper-constantan) thermocouple was secured to the cryoloop tip (**Figure 1** inset) to allow monitoring of the cryoloop temperature with a digital thermometer (HH506RA, Omega). Regulating the pump speed allowed the flow rate through the system to be controlled thereby enabling the temperature at the cryoloop tip to be maintained at the desired temperature.

The cryoloop was curved to maximize contact with the dorsolateral surface of the exposed IC. This placement was chosen to maximize the extent of cooling in areas in which the density of neurons projecting via the CoIC to the contralateral IC is greatest (Saldaña and Merchán, 1992; Malmierca et al., 1995, 2009). At no time was the temperature allowed to drop below 2°C to prevent cryo-trauma to the tissue. Temperature measurements within the IC were made using a needle thermocouple (HYP-0, Omega) that was advanced into the IC using a microdrive. In some cases the thermocouple was glued to a recording electrode so that temperature could be measured in the IC close to the site of neural recording.

Histological processing using standard methods followed by cresyl violet staining was performed in some experiments to reconstruct the penetrations of the thermocouple and in others to verify that cooling did not produce tissue damage.

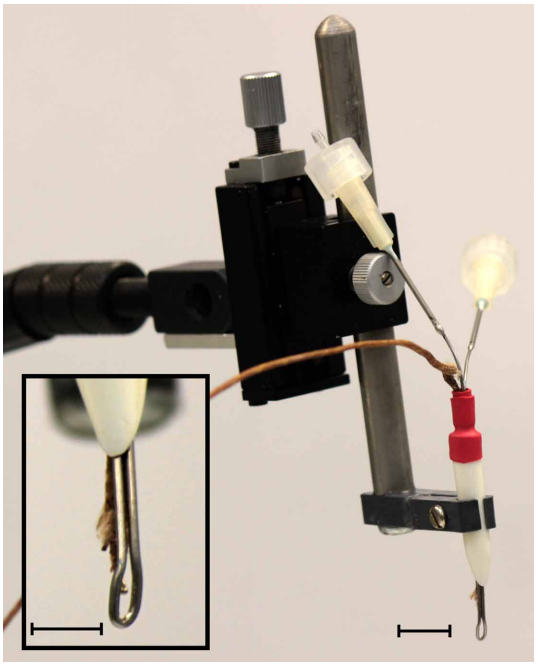

FIGURE 1 | Photograph of the cryoloop used to cool the IC held in a micromanipulator. Two 19 gauge needles soldered to each end of the stainless steel cryoloop tubing acted as the inlet and outlet ports for the coolant. The manipulator allowed precise placement of the loop in contact with the exposed IC. Inset: detail of the cryoloop. The thermocouple tip allows precise monitoring of the cryoloop temperature. The surface of the cryoloop was placed in contact with the dorso-rostral part of the exposed IC. Scale bars = 5 mm.

RESULTS

The principal aim of this study was to establish whether a cryoloop can be used to cool one IC selectively and reversibly to deactivate spiking whilst electrophysiological recordings are made in the contralateral IC. To address this question we first measured the temperature in several sites in both ICs while cooling the left IC. Implicit in this aim is that there should be no functionally significant spread of cooling to the other IC or other brainstem auditory structures, and that cooling should not produce tissue damage.

TEMPERATURE MEASUREMENTS IN THE COOLED IC

With the cryoloop placed on the IC with no coolant flow, the *cryoloop* temperature was typically 32–35°C, a few degrees below the maintained core temperature of 38°C. To establish how effectively our cryoloop system cooled the IC we measured temperature along vertical penetrations aligned with the electrode tracks made to record neural activity. Cooling was begun and the cryoloop tip held at 5°C for approximately 10 min (**Figure 2A**) before the thermocouple was lowered from the dorsal surface of the exposed IC. Temperature measurements were taken along the dorso-ventral penetration at 1 mm steps measured from the surface. The most laterally placed penetration reached the dorsal nucleus of the lateral lemniscus (DNLL). The temperatures recorded are represented by the color gradients on the schematic coronal section in **Figure 2A**. The temperature as a function of depth from the dorsal surface of the IC for the most lateral penetration in the cooled IC is plotted in **Figure 2B** (filled circles and solid line). For depths less than 2–2.5 mm the temperature was <20°C. As well as a gradient in depth, there is also a gradient across the IC with temperatures in the most medial track being higher than those more laterally. For comparison, we have also re-plotted temperature measurements (open circles and dashed lines) from Coomber et al. (2011) taken at different depths in the guinea pig auditory cortex when the surface was cooled to 2°C. The temperature gradient with depth is qualitatively similar in the two models.

TEMPERATURE MEASUREMENTS IN THE CONTRALATERAL IC, COCHLEAR NUCLEUS AND COCHLEA

The possible spread of cooling from the cooled IC to its contralateral counterpart was also assessed and the temperatures recorded in three penetrations in mirror image positions to those in the cooled side were measured (**Figure 2A**). At 1 mm below the surface the mean temperature recorded was 30.3 ± 0.9°C and increased with depth to 32.8 ± 0.60°C ($n = 3$) 4 mm from the surface. As in the left IC the temperature was lowest on the lateral side where 1 mm below the surface it was 28°C.

We also recorded temperatures in the right IC as a function of time over the course of the cooling cycle in three animals. The thermocouple tip was placed 1 mm below the surface of the contralateral IC in the mirror image position to that used to measure the IC cooled by the cryoloop. In each case the cryoloop temperature was reduced to ∼5°C and the temperature was measured in the contralateral IC after the temperature had stabilized. The lowest absolute temperatures measured in the contralateral IC ranged from 30.7 to 28.1°C, with a mean reduction of 4.3°C from control. The effect of varying the duration of cooling on the temperature in the contralateral IC was assessed by applying five cooling cycles which varied in duration between 0.5 and 30 min with the cryoloop temperature held at ∼5°C in each case (**Figure 3A**). The reduction in temperature in the contralateral IC ranged between 3.7°C after 3 min of cooling and 5.4°C after 30 min of cooling. The minimum temperature in each cooling cycle plotted as a function of cycle duration was fitted with a single phase exponential decay function ($r^2 = 0.96$; **Figure 3B**). These values demonstrate that the temperature of the IC remained stable over periods up to 30 min of cooling the contralateral IC.

The measurements described above were made with the cortex overlying the IC removed to facilitate placement of the thermocouple. In some cases we also compared temperature in the right IC contralateral to the cooled side before and after aspiration of the cortex. These measurements were made by introducing the thermocouple into the IC through the cortex using mirror image coordinates to those used for placement in the cooled IC. After making measurements the cortex was aspirated with the thermocouple in place and the measurements repeated and the recording positions relative to the right IC confirmed. The temperature measured 1 mm from the surface of the IC was ∼2°C warmer with the cortex intact indicating that the cortex served to insulate and warm the IC. At larger depths the difference in temperature was reduced to ∼0.5°C.

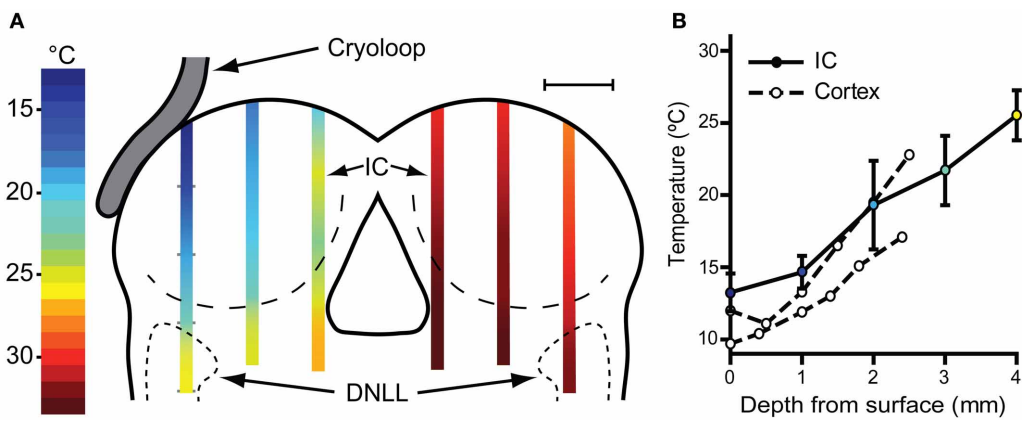

FIGURE 2 | (A) Schematic coronal section through the IC showing placement of the cryoloop and temperatures measured in the IC with a needle thermocouple during cooling in the left (cooled) and right IC. These measurements were made after removal of the overlying cortex. For electrophysiological recording experiments the cortex over the right IC was left intact with the result that the temperature would be ∼2°C warmer in the right IC (see text). **(B)** Mean ± SD of temperature measured in the lateral-most penetration of the left IC and three similar cases (filled circles, solid line). Open circles and dashed lines show temperature as a function of depth in guinea pig auditory cortex re-plotted from Coomber et al. (2011) for comparison.

We also measured the effect of cooling the IC on the temperature of two other structures in the auditory pathway: the cochlear nucleus and the cochlea. In both cases measurements were made from the structures ipsilateral to the cooled IC. This was done because we predicted that these structures were most likely to be affected by cooling and they provide the predominant input to the contralateral IC—the ultimate target of our electrophysiological recordings. The temperature of the cochlear nucleus never fell more than 2°C below control throughout 20 min of cooling (**Figure 3C**).

The temperature of the cochlea was measured in three ways. When the thermocouple tip was placed in contact with the round window, the temperature fell by 1.8°C during cooling (**Figure 3D**). A second set of measurements were made with the thermocouple placed on the first turn of the cochlea, and finally a small hole was made in the bony wall and the thermocouple tip placed inside the cochlea. In each case the temperature drop measured was <2°C from the control temperature (33.7°C) after the loop had been cooled to ∼5°C for 20 min.

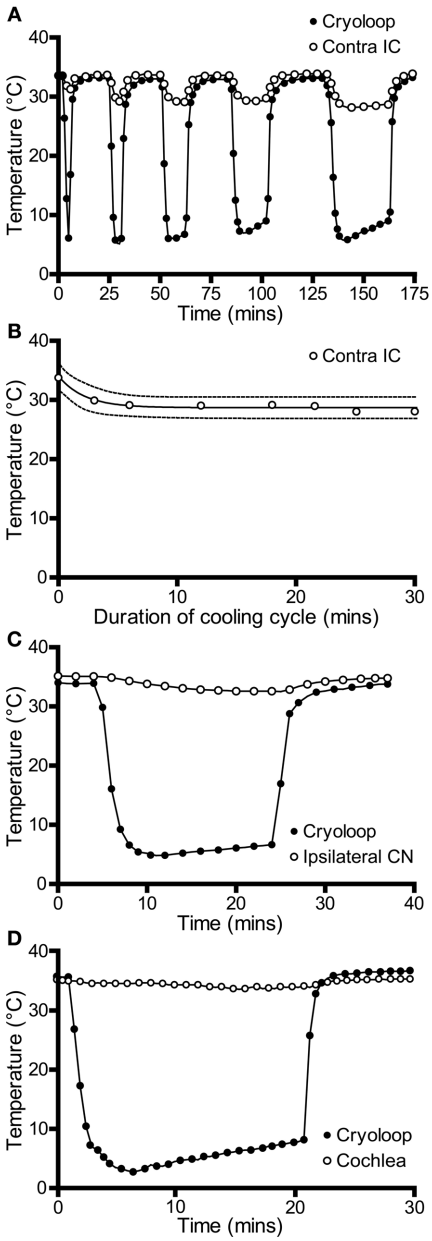

FIGURE 3 | (A) Temperature of the cryoloop (filled circles) and at 1-mm depth in the contralateral IC (open circles) during repeated cycles of cooling of different duration. The temperature in the contralateral IC falls only a few degrees below control temperature. **(B)** Temperature in the contralateral IC (open circles) is relatively stable as the duration of the cooling cycle is increased progressively to 30 min. **(C)** Cooling the IC resulted in a less than 2°C reduction in temperature in the ipsilateral cochlear nucleus (CN, open circles) and **(D)** in the ipsilateral cochlear duct (open circles).

HISTOLOGICAL ANALYSIS OF COOLED TISSUE

We used histology to assess the integrity of the neural tissue after its exposure to temperatures of ∼5°C. In six experiments in which the IC underwent multiple cooling cycles over the course of several hours, the animal was perfused and sections were cut through the IC at 50 μm thickness to check for signs of cryogenic tissue damage or ischemia. **Figure 4** shows a transverse section through the IC, cut approximately midway through the rostro-caudal axis, and stained with cresyl violet. The cortex that normally overlies the left IC was aspirated to allow placement of the cryoloop. In this, and the other cases, the shape and structure of the cooled IC appeared normal. There was some bleeding from the edges of the damaged cortex that formed small clots along the midline (black

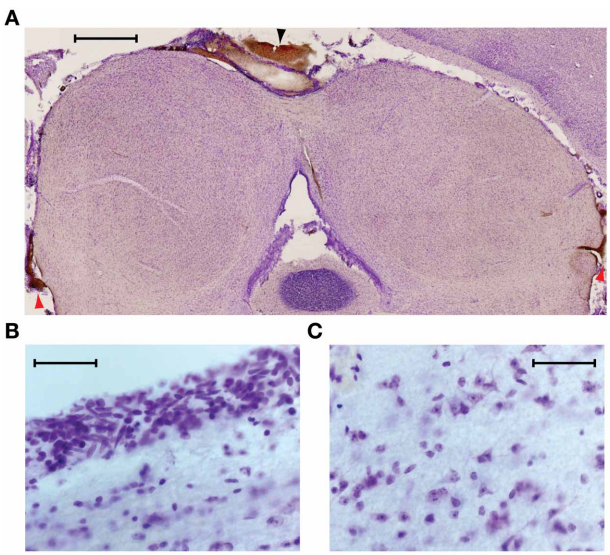

FIGURE 4 | (A) Near coronal section through the IC following an experiment. Aspiration of the cortex overlying the left IC and placement of the cryoloop did not produce any noticeable trauma to the tissue. Blood at the midline (black arrowhead) and bilaterally at the ventro-lateral edges of the tectum (red arrowheads) resulted from aspiration of the cortex. Scale bar = 1 mm. **(B)** Neurons near the dorsal surface of the IC contacted by the cryoloop show no sign of damage. **(C)** Neurons within the cooled IC have normal morphology and no signs of ischemia are present. Scale bar in **(B)** and **(C)** = 50 μm.

arrowhead) and at the ventro-lateral edges of the tectum, lateral to each sagulum (red arrowheads). There were no clots on the surface between the cryoloop tip and the IC, and no sign of vascular damage within the tissue.

Higher magnification images taken from the dorsal surface (**Figure 4B**) and the center of the cooled IC (**Figure 4C**) show cells with normal morphology and intact nucleoli. Comparison with tissue in the uncooled IC shows no discernible differences.

NEURAL ACTIVITY IN THE COOLED IC

The effect of cooling on sound-driven neural activity was assessed by recording single units and multi-unit clusters at different depths in the cooled IC. Recordings were completed for control, cool, and recovery phases from 33 single units and 9 multi-unit clusters, in 11 experiments. The responses to multiple repetitions of a pure tone 20 dB above threshold at CF were collected in each condition. To test for any change in firing rate, the number of spikes evoked per stimulus in each condition was assessed with a Friedman omnibus test. Multiple Wilcoxon signed ranks tests were used to determine differences between pairs of values between the three conditions. In order to be included in these analyses, the control and recovery data had to show no significant difference in the number of spikes per stimulus ($p > 0.017$, following Bonferroni correction) and the PSTH had to recover the same pattern as seen in the control condition. Of the 33 single units, 21 passed this criterion and are included here. The firing rate in the recovery condition of single units that reached criterion ranged from 72.0 to 127.6% of control (median = 95.2%; interquartile range (IQR) = 88.8–100.6%). Of the 9 multi-unit clusters, 7 passed the criterion for inclusion (median recovery firing rate = 98.7%; IQR = 85.0–106.6%; range = 71.5–121.3%).

The minimum cryoloop tip temperature differed for each single neuron to maximize the chances of holding the unit to obtain recovery data. If a neuron showed a marked reduction in firing rate, cooling was discontinued. The lowest cryoloop tip temperature was 2°C while the highest maximal cooling temperature applied was 20.3°C (median = 8.1°C). The firing rates of all included units were not normally distributed (D'Agostino-Pearson omnibus K2 test). A Friedman test showed a statistically significant difference in firing rate between the control, cool and recovery groups of all units ($\chi^2(2) = 53.5$, $p < 0.001$). Wilcoxon Signed Ranks Tests found significant differences in the control versus cool ($Z = -5.6$, $p < 0.001$) and cool versus recovery conditions ($Z = -5.4$, $p < 0.001$) but no significant difference in the control versus recovery conditions ($Z = -1.6$, $p = 0.11$).

CHANGES IN NEURAL ACTIVITY AS A FUNCTION OF TEMPERATURE

In 17 units we recorded tone driven responses while progressively cooling the IC. **Figure 5** shows the effect of cooling on the firing rate of 12 single neurons ordered by their depth in the IC. The effect of temperature on firing rate follows one of three

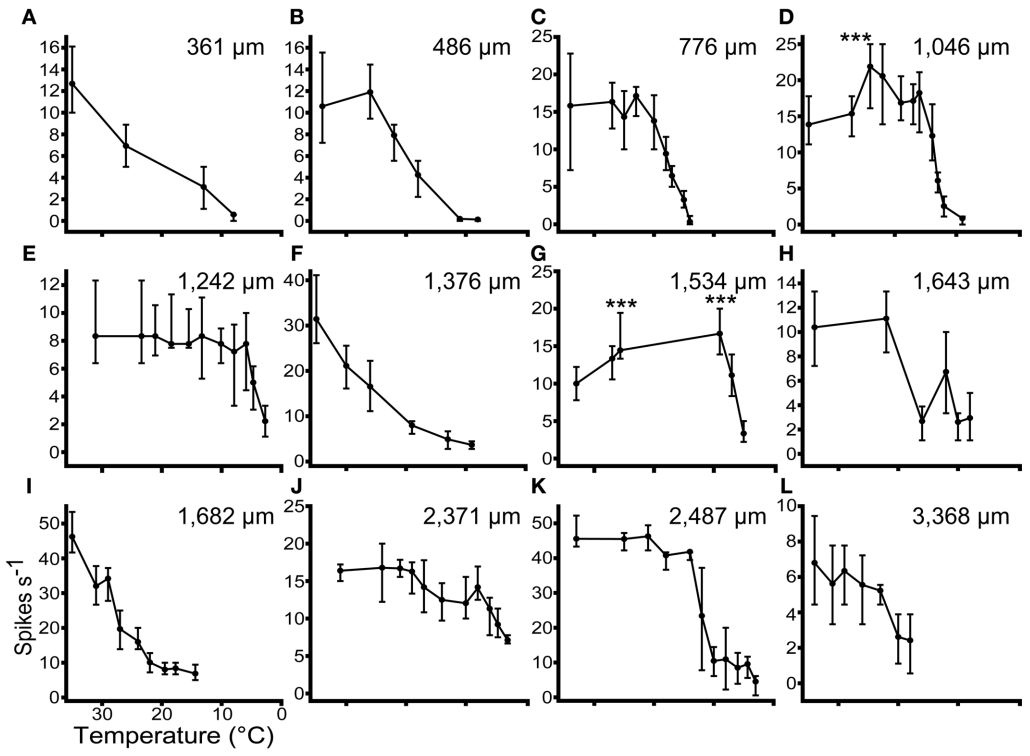

FIGURE 5 | The responses (Median ± IQR) of 12 single units to multiple presentations of a pure tone at CF, 20 dB re threshold, during stepwise cooling of the IC. Units were recorded along the dorso-ventral axis of the IC from 361 µm **(A)** to 3368 µm **(L)** from the dorsal surface. Cooling into the range 10–20°C induced a significant ($p < 0.001$) reduction in firing rate in all 12 units. In 2 units **(D** and **G)** firing rate increased significantly re control ($p < 0.001$) prior to decreasing at lower temperatures.

patterns. In the majority of cases firing rate remained relatively constant and then decreased as the temperature was reduced further (**Figures 5B,C,E,H,J,K,L**). A second group showed a similar decline in firing rate when the temperature fell below 20°C, but this was preceded by an elevation in firing rate when the temperature was in the range 20–26°C (e.g., **Figures 5D,G**). In a few units the firing rate began to decline immediately after the temperature was reduced (e.g., **Figures 5A,F,I**).

The occurrence of these types does not follow any specific pattern with recording depth. Across all the units tested with stepwise cooling, 4/17 (24%) showed a statistically significant increase in firing and 3/17 (18%) showed a reduction in firing at temperatures in the range 20–30°C. The remainder showed no statistically significant change over this temperature range. As the temperature was further reduced all units showed a statistically significant reduction in firing rate.

The PSTH and FRA of a neuron in response to tones before during and after cooling are shown in **Figure 6**. The neuron was characterized in the control condition as an "on-sustained" type (**Figure 6A**) with a V-shaped response area (**Figure 6D**) according to criteria defined previously (Rees et al., 1997; LeBeau et al., 2001).

Prior to cooling, the neuron fired 753 spikes in response to the 100 presentations of the PSTH stimulus (median = 8, IQR = 6–8). Maximal cooling resulted in the number of recorded spikes falling to 103 (median = 1, IQR = 0–2) with onset spikes accounting for the majority. Cessation of cooling produced an immediate recovery of spiking activity. When the temperature measured at the cryoloop tip returned to near the control value (33.5°C), the neuron fired 757 spikes in the PSTH paradigm (**Figure 6C**). In addition to the recovery in spike count, the shape of the PSTH returned to its original on-sustained form. Firing rate was modulated by cooling in a similar manner in response to monaural or binaural stimulation (not shown).

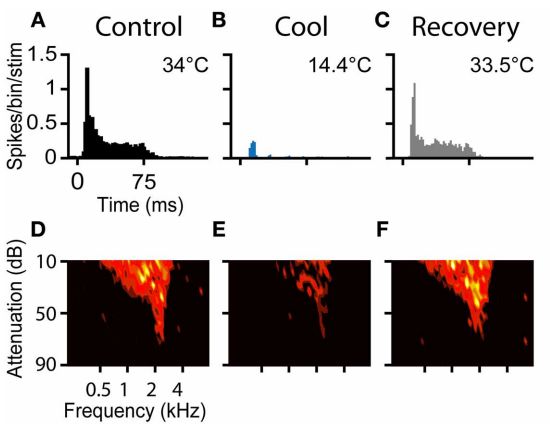

FIGURE 6 | (A–C) PSTHs and **(D–F)** FRAs during control, cool to 14.4°C, and recovery conditions, respectively for a unit with CF = 2.1 kHz. The unit had an on-sustained PSTH and a V-type FRA under control conditions. During cooling only an occasional spike near stimulus onset remained, but the frequency tuning was retained. On recovery the unit regained its original PSTH shape and firing as a function of frequency returned to control levels.

A Friedman test showed there was a statistically significant difference between the firing rates across the control, cool and recovery conditions ($\chi^2(2) = 150.4$, $p < 0.001$). *Post-hoc* analysis with Wilcoxon Signed Ranks Tests found a statistically significant difference between the control and cool ($Z = -8.6$, $p < 0.001$), and cool and recovery ($Z = -8.6$, $p < 0.001$) conditions, but no significant difference between the control and recovery conditions ($Z = -0.38$, $p = 0.71$).

The FRA of the unit had a threshold at 75 dB attenuation and a CF of 2.1 kHz, with a Q_{10} of 3.40 and a Q_{40} of 1.00 (**Figure 6D**). The unit fired to 173 of the 936 frequency-level combinations presented. When cooled the number of frequency-level combinations that elicited spikes fell to 87 (**Figure 6E**). Cooling increased the Q_{10} to 4.38 and the Q_{40} to 1.44, although throughout all stages of cooling, threshold and CF were unchanged. On recovery, the neuron regained tuning and firing rate properties similar to those in the pre-cooled condition (**Figure 6F**). The area of the FRA driven by sound increased to 182 bins with a concomitant reduction in Q_{10} to 3.40 and Q_{40} to 1.19.

NEURAL DEACTIVATION BY COOLING AS A FUNCTION OF DEPTH IN IC

To estimate the neural deactivation of the IC as a function of depth, we measured the responses of neurons at different frequencies and depths in the IC during cooling. To increase the sample size in this analysis we also sampled multi-unit clusters with the same procedure as for single unit recordings, except two or three neurons were recorded simultaneously. The responses of multi-unit clusters were modulated by cooling in similar manner to well-discriminated single units. **Figure 7** shows examples of data taken from one experiment where neural activity was recorded at approximately 1 mm intervals along a single electrode penetration following the dorsoventral axis of the IC (**Figure 7A**). The deviations from exact 1 mm steps along the track were to maximize the amplitude of the spike response in each position. The CF of the activity along the track followed the established tonotopic sequence with neurons tuned to low frequency dorsally and CF increased with depth.

All four locations were recorded with the cryoloop in the same position during cooling cycles of approximately 10-min duration with the cryoloop temperature held at 5 ± 3°C throughout. Cooling induced a gradient of neural deactivation along the track as revealed by the responses to monaural stimulation of the contralateral ear (**Figure 7B**) and similar responses to diotic stimulation (not shown). For the two most superficial positions firing rate was almost totally abolished, while for the two deeper positions there was a substantial reduction in firing in both cases.

Freidman's tests showed there was a statistically significant difference in firing rate between the control, cool, and recovery conditions in the three dorsal-most positions (26 μm: $\chi^2(2) = 73.2$; 1125 μm: $\chi^2(2) = 93.5$; 2210 μm: $\chi^2(2) = 26.0$; all $p < 0.001$). In the ventral-most position there was no significant difference in firing rate across groups ($\chi^2(2) = 1.10$, $p = 0.58$) despite a change in the PSTH morphology. *Post-hoc* analysis with the Wilcoxon Signed Ranks test for the dorsal-most position showed a statistically significant difference

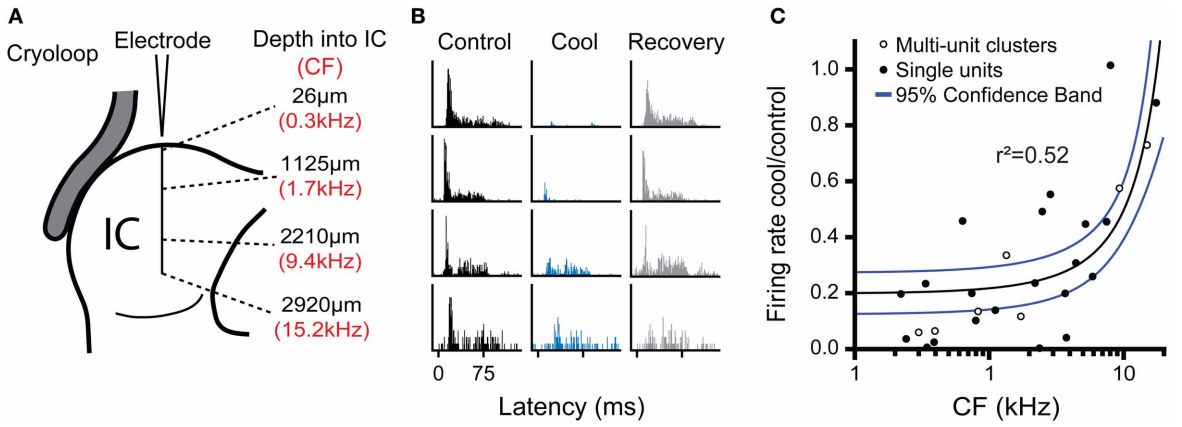

FIGURE 7 | (A) Schematic representation of multi-unit recordings made at approximately 1 mm steps in an electrode penetration along the dorso-ventral axis of the IC showing depth from the dorsal surface (black text) and CF of the recorded cluster (red text). **(B)** PSTHs for activity recorded at the four locations shown in **(A)** during control, cool, and recovery. Cooling resulted in a notable reduction of spiking in the three most dorsal positions, but had less effect in the deepest position. **(C)** Ratio of firing rate in the cool and control conditions as a function of unit CF for single and multi-unit cluster recordings pooled across experiments. The reduction in firing with cooling was most evident for low CFs (dorsal locations), while neurons with higher CFs in more ventral locations were less affected. Regression line (black) and 95% confidence limits (blue).

between the control and cool ($Z = -8.0$, $p < 0.001$) and the cool and recovery conditions ($Z = -6.0$, $p < 0.001$), but no significant difference between the control and recovery conditions ($Z = -1.1$, $p = 0.27$). The same pattern was found in the responses at 1125 μm from the dorsal surface. There was a significant difference between the control and cool ($Z = -8.4$, $p < 0.001$) and cool and recovery ($Z = -7.5$, $p < 0.001$) conditions, but no significant difference between the control and recovery conditions ($Z = -1.7$, $p = 0.082$). In the third position, the difference between the control and cool values had a lower Z statistic, but was still significant ($Z = -5.0$, $p < 0.001$). The same was true of the cool and recovery conditions ($Z = -5.1$, $p < 0.001$), with no significant difference between the control and recovery conditions ($Z = -1.9$, $p = 0.06$). In the ventral-most location there were no significant differences between any of the conditions.

Figure 7C shows the ratio of firing in the cool and control conditions for all the data collected in this analysis plotted as a function of the CF of the recording position. The maximal reduction in firing rate during cooling was fitted with a linear regression against CF ($r^2 = 0.52$, $p < 0.001$). The fit indicates that the cooling produced by the cryoloop in our configuration produced a 50% or greater reduction in firing rate for locations representing CFs up to 6–8 kHz.

Figure 8 summarizes the data collected for the effects of cooling on firing rate in the cooled IC, plotted in four frequency ranges. This plot confirms that cooling was effective in deactivating neural activity at CFs up to ∼8 kHz. For units with CFs greater than 8 kHz there was no significant difference between the firing rates in the control and cooled conditions. Temperatures measured at the depths in the IC at which the units were recorded indicate that cooling to below 25°C was necessary to produce a significant reduction in firing rate. This graph also demonstrates the recovery of firing rate after cooling was terminated and the tissue was allowed to rewarm.

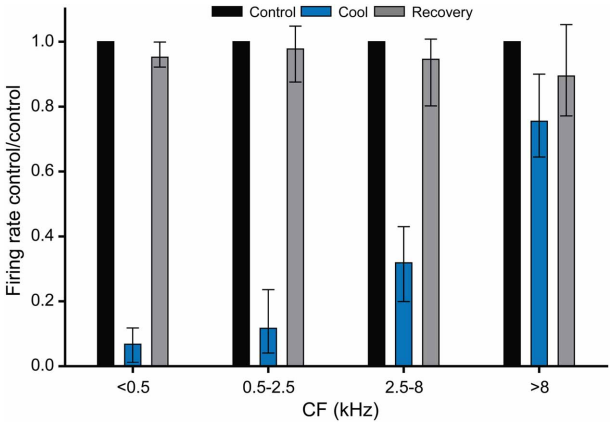

FIGURE 8 | Histograms showing the effect of cooling induced deactivation for single units grouped by CF. All units with a CF ≤ 8 kHz showed a statistically significant reduction in firing on cooling re their control (pre-cool) values, whereas units with CF >8 kHz did not show a statistically significant reduction in firing during cooling. In all cases firing rates recovered close to control values on rewarming.

CF WAS UNCHANGED BY DIRECT COOLING

FRAs were recorded under control, cool and recovery conditions from 14 single units and 2 multi-unit clusters in this sample. CFs ranged from 0.18 to 6.36 kHz in the control condition. Except for one unit in the cool and another unit in the recovery condition, the unit CFs were not substantially changed by the paradigm. During cooling, the median change was 1, with an IQR of 0.97–1.05, and a range of 0.86–1.24. Following recovery, the median change was again 1, the IQR was 0.93–1.08, and the range was 0.86–1.22. The largest change observed was an increase in CF from 1.7 to 2.1 kHz during cooling. This unit had a closed FRA and a small change in firing rate produced the 24% change in

CF. For the population, a Friedman test found no significant difference between CF in the control, cool, or recovery conditions ($\chi^2(2) = 0.84$, $p = 0.66$).

EFFECTS OF COOLING THE IC ON NEURAL RESPONSES IN THE CONTRALATERAL IC

After establishing the effects of cooling on neural activity in the IC, the second aim of this paper is to demonstrate its viability as a means of studying the influence of the IC on neural processing by its contralateral counterpart. Here we present examples of data in the form of single unit activity and LFPs showing the effects of cooling in the contralateral IC.

Figure 9A shows the PSTH of a single unit, which under control conditions (black) had a chopper response with three clearly identifiable peaks indicating a regular firing interval of ∼22 ms. This is confirmed by the single narrow peak centered on 22 ms in the interspike interval histogram (ISIH, **Figure 9B**). When the contralateral IC was cooled, the PSTH (blue) showed an overall reduction in the number of spikes per stimulus, as well as a notable increase in the latency to the first peak, a reduction in the number of peaks from three to two, and less regular firing exemplified by the lower and broader peaks in the PSTH. This is confirmed by the shift in the peak of the ISIH to a longer interval (∼44 ms) and the reduction in regularity is indicated by the lower height and broader width of the peak. When cooling was stopped, and the IC returned to near control temperature, the changes seen with cooling were reversed (gray).

In the second example illustrated in **Figure 10**, the effect of cooling is demonstrated under two different stimulus conditions: monaural contralateral stimulation (**Figure 10A**) and binaural diotic stimulation (**Figure 10B**). Under control conditions the

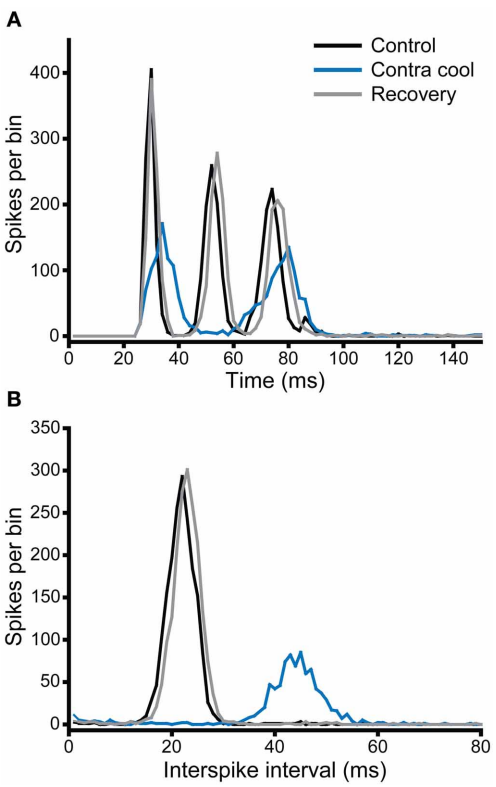

FIGURE 9 | (A) PSTH and **(B)** ISIH for a unit with a chopper response (CF = 1.1 kHz) that showed a change in firing rate and temporal pattern (mediated by an increase in ISI) during cooling of the contralateral IC. Both rate and ISI values recovered on re-warming to control temperature.

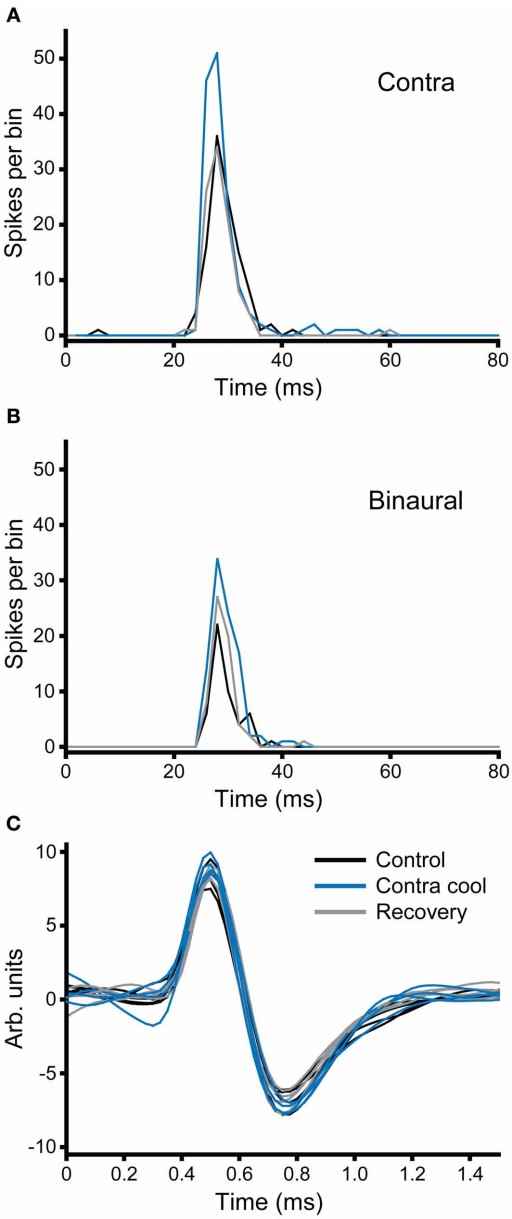

FIGURE 10 | (A,B) PSTHs of a broad-onset unit (CF = 8.1 kHz) recorded in the IC contralateral to the cryoloop before, during and after cooling. The number of spikes elicited to stimulation of the contralateral ear **(A)** increased during cooling and returned to the control value on recovery. In response to binaural stimulation **(B)** the unit showed an EI characteristic, but firing similarly increased with cooling. **(C)** Five examples of action potentials recorded during each of the three stages of the paradigm; the morphology of the action potential did not change during cooling of the contralateral IC.

unit fired fewer spikes with binaural stimulation indicating that it had an excitatory-inhibitory (EI) type response (black). In both conditions cooling the IC increased the firing rate (blue). The increase in firing rate was greater for contralateral stimulation, but the relative increase under both conditions was about the same. When the IC rewarmed, the changes observed with cooling were reversed (gray), but this was more complete for the case where stimuli were presented to the contralateral ear. **Figure 10C** shows examples of the action potential waveforms for this unit, color coded as for the PSTHs. The shape, size, and time course of the waveform remained the same in control, cool, and recovery conditions. The absence of any change in the action potentials makes it unlikely that the changes observed in the firing rate of the unit are attributable to temperature change in the recorded IC (Volgushev et al., 2000b; Cao and Oertel, 2005).

Figure 11 summarizes the changes in firing rate for a population of single units in the IC contralateral to cooling in response to repeated stimulation with a tone at their CF. Cooling led to an increase or decrease in firing rate in different neurons, and although the degree of change varied considerably between units in some cases it was substantial.

In addition to recording single unit activity, we assessed the impact of cooling the contralateral IC on the LFP. **Figure 12** shows examples of LFPs recorded from the IC before, during and after cooling of the contralateral IC under three stimulus conditions, contralateral, and ipsilateral monaural stimulation (**Figures 12A,B**, respectively) and diotic stimulation (**Figure 12C**). In the case of contralateral and binaural stimulation there was a pronounced upward-going component with a post-stimulus latency of ∼6 ms that corresponds to the afferent volley of activity to the IC followed by a biphasic waveform that returned to baseline at ∼30 ms. The afferent volley was less pronounced in the case of the response to ipsilateral stimulation. When the contralateral IC was cooled the magnitude and latency of the afferent volley was unchanged, but there were clear changes in the later potentials. The form and extent of the changes varied between the different stimulus conditions. In the case of contralateral stimulation the largest change occurred

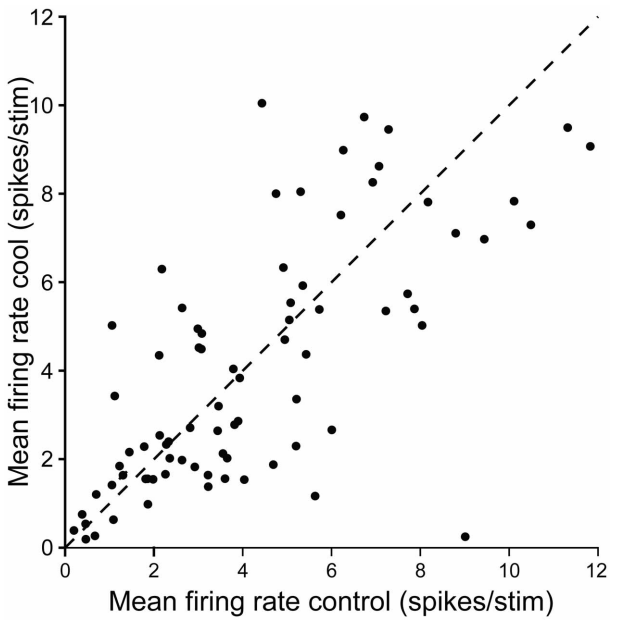

FIGURE 11 | Scatter plot showing control firing rate versus firing rate during cooling for single neurons recorded in the IC while cooling the contralateral IC. Dashed line shows the line of identity.

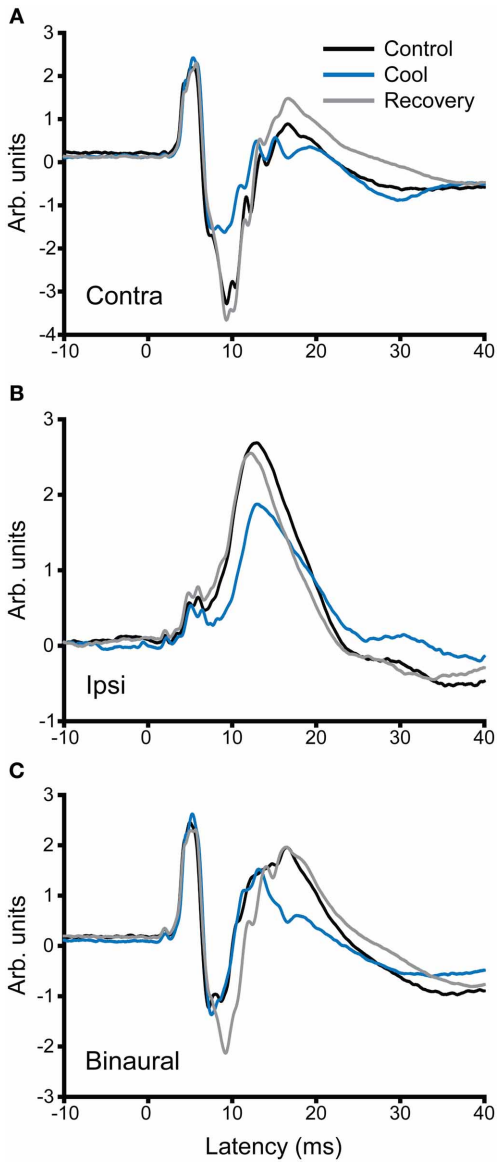

FIGURE 12 | Averaged local field potentials (100 sweeps) recorded in the IC in response to stimuli (1-ms duration tone pulses) presented at time zero to (A) the ear contralateral to the recorded IC, (B) the ipsilateral ear, and (C) binaural stimulation. Responses are shown for control conditions (black), during cooling (blue) and rewarming (gray) of the contralateral IC. Cooling has little effect on the first peak in the waveform, but changes the amplitude and time course of components occurring at and after 10 ms post stimulus onset.

in the first negative-going potential whereas with diotic stimulation the largest difference between cool and control was in the positive-going potential at ∼17 ms. With ipsilateral stimulation the single broad positive waveform was delayed, diminished in height and became broader.

DISCUSSION

Cooling has been demonstrated to be an effective means of deactivating brain tissue in many reports where it has been adopted for behavioral or electrophysiological studies (Schiller and Malpeli, 1977; Sherk, 1978; Girard and Bullier, 1989; Michalski et al., 1993; Payne et al., 1996; Lomber et al., 1999; Lomber and Malhotra, 2008; Girardin and Martin, 2009). The nature of the technique, however, requires that it be validated in each situation to which it is applied. The most important considerations are first that it is effective in deactivating the targeted center in a reversible manner, and second that the cooling effect is sufficiently restricted that it does not impact on other centers involved in the process under investigation. Our aim here was to establish the utility of cooling as a method for discovering how one IC is influenced by the other. If the technique can be demonstrated to be viable it would confer considerable advantages over the drug injection techniques used previously for this purpose (Malmierca et al., 2003, 2005). Our findings show that cooling the IC can fulfill both the required criteria.

Cooling has been applied to the auditory cortex in behavioral studies and to study its interactions with the medial geniculate body and the IC (Villa et al., 1991; Lomber and Malhotra, 2008; Nakamoto et al., 2008; Coomber et al., 2011), but it has not previously been applied directly to the IC itself. Indeed, the only previous reports of the application of cooling in the midbrain investigated superior colliculus function in cat and macaque both of which have a larger brain than guinea pig (Keating and Gooley, 1988; Lomber and Payne, 1996; Lomber et al., 2007b). Furthermore, in these studies the effect of deactivation was tested on behavior rather than on direct measures of neuronal function.

Our results demonstrate that spiking activity in the IC can be almost abolished only a few minutes after cooling begins and activity returns to control values within a few minutes of its termination, with in some cases an overshoot in activity following rewarming. Cooling was not homogenous throughout the depth of the IC. A temperature gradient extended along the dorsal to ventral axis of the IC corresponding to its well-established tonotopic gradient (Rose et al., 1963; Merzenich and Reid, 1974; Semple and Aitkin, 1979; Malmierca et al., 1995). Cooling appears to be effective to a depth of about 2 mm into the IC (**Figure 7**) when the cryoloop is cooled to 2–5°C. Cooling to this depth was sufficient to deactivate neurons representing frequencies up to 6–8 kHz. Although this covers only part of the auditory range, which extends to ∼50 kHz in the guinea pig (Heffner et al., 1971; Prosen et al., 1978), it encompasses key frequency ranges such as those over which interaural time and interaural level difference mechanisms dominate for sound localization.

The efficacy of cooling in the IC is similar to the ∼2 mm depth of deactivation reported when cryoloops were placed on the surface of the cerebral cortex in cat and guinea pig (Lomber and Payne, 2000; Lomber et al., 2007a; Girardin and Martin, 2009; Coomber et al., 2011). Intuitively, one might expect cooling to be more efficient in the IC since, in contrast to the relatively flat surface of the cortex in guinea pig, the exposed colliculus protrudes from the surrounding brainstem tissue, making a relatively larger part of its surface area accessible to contact with the cryoloop. On the other hand, the high blood flow in the IC might mitigate the cooling effect. The IC is highly vascular and demonstrates one of the highest blood flows of all brain regions and the vascularization is non-isotropic (Reivich et al., 1969; Gross et al., 1987; Dorr et al., 2007; Song et al., 2011). This high blood flow will warm the IC by convection and so counteract the cooling effect, and could also increase the rate of rewarming when the flow of coolant in the cryoloop circuit is stopped.

As reported by others, we found no anatomical evidence of tissue damage after cooling, even when the IC had been exposed to multiple cooling cycles to ∼5°C (Keating and Gooley, 1988; Lomber et al., 1999; Yang et al., 2006; Girardin and Martin, 2009). Following histological processing, cells were intact and there was no obvious difference between stained tissue from cooled and uncooled ICs. We were careful never to allow the cryoloop temperature to fall below 2°C and it is likely that even the tissue in immediate contact with the cryoloop would be higher than the cryoloop temperature. Consistent with the histological evidence, we found that in almost all cases the functional properties of the neurons in the cooled IC recovered to control values when the tissue was allowed to rewarm. In some cases there was rebound of neuronal firing, such that immediately after cooling was stopped firing rates temporarily exceeded control values.

Cooling had a profound effect on neuronal firing rate in the cooled IC. This is evident from several measures of neuronal function, including average firing rate and temporal firing patterns as represented by the PSTHs and FRAs. Although neuronal firing rates were significantly reduced by cooling, it was typical that neurons retained CFs similar to control (e.g., **Figures 6D–F**). This is consistent with the notion that cooling affects the synaptic efficacy of the afferent input to neurons, but stimulus selectivity is retained. A similar reduction in firing or synaptic potential, but with retention of stimulus selectivity has been observed for orientation tuning of neurons in visual cortex in cat (Michalski et al., 1993; Ferster et al., 1996; Girardin and Martin, 2009).

With a few notable exceptions (e.g., Michalski et al., 1993), most previous studies that employed cooling as a deactivation technique did not quantify the changes in response during the initial stages of cooling. Our results show that when the IC was progressively cooled all neurons showed a reduction in firing rate when the cryoloop temperature fell below about 20–10°C, consistent with previous reports (Michalski et al., 1993; Lomber et al., 1994, 1999), but three different patterns are apparent in the response over the first 10–15° of cooling. Most neurons show little change in firing rate over this range, but 24% show an elevation in firing rate and 18% show a notable decline in firing rate for temperatures below 30°C (**Figure 5**). These patterns did not correlate with recording depth in the IC so it is unlikely the effects are a consequence of the location of the neuron in the IC, rather it suggests that some neuronal types may be more sensitive to cooling than others. As well as revealing the direct influence of

cooling on individual neurons, such effects may also demonstrate the consequences of cooling in local networks. For example, a possible explanation for the severe reduction in firing with moderate cooling exhibited by some neurons is that by increasing the activation of inhibitory interneurons, moderate cooling leads to the more pronounced inhibition of neurons that receive this inhibitory input.

Biophysical studies, mainly *in vitro*, which have investigated how cooling influences neuronal responses show that it decreases synaptic efficacy by reducing the probability of transmitter release, and it has a differential effect on the operation of ion channels (Benita and Conde, 1972; Hardingham and Larkman, 1998; Volgushev et al., 2000a,b; Trevelyan and Jack, 2002; Cao and Oertel, 2005). At temperatures where neurons become virtually deactivated (∼10°C), firing fails as the biophysical changes induced by cold induce depolarization block although firing may still occur if the stimulus is sufficiently strong (Volgushev et al., 2000b). The progressive increase in membrane potential occurs as the conductances of passive and voltage-gated potassium channels are decreased while sodium conductances remain relatively unaffected. Such changes are consistent with our observations that some spikes occur even at very low temperature. At temperatures above the level of deactivation, in the range of 18–24°C, cooling may lead to an increase in excitability (e.g., Volgushev et al., 2000b). As a consequence, these authors pointed out that during cooling there may be a penumbra of tissue around the deactivated region in which neurons show elevated firing. Such effects are consistent with the elevation in firing rate above the uncooled value we observed in some neurons when the temperature was between 20 and 26°C. The consequences of this effect need to be borne in mind when interpreting cooling experiments. A possible advantage of the IC as a target for the technique is that it is organized as a stack of frequency band laminae in which interconnections along the dorso-ventral axis are less evident (Malmierca et al., 1995). This is in contrast to the cortex where processing depends on micro circuits involving neurons and connections distributed between the layers.

A key factor in determining the utility of cooling for deactivating the IC is the extent to which deactivation is limited to the cooled IC. Our measurements suggest that the temperature of structures neighboring the cooled IC are not significantly reduced by cooling the IC. Our measurements show that the ventral part of the IC (**Figures 7** and **8**) was not cooled sufficiently to deactivate neuronal function and therefore one would not expect the structures beneath it, including the DNLL, to be deactivated either.

In previous studies where cooling was used to deactivate auditory cortex in guinea pig a reduction in cochlear temperature was observed of up to 4°C on the side ipsilateral to the cooled cortex attributed to the proximity to the bulla of the jugular vein into which blood from the cortex ultimately drains (Coomber et al., 2011). We found that cooling the IC lead to a minimal effect on the cochlea, with the temperature reduced by less than 2°C from the animal's core temperature, and a similar change in the cochlear nucleus. This difference is presumably explained by differences in the vascular system serving the IC and the cortex, particularly the relative blood flow and venous drainage.

Since the aim of our application is to test the effect of unilateral IC deactivation on neural response to sounds, the spread of cold to the contralateral IC is a major concern. We found that cooling the IC does produce a small fall in temperature on the contralateral side, but always less than 5°C even after a prolonged cooling cycle of >30 min. Such effects can also be mitigated by keeping the cooling cycles as short as possible and using the warmest effective cooling temperature. However, our measurements in **Figures 2** and **3**, made after aspirating the cortex, underestimate the temperature of the contralateral IC when the cortex is intact. Removal of the cortex led to a fall in temperature of about 2°C at a depth of 1 mm in the uncooled IC. Without the cortex, the mean temperature of the contralateral IC during cooling was close to 30°C, but with the cortex intact its insulating and warming effect should maintain the temperature of the IC at ∼32°C. This is significant because when recording activity in the IC contralateral to the cooled IC our electrode penetrations are made through the cortex. This suggests the changes we observe in firing rate and temporal firing pattern are the consequence of blocking neural mechanisms in the contralateral, cooled IC, rather than direct cooling of the recorded neurons. Further evidence in support of this argument is our observation that changes in firing occur in the absence of significant changes in spike width, a direct measure of the effect of cooling (Volgushev et al., 2000b; Girardin and Martin, 2009).

Neural measurements of activity in the IC contralateral to the cooled IC provide evidence for an interaction between the two structures. These include changes in overall firing rate and in the temporal response properties of neurons that recover to pre-cool control values on rewarming. In addition, we found evidence for other changes in sound driven responses that will be reported separately. The summary data (**Figure 11**) show elevations and reductions in firing rate occur following deactivation of the contralateral IC. These are consistent with the findings reported when the contralateral IC is deactivated by drug injection (Malmierca et al., 2005). Such findings suggest that the commissural connections between the ICs mediate both excitatory and inhibitory effects, and the latter could be mediated by mono or disynaptic connections (Moore et al., 1998; Smith et al., 1998; Malmierca et al., 2005).

Given the extensive commissural fibers that interconnect the two ICs, blockade of these connections seems the most likely explanation for the changes we observed while cooling the other IC. However, an alternative mode of influence that could contribute to these effects is the modulation of descending activity from the IC since the neurons giving rise to descending fibers will also be deactivated by cooling. In guinea pig the IC sends descending projections to several upstream brainstem centers, both ipsilaterally and contralaterally (Malmierca et al., 1996; Schofield, 2001, 2010). Could the removal of descending input to these centers by cooling one IC explain the changes in neural activity we observed in the contralateral IC? Although we cannot rule out this possibility, evidence from LFP recordings suggests otherwise (**Figure 12**). In our recordings the first prominent peak in the LFP (particularly evident in responses to diotic stimuli or

stimuli applied to the ear contralateral to the recorded colliculus) had a latency of about 5–6 ms, about 1 ms shorter than the earliest spike latencies recorded in guinea pig IC. This latency also matched previous latency measurements of the P5 wave in the auditory brainstem response of guinea pig, and to LFPs recorded intracollicularly (Dum et al., 1981; Harrison and Palmer, 1984). It seems reasonable, therefore, to suggest that the first peak in the LFP corresponds to the latency of the incoming afferent volley to the IC and the synaptic activity that it generates. This short latency peak was minimally changed by cooling the other IC, both in terms of its amplitude and its latency. In contrast, the later components in the LFP, likely reflecting the activity of intracollicular processing, showed marked changes in morphology and latency with cooling. These changes could therefore represent the modulation of a commissurally-mediated influence over processing within the IC.

It could be argued that the LFP is not sufficiently sensitive to reflect the effect of descending control mediated by the IC, so although the conservative position is to assume that the effects of cooling one IC on the other are mediated by more than one pathway, given the strength of commissural input it is likely to be the dominant component. This limitation applies not only to cooling deactivation but to any method in which the circuitry of the IC is globally deactivated. If, as evidence suggests, different populations of neurons in the IC give rise to the descending and commissural projections (Okoyama et al., 2006), it may eventually be possible to selectively deactivate the descending and commissural systems, for example, by using optogenetic methods (Yizhar et al., 2011).

A further route whereby deactivation of one IC could affect the other is via a cortico-thalamic loop. Tracer studies show that the commissure contains some fibers that project from the IC to the contralateral auditory thalamus (Aitkin and Phillips, 1984) and there are descending connections from the contralateral cortex to the IC that probably involve the commissure (Winer et al., 2002; Bajo and Moore, 2005; Bajo et al., 2007). Deactivation of the IC would partially remove the drive to these centers and therefore could reduce the influence of their descending input to the contralateral IC. The contribution of these components to the commissure is, however, relatively small. Furthermore these fibers terminate mainly in the dorsal cortex and are therefore less likely to exert a direct effect in the central nucleus.

We conclude that cooling is a viable means of deactivating the IC and of studying the interaction between the two ICs. The rapid onset and reversibility of cooling, combined with the absence of any need for interference with the preparation during the cooling process, offer major advantages over drug injection methods. Like all deactivation methods that do not permit selective deactivation of different neuronal types, there is currently no way of isolating the contribution of commissural input from effects of descending connections to lower brainstem structures. Our results point to modulation of commissural input being the major effect of cooling the contralateral IC. This method produces changes in the response properties of IC neurons consistent with those observed with inactivation by drug injection, but offers the potential for more in depth studies of the role of the CoIC in auditory processing.

ACKNOWLEDGMENTS

Llwyd D. Orton was supported by a postgraduate studentship from Newcastle University. Paul W. F. Poon acknowledges the support of a visiting professorship from Newcastle University. We are grateful to David Perez Gonzalez for setting up the cooling system and to Alan Palmer for helpful advice about the cooling technique. This work was supported by a grant (BB/J008680/1) to Adrian Rees from the BBSRC.

REFERENCES

Adams, J. C. (1980). Crossed and descending projections to the inferior colliculus. *Neurosci. Lett.* 19, 1–5.

Aitkin, L. M., Gates, G. R., and Phillips, S. C. (1984). Responses of neurons in inferior colliculus to variations in sound-source azimuth. *J. Neurophysiol.* 52, 1–17.

Aitkin, L. M., and Phillips, S. C. (1984). The interconnections of the inferior colliculi through their commissure. *J. Comp. Neurol.* 228, 210–216.

Antunes, F. M., and Malmierca, M. S. (2011). Effect of auditory cortex deactivation on stimulus-specific adaptation in the medial geniculate body. *J. Neurosci.* 31, 17306–17316.

Bajo, V. M., and Moore, D. R. (2005). Descending projections from the auditory cortex to the inferior colliculus in the gerbil, *Meriones unguiculatus*. *J. Comp. Neurol.* 486, 101–116.

Bajo, V. M., Nodal, F. R., Bizley, J. K., Moore, D. R., and King, A. J. (2007). The ferret auditory cortex: descending projections to the inferior colliculus. *Cereb. Cortex* 17, 475–491.

Benita, M., and Conde, H. (1972). Effects of local cooling upon conduction and synaptic transmission. *Brain Res.* 36, 133–151.

Brooks, V. B. (1983). Study of brain-function by local, reversible cooling. *Rev. Physiol. Biochem. Pharmacol.* 95, 1–109.

Cao, X.-J., and Oertel, D. (2005). Temperature affects voltage-sensitive conductances differentially in octopus cells of the mammalian cochlear nucleus. *J. Neurophysiol.* 94, 821–832.

Coleman, J. R., and Clerici, W. J. (1987). Sources of projections to subdivisions of the inferior colliculus in the rat. *J. Comp. Neurol.* 262, 215–226.

Coomber, B., Edwards, D., Jones, S. J., Shackleton, T. M., Goldschmidt, J., Wallace, M. N., et al. (2011). Cortical inactivation by cooling in small animals. *Front. Syst. Neurosci.* 5:53. doi: 10.3389/fnsys.2011.00053

Delgutte, B., Joris, P. X., Litovsky, R. Y., and Yin, T. C. T. (1999). Receptive fields and binaural interactions for virtual-space stimuli in the cat inferior colliculus. *J. Neurophysiol.* 81, 2833–2851.

Diamond, M. E., Armstrong-James, M., Budway, M. J., and Ebner, F. F. (1992). Somatic sensory responses in the rostral sector of the posterior group (POm) and in the ventral posterior medial nucleus (VPM) of the rat thalamus: dependence on the barrel field cortex. *J. Comp. Neurol.* 319, 66–84.

Dorr, A., Sled, J. G., and Kabani, N. (2007). Three-dimensional cerebral vasculature of the CBA mouse brain: a magnetic resonance imaging and micro computed tomography study. *Neuroimage* 35, 1409–1423.

Dum, N., Schmidt, U., and von Wedel, H. (1981). Scalp distribution of the auditory evoked brainstem potentials in the guinea pig during monaural and binaural stimulation. *Hear. Res.* 5, 271–284.

Evans, E. F. (1979). "Single unit studies of the mammalian auditory nerve," in *Auditory Investigations: The Scientific and Technological Basis*, ed H. A. Beagley (Oxford: Oxford University Press), 324–367.

Ferster, D., Chung, S., and Wheat, H. (1996). Orientation selectivity of thalamic input to simple cells of cat visual cortex. *Nature* 380, 249–252.

Girard, P., and Bullier, J. (1989). Visual activity in area V2 during reversible inactivation of area 17 in the macaque monkey. *J. Neurophysiol.* 62, 1287–1302.

Girardin, C. C., and Martin, K. A. C. (2009). Cooling in cat visual cortex: stability of orientation selectivity despite changes in responsiveness and spike width. *Neuroscience* 164, 777–787.

González-Hernández, T. H., Galindo-Mireles, D., Castañeyra-Perdomo, A., and Ferres-Torres, R. (1991). Divergent projections of projecting

neurons of the inferior colliculus to the medial geniculate body and the contralateral inferior colliculus in the rat. *Hear. Res.* 52, 17–21.

Gross, P. M., Sposito, N. M., Pettersen, S. E., Panton, D. G., and Fenstermacher, J. D. (1987). Topography of capillary density, glucose metabolism, and microvascular function within the rat inferior colliculus. *J. Cereb. Blood Flow Metab.* 7, 154–160.

Hardingham, N. R., and Larkman, A. U. (1998). The reliability of excitatory synaptic transmission in slices of rat visual cortex *in vitro* is temperature dependent. *J. Physiol. (Lond.)* 507, 249–256.

Harrison, R. V., and Palmer, A. R. (1984). Neurone response latency in the inferior colliculus in relation to the auditory brainstem responses (ABR) in the guinea pig. *Scand. Audiol.* 13, 275–281.

Heffner, R., Heffner, H., and Masterton, B. (1971). Behavioral measurements of absolute and frequency-difference thresholds in guinea pig. *J. Acoust. Soc. Am.* 49, 1888–1895.

Jenkins, W. M., and Masterton, R. B. (1982). Sound localization: effects of unilateral lesions in central auditory system. *J. Neurophysiol.* 47, 987–1016.

Kayama, Y., Shosaku, A., and Doty, R. W. (1984). Cryogenic blockade of the visual cortico-thalamic projection in the rat. *Exp. Brain Res.* 54, 157–165.

Keating, E. G., and Gooley, S. G. (1988). Saccadic disorders caused by cooling the superior colliculus or the frontal eye field, or from combined lesions of both structures. *Brain Res.* 438, 247–255.

Kelly, J. B., and Kavanagh, G. L. (1994). Sound localization after unilateral lesions of inferior colliculus in the ferret (*Mustela putorius*). *J. Neurophysiol.* 71, 1078–1087.

LeBeau, F. E. N., Malmierca, M. S., and Rees, A. (2001). Iontophoresis *in vivo* demonstrates a key role for GABA(A) and glycinergic inhibition in shaping frequency response areas in the inferior colliculus of guinea pig. *J. Neurosci.* 21, 7303–7312.

Litovsky, R. Y., Fligor, B. J., and Traino, M. J. (2002). Functional role of the human inferior colliculus in binaural hearing. *Hear. Res.* 165, 177–188.

Lomber, S. G., Cornwell, P., Sun, J. S., MacNeil, M. A., and Payne, B. R. (1994). Reversible inactivation of visual processing operations in middle suprasylvian cortex of the behaving cat. *Proc. Natl. Acad. Sci. U.S.A.* 91, 2999–3003.

Lomber, S. G., and Malhotra, S. (2008). Double dissociation of 'what' and 'where' processing in auditory cortex. *Nat. Neurosci.* 11, 609–616.

Lomber, S. G., Malhotra, S., and Hall, A. J. (2007a). Functional specialization in non-primary auditory cortex of the cat: areal and laminar contributions to sound localization. *Hear. Res.* 229, 31–45.

Lomber, S. G., Malhotra, S., and Sprague, J. M. (2007b). Restoration of acoustic orienting into a cortically deaf hemifield by reversible deactivation of the contralesional superior colliculus: the acoustic "Sprague effect". *J. Neurophysiol.* 97, 979–993.

Lomber, S. G., and Payne, B. R. (1996). Removal of two halves restores the whole: reversal of visual hemineglect during bilateral cortical or collicular inactivation in the cat. *Vis. Neurosci.* 13, 1143–1156.

Lomber, S. G., and Payne, B. R. (2000). Translaminar differentiation of visually guided behaviors revealed by restricted cerebral cooling deactivation. *Cereb. Cortex* 10, 1066–1077.

Lomber, S. G., Payne, B. R., and Cornwell, P. (2001). Role of the superior colliculus in analyses of space: superficial and intermediate layer contributions to visual orienting, auditory orienting, and visuospatial discriminations during unilateral and bilateral deactivations. *J. Comp. Neurol.* 441, 44–57.

Lomber, S. G., Payne, B. R., and Horel, J. A. (1999). The cryoloop: an adaptable reversible cooling deactivation method for behavioral or electrophysiological assessment of neural function. *J. Neurosci. Methods* 86, 179–194.

Malmierca, M. S., and Hackett, T. A. (2010). "Structural organization of the ascending auditory pathway," in *The Auditory Brain*, eds A. Rees and A. R. Palmer (Oxford: Oxford University Press), 9–41.

Malmierca, M. S., Hernández, O., Antunes, F. M., and Rees, A. (2009). Divergent and point-to-point connections in the commissural pathway between the inferior colliculi. *J. Comp. Neurol.* 514, 226–239.

Malmierca, M. S., Hernández, O., Falconi, A., Lopez-Poveda, E. A., Merchán, M. A., and Rees, A. (2003). The commissure of the inferior colliculus shapes frequency response areas in rat: an *in vivo* study using reversible blockade with microinjection of kynurenic acid. *Exp. Brain Res.* 153, 522–529.

Malmierca, M. S., Hernández, O., and Rees, A. (2005). Intercollicular commissural projections modulate neuronal responses in the inferior colliculus. *Eur. J. Neurosci.* 21, 2701–2710.

Malmierca, M. S., LeBeau, F. E. N., and Rees, A. (1996). The topographical organization of descending projections from the central nucleus of the inferior colliculus in guinea pig. *Hear. Res.* 93, 167–180.

Malmierca, M. S., Rees, A., Le Beau, F. E. N., and Bjaalie, J. G. (1995). Laminar organization of frequency-defined local axons within and between the inferior colliculi of the guinea pig. *J. Comp. Neurol.* 357, 124–144.

McClurkin, J. W., and Marrocco, R. T. (1984). Visual cortical input alters spatial tuning in monkey lateral geniculate nucleus cells. *J. Physiol. (Lond.)* 348, 135–152.

Merrill, E., and Ainsworth, A. (1972). Glass-coated platinum-plated tungsten microelectrodes. *Med. Biol. Eng. Comput.* 10, 662–672.

Merzenich, M. M., and Reid, M. D. (1974). Representation of the cochlea within the inferior colliculus of the cat. *Brain Res.* 77, 397–415.

Michalski, A., Wimborne, B. M., and Henry, G. H. (1993). The effect of reversible cooling of cat's primary visual cortex on the responses of area 21a neurons. *J. Physiol. (Lond.)* 466, 133–156.

Moore, C. N., Casseday, J. H., and Neff, W. D. (1974). Sound localization: the role of the commissural pathways of the auditory system of the cat. *Brain Res.* 82, 13–26.

Moore, D. R. (1988). Auditory brainstem of the ferret: sources of projections to the inferior colliculus. *J. Comp. Neurol.* 269, 342–354.

Moore, D. R., Kotak, V. C., and Sanes, D. H. (1998). Commissural and lemniscal synaptic input to the gerbil inferior colliculus. *J. Neurophysiol.* 80, 2229–2236.

Nakamoto, K. T., Jones, S. J., and Palmer, A. R. (2008). Descending projections from auditory cortex modulate sensitivity in the midbrain to cues for spatial position. *J. Neurophysiol.* 99, 2347–2356.

Okoyama, S., Ohbayashi, M., Ito, M., and Harada, S. (2006). Neuronal organization of the rat inferior colliculus participating in four major auditory pathways. *Hear. Res.* 218, 72–80.

Oliver, D. L., and Huerta, M. F. (1992). "Inferior and superior colliculi," in *The Mammalian Auditory Pathway: Neuroanatomy*, eds D. B. Webster, A. N. Popper, and R. R. Fay (New York, NY: Springer-Verlag), 168–221.

Payne, B. R., Lomber, S. G., Villa, A. E., and Bullier, J. (1996). Reversible deactivation of cerebral network components. *Trends Neurosci.* 19, 535–542.

Prosen, C. A., Petersen, M. R., Moody, D. B., and Stebbins, W. C. (1978). Auditory thresholds and kanamycin-induced hearing loss in the guinea pig assessed by a positive reinforcement procedure. *J. Acoust. Soc. Am.* 63, 559–566.

Rees, A., Sarbaz, A., Malmierca, M. S., and Le Beau, F. E. N. (1997). Regularity of firing of neurons in the inferior colliculus. *J. Neurophysiol.* 77, 2945–2965.

Reivich, M., Jehle, J., Sokoloff, L., and Kety, S. S. (1969). Measurement of regional cerebral blood flow with antipyrine-^{14}C in awake cats. *J. Appl. Physiol.* 27, 296–300.

Rose, J. E., Greenwood, D. D., Goldberg, J. M., and Hind, J. E. (1963). Some discharge characteristics of single neurons in the inferior colliculus of the cat. I. Tonotopical organization, relation of spike-counts to tone intensity, and firing patterns of single elements. *J. Neurophysiol.* 26, 294–320.

Saldaña, E., and Merchán, M. (2005). "Intracollicular connections," in *The Inferior Colliculus*, eds J. A. Winer and C. Schreiner (New York, NY: Springer), 155–181.

Saldaña, E., and Merchán, M. A. (1992). Intrinsic and commissural connections of the rat inferior colliculus. *J. Comp. Neurol.* 319, 417–437.

Schiller, P. H., and Malpeli, J. G. (1977). The effect of striate cortex cooling on area 18 cells in the monkey. *Brain Res.* 126, 366–369.

Schofield, B. R. (2001). Origins of projections from the inferior colliculus to the cochlear nucleus in guinea pigs. *J. Comp. Neurol.* 429, 206–220.

Schofield, B. R. (2010). "Structural organization of the descending auditory pathway," in *The Auditory Brain*, eds A. Rees and A. R. Palmer (Oxford: Oxford University Press), 43–64.

Semple, M. N., and Aitkin, L. M. (1979). Representation of sound frequency and laterality by units in the central nucleus of cat inferior colliculus. *J. Neurophysiol.* 42, 1626–1639.

Sherk, H. (1978). Area 18 cell responses in cat during reversible inactivation of area 17. *J. Neurophysiol.* 41, 204–215.

Smith, P. H., Joris, P. X., and Yin, T. C. T. (1998). Anatomy and physiology of principal cells of

the medial nucleus of the trapezoid body (MNTB) of the cat. *J. Neurophysiol.* 79, 3127–3142.

Song, Y., Mellott, J. G., and Winer, J. A. (2011). Microvascular organization of the cat inferior colliculus. *Hear. Res.* 274, 5–12.

Trevelyan, A. J., and Jack, J. (2002). Detailed passive cable models of layer 2/3 pyramidal cells in rat visual cortex at different temperatures. *J. Physiol. (Lond.)* 539, 623–636.

Villa, A. E. P., Rouiller, E. M., Simm, G. M., Zurita, P., de Ribaupierre, Y., and de Ribaupierre, F. (1991). Corticofugal modulation of the information processing in the auditory thalamus of the cat. *Exp. Brain Res.* 86, 506–517.

Villa, A. E. P., Tetko, I. V., Dutoit, P., de Ribaupierre, Y., and de Ribaupierre, F. (1999). Corticofugal modulation of functional connectivity within the auditory thalamus of rat, guinea pig and cat revealed by cooling deactivation. *J. Neurosci. Methods* 86, 161–178.

Volgushev, M., Vidyasagar, T. R., Chistiakova, M., and Eysel, U. T. (2000a). Synaptic transmission in the neocortex during reversible cooling. *Neuroscience* 98, 9–22.

Volgushev, M., Vidyasagar, T. R., Chistiakova, M., Yousef, T., and Eysel, U. T. (2000b). Membrane properties and spike generation in rat visual cortical cells during reversible cooling. *J. Physiol. (Lond.)* 522, 59–76.

Winer, J. A., Chernock, M. L., Larue, D. T., and Cheung, S. W. (2002). Descending projections to the inferior colliculus from the posterior thalamus and the auditory cortex in rat, cat, and monkey. *Hear. Res.* 168, 181–195.

Yang, X.-F., Kennedy, B. R., Lomber, S. G., Schmidt, R. E., and Rothman, S. M. (2006). Cooling produces minimal neuropathology in neocortex and hippocampus. *Neurobiol. Dis.* 23, 637–643.

Yizhar, O., Fenno, L. E., Davidson, T. J., Mogri, M., and Deisseroth, K. (2011). Optogenetics in neural systems. *Neuron* 71, 9–34.

Yuan, B., Morrow, T. J., and Casey, K. L. (1986). Corticofugal influences of S1 cortex on ventrobasal thalamic neurons in the awake rat. *J. Neurosci.* 6, 3611–3617.

Conflict of Interest Statement: The authors declare that the research was conducted in the absence of any commercial or financial relationships that could be construed as a potential conflict of interest.

Received: 18 July 2012; accepted: 19 November 2012; published online: 14 December 2012.

Citation: Orton LD, Poon PWF and Rees A (2012) Deactivation of the inferior colliculus by cooling demonstrates intercollicular modulation of neuronal activity. Front. Neural Circuits ***6****:100. doi: 10.3389/fncir.2012.00100*

frontiers in
NEURAL CIRCUITS

ORIGINAL RESEARCH ARTICLE
published: 28 June 2012
doi: 10.3389/fncir.2012.00041

The selective neurotoxin DSP-4 impairs the noradrenergic projections from the locus coeruleus to the inferior colliculus in rats

Sebastián Hormigo*[1,2], *José de Anchieta de Castro e Horta Júnior*[3], *Ricardo Gómez-Nieto*[1,2,4] and *Dolores E. López*[1,2,4]

[1] *Institute for Neuroscience of Castilla y Leon, University of Salamanca, Salamanca, Spain*
[2] *Institute of Biomedical Research of Salamanca, University of Salamanca, Salamanca, Spain*
[3] *Biosciences Institute - Campus of Botucatu, São Paulo State University - UNESP-, São Paulo, Brazil*
[4] *Department of Cellular Biology and Pathology, University of Salamanca, Salamanca, Spain*

Edited by:
Eric D. Young, Johns Hopkins University, USA

Reviewed by:
Douglas L. Oliver, University of Connecticut Health Center, USA
Laura M. Hurley, Indiana University, USA

****Correspondence:***
Dolores E. López, Institute for Neuroscience of Castilla y Leon (INCYL), University of Salamanca, C/ Pintor Fernando Gallego, 1, 37007 Salamanca, Spain.
e-mail: lopezde@usal.es

The inferior colliculus (IC) and the locus coeruleus (LC) are two midbrain nuclei that integrate multimodal information and play a major role in novelty detection to elicit an orienting response. Despite the reciprocal connections between these two structures, the projection pattern and target areas of the LC within the subdivisions of the rat IC are still unknown. Here, we used tract-tracing approaches combined with immunohistochemistry, densitometry, and confocal microscopy (CM) analysis to describe a projection from the LC to the IC. Biotinylated dextran amine (BDA) injections into the LC showed that the LC-IC projection is mainly ipsilateral (90%) and reaches, to a major extent, the dorsal and lateral part of the IC and the intercollicular commissure. Additionally, some LC fibers extend into the central nucleus of the IC. The neurochemical nature of this projection is noradrenergic, given that tyrosine hydroxylase (TH) and dopamine beta hydroxylase (DBH) colocalize with the BDA-labeled fibers from the LC. To determine the total field of the LC innervations in the IC, we destroyed the LC neurons and fibers using a highly selective neurotoxin, DSP-4, and then studied the distribution and density of TH- and DBH-immunolabeled axons in the IC. In the DSP-4 treated animals, the number of axonal fibers immunolabeled for TH and DBH were deeply decreased throughout the entire rostrocaudal extent of the IC and its subdivisions compared to controls. Our densitometry results showed that the IC receives up to 97% of its noradrenergic innervations from the LC neurons and only 3% from non-coeruleus neurons. Our results also indicate that TH immunoreactivity in the IC was less impaired than the immunoreactivity for DBH after DSP-4 administration. This is consistent with the existence of an important dopaminergic projection from the substantia nigra to the IC. In conclusion, our study demonstrates and quantifies the noradrenergic projection from the LC to the IC and its subdivisions. The re-examination of the TH and DBH immunoreactivity after DSP-4 treatment provides insights into the source, extent, and topographic distribution of the LC efferent network in the IC, and hence, contributes to our understanding of the role of the noradrenaline (NA) system in auditory processing.

Keywords: biotinylated dextran amine, dopamine beta hydroxylase deficiency, immunohistochemistry, densitometry, neurotoxicity, noradrenergic efferents, noradrenergic modulation, tyrosine hydroxylase

Abbreviations: 4V, forth ventricle; 5n, trigeminal nerve; ABC, avidin biotin-peroxidase complex; Aq, Aqueduct (Sylvius); BDA, biotinylated dextran amine; CM, confocal microscopy; CN, cochlear nucleus; CNIC, central nucleus of the inferior colliculus; DAB, 3,3′ diaminobenzidine; DBH, dopamine beta hydroxylase; DCIC, dorsal cortex of the inferior colliculus; DNLL, dorsal nucleus of the lateral lemniscus; DSP-4, N-(2-chloroethyl)-N-ethyl-2-bromobenzylamine; LCIC, lateral cortex of the inferior colliculus; IA, Interaural level; IC, inferior colliculus; IHC, immunohistochemistry; ir, immunoreactivity; IS, injection site; LC, locus coeruleus; LM, light microscopy; ml, medial lemniscus; MNTB, medial nucleus of the trapezoid body; PB, phosphate buffer 0.1 M, pH 7.4; PBS, phosphate buffer saline; PnO, pontine reticular nucleus, oral part; NA, noradrenaline; TH, tyrosine hydroxylase; Tx, Triton X100; tz, trapezoid body; VNLL, ventral nucleus of the lateral lemniscus.

INTRODUCTION

The locus coeruleus (LC) is a structure located in the caudal central gray pons under the floor of the fourth ventricle. It was first described in 1809 by the German neuroanatomist Johann C. Reil, but it was not until 1812 that the Wenzel brothers coined the name (Toshihiro, 2000). The LC is involved in many of the sympathetic effects during stress due to an increased production of noradrenaline (NA). Electrophysiological studies support the hypothesis that the LC is activated by various stressful stimuli (Valentino et al., 1983; Page et al., 1992; Curtis et al., 1993; del C. Gonzalez et al., 1995; Singewald et al., 1995; Conti and

Foote, 1996; Dawe et al., 2001; Valentino and Van Bockstaele, 2008), noxious/nociceptive stimuli (Singewald et al., 1995; Couto et al., 2006; Viisanen and Pertovaara, 2007; Liu et al., 2008; Imbe et al., 2009; Tsuruoka et al., 2011), and physiological stimuli, such as hypotension, hypoxia, and visceral stimulation, which increase the firing of the neurons in this structure (Miao-Kun, 1995; Singewald et al., 1995; Lechner et al., 1997; Valentino et al., 2005; Ma et al., 2008).

The LC is the main source of NA for both the brainstem and the forebrain (Aston-Jones, 2004). Previous investigations have described the catecholamine biosynthetic pathways and their regulation in the nervous system. The metabolic pathways can be finely regulated when there is an increase in the demand of synthesis for NA, for instance in a stressful situation or in the detection of novelty stimuli (Potter et al., 1962; Snyder et al., 1965; Axelrod et al., 1969; Ciaranello et al., 1976).

Studies have shown that the neurotoxin N-(2-chloroethyl)-N-ethyl-2-bromobenzylamine (DSP-4) can be used for the temporary selective degradation of the central and peripheral noradrenergic neurons, mainly those from the LC (Fritschy and Grzanna, 1989; Grzanna et al., 1989; Fritschy et al., 1991). Based on these experiments, the authors described the existence of two separate subsystems of noradrenergic fibers, the LC and non-coerulean noradrenergic fibers, which differ not only in their projections but also with respect to the pharmacological properties of their axon terminals. The neurotoxin DSP-4 exclusively affects the noradrenergic fibers from the LC (Fritschy and Grzanna, 1989; Grzanna et al., 1989). It has been suggested that this selectivity of DSP-4 toward LC neurons may be related to the significant difference found in the affinity of DSP-4 for the NA uptake carrier in different brain structures (Zaczek et al., 1990). In rodents, a systemic injection of DSP-4 causes a depletion in the levels of NA, in the release capacity and in the activity of dopamine beta hydroxylase (DBH) (Ross et al., 1973; Ross, 1985). The effects of DSP-4 administration on the behavior of rats (open-field tests) can include neophobia (distorted reactions to new things or experiences), increased emotionality (more grooming activities and number of stools), defensive or submissive behavior, an altered resident/intruder paradigm, increased aggressiveness and a lack of fear to environmental factors (Spyraki et al., 1982; Delini-Stula et al., 1984; Cornwell-Jones et al., 1992; Harro et al., 1995; van den Buuse et al., 2001).

With regard to the auditory pathway, the LC provides noradrenergic inputs to the cochlear nuclei (Klepper and Herbert, 1991; Ebert, 1996; Thompson, 2003), the superior olivary complex (Mulders and Robertson, 2001), the cochlear root nucleus (Gómez-Nieto et al., 2008b) and the inferior colliculus (IC) (Klepper and Herbert, 1991). The IC is an important auditory nucleus in the brainstem with significant physiological implications, not only for hearing processing but also for adaptive mechanisms, such as the acoustic startle reflex (Jordan and Leaton, 1982; Leitner and Cohen, 1985; Li et al., 1998; Li and Yeomans, 2000; Li and Yue, 2002; Heldt and Falls, 2003; Nobre et al., 2003; Silva et al., 2005; Reimer et al., 2008; Satake et al., 2012). The LC and the IC are reciprocally connected (Klepper and Herbert, 1991; Freitas et al., 2006). Nevertheless, little is known about the projection pattern and target areas of the LC within the IC. The aim of this study was to investigate the noradrenergic innervation of the LC throughout the rostrocaudal extent of the IC and its subdivisions. We attempt to reveal the extensive LC noradrenergic efferent network within the IC using anterograde tract-tracing techniques combined with immunohistochemistry in addition to densitometry and colocalization studies of the catecholaminergic enzymes in control and DSP-4 treated rats. Based on the hypothesis that there are two separate subsystems of noradrenergic fibers and that the neurotoxin DSP-4 exclusively affects the noradrenergic fibers from the LC (Fritschy and Grzanna, 1989; Grzanna et al., 1989), we used DSP-4 as a highly selective neurotoxin to eliminate the projections from the LC. Using this approach, we studied the changes in DBH immunohistochemistry in the IC before and after DSP-4 treatment to evaluate the loss of the LC noradrenergic projections to the IC and quantified the difference.

MATERIALS AND METHODS

ANIMALS AND EXPERIMENTAL DESIGN

Seventeen adult albino rats (Wistar strain) weighting 250–300 g were used (Charles River, Barcelona, Spain). The experiments were conducted according to the guidelines for the use and care of laboratory animals of the European Communities Council Directive (DOCE L222; 24-08-1999) and with those established by the Spanish Government (RD 1201/2005). Animals were housed in groups of two or three prior to surgery and individually afterwards. All efforts were made to minimize the number of animals that were used and their suffering.

We designed a prospective study. In the first step, we studied the projections from the LC to the IC. Then, we demonstrated the noradrenergic nature of these projections in the IC through spatial overlapping techniques, and we described the noradrenergic immunoreactivity in the IC. Afterwards, we investigated the morphological modifications in animals treated with the neurotoxin DSP-4.

INJECTION OF NEURONAL TRACERS

To study the neuronal projections from the LC to the IC, we injected nine animals with biotinylated dextran amine (BDA, 10,000 MW, Molecular Probes, Eugene, OR, USA; 10% in distilled water) in the left LC. The neuronal tracer BDA was injected after deep anesthetization of the animal through an intramuscular administration of a mixture of xylazine (7 mg/kg) and ketamine (40 mg/kg). When necessary, additional anesthesia (one-fifth of the initial dose) was given during surgery. Each animal was placed in a stereotaxic frame (Kopf, Tujunga, CA, USA) using the head-positioning procedure described by Paxinos and Watson (2005). The skull was exposed by a midline scalp incision, and a craniotomy was performed over the injection coordinates (Fritschy and Grzanna, 1990). Because the LC is topographically organized, the injection sites were preferentially located in and around the dorsal half of the nucleus, where the ascending projections originate (Guyenet, 1980; Fritschy and Grzanna, 1990). BDA was injected iontophoretically via a glass micropipette (25 μm tip diameter) with 3 μA positive current pulses (7 s on/7 s off) for 15 min. Following the tracer injection, the pipette was left in place for 15 min without current passing to prevent the backflow, then

the scalp was sutured and the animal was allowed to recover for a minimum of 7 d (Gómez-Nieto et al., 2008a; Horta-Júnior et al., 2008).

VISUALIZATION OF NEUROTRACERS

At the end of the survival period, the animals were euthanized with a sodium pentobarbital overdose and then perfused transcardially with 100 ml of fresh Ringer calcium-free buffer (NaCl, 145.45 mM; KCl, 3.35 mM; $NaHCO_3$, 2.38 mM), pH 6.9, at 37°C, followed by 1000 ml of fresh depolymerized 4% paraformaldehyde in 0.1 M phosphate buffer, pH 7.4 (PB), at room temperature. For either light microscopy (LM) or confocal microscopy (CM), the brains were removed and cryoprotected for 48 h at 4°C in 30% sucrose in PB. Serial coronal sections (40 μm in thickness) were cut on a freezing stage sliding microtome (HM430; Microm, Heidelberg, Germany). The serial sections were collected in PB and divided into a series of 10 bins.

For LM, the tracers were visualized using a peroxide-based protocol with Tris-buffered saline containing 0.2% Triton X-100 (TBS-TX, #T9284; Sigma, St. Louis, MO, USA) in washing steps. To reveal the BDA tracer, free-floating sections were incubated with an avidin biotin-peroxidase complex (ABC, Standard-kit #PK 4000; Vector Laboratories, Burlingame, CA, USA) for 2 h and visualized with a 3,3′ diaminobenzidine tetrahydrochloride (DAB) and nickel ammonium sulfate solution (Hancock, 1982; Hsu and Soban, 1982).

TH AND DBH IMMUNOHISTOCHEMISTRY FOR LM

To study the pattern of TH and DBH immunoreactivity, we used eight animals. After the perfusion and serial section protocol, standard immunostaining procedures were followed for the respective sections, which entailed incubating the sections for 72 h at 4°C in a primary antibody solution diluted in TBS-Tx. The tissue was then washed and incubated in its corresponding biotinylated secondary antibody for 2 h at room temperature. The antibodies used and their dilution are shown in **Table 1**.

Following the removal of the secondary antibodies, the sections were reacted with ABC as described above, using DAB as the chromogen. All sections were mounted on slides, dehydrated and coverslipped with Entellan® Neu (Merck, Darmstadt, Germany). In addition, several series were counterstained with cresyl violet 0.1% (#5235, Merck) for cytoarchitectonic reference, chiefly to identify the subdivisions of the IC.

COLOCALIZATION EXPERIMENTS

To demonstrate the noradrenergic nature of the BDA-labeled fibers from the LC, we have performed experiments to highlight the colocalization between, tyrosine hydroxylase-immunoreactivity (TH-ir) and dopamine beta hydroxylase-immunoreactivity (DBH-ir) in the IC using CM. Free-floating sections were pretreated with phosphate buffer saline (PBS) 0.3% Triton X-100 and blocked for 1 h at room temperature with 6% normal goat serum (#S-1000, Vector Laboratories) in PBS. After overnight incubation at 4°C with primary antibodies, the sections were washed in PBS and incubated for 1 h at room temperature with the secondary antibody (**Table 1**). The BDA was revealed by incubation in Cy2-conjugated streptavidin (1/650; #016-220-084; Jackson ImmunoResearch). Later on, the sections were rinsed, mounted on slides and coverslipped with the ProLong® Antifade kit (#P7481; Molecular Probes).

In all immunohistochemistry experiments, the omission of the primary antibody resulted in no staining (see Results for more details).

NEUROTOXIC LESION WITH DSP-4

To study the TH-ir and DBH-ir fibers located in the IC following the administration of DSP-4 (Sigma-Aldrich Co, St. Louis, MO, USA), we performed immunohistochemistry for TH and BDH in five animals treated with DSP-4 and five control animals. We administrated a single intraperitoneal dose of 50 mg/kg of DSP-4 in five rats, as previously described (Ross, 1985; Grzanna et al., 1989; Fritschy et al., 1991). After 15 d, we sacrificed the rats.

IMAGE ANALYSIS

The sections processed for LM were studied using a microscope (#BX5; Olympus, Center Valley, PA, USA) equipped with a digital camera (Spot Rt®; Diagnostic Instruments, Sterling Heights, MI, USA). Low-magnification images were taken with a 5× objective lens, and high-magnification images were taken with a 20× objective lens.

Table 1 | List of antibodies and dilutions used for the immunohistochemical approaches.

Antigen	Primary antibody	Reference	Dilution	Secondary antibody	Reference	Dilution	Method
TH	Mouse anti-TH	#22941-Diasorin	1/10,000	Biotinylated goat anti-mouse	#BA-2000-Vector	1/200	LM
				Goat Cy5 anti-mouse IgG	#115-175-003-JI	1/250	CM
				Goat Cy2 anti-mouse	#115-225-003-JI	1/250	CM
DBH	Rabbit anti-DBH	#DZ1020-Affiniti	1/500	Biotinylated goat anti-rabbit	#BA-1000-Vector	1/200	LM
				Goat Cy5 anti-rabbit IgG	#111-175-003-JI	1/250	CM

Affinity Research Products, Nottingham, UK; Diasorin, Stillwater, MN, USA; JI: Jackson Immunoresearch, West Grove, PA, USA; Vector Laboratories, Burlingame, CA, USA. The specificity of the anti-TH antibody: the antibody recognizes an epitope present in the N-terminal region (between a 40–152) of both rodent and human tyrosine hydroxylase. It detects both the intact subunits and the 59/57 kDa doublet and an array of TH forms with decreasing molecular weights resulting from severe proteolysis. The specificity of the anti-DBH antibody: the dopamine β-hydroxylase precursor recombinant protein epitope signature tag (PrEST).

Immunogen sequence:

VQRTPEGLTLLFKRPFGTCDPKDYLIEDGTVHLVYGILEEPFRSLEAINGSGLQMGLQRVQLLKPNIPEPELPSDACTMEVQAPNIQIPSQETTYWCYIKELPKGFSRHHIIKYEPIV TKGN.

The sections processed for CM were first examined using a microscope (#BX5; Olympus) equipped with epifluorescence and a digital camera (Spot Rt®). Then, the sections were processed and analyzed using a Leica TCS SP2 confocal laser scanning microscope (Leica Microsystems, Mannheim, Germany) coupled to a Leica DM IRE2 inverted microscope and equipped with argon and helium neon lasers with excitation wavelengths of 458, 476, 488, 543, 568, and 633 nm. The fluorochromes Cy2 and Cy5 were detected sequentially, stack-by-stack, with the acousto-optical tunable filter system and triple dichroic mirror TD488/543/633 using laser lines 488–495, 546, and 633 nm. The background was controlled, and the photomultiplier voltage (800 V) was selected for maximum sensitivity in the linear range. The objectives used were Planapochromat 20×, oil immersion 40×, and 63×/numerical aperture 1.30, giving a resolution of ∼150 nm in the xy-plane and ∼300 nm along the z-axis (pinhole 1 Airy unit), as well as several electronic zoom factors up to 1.58×.

All photomicrographs shown in the figures were processed with minor modifications in brightness, contrast and to remove the tissue free background using Adobe Photoshop® (version 9.0; Adobe Systems Incorporated, San Jose, CA, USA). The IC fiber drawing was made using Adobe Photoshop® to mount digitalized slices from high-magnification images acquired with 20× objective lens and Canvas® (version X Build 885, ACD Systems Inc, USA) to draw the labeled fibers as well as the assemblage of all figures.

The densitometry of TH-ir and DBH-ir was made using the Canvas fiber drawings. The immunoreactive fibers in the IC were drawn with 0.176 mm thick black solid lines on a white background. The quantification of the mean gray level for the subdivisions of the IC in different rostrocaudal levels was performed on traces of stained sections using ImageJ software (version 1.43, Rasband, W.S., ImageJ, US National Institutes of Health, Bethesda, Maryland, USA, http://imagej.nih.gov/ij/, 1997–2011).

Different experimental conditions were compared using the unpaired Student's *t*-test. Data are reported as the means ± SD. The statistical package we employed was PASW Statistics 18.0.0 (SPSS Inc., Chicago, IL, USA). Statistical significance was accepted at $p < 0.05$.

RESULTS

LC SENDS PROJECTIONS TO THE IC

The tracer injection experiments resulted in a single BDA injection in the left LC (**Figure 1A**). The injection sites were elliptical with a typical size of ∼ 600 × 600 μm in the rostrocaudal and mediolateral axis, respectively. We only used those injections that did not spread to adjacent nuclei, e.g., to the laterodorsal tegmental nucleus (LDTg). The injections were restricted to the nuclear core of the LC. We also detected anterograde labeling in known LC targets, including the dorsal raphe (Kim et al., 2004), and brain structures of the somatosensory pathway, such as the somatosensory cortex, the ventrobasal nucleus of the thalamus, and the principal nucleus of the trigeminal nerve (Simpson et al., 1997). In all cases, we observed thick (1.04 ± 0.78 μm), straight BDA-labeled fibers with varicosities en passage (beaded fibers), and thin (0.8 ± 0.15 μm), branching BDA-labeled fibers with button-like varicosities (terminal plexus) in both the ipsilateral and contralateral IC (**Figures 1B,C,D,** and **E**). These terminal fibers were located predominantly in the lateral and dorsal cortices and in the intercollicular commissure.

The LC–IC projection was mainly ipsilateral (∼90%), although each LC directs some fibers to the contralateral IC (∼10%) (**Figure 1F**). We found a few labeled fibers from the LC in the central nucleus of the IC.

NEUROCHEMICAL IDENTITY OF LC TERMINAL FIBERS IN THE IC

Fibers that were immunoreactive for TH and DBH in the IC were similar in distribution and size to those described for the BDA-labeled fibers from the LC. We observed TH-ir and BDH-ir beaded fibers that branched into thinner TH-ir and BDH-ir fibers with button-like varicosities (**Figures 2B** and **3B**).

To show that the BDA-labeled endings from the LC contained catecholaminergic enzymes (TH and DBH), we combined a BDA injection in the LC with immunohistochemistry for TH or DBH. Our results show that BDA-labeled fibers from the LC colocalized with TH-positive fibers and terminals, indicating the catecholaminergic nature of the LC-IC projection (**Figure 2**). Furthermore, some labeled fibers in the IC from the LC were identified as noradrenergic because we observed colocalization between the BDA-labeled fibers and the DBH-ir fibers (**Figure 3**).

Despite the high degree of colocalization in the IC between TH-ir and DBH-ir fibers (**Figure 4**), not every catecholaminergic fiber was noradrenergic in nature. The immunoreactivity for TH had incomplete spatial overlapping with DBH-ir (**Figure 4**). This suggests that others structures in the brainstem and in other brain regions are sending dopaminergic projections to the IC.

DSP-4 ADMINISTRATION IMPAIRED PROJECTIONS FROM THE LC TO THE IC

On average, the weight of the treated rats was approximately 12% lower than that of control rats at one week post-treatment and approximately 9% lower than controls at two weeks after the DSP-4 administration. The administration of DSP-4 in rats also causes changes in urination (a loss of rhythm patterns of diurnal urination), a large increase in void volume and increased water intake, all of which are due to changes in TH (Ranson et al., 2003). We also observed disturbed sleep in which the sleep-wake cycle was altered during the first five post-treatment but then returned to control values.

To determine the total field of the LC projection to the entire rostrocaudal extent of the IC and its subdivisions, we used TH and DBH immunohistochemistry and re-examined the LC-IC projection after DSP-4 administration. In non-treated animals, we found intense immunoreactivity for both TH and DBH in the LC (**Figures 5A** and **B**). Within the LC, we found dark-stained fibers and cell bodies immunolabeled for both enzymes. As described elsewhere (Klepper and Herbert, 1991), we observed this immunolabeled pattern of fibers and cell bodies throughout the rostral-caudal extent of the LC. At 15 days post-administration in DSP-4 rats, the immunoreactivity for those enzymes decidedly decreased. Thus, large projection neurons and the fibers of the LC could no longer be visualized with TH and DBH immunohistochemistry after DSP-4 treatment (**Figures 5C** and **D**). This indicates that the efferents from the LC are affected

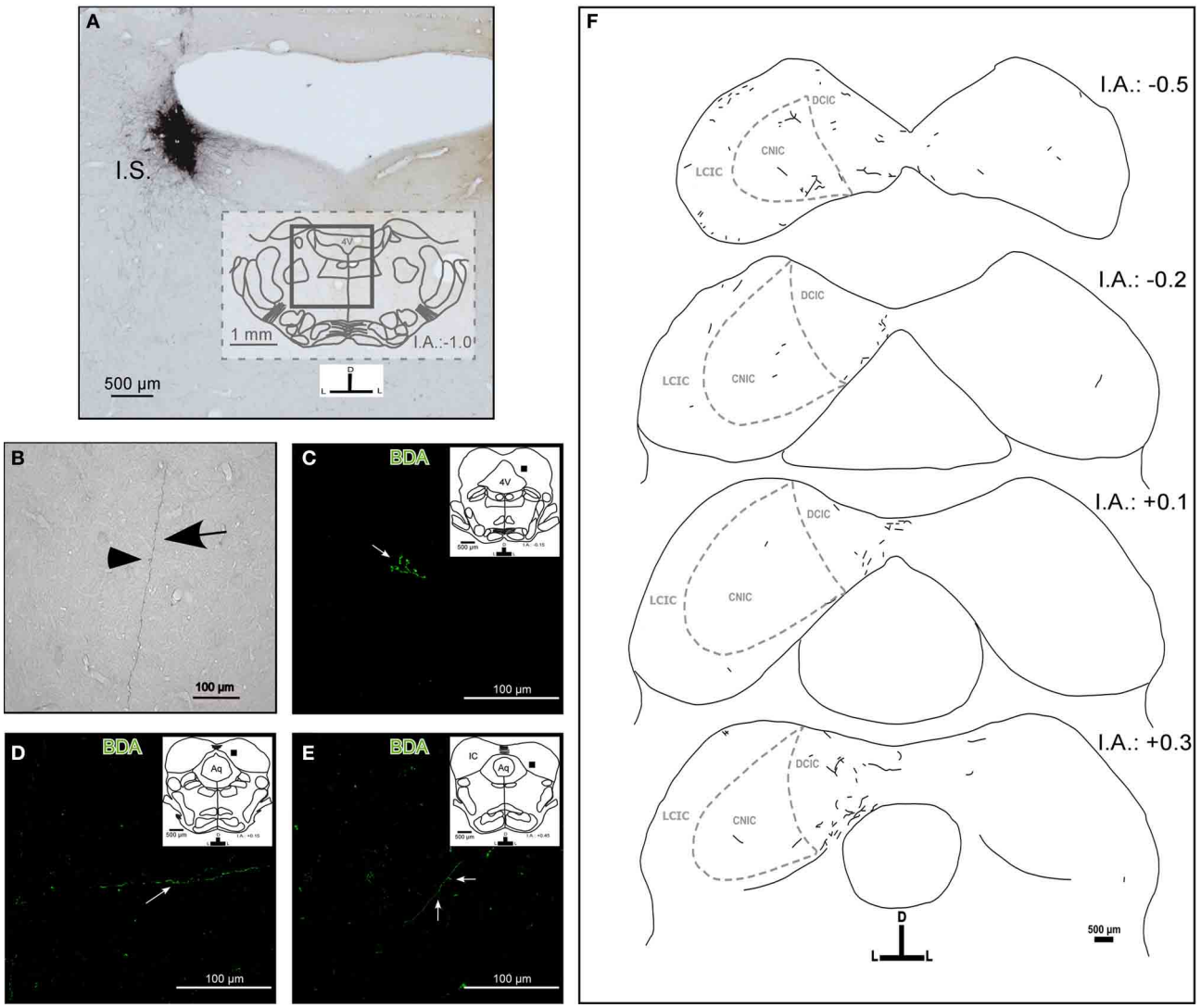

FIGURE 1 | The target areas and projection pattern of the locus coeruleus (LC) fibers within the inferior colliculus (IC). The inset schemes represent coronal sections at the rostrocaudal level as a reference, and the black square represents the area photographed in high magnification. **(A)** A representative photomicrograph of a typical injection site (I.S.). Left LC received a BDA stereotaxic injection (black). **(B)** A photomicrograph of a typical labeled fiber in the IC from the LC. The arrow indicates a fiber and the arrowhead indicates a varicosity. **(C–E)** Confocal photomicrographs of BDA-labeled fibers in the IC. **(C)** The arrow indicates possible synaptic buttons. **(D)** The arrow indicates single fibers. **(E)** The arrow indicates a fiber and the arrowhead indicates possible synaptic buttons. **(F)** A schematic representation of the BDA-labeled fibers from the LC found in the IC and the internal anatomic subdivisions of the IC. Notice that there are ipsi- and contralateral labeled fibers. The interaural level for coronal placement is displayed in millimeters. See the provided list for abbreviations.

by the action of the drug, including the noradrenergic fibers in the IC, as presented in the following results. The immunohistochemical negative controls (no primary antibody added) showed no immunoreactivity for TH or DBH (**Figures 5E,F,G,** and **H**).

For a better description of the results, we divided the rostrocaudal extension of the IC into three different parts: caudal, middle, and rostral. We found a dense TH-ir throughout the entire IC in the control animals, with the highest mean gray values at the caudal level, mainly in the DCIC and the CNIC (**Figure 6A**). The fibers spread homogeneously in the IC, and there was no significant difference in the distribution along the subdivisions ($p > 0.05$). There was a great reduction in TH fibers in all subdivisions of the IC in the animals treated with DSP-4 (**Figure 6B**). The most important diminutions were found in the caudal (72.9%, $p < 0.01$) and the middle (68.8%, $p < 0.01$) portions of the CNIC and in the whole length of the LCIC (caudal 73%, middle 72.3%, and rostral 50.9%, for all cases $p < 0.01$) (**Figures 6C,D,** and **E**), whereas the rostral part of the DCIC and the intercollicular commissure remained almost unaltered. The observed reduction was approximately 10% ($p < 0.05$) (**Figure 6E**), suggesting that approximately 90% of the labeled fibers in this region belong to the dopaminergic system.

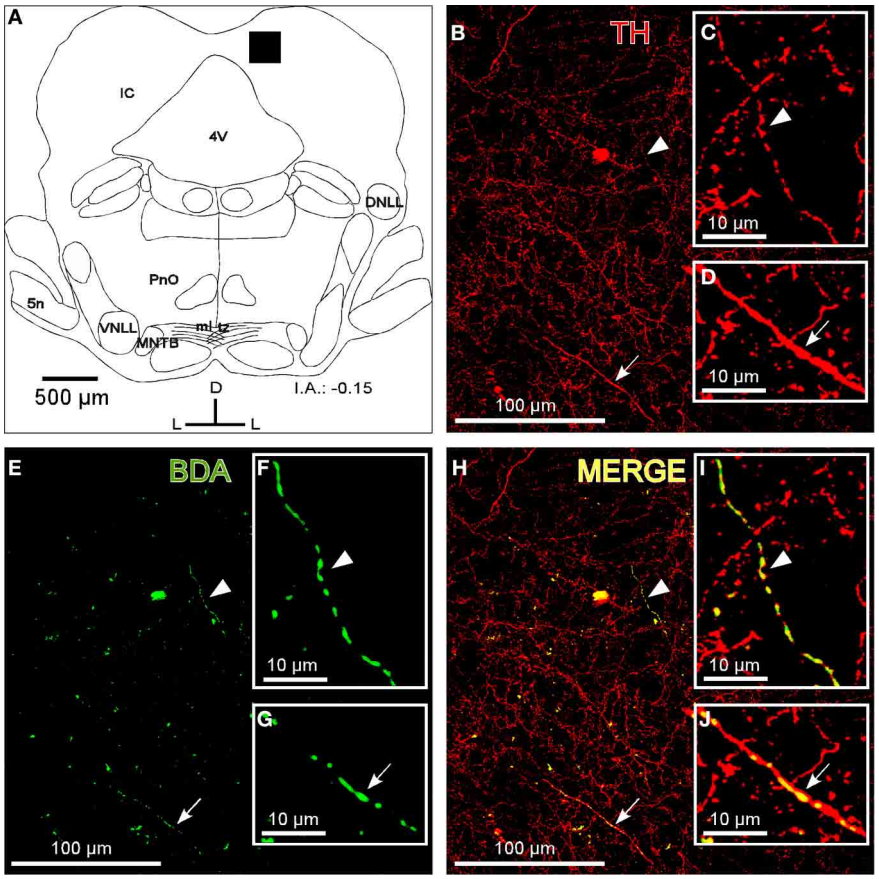

FIGURE 2 | The colocalization of locus coeruleus fibers with tyrosine hydroxylase (TH) in the dorsal cortex of the inferior colliculus (DCIC). **(A)** A schematic representation of the coronal section in which the following confocal photomicrographs were taken. The black square depicts the area of the confocal images. **(B)** The confocal image shows TH-ir in DCIC (red). The arrow and arrowhead indicate representative TH-labeled fibers magnified in **C** and **D**, respectively. **(E)** The confocal image shows labeled fibers (green) after BDA injection in the LC. The arrow and arrowhead indicate representative BDA-labeled fibers in the DCIC. The high magnification images of those fibers are shown in the insets **F** and **G**. **(H)** The merged composition of the photomicrographs in **B** and **E** (yellow). The arrowhead and arrow indicate the colocalization of BDA and TH on the representative fibers that are magnified in **I** and **J**, respectively. The interaural level for coronal placement is displayed in millimeters. See the provided list for abbreviations.

Similarly, we found dense DBH-ir in the entire IC in the control animals (**Figure 7A**). The caudal part presented the highest mean gray values, mainly in the DCIC and the CNIC. The fibers were uniformly distributed in the IC, and there was no significant difference in the distribution along the subdivisions ($p > 0.05$). However, the reduction in DBH fibers in animals treated with DSP-4 was extremely severe (**Figure 7B**). The decrease of DBH-ir took placed along the full length of the IC and in all its subdivisions, ranging from 89 to 97% (for all cases $p < 0.01$) (**Figures 7C,D,** and **E**).

Based on these data, we conclude that DSP-4 removes the majority of the noradrenergic fibers in the IC, leaving only a few fibers spread in the different divisions of the IC and in the commissure.

DISCUSSION

Our findings suggest there is a direct projection from the LC to the IC. We found that this projection is mainly ipsilateral, reaching the DCIC, the LCIC and the commissure of the IC. In agreement with these results, previous studies have shown that the efferent projection from the LC to other nuclei, such as those from the somatosensory pathway, is mainly ipsilateral (Simpson et al., 1997). The neurochemical nature of these projections is noradrenergic, given that TH and DBH colocalize with the BDA-labeled fibers from the LC. We also found a dense immunoreactivity for TH in the IC, even when DSP-4 was administrated. Similar to our observations in the IC, the levels of TH-immunoreactive axons within the hypothalamus, reticular formation, and brainstem motor nuclei appeared relatively unaffected following DSP-4 administration (Fritschy and Grzanna, 1989).

Consistent with Tong et al. (2005), our results also showed single-labeled fibers for TH and double-labeled fibers for TH and DBH in the IC. Moreover, phenylethanolamine-N-methyltransferase, an enzyme use to identify adrenergic neurons and fibers, is not localized in the IC (Tong et al., 2005). In our study, TH-ir was not totally eliminated in the IC after the administration of DSP-4, which indicates the presence of a strong dopaminergic innervation within the IC. These data suggest that

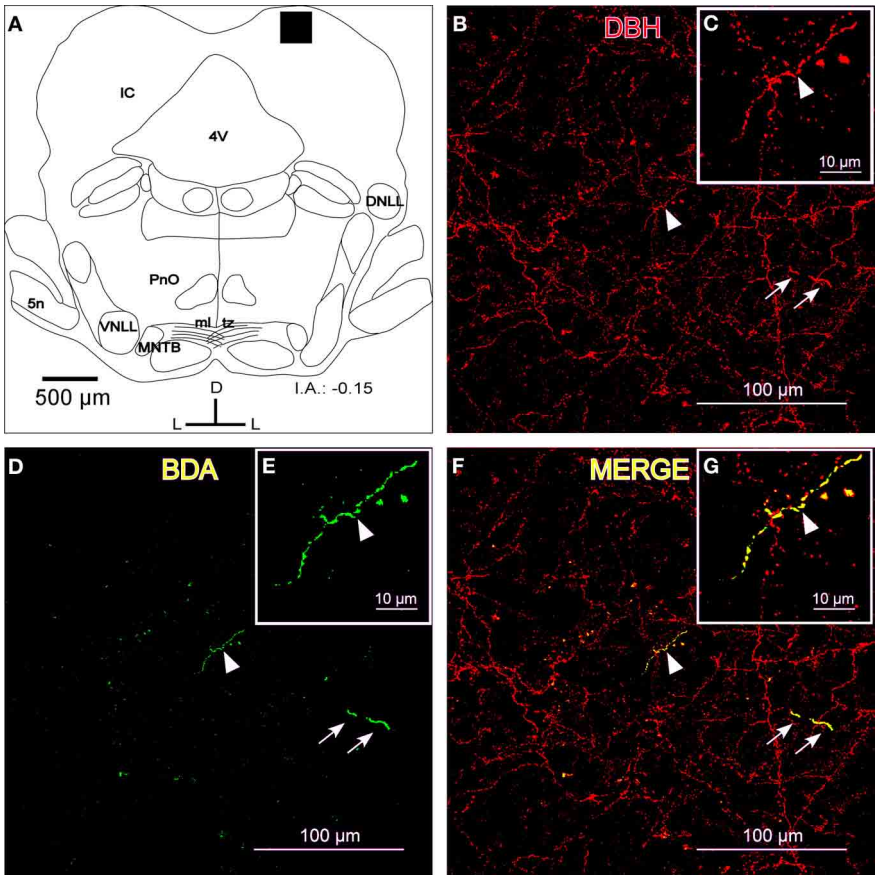

FIGURE 3 | The colocalization of locus coeruleus fibers with dopamine beta hydroxylase (DBH) in the dorsal cortex of the inferior colliculus (DCIC). (A) A schematic representation of the coronal section in which the following confocal photomicrographs were taken. The black square depicts the area of the confocal images. **(B)** A confocal image for DBH-ir (red). The arrows indicate a representative fiber in two parts, most likely due to the Z-axis frame, and the arrowhead shows another representative fiber that is magnified in **C**. **(D)** The confocal image shows labeled fibers (green) after BDA injection in the LC. The arrows indicate a representative fiber, and the arrowhead shows another representative fiber that is magnified in **E**. **(F)** The merged composition between **B** and **D** (yellow). The arrowhead indicates a merged fiber (yellow) that is magnified in **G**. The arrows show colocalization in another fiber (yellow). The interaural level for coronal placement is displayed in millimeters. See the provided list for abbreviations.

both dopaminergic and noradrenergic systems are present in the IC. The source of the dopaminergic innervation might be from the substantia nigra (Garcia-Munoz et al., 1982; Takada et al., 1987; Kemel et al., 1988; Yasui et al., 1991; Deniau and Chevalier, 1992; Moriizumi et al., 1992; Yasui et al., 1995; Richards et al., 1997).

THE LC-IC NORADRENERGIC INNERVATION AND THE EFFECTS OF DSP-4 ADMINISTRATION

Noradrenergic fibers in the IC have been widely studied (Swanson and Hartman, 1975; Levitt and Moore, 1979; Olazàbal and Moore, 1989; Fritschy and Grzanna, 1990); however, the subnuclei distributions of the catecholaminergic innervations in the IC were uncharacterized. Kromer and Moore (1980) described a diffuse pattern of DBH-ir fibers in all the subdivisions of the IC, whereas Klepper and Herbert (1991) clearly indicated a subnuclei distribution of noradrenergic fibers in the IC based on immunohistochemistry for DBH and retrograde tract-tracing studies after injections into the IC.

Klepper and Herbert (1991) demonstrated that the noradrenergic projection to the IC largely arises from the LC and evidenced that these projections were bilateral with predominance (2/1) toward the ipsilateral side. Because the injections sites in the IC were not considered in those retrograde tract-tracing studies (Klepper and Herbert, 1991), the projection field of the LC innervations in the IC remains unknown. Our anterograde track-tracing study verified that the LC–IC projection is mainly ipsilateral and further described the topographic distribution of the LC noradrenergic system in the rostrocaudal extent of the IC and its subdivisions.

Studies that describe the projections from the LC to the IC using anterograde tracers are often contradictory. The injection of lectin *Phaseolus vulgaris* leucoagglutinin (PHA-L) into the LC in combination with immunohistochemistry for DBH described axons that ran bilaterally into the inferior colliculi, but those LC axons appeared in a patch within sensory nuclei (Fritschy and Grzanna, 1990). Other authors, found very few labeled BDA fibers in the IC after BDA injections into the LC, with little difference

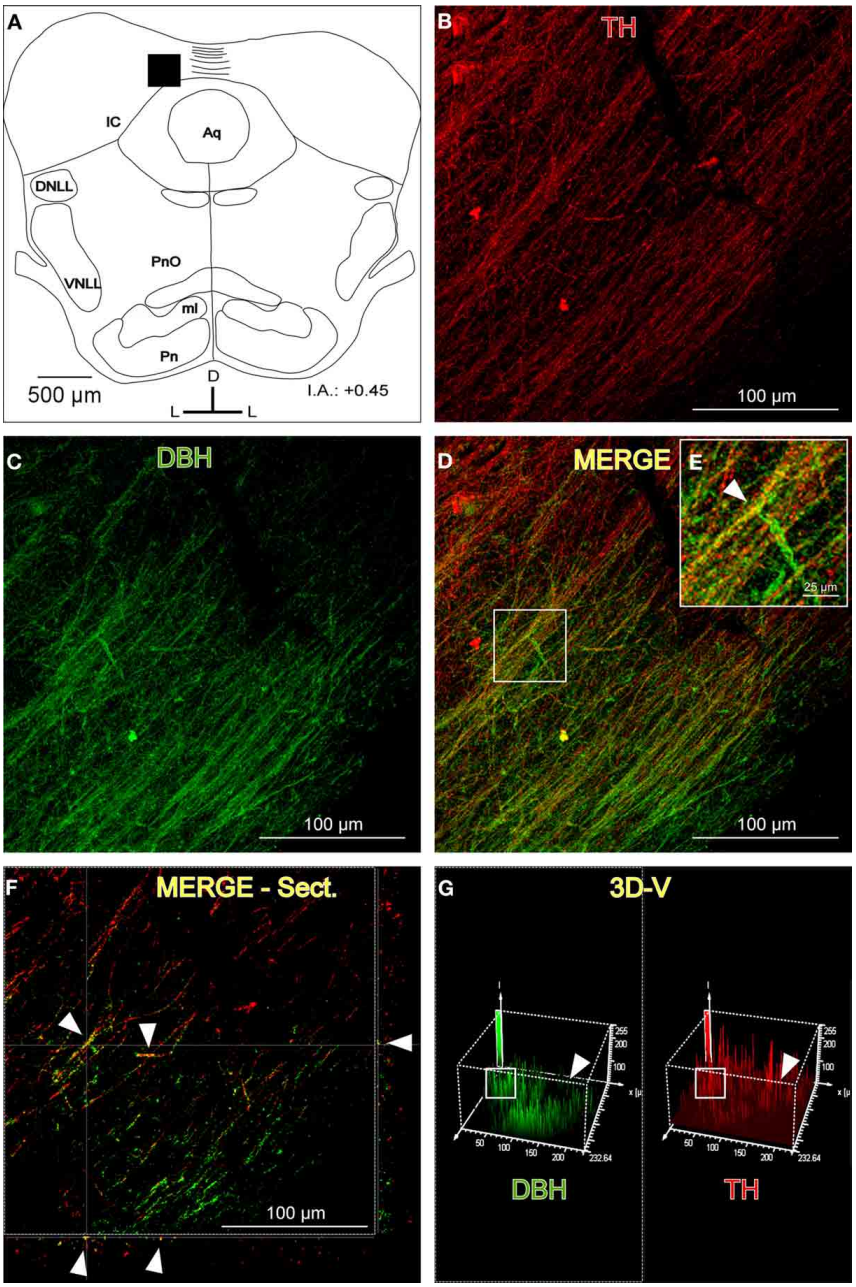

FIGURE 4 | The distribution of immunolabeled fibers for tyrosine hydroxylase (TH) and dopamine beta hydroxylase (DBH) in the inferior colliculus (IC). (A) Schematic representation of the coronal section in which the following confocal photomicrographs were taken. The black square depicts the exact placement of the confocal images, which were taken near the commissure. **(B)** The confocal image for TH-ir (red). **(C)** The confocal image for DBH-ir (green). **(D)** The merged composition between **B** and **C** (yellow). **(E)** A magnification of the white square in **D**. The arrowhead indicates merged fibers (yellow). **(F)** An orthogonal view of a section of the confocal fibers. The arrowheads indicate merged fibers and their place in the Z-axis. **(G)** A three-dimensional view of the two channels. The arrowheads show the difference between the signals in the upper right part of the images where there are TH-ir fibers (red) but not DBH-ir, which leads to the conclusion that dopaminergic fibers (not noradrenergic) exist in the IC. The white square indicates the zone where the colocalization was found. There is a similar pattern of signal distribution. The interaural level for the coronal placement is displayed in millimeters. See the provided list for abbreviations.

between the ipsi- and contralateral side (Mulders and Robertson, 2001).

On the other hand, there is another work that studied the afferent projections to the central nucleus of the IC in the rat that did not identify the LC as a source of afferents to this nucleus (Beyerl, 1978).

The LC is a nucleus with a considerably large caudo-rostral extension, and it has been described as a nucleus with a

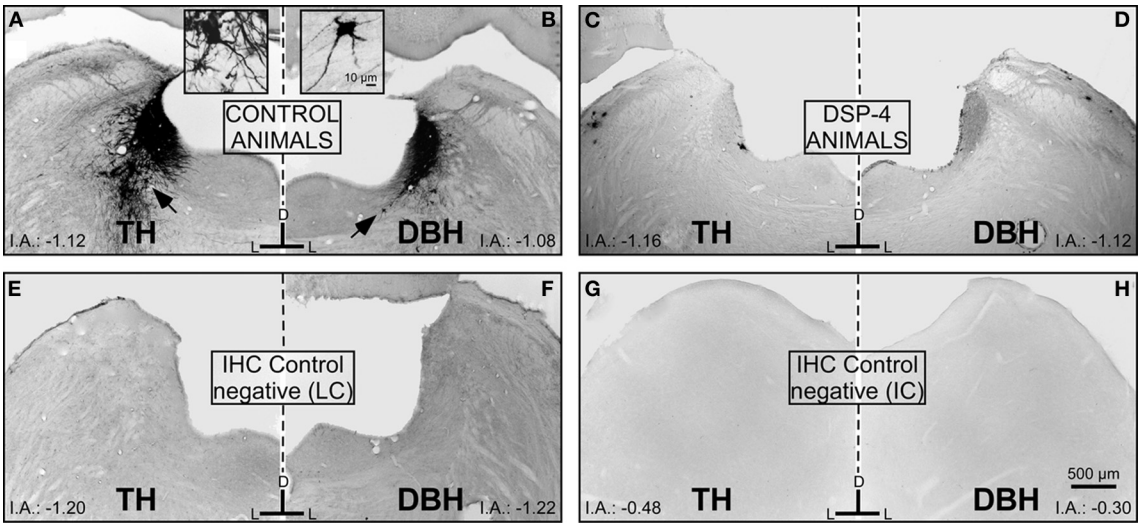

FIGURE 5 | The effects of DSP-4 administration in the locus coeruleus (LC) on immunohistochemistry (tyrosine hydroxylase and dopamine beta hydroxylase) compared to negative controls for the LC and the inferior colliculus (IC). (A) A photomicrograph of the locus coeruleus (LC) immunostained for tyrosine hydroxylase (TH) in a control animal. The black arrow represents a typical immunoreactive neuron, which is magnified in the inset. **(B)** A photomicrograph of the LC immunostained for dopamine-beta-hydroxylase (DBH) in a control animal. The black arrow represents a typical immunoreactive neuron, which is magnified in the inset. **(C)** A photomicrograph of the LC immunostained for TH in a DSP-4-treated animal. **(D)** A photomicrograph of the LC immunostained for DBH in a DSP-4-treated animal. Notice in this set of images how the immunoreactivity against the catecholaminergic enzymes is distinctly decreased compared to the controls. This reflects the immunoreactivity found in the IC in controls and treated animals. **E**,**F**,**G,** and **H** are images taken from the negative controls (no primary antibody added). The interaural level for the coronal placement is displayed in millimeters. See the provided list for abbreviations.

heterogeneous neuronal population, differentiating its projections according to topographical criteria: axons directed to the forebrain and axons directed to the spinal cord (Mason and Fibiger, 1979; Grzanna and Molliver, 1980; Nagai et al., 1981; Loughlin et al., 1986). The contributions of each neuronal type to a broad efferent network are presented in detail in those studies, but there is no description of the projections to the IC.

In our study, we injected an anterograde tracer into small portions of the LC to avoid spreading to adjacent nuclei, which also project to the IC (for instance, the LDTg). Due to the small size of the BDA injection sites, only a fraction of all LC neurons was labeled in each case, resulting in light density axonal labeling. To determine the total field of the LC innervations in the IC, we destroyed the LC neurons and fibers using a highly selective neurotoxin, DSP-4, and then studied the distribution and density of the TH and DBH immunolabeled axons in the IC. DSP-4 administration models induce noradrenergic degeneration, exclusively affecting the noradrenergic fibers originating in the LC (Fritschy and Grzanna, 1989; Grzanna et al., 1989; Fritschy et al., 1991). Therefore, the densitometry analysis of TH and DBH-ir throughout the IC in DSP-4-treated and non-treated control rats provided us with valuable information regarding the extent and topographical distribution of the LC efferent network in the IC.

After DSP-4 treatment, we found a loss of TH immunoreactive fibers in the dorsal cortex and lateral cortex of the IC and nearly all BDH immunoreactive fibers. Additionally, there were a few remaining DBH-ir that might belong to noradrenergic neurons distributed in the IC. These intrinsic noradrenergic neurons of the IC send descending projections to brainstem nuclei, including the LC (Tong et al., 2005; Freitas et al., 2006). In agreement with Fritschy and Grzanna (1989), our study verified the existence of two separate systems of noradrenergic fibers in the IC: the LC and non-coerulean noradrenergic systems. Our results further show that the sources of NA from non-coeruleus structures were much sparser than the lost of fibers from the LC. Therefore, our study verified that the LC system is the main source of NA in the IC and indicates that the fibers are distinctively distributed in the dorsal and lateral areas of the IC and the intercollicular commissure. These results might contribute to the understanding of the functional role of the IC–LC projection.

FUNCTIONAL IMPLICATIONS

Novelty detection is concerned with recognizing inputs that differ in some way from previous inputs. In all sensorial modalities, an unexpected and novel perception is highly effective in attracting and focusing attention. Both the IC and the LC play a major role in novelty detection. The IC constitutes an obligatory and highly integrative relay for the ascending and descending auditory pathways and also process multimodal information, including visual cues (Cooper and Young, 1976; Elverland, 1978; Morest and Oliver, 1984; Faye-Lund and Osen, 1985; Saldana et al., 1996). IC neurons respond selectively to novel sounds and show stimulus-specific adaptation (Pérez-González et al., 2005; Malmierca et al., 2009). Similarly, the LC neurons integrate multimodal information and increase their firing rates following the presentation of novel stimuli (Foote et al., 1980; Grant et al., 1988). Therefore, both midbrain nuclei (IC and LC) are essential for eliciting an

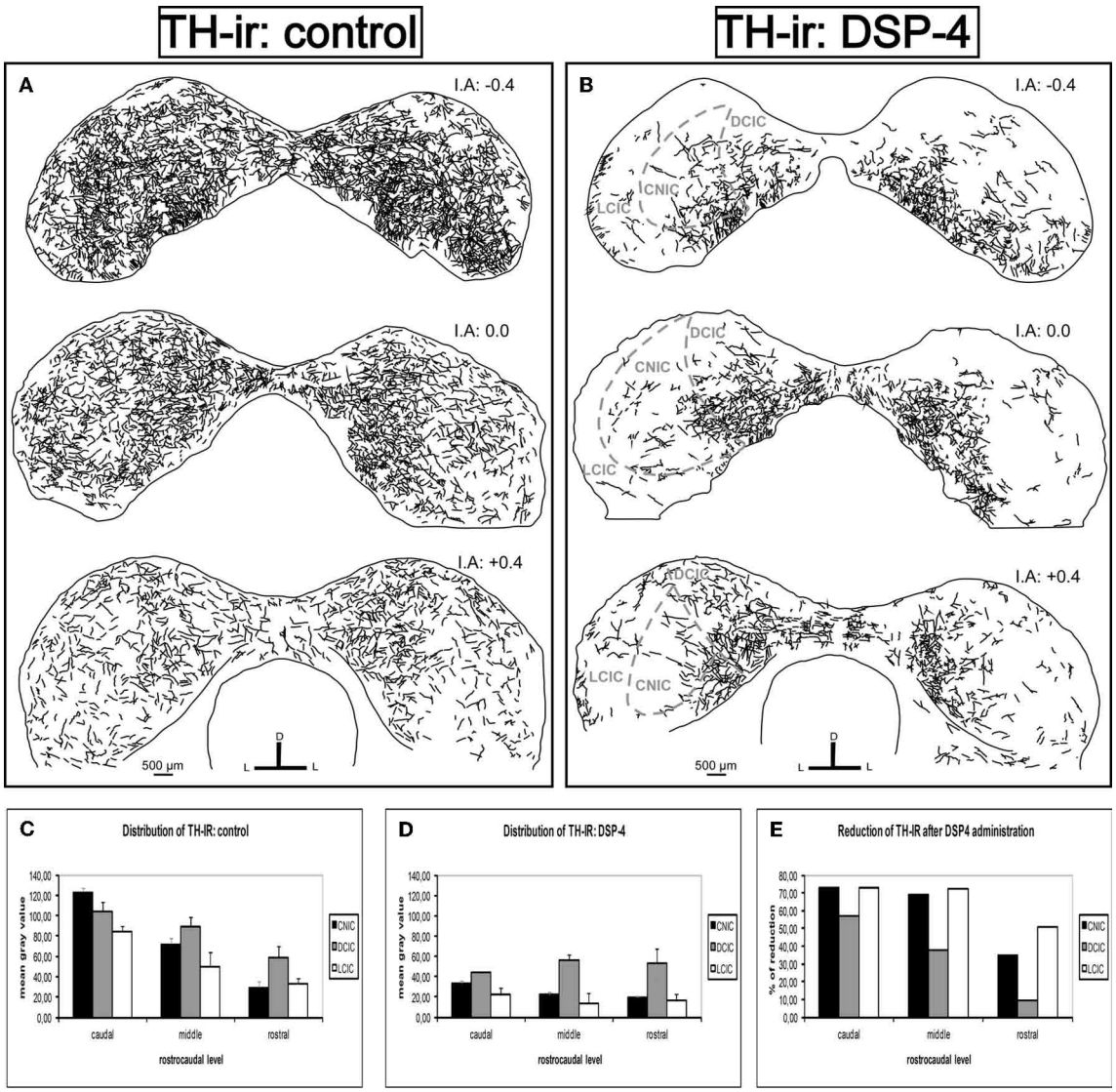

FIGURE 6 | The effects of DSP-4 administration in the tyrosine hydroxylase-immunoreactivity (TH-ir) within the inferior colliculus (IC). A schematic representation of TH-ir in the IC from the caudal to the rostral part. **(A)** Drawings of the TH-ir in control animals. **(B)** Drawings of the TH-ir in DSP-4-treated animals. Notice how the immunoreactivity is markedly decreased in treated animals compared to controls. **(C)** The mean gray value of the distribution of TH-ir in control animals at different rostrocaudal levels and subdivisions. **(D)** The mean gray value of the distribution of TH-ir in DSP-4-treated animals at different rostrocaudal levels and subdivisions. **(E)** The percent reduction in TH-ir following DSP-4 treatment. The interaural level for the coronal placement is displayed in millimeters. The bars represent means ± SD of 24 stained sections. See the provided list for abbreviations.

orienting response. Our study demonstrates a noradrenergic projection from the LC to the IC, suggesting a functional correlation between the two nuclei. In fact, the main target areas and projection pattern of the LC fibers within the IC are precisely the same IC areas where the population of novelty neurons is located.

In comparison with the neurons in the central nucleus of the IC, the neurons in the dorsal and lateral IC show a strong stimulus-specific adaptation that might contribute to auditory scene analysis, novelty detection, and selective attention (Pérez-González et al., 2005; Malmierca et al., 2009; Lumani and Zhang, 2010). Interestingly, our results showed that the noradrenergic projection from the LC projects to the dorsal and lateral cortex of the IC and, to a lesser extent, to the central nucleus of the IC. Modulators like NA might participate in stimulus-specific adaption given that NA blocks both Ca^{2+}- and Na^{+}-dependent K^{+} currents (Foehring et al., 1989). Such K^{+} currents underlie at least part of the cortical auditory adaptation in awake rats (Abolafia et al., 2011). This suggests that the noradrenergic LC–IC projection might contribute to the information that this population of IC neurons integrates for novelty detection.

As we have shown in the IC, the cochlear nucleus and the superior olivary complex also receive noradrenergic inputs from the LC (Klepper and Herbert, 1991; Ebert, 1996; Mulders and Robertson, 2001; Thompson, 2003). Therefore, all the major relay

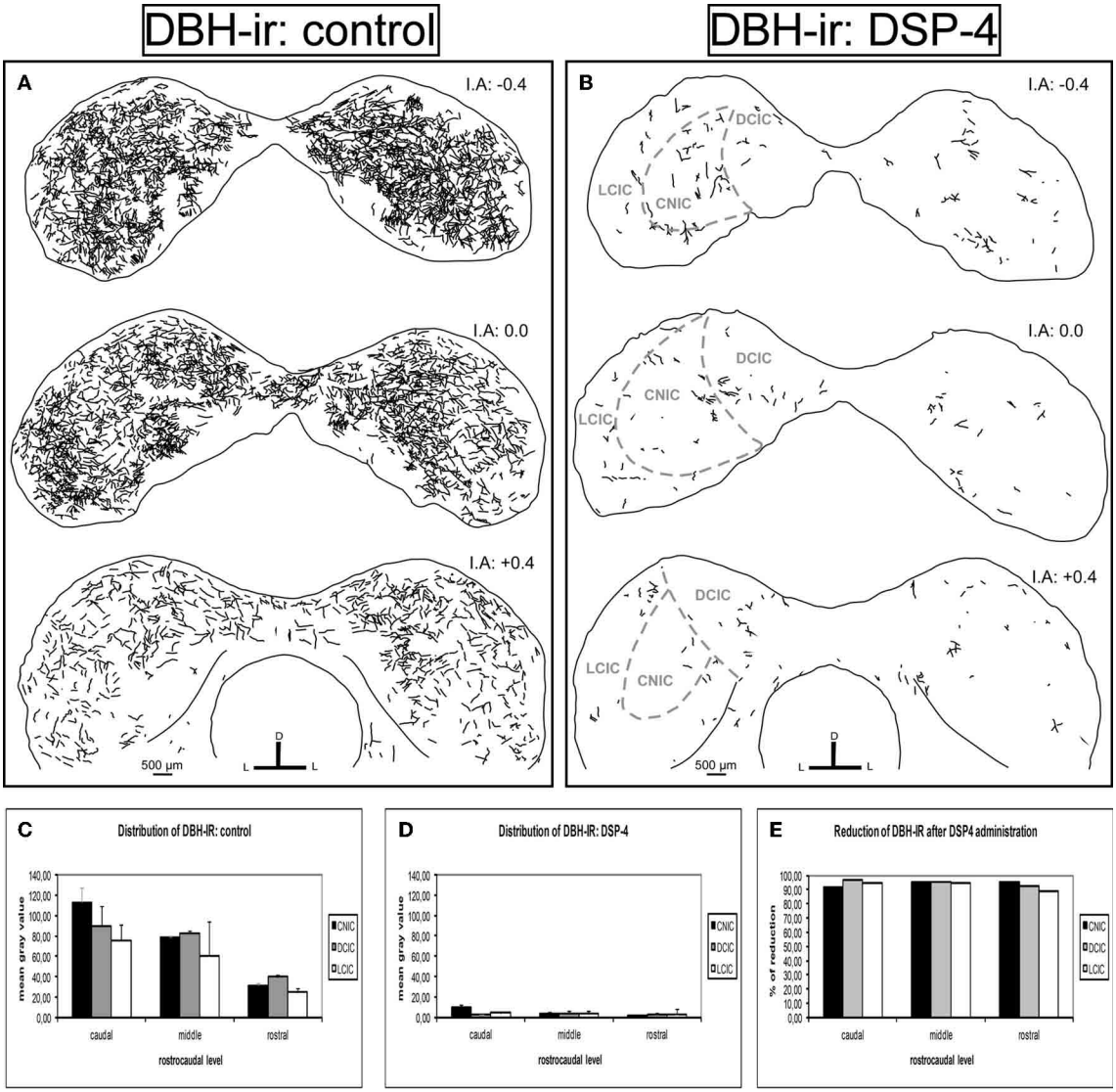

FIGURE 7 | The effects of DSP-4 administration on the dopamine beta hydroxylase-immunoreactivity (DBH-ir) in the inferior colliculus (IC). A schematic representation of DBH-ir in the IC from the caudal to the rostral part. **(A)** Drawings of the DBH-ir in control animals. **(B)** Drawings of the DBH-ir in DSP-4-treated animals. Notice how the immunoreactivity almost disappears in treated animals. **(C)** The mean gray value of the distribution of DBH-ir in control animals at different rostrocaudal levels and subdivisions. **(D)** The mean gray value of the distribution of DBH-ir in DSP-4-treated animals at different rostrocaudal levels and subdivisions. **(E)** The percent reduction in DBH-ir following DSP-4 treatment. The interaural level for the coronal placement is displayed in millimeters. The bars represent means ± SD of 24 stained sections. See the provided list for abbreviations.

nuclei for auditory information are influenced by the neuromodulator NA. In the context of the NA regulation of behaviors, the activation of the LC noradrenergic system is known to increase attentional processes and influence the target circuits involved in arousal states, learning and memory, alertness, and vigilance (Aston-Jones et al., 1991; Woodward et al., 1991; Berridge and Waterhouse, 2003; Lapiz and Morilak, 2006). This leads us to question how the LC noradrenergic system affects auditory perception and how auditory processing is carried out under different behavioral circumstances. In auditory cue detection, a recent study showed that α-2 adrenergic stimulation is effective in modulating accuracy and response latencies in non-stressed animals (Brown et al., 2012). This suggests that NA not only induces the arousal state to initiate attentional processing but also suggests a more specific role for NA in auditory signal versus non-signal discrimination (Brown et al., 2012). Because the cortex of the IC is particularly rich in α-2 adrenergic receptors (Probst et al., 1984), it is essential to know the target areas of the LC noradrenergic system within the IC. Our study indicates that the LC noradrenergic system massively innervates the dorsal and lateral portions of the IC and revealed that these innervations are significantly impaired in DSP-4-treated rats. These results might contribute to the design of new experiments focused on the role of α adrenergic receptors in the dorsal and lateral IC.

Additionally, the LC projects to the cochlear root nucleus, another midbrain nucleus, which processes unexpected acoustic stimuli and mediates auditory alerting and escape behaviors, such as the acoustic startle reflex (Lee et al., 1996; López et al., 1999; Gómez-Nieto et al., 2008b). The cochlear root nucleus projects to the facial motor neurons that promote pinna movements toward unexpected, loud sounds (Horta-Júnior et al., 2008) and also receives inputs from the IC via a short descending auditory pathway that relays in the ventral nucleus of the trapezoid body (Gómez-Nieto et al., 2008a). Because the IC plays a role in binaural inhibition and is critical for the modulation of the acoustic startle reflex by auditory stimuli (reviewed in Fendt et al., 2001), it is of great interest to study the connections between the IC, LC, and the cochlear root nucleus. The main goal of the present study was to re-examine the projections from the LC to IC in intact and DSP-4 treated rats. Our results demonstrate that the noradrenergic projection from the LC to the IC was drastically impaired after DSP-4 administration. This implies that DSP-4 might be used as a powerful tool to study the functional role of the projections from the LC to midbrain nuclei, such as the IC and the cochlear root nucleus, that are involved in novelty detection, orienting response, and alerting behaviors.

ACKNOWLEDGMENTS

We would like to express gratitude to the Spanish Ministry of Science and Innovation, (MICINN, # BFU2010-17754) and to the Sao Paulo State Research Foundation (FAPESP proc. 2008/02771-6) for their financial support. Moreover, we thank the AUIP (Programa de Becas de Movilidad Académica 2010–2011) for facilitating a fellowship in Brazil in which some parts of the experiments above took place.

REFERENCES

Abolafia, J. M., Vergara, R., Arnold, M. M., Reig, R., and Sanchez-Vives, M. V. (2011). Cortical auditory adaptation in the awake rat and the role of potassium currents. *Cereb. Cortex* 21, 977–990.

Aston-Jones, G. (2004). "Locus coeruleus, A5 and A7 noradrenergic cell groups," in *The Rat Nervous System,* ed G. Paxinos (San Diego, CA: Elsevier), 259–294.

Aston-Jones, G., Chiang, C., and Alexinsky, T. (1991). Discharge of noradrenergic locus coeruleus neurons in behaving rats and monkeys suggests a role in vigilance. *Prog. Brain Res.* 88, 501–520.

Axelrod, J., Kopin, I. J., and Waser, K. A. (1969). The uptake, storage, release and metabolism of noradrenaline in sympathetic nerves. *Prog. Brain Res.* 31, 21–32.

Berridge, C. W., and Waterhouse, B. D. (2003). The locus coeruleus-noradrenergic system: modulation of behavioral state and state-dependent cognitive processes. *Brain Res. Rev.* 42, 33–84.

Beyerl, B. D. (1978). Afferent projections to the central nucleus of the inferior colliculus in the rat. *Brain Res.* 145, 209–223.

Brown, D. C. 2nd, Co, M. S., Wolff, R. C., and Atzori, M. (2012). α-Adrenergic receptors in auditory cue detection: α(2) receptor blockade suppresses false alarm responding in the rat. *Neuropharmacology* 62, 2177–2182.

Ciaranello, R. D., Wooten, F. G., and Axelrod, J. (1976). Regulation of rat adrenal dopamine B-hydroxylase. II. Receptor interaction in the regulation of enzyme synthesis and degradation. *Brain Res.* 113, 349–362.

Conti, L. H., and Foote, S. L. (1996). Reciprocal cross-desensitization of locus coeruleus electrophysiological responsivity to corticotropin-releasing factor and stress. *Brain Res.* 722, 19–29.

Cornwell-Jones, C. A., Palfai, T., Krasenbaum, D., Byer, E. Jr., Clark, R., and Kinnard, K. (1992). Housing influences exploration and social interaction of control and DSP-4-treated rats. *Physiol. Behav.* 52, 271–276.

Couto, L. B., Moroni, C. R., Ferreira, C. M., Elias-Filho, D. H., Parada, C., Pel, I. R., and Coimbra, N. C. (2006). Descriptive and functional neuroanatomy of locus coeruleus-noradrenaline-containing neurons involvement in bradykinin-induced antinociception on principal sensory trigeminal nucleus. *J. Chem. Neuroanat.* 32, 28–45.

Cooper, M. H., and Young, P. A. (1976). Cortical projections to the inferior colliculus of the cat. *Exp. Neurol.* 51, 488–502.

Curtis, A. L., Drolet, G., and Valentino, R. J. (1993). Hemodynamic stress activates locus coeruleus neurons of unanesthetized rats. *Brain Res. Bull.* 31, 737–744.

Dawe, G. S., Huff, K. D., Vandergriff, J. L., Sharp, T., O'Neill, M. J., and Rasmussen, K. (2001). Olanzapine activates the rat locus coeruleus: *in vivo* electrophysiology and c-Fos immunoreactivity. *Biol. Psychiatry* 50, 510–520.

del C. Gonzalez, M. M., Debilly, G., Valatx, J. L., and Jouvet, M. (1995). Sleep increase after immobilization stress: role of the noradrenergic locus coeruleus system in the rat. *Neurosci. Lett.* 202, 5–8.

Delini-Stula, A., Mogilnicka, E., Hunn, C., and Dooley, D. J. (1984). Novelty-oriented behavior in the rat after selective damage of locus coeruleus projections by DSP-4, a new noradrenergic neurotoxin. *Pharmacol. Biochem. Behav.* 20, 613–618.

Deniau, J. M., and Chevalier, G. (1992). The lamellar organization of the rat substantia nigra pars reticulata: distribution of projection neurons. *Neuroscience* 46, 361–377.

Ebert, U. (1996). Noradrenaline enhances the activity of cochlear nucleus neurons in the rat. *Eur. J. Neurosci.* 8, 13006–13014.

Elverland, H. H. (1978). Ascending and intrinsic projections of the superior olivary complex in the cat. *Exp. Brain Res.* 32, 117–134.

Faye-Lund, H., and Osen, K. K. (1985). Anatomy of the inferior colliculus in rat. *Anat. Embryol.* 171, 1–20.

Fendt, M., Li, L., and Yeomans, J. S. (2001). Brain stem circuits mediating prepulse inhibition of the startle reflex. *Psychopharmacology (Berl.)* 156, 216–224.

Foehring, R. C., Schwindt, P. C., and Crill, W. E. (1989). Norepinephrine selectively reduces slow Ca2+- and Na+-mediated K+ currents in cat neocortical neurons. *J. Neurophysiol.* 61, 245–256.

Foote, S. L., Aston-Jones, G., and Bloom, F. E. (1980). Impulse activity of locus coeruleus neurons in awake rats and monkeys is a function of sensory stimulation and arousal. *Proc. Natl. Acad. Sci. U.S.A.* 77, 3033–3037.

Freitas, R. L., Ferreira, C. M. R., Ribeiro, S. J., Carvalho, A. D., Elias-Filho, D. H., Garcia-Cairasco, N., and Coimbra, N. C. (2006). Intrinsic neural circuits between dorsal midbrain neurons that control fear-induced responses and seizure activity and nuclei of the pain inhibitory system elaborating postictal antinociceptive processes: a functional neuroanatomical and neuropharmacological study. *Exp. Neurol.* 191, 225–242.

Fritschy, J. M., and Grzanna, R. (1989). Immunohistochemical analysis of the neurotoxic effects of DSP-4 identifies two populations of noradrenergic axon terminals. *Neuroscience* 30, 181–197.

Fritschy, J. M., and Grzanna, R. (1990). Distribution of locus coeruleus axons within the rat brainstem demonstrated by *Phaseolus vulgaris* leucoagglutinin anterograde tracing in combination with dopamine-beta-hydroxylase immunofluorescence. *J. Comp. Neurol.* 293, 616–631.

Fritschy, J. M., Grzanna, R., and Pompeiano, C. D. (1991). Chapter 20 Selective effects of DSP-4 on locus coeruleus axons: are there pharmacologically different types of noradrenergic axons in the central nervous system? *Prog. Brain Res.* 88, 257–268.

Garcia-Munoz, M., Patino, P., Aguilar, R., and Arbuthnott, G. (1982). Participation of projections from substantia nigra reticulata to the lower brain stem in turning behavior. *Exp. Neurol.* 78, 380–390.

Gómez-Nieto, R., Rubio, M. E., and López, D. E. (2008a). Cholinergic input from the ventral nucleus of the trapezoid body to cochlear root neurons in rats. *J. Comp. Neurol.* 506, 452–468.

Gómez-Nieto, R., Horta-Junior, J. A. C., Castellano, O., Herrero-Turrión, M. J., Rubio, M. E., and López, D. E. (2008b). Neurochemistry of the afferents to the rat cochlear root nucleus: possible synaptic modulation of the acoustic startle. *Neuroscience* 154, 51–64.

Grant, S. J., Aston-Jones, G., and Redmond, D. E. (1988). Responses of primate locus 'coeruleus neurons'

to 'simple and complex' sensory 'stimuli. *Brain Res. Bull.* 21, 401–410.

Grzanna, R., Berger, U., Fritschy, J. M., and Geffard, M. (1989). Acute action of DSP-4 on central norepinephrine axons: biochemical and immunohistochemical evidence for differential effects. *J. Histochem. Cytochem.* 37, 1435–1442.

Grzanna, R., and Molliver, M. E. (1980). The locus coeruleus in the rat: an immunohistochemical delineation. *Neuroscience* 5, 21–40.

Guyenet, P. G. (1980). The coeruleospinal noradrenergic neurons: anatomical and electrophysiological studies in the rat. *Brain Res.* 189, 121–133.

Hancock, M. B. (1982). DAB-Nikel substrate for the differential immunoperoxidase staining of nerve fibers and fiber terminals. *J. Histochem. Cytochem.* 30, 578.

Harro, J., Oreland, L., Vasar, E., and Bradwejn, J. (1995). Impaired exploratory behaviour after DSP-4 treatment in rats: implications for the increased anxiety after noradrenergic denervation. *Eur. Neuropsychopharmacol.* 5, 447–455.

Heldt, S. A., and Falls, W. A. (2003). Destruction of the inferior colliculus disrupts the production and inhibition of fear conditioned to an acoustic stimulus. *Behav. Brain Res.* 144, 175–185.

Horta-Júnior, J. A., López, D. E., Alvarez-Morujo, A. J., and Bittencourt, J. C. (2008). Direct and indirect connections between cochlear root neurons and facial motor neurons: pathways underlying the acoustic pinna reflex in the albino rat. *J. Comp. Neurol.* 507, 1763–1779.

Hsu, S. M., and Soban, E. (1982). Color modification of diaminobenzidine (DAB) precipitation by metallic ions and its application for double immunohistochemistry. *J. Histochem. Cytochem.* 30, 1079–1082.

Imbe, H., Okamoto, K., Donishi, T., Kawai, S., Enoki, K., Senba, E., and Kimura, A. (2009). Activation of ERK in the locus coeruleus following acute noxious stimulation. *Brain Res.* 1263, 50–57.

Jordan, W. P., and Leaton, R. N. (1982). Startle habituation in rats after lesions in the brachium of the inferior colliculus. *Physiol. Behav.* 28, 253–258.

Kemel, M. L., Desban, M., Gauchy, C., Glowinski, J., and Besson, M. J. (1988). Topographical organization of efferent projections from the cat substantia nigra pars reticulata. *Brain Res.* 455, 307–323.

Kim, M. A., Lee, H. S., Lee, B. Y., and Waterhouse, B. D. (2004). Reciprocal connections between subdivisions of the dorsal raphe and the nuclear core of the locus coeruleus in the rat. *Brain Res.* 1026, 56–67.

Klepper, A., and Herbert, H. (1991). Distribution and origin of noradrenergic and serotonergic fibers in the cochlear nucleus and inferior colliculus of the rat. *Brain Res.* 557, 190–201.

Kromer, L. F., and Moore, R. Y. (1980). A study of the organization of the locus coeruleus projections to the lateral geniculate nuclei in the albino rat. *Neuroscience* 5, 255–271.

Lapiz, M. D. S., and Morilak, D. A. (2006). Noradrenergic modulation of cognitive function in rat medial prefrontal cortex as measured by attentional set shifting capability. *Neuroscience* 137, 1039–1049.

Lechner, S. M., Curtis, A. L., Brons, R., and Valentino, R. J. (1997). Locus coeruleus activation by colon distention: role of corticotropin-releasing factor and excitatory amino acids. *Brain Res.* 756, 114–124.

Lee, Y., López, D. E., Meloni, E. G., and Davis, M. (1996). A primary acoustic startle pathway: obligatory role of cochlear root neurons and the nucleus reticularis pontis caudalis. *J. Neurosci.* 16, 3775–3789.

Leitner, D. S., and Cohen, M. E. (1985). Role of the inferior colliculus in the inhibition of acoustic startle in the rat. *Physiol. Behav.* 34, 65–70.

Levitt, P., and Moore, R. Y. (1979). Origin and organization of brainstem catecholamine innervations in rat. *J. Comp. Neurol.* 186, 505–528.

Li, L., Korngut, L. M., Frost, B. J., and Beninger, R. J. (1998). Prepulse inhibition following lesions of the inferior colliculus: prepulse intensity functions. *Physiol. Behav.* 65, 133–139.

Li, L., and Yeomans, J. S. (2000). Using intracranial electrical stimulation to study the timing of prepulse inhibition of the startle reflex. *Brain Res. Brain Res. Protoc.* 5, 67–74.

Li, L., and Yue, Q. (2002). Auditory gating processes and binaural inhibition in the inferior colliculus. *Hear. Res.* 168, 98–109.

Liu, L., Tsuruoka, M., Maeda, M., Hayashi, B., Wang, X., and Inoue, T. (2008). Descending modulation of visceral nociceptive transmission from the locus coeruleus/subcoeruleus in the rat. *Brain Res. Bull.* 76, 616–625.

López, D. E., Saldana, E., Nodal, F. R., Merchán, M. A., and Warr, W. B. (1999). Projections of cochlear root neurons, sentinels of the auditory pathway in the rat. *J. Comp. Neurol.* 415, 160–174.

Loughlin, S. E., Foote, S. L., and Grzanna, R. (1986). Efferent projections of nucleus locus coeruleus: morphologic subpopulations have different efferent targets. *Neuroscience* 18, 307–319.

Lumani, A., and Zhang, H. (2010). Responses of neurons in the rat's dorsal cortex of the inferior colliculus to monaural tone bursts. *Brain Res.* 1351, 115–129.

Ma, S., Mifflin, S. W., Cunningham, J. T., and Morilak, D. A. (2008). Chronic intermittent hypoxia sensitizes acute hypothalamic-pituitary-adrenal stress reactivity and Fos induction in the rat locus coeruleus in response to subsequent immobilization stress. *Neuroscience* 154, 1639–1647.

Malmierca, M. S., Cristaudo, S., Pérez-González, D., and Covey, E. (2009). Stimulus-specific adaptation in the inferior colliculus of the anesthetized rat. *J. Neurosci.* 29, 5483–5493.

Mason, S. T., and Fibiger, H. C. (1979). Regional topography within noradrenergic locus coeruleus as revealed by retrograde transport of horseradish peroxidase. *J. Comp. Neurol.* 187, 703–724.

Miao-Kun, S. (1995). Central neural organization and control of sympathetic nervous system in mammals. *Prog. Neurobiol.* 47, 157–233.

Moriizumi, T., Leduc-Cross, B., Wu, J. Y., and Hattori, T. (1992). Separate neuronal populations of the rat substantia nigra pars lateralis with distinct projection sites and transmitter phenotypes. *Neuroscience* 46, 711–720.

Morest, D. K., and Oliver, D. L. (1984). The neuronal architecture of the inferior colliculus in the cat: defining the functional anatomy of the auditory midbrain. *J. Comp. Neurol.* 222, 209–236.

Mulders, W. H. A. M., and Robertson, D. (2001). Origin of the noradrenergic innervation of the superior olivary complex in the rat. *J. Chem. Neuroanat.* 21, 313–322.

Nagai, T., Satoh, K., Imamoto, K., and Maeda, T. (1981). Divergent projections of catecholamine neurons of the locus coeruleus as revealed by fluorescent retrograde double labeling technique. *Neurosci. Lett.* 23, 117–123.

Nobre, M. J., Sandner, G., and Brandao, M. L. (2003). Enhancement of acoustic evoked potentials and impairment of startle reflex induced by reduction of GABAergic control of the neural substrates of aversion in the inferior colliculus. *Hear. Res.* 184, 82–90.

Olazàbal, U. E., and Moore, J. K. (1989). Nigrotectal projection to the inferior colliculus: horseradish perosidase transport and tyroxine hydroxylase immunohystochemical studies in rats, cats and bats. *J. Comp. Neurol.* 282, 98–118.

Page, M. E., Akaoka, H., Aston-Jones, G., and Valentino, R. J. (1992). Bladder distention activates noradrenergic locus coeruleus neurons by an excitatory amino acid mechanism. *Neuroscience* 51, 555–563.

Paxinos, G., and Watson, C. (2005). *The Rat Brain in Stereotaxic Coordinates: The New Coronal set–161 Diagrams, 5th edn*. San Diego, CA: Academic Press.

Pérez-González, D., Malmierca, M. S., and Covey, E. (2005). Novelty detector neurons in the mammalian auditory midbrain. *Eur. J. Neurosci.* 22, 2879–2885.

Potter, L. T., Axelrod, J., and Kopin, I. J. (1962). Differential binding and release of norepinephrine and tachyphylaxis. *Biochem. Pharmacol.* 11, 254–256.

Probst, A., Cortés, R., and Palacios, J. M. (1984). Distribution of α 2-adrenergic receptors in the human brainstem: an autoradiographic study using [3H]p-aminoclonidine. *Eur. J. Pharmacol.* 106, 477–488.

Ranson, R. N., Gaunt, K., Santer, R. M., and Watson, A. H. D. (2003). The effects of ageing and of DSP-4 administration on the micturition characteristics of male Wistar rats. *Brain Res.* 988, 130–138.

Reimer, A. E., Oliveira, A. R., and Brandao, M. L. (2008). Selective involvement of GABAergic mechanisms of the dorsal periaqueductal gray and inferior colliculus on the memory of the contextual fear as assessed by the fear potentiated startle test. *Brain Res. Bull.* 76, 545–550.

Richards, C. D., Shiroyama, T., and Kitai, S. T. (1997). Electrophysiological and immunocytochemical characterization of GABA and dopamine neurons in the substantia nigra of the rat. *Neuroscience* 80, 545–557.

Ross, S. B. (1985). DSP-4 and behavioural experiments. *Pharmacol. Sci.* 6, 237.

Ross, S. B., Johansson, J. G., Lindborg, B., and Dahlbom, R. (1973). Cyclizing compounds. I. Tertiary N-(2-bromobenzyl)-N-haloalkylamines with adrenergic

blocking action. *Acta Pharm. Suec.* 10, 29–42.

Saldana, E., Feliciano, M., and Mugnaini, E. (1996). Distribution of descending projections from primary auditory neocortex to inferior colliculus mimics the topography of intracollicular projections. *J. Comp. Neurol.* 371, 15–40.

Satake, S., Yamada, K., Melo, L. L., and Barbosa, S. R. (2012). Effects of microinjections of apomorphine and haloperidol into the inferior colliculus on prepulse inhibition of the acoustic startle reflex in rat. *Neurosci. Lett.* 509, 60–63.

Silva, R. C. B., Sandner, G., and Brandao, M. L. (2005). Unilateral electrical stimulation of the inferior colliculus of rats modifies the prepulse modulation of the startle response (PPI): effects of ketamine and diazepam. *Behav. Brain Res.* 160, 323–330.

Simpson, K. L., Altman, D. W., Wang, L., Kirifides, M. L., Lin, R. C., and Waterhouse, B. D. (1997). Lateralization and functional organization of the locus coeruleus projection to the trigeminal somatosensory pathway in rat. *J. Comp. Neurol.* 385, 135–147.

Singewald, N., Zhou, G. Y., and Schneider, C. (1995). Release of excitatory and inhibitory amino acids from the locus coeruleus of conscious rats by cardiovascular stimuli and various forms of acute stress. *Brain Res.* 704, 42–50.

Snyder, S. H., Glowinski, J., and Axelrod, J. (1965). The storage of norepinephrine and some of its derivatives in brain synaptosomes. *Life Sci.* 4, 797–807.

Spyraki, C., Arbuthnott, G. W., and Fibiger, H. C. (1982). The effect of DSP-4 on some positively reinforced operant behaviors in the rat. *Pharmacol. Biochem. Behav.* 16, 197–202.

Swanson, L. W., and Hartman, B. K. (1975). The central adrenergic system: an immunofluorescence study of the location of cell bodies and their efferent connections in the rat utilizing dopamine-β-hydroxylase as a marker. *J. Comp. Neurol.* 163, 467–506.

Takada, M., Li, Z. K., and Hattori, T. (1987). A note on the projections of pars compacta neurons within pars reticulata of the substantia nigra in the rat. *Brain Res. Bull.* 18, 285–290.

Thompson, A. M. (2003). Pontine sources of norepinephrine in the cat cochlear nucleus. *J. Comp. Neurol.* 457, 374–383.

Tong, L., Altschuler, R. A., and Holt, A. G. (2005). Tyrosine hydroxylase in rat auditory midbrain: distribution and changes following deafness. *Hear. Res.* 206, 28–41.

Toshihiro, M. (2000). The locus coeruleus: history. *J. Chem. Neuroanat.* 18, 57–64.

Tsuruoka, M., Tamaki, J., Maeda, M., Hayashi, B., and Inoue, T. (2011). The nucleus locus coeruleus/subcoeruleus contributes to antinociception during freezing behavior following the air-puff startle in rats. *Brain Res.* 1393, 52–61.

Valentino, R. J., Foote, S. L., and Aston-Jones, G. (1983). Corticotropin-releasing factor activates noradrenergic neurons of the locus coeruleus. *Brain Res.* 270, 363–367.

Valentino, R. J., and Van Bockstaele, E. (2008). Convergent regulation of locus coeruleus activity as an adaptive response to stress. *Eur. J. Pharmacol.* 583, 194–203.

Valentino, R. J., Van Bockstaele, E. J., and Steckler, T. (2005). "Chapter 4.4 Functional interactions between stress neuromediators and the locus coeruleus-norepinephrine system," in *Techniques in the Behavioral and Neural Sciences*, Part 1, Vol. 15, eds J. M. H. M. Reul, N. H. Kalin, and T. Steckler (Philadelphia, PA: Elsevier), 465–486.

van den Buuse, M., Lambert, G., Fluttert, M., and Eikelis, N. (2001). Cardiovascular and behavioural responses to psychological stress in spontaneously hypertensive rats: effect of treatment with DSP-4. *Behav. Brain Res.* 119, 131–142.

Viisanen, H., and Pertovaara, A. (2007). Influence of peripheral nerve injury on response properties of locus coeruleus neurons and coeruleospinal antinociception in the rat. *Neuroscience* 146, 1785–1794.

Woodward, D. J., Moises, H. C., Waterhouse, B. D., Yeh, H. H., and Cheun, J. E. (1991). Modulatory actions of norepinephrine on neural circuits. *Adv. Exp. Med. Biol.* 287, 193–208.

Yasui, Y., Nakano, K., Kayahara, T., and Mizuno, N. (1991). Non-dopaminergic projections from the substantia nigra pars lateralis to the inferior colliculus in the rat. *Brain Res.* 559, 139–144.

Yasui, Y., Tsumori, T., Ando, A., and Domoto, T. (1995). Demonstration of axon collateral projections from the substantia nigra pars reticulata to the superior colliculus and the parvicellular reticular formation in the rat. *Brain Res.* 674, 122–126.

Zaczek, R., Fritschy, J. M., Culp, S., De Souza, E. B., and Grzanna, R. (1990). Differential effects of DSP-4 on noradrenaline axons in cerebral cortex and hypothalamus may reflect heterogeneity of noradrenaline uptake sites. *Brain Res.* 522, 308–314.

Conflict of Interest Statement: The authors declare that the research was conducted in the absence of any commercial or financial relationships that could be construed as a potential conflict of interest.

Received: 30 March 2012; accepted: 12 June 2012; published online: 28 June 2012.

Citation: Hormigo S, Horta Júnior JAC, Gómez-Nieto R and López DE (2012) The selective neurotoxin DSP-4 impairs the noradrenergic projections from the locus coeruleus to the inferior colliculus in rats. Front. Neural Circuits ***6****:41. doi: 10.3389/fncir.2012.00041*

frontiers in
NEURAL CIRCUITS

METHODS ARTICLE
published: 27 June 2012
doi: 10.3389/fncir.2012.00039

Three-dimensional brain reconstruction of *in vivo* electrode tracks for neuroscience and neural prosthetic applications

Craig D. Markovitz[1]*†, Tien T. Tang[1†], David P. Edge[1] and Hubert H. Lim[1,2,3]

[1] *Department of Biomedical Engineering, University of Minnesota, Minneapolis, MN, USA*
[2] *Department of Otolaryngology, University of Minnesota, Minneapolis, MN, USA*
[3] *Institute for Translational Neuroscience, University of Minnesota, Minneapolis, MN, USA*

Edited by:
Manuel S. Malmierca, University of Salamanca, Spain

Reviewed by:
Yang Dan, University of California, USA
Douglas L. Oliver, University of Connecticut Health Center, USA

****Correspondence:***
Craig D. Markovitz, Department of Biomedical Engineering, University of Minnesota, 7-105 Hasselmo Hall, 312 Church Street SE, Minneapolis, MN 55455, USA.
e-mail: cdmarkovitz@gmail.com
† These authors contributed equally to this work.

The brain is a densely interconnected network that relies on populations of neurons within and across multiple nuclei to code for features leading to perception and action. However, the neurophysiology field is still dominated by the characterization of individual neurons, rather than simultaneous recordings across multiple regions, without consistent spatial reconstruction of their locations for comparisons across studies. There are sophisticated histological and imaging techniques for performing brain reconstructions. However, what is needed is a method that is relatively easy and inexpensive to implement in a typical neurophysiology lab and provides consistent identification of electrode locations to make it widely used for pooling data across studies and research groups. This paper presents our initial development of such an approach for reconstructing electrode tracks and site locations within the guinea pig inferior colliculus (IC) to identify its functional organization for frequency coding relevant for a new auditory midbrain implant (AMI). Encouragingly, the spatial error associated with different individuals reconstructing electrode tracks for the same midbrain was less than 65 μm, corresponding to an error of ∼1.5% relative to the entire IC structure (∼4–5 mm diameter sphere). Furthermore, the reconstructed frequency laminae of the IC were consistently aligned across three sampled midbrains, demonstrating the ability to use our method to combine location data across animals. Hopefully, through further improvements in our reconstruction method, it can be used as a standard protocol across neurophysiology labs to characterize neural data not only within the IC but also within other brain regions to help bridge the gap between cellular activity and network function. Clinically, correlating function with location within and across multiple brain regions can guide optimal placement of electrodes for the growing field of neural prosthetics.

Keywords: histology, imaging, inferior colliculus, neural prosthesis, deep brain stimulation, population coding, reconstruction, tonotopy

INTRODUCTION

The neuroscience field has experienced rapid technological advances over the past decade, including the development of multi-site array technologies that can record or stimulate across more than 100 sites (Lehew and Nicolelis, 2008; Falcone and Bhatti, 2011; Stevenson and Kording, 2011), the discovery of optogenetics in which neurons can be genetically altered to become excited or suppressed to different lights (Bamann et al., 2010; Fenno et al., 2011; Miesenbock, 2011), and advances in magnetic resonance imaging (MRI) techniques that have enabled non-invasive functional and anatomical mapping of the brain (Yacoub et al., 2008; Lenglet et al., 2009; Leergaard et al., 2010; Van Essen et al., 2012). These advances have led to more detailed and intricate studies in understanding how individual neurons interact and function as a network, leading to perception and action. In parallel, there have also been significant developments in brain stimulation approaches for treating various sensory, motor, and neurological disorders (Lozano and Hamani, 2004; Zhou and Greenbaum, 2009; Tierney et al., 2011). Two main examples are deep brain stimulation (DBS) for treating neurological disorders [e.g., Parkinson's or Essential Tremor; >75,000 DBS patients worldwide (Zrinzo et al., 2011)] and central auditory prostheses for hearing restoration [within the brainstem or midbrain; >1000 patients worldwide (Lim et al., 2011)]. The increased knowledge gained from basic neuroscience research has provided some insight into the function of neural circuitry relevant for brain stimulation devices. However, one major bottleneck in successful implementation of these different neural prosthetics has been the identification of optimal locations for stimulation to treat the health condition (Johnson et al., 2008; McCreery, 2008; Lim et al., 2009; Hemm and Wardell, 2010).

Neurophysiology experiments can provide spatial mapping of the brain down to a cellular scale. Thus, it would seem that understanding neural function at a sufficient spatial resolution for identifying appropriate brain locations for prosthetic stimulation would not be a major hurdle. However, neurophysiological

studies are not typically accompanied by detailed brain reconstructions identifying the actual locations of the recording and/or stimulation sites. For example, there are over a thousand studies related to auditory coding in the inferior colliculus (IC), the main auditory structure of the midbrain (e.g., using key words "IC" and "auditory" in PubMed). In contrast, there are only a handful of IC neurophysiology studies that provide detailed histological reconstruction of their recording or stimulation site locations (e.g., Merzenich and Reid, 1974; Malmierca et al., 2008; Loftus et al., 2010). Histological confirmation of the sites is typically used to indicate general placement within a nucleus rather than to systematically identify coding features across that nucleus. With the recent developments of an IC-based auditory prosthesis (auditory midbrain implant, AMI), it has become increasingly important to identify which regions of the IC are well-suited for electrical stimulation to restore intelligible hearing (Lim et al., 2007, 2009). Detailed neurophysiological mapping studies with sufficient spatial information are necessary to guide future IC stimulation strategies. Unfortunately, there is no consistent histological method used across labs that enables functional and anatomical data to be pooled across studies to lead to a more spatially complete picture of auditory coding in the IC. These limitations are not only observed in auditory research but throughout the neuroscience field.

Three-dimensional brain reconstruction and modeling is not a new concept, yet is one that needs to be revived in neurophysiology labs, especially as brain stimulation approaches become more widely implemented in patients. MRI techniques have provided a successful pathway for fusing anatomical organization with neural function (Yacoub et al., 2008; Lenglet et al., 2012; Van Essen et al., 2012). However, in parallel, neurophysiological mapping studies are still needed to understand the neural coding features at multiple spatial and time scales, rather than focusing solely on the indirect measure of the slow hemodynamic response captured by functional MRI (Sutton et al., 2009; Glover, 2011). The cellular structure and neurochemical function can also be investigated in stained histological slices and correlated with the neurophysiological mapping results (Cant and Benson, 2005; Dauguet et al., 2007; Bohland et al., 2009; Kleinfeld et al., 2011).

As a step toward bridging the gap between cellular function and network coding organization, especially in identifying appropriate locations within specific nuclei for neural prosthetic applications, we developed a simple and relatively inexpensive three-dimensional brain reconstruction method that uses standard histological techniques and equipment commonly available in research labs. The process uses a three-dimensional rendering software (Rhinoceros, Seattle, WA) that is inexpensive (~$200 for a student version). Although preparing the slices and creating the reconstructions requires a significant time commitment, the entire process is easy to learn and we have been able to recruit volunteer students to perform the reconstructions. The students benefit from this arrangement by participating in the neurophysiology experiments and being provided an initial reconstruction project to learn brain anatomy. Thus in an academic setting, it is possible to perform inexpensive, detailed brain reconstructions to supplement neurophysiology data using this approach.

The overall goal of this method is to establish a relatively simple and accessible standard for how different labs perform brain reconstructions that will be available online and enable data to be pooled across studies. Initially, we investigated our approach for reconstructing the IC due to immediate interests in guiding AMI stimulation strategies. In this paper, we will first present the detailed steps involved with the reconstruction approach in the Methods. The error analysis and the ability to consistently reconstruct electrode tracks and sites positioned across the frequency axis of the IC will then be presented in the Results. Finally, potential improvements and new directions for brain reconstructions will be presented in the Discussion.

METHODS

We have developed a reconstruction method combining histological brain slices and neurophysiological recordings to identify the tracks and site locations of acutely implanted electrode arrays in the IC. The detailed steps in performing the brain reconstructions are presented below. Additionally, a video simulation of the entire computer reconstruction process using Rhinoceros can be downloaded from soniclab.umn.edu.

ANIMAL SURGERY AND ELECTRODE ARRAY PLACEMENT

Electrophysiological experiments were performed on young Hartley guinea pigs (Elm Hill Breeding Labs, Chelmsford, MA) under ketamine (40 mg/kg) and xylazine (10 mg/kg) anesthesia in accordance with policies of the University of Minnesota Institutional Animal Care and Use Committee. Further details on the anesthesia and surgical approach have been presented previously (Lim and Anderson, 2007b; Neuheiser et al., 2010) and are only briefly described here. All animals had a mass of 330–380 g at the time of experiment. A silicon-substrate, multi-site Michigan electrode array (**Figure 1**; NeuroNexus Technologies, Ann Arbor, MI) was acutely implanted into the right IC. The probe consists of two shanks separated by 500 μm, with each shank having 16 iridium sites linearly spaced 100 μm apart (center-to-center). Before placement, the shanks were dipped 10 times

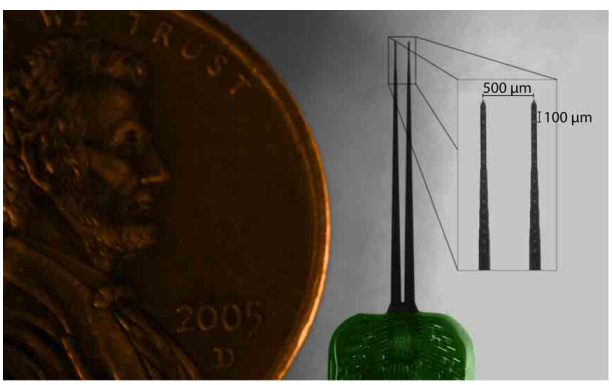

FIGURE 1 | Microscope image of acutely-implanted Michigan electrode array (NeuroNexus Technologies, Ann Arbor, MI) consisting of two shanks (10 mm long) each with 16 contacts (~400 μm^2 site area) spaced 100 μm apart center-to-center.

in a red fluorescent dye [3 mg Di-I (1,1′-dioctadecyl-3,3,3′,3′-tetramethylindocarbocyanine perchlorate) per 100 μL acetone; Sigma-Aldrich, St. Louis, MO], alternating between 10 s in and 10 s out of the dye. The Di-I is visible in brightfield images of brain slices, fluoresces for added visualization, and has been used successfully in previous studies without noticeably altering neural activity (DiCarlo et al., 1996; Jain and Shore, 2006; Lim and Anderson, 2007b). The probe was stereotaxically inserted at a 45° angle off the sagittal plane through the occipital cortex into the IC, with one shank placed approximately rostral to the other. The 45° angle aligns the probe along the tonotopic axis of the IC, while the bi-shank design allows for simultaneous recordings within isofrequency laminae. The fixed-distance bi-shank design is also crucial for identifying the location of individual electrode sites as described later in the Methods. The probe only needed to be stained prior to the first implantation location and the stained track could be visualized across multiple locations (up to 12 placements corresponding to 24 shank tracks) throughout the entire experiment. Each placement lasted approximately one hour for recording acoustic-driven neural activity that was later used for offline characterization of the functional organization.

HISTOLOGICAL SLICE PREPARATION

After our *in vivo* experiment, the animal was euthanized with an overdose (0.07 mL/mg) of Beuthanasia-D Special (Merck, Summit, NJ) into the heart. The animal was then decapitated and the head was fixed in 3.7% paraformaldehyde and stored in a 4°C refrigerator for 3–6 days, during which time most of the skull overlying the cortex was also removed to increase diffusion of the fixative into the brain. This duration sufficiently fixed the tissue to allow removal of the brain from the skull without damaging its bottom surface, which is used to later align and cut the tissue to extract the midbrain. The brain was immersed in fixative for about three more days after its removal from the skull. Future protocols should include transcardial perfusion to improve fixation of deeper structures, especially when attempting to histologically characterize cellular organization and function. However, based on previous studies (Bledsoe et al., 2003; Lim and Anderson, 2007b; Neuheiser et al., 2010) and as shown later in the Results, this simpler fixation protocol was sufficient to consistently reconstruct our brain tissue and electrode tracks.

To block the midbrain, a custom-made slicing box (specifications found at soniclab.umn.edu) was built to assure straight-edge cuts. Commercial brain blockers have a set mold that the full brain rests in and do not work for slicing partial brain regions, such as the midbrain. The custom slicing box has holes through which the brain can be pinned down and allows the full brain or partial regions to be blocked carefully along appropriate planes. Although this custom-made slicing box was used for the histological preparations in this paper, any preferred apparatus or method can be used to make straight-edge cuts. This slicing box was originally designed and used to increase the consistency in how different midbrains were blocked to improve normalization of data across animals. However, it was frequently observed that anatomical variations between brains could cause them to lie in the box with slightly different orientations, leading to different angled cuts across the edges of the extracted midbrains. Similar cutting issues occur when using commercial brain blockers (e.g., Kopf Instruments, Tujunga, CA). As described in detail in section "Normalizing Across Multiple Midbrains," a unique solution to this problem has been to identify consistent anatomical landmarks that can be used to align and normalize brains across animals without relying on the sliced edges. The only critical requirement for any slicing apparatus used for blocking the midbrain is that it can create a straight-edge cut along the correct midline of the midbrain important for the normalization procedure.

There are several steps that were used to block the midbrain. Initially, with the brain sitting on its ventral side and pinned down through the frontal lobes and the cerebellum, a coronal cut was made caudal to the cerebellum to remove the back portion of the spinal cord, allowing the brain to sit flat in the box (**Figure 2A**). Another coronal cut, made through the center of the temporal lobes, removed the rostral half of the brain (**Figure 2B**), and the cortex was peeled away from the midbrain (**Figure 2C**). Using a small razor, the cerebellum was then carefully pulled and cut away from the midbrain (**Figure 2D**). Finally, the left midbrain was pinned down in the box and a sagittal cut was made through the visible midline track to extract the right midbrain (**Figure 2E**).

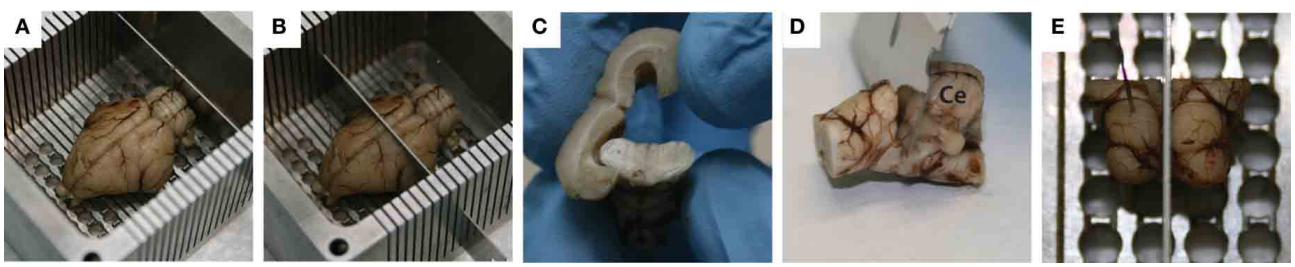

FIGURE 2 | Standard blocking procedure for extracting the midbrain. With the brain pinned to the custom-made slicing box through the frontal lobe and the cerebellum, a coronal slice was made caudal of the cerebellum to remove the spinal cord **(A)**, while a second coronal slice was made through the center of the temporal lobes to remove the rostral half of the brain **(B)**. A frontal view of the cortex being peeled away from the midbrain is shown in **(C)**, followed by removal of the cerebellum (labeled Ce in **D**) using a small razor. Finally, with the left midbrain pinned down, a mid-sagittal cut was made to extract the right midbrain **(E)**. Red dots on the right inferior colliculus show where the dyed shanks entered through its surface during the *in vivo* portion of the experiment.

For accurate alignment of the midbrain slices during reconstruction, three reference tracks were created in the lateral-to-medial direction in the right midbrain. With the midbrain resting on its medial edge, a small needle stained with Di-I was stereotaxically inserted perpendicular to the lateral surface and left for 15 min to allow the Di-I to diffuse into the tissue, while dripping a sucrose solution (15 g sucrose per 100 mL of 0.1 M PBS) on the midbrain to keep it moist. The first track was inserted into the intersection point of the superior colliculus (SC), thalamus, and the lateral extension from the IC as shown in **Figure 3C** (black arrow). This is a consistent anatomical landmark across animals (termed the "consistent reference track") and is critical for accurate alignment of the slices. As discussed later in the Methods, the lateral edge of this reference track is used to normalize across multiple brains, making its consistent placement vital to the method's success. To avoid misalignments due to slice rotation errors and tearing along the reference track, two additional perpendicular reference tracks were arbitrarily created within the tissue but outside of the IC as to not interfere with the electrode shank placements (gray tracks in **Figures 3E** and **F**). It is also possible to create angled reference tracks if angled electrode trajectories are not available to later aid in the alignment process. After creating the three reference tracks, the midbrain was placed into a sucrose solution until the tissue sank (∼1 day). The midbrain was then dipped in saline and frozen on its medial edge to –18°C for cryosectioning. Sagittal sections (60 μm thickness) were cut using a sliding microtome (Leica, Buffalo Grove, IL) and placed in wells filled with a phosphate buffer (9:1 di-ionized H_20 to PBS). The slices were dipped in a sodium acetate buffer and mounted onto slides for imaging. Each slice was labeled with the distance from the lateral edge of the IC and any slice with extreme tearing was discarded. Sagittal sectioning ensured that each slice showed a single point for each electrode track (placed at a 45° angle off the sagittal plane) and reference track (placed at a 90° angle off the sagittal plane).

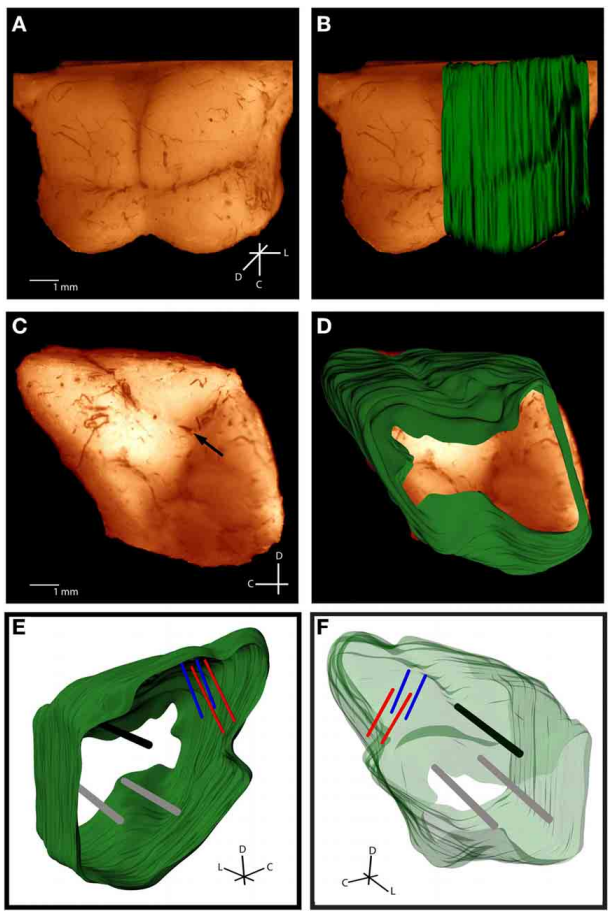

FIGURE 3 | Histological computer reconstruction of the midbrain overlaid on a top view (A,B) and lateral view (C,D) of the fixed midbrain. Images were digitally enhanced to improve visualization of the borders. The reconstructed midbrain was also slanted in **A** and **B** to align it with the angled view of the fixed midbrain, which was purposely presented in this way to visualize the lateral side of the right inferior colliculus. The placement of the "consistent reference track," which is through the intersection of the superior colliculus, thalamus, and lateral extension from the inferior colliculus, is indicated by the black arrow in **(C)**. Computer reconstructions are rotated to view them from the medial **(E)** and lateral **(F)** sides. The consistent reference track is shown in black, the two arbitrarily-placed reference points are in gray, and the two bi-shank probe pairs are in red and blue. C, caudal; D, dorsal; L, lateral.

IMAGING OF SECTIONS

Slice images were taken within a week of sectioning using a Leica MZ FLIII fluorescent stereomicroscope (Leica, Buffalo Grove, IL), Leica DFC420 C peltier cooled CCD camera, and Image-Pro software (MediaCybernetics, Bethesda, MD). At least two fluorescent images using a filter set with a 546/10 nm excitation and 590 nm emission were taken of each slice with varying degrees of exposure (**Figure 4**). Fluorescent images were taken while varying the exposure time (3–3.5 s) and gain (2.5–4×) to optimize the visualization points (i.e., higher values to see dull points, lower values to remove flare in bright points). A single reflective white light image using a variable intensity fiber optic light source (Fiber-Lite-PL800, Dolan-Jenner Industries, Boxborough, MA) was taken to determine the outline of each slice for tracing. Fluorescence images were later superimposed on the reflective white light images for visualization of the reference and electrode shank points. The images were then saved as .tif files and labeled with their distance from the lateral edge of the IC. All images were taken at the same zoom for consistency, and an additional image of a 1 mm scale ruler was taken to later calibrate the image size in the modeling software.

TRACING IMAGES

The .tif images were imported into Rhinoceros, a three-dimensional modeling tool for designers (Seattle, WA). A detailed view of the Rhinoceros interface is shown in **Figure 5**. Grid lines were placed (major every 100 μm, minor every 10 μm) and the snap spacing was enabled and set to 1 μm. At this point, distances within the Rhinoceros interface were arbitrary, but once all of the images were placed and traced, the 1 mm ruler image was used to scale all of the tracings to the correct physical size. The first bitmap was placed at the origin and a frame was created around the outline to place subsequent bitmaps (**Figures 5A** and **B**). Once the frame was in place, grid line snap was turned

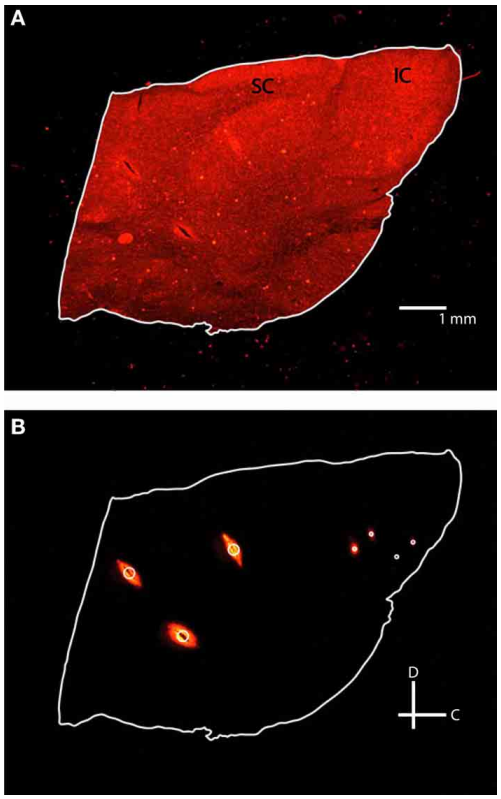

FIGURE 4 | Fluorescent images of the same 60 μm thick sagittal slice with reflective white light (A) and fluorescence (B) settings. Each slice was outlined in white and three reference points (large white circle) and two pairs of electrodes (small white circles) were identified. IC, inferior colliculus; SC, superior colliculus; C, caudal; D, dorsal.

off and grayscale was turned off to better visualize the slices. Each slice was traced using the InterpolateCurve command, ignoring tears that extended beyond the obvious border of the slice, and saved as a new layer. Any slice with significant tearing or folding was discarded (typically <5% of total slices). Once a reflective white light image outline was traced, the same slice's fluorescence image was overlaid to identify the reference points and shank placements, which were chosen using the Circle command with 3 μm and 1 μm radii, respectively (white circles in **Figure 4**). Lastly, each completed tracing was moved to the correct sagittal depth based on its distance from the lateral edge of the IC and spaced 60 μm from the neighboring slices assuming no torn slices were removed (**Figure 5C**).

ALIGNING SLICES

With the tracings in the correct position, they needed to be rotated and aligned to each other using the reference tracks and the electrode trajectories. First, the ICs were approximately arranged across slices, and slices that were mounted on the slides backwards were mirrored. The consistent reference track at the intersection of the SC, thalamus, and the lateral extension from the IC was aligned across slices. The tracings were then rotated to align the other two reference tracks through the midbrain and match the straight rostral edge created from the frontal cut during the blocking process (**Figures 5D–G**). The 45° angled electrode trajectories combined with the three reference tracks provided multiple axes to align all the slices while minimizing shifting of each slice relative to each other. Finally, the image of the 1 mm ruler was imported into Rhinoceros, traced, and used to scale the arbitrary distances within Rhinoceros to the actual physical dimensions of the slices.

CREATION OF BEST FIT LINES FOR ELECTRODE TRACKS

To visualize the complete electrode shank trajectories, we created a best fit line through the electrode shank placements across all the traced slices, examples of which are shown in **Figure 5H**. To create each best fit line, a new layer in Rhinoceros was created, the center snap feature was turned on, and the points making up a given track were selected across all the slices. Using the LineThroughPt command, a best fit line through all of the points was created and saved as the final trajectory. A similar fitting procedure was also performed for the reference tracks.

CONSTRUCTION OF 3D MESH

With all of the tracings aligned at the correct orientation, they needed to be meshed to create a complete surface. In a new layer, the Loft command in Rhinoceros was used. At least 50 control points were chosen on the outline of the tracings and a mesh was formed around those points. If more control points were selected, the mesh around the tracings became tighter and created a more jagged rendering of the three-dimensional surface. Also, the electrode best fit lines and the reference tracks were meshed for visualization purposes using the Loft command, creating tube-like trajectories (**Figure 5H**).

IDENTIFYING THE LOCATION OF ELECTRODE SITES

To identify the location of each electrode site along a shank track, a few extra steps and probe requirements were needed. First, during the *in vivo* portion of the experiment, the electrode array was initially inserted only partially within the IC. Neural activity was recorded on each site in response to 100 trials of 70 dB broadband noise (6 octaves wide centered at 5 kHz). The border of the IC, as shown in **Figure 6**, was identified as the location halfway between the last site showing a significant response [i.e., >76% correct in a signal detection theory paradigm (Green and Swets, 1966; Lim and Anderson, 2006; Middlebrooks and Snyder, 2007)] and the next superficial site (spaced 100 μm away). The electrode array was then inserted using a hydraulic micro-manipulator into the final location for experimentation, noting the additional distance the array was inserted into the midbrain.

Though the physical distance of each electrode site along a track within the IC was known for the *in vivo* preparation, the fixation process could cause the midbrain to change in size and modify the track and site locations. To address this issue, an electrode array with two shanks separated by a fixed distance (500 μm apart) was necessary for assessing how much the tissue changed during fixation. Assuming the brain changes size in a homogenous and isotropic manner, it was possible to take the average change in distance between pairs of shanks across all placements throughout the IC for a given animal and use that scaling factor to

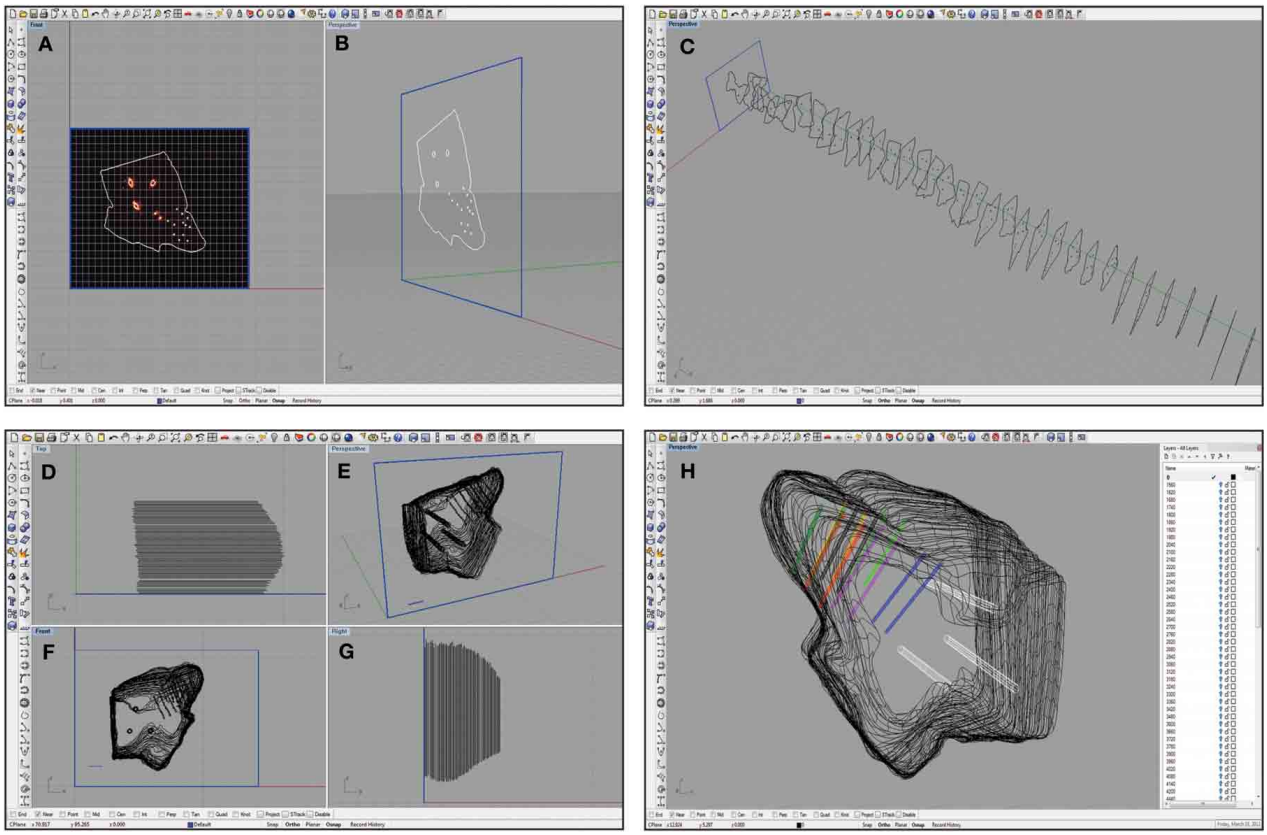

FIGURE 5 | Screen shots of the Rhinoceros software interface at various steps in the reconstruction process. A single slice was placed in a frame of arbitrary size (shown in blue) at the origin and traced as shown from a medial **(A)** and an oblique **(B)** view. This process was repeated for each slice that was also placed at the correct location on the medial-to-lateral axis **(C)**. Damaged slices that could not be accurately traced were not included, leaving larger gaps between the surrounding slices. The slices were then aligned using the three reference points as shown from a top view **(D)**, an oblique angle **(E)**, a medial view **(F)**, and from the caudal side **(G)**. Larger spacing in **(D)** and **(G)** indicate where torn slices were removed from the reconstruction. These slices were also scaled using a 1 mm ruler (shown in blue; **E** and **F**). Finally, the wireframe was meshed using approximately 50 control points around the shell of the midbrain, and the reference points (white) and electrode array tracks (multiple colors; bi-shank probe pairs are color-matched) were meshed to create tube-like trajectories **(H)**. The white menu on the right indicates the number of layers that can be turned on or off to increase visualization of specific features at any given time.

adjust the distance from the edge of the IC of each site measured *in vivo* to match the reconstructed IC dimensions. The scale factor across animals showed that the midbrain shrank an average of <4% from its *in vivo* size. Other studies have observed tissue shrinkage up to 10–15% (Cant and Benson, 2005; Dauguet et al., 2007), which was not observed for the protocol used in this study. The creative use of probes with fixed-shanks can partially correct for morphological changes that occur during the fixation process. Considering recent advances in multi-site array technologies in which three-dimensional configurations with micron level precision can be developed and are commercially available (e.g., NeuroNexus Technologies, Ann Arbor, MI), there are numerous opportunities for improving functional mapping of the brain through combined histological and neurophysiological reconstructions.

NORMALIZING ACROSS MULTIPLE MIDBRAINS

While the previous steps detail reconstruction of electrode locations for a single midbrain, mapping studies typically require researchers to pool data across multiple brains. Therefore, it is necessary to be able to align and normalize midbrains of different sizes and shapes (**Figure 7**). First, a standard midbrain, having the most average size and shape across the data-set, was chosen. To normalize a new midbrain to the standard midbrain, both were imported into Rhinoceros. All movements, including resizing and rotations, were done on the new midbrain only. The new midbrain was first translated to the correct sagittal location to align the medial surfaces of the two midbrains, and then scaled one-dimensionally to match the medial-to-lateral distance of the standard midbrain. The consistent reference tracks of each midbrain were aligned and the new midbrain was rotated so that both reference tracks were approximately in the same orientation. The consistent reference track of the new midbrain was then anchored only at the lateral edge (point of insertion, gray arrow in **Figure 7B**) and all scaling and rotations were performed relative to that point. This is a new approach developed for the normalization procedure in this paper that has produced quite consistent results across animals. It also minimizes alignment

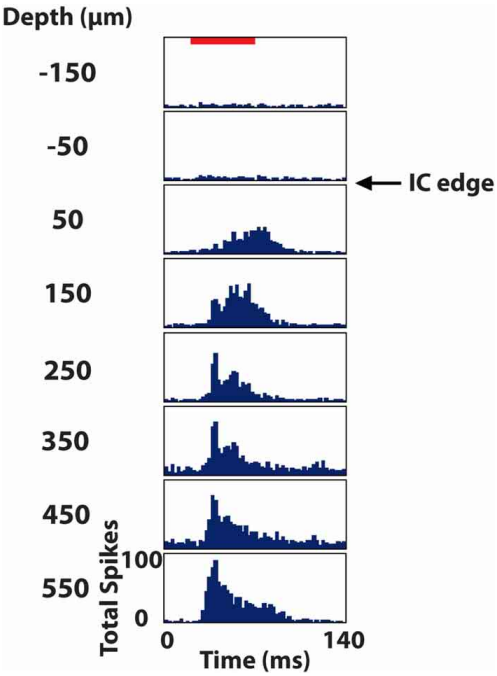

FIGURE 6 | Post stimulus time histograms of eight sites in the inferior colliculus (IC) in response to 100 trials of broadband noise (70 dB SPL, 6 octaves centered at 5 kHz). The red bar corresponds to the acoustic stimulus (60 ms duration) and depths are labeled relative to the superficial edge of the IC, which was approximated as the center point between the last electrode site responding significantly to the stimulus and the next site outside of the IC.

errors created during the blocking protocol. During the cutting process, the brain was placed into the customized slicing box and cut with straight edges. However, due to shape variations of each brain and how they laid in the box, each midbrain may have been cut and extracted with slightly different angles relative to each other. The anchoring process enabled the reconstructed midbrains from different animals to be rotated relative to a consistent landmark to minimize the errors associated with these cutting misalignments. Animals of similar age were used to minimize differences in size of the midbrains for normalization. However, to account for additional differences in size and shape of the midbrains across animals, a second two-dimensional scaling process was performed on the new midbrain. The new midbrain was iteratively scaled and rotated in different orientations to match surfaces of interest, including the caudal surface of the IC (red arrow), the caudal-dorsal surface of the IC (blue arrow), and the curvature of the IC extending from the dorsal to the lateral surface of the IC (orange arrow) as shown in **Figure 7**. The dip between the IC and SC was used as an additional landmark for normalization. The other edges and surfaces were not used since they depended on subjective and inconsistent cuts made during the blocking process.

CORRELATING LOCATION WITH FUNCTION

A key advantage of this reconstruction method is the ability to correlate functional neural activity with several anatomical locations for extensive mapping studies across animals. In this study, the spatial organization of three general frequency laminae within the central nucleus of the IC (ICC) across animals was reconstructed from the neurophysiological and anatomical

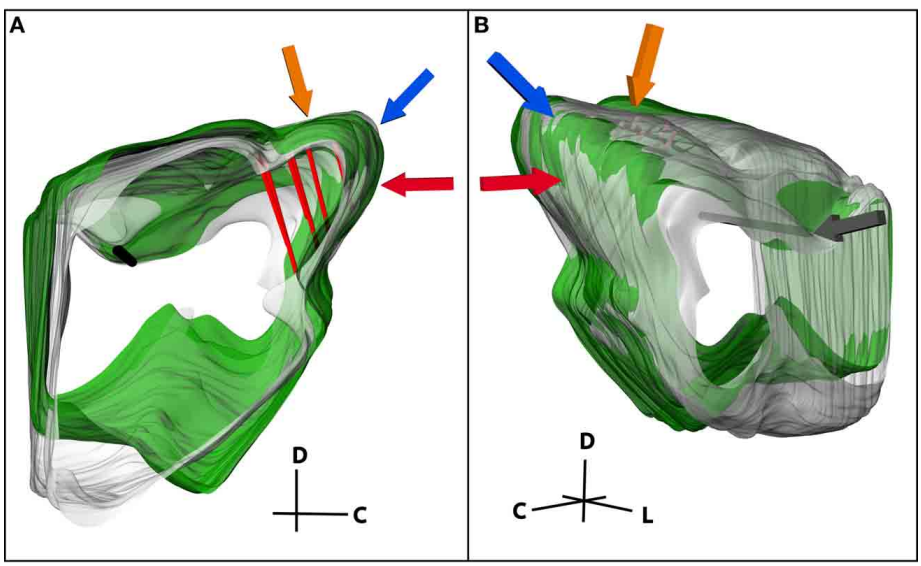

FIGURE 7 | (A) Medial and (B) lateral views of two midbrains (green and gray) normalized to each other. The consistent reference track is shown in black and three pairs of electrode tracks in red. Three of the landmarks used to normalize the midbrains are highlighted, including the caudal-dorsal surface of the inferior colliculus (IC; blue arrow), the curvature of the IC extending from the dorsal to the lateral surface (orange arrow), and the caudal surface of the IC (red arrow). The midbrains were anchored together on the lateral edge of the consistent reference track (gray arrow) and rotated and scaled relative to that point until the new midbrain (green) was normalized to the standard midbrain (gray). C, caudal; D, dorsal; L, lateral.

data. *In vivo* experiments were conducted within a sound attenuating, electrically-shielded room, and controlled by a computer using TDT hardware (Tucker-Davis Technology, Alachua, FL) and custom software written in MATLAB (MathWorks, Natick, MA). The TDT-MATLAB system digitally generates acoustic stimuli at a 200 kHz D/A sampling rate (24 bit sigma-delta). Acoustic stimulation was presented via a speaker coupled with the left ear canal by a custom-made hollow ear bar. The speaker-ear bar system was calibrated by coupling the tip of the ear bar with a 0.25-in ACO Pacific condenser microphone (Belmont, CA) via a short plastic tube that represents the ear canal. The neural data was sampled at a rate of 25 kHz (16-bit), passed through analog DC-blocking and anti-aliasing filters up to 7.5 kHz, and later digitally filtered between 0.3 and 3 kHz for spike analysis.

Neural activity was recorded in response to 100 trials of 70 dB SPL, 50 ms duration (0.5 ms rise/fall ramp times) broadband noise (6 octaves centered at 5 kHz) and post-stimulus time histograms were plotted for visualization. Additionally, frequency response maps were plotted by varying 50 ms (5 ms rise/fall ramp times) pure tones (1–40 kHz in 8 steps/octave) from 0 to 70 dB SPL and recording the normalized spike rates for four trials of each stimulus (**Figure 8**). The spike rate was calculated by finding when the voltage exceeded 3.5 standard deviations above the noise floor within a window of 5–65 ms following the onset of the acoustic stimulus. The best frequency (BF) of each electrode site was determined by taking the centroid of activity across frequencies at 10 dB above the visually-identified threshold level. This BF measure was used instead of characteristic frequency (i.e., frequency corresponding to the maximum activity at threshold) because it was less susceptible to noise and more consistent with what was visually estimated from the frequency response maps.

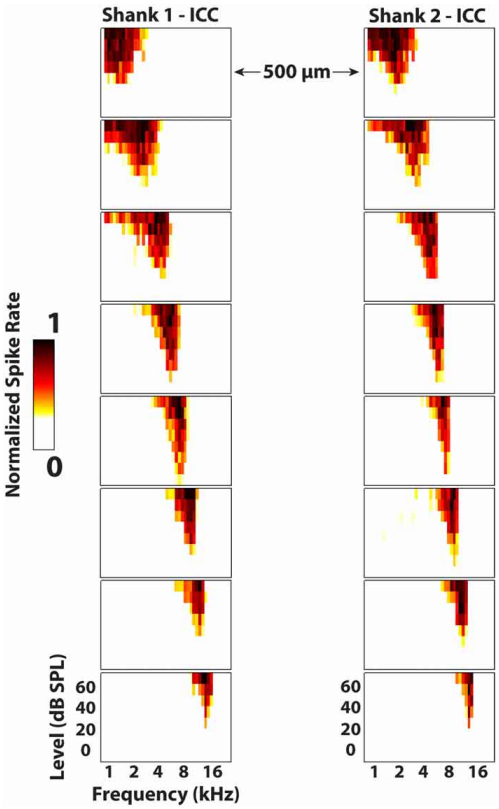

FIGURE 8 | Frequency response maps for two electrode shanks separated by 500 µm placed in the central nucleus of the inferior colliculus (ICC). ICC placements are characterized by sharp tuning and a consistent tonotopic shift from low (superficial sites) to high (deep sites) frequencies. Spike rates were normalized to the maximum number of spikes for each site across all stimuli. Every other site (200 µm spacing) along the electrode shank is plotted. The colorbar was adjusted to remove spontaneous activity to enhance visualization of the response maps.

RESULTS

The first validation of our method was to qualitatively compare our computer model (**Figures 3E** and **F**) of the midbrain to images of the midbrain taken a day before slicing. Overlaying our reconstruction on the fixed midbrain (dorsal view shown in **Figures 3A** and **B** and lateral view in **Figures 3C** and **D**) shows a close correspondence in shape and size of the midbrain. We also quantified the errors associated with the reconstruction process, starting with the accuracy of aligning slices. Another major source of error is due to the subjectivity involved with tracing and aligning the different slices together. Four trained individuals independently reconstructed the same midbrain and we calculated the variation in electrode and reference track locations across slices and for a fully reconstructed midbrain. When normalizing across different midbrains, there is the additional variation of midbrain size and shape that cannot be avoided. Even with this animal variation, we were able to consistently reconstruct several frequency laminae of the ICC across three different animals.

ALIGNMENT ERROR: ANALYSIS OF ELECTRODE SHANK BEST FIT LINES

The accuracy of aligning slices throughout a brain was determined by analyzing the variability in electrode shank points from the best fit line placed through them. Sources of error include tissue deformation while slicing and mounting the sections on slides and manually determining electrode shank locations. Twelve total electrode shanks were randomly chosen from three brains for the analysis. For each electrode shank location within a slice, a perpendicular line was drawn from the placement to the best fit line and measured. Across all of the placements, we found an average distance of 31 µm (standard deviation (σ) = 21 µm, maximum = 260 µm). A distribution of the measured distances (**Figure 9**) encouragingly shows that ~75% of the electrode shank locations are within 50 µm of their best fit line.

SINGLE SLICE ERROR: SELECTION OF ELECTRODE AND REFERENCE POINTS

The second analysis performed was to quantify the error of different individuals reconstructing slices and choosing the locations of electrode and reference points (**Figure 10**). Variations in measurements arise from several sources. For example, the Di-I diffuses through the tissue and the trained individual has to estimate the center of the electrode or reference point. Additionally, the reference needle can cause tearing in the surrounding tissue requiring subjective estimation of the center of the reference

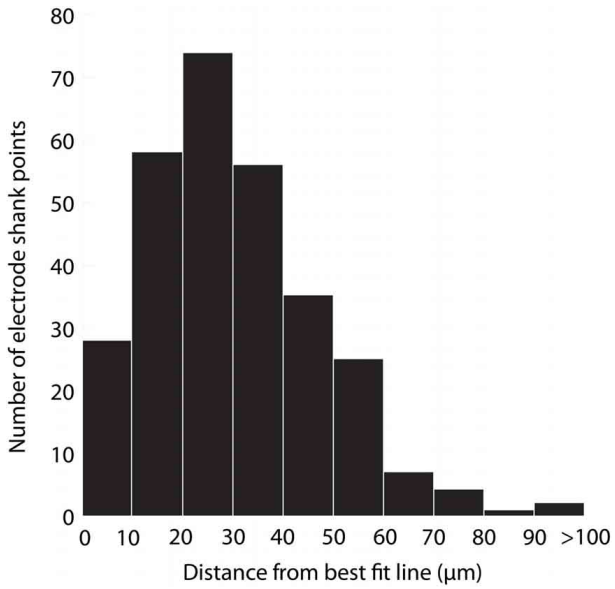

FIGURE 9 | Histogram of the distance of electrode shank points from their best fit line. Twelve total electrode shanks were randomly chosen from three brains. For each electrode shank, a perpendicular line was drawn between the electrode shank location (i.e., point) in each slice and the best fit line across slices. The distance of this perpendicular line was measured across slices, shanks and animals, and the values are displayed in the histogram, which presents the accuracy of alignment across slices. $N = 290$ electrode shank points.

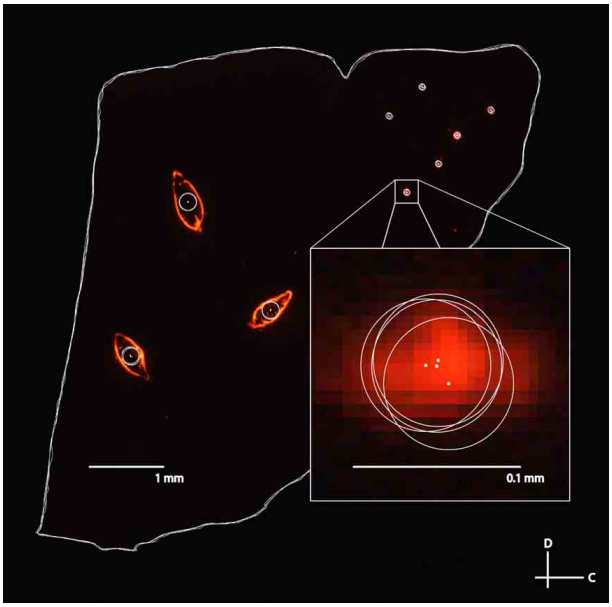

FIGURE 10 | A fluorescent image of a sagittal slice traced by four separate individuals for the second error analysis. The large white circles correspond to the three reference points and the small white circles correspond to the different electrode track placements (three bi-shank placements). Tracing error between individuals was determined by measuring the distance between the estimated electrode track point or reference point (i.e., the center of the circles indicated by white dots) between each pair of individuals, and averaging across all pairs of individuals and placements for five different slices. C, caudal; D, dorsal.

point. In order to quantify the individual variation, four individuals reconstructed the same five slices of a midbrain independently. Each slice consisted of three placements of the bi-shank electrode (for a total of six electrode points) and three reference points. The tracings for each slice were then superimposed directly on top of each other by aligning the frame used in Rhinoceros for tracing the slices and the distance between corresponding points across the four individuals were measured. The electrode placements were found to have an average distance of 12 μm ($\sigma = 9\,\mu$m, maximum = 61 μm) across all the points and slices. As expected, the reference points had a larger average error of 18 μm ($\sigma = 13\,\mu$m, maximum = 61 μm). Consistent localization of reference points is especially important as all of the slices are aligned according to these three points.

SINGLE MIDBRAIN ERROR: IDENTIFYING ELECTRODE TRACKS

While the second analysis provides the individual error associated with simply tracing the slices and selecting points of interest, the next step was to analyze the error associated with the entire three-dimensional reconstruction process, including differences between individuals and the subjective normalization process (**Figure 11**). Four individuals independently reconstructed the same midbrain. The midbrains were then normalized together as described in the Methods and shown in **Figure 8**, and five random slices each with six electrode track points (taken from the best fit lines for each electrode shank) were used for analysis. Using this technique and measuring the absolute distances between points for each track across individuals for the different electrode tracks and slices, the average electrode track error was 64 μm ($\sigma = 43\,\mu$m, maximum = 201 μm; **Figure 11i**), which is an error of ∼1.5% relative to the entire IC structure (4–5 mm diameter sphere). Since the true electrode track location is likely somewhere between the points estimated by each individual, we performed another analysis that would more closely depict the error of our reconstruction method (**Figure 11ii**). We calculated the average of the four individuals' best fit lines and assumed this was the actual electrode location for each track (white circle in **Figure 11ii**). Measuring the distance of each individual's electrode position to this averaged placement across electrode tracks and slices, we found an average error of 31 μm ($\sigma = 19\,\mu$m, maximum = 84 μm), corresponding to ∼0.7% of the IC structure.

NORMALIZING ACROSS MIDBRAINS: ISOFREQUENCY LAMINAE ANALYSIS

The final analysis sought to qualitatively determine whether our anatomical modeling method could reconstruct electrode site locations across three animals by aligning the neurophysiologically confirmed frequency layers of the ICC (**Figure 12**). This analysis incorporates both reconstruction errors and inter-animal variability. Based on the literature, layered isofrequency laminae in the ICC are generally accepted to be consistent across animals (Malmierca et al., 1995, 2008; Ehret, 1997; Schreiner and Langner, 1997; Oliver, 2005); thus we expected to see aligned frequency layers across the three animals assuming sufficient accuracy with

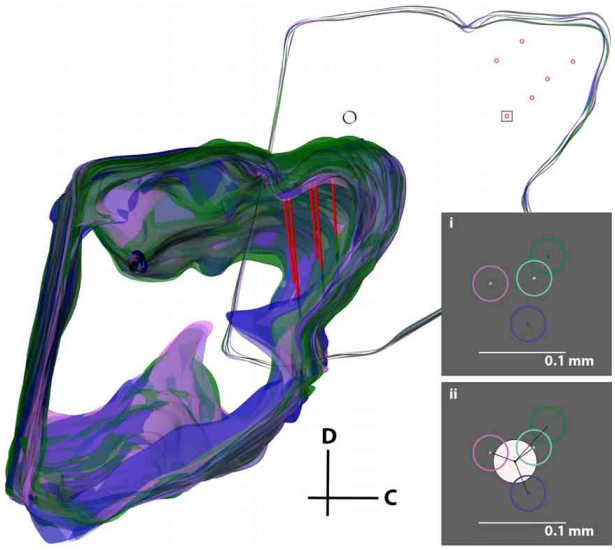

FIGURE 11 | Error analysis procedure incorporating all errors in the reconstruction process. The same midbrain was reconstructed by four different individuals (purple, pink, cyan, and green), aligned, and normalized to each other. The consistent reference track for each midbrain and three pairs of electrode tracks from one of the four midbrains (red) are displayed. A single slice was removed for analysis (top right), and a box around one electrode placement is shown in inserts **(i)** and **(ii)**. The error was either calculated (**i**) by taking the distance between each of the four electrode track points (center-to-center of the circles), or **(ii)** by finding the average of the four placements (white circle) and calculating the distance from its center to each electrode track point. The distances for each of the six electrode points across five slices were averaged to obtain the total error for this analysis. C, caudal; D, dorsal.

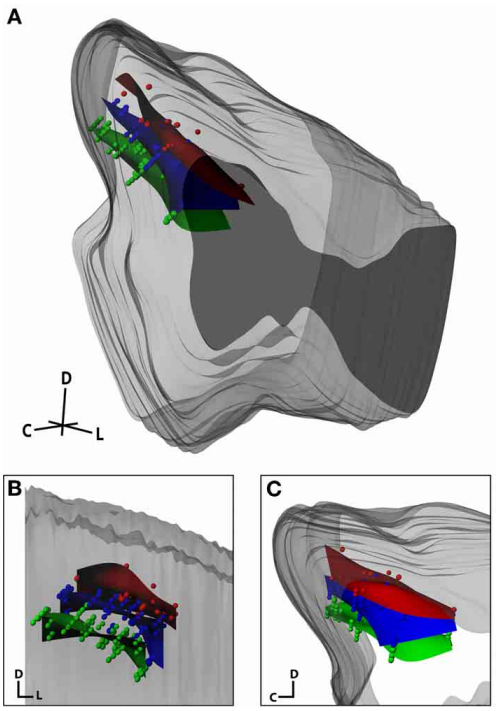

FIGURE 12 | Isofrequency laminae from three midbrains that were aligned and normalized together and shown within the standard midbrain in an isometric view (A), and magnified in a caudal (coronal; B) and lateral (sagittal; C) view. Dots correspond to individual electrode sites with best frequencies measured *in vivo* via frequency response maps. The curved planes were created in Rhinoceros as a best-fit to the electrode sites. The red, blue, and green planes correspond to low frequency (2–3.2 kHz; $n = 26$), middle frequency (5–8 kHz, $n = 72$), and high frequency (10–16 kHz, $n = 80$) sites, respectively. C, caudal; D, dorsal; L, lateral.

our reconstruction method. Each midbrain was reconstructed by the same individual and the locations of the isofrequency laminae were determined using *in vivo* recordings. Isofrequency laminae 0.6 octaves thick, likely corresponding to two critical bands (Schreiner and Langner, 1997; Egorova et al., 2006; Malmierca et al., 2008), were determined. We used 0.6 octaves to have a sufficient number of points per lamina for reconstruction of the layers and because it was not possible with our current method to spatially resolve individual laminae. Electrode site locations with BFs within three ranges—low (2–3.2 kHz), middle (5–8 kHz), and high (10–16 kHz) frequencies—were identified across the three animals and normalized to each other as shown in **Figure 12** using the standard midbrain. Encouragingly, the site locations for each lamina aligned consistently across animals and the planes displayed the characteristic ∼45° angle (**Figure 12B**, coronal view).

Ideally, these reconstructions can achieve accurate localization of the electrode track and site placements within and across animals. However, due to animal variability, distortions in midbrain shape due to the fixation and reconstruction process, and reconstruction subjectivity, there will always exist some errors that cannot be avoided. Also, this method does not yet possess the resolution to differentiate neighboring isofrequency laminae within the ICC. By using an array with closer sites and improving the reconstruction steps, it will be possible to increase the spatial resolution of the reconstructions. However, as shown in **Figure 12**, we were still able to differentiate isofrequency laminae separated by 1–2 octaves and map out locations across the ICC laminae. This is useful for studies investigating how coding properties vary within different subregions along the ICC laminae. Although our approach is not yet able to characterize the organization along a single, specific lamina, close-by laminae will likely exhibit similar properties and dimensions, and can be pooled together into one general lamina (Malmierca et al., 1995; Oliver, 2005; Seshagiri and Delgutte, 2007). For example, the low frequency laminae could have different shapes and dimensions than the high frequency laminae (Malmierca et al., 1995). Functional properties as well as afferent and efferent projections can also vary differently between low and high frequency ICC laminae (Ramachandran et al., 1999; Cant and Benson, 2003; Loftus et al., 2004; McMullen et al., 2005). Therefore, separating the ICC into several frequency groups that each may span several critical bands and reconstructing the functional properties and projection pathways along those grouped ICC laminae would provide important and useful information for central auditory processing and organization. Encouragingly, our lab has already identified the existence of functional subregions across and along the ICC laminae using many of the reconstruction steps presented in this paper. This includes both ascending

and descending functional and anatomical patterns (Lim and Anderson, 2007a,b; Neuheiser et al., 2010; Markovitz and Lim, 2012).

DISCUSSION

In this study we presented a relatively easy and consistent approach for creating three-dimensional reconstructions of electrode tracks within the IC as well as identifying BF laminae using functional data obtained via electrode sites along those tracks. While electrode locations cannot be perfectly determined due to processing errors, subjectivity within the method and variability between animals, general functional trends can be correlated with anatomical locations using this process. The reconstruction process requires a significant time commitment for tracing and aligning of the slices. However, since the method can be quickly learned, it can serve as a starting project for undergraduate students and even high schools students interested in obtaining initial exposure to neurophysiological and anatomical studies. Automating the different reconstruction steps has been attempted with varying degrees of success by other groups (Ju et al., 2006; Dauguet et al., 2007; Chklovskii et al., 2010; Cifor et al., 2011; Kleinfeld et al., 2011), but these algorithms may miss tissue abnormalities that can generally be fixed through visual and manual correction of the imaged tissue. The customized software packages and additional equipment required for automatic and semi-automatic reconstruction steps can also be quite expensive and not readily available to most neurophysiology labs. For example, four commonly used software packages, Neurolucida (MBF Bioscience, Williston, VT), Amira (Visage Imaging, Richmond VIC, Australia), Avizo (Visualization Science Group, Burlington, MA), and Analyze (AnalyzeDirect, Overland Park, KS), cost between $4000 and $6500 per license, which can become quite expensive when multiple licenses are required. As long as the software is low in cost and multiple licenses and computers can be purchased (e.g., we have four workstations for <$1500 each), a volunteer student infrastructure can provide sufficient personnel time to carefully assess the tissue slices and perform reliable reconstructions, making it more feasible to implement for typical neurophysiological labs. Other costs involved with the procedure can also be minimized, such as by preparing histological slices within the lab instead of outsourcing them to a histology center. While the training and equipment costs are greater initially, this approach is financially beneficial and ensures consistency in the long run.

While this study focused on reconstructing the guinea pig IC using sagittal slices, the process can be utilized across multiple brain regions, species, and slicing planes. One of the most crucial steps in this process is to identify consistent landmarks for normalizing across animals, which would need to be developed for the region of interest. The intersection of the SC, thalamus, and lateral extension from the IC (black arrow in **Figure 3C**) was used as the consistent landmark for IC reconstructions in guinea pigs. This landmark can be used regardless of the slicing plane, as long as additional reference tracks are made perpendicular to the slicing plane to initially align the slices. The consistent reference track can then be reconstructed and anchored at its lateral-most point for normalization. This landmark can also be used to reconstruct other surrounding and connected brain regions, such as the SC, various thalamic areas, and other brainstem regions. Reconstruction of cortical regions, such as the auditory cortex, may be possible by using the indentation along the pseudosylvian sulcus combined with the edges of the visual, temporal, and frontal cortices and the midline for normalization (cortex is shown in **Figures 2A** and **B**). However, since cortical regions are more easily warped during the histology process, other steps such as embedding the tissue in albumin-gelatin or paraffin wax, or slicing on a cryostat may be necessary for increased accuracy (see below for additional improvements).

There are still several hurdles that need to be overcome to create a standard reconstruction method that can be reliably used across research groups. A non-trivial issue with combining data across multiple labs using different software systems is the compatibility of data files. One of the formats that can be used in the Rhinoceros program is AutoCAD.dxf, which is compatible with files produced in Neurolucida, Amira, Avizo, and Analyze. In addition, Rhinoceros files can be saved in over 30 different file formats, allowing for easy manipulation of the data and the potential to fuse files developed from different software programs and research groups. Another issue with combining data across research groups is ensuring that similar fixation and slicing protocols are used to minimize size and shape variations that can affect the reconstructions (Bohland et al., 2009). Transcardial perfusion would improve reconstructions, and should be used for histological protocols to analyze cellular morphology and function. In our study, we did not perform transcardial perfusion since the various experiments in our laboratory typically last 15–20 h and it is not uncommon for the animal to die from the anesthesia before euthanization, preventing successful perfusion of the tissue. However, perfusion can be employed in place of our simple fixation method without changing the rest of the procedure. Even with transcardial perfusion, tissue deformations and shape changes can occur throughout several steps of the reconstruction process (Dauguet et al., 2007). There are global deformations and shrinkage caused by extraction of the brain from the skull and the fixation process as well as loss of cerebrospinal fluid and dehydration. There are also additional local deformations caused by the slicing, mounting of tissue onto the slides, and any additional staining or manipulations of the slices. As further discussed below, MRI reconstructions can be used to identify and address the global deformations, though this approach is not readily available to all labs and can be expensive for a large number of brain reconstructions. One solution is to embed the tissue in a gelatin albumin to prevent deformations cased by mounting the tissue. Another solution is to take images of the blocked tissue surface (i.e., blockface photograph) after each slice of tissue is removed (Dauguet et al., 2007; Bohland et al., 2009). Then the image of the slice mounted onto the slide can be adjusted using various software algorithms to match the blockface photograph. It is possible to also perform three-dimensional reconstruction of the blockface photographs with greater accuracy than with the histological slices. However, the fine anatomical features cannot be clearly identified without the use of appropriate stains that are possible with the histological slices. For our track reconstructions, it was not possible to consistently detect and reconstruct the red-stained

track trajectories in blockface photographs. Attempting to create a green filter microscope system combined with the microtome device for capturing both fluorescence and blockface photographs is not trivial and can be expensive. At this stage, it is more realistic to use the blockface photographs to fix the local deformations in the slices, and then use those imaged histological slices for the actual reconstruction process.

Another major hurdle is how to address animal variability, especially when attempting to normalize brains across different animal strains and ages. The normalization process depends on the consistency of anatomical landmarks and edge shapes across animals. For this study, we used guinea pigs that were the same strain and similar in age and weight. Based on visual inspection, we generally observed consistent brain shapes and landmarks across animals, though there were slight variations as observed in **Figure 7**. One approach to assess how much of these differences are due to the fixation and reconstruction process versus true animal variability is to use MRI to image the *in vivo* brains of the animals with high spatial resolution (Dauguet et al., 2007). While MRI images could provide confirmation of the histological brain reconstruction method and its consistency across different strains and ages, MRI facilities are not accessible to all neurophysiology labs. Also, morphological and neurochemical assessment of the tissue on the cellular level would not be possible with MRI alone. If MRI facilities and resources are readily available with reduced costs, then it could be possible to complement the histological reconstructions with MRI images. In terms of reconstruction of actual electrode locations throughout the target structure, it may be possible to induce electrolytic lesions large enough to be detected in the MRI images. In our study, we did not use lesions to mark the electrode locations to avoid excessive damage to the tissue, especially since several array placements were made during the experiment. Developing methods for marking the actual electrode locations *in vivo* without further compromising the neural tissue or functional responses will provide improvements for both histological and MRI reconstruction methods.

The results presented in this study, in addition to the financial and personnel infrastructure described above, are encouraging for developing a standard reconstruction approach that can be performed by multiple labs and used to pool data across animals for creating a more detailed three-dimensional functional model of the brain. One possibility is to have different labs provide their brain models online (i.e., as a Rhinoceros or other compatible file), allowing the community access to the data for further interpretation of coding properties. As long as consistent landmarks are used, groups can normalize the downloaded reconstructions to align with their models. This approach can also be used for brain reconstructions and functional mapping in humans. There has been a significant increase in patients being implanted with neural implants in different brain regions (Zhou and Greenbaum, 2009; Lyons, 2011; Tierney et al., 2011). Coupled with these implants is an enormous amount of perceptual data relating to the effects of stimulation of different locations. Initial identification of the electrode locations are currently achieved through non-invasive CT-MRI techniques. However, confirmation of these locations can also be achieved through histological reconstructions of the implanted brains that become available for research purposes. The functional trends found in humans can then be compared with those from animals.

In summary, our described method allows reconstruction of electrode sites at a spatial resolution of about 100 μm. Additional variability across animals and processing deformations limit identification of absolute locations throughout a structure. However, the use of reliable landmarks and proper normalization as described for our method enables consistent identification of electrode locations across animals to observe general spatial trends along a target nucleus. More sophisticated yet accessible methods and technologies will be necessary to achieve more spatially resolved reconstructions, especially at the cellular and synaptic levels (Bohland et al., 2009; Kleinfeld et al., 2011), and for pooling these data across studies and research groups. Clinically, better understanding of function versus location will help guide optimal electrode placements for neural prosthetic applications and brain-machine devices.

ACKNOWLEDGMENTS

The authors would like to thank Jessica Pohl, Kyle Wesen, and Patrick Hogan for performing independent reconstructions of the brains for data analysis and for their assistance in preparing figures for the manuscript as well as Sarah Offutt and Malgorzata Straka for feedback on the reconstruction approach and manuscript. We would also like to thank John Oja for assistance with the fluorescence microscopy and Nell Cant for providing her protocols in preparing the histological slices. This work was supported by NIH NIDCD R03-DC011589, NIH NIDA T32-DA022616, the University of Minnesota Institute for Engineering in Medicine Walter Barnes Lange Memorial Award, and start-up funds from the University of Minnesota (Institute for Translational Neuroscience and College of Science and Engineering).

REFERENCES

Bamann, C., Nagel, G., and Bamberg, E. (2010). Microbial rhodopsins in the spotlight. *Curr. Opin. Neurobiol.* 20, 610–616.

Bledsoe, S. C., Shore, S. E., and Guitton, M. J. (2003). Spatial representation of corticofugal input in the inferior colliculus: a multicontact silicon probe approach. *Exp. Brain Res.* 153, 530–542.

Bohland, J. W., Wu, C., Barbas, H., Bokil, H., Bota, M., Breiter, H. C., Cline, H. T., Doyle, J. C., Freed, P. J., Greenspan, R. J., Haber, S. N., Hawrylycz, M., Herrera, D. G., Hilgetag, C. C., Huang, Z. J., Jones, A., Jones, E. G., Karten, H. J., Kleinfeld, D., Kotter, R., Lester, H. A., Lin, J. M., Mensh, B. D., Mikula, S., Panksepp, J., Price, J. L., Safdieh, J., Saper, C. B., Schiff, N. D., Schmahmann, J. D., Stillman, B. W., Svoboda, K., Swanson, L. W., Toga, A. W., Van Essen, D. C., Watson, J. D., and Mitra, P. P. (2009). A proposal for a coordinated effort for the determination of brainwide neuroanatomical connectivity in model organisms at a mesoscopic scale. *PLoS Comput. Biol.* 5:e1000334. doi: 10.1371/journal.pcbi.1000334

Cant, N. B., and Benson, C. G. (2003). Parallel auditory pathways: projection patterns of the different neuronal populations in the dorsal and ventral cochlear nuclei. *Brain Res. Bull.* 60, 457–474.

Cant, N. B., and Benson, C. G. (2005). An atlas of the inferior colliculus of the gerbil in three dimensions. *Hear. Res.* 206, 12–27.

Chklovskii, D. B., Vitaladevuni, S., and Scheffer, L. K. (2010). Semi-automated reconstruction of neural circuits using electron microscopy. *Curr. Opin. Neurobiol.* 20, 667–675.

Cifor, A., Bai, L., and Pitiot, A. (2011). Smoothness-guided 3-D reconstruction of 2-D histological images. *Neuroimage* 56, 197–211.

Dauguet, J., Delzescaux, T., Conde, F., Mangin, J. F., Ayache, N., Hantraye, P., and Frouin, V. (2007). Three-dimensional reconstruction of stained histological slices and 3D non-linear registration with *in-vivo* MRI for whole baboon brain. *J. Neurosci. Methods* 164, 191–204.

DiCarlo, J. J., Lane, J. W., Hsiao, S. S., and Johnson, K. O. (1996). Marking microelectrode penetrations with fluorescent dyes. *J. Neurosci. Methods* 64, 75–81.

Egorova, M., Vartanyan, I., and Ehret, G. (2006). Frequency response areas of mouse inferior colliculus neurons: II. Critical bands. *Neuroreport* 17, 1783–1786.

Ehret, G. (1997). "The auditory midbrain, a "shunting yard" of acoustical information processing," in *The Central Auditory System,* eds G. Ehret and R. Romand (New York, NY: Oxford University Press, Inc.), 259–316.

Falcone, J. D., and Bhatti, P. T. (2011). Current steering and current focusing with a high-density intracochlear electrode array. *Conf. Proc. IEEE Eng. Med. Biol. Soc.* 2011, 1049–1052.

Fenno, L., Yizhar, O., and Deisseroth, K. (2011). The development and application of optogenetics. *Annu. Rev. Neurosci.* 34, 389–412.

Glover, G. H. (2011). Overview of functional magnetic resonance imaging. *Neurosurg. Clin. N. Am.* 22, 133–139, vii.

Green, D., and Swets, J. (1966). *Signal Detection Theory and Psychophysics.* New York, NY: Wiley.

Hemm, S., and Wardell, K. (2010). Stereotactic implantation of deep brain stimulation electrodes: a review of technical systems, methods and emerging tools. *Med. Biol. Eng. Comput.* 48, 611–624.

Jain, R., and Shore, S. (2006). External inferior colliculus integrates trigeminal and acoustic information: unit responses to trigeminal nucleus and acoustic stimulation in the guinea pig. *Neurosci. Lett.* 395, 71–75.

Johnson, M. D., Miocinovic, S., McIntyre, C. C., and Vitek, J. L. (2008). Mechanisms and targets of deep brain stimulation in movement disorders. *Neurotherapeutics* 5, 294–308.

Ju, T., Warren, J., Carson, J., Bello, M., Kakadiaris, I., Chiu, W., Thaller, C., and Eichele, G. (2006). 3D volume reconstruction of a mouse brain from histological sections using warp filtering. *J. Neurosci. Methods* 156, 84–100.

Kleinfeld, D., Bharioke, A., Blinder, P., Bock, D. D., Briggman, K. L., Chklovskii, D. B., Denk, W., Helmstaedter, M., Kaufhold, J. P., Lee, W. C., Meyer, H. S., Micheva, K. D., Oberlaender, M., Prohaska, S., Reid, R. C., Smith, S. J., Takemura, S., Tsai, P. S., and Sakmann, B. (2011). Large-scale automated histology in the pursuit of connectomes. *J. Neurosci.* 31, 16125–16138.

Leergaard, T. B., White, N. S., De Crespigny, A., Bolstad, I., D'arceuil, H., Bjaalie, J. G., and Dale, A. M. (2010). Quantitative histological validation of diffusion MRI fiber orientation distributions in the rat brain. *PLoS ONE* 5:e8595. doi: 10.1371/journal.pone.0008595

Lehew, G., and Nicolelis, M. A. L. (2008). "State-of-the-art microwire array design for chronic neural recordings in behaving animals," in *Methods for Neural Ensemble Recordings,* 2nd Edn. ed M. A. L. Nicolelis (Boca Raton, FL), 1–20.

Lenglet, C., Abosch, A., Yacoub, E., De Martino, F., Sapiro, G., and Harel, N. (2012). Comprehensive *in vivo* mapping of the human basal ganglia and thalamic connectome in individuals using 7T MRI. *PLoS ONE* 7:e29153. doi: 10.1371/journal.pone.0029153

Lenglet, C., Campbell, J. S., Descoteaux, M., Haro, G., Savadjiev, P., Wassermann, D., Anwander, A., Deriche, R., Pike, G. B., Sapiro, G., Siddiqi, K., and Thompson, P. M. (2009). Mathematical methods for diffusion MRI processing. *Neuroimage* 45, S111–S122.

Lim, H. H., and Anderson, D. J. (2006). Auditory cortical responses to electrical stimulation of the inferior colliculus: implications for an auditory midbrain implant. *J. Neurophysiol.* 96, 975–988.

Lim, H. H., and Anderson, D. J. (2007a). Antidromic activation reveals tonotopically organized projections from primary auditory cortex to the central nucleus of the inferior colliculus in guinea pig. *J. Neurophysiol.* 97, 1413–1427.

Lim, H. H., and Anderson, D. J. (2007b). Spatially distinct functional output regions within the central nucleus of the inferior colliculus: implications for an auditory midbrain implant. *J. Neurosci.* 27, 8733–8743.

Lim, H. H., Lenarz, M., and Lenarz, T. (2009). Auditory midbrain implant: a review. *Trends Amplif.* 13, 149–180.

Lim, H. H., Lenarz, M., and Lenarz, T. (2011). "Midbrain auditory prostheses," in *Auditory Prostheses: New Horizons,* eds F. G. Zeng, R. R. Fay, and A. N. Popper (New York, NY: Springer Science+Business Media, LLC), 207–232.

Lim, H. H., Lenarz, T., Joseph, G., Battmer, R. D., Samii, A., Samii, M., Patrick, J. F., and Lenarz, M. (2007). Electrical stimulation of the midbrain for hearing restoration: insight into the functional organization of the human central auditory system. *J. Neurosci.* 27, 13541–13551.

Loftus, W. C., Bishop, D. C., and Oliver, D. L. (2010). Differential patterns of inputs create functional zones in central nucleus of inferior colliculus. *J. Neurosci.* 30, 13396–13408.

Loftus, W. C., Bishop, D. C., Saint Marie, R. L., and Oliver, D. L. (2004). Organization of binaural excitatory and inhibitory inputs to the inferior colliculus from the superior olive. *J. Comp. Neurol.* 472, 330–344.

Lozano, A. M., and Hamani, C. (2004). The future of deep brain stimulation. *J. Clin. Neurophysiol.* 21, 68–69.

Lyons, M. K. (2011). Deep brain stimulation: current and future clinical applications. *Mayo Clin. Proc.* 86, 662–672.

Malmierca, M. S., Izquierdo, M. A., Cristaudo, S., Hernandez, O., Perez-Gonzalez, D., Covey, E., and Oliver, D. L. (2008). A discontinuous tonotopic organization in the inferior colliculus of the rat. *J. Neurosci.* 28, 4767–4776.

Malmierca, M. S., Rees, A., Le Beau, F. E., and Bjaalie, J. G. (1995). Laminar organization of frequency-defined local axons within and between the inferior colliculi of the guinea pig. *J. Comp. Neurol.* 357, 124–144.

Markovitz, C. D., and Lim, H. H. (2012). Dissecting the corticofugal pathways of the central auditory system: the effect of cortical stimulation on neural firing in the inferior colliculus. *Assoc. Res. Otolaryngol. Abstr.* 35, 274.

McCreery, D. B. (2008). Cochlear nucleus auditory prostheses. *Hear. Res.* 242, 64–73.

McMullen, N. T., Velenovsky, D. S., and Holmes, M. G. (2005). Auditory thalamic organization: cellular slabs, dendritic arbors and tectothalamic axons underlying the frequency map. *Neuroscience* 136, 927–943.

Merzenich, M. M., and Reid, M. D. (1974). Representation of the cochlea within the inferior colliculus of the cat. *Brain Res.* 77, 397–415.

Middlebrooks, J. C., and Snyder, R. L. (2007). Auditory prosthesis with a penetrating nerve array. *J. Assoc. Res. Otolaryngol.* 8, 258–279.

Miesenbock, G. (2011). Optogenetic control of cells and circuits. *Annu. Rev. Cell Dev. Biol.* 27, 731–758.

Neuheiser, A., Lenarz, M., Reuter, G., Calixto, R., Nolte, I., Lenarz, T., and Lim, H. H. (2010). Effects of pulse phase duration and location of stimulation within the inferior colliculus on auditory cortical evoked potentials in a guinea pig model. *J. Assoc. Res. Otolaryngol.* 11, 689–708.

Oliver, D. L. (2005). "Neuronal organization in the inferior colliculus," in *The Inferior Colliculus,* eds J. A. Winer and C. E. Schreiner (New York, NY: Springer Science+Business Media, Inc.), 69–114.

Ramachandran, R., Davis, K. A., and May, B. J. (1999). Single-unit responses in the inferior colliculus of decerebrate cats. I. Classification based on frequency response maps. *J. Neurophysiol.* 82, 152–163.

Schreiner, C. E., and Langner, G. (1997). Laminar fine structure of frequency organization in auditory midbrain. *Nature* 388, 383–386.

Seshagiri, C. V., and Delgutte, B. (2007). Response properties of neighboring neurons in the auditory midbrain for pure-tone stimulation: a tetrode study. *J. Neurophysiol.* 98, 2058–2073.

Stevenson, I. H., and Kording, K. P. (2011). How advances in neural recording affect data analysis. *Nat. Neurosci.* 14, 139–142.

Sutton, B. P., Ouyang, C., Karampinos, D. C., and Miller, G. A. (2009). Current trends and challenges in MRI acquisitions to investigate brain function. *Int. J. Psychophysiol.* 73, 33–42.

Tierney, T. S., Sankar, T., and Lozano, A. M. (2011). Deep brain stimulation emerging indications. *Prog. Brain Res.* 194, 83–95.

Van Essen, D. C., Ugurbil, K., Auerbach, E., Barch, D., Behrens, T. E., Bucholz, R., Chang, A., Chen, L., Corbetta, M., Curtiss, S. W., Della Penna, S., Feinberg, D., Glasser, M. F., Harel, N., Heath, A. C., Larson-Prior, L., Marcus, D., Michalareas, G., Moeller, S., Oostenveld, R., Petersen, S. E., Prior, F., Schlaggar, B. L., Smith, S. M., Snyder, A. Z., Xu, J., and Yacoub, E. (2012). The Human Connectome Project: a data acquisition perspective. *Neuroimage*. doi: 10.1016/j.neuroimage.2012.02.018. [Epub ahaed of print].

Yacoub, E., Harel, N., and Ugurbil, K. (2008). High-field fMRI unveils orientation columns in humans. *Proc. Natl. Acad. Sci. U.S.A.* 105, 10607–10612.

Zhou, D. D., and Greenbaum, E. (eds.). (2009). *Implantable Neural Prostheses 1: Devices and Applications.* New York, NY: Springer Science+Business Media, LLC.

Zrinzo, L., Yoshida, F., Hariz, M. I., Thornton, J., Foltynie, T., Yousry, T. A., and Limousin, P. (2011). Clinical safety of brain magnetic resonance imaging with implanted deep brain stimulation hardware: large case series and review of the literature. *World Neurosurg.* 76, 164–172; discussion 169–173.

Conflict of Interest Statement: The authors declare that the research was conducted in the absence of any commercial or financial relationships that could be construed as a potential conflict of interest.

Received: 06 April 2012; accepted: 08 June 2012; published online: 27 June 2012.

Citation: Markovitz CD, Tang TT, Edge DP and Lim HH (2012) Three-dimensional brain reconstruction of in vivo electrode tracks for neuroscience and neural prosthetic applications. Front. Neural Circuits ***6****:39. doi: 10.3389/fncir.2012.00039*

frontiers in
NEURAL CIRCUITS

ORIGINAL RESEARCH ARTICLE
published: 02 November 2012
doi: 10.3389/fncir.2012.00077

A computational model of inferior colliculus responses to amplitude modulated sounds in young and aged rats

Cal F. Rabang[1†], Aravindakshan Parthasarathy[2†], Yamini Venkataraman[1], Zachery L. Fisher[2], Stephanie M. Gardner[2] and Edward L. Bartlett[1,2]*

[1] Weldon School of Biomedical Engineering, Purdue University, West Lafayette, IN, USA
[2] Department of Biological Sciences, Purdue University, West Lafayette, IN, USA

Edited by:
Eric D. Young, Johns Hopkins University, USA

Reviewed by:
Paul B. Manis, University of North Carolina at Chapel Hill, USA
Donal G. Sinex, Utah State University, USA
Gerard Borst, Erasmus MC, Netherlands

***Correspondence:**
Edward L. Bartlett, Weldon School of Biomedical Engineering, 206 South Martin Jischke Drive, West Lafayette, IN 47906, USA.
e-mail: ebartle@purdue.edu

† Cal F. Rabang and Aravindakshan Parthasarathy have contributed equally to this work.

The inferior colliculus (IC) receives ascending excitatory and inhibitory inputs from multiple sources, but how these auditory inputs converge to generate IC spike patterns is poorly understood. Simulating patterns of *in vivo* spike train data from cellular and synaptic models creates a powerful framework to identify factors that contribute to changes in IC responses, such as those resulting in age-related loss of temporal processing. A conductance-based single neuron IC model was constructed, and its responses were compared to those observed during *in vivo* IC recordings in rats. IC spike patterns were evoked using amplitude-modulated tone or noise carriers at 20–40 dB above threshold and were classified as low-pass, band-pass, band-reject, all-pass, or complex based on their rate modulation transfer function tuning shape. Their temporal modulation transfer functions were also measured. These spike patterns provided experimental measures of rate, vector strength, and firing pattern for comparison with model outputs. Patterns of excitatory and inhibitory synaptic convergence to IC neurons were based on anatomical studies and generalized input tuning for modulation frequency. Responses of modeled ascending inputs were derived from experimental data from previous studies. Adapting and sustained IC intrinsic models were created, with adaptation created via calcium-activated potassium currents. Short-term synaptic plasticity was incorporated into the model in the form of synaptic depression, which was shown to have a substantial effect on the magnitude and time course of the IC response. The most commonly observed IC response sub-types were recreated and enabled dissociation of inherited response properties from those that were generated in IC. Furthermore, the model was used to make predictions about the consequences of reduction in inhibition for age-related loss of temporal processing due to a reduction in GABA seen anatomically with age.

Keywords: aging, neuron, inhibition, amplitude modulation, auditory, GABA, lateral lemniscus, superior olive

INTRODUCTION

The inferior colliculus (IC) is a major integrative center of auditory processing, receiving multiple ascending excitatory inputs from the contralateral ventral and dorsal cochlear nuclei (VCN and DCN, respectively) and from the contralateral lateral and medial superior olive (LSO and MSO) to form different functional zones within the IC (reviewed in Kelly and Caspary, 2005). These excitatory input patterns are superimposed upon similar functional zones formed by the inhibitory dorsal and ventral nuclei of the lateral lemniscus (DNLL and VNLL), as well as the superior olivary nucleus (Cant and Benson, 2006; Loftus et al., 2010). In addition, there are excitatory inputs from the contralateral IC, a network of inhibitory interneurons within the IC, local excitatory collaterals, and descending projections from auditory cortex (Oliver et al., 1991; Paloff et al., 1992; Coomes Peterson and Schofield, 2007). Excitatory projections are glutamatergic, acting on AMPA and NMDA receptors in the IC neurons (Adams and Wenthold, 1979; Wu et al., 2004). Inhibitory projections are primarily GABAergic, with a few glycinergic inputs (Caspary et al., 1990b; Winer et al., 1995; Helfert et al., 1999). This complex interplay of excitatory and inhibitory projections from various nuclei of the auditory pathway makes the IC an important nucleus for understanding how neural representations are transformed as they ascend the auditory pathway.

Age-related central auditory changes in auditory processing primarily manifest as deficits in temporal processing. This has been observed psychophysically in humans, where older listeners perform significantly worse than younger listeners in gap detection tasks (Schneider et al., 1994) or in word recognition tasks (Frisina and Frisina, 1997; Strouse et al., 1998) even when they have comparable hearing thresholds. These deficits are exacerbated in the presence of competing sounds or in the presence of background noise (Frisina and Frisina, 1997). We have previously demonstrated age-related deficits in temporal processing using envelope following responses in Fischer-344 rats. The strength of phase locking to the amplitude modulation showed age-related deficits primarily for faster modulation frequencies (Parthasarathy and Bartlett, 2012), under reduced modulation depth (Parthasarathy and Bartlett, 2011) or in the presence of background noise (Parthasarathy et al., 2010). At the level of the

single neuron, this has been observed in the cochlear nuclei (Schatteman et al., 2008) as well as the IC. One study in IC showed that aged animals had fewer units with rate coding for higher modulation frequencies compared to young animals, which had rate best modulation frequencies (rBMFs) >100 Hz and an increase in overall spike counts at low modulation frequencies (Walton et al., 2002). Other studies have also shown a shift in rate coding from band-pass to low-pass in aged animals (Palombi et al., 2001), as well as a increased in minimum gap thresholds for gap detection stimuli (Walton et al., 1998).

Inferior colliculus neurons represent sinusoidal amplitude-modulated tones (sAM) or noise (nAM) with action potentials synchronized to the stimulus modulation envelope. The IC is the first nucleus in the auditory pathway where rate coding becomes prominent and prevalent, with many neurons exhibiting band-pass (BP) coding (firing rate maximum tuned to a modulation frequency), band-reject (BR) coding (firing rate minimum tuned to a modulation frequency) or low-pass coding in discharge rate in addition to their temporally synchronized responses (Rees and Moller, 1987; Langner and Schreiner, 1988; Krishna and Semple, 2000). The neural mechanisms by which rate tuning for AM frequency emerge in IC remain unresolved. One approach to understanding the basis for IC responses is through computational models that incorporate synaptic and intrinsic properties measured *in vitro* to investigate how these mechanisms help generate auditory responses recorded *in vivo*. Previous IC models adjusted existing neuron models of cochlear nuclei to match physiological characteristics (Cai et al., 1998a,b) or were phenomenological models intended to explain experimental observations (Hewitt and Meddis, 1994; Nelson and Carney, 2004; Guerin et al., 2006). Although they did provide insight into potential input schemes for generating rate coded IC neurons, these models did not take into account IC-specific cellular properties, synaptic mechanisms, or short-term synaptic plasticity. A computational model of the IC which incorporates these elements and which can be validated against neuronal responses from the IC would help provide a better understanding of the neural mechanisms of temporal processing in the IC. This model can then be used to predict synaptic mechanisms that can replicate altered neural encoding of sound stimuli in aging.

In this study we have created single compartment models of IC neurons that use input trains derived from data recorded from LSO, DNLL, VNLL, DCN, and VCN from previous studies. We have also recorded single unit responses of IC neurons to AM stimuli from young and aged animals. Together, the input, synaptic and intrinsic properties of the models were able to reproduce the most common response types of the IC to these AM stimuli. Using these IC neuron models as a template, we have then attempted to change these input and synaptic properties, especially those pertaining to synaptic inhibition, to simulate the responses of the aged animals as observed in our study as well as from previous other studies.

MATERIALS AND METHODS

SINGLE UNIT RECORDINGS

Surgical procedures

Five young (4–6 months) and 4 aged (22–24 months) Fischer-344 rats were used in this study. All surgical protocols used were approved by the Purdue University animal care and use committee (PACUC 06-106). Auditory brainstem responses and frequency following responses were recorded from these animals a few days prior to surgery, to ensure all animals had hearing thresholds typical for their age and there were no signs of any other abnormal auditory pathologies. Surgeries and recordings were performed in a $9' \times 9'$ double walled acoustic chamber (Industrial Acoustics Corporation). Anesthesia was induced in the animals using a mixture of ketamine (VetaKet, 80 mg/kg for the young, 60 mg/kg for the aged) and medetomidine (Dexdomitor, 0.2 mg/kg for the young, and 0.1 mg/kg for the aged) administered intra-muscularly via injection. The reduced concentration of anesthesia for the aged was to account for their decreased liver function. The animals were maintained on oxygen through a manifold. The pulse rate and oxygen saturation were maintained using a pulse-oximeter to ensure they were within normal ranges. Supplementary doses of the anesthesia (20 mg/kg of ketamine, 0.05 mg/kg of medetomidine) were administered intra-muscularly as required to maintain areflexia and a surgical plane of anesthesia. An initial dose of dexamethasone and atropine was administered to reduce swelling and mucosal secretions. A constant physiological body temperature was maintained using a water-circulated heating pad (Gaymar) set at 37°C with the pump placed outside the recording chamber to eliminate audio and electrical interferences. A central incision was made along the midline, and the calvaria exposed. A stainless steel headpost was secured anterior to bregma using three screws drilled into the skull and a head-cap constructed of orthodontic resin (Dentsply). A craniotomy was performed posterior to the lambda suture and 1 mm lateral from the midline. The dura mater was kept intact, and the site of recording was estimated stereotaxically using a rat atlas (Paxinos and Watson, 2006) as well as using internal vasculature landmarks and physiological measurements.

Stimulus description and recording procedures

Sound stimuli were generated using SigGenRP (Tucker-Davis Technologies, TDT) at a 97.64 kHz sampling rate (standard TDT sampling rate) and presented through custom-written interfaces in OpenEx software (TDT) in a random order for each repetition. Sound waveforms were generated via a multichannel processor (RX6, TDT), amplified (SA1, TDT), and presented free-field through a Bowers and Wilkins DM601 speaker. The sounds were presented to the animal at azimuth 0° and elevation 0°, calibrated at a distance of 115 cm from speaker to ear, using a Bruel and Kjaer microphone and SigCal software (TDT). All stimuli used had a 5 ms cosine squared gate at onset and offset. Search stimuli used were 200 ms long BP filtered noise with center frequencies from 1 to 36 kHz in five steps per octave with a 0.5 octave bandwidth. The stimuli for the tuning curve were 200 ms long pure tones with frequencies from 500 to 40 kHz, with 10 steps per octave. Filtered noise and tuning curve stimuli were presented every 800 ms. The rate-level stimuli consisted of 100 or 200 ms long pure tones set at the center frequency (CF) of the neuron presented at varying sound levels from 5 to 85 dB SPL in 10 dB steps. Sinusoidally amplitude-modulated noise (nAM) and tone (sAM) stimuli were 750 ms long, with modulation frequency ranging from 8 to 1024 Hz in one octave steps. The nAM stimuli used broadband Gaussian noise as the carrier (0.1–44 kHz),

while the carrier frequency of the sAM stimuli were set to the CF of the neuron that was isolated. AM stimuli were presented every 2000–2500 ms and were 100% modulated.

Single unit activity and multiunit activity in the IC were recorded using a tungsten electrode (A-M Systems) encased in a glass capillary that was advanced using a hydraulic micro-drive (Narishige). The IC was identified based on short-latency driven responses to the 1/2 octave band-passed noise search stimuli. The central nucleus of the IC was identified using the ascending tonotopy, as well as narrowly tuned responses to pure tones of various frequencies. Once an auditory neuron was isolated using the search stimuli, a tuning curve was obtained to determine the CF of the neuron. Responses of the neuron to 5–10 repetitions of each sound stimulus were recorded (usually five repetitions for the tuning curve and 10 for other stimuli). Once the CF was determined, the responses of the neuron were obtained to nAM stimuli or sAM stimuli with the carrier frequency set at CF. The sound level of presentation for the sAM and nAM stimuli were set at the lowest sound level that produced a robust sustained response to the tone set at CF. This usually was 20–40 dB above threshold and corresponded to about 60–70 dB SPL for the young and 75–85 dB for the aged, comparable to the sound levels used in our previous studies of the envelope following responses in young and aged animals (Parthasarathy et al., 2010; Parthasarathy and Bartlett, 2011, 2012).

Stimulus generation, data acquisition, and recording

Neural signals were acquired using the tungsten electrode connected to a headstage (RA4, TDT) and amplified (RA4PA preamplifier, TDT). The digitized waveforms and spike times were recorded with a multichannel recording and stimulation system (RZ-5, TDT) at a sampling rate of 24.41 kHz (standard TDT sampling rate). The interface for acquisition and spike sorting were custom made using the OpenEx and RPvdsEx software (TDT). The single units acquired were filtered between 300 and 5000 Hz. Single units that were substantially above noise threshold were sorted visually online and then subsequently identified and isolated offline using the OpenEx interface based on waveform similarity. Typically the isolated single units had a signal-to-noise ratio of at least 6 dB. The acquired spikes were stored in data tank and analyzed using custom-written software in MATLAB. Offline sorting of the spike waveforms was performed in OpenExplorer (TDT) if necessary to isolate consistent single units from random background activity.

Data analysis and response type classification

Spontaneous rate was calculated as the mean rate of the 200 ms period that preceded each trial of the stimulus presentation. An auditory driven neuron was defined as a neuron that exhibited an overall firing rate that was at least two standard deviations (SD) higher than the spontaneous firing rate during the presentation of the search stimulus. Only neurons that produced a significant sound-evoked increase in firing rate were included in the analysis. The best frequency (BF) of a neuron was defined as the pure tone frequency that generated the highest firing rate in the recorded neuron. Best level was defined as the sound level that produced the highest firing rate at BF while threshold was defined as the lowest sound level that produced a firing rate which was at least 2 SD above the spontaneous firing rate. The ability of a neuron to synchronize was calculated using the vector strength (vs) of the response at each modulation frequency $VS = (1/n) * \sqrt{\left(\left(\sum \cos\varphi_i\right)^2 + \left(\sum \sin\varphi_i\right)^2\right)}$, where $n =$ total number of observed spikes, $\varphi_i =$ phase of observed spike relative to modulation frequency. Statistical significance was assessed using the Rayleigh statistic, to account for differences in the number of driven spikes between neurons, with a Rayleigh statistic value of greater than 13.8 considered to be statistically significant ($p < 0.001$; Mardia and Jupp, 2000).

Neurons were classified as either rate coded, synchronized, or both, depending on changes in firing rate as well as synchrony at different modulation frequencies. Based on rate, the modulation transfer function (rMTF) of a neuron was classified as low-pass (LP), band-pass (BP), all-pass (AP), band-reject (BR) or complex responses. For each neuron, a normalized firing rate was calculated across all the modulation frequencies tested, with the rate at the best modulation frequency (rBMF) denoted as 1, and rates at all other modulation frequencies scaled accordingly. This allowed the comparison of overall shapes of the rMTFs of various neurons with different absolute firing rates. A neuron was classified as BP if the normalized rate dropped below 75% on both sides of the maximum, as LP is the normalized rate dropped below 75% on the high side alone, AP if the normalized rate did not drop below 75% on either side of the maximum and as BR if the normalized rate fell below 66% for a range of modulation frequencies but recovered back up to above 75% on either side. All other neurons were classified as complex responses. The neurons recorded were also divided into synchronous (neurons that represented change in modulation frequency with changes in significant vs) and rate coded (neurons that represented change in modulation frequency with changes in firing rate), with the synchronous neurons classified into low-pass or band-pass based on their temporal modulation transfer function (tMTF) as measured by vector strength (vs) for the synchronous units. In addition, for the synchronous units, a temporal best modulation frequency (tBMF) was calculated as the modulation frequency that produced the greatest vs, and an F_{max} was calculated as the highest modulation frequency that synchronized with a Rayleigh statistic greater than 13.8.

SINGLE COMPARTMENT IC MODEL

Intrinsic properties

Two separate neuron models were developed based on intrinsic properties described in previous intracellular studies (Sivaramakrishnan and Oliver, 2001; Koch and Grothe, 2003; Wu et al., 2004; Tan et al., 2007), and these basic models were modified to produce other observed firing patterns for current injection. The sustained model consisted of a fast transient Na^+ current (I_{Na}), a delayed rectifier potassium current (I_{kDr}), a high-threshold potassium current (I_{kHT}), and a TEA-sensitive potassium current (I_{kTEA}). The adapting model consisted of a fast transient Na^+ current (I_{Na}), a delayed rectifier potassium current (I_{kDr}), a TEA-sensitive potassium current (I_{kTEA}), a low-threshold Ca2+ current (I_T), a high-threshold Ca2+ current (I_L), an apamin-sensitive calcium-activated potassium current (I_{Sk}), an apamin-insensitive, large conductance Ca^{2+} dependent potassium channel (I_{Bk}), and a

hyperpolarization-activated cation current (I_h). Both models also included synaptic currents (I_{syn}), an injected current (I_{inj}), and a leak current (I_{leak}). Model equations and constants are given in the Appendix.

The leak conductances for each model were adjusted so that their resting membrane potentials were approximately −70 mV. Subsequent small adjustments to membrane potential were done through constant injected current applied throughout the simulation run, at least 200 ms prior to synaptic stimulation, ensuring the membrane potential reaches steady state as noted and placing the membrane potential in the range found *in vivo* (Tan et al., 2007; Geis and Borst, 2009).

Synaptic inputs

The inputs to the IC model represented realistic *in vivo* responses from cochlear nucleus (Joris and Yin, 1998; Schatteman et al., 2008), superior olivary complex (Grothe et al., 1997; Joris and Yin, 1998), and lateral lemniscus (Yang and Pollak, 1997; Zhang and Kelly, 2006) to sAM stimuli.

Each individual input to the model IC neuron was modeled as a series of spike times. For a given input, each individual afferent spike train was created based on spike probabilities calculated from rate and temporal MTFs from responses to sAM stimuli in the ascending input sources listed above. The statistical model used to generate these inputs is given in the Appendix. Each trial for a given IC input train had a unique set of generated spike times. To use numbers of trials similar to that collected during typical *in vivo* recordings, 10 trials of a given stimulus were typically used to generate model responses using a given set of parameters. Modulation frequencies ranged from 8 to 1024 Hz in octave steps, similar to the *in vivo* recordings.

The generated input spike times were used to generate the synaptic currents in a method similar to a previous modeling study (Rabang and Bartlett, 2011). Each input spike time would trigger a synaptic event that produces a measured increase in synaptic conductance. The amplitude and time constants used to produce the synaptic events were adjusted to fit amplitude, rise and decay characteristics using data reported from *in vitro* studies of IC synaptic currents and given in the Appendix (Wu et al., 2004). Excitatory inputs consisted of an AMPA and NMDA component and inhibitory inputs consisted of a $GABA_A$ current. Synaptic depression of the AMPA and $GABA_A$ current was modeled via an interval-dependent amplitude scale factor of the resulting excitatory and inhibitory conductances, which were based on previous intracellular IC studies in rats (Wu et al., 2004; Sivaramakrishnan and Oliver, 2006).

The synaptic input characteristics, input spike times, and synaptic conductance values were written, generated and run through MATLAB (Mathworks, Inc.). Using these parameters, the adapting and sustained IC neuron model simulations were performed in the NEURON simulation environment (Hines and Carnevale, 2001). Analysis was done in MATLAB. All computation and analysis were performed on DELL workstations using the MS Windows 7 operating system. The simulation trials used an integration time step value $dt = 0.02$ ms. This value was empirically verified to be sufficient to simulate accurate ion channel and synaptic currents.

User-defined inputs

In addition to using physiologically derived rate and temporal characteristics to generate realistic synaptic inputs, we generated synaptic inputs that were shaped by user-defined input rate and temporal MTFs. We used these user-defined inputs to highlight transformation of input to output responses via the IC models. Excitatory inputs were based on normalized rate curves that were BP, AP, or LP. The tMTF of these inputs were similar to the LSO inputs (**Figure 3**). User-defined inhibitory inputs were either AP rate with DNLL LP tMTF characteristics, or BP rates generated with user-defined rBMF. Example user-defined shape input MTFs and model responses are shown and used in **Figure 3**.

Model data analysis

Unless otherwise noted, spike counts and firing rates were computed from the entire stimulus duration. Synchrony of the model response was analyzed similarly to the single unit recordings using vs and Rayleigh statistic. The time window for Rayleigh computation was 50 ms following stimulus onset through the duration of the 750 ms stimulus. Output responses were designated as onset or sustained, and either LP, AP, high-pass, BP, or BR by similar criteria used for experimental recordings.

IMMUNOHISTOCHEMISTRY

The ICs of four young (9–12 weeks) and four aged (92–95 weeks) Fischer-344 rats were processed for immunohistochemistry. Animals were euthanized with Beuthanasia (200 mg/kg). Once areflexive, they were perfused transcardially with 150–200 mL phosphate buffered saline with 0.1% heparin followed by 400–500 mL 4% paraformaldehyde. The brains were removed and stored overnight in 4% paraformaldehyde, after which they were transferred to 30% sucrose for cryoprotection and frozen. Thirty or 35 μm free-floating sections were obtained using a Shandon FE cryotome (Thermo-Electron). Free-floating sections were processed for immuno-histochemical labeling of GAD 65/67 and VGluT2. Rabbit anti –GAD 65/67 (1:1000, Millipore) was used as the primary antibody for GAD 65/67. Guinea pig anti-VGluT2 (1:500, Millipore) was used as the primary antibody for VGluT2. The specificities of these antibodies have been verified in previous studies (Belenky et al., 2008; Cooper and Gillespie, 2011). Biotinylated secondary antibodies (1:200, Vector Laboratories) were used for both. Tissue was then processed using the Vectastain ABC kit (Vector Laboratories), and antibody localization was visualized by DAB (diaminobenzidine). Sections were mounted onto Superfrost Plus slides, dehydrated, and cover slipped using Permount (Fisher). For two sets of the animals (one young and one aged animal being a set), the tissue was processed on the same day with the same reagents. All tissue was stained using aliquots from the same original vial of antibody. For every round of staining, two negative controls were used to verify the specificity of the signal from the oxidized DAB precipitate: (1) no primary antibody and (2) no secondary antibody.

Image analysis

ImageJ software (NIH) was used to analyze four random, 1600 μm^2 regions of interest (ROI's) from within the IC central nucleus of each selected section at 40× using a Zeiss AxioObserver.Z1. Pixel intensity values were normalized against unstained

cells to obtain the relative optical density (ROD). Unstained cells were characterized as such because their average pixel intensities were within one SD of the average pixel intensity values of the deep cortical white matter in the same section. Eight to ten sections per animal were analyzed, so the ROD for each animal was based on the average ROD of 32–40 ROIs. For illustrative purposes, ROD was shown as 1-ROD in figures so that high values correspond to dark pixel intensities.

RESULTS

RESPONSES OF NEURONS IN THE IC OF YOUNG ANIMALS TO AM STIMULI

Responses from 92 auditory neurons were recorded from the IC of four young animals. Of these, 37 (40%) neurons had non-synchronized, purely onset responses to AM stimuli that were not modulated by modulation frequency, and were discarded for the purposes of this study. These neurons were often encountered early in a dorso-ventral oriented track and were likely to be located in dorsal or external cortex of IC. The remaining neurons all responded to varying modulation frequencies either by change in rate or synchrony. Of these, the percentages of neurons exhibiting BP and LP rMTFs were 24% ($n = 13$) and 36% ($n = 20$), respectively. Forty percentage of the neurons not classified as either BP or LP rMTFs were distributed equally into AP ($n = 11$) and BR ($n = 11$) rMTFs with a few neurons ($n = 4$) showing complex rate tuning (see Materials and Methods for definitions). A small number ($n = 3$) of the neurons exhibited sustained discharges but were not synchronized to any modulation frequency and represented changes in modulation frequency purely by changes in rate. These neurons were not used in for the analysis of synchrony. Of the synchronized neurons, almost equal numbers exhibited LP (56%, $n = 31$) and BP (44%, $n = 24$) behavior in their tMTFs.

SINGLE COMPARTMENT IC MODEL – MEMBRANE AND SYNAPTIC PROPERTIES

Two basic single compartment models were created to simulate sustained and adapting firing patterns in IC (**Figures 1A,B**), which are the two most commonly observed firing patterns in response to current injection *in vivo* (Tan et al., 2007) and *in vitro* (Sivaramakrishnan and Oliver, 2001). The Sustained model produced regular firing to depolarizing current injections. The Adapting model produced a higher frequency onset burst followed by sustained spiking with rate adaptation to depolarizing currents. A low-threshold Ca^{2+} dependent current (I_T) produced rebound depolarization following hyperpolarization, and I_h was included for this model because it is commonly found in adapting neurons (Tan et al., 2007). **Figures 1A,B** shows the model responses to depolarizing and hyperpolarizing current pulses for Sustained and Adapting models, respectively. Each model had a resting membrane potential of −70 mV; a bias current was applied during each simulation to adjust membrane potential to between −64 and −56 mV, which accounts for mean depolarization provided by ongoing synaptic activity. This is within range of typical values recorded from IC neurons *in vivo* (Tan et al., 2007; Geis and Borst, 2009). The Sustained and Adapting model had calculated membrane resistances of 146 and 142 MΩ and a time constant of 4.4 and 5 ms, respectively, in line with previous measurements (Tan et al., 2007).

The basic Sustained and Adapting models were then elaborated to create Pause-Build (**Figure 1C**), Rebound-Sustained (**Figure 1D**), or Rebound-Transient (**Figure 1E**) models corresponding to response classes reported in previous studies (Sivaramakrishnan and Oliver, 2001; Tan et al., 2007). For the Pause-Build model, a rapidly inactivating potassium conductance was added, along with a small I_h current, while the high-threshold potassium conductance was removed and the low-threshold potassium and leak conductances were lowered (Appendix). While this did not affect responses to depolarizing current pulses, the presence of the A-type potassium conductance produced a delayed onset to firing when a depolarizing current followed hyperpolarization that deinactivated the potassium conductance (**Figure 1C**). The Rebound-Sustained model is the Sustained model with the presence of a T-type calcium conductance (**Figure 1D**), which affected responses mainly when hyperpolarized by inhibition or neuromodulators. To obtain the Rebound-Transient response, the Adapting model was adjusted by increasing the L-type calcium conductance and reversing the relative strengths of the SK and BK calcium-activated potassium conductances. In addition to producing transient burst responses (**Figure 1E**), these adjustments also produced depolarizing afterpotentials (not shown), as reported in Sivaramakrishnan and Oliver (2001). Onset responses to current injection have been reported as a small proportion of responses (Sivaramakrishnan and Oliver, 2001; Bal et al., 2002) or absent (Tan et al., 2007) in previous studies. The Onset model was configured differently than the Sustained or Adapting models. The Onset model contained a transient sodium, potassium delayed rectifier, low-threshold potassium (Rothman and Manis, 2003), and a hyperpolarization-activated cation current (Koch and Grothe, 2003). The conductances for each were adjusted to fit firing patterns to depolarizing current pulses (Sivaramakrishnan and Oliver, 2001). Onset model responses produced a single spike for depolarizing current pulses (**Figure 1F**). Because the Adapting and Sustained responses comprised the majority of IC responses, these have been used for the remainder of the results, leaving exploration of the interaction between subtype membrane and synaptic properties for future study. Adapting and Sustained model responses to identical stimuli typically produced similarly shaped rMTFs, although Sustained model responses exhibited higher rates overall at the same membrane potential. This is likely due to the larger membrane resistance in the Sustained model and the addition of potassium currents in the Adapting model. As a result, Sustained model responses often had lower vs values due to a larger number of action potentials observed within a given period and greater sensitivity to small membrane potential fluctuations. As the name implies, there was a gradual decline in firing rate for sustained synaptic stimulation in the Adapting model but not in the Sustained model.

Excitatory synaptic inputs consisted of AMPA and NMDA receptor components. Inhibitory inputs consisted of a $GABA_A$ receptor component. Both AMPA and $GABA_A$ components exhibited short-term synaptic depression, which was modeled from *in vitro* voltage clamp studies in rat IC (Wu et al., 2004). Example post-synaptic currents with pairs of inputs at 10 and 25 ms ISI are shown for each synaptic current on **Figures 1G–I**.

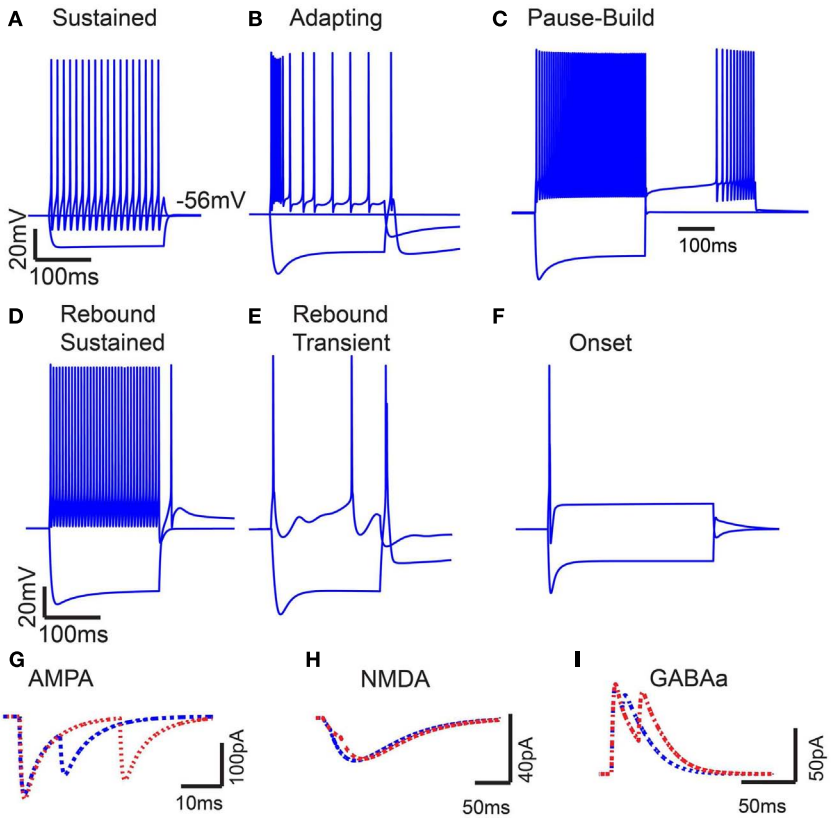

FIGURE 1 | Model intrinsic and synaptic properties. (A) IC Sustained model response to 200 pA depolarizing and hyperpolarizing current pulses. Voltage traces measured in mV (*Y*-axis) plotted versus time in ms (*X*-axis). **(B)** Adapting model response to 300 pA depolarizing and hyperpolarizing current pulses. **(C)** Pause-build responses to a 500 pA depolarizing pulse and a negative 500 pA hyperpolarizing current pulse, followed by a 500 pA depolarizing current pulse. **(D)** Rebound-Sustained response to 500 pA depolarizing and hyperpolarizing current pulses. **(E)** Rebound-Transient response to 400 pA depolarizing and hyperpolarizing current pulses. **(F)** Onset response to 800 pA depolarizing and hyperpolarizing current pulses. *Y*-axis represents voltage traces measured in mV and *X*-axis represents time in ms for **(A–F)**. **(G–I)** Current traces of paired post-synaptic AMPA, NMDA, and $GABA_A$ currents, respectively. *Y*-axis represents synaptic current in nA, and *X*-axis represents time ms. Paired inputs at 10 *(blue)* and 25 *(red)* ms ISI to show time course and magnitude of synaptic depression.

RATE AND TEMPORAL CHARACTERISTICS OF MODEL INPUTS

Three example excitatory input sources were chosen for synaptic input to the IC model; LSO, DCN, and VCN (Cant and Benson, 2006), and were also used as a means to represent different rate tuning shapes of physiological inputs to IC. The input rMTF and tMTFs for each example input are given in **Figures 2A–C**. DCN input rates (Schatteman et al., 2008) increased monotonically but over a relatively small range of rates with increasing modulation frequency. LSO input rates (Joris and Yin, 1998) were LP with peak rates and tMTF cut-off at 64 Hz. VCN input rates (Joris and Yin, 1998) were AP tuned. The tMTF curves for the DCN and LSO inputs were all LP. VCN input synchrony was BP tuned to 128 Hz, simulating the response to suprathreshold intensities (Møller, 1972; Frisina et al., 1990) while the rate tuning was flat for all modulation frequencies. These examples were culled from previous literature, but are not intended to represent the full response distributions of any given afferent to IC. Values for a given class of inputs could be adjusted easily to fit individual examples, if desired.

Two inhibitory input sources were used: DNLL and VNLL (Cant and Benson, 2006). The input rMTF and tMTFs are shown on **Figures 2D,E**. DNLL input rates were either high-pass (**Figure 2D**) or AP tuned, with LP synchrony. VNLL input rates were either BP or high pass with BP synchrony tuned between 64 and 128 Hz (**Figure 2E**). Each MTF was modeled from physiological data (Yang and Pollak, 1997; Zhang and Kelly, 2006).

COMPARISON OF MODEL INPUT AND OUTPUT RATE AND SYNCHRONY

In addition to physiologically derived input characteristics from previous studies, user-defined tuning shape input rates, and temporal MTFs were also produced to highlight the transformation of input to output responses via the IC models. By creating generalized LP, BP, and AP rate tuning shapes, it was easier to isolate transformations in responses generated by IC synaptic and membrane characteristics. User-defined EX inputs were based on normalized rate curves that were BP, AP, or LP. The EX inputs used a LP tMTF similar to the LSO inputs. User-defined IN inputs were either AP rate with DNLL LP tMTF characteristics, or BP rate with user-defined rBMF. Example model responses to EX inputs with corresponding input MTFs are shown in **Figure 3** for an Adapting neuron model. BP EX inputs typically produced similar model

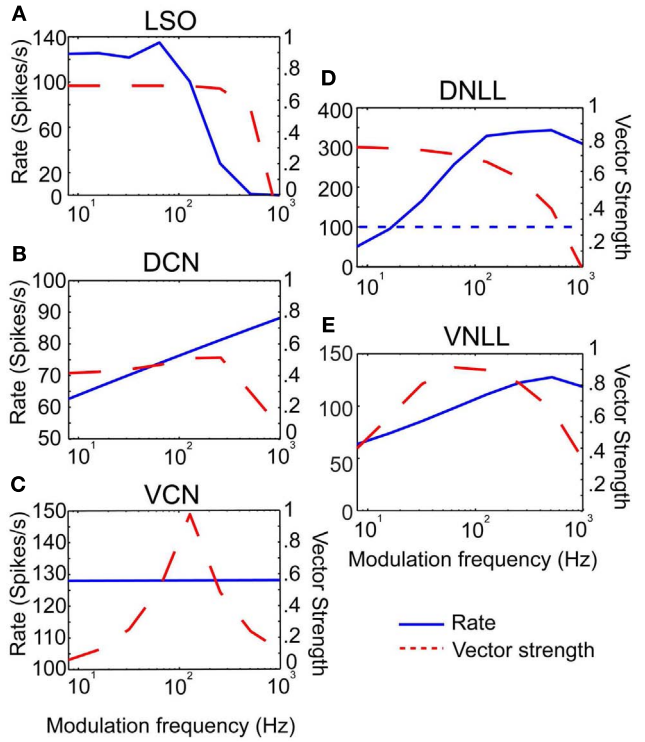

FIGURE 2 | Excitatory and inhibitory model input characteristics. (A–C) Rate in spikes/s *(blue)* and vector strength *(red)* curves characterizing inputs from LSO, DCN, and VCN, respectively. Rate and vector strength are marked on opposing *Y*-axes. Modulation frequency is marked along the *X*-axis in Hz. **(D–E)** Rate and vector strength curves characterizing inhibitory inputs from DNLL and VNLL. DNLL inputs either had all-pass or high-pass rate characteristics, as shown. Axes similar to **(A)**.

output rate responses, while LP and AP inputs produced nearly all LP rate responses. Similar results were observed for the Sustained model.

SIMULATION OF EXAMPLE *IN VIVO* RESPONSE TYPES USING SINGLE COMPARTMENT MODEL

Detailed response characteristics of example neurons are presented below. These were selected to represent neurons from four broad categories of rate coding – BP, LP, BR, and AP. The responses of these neurons with respect to rate and synchrony are described below and the parameters of the model that were modified to produce these specific neuronal types are also described. By changing a few physiologically relevant factors in the model, more than 90% of the neuronal response types encountered in the IC to AM stimuli were reproduced.

Low-pass rate responses

Thirty six percentage of the neurons recorded *in vivo* exhibited LP rMTFs as described in the Section "Materials and Methods." These LP rate responses typically produced rBMFs of 8–16 Hz, with the responses dropping below 75% (F_{max}) at frequencies from 32 to 128 Hz. These neurons also exhibited synchrony in a LP (60%) or BP (40%) manner, with the rBMFs and tBMFs typically differing for both response sub-types. **Figures 4A,C** shows a representative LP rate coded unit, Y27, which exhibited LP rMTF and tMTF for nAM stimuli presented at 65 dB SPL. In this example, the rBMF and the tBMF were both 16 Hz, with a rate of 23.7 spikes/s and vs of 0.85.

Low-pass model responses were most commonly generated with LP or AP excitatory inputs (i.e., LSO, VCN, user-defined EX inputs) coupled with inhibitory high-pass or AP inputs (VNLL, DNLL). Nearly all LP model rate responses produced a LP tMTF. An Adapting model response to AP VCN excitatory and high-pass DNLL inhibitory inputs shows an example of LP rate and synchrony (**Figures 4B,D**).

Band-pass rate tuning

Twenty-four percentage of the neurons encountered in young animals exhibited BP rMTFs. Of these, a majority of the neurons also exhibited BP coding for synchrony. The rBMF and the tBMF were the same for all but one neuron in this category. **Figures 4E,G** shows a representative neuron, Y30, exhibiting BP rate and synchrony coding to nAM stimuli presented at 75 dB SPL. In this example, the neuron exhibited strong onset responses and a few scattered action potentials that changed only minimally at all modulation frequencies except at 16–32 Hz, with a BMF of 32 Hz. At 32 Hz, the neuron strongly phase-locked to the modulation frequency, producing a concurrent increase in rate. The vs at BMF was 0.67, and the peak firing rate was 32.9 spikes/s.

Model BP responses could be generated using excitatory inputs that also were BP tuned (i.e., BP EX inputs, **Figure 3**), LP excitatory inputs coupled with BP inhibitory inputs tuned to lower (<64 Hz) frequencies (**Figure 11**) or LP excitatory inputs and LP inhibitory inputs with equal or higher corner frequency for the excitatory inputs (**Figures 4F,H**, Dicke et al., 2007). Synaptic inhibition is not necessarily required for BP rate tuning. However, preliminary testing suggests that other mechanisms that may produce BP mechanisms from only excitatory inputs (e.g., coincidence detection) are difficult to make compatible with the combination of input firing rates, membrane properties, and time constants, and synaptic properties and time constants. We did produce BP responses using only excitatory inputs. However, these were only produced using a limited set of parameters (**Figure A2** in Appendix). **Figures 4F,H** shows model BP rate and synchrony responses using LP excitatory inputs with LP inhibition with corner frequencies at 32 Hz.

A small number of neurons ($n = 4$) that exhibited BP rate coding also exhibited a LP coding for synchrony. This was reproduced in the model using low-pass LSO excitatory inputs and BP VNLL inputs (not shown).

All-pass, band-reject, and other rate responses

Forty percentage of the neurons encountered did not exhibit BP or LP rate tuning. Of these, half the neurons exhibited AP rate tuning and did not change in rate significantly with changes in modulation frequency, but selectively encoded these changes in modulation frequencies by changes in synchrony and in some cases changes in overall firing pattern. Another 36% of these units exhibited BR responses, where their normalized rates dropped below 67% for a small range of modulation frequencies but were flanked by higher rates for lower and higher modulation

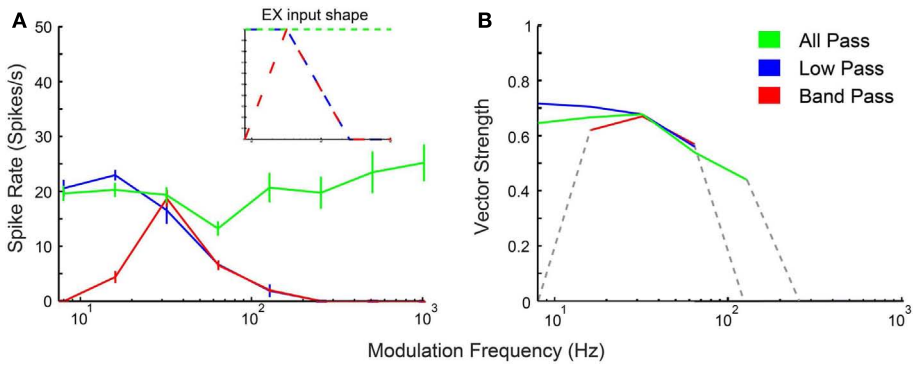

FIGURE 3 | IC model responses to general AM rate tuning of inputs. User-defined all-pass *(green)*, low-pass *(blue)*, and band-pass *(red)* excitatory inputs. Three excitatory inputs with LSO tuned synchrony coupled with two DNLL all-pass inhibitory inputs using the Adapting model. **(A)** Rate response shapes reflect input rate characteristics. Firing rate in spikes/second is marked along the *Y*-axis and modulation frequency in Hz is marked along the *X*-axis. *Inset:* Input rate shape characteristics. **(B)** Vector strength responses to user-defined inputs. Vector strength responses that only show significant synchrony (Rayleigh Stat >13.8, $p < 0.001$) are displayed. Vector strength is marked along the *Y*-axis and modulation frequency in Hz is marked along the *X*-axis.

frequencies. A small number ($n = 4$) also exhibited other rate responses, consisting of high-pass, double-peaked, or complex tuning.

Of these units that exhibited AP, BR or other rate response types, 68% exhibited LP tMTF characteristics and 32% exhibited BP tMTF characteristics. The tBMFs of these units typically ranged from 8 to 64 Hz, and the cut-off frequencies ranged from 16 to 256 Hz.

Figures 5A,C shows a representative neuron, Y34, which exhibited AP rate coding and a LP synchrony coding to sAM stimuli centered at 1.7 kHz presented at 65 dB SPL. The tBMF was 16 Hz with vs of 0.41 and the mean firing rate was 39.3 ± 5.9 spikes/s. AP model responses were generated using excitatory AP (VCN) or high-pass rate responses (DCN) with inhibitory high-pass or AP rate inputs (DNLL). These responses also produced a LP tMTF. An Adapting model response using DCN and DNLL inputs is shown on **Figures 5B,D**.

Figures 5E,G shows a representative neuron, Y22, exhibiting BR rate coding and LP synchrony coding to nAM stimuli presented at 65 dB SPL. In this example, the normalized rate dropped below 67% at 32 and 64 Hz AM, while staying above 75% on either side. The tBMF for this unit was 8 Hz, with vs of 0.50.

Band-reject rate coded model responses were produced using BP inhibitory inputs with VNLL synchrony coding. The BR region of the output response was typically produced at or within an octave range of the BP inhibitory input rBMF. BR rate coded responses were also created using inhibitory inputs that preceded excitatory inputs for a limited set of parameters (**Figure A3** in Appendix). The example in **Figures 5F,H** shows an Adapting model response to AP VCN excitatory inputs with BP VNLL synchrony coded inhibitory inputs with tBMF at 36 Hz.

DETERMINANTS OF OUTPUT tMTF

In vitro studies suggest a moderate number of inputs (1–10) converge on IC neurons (Smith, 1992; Wu et al., 2004). The balance of excitation and inhibition has varied substantially between IC models, ranging from no inhibition (Hewitt and Meddis, 1994) to dominant inhibition (Nelson and Carney, 2004). Using two to five excitatory and inhibitory inputs, with combinations where the number of excitatory and inhibitory inputs were nearly balanced or were dominated by inhibition, produced the best results. In terms of membrane potential fluctuations, we found that smaller numbers of excitatory inputs (2–3) produced more phasic and peaked membrane fluctuations for each stimulus modulation period, whereas larger numbers of excitatory inputs (7–9) generated smoother membrane potential fluctuations that followed the amplitude modulation contour (**Figures 7G–I**, number of inhibitory inputs fixed at five). These membrane potential fluctuations are similar to those described by Geis and Borst (2009). Other studies have also assumed inhibition would lag excitation (∼1 ms; Cai et al., 1998a,b; Borisyuk et al., 2002). However, our model does not show strong qualitative differences in responses to shifts of inhibition timing relative to excitation (±5 ms, data not shown), likely owing to multiple inputs with multiple spikes per cycle at lower modulation frequencies which renders delay less meaningful after the initial response.

One feature of this IC model is the use of short-term synaptic depression measured in previous *in vitro* studies (Wu et al., 2004). We compared a limited set of model responses with and without the presence of synaptic depression in the AMPA and $GABA_A$ receptor mediated currents. A noticeable change in rate was observed as responses without AMPA plasticity increased at nearly all modulation frequencies (**Figure 6A**). There were few qualitative changes in vs or changes in synchrony cut-off (**Figure 6B**), so AMPA plasticity under these conditions made these responses more energetically efficient, meaning that the same features could be represented with far fewer spikes, which are energetically costly (Attwell and Laughlin, 2001). Removing $GABA_A$ plasticity, however, reduced rate responses at all modulation frequencies (**Figure 6A**). In addition, synchrony cut-off was reduced due to low spike output (**Figure 6B**).

The model recovery time constant from synaptic depression was also varied by changing the value of TauR2 for AMPA and TauR for $GABA_A$ synaptic currents (**Table A4** in Appendix). Either increasing or decreasing the depression recovery time by 50%

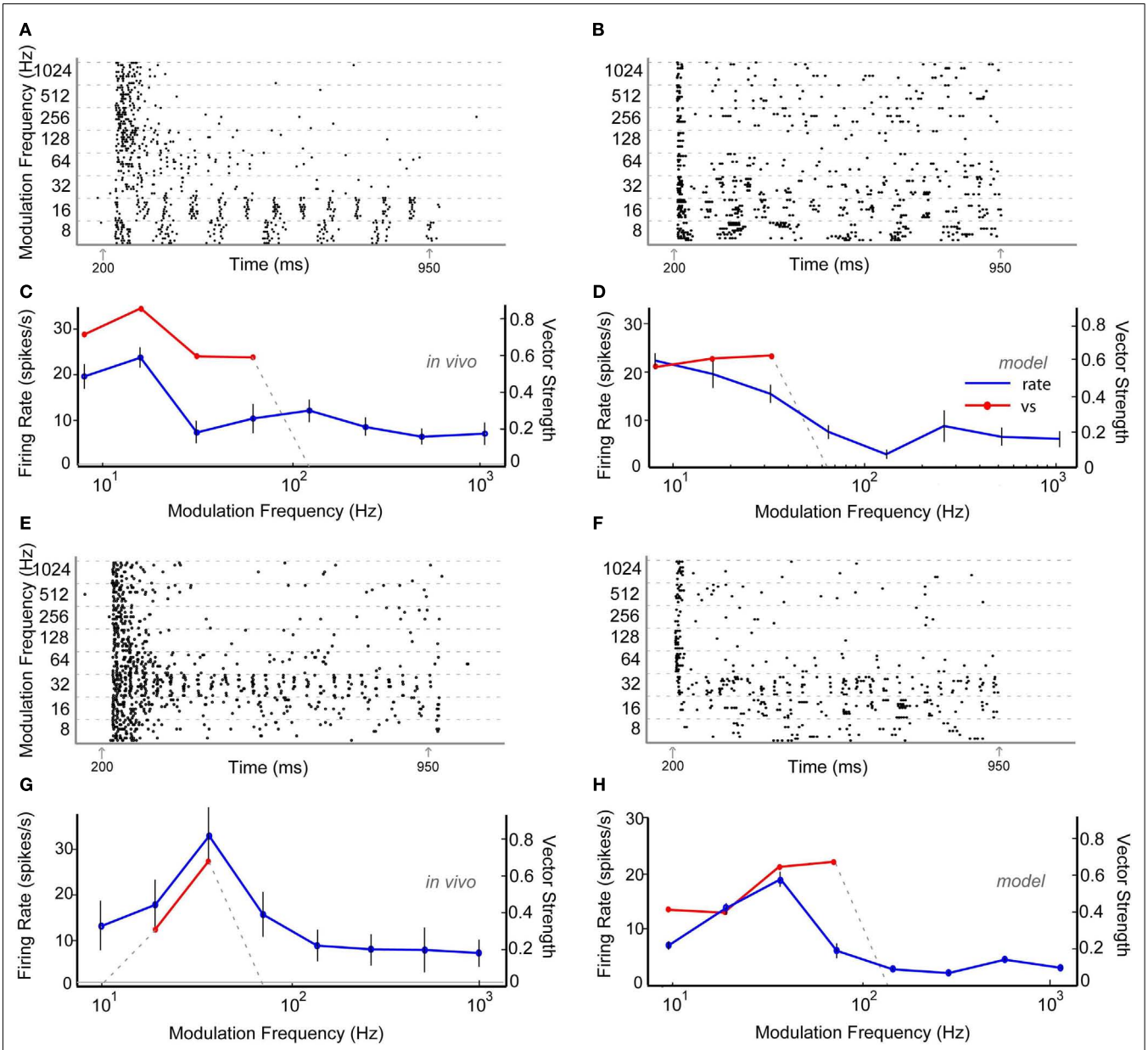

FIGURE 4 | Example *in vivo* and model neurons exhibiting either low-pass rMTF (A–D) or band-pass rMTF (E–H). (A) Dot-raster plot of responses of unit Y27 from the IC of a young animal to nAM stimuli presented at 65 dB SPL. For this example and other raster examples, modulation frequency is marked along the *Y*-axis in Hz and time along the *X*-axis in ms. Each black dot represents a single action potential. Gray arrows indicate beginning and end of sound stimulus. Each modulation frequency shows an aggregation of 10 trials. **(B)** Dot-raster plot of an Adapting model neuron using 2 VCN and 4 high-pass rate tuned DNLL inputs. **(C)** Mean firing rate and vector strength of neuron shown in **(A)** for various modulation frequencies, exhibiting low-pass rMTF and tMTF. Rate in spikes/s *(blue)* and significant vector strength *(red)* are marked on opposing *Y*-axes. Modulation frequency is marked along the *X*-axis in Hz. Horizontal gray line indicates mean spontaneous firing rate. Error bars indicate 1 standard deviation from mean firing rate. **(D)** Adapting IC model neuron using inputs described in **(B)** showing mean firing rate (blue) of 10 trials, and significant vector strength (red). Axes similar to **(C)**. **(E)** Dot-raster plot of responses of unit Y30 from the IC of a young animal to nAM stimuli presented at 75 dB SPL. **(F)** Dot-raster plot of a Sustained model neuron using three user-defined low-pass excitatory inputs with six low-pass inhibitory inputs, each with corner frequencies at 32 Hz. **(G)** Mean firing rate and vector strength of neuron shown in **(E)** for various modulation frequencies, exhibiting band-pass rMTF and tMTF. Axes similar to **(C)**. **(H)** Mean firing rate and vector strength of model neuron described in **(F)** for various modulation frequencies, showing mean firing rate (blue) of 10 trials, and significant vector strength (red). Axes similar to **(G)**.

for either the AMPA or $GABA_A$ plasticity produced similar rate responses at 8 Hz (**Figure 6C**). For higher modulation frequencies, differences were more evident, such as the five-fold difference in firing rates at 32 Hz between 50% GABA recovery tau versus 150% recovery tau. The range of synchrony was decreased when AMPA or $GABA_A$ recovery time was halved, while increasing the

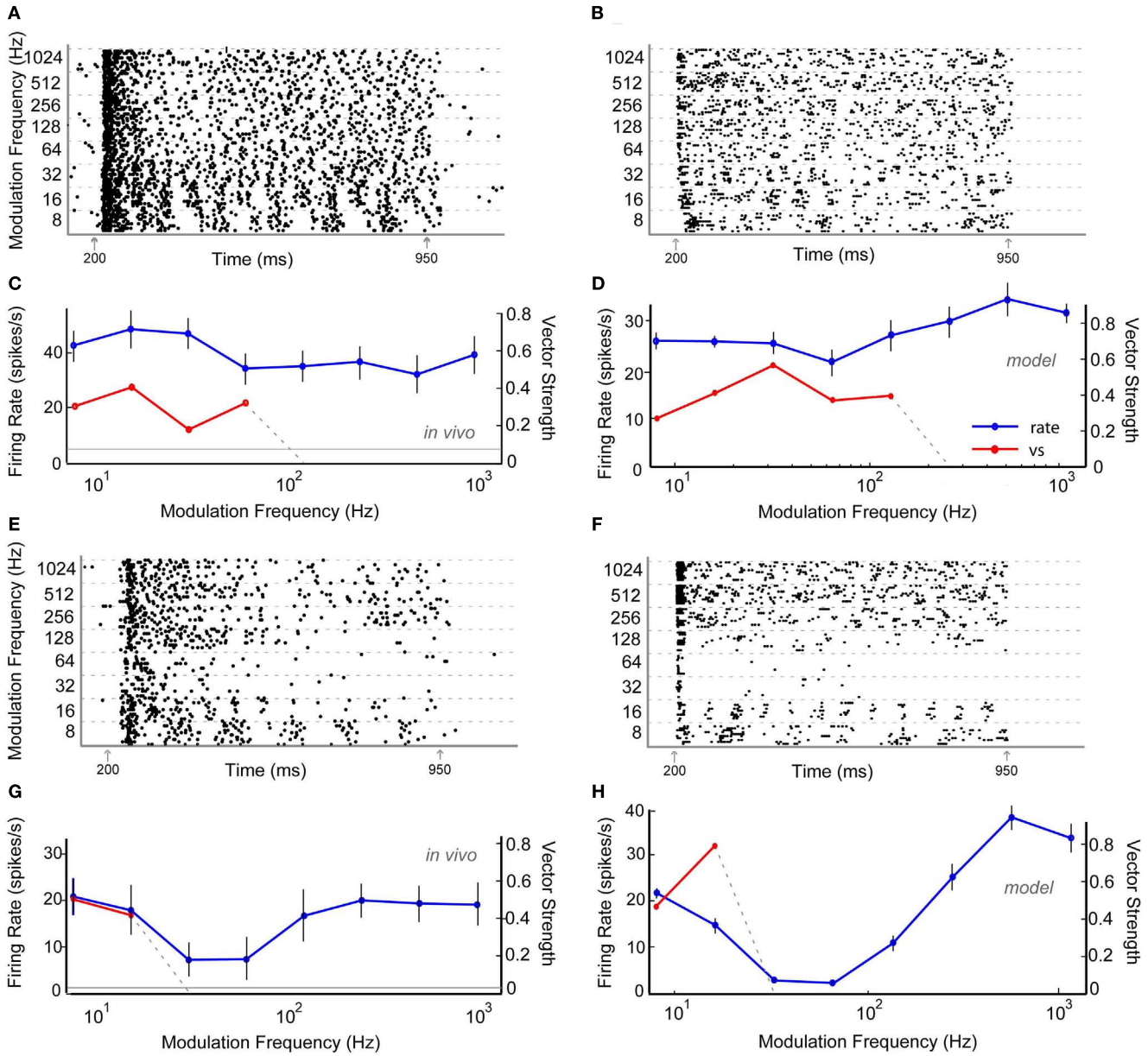

FIGURE 5 | Example *in vivo* and model neurons exhibiting all-pass rMTF and low-pass tMTF (A–D) or band-reject rMTF and low-pass tMTF (E–H). (A) Dot-raster plot of responses of unit Y34 from the IC of a young animal to nAM stimuli presented at 65 dB SPL. **(B)** Dot-raster plot of an Adapting model neuron using three DCN and two all-pass rate tuned DNLL inputs. **(C)** Mean firing rate and vector strength of neuron shown in **(A)** for various modulation frequencies, exhibiting all-pass rMTF and low-pass tMTF. **(D)** Mean firing rate and vector strength of the model neuron described in **(B)**. **(E)** Dot-raster plot of responses of unit Y22 from the IC of a young animal to nAM stimuli presented at 65 dB SPL. **(F)** Dot-raster plot of responses from an Adapting model neuron with 2 VCN and 6 VNLL band-pass rate tuned inputs (rBMF = 36 Hz). **(G)** Mean firing rate and vector strength of neuron shown in **(E)** for various modulation frequencies, exhibiting band-reject rMTF and low-pass tMTF. **(H)** Mean firing rate *(blue)* of 10 trials, and significant vector strength *(red)* of model neuron shown in **(F)**. All axes similar to **Figure 4**.

recovery time for $GABA_A$ increased synchronized response range (**Figure 6D**).

In addition to synaptic depression, other potentially important determinants of IC responses were tested in combination with one another to observe their effects on rMTF, including the conductances of AMPA and $GABA_A$, the $GABA_A$ inhibitory post-synaptic current (IPSC) decay time constant, and the number of excitatory and inhibitory inputs. Each of these parameters can influence the shape of the output rMTF. These values were adjusted in the model, and the output rMTFs were recorded. The summaries of the IC rMTF shapes are shown in **Figure 7**, using the rMTF shape definitions described in the Section "Materials and Methods." 4 VCN

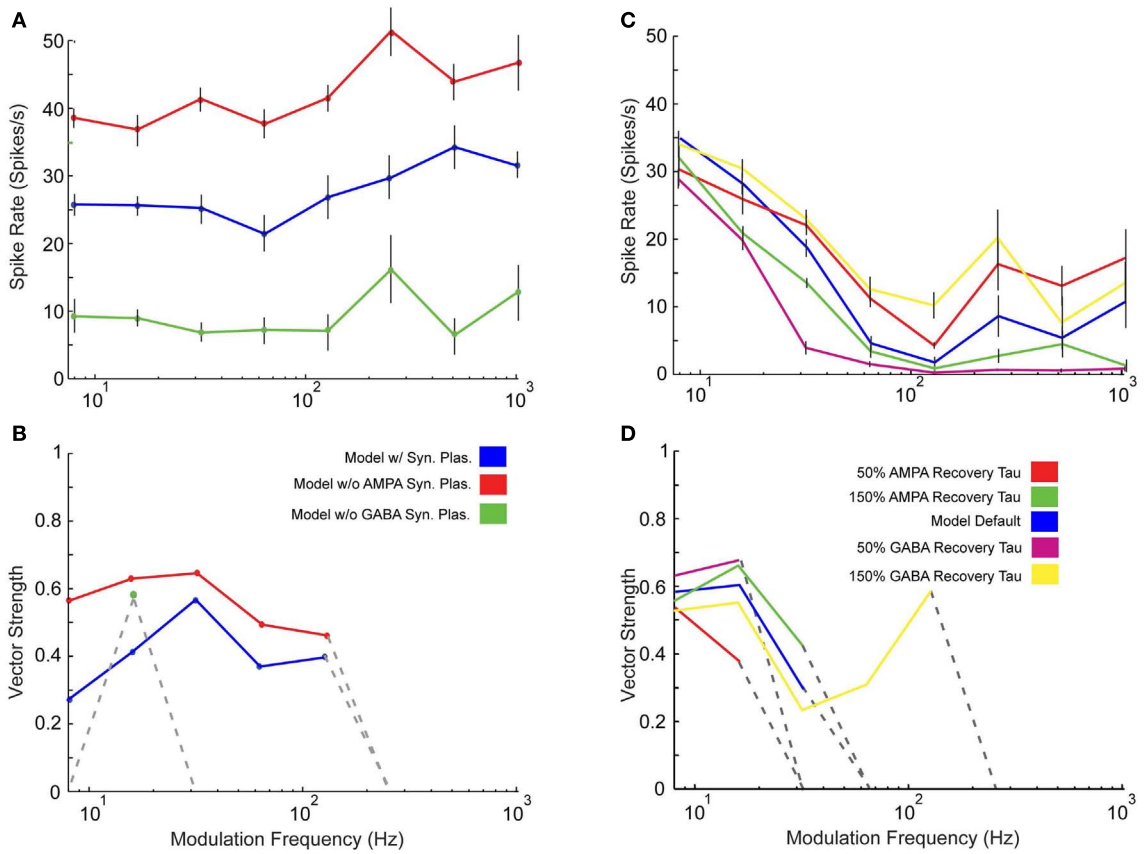

FIGURE 6 | Effects of synaptic plasticity on model responses. Changes in rate **(A)** and statistically significant vector strength **(B)** with modulation frequency in IC Adapting Model responses with 3 DCN and 2 DNLL all-pass inputs in the presence of synaptic depression *(blue)*, the absence of only AMPA synaptic depression *(red)* or the absence of only $GABA_A$ synaptic depression *(green)*. Changes in rate **(C)** and statistically significant vector strength **(D)** responses with modulation frequency in IC Adapting model with 2 VCN and 4 DNLL high-pass inputs under normal $GABA_A$ and AMPA recovery time constants *(blue)*, 50% reduction in AMPA *(red)* or $GABA_A$ *(purple)*, or 150% increase in AMPA *(green)* or $GABA_A$ *(yellow)* time constants. Synchrony range is increased with longer recovery time but decreased with shorter recovery time. Modulation frequency in Hz is marked along the *X*-axes for **(A–D)**, mean firing rate in spikes/s is marked along the *Y*-axes in **(A,C)** and vector strength is marked along the *Y*-axes in **(B,D)**.

(**Figures 7A–C**) or 4 DCN (**Figures 7D–F**) excitatory inputs and 4 DNLL high-pass inhibitory inputs were used. Model simulations using large $GABA_A$ conductances, large IPSC decay values, or large numbers of inhibitory inputs typically produced LP rate responses (blue x), while smaller inhibitory conductances, IPSC decay values or number of inhibitory inputs typically produced AP rate responses (red circles), which are indicated on the color plots (**Figures 7A–F**). BR responses were produced at intermediate values that separated regions of AP and LP rate responses (green diamonds). BP responses were not commonly observed using the combinations of either DCN/DNLL or VCN/DNLL inputs tested in these examples (black filled circles).

ANATOMIC CHANGES IN SYNAPTIC MARKERS IN AGED IC

A main goal in developing the IC model was to apply it to understanding central mechanisms of age-related decline in temporal processing (Schatteman et al., 2008; Parthasarathy and Bartlett, 2011). As a preliminary step to constrain potential mechanisms to test in the IC model, anatomic techniques were used to measure changes in the inhibitory and excitatory synaptic markers. The relative optical densities (RODs) of ROI in the IC central nucleus were compared between young and aged animals for sections immunostained for GAD65/67 a marker of presynaptic GABAergic axons or VGluT2 a marker of a population of glutamatergic axons (e.g., **Figure 8A**). GAD65/67 ROD showed a significant decrease in aged animals (**Figure 8B**, $p < 0.05$, unpaired t-test), consistent with previous studies showing a loss of inhibitory markers (Raza et al., 1994; Burianova et al., 2009). VGluT2 did not change significantly with age (**Figure 8B**), consistent with previous studies showing no loss in the number of excitatory terminals in the aged IC (Helfert et al., 1999), though the functionalities of the terminals and post-synaptic receptors are not known. These anatomical data suggested some data-constrained variables suitable for further exploration in the IC model.

COMPARISON OF *IN VIVO* RESPONSES FROM THE IC OF YOUNG AND AGED ANIMALS

Responses of 47 auditory neurons were recorded from the IC of three aged animals. Of these, 25 neurons had non-synchronized, purely onset responses to AM stimuli that were not modulated by

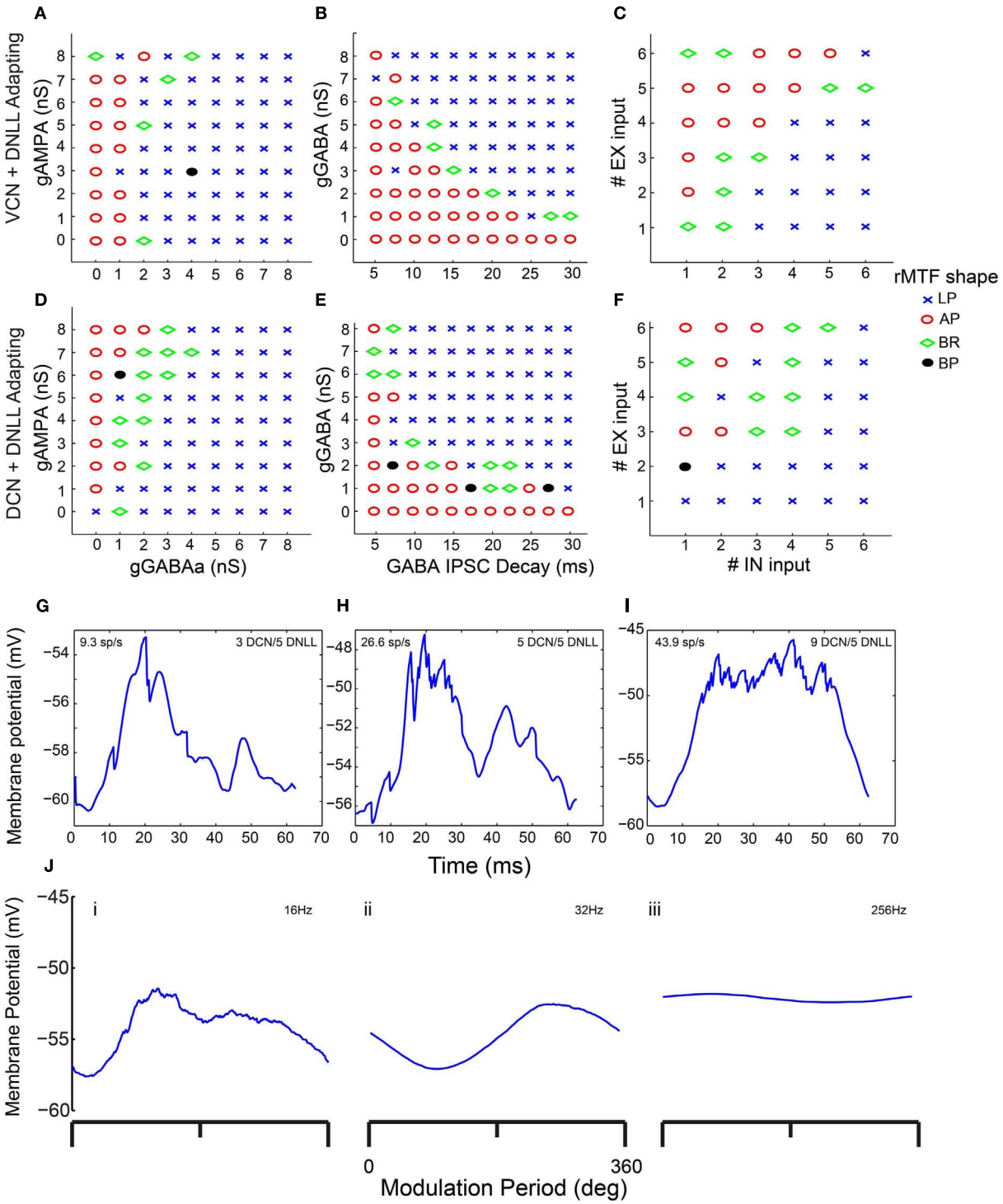

FIGURE 7 | Determinants of IC Model output and rMTF shape. Color plots showing various rate MTF response shapes using 4 VCN excitatory and 4 DNLL high-pass inhibitory **(A–C)** inputs with the IC Adapting model. LP – low-pass *(blue crosses)*, AP – all-pass *(red circles)*, BR – band-reject *(green diamonds)*, BP – band-pass *(black circles)*. **(A)** Rate shape plots as a result of adjusting $GABA_A$ synaptic conductance (nS, *X*-axis) and AMPA synaptic conductance (nS, *Y*-axis). **(B)** Rate shape plots corresponding to changes in $GABA_A$ ISPC decay (ms, *X*-axis) and $GABA_A$ synaptic conductance (nS, *Y*-axis) **(C)** Rate shape plots corresponding to changes in number of inhibitory (*X*-axis) and excitatory (*Y*-axis). **(D–F)** Color plots similar to **(A–C)**, using 4 DCN and 4 DNLL high-pass inputs in the Adapting model. **(G–I)** Voltage traces taken from a single trial, divided into 62.5 ms intervals (16 Hz) and averaged. Mean voltage trace from a trial using 3 DCN and 5 DNLL high-pass inputs **(G)**, 5 DCN and 5 DNLL high-pass inputs **(H)**, or 9 DCN and 5 DNLL high-pass inputs **(I)**. Membrane potential is marked along the *Y*-axis in mV and time is marked along the *X*-axis in ms. **(J)** Voltage traces taken from a single trial, divided into either 62.5 ms (16 Hz, i), 15.6 ms (64 Hz, ii) or 3.9 ms (256 Hz, iii) intervals and averaged. Mean voltage traces using 3 DCN and 5 DNLL high pass inputs. Membrane potential is marked along the *Y*-axis in mV and modulation period is marked along the *X*-axis in degrees.

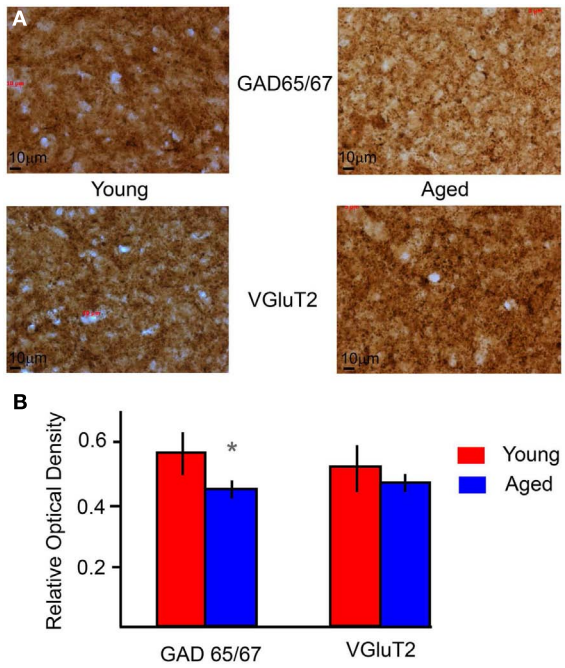

FIGURE 8 | Immuno-histochemical levels of GAD and VGluT2 in young and aged IC. (A) Example sections of the IC stained for GAD (top) and VGluT2 (bottom) for young (left) and aged (right) animals under 40× magnification. The dimensions of the sections are 208.2 × 156 μm. **(B)** Average relative optical densities of GAD 65/67 and VGluT2 from the IC of young (red) and aged (blue) animals. ROD is marked along the *Y*-axis, and the type of marker along the *X*-axis. Error bars indicate one standard deviation. Asterisks indicate significant difference ($p < 0.01$, unpaired *t*-test).

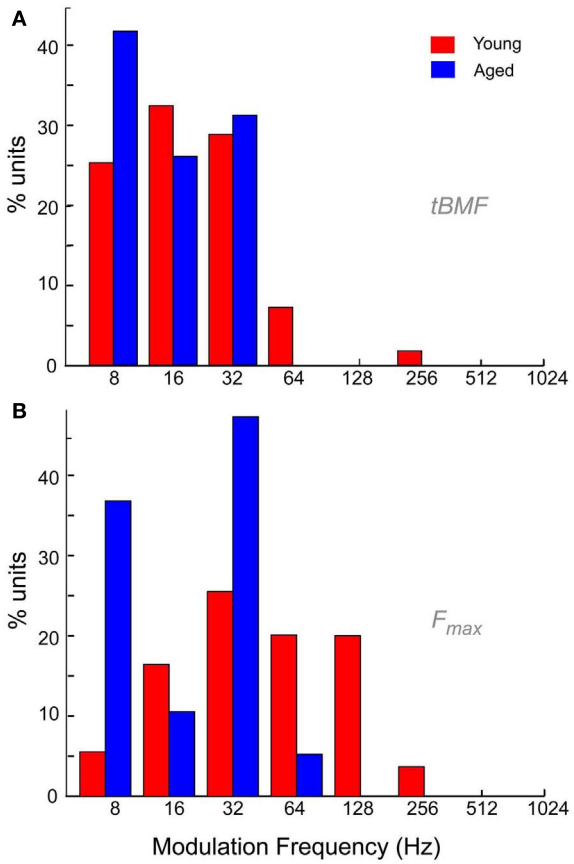

FIGURE 9 | Temporal characteristics of IC neurons from young and aged animals. (A) Distribution of best temporal modulation frequencies (tBMFs) in young (red) and aged (blue) animals among the recorded neurons in this study. Modulation frequency is marked along the *X*-axis in Hz and *Y*-axis indicates percentage of units with specified tBMF. **(B)** Distribution of temporal cut-off frequencies (F_{max}) in young (red) and aged (blue) animals among the neurons recorded in this study. Axes same as **(A)**.

modulation frequency. These neurons, encountered early in the track and likely to be located in the dorsal or external cortex of the IC, were discarded for the purposes of this study. The remaining neurons all responded to varying modulation frequencies by changes in rate and/or synchrony and were compared to responses obtained from the young animals. Of these neurons, 46% exhibited LP, 36% exhibited BP, and 18% exhibited AP rate tuning. No BR neurons were encountered in our aged sample. The proportion of neurons exhibiting LP characteristics compared to the other response types was slightly higher in the aged than the young. Of the synchronous neurons, the relative proportions of LP and BP tMTFs did not change significantly with age, with 58% exhibiting LP synchrony, and 42% exhibiting BP synchrony.

The distribution of tBMFs was LP in nature for both young and aged animals. Aged neurons generally had lower vs, and no aged neurons with tBMFs greater than 32 Hz were encountered (**Figure 9A**). The mean vs at tBMF was also significantly lower for in the aged (0.45 ± 0.12) compared to the young (0.56 ± 0.16, $p < 0.01$, rank-sum test). **Figure 9B** shows the distribution of F_{max} for the young and aged animals. The F_{max} or the cut-off frequencies were more band-pass in nature for the young, with the most number of units having a maximum phase locking from 32 to 64 Hz. In the aged, the distribution of F_{max} revealed no neurons that could synchronize to MFs greater than 64 Hz AM. The population of neurons that could synchronize to modulation frequencies of 64 Hz and higher, were significantly different between the young and the aged (52.7 vs. 5.3%, $p < 0.001$, χ^2 test). Thus overall, the aged neurons seemed to lack the ability to synchronize to faster modulation frequencies, and also showed more LP rate tuning and no BR rate tuning.

MODELING OF AGED UNITS BASED ON *IN VIVO* RESPONSES

Based on the decrease in markers of GABAergic inhibition seen at the anatomical level, $GABA_A$ conductance was modified to reproduce the results seen at the level of the single neuron. **Figure 10** shows an IC Sustained model with two DCN inputs and five DNLL high-pass inputs with LP rate and synchrony coding. **Figure 10A** (left) shows a voltage trace from the "young" model with full inhibition for an AM frequency of 16 Hz, demonstrating periodic firing at the modulation frequency. Upon reduction of $GABA_A$ conductance by 50%, the neuron remained more depolarized (**Figure 10A**, right), and the synchronized firing was abolished (**Figure 10B**). The neuron remained LP rate tuned with higher firing rates (blue dashed line). This decrease in synchrony was

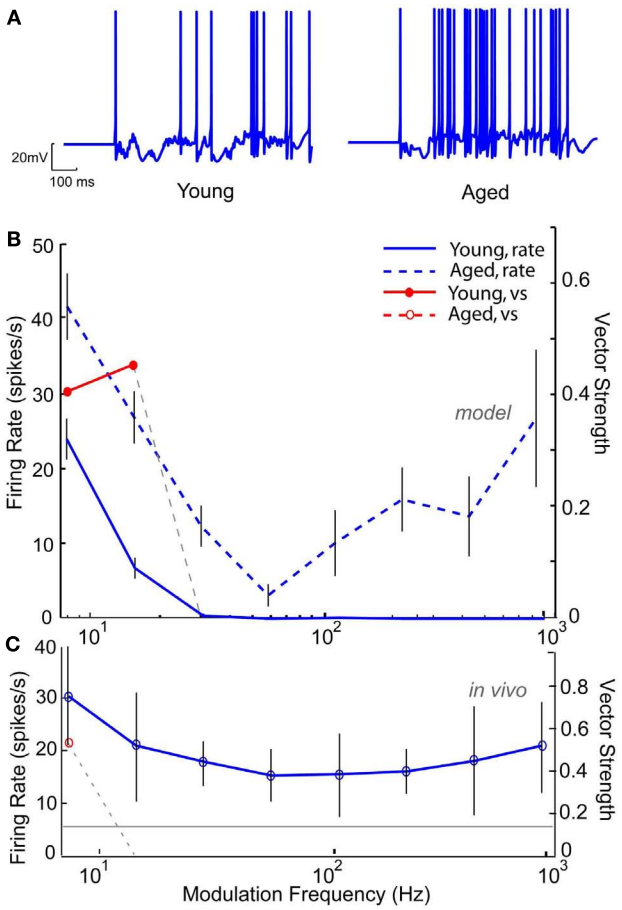

FIGURE 10 | Modeling age-related loss of synchrony through reduction in $GABA_A$. IC Sustained model with two LSO inputs and three DNLL all-pass and the membrane potential at −60 mV. **(A)** Example voltage traces from individual trials at 16 Hz modulation frequency for a young (left) and aged (right) model neuron. **(B)** Changes in mean firing rate shown for a young model neuron (blue solid line) and an aged model neuron with 50% reduction in $GABA_A$ (blue dashed lines). Significant vector strengths shown for a young model neuron (*filled red circles*) and an aged model neuron (*red open circles*, not present in the model). Firing rate, in spikes/s, and vector strength are marked along opposing *Y*-axes and modulation frequency in Hz is marked along the *X*-axis. Error bars indicate one standard deviation from the mean of 10 trials. **(C)** Representative neuron A15 from an aged animal showing a weak low-pass rMTF (*blue solid lines*) and reduced synchrony (*red open circle*) to sAM stimuli presented at 75 dB SPL and centered at 16 KHz. Gray line indicates mean spontaneous firing rate. Axes same as **(A)**.

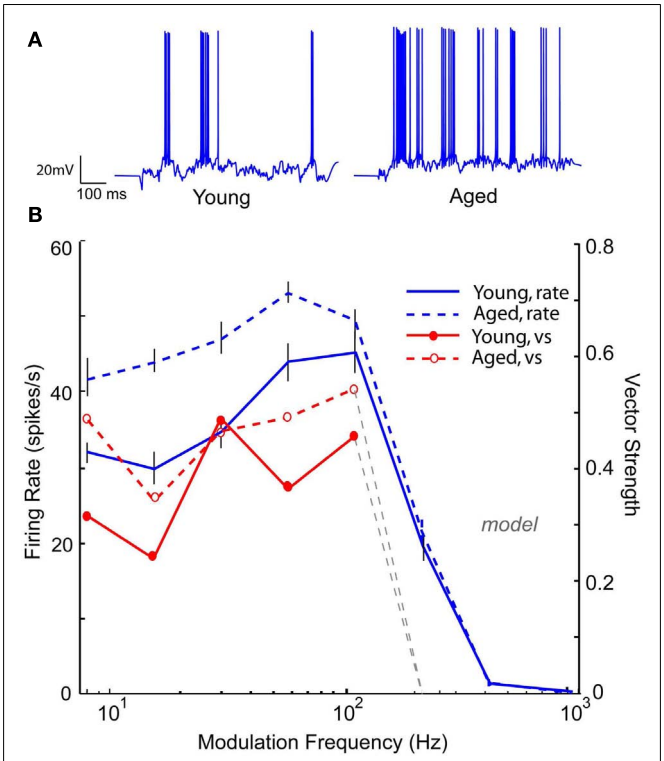

FIGURE 11 | Transformation of band-pass rMTF to low-pass rMTF by reducing $GABA_A$. IC Adapting model with 3 user-defined low-pass excitatory inputs (LSO sync tuning) and 3 VNLL band-pass inhibitory inputs (rBMF = 12 Hz). **(A)** Example voltage traces from individual trials at 16 Hz modulation frequency for a young (left) and aged (right) model neuron. **(B)** A band-pass rMTF (*solid blue*) from a model young neuron is transformed into a low-pass rMTF (*dashed, blue*) upon 50% reduction in $GABA_A$. The original vector strength (*solid red*) decreased (*dashed, red*) but the cut-off frequency remained the same. Firing rate, in spikes/s, and vector strength are marked along opposing *Y*-axes and modulation frequency is marked along the *X*-axis in Hz.

similar to those observed at the single neuron level in the aged, as illustrated by responses of an aged neuron, A21, to sAM stimuli centered at 16 kHz, presented at 75 dB SPL (**Figure 10C**). This example neuron exhibited a low-pass rMTF with an rBMF of 8 Hz (rate – 30.4 spikes/s) and LP tMTF with a tBMF of 8 Hz (vs – 0.42).

Neuronal responses from aged animals in a previous study (Palombi et al., 2001) revealed a significant increase in LP rate tuned responses, whereas a slight increase was seen in aged animals in the present study. **Figure 11** shows an IC Adapting model with four LSO LP excitatory inputs with six VNLL BP inhibitory inputs (rBMF = 12 Hz) with BP rate tuning. For 16 Hz AM, the voltage trace in the "young" model neuron (**Figure 11A**, left) shows a low but periodic firing rate. Upon decreasing $GABA_A$ conductance by 50%, the "aged" model neuron transformed into a LP rate coded neuron, which can be seen in **Figure 11B** (blue dashed line) while maintaining or even exceeding the vs of the "young" model neuron (**Figure 11B**, red lines). In this example, decreasing inhibition allowed the synchronized excitatory inputs to reach threshold, generating a synchronized response with a higher rate than in the young (**Figure 11A**, right).

Band-reject neurons or neurons with a "worst modulation frequency" have been reported in a significant percentage IC AM responses in young animals (Krishna and Semple, 2000; Krebs et al., 2008). These neurons are thought to be the result of an excitatory AP input spike train that coincided with a tuned inhibitory input upon an IC neuron. An IC Adapting model using three VCN inputs and five VNLL BP inputs (rBMF = 32 Hz) produced a BR response with a minimum at 64 Hz and a synchronized range from 16 to 32 Hz, as seen in **Figure 12B** (blue and red solid lines). Upon reduction of this tuned inhibition by 50% (blue dashed lines), the rate at the worst modulation frequency increased. The

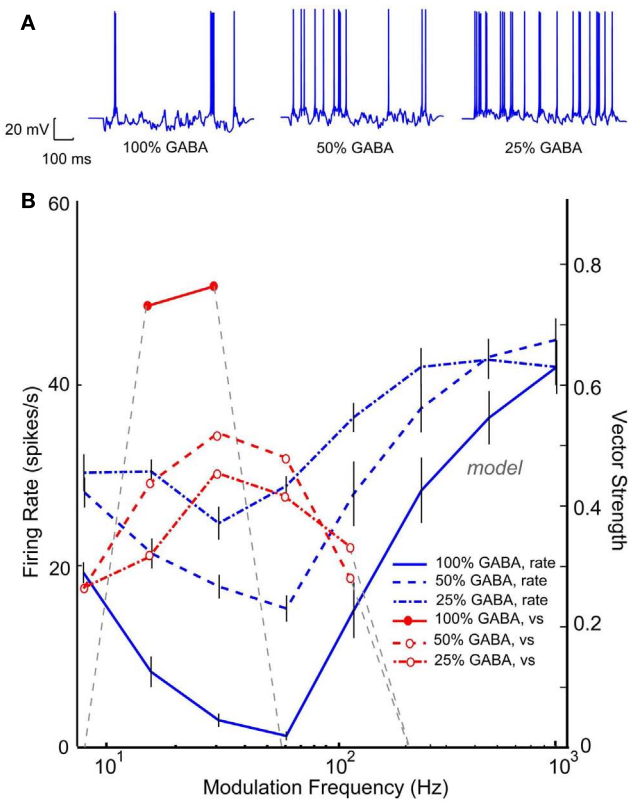

FIGURE 12 | Reduction in band-reject rMTFs due to reduction in $GABA_A$. IC Adapting model with 3 VCN inputs and 4 VNLL band-pass inputs (rBMF = 32 Hz). **(A)** Example voltage traces from individual trials at 16 Hz modulation frequency for a young (left) and aged (right) model neuron. **(B)** Changes in mean firing rate of a model neuron exhibiting band-reject rMTF (*solid blue*) with reduction in $GABA_A$ to 50% (*dashed blue*) or to 25% (*dot-dashed, blue*). The original vector strength (*solid red*) reduced for both conditions (*dashed, red,* and *dot-dashed red* respectively). Firing rate, in spikes/s, and vector strength are marked along opposing *Y*-axes and modulation frequency is marked along the *X*-axis in Hz.

neuron was still BR at 32–64 Hz, but the depth of rate modulation was much lower. Similar to **Figure 11**, reducing inhibition uncovered the synchrony of the excitatory inputs, resulting in synchronized responses from 8 to 128 Hz. Further reduction of 75% of the inhibitory conductance generated a high-pass rMTF (dash-dot lines), reflecting the VCN inputs and the lack of inhibition at high AM frequencies. This example demonstrates the complicated relationship between the balance in excitation and inhibition and the representation of temporal modulation. In this case, inhibition shaped selectivity for AM for both rate and synchrony in the "young" model, restricting the response to low modulation frequencies. Loss of inhibition resulted in a loss of selectivity but a more extensive range over which periodicity could be represented by a single IC neuron.

DISCUSSION

SUMMARY OF RESULTS

In this study, neuronal responses were recorded in the IC of young and aged Fischer-344 rats to using sAM and nAM stimuli. In young animals, these responses were primarily classified into LP, BP, BR, and AP responses based on their rate tuning. Neuronal tMTFs also showed LP and BP characteristics. These major types of responses were recreated using a single compartment IC neuron model with voltage-gated ion channels and synaptic ligand-gated channel characteristics derived from previous *in vitro* and *in vivo* studies, including physiologically realistic input rates and synaptic depression.

Predictions based on changes in response patterns due to aging, primarily due to decreased inhibition, were motivated by changes in anatomical markers as well as changes in responses to the same AM stimuli from the IC of aged animals. In addition, it was demonstrated that changes in the balance between excitation and inhibition (**Figure 7**), as well as changes in recovery timing of synaptic depression (**Figure 6**) produced decrements in temporal processing consistent with data from aged animals. Hence this model provides a powerful framework for understanding the cellular mechanisms of temporal processing in the IC, and predicting how they may change in cases of aberrant processing, such as those in aging.

CONSIDERATION OF MODEL PARAMETERS

The creation and use of the IC model uncovered important assumptions and needs for additional experimental data. A single compartment model of IC neurons was used in this study. Most neurons in the central nucleus of IC have disk-shaped morphology (Oliver, 1984; Peruzzi et al., 2000), where the dendrites are thick proximally and taper within about 50 μm, extending 100–150 μm from the cell body in the rat (Peruzzi et al., 2000). Many inhibitory synapses onto IC neurons are axosomatic (Ito et al., 2009), whereas excitatory synapses are found mainly along the dendrites (Oliver et al., 1999). Although dendritic filtering of synaptic inputs, which may be important in auditory brainstem neurons (Joris et al., 1998), was not accounted for, there are mechanisms in hippocampus and cortex that allow somatic EPSP amplitude to be largely independent of synaptic location (Magee and Cook, 2000). Hence a point model neuron was used as a first approximation lacking further evidence for how synapses and ion channels are distributed in IC neurons.

Although there are multiple sources of ascending excitatory and inhibitory projections to IC, studies of their synaptic properties, largely conducted using brain slices, have typically not dissociated the sources. Therefore, only the aggregate population synaptic characteristics are known (Smith, 1992; Wu et al., 2004; Sivaramakrishnan and Oliver, 2006), not the input-specific synaptic characteristics for each source. Moreover, the number of synaptic inputs used to model IC neurons has varied widely from 1 to 30 inputs (Reed and Blum, 1999; Shackleton et al., 2000; Nelson and Carney, 2004; Guerin et al., 2006). Data from *in vitro* recordings suggests a moderate number of inputs (1–10) converge on IC neurons (Smith, 1992; Wu et al., 2004). While this is clearly fewer than the number of synapses on a given neuron, it may provide an estimate of the number of functional levels of excitation or inhibition. Given that individual afferent axons often contribute more than one synapse onto a single neuron, it is useful to consider the functional levels that can be evoked by electrical stimulation as a lower estimate of the number of separate inputs evoked by

sound. These numbers were sufficient to drive IC rates comparable to those *in vivo*. Some IC models have suggested the use of balanced inhibition, while others (Nelson and Carney, 2004) have suggested that inhibition should dominate. This was often the case in our model, where even in the presence of 4–6 inhibitory inputs, 2–3 excitatory inputs could drive model IC neurons to rates comparable to those *in vivo* (e.g., **Figures 4**, **5**, and **10–12**). Moreover, we have verified that BP IC responses can be generated by LP excitatory inputs with equal or higher corner frequencies than LP inhibitory inputs (**Figures 4F,H**), as suggested by Dicke et al. (2007). Another assumption in the model is that a given neuron receives only one type of excitatory or inhibitory input. There have been excellent studies demonstrating functional zones of inputs to the IC (Malmierca et al., 2005; Cant and Benson, 2006; Loftus et al., 2010), but whether different excitatory or different inhibitory inputs converge on individual IC neurons has not been established. Finally, the effects of local excitatory and inhibitory collaterals in IC (Herrera et al., 1989; Oliver et al., 1991; Paloff et al., 1992) have been omitted from this iteration of the IC model but would be likely to enhance or suppress the sustained responses of IC neurons, respectively.

COMPARISON OF THE MODEL WITH PREVIOUS MODELS

Experimental parameters for the present study were obtained from IC studies using brain slices (Peruzzi et al., 2000; Wu et al., 2004; Sivaramakrishnan and Oliver, 2006) and from *in vivo* intracellular recordings (Tan and Borst, 2007; Tan et al., 2007; Geis and Borst, 2009). From these studies, it was possible to obtain values for membrane properties, synaptic amplitudes and time courses, and short-term synaptic plasticity. The setup of input tuning curves to generate different IC outputs in our model overlapped with schemes in previous models (Cai et al., 1998a,b; Nelson and Carney, 2004; Guerin et al., 2006; Dicke et al., 2007), which in most cases focused on BP tuned IC neurons and used much faster synaptic time constants than have been measured for IC neurons. This does not diminish the functional insights gained from these models, but the current model can generate the spectrum of IC responses using more recent synaptic data and membrane properties. For example, *in vivo* it is known that synaptic depression and facilitation can have significant influence on information transmission (Elhilali et al., 2004; Wolfart et al., 2005), especially using more realistic patterns of activity (Hermann et al., 2009). Although spontaneous activity may affect the steady state magnitude of depression (Hermann et al., 2007), the spontaneous rate of IC inputs is often low (Tan et al., 2007, **Figures 4**, **5**), and the spontaneous rates of many of the IC inputs are low (Yin and Chan, 1990; Bajo et al., 1999; Paolini and Clark, 1999), so it is still expected that some depression of inputs to the IC will be present for the initial sound-evoked activity. In addition, data from the calyx of Held synapses suggests that extracellular calcium concentration and intracellular calcium handling will affect the strength and time course of depression (Lorteije et al., 2009) and that *in vivo* extracellular calcium concentration is probably lower than typically used in brain slice experiments. However, activity dependent shifts in depression, or the balance of excitatory and inhibitory depression (**Figure 6**), may be an interesting way to regulate IC sustained activity. The advantage of using realistic intrinsic properties and synaptic properties for the IC is that they can be modified to make specific, testable mechanistic predictions about how changes in those properties, due to conditions such as aging or hearing loss, will affect IC model responses. In this study, the main focus has been on synaptic parameters that change, such as a decrease in GABAergic inhibition with age (**Figures 10–12**), but it is possible to test for other parameters that may be affected by aging, such as the influence of voltage-dependent ion channels, membrane properties, and changes in reversal potentials associated with impaired bioenergetics in aging (Mei et al., 1999; Melov, 2004).

COMPARISON OF *IN VIVO* RESPONSES WITH PREVIOUS STUDIES

The classification of rate MTFs followed earlier studies in the IC, with studies reporting LP, BP, and AP tuning (Rees and Moller, 1987; Langner and Schreiner, 1988; Rees and Palmer, 1989). Previous studies also reported BR rMTF tuning, as a worst modulation frequency (Krishna and Semple, 2000; Krebs et al., 2008). The BR tuning is thought to be due to the presence of tuned inhibitory inputs converging on an IC neuron along with an AP rate input, but it is also possible to get BR tuning with inhibition that precedes excitation (**Figure A3** in Appendix). Many other neurons in this study showed a LP or BP tMTF, with the distributions of tBMFs and F_{max} similar to those reported in earlier studies in rats (Rees and Moller, 1987). Though temporal coding of periodic stimuli is not generated in the IC and is inherited from the lower auditory inputs, these responses may be sharpened due to the effect of inhibition mediated by GABA in young animals (Caspary et al., 2002; Zhang and Kelly, 2003). It is the reduction in inhibition estimated by a reduction in GAD 65/67 staining seen in this study (**Figure 8**), as well as reported previously in various other studies that is thought to be a contributing factor to altered temporal responses with age (reviewed in Caspary et al. (2008). The reduction in GABAergic inhibition has robust effects on rate coding and vs, with an overall increase in rate and more complex effects on vs. Rate changes can transform rMTFs from BP tuning to LP tuning or from BR to AP or high-pass (**Figures 10–12**).

MECHANISMS DETERMINING AM PROCESSING CHARACTERISTICS IN YOUNG

The IC neuron model highlights several possible mechanisms of IC neurons that can influence responses to AM inputs, and it allows for adjustments of many parameters that modify intrinsic and synaptic properties.

Output response tuning to AM inputs can be inherited via combinations of different input tuning. **Figure 3** shows responses to different types of afferent rate tuning, which are compared to the corresponding output responses. Coupled with AP inhibition, excitatory inputs exhibiting distinct rate characteristics often produce rate responses that inherit and display similar rate curves.

Not surprisingly, regions of few excitatory and numerous inhibitory inputs suppressed firing and either produced purely subthreshold responses, or responses with very low spike counts. More interestingly, this combination could transform AP VCN excitatory inputs to LP IC rMTF outputs (**Figure 7C**). Predictably, numerous excitatory and few inhibitory inputs produced large spike rates that are either non-synchronized or take on the characteristics of their inputs, such as the AP responses in **Figures 7A,D**.

The best fits with data occurred when there were 1–3 more inhibitory inputs than excitatory inputs (**Figures 4**, **5**), suggesting that the inhibition dominated models of Nelson and Carney (2004) may fit the data best.

The $GABA_A$ IPSC decay time was another factor that significantly influenced the output response characteristics, particularly response rates. Increasing the IPSC decay value by 50% decreased spike rates at all modulation frequencies, due to larger hyperpolarization and increased summation of inhibitory inputs. This increase could also drive selectivity of the rMTF, as shown in **Figures 7B,E**, in a manner that was similar to increasing the peak conductance. Conversely, shortening IPSC decay values by 50% increased firing rates and reduced rMTF selectivity. This decrease sometimes reduced response vs measures and made the synchronized portion of its tMTF more similar to that of its inputs. Unlike IPSC decay time, adjustments to inhibition timing (±5 ms) relative to excitation produced only minor differences in rate or synchrony, similar to previous model studies (Nelson and Carney, 2004), which is probably due the integration of multiple inputs with multiple spikes per cycle. If the firing between the excitatory and inhibitory inputs were significantly correlated, rather than independently generated as they have been modeled in this study, delay would be more of a factor.

Finally, tuned rate responses could be obtained in a straightforward manner in the model using tuned excitatory inputs alone or in conjunction with tuned inhibitory inputs. This may be occurring for MSO inputs (Grothe, 1994) and for DNLL and VNLL inputs (Yang and Pollak, 1997; Zhang and Kelly, 2006). Tuned inhibition explains some results in young animals, such as a decrease in firing rate in the low AM frequency region of some BP units in IC generated by either BP or LP inhibitory inputs. However, it does not adequately explain on-rBMF inhibition and maintenance of BP tuning and rBMF during blockade of inhibition (Caspary et al., 2002). This appears to require additional mechanisms such as coincidence detection (Guerin et al., 2006) or cross-correlation (Nelson and Carney, 2004) except that slower synaptic time constants measured for IC neurons should be used. Further study is required to correlate subthreshold membrane potential contours with rMTF shape and with model responses, as was found in Geis and Borst (2009). However, **Figures 7G–I** from our study demonstrated that increasing the number of excitatory inputs smoothes the membrane potential contours, given a constant strength of inhibition. In addition, higher frequency inputs also smooth the membrane potential contours (**Figure 7J**), similar to Geis and Borst (2009).

MANIPULATIONS IN MODELS THAT PRODUCE AGING-LIKE RESPONSES AND COMPARISON WITH OTHER AGED IC STUDIES

Reduction in GABAergic inhibition was chosen for initial simulations of age-related changes in the IC model. Intrinsic parameters were largely ignored for this iteration of the model because there are very few data on age-related changes in membrane channels, though some changes have been observed with deafness or hearing loss (Kharkovets et al., 2000; Vale et al., 2003; Cui et al., 2007). A decrease in GAD65/67 has been observed in **Figure 8** and a number of previous studies (Raza et al., 1994; Burianova et al., 2009), signifying that the amount of GABA available may be lower in aged animals. There are also indications of alterations of the $GABA_A$ subunit composition (Backoff et al., 1999), suggesting that both pre- and post-synaptic components of fast inhibition in the IC are altered. A simple way to test the aggregate effect of these changes was to reduce the $GABA_A$ conductance in the model, though a finer-scale modeling of amplitude and kinetics could be possible. Although **Figure 8B** suggests that presynaptic markers of excitatory terminals are not affected by aging, evoked glutamate release (Caspary et al., 1990a) and glutamate receptor subunit composition (Marianowski et al., 2000; Holt et al., 2005) can both be affected by aging, so simple changes in excitatory function can be tested in conjunction with decreased inhibition in the future. Finally, recovery from sound gaps (Walton et al., 1998) or sequential stimuli (Finlayson, 2002) suggested that recovery from depression may be affected by aging, and **Figure 6** suggests that changing synaptic depression changes both rate and temporal selectivity in IC.

Manipulations that affected $GABA_A$ conductance shaped tuning in ways consistent with previous studies of aged animals. For units with LP responses (**Figure 10**), rates increased and vector strength often decreased. For units whose BP tuning was shaped by LP or BP inhibition, reducing inhibition led to a shift to LP tuning (**Figure 11**). For units with BR tuning, created by LP or AP excitation and BP or preceding AP inhibition, reducing inhibition led to high-pass or AP rMTF responses (**Figure 12**). These effects are similar to those observed in IC studies of young rats (Caspary et al., 2002; Zhang and Kelly, 2003), where a subset of BP units reverted to LP responses during bicuculline administration. Many of the units still had BP tuning with elevated rates, suggesting that the BP tuning was inherited from inputs or generated by synaptic and cellular filtering in IC. The results are also consistent with our small sample of aged units and studies of AM in aged animals (Palombi et al., 2001), where there was a higher percentage of LP responses. These examples demonstrate the versatility of the IC model in testing and making predictions about consequences of different changes in IC synaptic and neuron properties, but were intended to be illustrative rather than exhaustive.

MODEL PREDICTIONS AND GAPS IN NECESSARY EXPERIMENTAL DATA REVEALED BY MODEL

By using IC experimental data from rodents for model values where possible, construction of the model revealed experimental avenues for future study in order to more accurately simulate IC processing. The synaptic properties of the main ascending afferents to IC need to be dissociated and analyzed separately, for both the excitatory and inhibitory inputs. In addition, the anatomical convergence of afferents at the single neuron level needs to be examined in order to determine how many different ascending axons send terminals to a different neuron and whether different excitatory sources or different inhibitory sources often converge. Estimates were made based on current available data and the ability to recapitulate basic AM tuning with minimal manipulations, but this study has not focused on specific parameter fitting to individual neuron data. In addition, the inputs to the IC model were assumed to be normal, despite evidence that there are temporal processing deficits evident in single unit brainstem responses (Schatteman et al., 2008) and population neural responses that

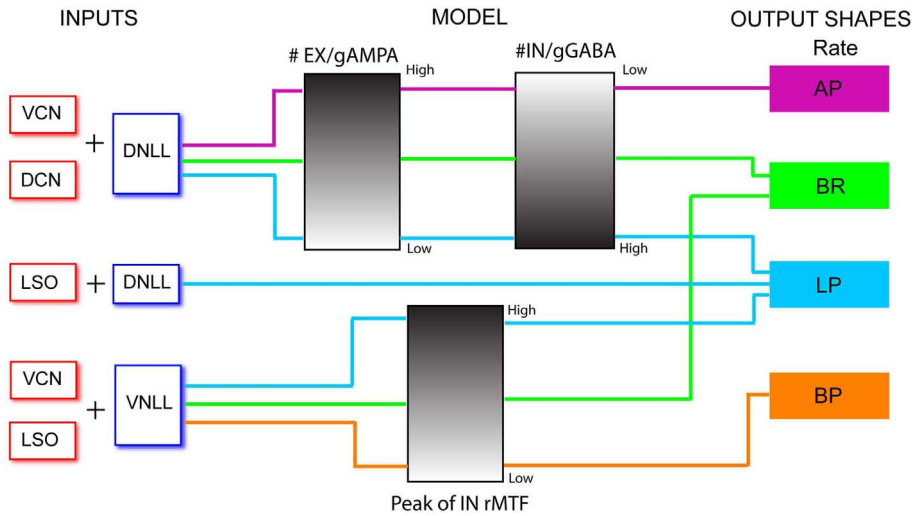

FIGURE 13 | Model output schematic. Diagram describes possible rate output shapes generated by different combinations of inputs (*left*) and changes in model parameters (to be read left to right). Excitatory inputs are shown in red boxes and inhibitory inputs are shown in blue boxes. Adjustment of model parameters (*center*), such as number of excitatory or inhibitory inputs, magnitude of synaptic conductances of AMPA or $GABA_A$, duration of inhibitory post synaptic currents (IPSCs), or frequency of peak inhibitory input rMTF can shape output rate response and lines through gradients indicate magnitude of each parameter. Similar colored lines correspond to different rate output shapes (*right*) produced by different combinations.

include brainstem and midbrain sources (Parthasarathy et al., 2010; Parthasarathy and Bartlett, 2011).

CONCLUDING REMARKS

The IC model presented here, using realistic voltage-dependent membrane channels and synaptic ion channels, is able to produce all *in-vivo* rMTF responses described in this study (**Figures 4**, **5**). **Figure 13** shows a schematic of the IC model with the different ascending input combinations, key model parameters, and the resulting output rMTFs generated. LP inputs, such as the LSO inputs (**Figure 2**), preserved their rate shape if coupled with either AP or high-pass inhibition (DNLL). AP inputs (DCN, VCN) with a large number of inhibitory inputs or BP inhibition tuned to high (>64 Hz) frequencies also produced a LP rate response. AP inputs preserved their rate shape when they outnumbered inhibitory inputs or, similarly, had large AMPA conductances. There was an intermediate regime between LP and AP responses (**Figures 7A–F**) where AP inputs (VCN, DCN) coupled with DNLL inhibition produced BR responses. In addition, BR responses could be generated when the AP excitatory inputs were coupled with inhibition tuned to intermediate modulation frequencies. BP responses were occasionally generated for specific parameter combinations (**Figures 7A–F**), but they could be reliably generated from LP LSO inputs coupled with VNLL BP inhibition tuned to low (<32 Hz) frequencies or from LP inhibitory inputs with a lower LP corner frequency. Based on these observations, there were predictable changes in rMTF when one aspect of age-related change was simulated by reducing GABAergic inhibition. This could cause BP responses to become LP (**Figure 11**) or BR responses to become AP or high-pass (**Figure 12**). Taken together, it appears that IC outputs will reflect the rMTFs and basic tMTF characteristics of their inputs, but this simple relay is shaped by inhibitory inputs to transform the AM rate selectivity within the IC, which is greatly diminished by reduced inhibition such as that found in aging.

ACKNOWLEDGMENTS

This study was supported by grants from the American Federation for Aging Research (AFAR), Deafness Research Foundation (DRF), and NIDCD (R01DC011580) to Edward L. Bartlett. Zachery Fisher was supported by a grant from the Howard Hughes Medical Institute and Stephanie M. Gardner was supported by NSF CCLI/TUES #0941921.

REFERENCES

Adams, J. C., and Wenthold, R. J. (1979). Distribution of putative amino-acid transmitters, choline-acetyltransferase and glutamate-decarboxylase in the inferior colliculus. *Neuroscience* 4, 1947–1951.

Attwell, D., and Laughlin, S. B. (2001). An energy budget for signaling in the grey matter of the brain. *J. Cereb. Blood Flow Metab.* 21, 1133–1145.

Backoff, P. M., Palombi, P. S., and Caspary, D. M. (1999). gamma-Aminobutyric acidergic and glycinergic inputs shape coding of amplitude modulation in the chinchilla cochlear nucleus. *Hear. Res.* 134, 77–88.

Bajo, V. M., Merchan, M. A., Malmierca, M. S., Nodal, F. R., and Bjaalie, J. G. (1999). Topographic organization of the dorsal nucleus of the lateral lemniscus in the cat. *J. Comp. Neurol.* 407, 349–366.

Bal, R., Green, G. G. R., Rees, A., and Sanders, D. J. (2002). Firing patterns of inferior colliculus neurons-histology and mechanism to change firing patterns in rat brain slices. *Neurosci. Lett.* 317, 42–46.

Belenky, M. A., Yarom, Y., and Pickard, G. E. (2008). Heterogeneous expression of gamma-aminobutyric acid and gamma-aminobutyric acid-associated receptors and transporters in the rat suprachiasmatic nucleus. *J. Comp. Neurol.* 506, 708–732.

Borisyuk, A., Semple, M. N., and Rinzel, J. (2002). Adaptation and inhibition underlie responses to time-varying interaural phase cues in a model of inferior colliculus neurons. *J. Neurophysiol.* 88, 2134–2146.

Burianova, J., Ouda, L., Profant, O., and Syka, J. (2009). Age-related changes in GAD levels in the central auditory system of the rat. *Exp. Gerontol.* 44, 161–169.

Cai, H., Carney, L. H., and Colburn, H. S. (1998a). A model for binaural response properties of inferior colliculus neurons. I. A model with interaural time difference-sensitive excitatory and inhibitory inputs. *J. Acoust. Soc. Am.* 103, 475–493.

Cai, H., Carney, L. H., and Colburn, H. S. (1998b). A model for binaural response properties of inferior colliculus neurons. II. A model with interaural time difference-sensitive excitatory and inhibitory inputs and an adaptation mechanism. *J. Acoust. Soc. Am.* 103, 494–506.

Cant, N. B., and Benson, C. G. (2006). Organization of the inferior colliculus of the gerbil (Meriones unguiculatus): Differences in distribution of projections from the cochlear nuclei and the superior olivary complex. *J. Comp. Neurol.* 495, 511–528.

Caspary, D. M., Arneric, S. P., Raza, A., and Finlayson, P. (1990a). Age related changes in the auditory system of the Fischer-344 Rat. *J. Am. Geriatr. Soc.* 38, A15–A15.

Caspary, D. M., Raza, A., Armour, B. A. L., Pippin, J., and Arneric, S. P. (1990b). Immunocytochemical and neurochemical evidence for age-related loss of GABA in the inferior colliculus – implications for neural presbycusis. *J. Neurosci.* 10, 2363–2372.

Caspary, D. M., Ling, L., Turner, J. G., and Hughes, L. F. (2008). Inhibitory neurotransmission, plasticity and aging in the mammalian central auditory system. *J. Exp. Biol.* 211, 1781–1791.

Caspary, D. M., Palombi, P. S., and Hughes, L. F. (2002). GABAergic inputs shape responses to amplitude modulated stimuli in the inferior colliculus. *Hear. Res.* 168, 163–173.

Coomes Peterson, D., and Schofield, B. R. (2007). Projections from auditory cortex contact ascending pathways that originate in the superior olive and inferior colliculus. *Hear. Res.* 232, 67–77.

Cooper, A. P., and Gillespie, D. C. (2011). Synaptotagmins I and II in the developing rat auditory brainstem: Synaptotagmin I is transiently expressed in glutamate-releasing immature inhibitory terminals. *J. Comp. Neurol.* 519, 2417–2433.

Cui, Y. L., Holt, A. G., Lomax, C. A., and Altschuler, R. A. (2007). Deafness associated changes in two-pore domain potassium channels in the rat inferior colliculus. *Neuroscience* 149, 421–433.

Dicke, U., Ewert, S. D., and Dau, T. (2007). A neural circuit transforming temporal periodicity information into a rate-based representation in the mammalian auditory system. *J. Acoust. Soc. Am.* 121, 310–326.

Elhilali, M., Fritz, J. B., Klein, D. J., Simon, J. Z., and Shamma, S. A. (2004). Dynamics of precise spike timing in primary auditory cortex. *J. Neurosci.* 24, 1159–1172.

Finlayson, P. G. (2002). Paired-tone stimuli reveal reductions and alterations in temporal processing in inferior colliculus neurons of aged animals. *J. Assoc. Res. Otolaryngol.* 3, 321–331.

Frisina, D. R., and Frisina, R. D. (1997). Speech recognition in noise and presbycusis: relations to possible neural mechanisms. *Hear. Res.* 106, 95–104.

Frisina, R. D., Smith, R. L., and Chamberlain, S. C. (1990). Encoding of amplitude modulation in the gerbil cochlear nucleus: I. A hierarchy of enhancement. *Hear. Res.* 44, 99–122.

Geis, H. R., and Borst, J. G. G. (2009). Intracellular responses of neurons in the mouse inferior colliculus to sinusoidal amplitude-modulated tones. *J. Neurophysiol.* 101, 2002–2016.

Grothe, B. (1994). Interaction of excitation and inhibition in processing of pure-tone and amplitude-modulated stimuli in the medial superior olive of the moustached bat. *J. Neurophysiol.* 71, 706–721.

Grothe, B., Park, T. J., and Schuller, G. (1997). Medial superior olive in the free-tailed bat: response to pure tones and amplitude-modulated tones. *J. Neurophysiol.* 77, 1553–1565.

Guerin, A., Jeannes Rle, B., Bes, J., Faucon, G., and Lorenzi, C. (2006). Evaluation of two computational models of amplitude modulation coding in the inferior colliculus. *Hear. Res.* 211, 54–62.

Helfert, R. H., Sommer, T. J., Meeks, J., Hofstetter, P., and Hughes, L. F. (1999). Age-related synaptic changes in the central nucleus of the inferior colliculus of Fischer-344 rats. *J. Comp. Neurol.* 406, 285–298.

Hermann, J., Grothe, B., and Klug, A. (2009). Modeling short-term synaptic plasticity at the calyx of held using in vivo-like stimulation patterns. *J. Neurophysiol.* 101, 20–30.

Hermann, J., Pecka, M., Von Gersdorff, H., Grothe, B., and Klug, A. (2007). Synaptic transmission at the calyx of held under in vivo like activity levels. *J. Neurophysiol.* 98, 807–820.

Herrera, M., Delcampo, F. S., Puchades, A., and Correa, J. (1989). Axonal patterns of disc-shaped cells in the central nucleus of the cat inferior colliculus. *Z. Mikrosk. Anat. Forsch.* 103, 515–525.

Hewitt, M. J., and Meddis, R. (1994). A computer model of amplitude-modulation sensitivity of single units in the inferior colliculus. *J. Acoust. Soc. Am.* 95, 2145–2159.

Hines, M. L., and Carnevale, N. T. (2001). NEURON: a tool for neuroscientists. *Neuroscientist* 7, 123–135.

Holt, A. G., Asako, M., Lomax, C. A., MacDonald, J. W., Tong, L., Lomax, M. I., et al. (2005). Deafness-related plasticity in the inferior colliculus: gene expression profiling following removal of peripheral activity. *J. Neurochem.* 93, 1069–1086.

Ito, T., Bishop, D. C., and Oliver, D. L. (2009). Two classes of GABAergic neurons in the inferior colliculus. *J. Neurosci.* 29, 13860–13869.

Joris, P. X., Smith, P. H., and Yin, T. C. (1998). Coincidence detection in the auditory system: 50 years after Jeffress. *Neuron* 21, 1235–1238.

Joris, P. X., and Yin, T. C. T. (1998). Envelope coding in the lateral superior olive. III. Comparison with afferent pathways. *J. Neurophysiol.* 79, 253–269.

Kelly, J. B., and Caspary, D. (2005). "Chapter 9: pharmacology of the inferior colliculus," in *The Inferior Colliculus With 168 Illustrations*, eds. J. A. Winer and C. Schreiner (New York, NY: Springer), 248–281.

Kharkovets, T., Hardelin, J. P., Safieddine, S., Schweizer, M., El-Amraoui, A., Petit, C., et al. (2000). KCNQ4, a K+ channel mutated in a form of dominant deafness, is expressed in the inner ear and the central auditory pathway. *Proc. Natl. Acad. Sci. U.S.A.* 97, 4333–4338.

Koch, U., and Grothe, B. (2003). Hyperpolarization-activated current (I-h) in the inferior colliculus: distribution and contribution to temporal processing. *J. Neurophysiol.* 90, 3679–3687.

Krebs, B., Lesica, N. A., and Grothe, B. (2008). The representation of amplitude modulations in the mammalian auditory midbrain. *J. Neurophysiol.* 100, 1602–1609.

Krishna, B. S., and Semple, M. N. (2000). Auditory temporal processing: responses to sinusoidally amplitude-modulated tones in the inferior colliculus. *J. Neurophysiol.* 84, 255–273.

Langner, G., and Schreiner, C. E. (1988). Periodicity coding in the inferior colliculus of the cat. I. Neuronal mechanisms. *J. Neurophysiol.* 60, 1799–1822.

Loftus, W. C., Bishop, D. C., and Oliver, D. L. (2010). Differential patterns of inputs create functional zones in central nucleus of inferior colliculus. *J. Neurosci.* 30, 13396–13408.

Lorteije, J. A. M., Rusu, S. I., Kushmerick, C., and Borst, J. G. (2009). Reliability and precision of the mouse calyx of held synapse. *J. Neurosci.* 29, 13770–13784.

Magee, J. C., and Cook, E. P. (2000). Somatic EPSP amplitude is independent of synapse location in hippocampal pyramidal neurons. *Nat. Neurosci.* 3, 895–903.

Malmierca, M. S., Saint Marie, R. L., Merchan, M. A., and Oliver, D. L. (2005). Laminar inputs from dorsal cochlear nucleus and ventral cochlear nucleus to the central nucleus of the inferior colliculus: two patterns of convergence. *Neuroscience* 136, 883–894.

Mardia, K. V., and Jupp, P. E. (2000). *Directional Statistics.* New York: Wiley.

Marianowski, R., Liao, W. H., Van Den Abbeele, T., Fillit, P., Herman, P., Frachet, B., et al. (2000). Expression of NMDA, AMPA and GABA(A) receptor subunit mRNAs in the rat auditory brainstem. I. Influence of early auditory deprivation. *Hear. Res.* 150, 1–11.

Mei, Y., Gawai, K. R., Nie, Z. Z., Ramkumar, V., and Helfert, R. H. (1999). Age-related reductions in the activities of antioxidant enzymes in the rat inferior colliculus. *Hear. Res.* 135, 169–180.

Melov, S. (2004). Modeling mitrochondiral function in aging neurons. *Trends Neurosci.* 27, 601–606.

Møller, A. R. (1972). Coding of amplitude and frequency modulated sounds in the cochlear nucleus of the rat. *Acta Physiol. Scand.* 86, 223–238.

Nelson, P. C., and Carney, L. H. (2004). A phenomenological model of peripheral and central neural responses to amplitude-modulated tones. *J. Acoust. Soc. Am.* 116, 2173–2186.

Oliver, D. L. (1984). Neuron types in the central nucleus of the inferior colliculus that project to the medial geniculate body. *Neuroscience* 11, 409–424.

Oliver, D. L., Kuwada, S., Yin, T. C. T., Haberly, L. B., and Henkel, C. K. (1991). Dendritic and axonal morphology of HRP-injected neurons in the inferior colliculus of the cat. *J. Comp. Neurol.* 303, 75–100.

Oliver, D. L., Ostapoff, E. M., and Beckius, I. E. (1999). Direct innervation

of identified tectothalamic neurons in the inferior colliculus by axons from the cochlear nucleus. *Neuroscience* 93, 643–658.

Paloff, A. M., Usunoff, K. G., and Hinovapalova, D. V. (1992). Ultrastructure of golgi-impregnated and gold-toned neurons in the central nucleus of the inferior colliculus in the cat. *J. Hirnforsch.* 33, 361–407.

Palombi, P. S., Backoff, P. M., and Caspary, D. M. (2001). Responses of young and aged rat inferior colliculus neurons to sinusoidally amplitude modulated stimuli. *Hear. Res.* 153, 174–180.

Paolini, A. G., and Clark, G. M. (1999). Intracellular responses of onset chopper neurons in the ventral cochlear nucleus to tones: evidence for dual-component processing. *J. Neurophysiol.* 81, 2347–2359.

Parthasarathy, A., and Bartlett, E. (2012). Two-channel recording of auditory-evoked potentials to detect age-related deficits in temporal processing. *Hear. Res.* 289, 52–62.

Parthasarathy, A., and Bartlett, E. L. (2011). Age-related auditory deficits in temporal processing in F-344 rats. *Neuroscience* 192, 619–630.

Parthasarathy, A., Cunningham, P. A., and Bartlett, E. L. (2010). Age-related differences in auditory processing as assessed by amplitude-modulation following responses in quiet and in noise. *Front. Aging Neurosci.* 2:152. doi:10.3389/fnagi.2010.00152

Paxinos, G., and Watson, C. (2006). *The Rat Brain in Stereotaxic Coordinates.* San Diego, CA: Academic Press.

Peruzzi, D., Sivaramakrishnan, S., and Oliver, D. L. (2000). Identification of cell types in brain slices of the inferior colliculus. *Neuroscience* 101, 403–416.

Rabang, C. F., and Bartlett, E. L. (2011). A computational model of cellular mechanisms of temporal coding in the medial geniculate body (MGB). *PLoS ONE* 6, e29375. doi:10.1371/journal.pone.0029375

Raza, A., Milbrandt, J. C., Arneric, S. P., and Caspary, D. M. (1994). Age-related changes in brain-stem auditory neurotransmitters – measures of GABA and acetylcholine function. *Hear. Res.* 77, 221–230.

Reed, M. C., and Blum, J. J. (1999). Model calculations of steady state responses to binaural stimuli in the dorsal nucleus of the lateral lemniscus. *Hear. Res.* 136, 13–28.

Rees, A., and Moller, A. R. (1987). Stimulus properties influencing the responses of inferior colliculus neurons to amplitude-modulated sounds. *Hear. Res.* 27, 129–143.

Rees, A., and Palmer, A. R. (1989). Neuronal responses to amplitude-modulated and pure-tone stimuli in the guinea pig inferior colliculus, and their modification by broadband noise. *J. Acoust. Soc. Am.* 85, 1978–1994.

Rothman, J. S., and Manis, P. B. (2003). The roles potassium currents play in regulating the electrical activity of ventral cochlear nucleus neurons. *J. Neurophysiol.* 89, 3097–3113.

Schatteman, T. A., Hughes, L. F., and Caspary, D. M. (2008). Aged-related loss of temporal processing: altered responses to amplitude modulated tones in rat dorsal cochlear nucleus. *Neuroscience* 154, 329–337.

Schneider, B. A., Pichorafuller, M. K., Kowalchuk, D., and Lamb, M. (1994). Gap detection and the precedence effect in young and old adults. *J. Acoust. Soc. Am.* 95, 980–991.

Shackleton, T. M., McAlpine, D., and Palmer, A. R. (2000). Modelling convergent input onto interaural-delay-sensitive inferior colliculus neurones. *Hear. Res.* 149, 199–215.

Sivaramakrishnan, S., and Oliver, D. (2006). Neuronal responses to lemniscal stimulation in laminar brain slices of the inferior colliculus. *J. Assoc. Res. Otolaryngol.* 7, 1–14.

Sivaramakrishnan, S., and Oliver, D. L. (2001). Distinct K currents result in physiologically distinct cell types in the inferior colliculus of the rat. *J. Neurosci.* 21, 2861–2877.

Smith, P. (1992). Anatomy and physiology of multipolar cells in the rat inferior collicular cortex using the in vitro brain slice technique. *J. Neurosci.* 12, 3700–3715.

Strouse, A., Ashmead, D. H., Ohde, R. N., and Grantham, D. W. (1998). Temporal processing in the aging auditory system. *J. Acoust. Soc. Am.* 104, 2385–2399.

Tan, M. L., and Borst, J. G. G. (2007). Comparison of responses of neurons in the mouse inferior colliculus to current injections, tones of different durations, and sinusoidal amplitude-modulated tones. *J. Neurophysiol.* 98, 454–466.

Tan, M. L., Theeuwes, H. P., Feenstra, L., and Borst, J. G. G. (2007). Membrane properties and firing patterns of inferior colliculus neurons: an in vivo patch-clamp study in rodents. *J. Neurophysiol.* 98, 443–453.

Vale, C., Schoorlemmer, J., and Sanes, D. H. (2003). Deafness disrupts chloride transporter function and inhibitory synaptic transmission. *J. Neurosci.* 23, 7516–7524.

Walton, J. P., Frisina, R. D., and O'Neill, W. E. (1998). Age-related alteration in processing of temporal sound features in the auditory midbrain of the CBA mouse. *J. Neurosci.* 18, 2764–2776.

Walton, J. P., Simon, H., and Frisina, R. D. (2002). Age-related alterations in the neural coding of envelope periodicities. *J. Neurophysiol.* 88, 565–578.

Winer, J. A., Larue, D. T., and Pollak, G. D. (1995). Gaba and glycine in the central auditory-system of the moustache bat – structural substrates for inhibitory neuronal organization. *J. Comp. Neurol.* 355, 317–353.

Wolfart, J., Debay, D., Le Masson, G., Destexhe, A., and Bal, T. (2005). Synaptic background activity controls spike transfer from thalamus to cortex. *Nat. Neurosci.* 8, 1760–1767.

Wu, S. H., Ma, C. L., and Kelly, J. B. (2004). Contribution of AMPA, NMDA, and GABA(A) receptors to temporal pattern of postsynaptic responses in the inferior colliculus of the rat. *J. Neurosci.* 24, 4625–4634.

Yang, L., and Pollak, G. D. (1997). Differential response properties to amplitude modulated signals in the dorsal nucleus of the lateral lemniscus of the mustache bat and the roles of GABAergic inhibition. *J. Neurophysiol.* 77, 324–340.

Yin, T. C., and Chan, J. C. (1990). Interaural time sensitivity in medial superior olive of cat. *J. Neurophysiol.* 64, 465–488.

Zhang, H., and Kelly, J. B. (2006). Responses of neurons in the rat's ventral nucleus of the lateral lemniscus to amplitude-modulated tones. *J. Neurophysiol.* 96, 2905–2914.

Zhang, H. M., and Kelly, J. B. (2003). Glutamatergic and GABAergic regulation of neural responses in inferior colliculus to amplitude-modulated sounds. *J. Neurophysiol.* 90, 477–490.

Conflict of Interest Statement: The authors declare that the research was conducted in the absence of any commercial or financial relationships that could be construed as a potential conflict of interest.

Received: 29 April 2012; accepted: 05 October 2012; published online: 02 November 2012.

*Citation: Rabang CF, Parthasarathy A, Venkataraman Y, Fisher ZL, Gardner SM and Bartlett EL (2012) A computational model of inferior colliculus responses to amplitude modulated sounds in young and aged rats. Front. Neural Circuits **6**:77. doi: 10.3389/fncir.2012.00077*

APPENDIX

The ionic channels for the model are described by the following equation:

$$I_x = g_x(V_m - E_x)$$

Where g_x is the time-varying conductance for an individual ion channel multiplied by the difference between the membrane potential, V_m and the reversal potential for that ion channel, E_x. The time course and magnitude of the activation and inactivation parameters are given for each of the channel equations listed below. The models were implemented in NEURON v7.1 (Hines and Carnevale, 2001) using a time step of 0.02 ms and a temperature of 34°C. Model cell capacitance for each type were set to a value of 1 μF/cm^2. Times are in ms, voltages are in mV, concentrations are in mM, and currents (unless otherwise stated) are in mA/cm^2.

FAST, TRANSIENT NA$^+$ CURRENT (TRAUB ET AL., 2003)

$$I_{Na} = g_{Na} m^3 h(V_m - E_{Na})$$
$$\tau_m = 1/(\alpha_m + \beta_h)$$
$$m_\infty = \alpha_m/(\alpha_m + \beta_m)$$
$$\alpha_m = [0.32(-(V_m + 39))]/[e^{(-(V_m+39)/4)} - 1]$$
$$\beta_m = [0.28 * ((V_m + 12)]/[e^{((V_m+12)/5)} - 1]$$
$$\tau_h = 1/(\alpha_h + \beta_h)$$
$$h_\infty = \alpha_h/(\alpha_h + \beta_h)$$
$$\alpha_h = 0.128e^{(-(V_m+35)/18)}$$
$$\beta_h = 4/[1 + \exp^{(-(V_m+12)/5)}]$$

POTASSIUM DELAYED RECTIFIER CURRENT (TRAUB ET AL., 2003)

$$I_{Kdr} = g_{Kdr} n^4 (V_m - E_K)$$
$$n_\infty = 1/[1 + e^{(-(V_m+5.3)/10.8)}]$$
$$\tau_n = 0.25 + 4.35e^{((V_m+10)/10)} \text{ for } V_m < -10\text{mV}$$
$$\tau_n = 0.25 + 4.35e^{((V_m+10)/10)} \text{ for } V_m > -10\text{mV}$$

POTASSIUM CURRENT (TEA-SENSITIVE; SIVARAMAKRISHNAN AND OLIVER, 2001; TRAUB ET AL., 2003)

$$I_{Ktea} = g_{Kdr} n^4 (V_m - E_K)$$
$$n_\infty = 1/[1 + e^{(-(V_m+7.2)/8.9)}]$$
$$\tau_n = 0.25 + 4.35e^{((V_m+10)/10)} \text{ for } V_m < -10\text{mV}$$
$$\tau_n = 0.25 + 4.35e^{((V_m+10)/10)} \text{ for } V_m \geq -10\text{mV}$$

I_H CHANNEL (KOCH AND GROTHE, 2003)

$$I_h = g_h m(V_m - E_h)$$
$$m_\infty = 1/[1 + e^{((V_m+79.5)/9.8)}]$$
$$\tau_m = 1.475 + 1/[e^{(-7.647-0.038V_m)+e(-1.533+0.046V_m)}]$$

I_H CHANNEL, ONSET (KOCH AND GROTHE, 2003)

$$I_h = g_h m(V_m - E_h)$$
$$m_\infty = 1/[1 + e^{((V_m+79.5)/9.8)}]$$
$$\tau_m = 3.21 + 1/[e^{(-7.63-0.042V_m)} + e^{(-1.22+0.052V_m)}]$$

LOW-THRESHOLD CA^{2+} CURRENT (I_T; HUGUENARD AND MCCORMICK, 1992)

$$I_T = P_{CaT} m^2 h G(V_m, Ca_o, Ca_i)$$
$$G(V, Ca_o, Ca_i) =$$
$$(Z^2F^2V_m/RT)[(Ca_i - Ca_o e^{(-ZFV_m/RT)})/(1 - e^{(-ZFV_m/RT)})]$$
$$m_\infty = 1/(1 + e^{(-(V_m+57)/6.2)})$$
$$h_\infty = 1/(1 + e^{((V_m+81)/4)})$$
$$\tau_m = 0.612 + 1.0/(\exp(-(v + 132)/16.7) + \exp((v + 16.8)/18.2))$$
$$\tau_h = e^{((V_m+467)/66.6)} \text{ for } V_m < -80$$
$$\tau_h = 28 + e^{(-(V_m+22)/10.5)} \text{ for } V_m \geq -80$$

HIGH-THRESHOLD CA^{2+} CURRENT (I_L; MCCORMICK AND HUGUENARD, 1992)

$$I_L = P_{CaL} m^2 h G(V_m, Ca_o, Ca_i)$$
$$G(V, Ca_o, Ca_i) =$$
$$(Z^2F^2V_m/RT)[(Ca_i - Ca_o e^{(-ZFV_m/RT)})/(1 - e^{(-ZFV_m/RT)})]$$
$$\alpha_m = 1.6/[1 + e^{(-0.072(V_m-5.0))}]$$
$$\beta_m = 0.02(V_m - 1.31)/[e^{((V_m-1.31)/5.36)} - 1]$$
$$m_\infty = \alpha_m/(\alpha_m + \beta_m)$$
$$\tau_m = 1/(\alpha_m + \beta_m)$$

CA-DEPENDENT POTASSIUM CHANNELS (BK/SK; ARADI AND HOLMES, 1999; SIVARAMAKRISHNAN AND OLIVER, 2001)

$$I_{KCa} = (g_{bk} + g_{sk})(V_m - E_K)$$
$$g_{bk} = g_{bk}\text{bar} * rs^2$$
$$g_{sk} = g_{sk}\text{bar}q^2$$
$$q = \alpha_q/(\alpha_q + \beta_q)$$
$$r = 7.5/(7.5 + \beta_r)$$
$$s = 1/(1 + 4/(1000 * Ca_i))$$
$$\alpha_q = 0.00246/e^{(12 \log 10(Ca_i)+28.48)/-4.5}$$
$$\beta_q = 0.006/e^{(12 \log 10(Ca_i)+60.4)/35}$$
$$\beta_r = 0.11/e^{((V_m-35)/14.9)}$$

LOW THRESHOLD POTASSIUM CHANNEL (ROTHMAN AND MANIS, 2003; ZHOU ET AL., 2005)

$$I_{KLT} = g_{KLT} * w^4 z * (V_m - E_K)$$
$$W_\infty = 1/(1 + e^{(-(V_m+48)/6)})^{1/4}$$
$$\tau_W = 1.5 + 100/(6e^{((V_m+60)/6)} + 16e^{(-(V_m+60)/45)})$$
$$Z_\infty = 0.5 + 0.5/(1 + e^{((V_m+71)/10)})$$
$$\tau_z = 50 + 1000/(e^{((V_m+60)/20)} + e^{(-(V_m+60)/8)})$$

HIGH THRESHOLD POTASSIUM CHANNEL (ROTHMAN AND MANIS, 2003; ZHOU ET AL., 2005)

$$I_{KHT} = g_{KHT} * (0.85n^2 + 0.15p) * (V_m - E_K)$$
$$n_\infty = 1/(1 + e^{(-(V_m+15)/5)})^2$$
$$\tau_n = 0.7 + 100/(11e^{((V_m+60)/24)} + 21e^{(-(V_m+60)/23)})$$
$$p_\infty = 1/(1 + e^{(-(V_m+23)/6)})$$
$$\tau_p = 5 + 100/(4e^{((V_m+60)/32)} + 5e^{(-(V_m+60)/22)})$$

RAPIDLY INACTIVATING POTASSIUM CHANNEL (ROTHMAN AND MANIS, 2003)

$$I_A = g_{kA} * (a^4)b * c * (V_m - E_K)$$
$$a_\infty = (1/(1 + e^{(-(V_m+31)/6)}))^{1/4}$$
$$b_\infty = (1/(1 + e^{((V_m+66)/7)}))^{1/2}$$
$$c_\infty = (1/(1 + e^{((V_m+66)/7)}))^{1/2}$$
$$\tau_a = 0.1 + (100/(7e^{((V_m+60)/14)} + 29e^{(-(V_m+60)/24)}))$$
$$\tau_b = 1 + (1000/(14e^{((V_m+60)/27)} + 29e^{(-(V_m+60)/24)}))$$
$$\tau_c = 10 + (90/(1 + e^{(-(66+V_m)/17)}))$$

IC ADAPTING MODEL

The IC Adapting model is based on the Rebound-adapting response neurons found in IC, which are characterized by adaptation during sustained firing to depolarizing current and calcium rebound following hyperpolarizing currents (Sivaramakrishnan and Oliver, 2001; Koch and Grothe, 2003; Tan et al., 2007). The membrane potential of this neuron model is described by the following equation:

$$C * (dV/dt) = I_{Na} + I_{Kdr} + I_h + I_T + I_L + I_{KCa} + I_{syn} + I_{leak}$$

Addition of the calcium activated potassium current I_{KCa} and the high threshold calcium current I_L contributes to the adaptation to depolarization. Inward rectification due to hyperpolarization is accomplished with the addition of I_h. The low threshold calcium current I_T produces the depolarizing rebound following hyperpolarization.

The Na^+ and delayed rectifier K^+ current equations were taken from Traub et al. (2003). The maximal conductance values were adjusted to produce current values similar to those observed in Sivaramakrishnan and Oliver (2001; **Table A1** in Appendix). Both the low-threshold and high-threshold calcium ion current equations were taken from a modeling study in the thalamus (Huguenard and McCormick, 1992). The values for maximal ion permeability P_{Ca} was adjusted to fit current values (**Table A1** in Appendix). Sivaramakrishnan and Oliver (2001) observed potassium channels that were calcium-dependent and could be affected by either apamin (small conductance channels, SK) or charybdotoxin (large conductance channels, BK). We take existing kinetic models for SK and BK calcium-dependent potassium channels from a modeling study of hippocampal dentate granule cells (Aradi and Holmes, 1999) and adjusted the maximal conductance values g_{bk} bar and g_{sk} bar to fit current values found in Sivaramakrishnan and Oliver (2001; **Table A1** in Appendix).

IC SUSTAINED MODEL

The sustained model is based on the sustained-regular cells, which have a nonadapting sustained firing pattern in response to depolarizing current.

$$C * (dV/dt) = I_{Na} + I_{Kdr} + I_{Ktea} + I_{KHT} + I_{syn} + I_{leak}$$

The Na^+ and delayed rectifier K^+ current equations were taken from Traub et al. (2003). The maximal conductance values were

Table A1 | Model parameters for sustained, adapting, pause-build, and rebound-transient patterns.

	Adapting	Sustained	Pause-build	Rebound-transient
Model surface area (μm^2)	373.93	334.9	334.9	373.93
Na^+ reversal potential (mV)	50	50	50	50
K^+ reversal potential (mV)	−90	−90	−90	−90
Membrane leak reversal potential (mV)	−70	−70	−70	−70
Max. transient Na^+ conductance (g_{Na}; S/cm^2)	0.2	0.1	0.1	0.2
Max. delayed rectifier K^+ conductance (g_{Kdr}; S/cm^2)	0.1	0.1	0.1	0.1
Max. T-type Ca^{2+} permeability (P_{CaT})	0.00002 cm/s			0.00002 cm/s
Max. L-type Ca^{2+} permeability (P_{CaL})	0.00001 cm/s			0.00003 cm/s
Max. Ca^{2+} Activated K^+ conductance (BK; S/cm^2)	0.00226			0.0375
Max. Ca^{2+} Activated K^+ conductance (SK)	0.03 S/cm^2			0.005 S/cm^2
Max. High-threshold K^+ conductance (g_{KHT}; S/cm^2)		0.005		
Max. Low-threshold K^+ conductance (g_{KLT}; S/cm^2)			0.0006	
Max. TEA-sensitive K^+ conductance (S/cm^2)		0.014	0.014	
Max. A-type K^+ conductance (g_{kA}; S/cm^2)			0.00125	
Max. hyperpolarization-activated cation current (g_h; S/cm^2)	0.000218		0.0002	0.0001
Leak conductance	0.0000149	0.00019	0.000028	0.00005
AMPA reversal potential (mV)	0	0	0	0
NMDA reversal potential (mV)	20	20	20	20
$GABA_A$ reversal potential (mV)	−80	−80	−80	−80

Table A2 | Onset model parameters.

	Onset
Model surface area (μm^2)	380.46
Na^+ reversal potential	50 mV
K^+ reversal potential	−85 mV
Membrane leak reversal potential	−73 mV
Max. transient Na^+ conductance (g_{Na})	0.22 S/cm^2
Max. delayed rectifier K^+ conductance (g_{Kdr})	0.01592 S/cm^2
Max. Low-threshold K^+ conductance (g_{KLT})	0.0035 S/cm^2
Max. TEA-sensitive K^+ conductance	0.01592 S/cm^2
Max. hyperpolarization-activated cation current (g_h)	0.000577 S/cm^2
Leak conductance	0.00025 S/cm^2
AMPA reversal potential	0 mV
NMDA reversal potential	20 mV

Table A3 | Synaptic current parameter values.

	A	tau1 (ms)	tau 2 (ms)
AMPA	1.0526	0.5464	6
NMDA	0.56	32	50
GABAA	1.4085	3	15

Table A4 | AMPA and GABA depression equation constants.

	AMPA	GABA
A1	0.378	1
A2	0.622	–
A3	115.4	–
A4	115.3	–
TauR (ms)	63.73	16.85
TauR2 (ms)	3.32	–
TauR3 (ms)	69.7	–
TauR4 (ms)	70.46	–

adjusted to produce current values similar to those observed in Sivaramakrishnan and Oliver (2001; **Table A1** in Appendix). Sivaramakrishnan and Oliver (2001) identified tetraethylammonium chloride (TEA-Cl) and 4-aminopyridine (4-AP) sensitive delayed rectifier K^+channels. For the Sustained, Pause-Build, and Onset models, we have added a TEA-sensitive delayed rectifier channel, I_{Ktea} by adjusting the steady-state activation equations from the delayed rectifier current I_{Kdr}. Equations for a high threshold potassium channel I_{kHT} were taken from a modeling study in medial superior olive (Zhou et al., 2005). Conductance values for I_{KHT} were adjusted to fit firing patterns to injected current pulses.

IC PAUSE-BUILD, REBOUND-SUSTAINED, REBOUND-TRANSIENT, ONSET MODELS

The pause-build model was created by modifying the IC Sustained Model and adjusting channel conductance values as shown in **Table A1** in Appendix, following the findings in Sivaramakrishnan and Oliver (2001). An A-type potassium conductance was added, along with a small I_h current, while the high-threshold potassium conductance was removed and the leak conductance were lowered somewhat.

The Rebound-Sustained model was created by modifying the IC Sustained Model, adding in a T-type calcium permeability (0.00002 S/cm^2) and a weak I_h current (0.0000644 S/cm^2).

The Rebound-Transient model was created by modifying the IC Adapting Model and adjusting the BK and SK Ca^{2+} channel conductance values such that the BK conductance was larger than the SK conductance, as reported by Sivaramakrishnan and Oliver (2001).

The Onset model, like the Sustained and Pause-Build model, has 4-AP and TEA-sensitive components of the delayed rectifier K+ current (**Table A2**). In addition, a low-threshold K+ current modeled from VCN neurons (Rothman and Manis, 2003) is also added. The kinetic equations for activation were adjusted according to Koch and Grothe (2003) to reflect rapid activation of I_h in IC onset neurons. The conductances of each were adjusted to fit firing patterns found in Sivaramakrishnan and Oliver (2001).

GENERATION OF INPUT SPIKE TIMES

Given the rMTF and tMTF of the input sources (**Figure 2**), the average spikes per cycle were generated. A standard deviation of 50% of the average spikes per cycle spikes was typically used, constrained by the total number of spikes per trial. Spike times were generated by selecting from a Gaussian distribution whose width was chosen to generate the vector strength given by the tMTF of the input. The Gaussian widths were determined empirically. A refractory period of 1.5 ms was used, encompassing absolute and relative refractory periods. This produced a series of spike times whose characteristics matched the input rates and vector strengths.

For LSO and VCN input sources, spike trains were generated such that the stimulus onset (∼15 ms) had a higher average spikes per cycle than the sustained portion of the input train (∼735 ms). The onset to sustained average spikes per cycle was set to a ratio of 4:1; however, the overall average spikes per cycle remained the same. This adjustment was made to match PSTH spike data taken from studies in LSO and VCN (Adam et al., 1999; Paolini and Clark, 1999).

GENERATION OF SYNAPTIC CURRENTS

The synaptic current to the computational model is given by the following equation:

$$I_{syn} = \sum I_{EX} + I_{IN}$$

where I_{EX} and I_{IN} are the sum of all independent excitatory or inhibitory synaptic inputs, respectively. The general equation for synaptic current is given as

$$I_{syn(i)} = g(V,t) * (V - E_{rev})$$

where the term g is voltage and time dependent and can be described in the following equation:

$$g(V,t) = g_{max} * p * [A * (\exp(-t/tau1) - \exp(-t/tau2))]$$

Values for A, tau1 and tau2 are given in **Table A3** for the AMPA, NMDA, and $GABA_A$ currents.

Table A5 | Figure parameters.

Figure	Model type	Ex	IN	AMPA (nS)	NMDA (nS)	$GABA_A$ (nS)	GABA decay (ms)	(mV)
Figure 3	A	3 LSO	2 DNLL (AP)	5	1.5	3	15	−60
Figure 4, low-pass	A	2 VCN	4 DNLL (HP)	5	1.5	4	15	−56
Figure 4, band-pass	S	3 LSO*	6 DNLL* (LP)	5	1.5	3	12	−60
Figure 5, all-Pass	A	3 DCN	2 DNLL (AP)	5	1.5	3	20	−56
Figure 5, band reject	A	2 VCN	6 VNLL (36 Hz)	5	1.5	4	15	−60
Figures 6A,B	A	3 DCN	2 DNLL (AP)	5	1.5	3	15	−56
Figures 6C,D	A	2 VCN	4 DNLL (HP)	5	1.5	3	15	−56
Figure 10	S	2 DCN	5 DNLL (HP)	5	1.5	3, 1.5	15	−56
Figure 11	A	4 LSO	6 VNLL (12 Hz)	5	1.5	4, 2	15	−60
Figure 12	A	3 VCN	5 VNLL (32 Hz)	5	1.5	4, 2, 1	15	−56

User-defined low-pass inputs were used for **Figures 4F,H. A, adapting; S, sustained.*

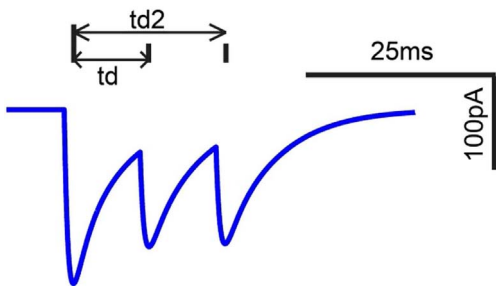

FIGURE A1 | AMPA current exhibiting synaptic depression. t_{d2} and t_d refers to interval relative to current (third) synaptic event.

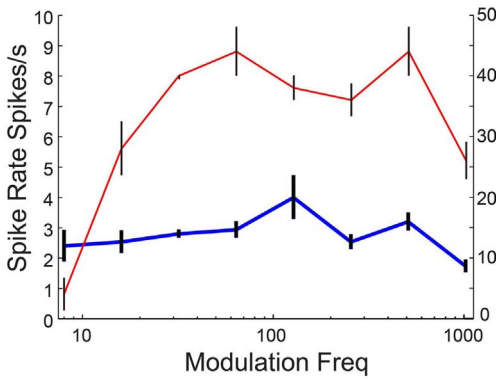

FIGURE A2 | Band-pass responses using excitatory inputs. Blue line shows rate responses taken from 750 ms stimulation duration (Y-axis scale, left). Red line shows rate responses taken from first 50 ms of stimulus onset (Y-axis scale, right).

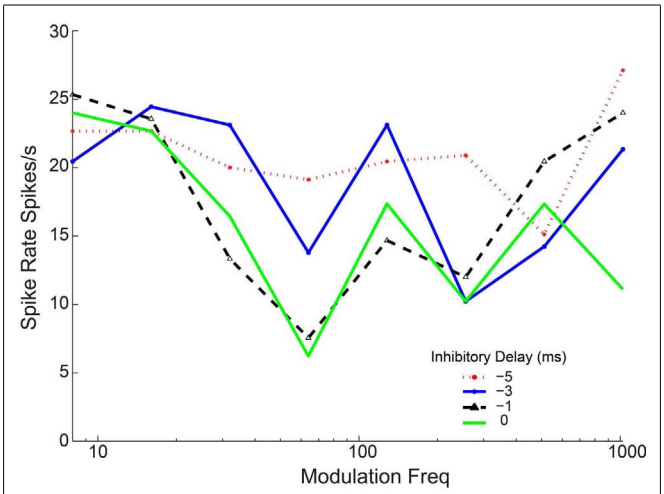

FIGURE A3 | Inhibition timing can affect rMTF response shape. Three VCN excitatory and three DNLL all-pass tuned inhibitory inputs to an Adapting model. Inhibitory inputs adjusted such that they are conincident (green) or precede excitation by 1, 3, or 5 ms (black, blue, red lines, respectively).

The term p refers to a scaling factor that reduces the synaptic conductance due to short-term synaptic plasticity. This scaling factor is dependent on the timing of the two preceding synaptic events and modeled from voltage clamp data from Wu et al., 2004. The general equation describing scaling due to short-term synaptic plasticity is given as follows:

$$P_{\mathrm{AMPA}} = (1 - \mathrm{A1} * \exp(-t_{\mathrm{d}}/\mathrm{tau}R) - \mathrm{A2} * \exp(-t_{\mathrm{d}}/\mathrm{tau}R2)) * (1 + \mathrm{A3} * \exp(-t_{\mathrm{d2}}/\mathrm{tau}R3) - \mathrm{A4} * \exp(-t_{\mathrm{d2}}/\mathrm{tau}R4))$$

$$\mathrm{P}_{\mathrm{GABAA}} = (1 - \mathrm{A1} * \exp(-t_{\mathrm{d}}/\mathrm{tau}R))$$

Here t_{d} refers to the time elapsed from the previous synaptic event in the given synaptic input. The value of t_{d2} refers to the time elapsed from the second previous synaptic event in the given synaptic input. A schematic depicting t_d and t_{d2} for a series of evoked AMPA currents is shown in **Figure A1**. If only two synaptic events are present, the values of A3 and A4 are zero. The equation is an approximation to the time course of synaptic depression, with values of A1–4 and TauR1–4 chosen in order to best fit the EPSC amplitude ratios described in Wu et al. (2004).

For NMDA receptor dependent excitatory currents, g is also voltage-dependent and given by the following equation:

$$B = 1/(1 + 0.28 * \exp(-0.062 * V_m))$$

GENERATION OF BAND-PASS AND BAND-REJECT RESPONSES

Caspary et al. (2002) found band-pass tuning in the presence of bicuculline, suggesting inhibition may not be necessary for band-pass rate tuning. We recreate band-pass responses shown above using an Adapting model and three excitatory VCN inputs with onset EPSPs exhibiting adaptation (**Figure A2** in Appendix). We use inputs using low input (50 spikes/s) rates, reduced AMPA and NMDA conductances (50 and 20%, respectively), and a more hyperpolarized membrane potential (−64 mV).

Band-reject responses were created using 3 VCN excitatory and 3 DNLL all-pass inhibitory inputs. We varied the input timing such that the inhibitory input either preceded (**Figure A3** in Appendix) or lagged excitation (not shown). When inhibition was coincident with (**Figure A3** in Appendix, green line) or briefly preceded excitation (**Figure A3** in Appendix, 0, −1, −3 ms relative to excitation), band-reject responses were observed. If inhibition preceded excitation by >3 ms, all-pass responses were observed (**Figure A3** in Appendix, red dashed line).

REFERENCES

Adam, T. J., Schwarz, D. W., and Finlayson, P. (1999). Firing properties of chopper and delay neurons in the lateral superior olive of the rat. *Exp. Brain Res.* 124, 489–502.

Aradi, I., and Holmes, W. R. (1999). Role of multiple calcium and calcium-dependent conductances in regulation of hippocampal dentate granule cell excitability. *J. Comput. Neurosci.* 6, 215–235.

Huguenard, J. R., and McCormick, D. A. (1992). Simulation of the currents involved in rhythmic oscillations in thalamic relay neurons. *J. Neurophysiol.* 68, 1373–1383.

McCormick, D. A., and Huguenard, J. R. (1992). A model of the electrophysiological properties of thalamocortical relay neurons. *J. Neurophysiol.* 68, 1384–1400.

Traub, R. D., Buhl, E. H., Gloveli, T., and Whittington, M. A. (2003). Fast rhythmic bursting can be induced in layer 2/3 cortical neurons by enhancing persistent Na+ conductance or by blocking BK channels. *J. Neurophysiol.* 89, 909–921.

Zhou, Y., Carney, L. H., and Colburn, H. S. (2005). A model for interaural time difference sensitivity in the medial superior olive: interaction of excitatory and inhibitory synaptic inputs, channel dynamics, and cellular morphology. *J. Neurosci.* 25, 3046–3058.

frontiers in
NEURAL CIRCUITS

ORIGINAL RESEARCH ARTICLE
published: 31 January 2013
doi: 10.3389/fncir.2013.00007

Intracellular responses to frequency modulated tones in the dorsal cortex of the mouse inferior colliculus

H.-Rüdiger A. P. Geis and J. Gerard G. Borst*

Department of Neuroscience, Erasmus MC, University Medical Center Rotterdam, Rotterdam, Netherlands

Edited by:
Manuel S. Malmierca, University of Salamanca, Spain

Reviewed by:
Douglas L. Oliver, University of Connecticut Health Center, USA
Zoltan M. Fuzessery, University of Wyoming, USA

***Correspondence:**
J. Gerard G. Borst, Department of Neuroscience, Erasmus MC, University Medical Center Rotterdam, Dr. Molewaterplein 50, Rotterdam, 3015 GE, Netherlands.
e-mail: g.borst@erasmusmc.nl

Frequency modulations occur in many natural sounds, including vocalizations. The neuronal response to frequency modulated (FM) stimuli has been studied extensively in different brain areas, with an emphasis on the auditory cortex and the central nucleus of the inferior colliculus. Here, we measured the responses to FM sweeps in whole-cell recordings from neurons in the dorsal cortex of the mouse inferior colliculus. Both up- and downward logarithmic FM sweeps were presented at two different speeds to both the ipsi- and the contralateral ear. Based on the number of action potentials that were fired, between 10 and 24% of cells were selective for rate or direction of the FM sweeps. A somewhat lower percentage of cells, 6–21%, showed selectivity based on EPSP size. To study the mechanisms underlying the generation of FM selectivity, we compared FM responses with responses to simple tones in the same cells. We found that if pairs of neurons responded in a similar way to simple tones, they generally also responded in a similar way to FM sweeps. Further evidence that FM selectivity can be generated within the dorsal cortex was obtained by reconstructing FM sweeps from the response to simple tones using three different models. In about half of the direction selective neurons the selectivity was generated by spectrally asymmetric synaptic inhibition. In addition, evidence for direction selectivity based on the timing of excitatory responses was also obtained in some cells. No clear evidence for the local generation of rate selectivity was obtained. We conclude that FM direction selectivity can be generated within the dorsal cortex of the mouse inferior colliculus by multiple mechanisms.

Keywords: patch-clamp, direction selectivity, rate selectivity, FM reconstruction, auditory midbrain

INTRODUCTION

Most natural sounds vary in the frequency domain. Frequency modulation (FM) is an important component of animal communication, including speech (Stein, 1968; Ryan, 1983; Kanwal et al., 1994; Holy and Guo, 2005; Zeng et al., 2005). In addition, FM has been described as a component of echolocation calls in bats and other animals (Simmons and Stein, 1980; Siemers et al., 2009). Within the auditory system, many neurons respond to FM stimuli and a subset of those cells preferentially fire action potentials in response to FM sweeps with a certain rate or direction. These neurons are considered rate- or direction-selective. FM direction selective neurons have been found in the major nuclei of the primary ascending auditory pathway, including the cochlear nucleus, inferior colliculus, medial geniculate body, and the auditory cortex (Whitfield and Evans, 1965; Erulkar et al., 1968; Hage and Ehret, 2003; Lui and Mendelson, 2003; Zhang et al., 2003; Kuo and Wu, 2012). However, there is still relatively little FM direction selectivity in the cochlear nucleus, a major source of inputs to the inferior colliculus. As a result, the mechanisms generating FM selectivity in the central nucleus of the inferior colliculus have received a lot of attention. These studies have demonstrated that spectrally asymmetric synaptic inhibition plays an important role in creating FM direction selectivity within the inferior colliculus (reviewed in Fuzessery et al., 2011; Pollak et al., 2011). In these cells, for the preferred sweep direction excitation precedes inhibition, whereas for the other direction inhibition coincides with excitation. It is still debated whether this mechanism can entirely explain FM direction selectivity within the inferior colliculus, or whether there is an additional role for upstream processing or the timing of excitatory inputs (Suga, 1965; Clopton and Winfield, 1974; Poon et al., 1992; Felsheim and Ostwald, 1996; Gittelman et al., 2009; Williams and Fuzessery, 2011; Kuo and Wu, 2012).

Selectivity for the rate of FM sweeps can also be created by the spectrotemporal interaction of inhibitory and excitatory inputs, but additional mechanisms are thought to play a role as well (Gordon and O'Neill, 1998; Fuzessery et al., 2006; Williams and Fuzessery, 2011, 2012). Much of the rate selectivity of inferior colliculus neurons appears to be already present in their synaptic inputs (Williams and Fuzessery, 2010, 2011; Gittelman and Li, 2011).

Much less is known about FM direction and rate selectivity in the lateral and dorsal cortex than in the central nucleus of the inferior colliculus. The available evidence suggests that the lateral cortex contains a larger proportion of FM selective cells than the dorsal cortex (Poon et al., 1992; Gordon and O'Neill, 2000). The dorsal cortex of the inferior colliculus receives inputs from the inferior colliculus and the auditory cortex, both of which contain

neurons selective for FM (Stiebler et al., 1997; Hage and Ehret, 2003). It is unclear whether direction selectivity can be generated in the dorsal cortex of the inferior colliculus itself. While extracellular recordings allow measuring rate and direction selectivity of neurons based on action potential firing rate, it is more difficult to assess if selectivity is generated in these cells or upstream, even though in combination with local pharmacological block of inhibition the essential role of inhibitory inputs in creating FM selectivity could be demonstrated in the bat inferior colliculus (reviewed in Fuzessery et al., 2011). This question can be more readily addressed with intracellular measurements, which allow the recording of postsynaptic responses to FM sweeps (Voytenko and Galazyuk, 2007; Gittelman et al., 2009; Gittelman and Li, 2011; Kuo and Wu, 2012). One possible approach is to compare the intracellular responses to simple tones at different frequencies and to FM sweeps in the same neuron. If the set of intracellular simple tone responses can be used to reconstruct the intracellular response to a FM sweep, it can be assumed that selectivity was generated *de novo* in this neuron by integration of synaptic inputs. In the auditory cortex, the time-shifted responses to simple tones have been compared to FM evoked responses to explore the contribution of excitation delays and spectral offsets between excitation and inhibition (Ye et al., 2010). A limitation of their approach was that the entire response to the simple tones was used, whereas an FM sweep resides only a limited time at each frequency. During FM responses, the onset responses at each frequency can be expected to be relatively important. Responses to simple tones can appear similar over a range of frequencies and sound pressure levels (SPLs), indicating the activation of a common set of inputs. Such "frequency channels" might be important for the prediction of FM evoked responses, because a FM sweep can reside for a prolonged period of time within the same channel. During this time, the same set of inputs would be activated, allowing adaptation of the response. To account for this, a prediction of FM evoked responses should put emphasis on changes and novelties in the responses to simple tones across frequencies to account for the activation of new frequency channels, while suppressing the influence of consistent responses to simple tones, reflecting the continued activation of the same frequency channel.

Here, we recorded intracellular responses to FM sweeps to study FM selectivity in the dorsal cortex of the inferior colliculus. We presented logarithmic up- and downward FM sweeps with different speeds to assess direction selectivity and rate selectivity. By comparing the responses to FM sweeps and simple tones between cells, we tested for a connection between frequency response areas (FRAs) and the responses to FM sweeps. To explore if FM selectivity can be generated in the dorsal cortex of the inferior colliculus, we reconstructed responses to FM sweeps from FRAs and we develop quantitative measures to quantify how well the reconstruction match the recorded responses.

Our data show that neurons in the dorsal cortex of the inferior colliculus can selectively respond to the direction or rate of FM sweeps. Neurons with similar responses to FM sweeps also had similar FRAs. Our reconstructions of responses to FM sweeps from FRAs suggest that FM selectivity can be generated in the dorsal cortex of the inferior colliculus. In most of the cells spectrally asymmetric inhibition appeared to be the underlying mechanism, but evidence for alternative mechanisms was also found.

MATERIALS AND METHODS

A detailed description of the "Materials and Methods" used was given in Geis et al. (2011).

SURGERY

All experiments were conducted as approved by the Erasmus MC animal care ethics committee. Measurements were done on 80 C57/BL6 mice (Harlan, The Netherlands) of postnatal age between day 21 and 79. Animals were initially anesthetized with an intraperitoneal injection of ketamine–xylazine (65 and 10 mg kg^{-1}). Ketamine–xylazine was supplemented as needed to reach and maintain a surgical level of anesthesia, which was assessed with the hind limb withdrawal reflex. To maintain body core temperature at 37–38°C, animals were placed on a heating pad with rectal feedback (40-90-8C; FHC, Bowdoinham, ME, USA). Eye ointment (Duratears; Alcon Nederland, Gorinchem, The Netherlands) was applied to keep the eyes moist. The skin overlying the skull was incised with a scalpel and lidocaine (Xylocaine 10%; AstraZeneca, Zoetermeer, The Netherlands) was applied to the surface before removing the bone skin. On the cleaned bone above the inferior colliculus, a titanium head plate was attached with super glue. A small hole was drilled more rostrally, above the neocortex, for the reference electrode, which was hooked between dura and bone. Both the head plate and the reference electrode were secured with dental acrylic (Simplex rapid; Associated Dental Products, Purton, UK). The bone overlying the inferior colliculus was thinned and opened via an opening in the center of the head plate. Before puncturing and deflecting the dura, bone wax was applied to the edge of the exposure. The surface of the inferior colliculus was kept moist with Ringer solution containing (in mM): NaCl 135, KCl 5.4, $MgCl_2$ 1, $CaCl_2$ 1.8, Hepes 5 (pH 7.2 with NaOH; Merck, Darmstadt, Germany).

AUDITORY STIMULATION

For closed field auditory stimulation, speaker probes were inserted into the ear canals and fixed with silicon elastomer (Kwik-Cast; WPI, Berlin, Germany). Auditory stimuli were computed in MATLAB v7.0.4 (The MathWorks, Natick, MA, USA), and played back via a TDT system 3 (RP2.1 processor, PA5.1 attenuator, ED1 electrostatic speaker driver, EC1 electrostatic speaker). Intensities were calibrated for frequencies between 1 and 48.5 kHz with a condenser microphone (ACO pacific Type 7017, MA3 stereo microphone amplifier, TDT SigCal). FM sweeps had a duration of 100 ms (fast sweep) or 300 ms (slow sweep), including 2.5 ms rise/decay. Frequency was modulated logarithmically from 1 to 48.5 kHz (upward sweep) or from 48.5 to 1 kHz (downward sweep). Modulated stimuli were presented at intensities between 0 and 80 dB SPL in steps of 10 dB. We compared the responses to FM stimuli with the response to simple tones, which, apart from eight cells, had already been reported previously (Geis et al., 2011; Geis and Borst, 2013). Simple tone stimuli had durations of 100 ms, including 2.5 ms rise/decay. Frequencies

between 1 and 48.5 kHz with five steps per octave were presented at intensities between 0 and 80 dB SPL in steps of 10 dB. Even at the highest intensities, we consider acoustic crosstalk between both ears unlikely to make a sizeable contribution, since recordings under similar conditions at the calyx of Held synapse, a strictly contralaterally innervated nucleus, did not show evidence for acoustic crosstalk even at high intensities (Lorteije and Borst, 2011). Stimulations were repeated 3–20 times, depending on the quality of the recording.

ELECTROPHYSIOLOGY

In vivo whole-cell recordings were done under 2-photon guidance with a custom built microscope (Mai Tai laser, 800 nm; Spectra Physics Lasers, Mountain View, CA, USA) using the "shadow-patching" method (Kitamura et al., 2008), as described earlier (Geis et al., 2011). Glass pipettes (Hilgenberg, Malsfeld, Germany) with 1–2 μm tip diameter were pulled with a horizontal puller (P-97; Sutter Instrument, Novato, CA, USA) and filled with internal solution containing (in mM): potassium gluconate 126, KCl 20, Na_2-phosphocreatine 10, Mg-ATP 4, Na_2-GTP 0.3, EGTA 0.5, Hepes 10 (pH 7.2 with KOH; Merck, Darmstadt, Germany). The internal solution also contained 0.5% biocytin (Sigma-Aldrich, Steinheim, Germany) to retrieve cells histologically and 40 μM Alexa Fluor 594 hydrazide (Invitrogen, Carlsbad, CA, USA) to visualize cells *in vivo*. The inferior colliculus was entered with an initial pipette pressure of 30 kPa and the pressure was adjusted to 3 kPa when approaching a neuron. The brain surface was stabilized with 2% Agar (Sigma-Aldrich, Steinheim, Germany; in Ringer solution). Measurements were amplified with a MultiClamp 700A (10 kHz low pass Bessel filter), digitized with a DigiData 1322A at a sampling rate of 25 kHz, and acquired with pCLAMP 9.2 (all from Molecular Devices, Sunnyvale, CA, USA). Membrane potentials were corrected for a junction potential of −11 mV.

ANALYSIS

Data were analyzed with Igor pro (version 6.2.2.2; WaveMetrics, Lake Oswego, OR, USA) using NeuroMatic (version 2.00; kindly provided by Dr. J. Rothman, University College London) and custom written functions. Action potentials were detected by a threshold criterion and truncated by linearly interpolating the membrane potential 1–3 ms preceding and following the spike. The truncated responses to individual FM stimuli were correlated across repetitions (Geis et al., 2011). If the resulting autocorrelation was significantly different from zero ($p < 0.001$; t-test), the cell was considered responsive to this FM stimulus and we determined the properties of the response. Depending on sweep length, the number of action potentials was counted up to 150 or 350 ms after stimulus onset following a minimum delay of 7 ms after stimulus onset. Evoked rates were corrected for spontaneous firing. The spontaneous firing rate was determined in the 50 ms period before stimulus onset. Truncated membrane potential traces were averaged across all stimulus repetitions. Peak membrane potential amplitudes were detected on the smoothed, averaged membrane potential recordings in the 150 ms following the onset of a fast sweep or in the 350 ms after the onset of a slow sweep.

Selectivity indices for the FM stimuli were calculated both for action potentials and for synaptic potentials. To determine the direction selectivity index (DSI), we divided the difference in response (spikes or potential) between upward (R_{up}) and downward (R_{down}) sweep by the sum of the response to the two sweep directions (Britt and Starr, 1976). Positive DSI values indicate a preference for upward and negative DSI values for downward FM.

$$\mathrm{DSI} = \frac{R_{up} - R_{down}}{R_{up} + R_{down}}$$

The rate selectivity index (RSI) was calculated by subtracting the ratio between the mean response (R_{mean}) and the maximal response (R_{max}) from 1, and multiply by 2 to have RSI values ranging from 0 (no rate preference) to 1 (high rate preference) (Brown and Harrison, 2009).

$$\mathrm{RSI} = 2 \times \left(1 - \left(\frac{R_{mean}}{R_{max}}\right)\right)$$

To compare the responsiveness to modulated and simple stimuli between neurons, we concatenated the measured membrane potentials of the whole FRA of a cell into one vector and the membrane potential in response to all FM sweeps into another vector. Each FRA vector had a total duration of 261 s, consisting of a total of 522 different 100 ms stimuli (29 different frequencies, at nine different intensities presented to both the contra- and ipsilateral ear), at an interstimulus interval of 400 ms. The FM vectors had a total duration of 36 s, containing contiguous 500 ms recordings segments of stimulations with four different FM sweeps (up, down, slow, and fast), at nine different intensities, presented to both the contra- and the ipsilateral ear. Stimulus duration was either 100 or 300 ms, depending on sweep speed. FRA and FM vectors were created for each repetition of the whole stimulus set and cross-correlated to all the corresponding vectors in another cell, excluding correlations of identical repetition number. The resulting cross-correlation values were averaged over repetitions, summarizing the similarity of responses to simple tones or FM sweeps between two neurons in one correlation value.

RECONSTRUCTION

We employed three different models to reconstruct responses to FM sweeps from responses to the simple tones used in the FRA. The simplest model, called "Delay," assumes only a time delay from the onset of the FM sweep until it reaches a specific frequency. Subthreshold potentials in response to simple tones were time shifted and averaged. Since we presented logarithmic FM sweeps and simple tones with logarithmic frequency spacing, for the reconstruction a linear increase in delay between simple tone responses was assumed. Delays for time shifting were therefore calculated by dividing the FM sweep duration by the number of simple tones. By linearly integrating the delay shifted responses to simple tones over the range from 1 to 48.5 kHz, this reconstruction does not take any temporal or spectral non-linearities into account, which might contribute to the generation of FM selective responses.

Our second model used the same time delay, but, in addition, emphasizes the onset response generated by simple tones. We only recorded responses to simple tones with a duration of 100 ms, while the FM sweeps we used passed through the entire frequency range between 1 and 48.5 kHz in 100 or 300 ms total. To reduce the impact of the late response during the response to a 100 ms simple tone and to increase the impact of onset responses, we convoluted subthreshold potential changes with an impulse function of the form $e^{(-(\ln(t/t_{onset})/width)^2)}$, where t was time, t_{onset} the average postsynaptic potential onset time for the given SPL and width was set to values of 0.12 for short and 0.32 for long sweeps. In this "Onset" model, after convolution the responses were time shifted, summed and scaled according to the overlap between the impulse function after time shift.

With our third model, called "Channel," we tried to highlight the influence of different frequency channels on the response to FM sweeps. FRAs contain areas with uniform responses to simple tones of different frequencies, suggesting that the cell receives the same set of inputs for all frequencies within that area. A FM sweep passing through such a frequency channel would activate the same inputs for a prolonged period of time, potentially leading to a reduced response due to prolonged activation. Assuming such an adaptation of the response if a FM sweep moves over frequencies within one frequency channel, and increased responsiveness if a FM sweep enters a new frequency channel, in our reconstruction we only used responses to simple tones if they were larger or if they were sufficiently different from the preceding simple tone responses in the FM reconstruction. Responses were considered larger if a line fit that was constrained to go through the origin in the graph in which the response that came later in the reconstruction is plotted against the earlier resulted in a slope bigger than one. Responses were considered different if the Pearson correlation between the earlier and the later response was less than 0.92. If responses were larger or sufficiently different, the difference between the two time-shifted responses was added to the reconstruction. If this was not the case, the reconstruction was scaled down using a vector. To get this vector, the two tone responses were subtracted after appropriate time shifting. The difference was divided by the maximum size of the absolute response to the earlier tone, clipped to a maximum value of one, after which it was subtracted from 1 and multiplied with the running sum. This strategy ensured that downscaling was proportional to the difference in the responses to the two simple tones.

RESULTS

We made whole-cell recordings from a total of 123 neurons in the dorsal cortex of the inferior colliculus. Their average resting membrane potential was -66 ± 1 mV. The median minimum threshold for postsynaptic potentials was 40 dB SPL. To determine their FM selectivity, we measured their response to logarithmic FM sweeps. A total of 121 neurons showed a consistent synaptic response to at least one FM stimulus. In 31 of these cells only contralateral FM stimulation evoked spikes, in 8 cells only ipsilateral, and in the remaining 26 cells both contra- and ipsilateral FM stimulation evoked spikes.

DIRECTION SELECTIVE NEURONS IN THE DORSAL CORTEX OF THE INFERIOR COLLICULUS

About 20% of neurons in the dorsal cortex of the inferior colliculus showed selectivity to the direction of FM sweeps. Three examples are shown in **Figures 1A–F**. In response to 80 dB FM stimuli presented to the contralateral ear, the cell shown in **Figure 1A** fired action potentials to upward fast or slow modulated sweeps, but not to downward (**Figure 1A**; top row). This firing behavior resulted in a DSI for spikes of +1 for both fast and slow sweeps. Upward FM sweep also evoked larger EPSPs while downward FM sweeps evoked a larger hyperpolarization (**Figure 1A**; bottom row). The difference in EPSP amplitude is reflected in the positive EPSP based DSI values of 0.56 for fast sweeps and 0.18 for slow sweeps.

A relatively frequently occurring mechanism underlying upward direction selective responses was the combination of low frequency excitation and high frequency inhibition. The responses to 80 dB SPL tones of the neuron displayed in **Figure 1A** show clear excitatory and inhibitory frequency areas (**Figure 1B**; right). At low frequencies (bottom arrow, left trace), the neuron responded with an EPSP to stimulation with a simple 100 ms tone (horizontal bar) presented to the contralateral ear at 80 dB SPL. In contrast, at high frequencies (top arrow, right trace) the stimulation evoked an IPSP. Another example of an upward direction selective neuron is shown in **Figures 1C** and **D**. This cell responded with IPSPs and subthreshold EPSPs to FM stimuli. EPSPs were largest for fast upward modulated sweep and very small for fast downward modulated sweeps. This difference resulted in a DSI of 0.62, classifying this cell as upward selective. Similar to the neuron showed in **Figures 1A**,**B**, the responses to 80 dB SPL tones of this neuron also showed low frequency excitation and high frequency inhibition (**Figure 1D**).

Whereas the combination of high frequency inhibition and low frequency excitation could underlie upward FM selective responses, the reverse could underlie downward FM selective responses. The neuron in **Figure 1E** fired more action potentials and showed larger EPSPs in response to downward FM sweeps. Based on a spike based DSI of −0.75 for fast and −0.8 for slow sweeps, as well as an EPSP based DSI of −0.32 for fast and −0.58 for slow sweeps, this cell was classified as downward FM selective. The responses to 80 dB SPL tones of this neuron showed inhibitory and excitatory frequency areas, with inhibition dominating at low frequencies and excitation more prominent at high frequencies (**Figure 1F**).

The majority of the neurons in the dorsal cortex showed little selectivity for the direction of FM sweeps. An example of a cell that was not selective for the direction of FM sweeps is shown in **Figure 1G**. This neuron had a DSI for spikes of −0.26 for fast FM sweeps and of −0.18 for slow sweeps, whereas DSIs for EPSPs were −0.13 and −0.14 for fast and slow sweeps, respectively. The responses to 80 dB SPL tones showed an EPSP, which was longer lasting at both the lowest and the highest frequencies (**Figure 1H**), providing an explanation for the two-peaked synaptic response during FM sweeps. The response to a fast downward modulated sweep did not show a clear second peak, probably owing to the larger delayed EPSP evoked at high frequencies.

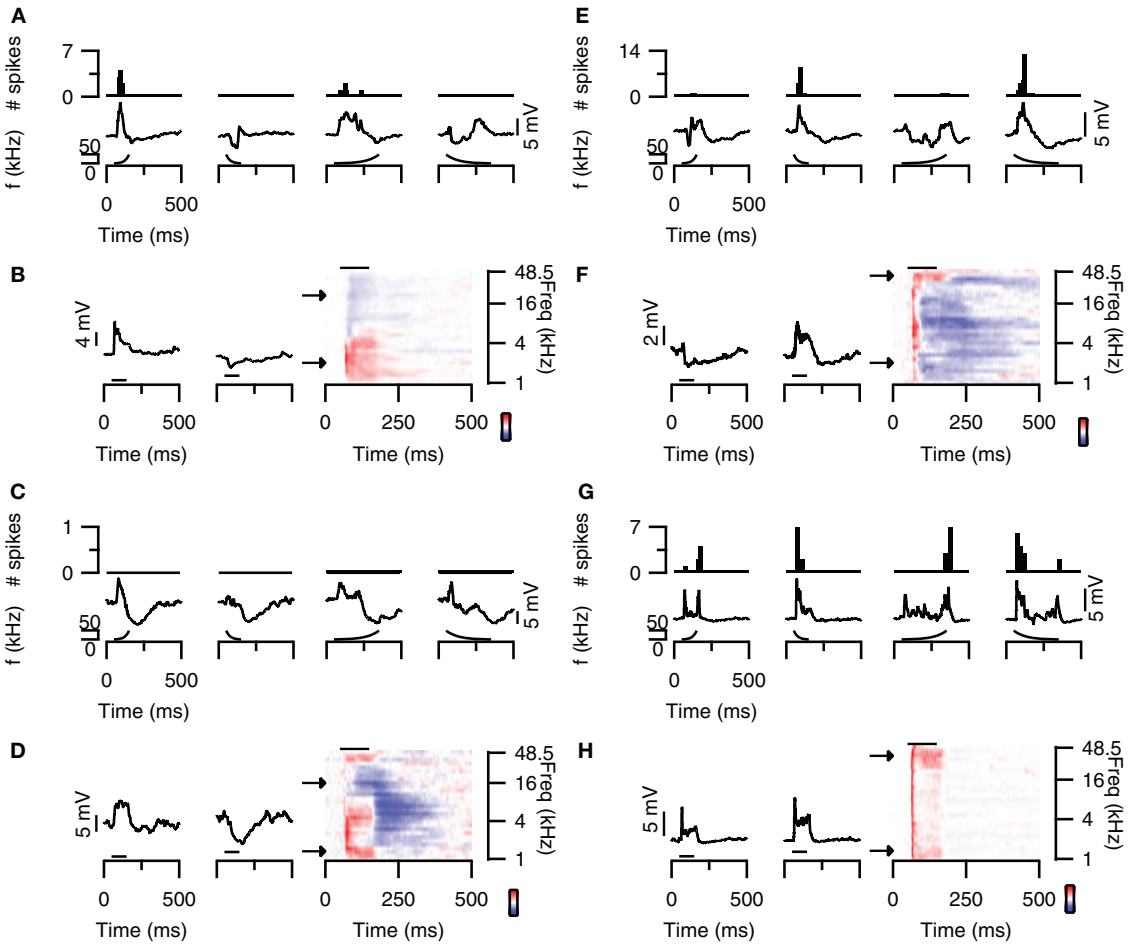

FIGURE 1 | FM direction selectivity in the dorsal cortex of the inferior colliculus. (A) Responses of an upward direction selective neuron. Poststimulus time histograms are shown in the top panel, underlying membrane potential changes in the bottom panel. Resting membrane potential was −64 mV. **(B)** Responses to 80 dB SPL tones of the neurons in **(A)** on the right with two example traces corresponding to the responses to simple tones at the frequencies indicated by the arrows. Color bar indicates ±13 mV. Horizontal bars mark the stimulus. **(C)** Responses of an EPSP-based upward selective neuron that did not fire action potentials. Layout as in **(A)**. Resting membrane potential was −69 mV. **(D)** Responses to 80 dB SPL tones of the neurons in **(C)** on the right with two example traces corresponding to the responses to simple tones at the frequencies indicated by the arrows. Color bar indicates ±12 mV. **(E)** Responses of a spike-based downward direction selective neuron. Layout matches **(A)**. Resting membrane potential was −64 mV. **(F)** Responses to 80 dB SPL tones of the neurons in **(E)** on the right with two example traces corresponding to the responses to simple tones at the frequencies indicated by the arrows. Color bar indicates ±5 mV. **(G)** Responses of a direction unselective neuron. Layout as in **(A)**. Resting membrane potential was −61 mV. **(H)** Responses to 80 dB SPL tones of the neurons in **(G)** on the right with two example traces corresponding to the responses to simple tones at the frequencies indicated by the arrows. Color bar indicates ±13 mV. Stimuli were presented to the contralateral ear at 80 dB SPL.

Figure 2 shows population data for direction selectivity. In most neurons the number of action potentials fired in response to contralateral stimulation with fast up- or downward FM sweeps was similar (**Figure 2A**). The two solid lines in **Figure 2A** indicate a DSI of +0.33 or −0.33, which we used as the cutoff for selectivity. Twenty percent of neurons showed direction selectivity for fast sweeps during contralateral stimulation. The majority of these cells (67%) lined up along the axes, indicating a DSI of +1 or −1. The number of up- and downward selective neurons was similar (**Figure 2C**; **Table 1**). A slightly larger percentage of cells (24%) showed direction selectivity in response to slow FM sweeps presented to the contralateral ear (**Figure 2B**). Of these, slightly more than half (55%) responded exclusively to the preferred direction. More than half (55%) of the neurons that showed direction selectivity to slow sweeps preferred upward sweeps (**Table 1**).

Fewer cells showed direction selectivity in response to ipsilateral stimulation (**Table 1**), but the overall distribution of DSIs was similar for ipsi- and contralateral stimulation (**Figure 2C**). In response to fast FM sweeps presented to the ipsilateral ear, 13% of cells were direction selective. About one third of these fired action potentials only to the preferred direction. No preferred direction was apparent (**Table 1**). Slow FM sweeps presented to the ipsilateral ear revealed 10% direction selective neurons, and 67% of these fired spikes only to sweeps in the preferred direction. Again, there was a somewhat higher percentage of upward than downward selective neurons (**Table 1**), suggesting a slight preference for

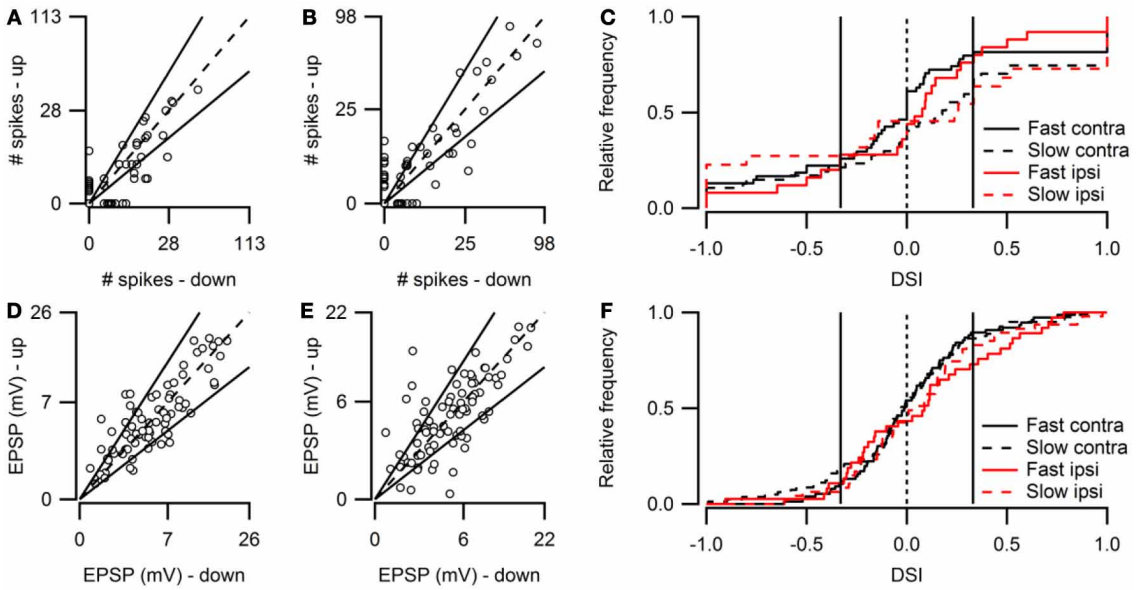

FIGURE 2 | Overview of FM direction selectivity. (A) Number of action potentials evoked by fast upward sweeps plotted against the number of spikes in response to fast downward sweeps presented to the contralateral ear ($n = 84$; 36 cells at origin). Solid lines next to identity line indicate DSI of ±0.33. **(B)** Action potentials fired in response to slow up- and downward sweeps presented to the contralateral ear ($n = 88$; 41 cells at origin). **(C)** Cumulative distribution of spike-based DSIs in response to fast or slow FM sweeps presented to the contra- or ipsilateral ear. Vertical solid lines indicate a DSI of ±0.33. **(D)** EPSP amplitudes in response to fast upward sweeps plotted against amplitudes in response to fast downward sweeps presented to the contralateral ear ($n = 76$). Solid lines indicate DSI of ±0.33. **(E)** EPSP amplitudes evoked by slow up- and downward sweeps presented to the contralateral ear ($n = 81$). **(F)** Cumulative distribution of EPSP amplitude based DSIs in response to fast or slow FM sweeps presented to the contra- or ipsilateral ear. Vertical solid lines indicate a DSI of ±0.33.

Table 1 | Direction and rate selectivity in the dorsal cortex of the inferior colliculus.

		Direction selectivity		Rate selectivity	
		Fast sweep	**Slow sweep**	**Up sweep**	**Down sweep**
Spikes	Contralateral	20% 10up/14down	24% 16up/13down	14% 5fast/12slow	17% 10fast/11slow
	Ipsilateral	13% 7up/9down	10% 8up/4down	11% 6fast/7slow	12% 7fast/8slow
EPSPs	Contralateral	13% 8up/8down	21% 11up/15down	6% 3fast/4slow	7% 4fast/4slow
	Ipsilateral	11% 10up/4down	10% 8up/4down	7% 2fast/7slow	7% 3fast/6slow

Percentage of direction and rate selective neurons for different sets of FM sweeps, as determined by the number of action potentials or the EPSP peak amplitude. FM stimuli were presented to the contra- or ipsilateral ear at 80 dB SPL.

upward modulation in the case of slow sweeps, regardless of the side of stimulation.

Based on EPSP amplitude, 13% of neurons in the dorsal cortex of the inferior colliculus showed direction selectivity to stimulation with fast and 21% to stimulation with slow FM sweeps. The peak amplitudes of the EPSPs in response to fast up- and downward FM sweeps presented to the contralateral ear are shown in **Figure 2D**. Most data points cluster around the unity line, indicating a low percentage of direction selective neurons. The number of neurons responding with larger EPSPs to fast up- or downward sweeps was similar, indicating no clear FM sweep direction preference in response to fast sweeps (**Table 1**). Slow sweeps evoked selective responses more often, with 21% of cells showing EPSP based direction selectivity (**Figure 2E**). There was a slight preference for downward sweeps (**Table 1**).

The distributions of DSIs resulting from stimulation with slow or fast FM sweeps presented to the ipsilateral ear were similar as for the contralateral ear (**Figure 2F**). A shift of the distribution to higher direction selectivity values, suggesting a preference for upward sweeps, was observed only for fast FM sweeps presented to the ipsilateral ear. Stimulation of the ipsilateral ear with fast FM sweeps revealed that 11% of cells were direction selective

(**Table 1**). Of these, 71% preferred upward modulated sweeps. Similar results were obtained for slow FM sweeps presented to the ipsilateral ear; 10% of cells were direction selective, with a preference for upward sweeps (**Table 1**).

The presence of excitatory and inhibitory areas in response to 80 DB SPL tones of different frequencies can explain direction selective responses in about half of the direction selective neurons. Of the eight upward direction selective neurons, five had responses to 80 dB SPL tones with excitatory areas at lower frequencies than their inhibitory areas (**Figure 3A**), similar to the cell shown in **Figures 1A**,**B**. Of the eight downward direction selective neurons, four had responses to 80 dB SPL tones with excitatory areas at higher frequencies and inhibitory areas extending to lower frequencies (**Figure 3B**), similar to the neuron shown in **Figures 1E**,**F**. Of the remaining seven cells, three had responses to 80 dB SPL tones with only excitatory areas (**Figure 1G**), two neurons showed only inhibitory areas and two cells showed a mix of excitatory and inhibitory areas that did not match their direction selectivity. In these seven cells, the direction selective response either was inherited from upstream nuclei, or it followed from a spectrotemporal interaction of excitatory and/or inhibitory conductances other than the mechanism that generated direction selectivity in the cells shown in **Figures 1A–F**.

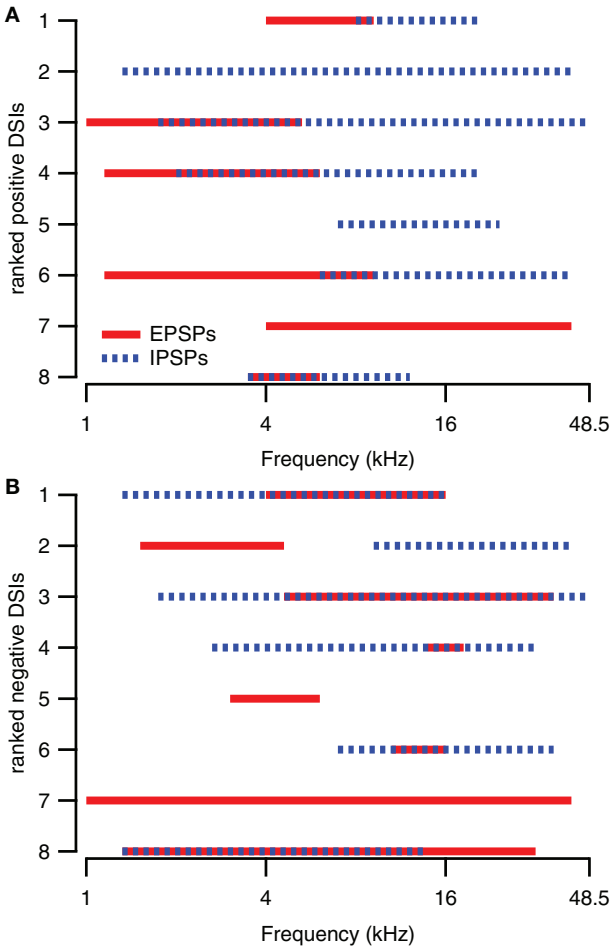

FIGURE 3 | Spectral integration of excitatory and inhibitory areas underlies direction selectivity in about half of the direction selective neurons. (A) Excitatory and inhibitory response areas of upward direction selective neurons (DSI >0.33) determined at 80 dB SPL. **(B)** Excitatory and inhibitory response areas of downward direction selective neurons (DSI <−0.33) determined at 80 dB SPL. The smallest rank was given to the neuron with the largest absolute DSI value.

RATE SELECTIVE NEURONS IN THE DORSAL CORTEX OF THE INFERIOR COLLICULUS

Some neurons in the dorsal cortex of the inferior colliculus showed rate selectivity for FM sweeps. **Figure 4A** (top) shows an example of a cell that mainly fired action potentials in response to fast sweeps. The spike based rate selectivity index was 1 for upward sweeps and 0.93 for downward sweeps. EPSP-based RSIs were much smaller in this cell, but followed the same trend with values of 0.07 for upward sweeps and 0.39 for downward sweeps (**Figure 4A**; bottom). The responses to 80 dB SPL tones of this cell were dominated by excitation, while weak onset inhibition was present at higher frequencies (**Figure 4B**). This inhibition might explain the preference for downward sweeps in this cell, as downward sweeps would first pass through an inhibitory area before entering an excitatory area. This observation, however, does not offer a basis for the observed rate selectivity, as the high frequency onset inhibition appears transient regardless of the downward sweep speed (**Figure 4A**; bottom panel). Instead, the time course of the EPSPs might offer an explanation for the rate selectivity, because at low frequencies EPSPs were more transient with shorter delays, whereas at higher frequencies EPSPs had longer delays and durations. These EPSPs are therefore expected to coincide during fast downward sweeps.

An example of an upward rate selective neuron is shown in **Figure 4C** (top). In this neuron the spike-based RSI was much larger for upward sweeps (0.71) than for downward sweeps (0.06). EPSP amplitudes also differed most between fast and slow upward sweeps, which led to RSIs of 0.40 for upward sweeps and 0 for downward sweeps (**Figure 4C**; bottom). The responses to 80 dB SPL tones of this neuron appeared fairly uniform across frequencies (**Figure 4D**). EPSPs were preceded by onset IPSPs and often followed by a late, slight hyperpolarization. In this rate selective neuron, the response to tones thus did not offer a good explanation for the rate selectivity.

Most neurons in the dorsal cortex of the inferior colliculus did not show FM rate selectivity. An example is shown in **Figure 4E**. Action potentials were elicited at fast and slow sweep rate, resulting in a RSI of 0 for upward and of 0.09 for downward sweeps (**Figure 4E**; top). EPSP amplitudes were also similar between sweep rates, resulting in EPSP-based RSI values of 0.05 for upward and 0.22 for downward sweeps (**Figure 4E**; bottom). The responses to 80 dB SPL tones showed onset excitation across most frequencies, which was followed by delayed excitation at low frequencies and delayed inhibition at higher frequencies (**Figure 4F**). Whereas the interaction between onset and delayed responses would represent a good substrate for rate selectivity in this neuron, we did not observe rate selective responses at the rates tested. Another example of a neuron

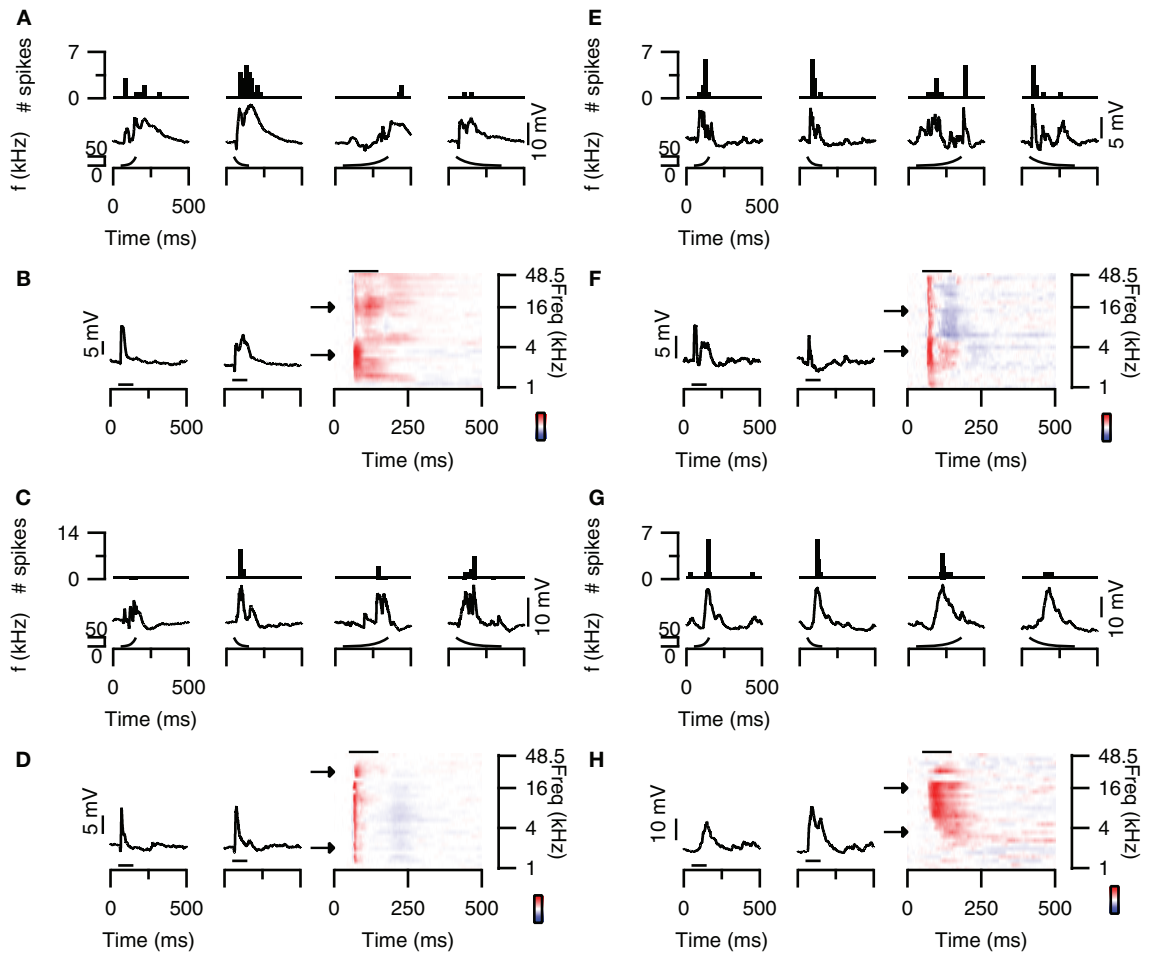

FIGURE 4 | FM rate selectivity. (A) Neuron with fast rate selectivity for downward sweeps. Poststimulus time histograms are shown in the top panel, underlying membrane potential changes in the bottom panel. Resting membrane potential was −58 mV. **(B)** Responses to 80 dB SPL tones of the neurons in **(A)** on the right with two example traces corresponding to the responses to simple tones at the frequencies indicated by the arrows. Color bar indicates ±15 mV. **(C)** Neuron with spike-based slow rate selectivity for upward sweeps. Layout matches **(A)**. Resting membrane potential was −68 mV. **(D)** Responses to 80 dB SPL tones of the neurons in **(C)** on the right with two example traces corresponding to the responses to simple tones at the frequencies indicated by the arrows. Color bar indicates ±15 mV. **(E)** Responses of a rate unselective neuron with EPSPs and IPSPs in the responses to 80 dB SPL tones. Layout as in **(A)**. Resting membrane potential was −65 mV. **(F)** Responses to 80 dB SPL tones of the neurons in **(E)** on the right with two example traces corresponding to the responses to simple tones at the frequencies indicated by the arrows. Color bar indicates ±9 mV. **(G)** Responses of a rate unselective neuron with a mainly excitatory responses to 80 dB SPL tones. Layout as in **(A)**. Resting membrane potential was −65 mV. **(H)** Responses to 80 dB SPL tones of the neurons in **(G)** on the right with two example traces corresponding to the responses to simple tones at the frequencies indicated by the arrows. Color bar indicates ±22 mV. Stimuli were presented to the contralateral ear at 80 dB SPL.

that did not show rate selectivity is displayed in **Figure 4G**. This cell fired action potentials in response to fast and slow upward as well as downward sweeps (**Figure 4G**; top). While the number of spike differed with sweep rate, the RSIs reached only 0.44 for upward sweeps and 0.5 for downward sweeps. EPSP amplitudes were even more similar, resulting in EPSP-based RSIs of 0.18 for upward and 0.04 for downward sweeps (**Figure 4G**; bottom). The responses to 80 dB SPL tones mainly showed excitatory inputs, which had longer delays at low frequencies than at high frequencies (**Figure 4H**). This frequency-dependent difference in delays could offer a mechanism for rate selectivity, except that we did not observe a rate selective response in this neuron at the rates tested.

Figure 5 provides population data for FM rate selectivity, illustrating that the majority of neurons in the dorsal cortex did not show rate selectivity for the rates tested. Based on the number of action potentials, 14% of neurons in the dorsal cortex of the inferior colliculus were selective for the rate of upward FM sweeps presented to the contralateral ear. In **Figure 5A** these cells are positioned outside the solid lines that indicate a RSI value of 0.6875. Fifty-nine percent of upward rate selective neurons fired action potentials only to the preferred sweep rate, resulting in an RSI of +1 and a position along one of the axes. Twenty-nine percent of upward rate selective neurons preferred fast sweep rates presented to the contralateral ear (**Table 1**), leading to a position close to the abscissa in **Figure 5A**.

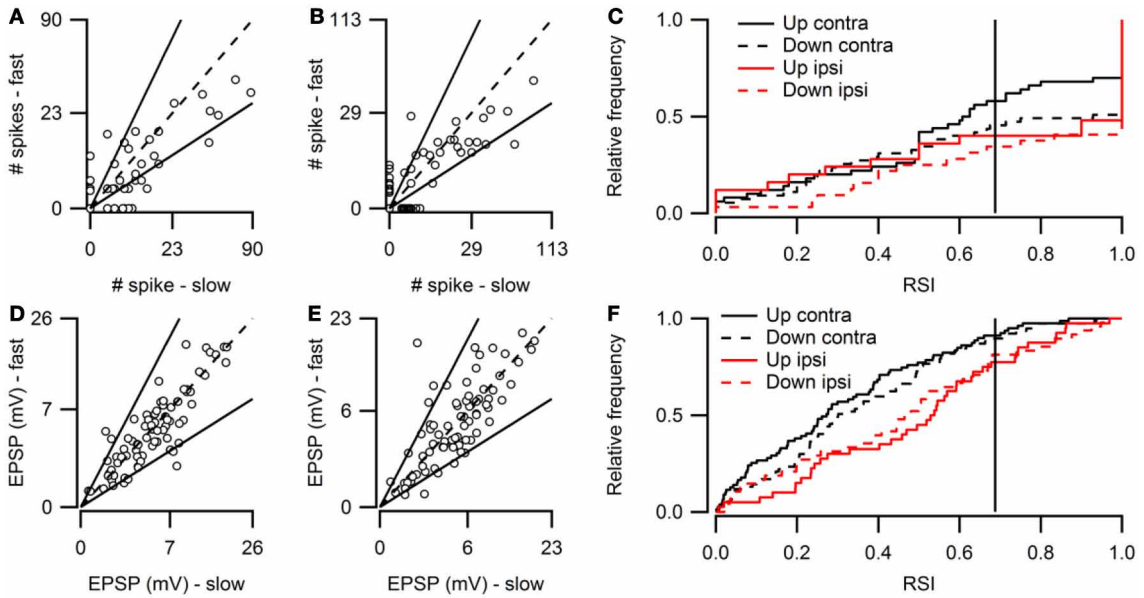

FIGURE 5 | Overview of FM rate selectivity. (A) Number of action potentials evoked by contralateral fast upward sweeps plotted against the number of spikes in response to contralateral slow upward sweeps ($n = 86$; 49 cells at origin). Solid lines next to identity line indicate RSI of 0.6875. **(B)** Action potentials fired in response to fast and slow downward sweeps presented to the contralateral ear ($n = 85$; 43 cells at origin). **(C)** Cumulative histogram of spike-based RSIs in response to up- or downward FM sweeps presented to the contralateral or ipsilateral ear. Vertical solid line indicates a RSI of 0.6875. **(D)** EPSP amplitudes in response to contralateral fast upward sweeps plotted against amplitudes in response to contralateral slow upward sweeps ($n = 77$). Solid lines indicate RSI of 0.6875. **(E)** EPSP amplitudes evoked by fast and slow downward sweeps presented to the contralateral ear ($n = 79$). **(F)** Cumulative histogram of EPSP amplitude based RSIs in response to up- or downward FM sweeps presented to the contralateral or ipsilateral ear. Vertical solid line indicates a RSI of 0.6875.

Based on action potential firing, 17% of cells were selective for the rate of a downward FM sweep presented to the contralateral ear (**Figure 5B**). Of these, 81% responded only to one sweep rate (**Figure 5C**). About half of downward sweep rate selective neurons preferred fast sweep rates. When stimuli were presented to the ipsilateral ear, 11% of cells showed rate selectivity with upward sweeps and 12% with downward sweeps (**Table 1**). Most of these rate selective cells responded to only a single FM rate (upward: 85%, downward: 87%).

Based on EPSP amplitude, only few neurons were rate selective for FM sweeps. Six percent of neurons were selective for the rate of upward sweeps presented to the contralateral ear (**Figure 5D**). Little rate selectivity (7%) was also observed for EPSP amplitudes when downward sweeps were presented to the contralateral ear (**Figure 5E**). RSI distributions were slightly shifted toward higher values for ipsilateral stimulation compared to contralateral stimulation (**Figure 5F**). Ipsilaterally presented sweeps evoked selective responses in 7% of neurons when modulated either up- or downward (**Table 1**).

CORRELATION BETWEEN SUPRA- AND SUBTHRESHOLD SELECTIVITY INDICES

Spike-based and EPSP-based DSIs were not very well correlated ($r = 0.42$). **Figure 6A** compares spike- and EPSP-based DSIs for contralateral stimulation ranging between 0 and 80 dB SPL. The distribution of EPSP-based DSIs was centered around zero, showing only few values close to $+1$ or -1. The distribution of spike-based DSIs was also centered around zero, but extreme values of -1 and $+1$ were more common.

The spike-based DSI was generally larger than the EPSP-based DSI (median DSI: 0.20 vs. 0.68, Mann–Whitney U = 36087, $n_1 = 160$, $n_2 = 302$, $P < 0.001$ two-tailed; **Figure 6B**).

Spike-based and EPSP-based RSIs showed little correlation (**Figure 6C**). Membrane potential based RSIs were generally low. The distribution was skewed to the right. In contrast, action potential based RSIs were distributed more evenly, except for a large peak at the maximum value of $+1$. This peak is responsible for the large difference between the medians of the two RSI indices (0.30 vs. 0.78, Mann–Whitney U = 52786, $n_1 = 218$, $n_2 = 330$, $P < 0.001$ two-tailed; **Figure 6D**).

FM RESPONSES CAN OFTEN BE PREDICTED BY TONE RESPONSES

We compared for each neuron pair in our dataset how similar responses to simple tones were, and compared this with the similarity of responses to FM sweeps. To calculate how similar tone responses were, we lumped together the membrane potential measurements during stimulation with all 29 simple tones presented at nine different SPLs to the contra- and ipsilateral ear, constituting the FRA. Correlation was then calculated as described in the "Materials and Methods." We also combined recordings during stimulation with the four types of FM sweeps presented at nine SPLs to the contra- and ipsilateral ear. Comparing the correlations in response to stimulation with simple tones and FM sweeps allowed us to explore if neurons

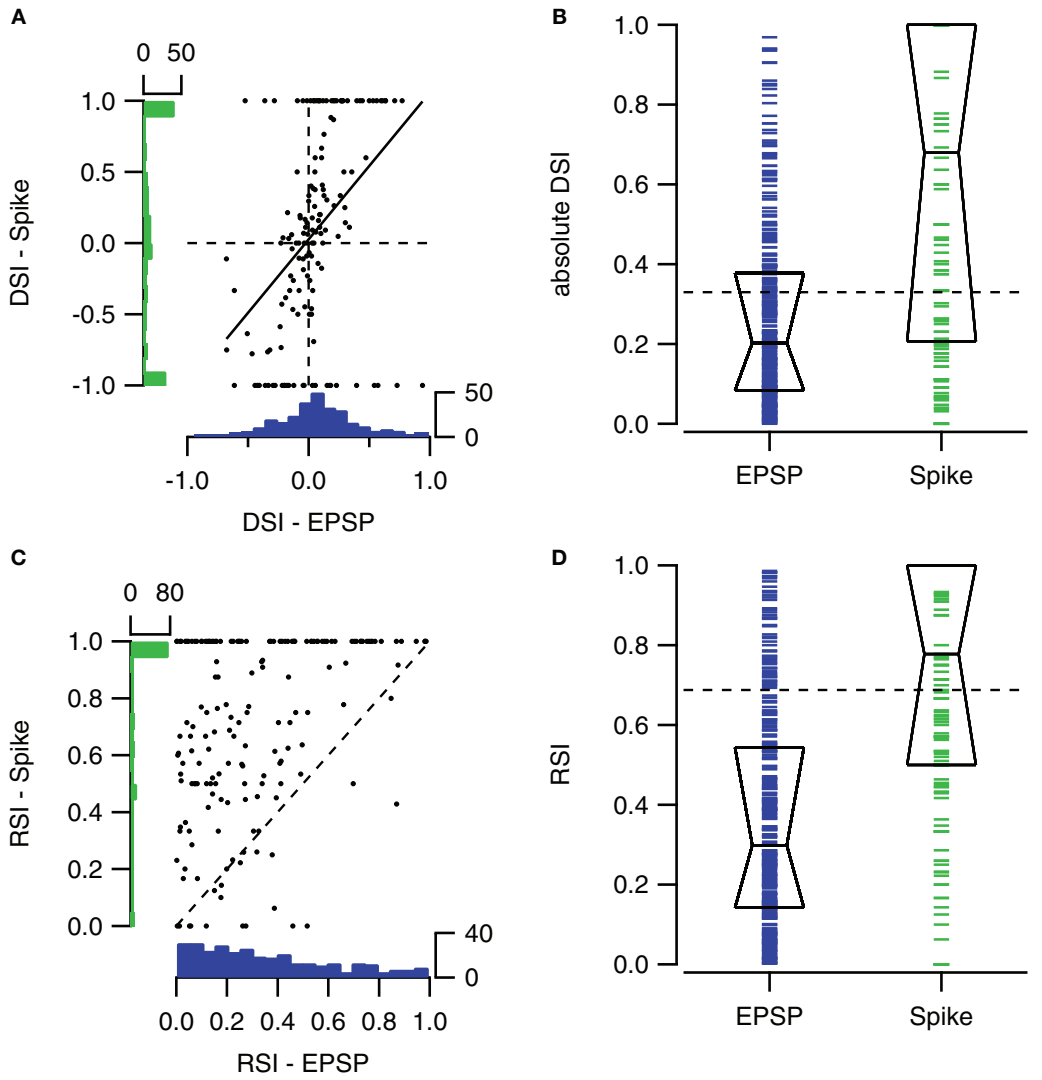

FIGURE 6 | Comparison of sub- and suprathreshold selectivity indices. **(A)** Scatter plot showing the relation between the fast sweep DSI for the number of action potentials and for EPSPs within the same cells for all sound intensities ranging from 0 to 80 dB SPL ($n = 153$ from 57 cells). Solid line shows the regression line ($r = 0.42$). At left and bottom the histograms of spike- and EPSP-DSI are shown. **(B)** Fast sweep DSIs for spikes ($n = 160$) are generally larger than for EPSP amplitudes ($n = 302$). Boxes indicate the median with first and third quartile. **(C)** Upward sweep RSIs for number of action potentials and for EPSPs ($r = 0.38$; $n = 172$ from 55 cells). **(D)** Upward sweep RSIs for spikes ($n = 181$) are generally larger than for EPSP amplitudes ($n = 330$). Boxes indicate the median with first and third quartile. Selectivity indices were determined using contralateral stimuli ranging from 0 to 80 dB SPL. EPSP-based DSIs and RSIs were only included when autocorrelation of the two underlying postsynaptic potentials were significant. Spike-based selectivity indices were only included if the cell fired in response to at least one of the two FM stimuli.

with similar FRAs also showed similar responses to FM sweeps. As shown in **Figure 7**, the two correlations correlated well ($r = 0.77$), suggesting that the responses to FM sweeps can be predicted from the FRA of a neuron.

USE OF THREE METHODS TO PREDICT FM RESPONSES FROM SIMPLE TONE RESPONSES

Two pieces of evidence suggest that FM selectivity can be generated within the dorsal cortex. Firstly, the spectral separation of inhibition and excitation in a subset of cells provides a well-known mechanism for the creation of direction selectivity (reviewed in Fuzessery et al., 2011; Pollak et al., 2011). Secondly, the observation that neurons with similar responses to tones also have similar responses to FM sweeps suggests that in many more neurons, the responses to FM sweeps are determined by the integration of synaptic inputs, rather than inherited from upstream structures. However, the positive correlation observed in **Figure 7** does not contain proof that responses are locally generated, since two neurons that inherit the same type of FM response may also inherit the same type of tone response. In addition, especially for the rate selective neurons, the underlying mechanism for the difference in the responses to fast and slow sweeps was generally not obvious in our dataset. To more directly investigate how well responses to FM can be predicted from the FRAs, we therefore

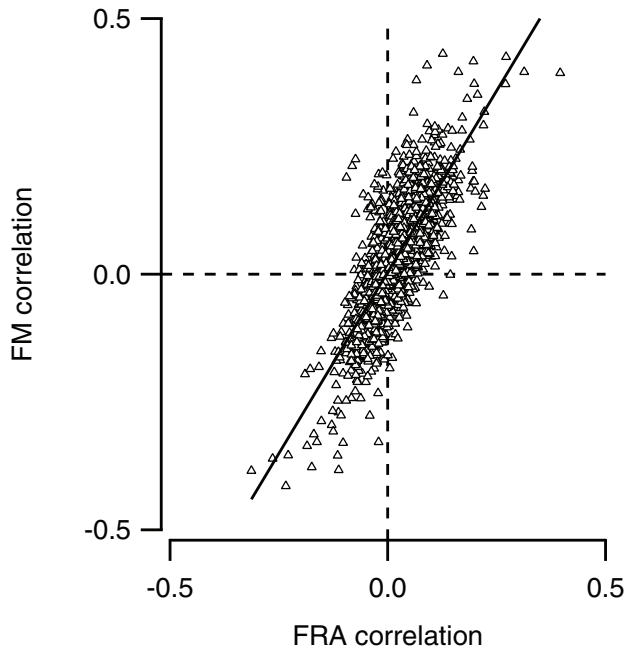

FIGURE 7 | Neurons with similar frequency response areas also respond similarly to FM sweeps. The Pearson correlation between the FM responses of any pair of neurons (FM correlation) is plotted against the Pearson correlation of the frequency response area as of the same pair (FRA correlation). Line shows a line fit though the data ($r = 0.77$).

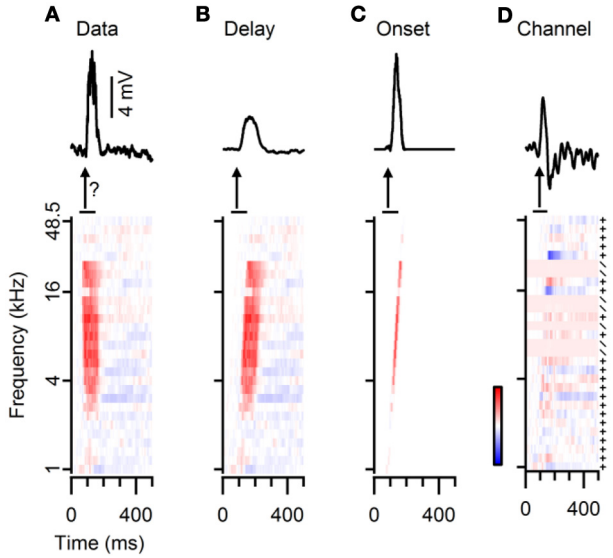

FIGURE 8 | Three different methods for reconstructing responses to FM sweeps from the responses to simple tones. (A) Average subthreshold potential responses to a fast upward FM sweep (top) and to simple tones (bottom). The question mark indicates that the goal of our reconstructions is to reproduce FM responses from tone responses. **(B)** "Delay" method: responses to simple tones were time shifted (bottom), followed by averaging to obtain the reconstruction (top). **(C)** "Onset" method: responses to simple tones were convoluted with an impulse function and time shifted (bottom) to create the reconstruction (top). **(D)** "Channel" method: differences in responses to simple tones of increasing frequencies were either added (+) or used as a scaling factor (/) to reconstruct the FM model (top). Color bar indicates ±10 mV.

tried to directly reconstruct FM responses from the responses to simple tones.

We used three different reconstruction methods, named "Delay," "Onset," and "Channel," as described in the "Materials and Methods" section. **Figure 8A** shows the responses to 80 dB SPL tones of a neuron together with the response to a fast upward FM sweep at the same sound intensity. In addition, the graph illustrates how the responses to 80 dB SPL tones were modified to calculate the three different reconstructions. In the "Delay" method merely an incremental delay was applied (**Figure 8B**). In the "Onset" method the same delay was applied, but only the onset of each component was used (**Figure 8C**). The "Channel" method used either addition or scaling, depending on the relative changes in the response to simple tones of neighboring frequencies (**Figure 8D**). All three reconstructions reproduced the excitatory nature of the FM evoked response in this example and captured some aspects of the EPSP timing. The reconstructions also exemplify some of the limitations of the three reconstruction methods. A relatively minor problem was the scaling of the reconstructions. In this example, the amplitudes of the Delay and of the Channel reconstructions were smaller than of the measured response (**Figures 8B**,**D**). This only hampers a comparison of EPSP amplitudes between different types of reconstructions, whereas a comparison within one reconstruction method and the calculation of DSI and RSI was not affected. A more specific issue concerning the Delay reconstructions can be seen in **Figure 8B**, as the reconstructed EPSP appears slightly delayed and broader than the recorded response to the FM stimulus. A slight delay was also introduced in the Onset reconstruction, but, by focusing on the onset responses to each simple tone, the reconstructed EPSP was not broadened and its amplitude matched that of the FM evoked response (**Figure 8C**). A drawback of the Channel reconstruction method was the relatively strong baseline fluctuations due to the scaling of the trace compared to the averaging done in the other reconstructions (**Figure 8D**). In addition, in this example an IPSP was artificially introduced that resulted from the difference between a simple tone stimulus that elicited an EPSP and one that did not elicit an obvious response. Compared to the Delay and the Onset reconstruction, the Channel reconstruction described the onset time of the response best. Owing to the averaging of time shifted responses, the amplitudes of our reconstructions often deviated from the amplitudes of FM evoked responses.

RECONSTRUCTION OF DIRECTION SELECTIVE FM RESPONSES FROM SIMPLE TONE RESPONSES

We then compared the predictions from the three models based on the responses to 80 dB SPL tones with the recorded FM responses. In some cells with spectrally separated excitatory and inhibitory tone response areas, reconstructions could reproduce FM responses well. An example is the neuron shown in **Figure 9A**, which responded with an EPSP to upward FM sweeps that was absent in response to downward sweeps. The responses to 80 dB

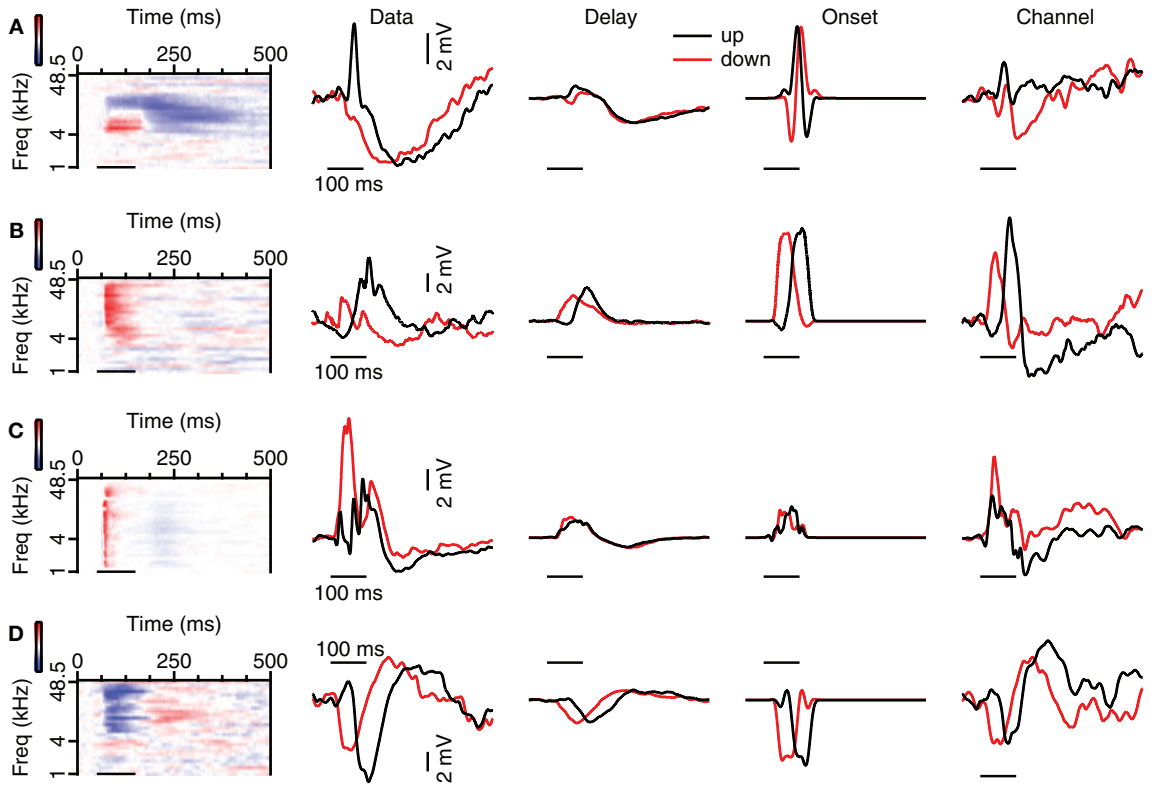

FIGURE 9 | Examples of reconstructions of up- and downward FM sweeps. (A) Neuron with strong correlation values for the Channel reconstructions, but weaker correlations for the Delay and Onset reconstructions. From left to right: responses to 80 dB SPL tones, averaged subthreshold response to fast FM sweep at 80 dB SPL ("Data"), Delay, Onset, and Channel reconstructions. Correlation values during stimulation: 0.11 (up Delay), −0.11 (down Delay), −0.34 (up Onset), −0.12 (down Onset), 0.97 (up Channel), 0.61 (down Channel). Selectivity error: 1.78 mV (Delay), 3.28 mV (Onset), 1.34 mV (Channel). Resting membrane potential was −71 mV. **(B)** Neuron with strong correlations for upward sweeps. Correlation values during stimulation: 0.89 (up Delay), 0.10 (down Delay), 0.96 (up Onset), 0.06 (down Onset), 0.97 (up Channel) and 0.67 (down Channel). Selectivity error: 2.10 mV (Delay), 2.94 mV (Onset), 1.66 mV (Channel). Resting membrane potential was −74 mV. **(C)** Neuron with variable correlations for the types of reconstructions. Correlation values during stimulation: 0.46 (up Delay), −0.0.33 (down Delay), 0.47 (up Onset), 0.56 (down Onset), −0.19 (up Channel), 0.79 (down Channel). Selectivity error: 2.94 mV (Delay), 4.78 mV (Onset), 0.13 mV (Channel). Resting membrane potential was −68 mV. **(D)** Neuron showing good correlations for most reconstruction methods. Correlation values during stimulation: 0.92 (up Delay), 0.34 (down Delay), 0.83 (up Onset), 0.70 (down Onset), 0.85 (up Channel) and 0.91 (down Channel). Selectivity error: 1.37 mV (Delay), 1.61 mV (Onset), 1.95 mV (Channel). Resting membrane potential was −58 mV.

SPL tones showed a low frequency excitatory area neighboring a high frequency inhibitory area. This configuration would allow the cell to respond with an EPSP followed by an IPSP to upward sweeps while a downward sweep would let the EPSP coincide with the IPSP. Our Delay and Channel reconstruction showed that the EPSP coincided with the IPSP during the upward sweep, while there was only a minor deflection in the response to the downward sweep. The overestimation of the EPSP in our simple reconstructions of responses to downward sweeps suggests that the impact of inhibition was underestimated. Despite these imperfections, FM direction selective responses could be reproduced with a method that did not require any free parameters, suggesting that the direction selectivity of this cell was generated locally in the dorsal cortex of the inferior colliculus based on the asymmetry of excitation and inhibition in its responses to 80 dB SPL tones. In a total of 7 of 9 fast sweep direction selective neurons that displayed asymmetric excitation and inhibition in response to 80 dB SPL tones direction selectivity was reproduced in at least one of the reconstructions. The same was true for 5 of 9 slow sweep direction selective cells that showed asymmetric excitation and inhibition.

The reconstructions also successfully reproduced FM responses in cells for which EPSP onset depended on tone frequency. The cell shown in **Figure 9B** responded with a larger EPSP to upward than to downward sweeps. This response behavior was also reflected in our reconstructions, indicating that the responses to 80 dB SPL tones contain the essential information required for direction selectivity generation. As the responses to 80 dB SPL tones in this cell were dominated by excitation, the interaction of excitatory inputs with different delays is the most parsimonious explanation for the observed direction selectivity. EPSPs delays appeared shortest at high frequencies and longer at lower frequencies. In this cell an upward sweep would first activate a long-latency EPSP, allowing the EPSPs to coincide later

during the sweep. We found evidence for differential delay of excitation as the underlying mechanism in a total of two fast sweep direction selective neurons and one slow sweep direction selective neuron.

Reconstructions could also reproduce FM responses in neurons for which the response to 80 dB SPL tones did not offer an obvious explanation for their FM selectivity. The neuron shown in **Figure 9C** is one of two neurons in which we could reconstruct the responses to fast FM sweeps, but for which the underlying mechanism was more subtle than in the neurons displayed in **Figures 9A**,**B**. As the difference reconstruction gave the best estimation of the FM response, the generation of direction selectivity might be linked to a sequential activation of frequency channels that favors responses to downward modulated sweeps. In six slow sweep direction selective neurons we could reconstruct the FM responses with at least one reconstruction method, suggesting that in these cells the direction selectivity also originated from the spectrotemporal interaction of synaptic inputs.

In other cases, reconstructions were unable to reproduce FM responses. An example is shown in **Figure 9D**. While we cannot exclude that more elaborate reconstruction methods would fare better, we consider it more likely that this cell received inputs that were already direction selective. Another class of cells in which reconstructions failed consisted of cells in which the response to FM sweeps was dominated by inhibition, but which showed a small EPSP for one direction, leading to a large DSI. Reconstructions did not capture direction selectivity in 6 of 16 fast sweep direction selective neurons and in 16 of 27 slow sweep direction selective neurons.

Reconstructions generally resembled the recorded FM evoked responses well. To have a measure for the quality of the reconstruction that is sensitive to the shape and overall timing of the response, but not to its amplitude, we chose to correlate our reconstructions with the recorded responses to FM sweeps. These correlations were limited to a time window matching the duration of the FM stimulus. **Figure 10** summarizes the correlations for direction selective neurons (|DSI|>0.33). Comparing the three reconstructions, the correlations were more similar for fast upward (Kruskal–Wallis H = 1.71, $df = 2$, $P = 0.43$) than for fast downward sweeps (Kruskal–Wallis H = 7.48, $df = 2$, $P < 0.05$). The Channel reconstruction yielded the highest correlations values, while the Delay and Onset reconstructions showed slightly lower correlations (**Figure 10A**; **Table 2**). The reconstructions of slow sweeps also yielded fairly high correlation values (**Figure 10B**; **Table 2**). The correlation values were similar for the three reconstructions of slow upward (Kruskal–Wallis H = 0.95, $df = 2$, $P = 0.62$) and slow downward sweeps (Kruskal–Wallis H = 0.35, $df = 2$, $P = 0.83$). The correlations of Delay, Onset, and Channel reconstructions of slow sweeps were generally lower than for fast sweeps, probably owing to the longer duration (**Table 2**).

Selective responses to fast sweeps were best reproduced by the Channel reconstruction whereas selective responses to slow sweeps were best reproduced by the Delay reconstruction. While the good correlations indicate that the reconstructions captured the temporal pattern of the response, it does not describe how well the reconstructions yielded the correct relative response amplitude. However, the correlation between the direction or rate selectivity indices of measured data and the reconstructions were poor (data not shown). A main reason for the poor correlation was that the measured EPSP sizes were often small, which had the effect that small errors in the reconstruction amplitudes led to large errors in DSI or RSI. To have a measure for the relative postsynaptic potential amplitude difference that was less sensitive to the absolute size of responses, we calculated the geometrical distance between a point describing the amplitudes of two FM sweeps and a second point with equal distance to the origin that has the same rate or DSI as resulting from the reconstruction amplitudes (**Figure 11A**). The calculated distance gives a selectivity error in millivolt that is independent of the absolute amplitudes of the reconstructions. For direction selective neurons (|DSI|>0.33) the selectivity error was generally in the range of a few millivolts. The median values for the three types of reconstructions were similar for fast (Kruskal–Wallis H = 0.21, $df = 2$, $P = 0.90$) and for slow sweeps (Kruskal–Wallis H = 1.57, $df = 2$, $P = 0.46$; **Figures 11B**,**C**; **Table 2**).

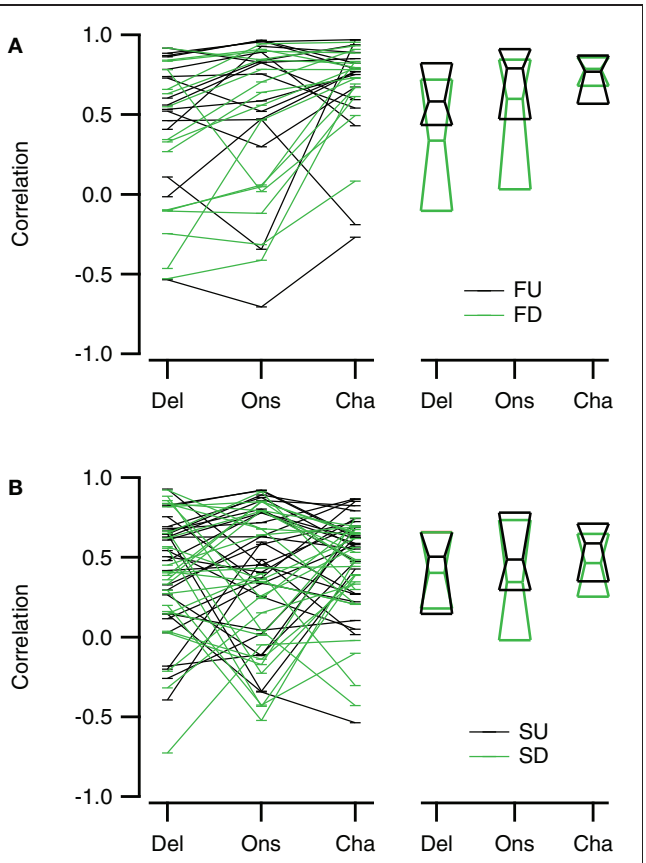

FIGURE 10 | Reconstructions of direction selective neurons generally correlate well with FM sweep evoked responses. (A) Correlations of the Delay ("Del"), Onset ("Ons"), and Channel ("Cha") reconstructions to responses to fast upward (FU, black) and fast downward (FD, green) FM sweeps ($n = 16$). **(B)** Correlation of the three reconstructions to responses evoked by slow upward (SU, black) and slow downward (SD, green) FM sweeps ($n = 27$). Scatter plots with lines connecting reconstructions of the same cell are shown on the left; median values and first and third quartiles are given on the right.

Table 2 | Correlations and selectivity errors of the three types of reconstructions.

		Direction selectivity				Rate selectivity			
		Fast sweeps		Slow sweeps		Up sweeps		Down sweeps	
		Up	Down	Up	Down	Fast	Slow	Fast	Slow
Delay	Correlation	0.58	0.34	0.50	0.40	0.52	0.64	0.69	0.39
	Error	2.1 mv		2.07 mV		1.26 mV		1.76 mV	
Onset	Correlation	0.79	0.60	0.49	0.35	0.57	0.69	0.59	0.64
	Error	2.4 mV		2.38 mV		2.2 mV		1.9 mV	
Channel	Correlation	0.77	0.79	0.59	0.46	0.88	0.68	0.77	0.54
	Error	1.58 mV		2.24 mV		2.65 mV		1.29 mV	

Errors and correlations are based on responses to contralateral stimulation at 80 dB SPL.

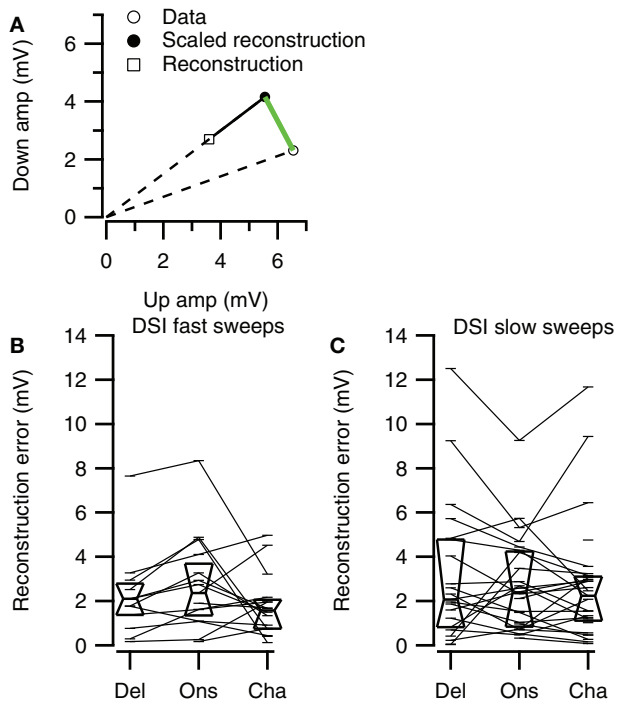

FIGURE 11 | Direction selectivity errors of the three reconstruction methods. (A) Illustration of the selectivity error calculation. Along a line from the origin through the reconstructed data point we determined the point with equal distance to the origin as the data point. The distance between this point and the data point (green line) was used as the selectivity error. **(B)** Selectivity errors for fast up- and downward sweeps (Del, $n = 13$; Ons, $n = 15$; Cha, $n = 16$). **(C)** Selectivity errors for slow up- and downward sweeps (Del, $n = 21$; Ons, $n = 24$; Cha, $n = 27$). Box plots show quartiles and medians.

RECONSTRUCTION OF RATE SELECTIVE FM RESPONSES FROM SIMPLE TONE RESPONSES

None of the three reconstruction methods generally reproduced rate selectivity well. Four different examples of reconstructions for two different FM sweep rates are shown in **Figure 12**. The reconstructions of the rate selective neuron shown in **Figure 12A** had low correlations for all three types of reconstructions in the time window matching the FM stimulation, among others because the EPSP that was present at low frequencies in the responses to 80 dB SPL tones did not show up in the recorded response to FM sweeps. The Delay, Onset, and Channel reconstructions yielded low selectivity errors (0.02, 0.06, 0.09 mV, respectively), indicating that all reconstructions captured the small relative difference in peak amplitude of the response. However, the small selectivity errors in this case probably result from the very small amplitude of the depolarization during FM stimulation, since the reconstructions showed a poor correlation with the FM responses. A total of 5 out of 7 upward sweep rate selective neurons could also not be reconstructed owing to the small size of the depolarization.

An example of a rate selective cell in which the relative amplitudes of the responses to FM sweeps could be approximated is shown in **Figure 12B**. Selectivity errors were low (Del: 0.52, Ons: 0.53, Cha: 0.36 mV). In addition, the reconstructions were also well correlated to the FM responses in the time window matching the FM stimulation (all $r > 0.77$). The high correlation values probably resulted from the successful reconstruction of the inhibitory potential, which was correct with respect to timing, and which dominated the responses to 80 dB SPL tones. The EPSP evoked by the slow sweep rate was fairly small but was reproduced in the Delay and the Onset reconstruction. Only in 2 out of 7 upward sweep rate selective neurons the relative amplitudes of the EPSPs could be approximated.

One cause for a failure to reconstruct rate selectivity was the underestimation of inhibitory inputs. The rate selective neuron in **Figure 12C** showed high correlations between reconstructions and the recorded response (all $r > 0.65$). However, the selectivity errors for Delay, Onset, and Channel reconstruction were all extremely high (12.6, 11.0, 15.9 mV, respectively), because all reconstructions underestimated the inhibition during the slow sweep. In a total of 5 out of 8 downward sweep rate selective neurons the reconstructions reflected the FM responses poorly. Possible reasons for the weak reconstructions could be very small EPSP amplitudes, potential shortcomings of our reconstruction methods or rate selective inputs.

Another reason why reconstructions could fail to reproduce rate selective responses was because they overestimated excitatory inputs. The correlation values during stimulation of the

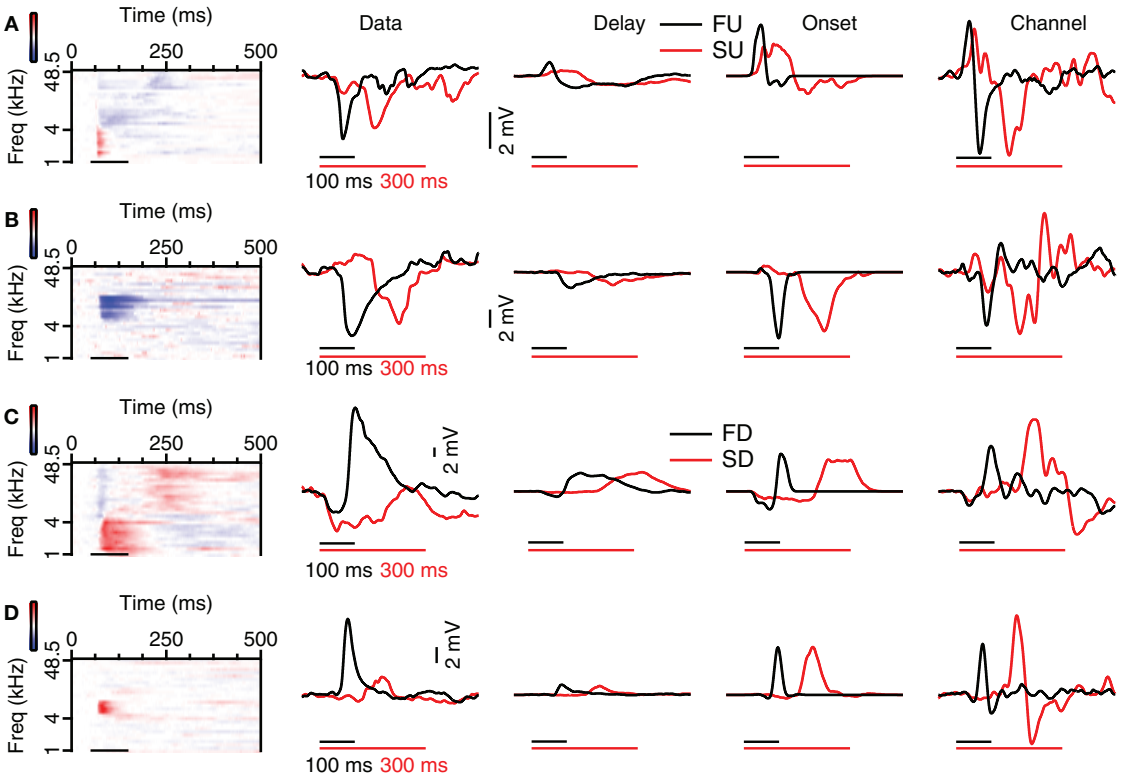

FIGURE 12 | Reconstruction of fast and slow FM sweeps. (A) Responses to 80 dB SPL tones (left) of a neuron with a small selectivity error for the Delay and the Onset reconstruction. The average of the truncated membrane potential (Data) is given next to the three different reconstructions (Delay, Onset, Channel). Resting membrane potential was −67 mV. **(B)** Neuron with a large selectivity error for the Delay reconstruction and smaller errors for the Onset and Channel reconstruction. Resting membrane potential was −67 mV. **(C)** Neuron with large selectivity errors for all three reconstruction methods. Resting membrane potential was −70 mV. **(D)** Cell with high reconstruction correlation values, capturing the temporal aspect of the response, but large selectivity error, showing that the reconstruction did not describe the relative amplitudes well. Resting membrane potential was −73 mV. Abbreviations: FU, fast upward; FD, fast downward; SU, slow upward; SD, slow downward.

reconstructions in **Figure 12D** were also high (all $r > 0.62$). The reconstruction selectivity errors were quite large (Del: 4.7, Ons: 5.4, Cha: 7.4 mV) because all reconstructions overestimated the amplitude of the slow downward sweeps. In 3 out of 8 downward sweep rate selective neurons some of the reconstructions yielded larger amplitudes for the preferred sweep rates, but in all these three neurons the reconstructions were fairly poor. Possible reasons for the weak performance of our reconstructions include that rate selectivity was more accidental, imperfections in the reconstruction algorithms, or the possibility that rate selectivity was inherited from upstream nuclei via rate selective inputs.

Channel reconstructions yielded the highest correlation values for fast sweeps and onset reconstructions resulted in the highest correlation values for slow sweeps in rate selective neurons (RSI >0.6875; **Figure 13**). Although the Delay, Onset, and Channel reconstructions generally yielded high correlations for up- and downward reconstructions, there were a larger number of downward reconstructions with relatively low correlation values, resulting in a larger spread. The three reconstruction methods yielded similar correlations for fast upward (Kruskal–Wallis H = 3.27, $df = 2$, $P = 0.21$), slow upward (Kruskal–Wallis H = 0.65, $df = 2$, $P = 0.70$), fast downward (Kruskal–Wallis H = 0.72, $df = 2$, $P = 0.68$), and slow downward sweeps (Kruskal–Wallis H = 1.34, $df = 2$, $P = 0.51$). The Channel reconstructions resulted in the highest correlation values for fast sweeps while the Onset reconstruction gave the highest correlation values for slow sweeps (**Table 2**). Finally, we also calculated the selectivity error for rate selective neurons, which had quite variable median values for the Delay, Onset, and Channel reconstruction (**Figure 14**; **Table 2**). The three reconstructions yielded similar reconstruction errors for upward sweeps (Kruskal–Wallis H = 2.89, $df = 2$, $P = 0.24$) but different errors for downward sweeps (Kruskal–Wallis H = 17.38, $df = 2$, $P < 0.001$).

DISCUSSION

Our results show that neurons in the dorsal cortex of the mouse inferior colliculus can respond selectively to the direction or rate of FM sweeps. We observed direction and rate selectivity both in suprathreshold spiking and in subthreshold EPSPs. Action potential based selectivity was predicted well by membrane potential based selectivity in case of direction but poorly in the case of rate. Neurons with similar FRAs also had similar responses to FM sweeps, suggesting that responses to FM sweeps could be predicted from FRAs. Our reconstructions show that FM evoked

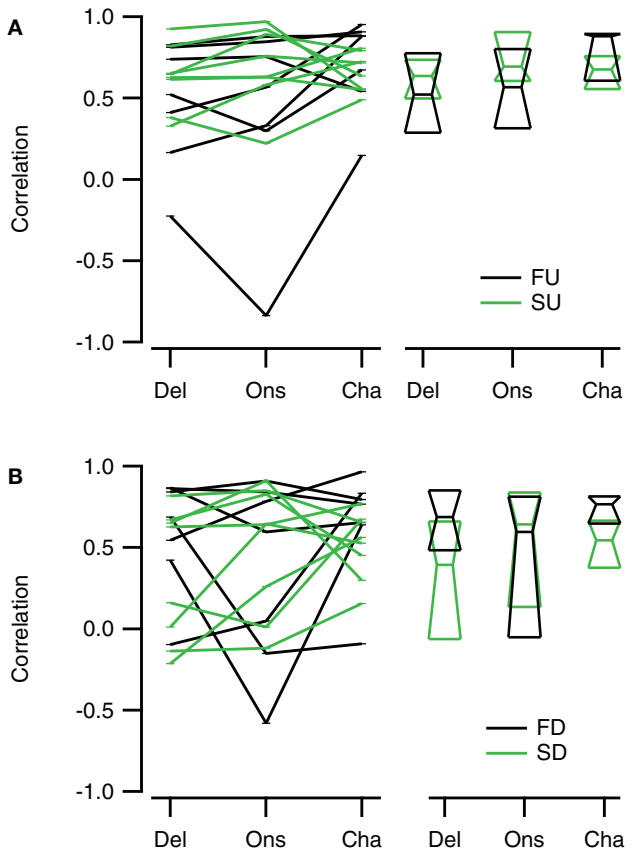

FIGURE 13 | Reconstructions of rate selective neurons correlate well to FM sweep evoked responses. (A) Correlations of the Delay ("Del"), Onset ("Ons"), and Channel ("Cha") reconstructions to responses to fast upward (FU, black) and slow upward (SU, green) FM sweeps ($n = 8$). **(B)** Correlation of the three reconstructions to responses evoked by fast downward (FD, black) and slow downward (SD, green) FM sweeps ($n = 8$). Scatter plots with lines connecting reconstructions of the same cell are shown on the left; median values and quartiles are given on the right.

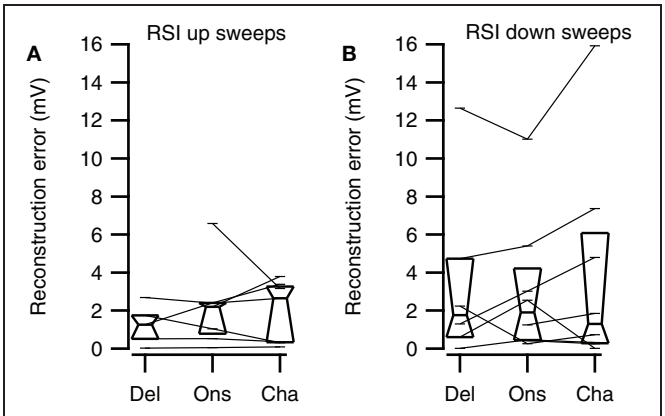

FIGURE 14 | Rate selectivity errors of the three reconstruction methods. (A) Selectivity errors for fast and slow upward sweeps (Del, $n = 5$; Ons, $n = 7$; Cha, $n = 7$). **(B)** Selectivity errors for fast and slow downward sweeps (Del, $n = 6$; Ons, $n = 8$; Cha, $n = 8$). Box plots show quartiles and medians.

responses could be reconstructed to a large extent from responses to simple tones, suggesting that some of the neurons in the dorsal cortex of the inferior colliculus can generate FM direction and rate selective responses.

DIRECTION SELECTIVITY IN THE DORSAL INFERIOR COLLICULUS

Based on both suprathreshold and subthreshold responses, we found FM direction selective neurons in the dorsal cortex of the mouse inferior colliculus. We found that the percentage of direction selective cells in the mouse dorsal cortex was relatively low, with values ranging between 13 and 24% for contralateral stimulation. This is still within the range of values observed in the rat central nucleus, where estimates from about 10% to over 50% of cells have been obtained (Poon et al., 1991, 1992; Felsheim and Ostwald, 1996; Kuo and Wu, 2012). As the inferior colliculus responds not only to contralateral but also to ipsilateral stimulation, we also determined the number of direction selective neurons in response to FM sweeps presented to the ipsilateral ear. With values ranging between 10 and 13%, fewer neurons were direction selective in response to FM sweeps presented to the ipsilateral ear. The DSI distribution indicated no clear preference for up- or downward sweeps in the dorsal cortex; only the EPSP-based DSIs for ipsilateral stimulation were slightly shifted toward higher (upward) values. In rats the proportion of up- and downward direction selective neurons in the inferior colliculus are typically similar, while in bats relatively many downward selective neurons are found, in accordance with the structure of their calls (Clopton and Winfield, 1974; Fuzessery, 1994; Felsheim and Ostwald, 1996; Andoni et al., 2007; Andoni and Pollak, 2011).

RATE SELECTIVITY IN THE DORSAL INFERIOR COLLICULUS

A subset of neurons in the dorsal cortex of the inferior colliculus responded selectively to the rate of FM sweeps. Large RSIs were common for suprathreshold responses but fairly rare for subthreshold responses. A high percentage of rate selective neurons has been observed in extracellular studies of the central nucleus of the inferior colliculus, while only 6–21% of cells in our dataset were selective for modulation rate (Felsheim and Ostwald, 1996; Fuzessery et al., 2006). A direct comparison is however difficult because of differences in the presented stimuli, including the number of different rates presented, the intensity of the stimuli, and the type of FM sweeps (logarithmic vs. linear). Both the analysis of action potentials and EPSPs revealed fewer modulation rate selective neurons if sweeps were presented to the ipsilateral ear than to the contralateral ear. However, these neurons showed higher rate selectivity than cells that were rate selective for contralateral stimulation. The functional significance of these differences between ipsi- and contralateral stimulation is not yet clear.

SPIKE THRESHOLD EFFECTS ON FM SELECTIVITY

FM selectivity indices for direction and rate were generally larger when based on action potentials compared to EPSPs. This observation can be attributed to a sharpening effect of the spike threshold on selectivity. Small changes in membrane potential can result in large changes in action potential firing, leading to larger

action potential based selectivity indices. We previously found a clear effect of the non-linear relation between membrane potential and spike probability on tuning for amplitude modulated (AM) responses in the central nucleus of the inferior colliculus (Geis and Borst, 2009). A spike threshold effect on FM selectivity has been put forward in studies of the direction and rate selectivity in the central nucleus of the inferior colliculus and the auditory cortex (Gittelman et al., 2009; Ye et al., 2010; Gittelman and Li, 2011). Many direction- or rate-selective neurons in our dataset only fired action potentials when stimulated with the preferred sweep. In addition, neurons with high selectivity indices often fired only few action potentials. In these cases there was often little underlying selectivity in EPSP sizes, suggesting that the rate selectivity for action potentials in these cells may have been accidental. Both points support the notion that spike threshold effects increase FM selectivity in the dorsal cortex of the inferior colliculus as well.

GENERATION OF FM SELECTIVITY IN THE DORSAL INFERIOR COLLICULUS

In our study, we compared the response to simple tones with the response to FM sweeps. This step can provide information about the question to what extent the FM responses are generated *de novo* by the recorded cell, or result from synaptic integration in auditory stations that are located upstream from the dorsal cortex. One indication that FM responses can be locally generated was our observation that pairs of neurons with similar responses to FM sweeps also had similar FRAs. This does not constitute proof for a causal relation since neurons can inherit both FM responses and tone responses, but did provide an impetus to test whether responses to FM sweeps can be predicted from the responses to simple tones composing the FRA.

Further evidence for the local generation of FM sweeps was obtained by comparing the FRAs for direction selective cells with the results obtained in the literature. Two main mechanisms have been proposed for the generation of direction selective responses (reviewed in Fuzessery et al., 2011; Pollak et al., 2011). The first mechanism relies on asymmetrical inhibition, resulting in direction-dependent differences in the relative timing of excitatory and inhibitory inputs. In about half of the FM direction selective neurons in our sample this mechanism most likely was responsible for the direction selectivity. In these direction selective cells the inhibitory area was at high frequencies for the upward selective cells and at low frequencies for downward direction selective cells. As a result, in the preferred direction, excitation would clearly precede the inhibition, whereas in the other direction, excitation and inhibition would coincide. In most of these cells, further support was obtained by the reconstructions, which showed that this mechanism provided a sufficient explanation for the observed direction selectivity.

The second proposed mechanism concerns the timing of excitatory inputs. In some neurons we recorded, differential latencies and EPSP time course appeared to underlie the response selectivity, including some direction selective neurons that displayed only excitatory FRAs. Even though this mechanism has been suggested to be responsible for creating direction selectivity in many studies (e.g., Suga and Schlegel, 1973; Phillips et al., 1985; Fuzessery et al., 2011), evidence for this mechanism is not as convincing as for the asymmetric inhibition. By reproducing the direction selectivity in the reconstructions we could show that this mechanism was a sufficient explanation for the creation of direction selectivity in some neurons in the dorsal cortex.

The presence of multiple mechanisms differs from the rat central nucleus, where it was found that asymmetric inhibition was responsible for direction selectivity in all neurons that were direction selective (Kuo and Wu, 2012), but agrees with results in the auditory cortex (Razak and Fuzessery, 2008; Ye et al., 2010) and in the bat central nucleus of the inferior colliculus (Fuzessery et al., 2011), where asymmetric inhibition, differential delay, and upstream mechanisms all are thought to contribute, even though it is still partly unclear to what extent these mechanisms are inherited from upstream nuclei.

The mechanisms underlying the observed rate selectivity were harder to deduce. The generation of rate selective responses is also thought to rely on the spectrotemporal interaction of synaptic inputs (reviewed in Fuzessery et al., 2011; Pollak et al., 2011). The mechanisms underlying rate selectivity have been mostly studied in the bat central nucleus of the inferior colliculus, where neurons generally show narrow excitatory tuning curves, in contrast to the broad tuning curves observed in our study. As the majority of rate selective neurons in our sample showed only small EPSPs in response to stimulation with FM sweeps, and the more responsive rate selective cells were poorly reconstructed, it remains to be established that clear rate selectivity can be generated within the dorsal cortex of the inferior colliculus.

COMPARISON OF THE THREE RECONSTRUCTION METHODS

To explore which aspect of the FRAs contributed to FM evoked response, we reconstructed FM evoked responses from responses to simple tones with three methods, each emphasizing a different response characteristic. Without employing any fitting, the reconstructions could reproduce responses to FM sweeps in the majority of neurons that showed direction selectivity to fast FM sweeps, but also in other cells. This is also remarkable because the three methods did not model the activation of voltage-dependent ion channels. In the cases where reconstruction was unsuccessful, our method does not allow to discriminate whether non-linear integration within the recorded neuron was responsible for the mismatch, or whether FM responses were inherited, although in cases where the fit was very poor the latter seems more likely.

The simplest reconstruction method we employed only considered the time shift introduced by the FM sweep. A comparable method has been utilized to reconstruct FM evoked responses in the auditory cortex (Ye et al., 2010). This Delay reconstruction often did not capture the temporal fine structure of FM evoked response and therefore correlations were mostly lower than for the other types of reconstructions. Although other reconstructions could yield lower selectivity errors, the Delay reconstruction resulted in the most consistent selectivity error values, suggesting that this simple method is the most stable one. Focusing on the response onset, the Onset reconstruction could reproduce the temporal pattern in response to fast sweeps better than in response to slow sweeps. The selectivity errors of the onset reconstruction usually exceeded that of the other methods,

emphasizing the lack of temporal integration as a drawback of this reconstruction method. The Channel reconstruction yielded the highest correlations and the lowest selectivity errors for fast sweeps, suggesting that for fast FM sweeps the concept of different frequency channels that are sequentially activated provides a good approximation. In reproducing responses to slow FM sweeps, the Channel reconstruction performed on a level comparable to the Delay reconstruction. As responses to simple tones do not contain information about direction or rate selectivity in response to FM sweeps, successful reconstructions of direction or rate selective responses indicate generation of this selectivity in neurons of the dorsal cortex of the inferior colliculus.

LIMITATIONS OF THE PRESENT RECONSTRUCTION METHODS

Even though we did not measure the underlying synaptic conductances and even though only a single duration was used for the simple tone stimuli, these data already allowed us to reconstruct the FM response with high fidelity in many cases. Obviously, it should be possible to obtain even more accurate reconstructions if a more extensive set of simple tone responses were obtained. Voltage clamp studies at different holding potentials can generate more quantitative information about both excitatory and inhibitory conductances than the current clamp recordings we made, although the high series resistance typically obtained for *in vivo* whole-cell recordings and the spatial clamp problems that are always present in intact neurons make appropriate controls essential (Kuo and Wu, 2012). We now simply added inhibitory and excitatory potentials, without taking into account the much smaller driving force for the IPSPs. The exact driving force was unknown in our experiments, because of the large access resistance of electrodes and the resulting incomplete dialysis of the cell with internal medium. Stimuli at different duration can provide information about the onset and offset of these synaptic conductances, which can be helpful to better match the tone duration to the time spent at each frequency at the different sweep rates, to take into account the effect of adaptation to prolonged tones, and to better include the responses to tone offsets. In combination with information about passive properties and voltage-dependent ion channels, an even better prediction of intracellular FM responses should thus be possible.

Another aspect of the quantitative relation between simple tones and FM sweeps that can still be further improved is related to the question what the contribution of individual inputs is to the measured FRA. As the FM sweep traverses this area, it will activate different inputs ("frequency channels"), depending on the individual receptive fields of the different presynaptic neurons. In our third model, we assumed that if simple tone responses changed little for adjacent stimulus frequencies, they were originating from the same set of presynaptic inputs. To test this more directly, a possible approach could be a systematic test for stimulus-specific adaptation using so-called "oddball" paradigms (Malmierca et al., 2009). If responses to simple tones of different frequencies co-adapt, it can be assumed that they are mediated by the same set of inputs (frequency channel). In combination with the conductance measurements, such an approach would also make it easier to discriminate between the appearance of inhibitory conductance and the disappearance of an excitatory conductance, which was now one of the hardest decisions in our current Channel model approach. Thus, it can be expected that an even better match between simple tone responses and FM responses can be obtained than was currently possible.

ACKNOWLEDGMENTS

This work was supported by a Neuro-BSIK grant (BSIK 03053; SenterNovem, The Netherlands) and a NeuroBasic PharmaPhenomics grant (AgentschapNL of the Ministry of Health, Welfare and Sports of the Netherlands). We thank C. Donkersloot for building and maintaining the two-photon microscope and Dr. M. van der Heijden for help with auditory stimulus generation.

REFERENCES

Andoni, S., Li, N., and Pollak, G. D. (2007). Spectrotemporal receptive fields in the inferior colliculus revealing selectivity for spectral motion in conspecific vocalizations. *J. Neurosci.* 27, 4882–4893.

Andoni, S., and Pollak, G. D. (2011). Selectivity for spectral motion as a neural computation for encoding natural communication signals in bat inferior colliculus. *J. Neurosci.* 31, 16529–16540.

Britt, R., and Starr, A. (1976). Synaptic events and discharge patterns of cochlear nucleus cells. II. Frequency-modulated tones. *J. Neurophysiol.* 39, 179–194.

Brown, T. A., and Harrison, R. V. (2009). Responses of neurons in chinchilla auditory cortex to frequency-modulated tones. *J. Neurophysiol.* 101, 2017–2029.

Clopton, B. M., and Winfield, J. A. (1974). Unit responses in the inferior colliculus of rat to temporal auditory patterns of tone sweeps and noise bursts. *Exp. Neurol.* 42, 532–540.

Erulkar, S. D., Butler, R. A., and Gerstein, G. L. (1968). Excitation and inhibition in cochlear nucleus. II. Frequency-modulated tones. *J. Neurophysiol.* 31, 537–548.

Felsheim, C., and Ostwald, J. (1996). Responses to exponential frequency modulations in the rat inferior colliculus. *Hear. Res.* 98, 137–151.

Fuzessery, Z. M. (1994). Response selectivity for multiple dimensions of frequency sweeps in the pallid bat inferior colliculus. *J. Neurophysiol.* 72, 1061–1079.

Fuzessery, Z. M., Razak, K. A., and Williams, A. J. (2011). Multiple mechanisms shape selectivity for FM sweep rate and direction in the pallid bat inferior colliculus and auditory cortex. *J. Comp. Physiol. A Neuroethol. Sens. Neural Behav. Physiol.* 197, 615–623.

Fuzessery, Z. M., Richardson, M. D., and Coburn, M. S. (2006). Neural mechanisms underlying selectivity for the rate and direction of frequency-modulated sweeps in the inferior colliculus of the pallid bat. *J. Neurophysiol.* 96, 1320–1336.

Geis, H.-R., and Borst, J. G. G. (2009). Intracellular responses of neurons in the mouse inferior colliculus to sinusoidal amplitude-modulated tones. *J. Neurophysiol.* 101, 2002–2016.

Geis, H. R. A. P., and Borst, J. G. G. (2013). Large GABAergic neurons form a distinct subclass within the mouse dorsal cortex of the inferior colliculus with respect to intrinsic properties, synaptic inputs, sound responses, and projections. *J. Comp. Neurol.* 521, 189–202.

Geis, H. R. A. P., Van Der Heijden, M., and Borst, J. G. G. (2011). Subcortical input heterogeneity in the mouse inferior colliculus. *J. Physiol.* 589, 3955–3967.

Gittelman, J. X., and Li, N. (2011). FM velocity selectivity in the inferior colliculus is inherited from velocity-selective inputs and enhanced by spike threshold. *J. Neurophysiol.* 106, 2399–2414.

Gittelman, J. X., Li, N., and Pollak, G. D. (2009). Mechanisms underlying directional selectivity for frequency-modulated sweeps in the inferior colliculus revealed by *in vivo* whole-cell recordings. *J. Neurosci.* 29, 13030–13041.

Gordon, M., and O'Neill, W. E. (1998). Temporal processing across frequency channels by FM selective auditory neurons can account for FM rate selectivity. *Hear. Res.* 122, 97–108.

Gordon, M., and O'Neill, W. E. (2000). An extralemniscal component of the mustached bat inferior colliculus

selective for direction and rate of linear frequency modulations. *J. Comp. Neurol.* 426, 165–181.

Hage, S. R., and Ehret, G. (2003). Mapping responses to frequency sweeps and tones in the inferior colliculus of house mice. *Eur. J. Neurosci.* 18, 2301–2312.

Holy, T. E., and Guo, Z. (2005). Ultrasonic songs of male mice. *PLoS Biol.* 3:e386. doi: 10.1371/journal.pbio.0030386

Kanwal, J. S., Matsumura, S., Ohlemiller, K., and Suga, N. (1994). Analysis of acoustic elements and syntax in communication sounds emitted by mustached bats. *J. Acoust. Soc. Am.* 96, 1229–1254.

Kitamura, K., Judkewitz, B., Kano, M., Denk, W., and Häusser, M. (2008). Targeted patch-clamp recordings and single-cell electroporation of unlabeled neurons *in vivo*. *Nat. Methods* 5, 61–67.

Kuo, R. I., and Wu, G. K. (2012). The generation of direction selectivity in the auditory system. *Neuron* 73, 1016–1027.

Lorteije, J. A. M., and Borst, J. G. G. (2011). Contribution of the mouse calyx of Held synapse to tone adaptation. *Eur. J. Neurosci.* 33, 251–258.

Lui, B., and Mendelson, J. R. (2003). Frequency modulated sweep responses in the medial geniculate nucleus. *Exp. Brain Res.* 153, 550–553.

Malmierca, M. S., Cristaudo, S., Pérez-González, D., and Covey, E. (2009). Stimulus-specific adaptation in the inferior colliculus of the anesthetized rat. *J. Neurosci.* 29, 5483–5493.

Phillips, D. P., Mendelson, J. R., Cynader, M. S., and Douglas, R. M. (1985). Responses of single neurones in cat auditory cortex to time-varying stimuli: frequency-modulated tones of narrow excursion. *Exp. Brain Res.* 58, 443–454.

Pollak, G. D., Xie, R., Gittelman, J. X., Andoni, S., and Li, N. (2011). The dominance of inhibition in the inferior colliculus. *Hear. Res.* 274, 27–39.

Poon, P. W. F., Chen, X., and Cheung, Y. M. (1992). Differences in FM response correlate with morphology of neurons in the rat inferior colliculus. *Exp. Brain Res.* 91, 94–104.

Poon, P. W. F., Chen, X., and Hwang, J. C. (1991). Basic determinants for FM responses in the inferior colliculus of rats. *Exp. Brain Res.* 83, 598–606.

Razak, K. A., and Fuzessery, Z. M. (2008). Facilitatory mechanisms underlying selectivity for the direction and rate of frequency modulated sweeps in the auditory cortex. *J. Neurosci.* 28, 9806–9816.

Ryan, M. J. (1983). Frequency modulated calls and species recognition in a neotropical frog. *J. Comp. Physiol. A* 150, 217–221.

Siemers, B. M., Schauermann, G., Turni, H., and Von Merten, S. (2009). Why do shrews twitter? Communication or simple echo-based orientation. *Biol. Lett.* 5, 593–596.

Simmons, J. A., and Stein, R. A. (1980). Acoustic imaging in bat sonar: echolocation signals and the evolution of echolocation. *J. Comp. Physiol. A* 135, 61–84.

Stein, R. C. (1968). Modulation in bird sounds. *Auk* 85, 229–243.

Stiebler, I., Neulist, R., Fichtel, I., and Ehret, G. (1997). The auditory cortex of the house mouse: left-right differences, tonotopic organization and quantitative analysis of frequency representation. *J. Comp. Physiol. A* 181, 559–571.

Suga, N. (1965). Analysis of frequency-modulated sounds by auditory neurones of echo-locating bats. *J. Physiol.* 179, 26–53.

Suga, N., and Schlegel, P. (1973). Coding and processing in the auditory systems of FM-signal-producing bats. *J. Acoust. Soc. Am.* 54, 174–190.

Voytenko, S. V., and Galazyuk, A. V. (2007). Intracellular recording reveals temporal integration in inferior colliculus neurons of awake bats. *J. Neurophysiol.* 97, 1368–1378.

Whitfield, I. C., and Evans, E. F. (1965). Responses of auditory cortical neurons to stimuli of changing frequency. *J. Neurophysiol.* 28, 655–672.

Williams, A. J., and Fuzessery, Z. M. (2010). Facilitatory mechanisms shape selectivity for the rate and direction of FM sweeps in the inferior colliculus of the pallid bat. *J. Neurophysiol.* 104, 1456–1471.

Williams, A. J., and Fuzessery, Z. M. (2011). Differential roles of GABAergic and glycinergic input on FM selectivity in the inferior colliculus of the pallid bat. *J. Neurophysiol.* 106, 2523–2535.

Williams, A. J., and Fuzessery, Z. M. (2012). Multiple mechanisms shape FM sweep rate selectivity: complementary or redundant? *Front. Neural Circuits* 6:54. doi: 10.3389/fncir.2012.00054

Ye, C.-Q., Poo, M.-M., Dan, Y., and Zhang, X.-H. (2010). Synaptic mechanisms of direction selectivity in primary auditory cortex. *J. Neurosci.* 30, 1861–1868.

Zeng, F. G., Nie, K., Stickney, G. S., Kong, Y. Y., Vongphoe, M., Bhargave, A., et al. (2005). Speech recognition with amplitude and frequency modulations. *Proc. Natl. Acad. Sci. U.S.A.* 102, 2293–2298.

Zhang, L. I., Tan, A. Y. Y., Schreiner, C. E., and Merzenich, M. M. (2003). Topography and synaptic shaping of direction selectivity in primary auditory cortex. *Nature* 424, 201–205.

Conflict of Interest Statement: The authors declare that the research was conducted in the absence of any commercial or financial relationships that could be construed as a potential conflict of interest.

Received: 02 October 2012; accepted: 13 January 2013; published online: 31 January 2013.

Citation: Geis H-RAP and Borst JGG (2013) Intracellular responses to frequency modulated tones in the dorsal cortex of the mouse inferior colliculus. Front. Neural Circuits 7:7. doi: 10.3389/fncir.2013.00007

frontiers in
NEURAL CIRCUITS

ORIGINAL RESEARCH ARTICLE
published: 31 August 2012
doi: 10.3389/fncir.2012.00060

Low-threshold potassium currents stabilize IID-sensitivity in the inferior colliculus

Anita Karcz*[1,2], *Rudolf Rübsamen*[2] *and Cornelia Kopp-Scheinpflug*[2,3]

[1] *Carl-Ludwig-Institute for Physiology, University of Leipzig, Medical School, Leipzig, Germany*
[2] *Faculty of Biosciences, Pharmacy and Psychology, University of Leipzig, Leipzig, Germany*
[3] *Medical Research Council UK, Toxicology Unit, Leicester, UK*

Edited by:
Manuel S. Malmierca, University of Salamanca, Spain

Reviewed by:
Henry Lütcke, University of Zurich, Switzerland
Dan Tollin, University of Colorado School of Medicine, USA

****Correspondence:***
Cornelia Kopp-Scheinpflug, MRC Toxicology Unit, University of Leicester, LE1 9HN, UK.
e-mail: cks7@le.ac.uk

The inferior colliculus (IC) is a midbrain nucleus that exhibits sensitivity to differences in interaural time and intensity (ITDs and IIDs) and integrates information from the auditory brainstem to provide an unambiguous representation of sound location across the azimuth. Further upstream, in the lateral superior olive (LSO), absence of low-threshold potassium currents in *Kcna1*$^{-/-}$ mice interfered with response onset timing and restricted IID-sensitivity to the hemifield of the excitatory ear. Assuming the IID-sensitivity in the IC to be at least partly inherited from LSO neurons, the IC IID-encoding was compared between wild-type (*Kcna1*$^{+/+}$) and *Kcna1*$^{-/-}$ mice. We asked whether the effect observed in the *Kcna1*$^{-/-}$ LSO is (1) simply propagated into the IC, (2) is enhanced and amplified or, (3) alternatively, is compensated and so no longer detectable. Our results show that general IC response properties as well as the distribution of IID-functions were comparable in *Kcna1*$^{-/-}$ and *Kcna1*$^{+/+}$ mice. In agreement with the literature IC neurons exhibited a higher level-invariance of IID-sensitivity compared to LSO neurons. However, manipulating the timing between the inputs of the two ears caused significantly larger shifts of IID-sensitivity in *Kcna1*$^{-/-}$ mice, whereas in the wild-type IC the IID functions were stable and less sensitive to changes of the temporal relationship between the binaural inputs. We conclude that the IC not only inherits IID-sensitivity from the LSO, but that the convergence with other, non-olivary inputs in the wild-type IC acts to quality-control, consolidate, and stabilize IID representation; this necessary integration of inputs is impaired in the absence of the low-threshold potassium currents mediated by Kv1.1.

Keywords: potassium channels, IID processing, temporal precision, sound localization

INTRODUCTION

Interaural intensity differences (IIDs) are essential cues to localize the source of high-frequency sounds. Individual IID-sensitive neurons in the auditory brainstem lateral superior olive (LSO) and in the auditory midbrain inferior colliculus (IC) integrate excitation received from one ear with inhibition received from the other ear, a computation that results in a specified firing rate for each IID (Boudreau and Tsuchitani, 1968; Sanes and Rubel, 1988; Tollin, 2003). The response rate of an individual neuron is tuned to a particular IID range. On a population level, this will result in IID functions that represent the whole range of physiological relevant IIDs. While the encoding of IID functions is quite well agreed in the LSO, in the IC there is some debate as to whether IID-sensitivity is generated de novo or is inherited from the upstream LSO (Park, 1998; Pollak et al., 2003; Gittelman et al., 2009). Although neurons in the IC receive strong excitatory projections from the contralateral LSO carrying information about IID-sensitivity, there are additional excitatory inputs from the contralateral VCN (Beyerl, 1978; Moore and Kitzes, 1985; Ross et al., 1988) and bilateral inhibitory inputs from the dorsal nucleus of the lateral lemniscus (DNLL) (Shneiderman et al., 1993). These non-olivary inputs create and moreover modify IID-sensitivity in the IC (Pollak et al., 2003).

As suggested by previous studies in the LSO and the IC, the arrival of the binaural inputs into a binaural level-detector within a submillisecond range of each other is crucial for their integration (Irvine et al., 1995; Joris and Yin, 1995). A delay in one input will result in a shift of the respective IID-function. Different models exist for the generation of positive (excitatory ear more intense) or negative (inhibitory ear more intense) IIDs, requiring the inputs to arrive either with a constant delay or to be coincident (Park et al., 1996). The time window for integrating synaptic inputs depends strongly on the neuronal membrane time constant and therefore on the ion channels that are open at a given membrane potential. Kv1.1 containing channels are activated at depolarizations very close to the resting membrane potential. They repolarize the membrane quickly and are therefore powerful means of restricting temporal summation (Oertel, 1985; Manis and Marx, 1991; Trussell, 1999; Johnston et al., 2010). In the LSO, the lack of Kv1.1 caused a limited IID representation with IIDs corresponding only to sounds in the ipsilateral hemifield (Karcz

et al., 2011). Here we aim to understand how a mismatched timing of the inputs into the IC alters the neurons' IID-sensitivity and how the presence of low-threshold potassium channel subunits like Kv1.1, prevents a disrupting influence of poorly-timed inputs. Using Kv1.1 knockout mice as a model allows us to study not only the effect of a shift in stimulus onset timing on IID encoding (as can be achieved also by the introduction of a stimulus delay) but also the effect of altered intrinsic excitability on the generation of each action potential that will be integrated to an IID response. We use single-unit recording *in vivo* from wild-type mice (*Kcna1*$^{+/+}$ mice) and also from mice whose temporal integration window is artificially extended through the lack of Kv1.1 containing channels (*Kcna1*$^{-/-}$ mice).

METHODS

A detailed description of the methods and mouse strains used in this study was described previously in (Karcz et al., 2011). In brief, the *Kcna1*^{tm1Tem} strain was generated as described in Smart et al. (1998). Mice used in this study were generated by intercrossing heterozygotes from the C3HeB/FeJ-*Kcna1*^{tm1Tem} line maintained at the University of Leipzig. The experiments were performed at the Neurobiology Laboratories of the Faculty of Bioscience, Pharmacy and Psychology of the University of Leipzig (Germany). All experimental procedures were approved by the Saxonian District Government, Leipzig, and were conducted according to European Communities Council Directive of 24th November 1986 (86/609/EEC). Genotyping was carried out on DNA isolated from tail clips of each mouse in a litter aged 7–10 days as described by Brew et al. (2003). Detailed protocols are available online (http://depts.washington.edu/tempelab/Protocols/KCNA1.html).

SURGICAL PREPARATION

During the experiments and surgical preparation, the animals were anaesthetized with a combined initial dose of 0.01 ml/g body weight of ketamine hydrochloride (100 mg/kg body weight; Parke-Davis, Berlin, Germany) and xylazine hydrochloride (5 mg/kg body weight; Bayer, Leverkusen, Germany). Anaesthesia was maintained throughout the recording experiments by hourly injections of one-third of the above dose. Ketamine is an antagonist of NMDA receptors. Ketamine-Xylazine anesthesia was employed in previous studies using the same mouse strain (Kopp-Scheinpflug et al., 2003; Karcz et al., 2011) and no differences in the depth or duration of anesthesia were found between genotypes. Other anesthetics like Isoflurane are less suited for the present experiments since it inhibits hyperpolarization-activated cyclic nucleotide modulated channels (Chen et al., 2009) which have a close structural resemblance to voltage-gated potassium channels. To avoid infections all instruments were wiped with a 70% alcohol before surgery. Recording and tracer solutions were filtered and electrodes were heat-sterilized. The incision site on the experimental animals head was cleaned with a chlorhexidine solution and the skull was exposed along the dorsal midsagittal line. A small metal bolt for supporting the animal in the stereotaxic recording device was glued to the bone overlaying the forebrain. Two holes were drilled in the skull, one to position the reference electrode in the superficial cerebellum, the other for insertion of recording electrodes. The second drill hole (500 μm diameter) was located 1.2 mm lateral to the midline and 1.8 mm caudal to the lambda suture. All recording experiments were performed in a sound-attenuated chamber (Industrial Acoustics, Type 400). During surgery and experiments the body temperature was kept between 36°C and 37.5°C by positioning the animal on a temperature-controlled heating pad (Harvard Apparatus) and maintaining the temperature of the sound-attenuated chamber at 25–30°C. Warmed lactated Ringer's (0.5–1 ml) was injected subcutaneously to prevent dehydration. At the end of the experiment, the head post was removed under anesthesia and a local analgesia (Xylocain Gel 2%; AstraZeneca GmbH) was applied to the wound, before closing the incision with histoacrylic glue. To help recovery from anesthesia mice were placed in oxygen-enriched air. Food pellets soaked in water were given to the mice for additional fluid supply. Over the duration of 4–5 days the animals were monitored daily for bodyweight, abnormal behavior or signs of infections.

DATA COLLECTION

Recordings were made using glass micropipettes (15–30 MΩ, 3 M KCl). The electrode was advanced vertically by a motorized micromanipulator (WPI, DC3001). The activity of isolated single units was identified by their relatively constant spike height, filtered (0.3–10 kHz), amplified (TDT, PC1) to the voltage range of the spike discriminator (TDT, SD1), and recorded at 100 kHz using custom-written software (Dr. M. Weick, University of Leipzig).

ACOUSTIC STIMULATION

Stimulus tones (100/40 ms duration, 5 ms rise-fall time, 100–300 ms inter-stimulus interval) were generated at a 97.7 kHz sampling rate using (TDT; RP2-1), amplified (TDT; ED1), delivered to electrostatic speakers (TDT; EC1) and fed via acoustic tubing to the outer ear approximately 5 mm from the animal's eardrum. For each neuron the following stimulation protocol was employed.

Excitatory response maps were measured by random presentation of pure-tone pulses (100 ms duration, 5 ms rise-fall time, 100 ms interstimulus interval) within a given matrix of 16 × 15 frequency/intensity pairs (240 combinations). The frequency range of this matrix typically included 5 octaves (4 tones/octave) with about three octaves below the estimated characteristic frequency (CF) and two octaves above. The intensity varied in 5 dB-steps between 90 and 20 dB SPL. Each frequency/intensity combination was presented five times in a predefined frequency/intensity array (1200 tone bursts). The timing and number of spikes were measured during the 100 ms period of stimulus presentation. Spontaneous activity was defined by the firing rate during eighty 100 ms-periods (8 s) with maximal attenuation (120 dB) of the stimulus randomly inserted in the stimulus protocol. Excitatory response areas were defined by the range of frequency/intensity combinations that evoked firing rates at or above the 10% significance level above spontaneous activity (Dorrscheidt, 1981). The outline of the response area defined the unit's frequency-threshold curve, from which

the CF and the threshold at CF were determined. Vice versa, inhibitory response areas were defined by a respective reduction of firing rates below the level of spontaneous rate (or below an acoustically evoked firing rate; for details see Karcz et al., 2011). Rate-level functions were calculated at CF by averaging the spike rates for each stimulus intensity (5 repetitions/stimulus). Median first spike latency and jitter (25–75% range of first spike latencies) were determined from 250 stimulus repetitions at CF and 80 dB SPL. Temporal response patterns were evaluated from peri-stimulus time histograms that display the number of APs occurring within 0.5 ms time intervals during stimulus presentation. Sensitivity to IIDs was tested by presenting a constant tone (40 ms) at CF, 20 dB (±15 dB) above threshold to the contralateral ear (using these parameters, similar firing rates could be achieved in both genotypes) and simultaneously stimulating the ipsilateral ear at CF with stimulus intensities pseudo-randomly varying from 20 to 90 dB SPL in 5 dB-steps. The acquired averaged IID functions (25 repetitions) were normalized; with AP firing rates during monaural contralateral stimulation corresponding to 100%. For further quantification of IID_{50} and slopes, IID functions were fit with four-parametric sigmoid functions from which IID values at 50% reduction of firing rate (IID_{50}) were determined (Wise and Irvine, 1985). Data were only considered if the fit had a minimum of 95% correlation.

STATISTICAL ANALYSES

Statistical analyses of the data were performed with SigmaPlot™ (Version 12; Systat Software Inc., San Jose, CA, USA). Unless indicated otherwise, results are expressed as mean ± standard error of the mean (S.E.M.) or for non-normal distributions as median (25%; 75% quartiles). Statistical significance was assessed using two-tailed tests; the Student's *t*-test for normally distributed data and the Mann-Whitney Rank Sum Test for non-normal distributions. Normality was assessed by the Shapiro-Wilk test. Significance levels are indicated by p-values that were corrected for nonhomogeneity of between cell-correlations by the Hunyh-Feldt method.

VERIFICATION OF RECORDING SITES

In each animal, all recording sites were verified histologically by iontophoretic injections (2 μA for 5 min) of hydroxystilbamidine (FG; Biotium; equivalent to FluoroGold™) at the end of the recording session. The mice were allowed to recover from anaesthesia and after 5 days (FG) the animals received a lethal anaesthetic injection and were then perfused via the left ventricle with 0.9% NaCl solution followed by fixative (2.5% paraformaldehyde in 0.1 M phosphate buffer, pH 7.4) for 20–25 min. The brains were sectioned on a vibratome and the tissue sections (30 μm thick) were examined using a fluorescence microscope (Zeiss, Axioskop, absorption/emission: 361/536 nm) and the electrode tracks and recording sites were identified.

RESULTS

This study is based on single-unit recordings of IID sensitive neurons in the IC, which receive contralateral excitation and ipsilateral inhibition. A sample of 19 wild-type (5 *Kcna1*$^{+/+}$ mice) and 19 knockout (5 *Kcna1*$^{-/-}$ mice, average age: 39 days) IC neurons was recorded and the neurons' basic response features assessed by their response to the excitatory ear. If the excitatory input conveys mainly inherited information from the LSO, the basic response features may not differ any more than in their input structure. Indeed, characteristic frequencies of 14.8 ± 1.1 kHz (*Kcna1*$^{+/+}$) and of 17.7 ± 2.2 kHz (*Kcna1*$^{-/-}$) did not differ between genotypes ($p = 0.247$). Spontaneous firing rates were low in both, *Kcna1*$^{+/+}$ mice (0.2 [0.0; 3.0] spikes/s) and *Kcna1*$^{-/-}$ mice (0.5 [0.0; 5.4] spikes/s; $p = 0.460$) and despite a 18 dB threshold elevation (*Kcna1*$^{+/+}$: 38 ± 3 dB SPL; *Kcna1*$^{-/-}$: 56 ± 4; $p = 0.002$), evoked firing rates at 20 dB above threshold did not differ significantly between both genotypes (*Kcna1*$^{+/+}$: 40 [18; 106] spikes/s; *Kcna1*$^{-/-}$: 16 [12; 32] spikes/s; $p = 0.072$; **Table 1**). The elevation of thresholds by 18 dB in *Kcna1*$^{-/-}$ IC neurons is similar to the threshold elevation found in the upstream LSO (Karcz et al., 2011). No further significant threshold elevation has been detected between IC neurons of *Kcna1*$^{+/+}$ nor of *Kcna1*$^{-/-}$ mice (Two Way ANOVA, interaction genotype vs. nucleus, $F_{(1, 93)} = 1.87$, $p = 0.175$, $\eta_p^2 = 0.02$). First spike latencies and their variability (jitter) as well as temporal response patterns were used to compare the timing precision in *Kcna1*$^{+/+}$ and *Kcna1*$^{-/-}$ neurons. Consistent with the changes found in the LSO of *Kcna1*$^{-/-}$ mice (Karcz et al., 2011) no significant genotype specific differences were found in latencies and jitter (**Table 1**). Interestingly, the distribution of temporal response patterns changed from chopper-PSTHs (dominant in wild-type) to more onset-PSTHs in the *Kcna1*$^{-/-}$ neurons, indicative for a change in the IC neurons' intrinsic response properties. The classification of the PSTHs was based on the definitions by Pfeiffer (1966). Chopper PSTHs exhibit several regularly spaced peaks with inter-peak distances unrelated to the stimulation frequency. In the present study, chopper units were not further divided into transient choppers which display the regular discharge pattern only at the beginning of the response, and in sustained choppers where prominent periodic discharge peaks were found throughout the entire duration of the response. Units classified as firing onset responses have PST histograms that are characterized by one or two initial peaks with little activity thereafter.

IID-SENSITIVITY IN IC NEURONS COVERS THE WHOLE RANGE OF PHYSIOLOGICAL RELEVANT IIDs

IID sensitivity between *Kcna1*$^{+/+}$ and *Kcna1*$^{-/-}$ IC neurons was compared based on the distribution of IID functions within the range of physiological relevant IIDs quantified by IID_{50} values (**Figures 1A,B**). The neurons' firing rates at sole stimulation of the excitatory (contralateral) ear was normalized and set to 100%. As differences in overall sound intensity will lead to a shift in IID-sensitivity at least in the LSO (Tsai et al., 2010; Karcz et al., 2011), the distribution of IID 50 values was evaluated for two conditions: (1) same excitatory intensity of 80 dB SPL for all neurons and (2) 20 dB above each unit's individual excitatory threshold. For both conditions, successively increasing the intensity at the inhibitory (ipsilateral) ear eventually reduced the

Table 1 | Response features of IID-sensitive IC neurons.

Parameter	*Kcnal*$^{+/+}$					*Kcnal*$^{-/-}$					Test	Significance
	Mean ± S.E.M.	Median	25%	75%	*n*	Mean ± S.E.M.	Median	25%	75%	*n*		
CF_{exc} (kHz)	14.8 ± 1.1	13.8	11.3	17.8	19	17.7 ± 2.2	13.8	11.0	24.4	19	*t*-test	$p = 0.247$
CF_{inh} (kHz)	19.3 ± 2.0	19.7	13.3	24.3	17	17.5 ± 2.8	13.8	11.5	22.9	11	MWRS-test	$p = 0.495$
$Threshold_{exc}$ (dB SPL)	38 ± 3	40	26	53	19	56 ± 4	63	50	69	19	*t*-test	$p = 0.002$
$Threshold_{inh}$ (dB SPL)	46 ± 5	45	35	65	17	61 ± 6	60	46	82	11	*t*-test	$p = 0.089$
Spont. rate (spikes/s)	2.3 ± 0.9	0.2	0.0	3.0	19	5.0 ± 2.2	0.5	0.0	5.4	19	MWRS-test	$p = 0.460$
Firing rate (spikes/s) 20 dB>thres.	57 ± 10	40	18	106	19	38 ± 11	16	12	32	19	MWRS-test	$p = 0.072$
Latency (ms)	12.0 ± 2.1	6.7	5.7	19.7	13	7.5 ± 0.7	6.5	5.5	8.7	18	*t*-test	$p = 0.238$
Jitter (ms)	1.7 ± 0.4	1.4	0.3	3.0	11	0.8 ± 0.3	0.4	0.2	0.8	18	MWRS-test	$p = 0.078$
PSTH (%)	Chopper	55			6/11	Chopper	12			2/17		
	Onset	45			5/11	Onset	65			11/17		
	Primary like	0			0/11	Primary like	18			3/17		
	Other	0			0/11	Other	6			1/17		
$11D_{50}$ (dB)80 dB	7.6 ± 3.1	10.5	0.9	13.8	7	7.2 ± 3.8	8.4	−2.0	15.5	7	*t*-test	$p = 0.938$
IIDslope 80 dB	4.8 ± 1.0	4.4	3.4	6.1	7	4.2 ± 0.8	4.2	2.6	6.0	7	*t*-test	$p = 0.645$
$11D_{50}$ (dB)20 dB > thres.	8.5 ± 4.8	10.7	0.5	22.8	11	8.5 ± 3.7	8.7	−0.3	16.1	8	*t*-test	$p = 0.992$
I I Dslope20 dB > thres.	3.9 ± 1.0	2.8	1.6	6.6	11	5.0 ± 1.4	4.3	1.8	6.2	8	MWRS-test	$p = 0.536$

MWRS-test: Mann–Whitney Rank sum-test.

firing rate to at least 50% (= IID_{50}). Neither condition showed genotype-specific differences, suggesting that the lack of Kv1.1 mediated currents did not change the distribution of IIDs on the IC population level (**Figures 1B,C** and **Table 1**). Analyses on the single neuron level in wild-type mice confirmed a lower sensitivity to overall sound intensity as has been reported for the IC compared to the LSO (Park et al., 2004): the shift of IID sensitivity elicited in *Kcna1*$^{+/+}$ IC neurons did not differ significantly from zero (one-sample *t*-test: $p = 0.782$) whereas level-dependence of IID responses was present in LSO neurons with shifts toward positive IIDs of 0.68 dB per dB excitatory level increase (shift IID_{50}, MWRS-test, $p = 0.023$; IC$^{+/+}$: −0.30 [−0.41; 0.70] dB/dB; LSO$^{+/+}$: 0.68 [0.48; 0.87] dB/dB; **Figure 2C**).

IN THE IC, LOW-THRESHOLD POTASSIUM CURRENTS PREVENT INTEGRATION OF INPUTS RAISED BY NON-PHYSIOLOGICAL IIDs

One function of the IC in IID processing is thought to be an additional modification of IID-sensitivity inherited from the LSO. It has already been suggested that IID-sensitivity in IC neurons is less sensitive toward changes in overall sound intensity (Park et al., 2004; Tsai et al., 2010). Here we explore the role of Kv1.1 low-threshold potassium currents in temporal integration of synaptic inputs into the IC. Therefore, the main excitatory input from the contralateral LSO remained unaltered and a temporal lead of 1, 2, 3, 4 or 5 ms to the stimulus at the ipsilateral ear was introduced. Temporally mismatched, additional non-olivary inputs will have a larger influence on the IID-sensitivity in the IC of *Kcna1*$^{-/-}$ mice as their integration window should be larger. The shift of IID_{50} values per temporal lead was calculated for each neuron including all IID functions that show 95% correlation with 4-parametric sigmoidal fits (**Figure 2**). Positive values represent shifts toward more positive IIDs and indicate more effective inhibition present at lower ipsilateral intensities of the temporally advanced stimulus. Accordingly, a negative shift in IID_{50} values per millisecond temporal lead displays the need for higher ipsilateral inhibitory intensities to suppress 50% of the contralaterally evoked firing rate. The initial contralateral firing rate was evoked by either stimulation at the neuron's CF and 80 dB SPL or at 20 dB above the neuron's threshold. Under both conditions, the introduction of a temporal lead of the inhibitory signal caused the IID functions of *Kcna1*$^{-/-}$ IC neurons to shift to more positive IIDs, whereas no consistent shift was detected in *Kcna1*$^{+/+}$ neurons (contra-intensity 80 dB: shift IID_{50}, *Kcna1*$^{+/+}$: 0.1 ± 0.5 dB/ms; *Kcna1*$^{-/-}$: 1.9 ± 0.6 dB/ms, $p = 0.03$; contra-intensity 20 dB above threshold: *Kcna1*$^{+/+}$: −0.3 −0.5; −0.1] dB/ms; *Kcna1*$^{-/-}$: 1.5 [0.7; 2.6] dB/ms, $p = 0.005$; **Figure 2F**). The effects are illustrated for a representative neuron of each genotype in **Figure 2**. The dot raster plots display the occurrence of an AP at a certain time point for five repetitions of each of the 16 tested IIDs (**Figures 2A,D**). In the wild-type example, different lead times did not systematically change IID sensitivity. The same data plotted in form of IID functions (**Figures 2B,E**) summarizes the weak influence of temporal lead on IID_{50} values in this *Kcna1*$^{+/+}$ neuron (shift of IID_{50}: 0.5 dB/ms). In contrast, the inhibitory effect in the *Kcna1*$^{-/-}$ neuron presented in **Figure 2** consistently increased with increasing ipsilateral inhibitory lead time, resulting in a shift of IID_{50} values of 3.5 dB/ms. On average, *Kcna1*$^{-/-}$ IC neurons have an increased susceptibility toward changes in the arrival times of the binaural inputs, resulting in IID_{50} shifts even outside the range of physiological

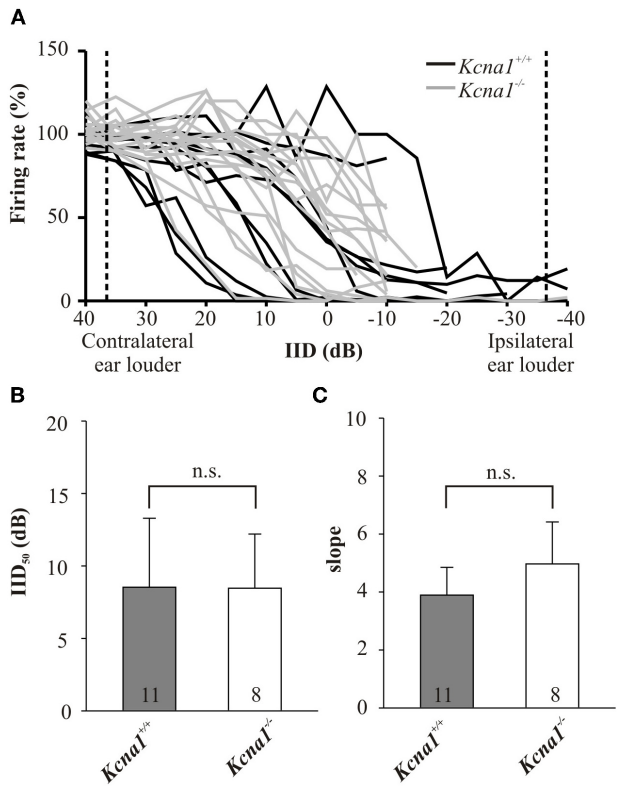

FIGURE 1 | (A–C) IID-sensitivity of IC neurons in wild-type and *Kcna1*$^{-/-}$ mice. **(A)** IID functions obtained from the IC of *Kcna1*$^{+/+}$ (black curves) and *Kcna1*$^{-/-}$ mice (gray curves) are equally distributed between negative and positive IIDs. Dotted lines represent the range of IIDs which a small headed species such as the mouse could possibly encounter in a natural environment (Chen et al., 1995). **(B)** IID curves were fitted by a 4-parametric sigmoid function from which IID values corresponding to a 50% rate reduction (IID_{50}) were determined. No genotype specific differences were found. **(C)** The slope of the IID functions (determined from the sigmoid fit) was also not significantly different between the two genotypes.

relevant IIDs (**Figure 2F**) where they would no longer add reliable information about the location of a sound source. In wild-type animals, the presence of Kv1.1 currents restricts the integration of such a temporal mismatch between LSO and non-olivary inputs and stabilizes the IID functions within the physiological range.

DISCUSSION

The presence of low-threshold potassium currents (Kv1.1) is known to limit action potential firing and restrict temporal summation of synaptic inputs. In the present study we used the *Kcna1*$^{-/-}$ mouse as a model to evaluate the impact of changes in the integration time on IID-sensitivity in the IC. Our results suggest that although a major part of the IID-sensitivity reflects the input from the LSO, correct additional integration of other, non-olivary inputs is necessary to stabilize IID-sensitivity against variations in input timing.

Kv1.1 CURRENTS CONTROL THE NEURONS' SYNAPTIC AND INTRINSIC FIRING PATTERN

Kv1.1 containing channels activate at membrane potentials around −40 mV which is only slightly positive to the neurons' resting membrane potential (Brew and Forsythe, 1995). As sodium currents are activated in a similar voltage range, Kv1.1 mediated currents and sodium currents compete, pulling the membrane potential in hyperpolarizing and depolarizing directions, respectively. Therefore, only strong and fast inputs, as found in cells with coincident inputs or in cells with giant calyceal input, activate sodium currents quickly enough to overcome the competition with Kv1.1 (Oertel, 1985; Manis and Marx, 1991; Trussell, 1999; Johnston et al., 2010). The resulting brief synaptic integration window will restrict temporal summation of synaptic inputs, excitatory and/or inhibitory, to a narrow coincidence window. Vice versa, the lack of Kv1.1 containing channels will allow temporal integration of more disperse inputs, which—in the present study—will lead to a less stable encoding of IID-sensitivity in the IC.

Besides restricting synaptic integration, Kv1.1 mediated currents also determine the intrinsic firing pattern of the neurons. These currents repolarize the membrane quickly and inactivate slowly, which makes firing of subsequent action potentials highly unlikely. Accordingly, Kv1.1 mediated currents are strongly associated with single-spike firing in response to prolonged depolarizations in patch-clamp studies from brain slices (Brew and Forsythe, 1995; Barnes-Davies et al., 2004; Cao et al., 2007). Although it appears as an obvious assumption, this single-spike firing phenotype does not necessarily correspond to single spike (onset) firing in responses to sound burst stimulation *in vivo*. In contrast to a prolonged depolarization by current injection *in vitro*, sound-evoked synaptic transmission is composed of many discrete transient events greatly varying in temporal succession and amplitudes and thus Kv1.1 mediated currents will foster single spiking to EPSP depolarizations at each of these events. Hence, the stronger expression of Kv1.1 will promote single spike responses to a sustained *in vitro* depolarization AND will at the same time enhance discrete firing as in chopper/tonic responses, *in vivo*. Thus, the temporal firing patterns change from wild-type to *Kcna1*$^{-/-}$ mice from single-spiking to multiple firing in the slice and from chopper/Primary-like (tonic) to onset (phasic) discharge patterns *in vivo*. Respective changes were observed in the probability of temporal firing patterns from chopper to onset in the LSO and the IC of *Kcna1*$^{-/-}$ mice (**Table 1**; Karcz, 2011). The prevalence of chopper responses in the wild-type LSO and IC suggests that this is the optimal response pattern for integrating temporally precise binaural inputs over several cycles of the stimulus, whereas in the *Kcna1*$^{-/-}$ mouse the respective information is restricted to the response onset.

ORIGIN OF IID SENSITIVITY IN IC NEURONS

One difficulty in the evaluation of the activity in IC neurons is the lack of knowledge about the origin of binaural response patterns. It is likely that the recorded cell population resembles a mixture of IC neurons that either (1) inherit their IID

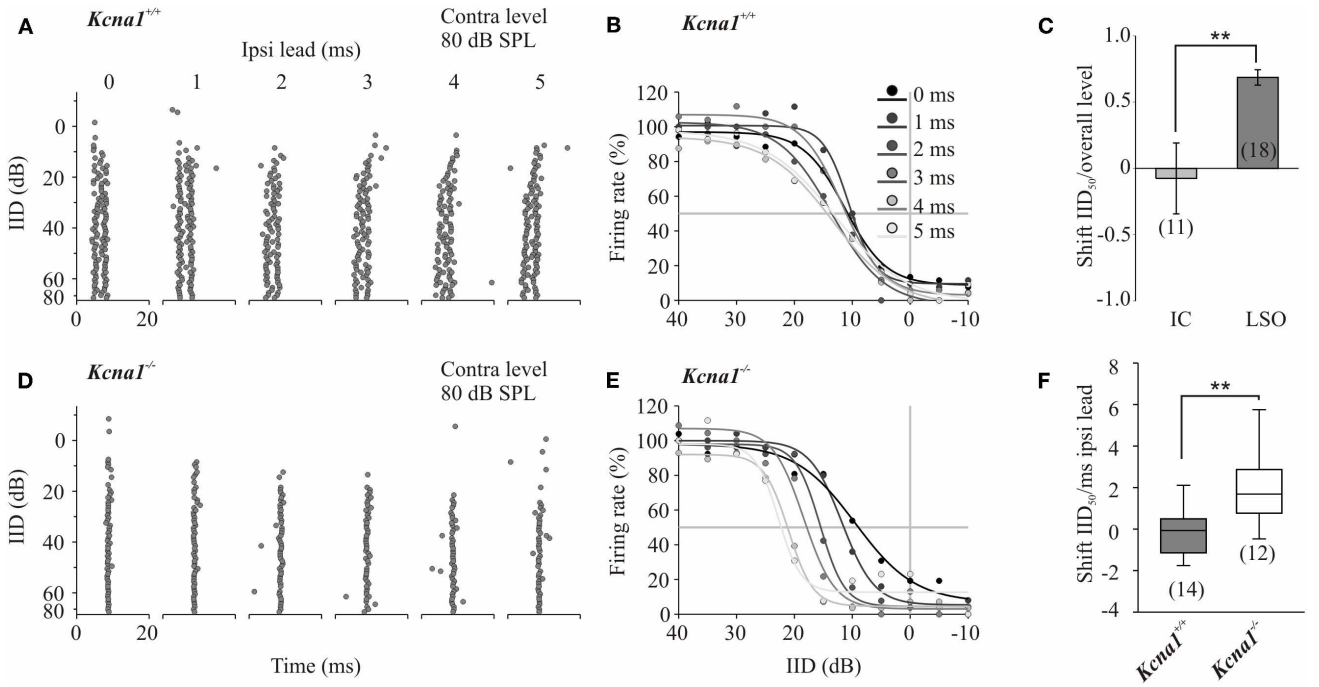

FIGURE 2 | (A–F) Increasing temporal mismatch between inputs shifts IID functions in the *Kcna1*$^{-/-}$ but not the wild-type mice. Instead of the simultaneous onset of the ipsi- and contralateral stimulus, the ipsilateral inhibitory stimulus was presented 1–5 ms in advance. **(A)** Dot raster displays of a representative *Kcna1*$^{+/+}$ neuron show no systematic change in response to different ipsilateral lead times. **(B)** IID functions of the same neuron shown in A did not vary in their IID_{50} values. **(C)** IID-sensitivity in wild-type IC neurons was not only stable toward temporal mismatch in the inputs; they also showed a larger stability toward overall changes in sound intensity compared to wild-type LSO neurons. **(D)** Increasing the delay between excitatory and inhibitory inputs caused increasingly more effective inhibition in *Kcna1*$^{-/-}$ neurons generating a remarkable shift of IID sensitivity toward more positive IIDs **(E)**. This shift in IID-functions with temporal lead of the inhibitory input is quantified in panel **(F)**.

sensitivity unmodified from neurons in the contralateral LSO, (2) inherit some IID sensitivity from neurons in the contralateral LSO which is modified in the IC by additional inputs from non-olivary nuclei, or (3) generate IID sensitivity *de novo* by receiving inputs from non-olivary nuclei converging at the level of the IC (for review see Pollak et al., 2002). The latter two options require precise temporal integration as secured by Kv1.1. One possible source assumed to play a role in shaping or in *de novo* generation of IID sensitivity in IC neurons is the DNLL. This nucleus is innervated by excitatory contralateral CN neurons as well as by ipsilateral and contralateral LSO neurons. DNLL principal neurons send inhibitory GABAergic projections to both ICs (Adams and Mugnaini, 1984; Kelly et al., 2009). Pollak et al. (2002) reported four differential effects on IE neurons of the IC, when GABAergic inhibition originating in the DNLL was blocked (Pollak et al., 2002). Most common was a shift of the IID function to more negative IID values. Hence, a more intense inhibitory stimulus was necessary to achieve maximal reduction of firing compared to the condition with an effective GABAergic DNLL inhibition. The application of bicuculline, a GABA antagonist, or the inactivation of the DNLL contralateral to the IC with kynurenic acid caused equivalent IID shifts. The authors assumed that IID sensitivity in DNLL and LSO neurons differs slightly in that complete inhibition is achieved in the DNLL whilst LSO neurons would still dynamically integrate excitatory and inhibitory inputs. Those differences in IID sensitivity between DNLL and LSO could result from different latency mismatches but involved circuitries are not yet clarified. Tsai et al. (2010) suggested a subtraction model to demonstrate the larger level invariance of IC compared to LSO neurons shown by Park et al. (2004) which was also confirmed is the present study. The subtraction model suggests that each LSO neuron's IID function has its mirror image IID function in a neuron of the opposite LSO (ipsilateral to the IC). The IC then integrates the excitatory responses conveyed by the contralateral LSO and the inhibitory mirror image responses transferred from the ipsilateral LSO via the contralateral DNLL (for details see Figure 5 in Tsai et al., 2010). On the level of the IC strong excitation would converge with weak inhibition. The interplay of the excitatory and inhibitory counterparts originating from the same source remove the bias in form of shift of IID functions due to overall level changes. Failure to integrate such non-olivary inputs as suggested for the *Kcna1*$^{-/-}$ mice, results in larger vulnerability toward changes in overall level or input timing. Besides the actual arrival time of the two inputs, the temporal jitter of the inputs is another parameter that can disrupt binaural integration (Gittelman and Pollak, 2011). Broadening the temporal jitter of at least one input results in

a displacement of the IID-functions in the LSO (Karcz et al., 2011).

Taken together, low-threshold potassium currents act on at least two different levels: I) control of intrinsic spike firing behavior and II) restriction of temporal summation of synaptic inputs. In the IC this results in a shift from chopper to onset response patterns, which can cause a loss of information normally obtained by integrating binaural information during subsequent cycles in the temporal response pattern following complex-structured acoustic signals. So it is conceivable that the contralateral LSO provides the IC neurons with the basic IID information while additional inhibitory inputs from non-olivary nuclei (arriving with a slight delay) are integrated at the level of the IC to remove level variance and to consolidate IID responses of physiologically timed binaural inputs. Inputs arriving outside the IC neurons' integration window might then be attributed to separate sound objects. A disruption of synaptic integration in the IC as in the *Kcna1*$^{-/-}$ mice can then interfere with such quality-control function performed by non-olivary inputs and subsequently result in impaired sound localization in *Kcna1*$^{-/-}$ mice (Allen and Ison, 2012).

ACKNOWLEDGMENTS

We are very grateful to I. D. Forsythe for helpful comments on an earlier version of this manuscript. We also like to thank B. L. Tempel (University of Washington, USA) for generating and sharing the *Kcna1*$^{-/-}$ mice. This work was supported by the German Academic Exchange Service DAAD-D/07/40536 (Anita Karcz) and Graduate School 1097 funded by the German Research Council (DFG) (Anita Karcz), the DFG (390/19-1, Rudolf Rübsamen) and by a HSP3-Habilitation-Fellowship of the Saxonian Government and the Schmitt Program on Integrative Brain Research (Cornelia Kopp-Scheinpflug).

REFERENCES

Adams, J. C., and Mugnaini, E. (1984). Dorsal nucleus of the lateral lemniscus: a nucleus of GABAergic projection neurons. *Brain Res. Bull.* 13, 585–590.

Allen, P. D., and Ison, J. R. (2012). Kcna1 gene deletion lowers the behavioral sensitivity of mice to small changes in sound location and increases asynchronous brainstem auditory evoked potentials but does not affect hearing thresholds. *J. Neurosci.* 32, 2538–2543.

Barnes-Davies, M., Barker, M. C., Osmani, F., and Forsythe, I. D. (2004). Kv1 currents mediate a gradient of principal neuron excitability across the tonotopic axis in the rat lateral superior olive. *Eur. J. Neurosci.* 19, 325–333.

Beyerl, B. D. (1978). Afferent projections to the central nucleus of the inferior colliculus in the rat. *Brain Res.* 145, 209–223.

Boudreau, J. C., and Tsuchitani, C. (1968). Binaural interaction in the cat superior olive S segment. *J. Neurophysiol.* 31, 442–454.

Brew, H. M., and Forsythe, I. D. (1995). Two voltage-dependent K^+ conductances with complementary functions in postsynaptic integration at a central auditory synapse. *J. Neurosci.* 15, 8011–8022.

Brew, H. M., Hallows, J. L., and Tempel, B. L. (2003). Hyperexcitability and reduced low threshold potassium currents in auditory neurons of mice lacking the channel subunit Kv1.1. *J. Physiol.* 548, 1–20.

Cao, X. J., Shatadal, S., and Oertel, D. (2007). Voltage-sensitive conductances of bushy cells of the Mammalian ventral cochlear nucleus. *J. Neurophysiol.* 97, 3961–3975.

Chen, Q. C., Cain, D., and Jen, P. H. (1995). Sound pressure transformation at the pinna of Mus domesticus. *J. Exp. Biol.* 198, 2007–2023.

Chen, X., Shu, S., Kennedy, D. P., Willcox, S. C., and Bayliss, D. A. (2009). Subunit-specific effects of isoflurane on neuronal Ih in HCN1 knockout mice. *J. Neurophysiol.* 101, 129–140.

Dorrscheidt, G. H. (1981). The statistical significance of the peristimulus time histogram (PSTH). *Brain Res.* 220, 397–401.

Gittelman, J. X., Li, N., and Pollak, G. D. (2009). Mechanisms underlying directional selectivity for frequency-modulated sweeps in the inferior colliculus revealed by *in vivo* whole-cell recordings. *J. Neurosci.* 29, 13030–13041.

Gittelman, J. X., and Pollak, G. D. (2011). It's about time: how input timing is used and not used to create emergent properties in the auditory system. *J. Neurosci.* 31, 2576–2583.

Irvine, D. R., Park, V. N., and Mattingley, J. B. (1995). Responses of neurons in the inferior colliculus of the rat to interaural time and intensity differences in transient stimuli: implications for the latency hypotheses. *Hear. Res.* 85, 127–141.

Johnston, J., Forsythe, I. D., and Kopp-Scheinpflug, C. (2010). Going native: voltage-gated potassium channels controlling neuronal excitability. *J. Physiol.* 588, 3187–3200.

Joris, P. X., and Yin, T. C. (1995). Envelope coding in the lateral superior olive. I. Sensitivity to interaural time differences. *J. Neurophysiol.* 73, 1043–1062.

Karcz, A. (2011). *The Significance of the Low Voltage-Gated Potassium ChannelSubunitv1.1fortheProcessing of Sound Source Location*. Ph.D. dissertation, University of Leipzig.

Karcz, A., Hennig, M. H., Robbins, C. A., Tempel, B. L., Rubsamen, R., and Kopp-Scheinpflug, C. (2011). Low-voltage activated Kv1.1 subunits are crucial for the processing of sound source location in the lateral superior olive in mice. *J. Physiol.* 589, 1143–1157.

Kelly, J. B., van Adel, B. A., and Ito, M. (2009). Anatomical projections of the nuclei of the lateral lemniscus in the albino rat (*Rattus norvegicus*). *J. Comp. Neurol.* 512, 573–593.

Kopp-Scheinpflug, C., Fuchs, K., Lippe, W. R., Tempel, B., and Rubsamen, R. (2003). Decreased temporal precision of auditory signaling in kcna1-null mice: an electrophysiological study *in vivo*. *J. Neurosci.* 23, 9199–9207.

Manis, P. B., and Marx, S. O. (1991). Outward currents in isolated ventral cochlear nucleus neurons. *J. Neurosci.* 11, 2865–2880.

Moore, D. R., and Kitzes, L. M. (1985). Projections from the cochlear nucleus to the inferior colliculus in normal and neonatally cochlea-ablated gerbils. *J. Comp. Neurol.* 240, 180–195.

Oertel, D. (1985). Use of brain slices in the study of the auditory system: spatial and temporal summation of synaptic inputs in cells in the anteroventral cochlear nucleus of the mouse. *J. Acoust. Soc. Am.* 78, 328–333.

Park, T. J. (1998). IID sensitivity differs between two principal centers in the interaural intensity difference pathway: the LSO and the IC. *J. Neurophysiol.* 79, 2416–2431.

Park, T. J., Grothe, B., Pollak, G. D., Schuller, G., and Koch, U. (1996). Neural delays shape selectivity to interaural intensity differences in the lateral superior olive. *J. Neurosci.* 16, 6554–6566.

Park, T. J., Klug, A., Holinstat, M., and Grothe, B. (2004). Interaural level difference processing in the lateral superior olive and the inferior colliculus. *J. Neurophysiol.* 92, 289–301.

Pfeiffer, R. R. (1966). Classification of response patterns of spike discharges for units in the cochlear nucleus: tone-burst stimulation. *Exp. Brain Res.* 1, 220–235.

Pollak, G. D., Burger, R. M., and Klug, A. (2003). Dissecting the circuitry of the auditory system. *Trends Neurosci.* 26, 33–39.

Pollak, G. D., Burger, R. M., Park, T. J., Klug, A., and Bauer, E. E. (2002). Roles of inhibition for transforming binaural properties in the brainstem auditory system. *Hear. Res.* 168, 60–78.

Ross, L. S., Pollak, G. D., and Zook, J. M. (1988). Origin of ascending projections to an isofrequency region of the mustache bat's inferior colliculus. *J. Comp. Neurol.* 270, 488–505.

Sanes, D. H., and Rubel, E. W. (1988). The ontogeny of inhibition and excitation in the gerbil lateral superior olive. *J. Neurosci.* 8, 682–700.

Shneiderman, A., Chase, M. B., Rockwood, J. M., Benson, C. G., and Potashner, S. J. (1993). Evidence for a GABAergic projection from the dorsal nucleus of the lateral lemniscus to the inferior colliculus. *J. Neurochem.* 60, 72–82.

Smart, S. L., Lopantsev, V., Zhang, C. L., Robbins, C. A., Wang, H., Chiu, S. Y., Schwartzkroin, P. A., Messing, A., and Tempel, B. L. (1998). Deletion

of the K(V)1.1 potassium channel causes epilepsy in mice. *Neuron* 20, 809–819.

Tollin, D. J. (2003). The lateral superior olive: a functional role in sound source localization. *Neuroscientist* 9, 127–143.

Trussell, L. O. (1999). Synaptic mechanisms for coding timing in auditory neurons. *Annu. Rev. Physiol.* 61, 477–496.

Tsai, J. J., Koka, K., and Tollin, D. J. (2010). Varying overall sound intensity to the two ears impacts interaural level difference discrimination thresholds by single neurons in the lateral superior olive. *J. Neurophysiol.* 103, 875–886.

Wise, L. Z., and Irvine, D. R. (1985). Topographic organization of interaural intensity difference sensitivity in deep layers of cat superior colliculus: implications for auditory spatial representation. *J. Neurophysiol.* 54, 185–211.

Conflict of Interest Statement: The authors declare that the research was conducted in the absence of any commercial or financial relationships that could be construed as a potential conflict of interest.

Received: 29 March 2012; accepted: 14 August 2012; published online: 31 August 2012.

Citation: Karcz A, Rübsamen R and Kopp-Scheinpflug C (2012) Low-threshold potassium currents stabilize IID-sensitivity in the inferior colliculus. Front. Neural Circuits ***6****:60. doi: 10.3389/fncir.2012.00060*

frontiers in
NEURAL CIRCUITS

REVIEW ARTICLE
published: 06 September 2012
doi: 10.3389/fncir.2012.00058

From behavioral context to receptors: serotonergic modulatory pathways in the IC

Laura M. Hurley* and Megan R. Sullivan

Department of Biology, Center for the Integrative Study of Animal Behavior, Indiana University, Bloomington, IN, USA

Edited by:
Manuel S. Malmierca, University of Salamanca, Spain

Reviewed by:
Michael R. Burger, Lehigh University, USA
Wilhelmina Mulders, University of Western Australia, Australia

****Correspondence:***
Laura M. Hurley, Department of Biology, Indiana University, 1001 E. Third St., Bloomington, IN 47405, USA.
e-mail: lhurley@indiana.edu

In addition to ascending, descending, and lateral auditory projections, inputs extrinsic to the auditory system also influence neural processing in the inferior colliculus (IC). These types of inputs often have an important role in signaling salient factors such as behavioral context or internal state. One route for such extrinsic information is through centralized neuromodulatory networks like the serotonergic system. Serotonergic inputs to the IC originate from centralized raphe nuclei, release serotonin in the IC, and activate serotonin receptors expressed by auditory neurons. Different types of serotonin receptors act as parallel pathways regulating specific features of circuitry within the IC. This results from variation in subcellular localizations and effector pathways of different receptors, which consequently influence auditory responses in distinct ways. Serotonin receptors may regulate GABAergic inhibition, influence response gain, alter spike timing, or have effects that are dependent on the level of activity. Serotonin receptor types additionally interact in nonadditive ways to produce distinct combinatorial effects. This array of effects of serotonin is likely to depend on behavioral context, since the levels of serotonin in the IC transiently increase during behavioral events including stressful situations and social interaction. These studies support a broad model of serotonin receptors as a link between behavioral context and reconfiguration of circuitry in the IC, and the resulting possibility that plasticity at the level of specific receptor types could alter the relationship between context and circuit function.

Keywords: serotonin, receptor, 5-HT1A, 5-HT1B, 5-HT2, 5-HT3, behavioral context

INTRODUCTION

The convergence of ascending, descending, and lateral circuitry in the inferior colliculus (IC) creates neural response properties important for decoding specific features of the auditory scene (Huffman and Henson, 1990; Vater et al., 1995; Kidd and Kelly, 1996; Thompson and Schofield, 2000; Malmierca et al., 2005a,b, 2009; Schofield and Coomes, 2006; Winer, 2006; Yavuzoglu et al., 2010; Oertel et al., 2011; Yavuzoglu et al., 2011). To build circuits that respond to changing behavioral contexts, information that is extrinsic to the auditory system must also be incorporated into this convergence. Inputs signaling behavioral context or internal state strongly influence the responses of neurons in the IC to auditory stimuli. For example, external cues indicating the presence of a social partner, or internal signals of stress or reproductive state, can alter evoked responses or gene expression in the IC and its homologs in nonmammalian vertebrates (Mello and Ribeiro, 1998; Miranda and Wilczynski, 2009a,b; Mazurek et al., 2010; Mangiamele and Burmeister, 2011). There are numerous mechanisms through which extra-auditory sources of information influence neural processing in the IC, including input pathways from visual and somatosensory systems or pathways from affective centers such as the amygdala (Groh et al., 2001; Marsh et al., 2002; Metzger et al., 2006; Zhou and Shore, 2006; Dehmel et al., 2008). Hormonal pathways (Greco et al., 1999; Charitidi and Canlon, 2010; Maney and Pinaud, 2011) and centralized neurochemical pathways (Levitt and Moore, 1979; Klepper and Herbert, 1991; Thompson et al., 1994; Habbicht and Vater, 1996; Wynne and Robertson, 1996; Kaiser and Covey, 1997; Tong et al., 2005; Ji and Suga, 2009; Motts and Schofield, 2009, 2011) also provide potential routes for nonauditory signals.

Neuromodulatory networks comprise a large class of mechanisms linking behavioral context and internal state to local changes in auditory processing within the IC. Multiple neuromodulators including norepinephrine, acetylcholine, serotonin, and dopamine are present in the IC (Levitt and Moore, 1979; Klepper and Herbert, 1991; Thompson et al., 1994; Habbicht and Vater, 1996; Wynne and Robertson, 1996; Kaiser and Covey, 1997; Tong et al., 2005; Ji and Suga, 2009; Motts and Schofield, 2009, 2011). Neurons synthesizing these modulatory signals typically respond to salient features of behavioral situations and communicate this information to the IC through axonal projections that may ramify widely in the IC and other regions of the central nervous system. Although in some cases auditory neurons contain these neurochemicals, they can also be found in centralized extra-auditory nuclei (Klepper and Herbert, 1991; Tong et al.,

Abbreviations: 8-OH-DPAT, 8-Hydroxy-2-(di-n-propylamino)tetralin; CP93129, 3-(1,2,3,6-tetrahydropyridin-4-yl)-1,4-dihydropyrrolo[3,2-b]pyridin-5-one; DNLL, dorsal nucleus of the lateral lemniscus; DOI, 2,5-dimethoxy-4-iodoamphetamine; DRN, nucleus raphe dorsalis; IC, inferior colliculus; MK212, 2-Chloro-6-(1-piperazinyl)pyrazine; mCPBG, m-chlorophenylbiguanidine; pCPA, parachlorophenylalanine; SERT, serotonin transporter; SSRI, selective serotonin reuptake inhibitor.

2005; Motts and Schofield, 2009). Neuromodulatory systems have the ability to profoundly alter auditory processing in the IC, facilitating signatures of associative and other types of plasticity, or altering excitatory-inhibitory interactions to change ongoing responses to stimuli (Farley et al., 1983; Habbicht and Vater, 1996; Yigit et al., 2003; Hurley et al., 2004; Ji and Suga, 2009).

This review will focus on how the serotonergic neuromodulatory system in particular alters the function of circuits in the IC. The first reason for this focus is that the serotonergic system is unambiguously extrinsic to the auditory system in adults (Klepper and Herbert, 1991; Thompson and Lauder, 2005; Thompson, 2006; Thompson and Thompson, 2009). The serotonergic system is thus a clear candidate source of nonauditory information to the IC. Second, the serotonergic system is potentially a conduit for several major classes of nonauditory information to the IC, including information on the sleep-wake cycle, stress, and social encounters or social status (Boutelle et al., 1990; Mas et al., 1995; Clement et al., 1998; Jacobs and Fornal, 1999; Portas et al., 2000). Lastly, serotonin strongly modulates the sound-evoked activity of IC neurons (Hurley and Pollak, 1999, 2001; Hurley et al., 2002).

SOURCES OF SEROTONIN ARE EXTRINSIC TO THE IC

Serotonergic innervation of the IC has been noted for decades. In adults, no auditory neurons contain serotonin, although during development neurons in some brainstem auditory nuclei are transiently immunopositive for the serotonin transporter (SERT) and accumulate serotonin (Thompson and Lauder, 2005; Thompson, 2006; Thompson and Thompson, 2009). Dense innervation of the auditory midbrain by serotonergic fibers is conserved across vertebrate groups, as is the relative density of fibers in different subnuclei (**Figure 1**; Klepper and Herbert, 1991; Kaiser and Covey, 1997; Zeng et al., 2007). Fibers are denser in shell regions such as the dorsal and external cortices, something that has been confirmed quantitatively (Klepper and Herbert, 1991; Thompson et al., 1994; Kaiser and Covey, 1997; Hurley and Thompson, 2001; Zeng et al., 2007; Matragrano et al., 2012; Papesh and Hurley, 2012). Although serotonergic projections are somewhat denser in cortical IC regions, substantial innervation by serotonergic fibers also occurs in the central subnucleus (Papesh and Hurley, 2012). Once released, serotonin may act either synaptically or extrasynaptically in some brain regions in a process known as volume release (Bunin and Wightman, 1999). A synaptic morphology suggestive of nonsynaptic release has been described for specialized serotonergic "basket terminals" found around a subset of GABAergic neurons in primary auditory cortex of cat (Defelipe et al., 1991). The structure of serotonergic release sites has not been explored in the IC, however.

The major source of serotonergic fibers to the IC is the dorsal raphe nucleus (DRN), a superior nucleus in a chain of serotonin-producing raphe nuclei in the vertebrate brain. Approximately 80% of raphe neurons that both contain an IC-injected retrograde tracer and co-label with an antibody to serotonin are found in the DRN, with smaller proportions found in other regions such as the median raphe nucleus (14%) (Klepper and Herbert, 1991). Beyond this simple characterization, little information is available regarding the significance of anatomical relationships between the raphe nuclei and the IC. For example, whether subgroups of DRN neurons disproportionately innervate the IC has not been established.

THE SEROTONERGIC SYSTEM PROVIDES INFORMATION ON EXTERNAL EVENTS AND INTERNAL STATE TO THE IC

Supporting the concept that the anatomical connection between the DRN and IC serves as a conduit for multiple types of nonauditory information into the IC, the DRN itself receives inputs from many other brain regions. These include relatively peripheral sensory areas such as the retina, vestibular nuclei, and purported multisensory regions that likely process sound (Kawano et al., 1996; Ye and Kim, 2001; Cuccurazzu and Halberstadt, 2008). They also include regions such as amygdala, preoptic areas, and prefrontal cortex (Peyron et al., 1998; Lee et al., 2003). As a consequence of these projections, the activity of DRN neurons is influenced by a wide range of behaviorally relevant factors. The tonic level of activity of DRN neurons depends heavily on the phase of the sleep-wake cycle, with firing rates higher in waking states. DRN neurons also respond transiently to simple sensory stimuli (Heym et al., 1982; Jacobs and Fornal, 1999), and follow

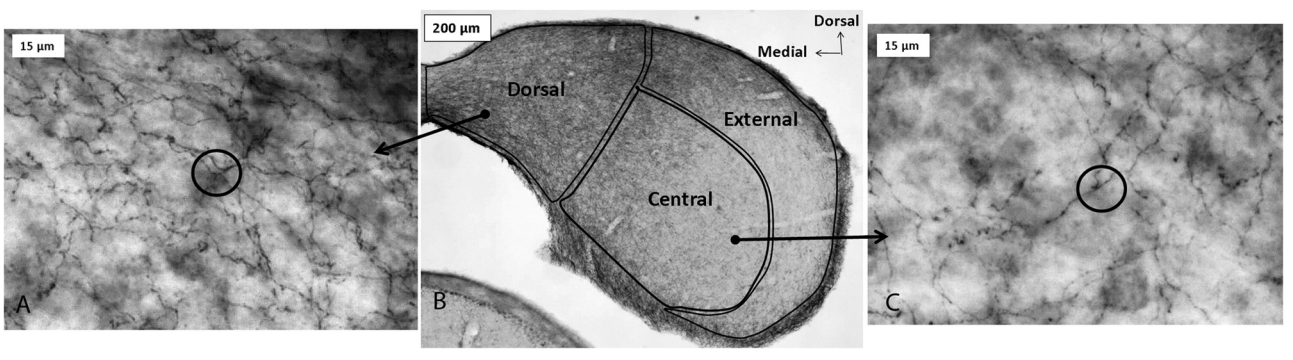

FIGURE 1 | Immunoreactivity for the serotonin transporter (SERT) in the IC of a CBA/J mouse, showing projections from raphe nuclei. Panel **(B)** contains a photomicrograph of a transverse section of IC processed with a SERT antibody, and panels **(A)** and **(C)** show higher-magnification images of positively immunostained fibers in the dorsal cortex and central IC, respectively. Circles in panels **(A)** and **(C)** depict software probes used to estimate fiber density. All panels were reprinted with permission from Elsevier; additional information on the source article can be found in the Acknowledgments.

higher-level features of behavioral paradigms such as the delay of a reward (Miyazaki et al., 2011).

There is also direct evidence that both behavioral state and the occurrence of external events regulate serotonin levels within the IC (**Figure 2**; reviewed in Hurley and Hall, 2011). As expected from the influence of the sleep/wake cycle on activity in the DRN, locally measured serotonin in the IC increases as mice wake from anesthesia (Hall et al., 2010). On top of this tonic change, serotonin increases within minutes in the IC in response to loud broadband noise and to restriction stress, but not to other simple stimuli that evoke strong behavioral responses such as the presentation of food or odor of a predator (Hall et al., 2010). Serotonin also increases in the IC over the course of social interactions including same-sex resident-intruder interactions (Hall et al., 2011) and opposite-sex encounters (unpublished data). The dynamics of serotonergic increases are distinct across different types of behavioral paradigms, such that increases during social interactions are more gradual than during the presentation of simple stressors (Hurley and Hall, 2011).

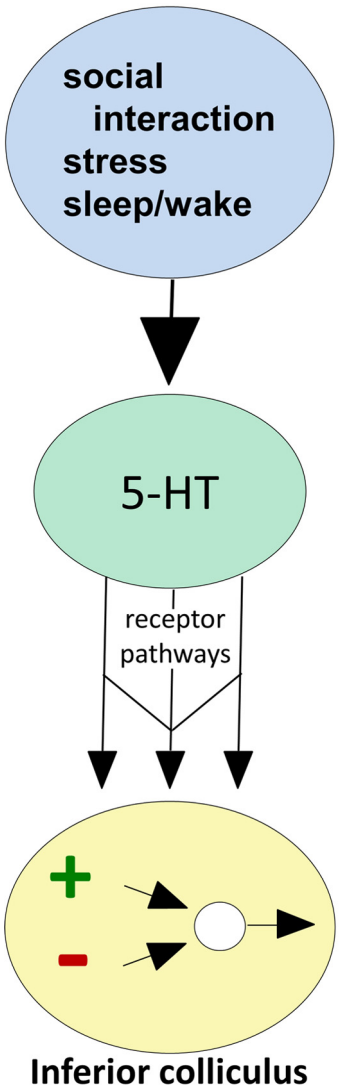

FIGURE 2 | Conceptual diagram illustrating how behavioral state modulates the function of circuitry in the IC, through serotonin receptor pathways. Behavioral factors (top oval) evoke serotonin release (middle oval), which then acts through multiple receptor types expressed by IC neurons (arrows) to influence excitatory-inhibitory circuitry (bottom oval).

SEROTONIN STRONGLY MODULATES AUDITORY RESPONSES IN THE IC

The local application of exogenous serotonin and the release of local stores of serotonin have strong effects on the auditory responses of single IC neurons, supporting the idea that context-specific changes in serotonin have functional consequences (Hurley and Pollak, 1999; Hall and Hurley, 2007). A prominent effect of serotonin is to control the gain of IC responses across the frequency tuning curve. In most cases, serotonin suppresses responses evoked by tones and FM sweeps, but in a minority of neurons, serotonin facilitates responses (Hurley and Pollak, 1999, 2001). Among the more interesting effects of serotonin observed in a subset of IC neurons are frequency-specific changes in firing rate. For these neurons, serotonin may strongly suppress or facilitate responses to tones at some frequencies, but leave responses to other frequencies in the tuning curve relatively unaffected (Hurley and Pollak, 2001). Either uniform gain control or frequency-specific effects can result in changes in the bandwidths of frequency response ranges (Hurley and Pollak, 2001). Such changes in tuning further result in changes in the selectivity of neurons for more complex sounds.

Not surprisingly, the pronounced changes in spike rate induced by serotonin are often accompanied by changes in multiple temporal features of spike trains, including initial spike latency and variance, interspike interval (ISI), and the response durations of IC neurons (Hurley and Pollak, 2005b). Changes in temporal response properties such as the initial spike latency often correspond to changes in spike rate, so that spike suppression is associated with increased latency, and spike facilitation with decreased latency, but can also occur independently of changes in spike rate. In addition to changing temporal response properties of IC neurons, serotonin also targets neurons with particular temporal characteristics. Across multiple studies, neurons with latencies of over approximately 10 ms, or with relatively low first-spike precision, show greater sensitivity to serotonergic agonists including serotonin, a 5-HT1A agonist, and a 5-HT3 agonist (Hurley and Pollak, 2005b; Hurley, 2007; Bohorquez and Hurley, 2009). These consistent findings suggest that longer-latency or lower-precision neurons either preferentially express some types of serotonin receptors or are more responsive to activation of these receptors. Interestingly, IC neurons with latencies of over 12 ms are also more reliably sensitive to NMDA receptor blockade and less sensitive to AMPA receptor blockade (Sanchez et al., 2007). Together, these studies hint at the existence of distinct sets of neurochemical sensitivities in groups of IC neurons defined by their temporal characteristics.

Studies at the level of single IC neurons thus illustrate that serotonin and its receptors are capable of broadly reshaping temporal features of evoked activity in the IC. In agreement

with this hypothesis, brain-wide depletion of serotonin using parachlorophenylalanine (pCPA) alters the latencies of auditory brainstem response (ABR) waves including wave V, which is likely to be influenced by activity in the IC (Funai and Funasaka, 1983; Kaga et al., 1999). The effect of pCPA may depend on the species under study or on stimulus parameters such as repetition rate, since the same type of serotonergic depletion has been reported to either decrease or increase ABR latencies (Revelis et al., 1998). Taken as a whole, however, these findings underscore the global effects of the manipulation of endogenous sources of serotonin on the timing of auditory activity.

SEROTONIN RECEPTOR TYPES DEFINE PARALLEL PATHWAYS FOR REGULATION OF IC CIRCUITRY

The strength and dynamics of the effects of endogenously released serotonin are regulated by local mechanisms in the IC, including high-affinity transporters expressed by serotonergic projections as well as lower-affinity organic cation transporters (Hoffman et al., 1998; Gasser et al., 2009; Hall et al., 2010). A particularly important aspect of local regulation of serotonergic effects is the expression of serotonin receptors by auditory neurons in the IC (Thompson et al., 1994; Hurley, 2006). Of all the classes of molecules regulating serotonergic signaling locally, different types of serotonin receptor have the most potential to provide insight into the wide range of serotonergic effects on IC neurons. This is because receptors are differentially expressed by IC neurons, and different receptor types have highly characteristic effector pathways and patterns of subcellular localization (Hannon and Hoyer, 2008). This diversity creates a wide range of potential neuromodulatory effects that are quite specific for the auditory circuitry of the IC, even though they originate from a diffusely projecting neurochemical system. Different serotonin receptor types therefore act as parallel pathways for altering specific features of circuitry in the IC (**Figure 2**).

Different serotonin receptor types represent an especially rich source of potential functional variability relative to receptors of other types of neuromodulators, because of the exceptionally wide array of serotonin receptor types. There are seven major families of serotonin receptors, several of which include multiple well-characterized and functionally distinct members (Hannon and Hoyer, 2008). Most of these families consist of G-protein coupled receptors. 5-HT3 receptors are the exception, and are cation channels similar in structure to nicotinic acetylcholine receptors (Chameau and Van Hooft, 2006). Consistent with this predominantly metabotropic set of effector pathways, the actions of serotonin receptors in the IC conform to classical models of neuromodulator function. That is, rather than directly creating responses to auditory stimuli, serotonin receptors reconfigure auditory circuits mediated by other neurotransmitters (Harris-Warrick, 2011). Although members of at least five families of serotonin receptor have been reported in the IC, members of only three of these have been explored in terms of their physiological function: 5-HT1, 5-HT2, and 5-HT3 receptors (Chalmers and Watson, 1991; Pompeiano et al., 1992; Thompson et al., 1994; To et al., 1995; Wright et al., 1995; Waeber et al., 1996; Morales and Bloom, 1997; Peruzzi and Dut, 2004; Hurley, 2006; Wang et al., 2008; Bohorquez and Hurley, 2009; Miko and Sanes, 2009).

Multiple studies on the function of specific serotonin receptor types in the IC have used the approach of extracellular recording of sound-evoked responses *in vivo* during the local iontophoresis of serotonin receptor agonists and antagonists (**Figure 3**; Hurley and Pollak, 1999, 2001, 2005a,b; Hurley, 2006, 2007; Hurley et al., 2008; Bohorquez and Hurley, 2009; Ramsey et al., 2010). In these types of studies, inferences on the influence of serotonin receptor types on particular features of the circuitry of the IC are based on three types of information: the demonstrated cellular mechanisms of these receptors throughout the brain, their specific effects in the IC, and their interaction with neurotransmitter systems in the IC. With several important exceptions that are described below, the cellular mechanisms of serotonergic action in the IC are therefore largely unexplored through *in vitro* recording techniques. In the remainder of this section, we present direct and indirect evidence supporting roles for specific serotonin receptor pathways in the modulation of inhibition, the suppression of responsiveness to input, and the mediation of activity-dependent plasticity. The interaction of some serotonin receptor types is also described.

SEROTONERGIC MODULATION OF INHIBITION

The IC contains a strong inhibitory network and excitatory-inhibitory balance is particularly important for acoustic processing in the IC (Yang et al., 1992; Casseday et al., 1994; Fuzessery and Hall, 1996; Lebeau et al., 1996; Casseday et al., 2000). Serotonergic modulation of inhibition is one type of mechanism that shifts the excitatory-inhibitory balance and selectively tunes sensory processing (Ciranna, 2006). GABA is a major inhibitory neurotransmitter in the IC and activates two types of receptors, $GABA_A$ and $GABA_B$ receptors (Wisden et al., 1992; Fubara et al., 1996). $GABA_A$ receptors directly pass Cl^- and have modulatory binding sites for benzodiazepines, barbiturates, neurosteroids, and ethanol (Macdonald and Olsen, 1994). In contrast, $GABA_B$ receptors couple to Ca^{2+} and K^+ channels via G proteins and second messengers (Bowery, 1989). Serotonergic inputs could also potentially modulate glycinergic inhibitory transmission, but there is currently little data on the effects of serotonin on glycinergic inhibition in the IC or other brain areas (Engelhardt et al., 2010). For this reason, we will focus on serotonergic modulation of GABAergic transmission by describing (1) the anatomical association between the serotonergic and GABAergic systems, and (2) the modulation of GABAergic transmission by serotonin.

Anatomical association between 5-HT receptors and inhibitory interneurons

The serotonergic nucleus providing most of the serotonergic fibers to the IC, the DRN, has a distinct relationship with GABAergic neurons in other brain regions that provides a useful comparison for the IC. In the hippocampus and cortex, selective serotonergic modulation of inhibitory neurons has been observed (Freund et al., 1990; Defelipe et al., 1991). In particular, the serotonergic raphe-hippocampal pathway forms multiple synaptic contacts with calbindin D-28k-containing GABAergic interneurons, but not parvalbumin-expressing GABAergic interneurons (Freund et al., 1990). Both calbindin and parvalbumin are calcium binding proteins usually located in inhibitory interneurons.

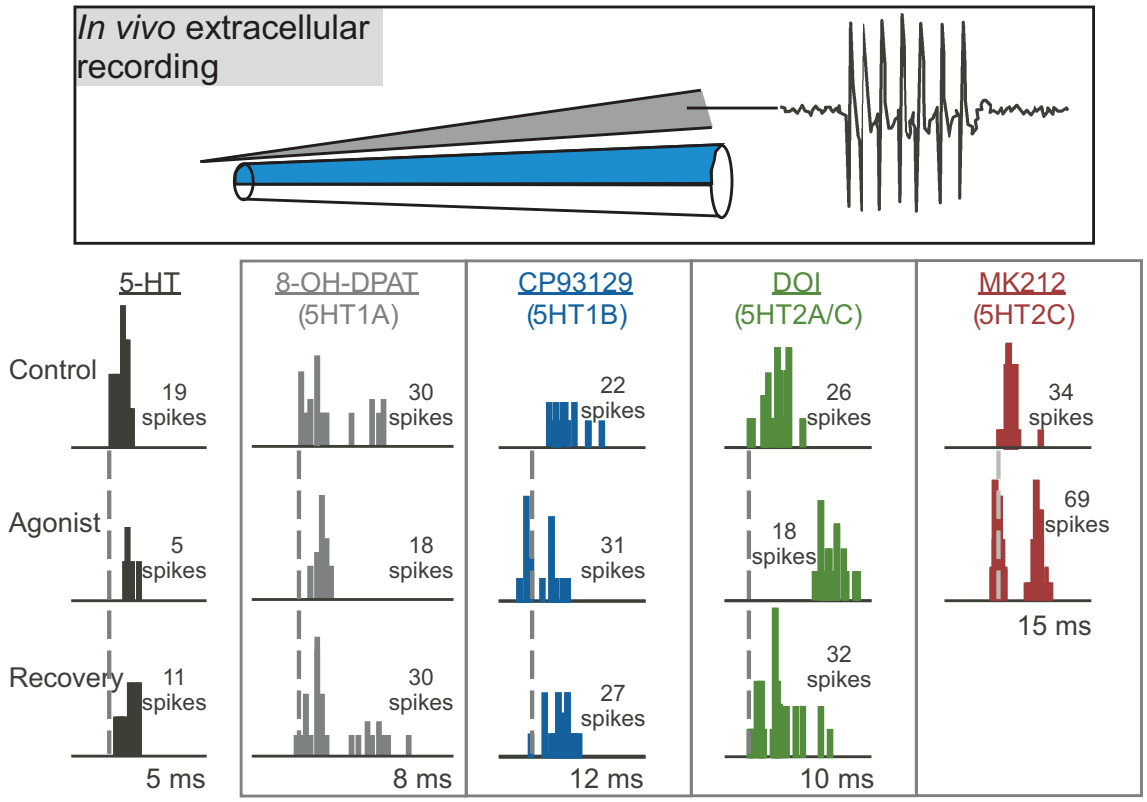

FIGURE 3 | Effects of different serotonin (5-HT) receptor agonists on spike number and latency in response to 32 repetitions of a tone at characteristic frequency. The top panel depicts a "piggyback" electrode used for combined extracellular recording of single neurons and drug iontophoresis. The lower panel shows PSTHs of responses in the control, during the iontophoresis of agonists, and in the recovery are shown for five different sample neurons in the IC. Specific agonists and the receptors they target appear above each neuron. Dashed vertical lines mark the latencies of the earliest spikes in the control condition. Stimuli were: for serotonin, a 10-kHz FM sweep centered at 25 kHz at 20 dB SPL; for 8-OH-DPAT, a 10-kHz FM sweep centered at 25 kHz at 40 dB SPL; for CP93129, a 20-kHz tone at 20 dB SPL; for DOI, a 7-kHz FM sweep centered at 21 kHz at 50 dB SPL; for MK212, a 5-kHz FM sweep centered at 19 kHz at 50 dB SPL. All stimuli were 10 ms in duration. The lower panel was reprinted from a journal published by the American Physiological Society; additional information on the source article can be found in the Acknowledgments.

This suggests that the serotonergic pathway may influence synaptic function through modulation of local inhibitory circuits. Similar anatomical targeting of projections from the DRN onto GABAergic neurons has been observed around somata and dendrites of GABAergic neurons in primary auditory cortex (Defelipe et al., 1991). In other cortical areas, inhibitory interneurons have also been identified as major targets of serotonergic synapses (Smiley and Goldmanrakic, 1996). This input specificity from raphe axons suggests a modulatory diversity in inhibitory cell types.

In the IC, it is not known whether serotonergic inputs to the IC target specific inhibitory neuron cell types as observed in the hippocampus and cortex. However, staining for both calbindin and parvalbumin, which label neuronal cell types targeted by raphe projections in the hippocampus and cortex, is localized to the superficial rim of the external cortex and dorsal cortex and is almost completely absent from the central nucleus (Celio, 1990; Lohmann and Friauf, 1996). To some extent, the distribution of these presumptive inhibitory interneurons therefore parallels the density of serotonergic fibers in the subregions of the IC.

In addition to targeting at the level of serotonergic projections, there is evidence for anatomical segregation of serotonergic effects based on the selective expression of serotonin receptors by different cell types (Jakab and Goldman-Rakic, 2000). In cortical neurons, 5-HT2A receptors are segregated from 5-HT3 receptors. 5-HT2A receptors are found in pyramidal neurons and in GABAergic interneurons expressing parvalbumin and calbindin. 5-HT3 receptors are found in small GABAergic interneurons with calbindin and medium calretinin-containing interneurons (Morales and Bloom, 1997; Jakab and Goldman-Rakic, 2000). This cellular segregation indicates a serotonin-receptor specific segmentation of the GABAergic inhibitory actions along the pyramidal neuronal arbor (Jakab and Goldman-Rakic, 2000).

There is some evidence for the expression of serotonin receptor types by GABAergic neurons in the IC. Approximately two-thirds of GABA-positive neurons are associated with 5-HT1A or 5-HT1B receptors, with neurons positive for 5HT1B receptors more numerous than neurons positive for 5HT1A receptors (Peruzzi and Dut, 2004). GABAergic neurons in the IC can additionally be subdivided into at least two groups based on soma size and their innervation by different types of glutamatergic terminals

(Ito et al., 2009), but whether serotonin differentially regulates these neural classes is unknown. This association between serotonin receptors and GABAergic neurons provides some suggestive evidence that serotonergic modulation may target the inhibitory network in the IC, similar to mechanisms in other brain regions (Peruzzi and Dut, 2004).

It is essential to note that IC neurons receive GABAergic inputs from a range of sources. The dorsal nucleus of the lateral lemniscus (DNLL) sends a bilateral GABAergic projection to IC that shapes binaural responses (Adams and Mugnaini, 1984; Shneiderman et al., 1988; Shneiderman and Oliver, 1989; Faingold et al., 1993; Shneiderman et al., 1993; Burger and Pollak, 2001; Pollak et al., 2002), and other nuclei of the lateral lemniscus also contain GABAergic neurons that project to IC (Zhang et al., 1998). GABAergic projections to IC also arise from neurons in the contralateral IC (Gonzalez-Hernandez et al., 1996; Hernandez et al., 2006). Small numbers of GABAergic neurons project to the IC from periolivary regions and cochlear nuclei (Gonzalez-Hernandez et al., 1996). IC neurons also receive projections from intrinsic GABAergic neurons, which constitute a substantial proportion of cell bodies in the IC (Roberts and Ribak, 1987; Oliver et al., 1994). Which of these populations of GABAergic neurons are modulated by the 5-HT1B and 5-HT2A receptors has not yet been explored, but this information could provide an important clue as to the functional consequences of the modulation of inhibition by serotonin receptors.

Modulation of GABAergic inhibition

Multiple studies have explored the functional interaction between serotonin receptors and GABAergic inhibition. *In vitro* evidence from one study suggests that the 5-HT2A receptor modulates GABAergic inhibition in the IC (Wang et al., 2008). In this study, serotonin enhanced the frequency and amplitude of spontaneous inhibitory postsynaptic currents (sIPSCs) in 70% of neurons recorded. A selective 5-HT2A agonist (α-methylserotonin) mimicked the effect of serotonin on sIPSCS. The observation of enhanced sIPSCs in the IC is consistent with data from other brain regions including the substantia nigra (Stanford and Lacey, 1996) and cortex (Zhou and Hablitz, 1999).

Additional support for a role of the 5-HT2 receptor dependent modulation of inhibition in the lateral superior olive (LSO) is supported by a series of experiments using whole cell voltage-clamp recordings of gerbil slices from postnatal days 6–13 (Fitzgerald and Sanes, 1999). These experiments identified an increase in spontaneous inhibitory postsynaptic currents (IPSCs) with the application of 5-HT. Upon further examination, a 5-HT2 agonist (α-Me-5-HT) reproduced the increase in spontaneous IPSCs and a 5-HT2 antagonist (ketanserin) blocked the induction of spontaneous IPSCs. This specific modulation of inhibition by the 5-HT2 receptor was developmentally dependent and generally not observed beyond postnatal day 8. It is not yet known if a similar developmentally dependent mechanism of serotonergic modulation might be observed in the IC or other regions in the auditory pathway.

Another type of serotonin receptor, the 5-HT1B receptor, may also affect GABAergic transmission. Activation of this receptor type strongly facilitates sound-evoked responses (Hurley, 2006). In other brain regions, the 5-HT1B receptor is localized to presynaptic axons or terminals and decreases the release of a range of neurotransmitters (Sari, 2004). These facts underlie the hypothesis that the 5-HT1B receptor decreases the release of inhibitory neurotransmitter in the IC. An *in vivo* study examined whether the 5-HT1B receptor influences responses to GABAergic inhibition in the IC by using the selective 5-HT1B agonist CP93129 in combination with the co-application of $GABA_A$ receptor antagonists (bicuculline or gabazine; **Figure 4**).

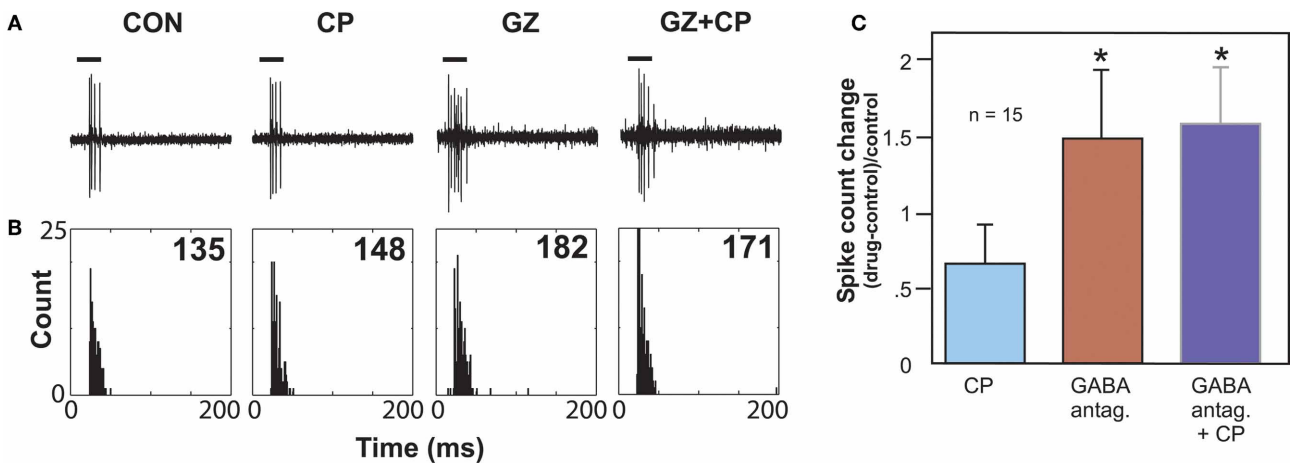

FIGURE 4 | Effects of $GABA_A$ antagonists alone and with 5-HT1B agonist CP93129. (A) Single voltage traces in response to a CF pure tone of 11 kHz for each drug condition. **(B)** PSTH plots consisting of 32 trials with a 250 ms duration for each trial and corresponding to the voltage traces in **(A)**. Numbers represent total spike counts for the 32 tone presentations. Both CP93129 (CP) and the $GABA_A$ antagonist gabazine (GZ) increased spikes alone, but CP93129 did not increase spikes in the presence of gabazine (GZ + CP) relative to gabazine alone. **(C)** Average changes in spike count at CF relative to the control condition for 15 neurons. Panel **(B)** was reprinted from a journal published by the American Physiological Society; additional information on the source article can be found in the Acknowledgments.

This combination tested the prediction that 5-HT1B activation and blockade of GABAergic inhibition would create similar effects. Indeed, 5-HT1B activation and $GABA_A$ blockage, when each manipulation was performed alone, had similar effects on the direction and magnitude of responses, frequency response bandwidths, and ISIs, although the effects of $GABA_A$ blockade were typically larger. Furthermore, following the increase in spike number induced by $GABA_A$ receptor antagonists alone, the addition of a 5-HT1B agonist did not cause a further facilitation, suggesting that blockage of $GABA_A$ receptors reduced the effect of activating 5-HT1B receptors (Hurley et al., 2008). Taken together with the localization of 5-HT1B receptors to presynaptic axons or terminals in other brain regions, these experiments provide evidence for modulation of GABAergic inhibition in the IC by the 5-HT1B receptor.

Multiple authors have found that GABAergic inhibition surrounding the characteristic frequencies of IC neurons sharpens frequency tuning (Yang et al., 1992; Fuzessery and Hall, 1996; Palombi and Caspary, 1996; Lebeau et al., 2001; Lu and Jen, 2001). A functional test of whether the 5-HT1B receptor regulates excitatory-inhibitory balance in these frequency regions was performed *in vivo* by suppressing the excitatory responses to a tone at the characteristic frequency with the co-presentation of tones at surrounding frequencies (Hurley et al., 2008). The effect of a 5-HT1B selective agonist (CP93129) on the excitatory-inhibitory balance was then tested using such two-tone stimuli. The 5-HT1B agonist often decreased the suppression of the tone at characteristic frequency by tones at surrounding frequencies (Hurley et al., 2008). The 5-HT1B agonist also expanded frequency tuning in many neurons, and in some cases the frequencies of expansion corresponded to frequencies at which reduction of suppression occurred. This suggests that the 5-HT1B receptor regulates the sharpness of frequency tuning in some IC neurons by reducing surround inhibition.

All of the studies described above indicate that GABAergic inhibition in the IC is regulated by multiple types of serotonin receptor, which influence GABAergic transmission in different ways.

SUPPRESSION OF RESPONSES BY SEROTONIN

A common effect of applying serotonin is the suppression, or decrease in magnitude, of evoked responses and spontaneous activity in IC neurons (Hurley and Pollak, 1999). Suppression by serotonin could be achieved through multiple serotonin receptor types and through pre- and postsynaptic mechanisms. The 5-HT1A receptor is likely to be one of the receptors, if not the predominant receptor, mediating suppression of responses. The expression of the 5-HT1A receptor is widespread throughout the IC including expression in inhibitory neurons (Duncan et al., 1998; Peruzzi and Dut, 2004). The 5-HT1A receptor is often located somatodendritically and typically decreases postsynaptic responses through an association with inward-rectifying potassium channels (Okuhara and Beck, 1994; Polter and Li, 2010).

Experiments in the IC of the mouse and Mexican free-tailed bat have shown that a 5-HT1A receptor agonist (8-OH-DPAT) suppress responses and shifts the temporal response profile to pure tones and FM sweeps (**Figure 5**; Hurley, 2006, 2007).

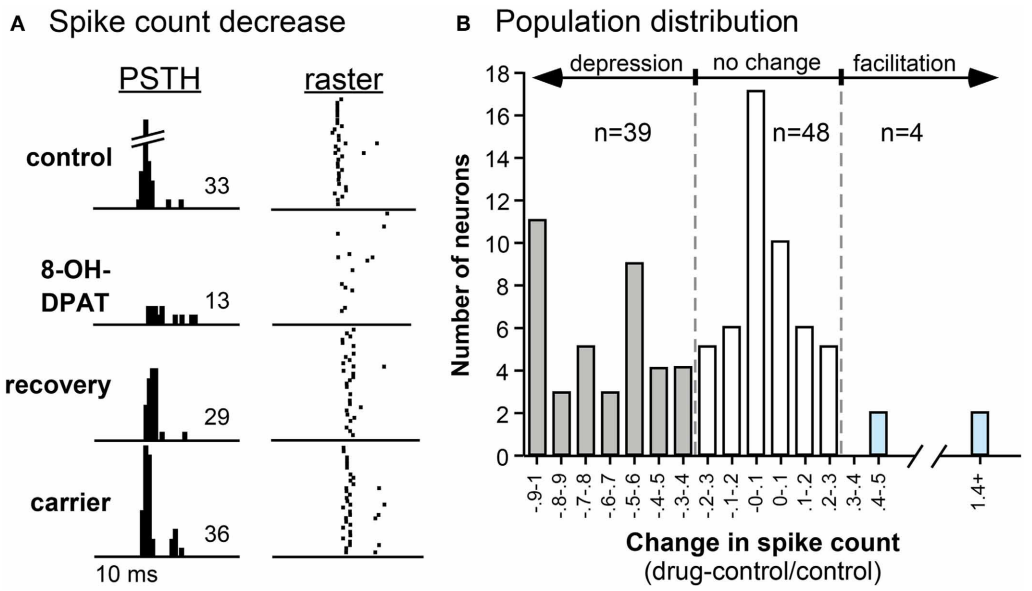

FIGURE 5 | Effects of the selective 5-HT1A agonist 8-OH-DPAT on a single neuron (A) and on a population of IC neurons (B). (A) PSTH and raster plots of the response of a neuron to an FM sweep in the control, during iontophoresis of 8-OH-DPAT, during the recovery, and during the iontophoresis of the carrier solution. The stimulus was a 30-dB SPL, 10-kHz FM sweep centered at 25 kHz. **(B)** Histogram of changes in spike count evoked by 8-OH-DPAT in 91 IC neurons. Negative values indicate decreases in spike count relative to the pre-drug control, and positive values indicate increases in spike count. Across the neuron population, the effect of 8-OH-DPAT is predominantly suppressive. All panels were reprinted with permission from Elsevier; additional information on the source article can be found in the Acknowledgments.

5-HT1A activation often increases the first-spike latency and ISI, while differentially suppressing secondary spikes in IC neurons (Hall and Hurley, 2007; Ramsey et al., 2010). Interestingly, the 5-HT1A receptor agonist produces the effects most similar to applying serotonin alone when compared to agonists for 5-HT1B and 5-HT2C receptors, suggesting that the 5-HT1A receptor may play a comparatively strong role in serotonergic modulation (Hurley, 2006).

Similar to the diversity of effects of serotonin (Hurley and Pollak, 1999), selective activation of the 5-HT1A receptor results in facilitation in a small number of IC neurons (Hurley, 2006). The net result of 5-HT1A receptor-induced hyperpolarization may depend on whether the receptors are present on an excitatory or inhibitory neuron. With an excitatory neuron, the result would be a direct suppression of responses. However, with an inhibitory neuron, the result could be facilitation of the responses of postsynaptic neurons. In several brain regions, the 5-HT1A receptor has been demonstrated to alter presynaptic GABA release (Kishimoto et al., 2001; Lee et al., 2008). Additional experiments in the IC with 5-HT1A agonists and antagonists in combination with $GABA_A$ receptor antagonists (bicuculline or gabazine) will be required to determine the interactions between the 5-HT1A receptor and GABAergic inhibition in the IC.

A common consequence of suppression by the 5-HT1A receptor is a narrowing in the frequency tuning curves of the neurons. Functionally, response suppression may therefore serve to increase the selectivity of responses to auditory stimuli. This would provide an additional mechanism in addition to direct shifts in the inhibitory-excitatory synaptic balance for tuning of responses to auditory stimuli. A range of mechanisms, including suppression and inhibition, likely acts concurrently to result in behavioral context-related changes in the IC. Suppression based on postsynaptic hyperpolarization may provide an important mechanism for serotonergic-dependent tuning of auditory processing.

SHORT-TERM PLASTICITY AND THE 5-HT3 RECEPTOR

Of all serotonin receptor types in the IC, 5-HT3 receptors might be expected to mediate the most rapid and neurotransmitter-like effects. 5-HT3 receptors have a pentameric structure similar to that of nicotinic acetylcholine receptors (Chameau and Van Hooft, 2006). Also similar to AChRs, 5-HT3 receptors are cation channels that allow the passage of Na+ and Ca2+ ions. Consistent with this mechanism of action, activation of 5-HT3 receptors does create rapid effects in some IC neurons, in seconds or less, comparable to application of neurotransmitters such as GABA and glutamate (Bohorquez and Hurley, 2009). For many IC neurons, however, the effects of activating the 5-HT3 receptor are much more slowly developing, with half-maximal effects occurring over a range from 10 to more than 150 s, with correspondingly long recovery times. Furthermore, in a majority of 55% of neurons that respond to a 5-HT3 agonist, the effects of 5-HT3 activation are suppressive rather than excitatory. One possible mechanism that could account for a suppressive effect of the 5-HT3 receptor is that it excites presynaptic inhibitory neurons such as GABAergic neurons (Shneiderman et al., 1993; Oliver et al., 1994; Gonzalez-Hernandez et al., 1996; Zhang et al., 1998). GABAergic neurons are a target of the 5-HT3 receptor in other sensory systems, making this a plausible mechanism (Morales and Bloom, 1997; Xiang and Prince, 2003). This potential regulation of GABergic pathways by the 5-HT3 receptor was assessed in one study by comparing the effects of a 5-HT3 receptor agonist in the presence versus absence of a $GABA_A$ antagonist. The rationale behind this experiment was similar to that used for assessing whether the 5-HT1B receptor interacted with GABAergic transmission, with the logic that blocking $GABA_A$ receptors should reduce the effect of 5-HT3 activation, if the 5-HT3 receptor acts by increasing GABA release. Unlike the 5-HT1B receptor, the effect of 5-HT3 activation was not decreased and was even accentuated in some neurons in the presence of a $GABA_A$ antagonist (Bohorquez and Hurley, 2009). This finding led to rejection of the hypothesis that the 5-HT3 receptor suppresses evoked activity in many IC neurons by exciting presynaptic GABAergic neurons.

A second hypothesis that could account for the range of effects of the 5-HT3 receptor in the IC is that this receptor has a genuinely modulatory influence via the admission of calcium into IC neurons. An interesting comparison between two independent studies examining the 5-HT3 receptor in the IC provides evidence for this hypothesis. One of these studies measured responses to current injection *in vitro* (Miko and Sanes, 2009). Following strong stimulation of lemniscal input fibers, the spiking response to a threshold-level current injection exhibited a short-term change in gain, usually facilitation, lasting seconds to minutes. Blockade of the 5-HT3 receptor removed or reduced the effect of fiber stimulation on gain control, at the same time reducing an associated depolarization of membrane potential. In contrast, antagonists of multiple other transmitter pathways, including ionotropic GABAergic and glycinergic receptors and both nicotinic and muscarinic cholinergic receptors, facilitated the change in gain. Furthermore, a similar decrease in positive gain was created by blockade of L-type calcium channels. These results all suggest an induction of plasticity in response gain by the 5-HT3 receptor, potentially by the postsynaptic admission of calcium (Miko and Sanes, 2009).

In a companion study *in vivo*, the effect of activating the 5-HT3 receptor corresponded to the level of spiking (Bohorquez and Hurley, 2009). Across the IC neuron population, higher rates of evoked spiking were associated with larger effects of 5-HT3 receptor activation. In a subset of single neurons, the effect of 5-HT3 receptor activation varied depending on the stimulus repetition rate and consequent spike rate per stimulus (**Figure 6**). As the stimulus presentation rate increased, associated with a decrease in the spike number, the effect of the 5-HT3 receptor shifted from relative suppression to relative facilitation. Functionally, the 5-HT3 agonist flattened the relationship between stimulus presentation rate and spike rate, in effect equalizing neural responses across different repetition rates. Together, these *in vitro* and *in vivo* studies suggest that the 5-HT3 receptor underlies a form of short-term plasticity in the IC, altering response gain in an activity-dependent manner, and potentially acting to stabilize the level of activity of IC neurons to stimulus trains.

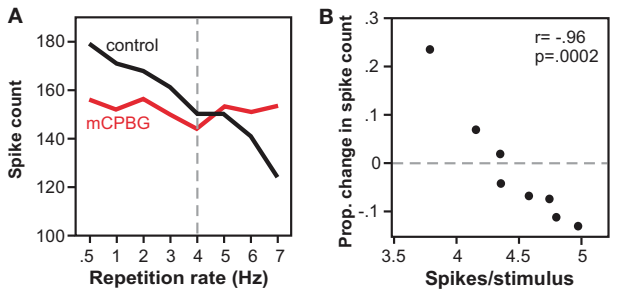

FIGURE 6 | Effects of the 5-HT3 receptor vary with stimulus repetition rate and spike rate. (A) Spike counts decrease with repetition rate in the control, but not during iontophoresis of a 5-HT3 agonist (mCPBG) for a single IC neuron. Stimulus consisted of a 20 ms tone at 13 kHz. **(B)** The same data as in **(A)** is plotted as a function of mCPBG-evoked change in spike count versus control spike rate. The 5-HT3 agonist increases spike count at low spike rates, and decreases spike count at high spike rates. All panels were reprinted with permission from Elsevier; additional information on the source article can be found in the Acknowledgments.

INTERACTIONS OF RECEPTORS CREATE NOVEL COMBINATIONS OF EFFECTS

As instructive as it is to understand the effects of individual serotonin receptor types, a realistic model of the effects of serotonin in the IC must involve some degree of receptor interaction, because multiple receptor types would likely be co-activated by the release of serotonin. With the diversity of receptor types in the IC, many of which have disparate cellular modes of action and distinct effects on evoked activity, predicting the nature of receptor interaction is not a straightforward matter. A study on the interactions of two specific serotonin receptor types within the same receptor family, the 5-HT1A and 5-HT1B receptor, illustrates this point.

The 5-HT1A and 5-HT1B receptors make an interesting comparison, since both are expressed widely among IC neurons (Thompson et al., 1994; Peruzzi and Dut, 2004), and activation of each receptor type correspondingly influences evoked responses of a large proportion of IC neurons. As described earlier, the effects of these receptors on evoked activity in response to tones are opposite, in that activation of the 5-HT1A receptor suppresses evoked responses and in some neurons reduces the bandwidth of frequency tuning, while activation of the 5-HT1B receptor facilitates evoked responses and often increases the bandwidth of frequency tuning. Each receptor also influences the timing of evoked responses for some neurons, with the 5-HT1A receptor usually increasing first-spike latency and ISI, and the 5-HT1B receptor often decreasing first-spike latency and ISI.

If they are not to simply antagonize each other, there are several potential ways for the 5-HT1A and 5-HT1B receptor to functionally interact. One of these is that they are segregated from each other on separate local circuits in the IC, so that they do not directly interact at all. In support of this, some IC neurons show disproportionately greater effects of activation of either the 5-HT1A or 5-HT1B receptors. Functional segregation of the two receptor types is not the complete solution to the puzzle of receptor interaction, however, because many IC neurons show substantial responses to individual activation of both receptor types (Ramsey et al., 2010). This suggests that both receptor types do influence the same local circuitry, as reflected in the activity of a single neuron. For these multiple-responsive neurons 5-HT1A and 5-HT1B receptors do not simply antagonize each other. When activated concurrently, an interesting differential effect of the two receptors types on spike rate versus spike timing emerges. For measures of evoked activity that reflect spike number, including spike rate at the characteristic frequency or the bandwidth of frequency tuning, the receptors do interact additively. That is, the effect of combinatorial activation of the two receptor types on spike rate can generally be predicted by summating the effect of each receptor type alone for a given neuron. In contrast, the 5-HT1A receptor dominates measures of spike timing including the first-spike latency and ISI, so that only the effect of the 5-HT1A receptor predicts the effect of the drug combination. These results fit the model of the 5-HT1A receptor as located postsynaptically on soma and dendrites, exerting control over the timing of spikes by causing potassium channels to open. These findings not only provide a resolution to the puzzle of receptor co-activation, but suggest that general suppression of responsiveness (5-HT1A) combined with presynaptic disinhibition (5-HT1B) can create novel aggregate effects, even for simple sounds such as tones at CF.

CONCLUSIONS

The experiments described above support the model of different serotonin receptor types as gates to separate but interacting effector pathways. As such, they are a critical node gating the route from behavioral context to the function of the circuitry of the IC. **Table 1** and **Figure 7** summarize the outcomes of studies on different receptor types in the IC and present a simplified model of the role of these receptors in the excitatory-inhibitory circuitry of the IC. Many features of this model, such as whether particular receptor types play special roles in specific contexts by virtue of their dynamics or closeness to serotonin release sites, are still murky. Nevertheless, the model provides a key for specific predictions in two broad areas of interest in understanding auditory function: (1) the role of the serotonergic system in specific behavioral contexts such as social interaction, and (2) how plasticity in the serotonergic system could alter the relationship between behavioral context and auditory processing or perception.

CONTEXT-DEPENDENCE OF SEROTONERGIC REGULATION

The measurement of serotonin in the IC of behaving animals suggests that serotonin regulates auditory processing in multiple behavioral contexts, including in waking states, in response to stressful or potentially threatening events, and during social interactions. Changes in serotonin that occur during the latter are worth examining in some detail, since they track behaviorally salient aspects of social interactions such as individual variation in social responses, experience, and age. In mice in which serotonin has been measured in the IC using voltammetry, individual differences in the serotonergic response to a novel social partner are quite pronounced, and correspond to social behaviors such as anogenital investigation and to nonsocial behaviors such as the overall level of activity (Hall et al., 2011). These behavioral correlations suggest that the serotonergic signal in the IC

Table 1 | Summary of the effects of different serotonin receptor types in the IC.

5-HT receptor type	Localization	Preparation	Effects in IC
1A	somatodendritic[1]	*in vivo*[a,b]	decreases evoked responses
1B	axonal/terminal[2]	*in vivo*[a,c]	increases evoked responses
2A	variable[3]	*in vitro*[d]	increases frequency and amplitude of GABAergic IPSCs
2C	postsynaptic density, somatodendritic[4]	*in vivo*[a]	increases evoked responses
2A/C	–	*in vivo*[a]	decreases evoked responses
3	variable[5]	*in vivo*, *in vitro*[e]	mixed gain control, activity-dependent

[1]Hannon and Hoyer, 2008; [2]Sari, 2004; [3]Bombardi, 2012; Jakab and Goldman-Rakic, 1998; [4]Anastasio et al., 2010; Liu et al., 2007; [5]Carrillo et al., 2010; [a]Hurley, 2006; [b]Hurley, 2007; [c]Hurley et al., 2008; [d]Wang et al., 2008; [e]Miko and Sanes, 2009; Bohorquez and Hurley, 2009.

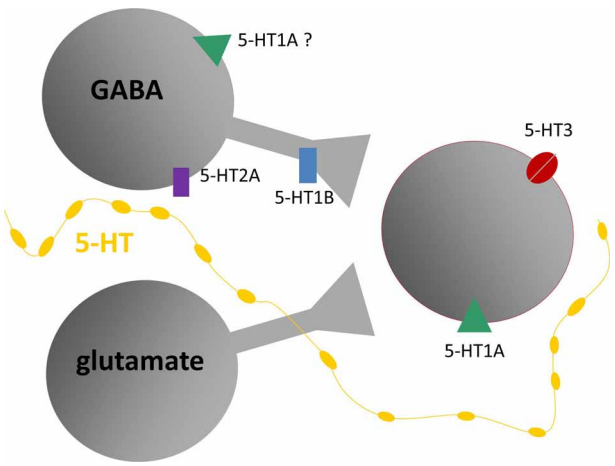

FIGURE 7 | Model of putative locations of 5-HT1A and 5-HT1B receptors relative to GABAergic and glutamatergic circuitry in the IC, based on *in vivo* and *in vitro* recordings. Gray shapes are auditory neurons that express serotonin (5-HT) receptors responding to release of serotonin by projections from raphe nuclei (yellow line). Red outline indicates neurons recorded in the IC, receiving inputs from presynaptic GABAergic and glutamatergic neurons. Diagram does not include all known types of serotonin receptors or types of inputs received by IC neurons.

conveys information about the responsiveness of individual mice to a social stimulus. Moreover, being in a social experiment leaves a long-lasting trace, since both the serotonergic signal in the IC and some behaviors are increased in male mice undergoing a second social encounter occurring one week later, although this could be an effect of either the social interaction itself or of stress (**Figure 8**). Finally, predictable factors like age also significantly correlate with not only the serotonergic response to a social encounter but also the density of serotonergic fibers, both of which decrease over a period of young adulthood (Hall et al., 2011). All of these results describe a regulatory signal that varies with socially salient information.

The IC and its homologs, including the torus semicircularis in amphibians and fish and the mesencephalicus lateralis, pars dorsalis (MLd) in birds, are important early processing centers for auditory signals produced in social interactions. Behaviorally, the auditory midbrain is necessary for responses to mate calls in some species (Endepols et al., 2003). Stimulus-evoked gene activity in the torus semicircularis reflects discrimination among different vocal signals, sometimes in a sex-specific manner (Hoke et al., 2004, 2010; Mangiamele and Burmeister, 2011). Furthermore, the processing of social vocalizations in auditory midbrain nuclei is context-dependent, in that neural responses vary with natural or experimental manipulation of reproductive state, or with salient factors such as the prospect of reward (Goense and Feng, 2005; Maney et al., 2006; Metzger et al., 2006; Miranda and Wilczynski, 2009a,b).

Consistent with these more global measures of the discrimination of social signals, individual IC neurons may themselves be selective for communication calls. With some exceptions, auditory midbrain neurons in a wide range of species show greater responses for auditory signals over nonvocalization sounds with similar characteristics (including time-reversed vocalizations), and may further be selective for specific vocalizations (Diekamp and Schneider, 1988; Bodnar and Bass, 1997; Crawford, 1997; Alder and Rose, 2000; Woolley et al., 2006; Andoni et al., 2007; Pincherli Castellanos et al., 2007; Suta et al., 2007, 2008; Andoni and Pollak, 2011; Elliott et al., 2011). In demonstrating selectivity for vocalizations, auditory midbrain neurons differ from neurons in some lower auditory nuclei. IC neurons show a higher level of vocalization selectivity than neurons that project to the IC from the dorsal and intermediate nuclei of the lateral lemniscus as a result of the convergence of inhibitory and excitatory inputs (Klug et al., 2002; Xie et al., 2005). Additional spectral or temporal coding mechanisms further contribute to selective midbrain responses (Epping, 1990; Bodnar and Bass, 1997; Leroy and Wenstrup, 2000; Bauer et al., 2002; Klug et al., 2002; Yavuzoglu et al., 2010; Andoni and Pollak, 2011; Pollak et al., 2011; Schneider and Woolley, 2011; Yavuzoglu et al., 2011), and patterns at the level of the neuron population may further increase the selectivity of vocalization encoding (Bodnar et al., 2001; Holmstrom et al., 2010; Schneider and Woolley, 2010).

Completing the link between serotonin and social situations, serotonin directly modifies the processing of social stimuli in the IC. In *in vivo* experiments in Mexican free-tailed bats, exogenously applied serotonin modulates the responses of individual IC neurons to playback of vocalizations from social interactions (Hurley and Pollak, 2005a). For most neurons, serotonin increases the selectivity of neural responses across a range of calls. Based on the regulation of less complex stimuli by different receptor types, reasonable predictions are that the modulation of vocalization responses by particular receptor types

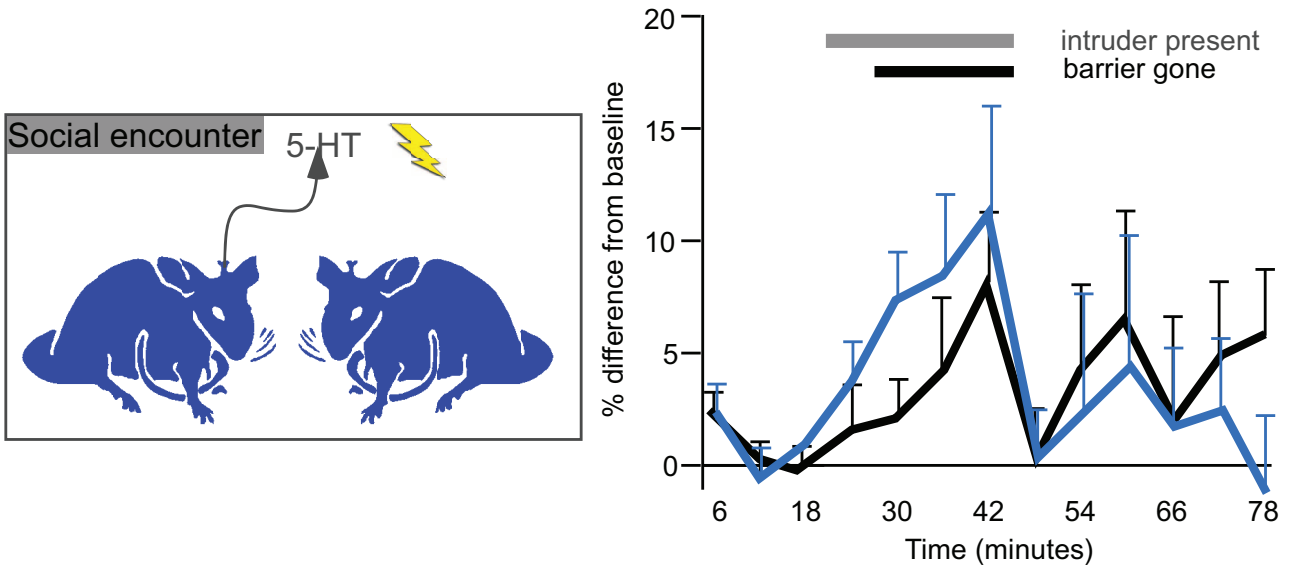

FIGURE 8 | Voltammetrically measured serotonin in the IC in resident male mice presented with a novel conspecific intruder (left panel). The right panel plots changes in serotonin over baseline measurements. The gray bar represents time in which an intruder male was placed in the cage of a resident. The black bar represents time in which a Plexiglass barrier was removed and males directly interacted. The black line represents the initial interactions, and the blue line represents interactions with a new intruder by the same residents one week later. Serotonin increases gradually during the social interaction, and declines abruptly afterwards. The right panel was reprinted from a journal published by the American Psychological Association; additional information on the source article can be found in the Acknowledgments.

should vary among neurons, should depend in part on the structure of a given call, and that different serotonin receptor types may interact to influence vocalization coding in novel ways.

All of this information on serotonergic function in the IC at multiple levels of analysis suggests a possible scenario of the role of serotonin in social encounters. During social interactions, serotonin in the IC would steadily increase over the course of a social interaction, and would be related to the magnitude of the behavioral response. Many IC neurons would show a parallel increase in selectivity for vocalizations or other sounds produced during the encounter. Overall, this could create population-level responses for different vocalizations that are more distinct from each other in the presence of serotonin. This scenario serves as the basis for an as yet untested prediction that behavioral responses to social vocalizations correspond to levels of serotonin in the IC.

SEROTONIN-AUDITORY PLASTICITY; A CHANNEL FOR PAST EXPERIENCE

An exciting prospect that has emerged as a result of work in the IC and other sensory regions is that plasticity in the infrastructure of the serotonergic system itself can provide a route for information about past events to influence neural circuitry. Plasticity in serotonergic-IC interactions occurs under a number of different conditions. The experience of acoustic trauma alters a fundamental aspect of the serotonergic system, the density of fibers within the IC. This is seen when a unilateral tonal trauma creates an imbalance in the density of serotonergic fibers between contralateral colliculi, with the IC contralateral to the traumatized ear having a lower density of fibers than the IC contralateral to the protected ear (**Figure 9**; Papesh and Hurley, 2012). Plasticity in the serotonergic system may also be guided by internal factors including age and reproductive state. Age influences both the density of serotonergic fibers and acute changes in serotonin, such that both fiber density and serotonin release during social encounters decline over young adulthood in mice (Hall et al., 2011; Papesh and Hurley, 2012). In older animals, serotonin content may rise again in the IC or other auditory regions (Cransac et al., 1996; Shim et al., 2012). Reproductive readiness, via gonadal hormones, also increases serotonergic fiber density in the avian auditory midbrain (Matragrano et al., 2012).

Plasticity is also observed at the level of serotonin receptors. With increasing age from adulthood through old age, the 5-HT2B receptor is upregulated in the IC (Tadros et al., 2007). Expression of this receptor type is further upregulated in old mice with severe hearing loss. The amount of expression of the 5-HT2B receptor is correlated with functional metrics of hearing such as the amplitude of the distortion product otoacoustic emission (DPOAE) and with the threshold of the ABR. In addition to age, peripheral damage leads to receptor plasticity. Following cochlear ablation, the expression of both 5-HT2C and 5-HT5B receptors is altered, but in different directions and with different dynamics. 5-HT2C expression increases from 3 through 90 days following ablation, and 5-HT5B receptor expression decreases from 5–21 days, and recovers by 90 days following ablation (Holt et al., 2005). Thus, the balance of different serotonin receptor types may be altered by plastic responses to aging or peripheral

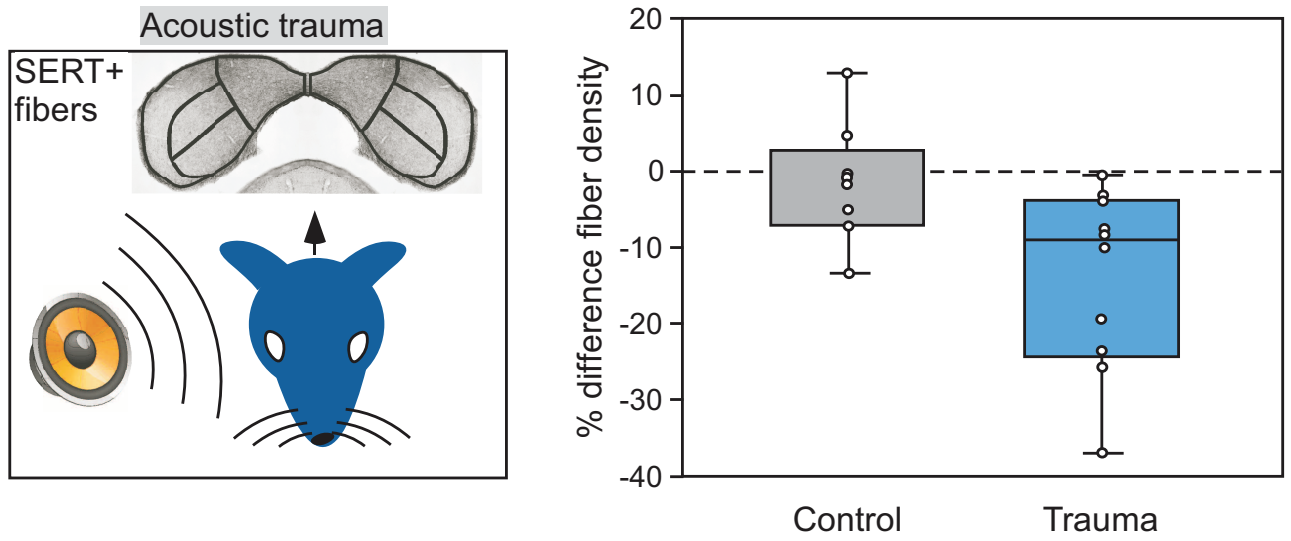

FIGURE 9 | Comparison of the density of serotonergic fibers in the IC contralateral versus ipsilateral to an ear exposed to 8 kHz acoustic trauma. Left panel depicts the monaural trauma and subsequent immunolabeling of SERT-positive projections in the IC. Right panel shows percentage differences in fiber density in the IC contralateral to acoustic trauma relative to the IC ipsilateral to the trauma, in 10 CBA/J mice. Fiber density is lower in the contralateral relative to the ipsilateral IC in the trauma group, but not for the control group that did not receive trauma. The right panel was reprinted with permission from Elsevier; additional information on the source article can be found in the Acknowledgments.

damage. Whether this creates qualitative changes in the modulatory effects of serotonin on auditory processing in the IC is unknown.

Predicting the functional importance of changes in the serotonergic infrastructure following events such as acoustic trauma is even more complex against the background of changes in other neurochemical signaling systems. Multiple events that create plasticity in the serotonergic system, such as acoustic trauma, are well-known for triggering plasticity in both excitatory and inhibitory neurotransmitter systems in the IC (Milbrandt et al., 2000; Dong et al., 2010; Browne et al., 2012). Such changes may result in shifts in excitatory-inhibitory balance in association with pathologies such as tinnitus and hyperacusis (Szczepaniak and Moller, 1996; Eggermont and Roberts, 2004). For example, experiments in the IC have demonstrated neurochemical and functional changes related to inhibition after acoustic trauma that have been associated with hyperexcitability of IC neurons (Salvi et al., 1990; Milbrandt et al., 2000; Salvi et al., 2000; Alvarado et al., 2005; Izquierdo et al., 2008; Browne et al., 2012). Given the evidence for serotonergic regulation of both inhibitory and excitatory neural responses in the IC, understanding exactly how events like acoustic trauma alter the regulation of excitability through particular receptor types is a topic that will require additional exploration.

Although plasticity at multiple levels is turning out to be a prominent feature of serotonergic-auditory interactions, whether particular types of changes represent developmental programs, homeostatic responses to peripheral damage, or pathological consequences of damage has not been addressed. Some insight into these issues may be gained from recent studies on the role of serotonin in visual plasticity. In rat visual cortex, ocular dominance plasticity, normally highly limited in adults relative to juveniles, is augmented by systemic administration of fluoxetine, a selective serotonin reuptake inhibitor (Maya Vetencourt et al., 2008). Other treatments that increase serotonin levels in the visual cortex, even behavioral treatments such as environmental enrichment, also augment ocular dominance plasticity (Baroncelli et al., 2010).

In light of this work, plasticity in the serotonergic system within the IC has several important implications for auditory function. One of these is based on the role of serotonin in mediating the influence of behavioral context. Plasticity in the serotonergic system could alter the relationship between behavioral context and auditory processing, leading to either more adaptive or pathological modulation of auditory responses during social interactions or stressful situations. If serotonin gates experience-dependent plasticity in the IC as it does in visual cortex, an alteration in the serotonergic system could additionally recast the ability of the auditory system to express adaptive plasticity. Both of these are exciting possibilities for future experimental attention.

GENERAL CONCLUSIONS

An increasing number of studies on the influence of serotonin in the IC have been completed in the last decade. Despite this, an understanding of serotonergic regulation in the IC, and indeed of the neuromodulation of auditory processing in general, is in its infancy. Here we have made the case that serotonin provides a channel for contextual information about internal state, external events, and even past experience. This information is then transformed into specific changes in the function of the neural circuits of the IC through parallel but interacting receptor pathways. Plasticity in the infrastructure of the serotonergic system, including within specific receptor pathways, could potentially alter the

relationship between behavioral context and circuit function in important ways that have yet to be explored.

ACKNOWLEDGMENTS

This work was supported in part by a grant from the National Institute on Deafness and Other Communication Disorders (DC-008963). **Figure 3** was reprinted from the *J. Neurophysiol.* Vol. 96, 2177–2188, Hurley, Copyright (2006), with permission from the American Physiological Society. Part of **Figure 4** was reprinted from the *J. Neurophysiol.* Vol. 100, 1656–1667, Hurley et al., Copyright (2008), with permission from the American Physiological Society. **Figure 5** was reprinted from *Brain Res.* Vol. 1181, 21–29, Hurley, Copyright (2007), with permission from Elsevier. **Figure 6** was reprinted from *Hear. Res.* Vol. 251, 29–38, Bohorquez and Hurley, Copyright (2009), with permission from Elsevier. Part of **Figure 8** was reprinted from *Behav. Neurosci.* Vol. 125, 501–511, Hall et al., Copyright (2011), with permission from the American Psychological Association. Part of **Figures 1** and **8** were reprinted from *Hear. Res.* Vol. 283, 89–97, Papesh and Hurley, Copyright (2012), with permission from Elsevier.

REFERENCES

Adams, J. C., and Mugnaini, E. (1984). Dorsal nucleus of the lateral lemniscus: a nucleus of GABAergic projection neurons. *Brain Res. Bull.* 13, 585–590.

Alder, T. B., and Rose, G. J. (2000). Integration and recovery processes contribute to the temporal selectivity of neurons in the midbrain of the northern leopard frog, *Rana pipiens*. *J. Comp. Physiol. A* 186, 923–937.

Alvarado, J. C., Fuentes-Santamaria, V., Franklin, S. R., Brunso-Bechtold, J. K., and Henkel, C. K. (2005). Unilateral cochlear ablation in adult ferrets results in upregulation in calretinin immunostaining in the central nucleus of the inferior colliculus. *Neuroscience* 136, 957–969.

Anastasio, N. C., Lanfranco, M. F., Bubar, M. J., Seitz, P. K., Stutz, S. J., McGinnis, A. G., Watson, C. S., and Cunningham, K. A. (2010). Serotonin 5-HT2C receptor protein expression is enriched in synaptosomal and post-synaptic compartments of rat cortex. *J. Neurochem.* 113, 1504–1515.

Andoni, S., Li, N., and Pollak, G. D. (2007). Spectrotemporal receptive fields in the inferior colliculus revealing selectivity for spectral motion in conspecific vocalizations. *J. Neurosci.* 27, 4882–4893.

Andoni, S., and Pollak, G. D. (2011). Selectivity for spectral motion as a neural computation for encoding natural communication signals in bat inferior colliculus. *J. Neurosci.* 31, 16529–16540.

Baroncelli, L., Sale, A., Viegi, A., Maya Vetencourt, J. F., De Pasquale, R., Baldini, S., and Maffei, L. (2010). Experience-dependent reactivation of ocular dominance plasticity in the adult visual cortex. *Exp. Neurol.* 226, 100–109.

Bauer, E. E., Klug, A., and Pollak, G. D. (2002). Spectral determination of responses to species-specific calls in the dorsal nucleus of the lateral lemniscus. *J. Neurophysiol.* 88, 1955–1967.

Bodnar, D. A., and Bass, A. H. (1997). Temporal coding of concurrent acoustic signals in auditory midbrain. *J. Neurosci.* 17, 7553–7564.

Bodnar, D. A., Holub, A. D., Land, B. R., Skovira, J., and Bass, A. H. (2001). Temporal population code of concurrent vocal signals in the auditory midbrain. *J. Comp. Physiol. A. Neuroethol. Sens. Neural. Behav. Physiol.* 187, 865–873.

Bohorquez, A., and Hurley, L. M. (2009). Activation of serotonin 3 receptors changes *in vivo* auditory responses in the mouse inferior colliculus. *Hear. Res.* 251, 29–38.

Bombardi, C. (2012). Neuronal localization of 5-HT2A receptor immunoreactivity in the rat hippocampal region. *Brain Res. Bull.* 87, 259–273.

Boutelle, M. G., Zetterstrom, T., Pei, Q., Svensson, L., and Fillenz, M. (1990). *In vivo* neurochemical effects of tail pinch. *J. Neurosci. Methods* 34, 151–157.

Bowery, N. (1989). GABAB receptors and their significance in mammalian pharmacology. *Trends Pharmacol. Sci.* 10, 401–407.

Browne, C. J., Morley, J. W., and Parsons, C. H. (2012). Tracking the expression of excitatory and inhibitory neurotransmission-related proteins and neuroplasticity markers after noise induced hearing loss. *PLoS ONE* 7:e33272. doi: 10.1371/journal.pone.0033272

Bunin, M. A., and Wightman, R. M. (1999). Paracrine neurotransmission in the CNS: involvement of 5-HT. *Trends Neurosci.* 22, 377–382.

Burger, R. M., and Pollak, G. D. (2001). Reversible inactivation of the dorsal nucleus of the lateral lemniscus reveals its role in the processing of multiple sound sources in the inferior colliculus of bats. *J. Neurosci.* 21, 4830–4843.

Carrillo, M., Ricci, L. A., Schwartzer, J. J., and Melloni, R. H. (2010). Immunohistochemical characterization of 5-HT(3A) receptors in the Syrian hamster forebrain. *Brain Res.* 1329, 67–81.

Casseday, J. H., Ehrlich, D., and Covey, E. (1994). Neural tuning for sound duration- role of inhibitory mechanisms in the inferior colliculus. *Science* 264, 847–850.

Casseday, J. H., Ehrlich, D., and Covey, E. (2000). Neural measurement of sound duration: control by excitatory-inhibitory interactions in the inferior colliculus. *J. Neurophysiol.* 84, 1475–1487.

Celio, M. R. (1990). Calbindin-d-28k and parvalbumin in the rat nervous-system. *Neuroscience* 35, 375–475.

Chalmers, D. T., and Watson, S. J. (1991). Comparative anatomical distribution of 5-HT1A receptor mRNA and 5-HT1A binding in rat brain–a combined *in situ* hybridisation/*in vitro* receptor autoradiographic study. *Brain Res.* 561, 51–60.

Chameau, P., and Van Hooft, J. A. (2006). Serotonin 5-HT(3) receptors in the central nervous system. *Cell Tissue Res.* 326, 573–581.

Charitidi, K., and Canlon, B. (2010). Estrogen receptors in the central auditory system of male and female mice. *Neuroscience* 165, 923–933.

Ciranna, L. (2006). Serotonin as a modulator of glutamate- and GABA-mediated neurotransmission: implications in physiological functions and in pathology. *Curr. Neuropharmacol.* 4, 101–114.

Clement, H. W., Kirsch, M., Hasse, C., Opper, C., Gemsa, D., and Wesemann, W. (1998). Effect of repeated immobilization on serotonin metabolism in different rat brain areas and on serum corticosterone. *J. Neural Transm.* 105, 1155–1170.

Cransac, H., Peyrin, L., Cottet-Emard, J. M., Farhat, F., Pequignot, J. M., and Reber, A. (1996). Aging effects on monoamines in rat medial vestibular and cochlear nuclei. *Hear. Res.* 100, 150–156.

Crawford, J. D. (1997). Feature-detecting auditory neurons in the brain of a sound-producing fish. *J. Comp. Physiol. A* 180, 439–450.

Cuccurazzu, B., and Halberstadt, A. L. (2008). Projections from the vestibular nuclei and nucleus prepositus hypoglossi to dorsal raphe nucleus in rats. *Neurosci. Lett.* 439, 70–74.

Defelipe, J., Hendry, S. H., Hashikawa, T., and Jones, E. G. (1991). Synaptic relationships of serotonin-immunoreactive terminal baskets on GABA neurons in the cat auditory cortex. *Cereb. Cortex* 1, 117–133.

Dehmel, S., Cui, Y. L., and Shore, S. E. (2008). Cross-modal interactions of auditory and somatic inputs in the brainstem and midbrain and their imbalance in tinnitus and deafness. *Am. J. Audiol.* 17, S193–S209.

Diekamp, B., and Schneider, H. (1988). Neuronal processing of conspecific and related calls in the torus semicircularis of *Rana r. ridibunda* Pall. (Anura): single-unit recordings. *J. Comp. Physiol. A* 163, 301–315.

Dong, S., Mulders, W. H., Rodger, J., Woo, S., and Robertson, D. (2010). Acoustic trauma evokes hyperactivity and changes in gene expression in guinea-pig auditory brainstem. *Eur. J. Neurosci.* 31, 1616–1628.

Duncan, G. E., Knapp, D. J., Breese, G. R., Crews, F. T., and Little, K. Y. (1998). Species differences in regional patterns of H-3-8-OH-DPAT and H-3-zolpidem binding in the rat and human brain. *Pharmacol. Biochem. Behav.* 60, 439–448.

Eggermont, J. J., and Roberts, L. E. (2004). The neuroscience of tinnitus. *Trends Neurosci.* 27, 676–682.

Elliott, T. M., Christensen-Dalsgaard, J., and Kelley, D. B. (2011). Temporally selective processing of communication signals by auditory midbrain neurons. *J. Neurophysiol.* 105, 1620–1632.

Endepols, H., Feng, A. S., Gerhardt, H. C., Schul, J., and Walkowiak, W. (2003). Roles of the auditory midbrain and thalamus in selective phonotaxis in female gray treefrogs (*Hyla versicolor*). *Behav. Brain Res.* 145, 63–77.

Engelhardt, J. K., Silveira, V., Morales, F. R., Pose, I., and Chase, M. H. (2010). Serotoninergic control of glycinergic inhibitory postsynaptic currents in rat hypoglossal motoneurons. *Brain Res.* 1345, 1–8.

Epping, W. J. (1990). Influence of adaptation on neural sensitivity to temporal characteristics of sound in the dorsal medullary nucleus and torus semicircularis of the grassfrog. *Hear. Res.* 45, 1–13.

Faingold, C. L., Anderson, C. A., and Randall, M. E. (1993). Stimulation or blockade of the dorsal nucleus of the lateral lemniscus alters binaural and tonic inhibition in contralateral inferior colliculus neurons. *Hear. Res.* 69, 98–106.

Farley, G. R., Morley, B. J., Javel, E., and Gorga, M. P. (1983). Single-unit responses to cholinergic agents in the rat inferior colliculus. *Hear. Res.* 11, 73–91.

Fitzgerald, K. K., and Sanes, D. H. (1999). Serotonergic modulation of synapses in the developing gerbil lateral superior olive. *J. Neurophysiol.* 81, 2743–2752.

Freund, T. F., Gulyas, A. I., Acsady, L., Gorcs, T., and Toth, K. (1990). Serotonergic control of the hippocampus via local inhibitory interneurons. *PNAS* 87, 8501–8505.

Fubara, B. M., Casseday, J. H., Covey, E., and Schwartzbloom, R. D. (1996). Distribution of GABA(A) GABA(B), and glycine receptors in the central auditory system of the big brown bat, *Eptesicus fuscus*. *J. Comp. Neurol.* 369, 83–92.

Funai, H., and Funasaka, S. (1983). Experimental study on the effect of inferior colliculus lesions upon auditory brain stem response. *Audiology* 22, 9–19.

Fuzessery, Z. M., and Hall, J. C. (1996). Role of GABA in shaping frequency tuning and creating FM sweep selectivity in the inferior colliculus. *J. Neurophysiol.* 76, 1059–1073.

Gasser, P. J., Orchinik, M., Raju, I., and Lowry, C. A. (2009). Distribution of organic cation transporter 3, a corticosterone-sensitive monoamine transporter, in the rat brain. *J. Comp. Neurol.* 512, 529–555.

Goense, J. B., and Feng, A. S. (2005). Seasonal changes in frequency tuning and temporal processing in single neurons in the frog auditory midbrain. *J. Neurobiol.* 65, 22–36.

Gonzalez-Hernandez, T., Mantolan-Sarmiento, B., Gonzalez-Gonzalez, B., and Perez-Gonzalez, H. (1996). Sources of GABAergic input to the inferior colliculus of the rat. *J. Comp. Neurol.* 372, 309–326.

Greco, B., Edwards, D. A., Michael, R. P., Zumpe, D., and Clancy, A. N. (1999). Colocalization of androgen receptors and mating-induced FOS immunoreactivity in neurons that project to the central tegmental field in male rats. *J. Comp. Neurol.* 408, 220–236.

Groh, J. M., Trause, A. S., Underhill, A. M., Clark, K. R., and Inati, S. (2001). Eye position influences auditory responses in primate inferior colliculus. *Neuron* 29, 509–518.

Habbicht, H., and Vater, M. (1996). A microiontophoretic study of acetylcholine effects in the inferior colliculus of horseshoe bats: implications for a modulatory role. *Brain Res.* 724, 169–179.

Hall, I. C., and Hurley, L. M. (2007). The serotonin releaser fenfluramine alters the auditory responses of inferior colliculus neurons. *Hear. Res.* 228, 82–94.

Hall, I. C., Rebec, G. V., and Hurley, L. M. (2010). Serotonin in the inferior colliculus fluctuates with behavioral state and environmental stimuli. *J. Exp. Biol.* 213, 1009–1017.

Hall, I. C., Sell, G. L., and Hurley, L. M. (2011). Social regulation of serotonin in the auditory midbrain. *Behav. Neurosci.* 125, 501–511.

Hannon, J., and Hoyer, D. (2008). Molecular biology of 5-HT receptors. *Behav. Brain Res.* 195, 198–213.

Harris-Warrick, R. M. (2011). Neuromodulation and flexibility in central pattern generator networks. *Curr. Opin. Neurobiol.* 21, 685–692.

Hernandez, O., Rees, A., and Malmierca, M. S. (2006). A GABAergic component in the commissure of the inferior colliculus in rat. *Neuroreport* 17, 1611–1614.

Heym, J., Trulson, M. E., and Jacobs, B. L. (1982). Raphe unit activity in freely moving cats: effects of phasic auditory and visual stimuli. *Brain Res.* 232, 29–39.

Hoffman, B. J., Hansson, S. R., Mezey, E., and Palkovits, M. (1998). Localization and dynamic regulation of biogenic amine transporters in the mammalian central nervous system. *Front. Neuroendocrinol.* 19, 187–231.

Hoke, K. L., Burmeister, S. S., Fernald, R. D., Rand, A. S., Ryan, M. J., and Wilczynski, W. (2004). Functional mapping of the auditory midbrain during mate call reception. *J. Neurosci.* 24, 11264–11272.

Hoke, K. L., Ryan, M. J., and Wilczynski, W. (2010). Sexually dimorphic sensory gating drives behavioral differences in tungara frogs. *J. Exp. Biol.* 213, 3463–3472.

Holmstrom, L. A., Eeuwes, L. B., Roberts, P. D., and Portfors, C. V. (2010). Efficient encoding of vocalizations in the auditory midbrain. *J. Neurosci.* 30, 802–819.

Holt, A. G., Asako, M., Lomax, C. A., Macdonald, J. W., Tong, L., Lomax, M. I., and Altschuler, R. A. (2005). Deafness-related plasticity in the inferior colliculus: gene expression profiling following removal of peripheral activity. *J. Neurochem.* 93, 1069–1086.

Huffman, R. F., and Henson, O. W. Jr. (1990). The descending auditory pathway and acousticomotor systems: connections with the inferior colliculus. *Brain Res. Brain Res. Rev.* 15, 295–323.

Hurley, L. M. (2006). Different serotonin receptor agonists have distinct effects on sound-evoked responses in inferior colliculus. *J. Neurophysiol.* 96, 2177–2188.

Hurley, L. M. (2007). Activation of the serotonin 1A receptor alters the temporal characteristics of auditory responses in the inferior colliculus. *Brain Res.* 1181, 21–29.

Hurley, L. M., Devilbiss, D. M., and Waterhouse, B. D. (2004). A matter of focus: monoaminergic modulation of stimulus coding in mammalian sensory networks. *Curr. Opin. Neurobiol.* 14, 488–495.

Hurley, L. M., and Hall, I. C. (2011). Context-dependent modulation of auditory processing by serotonin. *Hear. Res.* 279, 74–84.

Hurley, L. M., and Pollak, G. D. (1999). Serotonin differentially modulates responses to tones and frequency-modulated sweeps in the inferior colliculus. *J. Neurosci.* 19, 8071–8082.

Hurley, L. M., and Pollak, G. D. (2001). Serotonin effects on frequency tuning of inferior colliculus neurons. *J. Neurophysiol.* 85, 828–842.

Hurley, L. M., and Pollak, G. D. (2005a). Serotonin modulates responses to species-specific vocalizations in the inferior colliculus. *J. Comp. Physiol. A Neuroethol. Sens. Neural. Behav. Physiol.* 191, 535–546.

Hurley, L. M., and Pollak, G. D. (2005b). Serotonin shifts first-spike latencies of inferior colliculus neurons. *J. Neurosci.* 25, 7876–7886.

Hurley, L. M., and Thompson, A. M. (2001). Serotonergic innervation of the auditory brainstem of the Mexican free-tailed bat, *Tadarida brasiliensis*. *J. Comp. Neurol.* 435, 78–88.

Hurley, L. M., Thompson, A. M., and Pollak, G. D. (2002). Serotonin in the inferior colliculus. *Hear. Res.* 168, 1–11.

Hurley, L. M., Tracy, J. A., and Bohorquez, A. (2008). Serotonin 1B receptor modulates frequency response curves and spectral integration in the inferior colliculus by reducing GABAergic inhibition. *J. Neurophysiol.* 100, 1656–1667.

Ito, T., Bishop, D. C., and Oliver, D. L. (2009). Two classes of GABAergic neurons in the inferior colliculus. *J. Neurosci.* 29, 13860–13869.

Izquierdo, M. A., Gutierrez-Conde, P. M., Merchan, M. A., and Malmierca, M. S. (2008). Non-plastic reorganization of frequency coding in the inferior colliculus of the rat following noise-induced hearing loss. *Neuroscience* 154, 355–369.

Jacobs, B. L., and Fornal, C. A. (1999). Activity of serotonergic neurons in behaving animals. *Neuropsychopharmacology* 21, 9S–15S.

Jakab, R. L., and Goldman-Rakic, P. S. (1998). 5-Hydroxytryptamine2A serotonin receptors in the primate cerebral cortex: possible site of action of hallucinogenic and antipsychotic drugs in pyramidal cell apical dendrites. *Proc. Natl. Acad. Sci. U.S.A.* 95, 735–740.

Jakab, R. L., and Goldman-Rakic, P. S. (2000). Segregation of serotonin 5-HT2A and 5-HT3 receptors in inhibitory circuits of the primate cerebral cortex. *J. Comp. Neurol.* 417, 337–348.

Ji, W., and Suga, N. (2009). Tone-specific and nonspecific plasticity of inferior colliculus elicited by pseudo-conditioning: role of acetylcholine and auditory and somatosensory cortices. *J. Neurophysiol.* 102, 941–952.

Kaga, K., Yamada, K., Tsuzuku, T., and Uno, A. (1999). The long-term effect of bilateral inferior colliculus ablation on auditory brainstem response in awake cats. *Acta Otolaryngol.* 119, 128–131.

Kaiser, A., and Covey, E. (1997). "5-HT innervation of the auditory pathway in birds and bats," in *Acoustical Signal Processing in the Central Auditory System*, ed J. L. Syka (New York, NY: Plenum), 71–78.

Kawano, H., Decker, K., and Reuss, S. (1996). Is there a direct retina-raphe-suprachiasmatic nucleus pathway in the rat? *Neurosci. Lett.* 212, 143–146.

Kidd, S. A., and Kelly, J. B. (1996). Contribution of the dorsal nucleus of the lateral lemniscus to binaural responses in the inferior colliculus of the rat: interaural time delays. *J. Neurosci.* 16, 7390–7397.

Kishimoto, K., Koyama, S., and Akaike, N. (2001). Synergistic mu-opioid and 5-HT1A presynaptic inhibition of GABA release in rat periaqueductal gray neurons. *Neuropharmacology* 41, 529–538.

Klepper, A., and Herbert, H. (1991). Distribution and origin of noradrenergic and serotonergic fibers in the cochlear nucleus and inferior colliculus of the rat. *Brain Res.* 557, 190–201.

Klug, A., Bauer, E. E., Hanson, J. T., Hurley, L., Meitzen, J., and Pollak, G. D. (2002). Response selectivity for species-specific calls in the inferior colliculus of Mexican free-tailed bats is generated by inhibition. *J. Neurophysiol.* 88, 1941–1954.

Lebeau, F. E., Malmierca, M. S., and Rees, A. (2001). Iontophoresis *in vivo* demonstrates a key role for GABA(A) and glycinergic inhibition in shaping frequency response areas in the inferior colliculus of guinea pig. *J. Neurosci.* 21, 7303–7312.

Lebeau, F. E. N., Rees, A., and Malmierca, M. S. (1996). Contribution of GABA- and glycine-mediated inhibition to the monaural temporal response properties of neurons in the inferior colliculus. *J. Neurophysiol.* 75, 902–919.

Lee, H. S., Kim, M. A., Valentino, R. J., and Waterhouse, B. D. (2003). Glutamatergic afferent projections to the dorsal raphe nucleus of the rat. *Brain Res.* 963, 57–71.

Lee, J. J., Hahm, E. T., Lee, C. H., and Cho, Y. W. (2008). Serotonergic modulation of GABAergic and glutamatergic synaptic transmission in mechanically isolated rat medial preoptic area neurons. *Neuropsychopharmacology* 33, 340–352.

Leroy, S. A., and Wenstrup, J. J. (2000). Spectral integration in the inferior colliculus of the mustached bat. *J. Neurosci.* 20, 8533–8541.

Levitt, P., and Moore, R. Y. (1979). Origin and organization of brainstem catecholamine innervation in the rat. *J. Comp. Neurol.* 186, 505–528.

Liu, S., Bubar, M. J., Lanfranco, M. F., Hillman, G. R., and Cunningham, K. A. (2007). Serotonin2C receptor localization in GABA neurons of the rat medial prefrontal cortex: implications for understanding the neurobiology of addiction. *Neuroscience* 146, 1677–1688.

Lohmann, C., and Friauf, E. (1996). Distribution of the calcium-binding proteins parvalbumin and calretinin in the auditory brainstem of adult and developing rats. *J. Comp. Neurol.* 367, 90–109.

Lu, Y., and Jen, P. H. (2001). GABAergic and glycinergic neural inhibition in excitatory frequency tuning of bat inferior collicular neurons. *Exp. Brain Res.* 141, 331–339.

Macdonald, R. L., and Olsen, R. W. (1994). GABA(A) receptor channels. *Ann. Rev. Neurosci.* 17, 569–602.

Malmierca, M. S., Hernandez, O., Antunes, F. M., and Rees, A. (2009). Divergent and point-to-point connections in the commissural pathway between the inferior colliculi. *J. Comp. Neurol.* 514, 226–239.

Malmierca, M. S., Hernandez, O., and Rees, A. (2005a). Intercollicular commissural projections modulate neuronal responses in the inferior colliculus. *Eur. J. Neurosci.* 21, 2701–2710.

Malmierca, M. S., Saint Marie, R. L., Merchan, M. A., and Oliver, D. L. (2005b). Laminar inputs from dorsal cochlear nucleus and ventral cochlear nucleus to the central nucleus of the inferior colliculus: two patterns of convergence. *Neuroscience* 136, 883–894.

Maney, D. L., Cho, E., and Goode, C. T. (2006). Estrogen-dependent selectivity of genomic responses to birdsong. *Eur. J. Neurosci.* 23, 1523–1529.

Maney, D. L., and Pinaud, R. (2011). Estradiol-dependent modulation of auditory processing and selectivity in songbirds. *Front. Neuroendocrinol.* 32, 287–302.

Mangiamele, L. A., and Burmeister, S. S. (2011). Auditory selectivity for acoustic features that confer species recognition in the tungara frog. *J. Exp. Biol.* 214, 2911–2918.

Marsh, R. A., Fuzessery, Z. M., Grose, C. D., and Wenstrup, J. J. (2002). Projection to the inferior colliculus from the basal nucleus of the amygdala. *J. Neurosci.* 22, 10449–10460.

Mas, M., Fumero, B., and Gonzalez-Mora, J. L. (1995). Voltammetric and microdialysis monitoring of brain monoamine neurotransmitter release during sociosexual interactions. *Behav. Brain Res.* 71, 69–79.

Matragrano, L. L., Sanford, S. E., Salvante, K. G., Beaulieu, M., Sockman, K. W., and Maney, D. L. (2012). Estradiol-dependent modulation of serotonergic markers in auditory areas of a seasonally breeding songbird. *Behav. Neurosci.* 126, 110–122.

Maya Vetencourt, J. F., Sale, A., Viegi, A., Baroncelli, L., De Pasquale, R., O'leary, O. F., Castren, E., and Maffei, L. (2008). The antidepressant fluoxetine restores plasticity in the adult visual cortex. *Science* 320, 385–388.

Mazurek, B., Haupt, H., Joachim, R., Klapp, B. F., Stover, T., and Szczepek, A. J. (2010). Stress induces transient auditory hypersensitivity in rats. *Hear. Res.* 259, 55–63.

Mello, C. V., and Ribeiro, S. (1998). ZENK protein regulation by song in the brain of songbirds. *J. Comp. Neurol.* 393, 426–438.

Metzger, R. R., Greene, N. T., Porter, K. K., and Groh, J. M. (2006). Effects of reward and behavioral context on neural activity in the primate inferior colliculus. *J. Neurosci.* 26, 7468–7476.

Miko, I. J., and Sanes, D. H. (2009). Transient gain adjustment in the inferior colliculus is serotonin- and calcium-dependent. *Hear. Res.* 251, 39–50.

Milbrandt, J. C., Holder, T. M., Wilson, M. C., Salvi, R. J., and Caspary, D. M. (2000). GAD levels and muscimol binding in rat inferior colliculus following acoustic trauma. *Hear. Res.* 147, 251–260.

Miranda, J. A., and Wilczynski, W. (2009a). Female reproductive state influences the auditory midbrain response. *J. Comp. Physiol. A Neuroethol. Sens. Neural. Behav. Physiol.* 195, 341–349.

Miranda, J. A., and Wilczynski, W. (2009b). Sex differences and androgen influences on midbrain auditory thresholds in the green treefrog, *Hyla cinerea*. *Hear. Res.* 252, 79–88.

Miyazaki, K. W., Miyazaki, K., and Doya, K. (2011). Activation of the central serotonergic system in response to delayed but not omitted rewards. *Eur. J. Neurosci.* 33, 153–160.

Morales, M., and Bloom, F. E. (1997). The 5-HT3 receptor is present in different subpopulations of GABAergic neurons in the rat telencephalon. *J. Neurosci.* 17, 3157–3167.

Motts, S. D., and Schofield, B. R. (2009). Sources of cholinergic input to the inferior colliculus. *Neuroscience* 160, 103–114.

Motts, S. D., and Schofield, B. R. (2011). Cholinergic cells in the tegmentum send branching projections to the inferior colliculus and the medial geniculate body. *Neuroscience* 179, 120–130.

Oertel, D., Wright, S., Cao, X. J., Ferragamo, M., and Bal, R. (2011). The multiple functions of T stellate/multipolar/chopper cells in the ventral cochlear nucleus. *Hear. Res.* 276, 61–69.

Okuhara, D. Y., and Beck, S. G. (1994). 5-HT1A receptor linked to inward-rectifying potassium current in hippocampal CA3 pyramidal cells. *J. Neurophysiol.* 71, 2161–2167.

Oliver, D. L., Winer, J. A., Beckius, G. E., and Saint Marie, R. L. (1994). Morphology of GABAergic neurons in the inferior colliculus of the cat. *J. Comp. Neurol.* 340, 27–42.

Palombi, P. S., and Caspary, D. M. (1996). GABA inputs control discharge rate primarily within frequency receptive fields of inferior colliculus neurons. *J. Neurophysiol.* 75, 2211–2219.

Papesh, M. A., and Hurley, L. M. (2012). Plasticity of serotonergic innervation of the inferior colliculus in mice following acoustic trauma. *Hear. Res.* 283, 89–97.

Peruzzi, D., and Dut, A. (2004). GABA, serotonin and serotonin receptors in the rat inferior colliculus. *Brain Res.* 998, 247–250.

Peyron, C., Petit, J. M., Rampon, C., Jouvet, M., and Luppi, P. H. (1998). Forebrain afferents to the rat dorsal raphe nucleus demonstrated by retrograde and anterograde tracing methods. *Neuroscience* 82, 443–468.

Pincherli Castellanos, T. A., Aitoubah, J., Molotchnikoff, S., Lepore, F., and Guillemot, J. P. (2007). Responses of inferior collicular cells to species-specific vocalizations in normal and enucleated rats. *Exp. Brain Res.* 183, 341–350.

Pollak, G. D., Burger, R. M., Park, T. J., Klug, A., and Bauer, E. E. (2002). Roles of inhibition for transforming binaural properties in the brainstem auditory system. *Hear. Res.* 168, 60–78.

Pollak, G. D., Xie, R., Gittelman, J. X., Andoni, S., and Li, N. (2011). The dominance of inhibition in the inferior colliculus. *Hear. Res.* 274, 27–39.

Polter, A. M., and Li, X. H. (2010). 5-HT1A receptor-regulated signal transduction pathways in brain. *Cell. Signal.* 22, 1406–1412.

Pompeiano, M., Palacios, J. M., and Mengod, G. (1992). Distribution and cellular localization of mRNA coding for 5-HT1A receptor in the rat brain: correlation with receptor binding. *J. Neurosci.* 12, 440–453.

Portas, C. M., Bjorvatn, B., and Ursin, R. (2000). Serotonin and the sleep/wake cycle: special emphasis on microdialysis studies. *Prog. Neurobiol.* 60, 13–35.

Ramsey, L. C., Sinha, S. R., and Hurley, L. M. (2010). 5-HT1A and 5-HT1B receptors differentially modulate rate and timing of auditory responses in the mouse inferior colliculus. *Eur. J. Neurosci.* 32, 368–379.

Revelis, J., Thompson, A. M., Britton, B. H., and Thompson, G. C. (1998). Effects of para-chlorophenylalanine (pCPA) on the bush baby auditory brainstem response. *Hear. Res.* 116, 119–130.

Roberts, R. C., and Ribak, C. E. (1987). GABAergic neurons and axon terminals in the brainstem auditory nuclei of the gerbil. *J. Comp. Neurol.* 258, 267–280.

Salvi, R. J., Saunders, S. S., Gratton, M. A., Arehole, S., and Powers, N. (1990). Enhanced evoked response amplitudes in the inferior colliculus of the chinchilla following acoustic trauma. *Hear. Res.* 50, 245–257.

Salvi, R. J., Wang, J., and Ding, D. (2000). Auditory plasticity and hyperactivity following cochlear damage. *Hear. Res.* 147, 261–274.

Sanchez, J. T., Gans, D., and Wenstrup, J. J. (2007). Contribution of NMDA and AMPA receptors to temporal patterning of auditory responses in the inferior colliculus. *J. Neurosci.* 27, 1954–1963.

Sari, Y. (2004). Serotonin1B receptors: from protein to physiological function and behavior. *Neurosci. Biobehav. Rev.* 28, 565–582.

Schneider, D. M., and Woolley, S. M. (2010). Discrimination of communication vocalizations by single neurons and groups of neurons in the auditory midbrain. *J. Neurophysiol.* 103, 3248–3265.

Schneider, D. M., and Woolley, S. M. (2011). Extra-classical tuning predicts stimulus-dependent receptive fields in auditory neurons. *J. Neurosci.* 31, 11867–11878.

Schofield, B. R., and Coomes, D. L. (2006). Pathways from auditory cortex to the cochlear nucleus in guinea pigs. *Hear. Res.* 216–217, 81–89.

Shim, H. J., Lee, L. H., Huh, Y., Lee, S. Y., and Yeo, S. G. (2012). Age-related changes in the expression of NMDA, serotonin, and GAD in the central auditory system of the rat. *Acta Otolaryngol.* 132, 44–50.

Shneiderman, A., Chase, M. B., Rockwood, J. M., Benson, C. G., and Potashner, S. J. (1993). Evidence for a GABAergic projection from the dorsal nucleus of the lateral lemniscus to the inferior colliculus. *J. Neurochem.* 60, 72–82.

Shneiderman, A., and Oliver, D. L. (1989). EM autoradiographic study of the projections from the dorsal nucleus of the lateral lemniscus: a possible source of inhibitory inputs to the inferior colliculus. *J. Comp. Neurol.* 286, 28–47.

Shneiderman, A., Oliver, D. L., and Henkel, C. K. (1988). Connections of the dorsal nucleus of the lateral lemniscus: an inhibitory parallel pathway in the ascending auditory system? *J. Comp. Neurol.* 276, 188–208.

Smiley, J. F., and Goldmanrakic, P. S. (1996). Serotonergic axons in monkey prefrontal cerebral cortex synapse predominantly on interneurons as demonstrated by serial section electron microscopy. *J. Comp. Neurol.* 367, 431–443.

Stanford, I. M., and Lacey, M. G. (1996). Differential actions of serotonin, mediated by 5-HT1B and 5-HT2C receptors, on GABA-mediated synaptic input to rat substantia nigra pars reticulata neurons *in vitro*. *J. Neurosci.* 16, 7566–7573.

Suta, D., Popelar, J., Kvasnak, E., and Syka, J. (2007). Representation of species-specific vocalizations in the medial geniculate body of the guinea pig. *Exp. Brain Res.* 183, 377–388.

Suta, D., Popelar, J., and Syka, J. (2008). Coding of communication calls in the subcortical and cortical structures of the auditory system. *Physiol. Res.* 57(Suppl. 3), S149–S159.

Szczepaniak, W. S., and Moller, A. R. (1996). Effects of (-)-baclofen, clonazepam, and diazepam on tone exposure-induced hyperexcitability of the inferior colliculus in the rat: possible therapeutic implications for pharmacological management of tinnitus and hyperacusis. *Hear. Res.* 97, 46–53.

Tadros, S. F., D'souza, M., Zettel, M. L., Zhu, X., Lynch-Erhardt, M., and Frisina, R. D. (2007). Serotonin 2B receptor: upregulated with age and hearing loss in mouse auditory system. *Neurobiol. Aging* 28, 1112–1123.

Thompson, A. M. (2006). "Non-serotonergic" lateral superior olivary neurons of the neonatal mouse contain serotonin. *Brain Res.* 1122, 122–125.

Thompson, A. M., and Lauder, J. M. (2005). Postnatal expression of the serotonin transporter in auditory brainstem neurons. *Dev. Neurosci.* 27, 1–12.

Thompson, A. M., and Schofield, B. R. (2000). Afferent projections of the superior olivary complex. *Microsc. Res. Tech.* 51, 330–354.

Thompson, A. M., and Thompson, G. C. (2009). Serotonin-immunoreactive neurons in the postnatal MAO-A KO mouse lateral superior olive project to the inferior colliculus. *Neurosci. Lett.* 460, 47–51.

Thompson, G. C., Thompson, A. M., Garrett, K. M., and Britton, B. H. (1994). Serotonin and serotonin receptors in the central auditory system. *Otolaryngol. Head Neck Surg.* 110, 93–102.

To, Z. P., Bonhaus, D. W., Eglen, R. M., and Jakeman, L. B. (1995). Characterization and distribution of putative 5-ht7 receptors in guinea-pig brain. *Br. J. Pharmacol.* 115, 107–116.

Tong, L., Altschuler, R. A., and Holt, A. G. (2005). Tyrosine hydroxylase in rat auditory midbrain: distribution and changes following deafness. *Hear. Res.* 206, 28–41.

Vater, M., Casseday, J. H., and Covey, E. (1995). Convergence and divergence of ascending binaural and monaural pathways from the superior olives of the mustached bat. *J. Comp. Neurol.* 351, 632–646.

Waeber, C., Sebben, M., Bockaert, J., and Dumuis, A. (1996). Regional distribution and ontogeny of 5-HT4 binding sites in rat brain. *Behav. Brain Res.* 73, 259–262.

Wang, H. T., Luo, B., Huang, Y. N., Zhou, K. Q., and Chen, L. (2008). Sodium salicylate suppresses serotonin-induced enhancement of GABAergic spontaneous inhibitory postsynaptic currents in rat inferior colliculus *in vitro*. *Hear. Res.* 236, 42–51.

Winer, J. A. (2006). Decoding the auditory corticofugal systems. *Hear. Res.* 212, 1–8.

Wisden, W., Laurie, D. J., Monyer, H., and Seeburg, P. H. (1992). The distribution of 13-GABA-A receptor subunit messenger RNAs in the rat brain. 1. Telencephalon, diencephalon, mesencephalon. *J. Neurosci.* 12, 1040–1062.

Woolley, S. M., Gill, P. R., and Theunissen, F. E. (2006). Stimulus-dependent auditory tuning results in synchronous population coding of vocalizations in the songbird midbrain. *J. Neurosci.* 26, 2499–2512.

Wright, D. E., Seroogy, K. B., Lundgren, K. H., Davis, B. M., and Jennes, L. (1995). Comparative localization of serotonin1A, 1C, and 2 receptor subtype mRNAs in rat brain. *J. Comp. Neurol.* 351, 357–373.

Wynne, B., and Robertson, D. (1996). Localization of dopamine-beta-hydroxylase-like immunoreactivity in the superior olivary complex of the rat. *Audiol. Neurootol.* 1, 54–64.

Xiang, Z., and Prince, D. A. (2003). Heterogeneous actions of serotonin on interneurons in rat visual cortex. *J. Neurophysiol.* 89, 1278–1287.

Xie, R., Meitzen, J., and Pollak, G. D. (2005). Differing roles of inhibition in hierarchical processing of species-specific calls in auditory brainstem nuclei. *J. Neurophysiol.* 94, 4019–4037.

Yang, L., Pollak, G. D., and Resler, C. (1992). GABAergic circuits sharpen tuning curves and modify response properties in the mustache bat inferior colliculus. *J. Neurophysiol.* 68, 1760–1774.

Yavuzoglu, A., Schofield, B. R., and Wenstrup, J. J. (2010). Substrates of auditory frequency integration in a nucleus of the lateral lemniscus. *Neuroscience* 169, 906–919.

Yavuzoglu, A., Schofield, B. R., and Wenstrup, J. J. (2011). Circuitry underlying spectrotemporal integration in the auditory midbrain. *J. Neurosci.* 31, 14424–14435.

Ye, Y., and Kim, D. O. (2001). Connections between the dorsal raphe nucleus and a hindbrain region consisting of the cochlear nucleus and neighboring structures. *Acta Otolaryngol.* 121, 284–288.

Yigit, M., Keipert, C., and Backus, K. H. (2003). Muscarinic acetylcholine receptors potentiate the GABAergic transmission in the developing rat inferior colliculus. *Neuropharmacology* 45, 504–513.

Zeng, S., Li, J., Zhang, X., and Zuo, M. (2007). Distinction of neurochemistry between the cores and their

shells of auditory nuclei in tetrapod species. *Brain. Behav. Evol.* 70, 1–20.

Zhang, D. X., Li, L., Kelly, J. B., and Wu, S. H. (1998). GABAergic projections from the lateral lemniscus to the inferior colliculus of the rat. *Hear. Res.* 117, 1–12.

Zhou, F. M., and Hablitz, J. J. (1999). Activation of serotonin receptors modulates synaptic transmission in rat cerebral cortex. *J. Neurophysiol.* 82, 2989–2999.

Zhou, J., and Shore, S. (2006). Convergence of spinal trigeminal and cochlear nucleus projections in the inferior colliculus of the guinea pig. *J. Comp. Neurol.* 495, 100–112.

Conflict of Interest Statement: The authors declare that the research was conducted in the absence of any commercial or financial relationships that could be construed as a potential conflict of interest.

Received: 30 April 2012; accepted: 10 August 2012; published online: 06 September 2012.

Citation: Hurley LM and Sullivan MR (2012) From behavioral context to receptors: serotonergic modulatory pathways in the IC. Front. Neural Circuits ***6****:58. doi: 10.3389/fncir.2012.00058*

frontiers in
NEURAL CIRCUITS

REVIEW ARTICLE
published: 21 September 2012
doi: 10.3389/fncir.2012.00068

Immunocytochemical profiles of inferior colliculus neurons in the rat and their changes with aging

Ladislav Ouda* and Josef Syka

Institute of Experimental Medicine, Academy of Sciences of the Czech Republic, Prague, Czech Republic

Edited by:
Manuel S. Malmierca, University of Salamanca, Spain

Reviewed by:
Miguel A. Merchán, Universidad de Salamanca, Spain
Robert D. Frisina, University of South Florida, USA

****Correspondence:***
Ladislav Ouda, Institute of Experimental Medicine, Academy of Sciences of the Czech Republic, Vídeňská 1083, 142 20 Prague, Czech Republic.
e-mail: ouda@biomed.cas.cz

The inferior colliculus (IC) plays a strategic role in the central auditory system in relaying and processing acoustical information, and therefore its age-related changes may significantly influence the quality of the auditory function. A very complex processing of acoustical stimuli occurs in the IC, as supported also by the fact that the rat IC contains more neurons than all other subcortical auditory structures combined. GABAergic neurons, which predominantly co-express parvalbumin (PV), are present in the central nucleus of the IC in large numbers and to a lesser extent in the dorsal and external/lateral cortices of the IC. On the other hand, calbindin (CB) and calretinin (CR) are prevalent in the dorsal and external cortices of the IC, with only a few positive neurons in the central nucleus. The relationship between CB and CR expression in the IC and any neurotransmitter system has not yet been well established, but the distribution and morphology of the immunoreactive neurons suggest that they are at least partially non-GABAergic cells. The expression of glutamate decarboxylase (GAD) (a key enzyme for GABA synthesis) and calcium binding proteins (CBPs) in the IC of rats undergoes pronounced changes with aging that involve mostly a decline in protein expression and a decline in the number of immunoreactive neurons. Similar age-related changes in GAD, CB, and CR expression are present in the IC of two rat strains with differently preserved inner ear function up to late senescence (Long-Evans and Fischer 344), which suggests that these changes do not depend exclusively on peripheral deafferentation but are, at least partially, of central origin. These changes may be associated with the age-related deterioration in the processing of the temporal parameters of acoustical stimuli, which is not correlated with hearing threshold shifts, and therefore may contribute to central presbycusis.

Keywords: inferior colliculus, GABA, parvalbumin, calbindin, calretinin, aging, rat

INTRODUCTION

The inferior colliculus (IC) occupies a strategic position in the central auditory system. Almost all of the ascending projections from the lower auditory regions (cochlear nuclei, superior olivary complex, and lemniscus lateralis) converge in the central nucleus of the IC, thus making this structure a converging hub of the ascending as well as the descending auditory pathways of the auditory system (Beyerl, 1978; Druga and Syka, 1984a,b; Pollak and Casseday, 1986; Oliver and Huerta, 1992; Druga et al., 1997; Casseday et al., 2002). Simultaneously, the IC operates as a relay structure to the medial geniculate body (MGB) and subsequently to the auditory cortex.

With respect to its internal composition, the rat IC is subdivided into three major parts, the central nucleus and the dorsal and external (lateral) cortices. This division is visible in most histological and immunohistochemical stainings (Morest and Oliver, 1984; Faye-Lund and Osen, 1985; Malmierca et al., 1993), (**Figure 1**). In addition, the separation of the ventrolateral nucleus from the external cortex of the IC was proposed, based on homology with the ventrolateral nucleus in the cat (Loftus et al., 2008). The central nucleus of the IC (CIC) represents a part of the primary auditory pathway with a preserved tonotopy, sending primary ascending projections to the ventral subdivision of the MGB and receiving only weak descending projections from the telencephalon (Diamond et al., 1969; Druga and Syka, 1984a,b; Kudo and Nakamura, 1988; Schneiderman et al., 1988). In contrast, the dorsal (DIC) and external (EIC) cortices are more influenced by ascending monoaural pathways and by descending projections from layer V and, to lesser extent, from layer VI of the auditory and non-auditory cortical fields (Druga and Syka, 1984a,b; Saldana et al., 1996; Druga et al., 1997; Winer et al., 1998; Schofield, 2009). The external cortex of the IC possesses strong connections with non-auditory structures including the colliculus superior, substantia nigra, periaquaductal gray, and somatosensory cortex (Syka and Straschill, 1970; Syka and Radil-Weiss, 1971; Aitkin et al., 1978; Druga and Syka, 1984c; Tokunaga et al., 1984; Zhou and Shore, 2006).

Almost the entire GABAergic dorsal nucleus of the lateral lemniscus (Zhang et al., 1998) and the superior paraolivary nucleus (Kulesza and Berrebi, 2000; Saldaña et al., 2009) as well as a substantial portion of neurons from the ventral nucleus of the lateral lemniscus (Riquelme et al., 2001) send ascending inhibitory projections to the neurons of the IC (ipsi- and contralaterally), while excitatory ascending projections originate

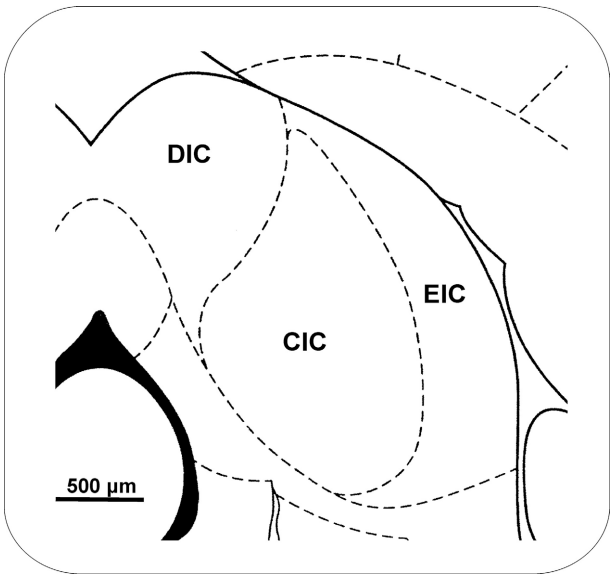

FIGURE 1 | Topographical schema of a frontal section through the IC. The drawing is based on Paxinos and Watson (1998). Bregma −8.6 mm. CIC, central nucleus of the inferior colliculus; DIC, dorsal cortex of the IC; EIC, external cortex of the IC.

predominantly from the lateral and medial superior olive and cochlear nuclei (Semple and Aitkin, 1980; Frisina et al., 1998; Malmierca et al., 1998; Riquelme et al., 2001; Davis, 2002; Malmierca et al., 2005). In addition, the contralateral IC is also a source of mostly inhibitory projections to the IC (González-Hernández et al., 1996). GABAergic perisomatic terminals are more prevalent on non-GABAergic neurons in the IC (Merchán et al., 2005).

The strong representation of GABA terminals as well as the high proportion of GABAergic cells in this structure in the rat suggests the presence of strong inhibitory processes in the IC (Gerken, 1996; Batra and Fitzpatrick, 2002; Merchán et al., 2005; Pollak et al., 2011). The GABAergic inhibitory system in the IC serves to modulate the spectral and temporal properties of IC responses with the aim of sharpening the responses to rapid complex sounds (Le Beau et al., 1996; Palombi and Caspary, 1996; Frisina, 2001; Walton et al., 2002).

Besides GABAergic inhibition, also present are significantly weaker glycinergic inhibitory projections onto the IC neurons from various sources (Saint Marie et al., 1989; Saint Marie and Baker, 1990). The presence of glycinergic neurons in the IC is controversial, since Merchán et al. (2005) reported no glycinergic neurons throughout the IC, while Fredrich et al. (2009) observed glycine immunoreactivity in about 1/6 of CIC neurons, however, always in colocalization with GABA. GABAergic puncta were observed both in the neurophil and in the contacts with neuronal somas, whereas very few glycinergic terminals contacted the somata (Merchán et al., 2005).

Auditory function in mammals, including humans, is known to be significantly affected by aging, ultimately resulting in presbycusis with alterations occurring both in the inner ear and in the central auditory system (Syka, 2002; Frisina and Rajan, 2005; Gates and Mills, 2005; Ohlemiller and Frisina, 2008; Frisina, 2009, 2010; Gordon-Salant et al., 2010). The central component of presbycusis is thought to be significantly associated with age-related alterations in the processing of the temporal parameters of complex acoustical stimuli within the central auditory system, especially the IC and auditory cortex (Strouse et al., 1998; Walton et al., 1998, 2002; Frisina and Walton, 2006; Walton et al., 2008; Walton, 2010; Suta et al., 2011). In the human population, a loss of speech understanding with aging constitutes an important health and social impairment (Frisina and Frisina, 1997; Mazelová et al., 2003; Gates and Mills, 2005; Gordon-Salant et al., 2007).

The significance of inhibition for the processing of information occurring in the IC is difficult to overemphasize, as reviewed in detail, e.g., by Pollak et al. (2011). Altered inhibition within the IC of animals may have a severe impact on survival in the wild, since it impairs their ability to refine the localization of a sound source in the environment (Litovsky and Delgutte, 2002; Pecka et al., 2007). In addition, under experimental conditions, the selectivity for features of incoming signals is significantly reduced or eliminated in the majority of IC cells when inhibition is blocked (Casseday et al., 2000; Malmierca et al., 2003; Nataraj and Wenstrup, 2005; Sanchez et al., 2007). Since GABA-mediated inhibition in the IC and auditory cortex is strongly involved in the temporal processing of complex acoustical stimuli, including human language (Walton et al., 1997, 1998; Strouse et al., 1998; Krishna and Semple, 2000; Walton et al., 2002; Suta et al., 2003; Simon et al., 2004), a functional decline in GABA-mediated inhibition may significantly contribute to a deterioration of hearing with aging, i.e., the central component of presbycusis.

In the last few years, we have evaluated age-related changes comprising mostly a decline in the expression of glutamate decarboxylase (GAD) and calcium binding proteins (CBPs) in the higher levels of the rat auditory pathway, including the IC and auditory cortex (Ouda et al., 2008; Burianova et al., 2009; Ouda et al., 2012b). An age-related decline in GABA levels in the IC was previously reported by other authors (Caspary et al., 1990; Gutiérrez et al., 1994; Raza et al., 1994; Caspary et al., 1995). A decreased number of GABA or GAD immunoreactive neurons was also documented in other parts of the rat brain, such as in the hippocampus (Shi et al., 2004; Stanley and Shetty, 2004; Ling et al., 2005), while no significant reduction was found in the sensorimotor or parietal cortex (Poe et al., 2001; Ling et al., 2005; Shi et al., 2006). Age-related changes in the levels of the CBPs in the auditory pathway were also evaluated in the cochlear nuclei and IC of mice. In addition, the reported changes were strain-dependant for all three proteins in the cochlear nuclei (Idrizbegovic et al., 2001, 2004) and for calretinin (CR) in the IC (Zettel et al., 1997).

In the following text, we first discuss in several chapters the quantitative data, the neuronal types and the distribution of particular immunoreactive neuronal populations in the IC of young adult animals. In the second half, we summarize the observed immunohistochemical age-related changes in the IC and their link to electrophysiological and behavioral findings.

HISTOCHEMICAL PROFILES OF THE INFERIOR COLLICULUS IN YOUNG RATS

TOTAL NUMBER OF NEURONS IN THE IC

The number of neurons in the IC, based on Nissl stained sections, in comparison with other central auditory structures in the rat has been reported in two recent papers (Kulesza et al., 2002; Ouda et al., 2012a). The rat IC contains about 350,000 neurons, with more than 200,000 neurons in the central nucleus alone, about 80,000 in the EIC and 45,000 in the DIC. This represents several times more neurons than in all lower auditory regions combined (cochlear nuclei—30,000 superior olivary complex—16,000–18,000 and lemniscus lateralis—15,000–18,000). In contrast to the IC, the next structure in the auditory pathway, the MGB, contains only about 60,000–70,000 neurons in the rat (with 40,000–45,000 in the ventral division of the MGB), which represents a large difference in comparison to the IC.

In this respect, the position of the MGB may be specific to some degree in the rodent, while the number of neurons in the MGB was reported to be significantly species-dependent, with markedly higher numbers in carnivores and especially in humans (Dorph-Petersen et al., 2009; Najdzion et al., 2011). On the other hand, the absolute number of neurons in the IC of rats and humans is suprisingly comparable, 350,000 vs cca 400,000 neurons (Sharma et al., 2009—a 5-month-old baby that died of postoperative complications after cardiac surgery). In addition, the total number of neurons in the rat auditory cortex is probably roughly the same as in the rat IC (Te1, Te2, Te3—about 600,000 neurons; Ouda et al., 2012a), while, e.g., in primates the divergence of the ascending auditory pathway rapidly increases further through the MGB to the auditory cortical areas. For example, the total number of neurons in the whole human neocortex is almost three orders of magnitude larger than in the whole rat neocortex (Pakkenberg and Gundersen, 1997; Herculano-Houzel and Lent, 2005). These findings strongly support the prominent role of the IC in the rodent central auditory system and suggest that the role of the MGB in rodents may be somewhat different than in other mammalian species.

GLUTAMATE DECARBOXYLASE

GABA is synthesized by the decarboxylation of glutamate, and the reaction is catalyzed by the key rate-limiting enzyme GAD. In the mammalian brain, two GAD isoforms of 65 and 67 kDa molecular weight (GAD 65 and GAD 67) are present (Erlander et al., 1991). Most GABA-expressing neurons contain both isoforms, and therefore GAD immunostaining is often used to identify GABAergic neurons (Erlander and Tobin, 1991; Feldblum et al., 1993; Esclapez et al., 1994; Hendrickson et al., 1994). In the rat, GAD65- and 67-immunoreactive(-ir) neurons are distributed throughout all three subdivisions of the IC (Merchán et al., 2005; Burianova et al., 2009) (**Figures 2A**, **3**).

In the CIC of rats, GAD-ir cell bodies of variable sizes are present, relatively homogenously distributed, with a variation in the intensity of immunostaining (Merchán et al., 2005; Burianova et al., 2009). With respect to morphology, the GAD-ir neurons are thought to correspond mostly to the less-flat neurons in the CIC (Malmierca et al., 1993, 1995a), which are homologous to stellate neurons in the CIC of the cat (Oliver, 1984; Oliver et al., 1994). Merchán et al. (2005) proposed that the majority of less-flat neurons are GABAergic, while the majority of flat neurons are excitatory cells (disc-shaped cells in the cat). GABAergic neurons were also reported to be larger on average in their somas when compared to non-GABA neurons in the IC, especially in the CIC (Merchán et al., 2005; Fredrich et al., 2009). In our experiments (Burianova et al., 2009), we did not quantify the size of GAD-ir neurons in comparison to immunonegative ones; however, in terms of morphology, the GAD-ir cells observed in the CIC belonged mostly to the less-flat neurons, with polygonal or oval shapes. In addition, we did not observe any distribution that resembled the location and orientation of the fibrodendritic laminae, which were described to comprise flat cells in the rat (Malmierca et al., 1993) or disc-shaped cells in cat (Morest and Oliver, 1984; Oliver and Morest, 1984).

In the external and dorsal cortices, the identification of morphological types is more complicated. The majority of GAD-ir neurons in the external cortex of the rat IC (EIC) are either large fusiform cells or smaller oval neurons, in both the second and third layers of the EIC. The GAD-ir neurons in the EIC resemble some types described with Rio-Hortega Golgi staining in the rat IC by Malmierca et al. (2011). Especially the large fusiform-like neurons, stained in our sections for GAD (Burianova et al., 2009), might correspond to the second major neuronal type in the EIC, called bitufted neurons with spindle, fusiform somas. In addition, Malmierca et al. (2011) also observed in the second layer of the rat EIC cluster-like groups of small neurons that may correspond to the modules described in detail by Chernock et al. (2004) and found in our own experiments as clusters of GAD-ir (and PV-ir) neurons (Ouda et al., 2008; Burianova et al., 2009). In the rat DIC, the situation is even more complex due to the large heterogeneity of neuronal shapes (Malmierca et al., 2011), which makes direct identification from immunostained sections practically impossible. In our GAD-staining, lower numbers, in comparison to the EIC and CIC, of predominantly small-sized immunoreactive neurons with a homogenous distribution were present in the rat DIC (Burianova et al., 2009).

The clusters of small neurons and intensely stained neuropil in the second layer of the rat EIC described by Chernock et al. (2004) are clearly visible in most sections to the naked eye (Chernock et al., 2004; Burianova et al., 2009). In addition to GAD, the clusters are immunopositive for NADPH-diaphorase and parvalbumin (PV), whereas they are immunonegative for glycine, CB, choline acetyltransferase, and SMI-32. These clusters or modules are absent in the mouse, squirrel, cat, bat, and macaque monkey, and so far they have been found only in rats and were suggested to possibly participate in the animal's spatial orientation (Chernock et al., 2004).

As already mentioned, the GABAergic neurons represent a substantial part of all neurons in the IC. In rats, the portion of inhibitory neurons in the IC seems to be larger than in the cat or bat; specifically; the CIC of the rat contains more than 30% of GABAergic neurons, whereas in the same structure of the cat or the bat they represent approximately 20% (Oliver et al., 1994; Winer et al., 1995; Merchán et al., 2005; Fredrich et al., 2009). The rat DIC and EIC are reported to contain about 20–25% of GABAergic neurons, while the data from other mammalian

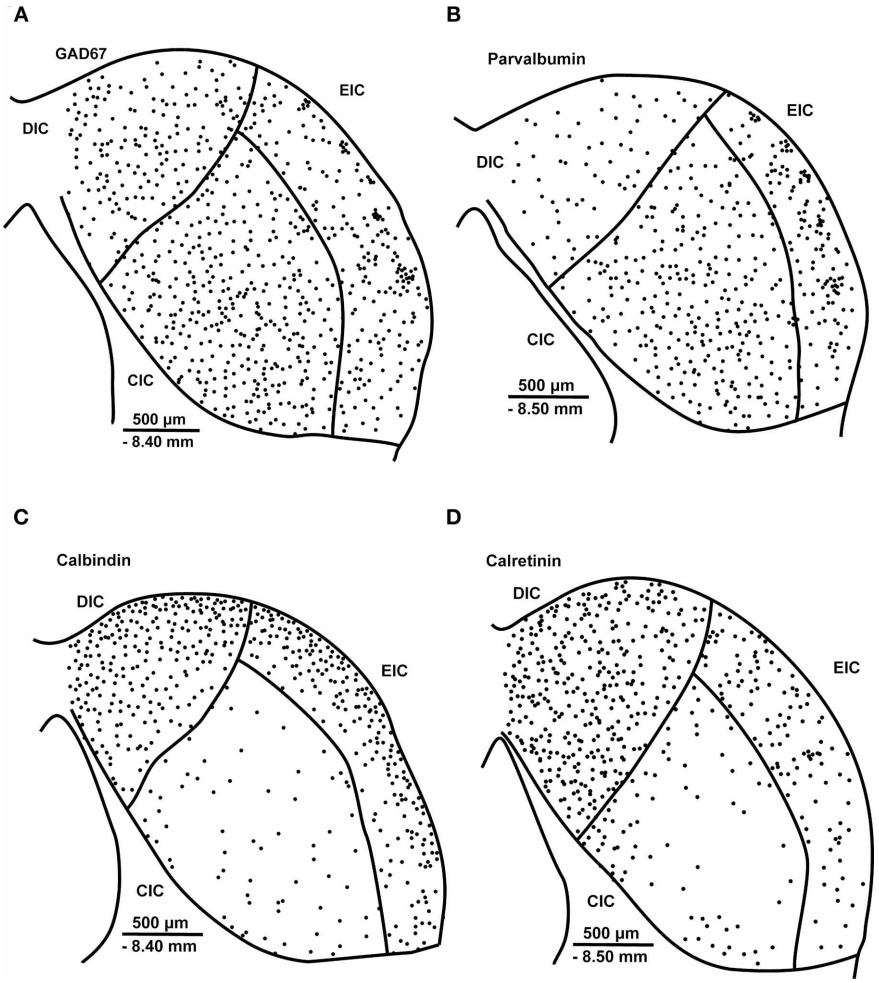

FIGURE 2 | Schematic illustration of the distribution of glutamate decarboxylase. GAD67 **(A)**, parvalbumin **(B)**, calbindin **(C)** and calretinin **(D)** immunoreactive neurons in a section containing all three major subdivisions of the IC, the central nucleus and the dorsal and external cortices, in young adult Long-Evans rats. CIC, central nucleus of the inferior colliculus; DIC, dorsal cortex of the inferior colliculus; EIC, external cortex of the inferior colliculus; GAD67, glutamate decarboxylase, isoform 67; PV, parvalbumin; CB, calbindin; CR, calretinin. The distance from bregma and scale bars are provided in each panel. The displayed schema is based on the distribution of GAD67-, PV-, CB-, and CR-ir neurons observed in our previous publications (Ouda et al., 2008; Burianova et al., 2009; Ouda et al., 2012b).

species are not known (Merchán et al., 2005). In addition to this, the GABAergic projection from the IC to the MGB has been reported to be more prominent in the rat than in some non-rodent species (Peruzzi et al., 1997; Ito et al., 2009). The reason for the difference from the known results in other mammalian orders is not clear. However, the next structure in the rat ascending auditory pathway, the MGB, contains almost no inhibitory neurons in the rat in contrast to other mammals. In the rat MGB, GABAergic neurons represent less than 1% of cells, while they form a significant portion (25%) of all neurons in the cat or primate MGB (Winer and Larue, 1996). Therefore, the only inhibition in the rat MGB is of extrinsic origin, which might be linked to the higher representation of GABAergic inhibition and projection in the rat IC.

The brainstem auditory nuclei, especially the dorsal and ventral nuclei of the lateral lemniscus as well as the superior paraolivary nucleus, have generally been considered to be a major source of inhibitory inputs to the neurons of the IC (ipsi- and contralaterally) (Zhang et al., 1998; Kulesza and Berrebi, 2000; Riquelme et al., 2001; Saldaña et al., 2009). However, the number of rat CIC GABAergic neurons, i.e., 30% of 200,000–230,000, which are either local circuit neurons or projecting neurons sending local collaterals within the IC (Oliver et al., 1991; Malmierca et al., 1995b; Ito et al., 2009), is markedly higher than the number of GABAergic neurons in all the lower brainstem auditory nuclei in total. Therefore, the most important source of GABAergic terminals on the rat IC neurons might be the intrinsic GABAergic IC neurons themselves.

Recently, two types of GABAergic neurons were described in the IC of the rat with different synaptic organization and axonal projections: smaller GABAergic neurons, which are predominatly local circuit interneurons, and larger GABAergic neurons,

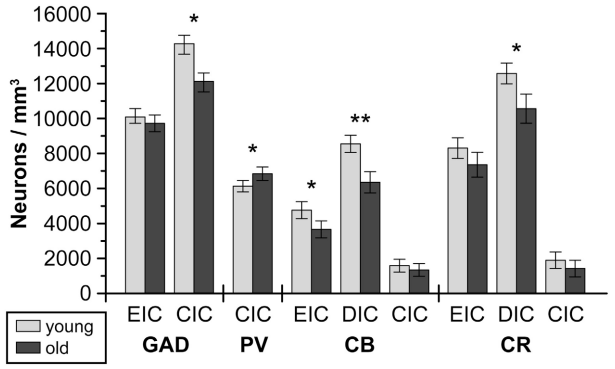

FIGURE 3 | The numerical density of GAD67-ir, PV-ir, CB-ir and CR-ir neurons in the external and dorsal cortices and in the central nucleus of the IC in young and old Long-Evans rats. CIC, central nucleus of the inferior colliculus; DIC, dorsal cortex of the inferior colliculus; EIC, external cortex of the inferior colliculus; GAD67, glutamate decarboxylase, isoform 67; PV, parvalbumin; CB, calbindin; CR, calretinin. The displayed results represent a summary of graphs from Ouda et al. (2008); Burianova et al. (2009); Ouda et al. (2012b). The error bars represent S.E.M. (* $P < 0.05$, ** $P < 0.01$).

predominantly projecting to the MGB (Ito et al., 2009). The projecting GABAergic neurons are more prevalent in the central nucleus of the IC and are densely covered perisomatically with glutamatergic synaptic contacts that could allow them to fire easily and rapidly. The exclusive presence of vesicular glutamate transporter 2 in presynaptic terminals suggests that the predominant sources of these synaptic connections are either collateral branches of IC glutamatergic neurons or fusiform cells in the dorsal cochlear nucleus. In addition, they possess very thick axons which may allow them to deliver inhibitory input to the MGB in advance of excitatory inputs from the glutamatergic IC neurons firing simultaneously (Ito et al., 2009).

In our previous study, we concluded that a minor neuronal population of about 10% of the neurons in all three major subdivisions of the IC of the rat expresses non-phosphorylated neurofilaments labeled by SMI-32 antibody (Ouda et al., 2012a). The SMI-32 antibody was shown to specifically label a subset of cortical and subcortical neurons in the mammalian brain, predominantly those with long and thick axonal projections (Sternberger and Sternberger, 1983; Kirkcaldie et al., 2002; Voelker et al., 2004; Molnár and Cheung, 2006). The non-phosporylated neurofilament content in neurons is thought to be associated with the large extent of axonal myelination and with large neuronal size (Campbell and Morrison, 1989; Tsang et al., 2000; Kirkcaldie et al., 2002). Since the GABAergic neurons in the rat IC are reported to be larger than non-GABAergic cells (Merchán et al., 2005), and simultaneously projection GABAergic neurons in the CIC and EIC, containing thick myelinated axons, are thought to be larger than non-projecting GABAergic neurons (Ito et al., 2009), we might speculate that the non-phosphorylated neurofilaments labeled by SMI-32 in the IC are preferentially expressed in a subset of the larger projecting GABA-ergic neuronal subpopulation. However, a double labeling study is necessary to confirm such a hypothesis.

CALCIUM BINDING PROTEINS

The calcium binding proteins (CBPs), CB, PV, and CR, represent major fast cytoplasmatic calcium buffers in the central nervous system and thus protect neurons from insults that induce an elevation of intracellular Ca^{2+} (Baimbridge et al., 1992; Elston and González-Albo, 2003). The disruption of neuronal calcium homeostasis and consequent molecular events affect neuronal viability and synaptic plasticity and may represent early steps in the development of neuronal degeneration (Foster, 2007). Changes in calcium homeostasis in the brain during aging or during different pathologies are thought to be tightly linked to a decline in neuronal performance (Khachaturian, 1989; Verkhratsky and Toescu, 1998; Toescu et al., 2004).

The distribution of calbindin-immunoreactive (CB-ir), calretinin immunoreactive (CR-ir) and parvalbumin-immunoreactive (PV-ir) neurons in the central nervous system of the rat was first described in summary by Celio (1990) and Résibois and Rogers (1992). Their distribution seems to be complementary to some extent with the major occurrence of PV in the primary (tonotopic) and CB and CR in the non-primary rat auditory regions (Lohmann and Friauf, 1996), as also described in mice (Cruikshank et al., 2001), chinchillas (Kelley et al., 1992), monkeys (Jones, 2003), and humans (Tardif et al., 2003; Sharma et al., 2009). Specifically in the IC, CB-ir, and CR-ir neurons are abundant in the dorsal and external cortices and relatively rare in the central nucleus of the IC, while PV-ir neurons are present in all three parts of the IC, with a predominant distribution in the CIC. The mutual colocalization of CB, PV, and CR in one neuron is known to be relatively rare, as they mainly represent three distinct neuronal populations; in the higher parts of the auditory pathway their expression is mostly found (in the case of PV almost exclusively) in GABAergic neurons (Demeulemeester et al., 1989; Kubota et al., 1994; Gonchar and Burkhalter, 1997; Jinno and Kosaka, 2002; Markram et al., 2004; Gonchar et al., 2007).

PARVALBUMIN

PV-ir neurons are present in all three subdivisions of the rat IC (Lohmann and Friauf, 1996; Ouda et al., 2008). In the CIC, neurons with a large variation in the size of their neuronal somas are rather uniformly distributed (**Figure 2B**). In our PV-ir staining, the intensity of their immunoreactivity varied from low to high and their morphology resembles the less-flat cells, similarly as in GAD immunostaining. In the EIC, the majority of PV-ir neurons belonged to the large spindle-like multipolar cells and smaller oval neurons (Ouda et al., 2008). The clusters of PV-immunoreactive somas and neuropil in the second layer of the EIC are very similar to the clusters in GAD immunostaining and visible in practically all examined rats, as in GAD immunostaining (Chernock et al., 2004; Ouda et al., 2008). The DIC contains a relatively low number of mostly oval, small-sized PV-immunoreactive neurons (Lohmann and Friauf, 1996; Ouda et al., 2008).

In the neocortex, the PV-expressing neurons mostly form a well-defined population of fast-spiking GABA-ergic basket cells that are essential for the generation of gamma oscillations, which are thought to provide a temporal framework for information processing in the brain (Kawaguchi and Kubota, 1998; Bartos

et al., 2007). These neurons comprise roughly 40–50% of all cortical GABAergic neurons; practically all PV-ir cortical cells are also GABAergic cells (Gonchar and Burkhalter, 1997; Gonchar et al., 2007). The co-expression of GAD and the functional importance of the PV-ir neuronal population in the IC are known to a lesser extent. From our experiments (Ouda et al., 2008), we can estimate that the number of GAD-ir neurons in the rat IC is roughly two times higher in the central nucleus and external cortex of the IC than the number of PV-ir neurons (**Figure 3**). On the other hand, Fredrich et al. (2009) identified almost all GAD-ir neurons in the central nucleus of the rat IC as co-expressing PV. The reason for this discrepancy is not clear; however, the different antibodies used and variations in the immunoreactivity of PV-ir somas pivotal for classifying a cell as PV-positive might be responsible to some degree for this difference. The potential preference for PV expression in some GABAergic subpopulations, especially larger GABAergic neurons projecting to the MGB vs. smaller local circuit interneurons (Ito et al., 2009), is open to further investigation. However, the PV-ir neurons in the CIC varied in size from small to large-sized in our staining, similarly as for GAD immunostaining (Ouda et al., 2008; Burianova et al., 2009), which may suggest the presence of PV in both of the above-mentioned GABAergic subpopulations.

In any case, the distribution of PV-ir neurons in the whole IC reflects relatively well the distribution of GABAergic (GAD-ir) neurons (compare **Figures 2A** and **2B**). Furthermore, the morphological types, at least of the neuronal somas, present in our immunostainings correspond relatively well to the same classification of GAD-ir neurons discussed in the previous section on GAD. In addition, the similar appearance of clusters in the EIC in both GAD and PV immunostaining (Chernock et al., 2004) supports the idea of a strong overlap of GAD and PV immunoreactivity in the IC. In addition, only one group of cellular clusters in the second layer of the EIC was evaluated by Malmierca et al. (2011) with Rio-Hortega Golgi staining. However, the precise extent of these overlaps, even in the discussed clusters in the second layer of the EIC, requires a double labeling study to determine, which has not yet been performed in the EIC.

CALBINDIN

CB-ir neurons are present in all three subdivisions of the rat IC; however, the majority of CB-ir cells are found in the dorsal and external cortices, while only a few weakly stained neurons are scattered throughout the central nucleus of the IC (Förster and Illing, 2000; Ouda et al., 2012b) (**Figure 2C**).

A relatively homogenous neuropil and a high numerical density of CB-ir neurons are typical for the rat DIC, with a gradual decrease from the cortical surface toward the borders with the central nucleus. The neuronal somata are mainly oval or polygonal with loosely stained dendrites (Ouda et al., 2012b). In the rat EIC, the numerical density of immunoreactive cells is lower (**Figure 3**) and decreases toward the CIC and toward the basal part of the IC. The cellular morphology in the EIC is more heterogenous with oval, elongated or triangular somas. No signs of cluster-like immunoreactivity are present in the EIC (Chernock et al., 2004; Ouda et al., 2012b). In both the DIC and CIC, the highest numerical density of CB-ir neurons can be found adjacent to the surface of the IC and decreases toward the central nucleus. The CIC is demarcated as an area with low CB neuropil staining and weakly stained sparse CB-ir neurons (Förster and Illing, 2000; Ouda et al., 2012b).

As mentioned previously, CBPs were reported to be expressed mostly by GABAergic neurons (Freund and Buzsáki, 1996; Gonchar and Burkhalter, 1997; Gonchar et al., 2007); however, calbindin most likely does not follow this rule. For example, some weakly stained CB-ir cells in the superficial cortical layers of the neocortex are known to be pyramidal neurons (Kubota et al., 1994; De Felipe, 1997). In the IC, the notable prevalence of calbindin (and also calretinin) in the dorsal and external cortices and its low occurrence in the CIC suggest that at least some of these neurons are not GABAergic. This suggestion is further supported by the fact that in our quantitative estimates, we found that the numerical density of calbindin- and calretinin-immunoreactive neurons in the DIC is even higher than the number of all GAD-ir neurons in the DIC (unpublished data). In addition, clusters of smaller oval neurons that are GAD-ir and PV-ir in the EIC are not visible in calbindin immunostaining (Ouda et al., 2012b). No double labeling study in the DIC or EIC has been undertaken so far, while in the CIC, Fredrich et al. (2009) did not report the colocalization of GABA and CB/CR using double staining.

CALRETININ

CR-ir neurons are found in all three subdivisions of the rat IC with a significant presence in the dorsal and external cortices (Lohmann and Friauf, 1996; Ouda et al., 2012b) (**Figure 2D**). In the CIC, a weaker positivity of the neuropil and a lower numerical density of CR-ir neurons are distinctive features, while in the DIC, a relatively homogenous neuropil and a very high numerical density of CR-ir neurons are dominant features (Ouda et al., 2012b).

In the rat EIC, an interesting feature of CR immunostaining that we could often find in our sections stained for calretinin is a strip-like distribution of CR-ir neurons and neuropil positivity throughout all three cortical layers, with patches with a higher concentration of immunoreactive neuropil and neurons that are surrounded by less stained neuropil. One might speculate about a link to the clusters evaluated by Chernock et al. (2004) that display GAD, parvalbumin and NADPH-diaphorase immunoreactivity. However, these *pro tempore* called strips or patches are not delineated as clearly and consistently or with such contrast as the clusters in GAD or PV immunostaining; furthermore, they are larger and situated deeper from the IC surface across the EIC (**Figure 2D**). Dual labeling will be necessary to determine any such potential relationship. The form of the CR-ir neuronal somas in the EIC ranges from small-sized to large neurons and oval or polygonal in shape, while a few cells with spindle-like morphology are present (Ouda et al., 2012b).

The correspondence of calretinin-expressing neurons with particular morphological types and specifically with the GABA-mediated system in the IC is more ambiguous than in the case of parvalbumin. As stated above, the numerical density of calbindin- and calretinin-immunoreactive neurons in the DIC is even higher than the number of all GAD-ir neurons in the DIC. However, in contrast to calbindin, the presence of a few large spindle-like

neurons and potential cluster-like immunoreactivity suggests a more pronounced overlap with the population of GAD-ir neurons, at least in the external cortex of the IC.

Interestingly, the distribution and numerical density of CR-ir neurons throughout the IC are similar to the distribution and numerical density of neurons positive for NADPH-diaphorase(-d), which identifies neurons capable of producing nitric oxide (Dawson et al., 1991; Hope et al., 1991; Druga and Syka, 1993; Loftus et al., 2008; Wu et al., 2008). In our estimation, the numerical density of NADPH-d-positive neurons in all three major divisions of the IC is close to the numerical density of CR-ir neurons (unpublished data). In the IC, the NADPH-d-positive neuronal subpopulation is known to be predominantly glutamatergic, while only a minority of NAPDH-diaphorase-positive cells in the IC is GABAergic neurons (Wu et al., 2008). No double labeling study of CR and NADPH-d was reported in the IC; however, a substantial colocalization of CR and NADPH-d expression in neurons was observed in the hippocampus and periaqueductal gray (Czéh et al., 2005; Barbaresi et al., 2012). On the other hand, the pattern of clusters in the second layer of the EIC labeled by NADPH-d staining apparently corresponds to the pattern of the clusters present in GAD and PV immunostaining (Chernock et al., 2004).

INFLUENCE OF AGING ON THE EXPRESSION OF IMMUNOCYTOCHEMICAL MARKERS

The inferior colliculus, similarly as other structures of the auditory pathway in the rat, undergoes essential changes with aging. To demonstrate these changes clearly, we decided to use for aging studies two rat strains (the inbred Fischer 344 strain and the outbred Long-Evans strain) with a wide variety of morphological, physiological and behavioral differences, including differently preserved hearing function with age (for review see Syka, 2010). For example, similarly as with other inbred strains, Fischer 344 rats display large cognitive deficits in different tests of spatial memory in the Morris water maze in contrast to wild rats and Long-Evans rats (Harker and Whishaw, 2002). While Long-Evans rats represent a strain with relatively well preserved peripheral hearing function up to late senescence, a rapid and pronounced deterioration of hearing function with aging is found in Fischer 344 rats, resulting in larger hearing threshold shifts, a decrease in the amplitude of click-evoked auditory brainstem responses, a diminution of distortion product otoacoustic emissions and a decrease in middle-ear compliance (Popelar et al., 2003, 2006). Age-related sensory deficits in F344 rats also include visual function, which is damaged due to retinal degeneration (Di Loreto et al., 1994). In spite of the differences between strains, we found that age-related changes in the immunocytochemical markers in the IC were almost identical in both strains.

GLUTAMATE DECARBOXYLASE

In GAD-65 and 67 immunoreactivity (Burianova et al., 2009), significant declines with aging were observed in the CIC and EIC comprising a decrease in the optical density of GAD-ir neuronal somas and a decrease in the number of GAD-ir cells (CIC only, **Figure 3**). These findings were supported by the results of western blot analysis that demonstrated a significant age-related decline of about 50% in the levels of GAD65 and GAD67 proteins in the IC of old rats in comparison with young animals (**Figure 4**). The analyzed samples for western blotting included the whole IC (i.e., all three subdivisions of the IC at once). The decline in GAD immunoreactivity was also similar in the auditory cortex, and the pattern of changes was very similar in both Long-Evans and Fischer 344 animals. Interestingly, the protein levels of both isoforms of glutamate decarboxylase (GAD65 and 67) were found to be approximately threefold higher (per unit of tissue weight) in the rat IC in comparison with the neocortical areas in both young and old animals (Sheikh et al., 1999; Burianova et al., 2009), which might further support a prominent role for inhibition in the rat IC.

An age-related decrease in the number of GABA-immunoreactive cells associated with a decrease in enzymatic activity, the levels of GABA and the release of GABA in the rat CIC was also reported by other authors (Caspary et al., 1990, 1995; Gutiérrez et al., 1994; Raza et al., 1994). Simultaneously, GABA-A and GABA-B receptor binding intensity was reported to decline, and the protein levels of the receptor subunits were found to be altered during aging in the IC of Sprague-Dawley and Fischer 344 rats (Gutiérrez et al., 1994; Milbrandt et al., 1994; Caspary et al., 1999; Schmidt et al., 2010). The compromised GABA-mediated inhibition in the IC could consequently result in a broadening of the excitatory areas and thus in the poorer tuning of the neuronal receptive fields. In turn, the reduction of fine-tuned receptive fields resulted in a poorer discrimination of the temporal parameters of sounds, as also demonstrated by

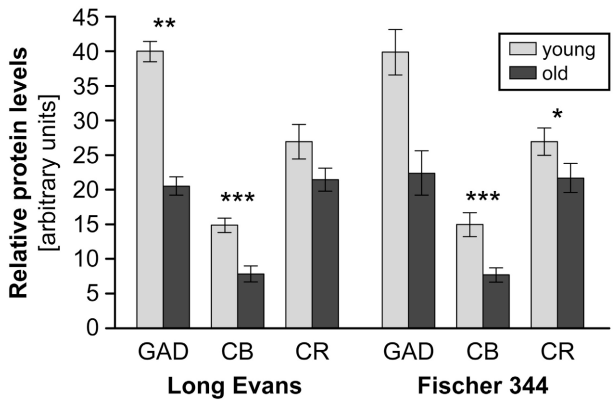

FIGURE 4 | The results of western blot protein analysis of GAD67, calbindin (CB) and calretinin (CR) in the IC of young and old Long-Evans and Fischer 344 rats. Arbitrary units were calculated as the ratio between the optical density of the examined protein and the optical density of actin (in scanned films analysed using ImageQuant software). The heights of the columns for GAD67, CB, and CR cannot be mutually compared; they are dependent on the ratio of protein levels between the IC and the cortical areas for each examined protein. The tall column for GAD67 (in arbitrary units) indicates a larger amount of GAD67 per unit tissue weight in the IC when compared to the cortex (and conversely for CB). Due to the limited number of old Fischer 344 rats available for GAD67 protein analysis, the data did not demonstrate statistically significant differences in this case. The graph is constructed from data presented in Burianova et al. (2009); Ouda et al. (2012b). The error bars represent S.E.M. ($^{*}P < 0.05$, $^{**}P < 0.01$, $^{***}P < 0.001$).

electrophysiological data in the IC (Palombi and Caspary, 1996; Walton et al., 1998, 2002; Simon et al., 2004).

CALCIUM BINDING PROTEINS

Despite the almost exclusive colocalization of GABA-ir and PV-ir in neurons in the IC and neocortex (Gonchar and Burkhalter, 1997; Gonchar et al., 2007; Fredrich et al., 2009), the age-related changes in parvalbumin immunoreactivity were different when compared with changes in GAD 65 and 67 (Ouda et al., 2008). In old Long Evans rats, the observed changes were rather mild: the number of PV-ir neurons in the CIC was slightly increased, associated with an increase in the optical density of PV-ir somas and a slight decrease in the mean neuronal volumes. In contrast, in old Fischer 344 rats a non-significant tendency toward a decrease in the number of PV-ir neurons in the IC and significantly smaller mean neuronal volumes were present. The observed changes could not be attributed to any specific type of neuron. In contrast to these findings, a significant reduction in the occurrence of PV-ir neurons was found in the auditory cortex of Fischer 344 animals with aging, whereas in Long Evans rats such a reduction was not observed.

The age-related changes in calbindin and calretinin immunoreactivity had a rather similar pattern and were relatively uniform, regardless of the examined rat strain or structure (IC and auditory cortex). We found similar significant age-related changes in CB immunoreactivity in the dorsal and external cortices of both Long Evans and Fischer 344 rats. The changes included a decrease in the number of CB-ir neurons and a significant decline in the average volumes of CB-ir neuronal somas (DIC only). In western blotting, the age-related changes were even more pronounced and resulted in a significant decline in the levels of calbindin in the whole IC of old rats of both species of almost 50%. In calretinin immunoreactivity, a tendency toward an age-related decline in the number of CR-ir neurons as well as a significant decrease in the mean volumes of the remaining CR-ir neuronal somas were found in the dorsal and external cortices of the IC. Western blot analysis demonstrated a significant decline, however, less pronounced when compared to calbindin and GAD, in calretinin protein levels of 22% in both rat strains (Ouda et al., 2012b). Summaries of the immunohistochemical age-related findings and western blot results are presented in **Figures 3**, **4**.

In an inter-species comparison, strain-dependent differences were found in the inferior colliculus of the CBA/CaJ and C57/BL/6J mouse strains: with aging, both strains showed a decline in the number of calbindin-ir neurons in the IC, similarly as in our study. However, the number of CR-ir neurons did not change with age in C57 mice and even significantly increased in the IC of CBA mice (a mouse strain with preserved hearing function up to an advanced age) (Zettel et al., 1997). In the case of calretinin, the changes were found to be activity-dependent, since early bilateral deafening prevented calretinin up-regulation in the DIC of aged CBA animals (Zettel et al., 2001). This difference from the findings in Long-Evans rats might reflect inter-species differences to some degree. A decline in the number of calcium binding protein (CBP)-ir neurons were observed in different brain neocortical areas in humans, including the auditory cortex, without any previous signs of psychiatric or neurological diseases (Bu et al., 2003). Increasing evidence has also accumulated about the mutual links among intracellular calcium regulation, alterations in intracellular CBP levels and neurodegenerative and neuropsychiatric disorders (for review see Woo and Lu, 2006; Mattson, 2007). The disruption of calcium homeostasis in neurons may consequently be involved in both the impairments that accompany normal aging and also in the different pathologies associated with age-related disorders (Khachaturian, 1989; Foster, 2007; Mattson, 2007; Riascos et al., 2011). In this context, it may be surprising that in mutant mice (CB-/-, CR-/- or PV-/-), the deleted individual CBP is not compensated for by the up-regulated expression of any other CBP (Schwaller et al., 2002). Nevertheless, the mice (of all three types) are not only able to survive, but actually display no significant changes in phenotype, either in the general morphology of the nervous system or their behavior under normal housing conditions. The morphological and functional changes are rather subtle and manifest during specific behavioral experiments, which may suggest a more complicated function for CBPs in neurons, not only as simple calcium buffers and thus as neuroprotective molecules, but also as complex components in intracellular calcium homeostasis involved in the subtle regulation and timing of calcium signals pre- or postsynaptically (Schwaller et al., 2002; Schwaller, 2010).

CHANGES IN THE TOTAL NUMBER OF NEURONS

The decreased number of immunoreactive neurons (GAD-, CB-, CR-ir, etc.,) in the IC observed in aging studies cannot be easily attributable to a general neuronal loss, because in our previous experiments we found that the reduction in the total number of neurons in the IC of old Long-Evans and Fischer 344 rats in Nissl-stained sections does not exceed 10% (unpublished data). This finding is in agreement with the data of other authors, who reported no significant changes accompanying aging in the total number of neurons in the rat inferior colliculus (Helfert et al., 1999) or other rat brain regions, including the hippocampus and cortical areas (Merrill et al., 2001; Poe et al., 2001; Stanley and Shetty, 2004). Specifically, in the IC of old Fischer 344 rats, the number of both inhibitory and excitatory synaptic terminals decreased while no age-related reduction in the total number of neurons was found (Helfert et al., 1999). For comparison, a stereological study demonstrated an age-related decrease in the total number of neurons in the human neocortex of fewer than 10% (Pakkenberg and Gundersen, 1997).

Therefore, the diminished expression of proteins in originally immunoreactive neurons may be the reason for the age-related reduction in the detectable numbers of immunoreactive neurons. Similarly, up-regulated or *de novo* expression in previously non-expressing neurons may be the reason for the increase in the number of immunoreactive neurons in situations such as the reported increase of CR-ir neurons in the IC of old CBA mice (Zettel et al., 1997).

THE LINK TO ELECTROPHYSIOLOGICAL AND BEHAVIORAL DATA

So far, it has not been known whether the age-related changes in the IC (and/or auditory cortex) are mainly the consequence of decreased ascending inputs from the deteriorated periphery or

rather part of the changes in the aging brain itself. Most immunohistochemical experiments concerning age-related changes in the GABA-mediated inhibition of central auditory system were undertaken in animal strains with a pronounced hearing loss and deterioration of the peripheral sensory organ with aging, which represented a complication for determining the cause of the observed changes (for review see Frisina, 2001, 2009, 2010; Syka, 2002; Caspary et al., 2008). In our experiments, the age-related decline in the number of GAD-ir, CB-ir, and CR-ir neurons as well as the decline in GAD, CB, and CR protein levels in the inferior colliculus (and auditory cortex) were found to be largely independent of the peripheral deterioration, including the levels of the hearing threshold shifts (Burianova et al., 2009; Ouda et al., 2012b).

Hearing function was shown to be altered in the absence of any significant damage to the peripheral sensory organ, since the age-related worsening of gap detection thresholds, the gap duration difference limen and the disappearing middle latency response to an increasing stimulus repetition rate are not correlated with hearing threshold shifts in Long-Evans rats (Suta et al., 2011). Specifically, the gap detection thresholds were shown to be based predominantly on subcortical structures, since the induced temporary inactivation of the left auditory cortex in the rat by the administration of muscimol resulted in a significant worsening of the gap duration difference limen, while gap detection thresholds were not significantly changed (Rybalko et al., 2010). Furthermore, the neural code necessary for behavioral gap detection is present in the temporal discharge patterns of the majority of IC neurons (Walton et al., 1997).

Similarly, in electrophysiological studies on aging Fischer 344 rats, the reduction in the maximum discharge rate or the increased number of units responding poorly to an auditory stimulus in the IC was not correlated with the observed hearing threshold shift. In addition, for spontaneous activity, first spike latency or dynamic range, no significant declines were observed with aging (Palombi and Caspary, 1996). Also in mice, spontaneous rates and the distribution of temporal discharge patterns did not differ significantly between young and old CBA/CaJ mice, and the age-related decline in the processing of temporal sound features or the coding of envelope periodicities was suggested to be likely related to a dysbalance between inhibitory and excitatory neuronal mechanisms (Walton et al., 1998, 2002). Significant central functional age-related hearing alterations in the IC were found in both the CBA/CaJ mouse strain, with relatively preserved peripheral hearing up to late senescence, and the C57/BL/6J mouse strain, which serve as a model of rapid and severe sensorineural presbycusis, though the particular character of the changes was different (Walton et al., 1998, 2002; Felix and Portfors, 2007).

In a recent age-related study, (Rybalko et al., in press) performed in our laboratory, the acoustic startle reflex (ASR) (a transient motor response to an intense unexpected stimulus) and the prepulse inhibition (PPI) were used as an indicator of the behavioral responsiveness to sound stimuli. While the ASR is an unconditioned reflex reaction, in the PPI procedure, the startle reaction is inhibited by a low-level sound that shortly precedes the intense startle stimulus (Davis et al., 1982; Koch, 1999). Animal studies have shown that in the auditory system, PPI is involved in the cochlear nucleus, the inferior and superior colliculi and the pedunculopontine tegmental nucleus (Nodal and López, 2003), with the cortex and hippocampus exhibiting a modulatory effect on the PPI (Koch, 1999). The PPI of ASR, which represents a basic inhibitory process regulating sensory inputs, can be used for estimating age-related changes in inhibitory function (Geyer and Braff, 1987; Swerdlow et al., 2001). In our experiments, both Long-Evans and Fischer 344 rats exhibited a similar age-related progression of PPI deterioration, with a significantly decreased inhibitory efficacy in aged rats. This decrease was not correlated with the observed hearing threshold shifts.

Therefore, we may suggest that the age-related decline in GAD expression in the rat IC and AC, as demonstrated in our experiments, does not depend exclusively on peripheral deafferentation but is, at least partially, of central origin. The age-related alterations in the IC involving the GABA-mediated inhibitory system and the decline in the number of neurons expressing glutamate decarboxylase and CBPs may significantly contribute to the observed behavioral impairment.

THE REVERSIBILITY OF CHANGES AND FUNCTIONAL IMPLICATIONS

The potential long-term reversibility or compensation of the age-related changes in the expression of glutamate decarboxylase or CBPs is open to further investigation. However, it is known that changes in the expression of selected neuronal markers in the IC neurons, including CBPs that are induced by experimental manipulations may be reversible to some extent.

For example, following monoaural cochlear ablation in the ferret, the CR-ir plexus in the contralateral CIC increased its optical density and the area of immunostaining (Fuentes-Santamaria et al., 2003). The increase in CR immunostaining was interpreted as an up-regulation of CR expression in a subset of IC afferents. In rats, a similar increase in the levels of CR was found after unilateral enucleation in the contralateral superior colliculus (Arai et al., 1993). Furthermore, the induced changes were found to be reversible to some degree after a longer time period. A unilateral ablation of the auditory cortex in rats resulted in a progressive increase in the number and optical density of CR-ir neurons in the dorsal and external cortices, i.e., the subdivisions of the IC more inervated by the cortico-collicular projection, which returned to control values during the long-term survival of the animals (Clarkson et al., 2010). Similarly, the number of NADPH-d-positive neurons in the inferior colliculus declined significantly after a lesion of the auditory cortex at short survival intervals in rats; however, this reduction diminished after longer survival intervals (Druga and Syka, 2001). The reversible character of the changes in protein expression supports the idea of the preservation of the affected neurons.

With respect to studies on aging, similar data are very limited. At the cortical level, a partial recovery of age-related deterioration was shown by De Villers-Sidani et al. (2010). The age-related hearing deficits and the decline in the number of PV-ir neurons in the auditory cortex of old rats were partially reversed after intensive auditory behavioral training. Similarly, in the visual cortex of old monkeys, deteriorated GABA-mediated function was observed with aging, while the local administration of GABA

temporarily improved the visual function of the neurons (Leventhal et al., 2003). Nevertheless, despite peripheral deterioration that leads to reduced input thoughout the auditory pathway to the IC and central neurochemical changes affecting the levels of neurotransmitters or CBPs, the compensatory mechanisms are probably highly active in sensory systems in aged animals and humans, as also emphasized by other authors (Palombi and Caspary, 1996; Syka, 2002; Caspary et al., 2008; Frisina, 2010).

CONCLUSIONS

The inferior colliculus may play an even more prominent role in the central auditory system of rats than usually thought, since the rat IC contains more neurons in total than all other subcortical auditory structures combined (Kulesza et al., 2002; Ouda et al., 2012a). In addition, inhibitory neurons in the rat IC, including GABAergic projections from the IC to the MGB, are present in abundant numbers when compared to the cat or bat, whereas intrinsic GABAergic neurons are practically absent in the MGB of rats and other rodents in contrast to other mammalian orders (Winer and Larue, 1996; Merchán et al., 2005; Ito et al., 2009).

Along with the auditory cortex, the IC plays a key role in the processing of the temporal parameters of sounds, which is strongly dependent on the function of the inhibitory systems. Both temporal parameter processing and GABA-mediated inhibition are known to be altered in aged rats (Syka, 2002; Caspary et al., 2008; Frisina, 2010). The decline in the number of neurons expressing glutamate decarboxylase and CBPs as well as the decline in the levels of these proteins occuring in the IC with aging, as observed in our experiments, could represent a basis for central functional deterioration (Ouda et al., 2008, 2012b; Burianova et al., 2009). Since the total number of neurons in the IC likely does not decline significantly with aging (Helfert et al., 1999), the diminished expression of proteins in originally immunoreactive neurons may be the reason for the age-related reduction in the detectable numbers of immunoreactive neurons. Furthemore, the age-related decline in the number of immunoreactive neurons and the levels of the proteins occurring in the central auditory system is not exclusively dependent on the loss of peripheral inputs, but may represent, at least partially, a feature of the aging brain and significantly contribute to the deterioration of hearing function known as central presbycusis.

Central presbycusis represents a complex process that includes alterations present in the subcortical auditory nuclei, the auditory cortex and other non-auditory regions, as well as the development of partial compensatory mechanisms. The potential reversibility or compensation of these age-related changes is open to further investigation. A better understanding of the mechanisms underlying impaired neuronal processing in the central auditory system with aging, resulting in the poor recognition of complex environmental sounds, species-specific vocalizations in animals and speech in man, may have important implications for the treatment or amelioration of the negative aspects of presbycusis in the future.

ACKNOWLEDGMENTS

This study was supported by the Grant Agency of the Czech Republic P304/12/1342 and P304/12/G069.

REFERENCES

Aitkin, L. M., Dickhaus, H., Schult, W., and Zimmermann, M. (1978). External nucleus of inferior colliculus: auditory and spinal somatosensory afferents and their interactions. *J. Neurophysiol.* 41, 837–847.

Arai, M., Arai, R., Sasamoto, K., Kani, K., Maeda, T., Deura, S., and Jacobowitz, D. M. (1993). Appearance of calretinin-immunoreactive neurons in the upper layers of the rat superior colliculus after eye enucleation. *Brain Res.* 613, 341–346.

Baimbridge, K. G., Celio, M. R., and Rogers, J. H. (1992). Calcium-binding proteins in the nervous system. *Trends Neurosci.* 15, 303–308.

Barbaresi, P., Quaranta, A., Amoroso, S., Mensà, E., and Fabri, M. (2012). Immunocytochemical localization of calretinin-containing neurons in the rat periaqueductal gray and colocalization with enzymes producing nitric oxide: a double, double-labeling study. *Synapse* 66, 291–307.

Bartos, M., Vida, I., and Jonas, P. (2007). Synaptic mechanisms of synchronized gamma oscillations in inhibitory interneuron networks. *Nat. Rev. Neurosci.* 8, 45–56.

Batra, R., and Fitzpatrick, D. C. (2002). Monaural and binaural processing in the ventral nucleus of the lateral lemniscus: a major source of inhibition to the inferior colliculus. *Hear. Res.* 168, 90–97.

Beyerl, B. D. (1978). Afferent projections to the central nucleus of the inferior colliculus in the rat. *Brain Res.* 145, 209–223.

Bu, J., Sathyendra, V., Nagykery, N., and Geula, C. (2003). Age-related changes in calbindin-D28k, calretinin, and parvalbumin-immunoreactive neurons in the human cerebral cortex. *Exp. Neurol.* 182, 220–231.

Burianova, J., Ouda, L., Profant, O., and Syka, J. (2009). Age-related changes in GAD levels in the central auditory system of the rat. *Exp. Gerontol.* 44, 161–169.

Campbell, M. J., and Morrison, J. H. (1989). Monoclonal antibody to neurofilament protein (SMI-32) labels a subpopulation of pyramidal neurons in the human and monkey neocortex. *J. Comp. Neurol.* 282, 191–205.

Caspary, D. M., Raza, A., Lawhorn Armour, B. A., Pippin, J., and Arneric, S. P. (1990). Immunocytochemical and neurochemical evidence for age-related loss of GABA in the inferior colliculus: implications for neural presbycusis. *J. Neurosci.* 10, 2363–2372.

Caspary, D. M., Holder, T. M., Hughes, L. F., Milbrandt, J. C., McKernan, R. M., and Naritoku, D. K. (1999). Age-related changes in GABAA receptor subunit composition and function in rat auditory system. *Neuroscience* 93, 307–312.

Caspary, D. M., Ling, L., Turner, J. G., and Hughes, L. F. (2008). Inhibitory neurotransmission, plasticity and aging in the mammalian central auditory system. *J. Exp. Biol.* 211, 1781–1791.

Caspary, D. M., Milbrandt, J. C., and Helfert, R. H. (1995). Central auditory aging: GABA changes in the inferior colliculus. *Exp. Gerontol.* 30, 349–360.

Casseday, J. H., Ehrlich, D., and Covey, E. (2000). Neural measurement of sound duration: control by excitatory-inhibitory interactions in the inferior colliculus. *J. Neurophysiol.* 84, 1475–1487.

Casseday, J. H., Fremouw, T., and Covey, E. (2002). "The inferior colliculus: a hub for the central auditory system," in *Integrative Functions in the Mammalian Auditory Pathway, Vol. 15*, eds D. Oertel, A. N. Popper, and R. R. Fay (New York, NY: Springer-Verlag), 238–318.

Celio, M. R. (1990). Calbindin D-28k and parvalbumin in the rat nervous system. *Neuroscience* 35, 375–475.

Chernock, M. L., Larue, D. T., and Winer, J. A. (2004). A periodic network of neurochemical modules in the inferior colliculus. *Hear. Res.* 188, 12–20.

Clarkson, C., Juíz, J. M., and Merchán, M. A. (2010). Long-term regulation in calretinin staining in the rat inferior colliculus after unilateral auditory cortical ablation. *J. Comp. Neurol.* 518, 4261–4276.

Cruikshank, S. J., Killackey, H. P., and Metherate, R. (2001). Parvalbumin and calbindin are differentially distributed within primary and secondary subregions of the mouse auditory forebrain. *Neuroscience* 105, 553–569.

Czéh, B., Hajnal, A., and Seress, L. (2005). NADPH-diaphorase positive neurons of the rat hippocampal formation: regional distribution, total number and colocalization with calcium binding proteins. *Prague Med. Rep.* 106, 261–274.

Davis, K. A. (2002). Evidence of a functionally segregated pathway from dorsal cochlear nucleus to inferior colliculus. *J. Neurophysiol.* 87, 1824–1835.

Davis, M., Gendelman, D., Tischler, M., and Gendelman, P. (1982). A primary acoustic startle circuit: lesion and stimulation studies. *J. Neurosci.* 6, 791–805.

Dawson, T. M., Bredt, D. S., Fotuhi, M., Hwang, P. M., and Snyder, S. H. (1991). Nitric oxide synthase and neuronal NADPH diaphorase are identical in brain and peripheral tissues. *Proc. Natl. Acad. Sci. U.S.A.* 88, 7797–7801.

De Felipe, J. (1997). Types of neurons, synaptic connections and chemical characteristics of cells immunoreactive for calbindin-D28K, parvalbumin and calretinin in the neocortex. *J. Chem. Neuroanat.* 14, 1–19.

De Villers-Sidani, E., Alzghoul, L., Zhou, X., Simpson, K. L., Lin, R. C., and Merzenich, M. M. (2010). Recovery of functional and structural age-related changes in the rat primary auditory cortex with operant training. *Proc. Natl. Acad. Sci. U.S.A.* 107, 13900–13905.

Demeulemeester, H., Vandesande, F., Orban, G. A., Heizmann, C. W., and Pochet, R. (1989). Calbindin D-28K and parvalbumin immunoreactivity is confined to two separate neuronal subpopulations in the cat visual cortex, whereas partial coexistence is shown in the dorsal lateral geniculate nucleus. *Neurosci. Lett.* 99, 6–11.

Diamond, J. T., Jones, E. G., and Powel, T. P. S. (1969). The projection of the auditory cortex upon the diencephalon and brainstem of the cat. *Brain Res.* 15, 305–340.

Di Loreto, D. Jr., Cox, C., Grover, D. A., Lazar, E., del Cerro, C., and del Cerro, M. (1994). The influences of age, retinal topography, and gender on retinal degeneration in the Fischer 344 rat. *Brain Res.* 647, 181–191.

Dorph-Petersen, K. A., Caric, D., Saghafi, R., Zhang, W., Sampson, A. R., and Lewis, D. A. (2009). Volume and neuron number of the lateral geniculate nucleus in schizophrenia and mood disorders. *Acta Neuropathol.* 117, 369–384.

Druga, R., and Syka, J. (1984a). Ascending and descending projections to the inferior colliculus in the rat. *Physiol. Bohemosl.* 33, 31–42.

Druga, R., and Syka, J. (1984b). Neocortical projections to the inferior colliculus in the rat. *Physiol. Bohemosl.* 33, 251–253.

Druga, R., and Syka, J. (1984c). Projections from auditory structures to the superior colliculus in the rat. *Neurosci. Lett.* 45, 247–252.

Druga, R., and Syka, J. (1993). NADPH-diaphorase activity in the central auditory structures of the rat. *Neuroreport* 4, 999–1002.

Druga, R., and Syka, J. (2001). Effect of auditory cortex lesions on NADPH-diaphorase staining in the inferior colliculus of rat. *Neuroreport* 12, 1555–1559.

Druga, R., Syka, J., and Rajkowska, G. (1997). Projections of auditory cortex onto the inferior colliculus in the rat. *Physiol. Res.* 46, 215–222.

Elston, G. N., and González-Albo, M. C. (2003). Parvalbumin-, calbindin-, and calretinin-immunoreactive neurons in the prefrontal cortex of the owl monkey (*Aotus trivirgatus*): a standardized quantitative comparison with sensory and motor areas. *Brain Behav. Evol.* 62, 19–30.

Erlander, M. G., Tillakaratne, N. J. K., Feldblum, S., Patel, N., and Tobin, A. J. (1991). Two genes encode distinct glutamate decarboxylase. *Neuron* 7, 91–100.

Erlander, M. G., and Tobin, A. J. (1991). The structural and functional heterogeneity of glutamic acid decarboxylase: a review. *Neurochem. Res.* 16, 215–226.

Esclapez, M., Tillakaratne, N. J., Kaufman, D. L., Tobin, A. J., and Houser, C. R. (1994). Comparative localization of two forms of glutamic acid decarboxylase and their mRNAs in rat brain supports the concept of functional differences between the forms. *J. Neurosci.* 14, 1834–1855.

Faye-Lund, H., and Osen, K. K. (1985). Anatomy of the inferior colliculus in rat. *Anat. Embryol.* 171, 1–20.

Feldblum, S., Erlander, M. G., and Tobin, A. J. (1993). Different distributions of GAD65 and GAD67 mRNAs suggest that the two glutamate decarboxylases play distinctive functional roles. *J. Neurosci. Res.* 34, 689–706.

Felix, R. A. 2nd, and Portfors, C. V. (2007). Excitatory, inhibitory and facilitatory frequency response areas in the inferior colliculus of hearing impaired mice. *Hear. Res.* 228, 212–229.

Foster, T. C. (2007). Calcium homeostasis and modulation of synaptic plasticity in the aged brain. *Aging Cell* 6, 319–325.

Förster, C. R., and Illing, R. B. (2000). Plasticity of the auditory brainstem: cochleotomy-induced changes of calbindin-D28k expression in the rat. *J. Comp. Neurol.* 416, 173–187.

Fredrich, M., Reisch, A., and Illing, R. B. (2009). Neuronal subtype identity in the rat auditory brainstem as defined by molecular profile and axonal projection. *Exp. Brain Res.* 195, 241–260.

Freund, T. F., and Buzsáki, G. (1996). Interneurons of the hippocampus. *Hippocampus* 6, 347–470.

Frisina, D. R., and Frisina, R. D. (1997). Speech recognition in noise and presbycusis: relations to possible neural mechanisms. *Hear. Res.* 106, 95–104.

Frisina, R. D. (2001). Subcortical neural coding mechanisms for auditory temporal processing. *Hear. Res.* 158, 1–27.

Frisina, R. D. (2009). Age-related hearing loss: ear and brain mechanisms. *Ann. N.Y. Acad. Sci.* 1170, 708–717.

Frisina, R. D. (2010). "Aging changes in the central auditory system," in *Handbook of Auditory Science: The Auditory Brain*, eds A. Rees and A. Palmer (Oxford: Oxford University Press), 415–436.

Frisina, R. D., and Rajan, R. (2005). "Inferior colliculus: aging and plasticity," in *The Inferior Colliculus*, eds J. Winer and C. Schreiner (New York, NY: Springer), 559–584.

Frisina, R. D., and Walton, J. P. (2006). Age-related structural and functional changes in the cochlear nucleus. *Hear. Res.* 217, 216–233.

Frisina, R. D., Walton, J. P., Lynch-Armour, M. A., and Byrd, J. D. (1998). Inputs to a physiologically-characterized region of the inferior colliculus of the young adult CBA mouse. *Hear. Res.* 115, 61–81.

Fuentes-Santamaria, V., Alvarado, J. C., Brunso-Bechtold, J. K., and Henkel, C. K. (2003). Upregulation of calretinin immunostaining in the ferret inferior colliculus after cochlear ablation. *J. Comp. Neurol.* 460, 585–596.

Gates, G. A., and Mills, J. H. (2005). Presbycusis. *Lancet* 366, 1111–1120.

Gerken, G. M. (1996). Central tinnitus and lateral inhibition: an auditory brainstem model. *Hear. Res.* 97, 75–83.

Geyer, M. A., and Braff, D. L. (1987). Startle habituation and sensorimotor gating in schizophrenia and related animal models. *Schizophr. Bull.* 13, 643–668.

Gonchar, Y., and Burkhalter, A. (1997). Three distinct families of GABAergic neurons in rat visual cortex. *Cereb. Cortex* 7, 347–358.

Gonchar, Y., Wang, Q., and Burkhalter, A. (2007). Multiple distinct subtypes of GABAergic neurons in mouse visual cortex identified by triple immunostaining. *Front. Neuroanat.* 1:1–11. doi: 10.3389/neuro.05.003.2007

González-Hernández, T., Mantolan, B., González, B., and Pérez, H. (1996). Sources of GABAergic input to the inferior colliculus of the rat. *J. Comp. Neurol.* 372, 309–326.

Gordon-Salant, S., Fitzgibbons, P. J., and Friedman, S. A. (2007). Recognition of time-compressed and natural speech with selective temporal enhancements by young and elderly listeners. *J. Speech Lang. Hear. Res.* 50, 1181–1193.

Gordon-Salant, S., Frisina, R. D., Popper, A., and Fay, R. R. (2010). *The Aging Auditory System*. New York, NY: Springer-Verlag.

Gutiérrez, A., Khan, Z. U., Morris, S. J., and De Blas, A. L. (1994). Age-related decrease of GABAA receptor subunits and glutamic acid decarboxylase in the rat inferior colliculus. *J. Neurosci.* 14, 7469–7477.

Harker, K. T., and Whishaw, I. Q. (2002). Place and matching-to-place spatial learning affected by rat inbreeding (Dark-Agouti, Fischer 344) and albinism (Wistar, Sprague-Dawley) but not domestication (wild rat vs. Long-Evans, Fischer-Norway). *Behav. Brain Res.* 134, 467–477.

Helfert, R. H., Sommer, T. J., Meeks, J., Hofstetter, P., and Hughes, L. F. (1999). Age-related synaptic changes in the central nucleus of the inferior colliculus of Fischer-344 rats. *J. Comp. Neurol.* 406, 285–298.

Hendrickson, A. E., Tillakaratne, N. J., Mehra, R. D., Esclapez, M., Erickson, A., Vician, L., and Tobin, A. J. (1994). Differential localization of two glutamic acid decarboxylases (GAD65 and GAD67) in adult monkey visual cortex. *J. Comp. Neurol.* 343, 566–581.

Herculano-Houzel, S., and Lent, R. (2005). Isotropic fractionator: a simple, rapid method for the quantification of total cell and neuron numbers in the brain. *J. Neurosci.* 25, 2518–2521.

Hope, B. T., Michael, G. J., Knigge, K. M., and Vincent, S. R. (1991). Neuronal NADPH diaphorase is a nitric oxide synthase. *Proc. Natl. Acad. Sci. U.S.A.* 88, 2811–2814.

Idrizbegovic, E., Bogdanovic, N., Willott, J. F., and Canlon, B. (2004). Age-related increases in calcium-binding protein immunoreactivity

in the cochlear nucleus of hearing impaired C57BL/6J mice. *Neurobiol. Aging* 25, 1085–1093.

Idrizbegovic, E., Canlon, B., Bross, L. S., Willott, J. F., and Bogdanovic, N. (2001). The total number of neurons and calcium binding protein positive neurons during aging in the cochlear nucleus of CBA/CaJ mice: a quantitative study. *Hear. Res.* 158, 102–115.

Ito, T., Bishop, D. C., and Oliver, D. L. (2009). Two classes of GABAergic neurons in the inferior colliculus. *J. Neurosci.* 29, 13860–13869.

Jinno, S., and Kosaka, T. (2002). Patterns of expression of calcium binding proteins and neuronal nitric oxide synthase in different populations of hippocampal GABAergic neurons in mice. *J. Comp. Neurol.* 449, 1–25.

Jones, E. G. (2003). Chemically defined parallel pathways in the monkey auditory system. *Ann. N.Y. Acad. Sci.* 999, 218–233.

Kawaguchi, Y., and Kubota, Y. (1998). Neurochemical features and synaptic connections of large physiologically-identified GABAergic cells in the rat frontal cortex. *Neuroscience* 85, 677–701.

Kelley, P., Frisina, R. D., Zettel, M. L., and Walton, J. P. (1992). Differential calbindin immunoreactivity in the brainstem auditory system of the chinchilla. *J. Comp. Neurol.* 320, 196–212.

Khachaturian, Z. S. (1989). The role of calcium regulation in brain aging: re-examination of a hypothesis. *Aging* 1, 17–34.

Kirkcaldie, M. T., Dickson, T. C., King, C. E., Grasby, D., Riederer, B. M., and Vickers, J. C. (2002). Neurofilament triplet proteins are restricted to a subset of neurons in the rat neocortex. *J. Chem. Neuroanat.* 24, 163–171.

Koch, M. (1999). The neurobiology of startle. *Prog. Neurobiol.* 59, 107–128.

Krishna, B. S., and Semple, M. N. (2000). Auditory temporal processing: responses to sinusoidally amplitude-modulated tones in the inferior colliculus. *J. Neurophysiol.* 84, 255–273.

Kubota, Y., Hattori, R., and Yui, Y. (1994). Three distinct subpopulations of GABA-ergic neurons in rat frontal agranular cortex. *Brain Res.* 649, 159–173.

Kudo, M., and Nakamura, Y. (1988). "Organization of the lateral lemniscal fibers converging onto the inferior colliculus in the cat: an anatomical review," in *Pathway: Structure and Function*, eds J. Syka and R. B. Masterton (New York, NY: Auditory Plenum Press), 171–183.

Kulesza, R. J. Jr., and Berrebi, A. S. (2000). Superior paraolivary nucleus of the rat is a GABAergic nucleus. *J. Assoc. Res. Otolaryngol.* 1, 255–269.

Kulesza, R. J., Viñuela, A., Saldaña, E., and Berrebi, A. S. (2002). Unbiased stereological estimates of neuron number in subcortical auditory nuclei of the rat. *Hear. Res.* 168, 12–24.

Le Beau, F. E., Rees, A., and Malmierca, M. S. (1996). Contribution of GABA- and glycine-mediated inhibition to the monaural temporal response properties of neurons in the inferior colliculus. *J. Neurophysiol.* 75, 902–919.

Leventhal, A. G., Wang, Y., Pu, M., Zhou, Y., and Ma, Y. (2003). GABA and its agonists improved visual cortical function in senescent monkeys. *Science* 300, 812–815.

Ling, L. L., Hughes, L. F., and Caspary, D. M. (2005). Age-related loss of the GABA synthetic enzyme glutamic acid decarboxylase in rat primary auditory cortex. *Neuroscience* 132, 1103–1113.

Litovsky, R. Y., and Delgutte, B. (2002). Neural correlates of the precedence effect in the inferior colliculus: effect of localization cues. *J. Neurophysiol.* 87, 976–994.

Loftus, W. C., Malmierca, M. S., Bishop, D. C., and Oliver, D. L. (2008). The cytoarchitecture of the inferior colliculus revisited: a common organization of the lateral cortex in rat and cat. *Neuroscience* 154, 196–205.

Lohmann, C., and Friauf, E. (1996). Distribution of the calcium-binding proteins parvalbumin and calretinin in the auditory brainstem of adult and developing rats. *J. Comp. Neurol.* 367, 90–109.

Malmierca, M. S., Blackstad, T. W., and Osen, K. K. (2011). Computer-assisted 3-D reconstructions of Golgi-impregnated neurons in the cortical regions of the inferior colliculus of rat. *Hear. Res.* 274, 13–26.

Malmierca, M. S., Blackstad, T. W., Osen, K. K., Karagulle, T., and Molowny, R. L. (1993). The central nucleus of the inferior colliculus in rat: a Golgi and computer reconstruction study of neuronal and laminar structure. *J. Comp. Neurol.* 333, 1–27.

Malmierca, M. S., Hernandez, O., Falconi, A., Lopez-Poveda, E. A., Merchan, M., and Rees, A. (2003). The commissure of the inferior colliculus shapes frequency response areas in rat: an *in vivo* study using reversible blockade with microinjection of kynurenic acid. *Exp. Brain Res.* 153, 522–529.

Malmierca, M. S., Leergaard, T. B., Bajo, V. M., Bjaalie, J. G., and Merchan, M. A. (1998). Anatomic evidence of a three-dimensional mosaic pattern of tonotopic organization in the ventral complex of the lateral lemniscus in cat. *J. Neurosci.* 18, 10603–10618.

Malmierca, M. S., Saint Marie, R. L., Merchan, M. A., and Oliver, D. L. (2005). Laminar inputs from dorsal cochlear nucleus and ventral cochlear nucleus to the central nucleus of the inferior colliculus: two patterns of convergence. *Neuroscience* 136, 883–894.

Malmierca, M. S., Seip, K. L., and Osen, K. K. (1995a). Morphological classification and identification of neurons in the inferior colliculus a multivariate analysis. *Anat. Embryol.* 191, 343–350.

Malmierca, M. S., Rees, A., Le Beau, F. E. N., and Bjaalie, J. G. (1995b). Laminar organization of frequency-defined local axons within and between the inferior colliculi of the guinea pig. *J. Comp. Neurol.* 357, 124–144.

Markram, H., Toledo-Rodriguez, M., Wang, Y., Gupta, A., Silberberg, G., and Wu, C. (2004). Interneurons of the neocortical inhibitory system. *Nat. Rev. Neurosci.* 5, 793–807.

Mattson, M. P. (2007). Calcium and neurodegeneration. *Aging Cell* 6, 337–350.

Mazelová, J., Popelar, J., and Syka, J. (2003). Auditory function in presbycusis: peripheral vs. central changes. *Exp. Gerontol.* 38, 87–94.

Merchán, M., Aguilar, L. A., Lopez-Poveda, E. A., and Malmierca, M. S. (2005). The inferior colliculus of the rat: quantitative immunocytochemical study of GABA and glycine. *Neuroscience* 136, 907–925.

Merrill, D. A., Chiba, A. A., and Tuszynski, M. H. (2001). Conservation of neuronal number and size in the entorhinal cortex of behaviorally characterized aged rats. *J. Comp. Neurol.* 438, 445–456.

Milbrandt, J. C., Albin, R. L., and Caspary, D. M. (1994). Age-related decrease in GABAB receptor binding in the Fischer 344 rat inferior colliculus. *Neurobiol. Aging* 15, 699–703.

Molnár, Z., and Cheung, A. F. (2006). Towards the classification of subpopulations of layer V pyramidal projection neurons. *Neurosci. Res.* 55, 105–115.

Morest, D. K., and Oliver, D. L. (1984). The neuronal architecture of the inferior colliculus of the cat: defining the functional anatomy of the auditory midbrain. *J. Comp. Neurol.* 222, 209–236.

Najdzion, J., Wasilewska, B., Równiak, M., Bogus-Nowakowska, K., Szteyn, S., and Robak, A. (2011). A morphometric comparative study of the medial geniculate body of the rabbit and the fox. *Anat. Histol. Embryol.* 40, 326–334.

Nataraj, K., and Wenstrup, J. J. (2005). Roles of inhibition in creating complex auditory responses in the inferior colliculus: facilitated combination-sensitive neurons. *J. Neurophysiol.* 93, 3294–3312.

Nodal, F. R., and López, D. E. (2003). Direct input from cochlear root neurons to pontine reticulospinal neurons in albino rat. *J. Comp. Neurol.* 460, 80–93.

Ohlemiller, K. K., and Frisina, R. D. (2008). "Clinical characterization of age-related hearing loss and its neural and molecular bases," in *Auditory Trauma, Protection and Treatment*, eds J. Schacht, A. Popper, and R. Fay (New York, NY: Springer-Verlag), 145–194.

Oliver, D. L. (1984). Neuron types in the central nucleus of the inferior colliculus that project to the medial geniculate body. *Neuroscience* 11, 409–424.

Oliver, D. L., and Huerta, M. F. (1992). "Inferior and superior colliculi," in *The Mammalian Auditory System: Neuroanatomy*, eds D. B. Webster, A. N. Popper, and R. R. Fay (New York, NY: Springer-Verlag), 168–221.

Oliver, D. L., Kuwada, S., Yin, T. C., Haberly, L. B., and Henkel, C. K. (1991). Dendritic and axonal morphology of HRP-injected neurons in the inferior colliculus of the cat. *J. Comp. Neurol.* 303, 75–100.

Oliver, D. L., and Morest, D. K. (1984). The central nucleus of the inferior colliculus in the cat. *J. Comp. Neurol.* 222, 237–264.

Oliver, D. L., Winer, J. A., Beckius, G. E., and Saint Marie, R. L. (1994). Morphology of GABAergic neurons in the inferior colliculus of the cat. *J. Comp. Neurol.* 340, 27–42.

Ouda, L., Druga, R., and Syka, J. (2008). Changes in parvalbumin immunoreactivity with aging in the central auditory system of the rat. *Exp. Gerontol.* 43, 782–789.

Ouda, L., Druga, R., and Syka, J. (2012a). Distribution of SMI-32-immunoreactive neurons in the central auditory system of the rat. *Brain Struct. Funct.* 217, 19–36.

Ouda, L., Burianova, J., and Syka, J. (2012b). Age-related changes in calbindin and calretinin

immunoreactivity in the central auditory system of the rat. *Exp. Geront*. 47, 497–506.

Pakkenberg, B., and Gundersen, H. J. (1997). Neocortical neuron number in humans: effect of sex and age. *J. Comp. Neurol.* 384, 312–320.

Palombi, P. S., and Caspary, D. M. (1996). Physiology of the aged Fischer 344 rat inferior colliculus: responses to contralateral monaural stimuli. *J. Neurophysiol.* 76, 3114–3125.

Paxinos, G., and Watson, C. (1998). *The Rat Brain in Stereotaxic Coordinates.* New York, NY: Academic Press.

Pecka, M., Zahn, T. P., Saunier-Rebori, B., Siveke, I., Felmy, F., Wiegrebe, L., Klug, A., Pollak, G. D., and Grothe, B. (2007). Inhibiting the inhibition: a neuronal network for sound localization in reverberant environments. *J. Neurosci.* 27, 1782–1790.

Peruzzi, D., Bartlett, E., Smith, P. H., and Oliver, D. L. (1997). A monosynaptic GABAergic input from the inferior colliculus to the medial geniculate body in rat. *J. Neurosci.* 17, 3766–3777.

Poe, B. H., Linville, C., and Brunso-Bechtold, J. (2001). Age-related decline of presumptive inhibitory synapses in the sensorimotor cortex as revealed by the physical disector. *J. Comp. Neurol.* 406, 285–298.

Pollak, G. D., and Casseday, J. H. (1986). *The Neural Basis of Echolocation in Bats*. New York, NY: Springer-Verlag.

Pollak, G. D., Xie, R., Gittelman, J. X., Andoni, S., and Li, N. (2011). The dominance of inhibition in the inferior colliculus. *Hear. Res.* 274, 27–39.

Popelar, J., Groh, D., Mazelova, J., and Syka, J. (2003). Cochlear function in young and adult Fischer 344 rats. *Hear. Res.* 186, 75–84.

Popelar, J., Groh, D., Pelanova, J., Canlon, B., and Syka, J. (2006). Age-related changes in cochlear and brainstem auditory functions in Fischer 344 rats. *Neurobiol. Aging* 27, 490–500.

Raza, A., Milbrandt, J. C., Arneric, S. P., and Caspary, D. M. (1994). Age-related changes in brainstem auditory neurotransmitters: measures of GABA and acetylcholine function. *Hear. Res.* 77, 221–230.

Résibois, A., and Rogers, J. H. (1992). Calretinin in rat brain: an immunohistochemical study. *Neuroscience* 46, 101–134.

Riascos, D., De Leon, D., Baker-Nigh, A., Nicholas, A., Yukhananov, R., Bu, J., Wu, C. K., and Geula, C. (2011). Age-related loss of calcium buffering and selective neuronal vulnerability in Alzheimer's disease. *Acta Neuropathol.* 122, 565–576.

Riquelme, R., Saldana, E., Osen, K. K., Ottersen, O. P., and Merchan, M. A. (2001). Colocalization of GABA and glycine in the ventral nucleus of the lateral lemniscus in rat: an *in situ* hybridization and semiquantitative immunocytochemical study. *J. Comp. Neurol.* 432, 409–424.

Rybalko, N., Bureš, Z., Burianová, J., Popelář, J., Poon, P. W. F., and Syka, J. (in press). Age-related changes in the acoustic startle reflex in Fischer 344 and Long Evans rats. *Exp. Geront*.

Rybalko, N., Suta, D., Popelár, J., and Syka, J. (2010). Inactivation of the left auditory cortex impairs temporal discrimination in the rat. *Behav. Brain Res.* 209, 123–130.

Saint Marie, R. L., and Baker, R. A. (1990). Neurotransmitter-specific uptake and retrograde transport of [3H]glycine from the inferior colliculus by ipsilateral projections of the superior olivary complex and nuclei of the lateral lemniscus. *Brain Res*. 524, 244–253.

Saint Marie, R. L., Ostapoff, E. M., Morest, D. K., and Wenthold, R. J. (1989). Glycine-immunoreactive projection of the cat lateral superior olive: possible role in midbrain ear dominance. *J. Comp. Neurol.* 279, 382–396.

Saldaña, E., Aparicio, M. A., Fuentes-Santamaría, V., and Berrebi, A. S. (2009). Connections of the superior paraolivary nucleus of the rat: projections to the inferior colliculus. *Neuroscience* 163, 372–387.

Saldana, E., Feliciano, M., and Mugnaini, E. (1996). Distribution of descending projections from primary auditory neocortex to inferior colliculus mimics the topography of intracollicular projections. *J. Comp. Neurol.* 371, 15–40.

Sanchez, J. T., Gans, D., and Wenstrup, J. J. (2007). Contribution of NMDA and AMPA receptors to temporal patterning of auditory responses in the inferior colliculus. *J. Neurosci.* 27, 1954–1963.

Schmidt, S., Redecker, C., Bruehl, C., and Witte, O. W. (2010). Age-related decline of functional inhibition in rat cortex. *Neurobiol. Aging* 31, 504–511.

Schneiderman, A., Oliver, D. L., and Henkel, C. K. (1988). Connections of the dorsal nucleus of the lateral lemniscus: an inhibitory parallel pathway in the ascending auditory system? *J. Comp. Neurol.* 276, 188–208.

Schofield, B. R. (2009). Projections to the inferior colliculus from layer VI cells of auditory cortex. *Neuroscience* 159, 246–258.

Schwaller, B. (2010). Cytosolic Ca2+ buffers. *Cold Spring Harb. Perspect. Biol*. 2, a004051

Schwaller, B., Meyer, M., and Schiffmann, S. (2002). 'New' functions for 'old' proteins: the role of the calcium-binding proteins calbindin D-28k, calretinin and parvalbumin, in cerebellar physiology. Studies with knockout mice. *Cerebellum* 1, 241–258.

Semple, M. N., and Aitkin, L. M. (1980). Physiology of pathway from dorsal cochlear nucleus to inferior colliculus revealed by electrical and auditory stimulation. *Exp. Brain Res*. 41, 19–28.

Sharma, V., Nag, T. C., Wadhwa, S., and Roy, T. S. (2009). Stereological investigation and expression of calcium-binding proteins in developing human inferior colliculus. *J. Chem. Neuroanat.* 37, 78–86.

Sheikh, S. N., Martin, S. B., and Martin, D. L. (1999). Regional distribution and relative amounts of glutamate decarboxylase isoforms in rat and mouse brain. *Neurochem. Int.* 35, 73–80.

Shi, L., Argenta, A. E., Winseck, A. K., and Brunso-Bechtold, J. K. (2004). Stereological quantification of GAD-67-immunoreactive neurons and boutons in the hippocampus of middle-aged and old Fischer 344 x Brown Norway rats. *J. Comp. Neurol.* 478, 282–291.

Shi, L., Pang, H., Linville, M. C., Bartley, A. N., Argenta, A. E., and Brunso-Bechtold, J. K. (2006). Maintenance of inhibitory interneurons and boutons in sensorimotor cortex between middle and old age in Fischer 344 X Brown Norway rats. *J. Chem. Neuroanat.* 32, 46–53.

Simon, H., Frisina, R. D., and Walton, J. P. (2004). Age reduces response latency of mouse inferior colliculus neurons to AM sounds. *J. Acoust. Soc. Am.* 116, 469–477.

Stanley, D. P., and Shetty, A. K. (2004). Aging in the rat hippocampus is associated with widespread reductions in the number of glutamate decarboxylase-67 positive interneurons but not interneuron degeneration. *J. Neurochem.* 89, 204–216.

Sternberger, L. A., and Sternberger, N. H. (1983). Monoclonal antibodies distinguish phosphorylated and nonphosphorylated forms of neurofilaments *in situ*. *Proc. Natl. Acad. Sci. U.S.A.* 80, 6126–6130.

Strouse, A., Ashmead, D. H., Ohde, R. N., and Grantham, D. W. (1998). Temporal processing in the aging auditory system. *J. Acoust. Soc. Am.* 104, 2385–2399.

Suta, D., Kvasnák, E., Popelár, J., and Syka, J. (2003). Representation of species-specific vocalizations in the inferior colliculus of the guinea pig. *J. Neurophysiol.* 90, 3794–3808.

Suta, D., Rybalko, N., Pelánová, J., Popelář, J., and Syka, J. (2011). Age-related changes in auditory temporal processing in the rat. *Exp. Gerontol*. 46, 739–746.

Swerdlow, N. R., Geyer, M. A., and Braff, D. L. (2001). Neural circuit regulation of prepulse inhibition of startle in the rat: current knowledge and future challenges. *Psychopharmacology* 156, 194–215.

Syka, J. (2002). Plastic changes in the central auditory system after hearing loss, restoration of function, and during learning. *Physiol. Rev.* 82, 601–636.

Syka, J. (2010). The Fischer 344 rat as a model of presbycusis. *Hear. Res.* 264, 70–78.

Syka, J., and Radil-Weiss, T. (1971). Electrical stimulation of the tectum in freely moving cats. *Brain Res.* 28, 567–572.

Syka, J., and Straschill, M. (1970). Activation of superior colliculus neurons and motor responses after electrical stimulation of the inferior colliculus. *Exp. Neurol.* 28, 384–392.

Tardif, E., Chiry, O., Probst, A., Magistretti, P. J., and Clarke, S. (2003). Patterns of calcium-binding proteins in human inferior colliculus: identification of subdivisions and evidence for putative parallel systems. *Neuroscience* 116, 1111–1121.

Toescu, E. C., Verkhratsky, A., and Landfield, P. W. (2004). Ca2+ regulation and gene expression in normal brain aging. *Trends Neurosci.* 27, 614–620.

Tokunaga, A., Sugita, S., and Otani, K. (1984). Auditory and non-auditory subcortical afferents to the inferior colliculus in the rat. *J. Hirnforsch.* 25, 461–472.

Tsang, Y. M., Chiong, F., Kuznetsov, D., Kasarskis, E., and Geula, C. (2000). Motor neurons are rich in non-phosphorylated neurofilaments: crossspecies comparison and alterations in ALS. *Brain Res.* 861, 45–58.

Verkhratsky, A., and Toescu, E. C. (1998). Calcium and neuronal ageing. *Trends Neurosci.* 21, 2–7.

Voelker, C. C., Garin, N., Taylor, J. S., Gähwiler, B. H., Hornung, J. P., and Molnár, Z. (2004). Selective neurofilament (SMI-32, FNP-7 and N200) expression in subpopulations of layer V pyramidal neurons *in vivo* and *in vitro*. *Cereb. Cortex* 14, 1276–1286.

Walton, J. P. (2010). Timing is everything: temporal processing deficits in the aged auditory brainstem. *Hear. Res.* 264, 63–69.

Walton, J. P., Barsz, K., and Wilson, W. W. (2008). Sensorineural hearing loss and neural correlates of temporal acuity in the inferior colliculus of the C57Bl/6 mouse. *J. Assoc. Res. Otolaryngol.* 9, 12–22.

Walton, J. P., Frisina, R. D., and O'Neill, W. E. (1998). Age-related alteration in processing of temporal sound features in the auditory midbrain of the CBA mouse. *J. Neurosci.* 18, 2764–2776.

Walton, J. P., Frisina, R. D., Ison, J. E., and O'Neill, W. E. (1997). Neural correlates of behavioral gap detection in the inferior colliculus of the young CBA mouse. *J. Comp. Physiol. A* 181, 161–176.

Walton, J. P., Simon, H., and Frisina, R. D. (2002). Age-related alterations in the neural coding of envelope periodicities. *J. Neurophysiol.* 88, 565–578.

Winer, J. A., and Larue, D. T. (1996). Evolution of GABAergic circuitry in the mammalian medial geniculate body. *Proc. Natl. Acad. Sci. U.S.A.* 93, 3083–3087.

Winer, J. A., Larue, D. T., and Pollak, G. D. (1995). GABA and glycine in the central auditory system of the mustache bat: structural substrates for inhibitory neural organization. *J. Comp. Neurol.* 352, 1–37.

Winer, J. A., Larue, D. T., Diehl, J. J., and Hefti, B. J. (1998). Auditory cortical projections to the cat inferior colliculus. *J. Comp. Neurol.* 400, 147–174.

Woo, N. H., and Lu, B. (2006). Regulation of cortical interneurons by neurotrophins: from development to cognitive disorders. *Neuroscientist* 12, 43–56.

Wu, M. D., Kimura, M., Hiromichi, I., and Helfert, R. H. (2008). A classification of NOergic neurons in the inferior colliculus of rat according to co-existence with classical amino acid transmitters. *Okajimas Folia Anat. Jpn.* 85, 17–27.

Zettel, M. L., Frisina, R. D., Haider, S. E., and O'Neill, W. E. (1997). Age-related changes in calbindin D-28k and calretinin immunoreactivity in the inferior colliculus of CBA/CaJ and C57Bl/6 mice. *J. Comp. Neurol.* 386, 92–110.

Zettel, M. L., O'Neill, W. E., Trang, T. T., and Frisina, R. D. (2001). Early bilateral deafening prevents calretinin up-regulation in the dorsal cortex of the inferior colliculus of aged CBA/CaJ mice. *Hear. Res.* 158, 131–138.

Zhang, D. X., Li, L., Kelly, J. B., and Wu, S. H. (1998). GABAergic projections from the lateral lemniscus to the inferior colliculus of the rat. *Hear. Res.* 117, 1–12.

Zhou, J., and Shore, S. (2006). Convergence of spinal trigeminal and cochlear nucleus projections in the inferior colliculus of the guinea pig. *J. Comp. Neurol.* 495, 100–112.

Conflict of Interest Statement: The authors declare that the research was conducted in the absence of any commercial or financial relationships that could be construed as a potential conflict of interest.

Received: 18 June 2012; accepted: 04 September 2012; published online: 21 September 2012.

Citation: Ouda L and Syka J (2012) Immunocytochemical profiles of inferior colliculus neurons in the rat and their changes with aging. Front. Neural Circuits ***6****:68. doi: 10.3389/fncir.2012.00068*

frontiers in
NEURAL CIRCUITS

ORIGINAL RESEARCH ARTICLE
published: 26 November 2012
doi: 10.3389/fncir.2012.00086

Cortical auditory deafferentation induces long-term plasticity in the inferior colliculus of adult rats: microarray and qPCR analysis

Cheryl Clarkson, M. Javier Herrero-Turrión and Miguel A. Merchán*

Instituto de Neurociencias de Castilla y León, Universidad de Salamanca, Salamanca, Spain

Edited by:
Eric D. Young, Johns Hopkins University, USA

Reviewed by:
Avril Genene Holt, Wayne State University, USA
Richard Altschuler, University of Michigan, USA

****Correspondence:***
Miguel A. Merchán, Laboratorio de Neurobiología de la Audición, Facultad de Medicina, Departamento de Biología Celular y Patología, Instituto de Neurociencias de Castilla y León, Universidad de Salamanca, C/Pintor Fernando Gallego, 1, Salamanca 37007, Spain.
e-mail: merchan@usal.es

The cortico-collicular pathway is a bilateral excitatory projection from the cortex to the inferior colliculus (IC). It is asymmetric and predominantly ipsilateral. Using microarrays and RT-qPCR we analyzed changes in gene expression in the IC after unilateral lesions of the auditory cortex, comparing the ICs ipsi- and contralateral to the lesioned side. At 15 days after surgery there were mainly changes in gene expression in the IC ipsilateral to the lesion. Regulation primarily involved inflammatory cascade genes, suggesting a direct effect of degeneration rather than a neuronal plastic reorganization. Ninety days after the cortical lesion the ipsilateral IC showed a significant up-regulation of genes involved in apoptosis and axonal regeneration combined with a down-regulation of genes involved in neurotransmission, synaptic growth, and gap junction assembly. In contrast, the contralateral IC at 90 days post-lesion showed an up-regulation in genes primarily related to neurotransmission, cell proliferation, and synaptic growth. There was also a down-regulation in autophagy and neuroprotection genes. These findings suggest that the reorganization in the IC after descending pathway deafferentation is a long-term process involving extensive changes in gene expression regulation. Regulated genes are involved in many different neuronal functions, and the number and gene rearrangement profile seems to depend on the density of loss of the auditory cortical inputs.

Keywords: brain injury, gene expression profiling, corticofugal projection, long-term post-lesion, adult lesion plasticity

INTRODUCTION

The inferior colliculus (IC) is an obligatory relay station for almost all ascending and descending auditory projections and it is a key nucleus for excitatory and inhibitory auditory input convergence (Malmierca and Merchán, 2004). The descending cortico-collicular projection acts as a filter for neuronal responses (Sun et al., 2007). It participates in a positive feedback loop which, in combination with lateral inhibition, sharpens, and adjusts the tuning of neurons in the auditory pathway (Zhang et al., 1997; Jen and Zhang, 1999). The descending auditory corticofugal projection is glutamatergic and therefore excitatory (Feliciano and Potashner, 1995). It is bilateral, but is denser on the ipsilateral side (Saldana et al., 1996; Bajo et al., 2007). Corticofugal deactivation results in unbalanced excitatory/inhibitory IC afferent projections, which induce alterations in the amplitude and latencies of IC neuronal responses (Nwabueze-Ogbo et al., 2002; Popelar et al., 2003), indicating that this projection affects directly the activity of IC neurons.

The developmental auditory system exhibits great ability for network reorganization induced by sensory deprivation (Kandler, 2004; Keuroghlian and Knudsen, 2007). In adults, this capability to induce plastic changes is reduced but still present. In the auditory pathway, plastic changes in the adult have been tested using acoustic stimulation (Norena and Eggermont, 2006), training-behavioral methods (Edeline and Weinberger, 1991a,b, 1992; Gao and Suga, 1998, 2000; Ma and Suga, 2005; Rutkowski and Weinberger, 2005), adaptation after sensory deafferentation (Holt et al., 2005, 2006; Illing et al., 2005; Illing and Reisch, 2006; Rubio, 2006), and auditory cortex lesion (Druga and Syka, 2001; Bowen et al., 2003; Rybalko et al., 2006; Clarkson et al., 2010a,b,c).

In the IC partial deafferentation of the ascending auditory pathway reduced sound-evoked inhibitory collicular responses (Semple and Kitzes, 1985; Bledsoe et al., 1995; McAlpine et al., 1997; Vale and Sanes, 2002). Whole cell patch recordings in brain slices showed that bilateral deafness induced a decrease in lateral lemniscus neurotransmitter release and synaptic strength variations in both excitatory and inhibitory IC synapses (Vale and Sanes, 2002). It is known that changes in the balance of excitation and inhibition trigger synaptic plasticity, adapting biophysical membrane properties (synaptic strength and axon conductance properties) or modifying the synthesis and trafficking of receptors (Perez-Otano and Ehlers, 2005; Turrigiano, 2012). Holt et al. (2005) suggested unbalanced excitation and inhibition as a basis for long-term (90 days) changes in adult IC gene expression after inactivation of the ascending auditory pathway by bilateral cochleotomy. Ascending lemniscal connections to the IC include both excitatory and inhibitory fibers (Riquelme et al., 2001). Therefore ascending deafferentation included a loss of both excitatory and inhibitory inputs. However, the descending pathway is solely excitatory, and its absence should lead to a strong

unbalance of excitation and inhibition with consequences in gene expression, which are currently unknown.

We have previously used an auditory cortical ablation model in adult rats to analyze long-term plastic changes in the IC (Clarkson et al., 2010a,b,c). We demonstrated that restricted cortical ablation in acoustically stimulated animals strongly decreased c-Fos immunoreactivity in IC neurons at 15 days post-lesion, with a significant recovery taking place after 90 days (Clarkson et al., 2010a). It is well known that c-Fos immunoreactivity is an anatomical marker of neuronal activity (Bullitt, 1995), and that its alteration may be related to changes in neuronal transcription (Kovacs, 2008). Based on our c-Fos results (Clarkson et al., 2010a), we suggest that time-dependent activation of IC neurons after long-term cortical deprivation may be a consequence of the reorganization of auditory pathway projections. In the Central Nervous System, mechanisms of neural plasticity underlying long-term network reorganization such as collateral sprouting and pruning, cell death, neurotransmitter regulation, or glial functional differences, are reflected in changes in levels of gene expression (Wieloch and Nikolich, 2006). To gain insights into long-term plastic changes after descending IC deafferentation, we have used in our auditory cortex ablation animal model (Clarkson et al., 2010a,b,c) a Gene Chip Microarray technology, validated by quantitative reverse transcription real-time PCR (RT-qPCR).

MATERIALS AND METHODS

EXPERIMENTAL ANIMALS

All experiments were performed according to national (R.D. 1201/2005) and EU regulations (DOCE L 222; 24-08-1999) for use and care of animals in research. Nine male rats (Wistar albino, Charles River Laboratories) weighing 230 g and 12 weeks of age at the beginning of experiments were used. Animals were free of ear infection and for a quick assessment of normal hearing we used in all cases bilateral finger friction test. For DNA microarrays analysis we used both IC (ipsilateral and contralateral) from three animals in each group (naïve control, 15 days post-lesion and 90 days post-lesion). For RT-qPCR three replicates from control and 90 days post-lesion group (both ICs) were randomly selected and run in triplicate twice for each gene product (25 genes).

SURGERY AND AUDITORY CORTEX LESION LOCALIZATION

Animals were anesthetized with ketamine chlorhydrate (30 mg/Kg, Imalgene® 1000, Rhone Méreuse, Lyon, France) and xylazine chlorhydrate (5 mg/Kg Rompun®, Bayer, Leverkusen, Germany). Unilateral ablation by aspiration of the left auditory cortices (primary – Au1, dorsal – AuD, and ventral – AuV areas), including cortical layers V and VI, was carried out under stereotaxic control using a stereotaxic frame (David Kopf Ins., Tujinga, CA, USA) following a procedure described in detail elsewhere (Clarkson et al., 2010b).

Following the appropriate number of days post-lesion, ablated, and naïve control animals were deeply anesthetized with sodium pentobarbital (60 mg/kg) and decapitated. After quickly exposing the brain stem, both ICs were removed and the brain was stored overnight in a solution of 4% paraformaldehyde in phosphate buffer (PB) 0.1 M, pH 7.4. Finally, the brains were cryoprotected in 30% sucrose in 0.1% PB and serially sectioned at 40 μm to quantify the percentage of auditory cortices affected by ablation (Clarkson et al., 2010a,b).

RNA ISOLATION

Collected ICs were homogenized and total RNA was purified using TRIZOL® (Gibco BRL, Gaithersburg, MD, USA). RNA quality was assessed and quantitated by Agilent 2100 Bioanalyzer software (Agilent Technologies, Palo Alto, CA, USA) associated with a RNA 6000 Nano kit. A RNA integrity number (RIN) >8.0 were found in all samples. In addition, further RNA purification using an RNeasy Mini Kit for RNA clean-up (Qiagen Sciences, Maryland, USA) was performed.

MICROARRAY, DATA, AND ONTOLOGICAL ANALYSIS

Microarray analyses were performed at the Cancer Research Center (Centro de Investigacion del Cancer – CIC) at the University of Salamanca (Spain). Labeling and hybridizations were performed according to Affymetrix protocols. One hundred to three hundred nanograms of total RNA were amplified and labeled using the WT Sense Target labeling and control reagents kit (Affymetrix Inc., Santa Clara, CA, USA), and hybridized to Rat Gene 1.0 ST Array (Affymetrix). Washes and scans were performed using GeneChip System of Affymetrix (GeneChip Hybridization Oven 640, GeneChip Fluidics Station 450, and GeneChip Scanner 7G).

Following image analysis, microarray data were imported into GeneSpring GX 7.3 (Agilent Technologies). RMA (Robust Multi-array Analysis), a method for normalizing and summarizing probe-level intensity measurements, was used. For this analysis, all genes that did not change between samples were excluded. We compared the experimental samples with naïve controls; all our samples passed a high data quality control, showing a high homogeneity intra-group (Datasheet 1 in Supplementary Material). Potential differential expression was determined with a one-way analysis of variance ANOVA (variances not assumed to be equal) and subsequently an unpaired t-test, $p < 0.05$, filtered for 1.5-fold was made in order to search differences in the gene expression (control samples were used as basal levels). Further processing including functional analysis and overrepresentation calculations based on Gene Ontology (GO) Annotation Tool and publication data from Database for Annotation, Visualization, and Integrated Discovery were made with GeneSpring GX 7.3 and Database for Annotation, Visualization, and Integrated Discovery (DAVID) Bioinformatics Resources 6.7 (http://david.abcc.ncifcrf.gov/; Dennis et al., 2003; Huang et al., 2009).

Only genes with a Fold Change (FC) >1.5 (up or down), were considered for analysis (Datasheet 1 in Supplementary Material). From this group of genes we centered our attention in categories reported altered in the IC after auditory cortical lesion or are related directly to post-lesional plasticity (genes shown in **Figures 2–4**).

QUANTITATIVE REVERSE TRANSCRIPTION REAL-TIME PCR

Total RNA (2 μg), primed with oligo-dT, was reverse-transcribed into cDNA at 37°C for 2 h using the first-strand cDNA synthesis kit (Promega Corporation, Madison, WI, USA). In all cases, a reverse transcriptase negative control was used for testing genomic DNA contamination. RT-qPCR was carried out on a real-time detection instrument (ABI Prism 7300 system) in 96-well optical plates

using TaqMan Universal PCR Master Mix and Assay on Demand primers and probes. Probe sets used are listed in Datasheet 2 in Supplementary Material. Reaction components included: 2X TaqMan Universal Master Mix with UNG, 450 nM unlabeled PCR primers, 125 nM FAM dye-labeled TaqMan MGB probe, and 1 μL cDNA reaction product in a 10 μL total reaction volume. PCR conditions were as follows: 2 min at 50°C, 10 min at 95°C and 40 cycles of 15 s at 95°C and 1 min at 60°C. Relative quantities were calculated using the $2^{-\Delta\Delta Ct}$ analysis method (Schmittgen and Livak, 2008) with *GAPDH* (*Glyceraldehyde-3-phosphate dehydrogenase*: Rn99999916_s1) as the endogenous control. $2^{-\Delta\Delta Ct}$ values were analyzed using One-way analysis of variance (ANOVA; $p < 0.05$) with a *post hoc* Student Newman-Keuls test ($p < 0.05$) was performed for statistical analysis.

RESULTS

We analyzed differences in gene expression profiling in the IC in the short (15 days) and long-term range (90 days) after unilateral auditory cortex ablation. In addition, as this is an anatomically asymmetric projection in terms of innervation density, we also studied the differences in gene expression between the ipsi- and contralateral IC at each time post-lesion. Comparisons between control and deafferented groups showed gene products corresponding to a total of 24,070 probes (of the 27,342 total probes on the arrays) which were confidently detected based on signal intensity at a fixed value above background level (See Material and Methods, Robust Multi-array Analysis, RMA).

To enhance biological interpretation of the differentially expressed genes we performed function enrichment analysis for these genes using the functional classification tool "DAVID Bioinformatics." Our results indicated that, although there were many over-represented biological function group of genes as shown in Datasheet 3 in Supplementary Material, the majority of them were related to a few functional categories. In our study the most relevant categories included genes related to neurotransmission and signal propagation such as receptors for glutamate, glycine, acetylcholine, or serotonin. This classification also involves enzymes and neurotransmitter transporters (glutamate, γ-aminobutyric acid (GABA), and glycine) and different types of channels (chloride, potassium, sodium, and calcium). Other functional categories notably detected include genes encoding proteins implicated in neural/synaptic plasticity, axonal growth/degeneration, myelin organization, and regulation, sprouting, neuroprotection, immune response, regulation of apoptosis, autophagy, and cell proliferation, migration, and differentiation.

All unilateral ablations were restricted in depth to the cortical gray matter (including layer 6) and their extension mainly affected the primary and secondary auditory cortices with an average of 69.74 + 4.7% for 15 days post-lesion group and 74.19 + 9.4% in the group 90 days post ablation (**Figure 1**).

CONTROL VS. 15 DAYS POST-LESION IN THE IPSILATERAL IC AND CONTROL VS. 15 DAYS POST-LESION IN THE CONTRALATERAL IC

Microarray comparisons between control and lesioned cases after 15 days showed that the genomic profile in the IC ipsilateral to the side of the lesion was slightly affected with 19 genes significantly up-regulated (FC > 1.5 and $p < 0.05$) and 14 genes significantly down-regulated (**Figure 2A** and Datasheet 1 in Supplementary Material). The IC contralateral to the side of the lesion also followed a similar trend with 16 genes up-regulated and three down-regulated (**Figure 2B** and Datasheet 1 in Supplementary Material).

After examining the potential function for each significantly affected gene per lesioned side we found that after 15 days post-lesion, the ipsilateral IC which had lost a denser cortical projection had a major up-regulation in several genes involved in inflammatory pathways (*Serglycin*, *Srgn; Podocalyxin*, *Podx; Complement Component 3*, *C3; and Claudin 5*, *Cldn5*) and stem cell regeneration (*Prominin 1*, *Prom1*). On the other hand, one gene directly related with neuroprotection (*Latexin*, *Lxn*) was clearly down-regulated (**Figure 2C**). Furthermore, the contralateral IC that had lost a weaker projection showed an up-regulation in genes involved in inflammation processes (*NADH dehydrogenase subunit 6* | *Cytochrome c oxidase subunit 3, Nd6*|*Cox3)* and synaptic growth (*Spinster*, *Spns*; **Figure 2D**).

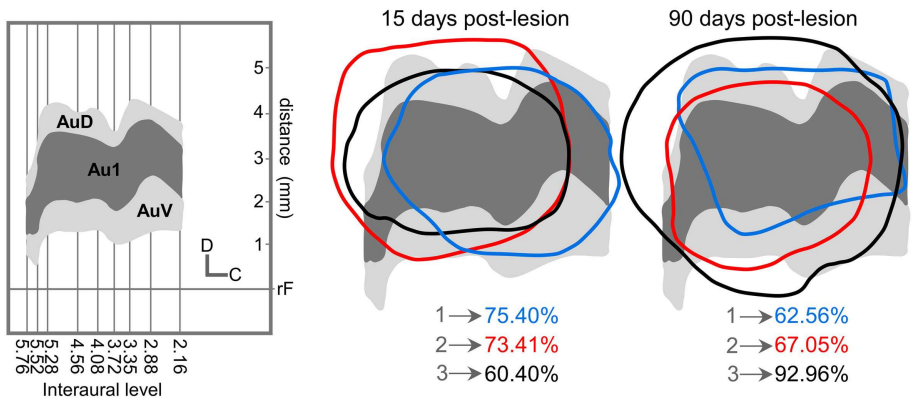

FIGURE 1 | Location and percentage of auditory cortical lesion for all cases used after 15 and 90 days post-lesion. On the left, the diagram shows the representation in our cases of primary and secondary auditory cortices (Clarkson et al., 2010a) for all interaural levels drawn by Paxinos and Watson (2005). We used like reference for the coordinates of the vertical axis the distance in mm from rhinal fissure. Right side, superimposition of each lesion contours over auditory cortex diagram. AuC, Primary auditory cortex; AuV, Ventral auditory cortex; AuD, Dorsal auditory cortex.

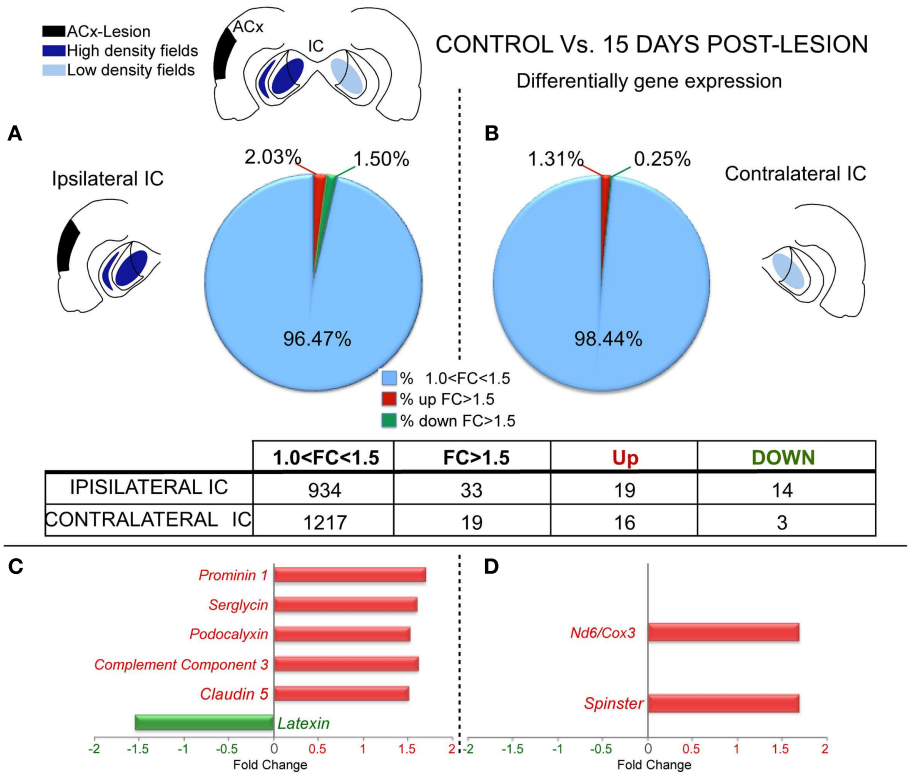

	1.0<FC<1.5	FC>1.5	Up	DOWN
IPISILATERAL IC	934	33	19	14
CONTRALATERAL IC	1217	19	16	3

FIGURE 2 | Differential gene expression between control and lesioned cases in the inferior colliculus 15 days after ablation of the auditory cortex. The insets show in black the unilateral auditory cortical lesion area and in blue the location of cortical projection fields in both IC. Notice that dark blue means a higher density of terminals and light blue a weaker cortical projection density. **(A,B)** Number of regulated genes in the IC ipsilateral **(A)** and contralateral **(B)** to the cortical lesion. The blue sector indicates the genes whose change was 1 < FC < 1.5. The red (up-regulation) and green (down-regulation) sectors indicate the percentage of genes whose change was greater than 1.5-fold. Notice for both ICs a predominant up-regulation in comparison to down-regulation of gene expression. **(C,D):** Bar graph showing functional analysis of the most representative genes for comparison between controls group and IC ipsilateral **(C)** and contralateral **(D)** IC to the cortical lesion. No changes *: Number of genes without significantly expression changes. Acx-Lesion, Auditory cortex lesion; IC, Inferior colliculus; *ND6/COX3, NADH dehydrogenase subunit 6 | cytochrome c oxidase subunit 3.*

CONTROL VS. 90 DAYS POST-LESION IN THE IPSILATERAL IC AND CONTROL VS. 90 DAYS POST-LESION IN THE CONTRALATERAL IC

The analysis of gene expression after 90 days post-lesion, on both the ipsi- and contralateral sides, showed greater changes compared to control than did the 15-days group. The ipsilateral side (90 days) displayed up-regulation of 322 genes and down-regulation in 108 genes (**Figure 3A** and Datasheet 1 in Supplementary Material). In the contralateral IC, 146 genes were up-regulated and 64 genes were down-regulated (**Figure 3B** and Datasheet 1 in Supplementary Material).

In particular, after 90 days post-lesion, gene function analysis showed that the ipsilateral IC had significant adjustments in genes involved in neurotransmission and signal propagation. Specifically, five were clearly down-regulated: *Calcium channel – voltage-dependent – γ3, Cacng3; Potassium inwardly rectifying channel, subfamily J, member 16, Kcnj16; Adducin 1 (alpha), Add1; Claudin 11, Cldn11; and Calsyntenin 3, Clstn3,* and one was up-regulated (*Sodium channel and clathrin linker 1, Sclt1*; **Figure 3C**). We also found up-regulation in the expression of genes potentially involved in apoptotic processes (*Programmed cell death 10, Pdcd10; Growth arrest-specific 2, Gas2; Fission 1, Fis1; and Cytochrome c oxidase subunit VIIb, Cox7b*) and down-regulation in an anti-apoptotic gene (*Gelsolin, Gsn*). At the same time, *the NADH dehydrogenase, subunit 6 |cytochrome c oxidase III (Nd6|Cox3)* gene involved in inflammatory response also showed up-regulation at this time post-lesion. Additionally, genes involved in synaptic growth, such as *Myelin-associated glycoprotein (Mag) and Cadherin 13 (Cdh13)*, also displayed down-regulated expression, accompanied by up-regulation in one gene related to axonal degeneration (*Calpain 7, Capn7*). Furthermore, *Gap junction proteins α1 and β6 (Gja1 and Gjb6)*, also named *Connexin 43* and *30, respectively*, showed down-regulation in gene expression. Finally, relevant genes for calcium regulation like (*Nucleobindin 1, Nucb1*) and calcium sensors like *Synaptotagmin XI (Syt11)* were down-regulated (**Figure 3C**).

Ninety days after the cortical lesion, the contralateral IC exhibited larger changes in the expression of genes related with neurotransmission than at 15 days, showing an up-regulation in *Dopamine receptor D1 interacting protein gene (Drd1ip, also named Calcyon); Synaptogyrin 3 (Syngr3); Synaptic vesicle related protein (SV2); Opioid receptor-like 1 (Oprl1); Potassium voltage*

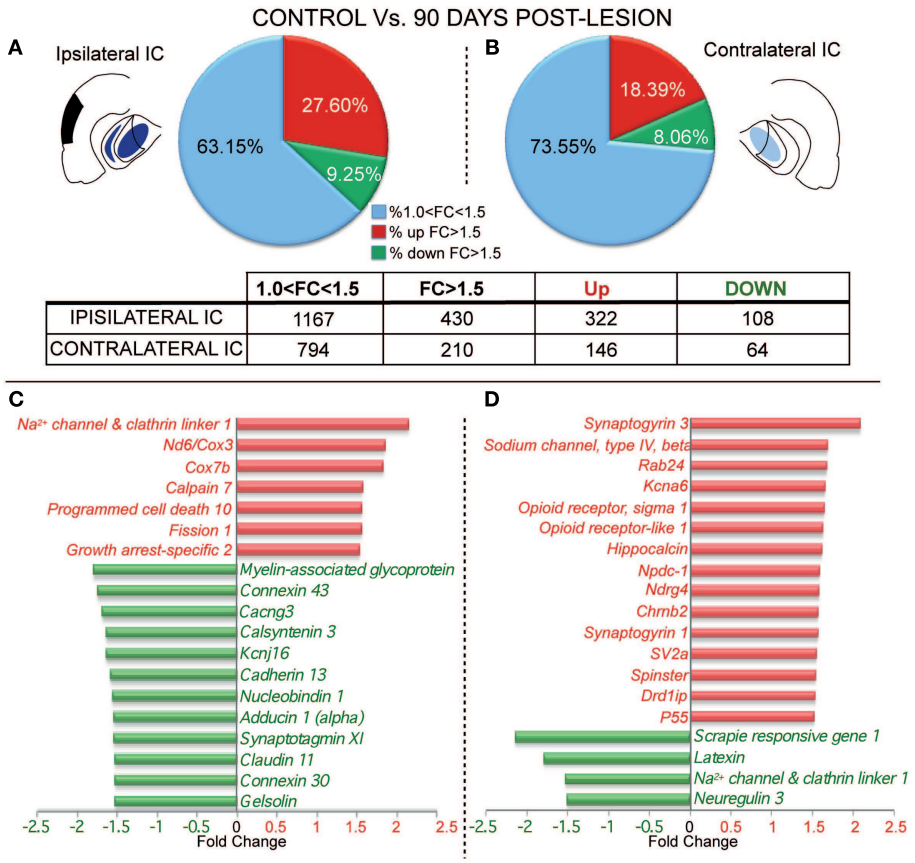

	1.0<FC<1.5	FC>1.5	Up	DOWN
IPISILATERAL IC	1167	430	322	108
CONTRALATERAL IC	794	210	146	64

FIGURE 3 | Differential gene expression between control and lesioned animals in the inferior colliculus 90 days after ablation of the auditory cortex. The insets show in black the unilateral auditory cortical lesion area and in blue the location of cortical projection fields in both IC. Notice that dark blue means a higher density of terminals and light blue a weaker cortical projection density. **(A,B)** Number of regulated genes in the IC ipsilateral **(A)** and contralateral **(B)** to the cortical lesion. The blue sector indicates the genes whose change was $1 < FC < 1.5$. The red (up-regulation) and green (down-regulation) sectors indicate the percentage of genes whose change was greater than 1.5-fold. Bar graph shows functional analysis of the most representative genes for comparison between control group and ipsilateral **(C)** and contralateral IC **(D)** to the cortical lesion. ATPase-6, CO-III, NADH dehydrogenase subunit 6 | cytochrome c oxidase subunit 3; COX subunit VIIb, Cytochrome c oxidase subunit VIIb; KCNJ16, Potassium inwardly rectifying channel, subfamily J, member 16; RAB24, RAB24, member RAS oncogene family; Kcna6, potassium voltage gated channel, shaker related subfamily, member 6; NPDC1, neural proliferation, differentiation and control, 1; Nrdg4, N-myc downstream regulated gene 4; SV2a, synaptic vesicle glycoprotein 2a; Drd1ip, dopamine receptor D1 interacting protein.

gated channel, shaker related subfamily, member 6 (*Kcna6*), *and Sodium channel, type IV, beta* gene (*Scn4b*; **Figure 3D**). Furthermore, *Neuregulin 3* (*Nrg3*) and *Sodium channel and clathrin linker 1 (Sclt1)* genes involved in neurotransmission were down-regulated. Interestingly, we found up-regulation in genes related to neural plasticity like *Opioid receptor, sigma 1* (*Oprs1*); *Hippocalcin* (*Hpca*); *P55; Synaptogyrin* family *(Syngr1 and 3)*, and also in genes that regulate synaptic growth, like *Spinster*, and cell proliferation, such as *N-myc downstream regulated gene 4*, (*Ndrg4*), and *Neural proliferation, differentiation and control, 1* (*Npdc1*; **Figure 3D**). In contrast, we found at this time/side down-regulation in *Latexin*, which is involved in neuroprotection. Mixes of genes related with autophagy were also affected, with an up-regulation in *RAB24, member RAS oncogene family* and a down-regulation in *Scrapie responsive gene 1* (*Scrg1*; **Figure 3D**).

IPSI- VS. CONTRALATERAL CHANGES AT 15 AND 90 DAYS POST-LESION

Unbalanced cortical inputs to the IC induced by unilateral cortical ablation seem to induce complex gene regulation patterns which are better appreciated by comparing the IC ipsi – and contralateral to the ablation side. In naïve control group, we did a comparison between ipsilateral and contralateral IC profiling and no significant FC in gene expression were found. Moreover, both ICs ipsi- and contralateral to the cortical lesion showed quantitatively slight alterations in gene expression after short-term post-lesion (15 days), with changes in 14 genes (Datasheet 2 in Supplementary Material). Of these genes, two have a known function as mediators of inflammatory processes and exhibit a down-regulation in the contralateral IC.

At long-term post-lesion (90 days), a much larger adjustment in gene expression was found, with 1659 probes significantly altered, i.e., 802 genes up-regulated and 857 genes down-regulated

(**Figure 4A** and Datasheet 1 in Supplementary Material). Analysis of genes function showed changes in 54 genes related with neurotransmission. These changes covered a wide range of neurotransmission processes, with up-regulation of glutamate receptor genes (*Glutamate receptor, ionotropic, N-methyl* D*-aspartate; Grin1, or Nmdar1*), glycine receptor (*Glycine receptor alpha 1*, *Glra1*), acetylcholine receptor subunits (*Cholinergic receptor, nicotinic, beta polypeptide 2; Chrnb2*), a serotonin receptor subunit (*5-hydroxytryptaine-serotonin receptor 1A, Htr1a*) and other receptor-like *Oprs1*. We also found up-regulation in five neurotransmitter synthesis enzyme genes [for glutamate: *Glutaminyl-tRNA synthetase* (*Qars*); for GABA: *Glutamic acid decarboxylase 1* (*Gad1*) and *4-aminobutyrate aminotransferase* (*Abat*); for glycine: *Glycyl-tRNA synthetase* (*Gars*); and for endocannabinoid mobilization through metabotropic glutamate receptors (mGluRs): *Dyacylglycerol lipase alpha* (*Dagla*)]. The neurotransmitter transporters also were affected. Two glutamate transporters genes were up-regulated *Solute carrier family 17 (sodium-dependent inorganic phosphate cotransporter) member 6, Slc17a6,* or also named *Vesicular glutamate transporter 2* (*VGlut2*); and *Solute carrier family 1 (Glial high affinity glutamate transporter) member 3, Slc1a3* or GLAST. Two GABA transporters (*Solute carrier family 6 – member 11 and family*

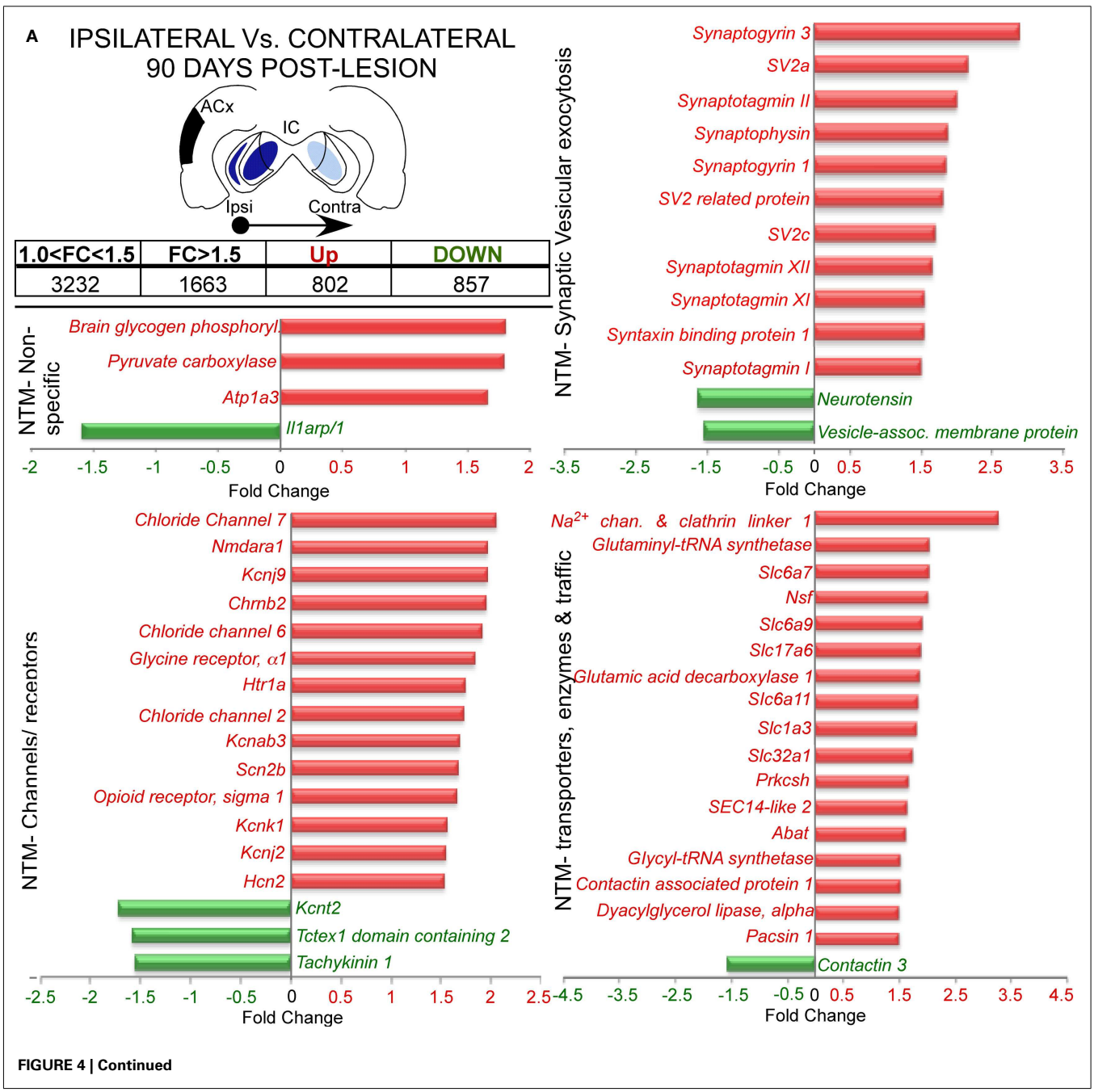

FIGURE 4 | Continued

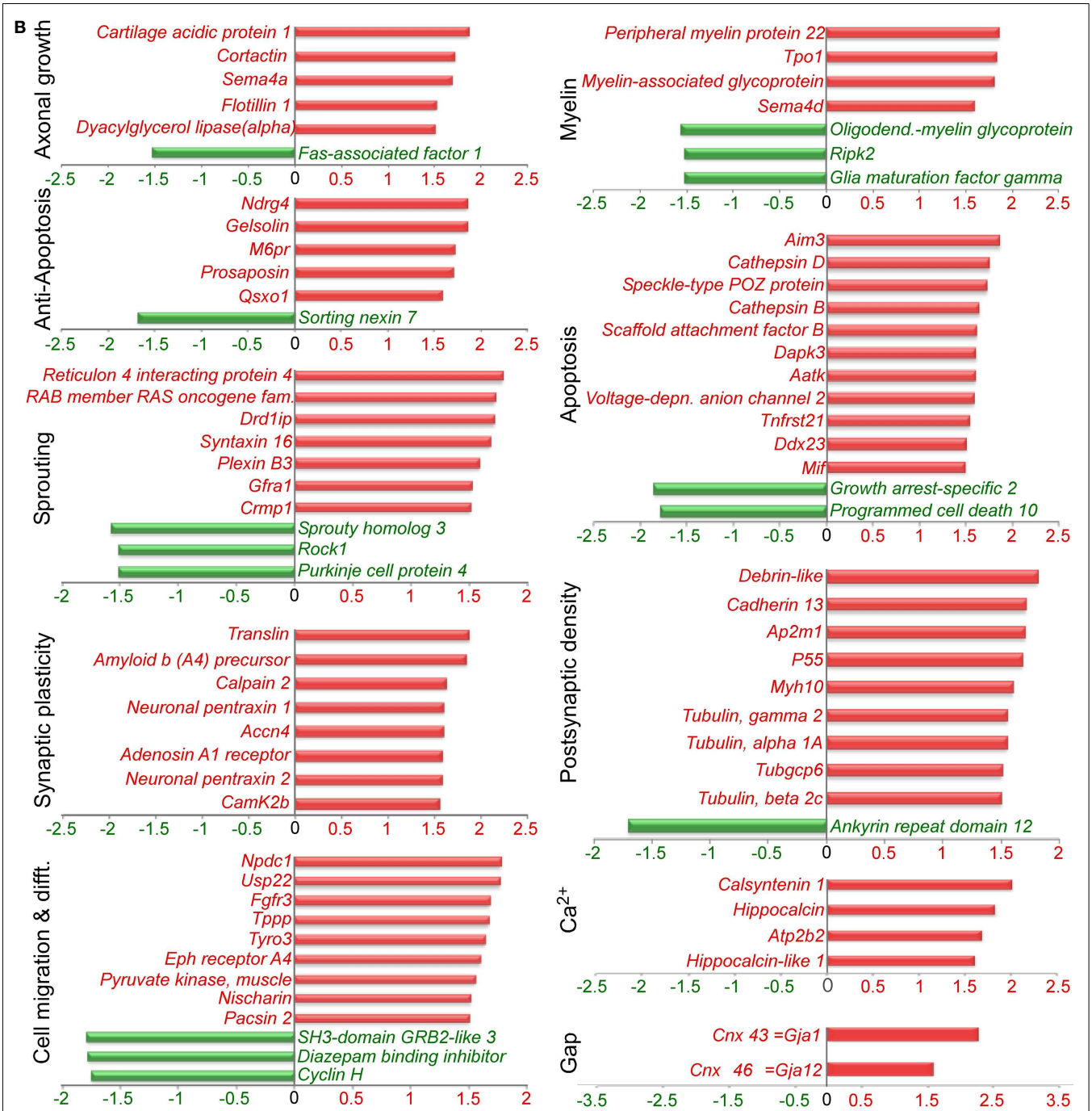

FIGURE 4 | Several of the most representative differentially expressed genes in the comparison between 90 days post-lesion in the ipsilateral IC vs. 90 days post-lesion in the contralateral IC. The inset shows in black the unilateral auditory cortical lesion area and in blues the location of cortical projection fields in both inferior colliculus. Notice that dark blue means a higher density of terminals and light blue a weaker cortical projection density. Graph bar showing functional analysis of the most representative genes in each functional category. **(A)** Neurotransmission (NTS). **(B)** Axonal growth, anti-apoptosis, sprouting, synaptic plasticity, cell migration and differentiation, myelin, apoptosis, postsynaptic density, Ca^{2+} and Gap junctions.

32 – member 1, *Slc6a11*, and *Slc32a1*, respectively), one glycine transporter [*Solute carrier family 6 member 9*, *Slc6a9*] and one proline transporter [*Solute carrier family 6 member 7*, *Slc6a7*] were also up-regulated. Up-regulation affected genes related with receptor trafficking as well, such as those for α-amino-3-hydroxy-5-methyl-4-isoxazolepropionic acid (AMPA) receptors: *N-ethylmaleimide sensitive fusion protein* (*Nsf*) and *Contactin associated protein 1* (*Cntnap1*). Also for acetylcholine receptors: *SEC14-like 2* and for

sodium channel internalization with *Sodium channel and clathrin linker 1 (SLCT1)*. Moreover, the *Contactin 1* (*Cntn1*) gene that regulates traffic and synaptic content of AMPA receptors showed down-regulation after 90 days post-lesion (**Figure 4A**).

In addition, voltage-operated and other non-ligand gated ion channel genes were also up-regulated. These included three *chloride channel* genes (*Clcn2*, *6*, *and 7*), five potassium channels [K^+ *inwardly rectifying channel subfamily J – members 2 and 9* (*Kcnj2 and 9*); K^+ *voltage gated channel shaker related subfamily* β*3* (*Kcnab3*); K^+ *channel subfamily K – member 1* (*Kcnk1*); and *Hyperpolarization activated cyclic nucleotide-gated* K^+ *channel 2* (*Hcn2*)] and a sodium channel [*sodium channel voltage-gate, type II*β (*Scn2b*)]. Additionally, a channel for potassium [K^+ *channel subfamily T – member 2* (*Kcnt2*)], another for calcium regulation (*Tctex1 domain containing 2*, *Tctex1d2)* and one receptor for substance P (*Tachykinin 1*, *Tac1*) were down-regulated (**Figure 4A**). It is important that the synaptic vesicular machinery was also affected, with an up-regulation of genes involved in neurotransmitter release, as well as calcium sensors for exocytosis, such as *Syngr1 and 3*, the *Synaptotagmin* family (*Syt1*, *2*, *11*, and *12*) and *SV* family (*SV2a* and *c*), and genes related with synaptic vesicle plasticity such as *Synaptophysin* and genes associated with synaptic vesicle docking and fusion (*Syntaxin binding protein 1*, *Stxbp1*, and *Syntaxin 16*, *Stx16*; **Figure 4A**).

Furthermore, as shown in **Figure 4B**, we found up- or down-regulation in genes involved in axonal growth and guidance, such as *cortactin* (*Cttn)* and *Dyacylglycerol lipase, alpha* (*Dagla*). At the same time, we detected changes in genes involved in myelin organization and regulation as *Peripheral myelin protein 22* (*Pmp22*) and *Developmentally regulated protein TPO1* (*Tpo1*), *Myelin-associated glycoprotein* (*Mag*), and *Oligodendrocyte-myelin glycoprotein* (*Omg*). We also found both types of regulation in genes involved in sprouting [*dopamine receptor D1 interacting protein* (*Drd1ip)*, *Sprouty homolog 3* (*Spry-3*), and *Rho-associated coiled-coil containing protein kinase 1* (*Rock1*)], in synaptic plasticity [*Amyloid beta (A4) precursor protein (App)*, *Neuronal pentraxin 2 (Nptx2)* and *Calcium/calmodulin-dependent protein kinase II*, β *Camk2b*] and in postsynaptic density reorganization (*p55*, and *Tubulins* γ*2*, α*1A, and* β*2C*). In addition, even after 90 days post-lesion, we still found regulations (up or down) in apoptotic genes, such as *Cathepsins B and D* (*Ctsb and Ctsd*), *Growth arrest-specific 2* (*Gas2*) and *Programmed cell death 10* (*Pdcd10*), but at the same time we found an increase in anti-apoptotic gene expression [*N-myc downstream regulated gene 4* (*Ndrg4)* and *Gelsolin* (*Gsn*)]. This regulation was accompanied by changes in genes involved in cell migration and differentiation [e.g., *Neural proliferation, differentiation and control, 1 (Npdc1)* and *Diazepam binding inhibitor* (*Dbi*)] and glial connexins [*Gap junction membrane channel protein alpha 12* (*Gja12*), and *gap junction protein, alpha 1* (*Gja1* or *Cnx43*)].

RT-qPCR ANALYSIS

RT-qPCR analysis was used to confirm a subset of gene expression changes observed in the microarray analysis. Genes chosen for RT-qPCR confirmation were mainly selected 90 days after cortical ablation, based on ontological categories with potential functional roles.

Differentially regulated genes confirmed by RT-qPCR belong to a majority of functional categories already described (neurotransmission, neural/synaptic plasticity, axonal growth/degeneration, myelin organization and regulation, sprouting, neuroprotection, regulation of apoptosis, and autophagy). Thus, as shown in **Table 1**, altered gene expression of the majority of genes, but not all, were confirmed by RT-qPCR.

Microarray analysis identified many neurotransmission-related genes with significant increases in expression at 90 days after unilateral auditory cortex ablation (**Figure 4A**). From these genes, 12 were further assessed with RT-qPCR and showed comparable changes. A serotonin receptor (*Htr1a*), a glutamate receptor (*Grin1 or NMDAR1*), an enzyme for GABA synthesis (*Glutamic acid decarboxylase 1*, *Gad1*), a gene involved in the regulation of AMPA receptors (*N-ethylmaleimide sensitive fusion protein, Nsf*), a glutamate transporter *Slc17a6* (=*VGlut2*), and two GABA transporters (*Slc32a1* and *Slc6a11*) showed significant increases of 4.09-, 1.81-, 2.13-, 1.48-, 1.79-, 1.52-, and 1.87-fold at 90 days in the contra- (vs. ipsilateral) IC, respectively. Increased gene expression at the same time point was seen for a cholinergic receptor (*Chrnb2*), NMDA receptor associated protein (*Grina*), *Neuronal pentraxin 2 (Nptx2)*, and the glutamate transporter *Slc1a3* (=*GLAST*) using microarrays analysis, whereas RT-qPCR did not confirm such a significant increase. Conversely, *Nsf* and *VGlut2* had increased levels of expression at 90 days in the ipsilateral IC and genes like *Grin1* and *Gad1* also had increased levels of expression at the same time point in the contralateral IC by RT-qPCR analysis, whereas the microarray data did not show a significant change. Also, RT-qPCR for *Nptx2* and a GABA transporter (*Slc32a1*) showed a 1.74- and 1.57-fold decrease in expression at 90 days in the ipsilateral IC after unilateral auditory cortex ablation, whereas microarrays did not show significant changes. In contrast, increased gene expression was seen at 90 days in the contralateral IC for the *Sodium channel, type IV, beta* (*Scn4b*) using microarrays analysis, whereas the RT-qPCR did not show a significant increase.

Microarray results for the neurogenesis-related genes or neuronal differentiation, such as *Amyloid beta (A4) precursor protein* (*App*), *Neural proliferation, differentiation and control, 1* (*Npdc1*), and *N-myc downstream regulated gene 4* (*Ndrg4)*, showed an increase in expression at 90 days in the contralateral IC vs. control and vs. ipsilateral IC, respectively, after unilateral auditory cortex ablation. On the other hand, decreased gene expression at 90 days in the contra vs. ipsilateral IC was seen in the *Diazepam binding inhibitor* (*Dbi*) using microarrays analysis, while the RT-qPCR did not show a significant increase. In contrast, this same gene showed 1.54-fold increase in expression at 90 days in the contralateral IC by RT-qPCR, whereas the microarray data did not show a significant change at this time point.

Other genes such as the enzyme involved in endocannabinoid mobilization *Dyacylglycerol lipase alpha* (*Dagla*), glial connexin *Gja1* (=*Cnx43*), *Apoptosis-inducing factor mitochondrion-associated 3* (*Aifm3*), *p55*, and *Gelsolin* (*Gsn*) assessed by RT-qPCR showed expression levels which were also increased at 90 days in the contra vs. ipsilateral IC, whereas *Myelin-associated glycoprotein* (*Mag*), *Rho-associated coiled-coil containing protein kinase 1 (Rock1)*, *Syt1,* and *Scrapie responsive gene 1* (*Scrg1*) did not show significant changes. Moreover, the gene encoding the gap junction

Table 1 | Comparison of gene expression at 90 days after unilateral auditory cortex ablation: Microarray vs. RT-qPCR data.

	Transcripts cluster ID	Gene description	Gene symbol	Control vs. 90dpl-Ipsi		Control vs. 90dpl-Contra		90dpl-ipsi vs. 90dpl-contra		Array PCR ID
				Microarray (1)	RT-qPCR (2)	Microarray (1)	RT-qPCR (2)	Microarray (1)	RT-qPCR (2)	
Neurotransmission: receptors, binding proteins, transports and metabolism, transport_ channels	10812879	5-hydroxytryptamine (serotonin) receptor 1A	Htr1a	NS	NS	NS	NS	**1.746**	**4,093 ± 1,23***	Rn00561409_s1
	10824517	Cholinergic receptor, nicotinic, beta polypeptide 2 (neuronal)	Chrnb2	NS	NS	NS	NS	**1.954**	NS	Rn00570733_m1
	10843400	Glutamate receptor, ionotropic, *N*-methyl d-aspartate 1	Grin1 = NMDAR1	NS	NS	NS	**2,509 ± 0,45***	**1.663**	**1,814 ± 0,33***	Rn01436038_m1
	10897146	Glutamate receptor, ionotropic, *N*-methyl d-aspartate-associated protein 1 (glutamate binding)	Grina	NS	NS	NS	NS	**1.967**	NS	Rn00596289_g1
	10836734	Glutamic acid decarboxylase 1	Gad1	NS	NS	NS	**3,607 ± 0,45***	**1.871**	**2,135 ± 0,27***	Rn00690300_m1
	10748118	*N*-ethylmaleimide sensitive fusion protein	Nsf	NS	**1,537 ± 0,03***	NS	**2,277 ± 0,10***	**2.028**	**1,481 ± 0,01***	Rn00612444_m1
	10760290	Neuronal pentraxin 2	Nptx2	NS	**−1,745 ± 0,07***	NS	NS	**1.584**	NS	Rn01756377_m1
	10909621	Sodium channel, type IV, beta	Scn4b	NS	NS	**1.683**	NS	NS	NS	Rn01418017_m1
	10821824	Solute carrier family 1 (glial high affinity glutamate transporter), member 3	Slc1a3 = Glast	NS	NS	NS	NS	**1.814**	NS	Rn00570130_m1
	10707325	Solute carrier family 17 (sodium-dependent inorganic phosphate cotransporter), member 6	Slc17a6 = VGlut2	NS	**2,375 ± 0,29***	NS	**4,270 ± 0,71***	**1.89**	**1,798 ± 0,30***	Rn00584780_m1
	10841774	Solute carrier family 32 (GABA vesicular transporter), member 1	Slc32a1	NS	**−1,570 ± 0,07***	NS	NS	**1.75**	**1,524 ± 0,05***	Rn00824654_m1
	10857916	Solute carrier family 6 (neurotransmitter transporter, GABA), member 11	Slc6a11	NS	NS	NS	NS	**1.848**	**1,871 ± 0,32***	Rn00577664_m1

(Continued)

Table 1 | Continued

	Transcripts cluster ID	Gene description	Gene symbol	Control vs. 90dpl-Ipsi		Control vs. 90dpl-Contra		90dpl-ipsi vs. 90dpl-contra		Array PCR ID
				Microarray (1)	RT-qPCR (2)	Microarray (1)	RT-qPCR (2)	Microarray (1)	RT-qPCR (2)	
Neurogenesis_ neuronal differentiation	10752811	Amyloid beta (A4) precursor protein	App	NS	NS	NS	**2,232 ± 0,30***	**1.848**	**1,697 ± 0,23***	Rn00570673_m1
	10931154	diazepam binding inhibitor	Dbi	NS	NS	NS	**1,543 ± 0,11***	**−1.778**	NS	Rn00821402_g1
	10834225	Neural proliferation, differentiation and control, 1	Npdc1	NS	NS	**1.585**	**1,971 ± 0,16***	**1.773**	**1,632 ± 0,13***	Rn01438701_g1
	10809100	*N*-myc downstream regulated gene 4	Ndrg4	NS	NS	**1.581**	**2,371 ± 0,13***	**1.858**	**1,347 ± 0,07***	Rn00582990_m1
Axonal growth_ sprouty_axonal branching	10728676	Diacylglycerol lipase, alpha	Dagla	NS	**−1,44 ± 0,10***	NS	NS	**1.509**	**1,546 ± 0,15***	Rn01454304_m1
	10720813	Myelin-associated glycoprotein	Mag	NS	NS	NS	NS	**1.811**	NS	Rn00567868_m1
	10803158	Rho-associated coiled-coil containing protein kinase 1	Rock1	NS	NS	NS	NS	**−1.509**	NS	Rn00579490_m1
Synaptic vesicular exocytosis_ calcium sensor	10902232	Synaptotagmin I	Syt1	NS	NS	NS	NS	**1.51**	NS	Rn00436862_m1
GLIA	10830189	Gap junction protein, alpha 1	Gja1 = Cnx43	**−1.749**	**−1,842 ± 0,16***	NS	**1,590 ± 0,05***	**1.593**	**2,928 ± 0,09***	Rn01433957_m1
Cell death_ apoptosis_autophagy	10755728	Apoptosis-inducing factor, mitochondrion-associated 3	Aifm3	NS	NS	NS	**3,588 ± 0,16***	**1.868**	**2,367 ± 0,11***	Rn01405066_m1
	10894498	P55	P55	NS	NS	**1.52**	**2,676 ± 0,34***	**1.684**	**1,831 ± 0,24***	Rn01509468_g1
	10791500	Scrapie responsive gene 1	Scrg1	NS	NS	**−2.141**	NS	**−1.79**	NS	Rn00583743_m1
	10835757	Gelsolin	Gsn	**−1.527**	NS	NS	NS	**1.854**	**2,033 ± 0,01***	Rn01438922_m1

(1)Change in intensity, expressed as fold change.

(2)Expressed as fold change ($2^{-\Delta\Delta Ct}$): mean ± SD.

NS, not statistically significant. Red indicates up-regulated; Green indicates down-regulated.

**$p < 0.05$.*

protein *Cnx43* and *p55* showed 1.84-fold decrease and 2.68-fold increase in expression at 90 days post-lesion in the ipsilateral and contralateral IC (vs. control), respectively, after unilateral auditory cortex ablation. A number of the RT-qPCR confirmation analysis (*Dagla* at 90 days in the ipsilateral IC, and *Cnx43* and *Aifm3* at 90 days in the contralateral IC) which did not reach statistical significance, demonstrated expression profiles similar to those observed in the microarray. On the other hand, *Gsn* at 90 days in the ipsilateral IC and *Scrg1* at 90 days in the contralateral IC, showed changes in gene expression levels in microarrays, whereas the RT-qPCR did not show a significant increase.

As shown in **Table 1**, we performed RT-qPCR analysis on 24 genes at 90 days in the contra vs. ipsilateral IC after unilateral auditory cortex ablation and 15 of them showed similar changes in expression levels using microarrays analysis. Therefore, we used RMA for normalization that reflects more accurately the expression level of genes and a statistical method sufficiently stringent in assigning significance. We have observed differences in expression of some genes (e.g., *Nptx2*, *Slc1a3,* and *Scn4b*) using microarray analysis whereas RT-qPCR did not confirm such a significant variation. This situation was also described after microarray analysis in the IC by Holt et al. (2005), mainly in genes that are constitutively expressed at low levels. It should not be surprising that when constitute expression of genes is extremely low the threshold of microarrays are higher than qPCR arrays.

DISCUSSION

Unilateral auditory cortical deafferentation induces bilateral and asymmetric changes in gene expression profiling in the IC. In adults, this plastic response is time-dependent, with more extensive regulation at long-term post-lesion (90 days) than at short-term (15 days). Also, the nature of this reorganization is different for each time post-lesion, supporting the concept of a plastic ability in adults.

Auditory cortical ablation affects a large number of genes simultaneously; at 15 days post-lesion we found 52 genes (33 in the ipsilateral side and 19 in the contralateral side) whose expression changes. Meanwhile, 90 days after the lesion this regulation affects 640 genes in the IC (430 in the ipsilateral side and 210 in the contralateral side). Unilateral cortical ablation strongly affects the ipsilateral lesioned side at both times post-lesion (15 and 90 days), due to the loss of a denser innervation. Ipsilateral regulation was greater after long-term (90 days) than after short-term. This "late" regulation suggests an important role for adult neural plasticity events in this key auditory nucleus. After 15 days post-lesion, gene expression regulation was mostly related to an inflammatory response, whereas after 90 days regulation was linked mainly to sprouting phenomena and synaptic transmission. We already know that the auditory system in adults is able to induce gene modulation in the IC even after long periods of peripheral deafferentation (Holt et al., 2005). Our approach has focused on a comparatively minor contralateral IC deafferentation and a stronger ipsilateral IC deafferentation resulting from unilateral cortical ablation. Our results show that this misbalance is enough to induce a rearrangement in gene expression profiles in the IC, involving the pathways necessary to trigger neuronal plasticity in adults. Neurons convert environmental stimuli using a complex array of signaling pathways and transcriptional mechanisms to orchestrate long-lasting changes in their physiology through the synaptic activity-regulated transcription of new gene products (Lyons and West, 2011). After auditory cortical lesions, these long-term transcriptional profiling changes in the bilateral ICs are an indication of adult synaptic plasticity triggers, which are dependent on both post-lesioned time and density deafferentation.

Our results are a first look at the entire post-lesional auditory plasticity process. To assess an IC reorganization after cortical ablation both genomic and proteomic analysis are necessary. Genomic results cannot be extrapolated to protein production since it is known that there exist some mismatches between genomic and proteomic data in both brain cell culture (Howley et al., 2012) and most specifically in auditory system nuclei (Bush and Hyson, 2008; Wang et al., 2009a,b). Wang et al. (2009b) found 80 days after sound exposure that GlyR α subunit message was increased in the dorsal cochlear nucleus. However, the protein level was decreased. Mechanisms for this mismatch are still unknown, but studies demonstrate that information regarding post-translational modifications of the proteins and their translocation is not inherently encoded in the gene sequences and cannot be derived from mRNA expression (see Benoit et al., 2011 review).

THE IPSI- AND CONTRALATERAL IC 15 DAYS AFTER THE LESION TO THE CORTEX

Functional analysis of IC gene profile expression 15 days after the lesion shows an up-regulation in *Serglycin,* a proteoglycan expressed primarily by immune cells (Kolset and Pejler, 2011) with a key role in inflammatory processes (Kolset and Tveit, 2008), suggesting that, in our model, cortical ablation induces in the short-term an inflammatory reaction in the ipsilateral IC which undergoes a larger loss of cortical descending afferents. In agreement with this finding, previous studies in the IC using a thiamine deficiency model to analyze inflammation, cellular stress, metabolism, and structural damage after focal neuronal death (Vemuganti et al., 2006) found an up-regulation in *Podocalyxin*, a cell adhesion regulator gene. More recently, other roles for this gene in neural development, neurite growth, branching, axonal fasciculation, and synapse formation after neuronal death or inflammation have been shown (Vitureira et al., 2010). In our experimental model, up-regulation of this gene in the ipsilateral IC suggests that this adjustment correlates with the density of the lesioned pathway. Furthermore, *Complement component 3* (*C3*), another inflammation-related gene, was found to be up-regulated in the IC in thiamin deficiency animals (Vemuganti et al., 2006) and in our ablated animals; supporting the idea of an ongoing inflammatory process at 15 days post-lesion which is stronger in the ipsilateral IC, accordingly with a heaviest preterminal fields degeneration after cortical ablation in the ipsilateral IC rather than the contralateral (Feliciano and Potashner, 1995). In addition, Stevens et al. (2007) have demonstrated that *C3* is a gene that tagged synapses to be eliminated during CNS development. These authors suggest that complement-mediated synapse elimination (synaptic stripping) may become aberrantly reactivated in neurological diseases. The process of synaptic elimination (pruning), even in adult animals, is important for rewiring neural circuits. Butz et al. (2009), using a model for analyzing cortical rewiring after deafferentation

showed that even small changes in homeostatic equilibrium imply formation of new synapses or pruning of existing ones.

On the other hand, in the ipsilateral IC at 15 days post-lesion we also found down-regulated genes, like *Latexin* which is a carboxypeptidase inhibitor which mediates inflammatory responses (Aagaard et al., 2005), but it also known to be expressed by astrocytes, providing neuroprotective mechanisms (Yata et al., 2011). However, our results suggest that a typical astrocytic reaction does not take place in the IC, because we did not find any regulation in marker genes for reactive astrocytes like *Vimentin* or *Glial fibrillary acidic protein (GFAP)* which in the case of a thiamine deficiency model were up-regulated (Vemuganti et al., 2006).

Analyses of the contralateral IC 15 days after the cortical lesion show an up-regulation in the *Spinster* (*Spns*) gene, which is a negative synaptic growth regulator. The Drosophila *Spns* mutant shows a 200% increase in the number of synaptic endings and a deficit in presynaptic release (Sweeney and Davis, 2002). *Spinster* is also linked to a novel caspase-independent cell death pathway mediated by autophagy (Yanagisawa et al., 2003). These data speak in favor of a rearrangement process in the contralateral IC that has lost a weaker corticofugal projection compared with the side ipsilateral to the lesion. The focus of this regulation may be in synaptic pruning, looking for an efficient synaptic rewiring (Butz et al., 2009), or it may be related to changes in presynaptic release after lesion (Birthelmer et al., 2003), which affects activity in IC neurons (Nwabueze-Ogbo et al., 2002; Popelar et al., 2003).

In summary, microarray analyses at 15 days post-lesion show that genes mainly related to inflammatory processes were up-regulated in the ipsilateral IC. The relative increase in the activity of genes related to inflammation could be a consequence of extensive brain injury (Block et al., 2005). However the asymmetry of the corticofugal projection (Saldana et al., 1996; Bajo et al., 2007) geared toward the ipsilateral side, along with an ipsilateral predominance of changes in gene expression suggest a local consequence of terminal degeneration in the IC. The biological functions of genes, whose regulation is affected, indicate that beyond an inflammatory response an emergent plastic process, probably related with sprouting, and pruning on the adult collicular network, takes place bilaterally in the ICs after short-term post-lesion.

THE IPSI- AND CONTRALATERAL IC 90 DAYS AFTER THE LESION TO THE CORTEX

A much larger gene expression regulation pattern was found in the IC 90 days after the cortical lesion. Microarray comparisons between control and ipsilateral IC showed that changes affected remarkably genes involved in apoptosis. We found an up-regulation in *Programmed cell death 10* (*Pdcd10*) whose overexpression is sufficient to induce neuronal apoptosis (Lin et al., 2010). *Fission 1* (*Fis1*) which participates in apoptotic mitochondrial fission (Youle and Karbowski, 2005) was also up-regulated and so were *Growth arrest-specific 2* (*Gas2*) gene, a substrate of Caspase-3 (Sgorbissa et al., 1999), and *Cytochrome c oxidase subunit VIIb* (*Cox7b*) which is one of the last subunits that join the assembling cytochrome oxidase complex inducing apoptosis and affecting mitochondrial integrity (Fornuskova et al., 2010). We also found an up-regulation in *Calpain 7 (Capn7),* which is associated after brain injury with neuron death and axonal degeneration (Saatman et al., 2010). In addition, we detected down-regulation of the *Calsyntenin 3* (*Clstn3*), a gene which overexpression accelerates neuronal death (Uchida et al., 2011). All this strongly suggests an ongoing cell death process in the ipsilateral IC at 90 days post-lesion. However we did not find changes in the expression of initiator or effector caspases genes triggering the apoptotic process. This could be related with limited microarray sensitivity. On the other hand, deprivation of auditory nerve input in adult animals does not result in significant neuronal loss in the cochlear nuclei (Harris et al., 2005), supporting the idea that in the auditory system mature neurons are less sensitive to apoptotic cell death. It could be that the regulation of apoptotic cascade genes observed by us may be related to other cellular pathways in which all these genes also performed a key role. Further specific proteomic experiments of caspases cell cascades will be needed to elucidate this problem, mainly because the regulation of apoptotic cascades is complex and involves transcriptional control as well as posttranscriptional protein modifications (Culmsee and Landshamer, 2006).

We also found in the ipsilateral IC 90 days after the lesion down-regulation of *Myelin-associated glycoprotein* (*Mag*), a gene able to inhibit axon regeneration after injury (Yiu and He, 2003). Studies *in vivo* demonstrate a modest but significant enhancement of axon regeneration in mice lacking *Mag* (Schnaar and Lopez, 2009). Down-regulation of this gene in our material could be an indication of axon elongation and indirectly of a sprouting process subsequent to lesion in the ipsilateral IC. However, at this same post-lesion time an oligodendrocyte-specific protein, *Claudin 11* (*Cldn11*), which encodes a molecular component present in tight junctions and which is also is involved in axon myelination, was down-regulated. This result probably indicates an inefficient axon myelination during axon elongation. *Cldn11* down-regulation may affect biophysical properties of myelinated axons in the IC, because it is known that *Cldn11*-null mice present a 60% decrease in conduction velocity (Devaux and Gow, 2008). A low effective compartmentalization of the myelin sheet of sprouting axon collaterals may be in accordance with previous results in which after 90 days of cortical lesion, sound stimulation-induced c-Fos immunoreactivity in the IC was only partially recovered (Clarkson et al., 2010a). In correspondence with this low activity in the IC at this survival time after the cortical lesion, genes related with synaptic activity also were affected with down-regulation in *Synaptotagmin-11* (*Syt11*, a Ca^{2+}-sensor during vesicular trafficking, Inoue et al., 2007), *Calcium channel – voltage-dependent – γ3* (*Cacng3*, a gene with modulatory effects on the electrophysiological characteristic of the $Ca_V2.1$ channel, Rousset et al., 2001) and also in *Potassium inwardly rectifying channel, subfamily J, member 16 (Kcnj16)* which plays a physiological role in the potassium buffering-action of brain astrocytes (Hibino et al., 2004). Holt et al. (2005) showed by RT-qPCR a rearrangement in synaptic transmission genes in the IC 90 days after cochlear ablation, with regulation affecting several glutamate and GABA receptors genes, supporting the hypothesis that, after long-term post-lesion, the adult auditory system is able to modify the gene neurotransmission machinery in the IC even after lack of auditory activity. Glial related genes such as *Connexin 30* and *43,* which are specific gap junction proteins that mediate cell-to-cell communication (Gemel et al., 2008) and *Cadherin 13* involved in regulation of cell growth, survival, and

astrocyte proliferation (Huang et al., 2003) were down-regulated. Recently studies from connexin 30 and 43 show that these gap junctions mediate astroglial networks scale synaptic activity, as they define the concentrations and dynamics of extracellular ions and neurotransmitters during synaptic activity (Pannasch et al., 2011). These glia gene regulations after ablation are important for tripartite synapses model, in which brain function actually arises from the coordinated activity of a network comprising both neurons and glia (Perea et al., 2009).

The idea that in the ipsilateral IC 90 days after cortical ablation plastic or adaptive reorganizations have been switched on is also reinforced by previous data showing that sound-induced c-Fos immunoreactivity progressively increases from 90 to 180 days after cortical ablation (Clarkson et al., 2010a), showing that neuronal activity is still on its way to recovery.

After 90 days of the lesion, the contralateral IC showed up-regulation in genes involved in neurotransmission/signal propagation/synaptic plasticity such as *Sodium channel, type IV, beta* (*Scn4b*) whose overexpression induces neurite outgrowth, causes thickening of dendrites and increases the post synaptic density of neuronal spines (Oyama et al., 2006). Also *Potassium voltage channel, shaker related subfamily, member 6* (*Kcna6*) was up-regulated. This potassium channel regulates miniature inhibitory postsynaptic currents (mIPSCs) by regulating glycine release from the endings (Shoudai et al., 2007). In astrocytes *Kcna6* underlies part of the delayed rectifier potassium current (Smart et al., 1997). Another family of potassium channels like KCNQ5 and KCNK15 has been localized to neurons in the IC and are modulated by hearing loss (Caminos et al., 2007; Dong et al., 2009). Furthermore, up-regulation in *opioid receptor, sigma 1* (*Oprs1*), found in our results, may be related to its role in neuronal plasticity, enhancing growth factor-induced neurite outgrowth (Hashimoto, 2010; Ruscher et al., 2011), and also regulating both Ca^{2+} entry and Ca^{2+} mobilization from endoplasmic reticulum stores (Monnet, 2005). Another opioid receptor involved in nociception, *Opioid receptor-like 1* (*Oprl1*) was also up-regulated, and is able to decrease acetylcholine release and dopamine release and elevates extracellular glutamate and GABA levels (Schlicker and Morari, 2000). All these changes were accompanied by an up-regulation in genes for neurotransmitter delivery at synaptic terminals. For example, in our material up-regulation of SV2a which exerts a main role in neurotransmitter uptake, vesicle targeting, and membrane fusion (Elferink and Scheller, 1995), as well as Synaptogyrin 1 and 3 (Syngr1 and 3), both of which play an essential function in synaptic plasticity without being required for neurotransmitter release (Belizaire et al., 2004). These data agrees with the idea that in adult animals the contralateral IC that loses the weaker projection from the cortex is still able, after long-term post-lesion, to enhance its genetic machinery to try to compensate the imbalance induced by lost cortical connections. This compensation could be the result of fine plastic modulations, which may include sprouting, pruning, and neurotransmission rearrangement. According to this idea, we also found an increase in *Hippocalcin* (*Hpca*) which encodes a calcium-binding protein considered relevant for synaptic plasticity, acting as a molecular link between Ca^{2+} entry through NMDA receptor and the subsequent endocytosis of AMPA receptor subunits in long-term depression (LTD; Palmer et al., 2005). Also it was shown that *Hpca* overexpression dramatically elongated neurites (Oh et al., 2008). Similarly, *Dopamine receptor D1 interacting protein* (*Drd1ip*) a known brain plasticity gene (Kruusmagi et al., 2007) that plays a specialized role in removal of synaptic AMPA receptor (Davidson et al., 2009) was up-regulated. So it was *N-myc downstream regulate gene 4* (*Ndrg4*) a contributor to neuronal differentiation, neurite formation, cell progression, and survival (Takahashi et al., 2005; Schilling et al., 2009), *Neural proliferation, differentiation, and control 1* (*Npdc1*) gene, which is able to down-regulate the proliferation of neural precursors (Dupont et al., 1997), and *Spinster* that is a negative regulator of synaptic regrowth (Sweeney and Davis, 2002) were also up-regulated. This balance between regrowth and growth suppression gene expression seems to be important to demonstrate rewiring network processes in the contralateral IC 90 days after lesion through activation of mechanisms involve in neuronal regulation.

In summary, up-regulation in genes related to axonal growth, receptor expression, and trafficking as well in channels and synaptic machinery may be compatible with plastic reorganization that is more active in the contralateral IC. These differences in the timing for plasticity activation between both sides may be explained by the asymmetrical loss of excitation due to the asymmetrical density of the descending connections from the cortex.

COMPARING IPSI- AND CONTRALATERAL CHANGES AT 15 AND 90 DAYS POST-LESION

Comparison between ipsi- and contralateral IC after 15 days shows a small number of altered genes (14), contrasting with the larger number of regulated genes in the comparison (ipsi- vs. contralateral) after 90 days subsequent to the cortical lesion (1659 genes). Gene expression analysis between ipsi- and contralateral IC after 90 days following the cortical lesion showed up-regulation in potassium and chloride channels, and cholinergic, serotoninergic, glycinergic receptors in the contralateral IC. Biological function of up-regulated genes speaks in favor of a more active synaptic plasticity in the contralateral IC after long-term post-lesion. In particular, the NMDA receptor subunit coded by *Grin1* (*glutamate receptor, ionotropic, N-methyl* D*-aspartate 1*) and its associated protein coded by *Grina* (*glutamate receptor, ionotropic, N-methyl* D*-aspartate-associated protein 1*) were up-regulated in the contralateral IC. NMDA receptors are important for activity-dependent synaptic plasticity (Kalev-Zylinska et al., 2009; Rebola et al., 2010). *In vitro* experiments demonstrated that activation of NMDA receptors mediated a dramatic increase of both *c-fos* expression and intracellular calcium (Lerea et al., 1992). In a previous work both Calretinin (an indirect marker of Ca^{2+} influx-Clarkson et al., 2010b) and c-Fos in the IC contralateral to the lesion (Clarkson et al., 2010a) showed stronger immunoreactivity relative to the ipsilateral side. Future experiments will be need to demonstrate in our *in vivo* model a direct correlation among NMDA receptor activation, c-Fos activation, and changes in the intracellular Ca^{2+} concentration.

An extensive group of genes potentially involved in neurotransmitter release, such as four members of the *Synaptotagmin* family (*Syt1, 2, 11,* and *12*; Chapman, 2008; Rizo and Rosenmund, 2008; Sudhof and Rothman, 2009), were

up-regulated in the contralateral side. In addition, genes involved both in expression and trafficking of *Synaptotagmin* family members, such as the *SV2* family (*SV2a*, *SV2c*, and *SV2 related protein*; Nowack et al., 2010) were also up-regulated in the contralateral IC. Not only were receptors and synaptic vesicle fusion genes up-regulated in the contralateral side after long-term lesion, but also this rearrangement was accompanied by an up-regulation in key enzymes for GABA (*4-aminobutyrate aminotransferase*, *Abat*, and *Glutamic acid decarboxylase 1*, *Gad1*), glycine (*Glycyl-tRNA synthetase*, *Gars*), glutamate (*Glutaminyl-tRNA synthetase*, *Qars*) and endocannabinoid synthesis (*Dyacylglycerol lipase alpha*, *Dagla*), all of them key components in short and long-term plastic synaptic changes. In addition, neurotransmitter transporters were up-regulated in the contralateral IC after long-term cortical ablation (for neuronal glutamate: *Vesicular glutamate transporter 2*, *VGlut2*, or *solute carrier family 17 member 6*, *Slc17a6*; for proline: *Slc6a7*; for glycine: *Slc6a9*; for GABA: *Slc6a11* and *Slc32a1;* and for glutamate: *Slc1a3* or *GLAST*). Up-regulation of both enzymes and transporter genes clearly suggests a post-lesion shift in the synthesis and recycling of neurotransmitters. These findings support the idea of a better recovery of neurotransmission in the contralateral IC probably due to the comparatively lower loss of excitation in that side after cortical lesion. All these data also suggest activity-dependent compensatory mechanisms in the contralateral IC, counteracting the most affected ipsilateral IC. In summary, these changes in gene expression are important due to the claim that regulation depends on the extent of deafferentation, and even in adult animals it is larger after long-term post-lesion with specific changes aimed at recovering activity loss in IC neurons.

AUTHOR CONTRIBUTION

Cheryl Clarkson Performed experiments, prepared figures and wrote the manuscript. M. Javier Herrero-Turrión. Performed RT-qPCRs experiments, analyzed statistically microarray data and drafted the manuscript. Miguel A. Merchán. Designed, coordinated, and supervised the study. All authors read and agreed the paper content.

ACKNOWLEDGMENTS

The authors would like to thank Dr. José Juiz for his critical review and very helpful suggestions and Ignacio Plaza for his excellent technical assistance. Financial support for this investigation was provided by the grant BFU2009-13754-CO2 from the Spanish Ministerio de Investigación e Innovación (Minciin).

SUPPLEMENTARY MATERIAL

The Supplementary Material for this article can be found online at http://www.frontiersin.org/Neural_Circuits/10.3389/fncir.2012.00086/abstract

Datasheet 1 | Naïve control vs. 15 days and 90 days post-lesion.

Datasheet 2 | Primers PCR arrays.

Datasheet 3 | Funtional annotation of diferentially expresed genes.

REFERENCES

Aagaard, A., Listwan, P., Cowieson, N., Huber, T., Ravasi, T., Wells, C. A., et al. (2005). An inflammatory role for the mammalian carboxypeptidase inhibitor latexin: relationship to cystatins and the tumor suppressor TIG1. *Structure* 13, 309–317.

Bajo, V. M., Nodal, F. R., Bizley, J. K., Moore, D. R., and King, A. J. (2007). The ferret auditory cortex: descending projections to the inferior colliculus. *Cereb. Cortex* 17, 475–491.

Belizaire, R., Komanduri, C., Wooten, K., Chen, M., Thaller, C., and Janz, R. (2004). Characterization of synaptogyrin 3 as a new synaptic vesicle protein. *J. Comp. Neurol.* 470, 266–281.

Benoit, C. E., Rowe, W. B., Menards, C., Sarret, P., and Quirion, R. (2011). Genomic and proteomic strategies to identify novel targets potentially involved in learning and memory. *Trends Pharmacol. Sci.* 32, 43–52.

Birthelmer, A., Ehret, A., Amtage, F., Forster, S., Lehmann, O., Jeltsch, H., et al. (2003). Neurotransmitter release and its presynaptic modulation in the rat hippocampus after selective damage to cholinergic or/and serotonergic afferents. *Brain Res. Bull.* 59, 371–381.

Bledsoe, S. C. Jr., Nagase, S., Miller, J. M., and Altschuler, R. A. (1995). Deafness-induced plasticity in the mature central auditory system. *Neuroreport* 7, 225–229.

Block, F., Dihne, M., and Loos, M. (2005). Inflammation in areas of remote changes following focal brain lesion. *Prog. Neurobiol.* 75, 342–365.

Bowen, G. P., Lin, D., Taylor, M. K., and Ison, J. R. (2003). Auditory cortex lesions in the rat impair both temporal acuity and noise increment thresholds, revealing a common neural substrate. *Cereb. Cortex* 13, 815–822.

Bullitt, E. (1995). Expression of c-fos-like protein as a marker for neuronal activity following noxious stimulation in the rat. *J. Comp. Neurol.* 296, 517–530.

Bush, A. L., and Hyson, R. L. (2008). Effects of lithium and deafferentation on expression of glycogen synthase kinase-3beta, NFkappaB, beta-catenin, and pCreb in the chick cochlear nucleus. *Brain Res.* 1203, 18–25.

Butz, M., van Ooyen, A., and Worgotter, F. (2009). A model for cortical rewiring following deafferentation and focal stroke. *Front. Comput. Neurosci.* 3:10. doi:10.3389/neuro.10.010.2009

Caminos, E., Garcia-Pino, E., Martinez-Galan, J. R., and Juiz, J. M. (2007). The potassium channel KCNQ5/Kv7.5 is localized in synaptic endings of auditory brainstem nuclei of the rat. *J. Comp. Neurol.* 505, 363–378.

Chapman, E. R. (2008). How does synaptotagmin trigger neurotransmitter release? *Annu. Rev. Biochem.* 77, 615–641.

Clarkson, C., Juíz, J. M., and Merchán, M. A. (2010a). Long-term regulation in calretinin staining in the rat inferior colliculus after unilateral auditory cortical ablation. *J. Comp. Neurol.* 518, 4261–4276.

Clarkson, C., Juíz, J. M., and Merchán, M. A. (2010b). Transient down-regulation of sound-induced c-fos protein expression in the inferior colliculus after ablation of the auditory cortex. *Front. Neuroanat.* 4:141. doi:10.3389/fnana.2010.00141

Clarkson, C., López, D. E., and Merchán, M. A. (2010c). Long-term functional recovery in the rat auditory system after unilateral auditory cortex ablation. *Acta Otolaryngol.* 130, 326–332.

Culmsee, C., and Landshamer, S. (2006). Molecular insights into mechanisms of the cell death program: role in the progression of neurodegenerative disorders. *Curr. Alzheimer Res.* 3, 269–283.

Davidson, H. T., Xiao, J., Dai, R., and Bergson, C. (2009). Calcyon is necessary for activity-dependent AMPA receptor internalization and LTD in CA1 neurons of hippocampus. *Eur. J. Neurosci.* 29, 42–54.

Dennis, G. Jr., Sherman, B. T., Hosack, D. A., Yang, J., Gao, W., Lane, H. C., et al. (2003). DAVID: database for annotation, visualization, and integrated discovery. *Genome Biol.* 4, P3.

Devaux, J., and Gow, A. (2008). Tight junctions potentiate the insulative properties of small CNS myelinated axons. *J. Cell Biol.* 183, 909–921.

Dong, S., Mulders, W. H., Rodger, J., and Robertson, D. (2009). Changes in neuronal activity and gene expression in guinea-pig auditory brainstem after unilateral partial hearing loss. *Neuroscience* 159, 1164–1174.

Druga, R., and Syka, J. (2001). Effect of auditory cortex lesions on NADPH-diaphorase staining in the inferior colliculus of rat. *Neuroreport* 12, 1555–1559.

Dupont, E., Sansal, I., Toru, D., Evrard, C., and Rouget, P. (1997). Identification of NPDC-1, gene involved in the control of proliferation and differentiation of neural and glial precursors. *C. R. Seances Soc. Biol. Fil.* 191, 95–104.

Edeline, J. M., and Weinberger, N. M. (1991a). Subcortical adaptive filtering in the auditory system: associative receptive field plasticity in the dorsal medial geniculate body. *Behav. Neurosci.* 105, 154–175.

Edeline, J. M., and Weinberger, N. M. (1991b). Thalamic short-term plasticity in the auditory system: associative returning of receptive fields in the ventral medial geniculate body. *Behav. Neurosci.* 105, 618–639.

Edeline, J. M., and Weinberger, N. M. (1992). Associative retuning in the thalamic source of input to the amygdala and auditory cortex: receptive field plasticity in the medial division of the medial geniculate body. *Behav. Neurosci.* 106, 81–105.

Elferink, L. A., and Scheller, R. H. (1995). Synaptic vesicle proteins and regulated exocytosis. *Prog. Brain Res.* 105, 79–85.

Feliciano, M., and Potashner, S. J. (1995). Evidence for a glutamatergic pathway from the guinea pig auditory cortex to the inferior colliculus. *J. Neurochem.* 65, 1348–1357.

Fornuskova, D., Stiburek, L., Wenchich, L., Vinsova, K., Hansikova, H., and Zeman, J. (2010). Novel insights into the assembly and function of human nuclear-encoded cytochrome *c* oxidase subunits 4, 5a, 6a, 7a, and 7b. *Biochem. J.* 428, 363–374.

Gao, E., and Suga, N. (1998). Experience-dependent corticofugal adjustment of midbrain frequency map in bat auditory system. *Proc. Natl. Acad. Sci. U.S.A.* 95, 12663–12670.

Gao, E., and Suga, N. (2000). Experience-dependent plasticity in the auditory cortex and the inferior colliculus of bats: role of the corticofugal system. *Proc. Natl. Acad. Sci. U.S.A.* 97, 8081–8086.

Gemel, J., Lin, X., Collins, R., Veenstra, R. D., and Beyer, E. C. (2008). Cx30.2 can form heteromeric gap junction channels with other cardiac connexins. *Biochem. Biophys. Res. Commun.* 369, 388–394.

Harris, J. A., Hardie, N. A., Bermingham-McDonogh, O., and Rubel, E. W. (2005). Gene expression differences over a critical period of afferent-dependent neuron survival in the mouse auditory brainstem. *J. Comp. Neurol.* 493, 460–474.

Hashimoto, K. (2010). Role of sigma-1 receptors in neural plasticity and in antipsychotic action. *Nihon Shinkei Seishin Yakurigaku Zasshi* 30, 123–127.

Hibino, H., Fujita, A., Iwai, K., Yamada, M., and Kurachi, Y. (2004). Differential assembly of inwardly rectifying K+ channel subunits, Kir4.1 and Kir5.1, in brain astrocytes. *J. Biol. Chem.* 279, 44065–44073.

Holt, A. G., Asako, M., Duncan, R. K., Lomax, C. A., Juíz, J. M., and Altschuler, R. A. (2006). Deafness associated changes in expression of two-pore domain potassium channels in the rat cochlear nucleus. *Hear. Res.* 216–217, 146–153.

Holt, A. G., Asako, M., Lomax, C. A., MacDonald, J. W., Tong, L., Lomax, M. I., et al. (2005). Deafness-related plasticity in the inferior colliculus: gene expression profiling following removal of peripheral activity. *J. Neurochem.* 93, 1069–1086.

Howley, R., Kinsella, P., Buckley, P. G., Alcock, L., Jansen, M., Heffernan, J., et al. (2012). Comparative genomic and proteomic analysis of high grade glioma primary cultures and matched tumor in situ. *Exp. Cell Res.* 318, 2245–2256.

Huang, D. W., Sherman, B. T., and Lempicki, R. A. (2009). Systematic and integrative analysis of large gene lists using DAVID bioinformatics resources. *Nat. Protoc.* 4, 44–57.

Huang, Z. Y., Wu, Y., Hedrick, N., and Gutmann, D. H. (2003). T-cadherin-mediated cell growth regulation involves G2 phase arrest and requires p21(CIP1/WAF1) expression. *Mol. Cell. Biol.* 23, 566–578.

Illing, R. B., Kraus, K. S., and Meidinger, M. A. (2005). Reconnecting neuronal networks in the auditory brainstem following unilateral deafening. *Hear. Res.* 206, 185–199.

Illing, R. B., and Reisch, A. (2006). Specific plasticity responses to unilaterally decreased or increased hearing intensity in the adult cochlear nucleus and beyond. *Hear. Res.* 216–217, 189–197.

Inoue, S., Imamura, A., Okazaki, Y., Yokota, H., Arai, M., Hayashi, N., et al. (2007). Synaptotagmin XI as a candidate gene for susceptibility to schizophrenia. *Am. J. Med. Genet. B Neuropsychiatr. Genet.* 144B, 332–340.

Jen, P. H., and Zhang, J. P. (1999). Corticofugal regulation of excitatory and inhibitory frequency tuning curves of bat inferior collicular neurons. *Brain Res.* 841, 184–188.

Kalev-Zylinska, M. L., Symes, W., Young, D., and During, M. J. (2009). Knockdown and overexpression of NR1 modulates NMDA receptor function. *Mol. Cell. Neurosci.* 41, 383–396.

Kandler, K. (2004). Activity-dependent organization of inhibitory circuits: lessons from the auditory system. *Curr. Opin. Neurobiol.* 14, 96–104.

Keuroghlian, A. S., and Knudsen, E. I. (2007). Adaptive auditory plasticity in developing and adult animals. *Prog. Neurobiol.* 82, 109–121.

Kolset, S. O., and Pejler, G. (2011). Serglycin: a structural and functional chameleon with wide impact on immune cells. *J. Immunol.* 187, 4927–4933.

Kolset, S. O., and Tveit, H. (2008). Serglycin – structure and biology. *Cell. Mol. Life Sci.* 65, 1073–1085.

Kovacs, K. J. (2008). Measurement of immediate-early gene activation-c-fos and beyond. *J. Neuroendocrinol.* 20, 665–672.

Kruusmagi, M., Zelenin, S., Brismar, H., and Scott, L. (2007). Intracellular dynamics of calcyon, a neuron-specific vesicular protein. *Neuroreport* 18, 1547–1551.

Lerea, L. S., Butler, L. S., and McNamara, J. O. (1992). NMDA and non-NMDA receptor-mediated increase of c-fos mRNA in dentate gyrus neurons involves calcium influx via different routes. *J. Neurosci.* 12, 2973–2981.

Lin, C., Meng, S., Zhu, T., and Wang, X. (2010). PDCD10/CCM3 acts downstream of {gamma}-protocadherins to regulate neuronal survival. *J. Biol. Chem.* 285, 41675–41685.

Lyons, M. R., and West, A. E. (2011). Mechanisms of specificity in neuronal activity-regulated gene transcription. *Prog. Neurobiol.* 94, 259–295.

Ma, X., and Suga, N. (2005). Long-term cortical plasticity evoked by electric stimulation and acetylcholine applied to the auditory cortex. *Proc. Natl. Acad. Sci. U.S.A.* 102, 9335–9340.

Malmierca, M. S., and Merchán, M. (2004). "The auditory system", in *The Rat Nervous System*, ed. G. Paxinos (San Diego: Academic Press), 995–1080.

McAlpine, D., Martin, R. L., Mossop, J. E., and Moore, D. R. (1997). Response properties of neurons in the inferior colliculus of the monaurally deafened ferret to acoustic stimulation of the intact ear. *J. Neurophysiol.* 78, 767–779.

Monnet, F. P. (2005). Sigma-1 receptor as regulator of neuronal intracellular Ca2+ : clinical and therapeutic relevance. *Biol. Cell* 97, 873–883.

Norena, A. J., and Eggermont, J. J. (2006). Enriched acoustic environment after noise trauma abolishes neural signs of tinnitus. *Neuroreport* 17, 559–563.

Nowack, A., Yao, J., Custer, K. L., and Bajjalieh, S. M. (2010). SV2 regulates neurotransmitter release via multiple mechanisms. *Am. J. Physiol. Cell Physiol.* 299, C960–C967.

Nwabueze-Ogbo, F. C., Popelar, J., and Syka, J. (2002). Changes in the acoustically evoked activity in the inferior colliculus of the rat after functional ablation of the auditory cortex. *Physiol. Res.* 51(Suppl. 1), S95–S104.

Oh, D. Y., Cho, J. H., Park, S. Y., Kim, Y. S., Yoon, Y. J., Yoon, S. H., et al. (2008). A novel role of hippocalcin in bFGF-induced neurite outgrowth of H19-7 cells. *J. Neurosci. Res.* 86, 1557–1565.

Oyama, F., Miyazaki, H., Sakamoto, N., Becquet, C., Machida, Y., Kaneko, K., et al. (2006). Sodium channel beta4 subunit: down-regulation and possible involvement in neuritic degeneration in Huntington's disease transgenic mice. *J. Neurochem.* 98, 518–529.

Palmer, C. L., Lim, W., Hastie, P. G., Toward, M., Korolchuk, V. I., Burbidge, S. A., et al. (2005). Hippocalcin functions as a calcium sensor in hippocampal LTD. *Neuron* 47, 487–494.

Pannasch, U., Vargová, L., Reingruber, J., Ezan, P., Holcman, D., Giaume, C., et al. (2011). Astroglial networks scale synaptic activity and plasticity. *Proc. Natl. Acad. Sci. U.S.A.* 108, 8467–8472.

Paxinos, G., and Watson, C. (2005). *The Rat Brain in Stereotaxic Coordinates*, 5th Edn, San Diego: Elsevier Academic Press.

Perea, G., Navarrete, M., and Araque, A. (2009). Tripartite synapses: astrocytes process and control synaptic information. *Trends Neurosci.* 32, 421–431.

Perez-Otano, I., and Ehlers, M. D. (2005). Homeostatic plasticity and NMDA receptor trafficking. *Trends Neurosci.* 28, 229–238.

Popelar, J., Nwabueze-Ogbo, F. C., and Syka, J. (2003). Changes in neuronal activity of the inferior colliculus in rat after temporal inactivation of the auditory cortex. *Physiol. Res.* 52, 615–628.

Rebola, N., Srikumar, B. N., and Mulle, C. (2010). Activity-dependent

synaptic plasticity of NMDA receptors. *J. Physiol.* 588(Pt 1), 93–99.

Riquelme, R., Saldana, E., Osen, K. K., Ottersen, O. P., and Merchán, M. A. (2001). Colocalization of GABA and glycine in the ventral nucleus of the lateral lemniscus in rat: an in situ hybridization and semiquantitative immunocytochemical study. *J. Comp. Neurol.* 432, 409–424.

Rizo, J., and Rosenmund, C. (2008). Synaptic vesicle fusion. *Nat. Struct. Mol. Biol.* 15, 665–674.

Rousset, M., Cens, T., Restituito, S., Barrere, C., Black, J. L. III, McEnery, M. W., and Charnet, P. (2001). Functional roles of gamma2, gamma3 and gamma4, three new Ca2+ channel subunits, in P/Q-type Ca2+ channel expressed in Xenopus oocytes. *J. Physiol. (Lond.)* 532, 583–593.

Rubio, M. E. (2006). Redistribution of synaptic AMPA receptors at glutamatergic synapses in the dorsal cochlear nucleus as an early response to cochlear ablation in rats. *Hear. Res.* 216–217, 154–167.

Ruscher, K., Shamloo, M., Rickhag, M., Ladunga, I., Soriano, L., Gisselsson, L., et al. (2011). The sigma-1 receptor enhances brain plasticity and functional recovery after experimental stroke. *Brain* 134, 732–746.

Rutkowski, R. G., and Weinberger, N. M. (2005). Encoding of learned importance of sound by magnitude of representational area in primary auditory cortex. *Proc. Natl. Acad. Sci. U.S.A.* 102, 13664–13669.

Rybalko, N., Suta, D., Nwabueze-Ogbo, F., and Syka, J. (2006). Effect of auditory cortex lesions on the discrimination of frequency-modulated tones in rats. *Eur. J. Neurosci.* 23, 1614–1622.

Saatman, K. E., Creed, J., and Raghupathi, R. (2010). Calpain as a therapeutic target in traumatic brain injury. *Neurotherapeutics* 7, 31–42.

Saldana, E., Feliciano, M., and Mugnaini, E. (1996). Distribution of descending projections from primary auditory neocortex to inferior colliculus mimics the topography of intracollicular projections. *J. Comp. Neurol.* 371, 15–40.

Schilling, S. H., Hjelmeland, A. B., Radiloff, D. R., Liu, I. M., Wakeman, T. P., Fielhauer, J. R., et al. (2009). NDRG4 is required for cell cycle progression and survival in glioblastoma cells. *J. Biol. Chem.* 284, 25160–25169.

Schlicker, E., and Morari, M. (2000). Nociceptin/orphanin FQ and neurotransmitter release in the central nervous system. *Peptides* 21, 1023–1029.

Schmittgen, T. D., and Livak, K. J. (2008). Analyzing real-time PCR data by the comparative C(T) method. *Nat. Protoc.* 3, 1101–1108.

Schnaar, R. L., and Lopez, P. H. (2009). Myelin-associated glycoprotein and its axonal receptors. *J. Neurosci. Res.* 87, 3267–3276.

Semple, M. N., and Kitzes, L. M. (1985). Single-unit responses in the inferior colliculus: different consequences of contralateral and ipsilateral auditory stimulation. *J. Neurophysiol.* 53, 1467–1482.

Sgorbissa, A., Benetti, R., Marzinotto, S., Schneider, C., and Brancolini, C. (1999). Caspase-3 and caspase-7 but not caspase-6 cleave Gas2 in vitro: implications for microfilament reorganization during apoptosis. *J. Cell. Sci.* 112(Pt 23), 4475–4482.

Shoudai, K., Nonaka, K., Maeda, M., Wang, Z. M., Jeong, H. J., Higashi, H., et al. (2007). Effects of various K+ channel blockers on spontaneous glycine release at rat spinal neurons. *Brain Res.* 1157, 11–22.

Smart, S. L., Bosma, M. M., and Tempel, B. L. (1997). Identification of the delayed rectifier potassium channel, Kv1.6, in cultured astrocytes. *Glia* 20, 127–134.

Stevens, B., Allen, N. J., Vazquez, L. E., Howell, G. R., Christopherson, K. S., Nouri, N., et al. (2007). The classical complement cascade mediates CNS synapse elimination. *Cell* 131, 1164–1178.

Sudhof, T. C., and Rothman, J. E. (2009). Membrane fusion: grappling with SNARE and SM proteins. *Science* 323, 474–477.

Sun, X., Xia, Q., Lai, C. H., Shum, D. K., Chan, Y. S., and He, J. (2007). Corticofugal modulation of acoustically induced Fos expression in the rat auditory pathway. *J. Comp. Neurol.* 501, 509–525.

Sweeney, S. T., and Davis, G. W. (2002). Unrestricted synaptic growth in spinster-a late endosomal protein implicated in TGF-beta-mediated synaptic growth regulation. *Neuron* 36, 403–416.

Takahashi, K., Yamada, M., Ohata, H., Honda, K., Yamada, M. (2005). Ndrg2 promotes neurite outgrowth of NGF-differentiated PC12 cells. *Neurosci. Lett.* 388, 157–162.

Turrigiano, G. (2012). Homeostatic synaptic plasticity: local and global mechanisms for stabilizing neuronal function. *Cold Spring Harb. Perspect. Biol.* 4, a005736. doi:10.1101/cshperspect.a005736

Uchida, Y., Nakano, S., Gomi, F., and Takahashi, H. (2011). Up-regulation of calsyntenin-3 by beta-amyloid increases vulnerability of cortical neurons. *FEBS Lett.* 585, 651–656.

Vale, C., and Sanes, D. H. (2002). The effect of bilateral deafness on excitatory and inhibitory synaptic strength in the inferior colliculus. *Eur. J. Neurosci.* 16, 2394–2404.

Vemuganti, R., Kalluri, H., Yi, J. H., Bowen, K. K., and Hazell, A. S. (2006). Gene expression changes in thalamus and inferior colliculus associated with inflammation, cellular stress, metabolism and structural damage in thiamine deficiency. *Eur. J. Neurosci.* 23, 1172–1188.

Vitureira, N., Andres, R., Perez-Martinez, E., Martinez, A., Bribian, A., Blasi, J., et al. (2010). Podocalyxin is a novel polysialylated neural adhesion protein with multiple roles in neural development and synapse formation. *PLoS ONE* 5, e12003. doi:10.1371/journal.pone.0012003

Wang, H., Turner, J. G., Ling, L., Parrish, J. L., Hughes, L. F., and Caspary, D. M. (2009a). Age-related changes in glycine receptor subunit composition and binding in dorsal cochlear nucleus. *Neuroscience* 160, 227–239.

Wang, H., Brozoski, T. J., Turner, J. G., Ling, L., Parrish, J. L., Hughes, L. F. et al. (2009b). Plasticity at glycinergic synapses in dorsal cochlear nucleus of rats with behavioral evidence of tinnitus. *Neuroscience* 164, 747–759.

Wieloch, T., and Nikolich, K. (2006) Mechanisms of neural plasticity following brain injury. *Curr. Opin. Neurobiol.* 16, 258–264.

Yanagisawa, H., Miyashita, T., Nakano, Y., and Yamamoto, D. (2003). HSpin1, a transmembrane protein interacting with Bcl-2/Bcl-xL, induces a caspase-independent autophagic cell death. *Cell Death Differ.* 10, 798–807.

Yata, K., Oikawa, S., Sasaki, R., Shindo, A., Yang, R., Murata, M., et al. (2011). Astrocytic neuroprotection through induction of cytoprotective molecules; a proteomic analysis of mutant P301S tau-transgenic mouse. *Brain Res.* 1410, 12–23.

Yiu, G., and He, Z. (2003). Signaling mechanisms of the myelin inhibitors of axon regeneration. *Curr. Opin. Neurobiol.* 13, 545–551.

Youle, R. J., and Karbowski, M. (2005). Mitochondrial fission in apoptosis. *Nat. Rev. Mol. Cell Biol.* 6, 657–663.

Zhang, Y., Suga, N., and Yan, J. (1997). Corticofugal modulation of frequency processing in bat auditory system. *Nature* 387, 900–903.

Conflict of Interest Statement: The authors declare that the research was conducted in the absence of any commercial or financial relationships that could be construed as a potential conflict of interest.

Received: 22 May 2012; accepted: 29 October 2012; published online: 26 November 2012.

*Citation: Clarkson C, Herrero-Turrión MJ and Merchán MA (2012) Cortical auditory deafferentation induces long-term plasticity in the inferior colliculus of adult rats: microarray and qPCR analysis. Front. Neural Circuits **6**:86. doi: 10.3389/fncir.2012.00086*

APPENDIX

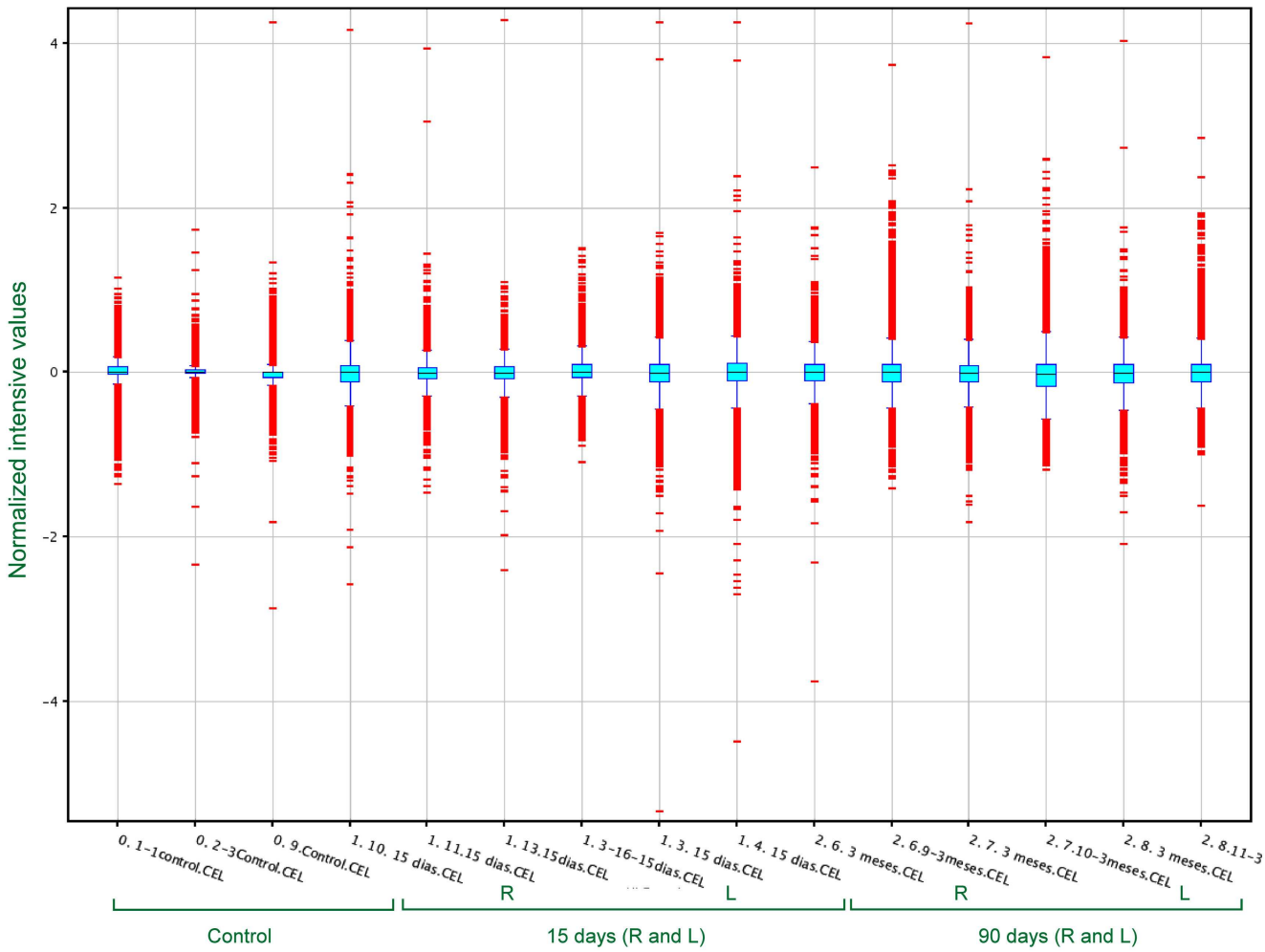

FIGURE A1 | Sample quality control. Box whisker diagram showing the data distribution of each of the samples. The diagram shows the dispersion of each of the samples [control, 15 and 90 days post-lesion; inferior colliculus right (R) and left (L)] and the degree of similarity between replicas.

frontiers in
NEURAL CIRCUITS

HYPOTHESIS AND THEORY ARTICLE
published: 28 June 2012
doi: 10.3389/fncir.2012.00042

Approaches to the study of neural coding of sound source location and sound envelope in real environments

Shigeyuki Kuwada*, Brian Bishop and Duck O. Kim

Department of Neuroscience, University of Connecticut Health Center, Farmington, CT, USA

Edited by:
Eric D. Young, Johns Hopkins University, USA

Reviewed by:
Adrian Rees, University of Newcastle, UK
Nicholas A. Lesica, University College London, UK

****Correspondence:***
Shigeyuki Kuwada, Department of Neuroscience, University of Connecticut Health Center, Farmington, CT 06030, USA.
e-mail: shig@neuron.uchc.edu

The major functions of the auditory system are recognition (what is the sound) and localization (where is the sound). Although each of these has received considerable attention, rarely are they studied in combination. Furthermore, the stimuli used in the bulk of studies did not represent sound location in real environments and ignored the effects of reverberation. Another ignored dimension is the distance of a sound source. Finally, there is a scarcity of studies conducted in unanesthetized animals. We illustrate a set of efficient methods that overcome these shortcomings. We use the virtual auditory space method (VAS) to efficiently present sounds at different azimuths, different distances and in different environments. Additionally, this method allows for efficient switching between binaural and monaural stimulation and alteration of acoustic cues singly or in combination to elucidate neural mechanisms underlying localization and recognition. Such procedures cannot be performed with real sound field stimulation. Our research is designed to address the following questions: Are IC neurons specialized to process what and where auditory information? How does reverberation and distance of the sound source affect this processing? How do IC neurons represent sound source distance? Are neural mechanisms underlying envelope processing binaural or monaural?

Keywords: AM envelope processing, inferior colliculus, sound localization, auditory distance, reverberation

INTRODUCTION

The goal here is to describe our approach to the study of neural mechanisms that underlie spatial and envelope coding of sounds in the mammalian auditory system. The ability to recognize and to localize a sound are the major functions of the auditory system. A key feature for recognition is the amplitude modulation (AM) envelopes present in natural sounds (Plomp, 1983). Key features for localization are interaural time (ITD) and level (ILD) differences and spectral cues that depend on sound source locations (Rayleigh, 1907; Blauert, 1997).

It is well established that sounds are transformed by the head and body (aka, head-related transfer function, HRTF) as well as by the acoustic environment (aka, binaural room transfer function, BRTF) in which they occur. Thus, it is surprising that the bulk of neural studies of envelope processing and localization used sounds that were delivered through headphones that lacked the important acoustic features created by HRTFs and BRTFs.

Despite decades of research devoted to the study of binaural cues in sound localization (see reviews by Palmer and Kuwada, 2005; Yin and Kuwada, 2010), there are relatively few studies that have investigated localization sensitivity in sound fields, either directly or through virtual auditory space (VAS) techniques. Even these studies have several shortcomings. First, the bulk of the studies were conducted under anesthesia which is known to alter binaural processing in the inferior colliculus (IC) (Kuwada et al., 1989; Tollin et al., 2004; D'Angelo et al., 2005). The findings using barbiturate anesthesia are consistent with the well known fact that barbiturates potentiate GABA-mediated inhibition (Barker and Ransom, 1978). Second, the bulk of the studies (exception: Sterbing et al., 2003; Behrend et al., 2004; Slee and Young, 2011) tested sound localization only in the frontal field resulting in an incomplete and perhaps inaccurate description of a neuron's spatial receptive field. Third, these studies did not systematically test the effects of stimulus level. Although it is generally recognized that azimuth tuning broadens with increasing stimulus level, the magnitude of broadening and the level tolerance of different neurons is poorly understood. Fourth, the bulk of the studies did not examine azimuth tuning to binaural and monaural stimulation (exception: Delgutte et al., 1999; Poirier et al., 2003). The extent to which azimuth tuning to binaural stimulation is disrupted under monaural stimulation indicates the importance of binaural cues. Fifth, the effect of sound source distance on neural responses is essentially ignored despite strong behavioral evidence linking reverberation to distance localization accuracy (Zahorik, 2002). Finally, the bulk of the studies (exception: Devore et al., 2009; Devore and Delgutte, 2010) have investigated spatial tuning in anechoic environments whereas real sound fields contain reverberations to different degrees. The above deficiencies collectively constitute a major void in our understanding of neural coding of sound source location in the auditory system.

Analogously, the bulk of neural studies of envelope processing used sounds delivered through headphones that lacked sound source location in an acoustic environments (see review by Joris et al., 2004). Lesica and Grothe (2008) studied temporal processing of natural sounds in IC neurons, with and without ambient noise, but not the effects of reverberation *per se*. Sayles and Winter

(2008) studied pitch processing in cochlear nucleus neurons in reverberation with a primary focus on monaural mechanisms in pitch processing. Despite decades of studies of neurons sensitive to AM envelopes using headphones little is known about the effects of sound source azimuth, distance and reverberation on envelope processing, an essential component of communication sounds.

Here, we outline our approach to alleviating these deficiencies. Our findings are from neurons in the IC of the unanesthetized rabbit. We used VAS stimuli because it is an efficient way to control the sound source location, and also used sinusoidally amplitude modulated (SAM) noise in order to simultaneously investigate neural sensitivities to location (where is the sound?) and envelope (what is the sound?). The VAS method has proven to be a valid method to study spatial tuning in humans (Wightman and Kistler, 1989; Kulkarni and Colburn, 1998) and in neurons (Keller et al., 1998; Behrend et al., 2004; Campbell et al., 2006). We summarize key findings of our recent published study (Kuwada et al., 2011) that focused on azimuth tuning in an anechoic environment. We also describe responses of an example neuron that outlines our approach to simultaneously examine azimuth tuning and envelope sensitivity at different distances and in different reverberant environments. Our research is designed to address the following questions: Are IC neurons specialized to process what and where auditory information? How does reverberation and distance of the sound source affect this processing? How do IC neurons represent sound source distance? Are neural mechanisms underlying envelope processing binaural or monaural?

MATERIALS AND METHODS

This study was approved by the University of Connecticut Health Center Animal Care Committee and was conducted according to the NIH guidelines. Neural recordings were performed in two female Dutch-Belted rabbits (1.5–2.5 kg). Surgical and experimental procedures have been described previously (e.g., Kuwada et al., 1987; Batra et al., 1989).

SURGICAL PROCEDURES

All surgery was performed using aseptic techniques on rabbits with clean external ears. Under anesthesia (sedation: 1 mg/kg, acepromazine, sc: anesthesia: 1.5–4% isoflurane inhalation, 1–2 liters/min oxygen) a brass plate with three threaded inserts (6–32) was anchored to the skull using screws and dental acrylic. At this time, custom ear molds were made for sound delivery using dental impression compound (Reprosil). After acoustic measurements were made (see below), the animal was again anesthetized, and a small craniotomy ($\sim$3 $\times$ 4 mm) was made over cortex overlying the IC. The craniotomy was bathed in chlorohexidine (0.2%), a cotton pellet placed over it and then covered with dental impression compound.

RECORDING PROCEDURES AND DATA COLLECTION

All recordings were conducted in a double-walled, sound-insulated chamber. The rabbit's body was wrapped with a surgical towel held in place with wide elastic bandages (ACE). It was then seated in a padded cradle, and further restrained using nylon straps. The wrap and straps provided only mild restraint, their primary purpose being to discourage movements that might cause injury to the rabbit. The rabbit's head was fixed by mating the head appliance to a horizontal bar with 6–32 threaded socket head screws. Once the rabbit was secured, the craniotomy was exposed. To eliminate possible pain or discomfort during the penetration of the electrode, a topical anesthetic (marcaine) was applied to the dura for approximately 5 min and then removed by aspiration. With these procedures, rabbits remained still for a period of 2 or more h, an important requirement for neural recording. Each rabbit participated in daily recording sessions over a period of several months. A session was terminated if the rabbit showed any signs of discomfort. The rabbit's comfort was a priority both for ethical reasons and because movements made it difficult to record from neurons.

Action potentials were recorded extracellularly with tungsten-in-glass microelectrodes (tip diameter of $\sim$1 μm, impedances of 5–10 MΩ). The recordings were amplified at a gain of 2–20 k and filtered (0.3–3 kHz) and the action potentials were triggered using a window discriminator (BAK Electronics, Germantown, MD) and timed relative to the stimulus onset with an accuracy of 10 μs. The recordings were from single-units or clusters comprising 2–3 units based on the height of their action potentials evaluated visually. The waveforms of the neural signals and the stimuli were recorded continuously (Adobe Audition) which allowed for subsequent re-examination.

MEASUREMENTS OF HRTFs/BRTFs

Each rabbits' HRTFs were measured in our anechoic chamber (9 $\times$ 4 $\times$ 4 m, anechoic between 0.11 and 200 kHz). The BRTFs were measured in our moderately reverberant room (6 $\times$ 5 $\times$ 3 m, T60 = 825 ms) and our highly reverberant room (6.5 $\times$ 5.7 $\times$ 5 m, T60 = 2,500 ms). These transfer functions were measured with an acoustic point source positioned at nine distances (10–160 cm in half doubling steps) and 25 azimuths ($\pm$165° in 15° steps) all at 0° elevation. These measurements were made with a blocked meatus approach with a miniature microphone (Knowles FG 23629) placed deep in each ear canal. This is done in the unanesthetized state and is highly advantageous because several sessions are required to complete these acoustic measurements and multiple sessions using anesthesia would increases the probability of death. The procedures for measuring HRTFs are described in (Kim et al., 2010).

GENERATION OF VIRTUAL AUDITORY SPACE (VAS) STIMULI

In various experiments we have used broad-band noise, 1-octave wide noise-based on the neuron's best frequency (BF), and 1-octave wide SAM noise. In all cases the source signals are filtered with the individual rabbit's HRTFs and BRTFs for each ear and each sound source location and acoustic environment. Comparisons of the SAM envelope at the source and in the ear canals in the different acoustic environments allow us to determine the acoustic transformations that the SAM envelope undergoes between the source and the ear canals for various source locations. This yields an acoustic modulation transfer function (MTF) of the system comprising the rabbit and sound source in a specific environment. In general, modulation gain in reverberation decreased with increasing modulation frequency and with

increasing distance. Furthermore, the ear opposite to the sound source was most affected.

These VAS stimuli are delivered to each ear through a Beyer DT-770 earphone coupled to a sound tube embedded in custom-fitted ear mold to form a closed system. The distal end of the sound tube is at the same location as the microphone used in the HRTF/BRTF measurements. The frequency responses of the sound delivery systems for the two ears is measured using a microphone (B&K type 4133) connected to a probe tube that extended to the tip of the sound delivery tube. Compensation of the system's frequency response was incorporated into sound stimuli.

In addition to the VAS stimuli, we stimulated both ears, as well as the ipsilateral and contralateral ear separately with sequential pure tones (100 ms every 300 ms repeated 4 times (4 ms rise/fall) between 0.2 and 32 kHz in 1/3rd octave steps at a constant level (30–70 dB SPL, re: 20 μPa) to measure each unit's BF). The tone frequencies were randomly presented.

RESULTS

AZIMUTH TUNING IN AN ANECHOIC ENVIRONMENT

Figure 1 shows our general approach to measure azimuth tuning of IC neurons. We first determined the unit's BF by delivering tone bursts as described above at 50 dB SPL. To determine the unit's threshold for VAS stimulation we set the azimuth to −75° and varied the stimulus level of a broad-band noise over a 70 dB range in 10 dB steps. We then delivered VAS stimuli at levels between 10 and 50 dB above its threshold for azimuths ranging between ±150° in 15° steps. These were delivered in random order and the response to the initial azimuth was discarded to minimize adaptation effects. **Figure 1A** displays this unit's response as dot rasters to binaural (red), ipsilateral (green) and contralateral stimulation, each 100 ms in duration and separated by 300 ms. This sequence was repeated 4 times at each azimuth. It is clear that this neuron is excited by binaural and contralateral ear stimulation and inhibited by ipsilateral ear stimulation. The strongest driven activity to binaural stimulation was in the contralateral sound field (i.e., 0–150°), whereas that to contralateral ear stimulation was omnidirectional. These features are also plotted in **Figure 1B** where the neural firing rates are plotted in Cartesian coordinates. These plots reflect the response during the stimulus burst. The spontaneous activity indicated was the mean of the last 100 ms of the silent period after binaural, ipsilateral and contralateral ear stimulation. In **Figure 1C**, the binaural and contralateral ear alone azimuth functions are displayed in polar coordinates after subtraction of the mean spontaneous activity. If this subtraction yielded negative values, we made the azimuth function positive by adding a constant (absolute value of the minimum). Although recordings were not made at 180° we interpolated and smoothed the function over the full range. Also shown are the actual responses at each azimuth for binaural (red open circle) and contralateral ear stimulation (blue open circles) after subtraction of the spontaneous rate. This neuron displays binaural facilitation (binaural response > contralateral ear response) in the contralateral sound field and binaural suppression (binaural response < contralateral ear response) in the ipsilateral sound field. The interpolation to ±180° allowed the calculation of vector strength (VS) and vector angle (VA) as a measure of the neuron's sharpness of azimuth tuning and its preferred azimuth direction (magenta line), respectively. VS and angle measures were computed using the original definition of Goldberg and Brown (1969). Best azimuth (BA, azimuth at the maximum response) is included as a comparison with VA.

Figure 2 displays the distributions of VS (red), VA (blue), and BA (black) to binaural stimulation as a function of stimulus level (upper five rows). In the bottom row is a summary of these distributions in the form of the median ± semi-interquartile range. The sharpness of azimuth tuning broadened with increasing stimulus level as evidenced by VS decreasing from 0.44 to 0.22. The direction of azimuth tuning as measured by VA shifted from −68° at 10 dB to −93° at 50 dB and its distribution became tighter with increasing stimulus level. BA shifted from −62° to −82°, but its distribution became broader with stimulus level.

The degree of level tolerance in azimuth tuning varies among neurons. We investigated the hypothesis that certain neurons exhibit level tolerant azimuth tuning, i.e., no significant changes in VS and VA across stimulus levels. To test this hypothesis we first selected units that were tested at 10, 30, and 50 dB and rank ordered this sample based on VS at 50 dB. We then subdivided it into three sub populations, top 10%, top 50%, and all for stimulus levels at 10, 30, and 50 dB and averaged their rate azimuth functions (**Figure 3**, top 3 rows). For each population, VS and VA are plotted in the fourth and fifth rows, respectively. For binaural stimulation, VS and angle remain relatively stable across stimulus level in all three subpopulations. There were no statistically significant differences in vector strength across stimulus level (1 way repeated measures ANOVA, $F = 4.74$, df $= 122$, $p > 0.01$) for the top 37% of the units, indicating level tolerant behavior for this subpopulation. There were no statistically significant differences in vector angle across stimulus level ($F = 4.93$, df $= 50$, $p > 0.01$) for only the top 15% of the units. Thus, if we require no significant change in both vector strength and vector angle across stimulus levels, then the top 15% satisfied this combined criterion. For all three subpopulations, the mean VA was in the frontal contralateral quarter field (∼−60°) at 10 dB and shifted backwards to ∼−90° at 30 and 50 dB. This shift reflects the fact that the responses in the back and front quarter fields become more symmetrical at higher stimulus levels.

In contrast, contralateral ear stimulation yielded VSs and angles comparable to binaural stimulation only at 10 dB and precipitously decreased with increasing stimulus level. VA at 30 and 50 dB are not plotted because the VS did not reach our minimal criterion (≥0.15). When the response was greater to binaural stimulation than to contralateral ear stimulation, we defined the difference summated over a region of azimuth to be the binaural facilitation area; when the relationship was reversed, we defined the difference to be the binaural suppression area. These measures are same as those used by Delgutte et al. (1999). The facilitation and suppression areas for our three subpopulations are plotted as a function of stimulus level in the bottom row (**Figure 3**). The strengths of binaural suppression and facilitation increased with increasing stimulus level. The combined consequence of this facilitation and suppression is to confine the azimuth tuning to the contralateral field over a wide range of stimulus levels.

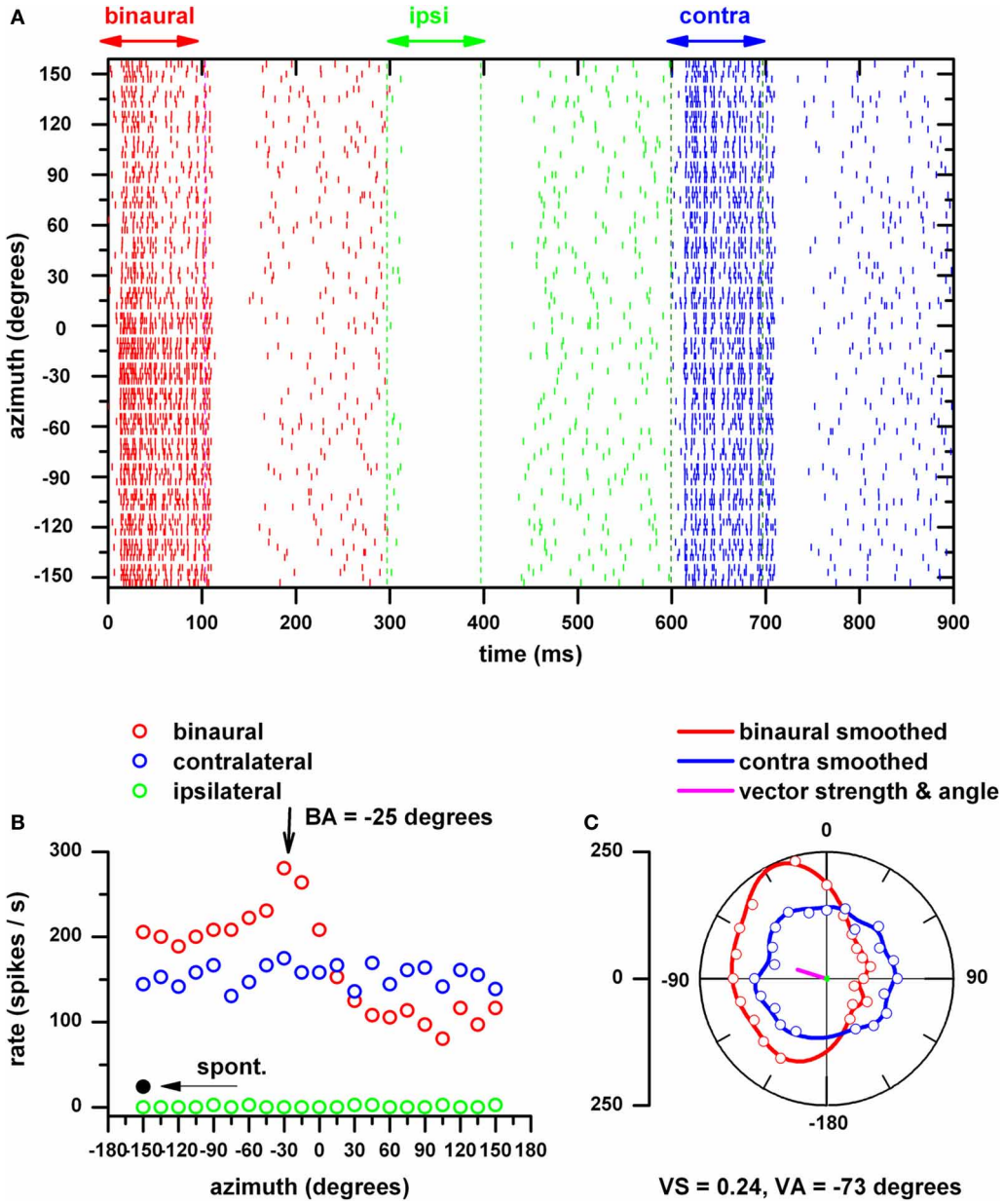

FIGURE 1 | Procedure for assessing a neuron's azimuth tuning. **(A)** IC neurons response (BF = 3.2 kHz) to wide-band noise (0.2–20 kHz) presented to both ears (red), to the ipsilateral ear (green) and to the contralateral ear, each 100 ms in duration and separated by 300 ms as dot rasters at azimuths between ±150° in 15° steps at a maximum of 45 dB SPL. This sequence was repeated 4 times at each azimuth and azimuths were presented in a random order. Negative azimuths correspond to sounds in the contralateral hemifield (re: recording site). **(B)** Firing rates as a function of azimuth are plotted in Cartesian coordinates for binaural, ipsilateral and contralateral stimulation. These plots reflect the response during the stimulus burst and the mean spontaneous firing rate (measured during the last 100 ms of each silent period) is indicated. **(C)** The azimuth functions in **(B)** after subtraction of the mean spontaneous firing rate and after interpolation and smoothing over a ±180° range are displayed in polar coordinates. Also shown are the actual responses at each azimuth for binaural (red open circle) and contralateral ear stimulation (blue open circles) after subtraction of the spontaneous rate. Vector strength (VS) and vector angle (VA) (magenta line) were calculated from the azimuth function to binaural stimulation and used as a measure of the neuron's sharpness of azimuth tuning (VS) and its preferred azimuth direction (VA). Best azimuth (BA, azimuth at the maximum response) is included as a comparison with VA.

CODING OF AZIMUTH AND ENVELOPE IN REVERBERANT ENVIRONMENTS

These experiments simultaneously examine coding of location and envelope in different acoustic environments by presenting SAM noise at different azimuths and distances. The carrier sound was a 1-octave wide noise centered at the unit's BF. Using this noise band we determine the unit's threshold by presenting sounds from 0 to 70 dB SPL binaurally and separately to

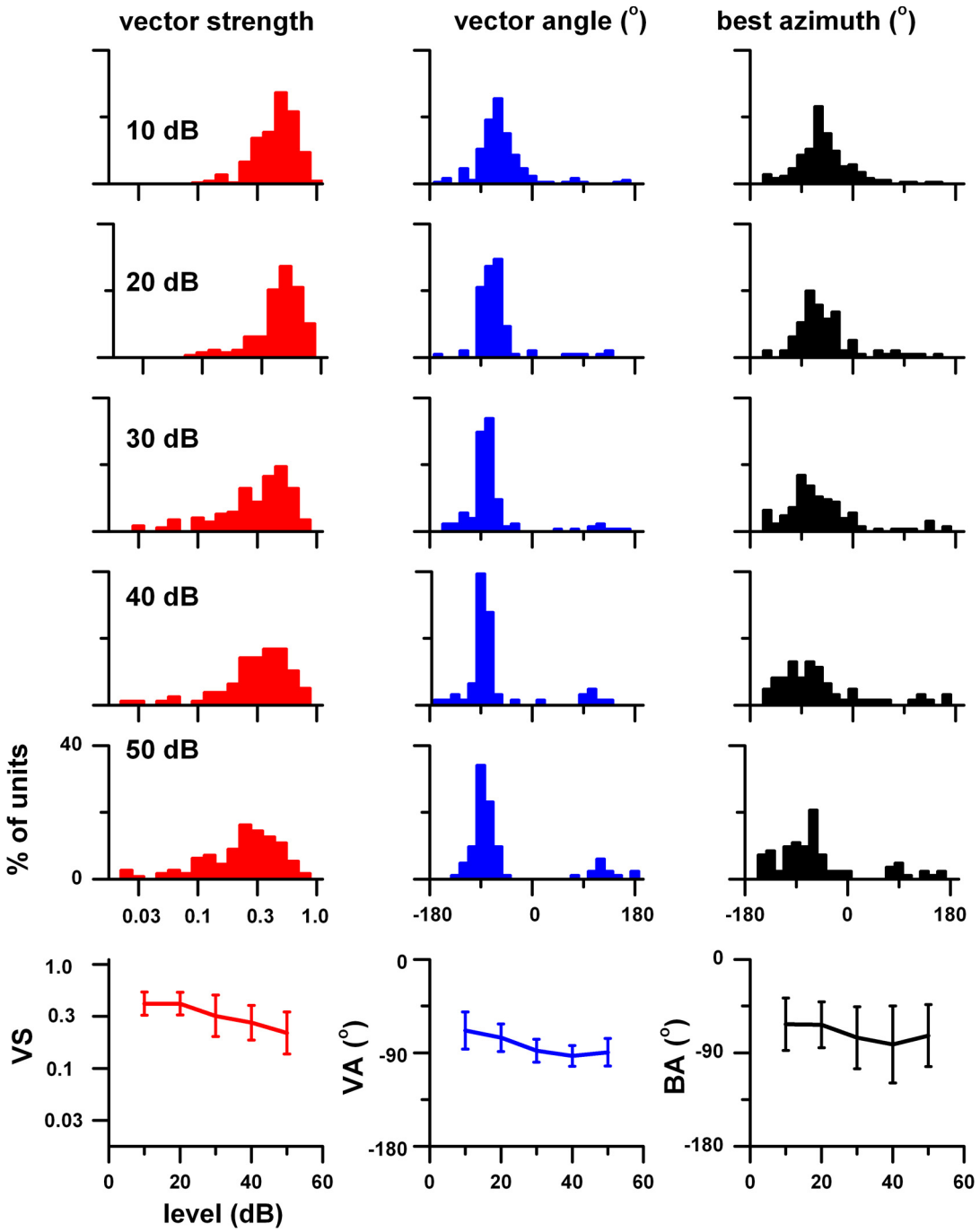

FIGURE 2 | ***Top 5 rows*****: Distributions of vector strength (VS, red), vector angle (VA, blue), and best azimuth (BA, black) at stimulus levels between 10 and 50 dB (re: neural threshold).** *Bottom row*: Plot of the median and semi-interquartile range of these three measures of azimuth tuning as a function of stimulus level. The sample size was: 10 dB, 178 units; 20 dB, 102 units; 30 dB, 155 units; 40 dB, 74 units; 50 dB, 115 units. Adapted from Kuwada et al. (2011).

the ipsilateral and contralateral ear at −75° azimuth (a value that approximates the BA of most units). We then determine the unit's azimuth functions to binaural, ipsilateral, and contralateral ear stimulation at 30 dB above threshold at a distance of 80 cm in the anechoic environment. Next, we determined its MTF to modulation frequencies between 2 and 512 Hz in 1-octave steps (100% depth) at the unit's BA, at a distance of 80 cm, and a level 30 dB above its threshold. Based on its MTF, the modulation depth of its best modulation frequency was varied between 12.5 and 100% in 3 dB

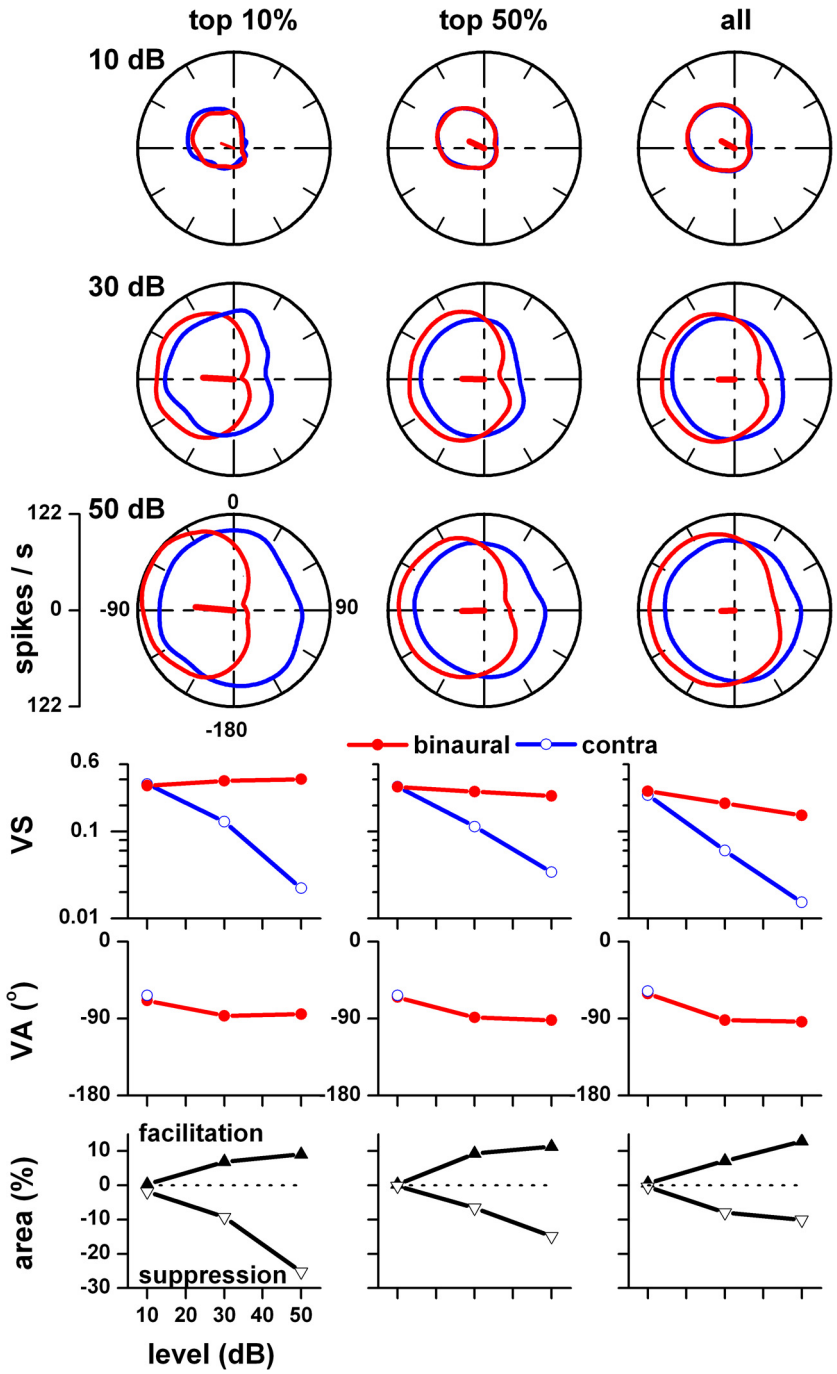

FIGURE 3 | Population azimuth tuning to binaural (red) and contralateral ear alone (blue) stimulation as a function of stimulus level. Only those units that were tested to both binaural and contralateral ear stimulation at 10, 30, and 50 dB ($n = 75$) were included. This sample was rank ordered based on vector strength to binaural stimulation at 50 dB and subdivided into three sub populations, top 10%, top 50%, and all. Top three rows: 10, 30, and 50 dB (re: threshold). Fourth row: vector strength versus stimulus level. Fifth row: vector angle versus stimulus level. Vector angles were plotted only when the corresponding vector strength was ≥0.15. Fifth row: binaural facilitation (solid triangles) and binaural suppression (open triangles) versus stimulus level. Adapted from Kuwada et al. (2011).

steps. We then selected a modulation depth that was approximately in the center of its range that produced significant ($p < 0.001$) neural synchrony based on circular statistics (Mardia, 1972).

Figure 4 displays the response of an IC neuron that had a BF of 628 Hz to the above type SAM noise (444–888 Hz, 32 Hz modulation, 70.7% depth, 50 dB SPL). The top dot raster displays the unit's response to the above stimuli presented binaurally

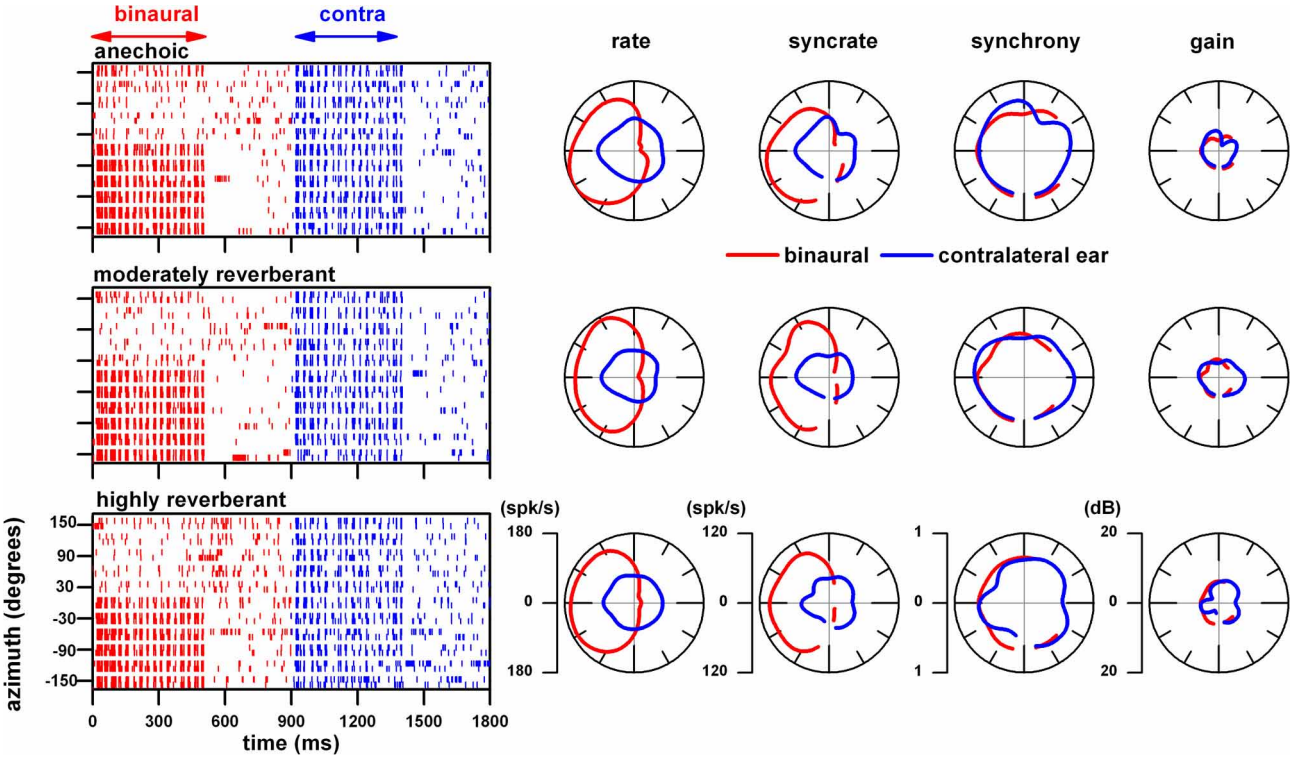

FIGURE 4 | Response of an IC neuron (BF = 628 Hz) to a SAM 1-octave band noise delivered binaurally and to the contralateral ear alone as a function of azimuth at a fixed distance of 10 cm. *Top row*: responses to different azimuths in the anechoic condition displayed as spike time rasters. The corresponding polar plots represent four measures derived from the responses depicted in the raster plot: rate, syncrate (synchrony × rate), synchrony, and neural modulation gain (20 × log (2 × neural synchrony/modulation depth in the ear). *Middle row*: responses of the same neuron to sounds in the moderately reverberant chamber. *Bottom row*: responses of the same neuron to sounds in the highly reverberant chamber. Responses to binaural stimulation are depicted as red and those to contralateral ear stimulation as blue. Stimulus parameters: 500 ms duration every 900 ms, 444–888 Hz band width, 32 Hz modulation frequency, 70.7% modulation depth, 30 dB above neural threshold (50 dB SPL).

(red) and to the contralateral ear alone (blue) in the anechoic environment at our closest sound source distance (10 cm). The corresponding polar plots of azimuth represent four measures derived from the responses depicted in the dot raster. The rate azimuth function shows that the binaural response is strongest in the contralateral sound field whereas those to the contralateral ear are omnidirectional. The combination of binaural facilitation in the contralateral sound field and the binaural suppression in the ipsilateral sound field described in **Figures 1**, **3** is also present here. The remaining 3 polar plots represent the neuron's response to the envelope. Because recordings were not made at 180° and because these measures require significant synchrony to the envelope, these polar plots have a gap at this azimuth. The syncrate measure is defined as a product of synchrony to the modulation envelope and firing rate. The significance of syncrate depends entirely on whether synchrony is significant or not ($p < 0.001$). The synchrony azimuth function was similar between binaural and contralateral stimulation. Consequently, the syncrate azimuth function resembled the rate azimuth function. The rightmost polar plot represents the neural modulation gain. It is defined as 20 × log (2 × neural synchrony/modulation depth in the ear) and was approximately 5 dB for binaural and monaural stimulation.

The middle and bottom row of **Figure 4** represents the responses of the same neuron to the same stimuli but presented in our moderately reverberant and highly reverberant environments, respectively. At this close distance (10 cm), the responses in these two reverberant environments are remarkably similar to each other and to those in the anechoic condition.

In **Figure 5** we display the responses of the same neuron to the same stimuli but at a further sound source distance (80 cm). In contrast to the responses at 10 cm (**Figure 4**), at 80 cm, the acoustic environment had noticeable effects on spike rate, syncrate, synchrony and gain azimuth functions.

The responses in the anechoic environment at 80 cm (**Figure 5**, top row) are very similar to those at 10 cm (**Figure 4**, top row). However, the responses in the two reverberant environments at 80 cm (**Figure 5**, middle and bottom rows) differed considerably from those in the anechoic condition (**Figure 5**, top row) and from those at 10 cm (**Figure 4**, middle and bottom rows). In reverberation, the firing rate to binaural stimulation in the contralateral sound field decreased relative to the anechoic condition. Additionally, the binaural facilitation and suppression in the rate azimuth function in the moderately reverberant environment was less pronounced and binaural suppression in the highly reverberant environment was absent. The firing rate to contralateral ear

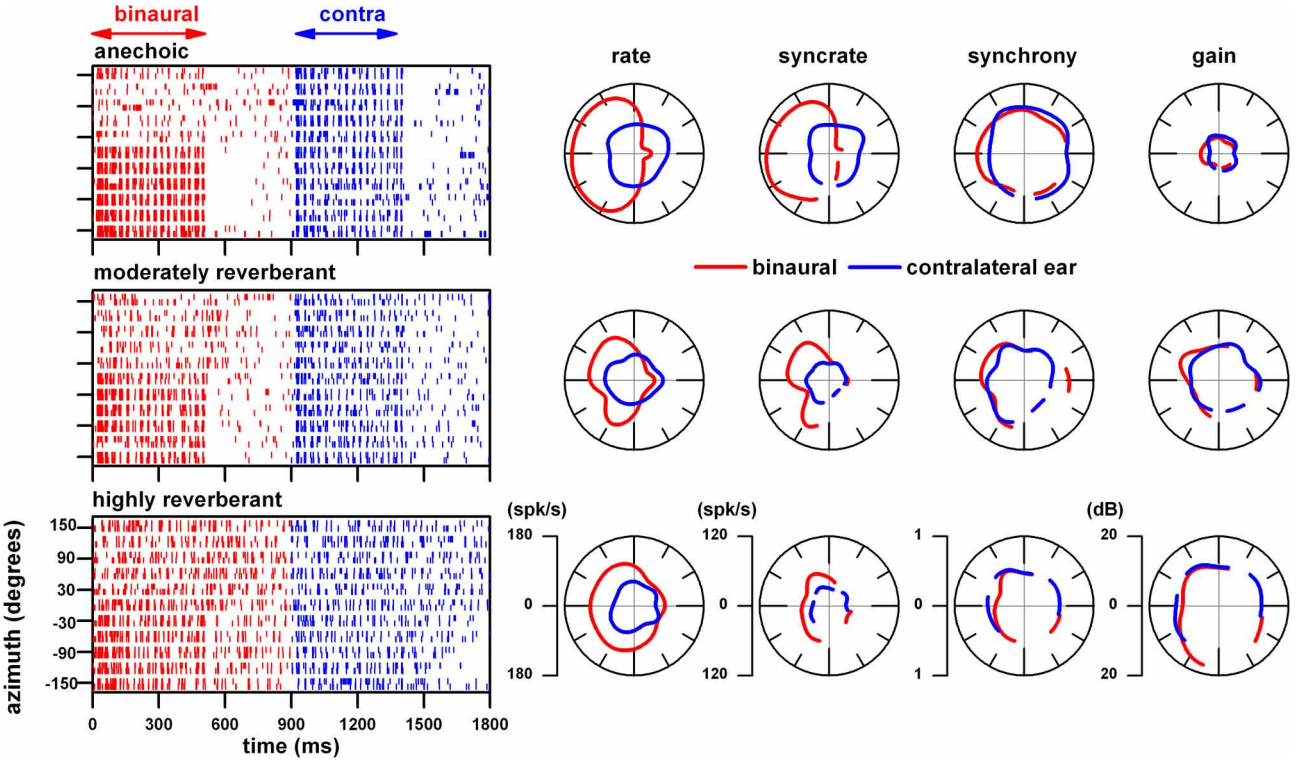

FIGURE 5 | Response of the same neuron in Figure 4 to the same stimuli but at a distance of 80 cm. Same format as **Figure 4**.

stimulation remained omnidirectional in all three environments. The synchrony to the modulation envelope to both binaural and monaural stimulation declined and was the weakest in the highly reverberant environment. Surprisingly, in the moderately reverberant environment, the mean neural modulation gain in the contralateral sound field to both binaural and contralateral ear stimulation reached 10 dB and further increased to 13 dB in the highly reverberant environment. These gains represent enhancements of 5 and 8 dB over the anechoic condition.

The strong firing rate of this neuron to binaural stimulation in the anechoic environment was confined to the contralateral sound field (**Figures 5**, **6**, top rows). In order to elucidate mechanisms underlying this azimuth tuning we altered the ITD cue in the fine structure by decorrelating the sounds between the two ears. In **Figure 6**, using the same neuron as in **Figures 4**, **5**, we show the effect of delivering decorrelated sounds to the ears. The upper row shows the dot rasters and polar plots when the same normal sound was delivered to the ears in our anechoic chamber at a distance of 160 cm. Note that as in the 10 and 80 cm distances (**Figures 4**, **5**, top rows), the azimuth rate response is primarily confined to the contralateral sound field whereas that to monaural stimulation is omnidirectional. In all cases, binaural facilitation in the contralateral sound field and binaural suppression in the ipsilateral sound field is prominent. However, when the sound to the ears is uncorrelated (**Figure 6**, bottom row), azimuth tuning to binaural stimulation becomes omnidirectional and very similar to monaural stimulation. The fact that azimuth tuning to binaural stimulation was destroyed is strong evidence that ITD plays the key role in azimuth tuning for this neuron. ILD play a negligible role because this cue is <1 dB at 160 cm in frequency range used (1-octave centered at 628 Hz). Synchrony to binaural and monaural stimulation remained relatively unchanged under the decorrelated condition. This indicates that the envelope coding mechanism for this neuron is monaural.

We recorded the responses of this neuron not only at 10 cm (**Figure 4**), 80 cm (**Figure 5**) and 160 cm (**Figure 6**), but also at sound source distances of 20 and 40 cm. **Figure 7** provides a summary of our findings at sound source distances between 10 and 160 cm. Plots E–L reflect the responses averaged in the contralateral sound field. The stimulus level was adjusted at each distance such that the absolute level was kept constant.

The sharpness of azimuth tuning as reflected by azimuth VS is plotted as a function of distance for binaural (panel A) and contralateral ear (panel B) stimulation. The VS to binaural stimulation remained constant across distance in the anechoic environment whereas it systematically decreased with distance in reverberation and most dramatically in the highly reverberant environment. This decrease in azimuth tuning with distance to binaural stimulation in the reverberant environments is likely due to a decrease in interaural correlation of the stimulus with distance. From 10 to 160 cm, the mean interaural correlation measured in the contralateral sound field systematically decreased from 0.98 to 0.74 in the highly reverberant environment, whereas it remained constant (0.997 ± 0.002) in the anechoic condition. Recall that decorrelation destroyed azimuth tuning (**Figure 6**).

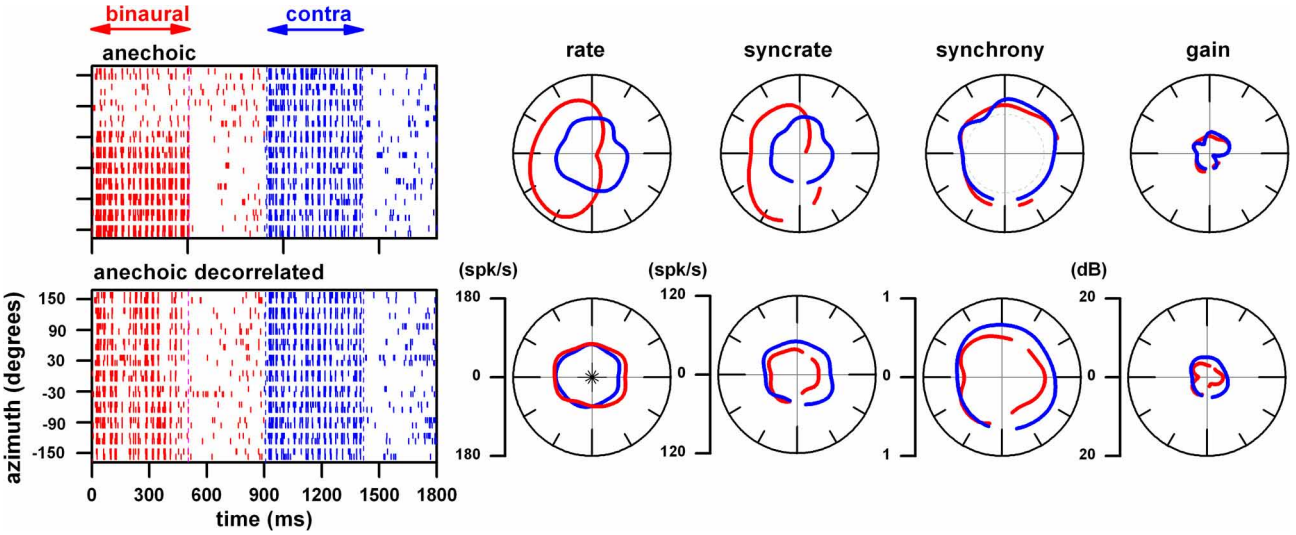

FIGURE 6 | Effect of presenting noise to each ear that is uncorrelated. Same neuron as in **Figures 5**, **6**. *Top row*: responses when the normal, correlated sound was delivered to the ears in our anechoic chamber at a distance of 160 cm. *Bottom row*: responses when the sound to the ears is uncorrelated.

Thus, the decrease in correlation with distance in reverberation parallels the observed decrease in azimuth VS, and the constant and high interaural correlation seen in the anechoic condition parallels the observed constant and strong azimuth VS.

Although azimuth VS to binaural stimulation decreased with distance in reverberation, azimuth VA remained relatively constant with distance (panel C). For contralateral stimulation (panel B), the azimuth VS across conditions was too small to meet our criterion for azimuth tuning (VS = 0.15). Consequently, none are plotted for azimuth VA to contralateral stimulation (panel D).

The mean rates to binaural and contralateral ear stimulation in the contralateral sound field are plotted in panels E and F, respectively. The rate to binaural stimulation remained relatively constant with distance in the anechoic environment (black) but gradually declined in the two reverberant environments to a maximum decline of 30% at 160 cm in the highly reverberant condition (blue). The decrease in rate to binaural stimulation in the contralateral sound field with distance in the reverberant environments is likely due to a decrease in interaural correlation as outlined above. Specifically, this decline in firing rate is consistent with decreasing interaural correlation with distance. The response rate to contralateral ear stimulation was about half that to binaural stimulation and there was no clear relationship with distance in the two reverberant environments. However, the firing rates averaged across distance in the moderate and highly reverberant environments were 9 and 14% less, respectively, compared to that in the anechoic environment.

The syncrate functions across distance to binaural and contralateral ear stimulation are shown in panels G and H, respectively. At 160 cm in the highly reverberant environment, syncrate was not significant to contralateral ear stimulation. Thus, this point is absent in panel H. The syncrate functions show a steeper decline with distance than the rate functions because both rate and synchrony decrease with distance.

Synchrony to binaural and contralateral ear stimulation remained essentially constant in the anechoic condition. In reverberation, synchrony remained essentially constant for distances up to 40 cm and then declined (panels I and J). At 160 cm in the highly reverberant environment, synchrony was not significant to contralateral ear stimulation. Thus, this point is absent in panel J.

The neural modulation gain as a function of distance is plotted in panels K and L for binaural and contralateral ear stimulation, respectively. The mean gain across distance in the anechoic condition for both types of stimulation was 5 dB. However, at far distances it increased with reverberation to a maximum of 15 dB to binaural stimulation and 13 dB to contralateral ear stimulation.

DISCUSSION

We have provided a synopsis of our previous findings on azimuth coding in anechoic conditions (Kuwada et al., 2011). We have also provided an example neuron illustrating our current approach that investigates coding of sound source distance, azimuth and AM envelope in anechoic and reverberant environments. In the Introduction we described the motivation for our research strategy and four questions that our strategy is designed to answer. We will discuss in turn these questions and the answers provided by our example neuron.

ARE IC NEURONS SPECIALIZED TO PROCESS WHAT AND WHERE AUDITORY INFORMATION?

The example neuron was able to code both azimuth and envelope (e.g., **Figures 4**–**7**), i.e., not specialized for envelope or azimuth coding. Other neurons show varying degrees of specialization for envelope or azimuth coding.

It has been firmly established that different specialized auditory cortical areas mediate recognition (anterior auditory field, AAF) and localization (posterior auditory field, PAF) of sounds

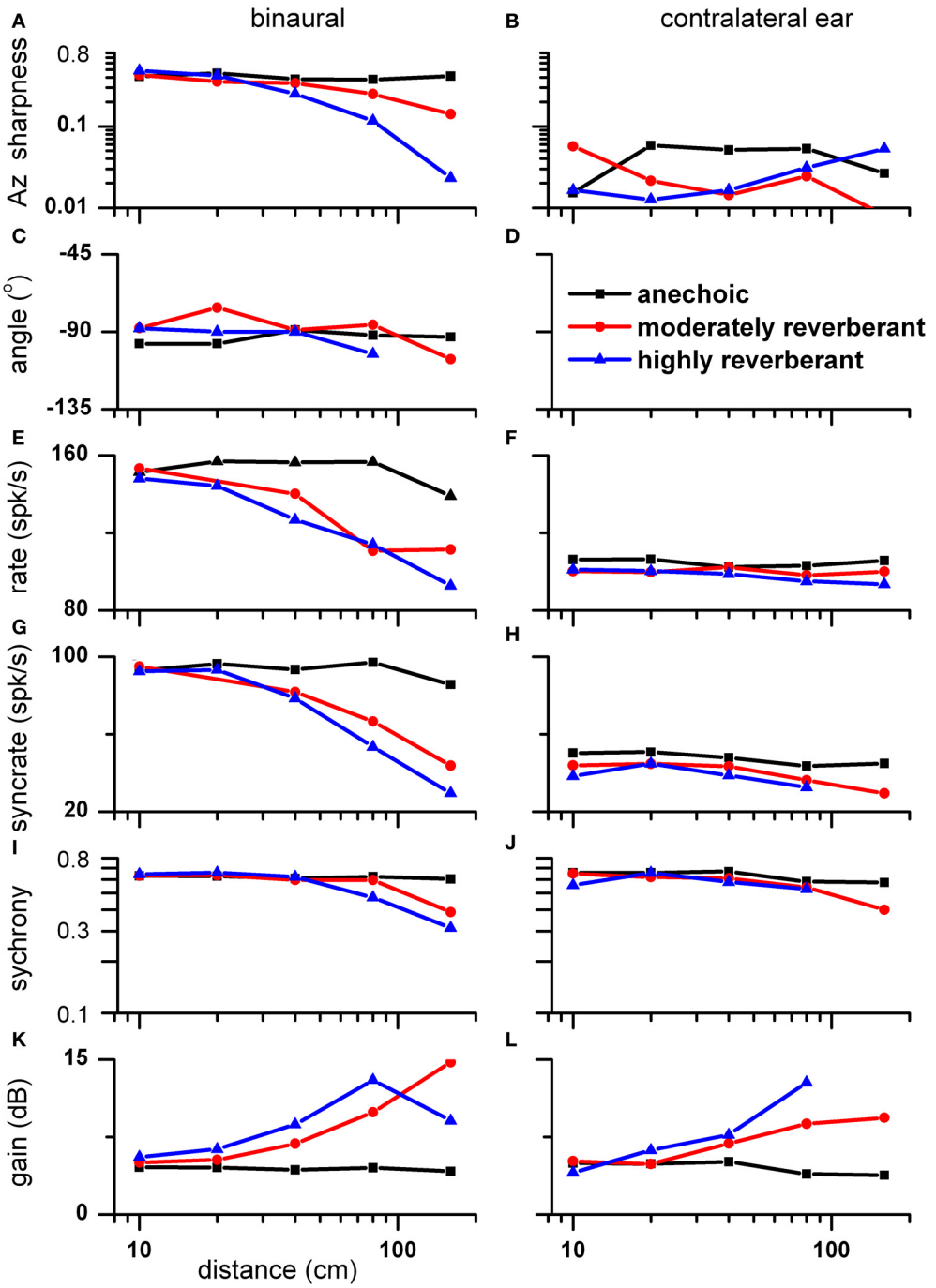

FIGURE 7 | Azimuth tuning and envelope sensitivity as a function of distance (10-160 cm) for the same neuron in Figures 4, 6, 7. Plots E–L reflect the responses averaged in the contralateral sound field. **(A,B)** Sharpness of azimuth tuning as measured by vector strength of rate azimuth function versus distance and environment to binaural **(A)** and contralateral ear stimulation **(B)**. **(C,D)** Direction of azimuth tuning as measured by vector angle of rate azimuth function. **(E,F)** Firing rate. **(G,H)** Syncrate, i.e., product of synchrony and rate. **(I,J)** Synchrony to the modulation envelope. **(K,L)** Neural modulation gain.

(Lomber and Malhotra, 2008). Their finding that the PAF mediates localization is consistent with the finding that neural population coding of space in the PAF is more accurate than that in the primary auditory field (AI) (Stecker et al., 2003). It remains to be determined whether neurons in the PAF are poor in coding envelope and whether neurons in the AAF are specialized for pattern recognition and poor in coding location as predicted by Lomber and Malhotra (2008).

The specialized processing in the cortex may be created *de novo*. This would be the logical case if IC neurons are not

specialized for what and where processing. On the other hand, the specialized processing in the cortex may reflect inputs from specialized neuron in the IC that project selectively via the thalamus to the appropriate cortical areas.

HOW DOES REVERBERATION AND DISTANCE OF THE SOUND SOURCE AFFECT NEURAL PROCESSING OF ENVELOPE AND AZIMUTH?

In response to binaural stimulation the synchrony to envelope in our example neuron showed immunity to reverberation for distances between 10 and 40 cm and a modest reduction in reverberation at 80 and 160 cm. Similarly, the sharpness of azimuth tuning showed immunity to reverberation for distances between 10 and 40 cm. However, at 160 cm in the highly reverberant environment the azimuth tuning was markedly degraded. This degradation is likely due to a reduction in interaural correlation caused by reverberation at far distances. This interpretation was supported by the same neuron's response to decorrelated stimuli (**Figure 6**). These observations are consistent with the finding that the ITD sensitivity of IC neurons systematically decreased with decreasing interaural correlation (Yin et al., 1987). In a classic model of sound localization (Jeffress, 1948), ITD sensitive neurons act like coincidence detectors. Thus, when the signals at the two ears are in-phase there is binaural facilitation and when they are out-of-phase there is binaural suppression (Goldberg and Brown, 1969). VS of azimuth tuning is a reflection of the strength of binaural facilitation and suppression. The decrease in interaural correlation with increasing distance in reverberation is a consequence of a decrease in the direct to reverberant energy ratio (D/R) with increasing distance (Zahorik, 2002).

HOW DO IC NEURONS REPRESENT SOUND SOURCE DISTANCE?

The firing rate of the example neuron to binaural stimulation in reverberation systematically decreased with increasing distance thus providing a rate code for distance. In contrast, in the anechoic condition, its rate was nearly constant. This decrease was not due to changes in stimulus level because it was kept constant across distance. Interestingly, the same mechanism proposed for changes in azimuth tuning, coincidence detection governed by strength of interaural correlation, produces a sensitivity to sound source distance. The fact that this neuron's firing rate to monaural stimulation remained nearly constant across distance is consistent with our view that a binaural mechanism (i.e., coincidence detection) underlies its ability to code sound source distance. Providing a distance code is a new role played by the coincidence detection mechanism that has not been described. The neural coding of sound source distance is vastly understudied and our strategy is designed to fill this void.

ARE NEURAL MECHANISMS UNDERLYING ENVELOPE PROCESSING BINAURAL OR MONAURAL?

Our example neuron displayed similar envelope synchrony to binaural and monaural stimulation. Relatedly, neural modulation gain of this neuron was high in reverberation at far distances and was essentially the same to binaural or monaural stimulation. These properties imply that monaural mechanisms underlie this neuron's envelope synchrony and modulation gain. This was validated by the finding that synchrony remained unchanged when the signals at the two ears were decorrelated (**Figure 6**).

Measurements in the auditory nerve (Kim et al., 1990; Joris and Yin, 1992) using conventional earphone stimuli indicate gains between −10 and 10 dB. In the olivocochlear efferent auditory nerve fibers, modulation gains were higher (up to 12 dB) than in afferent nerve fibers (Gummer et al., 1988). In the cochlear nucleus higher gains (often reaching 10–13 dB) were found (Frisina et al., 1990; Kim et al., 1990). In the IC even higher gains (reaching 15–20 dB) were found (Rees and Moller, 1983; Rees and Palmer, 1989; Krishna and Semple, 2000).

The larger gains in the reverberant compared to the anechoic condition in this example neuron may represent a compensatory monaural mechanism that counteracts the deleterious effects of reverberation. In a related behavioral study, it was shown that human AM sensitivity in reverberation was more sensitive than predicted by the acoustical MTFs (Zahorik et al., 2011). At an azimuth of −90° this enhancement effect was present whether the stimulation was monaural or binaural. However, a binaural advantage was seen at 0°, consistent with previous results (Danilenko, 1969).

ACKNOWLEDGMENTS

We thank Xi Bie, Jason Sijie Wang, Caitlin Alex, and Daniel Condit for their assistance. This study was supported by NIH grant R01 DC002178.

REFERENCES

Barker, J. L., and Ransom, B. R. (1978). Pentobarbitone pharmacology of mammalian central neurones grown in tissue culture. *J. Physiol.* 280, 355–372.

Batra, R., Kuwada, S., and Stanford, T. R. (1989). Temporal coding of envelopes and their interaural delays in the inferior colliculus of the unanesthetized rabbit. *J. Neurophysiol.* 61, 257–268.

Behrend, O., Dickson, B., Clarke, E., Jin, C., and Carlile, S. (2004). Neural responses to free field and virtual acoustic stimulation in the inferior colliculus of the guinea pig. *J. Neurophysiol.* 92, 3014–3029.

Blauert, J. (1997). *Spatial Hearing: the Psychophysics of Human Sound Localization,* Revised Edn. Cambridge, MA: MIT Press.

Campbell, R. A., Doubell, T. P., Nodal, F. R., Schnupp, J. W., and King, A. J. (2006). Interaural timing cues do not contribute to the map of space in the ferret superior colliculus: a virtual acoustic space study. *J. Neurophysiol.* 95, 242–254.

D'Angelo, W. R., Sterbing, S. J., Ostapoff, E. M., and Kuwada, S. (2005). Role of GABAergic inhibition in the coding of interaural time differences of low-frequency sounds in the inferior colliculus. *J. Neurophysiol.* 93, 3390–3400.

Danilenko, L. (1969). [Binaural hearing in non-stationary diffuse sound field]. *Kybernetik* 6, 50–57.

Delgutte, B., Joris, P. X., Litovsky, R. Y., and Yin, T. C. (1999). Receptive fields and binaural interactions for virtual-space stimuli in the cat inferior colliculus. *J. Neurophysiol.* 81, 2833–2851.

Devore, S., and Delgutte, B. (2010). Effects of reverberation on the directional sensitivity of auditory neurons across the tonotopic axis: influences of interaural time and level differences. *J. Neurosci.* 30, 7826–7837.

Devore, S., Ihlefeld, A., Hancock, K., Shinn-Cunningham, B., and Delgutte, B. (2009). Accurate sound localization in reverberant environments is mediated by robust encoding of spatial cues in the auditory midbrain. *Neuron* 62, 123–134.

Frisina, R. D., Smith, R. L., and Chamberlin, S. C. (1990). Encoding of amplitude modulation in the gerbil cochlear nucleus: I. A hierarchy of enhancement. *Hear. Res.* 44, 99–122.

Goldberg, J. M., and Brown, P. B. (1969). Response properties of binaural neurons of dog superior olivary complex to dichotic tonal stimuli: some physiological mechanisms of sound localization. *J. Neurophysiol.* 32, 613–636.

Gummer, M., Yates, G. K., and Johnstone, B. M. (1988). Modulation transfer function of efferent neurons in the guinea pig cochlea. *Hear. Res.* 36, 41–52.

Jeffress, L. A. (1948). A place code theory of sound localization. *J. Comp. Physiol. Psychol.* 41, 35–39.

Joris, P. X., Schreiner, C. E., and Rees, A. (2004). Neural processing of amplitude-modulated sounds. *Physiol. Rev.* 84, 541–577.

Joris, P. X., and Yin, T. C. (1992). Responses to amplitude-modulated tones in the auditory nerve of the cat. *J. Acoust. Soc. Am.* 91, 215–232.

Keller, C. H., Hartung, K., and Takahashi, T. T. (1998). Head-related transfer functions of the barn owl: measurement and neural responses. *Hear. Res.* 118, 13–34.

Kim, D. O., Bishop, B., and Kuwada, S. (2010). Acoustic cues for sound source distance and azimuth in rabbits, a racquetball and a rigid spherical model. *J. Assoc. Res. Otolaryngol.* 11, 541–557.

Kim, D. O., Sirianni, J. G., and Chang, S. O. (1990). Responses of DCN-PVCN neurons and auditory nerve fibers in unanesthetized decerebrate cats to AM and pure tones: analysis with autocorrelation/power-spectrum. *Hear. Res.* 45, 95–113.

Krishna, B. S., and Semple, M. N. (2000). Auditory temporal processing: responses to sinusoidally amplitude-modulated tones in the inferior colliculus. *J. Neurophysiol.* 84, 255–273.

Kulkarni, A., and Colburn, H. S. (1998). Role of spectral detail in sound-source localization. *Nature* 396, 747–749.

Kuwada, S., Batra, R., and Stanford, T. R. (1989). Monaural and binaural response properties of neurons in the inferior colliculus of the rabbit: effects of sodium pentobarbital. *J. Neurophysiol.* 61, 269–282.

Kuwada, S., Bishop, B., Alex, C., Condit, D., and Kim, D. (2011). Spatial tuning to sound-source azimuth in the inferior colliculus of the unanesthetized rabbit. *J. Neurophysiol.* 106, 2698–2708.

Kuwada, S., Stanford, T. R., and Batra, R. (1987). Interaural phase-sensitive units in the inferior colliculus of the unanesthetized rabbit: effects of changing frequency. *J. Neurophysiol.* 57, 1338–1360.

Lesica, N. A., and Grothe, B. (2008). Efficient temporal processing of naturalistic sounds. *PLoS ONE* 3:e1655. doi: 10.1371/journal.pone.0001655

Lomber, S. G., and Malhotra, S. (2008). Double dissociation of 'what' and 'where' processing in auditory cortex. *Nat. Neurosci.* 11, 609–616.

Mardia, K. (1972). *Statistics of Directional Data.* New York, NY: Academic Press.

Palmer, A., and Kuwada, S. (2005). "Binaural and spatial coding in the inferior colliculus," in *The Inferior Colliculus,* eds J. A. Winer and C. E. Schreiner (New York, NY: Springer-Verlag), 377–410.

Plomp, R. (1983). "The role of modulations in hearing," in *Hearing: Physiological Bases and Psychophysics,* eds R. Klinke and R. Hartmann (New York, NY: Springer Verlag), 270–275.

Poirier, P., Samson, F. K., and Imig, T. J. (2003). Spectral shape sensitivity contributes to the azimuth tuning of neurons in the cat's inferior colliculus. *J. Neurophysiol.* 89, 2760–2777.

Rayleigh, L. (1907). On our perception of sound direction. *Philos. Mag.* 13, 214–232.

Rees, A., and Moller, A. R. (1983). Responses of neurons in the inferior colliculus of the rat to AM and FM tones. *Hear. Res.* 10, 301–330.

Rees, A., and Palmer, A. R. (1989). Neuronal responses to amplitude-modulated and pure-tone stimuli in the guinea pig inferior colliculus, and their modification by broadband noise. *J. Acoust. Soc. Am.* 85, 1978–1994.

Sayles, M., and Winter, I. M. (2008). Reverberation challenges the temporal representation of the pitch of complex sounds. *Neuron* 58, 789–801.

Slee, S. J., and Young, E. D. (2011). Information conveyed by inferior colliculus neurons about stimuli with aligned and misaligned sound localization cues. *J. Neurophysiol.* 106, 974–985.

Stecker, G. C., Mickey, B. J., Macpherson, E. A., and Middlebrooks, J. C. (2003). Spatial sensitivity in field PAF of cat auditory cortex. *J. Neurophysiol.* 89, 2889–2903.

Sterbing, S. J., Hartung, K., and Hoffmann, K. P. (2003). Spatial tuning to virtual sounds in the inferior colliculus of the Guinea pig. *J. Neurophysiol.* 90, 2648–2659.

Tollin, D. J., Populin, L. C., and Yin, T. C. (2004). Neural correlates of the precedence effect in the inferior colliculus of behaving cats. *J. Neurophysiol.* 92, 3286–3297.

Wightman, F. L., and Kistler, D. J. (1989). Headphone simulation of free-field listening. II: psychophysical validation. *J. Acoust. Soc. Am.* 85, 868–878.

Yin, T., and Kuwada, S. (2010). "Binaural localization cues," in *The Auditory Brain,* Vol. 2, eds A. R. Palmer and A. Rees (Oxford, UK: Oxford University Press), 271–302.

Yin, T. C., Chan, J. C., and Carney, L. H. (1987). Effects of interaural time delays of noise stimuli on low-frequency cells in the cat's inferior colliculus. III. Evidence for cross-correlation. *J. Neurophysiol.* 58, 562–583.

Zahorik, P. (2002). Assessing auditory distance perception using virtual acoustics. *J. Acoust. Soc. Am.* 111, 1832–1846.

Zahorik, P., Kim, D. O., Kuwada, S., Anderson, P. W., Brandewie, E., and Srinivasn, N. K. (2011). "Amplitude Modulation Detection by Human Listeners in Sound Fields," in *Proceedings of Meetings on Acoustics*, Vol. 12, (Seattle, WA), 050005.

Conflict of Interest Statement: The authors declare that the research was conducted in the absence of any commercial or financial relationships that could be construed as a potential conflict of interest.

Received: 24 April 2012; accepted: 13 June 2012; published online: 28 June 2012.

Citation: Kuwada S, Bishop B and Kim DO (2012) Approaches to the study of neural coding of sound source location and sound envelope in real environments. Front. Neural Circuits ***6****:42. doi: 10.3389/fncir.2012.00042*

frontiers in
NEURAL CIRCUITS

ORIGINAL RESEARCH ARTICLE
published: 10 May 2013
doi: 10.3389/fncir.2013.00090

Frequency response areas in the inferior colliculus: nonlinearity and binaural interaction

Jane J. Yu and Eric D. Young*

Center for Hearing and Balance, Department of Biomedical Engineering, Johns Hopkins University, Baltimore, MD, USA

Edited by:
Manuel S. Malmierca, University of Salamanca, Spain

Reviewed by:
Nicholas A. Lesica, Ludwig-Maximilians-University Munich, Germany
Christine Portfors, Washington State University, USA

***Correspondence:**
Eric D. Young, Center for Hearing and Balance, Department of Biomedical Engineering, Johns Hopkins University, 505 Traylor Bldg., 720 Rutland Ave., Baltimore, MD 21205, USA.
e-mail: eyoung@jhu.edu

The tuning, binaural properties, and encoding characteristics of neurons in the central nucleus of the inferior colliculus (CNIC) were investigated to shed light on nonlinearities in the responses of these neurons. Results were analyzed for three types of neurons (I, O, and V) in the CNIC of decerebrate cats. Rate responses to binaural stimuli were characterized using a 1st- plus 2nd-order spectral integration model. Parameters of the model were derived using broadband stimuli with random spectral shapes (RSS). This method revealed four characteristics of CNIC neurons: (1) Tuning curves derived from broadband stimuli have fixed (i. e., level tolerant) bandwidths across a 50–60 dB range of sound levels; (2) 1st-order contralateral weights (particularly for type I and O neurons) were usually larger in magnitude than corresponding ipsilateral weights; (3) contralateral weights were more important than ipsilateral weights when using the model to predict responses to untrained noise stimuli; and (4) 2nd-order weight functions demonstrate frequency selectivity different from that of 1st-order weight functions. Furthermore, while the inclusion of 2nd-order terms in the model usually improved response predictions related to untrained RSS stimuli, they had limited impact on predictions related to other forms of filtered broadband noise [e. g., virtual-space stimuli (VS)]. The accuracy of the predictions varied considerably by response type. Predictions were most accurate for I neurons, and less accurate for O and V neurons, except at the lowest stimulus levels. These differences in prediction performance support the idea that type I, O, and V neurons encode different aspects of the stimulus: while type I neurons are most capable of producing linear representations of spectral shape, type O and V neurons may encode spectral features or temporal stimulus properties in a manner not easily explained with the low-order model. Supported by NIH grant DC00115.

Keywords: inferior colliculus, tuning, nonlinearity, binaural, model, random spectral shape, level tolerant, dynamic range

INTRODUCTION

The central nucleus of the inferior colliculus (CNIC) is an important site of convergence in the auditory system (Adams, 1979; Brunso-Bechtold et al., 1981; Winer, 2005). Ascending inputs to the CNIC terminate in tonotopically organized layers, but afferents from different brainstem sources innervate overlapping domains within the layers (Oliver et al., 1997; Henkel et al., 2003; Cant and Benson, 2008; Malmierca et al., 2009; Loftus et al., 2010). Despite the diversity of inputs, the cellular organization of CNIC is relatively homogeneous, with only a small number of morphological cell types that are not gathered into subnuclei or into an organized microstructure (Oliver and Morest, 1984; Malmierca et al., 1993; Ito and Oliver, 2012; Wallace et al., 2012). Studies of neurons' responses and electrophysiological characteristics are consistent with this anatomical evidence, in that neurons showing a relatively small number of response patterns are scattered throughout CNIC (e.g., Ramachandran et al., 1999; Sivaramakrishnan and Oliver, 2001).

The lack of distinct morphological cell types and organized microstructure suggests that progress on the representation of sound in the CNIC will depend on physiologically defined neuron classes. One basis for such classes is the pattern of frequency selectivity of CNIC neurons in response to tones (Davis, 2005). Tone responses can serve to define response classes; however, the most commonly encountered stimuli in the natural environment are broadband. Because tone responses typically do not accurately predict selectivity for broadband or natural stimuli (Nelken et al., 1997; Holmstrom et al., 2007; May et al., 2008), it seems important to derive models of spectral integration on the basis of responses to broadband stimuli.

The tuning of neurons to broadband sounds can be studied using a method like reverse correlation (De Boer and De Jongh, 1978; Aertsen and Johannesma, 1981) that derives an equivalent filter consistent with the neuron's responses to broadband or natural stimuli. In the CNIC, neurons have been characterized using the so-called spectro-temporal receptive field (STRF) which is based on the assumption that neurons perform a 1st-order (linear) spectro-temporal weighting of the stimulus (e.g., Klein et al., 2000; Theunissen et al., 2000; Escabi and Read, 2005; Eggermont, 2011). However there are a number of important questions remaining. The STRF has been successful in describing various aspects of neural responses [e.g., stimulus-dependence of

responses, (Theunissen et al., 2000); motion sensitivity, (Andoni and Pollak, 2011); spatial organization of response properties, (Chen et al., 2012); and comparison of response complexity between CNIC and auditory cortex, Atencio et al., 2012; etc.], but often STRFs do not predict the responses to test stimulus ensembles accurately (Machens et al., 2004; Versnel et al., 2009; Eggermont, 2011). Significant improvements in the models and in prediction have been made recently (Ahrens et al., 2008; Calabrese et al., 2011), but the reasons for the limited performance are not fully understood. In this work, we study three likely causes of limited prediction performance.

First, it seems likely that the performance of existing models is limited by the nonlinearity of auditory neural integration (Johnson, 1980; Christianson et al., 2008). Models have sometimes taken a "linear-nonlinear" form in which a 1st-order weighting of the stimulus is followed by a static nonlinearity to match the growth of response with stimulus level (Sharpee et al., 2004; Nagel and Doupe, 2006; Lesica and Grothe, 2008a). In other models, an input nonlinearity is postulated (most simply, using the log of the stimulus amplitude instead of the amplitude or power; Escabi et al., 2003; Ahrens et al., 2008), but nonlinearities intrinsic to the frequency response itself have not been considered.

Second, models have usually been studied at one or two sound levels only (but see Bandyopadhyay et al., 2007; Ahrens et al., 2008; Lesica and Grothe, 2008a; Pienkowski and Eggermont, 2011), while auditory nonlinearities often change significantly across sound levels (Nelken et al., 1997; Bandyopadhyay et al., 2007). For example, in the dorsal cochlear nucleus, neurons behave in a relatively linear manner at low sound levels, but exhibit nonlinearity at higher levels where so-called "type II" inhibitory interneurons are active. Thus there is a need for systematic examination of the effects of sound level on auditory spectral integration.

Finally, most studies of spectral representation in CNIC (and auditory cortex) have not investigated the separate contributions of the two ears in a systematic manner; stimulus presentations have been either monaural or free-field (but see Schnupp et al., 2001; Qiu et al., 2003). Thus, the possibility that nonlinear interactions occur between neural inputs from the two ears has also not been investigated sufficiently.

Here we describe spectral integration in three common response types of CNIC neurons (I, V, and O; Ramachandran et al., 1999) in unanesthetized (decerebrate) cats. The rate responses to broadband stimuli are used to construct weighting function models (Yu and Young, 2000; Young and Calhoun, 2005) that measure 1st and 2nd-order relationships between stimulus spectra and average discharge rates across a range of stimulus levels. Neural responses to the temporal aspects of the stimuli are not addressed in this paper. In the three response types, tuning observed in response to broadband stimuli is substantially more level tolerant than tuning to tones. Moreover, although contributions of the ipsilateral ear to neural responses are usually weak relative to contributions of the contralateral ear, they are still significant in many neurons. Finally, 2nd-order nonlinearities are significant and take a form that is poorly captured by the linear-nonlinear model. These results point the way for improvements in models of central auditory neurons. They also support previous suggestions (Davis, 2005) that the representation of stimuli in CNIC occurs in parallel pathways with characteristics that provide differing information about aspects of the stimulus.

MATERIALS AND METHODS

ANIMAL PREPARATION AND RECORDING

The experimental protocol was approved by the Johns Hopkins Animal Care and Use Committee. Data were obtained from eight adult male cats (3–4 kg) with clean ears and clear tympanic membranes. The cats were anesthetized with xylazine (2 mg im) plus ketamine (40 mg/kg im), then treated with dexamethasone (2–4 mg im) and atropine (0.1 mg im) to delay the onset of edema and minimize mucous secretions, respectively. A tracheostomy was performed to facilitate quiet breathing. Supplemental doses of ketamine (15 mg/kg iv) were given as needed during surgery. Body temperature was maintained between 37 and 40°C. A supracollicular decerebration was performed by aspiration. Anesthesia was then discontinued.

The ear canals were transected and hollow ear bars inserted to prepare for stimulus delivery. Polyethylene tubing (PE-200, approximately 40 cm in length) was inserted into each bulla to prevent static pressure buildup in the middle ear. A craniotomy was performed, tissue was aspirated, and dura was opened to expose the IC. In experiments that lasted several days, cats were given intravenous lactated ringers to maintain body fluids. Experiments were terminated when vascular pulsations or edema at the recording site prevented single neuron isolation. Animals were euthanized with a lethal intravenous injection of sodium pentobarbital.

An electrostatic speaker was coupled to each ear bar for stimulus delivery. The sound in each ear was calibrated near the tympanic membrane with a probe microphone. Sample acoustic calibrations are shown in **Figure 1A**.

A platinum-iridium microelectrode was inserted dorsoventrally into the IC (at an angle of 5–15° from vertical) under visual guidance, and single neurons were isolated from the amplified, filtered electrode signal using a Schmitt trigger. Each neuron was characterized by its best frequency (BF) and threshold in response to tones in the contralateral ear. Here, we define BF as the frequency at which a response is observed at the lowest sound level of the stimulus. The excitatory (E) or inhibitory (I) nature of the responses to contralateral and ipsilateral stimuli was determined by presenting monaural tones to each ear at BF. All neurons were binaural, although the responses of some neurons to ipsilateral stimuli were weak. Most neurons were EE or EI; that is, they were either excited by tones in both ears (EE), or excited by tones in the contralateral ear and inhibited by tones in the ipsilateral ear (EI).

Contralateral and ipsilateral response maps (shown below in **Figures 2–4**) were obtained by recording discharge rates in response to sequences of tones in the contralateral and ipsilateral ears, respectively. The frequencies of the tones in each ear were logarithmically spaced and spanned up to 4 octaves. Tone sequences were presented monaurally as 200-ms tone bursts, once per second, at fixed attenuation levels. Driven rates were averaged across the tone duration, and spontaneous rates were averaged

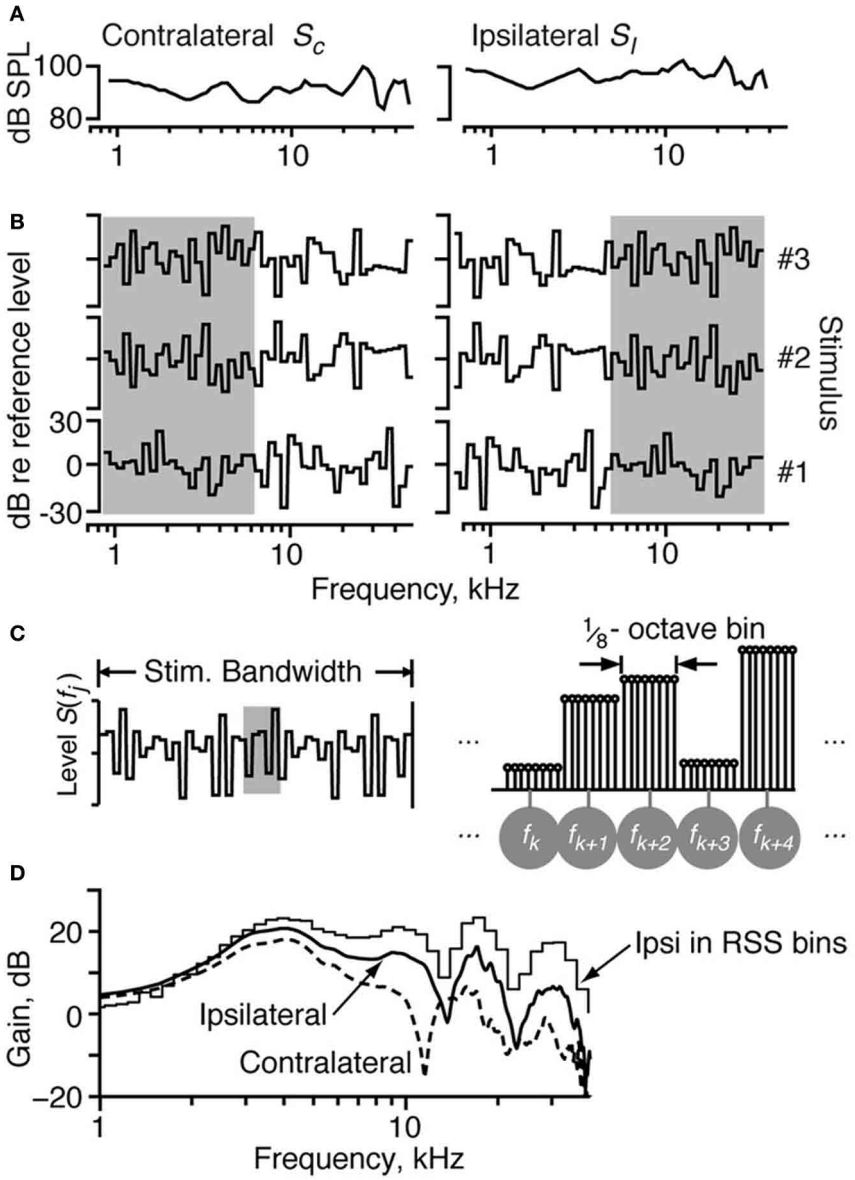

FIGURE 1 | The properties of the RSS stimuli. (A) The acoustic calibration of the two ears in one animal, showing the sound pressure level as a function of frequency at 0 dB attenuation. These were determined using a calibrated probe tube placed within 2 mm of the eardrum. The spectra of sounds were modified by filtering with these transfer functions. **(B)** Spectra of three example RSS stimuli, out of the set of 200, shown as the dB spectrum level vs. log frequency. The sound levels of individual frequency bins (of width 1/8 octave) are symmetrically distributed around a mean value of 0 dB, with SD 12 dB. The reference 0-dB sound level is varied with an attenuator, usually over a 50–70 dB range. Note that the spectra presented to the ipsilateral ear are frequency-shifted versions of the spectra presented to the contralateral ear (e.g., compare gray areas). **(C)** Spectral shape of the RSS stimuli in more detail. Each frequency bin consists of 8 tones, logarithmically spaced at 1/64 octave. Individual tones are shown in the line spectrogram at right, which corresponds to the shaded region of the stimulus spectrum at left. The eight tones in each bin (1/8 octave wide) have equal sound level. Frequencies of the bin centers are indicated by the symbols in gray circles. **(D)** Spectra of white noise filtered with two cat HRTFs. The ipsilateral and contralateral HRTFs approximate the spectral shapes in the ipsilateral and contralateral ears of a broadband noise stimulus played at 15° azimuth, 30° elevation. The stepped-function ("Ipsi in RSS bins") shows the stimulus energy for the ipsilateral spectrum in bins corresponding to the RSS stimuli at a sampling rate of 100 kHz.

across the last 400 ms of the stimulus-off period. Response maps were based on one presentation of each tone frequency at each sound level.

For the estimation and testing of weight-function models, broadband stimuli with random spectral shape (RSS) were presented to both ears simultaneously in 400-ms bursts, once per second, at fixed attenuation levels. Discharge rates were averaged across the 400-ms stimulus-on interval, and spontaneous rates were averaged across the last 400 ms of the stimulus-off intervals. Models were usually constructed from a single presentation of an

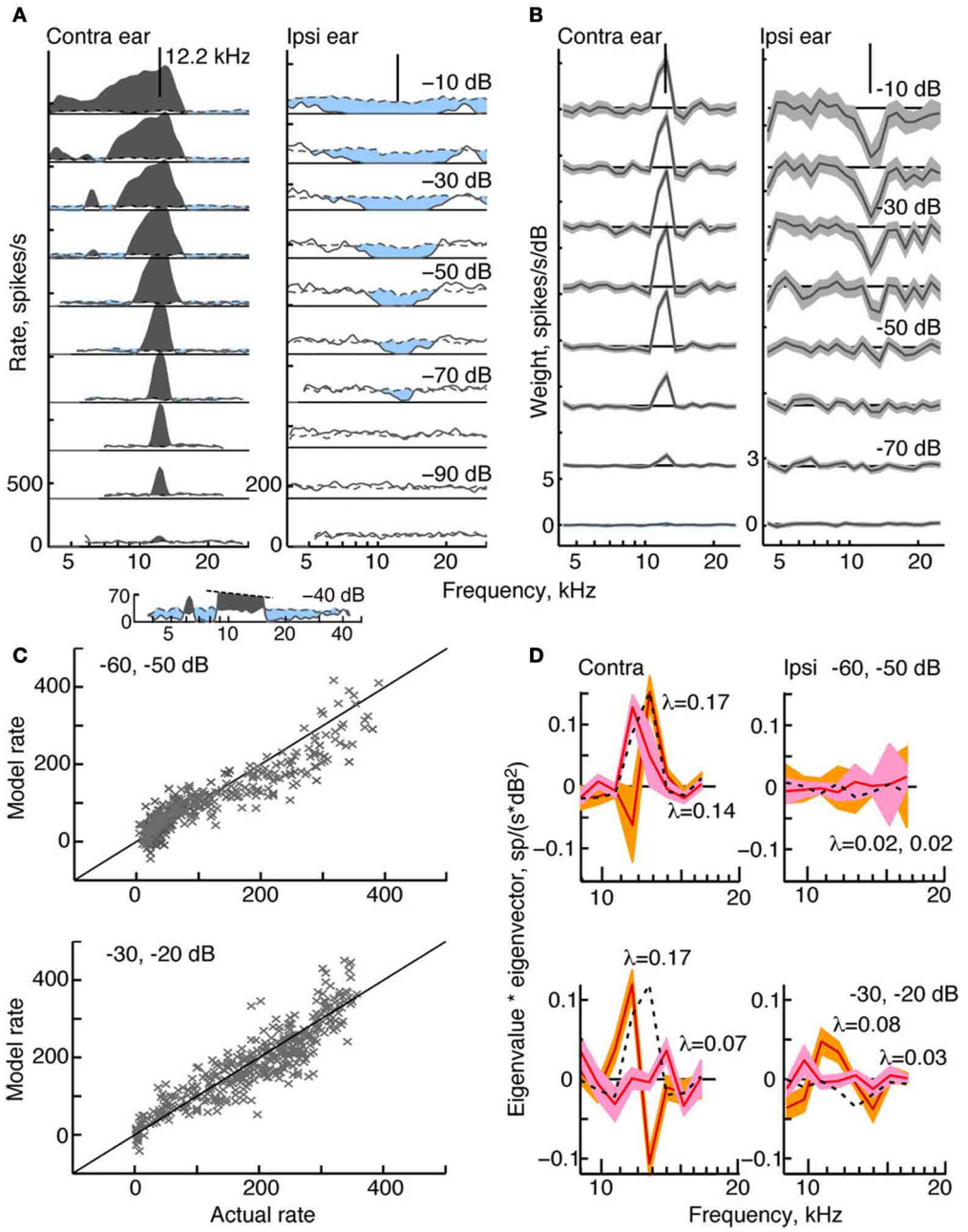

FIGURE 2 | Response characteristics for a type I neuron, BF 12.2 kHz. **(A)** Tone response maps showing rate responses to 200-ms tone bursts, plotted against the tone frequency at a fixed attenuation. Rates were computed from single tone presentations and smoothed (5-bin triangular filter) for display. Attenuations are shown at right. Zero dB attenuation was 94 dB SPL at the neuron's BF. Response maps were created by presenting tones in the contralateral ear only (left) and ipsilateral ear only (right). Discharge rates across the duration of the tone are shown by solid lines. Spontaneous rates are shown by dashed lines. The horizontal solid straight line indicates 0 spikes/s, and the rate scale is given at bottom left (different in the two ears). Excitatory responses are colored gray and inhibitory responses are light blue. The vertical lines at the top of the plots show the BF in the contralateral ear (12.2 kHz). **(B)** Weight functions estimated from responses to binaural RSS stimuli presented across a range of attenuations. First-order weights (w_C and w_I in Equation 1) are plotted on the same frequency axis as in **(A)**. Weight estimates are shown as black lines, and gray regions indicate ±1 SEM. Contralateral and ipsilateral weight functions were derived from the same 200 responses to the binaural stimulus set. Note that the weight scales on the ordinate differ. **(C)** Rates predicted by the model (ordinate) vs. experimental rates (abscissa) in leave-one-out model testing. For each plot, data for two attenuations (indicated in the legend) were combined for the leave-one-out procedure. **(D)** Second-order effective filters (i. e., eigenvectors of $\mathbf{M}_C$ and $\mathbf{M}_I$ in Equation 3) for the same two fits shown in **(C)**. Eigenvectors multiplied by their corresponding eigenvalue are plotted against frequency. The 1st-order weights, scaled to the same maximum value in each plot, are shown as black dotted lines. Only eigenvectors with the two largest positive eigenvalues λ are shown (largest λ, orange; second-largest λ, pink). The colored regions indicate ±1 SEM. The negative eigenvalues are smaller than the positive eigenvalues (<0.03, top case; <0.1, bottom case) and the corresponding eigenvectors are noisy (not shown).

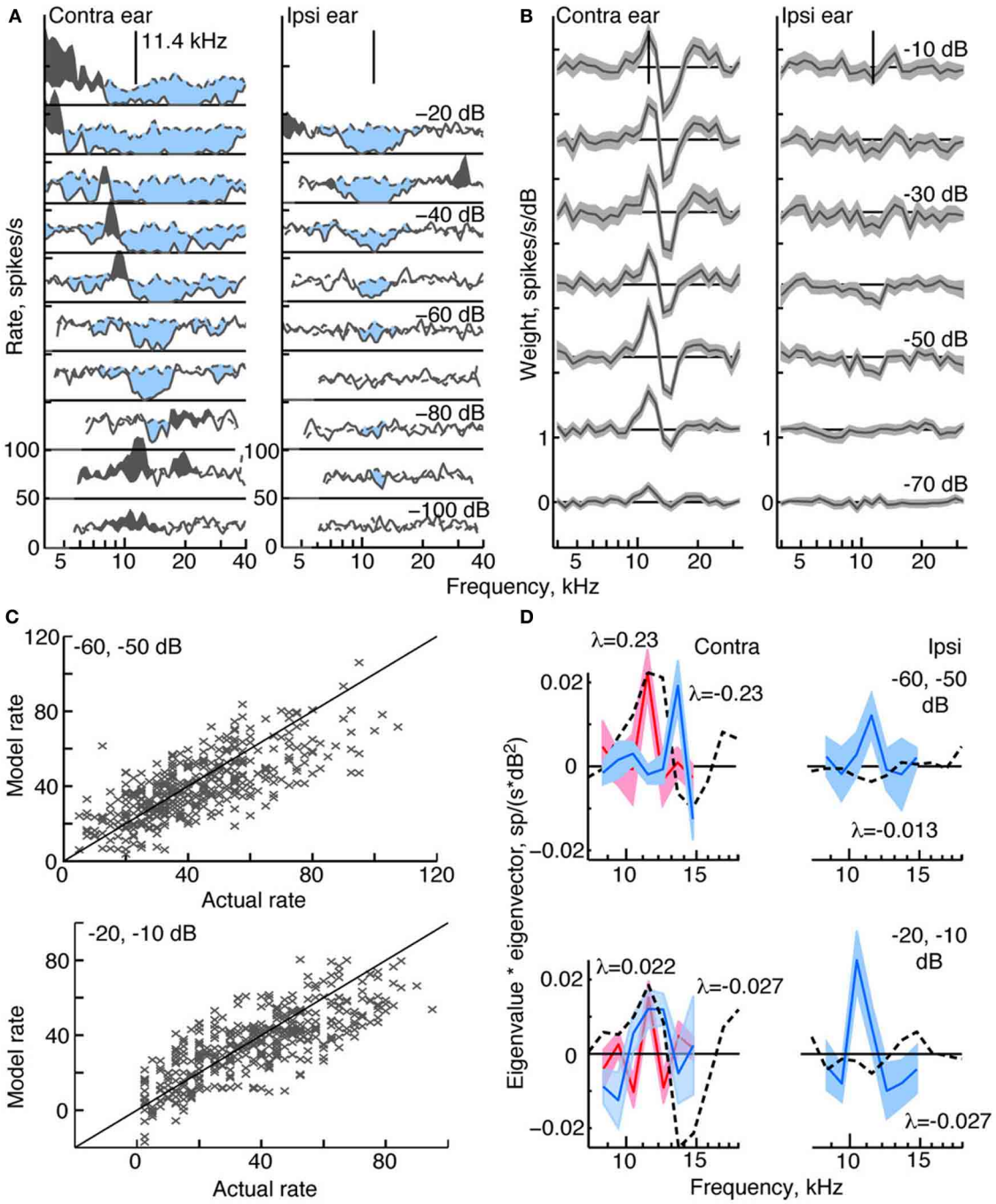

FIGURE 3 | Response characteristics for a type O neuron, BF 11.4 kHz. **(A,B)** Tone response maps and RSS weight functions, plotted as in **Figure 2**. Note the large inhibitory area centered on BF in the contralateral and ipsilateral tone response maps. Also note the difference in shape of the tone and weight-function maps. 0 dB attenuation is 98 dB SPL at the BF of the neuron. **(C)** Prediction performance as in **Figure 2**. *fv*-values are 0.54 for the stimuli at −60/−50 dB, and 0.51 at −20/−10 dB. **(D)** 2nd-order weight functions with the largest eigenvalues, given in the legends. Weights with positive eigenvalues are shown in red, and weights with negative eigenvalues are shown in blue.

ensemble of 200 RSS stimuli. In the few cases where multiple presentations of the same stimulus ensemble were performed, the resulting models were essentially the same as those based on a single presentation.

RESPONSE TYPES

CNIC neurons have been classified according to tone-based response maps using various criteria [e.g., Yang et al., 1992; Egorova et al., 2001; Lebeau et al., 2001; reviewed by Davis

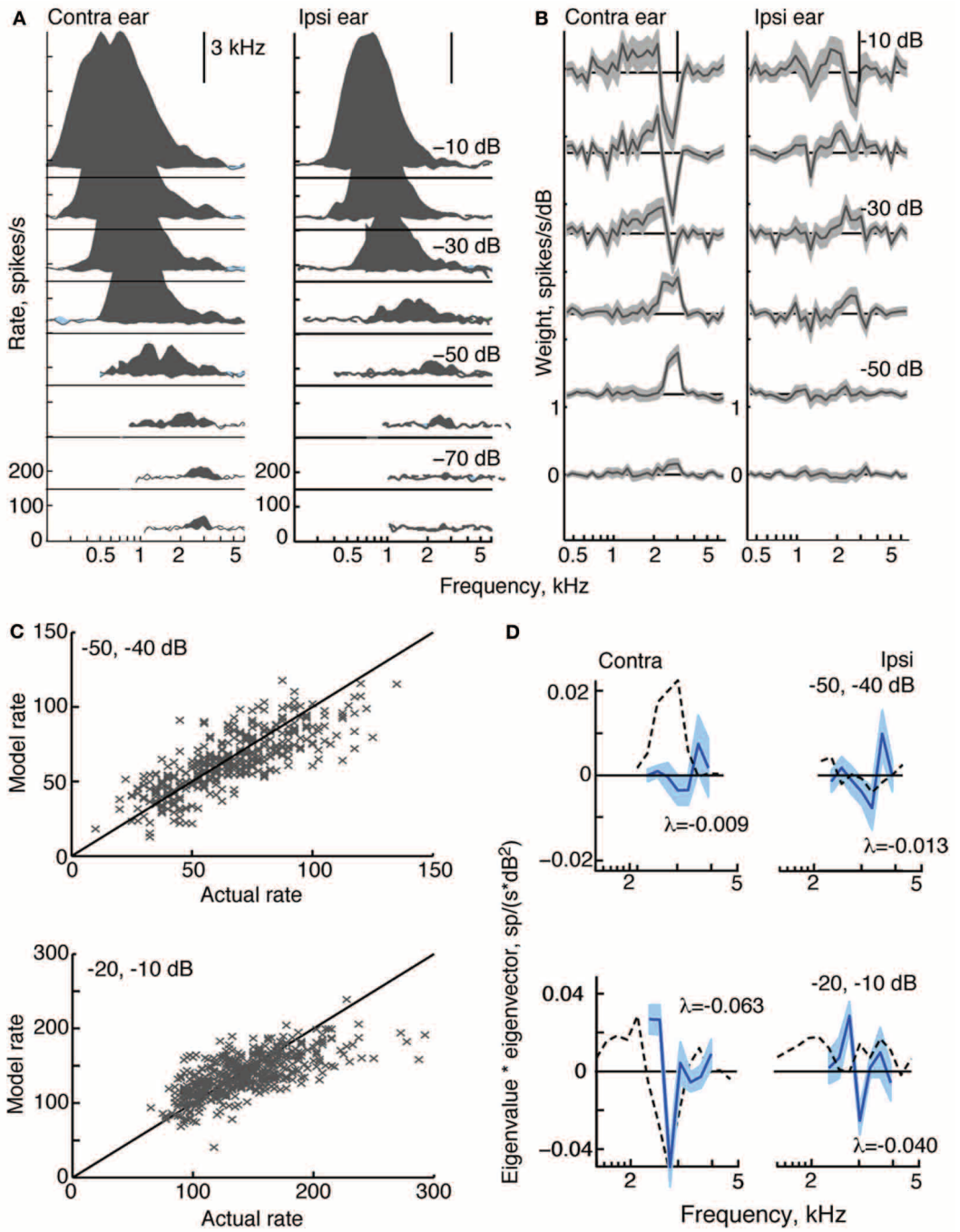

FIGURE 4 | Response characteristics for a type V neuron, *BF* = 3 kHz. **(A)** Response maps, plotted as in **Figure 2**. Zero dB attenuation was 98 (contra) and 95 (ipsi) dB SPL at the BF of the neuron. **(B)** At high sound levels, 1st-order weight functions suggest a substantial inhibitory area around BF–a pattern consistent with the weak responses to tones near BF in **(A)**. **(C)** Prediction performance as in **Figure 2**. *fv*-values are 0.61 for the stimuli at −50/−40 dB, and 0.41 at −20/−10 dB. **(D)** 2nd-order weights with the largest negative eigenvalues, given in the legends.

(2005)]. Here, we group neurons based on response map patterns and binaural properties—a classification scheme found most appropriate for the CNIC in decerebrate cats (Davis et al., 1999; Ramachandran et al., 1999). Type I ("eye") neurons demonstrate sharply tuned excitatory responses to contralateral tones at frequencies surrounding BF, and inhibitory responses to ipsilateral tones at frequencies equal to and surrounding the contralateral BF (EI). This pattern remains stable across all sound levels tested (see **Figure 2**). By contrast, Type V ("vee") neurons, which usually have a BF less than 3–4 kHz (in cats), demonstrate

broad excitatory responses to contralateral and ipsilateral tones (EE). Type V response maps frequently also suggest that some degree of inhibition exists at and above BF at high sound levels (see **Figure 4**). Finally, Type O neurons are strongly nonmonotonic (**Figure 3**): tones near BF presented to the contralateral ear produce excitatory responses at low sound levels and inhibitory responses at higher sound levels. For Type O neurons, responses to ipsilateral-ear stimuli are inhibitory at all sound levels tested. The CNIC also contains relatively few onset neurons (<10%), which do not give sustained responses to tones. Note that these classification criteria are qualitative: they are determined mainly by the binaural ipsilateral/contralateral response type (EI or EE) and the degree to which contralateral tones inhibit responses around BF. A number of quantitative properties for these different response types have been documented (Davis et al., 1999; Ramachandran et al., 1999), but these were not necessary for neuron classification.

RANDOM-SPECTRAL-SHAPE (RSS) AND VIRTUAL-SPACE (VS) STIMULI

Random-spectral-shape stimuli spanning a frequency range of 5.7 octaves (0.8–43 kHz) were used to explore the spectral sensitivity of IC neurons to broadband stimuli. The spectra of these stimuli are comprised of 1/8-octave bins, where each bin contains 8 tones of the same level spaced 1/64 octave apart. Sound levels across the bins were independently drawn from a Gaussian distribution with a mean of zero dB and a standard deviation of 12 dB. Here, zero dB serves as the reference sound level of the stimulus, which usually varied over a 50–70 dB range of absolute intensities. Stimulus waveforms were constructed by summing the tones with a baseline sampling rate of 100 kHz; the starting phases for the tones were randomized to prevent a click at time 0. Because the stimuli are defined on a log frequency axis, changing the sampling rate simply shifts the stimuli along the log frequency axis without changing their spectral shapes, binwidths, or the log-frequency spacing of the tones. As such, whenever possible, the sampling rates of the RSS stimuli were changed to place the BF of the neuron between one-half and two-thirds of the total frequency range of the stimulus.

In order to estimate parameters for the weight-function model, we constructed 192 binaural RSS stimuli with unique spectral shapes. The spectra of three such stimuli are shown in **Figures 1B,C**. Each RSS stimulus is characterized by $S(f)$, the sound levels in dB of the bins centered at frequencies f. Binaural stimuli are represented as two vectors $\vec{s}_C$ and $\vec{s}_I$ whose elements are dB sound levels $S_C(f_j)$ and $S_I(f_j)$ at each frequency in the contralateral and ipsilateral stimuli, respectively. Note that for each binaural stimulus pair, the low-frequency half of the stimulus in one ear is equal to the high-frequency half of the stimulus in the other ear (gray boxes in **Figure 1B**). This circular frequency shift ensures that ipsilateral spectra are orthogonal to contralateral spectra across half the stimulus bandwidth. Because the half-bandwidth of the stimuli (2.85 octaves) was wider than the bandwidth of the neurons, this symmetry did not confound characterization of a neuron's response patterns.

In addition to the 192 stimuli with RSS, we constructed eight binaural stimuli in which all levels are at the reference level: that is, $S(f) = 0$ dB for all f. These flat spectra stimuli were used to check the estimation of parameter R_0 in the weight-function model described below.

Virtual-space stimuli (VS) were generated by filtering a broadband (50-kHz wide) flat-spectrum noise stimulus with head-related transfer functions (HRTFs) that were measured in cat [**Figure 1D** from Rice et al. (1992)]. HRTF filtering produces noise at the eardrum similar to that which would have been produced if the noise were presented in free field. HRTFs representing 100 spatial locations (range: −60 to +60° azimuth, −30 to +45° elevation) were presented to the ears in binaural pairs that provided a virtual space simulation (assuming that the contralateral and ipsilateral ears of the cat are identical). For example, if the sound presented to the contralateral ear were filtered by the HRTF for −7.5° elevation and 15° azimuth, then the sound presented to the ipsilateral ear was filtered by the HRTF for −7.5° elevation and −15° azimuth. Because the same 50-kHz noise stimulus was applied to all HRTF filters, the resulting binaural signals also had appropriate interaural time, interaural level, and spectral cues. The responses to VS stimuli were used to test the models derived from responses to RSS stimuli.

WEIGHT-FUNCTION MODEL

The spectral sensitivity of neurons responding to broadband stimuli was characterized using the following model.

$$r = R_0 + \sum_{j=n_1}^{n_2} w_{Cj} S_C(f_j) + \sum_{j=n_1}^{n_2} w_{Ij} S_I(f_j) + \sum_{j=n_3}^{n_4} \sum_{k=j}^{n_4} m_{Cjk} S_C(f_j) S_C(f_k) + \sum_{j=n_3}^{n_4} \sum_{k=j}^{n_4} m_{Ijk} S_I(f_j) S_I(f_k) + \sum_{j=n_5}^{n_6} \sum_{k=n_5}^{n_6} b_{jk} S_C(f_j) S_I(f_k) \quad (1)$$

This model has previously been applied to auditory nerve fibers (ANF) (Young and Calhoun, 2005), brainstem neurons (Yu and Young, 2000; Tollin and Koka, 2010), and neurons in the auditory cortex (Barbour and Wang, 2003); however, in the present study, binaural processing is also explicitly represented. In this model, the discharge rate of the neuron r is the sum of six terms: constant R_0 which is the response to the flat-spectrum stimuli with all levels at 0 dB; 1st-order weightings of the spectral levels in each ear (the second and third terms); 2nd-order weightings of the levels in each ear, (the fourth and fifth terms); and a 2nd-order contribution related to a binaural interaction (the sixth term). Parameters w_{Cj} and w_{Ij} are 1st-order weights on stimulus levels at frequency f_j in the contralateral and ipsilateral ears, respectively. First-order weights represent gains of the rate response to energy at each frequency in spikes/(s·dB), and first-order weight functions show these gains for each stimulus frequency bin. Parameters m_{Cjk} and m_{Ijk} are 2nd-order weights which describe an interaction between spectral level pairs associated with the same ear [e.g., m_{Cjk} is the weighting on the multiplicative interaction $S_C(f_j)\ S_C(f_k)$]. Finally, parameter b_{jk} is a binaural weight measuring an interaction of spectral level pairs from opposite ears [i. e., b_{jk} is the interaction of $S_C(f_j)$ in the contralateral ear and $S_I(f_k)$ in the ipsilateral ear].

The model of Equation 1 is a linear function of the unknown parameters R_0, $\{w_{Cj}\}$, $\{w_{Ij}\}$, $\{m_{Cjk}\}$, $\{m_{Ijk}\}$, and $\{b_{jk}\}$. The parameters are estimated from discharge rates r, which are the responses

to 192 RSS and 8 flat-spectrum 0-dB stimuli. At each reference sound level (expressed in dB attenuation), weights were estimated by solving 200 simultaneous linear equations in the form of Equation 1—that is, one equation for each stimulus presented. Weight estimates were obtained by using either the method of normal equations or singular-value decomposition (Press et al., 2007, chapter 15)—both of which minimize the mean square error between the actual discharge rates and those predicted by the model. For the estimates computed here, the two methods give identical results. Plots of the estimated weights against frequency at each of the reference sound levels were aggregated to form weight-function maps.

Weights were also computed by combining responses at two or more reference sound levels—a calculation which mainly affected estimates for 2nd-order weights. A model with combined sound levels usually predicted rate responses to RSS stimuli (but not HRTF stimuli) more accurately than models estimated at only one sound level: median improvements in the goodness of fit for the predictions (i. e., *fv*; defined in the next section) are 0.12, 0.15, and 0.12 for I, V, and O neurons, respectively. The performance improvement presumably reflects the fact that a larger amount of data (400 vs. 200 data points) and a wider range of stimulus levels were used to fit the model. Response predictions generated by combining data from multiple levels are mixed with single-attenuation fits in **Figures 2C**, **3C**, **4C**, **7**, **9**.

The frequencies that are assumed to contribute to a neuron's responses are additional parameters in the model. These parameters, which are shown as limits on the summations $\{n_1, n_2, n_3, n_4, n_5, n_6\}$ in Equation 1, define the sequential set of weights (including BF) that lead to the model's best prediction performance. These frequency limits are determined by systematically varying the span of frequencies used during weight estimation and prediction. Parameters $\{n_1, n_2\}$ are varied first, followed by $\{n_3, n_4\}$ and finally $\{n_5, n_6\}$. Specifically, beginning with one weight at BF, weights are added below and above BF, one at a time, only as long as they improve prediction performance. When the 2nd-order weight limits are being determined, the 1st-order weight limits are fixed at the best performance of the 1st-order model. Similarly, when the binaural weight limits are being determined, both the 1st- and 2nd-order weight limits are fixed. Note that all weights in the current set, as specified by the $\{n_j\}$, are estimated simultaneously at each step, so that as 2nd-order weights are added, the 1st-order weights usually change. Neither the weights nor the prediction error are strong functions of $\{n_j\}$, especially near the edge of the response area, so the order in which the $\{n_j\}$ are tested does not change the model or error.

PREDICTION

Increasing the limits on summation in the model amounts to increasing the number of weights that need to be estimated. To prevent overfitting the model, we consider only weights in the model that are needed to accurately predict responses to broadband stimuli. To test the model, we use a leave-one-out cross-validation procedure where each of the 200 rates is set aside as a test response while the remaining 199 rates are used to estimate weights. The procedure is repeated for each of the 200 rates. This method produces results similar to bootstrap; however, it is preferred over bootstrap because it yields 200 separate prediction tests while also using the largest number of data points to fit the model. The SEMs of the weights are estimated from the leave-one-out calculations as $(n-1)\,\sigma_p/\sqrt{n}$, where n is the number of data points (200) and σ_p is the standard deviation of the weights in the 200 leave-1-out trials [Equation 10.9 in Efron and Tibshirani (1986)].

The quality of prediction is measured with fraction of variance, defined as:

$$fv = 1 - \frac{\sum (r_j - r_{mj})^2}{\sum (r_j - \hat{r})^2} \tag{2}$$

where r_j are the rates in the test data set, r_{mj} are the rates predicted by the model, and $\hat{r}$ is the mean of the r_j. The value of *fv* is 1 for a perfect fit and decreases as the fit worsens. The *fv* is zero if the model predicts the data no better than the mean rate, and the *fv* can be negative for very bad fits. We have chosen *fv* as a measure of fit because, unlike the often-used correlation coefficient (R), *fv* is sensitive to constant rate errors (i. e., differences in the mean rates between model and data). Such errors can be a problem for a model with even-order terms. Empirical comparisons of *fv* and R^2 based on the present data and auditory nerve data (Young and Calhoun, 2005) show that $R^2 \geq fv$ in all cases, and that the two measures are approximately equal for good fits (taken to be values of *fv* above ∼0.5). Noise in the rate measurements cannot be fit by the model and therefore decreases *fv*. A Poisson assumption for the rate statistics suggests that the maximum possible *fv* is about 0.8—a value consistent with the data (**Figure 7B**, assuming values above 0.8 are random scatter).

During this fitting process, *fv* for the 1st-order model usually did not change dramatically as the number of weights (n_1 and n_2) changed. However, the addition of 2nd-order weights to the best-performing 1st-order model (i. e., the 1st-order model with the largest *fv*) usually yielded increases in *fv* by up to 0.4, even when only one 2nd-order weight was introduced. The inclusion of additional 2nd-order weights (beyond the first one) also produced only small incremental changes in *fv*. This behavior, which was observed in 314/337 cases, suggests that the 2nd-order model provides information about spectral integration in these neurons that is not present in the 1st-order model. Note that binaural weights usually added little to the prediction quality of the best 1st- or 2nd-order models—improving *fv* by less than 0.01 in 225/310 cases.

Weight function models derived from RSS responses were used to predict responses to HRTF stimuli. Because the HRTF stimuli did not have an all-0-dB reference for the estimation of R_0, a modified prediction procedure was used. For these predictions, the reference stimulus was chosen to be the average of the four HRTF stimuli with the flattest spectral shape within 0.5 octave of the neuron's BF. R_0 was set to the average of the rates produced by those stimuli. HRTF responses were then predicted as differences between the response to the averaged reference stimulus and responses to each of the other 96 HRTF stimuli. This method produced usable predictions, but there were still errors in the rate predictions; specifically, there was often a shift in the means of the actual and predicted rates (see **Figure 8B**). As such, R^2 (i.e., the

square of the Pearson product-moment correlation coefficient), and not *fv*, was used to quantify errors between the actual and predicted rates (in **Figure 8C** only). Unlike *fv*, R^2 is sensitive to correlated rate fluctuations but not to errors in average rate or overall rate gain.

SECOND-ORDER FILTERS

The frequency selectivity implicit in the 2nd-order weights may be better understood by interpreting the terms in Equation 1 as filters (e.g., Lewis et al., 2002; Reiss et al., 2007). Equation 1 can be written in vector-matrix form as:

$$r = R_0 + \vec{w}_C^T\vec{s}_C + \vec{w}_I^T\vec{s}_I + \vec{s}_C^T\mathbf{M}_C\vec{s}_C + \vec{s}_I^T\mathbf{M}_I\vec{s}_I + \vec{s}_C^T\mathbf{M}_B\vec{s}_I \quad (3)$$

where the stimulus vectors $\vec{s}_C$ and $\vec{s}_I$ are defined above. Weight vectors $\vec{w}_C$ and $\vec{w}_I$ contain the 1st-order weights. Matrices $\mathbf{M}_C$, $\mathbf{M}_I$, and $\mathbf{M}_B$ contain 2nd-order and binaural weights corresponding to frequency pairs. Because the 2nd-order matrices $\mathbf{M}_C$ and $\mathbf{M}_I$ are real and symmetric, they can be written as

$$M = \sum_{j=1}^{N} \lambda_j \vec{e}_j \vec{e}_j^T \quad (4)$$

where λ_j are real eigenvalues of $\mathbf{M}$ and $\vec{e}_j$ are orthonormal eigenvectors. As such, each 2nd-order term in Equations 1 and 3 can be written as:

$$\vec{s}^T\mathbf{M}\vec{s} = \vec{s}^T\left(\sum_{j=1}^{N} \lambda_j \vec{e}_j \vec{e}_j^T\right)\vec{s} = \sum_{j=1}^{N} \lambda_j \left(\vec{s}^T\vec{e}_j\right)^2. \quad (5)$$

Examination of Equation 5 shows that an eigenvector $\vec{e}_j$ can be viewed as an "equivalent 2nd-order filter." However, because the filtering operation $\vec{s}^T\vec{e}_j$ is squared, the excitatory or inhibitory nature of the 2nd-order filter is determined by the sign of the eigenvalue, where a positive eigenvalue indicates an excitatory contribution and a negative eigenvalue indicates an inhibitory contribution. Furthermore, the magnitude of the eigenvalue quantifies the importance of the associated filter. In this paper, filters are shown for only the largest one or two eigenvalues.

RESULTS

Neurons in the CNIC show a variety of patterns of frequency sensitivity, as measured by responses to tones [reviewed by Davis (2005)]. Here, we use response types described by Ramachandran and colleagues in decerebrate cat (Davis et al., 1999; Ramachandran et al., 1999), as detailed in Materials and Methods. As stated previously, there are three types of tonic responses: types V, I, and O. **Figures 2** through **4** provide examples of tone and broadband tuning for these neuron types. Data presented in this paper are from neurons for which complete tone and RSS responses were obtained across a range of sound levels. These include 12 V neurons (BFs 0.8–4.1 kHz), 13 I neurons (BFs 1.8–21 kHz), and 10 O neurons (BFs 2.2–21 kHz). Onset neurons were also encountered during the study—comprising 9% of the total sample—and all gave reliable tonic responses to RSS stimuli. However, onset neurons were not studied completely and are not discussed here.

RESPONSE MAPS

Type I tuning

Figure 2A shows a tone response map typical of a type I neuron. Contralateral response maps (left) show a narrow excitatory area centered on BF (in this case, 12.2 kHz) and inhibitory sidebands at frequencies below and above the excitatory area (light blue). To better visualize the inhibitory areas, the response at −40 dB is shown on an expanded scale at the bottom of **Figure 2A**. Ipsilateral response maps (right), by contrast, show mainly inhibitory areas that are well tuned and centered on approximately the same BF. Like all type I neurons that were analyzed in the study, this neuron is EI in its responses near BF.

The effective tuning of a type I neuron for broadband noise can be inferred from the 1st-order weight functions (**Figure 2B**). First-order weight functions computed for the contralateral ear (at left) resemble contralateral response maps in that they show large positive peaks at BF. Similarly, 1st-order weight functions for the ipsilateral ear are negative at frequencies where responses to ipsilateral tones are inhibitory. This pattern of excitation and inhibition inferred by the weight-function maps is typical of all type I neurons studied.

To better understand the nature of 2nd-order weight functions, eight 2nd-order filters (Equation 5) were computed for the type I neuron featured in **Figure 2**. At low sound levels, negative eigenvalues for this neuron are small compared to the positive eigenvalues—a finding that supports a predominantly excitatory contribution of 2nd-order weights. However, inhibitory 2nd order effects are present at higher sound levels, where negative and positive eigenvalues reach comparable values (<0.1, not shown). The two filters corresponding to the largest positive eigenvalues are shown in **Figure 2D**. As indicated by the shaded areas (±1 SEM), most of the second-order weights are significantly different from zero. First-order weight functions at the same sound levels are superimposed for comparison (black dashed lines). Some of the contralateral 2nd-order filters are shown to have plus-minus shapes that differ significantly from 1st-order weight functions. For example, peaks are present at frequencies below BF rather than on BF, and substantial gain slopes occur near the BF. These differences suggest that 2nd-order filters change the frequency selectivity of the neuron.

The meaningfulness of the second-order weight function was evaluated by testing how well the model predicted responses to RSS stimuli not used in parameter estimation. Predictions were performed at the same sound levels featured in **Figure 2B**, and the results for two sound levels are shown (**Figure 2C**). Here, each data point is the predicted rate response to each left-out test stimulus (ordinate), plotted against the actual rate response to that stimulus. The *fv*-values (Equation 2), which measure the accuracy of the prediction, are 0.85 and 0.79 at the sound levels shown. For this type I neuron, the contribution of the 2nd-order terms in the weight-function model is significant: when all 2nd-order weights are excluded from the model, *fv*-values decrease to 0.32 and 0.58, respectively.

Type O tuning

Response maps and weight functions of a type O neuron are shown in **Figures 3A,B**, respectively. At low sound levels, the

contralateral response map for the type O neuron (**Figure 3A**, left) shows an excitatory response to low-level tones near BF (11.4 kHz at −90 dB); at higher levels, the response map demonstrates a strong inhibitory response around BF, and a mixture of excitatory and inhibitory responses at frequencies away from BF. Given that the responses to ipsilateral tones (**Figure 3A**, right) were predominantly inhibitory, the neuron was classified as EI, as were all type O neurons studied. Unlike the type I neuron (**Figure 2**), contralateral weight functions computed from responses to RSS stimuli (**Figure 3B**, left) differ significantly from the tone-based response map: rather than having large areas of inhibition at BF, the weight functions show a combination of positive gains near BF and negative gains above BF across a range of sound levels. Ipsilateral weight functions (**Figure 3B**, right), on the other hand, are similar to the response maps in that they mainly show weak inhibition near BF at most sound levels.

The equivalent 2nd-order filters show substantial inhibitory and excitatory contributions (**Figure 3D**), possessing both large negative (blue filters), and large positive eigenvalues (red filters). The contralateral and ipsilateral 2nd-order filters are statistically different from zero, and their shapes differ significantly from their corresponding 1st-order weight functions.

Compared to the weight-function model for the type I neuron, the model for the type O neuron is a less accurate predictor of responses to novel stimuli (**Figure 3C**). For this type O example, the general trend in the data is captured by the model; however, the *fv*-values are only 0.54 and 0.51 at the two sound levels shown. The 2nd-order terms are important to the model, as exclusion of these terms produces *fv*-values (for the best-fitting 1st-order model) of only 0.38 and 0.28, respectively.

Type V tuning

Like all type V neurons in this study, the neuron in **Figure 4** is EE, exhibiting broad excitatory responses to contralateral and ipsilateral tones (**Figure 4A**). At high sound levels, the weak response near BF, in addition to apparent limits on the spread of excitation to frequencies above BF, suggests that the response of the neuron is sculpted by inhibition. Although this behavior is observed in many V neurons (Davis et al., 1999), responses to tones that are strictly inhibitory (i. e., with rates below spontaneous rate) are small and rarely observed. Note that type V neurons were also encountered for which either, or both, response maps did not show signs of inhibition (not shown).

At low sound levels, weight functions for the type V neuron in **Figure 4B** resemble tone response maps in that weights are significantly positive at BF. Weight functions at higher sound levels show negative weights around BF in a manner consistent with the inhibitory sculpting described above. Second-order filters (**Figure 4D**) corroborate the inhibitory nature of this neuron's response: the largest eigenvalues are negative, and increases in sound level produce even larger negative eigenvalues.

In **Figure 4C**, the weight-function model predicts responses of the type V neuron with moderate accuracy. The *fv*-values for the 2nd-order model are 0.61 and 0.41 at the two sound levels shown. Exclusion of 2nd-order weights from the model reduces *fv*-values to 0.54 and 0.26, respectively.

LEVEL TOLERANCE

In this section, we compare the tuning of neurons responding to tones against the tuning implicit in responses to RSS stimuli. Specifically we compare areas of activity observed in tone response maps with those seen in weight-function maps at equivalent sound levels (dB re threshold). For type I neurons, this comparison is robust and straightforward. In the tone maps of type I neurons, edges of activity are taken to be the frequencies at which rate responses first go to zero on either side of BF (**Figure 5A**, blue line). These edges define a central excitatory region flanked by inhibitory sidebands. Analogously, in weight-function maps, edges of activity are taken to be the frequencies at which 1st-order weights are first indistinguishable from zero on either side of BF (i.e., within ±1-SEM of zero; **Figure 5B**, dashed green lines). In this example, as sound level increases, tone-based tuning (blue curve) broadens, as is commonly observed for auditory neurons in many parts of the brain. By contrast, the tuning apparent in noise-based weight-function maps is level tolerant: that is, bandwidths are relatively fixed over the range of sound levels studied (dashed green curve).

The comparison of tone- and noise-based tuning in **Figure 5** is typical of type I neurons. This is shown in **Figure 6A** where upper and lower edges of tuning curves are shown for type I

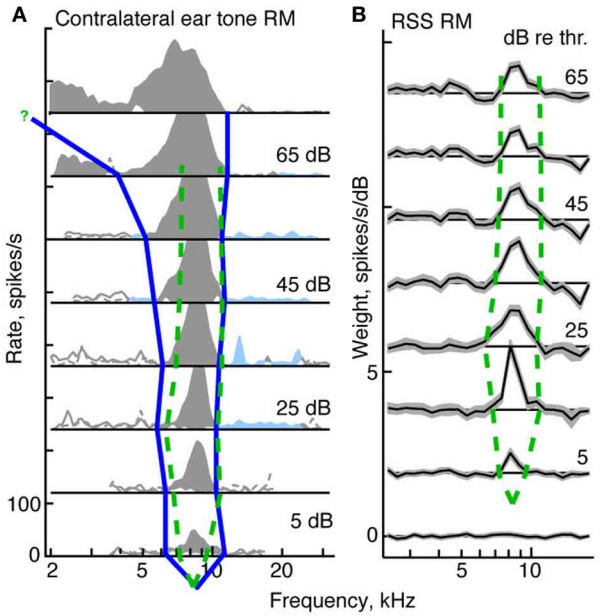

FIGURE 5 | Derivation of tuning curves from response maps for a type I neuron (*BF* = 8.3 kHz). (A) Tone response map for the contralateral ear. The blue curve shows the tuning curve edges for the tone response map, derived as described in the text. The green dashed curve in both **(A)** and **(B)** shows the edges of the tuning curve for the weight-function map. **(B)** Weight-function map for the same neuron. The dB scale in both parts is dB re threshold for BF tones **(A)** or RSS stimuli **(B)**. The tuning curve near the BF tip is not well specified by the response maps. For the tone response maps, the threshold at BF is determined from a rate-level function; for the weight-function maps, the threshold is set halfway between levels that do and do not produce weights that are significantly different than zero.

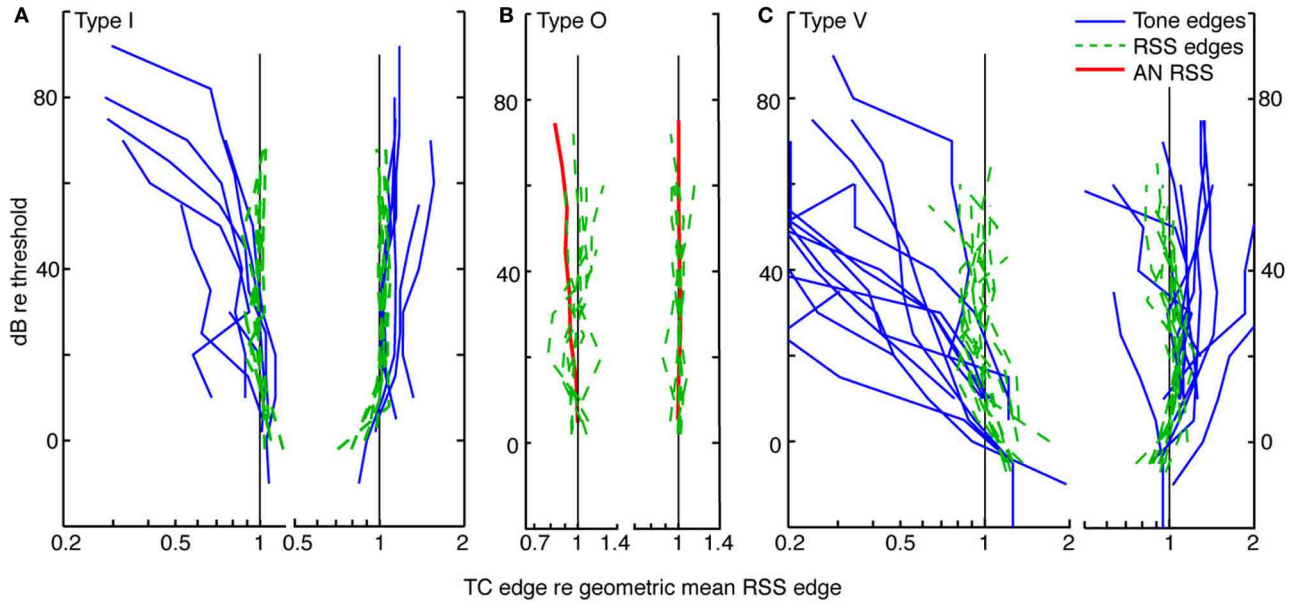

FIGURE 6 | Level tolerance of the edges of tone and weight-function response maps for populations of type I (A), O (B), and V (C) neurons. Frequency edges computed as in **Figure 5** are shown for *contralateral* stimuli only. Lower-(left) and upper-(right) frequency edges derived from tone response maps (blue lines) are overlaid on those derived from weight-function maps (dashed green lines) at equivalent sound levels, in dB re threshold. The point at BF is not included. For each neuron, lower (or upper) edge frequencies are plotted relative to the geometric mean across levels of the lower (or upper) edge frequencies of the weight-function maps. Slopes of lower frequency edges of tone maps differ significantly from those observed in weight-function maps (type I: $P = 0.1$; type V: $P < 0.01$; signed rank sum comparisons of slopes of best-fit lines). Upper-frequency edges do not differ. Tone maps were not analyzed for type O neurons (see text). The red curves in **(B)** show mean weight-function edges for auditory nerve fibers [ANF; data from Figure 5 of Young and Calhoun (2005)]. Here, frequencies are normalized by the average frequency edge at the lowest two sound levels. As sound level increases, the slopes of lower-frequency edges of CNIC weight-functions differ from those observed in ANF. Specifically, slopes suggest a relative narrowing in type I and type O data ($P = 0.02$), and relative widening in type V neurons ($P = 0.07$). For all weight-function types, upper frequency edges are not significantly different from those seen in ANFs. All Ps are Bonferroni corrected.

neurons. Frequency edges derived from weight-function maps (green dashed curves, as in **Figure 5**) are overlaid on those derived from tone-based response maps (blue lines, as in **Figure 5A**). To enable comparison of tuning curve slopes across neurons with different BFs, lower (or upper) frequency edges for each tuning curve (i. e., tone response maps and weight-function maps) are plotted relative to the geometric mean of lower (or upper) edge frequencies across all sound levels of the weight-function map. The lower and upper edges are plotted separately and the point at BF is not included.

Type I tuning in weighting functions is level tolerant: as sound level increases, upper and lower frequency edges remain relatively fixed. Level tolerance, however, was not observed in tone response maps, where increases in sound level typically yielded a broadening of response maps at the lower frequency edge: the slopes differ significantly between tone and weight-function maps on the low-frequency side ($P = 0.1$, Bonferroni corrected signed-rank-sum comparisons of slopes of best-fit lines), but not the high-frequency side.

For type O neurons, a direct comparison of tone- and noise-based tuning was not done because the patterns of excitation and inhibition in tone maps are complex and vary significantly from sound level to sound level (as in **Figure 3A**); thus, it is not clear how a meaningful and consistent bandwidth measure would be chosen. However, weight-function maps could be analyzed as described above for type I neurons. Because type O neurons often have distinct excitatory *and* inhibitory regions that are prominent near BF (as in **Figure 3B**, 3/7 cases), frequency edges in type O maps were chosen to include all statistically significant features that persisted across sound level (i. e., weights exceeding ± 1 SEM). For the map in **Figure 3B**, the persistent feature that was selected consists of both the excitatory lobe near BF and the inhibitory lobe above BF. The choice of persistent feature is not critical, for as long as the same feature definition is applied consistently across sound level, the result does not change for the sample of type O neurons studied. In **Figure 6B**, upper and lower frequency edges are shown for a population of type O neurons. Note that the frequency edges are roughly constant at the different sound levels, thus implying that broadband frequency selectivity in type O neurons is tolerant to increases in noise level.

A similar analysis for a population of type V neurons is shown in **Figure 6C**. As with type I neurons, edges of activity in tone-based response maps were taken to be frequencies at which rate responses first go to zero on either side of BF. This area of activity included frequencies at and above BF where responses were excitatory but appear dampened by inhibition (e. g., **Figure 4A**). As with type O neurons, frequency edges for weight-function maps were defined to encompass distinct statistically significant features. However, unlike type O neurons, the excitatory and inhibitory nature of those features often changed with changes

in sound level, as in **Figure 4B**. In such cases, all features near BF were included as part of a response area if they persisted over at least two levels. Because of the variability in weight-function maps, there is considerable variation in the width of type V tuning with changes in sound level (green dashed curves in **Figure 6C**). Weight-function tuning usually broadens near threshold, and in some cases narrows at high sound levels. However, lower frequency edges of weight-function maps remained relatively fixed compared to lower frequency edges of tone-based response maps ($P < 0.01$, signed rank sum test comparisons of slopes of best-fit lines).

Thus, the three CNIC neuron types—I, O, and V—exhibit level-tolerant tuning in response to broadband stimuli, but not in response to tones. For comparison, the edges of weight-function maps for a population of ANF were averaged and plotted in **Figure 6B** (red). For ANFs, the upper and lower frequency edges delineate an area of excitation that is centered on BF. The ANF weight-function map broadens slightly with increasing noise level at the lower frequency edge, exhibiting more widening than observed in type I and O edges ($P = 0.02$; signed rank sum test of slopes of best-fit lines). By contrast, ANF tuning widens less than that of type V neurons ($P = 0.07$).

QUALITY OF MODEL PREDICTIONS AND THE IMPORTANCE OF 2ND-ORDER TERMS

The weight-function model in Equation 1 predicts responses of the three CNIC neuron types with different degrees of accuracy. **Figure 7A** shows the distributions (left) and cumulative distributions (right) of *fv*-values for predictions computed using the leave-one-out procedure. Of the three response types, the model performs best for type I neurons where the median value of *fv* is 0.51 (gray). For the type V and O populations, median values of *fv* are only 0.30 (red) and 0.21 (blue), respectively. The differences in the medians of the *fv* distributions are statistically significant (see the figure caption).

The accuracy of the model predictions depends substantially on the inclusion of 2nd-order terms. The scatterplot of **Figure 7B** compares the performance of two models for each test response—a model which includes all 1st- and 2nd-order terms (abscissa), and another which includes only the 1st-order terms (ordinate). All data points are located below the diagonal line, meaning that the addition of 2nd-order terms consistently improves model performance. This was found to be true regardless of the quality of the 1st-order fit or the neuron type. Specifically, the median improvement in *fv* (calculated as the difference in *fv*-values for the 2nd- and 1st-order models) is 0.23 for I, 0.16 for V, and 0.18 for O neurons. Although it is not shown here, the binaural term (i. e., the sixth term of Equation 1) has a negligible impact on the quality of the prediction. In 225/310 cases, the improvement in *fv* resulting from the addition of binaural weights was less than 0.01.

Generally the accuracy of model predictions declines as sound level increases. **Figure 8A** shows the relationship between prediction accuracy (*fv*) and RSS stimulus level. The weight-function model most accurately predicts responses of type I neurons (gray lines), and this prediction performance declines slightly with sound level ($R = -0.17$, NS). Prediction performance for type V and type O neurons is relatively less accurate across sound

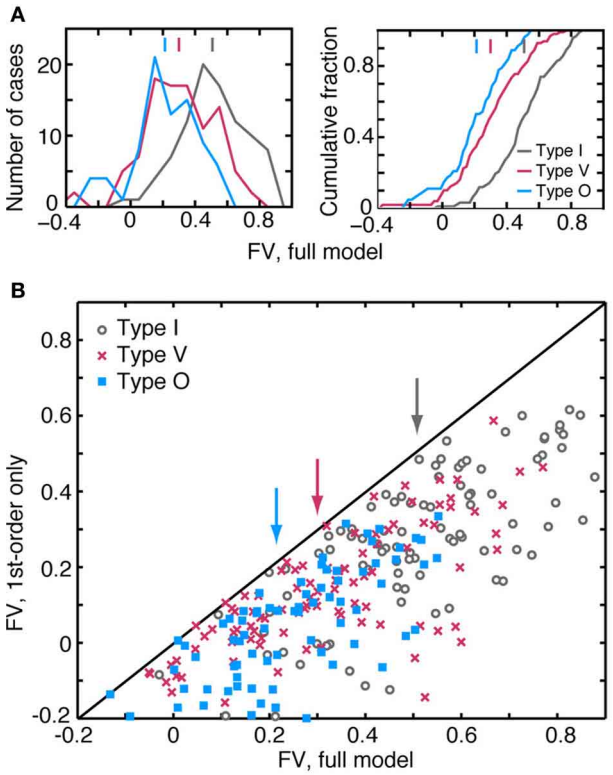

FIGURE 7 | Quality of the model predictions as measured by *fv* in leave-one-out cross validation tests. Each plot contains an aggregation of prediction data obtained at different sound levels. A neuron is usually represented multiple times, once at each sound level and also at pairs of adjacent sound levels. **(A)** Distribution (left) and cumulative distribution (right) of *fv*-values for the three response types. Vertical lines at the top of the plots show median *fv*-values. Differences in the distributions across the neuron types are statistically significant (rank sum test with Bonferroni correction; I vs. V and I vs. O, $P << 0.001$; V vs. O, $P < 0.02$). **(B)** Comparison of the best prediction quality (*fv*) for a full binaural model containing all 2nd-order terms (abscissa) and a model containing only 1st-order terms (ordinate). Ten data points with ordinate values < -0.2 are not shown, but are included in the statistics. Vertical arrows indicate median *fv*-values for each of the neuron types.

levels (red and blue lines), suggesting that nonlinearities not captured by the weight-function model have a marked impact on the rate responses in these neurons. The decline in prediction accuracy with sound level is significant in V neurons ($R = -0.5$, $P < 0.001$), but not in O neurons ($R = -0.04$, NS).

An important test of a model is whether it can predict responses to stimulus types different from those used to estimate model parameters. For this purpose, we tested the model with a functionally relevant stimulus set—specifically, broadband noise filtered by HRTFs (**Figure 1D**) that simulate natural sound localization cues. As described in Methods, the absence of a reference stimulus for the estimation of R_0 required a modified prediction approach. In **Figure 8B**, VS response predictions computed in this manner are shown for type I and type O neurons. Whereas rate fluctuations are qualitatively similar between the actual (green lines) and model (blue lines) rates, there are errors in average rate, especially in the type O example (**Figure 8B**). To deemphasize

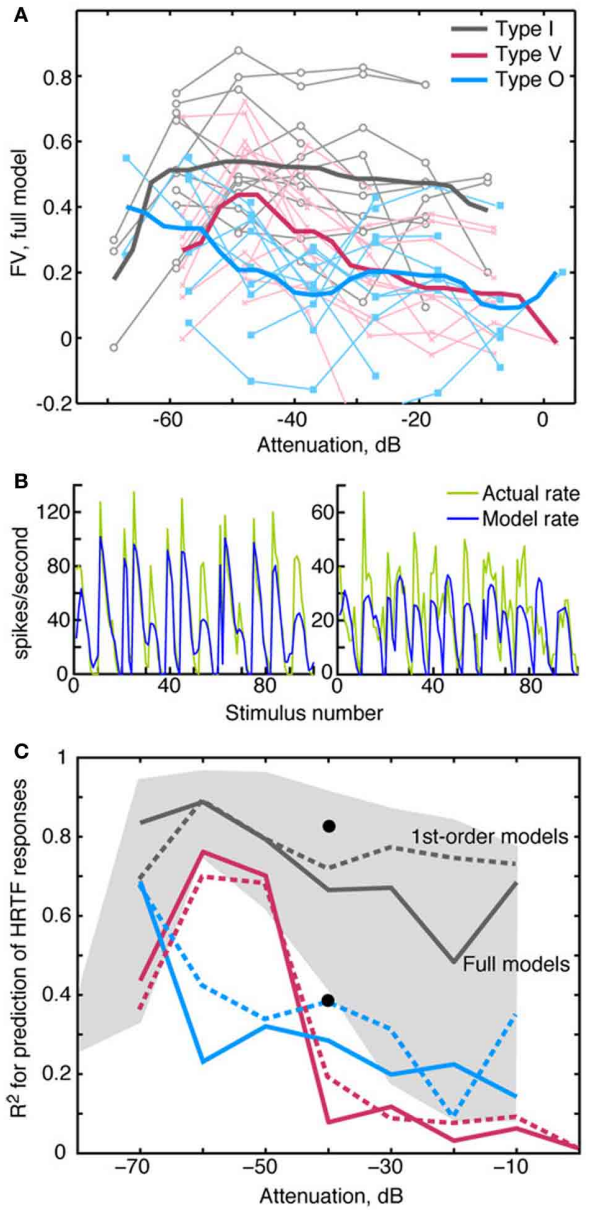

FIGURE 8 | Prediction quality for RSS and HRTF stimuli by sound level. **(A)** Quality of RSS response predictions (*fv*) plotted against the sound level of the stimulus. Light colored symbols connected by lines show data obtained from one neuron. Heavy colored lines show median *fv*-values for the 3 neuron types. For clarity in plotting, 1 dB was added to the attenuations for V neurons, and 2 dB was added to the attenuations for O neurons. **(B)** Predicted rate responses to HRTF-filtered noise (VS stimuli), computed using weight-function models derived at the same overall sound level (−40 dB). Predictions for a type I (left) and a type O (right) neuron were computed using the difference method (see text). Actual rates are shown in green and predicted rates are shown in blue. The goodness of fit for these predictions are as follows: Type I (left): $R^2 = 0.82$, $fv = 0.7$; type O (right): $R^2 = 0.39$, $fv = 0$. **(C)** Median R^2 for the three neuron types. Solid lines indicate median R^2-values obtained when the full model was used to predict responses to VS stimuli; dashed lines indicate median R^2-values based only on 1st-order terms. The black dots show the positions of the two examples in **(B)**. The gray shaded region indicates the range of R^2-values that were observed for type I neurons at each attenuation level.

differences in the means of the actual and predicted rates, the Pearson correlation coefficient R^2—instead of *fv*—was used to quantify the model fit (see Materials and Methods). **Figure 8C** shows median values of R^2 for the three neurons types. Consistent with **Figure 7**, the fits are best for type I neurons (gray lines), which maintain good fits (median $R^2 > 0.5$) over the range of sound levels; however, the range of R^2-values is quite wide, especially at high sound levels (gray shaded region). At each sound level, R^2-values for type V and type O neurons were comparable to those of type I neurons with the poorest fits.

HRTF response predictions, unlike RSS response predictions, were generally not improved with the addition of 2nd-order terms. In fact, at high sound levels, median R^2-values were slightly better for 1st-order models, as shown by the dashed lines in **Figure 8C**.

IMPORTANCE OF THE CONTRALATERAL EAR

Although it is well known that neurons in the CNIC have tuned responses to both contralateral and ipsilateral stimuli, the importance of ipsilateral inputs to spectral selectivity of neurons has not been studied extensively. We investigated this question by fitting a contralateral-only model to the data—that is, a model incorporating only the first, second, and fourth terms of Equation 1. We then used the monaural model to predict responses to test stimuli and compared the quality of those predictions to the quality achieved using the full binaural model (**Figure 9A**). The exclusion of ipsilateral information from the model was found to reduce the quality of the predictions: most of the data points in **Figure 9A** lie below and to the right of the diagonal line. However, the impact of the ipsilateral contribution is relatively small, as inclusion of ipsilateral weights in the model improved *fv* by more than 0.2 for only about 10% of the data.

Ipsilateral weights have a relatively weak impact on the accuracy of the model, partly because they are smaller in magnitude than contralateral weights. This difference in magnitude—which is evident in **Figures 2B**, **3B**, **4B**—are summarized in **Figure 9B**. Here, amplitudes of 1st-order contralateral weight vectors (abscissa) are plotted against amplitudes of 1st-order ipsilateral weight vectors (ordinate). These amplitudes are computed as the norm (or length) of the corresponding weight vector. Only type V neurons frequently exhibit ipsilateral norms that are larger than contralateral norms. By contrast, the ipsilateral norms for type I and type O neurons are usually relatively small. In **Figure 9B**, the dashed line indicates where ipsilateral norms are one-fourth the size of contralateral norms. For type I and type O neurons, median contralateral and ipsilateral norms (for contralateral norms greater than 0.6) are roughly approximated by this line. The norms of 2nd-order weights behave similarly (not shown).

EFFECT OF SOUND LEVEL ON SPECTRAL REPRESENTATIONS

A neuron that provides a robust rate-based spectral representation should respond over as wide a range of discharge rates as possible in response to changing spectral features. The neuron should also adapt the range of response rates to changing stimulus level (Rees and Palmer, 1988; Dean et al., 2008). Each column of **Figure 10A** shows rate responses of a type I neuron to the RSS

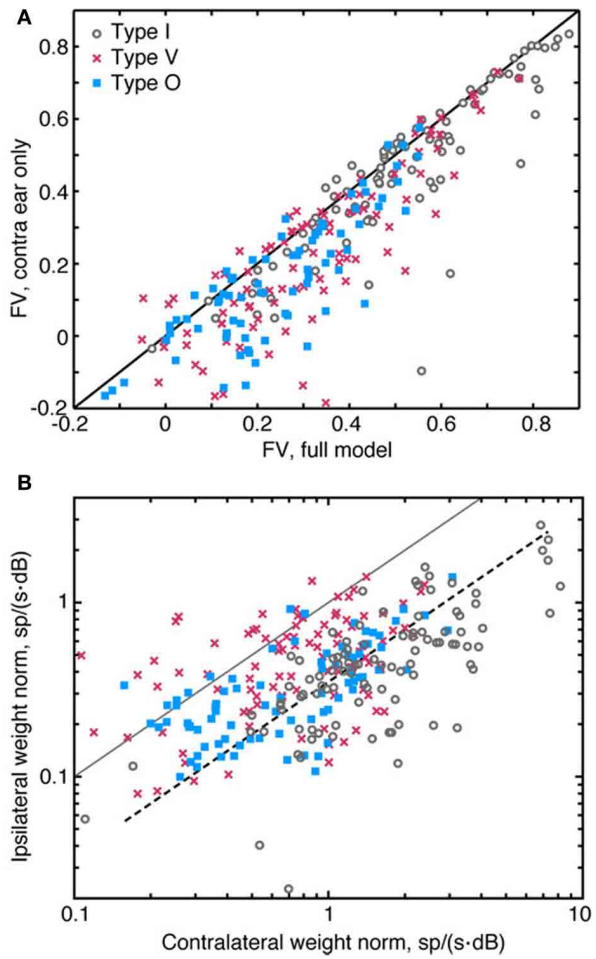

FIGURE 9 | Relative contribution of ipsilateral and contralateral weights. (A) Comparison of the prediction quality (*fv*) for a full 2nd-order binaural model (abscissa) and a model which assumes a purely contralateral input [i. e., $S_I(f) = 0$ for all *f*, ordinate]. Data from one experiment showing little or no effect of the ipsilateral inputs are included in this plot. **(B)** Plot of the amplitude of the 1st-order weight vector in the contralateral ear (abscissa) vs. the weight amplitude in the ipsilateral ear (ordinate). The amplitudes of the weights are measured as the norm of 1st-order weight vectors (the square root of the sum of the weights squared). The solid diagonal line indicates where weight vector norms are equal in amplitude. The dashed line indicates where ipsilateral norms are one-fourth the size of contralateral norms. Note the use of logarithmic axes in **(B)**. Also note that data points shown in **(A)** and **(B)** were aggregated across all sound levels of stimulus presentation.

stimulus set at two sound levels. The neuron in the left column responds at both sound levels with the full range of rates available to the neuron at the given sound level. By contrast, the neuron in the right column responds at the higher level over roughly half its full rate range due to rate saturation. To evaluate differences in the range of rate responses across sound level, we use the fractional rate ratio (*FRR*), which is defined as ([Rate at 97.5 percentile] – [Rate at 2.5 percentile])/[Rate at 97.5 percentile]. Here, the percentiles (horizontal dashed lines in **Figure 10A**) are used to reduce the effect of occasional rate outliers. *FRRs* for these examples are 0.97 and 0.98 in the left column and 1.0 and 0.50 in the right column. *FRR* is normalized by the maximum rate at a particular level—not the maximum rate across all levels. The latter would produce an increase in *FRR* at low levels that reflects the strength of the response rather than the neuron's use of the range of rates available to it.

As shown in **Figure 10B**, the dynamic range of rate responses are well-maintained in CNIC neurons across sound levels. Here, *FRR* is plotted against sound level for individual neurons (symbols), and heavy colored lines indicate the median *FRRs* for each neuron type. Median *FRRs* are also shown for low, medium, and high spontaneous rate ANFs (dashed lines) responding to the same stimulus set.

In type I and type V neurons, the largest *FRRs* occur at low sound levels and decline monotonically at higher levels. The *FRRs*, which tend to be larger for type I than for type V neurons, are generally comparable to those of low and medium spontaneous rate ANF. Type O neurons have the opposite behavior, showing higher *FRRs* at high sound levels. FRR values across the three groups are statistically different at the levels between −30 and 0 dB attenuation ($P < 0.001$ ranksum with Bonferroni correction).

When normalized by their peak value, median contralateral weight vector norms (i. e., amplitudes) of type I, type V, and type O neurons similarly increase at low sound levels and gradually peak between 40 and 30 dB attenuation (**Figure 10C**; solid colored lines). In a comparison of these amplitudes with those of ANFs (black dashed lines), median amplitudes of type I and O neurons correspond closely with those of high SR fibers at low sound levels. This finding suggests that high SR fibers alone can account for the responses of CNIC neurons to RSS stimuli at low sound levels., However, median amplitudes of high SR fibers decrease rapidly above 50 dB attenuation (presumably as a consequence of rate saturation; Young and Calhoun, 2005) whereas CNIC amplitudes continue to peak. The relationship between weight vector amplitudes and attenuation level at these higher sound levels more closely resembles that of low- and medium-SR fibers. Thus, weight vector amplitudes of CNIC neurons seem to reflect the behavior of the most responsive groups of AN fibers at each sound level.

DISCUSSION

THE WEIGHT-FUNCTION MODEL

Unlike STRFs, weight-function maps computed in this study do not describe the temporal selectivity of CNIC neurons. Rather, weight functions can be viewed as a frequency marginal of the STRF, providing an average of STRFs across the time dimension (Kim and Young, 1994). In neurons where STRFs are separable—that is, where STRFs can be written as the product of a frequency function, $A(f)$, and time function, $B(t)$, [i. e., $A(f)B(t)$]—weight functions can be viewed as similar to the frequency function $A(f)$. At lower sound levels, STRFs of most CNIC neurons have been found to be separable (Qiu et al., 2003; Lesica and Grothe, 2008a), but as stimulus levels increase, STRFs lose separability (Lesica and Grothe, 2008a). This observation may mirror the complex shape changes observed in RSS-derived weight functions, particularly among type V and O neurons. A clear example of neurons with inseparable characteristics that can't be modeled

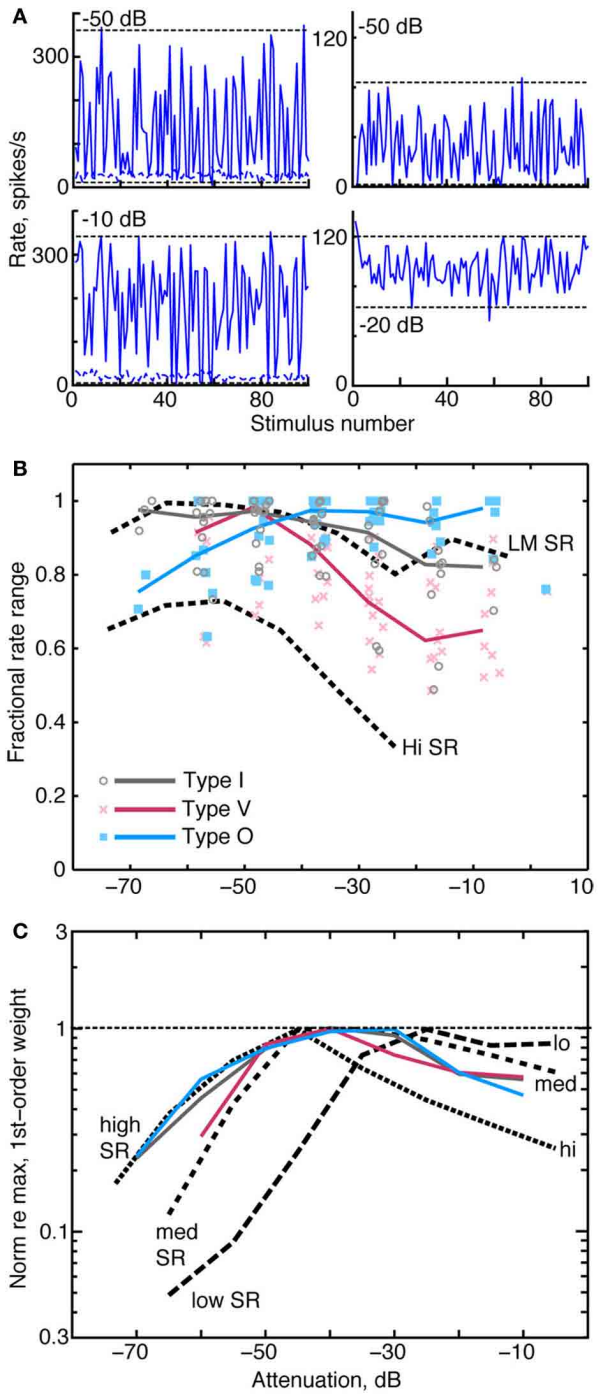

FIGURE 10 | Relationships between rate dynamic range, weight amplitude, and stimulus level. (A) Rate responses of two type I neurons to RSS stimuli. Each column contains data from one neuron, presented at two sound levels, as given by the legends. Horizontal dashed lines indicate rates at the 2.5 and 97.5 percentiles of the distribution of rates. *FRR* is calculated from these rates, see text. **(B)** *FRR*s of type I, O, and V populations at different attenuations of the RSS stimuli. Symbols mark the *FRR* of one neuron's responses at the indicated sound level. Abscissa positions of the data points are dithered by ±3 dB to improve clarity. Solid colored lines are the median *FRR*s for the neuron types in 10 dB bins.

(Continued)

FIGURE 10 | Continued
Black dashed lines are the median *FRR*s of 355 ANFs with high spontaneous rate (*Hi SR*) and low-to-medium spontaneous rate (*LM SR*) [from Young and Calhoun (2005)]. Low and medium SR fibers have been combined because they exhibit identical behavior. **(C)** Median norms of 1st-order weight vectors for CNIC neurons (contralateral only; colored lines) and ANFs [dashed lines; from Young and Calhoun (2005)]. For each neuron type, median norms have been scaled to a maximum value of 1 for comparison. Median norms peak at the following values, in spikes/s/dB: type I, 2.4; type V, 1.4; type O, 1.4; low-SR ANF, 3.0; medium-SR ANF, 3.0; and high-SR ANF, 2.9.

with weight functions are those with directional responses to frequency sweeps (Andoni and Pollak, 2011). In addition, a strictly spectral model is not useful in describing responses to stimuli with substantial amplitude or frequency modulation (Delgutte et al., 1998; Lesica and Grothe, 2008b; Zheng and Escabi, 2008).

Despite these limitations, the weight-function model has advantages over other approaches to broadband characterization of auditory neurons. One is that it is easy to express the responses in terms of nonlinear stimulus dimensions that are natural for the auditory system, i.e., log frequency and log sound level. The appropriateness of log frequency is clear from the layout of frequencies on the basilar membrane and in central auditory maps. The appropriateness of log sound level is suggested by amplitude compression in the response of the basilar membrane [reviewed by Robles and Ruggero (2001)] and by the fact that discharge rate is locally linear with dB amplitude in AN fibers (Sachs et al., 2006) and neurons in the cochlear nucleus (May et al., 1998). Further evidence is the fact that computing STRFs with a logarithmic stimulus-amplitude scale results in better fits in prediction tests compared to a linear or power scale (Escabi et al., 2003; Gill et al., 2008).

The actual functional form of the best-fitting input nonlinearity was determined from data by Ahrens et al. (2008) in auditory cortex neurons. Their input nonlinearities were expressed as functions on a log stimulus amplitude scale, i.e., as an additional nonlinearity beyond the logarithm. In most cases, the functions were linear over some portion of the log scale, consistent with the model used here, but modified by rectification and sometimes saturation at low and high levels. Another approach to describing input nonlinearities, which was mentioned in the introduction (Bandyopadhyay et al., 2007), is to incorporate an intensity nonlinearity into a 1st-order weight function for neurons in dorsal cochlear nucleus. In this case, the nonlinearity is frequency-dependent and cannot be represented with a single input nonlinearity.

IMPORTANCE OF SECOND-ORDER FILTERS

Previous studies of CNIC neurons have yielded conflicting perspectives on the importance of 2nd-order filters. In the bat, 2nd-order filters have been shown to be important in describing CNIC neuron responses (Andoni and Pollak, 2011); by contrast, in the cat, 2nd-order filters have been found not to be useful (Atencio et al., 2012). Reasons for these differences are not clear. However, the results of the current study clearly support the view that 2nd-order filters are important in the CNIC. As shown in **Figure 7B**, the accuracy of the spectral integration model for

CNIC neurons is improved with the addition of 2nd-order terms. In fact, in 93% of neurons studied, the addition of one or two judiciously chosen 2nd-order weights increased *fv*-values to levels not achievable through the addition of 1st-order weights alone (data not shown). The latter observation indicates that improvements in prediction accuracy depend specifically on 2nd-order terms and do not merely reflect the inclusion of a larger number of model parameters. Similar improvements to 1st-order models achieved through the inclusion of 2nd-order terms have been described for temporal responses in auditory cortex (Pienkowski et al., 2009).

The improvement in prediction performance achieved with 2nd-order filters may simply reflect the addition of static nonlinearities that match the curvature of a neuron's rate-level function. In models based on the STRF, prediction quality is often improved by following the linear STRF with a static nonlinear function—one that matches the amplitude of the STRF output to the neuron's response rate (e.g., Escabi et al., 2005; Nagel and Doupe, 2006; Lesica and Grothe, 2008a; Sharpee et al., 2008; Atencio et al., 2012). In these so-called "linear-nonlinear models," the nonlinear segment often bears the shape of a parabola that is dominated by a 2nd-order term. In the current study, the 2nd-order filters are equivalent to such models insofar as the 2nd-order filter and 1st-order weight functions demonstrate the same frequency selectivity. This was sometimes observed in the CNIC, as with the type O neuron in **Figure 3D** (blue filter, bottom left). However, in almost all cases, 2nd-order filters exhibited frequency selectivity that differed significantly from that of 1st-order weight functions (see part **D** of **Figures 2** through **4**). This suggests that a response function in the CNIC often cannot be described by simply appending a single nonlinear filter to a linear one. This finding has important functional implications, as it reveals a complexity in the frequency selectivity of CNIC neurons that is not captured by a 1st-order model alone.

However, the 2nd-order terms in weight functions are not universally useful, as was found for responses to HRTF filtered noise (**Figure 8C**). Although the addition of 2nd-order terms improved RSS response predictions, this was not true for HRTF response predictions. In fact, on average, weight-function models predicted HRTF responses better without the 2nd-order terms. Errors resulting from the inclusion of 2nd-order terms may reflect inaccuracies in modeling the average rate responses to those stimuli. When 2nd-order terms were added, errors in average rate were found to be larger than gains in the rate fluctuations. This suggests that the estimation of 2nd-order terms is more stimulus-dependent than the estimation of 1st-order terms. This interpretation is consistent with the general finding that STRF models perform better for the stimulus type to which they are fit (e.g., Theunissen et al., 2000; Machens et al., 2004). A similar result was recently obtained while trying to predict the binaural responses of neurons in the nucleus of the brachium of the inferior colliculus (Slee and Young, 2013). Here, the responses to binaural VS were well-predicted by an RSS model with only1st-order terms.

BINAURAL INTERACTION

As in previous studies of decerebrate cats (Davis et al., 1999; Chase and Young, 2005), CNIC neurons in the present sample were found to be binaural: that is, monaural stimuli presented to either ear yielded a response with a clear BF. Frequency selectivity in binaural CNIC neurons is often studied using monaural stimuli, where stimuli are presented either to the contralateral ear alone or in free field. But auditory neurons rarely encounter stimuli that are truly monaural in a natural environment. Studies involving binaural free-field stimulation, which are often based on a more natural stimulus presentation, may also be problematic in that they usually do not account for the varying dichotic nature of the stimuli. As such, responses dependent on the interaction of contralateral and ipsilateral inputs—e. g., sensitivity of neurons to interaural level differences (Delgutte et al., 1999)—are often not analyzed in a systematic manner that is frequency-specific.

In this work, independent RSS stimuli were presented to the two ears simultaneously. This binaural stimulus presentation enabled interactions between contralateral and ipsilateral inputs—as well as contralateral and ipsilateral frequency selectivity—to be investigated in a controlled manner. Furthermore, frequency selectivity, which was computed in the form of weights, could be compared between the two ears. For type I and O neurons, contralateral weights were almost always found to be larger in magnitude than ipsilateral weights (**Figure 9B**), suggesting that the responses of these neurons are more strongly influenced by spectra presented to the contralateral ear. Studies of CNIC neurons based on STRFs corroborate this finding, indicating that ipsilateral STRFs—which were found to be significant for only 36% of CNIC neurons studied—usually provide weak spectral representations (Qiu et al., 2003). For some binaural CNIC neurons, the contralateral weight functions alone appear sufficient to describe rate responses (e. g., the points on the diagonal line in **Figure 9A**), suggesting that these neurons are weakly responsive to ipsilateral RSS inputs. Prediction testing does suggest, however, that inputs from the ipsilateral ear contribute significantly to the responses of many CNIC neurons. **Figure 9A** indicates that spectral integration models that ignore inputs to the ipsilateral ear may yield errors in a large number of neurons. Difficulties reported in using STRFs to predict CNIC responses may reflect, to some extent, omission of ipsilateral inputs.

The consistently small size of binaural interaction weights (i. e., b_{jk}, the sixth term in Equation 1) suggests that binaural interactions, as they pertain to stimulus spectra (i. e., interaural level differences), are primarily additive rather than multiplicative. This conclusion is subject to the reservation that binaural interactions related to interaural time differences are not addressed here.

LEVEL-TOLERANT TUNING

The tuning of response areas—whether derived from noise or tone stimuli—becomes more level tolerant across the ascending pathway from the cochlea to the auditory cortex. For tones, neurons show sharper tuning in CNIC than in the cochlea (measured by Q40; Ramachandran et al., 1999; McLaughlin et al., 2007), and fully level-tolerant tone response maps have only been reported in auditory cortex (Sutter, 2000; Sadagopan and Wang, 2008). Tuning to broadband stimuli is more level tolerant than tuning to tones, even at the level of the auditory nerve

(Carney and Yin, 1988; Young and Calhoun, 2005) where level tolerance is believed to reflect cochlear suppression. In this study, we show weight-function maps that are more level tolerant than auditory nerve maps (**Figure 6B**), and tuning in type I and O neurons that is fully level tolerant. Experiments based on antagonists to inhibitory neurotransmitters (Yang et al., 1992; Lebeau et al., 2001), small cochlear lesions (Snyder and Sinex, 2002), and stimulus-driven adaptation suggest that sharpening of tone tuning can be attributed to inhibitory inputs at frequencies away from BF. The level tolerance observed in CNIC weighting functions is likely also shaped by this inhibition. From a functional perspective, level tolerance is significant: it suggests that CNIC neurons are capable of maintaining selectivity for narrow spectral features—such as those found in HRTFs—across a wide range of stimulus levels.

RESPONSE TYPES IN THE CNIC

The results shown here add to the current understanding of neural response types in the cat CNIC. The classification scheme applied in this study is based on spectral tuning for tones (Ramachandran et al., 1999; Greene et al., 2010), analysis of masking patterns (Ramachandran et al., 2000), and binaural processing (Davis et al., 1999; Ramachandran and May, 2002). The validity of this scheme is supported by the fact that class definitions incorporate multiple aspects of a neuron's response properties. Moreover, similar response types have been described in a number of animal species (when effects of anesthesia and stimulus design are taken into account; for example: bat, Yang et al., 1992; guinea pig, Lebeau et al., 2001; mouse, Egorova et al., 2001; rat, Hernández et al., 2005). The relative prevalence of the three response types does varies widely across species (Davis, 2005). Neurons resembling types I and V are found in all species, but the prevalence of type O neurons, which are most common in cats, varies significantly. This suggests that there are significant species differences in the representation of sound in IC.

In contrast to tone maps, the shapes of weight-function maps as described in this study do not clearly define the response types nor allow them to be differentiated. In type I neurons, weight-function maps usually exhibit on-BF positive (excitatory) peaks for the contralateral ear and on-BF negative troughs (inhibition) for the ipsilateral ear (as in **Figure 2**). It can also be stated that in type O and type V neurons, contralateral and ipsilateral weight-function maps usually contain areas of inhibition near BF that are more prominent than those for type I neurons (as in **Figures 3**, **4**). However, patterns of excitation and inhibition observed in weight-function maps—within a single response type—vary significantly, particularly within the type V and O classes. As a result, weight-function maps do not in themselves support a well-defined classification scheme. Likewise, studies of STRFs have yet to define a classification scheme for auditory neurons in CNIC or elsewhere [although see Woolley et al. (2009) in bird cortex].

On the other hand, results of this study do support the functional relevance of the type I, V, and O classification scheme. Specifically, the nature of spectral sensitivity differs for the three classes. As demonstrated in **Figures 7**, **8**, each of the neuron types is sensitive to spectral shape, as rate responses vary with changes in stimulus spectrum. For type I neurons, a low-order model containing only 1st- and 2nd-order terms typically accounts for most of the variance in rate responses—and thus spectral sensitivity—at stimulus levels up to 50–60 dB above threshold. By comparison, a low-order model is a less accurate description of type V and O rate responses, except at the lowest stimulus levels (**Figure 8**). The nature of spectral encoding therefore appears to be different for type I, V, and O neurons.

Differences in spectral encoding between type I, V, and O neurons support the idea of parallel representations of auditory stimuli (Yu and Young, 2000; Escabi and Schreiner, 2002; Woolley et al., 2009). Type I neurons, like chopper neurons in the ventral cochlear nucleus, produce linear representations of spectral shape. The weight function model did successfully capture the variation in rate responses across a set of untrained, functionally relevant VS stimuli (see **Figures 8B,C**). On the other hand, type O and V neurons exhibit nonlinear relationships between spectral level and discharge rate that imply other functional possibilities. One possibility is that "nonlinear" neurons may be encoding specific features of the stimulus—e. g., spectral notches or rising spectral edges, as are present in VS stimuli—in a manner not easily explained with a linear spectral integration model. Such neurons have been observed in the dorsal cochlear nucleus and CNIC (Davis et al., 2003; Escabi et al., 2005; Reiss and Young, 2005). Alternatively, the responses of nonlinear neurons may be more strongly influenced by properties of the stimulus other than the spectra, such as features encoded in the time domain. For example, type V neurons seem to be specialized for encoding interaural time differences (Ramachandran and May, 2002; Chase and Young, 2005), which were not controlled in RSS stimuli presentations. A full exploration of the link between response nonlinearity, feature selectivity, and temporal sensitivity remains to be done.

ACKNOWLEDGMENTS

Supported by grant DC-000115 from NIDCD. The technical assistance of Ron Atkinson, Phyllis Taylor, and Qian Li facilitated this work. Data acquisition software was written by Alon Fishbach.

REFERENCES

Adams, J. C. (1979). Ascending projections to the inferior colliculus. *J. Comp. Neurol.* 183, 519–538.

Aertsen, A. M. H. J., and Johannesma, P. I. M. (1981). The spectro-temporal receptive field. A functional characteristic of auditory neurons. *Biol. Cybern.* 42, 133–143.

Ahrens, M. B., Linden, J. F., and Sahani, M. (2008). Nonlinearities and contextual influences in auditory cortical responses modeled with multilinear spectrotemporal methods. *J. Neurosci.* 28, 1929–1942.

Andoni, S., and Pollak, G. D. (2011). Selectivity for spectral motion as a neural computation for encoding natural communication signals in bat inferior colliculus. *J. Neurosci.* 31, 16529–16540.

Atencio, C. A., Sharpee, T. O., and Schreiner, C. E. (2012). Receptive field dimensionality increases from the auditory midbrain to cortex. *J. Neurophysiol.* 107, 2594–2603.

Bandyopadhyay, S., Reiss, L. A., and Young, E. D. (2007). Receptive field for dorsal cochlear nucleus neurons at multiple sound levels. *J. Neurophysiol.* 98, 3505–3515.

Barbour, D. L., and Wang, X. (2003). Auditory cortical responses elicited in awake primates by random

spectrum stimuli. *J. Neurosci.* 23, 7194–7206.

Brunso-Bechtold, J. K., Thompson, G. C., and Masterton, R. B. (1981). HRP study of the organization of auditory afferents ascending to central nucleus of inferior colliculus in cat. *J. Comp. Neurol.* 197, 705–722.

Calabrese, A., Schumacher, J. W., Schneider, D. M., Paninski, L., and Woolley, S. M. (2011). A generalized linear model for estimating spectrotemporal receptive fields from responses to natural sounds. *PLoS ONE* 6:e16104. doi: 10.1371/journal.pone.0016104

Cant, N. B., and Benson, C. G. (2008). Organization of the inferior colliculus of the gerbil (*Meriones unguiculatus*): projections from the cochlear nucleus. *Neuroscience* 154, 206–217.

Carney, L. H., and Yin, T. C. T. (1988). Temporal coding of resonances by low-frequency auditory nerve fibers: single-fiber responses and a population model. *J. Neurophysiol.* 60, 1653–1677.

Chase, S. M., and Young, E. D. (2005). Limited segregation of different types of sound localization information among classes of units in the inferior colliculus. *J. Neurosci.* 25, 7575–7585.

Chen, C., Rodriguez, F. C., Read, H. L., and Escabi, M. A. (2012). Spectrotemporal sound preferences of neighboring inferior colliculus neurons: implications for local circuitry and processing. *Front. Neural Circuits* 6:62. doi: 10.3389/fncir.2012.00062

Christianson, G. B., Sahani, M., and Linden, J. F. (2008). The consequences of response nonlinearities for interpretation of spectrotemporal receptive fields. *J. Neurosci.* 28, 446–455.

Davis, K. A. (2005). "Spectral processing in the inferior colliculus," in *Auditory Spectral Processing*, eds M. S. Malmierca and D. R. F. Irvine (Amsterdam: Elsevier), 169–205.

Davis, K. A., Ramachandran, R., and May, B. J. (1999). Single-unit responses in the inferior colliculus of decerebrate cats II. Sensitivity to interaural level differences. *J. Neurophysiol.* 82, 164–175.

Davis, K. A., Ramachandran, R., and May, B. J. (2003). Auditory processing of spectral cues for sound localization in the inferior colliculus. *J. Assoc. Res. Otolaryngol.* 4, 148–163.

Dean, I., Robinson, B. L., Harper, N. S., and McAlpine, D. (2008). Rapid neural adaptation to sound level statistics. *J. Neurosci.* 28, 6430–6438.

De Boer, E., and De Jongh, H. R. (1978). On cochlear encoding: potentialities and limitations of the reverse-correlation technique. *J. Acoust. Soc. Am.* 63, 115–135.

Delgutte, B., Hammond, B. M., and Cariani, P. A. (1998). "Neural coding of the temporal envelope of speech: relation to modulation transfer functions," in *Psychophysical and Physiological Advances in Hearing*, eds A. R. Palmer, A. Rees, A. Q. Summerfield, and R. Meddis (London: Whurr Publ. Inc.), 595–603.

Delgutte, B., Joris, P. X., Litovsky, R. Y., and Yin, T. C. T. (1999). Receptive fields and binaural interactions for virtual-space stimuli in the cat inferior colliculus. *J. Neurophysiol.* 81, 2833–2851.

Efron, B., and Tibshirani, R. J. (1986). Bootstrap methods for standard errors, confidence intervals, and other measures of statisitical accuracy. *Stat. Sci.* 1, 54–77.

Eggermont, J. J. (2011). Context dependence of spectro-temporal receptive fields with implications for neural coding. *Hearing Res.* 271, 123–132.

Egorova, M., Ehret, G., Vartanian, I., and Esser, K. H. (2001). Frequency response areas of neurons in the mouse inferior colliculus I. Threshold and tuning characteristics. *Exp. Brain Res.* 140, 145–161.

Escabi, M. A., Miller, L. M., Read, H. L., and Schreiner, C. E. (2003). Naturalistic auditory contrast improves spectrotemporal coding in the cat inferior colliculus. *J. Neurosci.* 23, 11489–11504.

Escabi, M. A., Nassiri, R., Miller, L. M., Schreiner, C. E., and Read, H. L. (2005). The contribution of spike threshold to acoustic feature selectivity, spike information content, and information throughput. *J. Neurosci.* 41, 9524–9534.

Escabi, M. A., and Read, H. L. (2005). Neural mechanisms for spectral analysis in the auditory midbrain, thalamus, and cortex. *Int. Rev. Neurobiol.* 70, 207–252.

Escabi, M. A., and Schreiner, C. E. (2002). Nonlinear spectrotemporal sound analysis by neurons in the auditory midbrain. *J. Neurosci.* 22, 4114–4131.

Greene, N. T., Lomakin, O., and Davis, K. A. (2010). Monaural spectral processing differs between the lateral superior olive and the inferior colliculus: physiological evidence for an acoustic chiasm. *Hearing Res.* 269, 134–145.

Gill, P., Woolley, S., Fremouw, T., and Theunissen, F. E. (2008). What's that sound? Auditory area CLM encodes stimulus surprise, not intensity or intensity changes. *J. Neurophysiol.* 99, 2809–2820.

Henkel, C. K., Fuentes-Santamaria, V., Alvarado, J. C., and Brunso-Bechtold, J. K. (2003). Quantitative measurement of afferent layers in the ferret inferior colliculus: DNLL projections to sublayers. *Hearing Res.* 177, 32–42.

Hernández, O., Espinosa, N., Pérez-González, D., and Malmierca, M. S. (2005). The inferior colliculus of the rat: a quantitative analysis of monaural frequency response areas. *Neuroscience* 132, 203–217.

Holmstrom, L., Roberts, P. D., and Portfors, C. V. (2007). Responses to social vocalizations in the inferior colliculus of the mustached bat are influenced by secondary tuning curves. *J. Neurophysiol.* 98, 3461–3472.

Ito, T., and Oliver, D. L. (2012). The basic circuit of the IC: tectothalamic neurons with different patterns of synaptic organization send different messages to the thalamus. *Front. Neural Circuits* 6:48. doi: 10.3389/fncir.2012.00048

Johnson, D. H. (1980). Applicability of white-noise nonlinear system analysis to the peripheral auditory system. *J. Acoust. Soc. Am.* 68, 876–884.

Kim, P. J., and Young, E. D. (1994). Comparative analysis of spectro-temporal receptive fields, reverse correlation functions, and frequency tuning curves of auditory-nerve fibers. *J. Acoust. Soc. Am.* 95, 410–422.

Klein, D. J., Depireux, D. A., Simon, J. Z., and Shamma, S. A. (2000). Robust spectrotemporal reverse correlation for the auditory system: optimizing stimulus design. *J. Comput. Neurosci.* 9, 85–111.

Lebeau, F. E. N., Malmierca, M. S., and Rees, A. (2001). Iontophoresis *in vivo* demonstrates a key role for GABAA and glycinergic inhibition in shaping frequency response areas in the inferior colliculus of guinea pig. *J. Neurosci.* 21, 7303–7312.

Lesica, N. A., and Grothe, B. (2008a). Dynamic spectrotemporal feature selectivity in the auditory midbrain. *J. Neurosci.* 28, 5412–5421.

Lesica, N. A., and Grothe, B. (2008b). Efficient temporal processing of naturalistic sounds. *PLoS ONE* 3:e1655. doi: 10.1371/journal.pone.0001655

Lewis, E. R., Henry, K. R., and Yamada, W. M. (2002). Tuning and timing in the gerbil ear: Wiener-kernel analysis. *Hearing Res.* 174, 206–221.

Loftus, W. C., Bishop, D. C., and Oliver, D. L. (2010). Differential patterns of inputs create functional zones in central nucleus of inferior colliculus. *J. Neurosci.* 30, 13396–13408.

Machens, C. K., Wehr, M. S., and Zador, A. M. (2004). Linearity of cortical receptive fields measured with natural sounds. *J. Neurosci.* 24, 1089–1100.

Malmierca, M. S., Blackstad, T. W., Osen, K. K., Karagülle, T., and Molowny, R. L. (1993). The central nucleus of the inferior colliculus in rat: a Golgi and computer reconstruction study of neuronal and laminar structure. *J. Comp. Neurol.* 333, 1–27.

Malmierca, M. S., Hernández, O., Antunes, F. M., and Rees, A. (2009). Divergent and point-to-point connections in the commissural pathway between the inferior colliculi. *J. Comp. Neurol.* 514, 226–239.

May, B. J., Anderson, M. J., and Roos, M. (2008). The role of broadband inhibition in the rate representation of spectral cues for sound localization in the inferior colliculus. *Hearing Res.* 238, 77–93.

May, B. J., Leprell, G. S., and Sachs, M. B. (1998). Vowel representations in the ventral cochlear nucleus of the cat: effects of level, background noise, and behavioral state. *J. Neurophysiol.* 79, 1755–1767.

McLaughlin, M., Van De Sande, B., Van Der Heijden, M., and Joris, P. X. (2007). Comparison of bandwidths in the inferior colliculus and the auditory nerve. I. Measurement using a spectrally manipulated stimulus. *J. Neurophysiol.* 98, 2566–2579.

Nagel, K. I., and Doupe, A. J. (2006). Temporal processing and adaptation in the songbird auditory forebrain. *Neuron* 51, 845–859.

Nelken, I., Kim, P. J., and Young, E. D. (1997). Linear and non-linear spectral integration in type IV neurons of the dorsal cochlear nucleus: II. Predicting responses using nonlinear methods. *J. Neurophysiol.* 78, 800–811.

Oliver, D. L., Beckius, G. E., Bishop, D. C., and Kuwada, S. (1997). Simultaneous anterograde labeling of axonal layers from lateral superior olive and dorsal cochlear nucleus in the inferior colliculus of cat. *J. Comp. Neurol.* 382, 215–229.

Oliver, D. L., and Morest, D. K. (1984). The central nucleus of the inferior colliculus in the cat. *J. Comp. Neurol.* 222, 237–264.

Pienkowski, M., and Eggermont, J. J. (2011). Sound frequency representation in primary auditory cortex is level tolerant for moderately loud,

complex sounds. *J. Neurophysiol.* 106, 1016–1027.

Pienkowski, M., Shaw, G., and Eggermont, J. J. (2009). Wiener-Volterra characterization of neurons in primary auditory cortex using poisson-distributed impulse train inputs. *J. Neurophysiol.* 101, 3031–3041.

Press, W. H., Teukolsky, S. A., Vetterling, W. T., and Flannery, B. P. (2007). *Numerical Recipes: The Art of Scientific Computing*. Cambridge: Cambridge University Press.

Qiu, A., Schreiner, C. E., and Escabi, M. A. (2003). Gabor analysis of auditory midbrain receptive fields: spectro-temporal and binaural composition. *J. Neurophysiol.* 90, 456–476.

Ramachandran, R., Davis, K. A., and May, B. J. (1999). Single-unit responses in the inferior colliculus of decerebrate cats I. Classification based on frequency response maps. *J. Neurophysiol.* 82, 152–163.

Ramachandran, R., Davis, K. A., and May, B. J. (2000). Rate representation of tones in noise in the inferior colliculus of decerebrate cats. *J. Assoc. Res. Otolaryngol.* 1, 144–160.

Ramachandran, R., and May, B. J. (2002). Functional segregation of ITD sensitivity in the inferior colliculus of decerebrate cats. *J. Neurophysiol.* 88, 2251–2261.

Rees, A., and Palmer, A. R. (1988). Rate-intensity functions and their modification by broadband noise for neurons in the guinea pig inferior colliculus. *J. Acoust. Soc. Am.* 83, 1488–1498.

Reiss, L. A., Bandyopadhyay, S., and Young, E. D. (2007). Effects of stimulus spectral contrast on receptive fields of dorsal cochlear nucleus neurons. *J. Neurophysiol.* 98, 2133–2143.

Reiss, L. A., and Young, E. D. (2005). Spectral edge sensitivity in neural circuits of the dorsal cochlear nucleus. *J. Neurosci.* 25, 3680–3691.

Rice, J. J., May, B. J., Spirou, G. A., and Young, E. D. (1992). Pinna-based spectral cues for sound localization in cat. *Hearing Res.* 58, 132–152.

Robles, L., and Ruggero, M. A. (2001). Mechanics of the mammalian cochlea. *Physiol. Rev.* 81, 1305–1352.

Sachs, M. B., May, B. J., Le Prell, G. S., and Hienz, R. D. (2006). "Adequacy of auditory-nerve rate representations of vowels: comparison with behavioral measures in cat," in *Listening to Speech: An Auditory Perspective*, eds S. Greenberg and W. A. Ainsworth (London: Psychology Press), 115–127.

Sadagopan, S., and Wang, X. (2008). Level invariant representation of sounds by populations of neuron in primary auditory cortex. *J. Neurosci.* 28, 3415–3426.

Schnupp, J. W. H., Mrsic-Flogel, T. D., and King, A. J. (2001). Linear processing of spatial cues in primary auditory cortex. *Nature* 414, 200–204.

Sharpee, T., Rust, N. C., and Bialek, W. (2004). Analyzing neural responses to natural signals: maximally informative dimensions. *Neural Comput.* 16, 223–250.

Sharpee, T. O., Miller, K. D., and Stryker, M. P. (2008). On the importance of static nonlinearity in estimating spatiotemporal neural filters with natural stimuli. *J. Neurophysiol.* 99, 2496–2509.

Sivaramakrishnan, S., and Oliver, D. L. (2001). Distinct K currents result in physiologically distinct cell types in the inferior colliculus of the rat. *J. Neurosci.* 21, 2861–2877.

Slee, S. J., and Young, E. D. (2013). Linear processing of interaural level difference underlies spatial tuning in the nucleus of the brachium of the inferior colliculus. *J. Neurosci.* 33, 3891–3904.

Snyder, R. L., and Sinex, D. G. (2002). Immediate changes in tuning of inferior colliculus neurons following acute lesions of cat spiral ganglion. *J. Neurophysiol.* 87, 434–452.

Sutter, M. L. (2000). Shapes and level tolerances of frequency tuning curves in primary auditory cortex: quantitative measures and population codes. *J. Neurophysiol.* 84, 1012–1025.

Theunissen, F. E., Sen, K., and Doupe, A. J. (2000). Spectral-temporal receptive fields of nonlinear auditory neurons obtained using natural sounds. *J. Neurosci.* 20, 2315–2331.

Tollin, D. J., and Koka, K. (2010). "Linear and nonlinear coding of sound spectra by discharge rate in neurons comprising the ascending pathway through the lateral superior olive," in *The Neurophysiological Bases of Auditory Perception*, eds E. A. Lopez-Poveda, A. R. Palmer, and R. Meddis (New York, NY: Springer), 143–153.

Versnel, H., Zwiers, M. P., and Van Opstal, A. J. (2009). Spectrotemporal response properties of inferior colliculus neurons in alert monkey. *J. Neurosci.* 29, 9725–9739.

Wallace, M. N., Shackleton, T. M., and Palmer, A. R. (2012). Morphological and physiological characteristics of laminar cells in the central nucleus of the inferior colliculus. *Front. Neural Circuits* 6:55. doi: 10.3389/fncir.2012.00055

Winer, J. A. (2005). "Three systems of descending projections to the inferior colliculus," in *The Inferior Colliculus*, eds J. A. Winer and C. E. Schreiner (New York, NY: Springer), 231–247.

Woolley, S. M., Gill, P. R., Fremouw, T., and Theunissen, F. E. (2009). Functional groups in the avian auditory system. *J. Neurosci.* 29, 2780–2793.

Yang, L., Pollak, G. D., and Resler, C. (1992). GABAergic circuits sharpen tuning curves and modify response properties in the mustache bat inferior colliculus. *J. Neurophysiol.* 68, 1760–1774.

Young, E. D., and Calhoun, B. M. (2005). Nonlinear modeling of auditory-nerve rate responses to wideband stimuli. *J. Neurophysiol.* 94, 4441–4454.

Yu, J. J., and Young, E. D. (2000). Linear and nonlinear pathways of spectral information transmission in the cochlear nucleus. *Proc. Natl. Acad. Sci. U.S.A.* 97, 11780–11786.

Zheng, Y., and Escabi, M. A. (2008). Distinct roles for onset and sustained activity in the neuronal code for temporal periodicity and acoustic envelope shape. *J. Neurosci.* 28, 14230–14244.

Conflict of Interest Statement: The authors declare that the research was conducted in the absence of any commercial or financial relationships that could be construed as a potential conflict of interest.

Received: 28 January 2013; accepted: 22 April 2013; published online: 10 May 2013.

Citation: Yu JJ and Young ED (2013) Frequency response areas in the inferior colliculus: nonlinearity and binaural interaction. Front. Neural Circuits 7:90. doi: 10.3389/fncir.2013.00090

frontiers in
NEURAL CIRCUITS

ORIGINAL RESEARCH ARTICLE
published: 05 September 2012
doi: 10.3389/fncir.2012.00061

Distribution of visual and saccade related information in the monkey inferior colliculus

David A. Bulkin[1]* and Jennifer M. Groh[2,3,4]

[1] *Department of Psychology, Cornell University, Ithaca, NY, USA*
[2] *Department of Neurobiology, Duke University, Durham, NC, USA*
[3] *Department of Psychology and Neuroscience, Duke University, Durham, NC, USA*
[4] *Center for Cognitive Neuroscience, Duke University, Durham, NC, USA*

Edited by:
Manuel S. Malmierca, University of Salamanca, Spain

Reviewed by:
Yang Dan, University of California, Berkeley, USA
Christopher I. Petkov, Newcastle University, UK

****Correspondence:***
David A. Bulkin, Department of Psychology, Cornell University, 243 Uris Hall, Ithaca, NY 14853, USA.
e-mail: dab433@cornell.edu

The inferior colliculus (IC) is an essential stop early in the ascending auditory pathway. Though normally thought of as a predominantly auditory structure, recent work has uncovered a variety of non-auditory influences on firing rate in the IC. Here, we map the location within the IC of neurons that respond to the onset of a fixation-guiding visual stimulus. Visual/visuomotor associated activity was found throughout the IC (overall, 84 of 199 sites tested or 42%), but with a far reduced prevalence and strength along recording penetrations passing through the tonotopically organized region of the IC, putatively the central nucleus (11 of 42 sites tested, or 26%). These results suggest that visual information has only a weak effect on early auditory processing in core regions, but more strongly targets the modulatory shell regions of the IC.

Keywords: multisensory, auditory, vision, cross-modal

INTRODUCTION

Recent work has implicated the inferior colliculus (IC) in audio-visual integration. IC neurons can show different responses to auditory stimuli when presented with concurrent visual stimuli, and can even exhibit overt responses in the absence of a sound (Mascetti and Strozzi, 1988; Gutfreund et al., 2002; Porter et al., 2007; Bergan and Knudsen, 2009) (for review, see Gruters and Groh, this issue). The IC is a critical site of convergence along the ascending auditory pathway: virtually all auditory signals from the brainstem must stop in the IC before reaching thalamus and eventually cortex (Aitkin and Phillips, 1984; Winer and Schreiner, 2005). Thus, visual effects in the IC have the potential to exert a powerful influence on subsequent auditory processing. However, the subnuclei of the IC have dramatically different connectivity patterns. In order to interpret the implications of visually sensitive neurons in the IC it is essential to localize them within the structure.

Recently, our group demonstrated visually sensitive neurons in the macaque IC during a visual fixation task (Porter et al., 2007). A large proportion of sampled units (64%) showed changes in activity that were time-locked to either the onset of a visual fixation cue and/or eye movements that followed. However, because recording location was not systematically varied, it has remained unclear whether these responses are found throughout the IC or are confined to a subregion. In owls, visual modulation of activity has been localized within the lateral nucleus (Gutfreund et al., 2002; Bergan and Knudsen, 2009), but comparable data for other species are sparse and the possibility remains that other regions also show visual sensitivity.

Identifying the precise location of recordings by combining physiology and histology is particularly challenging in large animals such as, macaques. Physiological data are collected over several months, with many repeated electrode penetrations, and individual animals often participate in several experiments. Thus, by the time anatomical data are collected and analyzed, the location at which individual units were recorded is unclear. If only a few histologically-confirmed recording sites can be established for each animal, the time, effort, and cost involved in accumulating a sufficient sample is prohibitive.

One alternative to direct anatomical methods is to utilize known topographic patterns to form a functional map. This approach provides an indirect estimate of location, but allows measures that are centered on the recording electrode specific to each recording penetration. In this manner, the location of neurons possessing a particular functional feature (i.e., sensitivity to visual and visuomotor events) can be assessed using a previously ascertained organization (i.e., functional auditory topography).

We recently defined such a functional map by systematically sampling auditory responses in macaques (Bulkin and Groh, 2011). We measured multiunit neuronal activity throughout the midbrain of six macaques while presenting sounds, allowing delineation of several subregions of the macaque IC consisting of an area showing a tonotopic organization, a surrounding area with neurons tuned for low frequency sounds (tuned area), and a peripheral area in which neurons were either not tuned for tone frequency or not responsive to tones (untuned area). Using this functional map, we presently identify the locations of visually responsive neurons.

Overall, 84 of 199 (~42%) sampled locations showed a change in firing rate following the onset of the fixation stimulus. Responses were most common and most powerful in recordings taken along untuned penetrations, located chiefly in the rostral portion of our recording zone. In penetrations passing through the low frequency tuned, non-tonotopically organized, region of the IC, fewer (and weaker) responses were found. Along tonotopic penetrations, we found only subtle (though significant) effects

of visual stimulus presentations. Despite the lack of robust spiking responses in the tonotopically organized region of the IC, evoked potentials from this area were on par with recordings from neighboring subregions.

These results exhibit similarities and differences compared to our recent findings concerning the distribution of eye-position sensitivity in the IC (Bulkin and Groh, 2012). Neurons sensitive to the orientation of the eyes were most prevalent in recordings in tuned and untuned penetrations, like we report here for visual sensitivity. However, the amplitude of eye position modulation was similar throughout all regions of the IC, whereas we report here that modulation of neuronal activity in response to visual stimuli was much weaker along tonotopic penetrations, putatively the central nucleus of the IC, than in other areas. Taken together, the pattern of overt visual responses and eye position sensitivity supports the view that these multisensory influences are generally more powerful in the tuned and untuned areas, where neuronal activity was strongly related to both the position of the eyes and presentation of visual stimuli, than in the tonotopic area. The dissociation of these two effects in the tonotopically organized IC suggests these two signals may play somewhat different roles in the core ascending auditory pathway.

MATERIALS AND METHODS

SURGICAL PREPARATION, RECORDING PROCEDURES, AND INCLUSION CRITERIA

Three male and three female rhesus monkeys participated in the experiments. All procedures were approved by the Institutional Animal Care and Use Committees at Dartmouth College and Duke University, and were conducted in accordance with the principles of laboratory animal care of the National Institutes of Health (publication 86-23, revised 1985). Surgical procedures were performed using isoflurane anesthesia and aseptic techniques as well as postoperative analgesia. The monkeys underwent an initial surgery to implant a head post for restraining the head and a scleral eye coil for monitoring eye position (Robinson, 1963; Judge et al., 1980). After recovery, an additional surgery was performed to make a craniotomy and to implant a recording cylinder positioned to allow electrodes to approach the left IC at an angle approximately 30° from vertical in the coronal plane. The chamber contained a fixed grid of holes (Crist Instruments, Gaithersburg, MD) aligned such that electrode penetrations could be made in 1 mm increments in the anterior/posterior and (tilted) medial/lateral dimensions.

Recordings were made using tungsten microelectrodes (1–3 MΩ; FHC Inc., Bowdoin, ME). Multiunit clusters were selected using a window discriminator (Monkeys A,W: Plexon Inc., Dallas, TX; Monkeys E,M: Bak Electronics, Germantown, MD) and times of action potentials were stored for off-line analysis. A separate local field potential (LFP) signal (band pass filtered between 0.7 and 300 Hz) was collected and digitized (sampling rate 20 KHz). The location of the IC was determined using an anatomical MRI scan in which the recording chamber and plastic grid could be visualized, and was verified using physiological responses. Using MRI, we estimated all of the borders of the IC except on the rostral aspect, where a clear definition was not visible. This study was part of a larger mapping study in which we sampled neuronal activity throughout the region (in 1 mm increments in the transverse plane and 0.5 mm increments along the depth axis of our recording penetrations) to form a functional map of the region (Bulkin and Groh, 2011). Recordings to assess visual sensitivity were taken at a subset of locations, limited by the behavioral performance of the monkeys, which was required for the visual assessment but not for auditory assessment. Recording sessions began and ended at depths above and below the putative IC to ensure that the entire structure was covered. Analysis of visual response data was limited to locations within the borders measured by MRI scans ±1.5 mm, and meeting auditory response criteria. Sites were included if responses to sounds exceeded 3 SDs of baseline for 10 ms consecutively in a 50 ms window following auditory stimulus onset, and at least three sites within a penetration had to show such responses.

We tested a subset of sites, notably those in the rostral-most penetrations in monkey A, with microstimulation to rule out that they were in the superior colliculus (SC). The SC is an oculomotor structure rostral and dorsal to the IC, and it exhibits auditory responsiveness when animals are engaged in auditory saccade tasks (Jay and Sparks, 1984; Populin et al., 2004). Saccades can be elicited by stimulation in the SC (Robinson, 1972) but are not expected to be elicited from the IC. The absence of stimulation-evoked saccades can therefore help confirm that the MRI-based and physiological inclusion criteria described above are sufficient to limit auditory-responsive sites to those in the IC. Saccades were only elicited at 2 of 51 tested sites included in the auditory data set, confirming the adequacy of anatomical and physiological criteria. Neither of these sites was probed for visual responses, so they were not analyzed further for the present study. In more dorsal, also non-included locations, saccades were frequently observed following stimulation, with a predictable topographic organization of evoked saccade vectors. Such sites were probably in the SC.

STIMULUS PRESENTATION AND BEHAVIORAL TASK

Experiments were conducted in complete darkness in a single-walled sound isolation booth (International Acoustics Company, New York, NY). Echo-absorbent material lined the walls and ceiling (3 inches, Sonex Painted One acoustic foam), as well as the floor (carpet). The head of the monkey was restrained throughout the experiment. Visual stimuli consisted of light emitting diodes (LEDs; luminance ∼26.4 cd/m^2) presented from an array located ∼57 inches in front of the head.

In designing a task for this study, we were motivated by several considerations. The previous finding of visual responses in the monkey IC was a somewhat opportunistic one: visual responses were observed in conjunction with the onset of, or saccade to, a visual fixation target in a task in which visual fixation was followed by sound presentations (Porter et al., 2007). We wanted the task in the current study to also involve a visual fixation stimulus, and a similar time course, so that we would be able to make direct comparisons with the previous study. The task used previously included the presentation of a sound. This auditory stimulus was presented after the periods probed for visual-related responses, but we could not rule out the possibility that anticipation of the sound contributed to visual responsiveness. Here, we wanted to eliminate any chance that a temporally-linked auditory stimulus

might be connected to the observed visual effects. Thus, in the present experiments we used tasks that contained no auditory stimuli.

Monkeys were trained using operant conditioning to fixate visual stimuli for a fluid reward. At each recording site approximately 200 rewarded trials were collected. Two task designs were used and are depicted in **Figure 1**. Both tasks began with the fixation of an LED presented at eye level. Subsequently an additional "probe" LED was briefly flashed at 1 of 12 locations. Monkeys E and M were trained to make an additional saccade to the probe stimulus following the offset of the initial fixation LED (**Figure 1A**). Monkeys A and W were trained to ignore the probe LED and maintain fixation on the initial LED (**Figure 1B**). To allow comparison with our previous study and across monkeys within this study, all of the neurophysiological responses reported in this paper derive from epochs associated with the onset of this fixation target and its associated saccade (the shaded regions in **Figure 1**), i.e., when the task was similar across subjects and studies. If the monkey failed to fixate the appropriate target, or broke fixation, the trial was unrewarded and not included in the analysis. A variable interval ranging from 1 to 2 s followed the reward or error during which no stimuli were presented.

Acoustic stimuli used to ascertain tuning characteristics were presented in separate blocks at the sites probed for visual responses, as well as at numerous sites not tested for visual responsiveness. Auditory stimuli were presented on unrewarded trials with no other stimuli or performance requirements, and consisted of tones of 16 frequencies ranging from 0.4 to 12 kHz (approximately ¼ octave increments), as well as broadband noise (spectrum ranging from 0.5 to 18 kHz). Sounds were generally presented using loudspeakers (Audax Model TWO25V2 or Bose Acoustimas cube speakers) located 90° contralateral to the recording chamber and 57 in. from the subject's head. In all monkeys sounds were presented at 50 dB SPL, calibrated to within 1 dB of the target amplitude using a sound meter (Brüel & Kjær, model 2237 with model 4137 condenser microphone; A-weighted) placed at the position that the monkey's head would occupy in the experiment. The neural responses to sounds were used to classify recordings in a map of IC auditory topography.

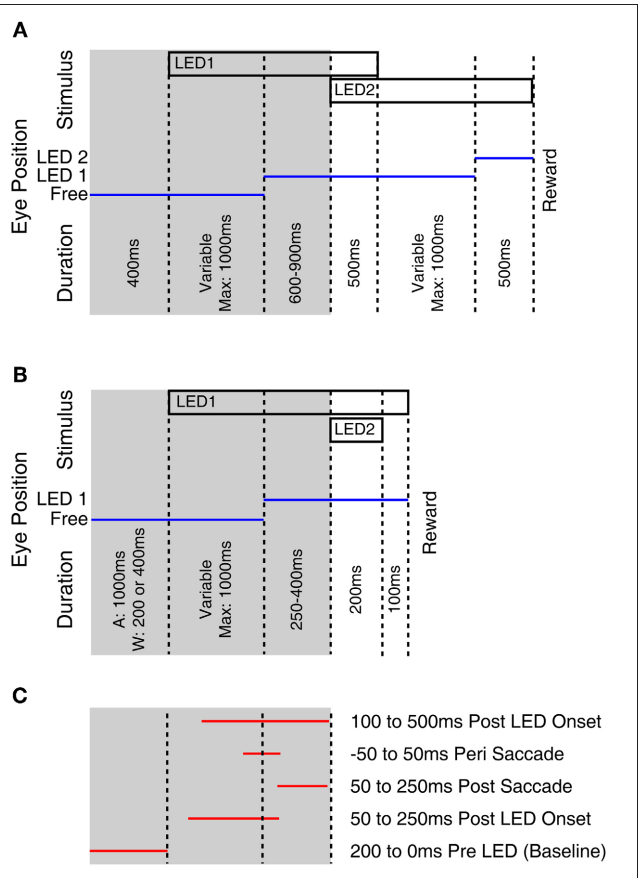

FIGURE 1 | Fixation tasks used to probe for visual responses. This figure illustrates the behavioral tasks used to probe for visual stimuli. Monkeys E and M performed a multiple fixation task **(A)** whereas monkeys A and W held fixation while ignoring a probe stimulus **(B)**. Temporal intervals tested for visual modulation of activity **(C)** used only the first part of the trials, that was common across monkeys. The tested epochs indicated in **(C)** are not drawn to scale as trials involved variable time intervals.

DATA ANALYSIS

Data were analyzed off-line to determine which sites along a penetration showed auditory responses. Auditory penetrations (showing three or more responsive sites) were classified as tonotopic if they showed a systematic progression of increasing tuned frequency with depth, tuned if three or more recordings within a penetration showed frequency tuning (but no systematic progression of tuned frequency), or untuned if the sites either did not respond to tones or did but responded similarly for all tone frequencies. The methods for the auditory response analysis have been described previously (Bulkin and Groh, 2011).

To determine if visual stimuli elicited a response, we compared firing rates during a baseline period (200 ms preceding stimulus onset) to the firing rate during four response epochs: 50–250 ms following the LED illumination, 50–250 ms following the saccade to the LED, 100 ms centered on the saccade, and 100–500 ms following onset of the LED (**Figure 1C**, **Table 2**). We used a two-tailed paired *t*-test to look for significant changes in activity, with a Bonferroni corrected criterion alpha value (i.e., $p < 0.0127$). The rationale for probing for responses in these epochs was to detect sites with different response properties. For example, sites with receptive fields in different locations might exhibit responses during different time periods, based on the eye movements required to perform the task. Sites with extra-foveal receptive fields might respond during the initial appearance of the LED if it happened to lie within that receptive field. Sites with foveal receptive fields would be more likely to show a response at the completion of a saccade to the LED, which would bring the LED onto the fovea. Sites with activity coupled to the saccade would show activity during the time window centered on the saccade. And we have previously observed some sites with slowly increasing activity following the onset of the stimulus (Porter et al., 2007).

Occasionally, electrical noise generated by the LED apparatus influenced recording equipment and generated a spurious response. Artifacts were readily detected as increases in activity

following the onset of the LED with no latency. These sites were removed from analysis by probing for increases in activity exceeding two standard deviations of baseline firing during the first 20 ms of following stimulus onset. Seventeen recordings were excluded from analysis due to too-short latency changes in firing rate.

To investigate spatial sensitivity to visual stimuli, we fit a two-dimensional Gaussian surface to the response (in each of the windows used for response detection described above) as a function of the horizontal and vertical location of the retinal or eye-centered stimulus location.

$$f(x, y) = \mathrm{C} + \mathrm{A}e^{-\left(\frac{(x-\mu_x)^2}{2\sigma_x^2} + \frac{(y-\mu_y)^2}{2\sigma_y^2}\right)}$$

$f(x, y)$ is the estimated firing rate response at eye-centered horizontal (x) and vertical (y) locations of the stimulus at onset. As the eyes were freely moving before the initial fixation cue, there was spontaneous variation in the retinal position of the stimulus. Estimates of μ_x and μ_y define the center of the receptive field, and σ_x and σ_y the spread of the responsive area in the horizontal and vertical dimensions. The amplitude, A, describes the ratio between responsive and unresponsive regions. We allowed both positive and negative amplitude Gaussian fits, meaning that the center of the surface could represent a peak or trough. To compare receptive fields across the population we calculated the diameters of an ellipse made by the Gaussian at half the height of the peak with respect to the offset:

$$\mathrm{FWHM}_x = \sigma_x \cdot 2\sqrt{2\ln 2}$$
$$\mathrm{FWHM}_y = \sigma_y \cdot 2\sqrt{2\ln 2}$$

RESULTS

We tested for visual responses in the activity of multiunit clusters distributed throughout the IC of four rhesus macaques. A total of 84 of 199 recording sites showed a response to the presentation and fixation of an LED in at least one of four tested epochs surrounding the events (**Tables 1**, **2**). Our most extensive sample came from monkey A due to improvements in the techniques we used to target potential recording sites.

Figure 2 displays example response patterns of multiunit clusters from three recording locations. IC cells show a mix of visual and visuomotor activity (Porter et al., 2007). Objectively classifying responses as related to visual or motor events is impossible in a simple fixation task as the onset of the LED is temporally linked to the onset of the saccade. Further confusing the issue, IC visual responses show spatial sensitivity, so a response temporally aligned with saccades may indicate either motor related activity (if it occurs prior to the saccade) or the repositioning of the visual stimulus on the retina (if it occurs following the saccade). Nonetheless, conjectures about the event best linked to responses can be garnered by investigating raster plots sorted on the time of the saccade. **Figures 2A–C** shows histograms and raster plots aligned on the onset of the LED. Rasters have been sorted on reaction time such that the slowest (i.e., longest duration between LED onset and saccade) responses are shown at the bottom of the panels. The red trace indicates the time the eyes entered the criterion target fixation window. At the top of the raster a number of trials are seen with no response latency; in these trials the monkey's eyes were directed at a point within the criterion window when the LED came on (though a small saccade within the window may have followed).

The examples in this figure show the range of different kinds of response patterns observed in our data. The increase in firing rate in Example 1 (panel A) appears time locked to the onset of the LED. The activity increased following the onset of the LED, and then decreased following the saccade. Whether this subsequent decrease is directly related to the saccade, or to the new position of the stimulus on the retina following the saccade (i.e., the fovea) is unclear. Example 2 (panel B) shows an increase around

Table 1 | Proportion of visual/visuomotor sensitive sites in functionally defined locations.

	Monkey				
	A	**W**	**E**	**M**	**Total**
Tonotopic	6/27 (22.2)	5/13 (38.5)	0/0	0/2 (0)	11/42 (26.2)
Tuned	28/82 (34.1)	2/8 (25)	3/14 (21.4)	2/6 (33.3)	35/110 (31.8)
Untuned	34/43 (79.1)	3/3 (100)	1/1 (100)	0/0	38/47 (80.9)
Total	68/152 (44.7)	10/24 (41.7)	4/15 (26.7)	2/8 (25)	84/199 (42.2)

Table 2 | Proportion of visual/visuomotor sensitive sites in functionally defined locations by response epoch.

	Epoch 1 50–250 ms LED onset (%)	**Epoch 2 50–250 ms saccade (%)**	**Epoch 3 100–500 ms LED onset (%)**	**Epoch 4 −50 to 50 ms saccade (%)**	**Group 1 Epochs 1 or 2 or 3 (%)**	**Group 2 Group 1, not epoch 4 (%)**	**Group 3 Epoch 4. not group 1 (%)**
Tonotopic ($n = 42$)	6 (14.3)	8 (19)	8 (19)	7 (16.7)	9 (21.4)	4 (1)	0 (0)
Tuned ($n = 110$)	22 (20)	17 (15.5)	22 (20)	17 (15.5)	33 (30)	18 (16.4)	2 (0.2)
Untuned ($n = 47$)	32 (68.1)	25 (53.2)	32 (68.1)	34 (72.3)	36 (76.6)	4 (0.9)	2 (0.4)
Total ($n = 199$)	60 (30.2)	50 (25.1)	62 (31.2)	58 (29.1)	78 (39.2)	26 (13.1)	4 (0.2)

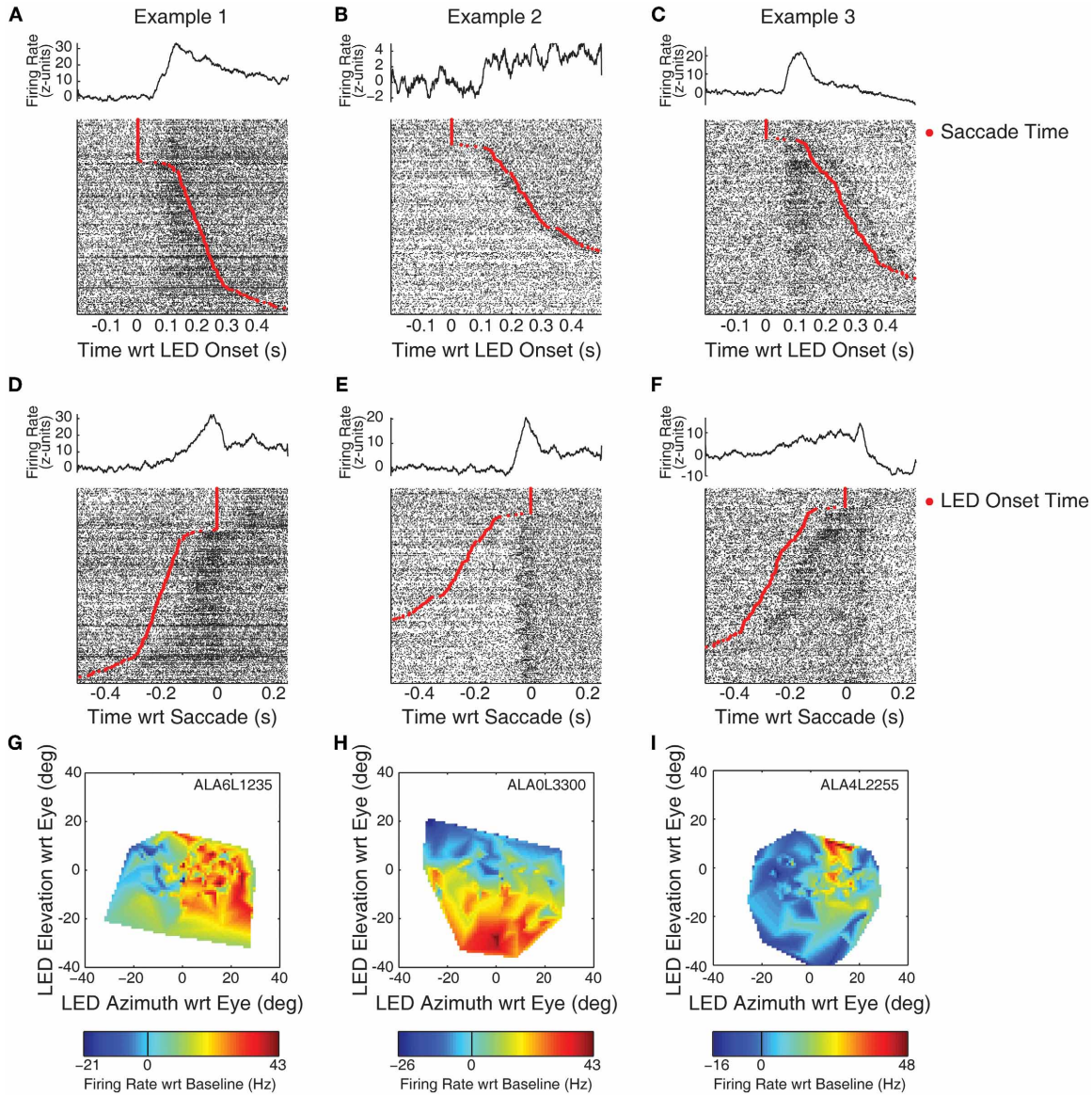

FIGURE 2 | Example recordings with visual and visuomotor related activity. Neural spiking data is plotted for each of three example recording sites in the IC. Panels **(A–C)** display PSTHs and rasters aligned on the onset of the LED. The time of the saccade is indicated by red points in the rasters. An increase in firing rate, time-locked to the onset of the LED, can be observed in panels **(A)** and **(C)**. Panels **(D–F)** display the same data, but aligned instead on the time at which the monkey's eyes entered the criterion fixation window (i.e., on the red points in **A–C**). Here, a seemingly motor-related response can be seen in panel **(E)**. Panels **(G–I)** indicate the spatial tuning properties of the responses using spontaneous changes in eye orientation at the time of LED onset. The ordinate and abcissa indicate the location of the fixation stimulus in eye-centered co-ordinates. Color tracks the firing rate (subtracting baseline), warmer colors indicate increases in firing rate, while cooler colors indicate decreases.

the time of the saccade. This increase is much clearer when the same data are aligned on the time the subject's eyes entered the fixation window (panel E). The increase in activity began immediately preceding the saccade, clearly distinguishable from a visual-related response. Nonetheless, the activity remains above baseline following the saccade, perhaps indicating the presence of a foveal receptive field. Example 3 shows increases in firing rate following both the onset of the LED and the fixation response. In both stimulus-aligned (**Figure 2C**) and response-aligned plots (**Figure 2F**), a transient increase in activity is seen following both the onset of the LED and the saccade.

Table 2 provides the results according to the epochs that indicated significant effects. Generally, sites that showed an increase in activity potentially corresponding to visual-related activity (epochs 1, 2, and 3) also showed a response in the saccade related epoch (epoch 4). (Again, note that although epoch 2 is aligned on the time of the saccade, activity during this temporal window would correspond to a visual effect, with the stimulus occupying a

new location on the retina following the saccade.) Because epoch 4 overlaps with epochs 1 and 3, the data cannot unambiguously distinguish visual from motor responses. Nonetheless, virtually all sites marked as responsive in epoch 4 were also marked in one of the other epochs, suggesting a low incidence of purely motor related activity. These results generally resemble our previous findings at the single-unit level (Porter et al., 2007).

The spatial sensitivity of responses was analyzed by relating activity to the location of the LED with respect to the direction of gaze when it was illuminated. **Figures 2G–I** show estimates of spatial tuning for the three examples. Negative numbers on the x-axis indicate locations in the ipsilateral hemifield; negative numbers on the y axis indicate locations below fixation. Color indicates firing rate, from the epoch that best captured the response (G,I: 50–250 ms following LED onset; H: a 100 ms window centered on the saccade). Warmer colors, indicating increases in firing rate relative to baseline, are seen on the right of panel G: this site showed the largest responses to locations in the contralateral hemifield. Example 2 showed a receptive field in the lower half of the plot, this site responded best when stimuli were below spontaneous pre-trial fixation. Example 3 showed a smaller receptive field, with maximal responses when the LED was in the contralateral hemifield and near or above spontaneous pre-trial eye orientation. A similar plot based on responses in a peri-saccade window was virtually identical (data not shown).

ANATOMICAL DISTRIBUTION OF VISUALLY EVOKED CHANGES WITHIN THE IC

Visually responsive recording sites were not restricted to a small region within the IC. **Figure 3** presents a three-dimensional reconstruction of recording penetrations. Grey vertical lines indicate the trajectory of recordings, which traversed through the midbrain along a dorsolateral to ventromedial course (see Materials and Methods). Along the penetrations, regions showing auditory responses are indicated by colored lines according to the categorical assignment of the penetration's auditory response (Bulkin and Groh, 2011). The locations of visually probed sites are indicated with black circles along the lines, filled markers show a change in firing rate in any of the temporal epochs tested. On occasion, the same location was tested on multiple penetrations. In these cases, a location is marked as visually responsive if any of the recordings showed a response. Responsive sites are found throughout the probed region in monkey A, and no completely unresponsive region is seen. As illustrated in **Table 2**, this was true for each of the different response epochs that we tested. These data indicate that modulation of activity following presentation of visual stimuli is not limited to a small subregion of the IC; rather it spanned the extent of our recordings.

A greater proportion of visually sensitive sites are evident along the peripheral, untuned penetrations in **Figure 3**. Indeed, visual sensitivity was observed at the majority of sites in untuned

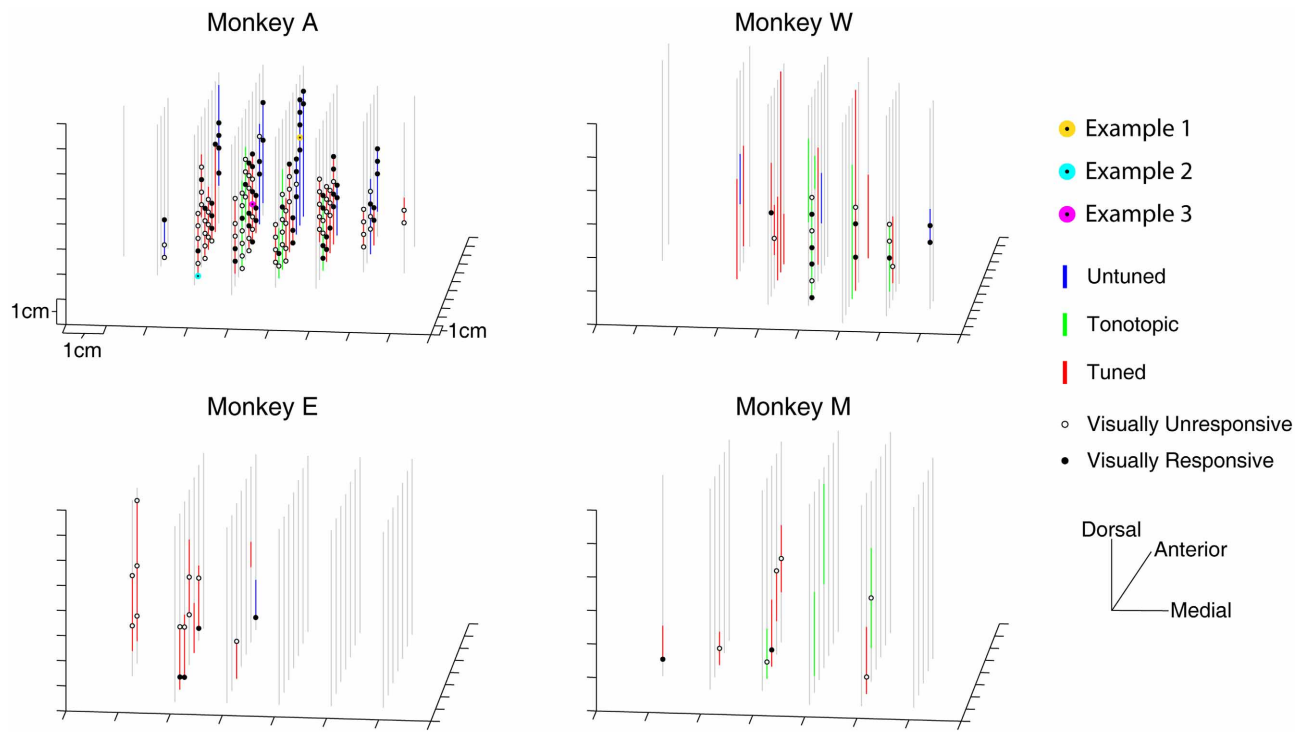

FIGURE 3 | Three dimensional map of locations of tested and responsive recording sites. The location of visually sampled sites are portrayed in a three dimensional representation. Auditory responsive regions are indicated with colored lines untuned penetrations: blue lines; tonotopic penetrations: green lines; tuned penetrations: red lines; (Bulkin and Groh, 2011). Sites that were tested for visual responses, but did not show a significant change in firing rate are indicated with open circles, responsive locations are indicated with filled circles. The locations of the recording sites used for examples in **Figure 2** are marked with yellow, cyan, and magenta circles (all were taken from Monkey A).

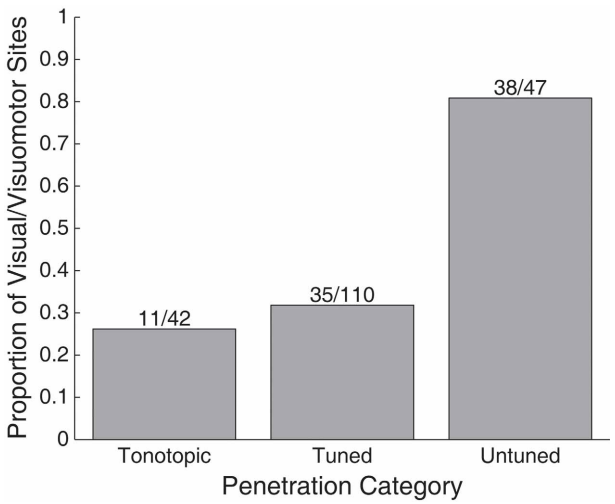

FIGURE 4 | Proportion of visually responsive recordings in tonotopic, tuned, and untuned recording penetrations. The height of bars indicates the proportion of sites showing visual sensitivity in each auditory class of recording penetration. Untuned penetrations contained the largest proportion of sites, tuned, and tonotopic penetrations contained far fewer.

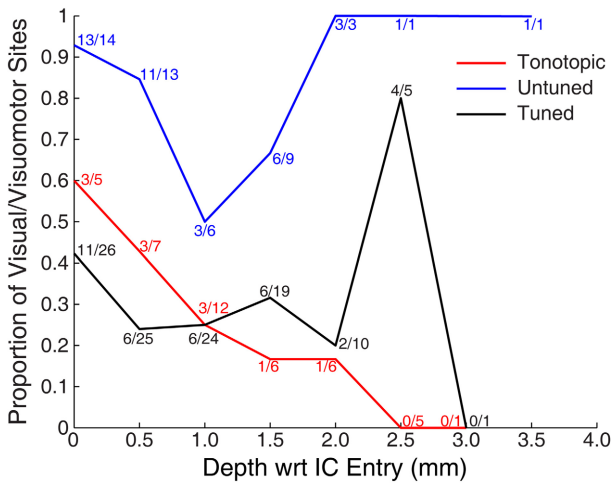

FIGURE 5 | Proportion of visually responsive recordings across recording depth. Data were aligned on the entry into the IC (as measured by the first auditory response in a penetration, i.e., the top of the colored lines in **Figure 3**). Points indicate the proportion of visually sensitive sites at each relative depth, and are marked with the number of responsive and tested sites. Recordings were less common at deeper locations, in part because of the somewhat spherical shape of the IC, and in part because monkeys reached satiety over the course of early recordings.

penetrations, largely found along rostral penetrations in monkey A (**Figure 4**). Importantly, note that these recordings were not taken from the nearby SC. We confirmed the location of the SC was dorsal to our most rostral recordings using microstimulation to probe for evoked saccades (see Materials and Methods for details).

Figure 5 shows the proportion of responsive sites as a function of recording depth for each of the penetration categories. Penetrations were aligned based on the first identified auditory responsive site (i.e., the entry into the IC). The figure provides some indication that deeper recordings within tonotopic penetrations were less likely to exhibit visual responses. However, this result should be interpreted with caution: due to variance in the length of penetrations and the alignment of the earliest sites, deep locations were somewhat undersampled. A total of 5 out of 30 sites located $\geq$1 mm along tonotopic penetrations showed visual responsiveness (16.7%). Although small, this proportion significantly exceeds the proportion expected by chance alone of 5% (binomial $p < 0.05$). Although not definitive, this suggests that visual responses within tonotopic penetrations are not limited to IC shell regions that the electrode passed through en route to the central nucleus.

Although, visual-related signals were present and statistically significant in all three functionally defined regions, the vigor and time course of the responses differed. **Figure 6** shows PSTHs for the individual responsive sites (black traces) as well as average population PSTHs (red traces) for each of the penetration categories. At untuned sites, visual responses are robust and strongly locked to the onset of the visual stimulus. At tuned sites, the responses are weaker, but some are still quite powerful and clearly locked to the visual stimulus onset. However, the pattern at tonotopic sites is quite different: the PSTHs deviate from baseline (and it is therefore clear why they are categorized as responsive) but they are weaker, and do not show the kind of crisp coupling to the LED or the saccade evident in at least at some of the sites for the other two categories. In addition, the responses appear to be equally likely to be inhibitory as excitatory.

The tendency of tonotopic sites to show much weaker visual-related signals is captured differently in **Figure 7**, which shows the distribution of average normalized (units of standard deviation of baseline) firing rate in the epochs used to mark visual responses. Visually sensitive sites in tuned and untuned penetrations generally showed excitatory responses, with untuned penetrations showing larger increases in firing rate. Visual responses in tonotopic penetrations, when found, were much smaller and frequently showed an inhibitory effect. The inset shows the distribution of firing rates for sites not marked as significantly responsive, these distributions were highly similar across categories.

LFPs also showed clear changes following onset of the visual stimulus. **Figures 8A–C** shows normalized LFPs aligned to the onset of the LED for all recorded sites in Monkey A (including both those that showed a significant spiking response as well as those that did not). Interestingly, despite the clear differences seen between spiking responses in each of the functionally defined subregions (**Figures 7**, **8**), LFPs were quite similar. It is unclear whether changes in evoked potentials recorded are truly indicative of dendritic synaptic activity within each of subregions, or if they are merely volume-conducted changes from nearby regions. Clear differences are seen between LFPs following presentation of auditory stimuli in each of these subregions (**Figures 8D–F**), suggesting that this measure can reveal differences locally within the IC. These results support the view that despite the lack of plentiful and powerful overt spiking responses in the tonotopic IC, visual information may potentially reach this subregion.

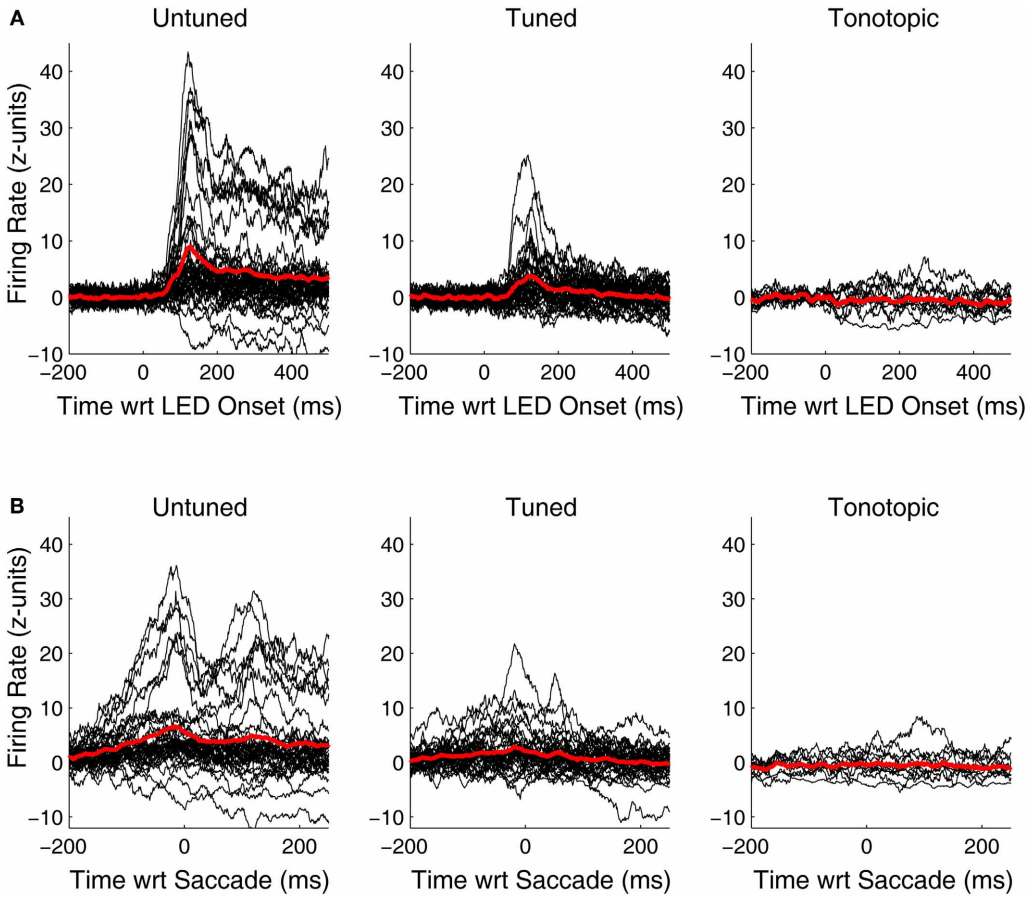

FIGURE 6 | Peri-stimulus and peri-saccade spiking histograms for visually responsive recordings in tonotopic, tuned, and untuned penetrations. Traces of the firing rate over time for all visually sensitive sites, aligned on the onset of the LED **(A)** and the saccade **(B)** are shown in black. Spiking information was binned in 1 ms intervals, smoothed with a 20 ms moving average, and normalized in standard units of baseline (i.e., z-scores). Averages of all significantly sensitive sites (red) are overlaid. In addition to being more common, visual responses along penetrations that showed little to no frequency tuning in the auditory domain, were generally more vigorous than others. Penetrations classified as tonotopic showed only subtle changes in firing rate following presentation of a visual stimulus.

To summarize, the sample along tonotopic penetrations is limited, and spiking responses at these sites tend to be subtle. This makes it difficult to be sure whether there are indeed signals that can reasonably be referred to as "visual" along these penetrations. The available evidence suggests that, if present, visual signals are sparser, weaker, and less temporally coupled to the onset of the visual stimulus in the tonotopic part (putatively the central nucleus) than in other regions of the IC. Nonetheless, it is clear that visually sensitive cells are not confined to a single region in the tissue surrounding the central nucleus.

SPATIAL SENSITIVITY

Though a variety of visual receptive field shapes and sizes among IC neurons were identified in our previous study (Porter et al., 2007), population analysis was previously precluded by a data set that was not collected from locations distributed throughout the structure. To summarize spatial receptive field characteristics, we fit two-dimensional Gaussian surfaces to the activity in each of the epochs used for assessing visual responses based on the eye-centered location of the stimulus (see Materials and Methods). We allowed both positive (i.e., peaks) and negative amplitude (i.e., troughs) surfaces. A negative amplitude function was not necessarily indicative of an inhibitory response, the spatial sensitivity was simply better characterized by a circumscribed lower-response region than a circumscribed higher-response region.

The strongest trends were seen when using a response window 50–250 ms window following stimulus onset (this result is predicted as this window was chosen to capture extrafoveal visual sensitivity). **Figure 9** shows the receptive field locations of all sites that both showed a significant response in this window (t-test, $p < 0.05$) and were successfully fit by a Gaussian function (f-test, $p < 0.05$). Of 71 sites meeting the first of these criteria, 29 sites (~41%) met both. Red points in **Figure 9** indicate the locations of centers of positive amplitude Gaussian fits, and blue points indicate locations of centers of negative amplitude Gaussian fits. Ellipses show the full width half maximum in the horizontal and vertical dimensions, indicating the size and

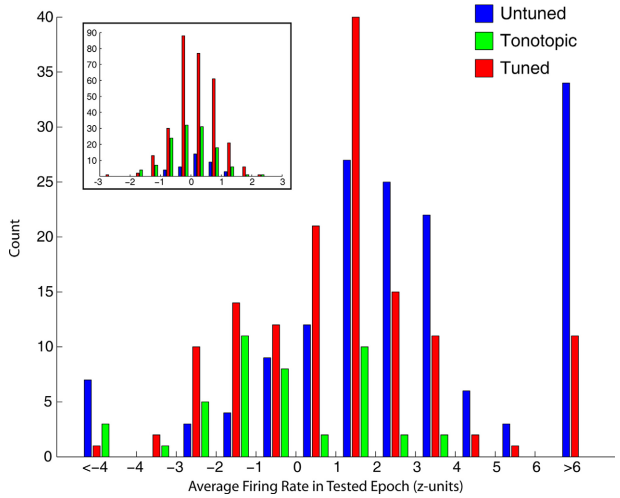

FIGURE 7 | Strength of visual responses in tonotopic, tuned, and untuned recording penetrations. For each of the four epochs tested for visual responses, we computed the average firing rate (normalized in standard deviation units of baseline). This histogram shows the distribution of firing rates across all temporal windows in visually responsive recordings, for each of the auditory penetration categories. Visually responsive sites along untuned (blue) and tuned (red) recording penetrations showed responses of greater magnitude, and were typically excitatory. In contrast, tonotopic penetrations (green) contained sites that showed only small changes in firing rate, and were frequently inhibitory. The inset shows histograms of sites not categorized as visually sensitive, firing rate in sites marked as unresponsive was normally distributed around baseline.

shape of the receptive field. Positive amplitude Gaussian functions dominate the right hand side of the figure, and negative amplitude functions dominate the left. These results show that, across the population, recordings were more likely to show excitatory visual responses when the stimulus was in the contralateral hemifield. Indeed, points in **Figure 9** that do not fit the trend show very small receptive fields, perhaps indicative of spurious receptive field identification. An alternative analysis using multivariate regressions to characterize spatial tuning produced comparable results: slopes of the horizontal component of regressions were biased in favor of increased activity when the stimulus was in the contralateral hemifield (data not shown). The design of our study did not allow for establishing the frame of reference of these response patterns. However, if visual information were strongly and uniformly head-centered, the eye-centered analysis employed here would have been handicapped at revealing spatial sensitivity.

DISCUSSION

We presently report that visual responses in the IC are not confined to a single subregion: they are well spread in the structure. In our most peripheral recordings, along penetrations that showed little to no evidence of tuning to sound frequency, the majority of sites were visually sensitive (38/47 sites). In recordings along penetrations that showed tuning to sounds, but no evidence of a tonotopic progression, we found fewer visual-related responses (35/110 sites). Along tonotopic penetrations, those that likely passed through the central nucleus, a connection was seen between visual stimuli and neural response (11/42 sites), but it involved notably weaker responses as seen in **Figures 7**, **8**.

The fact that visually responsive neurons are not confined to a small subregion within the IC has important implications. Somatosensory inputs to the IC in the cat are restricted. Their presence has been identified both anatomically and physiologically in the lateral nucleus of the structure but not elsewhere (Aitkin et al., 1978, 1981). Interestingly, the same lateral region has been highlighted in research in owls as a putative site of audiovisual integration (Feldman and Knudsen, 1997; DeBello et al., 2001). Auditory responses of neurons in the owl lateral nucleus can be modulated by a visual stimulus (Bergan and Knudsen, 2009), and exhibit overt visual responses when inhibitory signals from the optic tectum are blocked pharmacologically (Gutfreund et al., 2002). Coupled with results in the somatosensory domain, this suggests the lateral nucleus may have a specialized role in multisensory integration: computations underlying the combination of the senses might be handled by a discrete set of circuits in a localized part of the IC.

Our findings offer partial support for but also refinement of this view. In primates, the effects of visual stimuli are spread through the IC, but are clearly stronger in the regions showing untuned or tuned but not tonotopic auditory responses. We found only minimal sensitivity to visual stimuli along tonotopic penetrations. This suggests that visual signals in the central nucleus, the principal ascending auditory region of the IC, are, if indeed present, weaker/sparser. The IC is a three dimensional structure, so recording penetrations through the central nucleus likely passed through shell regions as well. Indeed, it is possible that the small visual signals we did observe along tonotopic penetrations may have come from the shell locations before or after the tonotopic domain. Additional sampling with finer spacing along tonotopic penetrations is necessary to confirm that visual responses are found at above chance levels within this region. Thus, compelling proof of whether or not neurons in the central nucleus show modulation based on visual signals is still needed. In any event, it is now apparent that the strength and prevalence of visual influences is certainly reduced in the tonotopic area relative to surrounding tissue. Subthreshold evoked potentials, however, were fairly similar across subregions of the IC. These results indicate the potential for visual *modulation* of auditory activity in all regions of the IC when stimuli are presented concurrently. Indeed, auditory cortex has shown LFP changes to non-auditory stimuli in the absence of changes in firing rate (Lakatos et al., 2007). This input can modulate bimodal spiking activity without having a unimodal effect, a pattern also seen in the owl IC (Bergan and Knudsen, 2009).

Anatomical studies have revealed multiple visually sensitive regions that project to shell regions of the IC, including connections from visual and parietal cortices (Cooper and Young, 1976; Coleman and Clerici, 1987; Druga et al., 1997), the retina (Itaya and Van Hoesen, 1982; Yamauchi and Yamadori, 1982; Herbin et al., 1994), and the SC (Adams, 1980; Coleman and Clerici, 1987; Covey et al., 1987). Direct inputs to the central nucleus from visual areas have not been conclusively demonstrated, though such information could potentially reach the IC through less direct routes. The weak visual modulation we observed along

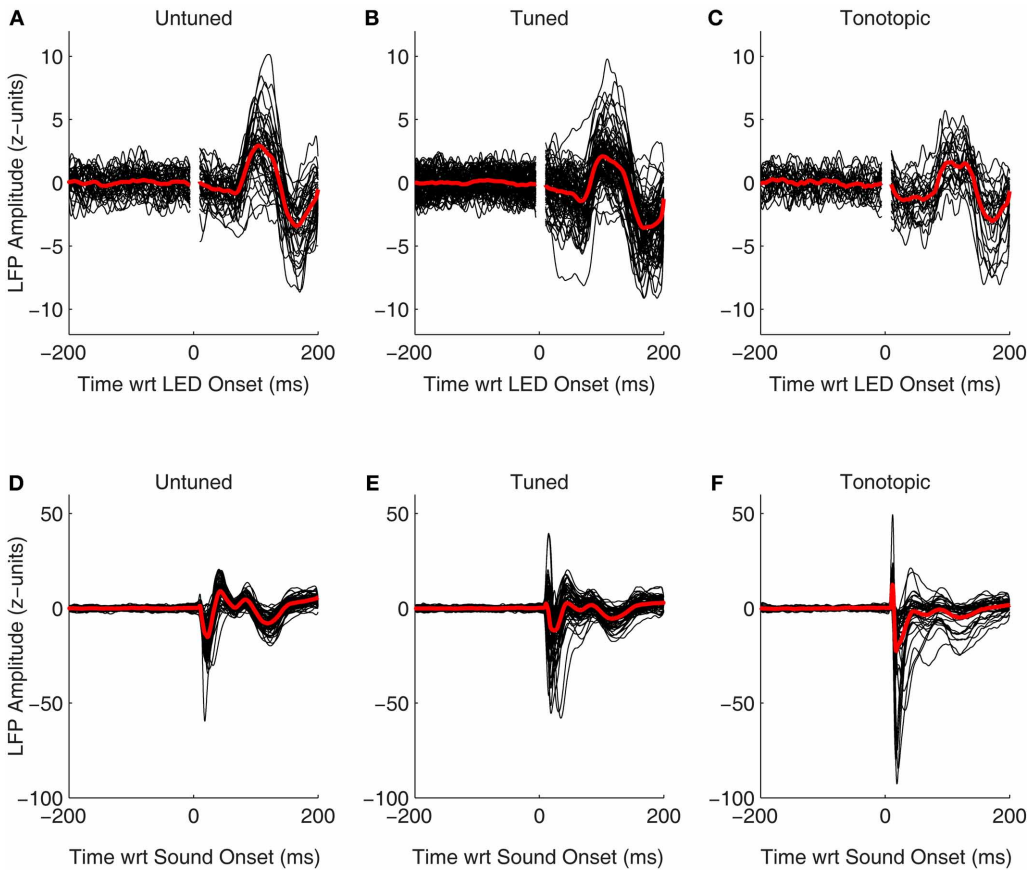

FIGURE 8 | Evoked visual and auditory potentials. The normalized local field potentials for each site, including both those that showed significant spiking responses as well as those that did not, is plotted aligned on onset of the visual **(A–C)** and auditory stimuli (**D–F**; collected from separate blocks, see Materials and Methods). For display, traces were smoothed by convolving the raw data with a 10 ms Gaussian kernel normalized to sum to 1. The red traces indicate the mean of the responses, means were taken from the unsmoothed data.

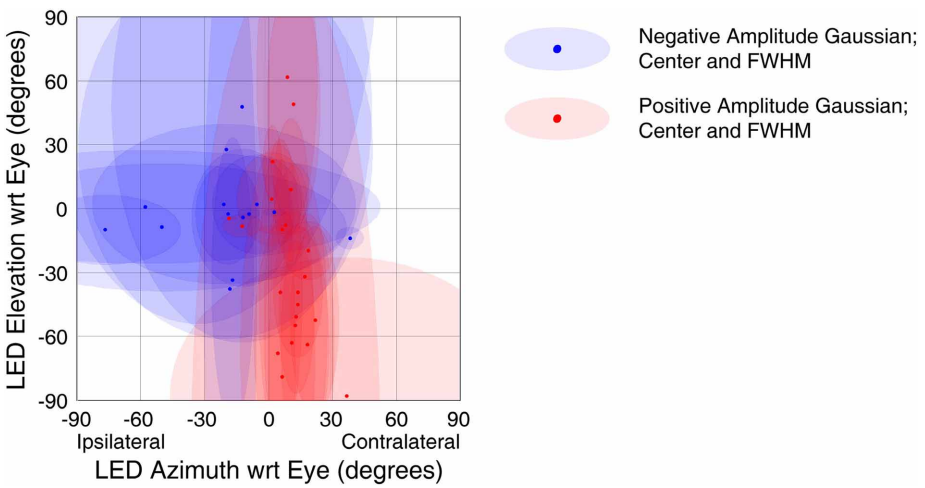

FIGURE 9 | Spatial tuning of visual responses. Receptive fields across all visually sensitive sites were summarized using a Gaussian fitting procedure (see Materials and Methods). The centers of the Gaussian functions are shown with red (Gaussian peaks) and blue (Gaussian troughs) points, and ellipses showing the width in the horizontal and vertical dimensions at half the maximum height of the Gaussian (with respect to its offset). Visually responsive recordings reliably showed increased firing rates to stimuli presented in the contralateral hemifield.

tonotopic penetrations might have arisen through such connections. Future studies with concentrated sampling in the central nucleus will be able to conclusively indicate whether centrally located neurons are sensitive visual input.

Visual information may also reach the IC through descending connections within the auditory pathway. A number of papers have reported both modulation and overt effects of visual stimuli in the core and belt regions of auditory cortex [humans: (Sams et al., 1991; Calvert et al., 1999; Giard and Peronnet, 1999; Callan et al., 2003; Wright et al., 2003; Besle et al., 2004, 2008; Molholm et al., 2004; van Wassenhove et al., 2005; Martuzzi et al., 2007; Luo et al., 2010); monkeys: (Barraclough et al., 2005; Brosch et al., 2005; Ghazanfar et al., 2005; Kayser et al., 2007, 2008, 2010); ferrets: (Bizley et al., 2007; Bizley and King, 2008); reviews: (Calvert, 2001; Ghazanfar and Schroeder, 2006; Kayser et al., 2009); appendix]. Descending connections from the auditory cortex more heavily target the shell regions of the IC than the central nucleus (Diamond et al., 1969; Andersen et al., 1980; Druga and Syka, 1984a,b; Coleman and Clerici, 1987; Saldaña et al., 1996; Druga et al., 1997; Winer et al., 2002; Schofield, 2009), consistent with the response trend we observed.

We also conducted the first population analysis of spatial sensitivity to visual stimuli in the IC. We found that spatial tuning was powerfully lateralized with the largest increases in firing rate coming from stimuli in the contralateral hemifield. Auditory responses show similar spatial sensitivity: IC neurons show monotonoic sensitivity with increasing response amplitude as stimuli are presented farther contralaterally (Groh et al., 2003). Further study on single unit responses will be necessary to determine whether individual cells show a relationship between visual and auditory tuning, but evidence from the population suggests that there may be a link.

The contralateral pattern of visual receptive fields parallels that observed for eye position, where firing rates increase as the eyes are oriented more contralaterally (Bulkin and Groh, 2012) However, the two effects are distinct, and neither can fully account for the other. For example, if the IC were not actually sensitive to visual stimulus location but only to eye position, this would appear in our study as a preference for visual stimulus locations in the opposite hemifield. When the eyes are directed more contralaterally, evoking higher eye-position related activity, the location of the fixation LED would lie more ipsilaterally on the retina, and neurons would appear to have ipsilateral visual receptive fields. We did not observe this pattern, suggesting that eye position and visual signals influence IC neurons independently.

These results raise questions about how auditory, visual, and eye-position signals interact in the IC. To combine the senses, the brain must reconcile signals that arise in different frames of reference: auditory localization is anchored to the head, and visual localization is anchored to the (independently moveable) eyes. In our assessment of spatial sensitivity we used an eye-centered definition of visual location, but the coordinate system used by the brain may be different. On average, auditory information in the IC is not encoded in head-centered frame of reference (as might be assumed given the head centered methods for assessing sound location). Rather auditory response patterns are modulated by the position of the eyes, though not enough to transform them fully into eye-centered co-ordinates (Groh et al., 2001; Zwiers et al., 2004; Porter et al., 2007; Maier and Groh, 2010). Visual signals may show a similar pattern, with receptive fields that are not fully described in a retinotopic reference frame. Such results have been observed in lateral and medial intraparietal cortex, representations of visual and acoustic information span a continuum from head- to eye-centered (Mullette-Gillman et al., 2005, 2009).

Along tonotopically organized penetrations through the IC, putatively the central nucleus, overt visual effects are weak at best while eye position modulation is still quite strong (Bulkin and Groh, 2012). While responses to visual stimuli are weak in the central nucleus, the effect of visual cues during bimodal stimulus presentation remains untested. Visual input may reach the central nucleus, but be ineffective in changing spike rate in the absence of auditory stimuli, a pattern similar observed with somatosensory effects in auditory cortex (Lakatos et al., 2007). Future work using presentations of bimodal stimuli will investigate this possibility.

REFERENCES

Adams, J. C. (1980). Crossed and descending projections to the inferior colliculus. *Neurosci. Lett.* 19, 1–5.

Aitkin, L. M., Dickhaus, H., Schult, W., and Zimmermann, M. (1978). External nucleus of inferior colliculus: auditory and spinal somatosensory afferents and their interactions. *J. Neurophysiol.* 41, 837–847.

Aitkin, L. M., Kenyon, C. E., and Philpott, P. (1981). The representation of the auditory and somatosensory systems in the external nucleus of the cat inferior colliculus. *J. Comp. Neurol.* 196, 25–40.

Aitkin, L. M., and Phillips, S. C. (1984). Is the inferior colliculus and obligatory relay in the cat auditory system? *Neurosci. Lett.* 44, 259–264.

Andersen, R. A., Snyder, R. L., and Merzenich, M. M. (1980). The topographic organization of corticocollicular projections from physiologically identified loci in the AI, AII, and anterior auditory cortical fields of the cat. *J. Comp. Neurol.* 191, 479–494.

Barraclough, N. E., Xiao, D., Baker, C. I., Oram, M. W., and Perrett, D. I. (2005). Integration of visual and auditory information by superior temporal sulcus neurons responsive to the sight of actions. *J. Cogn. Neurosci.* 17, 377–391.

Bergan, J. F., and Knudsen, E. I. (2009). Visual modulation of auditory responses in the owl inferior colliculus. *J. Neurophysiol.* 101, 2924–2933.

Besle, J., Fischer, C., Bidet-Caulet, A., Lecaignard, F., Bertrand, O., and Giard, M. H. (2008). Visual activation and audiovisual interactions in the auditory cortex during speech perception: intracranial recordings in humans. *J. Neurosci.* 28, 14301–14310.

Besle, J., Fort, A., Delpuech, C., and Giard, M. H. (2004). Bimodal speech: early suppressive visual effects in human auditory cortex. *Eur. J. Neurosci.* 20, 2225–2234.

Bizley, J. K., and King, A. J. (2008). Visual-auditory spatial processing in auditory cortical neurons. *Brain Res.* 1242, 24–36.

Bizley, J. K., Nodal, F. R., Bajo, V. M., Nelken, I., and King, A. J. (2007). Physiological and anatomical evidence for multisensory interactions in auditory cortex. *Cereb. Cortex* 17, 2172–2189.

Brosch, M., Selezneva, E., and Scheich, H. (2005). Nonauditory events of a behavioral procedure activate auditory cortex of highly trained monkeys. *J. Neurosci.* 25, 6797–6806.

Bulkin, D. A., and Groh, J. M. (2011). Systematic mapping of the monkey inferior colliculus reveals enhanced low frequency sound representation. *J. Neurophysiol.* 105, 1785–1797.

Bulkin, D. A., and Groh, J. M. (2012). Distribution of eye position information in the monkey inferior colliculus. *J. Neurophysiol.* 107, 785–795.

Callan, D. E., Jones, J. A., Munhall, K., Callan, A. M., Kroos, C., and Vatikiotis-Bateson, E. (2003).

Neural processes underlying perceptual enhancement by visual speech gestures. *Neuroreport* 14, 2213–2218.

Calvert, G. A. (2001). Crossmodal processing in the human brain: insights from functional neuroimaging studies. *Cereb. Cortex* 11, 1110–1123.

Calvert, G. A., Brammer, M. J., Bullmore, E. T., Campbell, R., Iversen, S. D., and David, A. S. (1999). Response amplification in sensory-specific cortices during crossmodal binding. *Neuroreport* 10, 2619–2623.

Coleman, J. R., and Clerici, W. J. (1987). Sources of projections to subdivisions of the inferior colliculus in the rat. *J. Comp. Neurol.* 262, 215–226.

Cooper, M. H., and Young, P. A. (1976). Cortical projections to the inferior colliculus of the cat. *Exp. Neurol.* 51, 488–502.

Covey, E., Hall, W. C., and Kobler, J. B. (1987). Subcortical connections of the superior colliculus in the mustache bat, *Pteronotus parnellii*. *J. Comp. Neurol.* 263, 179–197.

DeBello, W. M., Feldman, D. E., and Knudsen, E. I. (2001). Adaptive axonal remodeling in the midbrain auditory space map. *J. Neurosci.* 21, 3161–3174.

Diamond, I. T., Jones, E. G., and Powell, T. P. (1969). The projection of the auditory cortex upon the diencephalon and brain stem in the cat. *Brain Res.* 15, 305–340.

Druga, R., and Syka, J. (1984a). Neocortical projections to the inferior colliculus in the rat. (An experimental study using anterograde degeneration techniques). *Physiol. Bohemoslov.* 33, 251–253.

Druga, R., and Syka, J. (1984b). Ascending and descending projections to the inferior colliculus in the rat. *Physiol. Bohemoslov.* 33, 31–42.

Druga, R., Syka, J., and Rajkowska, G. (1997). Projections of auditory cortex onto the inferior colliculus in the rat. *Physiol. Res.* 46, 215–222.

Feldman, D. E., and Knudsen, E. I. (1997). An anatomical basis for visual calibration of the auditory space map in the barn owl's midbrain. *J. Neurosci.* 17, 6820–6837.

Ghazanfar, A. A., Maier, J. X., Hoffman, K. L., and Logothetis, N. K. (2005). Multisensory integration of dynamic faces and voices in rhesus monkey auditory cortex. *J. Neurosci.* 25, 5004–5012.

Ghazanfar, A. A., and Schroeder, C. E. (2006). Is neocortex essentially multisensory? *Trends Cogn. Sci.* 10, 278–285.

Giard, M. H., and Peronnet, F. (1999). Auditory-visual integration during multimodal object recognition in humans: a behavioral and electrophysiological study. *J. Cogn. Neurosci.* 11, 473–490.

Groh, J. M., Kelly, K. A., and Underhill, A. M. (2003). A monotonic code for sound azimuth in primate inferior colliculus. *J. Cogn. Neurosci.* 15, 1217–1231.

Groh, J. M., Trause, A. S., Underhill, A. M., Clark, K. R., and Inati, S. (2001). Eye position influences auditory responses in primate inferior colliculus. *Neuron* 29, 509–518.

Gutfreund, Y., Zheng, W., and Knudsen, E. I. (2002). Gated visual input to the central auditory system. *Science* 297, 1556–1559.

Herbin, M., Reperant, J., and Cooper, H. M. (1994). Visual system of the fossorial mole-lemmings, *Ellobius talpinus* and *Ellobius lutescens*. *J. Comp. Neurol.* 346, 253–275.

Itaya, S. K., and Van Hoesen, G. W. (1982). Retinal innervation of the inferior colliculus in rat and monkey. *Brain Res.* 233, 45–52.

Jay, M. F., and Sparks, D. L. (1984). Auditory receptive fields in primate superior colliculus shift with changes in eye position. *Nature* 309, 345–347.

Judge, S. J., Richmond, B. J., and Chu, F. C. (1980). Implantation of magnetic search coils for measurement of eye position: an improved method. *Vision Res.* 20, 535–538.

Kayser, C., Logothetis, N. K., and Panzeri, S. (2010). Visual enhancement of the information representation in auditory cortex. *Curr. Biol.* 20, 19–24.

Kayser, C., Petkov, C. I., Augath, M., and Logothetis, N. K. (2007). Functional imaging reveals visual modulation of specific fields in auditory cortex. *J. Neurosci.* 27, 1824–1835.

Kayser, C., Petkov, C. I., and Logothetis, N. K. (2008). Visual modulation of neurons in auditory cortex. *Cereb. Cortex* 18, 1560–1574.

Kayser, C., Petkov, C. I., and Logothetis, N. K. (2009). Multisensory interactions in primate auditory cortex: fMRI and electrophysiology. *Hear. Res.* 258, 80–88.

Lakatos, P., Chen, C. M., O'Connell, M. N., Mills, A., and Schroeder, C. E. (2007). Neuronal oscillations and multisensory interaction in primary auditory cortex. *Neuron* 53, 279–292.

Luo, H., Liu, Z., and Poeppel, D. (2010). Auditory cortex tracks both auditory and visual stimulus dynamics using low-frequency neuronal phase modulation. *PLoS Biol.* 8:e1000445. doi: 10.1371/journal.pbio.1000445

Maier, J. X., and Groh, J. M. (2010). Comparison of gain-like properties of eye position signals in inferior colliculus versus auditory cortex of primates. *Front. Integr. Neurosci.* 4:121. doi: 10.3389/fnint.2010.00121

Martuzzi, R., Murray, M. M., Michel, C. M., Thiran, J.-P., Maeder, P. P., Clarke, S., and Meuli, R. A. (2007). Multisensory interactions within human primary cortices revealed by BOLD dynamics. *Cereb. Cortex* 17, 1672–1679.

Mascetti, G. G., and Strozzi, L. (1988). Visual cells in the inferior colliculus of the cat. *Brain Res.* 442, 387–390.

Molholm, S., Ritter, W., Javitt, D. C., and Foxe, J. J. (2004). Multisensory visual-auditory object recognition in humans: a high-density electrical mapping study. *Cereb. Cortex* 14, 452–465.

Mullette-Gillman, O. A., Cohen, Y. E., and Groh, J. M. (2005). Eye-centered, head-centered, and complex coding of visual and auditory targets in the intraparietal sulcus. *J. Neurophysiol.* 94, 2331–2352.

Mullette-Gillman, O. A., Cohen, Y. E., and Groh, J. M. (2009). Motor-related signals in the intraparietal cortex encode locations in a hybrid, rather than eye- centered reference frame. *Cereb. Cortex* 19, 1761–1775.

Populin, L. C., Tollin, D. J., and Yin, T. C. (2004). Effect of eye position on saccades and neuronal responses to acoustic stimuli in the superior colliculus of the behaving cat. *J. Neurophysiol.* 92, 2151–2167.

Porter, K. K., Metzger, R. R., and Groh, J. M. (2007). Visual- and saccade-related signals in the primate inferior colliculus. *Proc. Natl. Acad. Sci. U.S.A.* 104, 17855–17860.

Robinson, D. A. (1963). A method of measuring eye movement using a scleral search coil in a magnetic field. *IEEE Trans. Biomed. Eng.* 10, 137–145.

Robinson, D. A. (1972). Eye movements evoked by collicular stimulation in the alert monkey. *Vision Res.* 12, 1795–1808.

Saldaña, E., Feliciano, M., and Mugnaini, E. (1996). Distribution of descending projections from primary auditory neocortex to inferior colliculus mimics the topography of intracollicular projections. *J. Comp. Neurol.* 371, 15–40.

Sams, M., Aulanko, R., Hamalainen, M., Hari, R., Lounasmaa, O. V., Lu, S. T., and Simola, J. (1991). Seeing speech: visual information from lip movements modifies activity in the human auditory cortex. *Neurosci. Lett.* 127, 141–145.

Schofield, B. R. (2009). Projections to the inferior colliculus from layer VI cells of auditory cortex. *Neuroscience* 159, 246–258.

van Wassenhove, V., Grant, K. W., and Poeppel, D. (2005). Visual speech speeds up the neural processing of auditory speech. *Proc. Natl. Acad. Sci. U.S.A.* 102, 1181–1186.

Winer, J. A., Chernock, M. L., Larue, D. T., and Cheung, S. W. (2002). Descending projections to the inferior colliculus from the posterior thalamus and the auditory cortex in rat, cat, and monkey. *Hear. Res.* 168, 181–195.

Winer, J. A., and Schreiner, C. E., (2005). "The central auditory system: a functional analysis," in *The Inferior Colliculus*, eds J. A. Winer and C. E. Schreiner (New York, NY: Springer), 1–68.

Wright, T. M., Pelphrey, K. A., Allison, T., McKeown, M. J., and McCarthy, G. (2003). Polysensory interactions along lateral temporal regions evoked by audiovisual speech. *Cereb. Cortex* 13, 1034–1043.

Yamauchi, K., and Yamadori, T. (1982). Retinal projection to the inferior colliculus in the rat. *Acta Anat. (Basel)* 114, 355–360.

Zwiers, M. P., Versnel, H., and Van Opstal, A. J. (2004). Involvement of monkey inferior colliculus in spatial hearing. *J. Neurosci.* 24, 4145–4156.

Conflict of Interest Statement: The authors declare that the research was conducted in the absence of any commercial or financial relationships that could be construed as a potential conflict of interest.

Received: 05 May 2012; accepted: 18 August 2012; published online: 05 September 2012.

Citation: Bulkin DA and Groh JM (2012) Distribution of visual and saccade related information in the monkey inferior colliculus. Front. Neural Circuits ***6****:61. doi: 10.3389/fncir.2012.00061*

frontiers in
NEURAL CIRCUITS

REVIEW ARTICLE
published: 11 December 2012
doi: 10.3389/fncir.2012.00096

Sounds and beyond: multisensory and other non-auditory signals in the inferior colliculus

***Kurtis G. Gruters*[1]* and *Jennifer M. Groh*[1,2,3,4]**

[1] *Department of Psychology and Neuroscience, Duke University, Durham, NC, USA*
[2] *Department of Neurobiology, Duke University, Durham, NC, USA*
[3] *Duke Institute for Brain Sciences, Duke University, Durham, NC, USA*
[4] *Center for Cognitive Neuroscience, Duke University, Durham, NC, USA*

Edited by:
Manuel S. Malmierca, University of Salamanca, Spain

Reviewed by:
Sarah L. Pallas, Georgia State University, USA
Susan Shore, University of Michigan, USA

****Correspondence:***
Kurtis G. Gruters, Department of Psychology and Neuroscience, Duke University, 308 Research Drive, Box 90999, Durham, NC 27708, USA.
e-mail: kurtis.gruters@gmail.com

The inferior colliculus (IC) is a major processing center situated mid-way along both the ascending and descending auditory pathways of the brain stem. Although it is fundamentally an auditory area, the IC also receives anatomical input from non-auditory sources. Neurophysiological studies corroborate that non-auditory stimuli can modulate auditory processing in the IC and even elicit responses independent of coincident auditory stimulation. In this article, we review anatomical and physiological evidence for multisensory and other non-auditory processing in the IC. Specifically, the contributions of signals related to vision, eye movements and position, somatosensation, and behavioral context to neural activity in the IC will be described. These signals are potentially important for localizing sound sources, attending to salient stimuli, distinguishing environmental from self-generated sounds, and perceiving and generating communication sounds. They suggest that the IC should be thought of as a node in a highly interconnected sensory, motor, and cognitive network dedicated to synthesizing a higher-order auditory percept rather than simply reporting patterns of air pressure detected by the cochlea. We highlight some of the potential pitfalls that can arise from experimental manipulations that may disrupt the normal function of this network, such as the use of anesthesia or the severing of connections from cortical structures that project to the IC. Finally, we note that the presence of these signals in the IC has implications for our understanding not just of the IC but also of the multitude of other regions within and beyond the auditory system that are dependent on signals that pass through the IC. Whatever the IC "hears" would seem to be passed both "upward" to thalamus and thence to auditory cortex and beyond, as well as "downward" via centrifugal connections to earlier areas of the auditory pathway such as the cochlear nucleus.

Keywords: multisensory, inferior colliculus, auditory, sound localization, communication

INTRODUCTION

Organisms gather information about their environment from a variety of sensory systems, but how these sensory systems interact with each other is poorly understood. Multisensory integration is sufficiently common in cortical regions that the cortex has been described as a fundamentally multisensory processor [for review, see Ghazanfar and Schroeder (2006)]. In contrast, relatively little attention has been given to the subcortical systems that provide sensory information to the cortex. Much of the sensory information passed along to the cortex from subcortical areas is already multisensory in nature, and is influenced by behavioral state and relevance of stimuli. In this review, we focus on the multisensory and context-related connections and response properties of the inferior colliculus (IC), an important subcortical node in the auditory pathway.

The IC is particularly interesting in regard to multisensory and other non-auditory contributions to hearing as it is a necessary relay for nearly all ascending and descending auditory information [for review see Winer and Schreiner (2005)]. Situated relatively early in the auditory system, the IC is comprised of a central nucleus (ICC; see **Table 1** for list of abbreviations) and various surrounding shell nuclei (shell nuclei of the IC[1]; sIC collectively), including, but not limited to, the external IC (ICX), pericentral nucleus of the IC (ICP), dorsal and lateral cortices of the IC, and brachium of the IC. The ICC primarily sends ascending auditory information to the thalamus (e.g., Kudo and Niimi, 1980; Calford and Aitkin, 1983) which then proceeds toward the cortex. The sIC also send ascending projections to the thalamus (ICP and ICX projections: Kudo and Niimi, 1980; and

[1]Though the subnuclear anatomy of the IC has been well described elsewhere (e.g., Morest and Oliver, 1984), the names and precise borders of these nuclei are not used consistently in the studies discussed in this review. Therefore, this core-shell nomenclature is adopted to avoid potentially applying these more precise subnuclear definitions inappropriately, particularly when such information is missing or ambiguous. When information about subnuclear locations is available for a given study, we have attempted to include the terminology used by the authors in our description of their findings.

Table 1 | List of anatomical abbreviations.

Abbreviation	Full name
AN	Auditory nerve
BLA	Basal lateral amygdala
DCN	Dorsal cochlear nucleus
FNc	Fastigial nucleus of the cerebellum
GP_C	Caudal portion of the globus pallidus
IC	Inferior colliculus
ICC	Central nucleus of the inferior colliculus
ICP	Pericentral nucleus of the inferior colliculus
ICX	External nucleus of the inferior colliculus
NAm	Nucleus ambiguus
nDC	Dorsal column nuclei
PAG	Periaquaductal gray
SC	Superior colliculus
sIC	Shell nuclei of the inferior colliculus
SN_l	Substantia nigra *pars lateralis*
TN	Trigeminal nerve
TN_{op}	Ophthlamic branch of the trigeminal nerve
TNG	Trigeminal nerve ganglion
VTA	Ventral tegmental area

Calford and Aitkin, 1983) as well as the superior colliculus (SC) (brachium of the IC, ICX: Van Buskirk, 1983; dorsomedial part of the IC, ICX: Druga and Syka, 1984; ICX: Zhang et al., 1987; rostal pole of the IC: Harting and Van Lieshout, 2000), and descending information back to the auditory brainstem (including the ICC) (Huffman and Henson, 1990).

Converging anatomical and physiological evidence indicates that cells within the IC are sensitive to visual, oculomotor, eye position, and somatosensory information as well as to signals relating to behavioral context and reward (**Figure 1**). Auditory perception and behavior are likely to be shaped by these non-auditory inputs to the IC.

NON-AUDITORY INFLUENCES ON NEURAL ACTIVITY IN IC

VISION AND OCULOMOTOR INFLUENCES

Numerous anatomical studies have established the existence of direct retinal innervation of the contralateral IC (rat, monkey: Itaya and Van Hoesen, 1982; rat: Yamauchi and Yamadori, 1982; guinea pig, hamster, rat: Zhang, 1984; mole-lemming: Herbin et al., 1994). Projections from the retina pass through the contralateral SC and into the ICP near the midline, fanning out dorsolaterally, before being pruned back during early neural development (Cooper and Cowey, 1990). Enucleation of the contralateral eye causes the degeneration of these connections in adult animals (Paloff et al., 1985). In addition to receiving retinal efferents, both the ICC and sIC (in particular, the ICX) receive inputs from the visual cortex (primarily ipsilateral) (cat: Cooper and Young, 1976) and the ipsilateral SC, a visually responsive structure involved in programming saccadic eye movements (cat: Adams, 1980; bat: Covey et al., 1987; rat: Coleman and Clerici, 1987; barn owl: Hyde and Knudsen, 2000) [for review of saccade generation in the SC, see Gandhi and Katnani (2011)].

The presence of anatomical connections from visual processing sources suggests that IC neurons should be responsive to visual stimuli. Several physiological studies have investigated this hypothesis and established that there are cells in the IC whose auditory responses are modulated by a concurrent visual stimulus (Syka and Radil-Weiss, 1973; Tawil et al., 1983), or that are capable of responding directly to visual stimuli without an accompanying sound (Mascetti and Strozzi, 1988; Porter et al., 2007; Bulkin and Groh, 2012b). Early reports using anesthetized and paralyzed cats suggested that 8–9% of IC neurons were visually responsive (Tawil et al., 1983: 112 total cells tested; Mascetti and Strozzi, 1988: 91 total cells tested), but later work involving more extensive statistical testing as well as awake and behaving monkeys performing a visually guided saccade task suggests that the proportion is much higher (Porter et al., 2007; Bulkin and Groh, 2012b). Porter et al. (2007) found a variety of response profiles including excitation (35%) or inhibition (5.5%) in response to a visual stimulus, excitation in conjunction with a visual stimulus and its accompanying saccade (15%), or excitation just during the saccade (4.5%). An additional 6% exhibited delayed activity increases or activity that differed in a non-specific but statistically significant fashion from baseline during stimulus presentation and/or the saccade. Overall, 64% of the tested neuronal population ($n = 180$) displayed statistically significant responses to visual stimuli and/or saccade-related activity.

A more detailed mapping of the locations of visual- and saccade-related responses in the IC has revealed that visual response properties are not uniform throughout the IC. Bulkin and Groh (2012b) localized visually responsive neurons with respect to a previous systematic mapping of auditory function in the region (Bulkin and Groh, 2011) (**Figure 2**). To define this functional map, Bulkin and Groh (2011) used a combination of electrophysiological recording, stereotaxic coordinates, MRI, histology, and known physiological properties of IC subdivisions to identify and demarcate three regions with distinct response properties. A central tonotopic region (red region in **Figures 2A,B**; example penetration given in **Figure 2E**), likely situated well within the ICC, exhibited cells whose best frequency increased as the electrode advanced along a dorsolateral to ventromedial trajectory. The surrounding region contained neurons tuned for low-frequency sounds but lacked a tonotopic gradient (low-frequency tuned area; purportedly overlapping with the outer portions of the ICC as well as the sIC) (green region of **Figures 2A,B**; example penetration in **Figure 2D**). Cells within the final region at the periphery of the IC were either unresponsive to pure tones or non-selective for tone frequency (blue region of **Figures 2A,B**; example penetration in **Figure 2C**).

Visual- and visuomotor-responses were found distributed throughout the IC (Bulkin and Groh, 2012b). However the different regions exhibited different proportions of sites sensitive to visual stimuli as well as different patterns of responses at those sites. Untuned auditory areas showed robust visual- or saccade-related responses in 81% of the tested units. Low-frequency tuned sites also showed vigorous visual- and saccade-related firing, but the responses were less strong than untuned sites and were found in only 31% of these cells. Tonotopic penetrations yielded

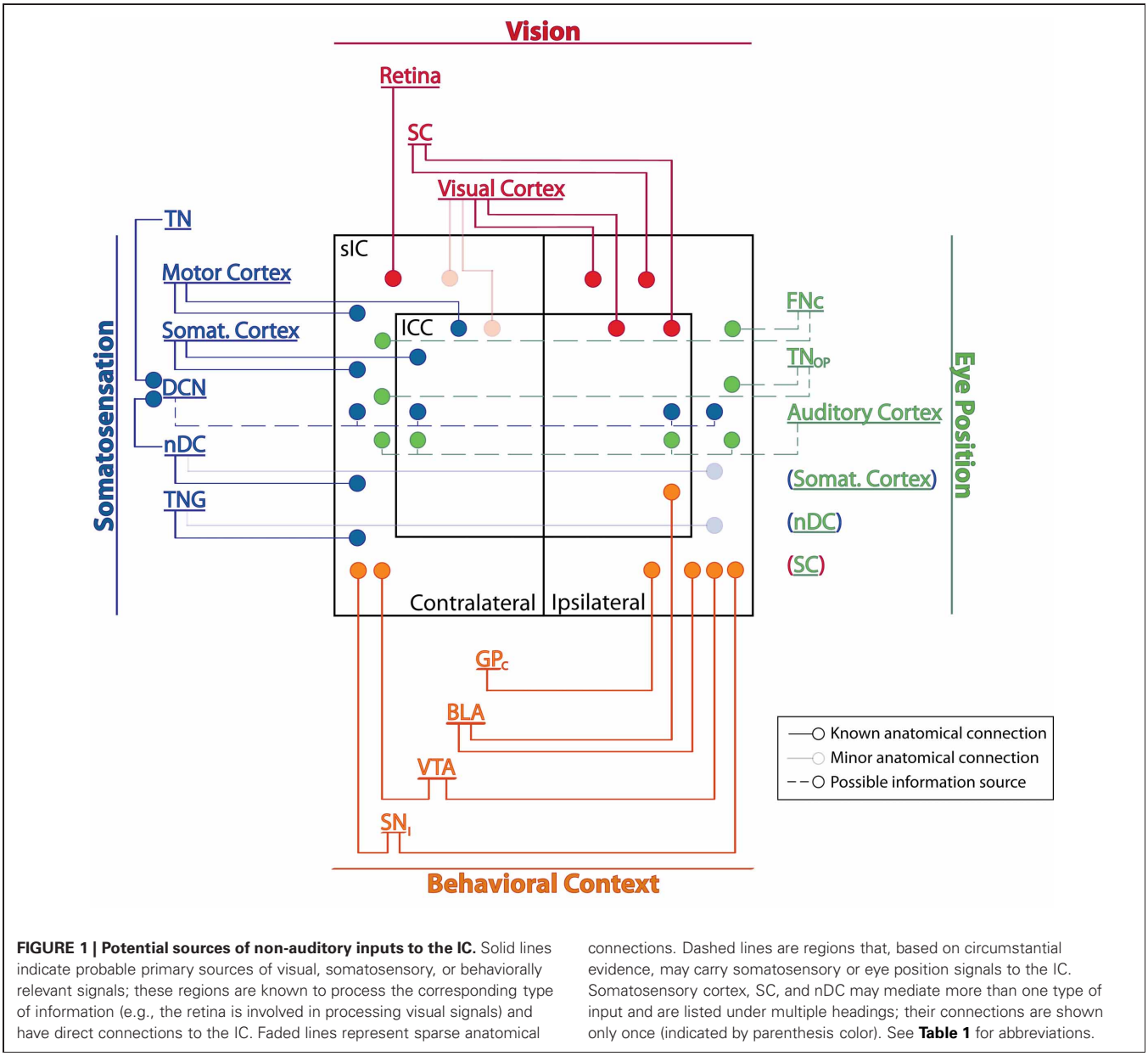

FIGURE 1 | Potential sources of non-auditory inputs to the IC. Solid lines indicate probable primary sources of visual, somatosensory, or behaviorally relevant signals; these regions are known to process the corresponding type of information (e.g., the retina is involved in processing visual signals) and have direct connections to the IC. Faded lines represent sparse anatomical connections. Dashed lines are regions that, based on circumstantial evidence, may carry somatosensory or eye position signals to the IC. Somatosensory cortex, SC, and nDC may mediate more than one type of input and are listed under multiple headings; their connections are shown only once (indicated by parenthesis color). See **Table 1** for abbreviations.

the lowest proportion of responsive cells (26%). Visual-related responses observed on these penetrations were weak, deviating only slightly from baseline, and did not exhibit the same clear stimulus- or saccade-onset timing present in untuned and low-frequency tuned populations.

The relative contributions of each of the potential anatomical sources of visual input to the IC are not known. Response latency is only moderately informative: signals within the IC cannot occur faster than their source signal, but reported latencies span a range consistent with any of the potential sources. Tawil et al. (1983) reported latencies ranging between 20 and 30 ms for the nine visually responsive cells recorded from within the cat IC, consistent with direct retinal innervation (latency in cat optic tract ≈20 ms: Freund et al., 1972), but excluding presumably longer latency inputs from the SC or visual cortex. However, in monkeys, latencies were reported to range from 60 to 115 ms (Porter et al., 2007), compatible with visual latencies from visual cortex, SC, and even the retina under low intensity stimulation (latency in monkey visual cortex ≈55–130 ms: Schmolesky et al., 1998; monkey SC ≈ 60–100 ms: Bell et al., 2006; monkey optic tract ≥40 ms: Inoue et al., 2000).

Likewise, the properties of the visual receptive fields (vRFs) found in the IC do not obviously implicate any one of the known inputs to the exclusion of the others. Like all three potential input sources, the IC's representation favors the contralateral field, but unlike the possible inputs, no topographic organization within the contralateral field has been observed in mammals. The vRFs of individual cells are variable in size, ranging from tens of degrees to nearly half of the visual field (Mascetti and Strozzi, 1988; Porter et al., 2007; Bulkin and Groh, 2012b).

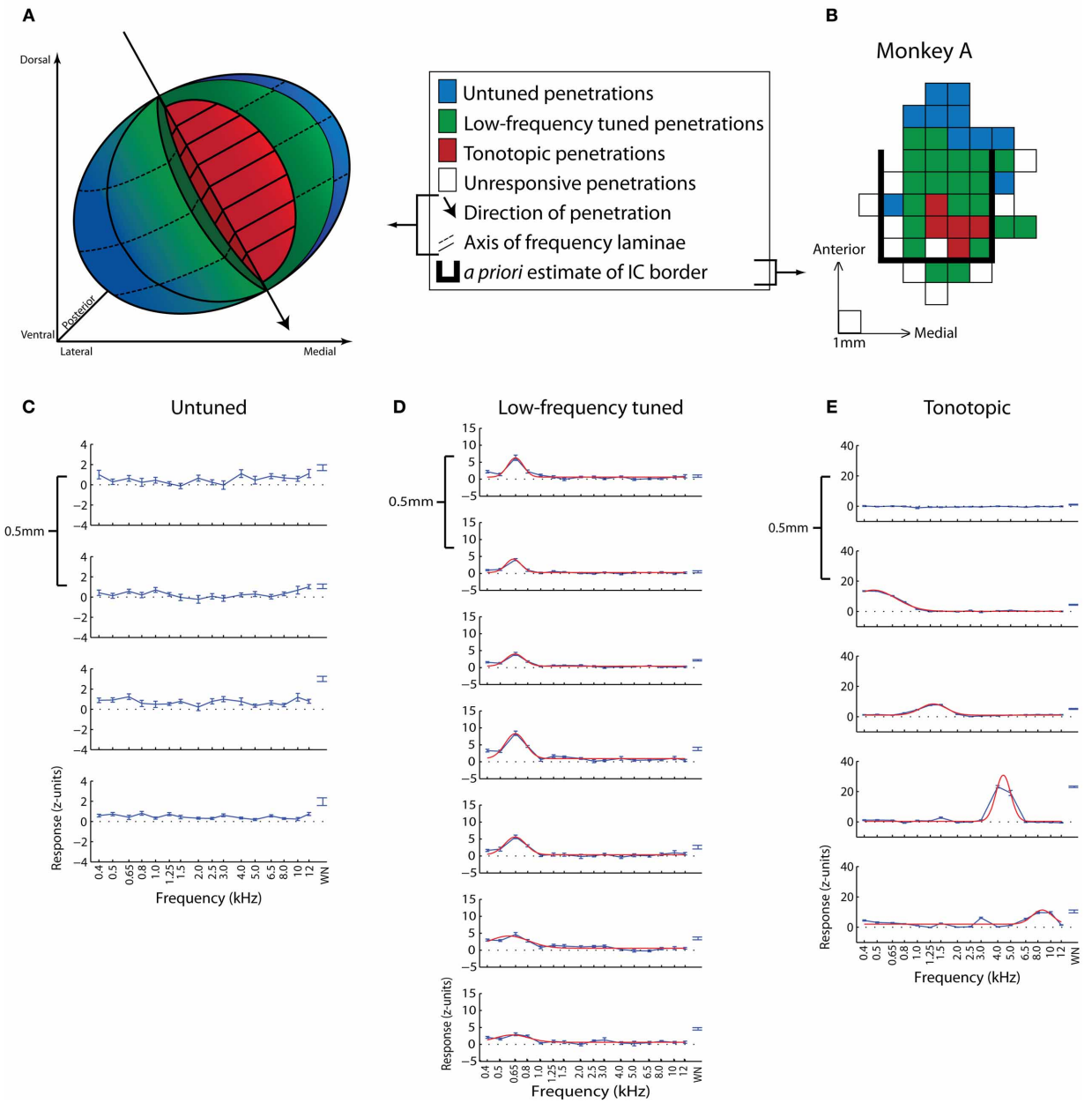

FIGURE 2 | Map of sound frequency representation in the monkey IC. **(A,B)** Three-dimensional schematic of sound frequency representation **(A)** based on a representative example dataset **(B)** from Bulkin and Groh (2011). Untuned sites are presumed to be in the outer sIC, low-frequency tuned sites from near the sIC-ICC border, and tonotopic sites from the center of the ICC. The grid in **(B)** is a top-down view of the recording grid for one monkey in the study. Each square represents a penetration site and is colored based on the response properties of that site. The bold black line delineates the *a priori* estimated boundaries of the IC based on MRI scans. **(C–E)** Example penetrations from untuned **(C)**, low-frequency tuned but not tonotopic **(D)**, and tonotopic **(E)** penetration locations. Each series is comprised of multiple recordings taken from a single example penetration. Frequency response functions were recorded at 0.5 mm increments along the dorsolateral-ventromedial penetration axis. The first graph in each series corresponds to the first, i.e., most dorsal, site to show responses to auditory stimuli along that penetration. Absolute depths of first responsive sites varied across penetrations. Blue lines **(C–E)** indicate the normalized average response over a 200 ms period as a function of sound frequency, and red lines **(D,E)** show the best Gaussian curve fit to tonal data. **(B–E)** Adapted from Bulkin and Groh (2011).

This is larger than the typical RFs found in retinal ganglion cells, visual cortex, or the SC (striate cortex: Wurtz, 1969; SC: Goldberg and Wurtz, 1972; retinal ganglion cells: Hammond, 1974; and Cleland et al., 1979).

The types of stimulus selectivity seen in IC neurons are also evident in more than one of the potential input sources. For example, visually responsive neurons in the IC tend to respond well to both static (Porter et al., 2007; Bulkin and Groh,

2012b) and moving (Mascetti and Strozzi, 1988) stimuli, properties observed in both the visual cortex (Wurtz, 1969) and retina (Shapley and Perry, 1986). IC cells that respond to moving stimuli are not tuned to a particular direction of stimulus motion (Mascetti and Strozzi, 1988), which is similar to a subset of SC neurons that are directionally untuned (Humphrey, 1968; Rhoades and Chalupa, 1976). Thus, the retina, visual cortex, and the SC all share some aspects of stimulus selectivity with IC neurons. Additional research is therefore necessary to explore receptive fields and stimulus selectivity in more detail before reaching conclusions on the potential source, or synthesis of multiple sources, responsible for IC vRFs and response properties.

Visual sensitivity has also been reported in the barn owl IC, but in contrast to mammalian studies, visual spatial sensitivity in the barn owl ICX appears to be well organized and tuned to the auditory space map in the same region (Bergan and Knudsen, 2009). Visual modulation fields [vMFs; defined as the region of visual space in which a stimulus exhibits ≥50% of its maximal modulatory effects on the paired auditory stimulus (see **Figure 3**)] of neurons throughout the ICX are well correlated with the location predicted by auditory localization cues. That is, a visual stimulus occurring at a given location in the visual field can modulate the ICX response to sounds originating from a similar point in space (**Figure 3**). Also in contrast to mammals, neurons in the owl ICX do not appear to respond to visual stimuli alone (Gutfreund et al., 2002; Bergan and Knudsen, 2009). Instead, visual information projecting from the owl's optic tectum (OT; homologous to the mammalian SC) to the ICX is gated via GABAergic inhibition in the OT (Gutfreund et al., 2002). Multiunit activity in the ICX is sensitive to visual stimulation only if inhibition is blocked in the region of OT corresponding to those units' preferred auditory location.

A variety of potential factors might influence the proportions and response patterns of visually sensitive cells in the IC. First, different species may utilize visual information in different ways depending on their ecological niche. For instance, diurnal species such as monkeys (e.g., Porter et al., 2007; Bulkin and Groh, 2012b) may exhibit response patterns that differ from those of nocturnal species such as cats or barn owls (e.g., Tawil et al., 1983; Mascetti and Strozzi, 1988; Bergan and Knudsen, 2009). Second, the cognitive state of the animal may be an important factor: Porter et al. (2007), and Bulkin and Groh (2012b) both used awake and behaving animals and found the highest proportion of visually responsive cells in comparison to other studies. Bergan and Knudsen (2009) estimated a slightly lower proportion in their awake but restrained birds[2], while the anesthetized preparations used by Tawil et al. (1983) and Mascetti and Strozzi (1988) yielded the smallest proportions. As discussed in detail in the section on "Behavioral context" of this review, behavioral state has a profound effect on neural activity in the IC. The report by Gutfreund et al. (2002) suggests that behavioral state might exert

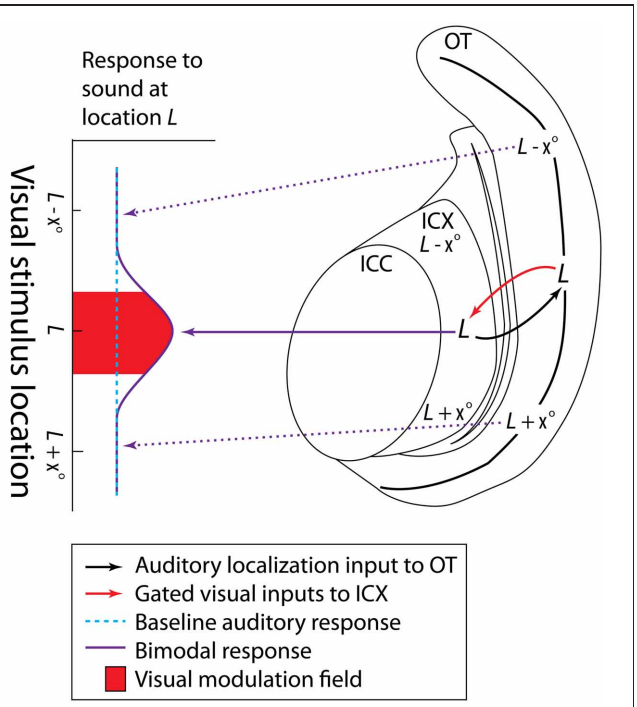

FIGURE 3 | Visual information modulates activity of cells in the owl ICX when auditory and visual inputs are closely aligned in space. Cells in the owl ICX respond best to a sound from some fixed location *L* in space (determined by interaural timing and level cues) (dotted blue line; note that the location of the auditory stimulus does not change in this schematic) and that information is transmitted to the corresponding location within the OT (black arrow). When a visual cue occupies the same or some nearby location in space, gated feedback from the OT (red arrow) enhances auditory responses (solid purple arrow); visual cues at other locations will not enhance auditory responses (dotted purple arrows). The visual field corresponding to ≥50% of the max auditory modulation is defined as the visual modulation field (red field). Adapted from Gutfreund et al. (2002); and Bergan and Knudsen (2009).

a specific influence over visual responsiveness in the IC by gating the passage of visual information into the IC. Importantly, the SC (or OT) is commonly implicated in both oculomotor (Gandhi and Sparks, 2007) and attentional control (e.g., Shen et al., 2011), and serves as one of the routes by which visual input can reach the IC. The use of a saccade task might therefore have been an important factor increasing the proportion of visually responsive cells in both Porter et al. (2007) and Bulkin and Groh (2012b). Other influential factors may include the breadth of sampling of visual space and the type of visual stimuli used. Visually responsive neurons in other brain areas are known to respond only to stimuli presented within spatially restricted receptive fields and to stimuli of preferred orientations, colors, shapes, and so forth (Schiller, 1986). It is likely that the set of visual stimuli used in the aforementioned studies did not exhaust all of the parameters for which visually responsive cells in the IC are selective. Therefore, the reported proportions may well be an underestimate of the actual proportion of visually responsive cells.

The functional purpose of visual signals in the IC is unknown. One potential role is to help calibrate the representation of

[2]They estimated that approximately one-third of their sampled neurons were sensitive to audiovisual stimuli; however, the aim of their study was to describe the response patterns of these neurons, so they did not report an exact proportion.

auditory space. This hypothesis has been tested thoroughly in the owl [for a review, see Knudsen (2002)], where visual space maps in the OT are functionally and anatomically connected to the auditory space maps of the ICX (Bergan and Knudsen, 2009). Barn owls reared with prisms that displace visual space show altered auditory spatial sensitivity in the ICX (Brainard and Knudsen, 1993), altered connectivity between the ICC and ICX (Debello et al., 2001), and altered connectivity patterns from the ICX to OT (Hyde and Knudsen, 2002; Linkenhoker and Knudsen, 2002). Ocular enucleation in rats appears to alter auditory spatial sensitivity as well (Pageau et al., 2008). This may be due to visual deprivation, though impaired eye position signals are also likely to result from enucleation and should not be dismissed as a contributing factor (see the section on "Eye position"). Together, these studies indicate that coding of auditory location is at least partially dependent on visual input. However, calibration of auditory space may not be the only role of visual signals in the IC. A possible role of visual signals in the sIC for communication is discussed in the section on "Communication."

EYE POSITION

The eyes and ears necessarily receive visual and auditory spatial information, respectively, within a different frame of reference. Specifically, visual space is initially encoded based on where the image falls on the retina (a so-called eye-centered reference frame) while auditory space is calculated based on the position of the sound relative to the ears and the head (a head-centered reference frame). In species where the eyes are able to move to a substantial degree within the head (e.g., rhesus monkeys and cats but not rodents or barn owls), the visual and auditory reference frames are not fixed to each other (**Figure 4**). Because of this constantly changing relationship between reference frames, aligning visual and auditory space requires factoring in both the orbital position of the eyes and sound localization cues.

Groh et al. (2001) identified a subset of cells in the IC (approximately one-third: 24/73) that altered their firing patterns in response to an auditory stimulus depending on where the eyes were positioned in their orbits with respect to the head. More specifically, the firing rate of individual neurons usually tended to increase as a monotonic function of eye position, with the population favoring contralateral eye positions (relative to IC hemisphere) (Porter et al., 2006) (**Figure 5A**). Additionally, eye position sensitivity appeared to be more common among neurons insensitive to sound location (up to 32% for sound location sensitive units and 56% for insensitive units; Porter et al., 2006), suggesting somewhat segregated subpopulations for eye position and sound location sensitive units in the IC. Eye position sensitivity has also been found for vertical eye positions (Zwiers et al., 2004; Bulkin and Groh, 2012a), as well as during both task-related and spontaneous fixations, and with or without the presence of a concurrent sound stimulus (Porter et al., 2006; Bulkin and Groh, 2012a). Collectively, these results indicate that eye position signals are an important aspect of IC processing and are separable from signals related to head-centered sound location, vision, and eye movements.

The reference frame in the IC has been found to be neither head-centered nor eye-centered but somewhere in between. Porter et al. (2006) reported that only 16% of tested units were head-centered, whereas 9% were more eye-centered; the remaining 75% of the tested units were approximately equally consistent with either head- or eye-centered reference frames (**Figure 5B**). A model trained on these data was able to provide an output that closely approximated a particular sound location via either head- or eye-centered coordinates (Porter et al., 2006). The brain seems to maintain this hybrid encoding scheme until the time of saccade generation. Specifically, the hybrid scheme is similar in the IC, auditory cortex (Werner-Reiss et al., 2003; Porter et al., 2006), and the visual intraparietal sulcus (Mullette-Gillman et al., 2005, 2009) as well as in the sensory signals in the SC (Jay and Sparks, 1984; Populin et al., 2004; Lee and Groh, 2012). However, a motor output command is eventually developed in eye-centered coordinates in the SC at the time of saccade generation (Lee and Groh, 2012).

The location of eye position sensitive cells within the IC was recently mapped in detail (Bulkin and Groh, 2012a) with respect to the functional response map previously described (Bulkin and Groh, 2011; see the section on "Vision and oculomotor influences," and **Figure 2**). Eye position sensitivity was found throughout the IC, but the proportions varied according to the functional response patterns of the recording site. Eye position effects were detected in 25% of tonotopic sites, 33% of low-frequency tuned sites, and 42% of untuned sites. As noted previously, these responses are likely to coincide with the central-most part of the ICC, the edges of the ICC and the inner part of the sIC, and the outer sIC respectively (Bulkin and Groh, 2011).

Despite the physiological studies identifying eye position signals in the IC, the anatomical sources of these signals have yet to be identified. It is not clear whether such signals are a result of corollary discharge from oculomotor outputs [e.g., the SC, or the fastigial nucleus of the cerebellum (Carpenter, 1959; Earle and Matzke, 1974)], proprioceptive feedback from muscles controlling eye position [along, for instance, the opthalamic tract of the trigeminal nerve (TN) (Steinbach, 1987); cuneate nuclei (Porter, 1986); or from the somatosensory cortex (Zhang et al., 2008)], or some combination of both. These signals may also come from other auditory areas. For instance, the primary auditory cortex contains eye position signals (Werner-Reiss et al., 2003) and sends anatomical projections to the IC (Winer et al., 1998). It is possible that eye position signals are sent through this route via corollary discharge from cortical regions important for eye position and movements (after Sommer and Wurtz, 2008). Further investigation will be necessary to identify the connectivity of eye position sensitive neurons in the IC.

SOMATOSENSATION

The IC also receives input from the somatosensory system. Connections from various brainstem nuclei—including the trigeminal nerve ganglion (TNG) and nuclei of the dorsal column (nDC)—have been identified in both the intercollicular region (cat: Anderson and Berry, 1959; opossum: Robards et al., 1976), and the ICX (opossum: Robards, 1979; cat: Aitkin et al., 1981; monkey: Wiberg et al., 1987; rat: Coleman and Clerici, 1987; hedgehog: Kunzle, 1998). Additionally, both the motor and somatosensory cortices project to the ipsilateral ICC and ICX

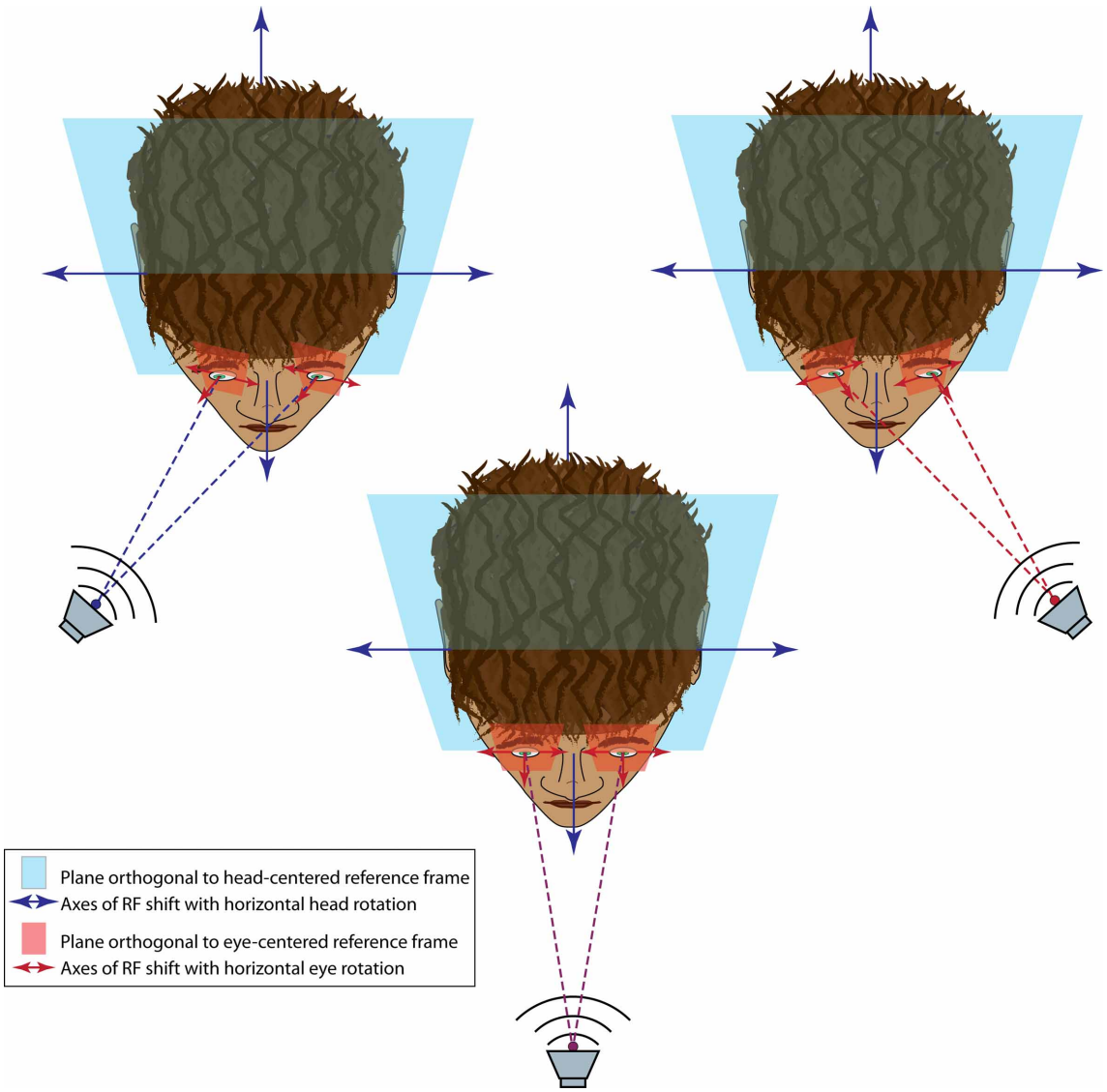

FIGURE 4 | Audiovisual reference frame problem. When an audiovisual target is straight ahead (center panel), the auditory and visual reference frames coincide; that is, a plane orthogonal to the auditory head-centered reference frame (blue field) is parallel to the plane orthogonal to the visual eye-centered reference frame (red field), and both are perpendicular to the audiovisual information source (speaker). When the target is moved eccentrically (upper panels), the head-centered and eye-centered reference frames are no longer parallel, with the eye-centered reference frame having rotated around a vertical axis (for horizontal eye movements). In this example, the eye-centered reference frame is still perpendicular to the audiovisual target but the head-centered reference frame is not.

(Cooper and Young, 1976). The ICC may also receive somatosensory signals from other areas along the auditory pathway. For example, the ICC is heavily innervated by the dorsal cochlear nucleus (DCN) (e.g., Cant and Benson, 2008), which is also known to receive direct innervation from the nDC (Li and Mizuno, 1997) and the TN (Zhou et al., 2007), and whose principle output cells are modulated by TN stimulation (Koehler et al., 2011). The ICX, meanwhile, receives convergent inputs from the DCN and spinal trigeminal nucleus (Zhou and Shore, 2006), suggesting that multiple, overlapping circuits may be involved in creating somatosensory-sensitive cells in the IC.

As suggested by these anatomical connections, neurons in both the ICC and ICX are sensitive to somatosensory inputs from the spinal cord [i.e., inputs from the spinal dorsal column (DC), peripheral nerves, and body, presumably via the nDC]. Specifically, cells may respond to unimodal somatosensory stimulation or alter their firing rate to auditory stimuli when sounds are paired with concurrent somatosensory stimulation. This was first demonstrated in the IC of anesthetized rats, where neurons changed their response to a pure tone stimulus in the presence of concurrent sciatic nerve stimulation (Syka and Radil-Weiss, 1973). Similar results have been reported using electrical

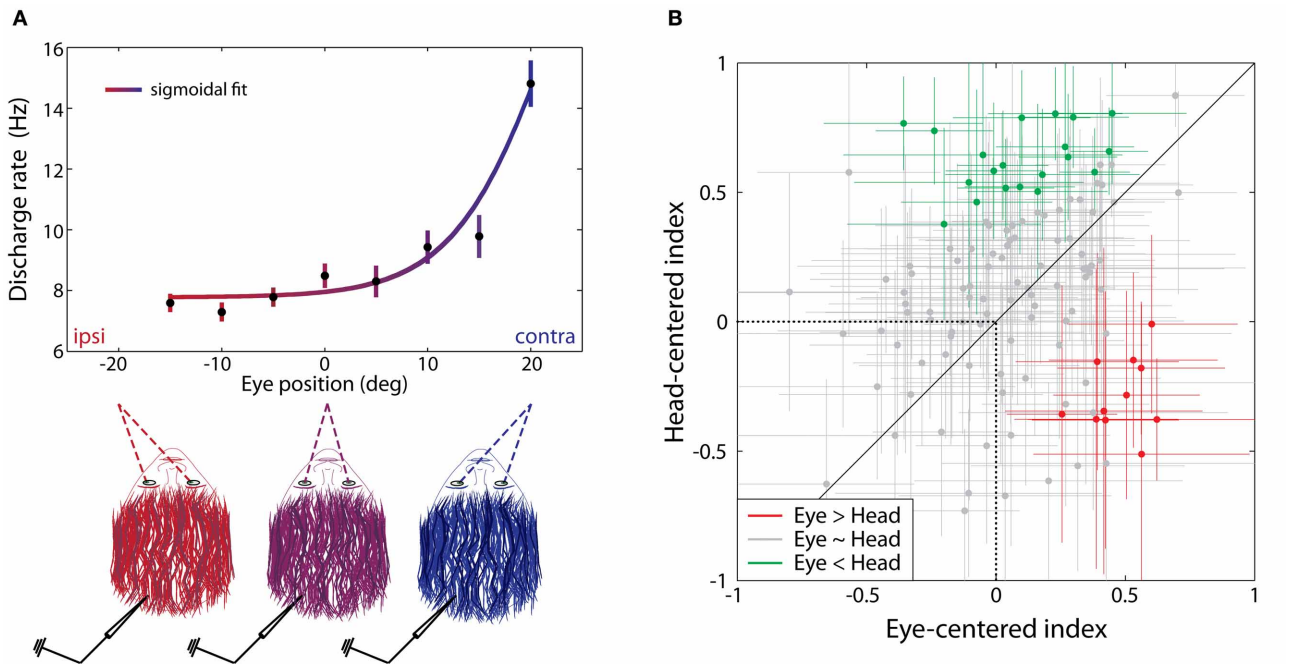

FIGURE 5 | Eye position gain and reference frame of IC cells. **(A)** Contralateral gain as a function of eye position in azimuth. The firing rate of eye position sensitive cells in the IC tends to increase with contralateral fixations. **(B)** The reference frame of individual IC cells was determined by calculating correlation coefficients between eye position during sound presentation, and sound locations defined (1) with respect to the eyes (eye-centered index) and (2) with respect to the head (head-centered index). A value of 1 indicates that the response function of a cell is perfectly aligned with the sound source in a particular reference frame (eye-centered or head-centered), while a value of −1 indicates perfect anti-correlation. Crosses centered on individual points indicate 95% confidence intervals for reference frame values. The reference frame of individual cells may be more head-centered (green) or eye-centered (red), or cells may have a hybrid reference frame (gray). **(B)** Reprinted from Porter et al. (2006).

stimulation of the median nerve in anesthetized rats (Szczepaniak and Moller, 1993) as well as the tibial nerve (Aitkin et al., 1978) and DC (Aitkin et al., 1978; Tawil et al., 1983) of anesthetized cats. In the case of DC stimulation, ≈5–20% of the IC cell population responded to electrical DC stimulation alone (this range may be partially due to variations in stimulation parameters across studies) and roughly 55% responded differentially to a combination of DC stimulation and concurrent sound presentation compared to sound alone. DC stimulation enhanced the acoustic response in about one-third of the bisensory units and inhibited the other two thirds. Additionally, cells in the ICX of anesthetized cats were found to respond to manual tactile stimulation of the skin and hair across the entire surface of the body (individual neurons had bodily receptive fields at varying locations and of variable sizes, with the full body surface represented across the population) (Aitkin et al., 1978, 1981). The proportion of cells responsive to tactile stimulation was somewhat lower than that responsive to DC stimulation: out of 261 cells (Aitkin et al., 1981) only 16% responded to unimodal tactile stimuli while 4% responded differentially to concurrent tactile and auditory stimulation compared to sound alone.

In addition to inputs carried via the spinal cord, the IC is also sensitive to influences mediated via cranial nerves, specifically from the TN and TNG. Electrical stimulation of the TNG in the absence of a sound stimulus causes increased metabolic activity within the IC cell population when compared to non-stimulated control animals [as measured by uptake of [14C]2-deoxyglucose (2DG); El-Kashlan and Shore, 2004]. Moreover, uptake of 2DG in response to TNG stimulation was qualitatively similar in the IC to uptake in response to sound stimulation. Similarly, electrical TN stimulation paired with sound modulated the response patterns of approximately two-thirds of the cells in the ICX of anesthetized guinea pigs (Jain and Shore, 2006). Specifically, auditory responses were inhibited by paired TN stimulation in nearly half of the tested units (60/126, 48%) and enhanced in 23 units (18%). TN stimulation alone did not appear to elicit responses in the absence of a sound.

Functionally, somatosensory inputs to the IC may serve numerous different roles within the auditory system[3]. Consider, for instance, the proposed role for eye position signals within the IC: aligning the neural representation of visual and auditory reference frames. In a relatively simple case of fixating on a sound source near the fovea, eye position and sound location cues appear to be sufficient information to execute the appropriate saccade. In more complex cases involving head, trunk, and limb motion, the brain must coordinate numerous effector muscles in order to orient toward (or away from) a sound source. Eye position, and possibly somatosensory, signals in the IC likely provide the information necessary to localize and act on some sound

[3]A possible role in communication behaviors will be discussed in the section on "Communication."

source. Additionally, the orientation of the pinnae must be factored into the interpretation of direction-dependent spectral cues in species that make guided ear movements in response to sounds (e.g., the cat: Populin and Yin, 1998). This information appears to be present in the DCN via nDC and TN inputs (Kanold and Young, 2001), and may be transmitted to the IC either directly from one or both of these somatosensory nuclei, or by way of the DCN. The IC, therefore, is presumably important for this behavior in that it may contribute sound location cues relative to eye position and pinnae-position to higher-order orientation circuitry.

Moreover, reflexive auditory orientation and startle behaviors involving the head may involve IC signaling (e.g., Leitner and Cohen, 1985). Thompson and Masterton (1978) found that shallow lesions at the level of the IC degrade the accuracy and latency of reflexive head orientation toward unexpected sounds in cats, but the response was still initiated toward the correct hemifield. In contrast, deep lesions that sever the connections from the DCN to IC cause startle responses targeted toward the wrong hemisphere. Such behaviors may be different from saccades: the reaction times (40 ms on average) were much faster than typical saccade latencies (150–300 ms: e.g., Carpenter, 1988; Jay and Sparks, 1990). These data suggest that an auditory orientation reflex is dependent on the IC and its inputs. Reflexive orientation likely requires a body-to-head (or head-to-body) reference frame transformation to execute a response in the appropriate direction, and the convergence of somatosensory and sound location information in the IC indicates that this is possible.

In addition to contributing to these various types of sound localization behaviors, all of these input sources would be useful in suppressing self-generated noise, including vocalizations, mastication, and respiration (Jain and Shore, 2006), as well as locomotion and visceral function. Motor structures may send corollary discharge signals to the IC (and other auditory regions) to suppress noises resulting from the ensuing behaviors. An example of this has been observed in crickets: auditory processing regions are inhibited via corollary discharge of the motor signals used to produce singing behaviors (Poulet and Hedwig, 2002). Similar mechanisms for attenuating self-generated sounds have been observed in more complex neural systems, including the bat auditory system (Suga and Shimozawa, 1974).

BEHAVIORAL CONTEXT

An animal's behavioral state influences neural activity in the IC, seemingly depending on task engagement and expected outcome. In rats, the activity of cells in the IC was found to increase as an expected rewarding (Nienhuis and Olds, 1978) or aversive (Ruth et al., 1974) stimulus draws near, at reinforcement intervals ranging from seconds to minutes (**Figures 6A,B**). Curare blocks the apparent anticipatory build up response for aversive stimulation, indicating that acetylcholine plays a role in this build up activity (Ruth et al., 1974). Similar reward-anticipation and task performance effects have been observed in the monkey IC. An estimated 60% of IC neurons show a general increase in firing rate when a monkey is engaged in active behavior as opposed to passive listening (46/80 cells: Ryan and Miller, 1977; Ryan et al., 1984). Additionally, the activity of IC neurons increases in apparent anticipation of a reward (**Figures 6C,D**), and the amount of increase depends on the size of the reward (Metzger et al., 2006). The trend appears to be the same in humans: attending to changing pitches in one ear while ignoring pitch changes in the other activates the contralateral IC (relative to attended ear) more than the ipsilateral IC (Rinne et al., 2008). Collectively, these data indicate that cells within the IC are sensitive to engagement in a task, and that they exhibit anticipation for some upcoming rewarding or aversive stimulus. It is particularly striking that these cells seem to be capable of anticipating over extended time periods of 30 s or more. Presumably, the increased activity reflects heightened sensitivity to behaviorally relevant stimuli.

These findings are consistent with known anatomical connections to the IC from regions typically associated with subjective value and emotion. Specifically, the sIC receive inputs from the ipsilateral caudal globus pallidus (GP; for cats and rodents in which these tracing studies have been carried out, the GP is equivalent to the external capsule of the GP in primates) (inputs primarily target ICX) (Yasui et al., 1990; Shinonaga et al., 1992; Shammah-Lagnado et al., 1996) as well as GABAergic inputs from the substantia nigra pars lateralis, bilaterally (SN_1) (specified ICX: Coleman and Clerici, 1987; unspecified: Yasui et al., 1991; and Moriizumi et al., 1992). The ICX also receives bilateral projections from the ventral tegmental area (VTA) (Herbert et al., 1997) while both the ICC and sIC receive ipsilateral inputs from the basal nucleus of the amygdala (Hopkins and Holstege, 1978; Marsh et al., 2002). All of these regions have a substantial body of literature implicating them in various habitual (e.g., Yin and Knowlton, 2006) and motivated (e.g., Ono et al., 2000) behaviors. It seems likely that these regions and their IC connections inform the processing of auditory stimulation and bias cells within the IC toward processing behaviorally important sounds. It is possible that the firing rate modulations found in these studies help to focus attention on a particular sound within the environment that will prove useful in, for example, detecting food or avoiding predators and other environmental dangers.

COMMUNICATION

Another form of specialized processing for which the IC appears to be particularly important is vocal communication. The role of the IC in this regard seems to lie somewhere between the basic auditory processing of lower brainstem regions and the more complex representation of communication calls found in cortical regions (Portfors and Sinex, 2005). Both auditory and non-auditory signals likely contribute to processing communication stimuli, and in this section, we also consider how somatosensory signals may be particularly important for audiomotor learning and maintenance of vocalizations.

Evidence implicating the IC in vocal communication comes from a variety of species. Specifically, some neurons respond better to conspecific calls than to either white noise and pure tones [around 75% of cells in sIC (82% in ICX, 72% in dorsal cortex) and 25% in ICC of cats (Aitkin et al., 1994)], or to time-reversed calls [approximately one-third of cells in guinea pig, all subdivisions (Suta et al., 2003); and in the rat ICC (Pincherli Castellanos et al., 2007)], while others fire selectively to particular conspecific calls (ICC of bats: Klug et al., 2002). Furthermore, some neurons

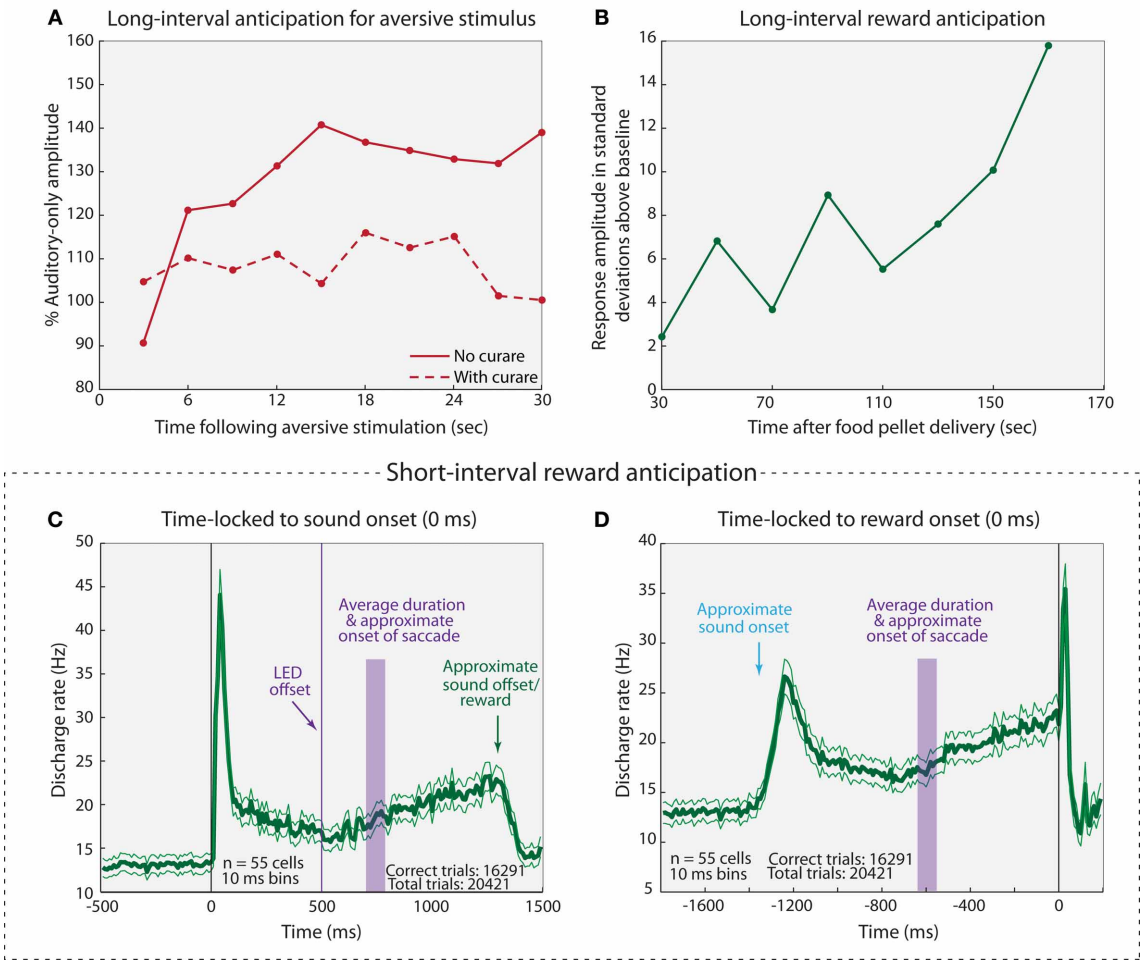

FIGURE 6 | Anticipatory responses of IC cells. (A) Average-evoked potential recorded from the IC in response to sounds presented at 3 s intervals following aversive stimulation of the mesencephalic central gray (MCG) with (dashed line) and without (solid line) curare. MCG stimulation occurred at a fixed interval of 30 s (thus, 0 s post-MCG stimulation may be thought of as 30 s pre-MCG stimulation for the following trial). **(B)** Representative example of a multi-unit response to sound presentation following rewarding stimulus. Sounds were played at varying intervals (up to 180 s) following reward, and the next reward was delivered after a second variable interval. Note that no error bars were provided in the source materials for panels **(A,B)** so the variability and potential statistical significance of the finding cannot be assessed. **(C,D)** Average response (± standard error) of IC cell population time-locked to sound onset **(C)** and reward onset **(D)**. Briefly, monkeys fixated on an LED while a sound was played. The LED was extinguished and the monkeys made a saccade to the auditory target. They were rewarded if the auditory saccade was within the appropriate fixation window (8–11°, depending on target distance from LED). Both rewarded and unrewarded trials were included in this analysis. Adapted from **(A)** Ruth et al. (1974); **(B)** Nienhuis and Olds (1978); **(C,D)** Metzger et al. (2006).

in the ICX of squirrel monkeys are suppressed by self-generated calls despite responding to acoustically similar vocalizations from other monkeys and other sounds (Tammer et al., 2004). In humans, unilateral lesions to the IC have been reported to impair recognition of speech sounds when presented to the contralateral ear (Fischer et al., 1995; Champoux et al., 2007). These data suggest that one possible role of the IC in communication processing is generally identifying species-specific and self-generated vocalizations.

The presence of non-auditory signals in the IC may contribute to communication processing in this region. Numerous studies in animals have illustrated integration of visual and auditory components of communication at other levels of the auditory pathway (e.g., Ghazanfar et al., 2005; Romanski, 2007), and in humans, visual stimuli such as lip-motion can change the perception of speech sounds (e.g., the McGurk effect: McGurk and MacDonald, 1976)[4]. One patient with a circumscribed unilateral lesion to the right IC [the same reported in Champoux et al. (2007)] displayed a deficit in processing McGurk stimuli when visual stimuli were shown in the contralateral (left)

[4]The McGurk effect (McGurk and MacDonald, 1976) is a common paradigm used to test audiovisual speech perception. In this and related studies, the auditory sound /ba/ is combined with a video of a person saying /ga/ (or some similar pair of related phonemes). Typically, an observer of the incongruent audiovisual pairing will perceive the intermediate phoneme /da/.

visual hemifield (Champoux et al., 2006). Although this is only one patient, the results suggest that the IC may play a role in audiovisual speech processing.

In addition to a possible visual influence on the processing of speech and other vocal communication in the IC, somatosensation may be extremely important for learning and fine-tuning the IC's responses to vocal communication. The motor system is also presumed to be heavily involved in speech learning and production [for a review of the motor theory of speech learning, see Hickok et al. (2011); and Hickok (2012)]. Briefly, it is thought that an efference copy of the motor command sent to the effector muscles involved in speech is also sent to the auditory system. This allows for a comparison of the motor command and the resulting emitted sound, both during early development and during later maintenance of vocal performance. Indeed, proper somatosensory feedback appears important for maintaining consistent generation of speech sounds. In particular, numbing of the lingual nerve (a peripheral branch of the trigeminal cranial nerve) results in abnormal and inconsistent (across individuals) speech generation deficits for vowels (Niemi et al., 2002), diphthongs (Niemi et al., 2004), and sibilant /s/ sounds (Niemi et al., 2006). It has also been found that both deaf and normal-hearing people are sensitive to perturbations of jaw movements during speech regardless of auditory feedback (Nasir and Ostry, 2008). These data collectively indicate that somatosensory feedback from the articulators is necessary for maintaining proper speech production, and that perturbations to the system are corrected based on the same, non-auditory, feedback. Because the lingual branch of the TN is apparently important in this process, connections from the TN to the IC provide a likely candidate for a site of the audiomotor integration involved in speech learning and maintenance.

The convergence of auditory and motor feedback in the IC, and the resulting shaping of vocal communication responses and learning, may be mediated by projections from the periaquaductal gray matter (PAG) to the sIC (including ICX) (Dujardin and Jurgens, 2005). Previous studies have shown that vocalizations can be elicited through electrical stimulation of the PAG (rhesus monkey and cat: Magoun et al., 1937; squirrel monkey: Jurgens and Ploog, 1970; gibbon: Apfelbach, 1972; bat: Suga et al., 1973; guinea pig: Martin, 1976; rat: Yajima et al., 1976). Transections of the forebrain and SC preserve species-specific vocalizations in cats whereas transections caudal to the IC render these animals mute (Bazett and Penfield, 1922). Jurgens and Pratt (1979) investigated the role of the PAG in emotional expressions of squirrel monkeys with a series of lesions and stimulations. They found that lesions to the PAG disrupted induced vocalizations, and that motor output is likely accomplished via direct connections from the PAG to the nucleus ambiguus (NAm), the projection site for laryngeal motor neurons. One interesting possibility is that the PAG sends a corollary discharge to both the NAm and IC. This in turn may be used to cancel out the reafferent vocalization signal, which could explain why cells within the ICX do not respond to self-generated calls but still respond to calls from conspecifics (Tammer et al., 2004). Should this prove to be the case, there is evidence that the mechanism behind this process could be direct inhibition of the auditory system (after Suga and Shimozawa, 1974; Klug et al., 2002), or a more complex reafference-canceling signal that is susceptible to plastic changes according to the needs of the organism at that time (e.g., Bell, 1981).

While few of these studies have focused on the IC to date, the prominent innervation of IC from somatosensory and behaviorally relevant sources suggests that it may be a crucial relay point in audiomotor feedback for vocal learning and maintenance of proper vocal production. It is possible that vocal motor commands that are sent from cortical control regions (e.g., the classic speech pathway) converge on the IC with auditory and somatosensory feedback. This potential circuit would allow for a direct comparison between the intended audiomotor output and the actual audiomotor execution at the level of the IC, which would in turn help to tune cortical audiomotor control mechanisms (**Figure 7**). This potential microcircuit has yet to be tested with respect to vocal communication. However, these pieces of circumstantial evidence suggest that non-auditory inputs to the IC may be involved in developing and maintaining vocal communication.

CONSIDERATIONS FOR PAST RESULTS AND FUTURE RESEARCH

The presence of non-auditory signals throughout all subdivisions of the IC—including both ascending and descending regions—provides a point of entry for these signals to reach auditory processing at all stages from brainstem to cortex (note, for example, projections from the IC to both the thalamus and cochlear nucleus: Coomes and Schofield, 2004). In addition to having implications for our understanding of the role of the IC in auditory-guided behavior, as discussed in the preceding sections, there are several practical implications from a methodological perspective. Specifically, the presence of these signals suggests that non-auditory sensory stimuli and behavioral state must be included on the list of factors to be controlled, monitored, or randomized. This is true regardless of what level of the auditory pathway is under investigation, since signals present in the IC can be assumed to propagate to most, and probably all, areas of the auditory pathway.

In addition, certain surgical practices may affect the signals reaching the IC. For example, in order to more easily access the IC for electrophysiological recordings, the visual cortex is sometimes aspirated. Aspiration of the visual cortex is likely to alter the function of IC cells, and may do so in anywhere up to 80% of cells in the sIC and up to 25% of cells in the ICC [based on the proportions found by Bulkin and Groh (2012b)]. While these proportions assume the worst-case-scenario that all visual cells in the IC receive either direct or indirect influence from the visual cortex, clearly a substantial proportion of cells may undergo changes in their inputs after cortical aspiration. How this might affect auditory responses is uncertain.

Similarly, decerebration limits or destroys many of the described non-auditory and descending auditory inputs to the IC. While this method in particular has given (and continues to give) valuable insight into basic auditory processing, a complete understanding of more complex auditory processes, including sound localization and communication behaviors, will require that the brain be fully intact (Bazett and Penfield, 1922).

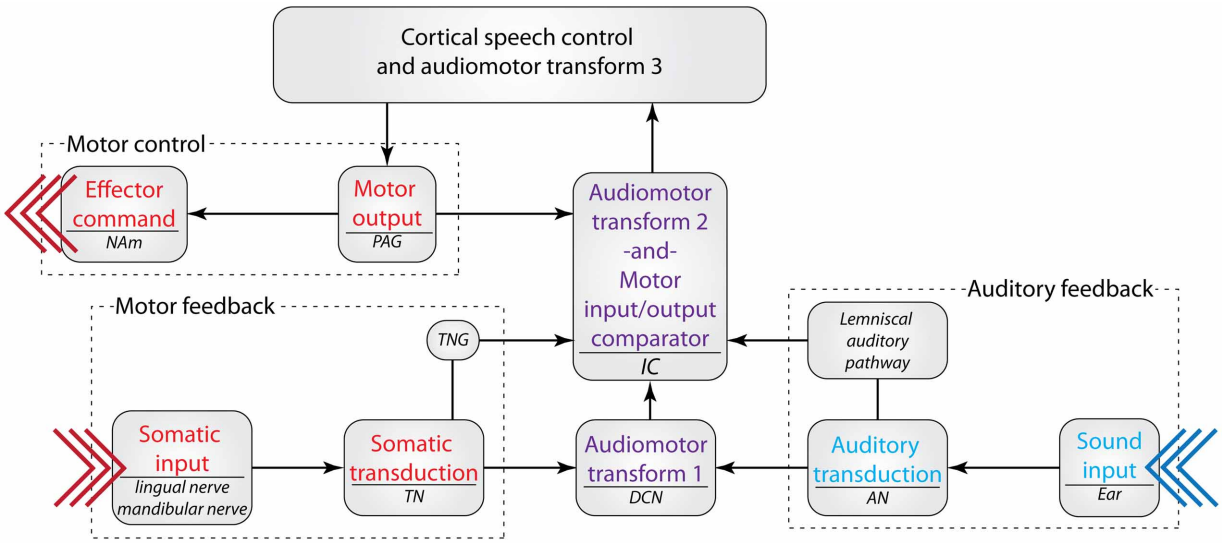

FIGURE 7 | A possible role for the inferior colliculus in audiomotor feedback during vocal communication. The IC receives anatomical inputs from the PAG, TNG, DCN, and other auditory regions. This circuit, in theory, allows for a comparison between premotor commands sent from the PAG and somatic feedback from the vocal apparatus via the TN and TNG. The resulting comparison could yield a vocalization motor error: expected motor execution (output) minus actual motor execution (feedback) equals motor error. This information could be used to adjust the motor output of vocalization in order to achieve a desired auditory structure [presumably determined by cortical planning regions; see Hickok (2012)]. If the motor error = 0, self-generated vocalization reafference is cancelled out (Tammer et al., 2004) and no adjustment is necessary; if the motor error ≠ 0, the corresponding audiomotor error is sent to cortical control regions for further analysis and correction. The potential role of the DCN in this circuit is currently unknown, but may be associated with monitoring audiomotor feedback of non-vocalization signals. See **Table 1** for abbreviations.

Pharmacological manipulations may also affect a substantial number of cells in the IC. Anesthetization of animal models has been shown to alter processing in the auditory cortex and thalamus (Zurita et al., 1994; Szalda and Burkard, 2005), IC (Kuwada et al., 1989; Szalda and Burkard, 2005), and CN (Evans and Nelson, 1973; Chen and Godfrey, 2000; Anderson and Young, 2004). With regard to non-auditory influences, anesthetization presumably has a substantial impact on the dynamic firing patterns of task-related neurons in the IC, a proportion consistently reported to be over half of the cells in this brain area. Induced paralysis, meanwhile, has the potential to influence the somatosensory signals in up to 75% of IC cells. In either case, pharmacological manipulations run the risk of inducing unintended alterations of auditory function, especially in the IC.

The above practices have given invaluable insight into numerous aspects of auditory processing. However, they may alter auditory function in unanticipated ways. Without explicitly testing the changes these methods may impart on the auditory system, there is no way to correct acquired data *post-hoc*. A thorough understanding of how the auditory system operates, particularly in its natural cognitive and broader sensory milieu, requires avoiding the unintended effects of structural and persistent pharmacological manipulations as much as possible. In particular, the use of awake and intact animals, when feasible, ensures that such pitfalls are circumvented.

Finally, we note that this review drew on the available evidence from a wide array of species, including mammals such as rodents, cats, and monkeys as well as birds such as barn owls. The demands on the sensory systems of different species may be different, and the neural organization and connections between sensory systems may differ accordingly. Further comparative work will ultimately be required to shed light on how the evolutionary history and ecological niche of different species are reflected in the patterns of non-auditory signals present in their ICs.

CONCLUDING REMARKS

The anatomical and physiological evidence that non-auditory factors contribute to IC activity is extensive. The roles played by the visual, oculomotor, eye position, somatosensory, and task-related signals are at present poorly understood, and may span a range of different aspects of auditory, multisensory, cognitive, and behavioral functions. Notable possibilities include integrating visual and auditory space, orienting to sounds, distinguishing self-generated from external sounds, accurately perceiving communication sounds, and monitoring vocal-related signals to achieve desired auditory performance. That such signals exist at an early, pre-cortical stage of the auditory pathway only a few synapses removed from sensory transduction in the cochlea highlights the importance of such constructive processes in the brain in interpreting sound.

ACKNOWLEDGMENTS

We would like to sincerely thank Dr. Nell Cant, Dr. Marty Woldorff, and Dr. Henry Yin for their thoughtful and helpful comments on this document. This work was written under the financial support of the National Institutes of Health grant number R01 NS50942 and the National Science Foundation grant number 0924750 to Jennifer M. Groh.

REFERENCES

Adams, J. C. (1980). Crossed and descending projections to the inferior colliculus. *Neurosci. Lett.* 19, 1–5.

Aitkin, L., Tran, L., and Syka, J. (1994). The responses of neurons in subdivisions of the inferior colliculus of cats to tonal, noise and vocal stimuli. *Exp. Brain Res.* 98, 53–64.

Aitkin, L. M., Dickhaus, H., Schult, W., and Zimmermann, M. (1978). External nucleus of inferior colliculus: auditory and spinal somatosensory afferents and their interactions. *J. Neurophysiol.* 41, 837–847.

Aitkin, L. M., Kenyon, C. E., and Philpott, P. (1981). The representation of the auditory and somatosensory systems in the external nucleus of the cat inferior colliculus. *J. Comp. Neurol.* 196, 25–40.

Anderson, F. D., and Berry, C. M. (1959). Degeneration studies of long ascending fiber systems in the cat brain stem. *J. Comp. Neurol.* 111, 195–229.

Anderson, M. J., and Young, E. D. (2004). Isoflurane/N2O anesthesia suppresses narrowband but not wideband inhibition in dorsal cochlear nucleus. *Hear. Res.* 188, 29–41.

Apfelbach, R. (1972). Electrically elicited vocalizations in the gibbon hylobates lar (Hylobatidae), and their behavioral significance. *Z. Tierpsychol.* 30, 420–430.

Bazett, H. C., and Penfield, W. G. (1922). A study of the sherrington decerebrate animal in the chronic as well as the acute condition. *Brain* 45, 185–265.

Bell, A. H., Meredith, M. A., Van Opstal, A. J., and Munoz, D. P. (2006). Stimulus intensity modifies saccadic reaction time and visual response latency in the superior colliculus. *Exp. Brain Res.* 174, 53–59.

Bell, C. C. (1981). An efference copy which is modified by reafferent input. *Science* 214, 450–453.

Bergan, J. F., and Knudsen, E. I. (2009). Visual modulation of auditory responses in the owl inferior colliculus. *J. Neurophysiol.* 101, 2924–2933.

Brainard, M. S., and Knudsen, E. I. (1993). Experience-dependent plasticity in the inferior colliculus: a site for visual calibration of the neural representation of auditory space in the barn owl. *J. Neurosci.* 13, 4589–4608.

Bulkin, D. A., and Groh, J. M. (2011). Systematic mapping of the monkey inferior colliculus reveals enhanced low frequency sound representation. *J. Neurophysiol.* 105, 1785–1797.

Bulkin, D. A., and Groh, J. M. (2012a). Distribution of eye position information in the monkey inferior colliculus. *J. Neurophysiol.* 107, 785–795.

Bulkin, D. A., and Groh, J. M. (2012b). Distribution of visual and saccade related information in the monkey inferior colliculus. *Front. Neural Circuits* 6:61. doi: 10.3389/fncir.2012.00061

Calford, M. B., and Aitkin, L. M. (1983). Ascending projections to the medial geniculate body of the cat: evidence for multiple, parallel auditory pathways through thalamus. *J. Neurosci.* 3, 2365–2380.

Cant, N. B., and Benson, C. G. (2008). Organization of the inferior colliculus of the gerbil (*Meriones unguiculatus*): projections from the cochlear nucleus. *Neuroscience* 154, 206–217.

Carpenter, M. B. (1959). Lesions of the fastigial nuclei in the rhesus monkey. *Am. J. Anat.* 104, 1–33.

Carpenter, R. H. S. (1988). *Movements of the Eyes.* London: Pion.

Champoux, F., Paiement, P., Mercier, C., Lepore, F., Lassonde, M., and Gagne, J. P. (2007). Auditory processing in a patient with a unilateral lesion of the inferior colliculus. *Eur. J. Neurosci.* 25, 291–297.

Champoux, F., Tremblay, C., Mercier, C., Lassonde, M., Lepore, F., Gagne, J. P., et al. (2006). A role for the inferior colliculus in multisensory speech integration. *Neuroreport* 17, 1607–1610.

Chen, K., and Godfrey, D. A. (2000). Sodium pentobarbital abolishes bursting spontaneous activity of dorsal cochlear nucleus in rat brain slices. *Hear. Res.* 149, 216–222.

Cleland, B. G., Harding, T. H., and Tulunay-Keesey, U. (1979). Visual resolution and receptive field size: examination of two kinds of cat retinal ganglion cell. *Science* 205, 1015–1017.

Coleman, J. R., and Clerici, W. J. (1987). Sources of projections to subdivisions of the inferior colliculus in the rat. *J. Comp. Neurol.* 262, 215–226.

Coomes, D. L., and Schofield, B. R. (2004). Separate projections from the inferior colliculus to the cochlear nucleus and thalamus in guinea pigs. *Hear. Res.* 191, 67–78.

Cooper, A. M., and Cowey, A. (1990). Development and retraction of a crossed retinal projection to the inferior colliculus in neonatal pigmented rats. *Neuroscience* 35, 335–344.

Cooper, M. H., and Young, P. A. (1976). Cortical projections to the inferior colliculus of the cat. *Exp. Neurol.* 51, 488–502.

Covey, E., Hall, W. C., and Kobler, J. B. (1987). Subcortical connections of the superior colliculus in the mustache bat, *Pteronotus parnellii*. *J. Comp. Neurol.* 263, 179–197.

Debello, W. M., Feldman, D. E., and Knudsen, E. I. (2001). Adaptive axonal remodeling in the midbrain auditory space map. *J. Neurosci.* 21, 3161–3174.

Druga, R., and Syka, J. (1984). Projections from auditory structures to the superior colliculus in the rat. *Neurosci. Lett.* 45, 247–252.

Dujardin, E., and Jurgens, U. (2005). Afferents of vocalization-controlling periaqueductal regions in the squirrel monkey. *Brain Res.* 1034, 114–131.

Earle, A. M., and Matzke, H. A. (1974). Efferent fibers of the deep cerebellar nuclei in hedgehogs. *J. Comp. Neurol.* 154, 117–131.

El-Kashlan, H. K., and Shore, S. E. (2004). Effects of trigeminal ganglion stimulation on the central auditory system. *Hear. Res.* 189, 25–30.

Evans, E. F., and Nelson, P. G. (1973). The responses of single neurones in the cochlear nucleus of the cat as a function of their location and the anaesthetic state. *Exp. Brain Res.* 17, 402–427.

Fischer, C., Bognar, L., Turjman, F., and Lapras, C. (1995). Auditory evoked potentials in a patient with a unilateral lesion of the inferior colliculus and medial geniculate body. *Electroencephalogr. Clin. Neurophysiol.* 96, 261–267.

Freund, H. J., Wita, C. W., and Brustle, R. (1972). Latency differences between inhibitory and excitatory responses of cat optic tract units. *Exp. Brain Res.* 16, 60–74.

Gandhi, N. J., and Katnani, H. A. (2011). Motor functions of the superior colliculus. *Annu. Rev. Neurosci.* 34, 205–231.

Gandhi, N. J., and Sparks, D. L. (2007). Dissociation of eye and head components of gaze shifts by stimulation of the omnipause neuron region. *J. Neurophysiol.* 98, 360–373.

Ghazanfar, A. A., Maier, J. X., Hoffman, K. L., and Logothetis, N. K. (2005). Multisensory integration of dynamic faces and voices in rhesus monkey auditory cortex. *J. Neurosci.* 25, 5004–5012.

Ghazanfar, A. A., and Schroeder, C. E. (2006). Is neocortex essentially multisensory? *Trends Cogn. Sci.* 10, 278–285.

Goldberg, M. E., and Wurtz, R. H. (1972). Activity of superior colliculus in behaving monkey. I. Visual receptive fields of single neurons. *J. Neurophysiol.* 35, 542–558.

Groh, J. M., Trause, A. S., Underhill, A. M., Clark, K. R., and Inati, S. (2001). Eye position influences auditory responses in primate inferior colliculus. *Neuron* 29, 509–518.

Gutfreund, Y., Zheng, W., and Knudsen, E. I. (2002). Gated visual input to the central auditory system. *Science* 297, 1556–1559.

Hammond, P. (1974). Cat retinal ganglion cells: size and shape of receptive field centres. *J. Physiol.* 242, 99–118.

Harting, J. K., and Van Lieshout, D. P. (2000). Projections from the rostral pole of the inferior colliculus to the cat superior colliculus. *Brain Res.* 881, 244–247.

Herbert, H., Klepper, A., and Ostwald, J. (1997). Afferent and efferent connections of the ventrolateral tegmental area in the rat. *Anat. Embryol. (Berl.)* 196, 235–259.

Herbin, M., Reperant, J., and Cooper, H. M. (1994). Visual system of the fossorial mole-lemmings, *Ellobius talpinus* and *Ellobius lutescens*. *J. Comp. Neurol.* 346, 253–275.

Hickok, G. (2012). Computational neuroanatomy of speech production. *Nat. Rev. Neurosci.* 13, 135–145.

Hickok, G., Houde, J., and Rong, F. (2011). Sensorimotor integration in speech processing: computational basis and neural organization. *Neuron* 69, 407–422.

Hopkins, D. A., and Holstege, G. (1978). Amygdaloid projections to the mesencephalon, pons and medulla oblongata in the cat. *Exp. Brain Res.* 32, 529–547.

Huffman, R. F., and Henson, O. W. (1990). The descending auditory pathway and acousticomotor systems: connections with the inferior colliculus. *Brain Res. Brain Res. Rev.* 15, 295–323.

Humphrey, N. K. (1968). Responses to visual stimuli of units in the superior colliculus of rats and monkeys. *Exp. Neurol.* 20, 312–340.

Hyde, P. S., and Knudsen, E. I. (2000). Topographic projection from the optic tectum to the auditory space map in the inferior colliculus of the barn owl. *J. Comp. Neurol.* 421, 146–160.

Hyde, P. S., and Knudsen, E. I. (2002). The optic tectum controls visually guided adaptive plasticity in the owl's auditory space map. *Nature* 415, 73–76.

Inoue, Y., Takemura, A., Kawano, K., and Mustari, M. J. (2000). Role of the pretectal nucleus of the optic

tract in short-latency ocular following responses in monkeys. *Exp. Brain Res.* 131, 269–281.

Itaya, S. K., and Van Hoesen, G. W. (1982). Retinal innervation of the inferior colliculus in rat and monkey. *Brain Res.* 233, 45–52.

Jain, R., and Shore, S. (2006). External inferior colliculus integrates trigeminal and acoustic information: unit responses to trigeminal nucleus and acoustic stimulation in the guinea pig. *Neurosci. Lett*. 395, 71–75.

Jay, M. F., and Sparks, D. (1990). "Localization of auditory and visual targets for the initiation of saccadic eye movements," in *Comparative Perception Vol I Basic Mechanisms*, eds M. A. Berkley and W. C. Stebbins (New York, NY: John Wiley and Sons), 527.

Jay, M. F., and Sparks, D. L. (1984). Auditory receptive fields in primate superior colliculus shift with changes in eye position. *Nature* 309, 345–347.

Jurgens, U., and Ploog, D. (1970). Cerebral representation of vocalization in the squirrel monkey. *Exp. Brain Res.* 10, 532–554.

Jurgens, U., and Pratt, R. (1979). Role of the periaqueductal grey in vocal expression of emotion. *Brain Res.* 167, 367–378.

Kanold, P. O., and Young, E. D. (2001). Proprioceptive information from the pinna provides somatosensory input to cat dorsal cochlear nucleus. *J. Neurosci.* 21, 7848–7858.

Klug, A., Bauer, E. E., Hanson, J. T., Hurley, L., Meitzen, J., and Pollak, G. D. (2002). Response selectivity for species-specific calls in the inferior colliculus of Mexican free-tailed bats is generated by inhibition. *J. Neurophysiol.* 88, 1941–1954.

Knudsen, E. I. (2002). Instructed learning in the auditory localization pathway of the barn owl. *Nature* 417, 322–328.

Koehler, S. D., Pradhan, S., Manis, P. B., and Shore, S. E. (2011). Somatosensory inputs modify auditory spike timing in dorsal cochlear nucleus principal cells. *Eur. J. Neurosci.* 33, 409–420.

Kudo, M., and Niimi, K. (1980). Ascending projections of the inferior colliculus in the cat: an autoradiographic study. *J. Comp. Neurol.* 191, 545–556.

Kunzle, H. (1998). Origin and terminal distribution of the trigeminal projections to the inferior and superior colliculi in the lesser hedgehog tenrec. *Eur. J. Neurosci.* 10, 368–376.

Kuwada, S., Batra, R., and Stanford, T. R. (1989). Monaural and binaural response properties of neurons in the inferior colliculus of the rabbit: effects of sodium pentobarbital. *J. Neurophysiol.* 61, 269–282.

Lee, J., and Groh, J. M. (2012). Auditory signals evolve from hybrid- to eye-centered coordinates in the primate superior colliculus. *J. Neurophysiol.* 108, 227–242.

Leitner, D. S., and Cohen, M. E. (1985). Role of the inferior colliculus in the inhibition of acoustic startle in the rat. *Physiol. Behav.* 34, 65–70.

Li, H., and Mizuno, N. (1997). Collateral projections from single neurons in the dorsal column nucleus to both the cochlear nucleus and the ventrobasal thalamus: a retrograde double-labeling study in the rat. *Neurosci. Lett.* 222, 87–90.

Linkenhoker, B. A., and Knudsen, E. I. (2002). Incremental training increases the plasticity of the auditory space map in adult barn owls. *Nature* 419, 293–296.

Magoun, H. W., Atlas, D., Ingersoll, E. H., and Ranson, S. W. (1937). Associated facial, vocal and respiratory components of emotional expression: an experimental study. *J. Neurol. Psychopathol.* 17, 241–255.

Marsh, R. A., Fuzessery, Z. M., Grose, C. D., and Wenstrup, J. J. (2002). Projection to the inferior colliculus from the basal nucleus of the amygdala. *J. Neurosci.* 22, 10449–10460.

Martin, J. R. (1976). Motivated behaviors elicited from hypothalamus, midbrain, and pons of the guinea pig (*Cavia porcellus*). *J. Comp. Physiol. Psychol.* 90, 1011–1034.

Mascetti, G. G., and Strozzi, L. (1988). Visual cells in the inferior colliculus of the cat. *Brain Res.* 442, 387–390.

McGurk, H., and MacDonald, J. (1976). Hearing lips and seeing voices. *Nature* 264, 746–748.

Metzger, R. R., Greene, N. T., Porter, K. K., and Groh, J. M. (2006). Effects of reward and behavioral context on neural activity in the primate inferior colliculus. *J. Neurosci.* 26, 7468–7476.

Morest, D. K., and Oliver, D. L. (1984). The neuronal architecture of the inferior colliculus in the cat: defining the functional anatomy of the auditory midbrain. *J. Comp. Neurol.* 222, 209–236.

Moriizumi, T., Leduc-Cross, B., Wu, J. Y., and Hattori, T. (1992). Separate neuronal populations of the rat substantia nigra pars lateralis with distinct projection sites and transmitter phenotypes. *Neuroscience* 46, 711–720.

Mullette-Gillman, O. A., Cohen, Y. E., and Groh, J. M. (2005). Eye-centered, head-centered, and complex coding of visual and auditory targets in the intraparietal sulcus. *J. Neurophysiol.* 94, 2331–2352.

Mullette-Gillman, O. A., Cohen, Y. E., and Groh, J. M. (2009). Motor-related signals in the intraparietal cortex encode locations in a hybrid, rather than eye-centered reference frame. *Cereb. Cortex* 19, 1761–1775.

Nasir, S. M., and Ostry, D. J. (2008). Speech motor learning in profoundly deaf adults. *Nat. Neurosci.* 11, 1217–1222.

Niemi, M., Laaksonen, J. P., Aaltonen, O., and Happonen, R. P. (2004). Effects of transitory lingual nerve impairment on speech: an acoustic study of diphthong sounds. *J. Oral Maxillofac. Surg.* 62, 44–51.

Niemi, M., Laaksonen, J. P., Ojala, S., Aaltonen, O., and Happonen, R. P. (2006). Effects of transitory lingual nerve impairment on speech: an acoustic study of sibilant sound/s. *Int. J. Oral Maxillofac. Surg.* 35, 920–923.

Niemi, M., Laaksonen, J. P., Vahatalo, K., Tuomainen, J., Aaltonen, O., and Happonen, R. P. (2002). Effects of transitory lingual nerve impairment on speech: an acoustic study of vowel sounds. *J. Oral Maxillofac. Surg.* 60, 647–652. discussion: 653.

Nienhuis, R., and Olds, J. (1978). Changes in unit responses to tones after food reinforcement in the auditory pathway of the rat: intertrial arousal. *Exp. Neurol.* 59, 229–242.

Ono, T., Nishijo, H., and Nishino, H. (2000). Functional role of the limbic system and basal ganglia in motivated behaviors. *J. Neurol.* 247(Suppl. 5), V23–V32.

Pageau, C., Champoux, F., Martin, A., Bacon, B. A., Lepore, F., and Guillemot, J. P. (2008). Visual deprivation modifies auditory directional tuning in the inferior colliculus. *Neuroreport* 19, 1797–1801.

Paloff, A. M., Usunoff, K. G., Hinova-Palova, D. V., and Ivanov, D. P. (1985). Retinal innervation of the inferior colliculus in adult cats: electron microscopic observations. *Neurosci. Lett.* 54, 339–344.

Pincherli Castellanos, T. A., Aitoubah, J., Molotchnikoff, S., Lepore, F., and Guillemot, J. P. (2007). Responses of inferior collicular cells to species-specific vocalizations in normal and enucleated rats. *Exp. Brain Res.* 183, 341–350.

Populin, L. C., Tollin, D. J., and Yin, T. C. (2004). Effect of eye position on saccades and neuronal responses to acoustic stimuli in the superior colliculus of the behaving cat. *J. Neurophysiol.* 92, 2151–2167.

Populin, L. C., and Yin, T. C. T. (1998). Pinna movements of the cat during sound localization. *J. Neurosci.* 18, 4233–4243.

Porter, J. D. (1986). Brainstem terminations of extraocular muscle primary afferent neurons in the monkey. *J. Comp. Neurol.* 247, 133–143.

Porter, K. K., Metzger, R. R., and Groh, J. M. (2006). Representation of eye position in primate inferior colliculus. *J. Neurophysiol.* 95, 1826–1842.

Porter, K. K., Metzger, R. R., and Groh, J. M. (2007). Visual- and saccade-related signals in the primate inferior colliculus. *Proc. Natl. Acad. Sci. U.S.A.* 104, 17855–17860.

Portfors, C. V., and Sinex, D. G. (2005). "Coding of communication sounds in the inferior colliculus," in *The Inferior Colliculus*, eds W. Ja and C. Schreiner (New York, NY: Springer), 411–425.

Poulet, J. F., and Hedwig, B. (2002). A corollary discharge maintains auditory sensitivity during sound production. *Nature* 418, 872–876.

Rhoades, R. W., and Chalupa, L. M. (1976). Directional selectivity in the superior colliculus of the golden hamster. *Brain Res.* 118, 334–338.

Rinne, T., Balk, M. H., Koistinen, S., Autti, T., Alho, K., and Sams, M. (2008). Auditory selective attention modulates activation of human inferior colliculus. *J. Neurophysiol.* 100, 3323–3327.

Robards, M. J. (1979). Somatic neurons in the brainstem and neocortex projecting to the external nucleus of the inferior colliculus: an anatomical study in the opossum. *J. Comp. Neurol.* 184, 547–565.

Robards, M. J., Watkins, D. W. 3rd., and Masterton, R. B. (1976). An anatomical study of some somesthetic afferents to the intercollicular terminal zone of the midbrain of the opossum. *J. Comp. Neurol.* 170, 499–524.

Romanski, L. M. (2007). Representation and integration of auditory and visual stimuli in the primate ventral lateral prefrontal cortex. *Cereb. Cortex* 17(Suppl. 1), i61–i69.

Ruth, R. E., Rosenfeld, J. P., Harris, D. M., and Birkel, P. (1974). Effects of aversive and rewarding electrical brain stimulation on auditory evoked responses in albino rat tectum. *Physiol. Behav.* 13, 729–735.

Ryan, A., and Miller, J. (1977). Effects of behavioral performance on single-unit firing patterns in inferior colliculus of the rhesus monkey. *J. Neurophysiol.* 40, 943–956.

Ryan, A. F., Miller, J. M., Pfingst, B. E., and Martin, G. K. (1984). Effects

of reaction time performance on single-unit activity in the central auditory pathway of the rhesus macaque. *J. Neurosci.* 4, 298–308.
Schiller, P. H. (1986). The central visual system. *Vision Res.* 26, 1351–1386.
Schmolesky, M. T., Wang, Y., Hanes, D. P., Thompson, K. G., Leutgeb, S., Schall, J. D., et al. (1998). Signal timing across the macaque visual system. *J. Neurophysiol.* 79, 3272–3278.
Shammah-Lagnado, S. J., Alheid, G. F., and Heimer, L. (1996). Efferent connections of the caudal part of the globus pallidus in the rat. *J. Comp. Neurol.* 376, 489–507.
Shapley, R., and Perry, V. H. (1986). Cat and monkey retinal ganglion-cells and their visual functional roles. *Trends Neurosci.* 9, 229–235.
Shen, K., Valero, J., Day, G. S., and Pare, M. (2011). Investigating the role of the superior colliculus in active vision with the visual search paradigm. *Eur. J. Neurosci.* 33, 2003–2016.
Shinonaga, Y., Takada, M., Ogawa-Meguro, R., Ikai, Y., and Mizuno, N. (1992). Direct projections from the globus pallidus to the midbrain and pons in the cat. *Neurosci. Lett.* 135, 179–183.
Sommer, M. A., and Wurtz, R. H. (2008). Brain circuits for the internal monitoring of movements. *Annu. Rev. Neurosci.* 31, 317–338.
Steinbach, M. J. (1987). Proprioceptive knowledge of eye position. *Vision Res.* 27, 1737–1744.
Suga, N., Schlegel, P., Shimozawa, T., and Simmons, J. (1973). Orientation sounds evoked from echolocating bats by electrical stimulation of the brain. *J. Acoust. Soc. Am.* 54, 793–797.
Suga, N., and Shimozawa, T. (1974). Site of neural attenuation of responses to self-vocalized sounds in echolocating bats. *Science* 183, 1211–1213.
Suta, D., Kvasnak, E., Popelar, J., and Syka, J. (2003). Representation of species-specific vocalizations in the inferior colliculus of the guinea pig. *J. Neurophysiol.* 90, 3794–3808.
Syka, J., and Radil-Weiss, T. (1973). Acoustical responses of inferior colliculus neurons in rats influenced by sciatic nerve stimulation and light flashes. *Int. J. Neurosci.* 5, 201–206.
Szalda, K., and Burkard, R. (2005). The effects of nembutal anesthesia on the auditory steady-state response (ASSR) from the inferior colliculus and auditory cortex of the chinchilla. *Hear. Res.* 203, 32–44.
Szczepaniak, W. S., and Moller, A. R. (1993). Interaction between auditory and somatosensory systems: a study of evoked potentials in the inferior colliculus. *Electroencephalogr. Clin. Neurophysiol.* 88, 508–515.
Tammer, R., Ehrenreich, L., and Jurgens, U. (2004). Telemetrically recorded neuronal activity in the inferior colliculus and bordering tegmentum during vocal communication in squirrel monkeys (*Saimiri sciureus*). *Behav. Brain Res.* 151, 331–336.
Tawil, R. N., Saade, N. E., Bitar, M., and Jabbur, S. J. (1983). Polysensory interactions on single neurons of cat inferior colliculus. *Brain Res.* 269, 149–152.
Thompson, G. C., and Masterton, R. B. (1978). Brain stem auditory pathways involved in reflexive head orientation to sound. *J. Neurophysiol.* 41, 1183–1202.
Van Buskirk, R. L. (1983). Subcortical auditory and somatosensory afferents to hamster superior colliculus. *Brain Res. Bull.* 10, 583–587.
Werner-Reiss, U., Kelly, K. A., Trause, A. S., Underhill, A. M., and Groh, J. M. (2003). Eye position affects activity in primary auditory cortex of primates. *Curr. Biol.* 13, 554–562.
Wiberg, M., Westman, J., and Blomqvist, A. (1987). Somatosensory projection to the mesencephalon: an anatomical study in the monkey. *J. Comp. Neurol.* 264, 92–117.
Winer, J. A., Larue, D. T., Diehl, J. J., and Hefti, B. J. (1998). Auditory cortical projections to the cat inferior colliculus. *J. Comp. Neurol.* 400, 147–174.
Winer, J. A., and Schreiner, C. E. (eds.). (2005). *The Inferior Colliculus*. New York, NY: Springer.
Wurtz, R. H. (1969). Visual receptive fields of striate cortex neurons in awake monkeys. *J. Neurophysiol.* 32, 727–742.
Yajima, Y., Hada, J., and Yoshii, N. (1976). Functional representation of ultrasonic vocalization evoked from rats by electrical stimulation of the brain. *Med. J. Osaka Univ.* 27, 25–32.
Yamauchi, K., and Yamadori, T. (1982). Retinal projection to the inferior colliculus in the rat. *Acta Anat. (Basel)* 114, 355–360.
Yasui, Y., Kayahara, T., Kuga, Y., and Nakano, K. (1990). Direct projections from the globus pallidus to the inferior colliculus in the rat. *Neurosci. Lett.* 115, 121–125.
Yasui, Y., Nakano, K., Kayahara, T., and Mizuno, N. (1991). Non-dopaminergic projections from the substantia nigra pars lateralis to the inferior colliculus in the rat. *Brain Res.* 559, 139–144.
Yin, H. H., and Knowlton, B. J. (2006). The role of the basal ganglia in habit formation. *Nat. Rev. Neurosci.* 7, 464–476.
Zhang, A. B. (1984). Retinotectal pathways in rodents: particularly from the retinal ganglion cells to the inferior colliculus. *Taiwan Yi Xue Hui Za Zhi* 83, 1–8.
Zhang, M., Wang, X., and Goldberg, M. E. (2008). Monkey primary somatosensory cortex has a proprioceptive representation of eye position. *Prog. Brain Res.* 171, 37–45.
Zhang, S. Q., Sun, X. D., and Jen, P. H. (1987). Anatomical study of neural projections to the superior colliculus of the big brown bat, *Eptesicus fuscus*. *Brain Res.* 416, 375–380.
Zhou, J., Nannapaneni, N., and Shore, S. (2007). Vessicular glutamate transporters 1 and 2 are differentially associated with auditory nerve and spinal trigeminal inputs to the cochlear nucleus. *J. Comp. Neurol.* 500, 777–787.
Zhou, J., and Shore, S. (2006). Convergence of spinal trigeminal and cochlear nucleus projections in the inferior colliculus of the guinea pig. *J. Comp. Neurol.* 495, 100–112.
Zurita, P., Villa, A. E., De Ribaupierre, Y., De Ribaupierre, F., and Rouiller, E. M. (1994). Changes of single unit activity in the cat's auditory thalamus and cortex associated to different anesthetic conditions. *Neurosci. Res.* 19, 303–316.
Zwiers, M. P., Versnel, H., and Van Opstal, A. J. (2004). Involvement of monkey inferior colliculus in spatial hearing. *J. Neurosci.* 24, 4145–4156.

Conflict of Interest Statement: The authors declare that the research was conducted in the absence of any commercial or financial relationships that could be construed as a potential conflict of interest.

Received: 18 June 2012; accepted: 15 November 2012; published online: 11 December 2012.
Citation: Gruters KG and Groh JM (2012) Sounds and beyond: multisensory and other non-auditory signals in the inferior colliculus. Front. Neural Circuits ***6****:96. doi: 10.3389/fncir.2012.00096*

frontiers in
NEURAL CIRCUITS

HYPOTHESIS AND THEORY ARTICLE
published: 27 December 2012
doi: 10.3389/fncir.2012.00107

Variability of the time course of stimulus-specific adaptation in the inferior colliculus

David Pérez-González[1]* and Manuel S. Malmierca[1,2]*

[1] Auditory Neurophysiology Laboratory, Institute of Neuroscience of Castilla y León, University of Salamanca, Salamanca, Spain
[2] Department of Cell Biology and Pathology, University of Salamanca, Salamanca, Spain

Edited by:
Eric D. Young, Johns Hopkins University, USA

Reviewed by:
Yoram Gutfreund, Technion - Israel Institute of Technology, Israel
Huiming Zhang, University of Windsor, Canada

***Correspondence:**
David Pérez-González or Manuel S. Malmierca, Auditory Neurophysiology Laboratory (Lab 1), Institute of Neuroscience of Castilla y León, University of Salamanca, C/ Pintor Fernando Gallego, 1, 37007 Salamanca, Spain.
e-mail: davidpg@usal.es; msm@usal.es

Stimulus-specific adaptation (SSA) is the ability of some neurons to respond better to rare than to frequent, repetitive stimuli. In the auditory system, SSA has been found at the level of the midbrain, thalamus, and cortex. While previous studies have used the whole overall neuronal response to characterize SSA, here we present a detailed analysis on the variations within the time course of the evoked responses. The extracellular activity of well isolated single neurons from the inferior colliculus (IC) was recorded during stimulation using an oddball paradigm, which is able to elicit SSA. At the same time, these responses were evaluated before, during, and after the microiontophoretic application of gabazine, a specific antagonist of $GABA_A$ receptors, to study the contribution of inhibition to the responses of these neurons. We then analyzed the difference signal (DS), which is the difference in the PSTH in response to rare and frequent stimuli. We found that, even in a sample of neurons showing strong SSA (i.e., showing larger preference for rare stimuli), the DS was variable and one third of the neurons contained portions that responded significantly better to the frequent stimuli than to the rare. This variability is not observed when averaging the responses of multiple cells. Furthermore, the blockade of $GABA_A$ receptors increased the number of neurons showing portions that responded better to the frequent stimuli, indicating that inhibition in the IC refines and sharpens SSA in the neural responses.

Keywords: auditory, stimulus-specific adaptation, inhibition, GABA-A receptor, microiontophoresis, single unit activity

INTRODUCTION

Since the original paper by Ulanovsky and colleagues (Ulanovsky et al., 2003), a number of studies have appeared in the last decade exploring the phenomenon so-called stimulus-specific adaptation (SSA), which consists on the ability of some neurons to reduce their responses to repetitive stimuli, while keeping their responsiveness to different, albeit similar, stimuli. SSA is elicited by presenting the stimuli in an oddball paradigm (Ulanovsky et al., 2003), in which each trial of a sequence contains one of two different stimuli, which have different probabilities of occurrence. The one appearing with the higher probability is referred to as the standard stimulus, while the other, at the lower probability, is known as the deviant stimulus. The frequent repetitions of the standard cause a gradual reduction of the response on these neurons, but whenever a deviant appears, the neurons are still able to respond promptly and robustly. SSA has been suggested to play a role in auditory scene analysis (Winkler et al., 2009), attention (Escera et al., 1998; Fritz et al., 2007), and novelty or change detection (Jääskeläinen et al., 2004; Nelken and Ulanovsky, 2007; Slabu et al., 2010; Grimm et al., 2011; Gutfreund, 2012).

Thus far, SSA has been found at the levels of the auditory midbrain (Pérez-González et al., 2005, 2012; Malmierca et al., 2009a; Lumani and Zhang, 2010; Zhao et al., 2011; Anderson and Malmierca, 2012; Patel et al., 2012), thalamus (Anderson et al., 2009; Yu et al., 2009; Antunes et al., 2010; Antunes and Malmierca, 2011), and cortex (Ulanovsky et al., 2003, 2004; von der Behrens et al., 2009; Farley et al., 2010; Taaseh et al., 2011; Yaron et al., 2012). The inferior colliculus (IC) is the main auditory center of the midbrain, acting as a site for convergence of most ascending auditory inputs (Oliver and Shneiderman, 1991; Malmierca, 2003) and where auditory information is integrated by combining the multiple excitatory and inhibitory projections arising from lower nuclei, the auditory cortex, as well as commissural and intrinsic connections (Malmierca, 2003; Malmierca et al., 2009b; Malmierca and Ryugo, 2011, 2012). Therefore, the IC stands as a unique auditory center that combines the attributes necessary for the formation of functional microcircuits. In turn, the IC sends the processed auditory information to the cortex, through the thalamus. Inhibition, in particular that mediated by GABA, has been found to play a key role in the sound processing that takes place in the IC (LeBeau et al., 1996; Wu et al., 2004; Gittelman et al., 2012), regulating several properties including sound intensity (Sivaramakrishnan et al., 2004), amplitude modulation (Caspary et al., 2002; Zhang and Kelly, 2003), frequency selectivity (Palombi and Caspary, 1996; Koch and Grothe, 1998; LeBeau et al., 2001), sound localization (Ingham and McAlpine, 2005), or sound duration (Casseday et al., 1994, 2000; Covey et al., 1996). SSA has been found to be a unique property of the non-lemniscal subcortical nuclei (Malmierca et al., 2009a; Antunes et al., 2010; Antunes and Malmierca, 2011; Duque et al., 2012). In this respect, it should be emphasized that there are between 10 and 20 times more

GABAergic than glycinergic puncta (Merchán et al., 2005) in the dorsal and lateral cortical areas of the IC, i.e., in the non-lemniscal areas, which suggest that in these IC regions GABA plays a key role in the processing of auditory stimuli through inhibition.

While SSA is commonly estimated from the whole evoked response of the neuron, several studies have described its variations across the response, either based on single unit recordings (Ulanovsky et al., 2003; Malmierca et al., 2009a; von der Behrens et al., 2009; Zhao et al., 2011), multiunit recordings (Ulanovsky et al., 2003; von der Behrens et al., 2009; Farley et al., 2010; Bäuerle et al., 2011), or local field potentials (LFPs) (von der Behrens et al., 2009; Patel et al., 2012). However, these studies tend to report the aggregated variations at the population level, a fact that will not reflect the details in the temporal variability on the responses of single neurons. We have used a data set that was published previously with a different purpose (Pérez-González et al., 2012), in order to perform a detailed analysis of the time course of the responses evoked during SSA. The original data set comprises single neurons located in the dorsal, lateral, and rostral cortices of the IC (Malmierca et al., 1993, 2011). Neurons located in those regions display a high degree of SSA. These neurons were tested for SSA using an oddball paradigm while blocking local $GABA_A$ receptors, using the powerful technique of microiontophoresis, which allows examining the contribution of inhibition to the neuronal responses.

MATERIALS AND METHODS

DATA SET AND DATA COLLECTION

We analyzed a data set comprising extracellular recordings of 46 single units from the IC of Long Evans adult rats. The neurons were located in the dorsal, lateral, and rostral cortices of the IC, which display a large amount of SSA (Pérez-González et al., 2005; Malmierca et al., 2009a). All cases from the original set were included in the analysis. The original data were collected and analyzed for other purposes (Pérez-González et al., 2012); therefore, here it suffices a brief description of the most relevant aspects of the data collection.

The experiments were conducted on urethane-anesthetized animals, which were placed in a stereotaxic frame and subjected to closed-field auditory stimulation (Rees, 1990; Rees et al., 1997; Malmierca et al., 2008, 2009a,b). A craniotomy was performed to allow for access to the IC through the cortex. The extracellular activity of single neurons in the IC was recorded with tungsten electrodes, and the spike times were stored for further analysis. The recording electrodes were attached to multibarrel pipettes, filled with either 20 mM gabazine (SR-95531, Sigma-Aldrich) or 1 mM NaCl for current compensation. Gabazine is a selective antagonist of $GABA_A$ receptors, which lacks the side effect on calcium-dependent potassium channels of bicuculline, the other typical antagonist of $GABA_A$ receptors (Kurt et al., 2006). Gabazine was released by microiontophoresis (Neurophore BH-2 System, Harvard Apparatus), applying currents to the pipettes (typically 40–50 nA), to locally block the $GABA_A$ receptors at the recording site. Controls were conducted to rule out current artifacts. Data were collected before (*control condition*), during (*gabazine condition*), and after (*recovery condition*, not analyzed here) the application of gabazine, and comparisons were made between the different conditions.

Acoustic stimuli were delivered monaurally through calibrated speakers (model EC1, TDT; Tucker-Davis Technologies), to the ear contralateral to the recording side. Stimulation and recording was performed by TDT System II equipment, controlled with custom software. Search stimuli included white noise and pure tones whose frequency was changed often to reduce neuronal adaptation. The experimental stimuli were pure tones with duration of 75 ms, including 5 ms rise/fall ramps, at a rate of 4/s. The frequency response area (FRA) of the neuron was determined using an automated procedure (Duque et al., 2012; Pérez-González et al., 2012) and was used to establish the best frequency (the frequency that evoked a response at the lowest intensity) and the threshold (the lowest intensity able to evoke a response). The stimuli were chosen to fall within the response area of the neuron. For each neuron, a pair of pure tones of different frequencies (f_1 and f_2; 0.36–0.53 octaves apart, relative to the lowest frequency of the pair) that elicited a similar firing rate at the same sound level (10–40 dB above threshold) were presented in an oddball paradigm (Näätänen, 1992; Ulanovsky et al., 2003, 2004; Malmierca et al., 2009a; Duque et al., 2012). This paradigm consisted of a sequence of 400 stimuli containing either frequency in a probabilistic manner. One frequency (f_1) was presented as the standard (i.e., high probability within the sequence, 90%); interspersed randomly among the standards were the deviant stimuli (i.e., low probability, 10%) at the second frequency (f_2). Afterwards the relative probabilities of the two stimuli were reversed, with f_2 as the standard and f_1 as the deviant (e.g., **Figure 1A**). The original and the reverse sequence were alternated during the whole course of the experiment.

DATA ANALYSIS

The spike times in response to the oddball paradigm were used to calculate peristimulus-time histograms (PSTH) separately for the deviant and the standard stimuli (e.g., **Figures 1B,C**, red and blue traces, respectively). The width of the PSTH bins was 1 ms. For each neuron we obtained eight PSTH: two frequencies (f_1, f_2), at two probabilities (10% for deviants, and 90% for standards), in two conditions (*control* and *gabazine*, i.e., before and during the application of gabazine). Due to the different probabilities, the PSTH were derived from different numbers of trials (40 trials in the case of the deviants and 360 trials in the case of the standards). The firing rates were expressed as spikes per second (spk/s) in order to properly compare the responses.

The PSTH of the neurons was classified based on the firing pattern. After correcting for spontaneous activity, the PSTH of a neuron was considered onset if 99% of the response was included in a 30 ms window; otherwise it was considered sustained. For simplicity, we did not perform a more detailed classification of the firing pattern. The 30-ms limit for onset responses has been used previously for neurons in the IC (LeBeau et al., 1996; Lumani and Zhang, 2010), while the 99% criterion avoids misclassification of neurons with spurious late spikes that otherwise would be considered purely onset. Since the firing pattern has been found to depend on the type of stimulus (Pérez-González et al., 2012), this classification was done separately for the responses to deviants

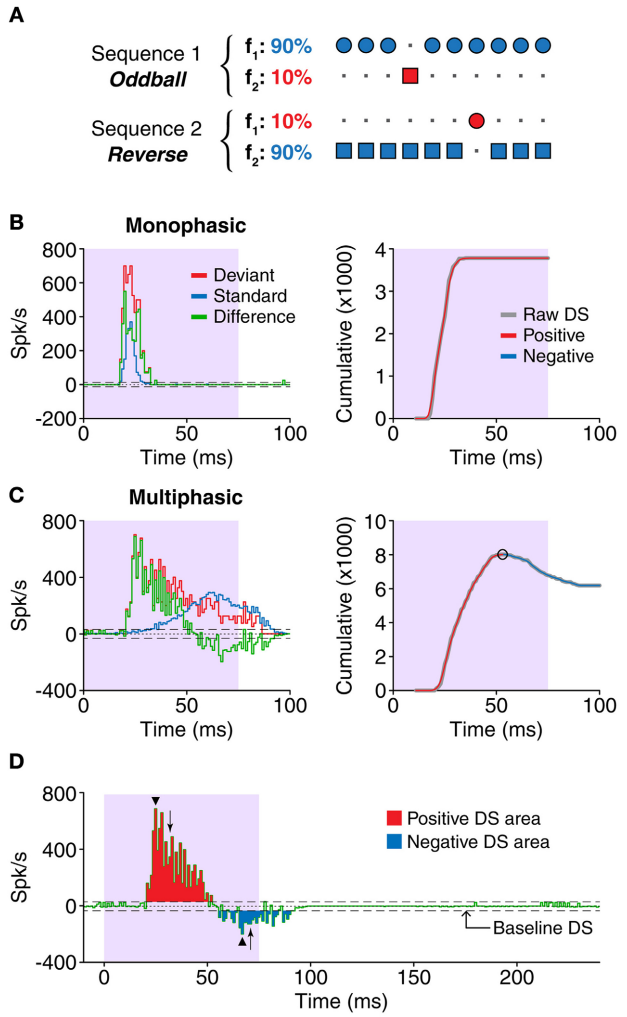

FIGURE 1 | (A) In the oddball paradigm, a sequence is built containing two different stimuli, in this case, two pure tones at different frequencies (f_1, f_2). The stimuli are equally spaced, but their probabilities are different. One of the tones, the standard (blue), appears in 90% of the trials, while the other, called deviant (red), appears in the remaining 10%. A complimentary sequence is presented afterwards, with the probabilities of the stimuli reversed. Thus, comparisons can be drawn for each of the tones when they are presented as deviants or standards. **(B,C)** Left panels show examples of responses (PSTH) to one tone presented as standard (blue) or deviant (red). The difference signal (DS, green) was calculated as deviant–standard. We classified the shapes of the DS as ***monophasic*** **(B)** or ***multiphasic*** **(C)**. The bin size for all the histograms in this study was 1 ms. The shaded background indicates the duration of the stimulus. Right panels show the cumulative functions of each corresponding DS. The raw cumulative sum function (gray) was smoothed, and the peaks and valleys (circles) were found (see "Materials and Methods"). The increasing sections between peaks (red) indicate portions were the DS is positive, while the decreasing sections indicate the negative portions of the DS. The extent of the negative portions was used to determine the type of DS. **(D)** Only DS values larger than the baseline DS were considered for the study. The positive (red) and negative (blue) portions of the DS were measured separately. The measurements included the latency and magnitude of the peaks (arrowheads), the duration and total area of each portion (red and blue areas), and the latency of the median spike (arrows). The horizontal dashed lines represent the threshold for the baseline activity, i.e., random fluctuations of the DS (mean + 3SD).

and to standards. We used a two-letter nomenclature to define the response of each neuron, the first letter corresponding to the firing pattern in response to standards, and the second in response to deviants. This way, neurons were classified as O-S when the standard was onset but the deviant was sustained, S-O when only the deviant was onset, O-O when both the deviant and the standard were onset and S-S when both were sustained.

The difference signal (DS) was calculated as the difference (in a per-bin basis) between the PSTH for the deviants and the standards ($PSTH_{deviant} - PSTH_{standard}$) in response to the same frequency, in the same condition (e.g., **Figures 1B,C**, green trace). Thus, positive values of the DS indicate that the response to a stimulus when deviant was larger than the response to the same stimulus when standard, and vice versa.

All the calculations based on the DS were corrected for the baseline fluctuations related to the spontaneous activity (i.e., the activity outside of the evoked response), calculated from a window of 50 ms at the end of each trial. The DS from this time window was obtained, the absolute value of those bins was calculated, and the mean + 3SD was used as threshold for separating the baseline activity. Only the bins whose absolute value was larger than this figure were considered to be significantly different to the baseline DS. In the calculations regarding the magnitude of the DS, this value was subtracted from each significant bin.

We categorized each DS based on its fluctuations during the course of the response. For this purpose, we calculated the cumulative function of the DS (after correcting for baseline activity) and applied a moving average filter (2 passes, 3-bin wide) to smooth high frequency variations. In this cumulative function, the increasing sections reflect positive DS values while the decreasing ones represent the negative DS values. To differentiate the positive from the negative sections, we identified the peaks and valleys of the function, excluding those smaller than 5% of the average firing rate of the neuron. This way, we classified the DSs as ***monophasic***, when the corresponding cumulative function did not contain such peaks or valleys, or ***multiphasic***, in the opposite case. Examples of neurons with monophasic and multiphasic DSs are shown in **Figures 1B,C**, respectively, as well as the cumulative functions that illustrate the classification process.

We performed a number of calculations in order to characterize the timing and magnitude of the positive and negative portions of the DS, on each neuron. After removing the baseline activity, we applied a time window that included only the evoked response, as judged by visual inspection of the PSTH. Since the response latency and duration were very variable, we considered this time window on a case-by-case basis, as we think this approach is more appropriate than establishing a fixed window for all the cases. First, we calculated the number of positive and negative bins as estimation of the duration of each portion (**Figure 1D**, red and blue bins, respectively). The area of the positive or negative bins (**Figure 1D**, red and blue areas, respectively), indicated the magnitude of each portion, and their timing was estimated from the latency of the median spike, relative to the onset of the stimulus (**Figure 1D**, arrows). On the other hand, we also calculated parameters relative to the peak of each portion (i.e., the bin with the largest positive or negative magnitude; **Figure 1D**, arrowheads), in particular the latency

and the firing rate. For neurons with multiple positive or negative peaks, these calculations were based on the largest positive or negative peak, respectively. All the calculations were corrected for the baseline activity (**Figure 1D**, dashed line) as described above. Differences between groups were compared using either a Two-Way ANOVA test [**Figures 3C**, **4C**, **5C**, **6C**; factors: sign of DS (positive or negative) and condition (control or gabazine) and **Figures 3G,H**, **4G,H**, **5G,H**, **6G,H**; factors: sign of DS (positive or negative) and firing pattern (S-S, S-O, O-S, or O-O)] or a Three-Way ANOVA test [**Figures 3D**, **4D**, **5D**, **6D**; factors: sign of DS (positive or negative), type of DS (monophasic or multiphasic) and condition (control or gabazine)] and corrected for multiple comparisons using the Tukey–Kramer method. Results were considered significant when $p < 0.05$.

The probability of occurrence of a positive or negative DS was calculated as the percentage of cases that contained a significantly positive or negative DS value in each particular bin. The results of this calculation are illustrated on **Figure 7**.

RESULTS

We calculated the PSTH of the responses of 46 neurons in the IC tested in an oddball paradigm, before and during the iontophoretic application of the $GABA_A$ antagonist gabazine. Each of the frequencies presented in the oddball paradigm for each neuron was considered separately for the analyses, so the number of cases is 92 frequencies. For each of these cases we calculated the DS, as the difference between the PSTH for deviants and standards (**Figures 1B,C**). The DS is an indicator of the parts of the response that prefer the deviant stimuli (positive DS) or the standard ones (negative DS).

PSTH OF THE POPULATION

As a first approximation, we calculated the grand average of all the responses, for all the neurons (**Figure 2**). During the control condition (**Figure 2A**), this resulted in a mainly onset PSTH, with a low-firing sustained part, for both standards and deviants. The peak response to the deviants (184.8 spk/s) was considerably larger than the peak response to the standards (31.2 spk/s). The latencies of the peak response for the deviant and the standard were similar (29.5 and 31.5 ms, respectively), although it has been shown that in individual neurons the latency in response to deviants is significantly shorter than in response to standards (Malmierca et al., 2009a; Antunes et al., 2010; Duque et al., 2012; Pérez-González et al., 2012). The resulting DS was positive during the whole evoked response (peak: 161.3 spk/s; peak latency: 28.5 ms). In the gabazine condition (**Figure 2B**) the peak rates were much larger in response to both deviant (441.3 spk/s) and standard stimuli (127.4 spk/s), but the response to the deviant stimuli remained substantially larger than the one to the standard stimuli. The shape of the PSTH became broader in both cases, while the latencies for the peak response were slightly longer (33.5 ms for the deviant; 32.5 ms for the standard). The DS of the population grand average was also positive for the duration of the evoked response (peak: 316.2 spk/s; peak latency: 31.5 ms). Together, the data from the averaged responses are consistent with the previously reported effect of $GABA_A$-mediated inhibition (Pérez-González et al., 2012), wherein inhibition would modify

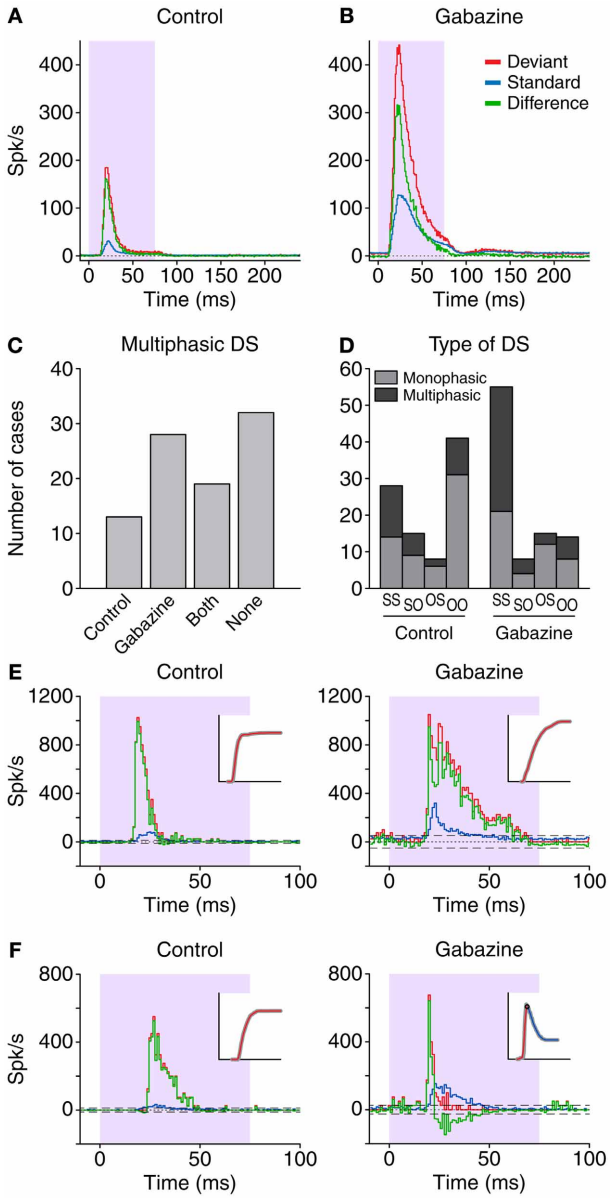

FIGURE 2 | Grand average PSTH from the sample of neurons in the control (A) and gabazine (B) conditions. The red lines correspond to the responses to the deviant stimuli, while the blue lines represent the responses to the standard stimuli. The difference signal (DS; deviant-standard) is represented in green. The shaded background indicates the duration of the stimulus. The length of the histogram bins is 1 ms. **(C)** Distribution of the cases were the DS was classified as multiphasic. The *Control* and *Gabazine* groups indicate the number of cases that only presented a negative DS during one of those conditions. *Both* indicates the neurons that had a negative part in both conditions, while neurons that did not have a negative portion under any condition are labeled as *None*. **(D)** Distribution of the cases based on the firing pattern. *S-S*, both standard and deviant were sustained; *S-O*, only the deviant was onset; *O-S*, only the standard was onset; *O-O*, both the deviant and the standard were onset. **(E,F)** Examples from two different neurons during the control and gabazine conditions. In both cases, the DS type is monophasic during the control condition, but in **(F)** the DS type transforms to multiphasic during the gabazine condition. The insets show the cumulative function of the DS, used for the classification.

the contrast between responses to standard and deviant by providing a control of the response gain, in what is known as "iceberg effect" (Rose and Blakemore, 1974; Isaacson and Scanziani, 2011).

While the DS was always positive in the averaged population response, this was not the case in the individual responses. All the individual DS had a positive part, but 34.8% (32/92) in the control condition also had significant negative portions, and were thus classified as multiphasic. In the gabazine condition, 51.1% (47/92) of the cases were classified as multiphasic. Not all the neurons that were multiphasic in the control condition maintained this classification during the gabazine condition; only 20.7% (19/92) of the cases were multiphasic during both control and gabazine conditions, while 14.1% (13/92) were multiphasic only during the control condition and 30.4% (28/92) only during the gabazine condition (**Figure 2C**). Thirty-five percent (32/92) of the cases did not show a negative part during any of the conditions.

Figure 2D shows the distribution of the types of DS and the firing patterns. During the control condition, the most common combination was monophasic neurons with onset patterns for both types of stimuli, deviant and standard (group O-O, 31/92). In contrast, during the gabazine condition, the most common combination was multiphasic neurons with sustained patterns in response to both deviants and standards (group S-S, 34/92). **Figures 2E,F** show the responses of two different neurons. Both of them displayed a DS (green trace) categorized as monophasic in the control condition (left panels), but the application of gabazine (right panels) modified substantially the response of the neuron in **Figure 2F**, to the point that the DS became multiphasic (see insets).

DURATION OF THE DIFFERENCE SIGNAL

The duration of the positive and negative parts of the DS was estimated as the number of 1-ms bins which were significantly different from the baseline DS. The duration of the positive parts in the control condition was on average 19.1 ± 12.7 ms, and increased to 34.7 ± 19.7 ms in the gabazine condition (**Figure 3A**). The application of gabazine caused an increment of the duration of the positive part on 75% of the cases (69/92), while 24% of the cases (22/92) showed a decrement. Taking all the cases into account, the average increment of the duration of the positive parts during the gabazine condition was 15.6 ± 22.8 ms. On the other hand, the duration of the negative parts was only 4.4 ± 7.4 ms in the control condition and 11.3 ± 15.9 in the gabazine condition (**Figure 3B**). Only 50% (46/92) of the cases showed an increment of the duration of the negative parts during the gabazine condition, while 27% of the cases (25/92) showed a decrement. In 3 cases (3%), the duration of the negative parts was the same in the control and gabazine conditions. In 18 cases (20%), there was no negative part during either the control or the gabazine conditions. Taking all the cases into account, the average increment of the duration of the negative parts during the gabazine condition was 6.9 ± 16.3 ms.

When pooling all cases together (**Figure 3C**), we found significant differences between the duration of the positive and the negative parts, in both the control and the gabazine conditions. In addition, the duration of both parts was significantly increased

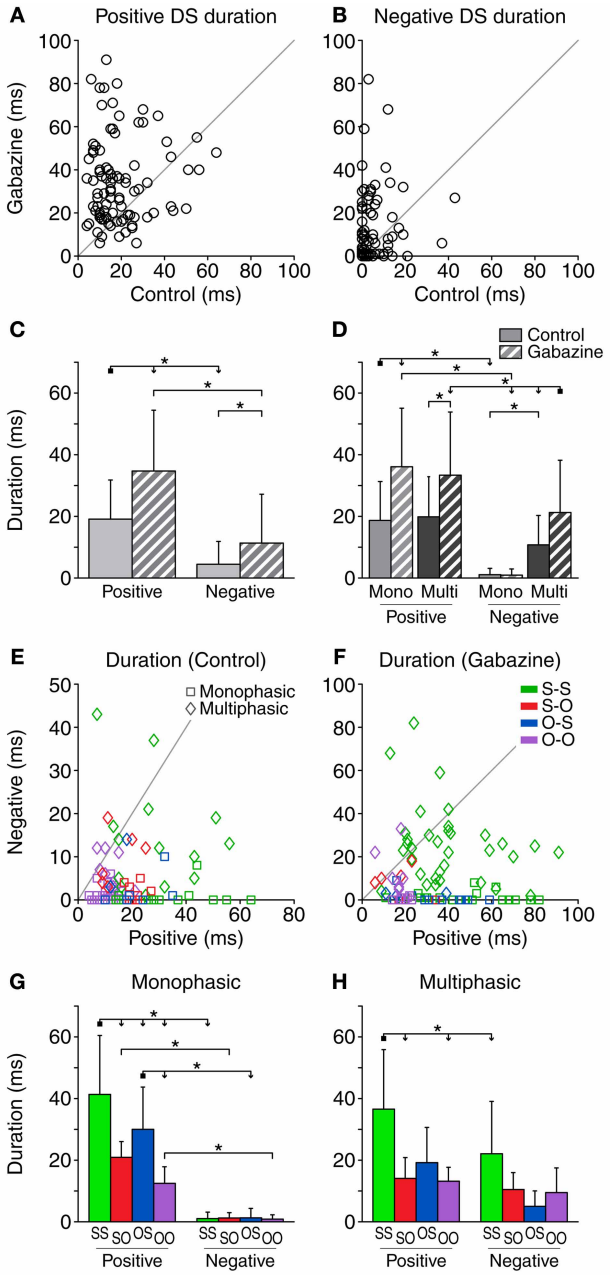

FIGURE 3 | Duration of the DS (number of 1-ms bins where the response is significantly larger than the baseline DS). The duration of both the positive **(A)** and negative **(B)** parts of the DS increased during the application of gabazine. **(C)** Mean and standard deviation of the duration for all the cases pooled together, in the control (solid fill) and gabazine (pattern fill) conditions. **(D)** Mean and standard deviation of the duration, grouped by DS type. The duration of the negative part of the DS was shorter than the duration of the positive part for most neurons, both in the control **(E)** and the gabazine **(F)** conditions. The axes in these panels have been plotted at different scales for a better visualization of the data. **(G)** Mean and standard deviation of the different firing pattern groups for the monophasic or **(H)** multiphasic units, including units in both the control and gabazine conditions. *Mono*, monophasic; *Multi*, multiphasic. *S-S*, standard and deviant sustained; *S-O*, standard sustained and deviant onset; *O-S*, standard onset and deviant sustained; *O-O*, standard and deviant onset.

(Continued)

FIGURE 3 | Continued
Asterisks indicate $p < 0.05$. For all the scatter plots in this and similar figures, $n = 92$ unless stated otherwise. In this and similar figures, some of the significance brackets have been collapsed into a complex bracket, to reduce clutter. They indicate significant differences ($p < 0.05$) between the group at the square end and every group under an arrowhead.

during the gabazine condition. We did a similar analysis sorting the cases into DS and firing pattern types (**Figure 3D**). We found that the duration of the positive parts of both the monophasic and multiphasic types was significantly affected by gabazine, but the duration of the negative parts was only affected by gabazine in the case of the multiphasic units. The duration of the positive parts was very similar for monophasic and multiphasic neurons, but the duration of the negative parts of the monophasic units was significantly smaller than that of the multiphasic units. In addition, the duration of the positive parts was significantly larger than the duration of the negative parts in all the groups but the multiphasic/control.

The duration of the positive part of the DS was longer than the negative part in most of the cases [93.5% (86/92) during the control condition and 84.8% (78/92) during the gabazine condition], as shown in **Figures 3E,F**. On average, the positive part of the DS was 14.6 ± 14.1 ms longer than the negative part in the control condition. This difference increased notably in the gabazine condition, where the positive part was 23.4 ± 25.8 ms longer than the negative.

A detailed analysis of the firing pattern groups, including units in both the control and gabazine conditions, showed that the S-S group had the longest positive DS duration. For the monophasic units, all the groups had longer positive durations than negative (**Figure 3G**), while for the multiphasic units only the S-S group had significantly different positive and negative DS durations (**Figure 3H**).

AREA OF THE PARTS OF THE DIFFERENCE SIGNAL

We calculated the total area of the positive and negative parts of the DS for each stimulus (e.g., red and blue areas in **Figure 1D**). The average area of the positive DS parts was 1.8 ± 1.3 spk per trial in the control condition, and in increased to 6.77 ± 6.44 spk per trial in the gabazine condition (**Figure 4A**). Gabazine caused an increment of the area of the positive DS in 85% (78/92) of the cases, and a decrement in the resting 15% (14/92). Taking all the cases into account, the area of the positive DS parts increased an average of 4.9 ± 6.4 spk per trial in the gabazine condition. The area of the negative DS in the control condition was only 0.06 ± 0.17 spk per trial, while in the gabazine condition it increased up to 0.47 ± 1.0 spk per trial (**Figure 4B**). Only 54% of the cases (50/92) showed a larger negative area in the gabazine condition relative to the control condition, while in 25% of the cases (23/92) the negative area was smaller. In 1 case (1%), the area of the negative DS parts was the same in the control and gabazine conditions. In 18 cases (20%), there was no negative part during either the control or the gabazine conditions. Taking all the cases into account, the average increment of the area of the negative parts during the gabazine condition was 0.41 ± 1.05 ms.

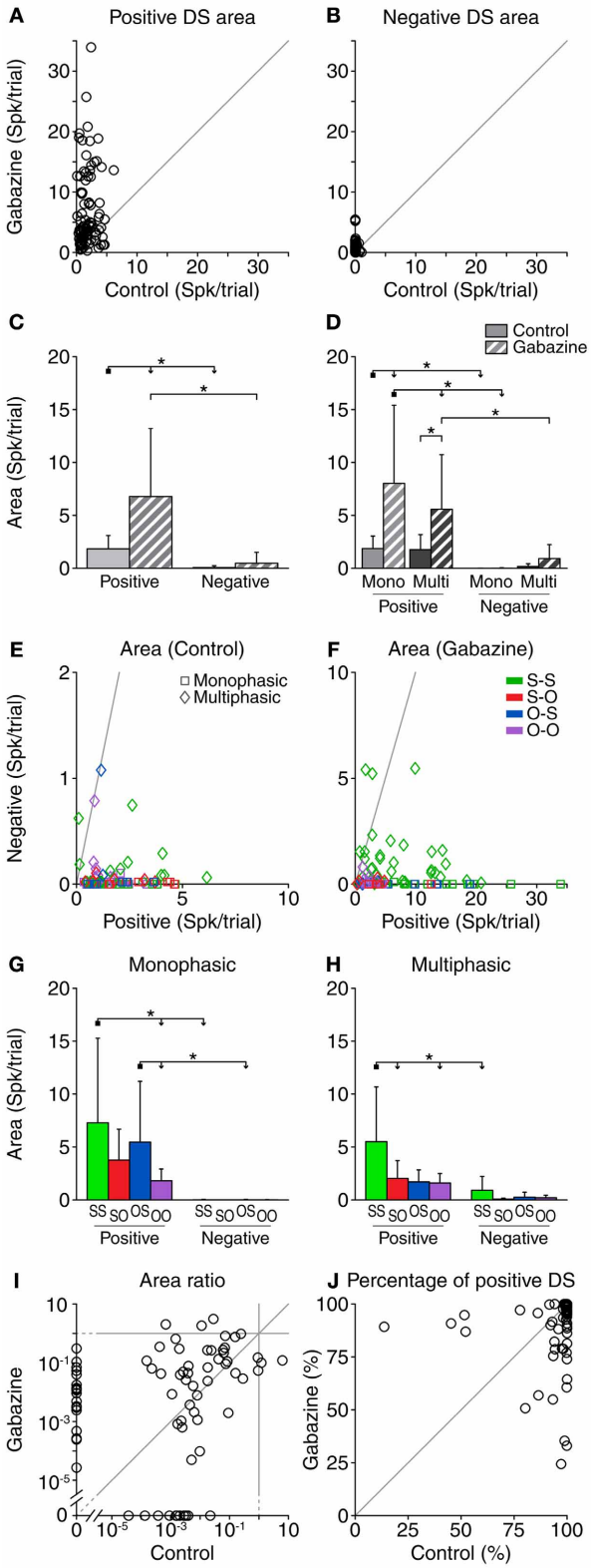

FIGURE 4 | Area (accumulated response) of the DS for each neuron, corrected for the baseline DS. The area of both the positive **(A)** and negative **(B)** portions of the DS increased during the gabazine condition.
(Continued)

FIGURE 4 | Continued
(C) Mean and standard deviation of the area for all the cases pooled together, in the control (solid fill) and gabazine (pattern fill) conditions. **(D)** Mean and standard deviation of the area, grouped by DS type. The area of the positive portions of the DS was larger than that of the negative ones for most neurons, both in the control **(E)** and the gabazine **(F)** conditions. The axes in these panels have been plotted at different scales for a better visualization of the data. **(G)** Mean and standard deviation of the different firing pattern groups for the monophasic or **(H)** multiphasic units, including units in both the control and gabazine conditions. The area ratio (negative area/positive area) **(I)** and the percentage of positive area **(J)** for each individual DS show that, while the amount of positive and negative DS portions changed during the gabazine condition, there was no clear trend. *Mono*, monophasic; *Multi*, multiphasic. *S-S*, standard and deviant sustained; *S-O*, standard sustained and deviant onset; *O-S*, standard onset and deviant sustained; *O-O*, standard and deviant onset. Asterisks indicate $p < 0.05$.

When all cases were pooled, gabazine only had a significant effect on the area of the positive parts of the DS (**Figure 4C**). Nevertheless, the positive area was significantly larger than the negative in both the control and gabazine conditions. When sorting the cases in DS and firing pattern types (**Figure 4D**), the results were similar to the analysis of the duration of the DS parts. The positive DS area increased significantly for the monophasic and multiphasic groups, but not the negative DS area. Likewise, the positive DS area was significantly larger than the negative DS area for the monophasic group (in both control and gabazine conditions), but for the multiphasic group it was larger only during the gabazine condition.

The area of the positive DS was larger than the area of the negative DS in almost every case, both in the control (98%, 90/92) and the gabazine conditions (97%, 89/92). Only 2 cases in the control condition and 3 cases in the gabazine condition showed a negative DS larger than the positive DS (**Figures 4E,F**).

Not surprisingly, the area of the negative DS parts was negligible for the monophasic units. The largest positive and negative DS areas corresponded to the neurons classified as S-S, while the smallest DS areas were those of the neurons classified as O-O (**Figures 4G,H**).

The area ratio (negative area/positive area) was larger in the gabazine condition than in the control condition for 64% (47/74) of the cases (**Figure 4I**). The area of the positive DS accounted for $95.8 \pm 12.9\%$ of the total DS area in the control condition, and $91.5 \pm 15.6\%$ in the gabazine condition (**Figure 4J**).

PEAK RATE OF THE DIFFERENCE SIGNAL

Similarly to the area of the DS, we quantified the peak rate of firing for the positive and negative portions of the DS (**Figures 5A,B**). The average peak rate of the positive portions was 344.4 ± 183.9 spk/s in the control condition and 558.2 ± 252.7 spk/s in the gabazine condition (**Figure 5A**). Gabazine caused an increment of the peak firing rate of the positive DS portions in 77% of the cases (71/92) and a decrement in the resting 23% (21/92). Considering all the cases, the average increment of the peak firing rate of the positive DS parts during the gabazine condition was 213.8 ± 293.9 spk/s. The peak firing rate of the negative parts was 18.9 ± 54.2 spk/s in the control condition,

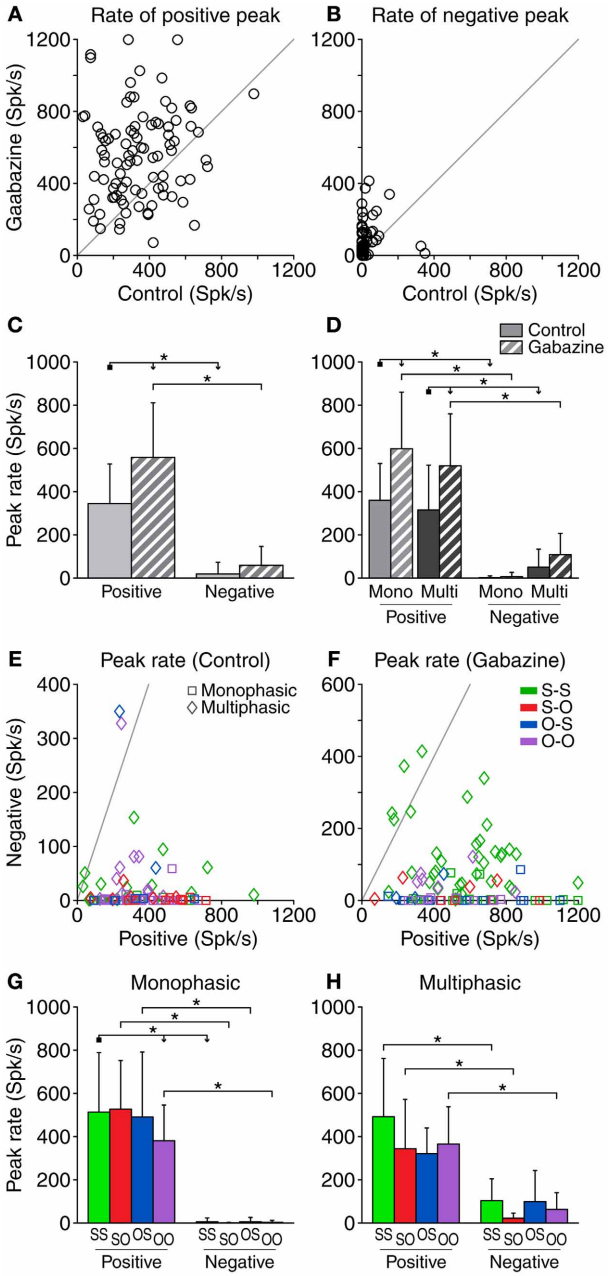

FIGURE 5 | Peak firing rate of the DS for each neuron. The most positive (positive peak) and most negative (negative peak) values of the DS for each neuron are represented here in absolute value. The effect of removing $GABA_A$ inhibition is depicted in **(A)** and **(B)**. Both the positive peak rates **(A)** and the negative **(B)** tend to increase due to the application of gabazine, to the point of the appearance of negative parts in the DS where there was previously none in the control condition **(B)**. **(C)** Mean and standard deviation of the peak firing rate for all the cases pooled together, in the control (solid fill) and gabazine (pattern fill) conditions. **(D)** Mean and standard deviation of the peak firing rate grouped by DS type. In the control condition **(E)**, the peak positive DS extended over a wide range of values, while the negative peak was limited to much smaller rates. During the gabazine condition **(F)**, both positive and negative peaks became slightly larger. In almost every case, the positive peak was much larger than the negative peak. The axes in these panels have been plotted at different

(Continued)

FIGURE 5 | Continued
scales for a better visualization of the data. **(G)** Mean and standard deviation of the different firing pattern groups for the monophasic or **(H)** multiphasic units, including units in both the control and gabazine conditions. *Mono*, monophasic; *Multi*, multiphasic. *S-S*, standard and deviant sustained; *S-O*, standard sustained and deviant onset; *O-S*, standard onset and deviant sustained; *O-O*, standard and deviant onset. Asterisks indicate $p < 0.05$.

and increased to 58.5 ± 87.7 spk/s during the gabazine condition (**Figure 5B**). Fifty-eight percent of the cases (53/92) showed an increment of the peak firing rate of the negative DS portions during the gabazine condition, while 20% (18/92) showed a decrement. In 18 cases (20%), there was no negative part during either the control or the gabazine conditions. Taking all the cases into account, the average increment of the peak firing rate of the negative parts during the gabazine condition was 39.6 ± 93.6 spk/s.

When considering all the cases together, the average peak firing rate of the positive parts was significantly larger than that of the negative parts, both in the control and gabazine conditions. In addition, gabazine had a significant effect on the rate of the positive portions of the DS, but not on the negative ones (**Figure 5C**). The analysis of the peak firing rate grouping the data by DS and firing pattern types (**Figure 5D**) was similar to the case of the area of the DS parts (**Figure 4D**), with the exceptions that now there is a significant difference between the positive and negative peak firing rates for multiphasic units in the control condition, and the positive peak firing rates of monophasic and multiphasic units in the gabazine condition are not significantly different.

The DS did not have a negative portion in 36 cases during the control condition and in 29 during the gabazine condition. In a large majority of the cases showing a negative part, the peak firing rate of the positive part was larger than that of the negative part, both in the control (95%, 53/56) and the gabazine (94%, 59/63) conditions (**Figures 5E,F**).

The peak firing rate of the positive DS parts was larger than that of the negative parts for all the firing pattern groups, both for the monophasic and the multiphasic neurons, with the only exception of the O-S group of the multiphasic units (**Figures 5G,H**). For each DS type (monophasic or multiphasic) and DS part (positive or negative), the mean peak firing rate was quite similar among all firing pattern groups, with the exception of the peak firing rate of the positive DS parts of the monophasic units, where there was a significant difference between the S-S and O-O groups.

TIMING OF THE DIFFERENCE SIGNAL

Regarding the timing of the different parts of the DS, we calculated the latency of the DS peaks (**Figure 6**). The average latency of the positive peaks was very similar in the control (22.1 ± 8.4 ms) and the gabazine (21.7 ± 5.7 ms) conditions (**Figure 6A**). The application of gabazine caused an increment of the latency of the positive peak on 39% of the cases (36/92), while 51% of the cases (47/92) showed a decrement. Taking all the cases into account, the average increment of the latency of the positive

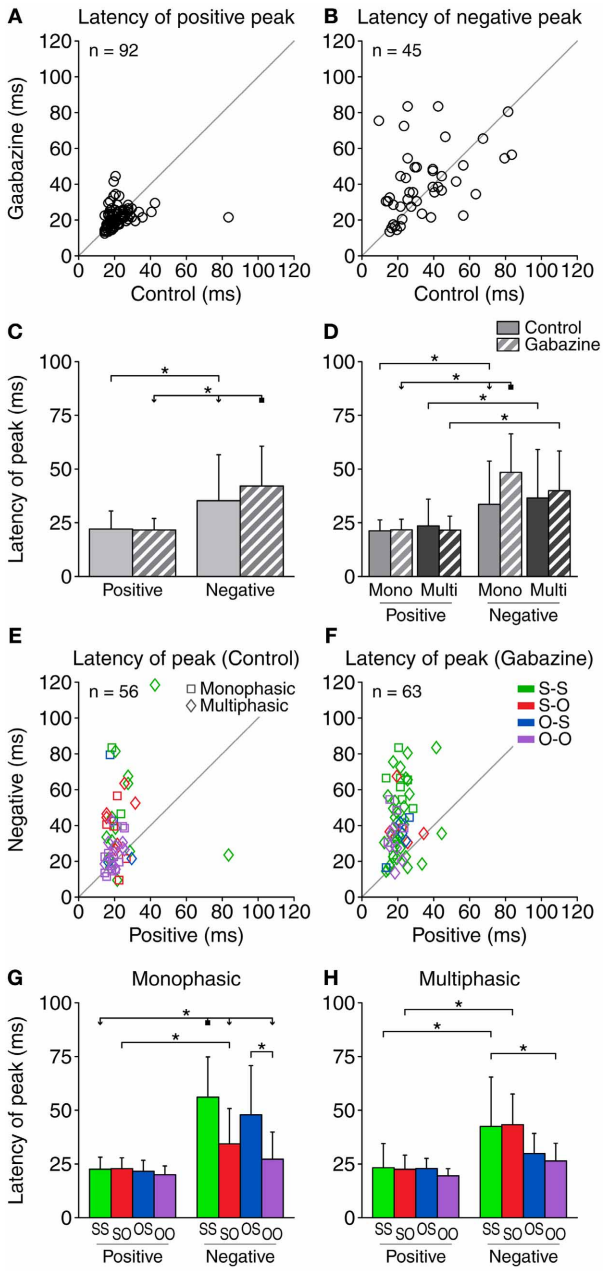

FIGURE 6 | The latency of the positive DS peak was relatively short (10–40 ms) and was little affected by gabazine (A), while the latency of the negative peak extended over a longer range of values (B). Some of the cases did not contain a negative part of the DS, so the corresponding latencies could not be calculated. The number of cases plotted is indicated inside each panel. **(C)** Mean and standard deviation of the latency of the peaks for all the cases pooled together, in the control (solid fill) and gabazine (pattern fill) conditions. **(D)** Mean and standard deviation of the latency of the peaks, grouped by DS type. In both the control **(E)** and the gabazine **(F)** condition, the latency of the positive DS peak was shorter than the latency of the negative peak for most neurons. **(G)** Mean and standard deviation of the different firing pattern groups for the monophasic or **(H)** multiphasic units, including units in both the control and gabazine conditions. *Mono*, monophasic; *Multi*, multiphasic. *S-S*, standard and deviant sustained; *S-O*, standard sustained and deviant onset; *O-S*, standard onset and deviant sustained; *O-O*, standard and deviant onset. Asterisks indicate $p < 0.05$.

peak during the gabazine condition was -0.4 ± 9.1 ms. The average latency of the negative peaks (**Figure 6B**) was longer in the control condition (35.3 ± 21.4 ms), and even longer in the gabazine condition (42.1 ± 18.6 ms). Only 45 neurons showed a negative portion in both the control and gabazine conditions. Of those, 47% of the cases (21/45) showed an increment of the latency of the negative peak during the gabazine condition, and 44% of the cases (20/45) showed a decrement. Taking these 45 cases into account, the average increment of the latency of the negative peak during the gabazine condition was 6.1 ± 20.7 ms. Additionally, the individual latencies were more dispersed.

When considering all the cases together, the latency of the negative peaks was significantly longer than the latency of the positive peaks in both the control and gabazine conditions. Only for the negative peaks, the latency was significantly affected by gabazine (**Figure 6C**). When grouping the data by DS and firing pattern type (**Figure 6D**), we found that the latency of the negative peaks was significantly longer than the latency of the positive peaks for both the monophasic and the multiphasic groups, in both control and gabazine conditions. Qualitatively similar results have been obtained for the median latency (data not shown).

Gabazine increased the number of cases where the latency of the positive peak was shorter than the negative from 73% (41/56; in 36 cases there was no negative part) of the cases during the control condition, to 90% (57/63; in 29 cases there was no negative part) during the application of gabazine (**Figures 6E,F**).

The latency of the positive DS peaks did not differ among firing pattern groups (**Figures 6G,H**). The latency of the negative DS peaks was significantly larger for the S-S and the S-O groups, but not for the others.

PROBABILITY OF SIGNIFICANT DIFFERENCE SIGNAL

Since we found that most neurons presented both positive and negative portions on their DS, we calculated the probability of observing a positive or negative DS value for each bin of the PSTH (**Figure 7**). In the control condition, the maximum probability of evoking a positive DS was 74%, with a latency of 21.5 ms after the stimulus onset. On the other hand, the maximum probability of a negative DS was only 11% and happened later, with a latency of 30.5 ms. The application of gabazine caused an increment of these figures, with a maximum positive DS probability of 89%, 23.5 ms after the onset of the stimulus, and maximum negative DS probability of 22% with a latency of 38.5 ms. When considering a window of 10–115 ms after the stimulus onset (which encompasses approximately the evoked portion of the responses), during the control condition the occurrence of a positive DS was 4.09 times more likely than a negative one. On the other hand, during the gabazine condition this ratio was reduced to 2.96. This way, inhibition increases the contrast between the positive and the negative portions of the DS in neurons showing strong SSA. These probability functions remark that SSA in the IC is stronger at the beginning of the stimulus, as a consequence of the shorter latencies in response to deviants. Nevertheless, even highly adapting neurons (such as those in this sample) may still momentarily respond better to standards than to deviants afterwards.

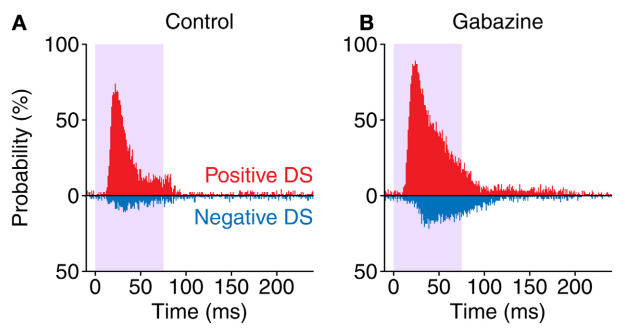

FIGURE 7 | Probability of occurrence of a positive (red) DS value or a negative one (blue) along time. Note how in the gabazine condition **(B)** the probabilities are higher and skewed toward longer latencies, compared to the control condition **(A)**.

DISCUSSION

In this study we report that even in a sample comprised of neurons showing very strong SSA (i.e., they respond more intensely to deviant stimuli overall), a subset of the neurons (one third of the cases in the control condition) contain portions that responded significantly better to the standard stimuli than to the deviants. Furthermore, the blockade of $GABA_A$ receptors increases the number of neurons showing portions that responded better to the standard stimuli, indicating that in the IC, inhibition refines the responses to SSA by sharpening or "cleaning" the "noise" produced by the portions that respond better to standards.

Due to the large variability in the timing of the negative portions of the DS (**Figure 6**), when considering the population as a whole these parts get averaged out (**Figures 2A,B**) and become unnoticed, both before and during application of gabazine. On the other hand, the smaller variability of the latencies of the positive portions contributes to the large peak observed in the averaged representations, like in **Figures 2A,B**. Other previous studies describing the average response in form of PSTH in the IC (Malmierca et al., 2009a; Zhao et al., 2011; Duque et al., 2012), auditory thalamus (Yu et al., 2009; Antunes et al., 2010; Bäuerle et al., 2011), and cortex (Ulanovsky et al., 2003; von der Behrens et al., 2009; Farley et al., 2010) have shown similar results at the population level, but they have not studied the influence of inhibition. It is only when analyzing the responses of individual neurons when these negative portions of the DS become noticeable. As a result, other types of measurements that depend of the global activity of a large number of neurons (like evoked potential recordings) are unlikely to reflect these particular details from the individual neurons. However, the negative DS at the single neuron level contributes to reduce the magnitude of the population signal at long latencies, narrowing the onset response, which can improve temporal accuracy.

The presence of negative portion in the DS was closely related to the type of firing pattern of the neuron in response to standard and deviant stimuli (**Figure 2D**). Taking together the control and gabazine conditions, the group with the largest proportion of multiphasic units was S-S (58%, 48/83), followed by S-O (44%, 10/23), O-O (29%, 16/55) and O-S (26%, 6/23). This indicates

that a sustained response to deviants facilitates the occurrence of negative DS parts. The larger number of multiphasic units found during the application of gabazine appears to be related to the lengthening of the neuronal responses caused by the reduction of the incoming inhibition, which increased the number of units classified as S-S. This type of firing pattern stands out from the others, as the neurons in this group are among the ones with the largest positive and negative DS duration, area, and peak firing rate, as well as the largest negative DS latency.

The latency of the negative DS part was generally longer than the latency of the positive DS part, both when measuring the latency of the peak DS (**Figure 6**) or the latency of the median spike (not shown). This is especially notable for the neurons that respond with a sustained firing rate to both standards and deviants (group S-S), since the longer duration of the responses allows for a better temporal separation of the positive and negative parts of the DS. However, even in the least favorable case, which the shortest responses to both standards and deviants (group O-O), the average latency of the negative parts of the DS is longer than the latency of the positive parts (**Figures 6G,H**), although the differences are not significant. The latencies of the positive parts (∼22 ms on average for the peak) fall within the range of onset responses in the cortical areas of the IC (e.g., Lumani and Zhang, 2010). The longer latencies of the negative DS parts, observed in the majority of neurons, reflect the differential responses to deviant and standard stimuli. A faster response to deviants is responsible for the early, positive DS peak, while a slower response to the standards produces the negative DS peak. These differences in the latency of the response to the stimuli with different probabilities have been reported previously in the IC (Malmierca et al., 2009a; Lumani and Zhang, 2010; Zhao et al., 2011; Duque et al., 2012; Pérez-González et al., 2012).

COMPARISON TO OTHER STUDIES

Several previous studies have reported the time course of neuronal responses related to SSA. Due to the lack of testing of the contribution of inhibition to SSA in previous studies, the following comparisons will refer only to our results in the control condition.

In an initial report of SSA in the IC, we showed (Malmierca et al., 2009a) that the PSTH-based population DS was mostly positive in different stimulation conditions, with peak latencies of 25–30 ms. We also found that the responses to deviant stimuli had shorter latencies than the responses to standard stimuli, which agrees with the present study. This finding was also reported in the dorsal cortex of the IC in rats (Lumani and Zhang, 2010). A study of the dynamics of adaptation in neurons through the IC showed that the general shape of the population DS was maintained at interstimulus intervals of up to 2 s, which is rather slow for this nucleus (Ayala and Malmierca, 2012). In the dorsal cortex of the IC, SSA was also reflected in the negative deflection of LFPs (Patel et al., 2012). The time course of the difference between the LFPs evoked by deviants and standards was comparable to that of the PSTH-based population DS, since in both cases the magnitude of the responses to deviants was consistently larger than that of the standards. In other words, neither the LFP nor the population DS did reflect the negative DS portions that we have shown here in single neurons, suggesting that they are averaged out in population measures.

In the medial geniculate body of the thalamus (Antunes et al., 2010), the population DS seems to be quite similar to that reported here for the IC. Some of the figures in Bäuerle et al. (2011) show the DS for some individual units, and several cases show consistent negative DS portions, although they do not discuss it. In any case, their sample of neurons from the ventral nucleus of the medial geniculate body showed a small degree of SSA, so that kind of response is as expected.

In the auditory cortex of an anesthetized preparation (Ulanovsky et al., 2003; Farley et al., 2010; Taaseh et al., 2011; Yaron et al., 2012), the first place where auditory SSA was described, the population DS seems to be more sustained. This contrasts with awaken animal preparations, were the neuronal responses are onset-like (von der Behrens et al., 2009). Due to this firing pattern, the calculated population DS in the cortex of an awaken preparation resulted to be significant at latencies of 12–28 ms, which is comparable to the latency of the positive peaks found in the IC (22.1 ± 8.4 ms).

EFFECT OF GABAZINE

Blocking $GABA_A$ receptors in the IC has been reported to increase the firing rates in response to stimuli, modify the response patterns and reduce the first spike latency in response to deviant stimuli (Pérez-González et al., 2012). By making the responses to standard relatively slower and more sustained than the responses to deviants, these effects may explain the stronger negative DS that is found during the gabazine condition, as well as the larger percentage of the overall response that is negative during the gabazine condition. Furthermore, this may be the reason of the increment in the number of multiphasic neurons during this condition.

As GABA is the main inhibitory neurotransmitter in the dorsal and lateral cortices of the IC, as indicated by the much larger numbers of GABAergic than glycinergic puncta (Merchán et al., 2005), the application of gabazine reflects a situation where inhibition is largely reduced and excitation is the most prominent driving force of these neurons. Based on these findings, we propose that excitation alone generates responses to deviant and standard stimuli that are quite different in shape and latency, resulting in DS that are more prone to variability during the response (e.g., changing from positive to negative). In addition to providing a mechanism of gain control that modulates the strength of SSA (Pérez-González et al., 2012), inhibition would reduce this variability of the responses, affecting mostly the negative parts of the DS, and thus sharpening the response to SSA.

In conclusion, the variability of the time course of the responses of neurons that show SSA, responsible for negative DS portions even in neurons that overall prefer deviant stimuli, is reduced by GABA and seems to be only evident on a single neuron level. Most studies on SSA tend to report aggregated data at the population level, which obscures this variability. Our study emphasizes the importance of reporting the details of the responses of single neurons, since paying attention only to the big picture may result in the omission of important functional features.

ACKNOWLEDGMENTS

Financial support was provided by the Spanish MINECO (BFU2009-07286) and (EUI2009-04083) in the frame of the ERA-NET NEURON to Manuel S. Malmierca, and by a postdoctoral fellowship from the Botín Foundation to David Pérez-González. The funders had no role in study design, data collection and analysis, decision to publish, or preparation of the manuscript.

REFERENCES

Anderson, L. A., Christianson, G. B., and Linden, J. F. (2009). Stimulus-specific adaptation occurs in the auditory thalamus. *J. Neurosci.* 29, 7359–7363.

Anderson, L. A., and Malmierca, M. S. (2012). The effect of auditory cortex deactivation on stimulus-specific adaptation in the inferior colliculus of the rat. *Eur. J. Neurosci.* doi: 10.1111/ejn.12018. [Epub ahead of print].

Antunes, F. M., and Malmierca, M. S. (2011). Effect of auditory cortex deactivation on stimulus-specific adaptation in the medial geniculate body. *J. Neurosci.* 31, 17306–17316.

Antunes, F. M., Nelken, I., Covey, E., and Malmierca, M. S. (2010). Stimulus-specific adaptation in the auditory thalamus of the anesthetized rat. *PLoS ONE* 5:e14071. doi: 10.1371/journal.pone.0014071

Ayala, Y. A., and Malmierca, M. S. (2012). Stimulus-specific adaptation and deviance detection in the inferior colliculus. *Front. Neural Circuits* 6:89. doi: 10.3389/fncir.2012.00089

Bäuerle, P., von der Behrens, W., Kössl, M., and Gaese, B. H. (2011). Stimulus-specific adaptation in the gerbil primary auditory thalamus is the result of a fast frequency-specific habituation and is regulated by the corticofugal system. *J. Neurosci.* 31, 9708–9722.

Caspary, D. M., Palombi, P. S., and Hughes, L. F. (2002). GABAergic inputs shape responses to amplitude modulated stimuli in the inferior colliculus. *Hear. Res.* 168, 163–173.

Casseday, J. H., Ehrlich, D., and Covey, E. (1994). Neural tuning for sound duration: role of inhibitory mechanisms in the inferior colliculus. *Science* 264, 847–850.

Casseday, J. H., Ehrlich, D., and Covey, E. (2000). Neural measurement of sound duration: control by excitatory-inhibitory interactions in the inferior colliculus. *J. Neurophysiol.* 84, 1475–1487.

Covey, E., Kauer, J. A., and Casseday, J. H. (1996). Whole-cell patch-clamp recording reveals subthreshold sound-evoked postsynaptic currents in the inferior colliculus of awake bats. *J. Neurosci.* 16, 3009–3018.

Duque, D., Pérez-González, D., Ayala, Y. A., Palmer, A. R., and Malmierca, M. S. (2012). Topographic distribution, frequency, and intensity dependence of stimulus-specific adaptation in the inferior colliculus of the rat. *J. Neurosci.* 32, 17762–17774.

Escera, C., Alho, K., Winkler, I., and Näätänen, R. (1998). Neural mechanisms of involuntary attention to acoustic novelty and change. *J. Cogn. Neurosci.* 10, 590–604.

Farley, B. J., Quirk, M. C., Doherty, J. J., and Christian, E. P. (2010). Stimulus-specific adaptation in auditory cortex is an NMDA-independent process distinct from the sensory novelty encoded by the mismatch negativity. *J. Neurosci.* 30, 16475–16484.

Fritz, J. B., Elhilali, M., David, S. V., and Shamma, S. A. (2007). Auditory attention–focusing the searchlight on sound. *Curr. Opin. Neurobiol.* 17, 437–455.

Gittelman, J. X., Wang, L., Colburn, H. S., and Pollak, G. D. (2012). Inhibition shapes response selectivity in the inferior colliculus by gain modulation. *Front. Neural Circuits* 6:67. doi: 10.3389/fncir.2012.00067

Grimm, S., Escera, C., Slabu, L., and Costa-Faidella, J. (2011). Electrophysiological evidence for the hierarchical organization of auditory change detection in the human brain. *Psychophysiology* 48, 377–384.

Gutfreund, Y. (2012). Stimulus-specific adaptation, habituation and change detection in the gaze control system. *Biol. Cybern.* 106, 657–668.

Ingham, N. J., and McAlpine, D. (2005). GABAergic inhibition controls neural gain in inferior colliculus neurons sensitive to interaural time differences. *J. Neurosci.* 25, 6187–6198.

Isaacson, J. S., and Scanziani, M. (2011). How inhibition shapes cortical activity. *Neuron* 72, 231–243.

Jääskeläinen, I. P., Ahveninen, J., Bonmassar, G., Dale, A. M., Ilmoniemi, R. J., Levänen, S., et al. (2004). Human posterior auditory cortex gates novel sounds to consciousness. *Proc. Natl. Acad. Sci. U.S.A.* 101, 6809–6814.

Koch, U., and Grothe, B. (1998). GABAergic and glycinergic inhibition sharpens tuning for frequency modulations in the inferior colliculus of the big brown bat. *J. Neurophysiol.* 80, 71–82.

Kurt, S., Crook, J. M., Ohl, F. W., Scheich, H., and Schulze, H. (2006). Differential effects of iontophoretic *in vivo* application of the $GABA_A$-antagonists bicuculline and gabazine in sensory cortex. *Hear. Res.* 212, 224–235.

LeBeau, F. E., Malmierca, M. S., and Rees, A. (2001). Iontophoresis *in vivo* demonstrates a key role for $GABA_A$ and glycinergic inhibition in shaping frequency response areas in the inferior colliculus of guinea pig. *J. Neurosci.* 21, 7303–7312.

LeBeau, F. E., Rees, A., and Malmierca, M. S. (1996). Contribution of GABA- and glycine-mediated inhibition to the monaural temporal response properties of neurons in the inferior colliculus. *J. Neurophysiol.* 75, 902–919.

Lumani, A., and Zhang, H. (2010). Responses of neurons in the rat's dorsal cortex of the inferior colliculus to monaural tone bursts. *Brain Res.* 1351, 115–129.

Malmierca, M. S. (2003). The structure and physiology of the rat auditory system: an overview. *Int. Rev. Neurobiol.* 56, 147–211.

Malmierca, M. S., Blackstad, T. W., and Osen, K. K. (2011). Computer-assisted 3-D reconstructions of Golgi-impregnated neurons in the cortical regions of the inferior colliculus of rat. *Hear. Res.* 274, 13–26.

Malmierca, M. S., Blackstad, T. W., Osen, K. K., Karagulle, T., and Molowny, R. L. (1993). The central nucleus of the inferior colliculus in rat: a Golgi and computer reconstruction study of neuronal and laminar structure. *J. Comp. Neurol.* 333, 1–27.

Malmierca, M. S., Cristaudo, S., Pérez-González, D., and Covey, E. (2009a). Stimulus-specific adaptation in the inferior colliculus of the anesthetized rat. *J. Neurosci.* 29, 5483–5493.

Malmierca, M. S., Hernandez, O., Antunes, F. M., and Rees, A., (2009b). Divergent and point-to-point connections in the commissural pathway between the inferior colliculi. *J. Comp. Neurol.* 514, 226–239.

Malmierca, M. S., Izquierdo, M. A., Cristaudo, S., Hernández, O., Pérez-González, D., Covey, E., et al. (2008). A discontinuous tonotopic organization in the inferior colliculus of the rat. *J. Neurosci.* 28, 4767–4776.

Malmierca, M. S., and Ryugo, D. K. (2011). "Descending connections of auditory cortex to the midbrain and brainstem," in *The Auditory Cortex,* eds J. A. Winer and C. E. Schreiner (New York, NY: Springer-Verlag), 189–208.

Malmierca, M. S., and Ryugo, D. K. (2012). "Sensory systems: Auditory," in *The Mouse Nervous System*, eds C. Watson, G. Paxinos and L. Puelles (San Diego, CA: Academic Press), 607–645.

Merchán, M., Aguilar, L. A., Lopez-Poveda, E. A., and Malmierca, M. S. (2005). The inferior colliculus of the rat: quantitative immunocytochemical study of GABA and glycine. *Neuroscience* 136, 907–925.

Näätänen, R. (1992). *Attention and Brain Function.* Hillsdale, NJ: Erlbaum.

Nelken, I., and Ulanovsky, N. (2007). Mismatch negativity and stimulus-specific adaptation in animal models. *J. Psychophysiol.* 21, 214–223.

Oliver, D. L., and Shneiderman, A. (1991). "The anatomy of the inferior colliculus. A cellular basis for integration of monaural and binaural information," in *Neurobiology of Hearing*, eds R. A. Altschuler, R. P. Bobbin, B. M. Clopton, and D. W. Hoffmann (New York, NY: Raven Press), 195–222.

Palombi, P. S., and Caspary, D. M. (1996). GABA inputs control discharge rate primarily within frequency receptive fields of inferior colliculus neurons. *J. Neurophysiol.* 75, 2211–2219.

Patel, C. R., Redhead, C., Cervi, A. L., and Zhang, H. (2012). Neural sensitivity to novel sounds in the rat's dorsal cortex of the inferior colliculus as revealed by evoked local field potentials. *Hear. Res.* 286, 41–54.

Pérez-González, D., Hernández, O., Covey, E., and Malmierca, M. S. (2012). $GABA_A$-mediated inhibition modulates stimulus-specific adaptation in the inferior colliculus. *PLoS ONE* 7:e34297. doi: 10.1371/journal.pone.0034297

Pérez-González, D., Malmierca, M. S., and Covey, E. (2005). Novelty detector neurons in the mammalian auditory midbrain. *Eur. J. Neurosci.* 22, 2879–2885.

Rees, A. (1990). A closed field sound system for auditory neurophysiology. *J. Physiol.* 430, 6.

Rees, A., Sarbaz, A., Malmierca, M. S., and LeBeau, F. E. (1997). Regularity of firing of neurons in the inferior colliculus. *J. Neurophysiol.* 77, 2945–2965.

Rose, D., and Blakemore, C. (1974). Effects of bicuculline on functions of inhibition in visual cortex. *Nature* 249, 375–377.

Sivaramakrishnan, S., Sterbing-D'Angelo, S. J., Filipovic, B., D'Angelo, W. R., Oliver, D. L., and Kuwada, S. (2004). GABA(A) synapses shape neuronal responses to sound intensity in the inferior colliculus. *J. Neurosci.* 24, 5031–5043.

Slabu, L., Escera, C., Grimm, S., and Costa-Faidella, J. (2010). Early change detection in humans as revealed by auditory brainstem and middle-latency evoked potentials. *Eur. J. Neurosci.* 32, 859–865.

Taaseh, N., Yaron, A., and Nelken, I. (2011). Stimulus-specific adaptation and deviance detection in the rat auditory cortex. *PLoS ONE* 6:e23369. doi: 10.1371/journal.pone.0023369

Ulanovsky, N., Las, L., Farkas, D., and Nelken, I. (2004). Multiple time scales of adaptation in auditory cortex neurons. *J. Neurosci.* 24, 10440–10453.

Ulanovsky, N., Las, L., and Nelken, I. (2003). Processing of low-probability sounds by cortical neurons. *Nat. Neurosci.* 6, 391–398.

von der Behrens, W., Bäuerle, P., Kössl, M., and Gaese, B. H. (2009). Correlating stimulus-specific adaptation of cortical neurons and local field potentials in the awake rat. *J. Neurosci.* 29, 13837–13849.

Winkler, I., Denham, S. L., and Nelken, I. (2009). Modeling the auditory scene: predictive regularity representations and perceptual objects. *Trends Cogn. Sci.* 13, 532–540.

Wu, S. H., Ma, C. L., and Kelly, J. B. (2004). Contribution of AMPA, NMDA, and GABA(A) receptors to temporal pattern of postsynaptic responses in the inferior colliculus of the rat. *J. Neurosci.* 24, 4625–4634.

Yaron, A., Hershenhoren, I., and Nelken, I. (2012). Sensitivity to complex statistical regularities in rat auditory cortex. *Neuron* 76, 603–615.

Yu, X. J., Xu, X. X., He, S., and He, J. (2009). Change detection by thalamic reticular neurons. *Nat. Neurosci.* 12, 1165–1170.

Zhang, H., and Kelly, J. B. (2003). Glutamatergic and GABAergic regulation of neural responses in inferior colliculus to amplitude-modulated sounds. *J. Neurophysiol.* 90, 477–490.

Zhao, L., Liu, Y., Shen, L., Feng, L., and Hong, B. (2011). Stimulus-specific adaptation and its dynamics in the inferior colliculus of rat. *Neuroscience* 181, 163–174.

Conflict of Interest Statement: The authors declare that the research was conducted in the absence of any commercial or financial relationships that could be construed as a potential conflict of interest.

Received: 04 July 2012; accepted: 03 December 2012; published online: 27 December 2012.

Citation: Pérez-González D and Malmierca MS (2012) Variability of the time course of stimulus-specific adaptation in the inferior colliculus. Front. Neural Circuits ***6****:107. doi: 10.3389/fncir.2012.00107*

frontiers in
NEURAL CIRCUITS

REVIEW ARTICLE
published: 17 January 2013
doi: 10.3389/fncir.2012.00089

Stimulus-specific adaptation and deviance detection in the inferior colliculus

Yaneri A. Ayala [1] ***and Manuel S. Malmierca*** [1,2] *******

[1] *Laboratory for the Neurobiology of Hearing, Auditory Neurophysiology Unit, Institute of Neuroscience of Castilla y León, University of Salamanca, Salamanca, Spain*
[2] *Department of Cell Biology and Pathology, Faculty of Medicine, University of Salamanca, Salamanca, Spain*

Edited by:
Eric D. Young, Johns Hopkins University, USA

Reviewed by:
Adrian Rees, Newcastle University, UK
Eric D. Young, Johns Hopkins University, USA

****Correspondence:***
Manuel S. Malmierca, Auditory Neurophysiology Unit (Lab. 1), Institute of Neuroscience of Castilla y León, University of Salamanca, Laboratory for the Neurobiology of Hearing, C/ Pintor Fernando Gallego, 1, 37007 Salamanca, Spain.
e-mail: msm@usal.es

Deviancy detection in the continuous flow of sensory information into the central nervous system is of vital importance for animals. The task requires neuronal mechanisms that allow for an efficient representation of the environment by removing statistically redundant signals. Recently, the neuronal principles of auditory deviance detection have been approached by studying the phenomenon of stimulus-specific adaptation (SSA). SSA is a reduction in the responsiveness of a neuron to a common or repetitive sound while the neuron remains highly sensitive to rare sounds (Ulanovsky et al., 2003). This phenomenon could enhance the saliency of unexpected, deviant stimuli against a background of repetitive signals. SSA shares many similarities with the evoked potential known as the "mismatch negativity," (MMN) and it has been linked to cognitive process such as auditory memory and scene analysis (Winkler et al., 2009) as well as to behavioral habituation (Netser et al., 2011). Neurons exhibiting SSA can be found at several levels of the auditory pathway, from the inferior colliculus (IC) up to the auditory cortex (AC). In this review, we offer an account of the state-of-the art of SSA studies in the IC with the aim of contributing to the growing interest in the single-neuron electrophysiology of auditory deviance detection. The dependence of neuronal SSA on various stimulus features, e.g., probability of the deviant stimulus and repetition rate, and the roles of the AC and inhibition in shaping SSA at the level of the IC are addressed.

Keywords: auditory, non-lemniscal pathway, frequency deviance, change detection, GABA-mediated inhibition, corticofugal modulation, mismatch negativity

THE AUDITORY SYSTEM IS HIGHLY SENSITIVE TO DEVIANT STIMULI

An animal's behavioral responses to unexpected changes in the continuous flow of sensory, including acoustic, information are critical for its survival. These responses depend on the ability to detect deviancy in an ongoing stimulus. In order for the nervous system to determine whether a sound is deviant, there must be an ongoing storage of information about the sounds that have already occurred, as well as a comparison of new sounds with previous ones.

Auditory deviance detection has been widely explored in human electroencephalogram (EEG) studies (for a review see Grimm and Escera, 2012). Those studies have shown that the waveform elicited by a deviant (low probability) stimulus differs from that elicited by a predictable (high probability) stimulus. Deviance detection has been associated with a particular evoked potential derived from the human EEG, namely the "mismatch negativity" (MMN; Näätänen et al., 1978; for recent review, see Näätänen et al., 2007). The MMN is measured as the difference between the evoked potential elicited to a sequentially repeated (high probability) stimulus, referred to as the "standard," and that elicited by a rarely occurring (low probability) sound referred to as the "deviant" that differs in any of its attributes such as location, pitch, intensity, or duration (**Figure 1A**). The MMN usually peaks at 150–200 ms from the onset of a change. It has a frontocentral scalp distribution, with positive voltages at electrode positions below the Sylvian fissure, indicating generator sources located bilaterally on the supratemporal plane of the auditory cortex (AC) (Huotilainen et al., 1998) with an additional prefrontal contribution (Shalgi and Deouell, 2007). The MMN is useful for the study of deviance detection in humans because (1) it provides a reliable signal of auditory change detection (e.g., Escera et al., 2000), and (2) it can be recorded passively, i.e., with no specific instruction given to the subjects, which makes it suitable for studying non-cooperative populations, such as patients with cerebral lesions, neurodegenerative diseases, or psychiatric disorders (e.g., Duncan et al., 2009; Luck et al., 2011), as well as newborns (Carral et al., 2005a) and fetuses (Draganova et al., 2005).

Because deviance detection requires information storage and comparison over time, it could be thought of as a form of cognitive processing, or "primitive intelligence" (Näätänen et al., 2001). For this reason, it has been commonly assumed that deviance detection must be accomplished at the level of the cortex. This assumption has persisted not only for theoretical reasons, but also because it is difficult to pinpoint the site at which EEG waveforms are generated, especially in the case of subcortical structures. However, the fact that the MMN persists during sleep or anesthesia suggests that it is "preattentive" in origin (Tiitinen et al., 1994)

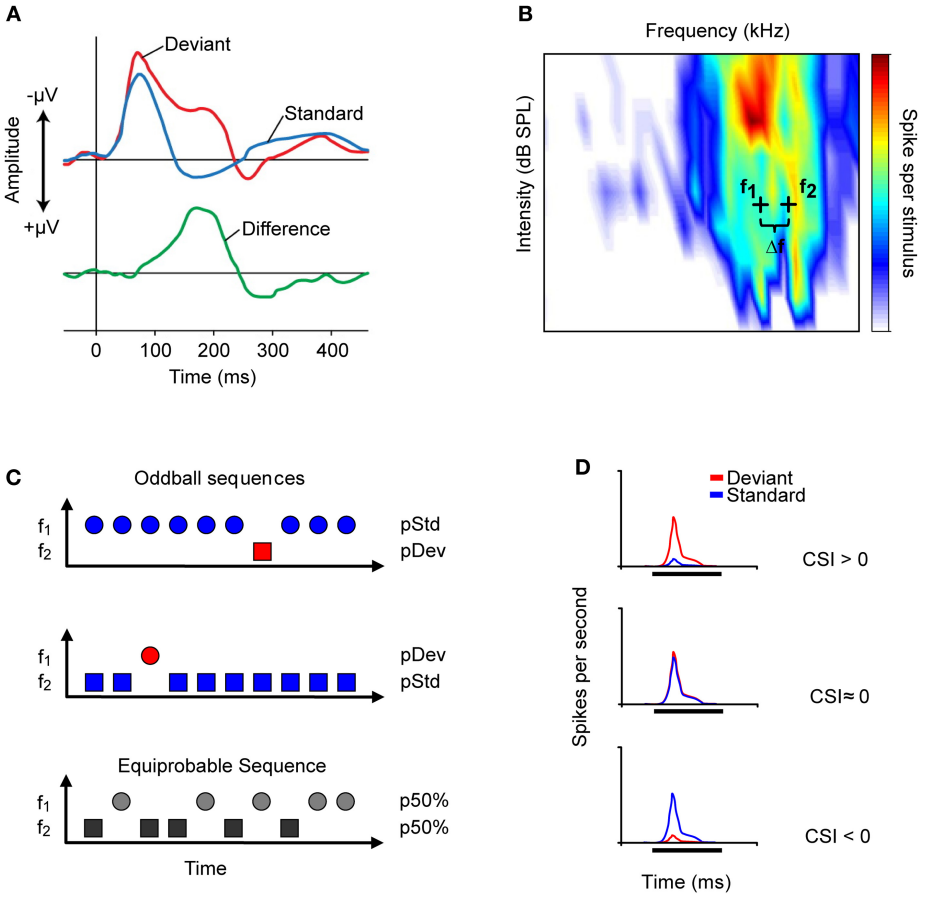

FIGURE 1 | Auditory change detection is studied by recording the evoked potentials of populations of neurons or the responses of single-units. (A) Schematic representation of the evoked potential known as the mismatch negativity (MMN) recorded through an electroencephalogram. The MMN is associated with the detection of deviant auditory events. It is measured as the difference (green line) between the potential elicited by a sequentially repeated stimulus (standard, blue line), and that elicited by a sound "deviating" in any of its attributes (deviant, red line). The peak of the MMN wave usually occurs at 150–200 ms from the onset of the deviant stimulus. **(B)** Frequency response area (FRA, combination of frequencies and intensities capable of evoking a response) of an IC neuron. Based on the FRA, the experimenter chooses a pair of frequencies (f_1 and f_2, black crosses) with a fixed physical separation (Δf) and at the same level to present in the oddball paradigm. Usually, in studies of the IC, a Δf of 0.058, 0.144, or 0.53 octaves is used. **(C)** Representation of the oddball paradigm used to study the detection of frequency deviance. In one oddball sequence (top), one frequency (f_1) is presented as the standard stimulus with a high probability of occurrence (blue symbol), while the second (f_2) is the rarely occurring deviant stimulus (red symbol), interspersed randomly among the standards. In a second oddball sequence (middle), the relative probabilities of the two stimuli are reversed, with f_2 as the standard (blue) and f_1 as the deviant (red). As a control (bottom), both frequencies are presented with the same probability of occurrence [equiprobable condition; $p(f_1) = p(f_2) = 50\%$]. **(D)** The common-SSA index (CSI) is a widely used metric to quantify the extent of SSA in the neuronal responses. The three PSTHs represents the response to deviant (red) and to standard (blue) tone of neurons exhibiting different values of CSI. The CSI compares the responses to deviant and to standard stimuli from the two oddball sequences by normalizing the responses in terms of spikes per stimulus (see text). The normalization corrects for the different number of presentations of the standard and deviant stimuli in each sequence. The possible values of the CSI range from +1 to −1, with positive values indicating that the response magnitude to the deviant is higher than that to the standard stimulus (upper PSTH); zero indicating that the two stimuli elicit equal responses (middle PSTH); and negative values indicating that the response to the standard stimulus is greater than that to the deviant stimulus (bottom PSTH).

and therefore could originate subcortically. This idea was largely untested and controversial until recently, as deviant occurrence is also reflected in the middle latency response (MLR) range of the evoked-activity, indicating that auditory change detection already occurs in early stages of human auditory processing (Slabu et al., 2010, 2012; Grimm et al., 2011).The MLR is a sequence of waveforms in the range of 12–50 ms from sound onset that precedes the well-studied MMN and it is generated by activation of subcortical areas as well as primary and secondary cortical areas (Grimm and Escera, 2012). Moreover, Slabu et al. (2012) showed that the human auditory brainstem is able to encode regularities in the recent auditory past that could be used for comparison to deviant events, and confirmed multiple anatomical and temporal scales of human deviance detection.

Finally, it is worth mentioning that MMN-like auditory-evoked potentials have also been recorded in laboratory animals in the AC (Javitt et al., 1994; Ruusuvirta et al., 1998; Eriksson and Villa, 2005; Astikainen et al., 2006, 2011; Tikhonravov et al., 2008; Nakamura et al., 2011) and subcortical structures: thalamus of the guinea pig (Kraus et al., 1994; King et al., 1995) and

inferior colliculus (IC) of the rat (Patel et al., 2012). Overall, these studies suggest that deviance detection may be a basic property of the functional organization of the auditory system occurring on multiples levels along the auditory pathway (Grimm et al., 2011; Grimm and Escera, 2012). Nevertheless, identification of the neuronal microcircuits and functional mechanisms underlying deviance detection remains a challenge in auditory neuroscience.

STIMULUS-SPECIFIC ADAPTATION: A NEURAL MECHANISM FOR DETECTION OF DEVIANT STIMULI

A decade ago, Nelken and colleagues (Ulanovsky et al., 2003) published a pioneering study that described a phenomenon similar to MMN and occurring at the cellular level in the mammalian AC. The single-neuron phenomenon was referred to as stimulus-specific adaptation (SSA) [a term originally coined by Movshon and Lennie (1979)] and it is proposed to be a neuronal mechanism that could be contributing to auditory deviance detection (Ulanovsky et al., 2003; Jääskeläinen et al., 2007). SSA is the reduction in the responsiveness of a neuron to a common or repetitive sound while the response decrement does not generalize to others sounds that are rarely presented. In this sense, SSA is a phenomenon of neuronal adaptation to the history of the stimulus rather than to the activity of the neuron (Nelken and Ulanovsky, 2007; Netser et al., 2011; Gutfreund, 2012). Although, MMN and SSA share several features such as their dependence on stimulation rate, they also greatly differ in their latencies and level of the neural structures involved (Nelken and Ulanovsky, 2007; Grimm and Escera, 2012). In addition, MMN is elicited by deviant stimuli immersed in complex forms of regularities (Carral et al., 2005b; Cornella et al., 2012; Recasens et al., 2012) that remained to be tested in single-unit recordings.

SSA is a widespread phenomenon in the brain exhibited by neurons of the visual (Woods and Frost, 1977; Sobotka and Ringo, 1994; Müller et al., 1999), somatosensory (Katz et al., 2006) and auditory (Ulanovsky et al., 2003; Malmierca et al., 2009a; Reches and Gutfreund, 2008; Anderson et al., 2009; Antunes et al., 2010) systems.

Auditory neurons that exhibit SSA for frequency deviance have been described in the IC (Pérez-González et al., 2005; Reches and Gutfreund, 2008; Malmierca et al., 2009a; Lumani and Zhang, 2010; Netser et al., 2011; Zhao et al., 2011), medial geniculate body (MGB) (Anderson et al., 2009; Yu et al., 2009; Antunes et al., 2010; Baüerle et al., 2011), and primary AC (Ulanovsky et al., 2003, 2004; Von Der Behrens et al., 2009; Taaseh et al., 2011). In the brainstem, SSA has been recently explored in the ventral and dorsal cochlear nucleus of the rat and the results suggest that all cochlear nucleus neurons tested lack SSA (Ayala et al., 2012). Thus, the IC is the earliest center where SSA has been described (Malmierca et al., 2009a), although it remains to be tested whether or not other brainstem nuclei located in between the cochlear nucleus and IC show some degree of SSA. In this review, we will focus on a description of SSA occurring at the IC, which is the major auditory station in the midbrain for the integration of ascending, descending, intrinsic, and commissural inputs (Malmierca, 2003; Malmierca et al., 2003, 2005a,b, 2009b; Cant and Benson, 2006; Loftus et al., 2010; Malmierca and Hackett, 2010; Malmierca and Ryugo, 2011).

STIMULUS-SPECIFIC ADAPTATION IN SINGLE-NEURON RESPONSE

Most of the studies of SSA in the IC have been carried out in the anesthetized rat (Pérez-González et al., 2005, 2012; Malmierca et al., 2009a; Lumani and Zhang, 2010; Zhao et al., 2011; Patel et al., 2012). Initially, Pérez-González et al. (2005) found that cortical IC neurons of the rat show adaptation to the repetitive stimulation of an acoustic parameter, but they resume firing if the sound parameter was changed. Responses similar to those reported by Pérez-González and colleagues were originally described in the midbrain of frogs (Bibikov, 1977; Bibikov and Soroka, 1979).

More recent studies have explored sensitivity to frequency deviance using an "oddball paradigm," similar to that used to record MMN responses in human studies (Näätänen, 1992). In this paradigm two tones are selected within the frequency response area of the neuron (**Figure 1B**) and randomly presented with different probabilities of occurrence. The high probability tone is usually referred to as the standard stimulus; interspersed among the standard stimuli are the low probability or deviant stimuli. In a second sequence of stimulation, the relative probabilities are reversed so that both frequencies are presented as standard and deviant. Usually, the neuronal responses are also recorded under an equiprobable condition, in which both frequencies have the same probability of occurrence (**Figure 1C**).

The amount of SSA is quantified by an index that reflects the extent to which a neuron responds to tones when they are presented as the deviant stimulus compared to when they are presented as the standard stimulus. This index is referred as the common SSA index (CSI) defined as $\mathrm{CSI} = [d(f_1) + d(f_2) - s(f_1) - s(f_2)]/[d(f_1) + d(f_2) + s(f_1) + s(f_2)]$, where $d(f)$ and $s(f)$ are responses measured as spike rate to frequencies f_1 or f_2 used as either the deviant (d) or standard (s) stimulus. The CSI values range from -1 to $+1$, being positive when the response to the deviant stimulus is stronger, and negative when the standard stimulus evokes more spikes (**Figure 1D**).

SSA to frequency deviance has been found to be stronger in the non-lemninscal regions, i.e., in the dorsal (DCIC), rostral (RCIC), and lateral cortices (LCIC), than in the central nucleus (CNIC) (Pérez-González et al., 2005; Malmierca et al., 2009a, 2011; Lumani and Zhang, 2010; Duque et al., 2012) (**Figure 2**). Studies of specific adaptation have also been reported in the awake barn owl (Reches and Gutfreund, 2008; Netser et al., 2011) and bat (Thomas et al., 2012).

Sensitivity to intensity and duration deviance has been observed in the AC (Ulanovsky et al., 2003; Farley et al., 2010) but it is not as robust as frequency deviance. These other stimulus features, i.e., intensity and duration, have not been tested under the oddball paradigm in the IC, but it seems likely that subcortical neurons that show SSA to frequency may also be able to detect deviance in other stimulus dimensions, as occurs with neurons of the midbrain of avians. Neurons in the optic tectum (analogous to the superior colliculus of mammals) of the barn owl exhibit SSA to sound frequencies, amplitude, and interaural time and level difference (Reches and Gutfreund, 2008).

The great majority of neurons with high levels of SSA display transient onset responses and have low or absent spontaneous

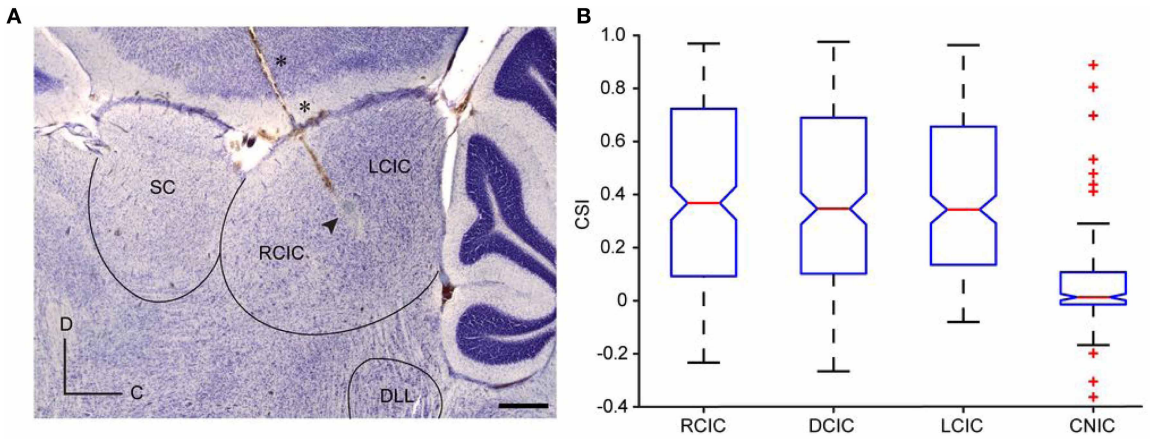

FIGURE 2 | Anatomical location of SSA in the IC. (A) Photomicrography showing a sagittal section of the IC with a typical electrode track (asterisks) and the electrolytic lesion generated (arrowhead). Scale bar = 500 μm. C, caudal; D, dorsal. **(B)** Box plot with the median value (red line) of CSI sorted by anatomic regions. The blue box delimits the 25th and 75th percentile and dashed lines show the most extreme data points not considered outliers. Red crosses indicate outliers. Cortical regions (RCIC, DCIC, and LCIC) are significantly different from the CNIC (Kruskal–Wallis test, $p < 0.001$). Reproduced from Duque et al. (2012).

activity in anesthetized rats (Pérez-González et al., 2005, 2012; Malmierca et al., 2009a; Lumani and Zhang, 2010; Duque et al., 2012). This finding is consistent with a higher incidence of SSA in the non-lemniscal IC since a large proportion of neurons in the dorsal regions of the IC have onset responses (Reetz and Ehret, 1999; LeBeau et al., 1996). Moreover, for adapting neurons with other types of responses, i.e., on-sustained and on-off (Rees et al., 1997), the largest difference between responses to deviant and standard stimuli is signaled by the onset component (Malmierca et al., 2009a; Duque et al., 2012).

Another feature of neurons that exhibit SSA is their broad frequency response area (Malmierca et al., 2009a; Duque et al., 2012). In the IC of the rat, neurons in the DCIC and RCIC regions possess widespread dendritic arbors (Malmierca et al., 1993, 1995, 2011), and broader frequency tuning than the CNIC (Syka et al., 2000; Duque et al., 2012). A possible functional consequence of neurons with large dendritic arbors is the integration of inputs over a broad frequency range. Among cortical IC neurons the broader the frequency response area the higher the level of SSA observed (Duque et al., 2012). In the bat IC, SSA is present in a subset of non-specialized neurons which are broadly tuned to frequency and non-selective for spectrotemporal pattern (Thomas et al., 2012) suggesting a complex input processing. Furthermore, SSA is not a property homogeneously distributed throughout the neuron's frequency response area. Duque et al. (2012) compared the degree of SSA at multiple combinations of frequencies and intensities in single-unit recordings in the IC of the anesthetized rat. They found that adapting neurons exhibit stronger SSA at the high frequency edge of the response area and low sound intensities (**Figure 3**). This study concluded that SSA is not constant within the neuronal receptive field, and therefore is not a characteristic property of the neuron, instead the neuron's inputs contribute to its generation.

In addition to encoding deviance by spike count, IC neurons can also encode deviance information through their spike timing. In neurons that exhibit SSA, the first spike latency (FSL) in the response evoked by the deviant tone is shorter than that evoked by the standard tone (Malmierca et al., 2009a; Zhao et al., 2011; Duque et al., 2012). This phenomenon is known as "latency adaptation" and seems to be a unique feature of subcortical neurons (Malmierca et al., 2009a; Antunes et al., 2010; Duque et al., 2012). The neurons in the DCIC that show SSA have much longer FSLs than neurons in the CNIC (Lumani and Zhang, 2010). Thus, temporal coding appears to play a key role in the signaling of deviance.

STIMULUS-SPECIFIC ADAPTATION AND ITS RELATIONSHIP TO STIMULATION PARAMETERS

A hallmark of SSA in the different auditory areas is its sensitivity to a variety of stimulus parameters such as the deviant probability, the frequency separation, and the time interval (stimulation rate) between stimuli (Ulanovsky et al., 2003; Malmierca et al., 2009a; Yu et al., 2009; Von Der Behrens et al., 2009; Antunes et al., 2010; Zhao et al., 2011). This dependency is also present for the processing of other stimulus features such as interaural time- and level-differences and amplitude deviants (Ulanovsky et al., 2003; Reches and Gutfreund, 2008).

The manipulation of the probability of occurrence of the deviant and, consequently, of the standard stimulus has a strong effect on the extent of SSA observed (Malmierca et al., 2009a; Patel et al., 2012). Deviant probabilities of 30 and 10% have been explored; SSA increases as the deviant probability decreases. Thus, neurons are sensitive to stimulus probability with greater sensitivity to tones that are less likely to occur (Malmierca et al., 2009a).

The sensitivity to deviance increases proportionally with the extent of physical separation between tones. The frequency contrast is expressed as $\Delta f = (f_2 - f_1)/(f_2 \times f_1)^{1/2}$; where f_2 and f_1 correspond to the frequencies tested (Ulanovsky et al., 2003) (**Figure 1B**). Most studies of SSA have employed pure tones

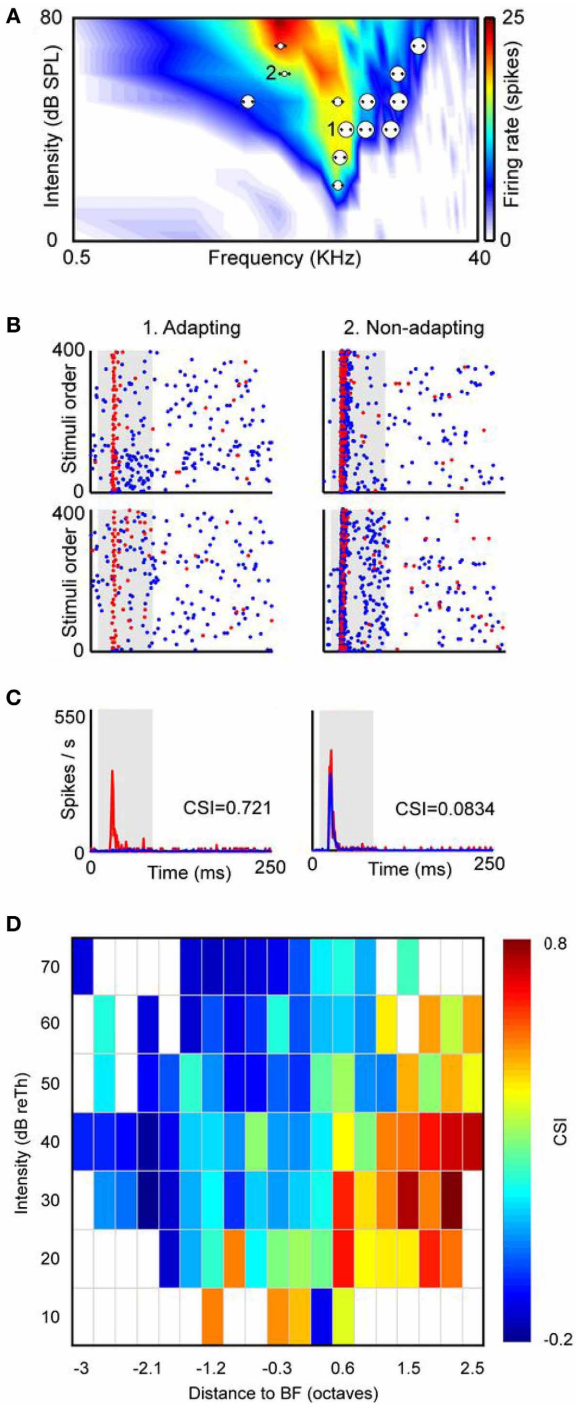

FIGURE 3 | SSA is not homogeneously distributed within the frequency response area of IC neurons. (A) Example of a neuron with a broad V-shaped response area and the distribution of the several pairs of frequencies presented under the oddball paradigm (dots). Each pair of dots is associated to a circle the size of which is proportional to the level of CSI evoked. An example of an adapting pair of frequencies (i.e., frequencies that elicited SSA) is marked as 1 and another example of a non-specifically adapting pair of frequencies is marked as 2. **(B)** Dot raster plots obtained with the adapting pair (left panels) and with the non-specifically adapting (right panels) pair of frequencies. The blue dots represent spikes evoked by *(Continued)*

FIGURE 3 | Continued
the standard stimulus (90% probability), while the red dots represent those evoked by the deviant stimulus (10% probability). Stimulus presentations are accumulated in the temporal domain along the vertical axis. In the adapting examples red dots are more visible because of the specific decrease of the response to the standard stimulus. The upper panels are the ones obtained when f_1 was the standard tone and f_2 was the deviant, and the bottom panels represent the response when the relative probabilities were inversed, that is, f_1 was the deviant and f_2 the standard. **(C)** Averaged PSTH for both frequencies when deviant (red) or standard (blue). CSI values obtained in each pair of frequencies are showed as insets in the PSTH. The shaded backgrounds in the dot raster and PSTH plots indicate the duration of the stimulus. **(D)** Distribution of the CSI values sorted relatively to the best frequency (BF) and the threshold (Th) of the response area of a sample of IC neurons (almost 80% are from the cortical region, $n = 124$). Higher CSI values are confined to the high-frequency edge and at low sound intensities. Reproduced from Duque et al. (2012).

centered on the best (Malmierca et al., 2009a; Pérez-González et al., 2012) or characteristic frequency (Zhao et al., 2011) of the neurons. The differential adaptation of the responses to deviant and standard stimuli is more prominent when Δf increases from 0.04 to 0.1 to 0.37 (0.058, 0.144, and 0.531 octaves, respectively) (Malmierca et al., 2009a). Neurons with strong SSA in the IC, as in the MGB and primary AC, show hyperacuity, that is, a strong and highly sensitive adaptation for frequency ratios as small as 4% ($\Delta f = 0.04$). This frequency ratio is smaller than the width of their frequency response areas (Ulanovsky et al., 2004; Moshitch et al., 2006; Malmierca et al., 2009a).

The highest levels of SSA are elicited by IC neurons at an ISI of 250 ms with a deviant probability of 10% compared to shorter (125 ms) or longer ISIs (500 ms) (Malmierca et al., 2009a). Few studies have explored SSA at very long ISIs. It has been reported that IC neurons are still capable of detecting frequency deviants at ISIs up to 1 s (repetition rate of 1 Hz) (Pérez-González et al., 2005; Reches and Gutfreund, 2008; Zhao et al., 2011). Indeed, we have recorded neurons that exhibit SSA at even slower repetition rates (ISI = 2000 ms) (Malmierca et al., 2010). **Figure 4** illustrates an example of the response of an IC neuron that exhibits SSA in the anesthetized rat. This neuron was very broadly tuned with a complex non-monotonic rate-level function and a transient onset firing pattern (**Figures 4A–C**). For this neuron, a pair of frequencies (black crosses; f_1 and f_2) with a physical separation of 0.216 octaves ($\Delta f = 0.15$) was chosen for presentation in the oddball paradigm with an ISI of either 2000 or 1000 ms. **Figures 4D,E** depict the responses to the deviant and standard stimuli as dot rasters and the corresponding peri-stimulus time histogram (PSTH) obtained with 0.5 and 1 Hz repetition frequencies, respectively. Under these conditions, the neuron showed SSA (CSI: 0.3–0.4), resulting in higher-evoked spiking to the deviant frequency (red color). **Figure 5A** shows the average PSTHs of a subset of neurons recorded with ISIs of 2000, 1000, and 500 ms. It is evident that there is an increasing difference between responses to deviant and standard tones as the frequency separation is increased (insets). Under these extreme stimulation rates, the FSLs evoked by the deviant tone were earlier than those evoked by the same tone when it was used as the standard, suggesting that the cellular mechanisms that discriminate between

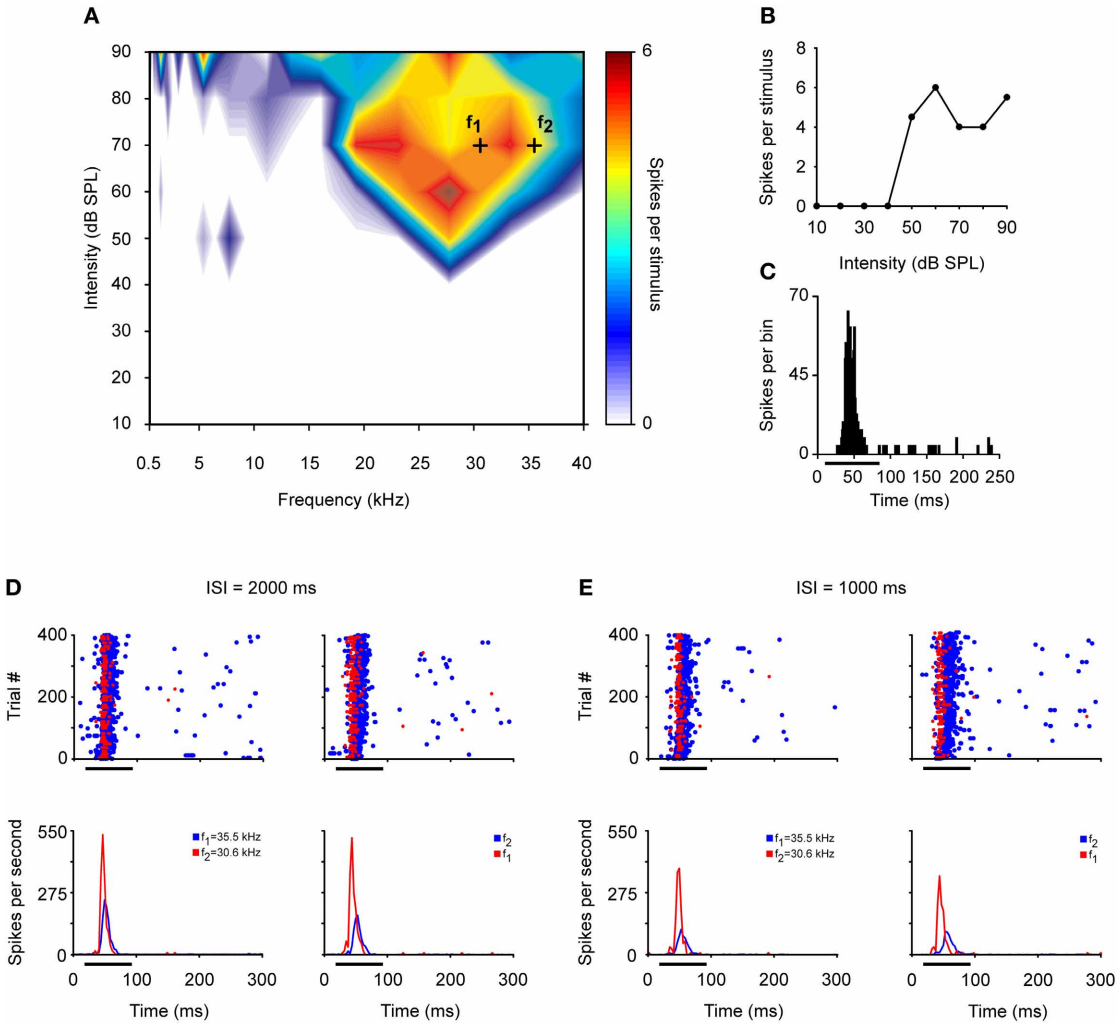

FIGURE 4 | Example of an IC neuron that exhibits SSA at low repetition frequencies. (A) Broad frequency response area displayed in color code according to the strength of the response. Black crosses represent a frequency pair—f_1 (30.6 kHz) and f_2 (35.5 kHz)—with a physical separation of 0.216 octaves ($\Delta f = 0.15$) at 70 dB SPL. **(B)** The neuron exhibits a non-monotonic rate-level function at its best frequency (27.1 kHz). **(C)** PSTH of the accumulated responses to all the frequencies (0.5–40 kHz) and intensities (10–90 dB SPL) presented (1 ms bins). **(D)** Top panels. Dot rasters of the response to oddball sequences of 400 stimulus presentations with a repetition rate of 0.5 Hz (ISI = 2000 ms). The frequencies used as the deviant stimulus (probability of 10%, red dots) and the standard or repetitive stimulus (probability of 90%, blue dots) are reversed in the left and right panels. The bottom panels show the corresponding normalized PSTHs to deviant (red line) and standard (blue line) stimuli. **(E)** Response to the oddball sequences presented at a higher repetition rate of 1 Hz (ISI = 1000 ms). Format same as for panel **(D)**.

deviant and standard responses are functional at the temporal scale of seconds (**Figures 5B,C**). As highlighted by Nelken and Ulanovsky (2007), the neuronal mechanisms for deviance detection become more important at more extreme stimulation values, e.g., slow stimulation rates and very similar stimulus frequencies.

Long interstimulus intervals affect the long-term dynamics of SSA, prolonging the time course of adaptation from several seconds at ISI of 125 ms, to tens of seconds when ISI is increased to 1000 ms. The frequency resolution of neurons is also modified by the repetition rate (Malmierca et al., 2009a; Antunes et al., 2010; Zhao et al., 2011). Frequencies separated by $\Delta f = 0.04$ do not elicit SSA in the IC or in the MGB of the rat (Antunes et al., 2010) when tested with the longest ISI of 2000 ms. Together these data indicate that the timing between stimuli affect both the extent and frequency resolution of SSA.

SSA at the time scale of 2000 ms has been found in primary AC, but cortical neurons do not adapt at ISIs longer than 2000 ms (Ulanovsky et al., 2003). SSA also occurs at an ISI of 2000 ms in the MGB, a mandatory processing station between the IC and the AC (Antunes et al., 2010). The presence of SSA in subcortical structures such as the IC and MGB on a time scale of the magnitude of seconds, similar to the time scale of cognition (Ulanovsky et al., 2003, 2004; Nelken and Ulanovsky, 2007), suggests that deviance detection at these early neuronal stages could be contributing to the perceptual organization of the

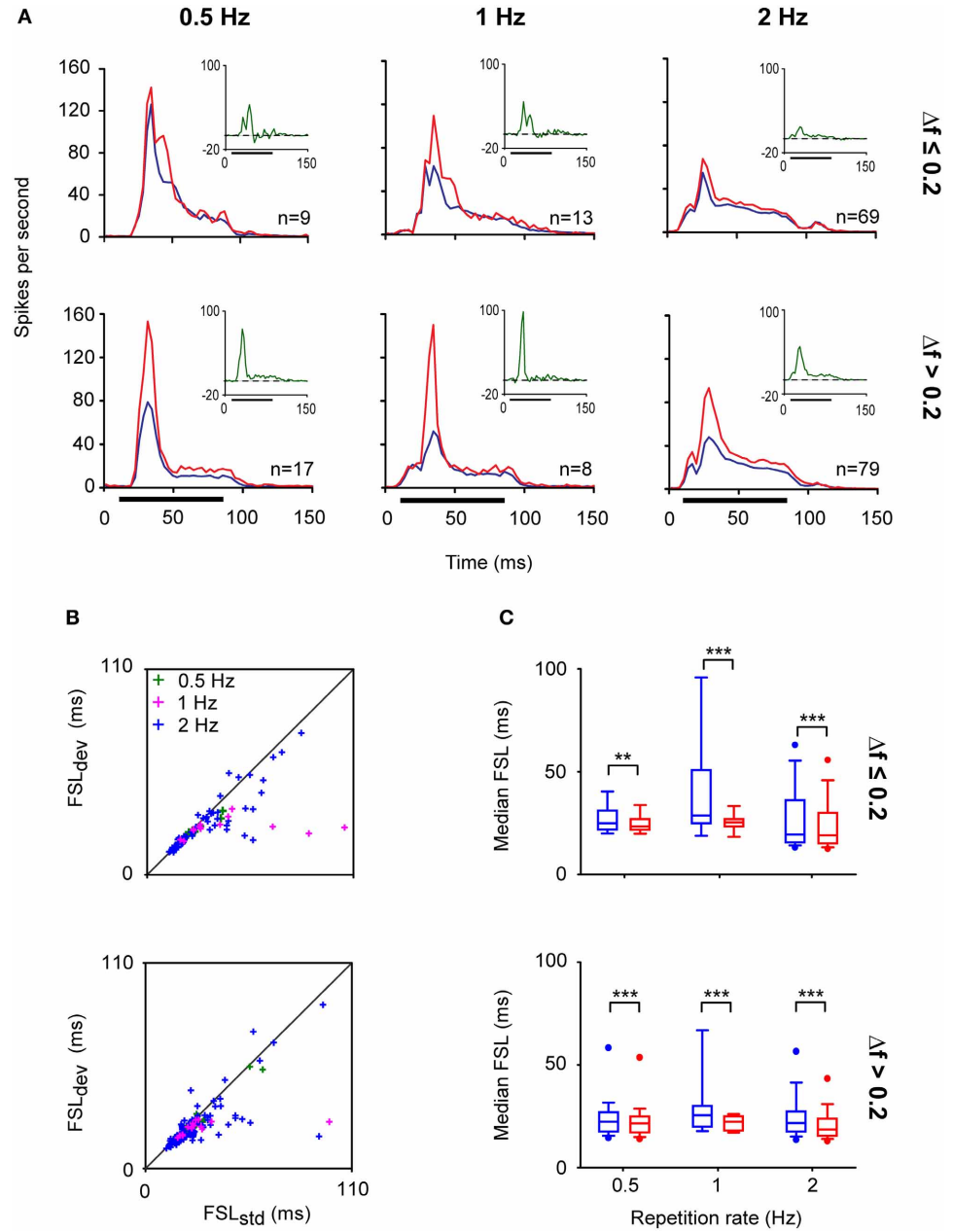

FIGURE 5 | IC neurons exhibit SSA even at very low repetition rates. **(A)** Population PSTHs of the IC neuronal responses to a deviant (red line) and to a standard (blue line) stimulus presented at different repetition rates; 0.5 (ISI = 2000 ms), 1 (ISI = 1000 ms), and 2 Hz (ISI = 500 ms). The physical separations between frequencies were grouped into $\Delta f \leq 0.2$ (≤ 0.288 octaves) (top panels) and $\Delta f > 0.2$ (bottom panels). The firing rates of individual neurons were averaged and normalized to account for the different number of stimulus presentations due to the different probabilities of the tones (deviant; 10%, standard; 90%). The insets shown in the right upper quadrants of each graph correspond to the averaged difference between the responses to the deviant and standard stimuli (green lines). The horizontal black bars indicate the duration of the stimulus. **(B)** Scatter plots of the first spike latency (FSL) of the neuronal responses evoked by f_1 and f_2 when they were the deviant (FSL_{dev}) or the standard (FSL_{std}) stimulus according to their frequency separation ($\Delta f \leq 0.2$ and $\Delta f > 0.2$) and across different repetition rates (0.5, 1, and 2 Hz). **(C)** Box plots of the population FSL indicating that even at very low repetition rates the FSLs evoked by the deviant tone (red boxes) are shorter than those evoked by the standard stimulus (blue boxes). (Signed-Rank Test; $^{**}p < 0.01$, $^{***}p < 0.001$).

components of complex auditory stimuli (Winkler et al., 2009) and to the change detection recorded in local field potentials (Slabu et al., 2010; Grimm et al., 2011). This temporal scale is consistent with the duration of sensory (echoic) memory in monkeys and humans, which is estimated to be in the order of a few seconds (Javitt et al., 1994; Näätänen and Escera, 2000).

The same systematic dependence on deviant probability, frequency contrast, and repetition rate seen in single neurons is

also present in the activity of ensembles of neurons in the IC (**Figure 6**). In a recent study the evoked local field potentials of DCIC neurons of the rat were recorded while stimulating with tone bursts under an oddball paradigm (Patel et al., 2012). The auditory response is a waveform with a relatively small positive deflection (D_P) followed by a large negative reflection (D_N) (**Figure 6A**). The degree of SSA is quantified by comparing the amplitude of the waves evoked by the deviant and standard stimuli using an amplitude-based, frequency-specific, SSA index for D_P and D_N ($SSAI_{Am}$). As expected, the amplitude of the local field potential is larger to a tone burst presented as deviant than as standard, and the difference is greater when the deviant stimulus is less likely to occur (deviant probability of 10% rather than 30%) (**Figures 6B,C**). The difference between responses to deviant and standard tones occurs after the initial rising phase of the dominant deflection (D_N), and no difference is elicited at the beginning of the response in D_P. Overall, the results by Patel et al. (2012) suggest that frequency deviance coding is detectable in ensembles or neuronal microcircuits of subcortical neurons as an evoked response with a larger amplitude and longer peak latency. There are some differences, however, compared to the SSA observed in single-units. The frequency separation required to elicit SSA is greater ($\Delta f = 0.37$ rather than $\Delta f = 0.1$); the strongest SSA

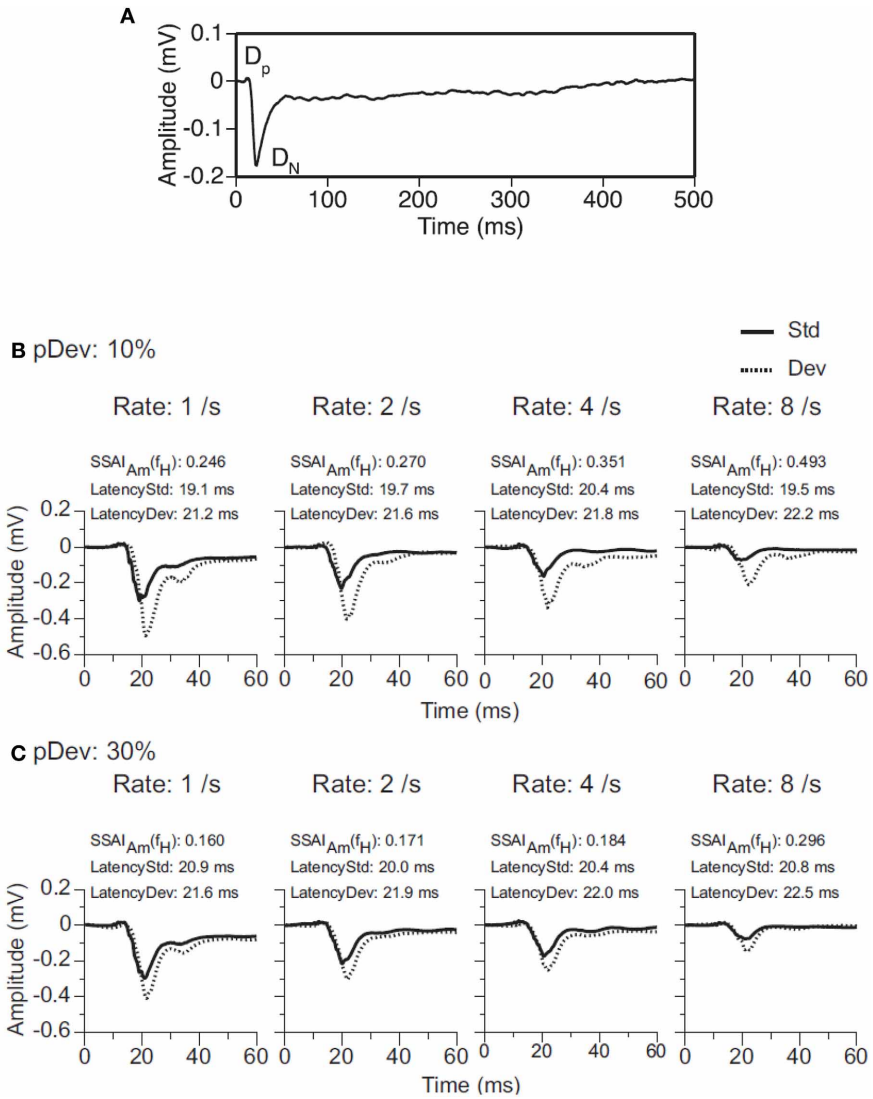

FIGURE 6 | Evoked local field potentials (LFP) recorded in the DCIC. (A) An average LFP is a waveform with a relatively small positive deflection (D_P) followed by a large negative deflection (D_N). Together, the two deflections are about 40 ms in total duration. (**B,C**) Evoked LFPs in response to a tone burst presented as standard stimulus (Std, solid line) or deviant stimulus (Dev, dotted line) in a pair of oddball sequences with probabilities of occurrence of the deviant of 10% (panel **B**) or 30% (panel **C**). Data were obtained for pairs of tones ($f_1 = 2.25$ kHz and $f_2 = 3.24$ kHz.) separated by a $\Delta f = 0.37$ and presented at 1, 2, 4 and 8 Hz. The BF of the recording site was 2.7 kHz. An amplitude-based, frequency-specific, stimulus-specific adaptation index [$SSAI_{Am}(f_X)$], along with the peak latencies of the responses evoked by the sound as standard and deviant stimuli, is shown at the top of each graph. Reproduced from Patel et al. (2012).

is elicited with a higher repetition rate (8 Hz); and the peak latency of the response to standard tone bursts is shorter than that to the deviant tone burst (contrary to the shorter latencies for deviants in single-unit recordings). As the authors suggested, these differences may be attributed to the fact that an evoked local field potential reflects a weighted average of voltage changes generated by multiple excitatory and inhibitory events in the vicinity of the recording electrode so that individual differences among neurons are largely averaged out. The short latency of responses in subcortical nuclei suggests that these responses could contribute to the earliest components of the evoked potential associated with the occurrence of a deviant acoustic event (Pa waveform in the MLR; peak at about 30 ms) (Grimm and Escera, 2012).

CORTICOFUGAL MODULATION

It was originally proposed that auditory SSA has a cortical origin and is propagated to subcortical nuclei through direct corticofugal projections (Ulanovsky et al., 2003; Nelken and Ulanovsky, 2007). Indeed, in the IC and MGB, the strongest SSA has been described in the extralemniscal regions (cortical regions of the IC: Malone et al., 2002; Pérez-González et al., 2005; Malmierca et al., 2009a; Lumani and Zhang, 2010; medial division of the MGB: Antunes et al., 2010), which operate under strong cortical control (Loftus et al., 2008; He and Yu, 2010; Lee and Sherman, 2011; Malmierca and Ryugo, 2011).

In a recent study, Anderson and Malmierca (2013) addressed whether SSA in the IC is dependent upon the AC for its generation. The authors reversibly deactivated the AC by cooling through a cryoloop device (Lomber et al., 1999; Lomber and Malhotra, 2008) and recorded the changes in SSA sensitivity exhibited by IC neurons. This technique has been successfully used to study the influence of the corticofugal system in the auditory system, including a study of sensitivity in IC neurons to cues for spatial position (Nakamoto et al., 2008) and sensitivity to deviance in the MGB (Antunes and Malmierca, 2011).

The neuronal responses to the oddball paradigm (with a deviant probability of 10% and a frequency separation between deviant and standard stimuli of 0.531 octaves) were recorded before, during and after the cooling of the AC. At the population level, the main finding was that deactivation of the ipsilateral AC did not eliminate SSA exhibited by IC neurons. A decrease in firing rate to both the deviant and standard stimuli was observed during the cooling condition, but the response was still higher to the deviant stimulus (**Figure 7A**). Thus, the deviant salience in the IC was preserved even after the deactivation of cortical inputs. Interestingly, at the single-neuron level Anderson and Malmierca identified IC neurons that showed SSA and were insensitive to the cooling of the AC (**Figure 7B**). Those neurons exhibited different levels of SSA covering the full CSI spectrum, from zero to one. On the other hand, the adaptive properties of about half of the IC neurons with SSA (52%) were differentially affected throughout the period of cortical cooling, increasing (**Figure 7C**) or decreasing (**Figure 7D**) their SSA sensitivity. Examples of single neurons are shown in **Figures 8** and **9**. During the cooling period, the neuron displayed in **Figure 8** increased its response area (**Figure 8A**), and its spontaneous and evoked firing rate. The increase was greater in response to the standard presentations (by a factor of seven) (**Figures 8B–D**, blue) than to the deviant ones (by a factor of three) (**Figures 8B–D**, red), resulting in a drop of its CSI (**Figure 8D**). On the other hand, the neuronal response illustrated in **Figure 9** exhibited a disproportionately decrease in the firing rate with an almost extinguished response to the standard stimulus, thus, increasing its CSI. The

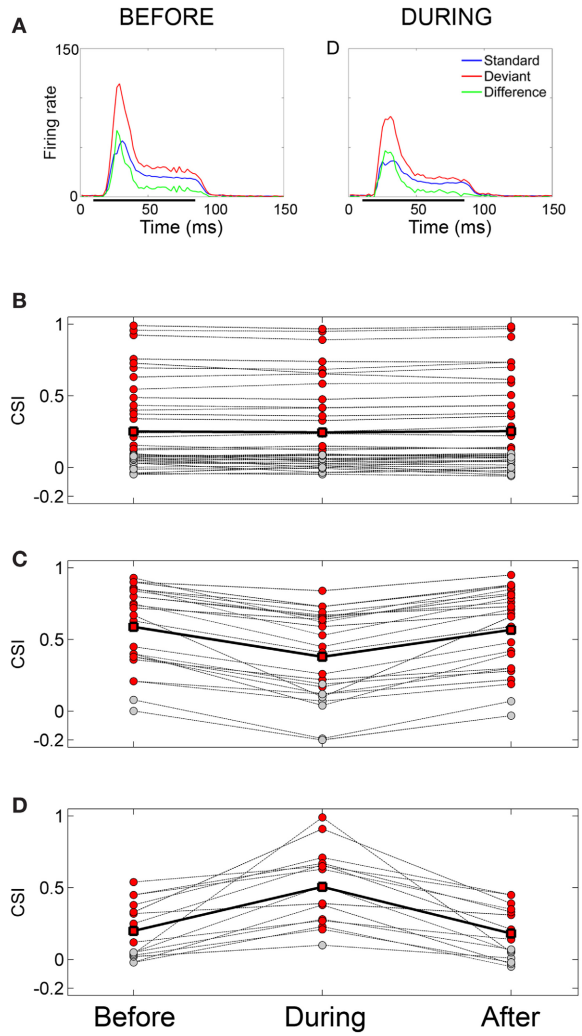

FIGURE 7 | Effect of cortical deactivation on SSA exhibited by IC neurons. (A) Mean population PSTHs from IC recordings ($n = 82$) in response to tones presented as standard (blue) or deviant (red) before and during cooling the ipsilateral AC. The difference between the two is plotted in green. Deactivation of the auditory cortex does not eliminate the deviant saliciency in the averaged signal. **(B)** Population of neurons which showed no significant change in SSA during cooling, red circles indicate significant SSA, those in gray indicate non-significant CSI values. The solid line connected with square symbols indicates the mean CSI values for the three conditions. **(C)** Population which shows a decrease in SSA during cooling. Note that on cooling some neurons cease to show significant SSA. **(D)** Population which shows an increase in SSA during cooling. Note that on cooling some neurons which previously did not show significant SSA now become significant. Figure layout in **(C)** and **(D)** is the same as in **(A)**. Reproduced from Anderson and Malmierca (2013).

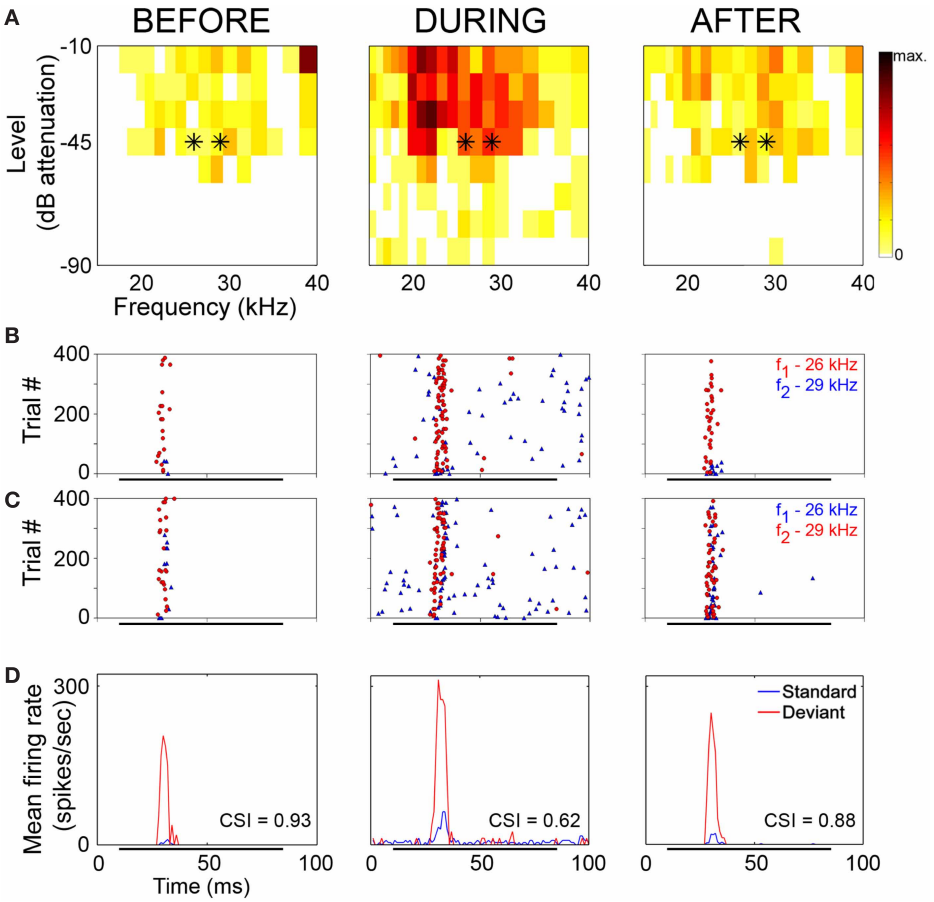

FIGURE 8 | Example of an IC neuron which shows a decrease in its adaptive properties with cooling. (A) Frequency response areas recorded before (left), during (middle), and after (right) cooling. Black asterisks indicate the frequencies used in the oddball paradigm, firing rate (spikes/sec) indicated by the color scale which applies to all response areas in this figure. **(B)** Raster plots showing response to f_1 (lower frequency) as deviant (red circles) and f_2 (higher frequency) as standard (blue triangles). **(C)** Raster plots showing response to f_1 as standard (blue triangles) and f_2 as deviant (red circles). **(D)** PSTH showing mean response to standard (blue) and deviant (red) stimuli. CSI values for each period are superimposed onto the relevant PSTH. Reproduced from Anderson and Malmierca (2013).

authors suggest that the disproportionate changes in the neuron's firing rate to standard or deviant stimulus caused by the cortical inactivation may indicate the occurrence of a gain control modulation similar to that observed in the MGB under a similar manipulation (Antunes and Malmierca, 2011) and elicited by $GABA_A$-mediated inhibition in the IC (Pérez-González and Malmierca, 2012; Pérez-González et al., 2012) which is clearly compatible with the "iceberg effect" notion described by, e.g., Isaacson and Scanziani (2011, see below).

Overall, a decrease in SSA was the predominant response, although the majority of IC neurons continued to show significant SSA after the deactivation of the cortical inputs. The extreme effects of cortical cooling were exhibited by (1) IC neurons that lost their pre-existing deviance sensitivity during the cooled condition and (2) non-adapting neurons that began to exhibit SSA. The existence of sets of IC neurons differentially affected by the AC deactivation suggests that the ipsilateral AC may relay SSA to a small group of neurons, but that corticofugal inputs do not account significantly for the SSA exhibited by the majority of adapting neurons. Using the same cooling technique, Antunes and Malmierca (2011) demonstrated that SSA persisted in the MGB neurons regardless of the lack of functional corticofugal feedback, suggesting that SSA is inherited through lower input channels in a bottom-up manner and/or generated *de novo* at each level of the auditory pathway. Pharmacological manipulation in the IC suggests that local circuits may operate intrinsically to shape SSA at this neuronal station (Pérez-González and Malmierca, 2012; Pérez-González et al., 2012; see below).

ROLE OF INHIBITORY INPUTS IN SHAPING SSA AND POSSIBLE MECHANISMS UNDERLYING SSA IN THE IC

It is well known that the IC integrates ascending and descending inputs from multiple sources (Malmierca, 2003; Malmierca and Ryugo, 2011) and possesses a dense and complex microcircuitry of local connections (Malmierca et al., 2003, 2005a, 2009b; Malmierca and Hackett, 2010). The IC is a major center for the convergence of both excitatory and inhibitory inputs and for combination of information across frequency-specific channels,

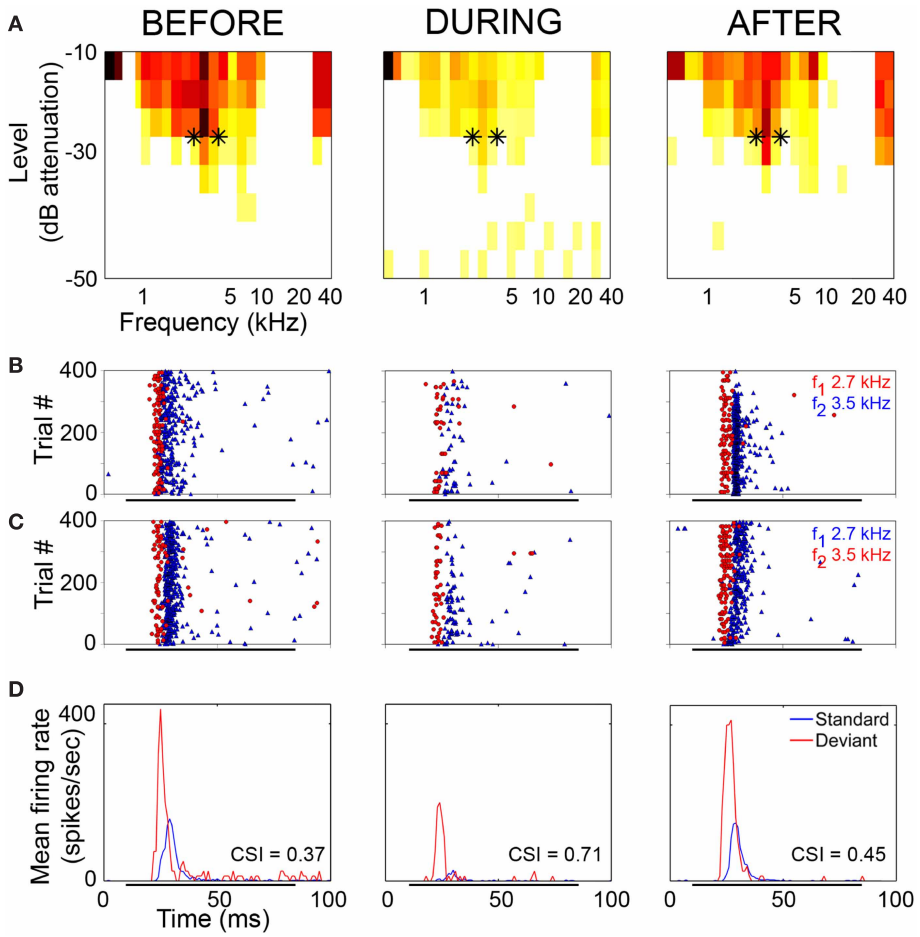

FIGURE 9 | Example of an IC neuron which shows stimulus-specific adaptation under normal conditions and increased SSA during the period of cortical cooling. (A) Frequency response areas recorded before (left), during (middle) and after (right) cooling of AC. Black asterisks indicate the frequencies used in the oddball paradigm and the firing rate (spikes/sec) are indicated by the same colour scale that appears in **Figure 8A**. **(B)** Raster plots showing response to f_1 (lower frequency) as deviant (red circles) and f_2 (higher frequency) as standard (blue triangles). **(C)** Raster plots showing response to f_1 as standard (blue triangles) and f_2 as deviant (red circles). **(D)** PSTH showing mean response to standard (blue) and deviant (red) stimuli. CSI values for each period are superimposed onto the relevant PSTH. Reproduced from Anderson and Malmierca (2013).

especially in the non-lemnical regions (Malmierca et al., 2011). Inhibitory neurotransmission in the IC is mediated by GABAergic and glycinergic receptors (Palombi and Caspary, 1996; Caspary et al., 2002; Sivaramakrishnan et al., 2004; Ingham and McAlpine, 2005; Hernández et al., 2005; Malmierca et al., 2005a; Merchán et al., 2005). GABAergic inputs come from several sources, including bilateral projections from the dorsal nucleus of the lateral lemniscus and ipsilateral projections from the ventral nucleus of the lateral lemniscus as well as intrinsic and commissural GABAergic IC neurons (Hernández et al., 2005; Malmierca et al., 2003, 2005a). Glycinergic inputs originate from the ipsilateral lateral superior olive and from the ipsilateral ventral nucleus of the lateral lemiscus (Kelly and Li, 1997; Moore et al., 1998; Riquelme et al., 2001). Pharmacological manipulation of inhibitory neurotransmitters has strong effects on neuronal response area (LeBeau et al., 2001), firing rate (Palombi and Caspary, 1996), temporal response properties (LeBeau et al., 1996), tuning for sound duration (Casseday et al., 1994, 2000) as well as for frequency (Koch and Grothe, 1998) and amplitude modulation (Caspary et al., 2002).

Recently, in a first attempt to study the role of GABAergic neurotransmission in the generation and/or modulation of SSA, gabazine an antagonist of $GABA_A$ receptors was applied microiontophoretically, and the firing rate of neurons exhibiting SSA was recorded before, during and after the drug injection (**Figures 10A–C**; Pérez-González et al., 2012). The response magnitude (**Figure 10D**), discharge pattern and latency remained distinct for the deviant and standard stimuli. The main finding was that the blockade of $GABA_A$ receptors modified the temporal dynamics of SSA but did not abolish it completely, although the CSI index was generally reduced. Adaptation to the standard stimulus still occurred in the absence of $GABA_A$-mediated inhibition but it was slower, especially at the beginning of stimulation.

The time course of the adaptation to the standard stimulus has a rapid- and a slow-decay component, after which the

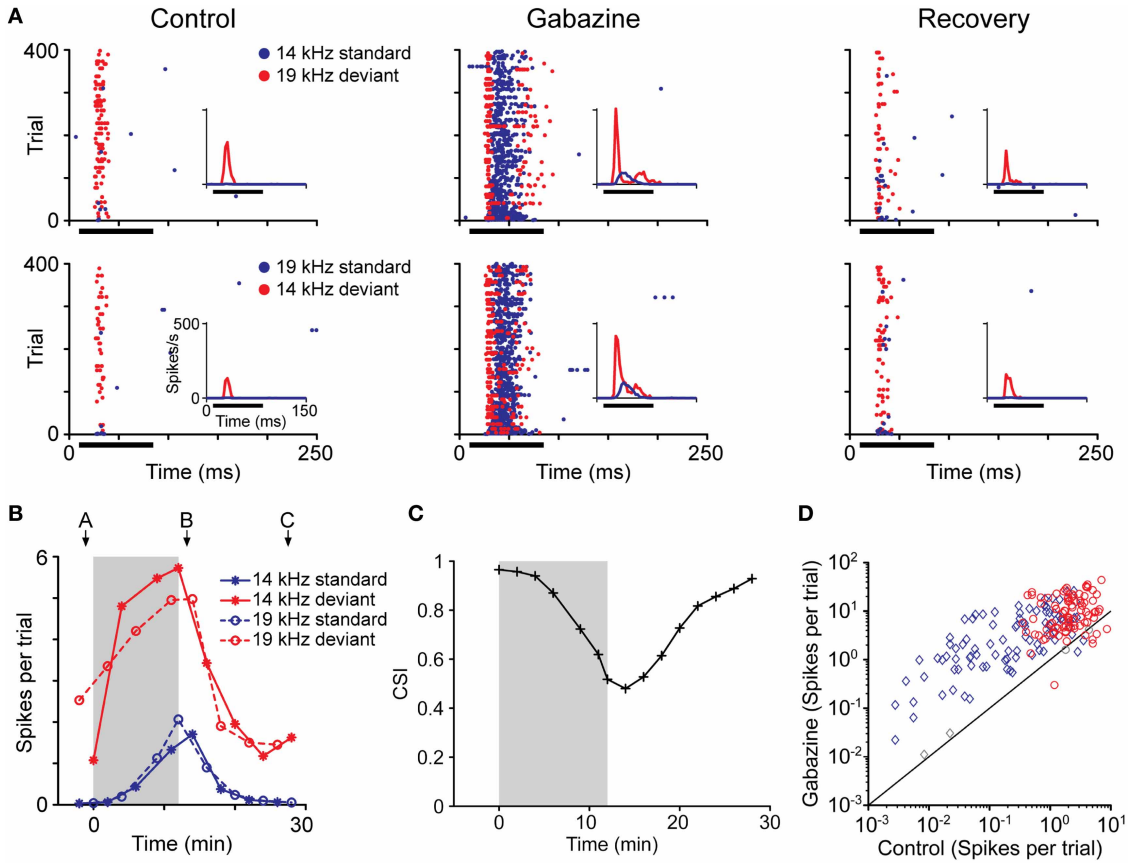

FIGURE 10 | Effect of the blockade of $GABA_A$ receptors on the response magnitude for deviant and for standard stimuli. (A) Dot rasters showing the effect of gabazine blockade of $GABA_A$ receptors on the responses of a neuron with SSA. The frequencies tested in the oddball paradigm were 14 kHz and 19 kHz ($\Delta f = 0.3$, 0.43 octaves). The insets show a PSTH of the response (3 ms bin size); the horizontal black bar indicates the duration of the stimulus. Before the application of gabazine, this neuron responded much more strongly to both frequencies when they were presented as the deviant than when they were presented as the standard stimulus, resulting in a CSI of 0.965. The application of gabazine for 12 min increased the response to both types of stimuli, but the relative increment was larger for the standards, causing the CSI to drop to 0.480. Fifteen minutes after the end of gabazine application, the neuron's response recovered to the control level, and the CSI increased to 0.926. **(B)** Evolution of the response magnitude of the neuron (mean spikes per trial) shown in **(A)** in response to standards (blue lines) and deviants stimulus (red lines). Note that the changes are similar for both frequencies (asterisk and circles) and the main differences are due to the probability condition. The shaded background represents the application of gabazine, which starts at $T = 0$. The arrows indicate the times corresponding to the dot rasters in **(A)**. **(C)** Evolution of CSI during the experiment. The symbols indicate the time at the end of a testing oddball sequence, so all times at or before 0 represent recordings completed before the start of the injection. **(D)** Effect of gabazine on response magnitude in the population of neurons. Gabazine increased the response (spikes per trial) of almost all neurons recorded, but the effect was different for standards (blue diamonds) than for deviants (red circles). Each symbol corresponds to one of the pair of stimuli for each neuron. Colored symbols indicate that the effect of gabazine was significant (Bootstrapping, 95% ci). Gray symbols represent changes that were not statistically significant. Reproduced from Pérez-González et al. (2012).

response reaches a steady-state (**Figures 11A–F**). Both decay components are faster for the neurons exhibiting higher levels of SSA (CSI > 0.5) than for the neurons with less SSA (CSI < 0.5). The blockade of the $GABA_A$ receptors slowed down both components and GABA inhibits more profoundly the steady-state component of the response of the neurons with the highest levels of SSA. As expected from previous results (Malmierca et al., 2009a; Zhao et al., 2011), Pérez-González et al. (2012) also found that the deviant-related activity did not decrease, showing a linear time course across the trials. The authors concluded that $GABA_A$-mediated inhibition acts as a gain control mechanism that enhances SSA by controlling the neuron's gain and responsiveness. Thus, synaptic inhibition via $GABA_A$ receptors seems to increase the saliency of the deviant stimulus (**Figure 12**). The role of inhibition in shaping contrast between stimuli has been described in detail in what is referred to as "the iceberg effect." Briefly, the iceberg effect describes the observation whereby a neuron's spike output is more sharply tuned than the underlying membrane potential since only the strongest excitatory input sufficiently depolarizes the membrane to reach threshold for spike generation (Isaacson and Scanziani, 2011).

The results by Pérez-González and colleagues suggest that other factors must be involved in the generation of SSA, leading to an interest in exploring the role of $GABA_B$ and glycinergic-mediated inhibition as well as neuromodulatory influences. $GABA_B$ receptors may be key players in shaping SSA. These

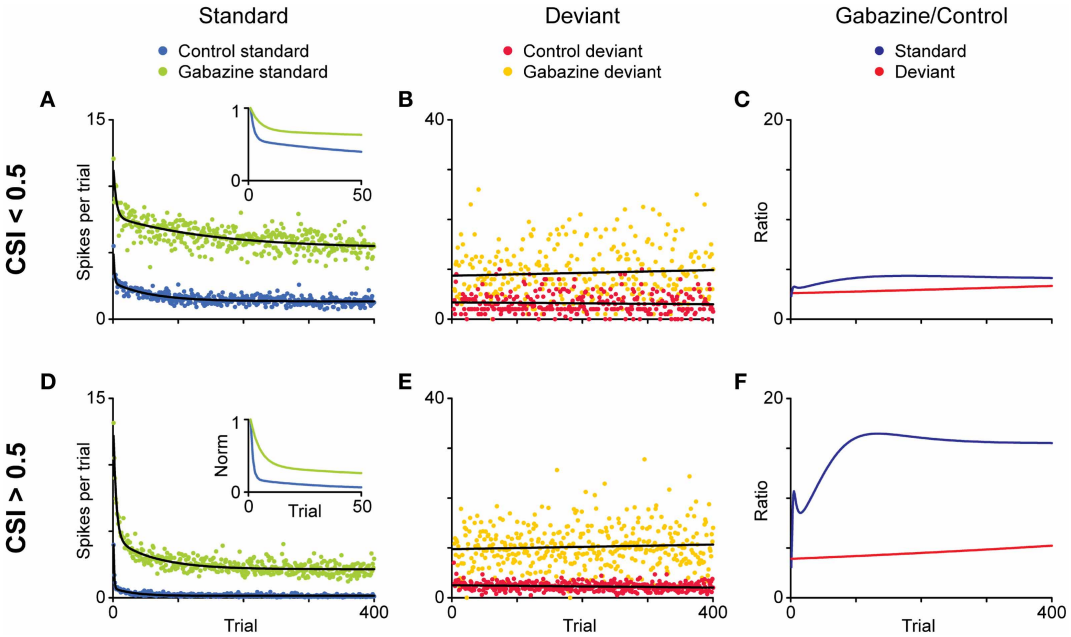

FIGURE 11 | Effect of the blockade of $GABA_A$ receptors on the time course of adaptation and a model of SSA modulation by inhibition. **(A,B; D,E)** Average discharge across the population of neurons for each position (trial) in the oddball sequence, separately for standard **(A,D)** and deviant **(B,E)** stimuli. The minimally adapting neurons (**A–C**; CSI < 0.5 in the control condition) and the highly adapting ones (**D,E**; CSI.0.5 in the control condition) were analyzed separately. Then the time course of habituation in the control condition and during application of gabazine was compared. The data for standard stimuli were fitted by a double exponential function (black lines), and the data for deviant stimuli, by a linear function. The insets show a magnified view of the normalized functions during the first 50 trials. Note the different ordinate scales for standard and deviant. **(C,F)** Ratio of gabazine/control for each type of stimulus during gabazine application. Reproduced from Pérez-González et al. (2012).

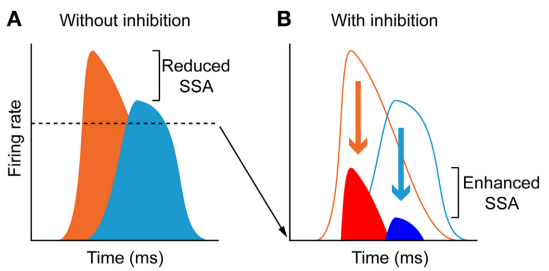

FIGURE 12 | The iceberg effect. **(A)** Schematic representation of a model of the iceberg effect indicating that in the absence of inhibition, neurons respond to deviants (orange) and standards (light blue) with high firing rates, and thus the deviant to standard ratio is small. **(B)** Inhibition reduces the responses to both deviants (red) and standards (dark blue) increasing the deviant to standard ratio and thus enhancing SSA. The dashed line in **(A)**, delimit the amount of activity (bottom area of the histograms) that decreases due to inhibition. Reproduced from Pérez-González et al. (2012).

receptors seem to be involved in the processing of novel visual stimuli in the superior colliculus (Binns and Salt, 1997) and they regulate the release of glutamate from excitatory terminals in the DCIC through presynaptic mechanisms (Scanziani, 2000; Sun and Wu, 2009). Then, both pre- and postsynaptic mechanisms are likely to contribute to a reduction in the membrane depolarization after initial excitation. To dissect the interplay of synaptic excitation and inhibition is also necessary to understand the cellular and network mechanisms underlying SSA. Previously, Binns and Salt (1995) demonstrated that the activity mediated by the NMDA and AMPA/Kainate receptors modulates response habituation in the superior colliculus. Hitherto, no attempt has been made to determine whether SSA in single-unit activity in the IC depends on local glutamatergic neurotransmission.

Since the level of SSA varies within the neuronal frequency response area (Duque et al., 2012), it is likely that the mechanisms underlying SSA act at the sites of synaptic inputs on the IC neuron. The specific decrement to repetitive stimuli seen in neurons exhibiting SSA could be explained by adaptation occurring at frequency-segregated input channels (Eytan et al., 2003). The persistence of SSA at long ISI suggests that it is not merely a result of mechanisms such as synaptic fatigue (e.g., reduction in neuronal responses independently of the stimulus due to depletion of neurotransmitter vesicles). This is less likely to occur at very long interstimulus gaps. Delayed synaptic inhibition might account for the specific response suppression to a highly repetitive stimulus. This idea is supported by intracellular recording suggesting that excitation in neurons throughout the IC is often followed by long-lasting hyperpolarization, possibly due to synaptic inhibition (Covey et al., 1996; Syka et al., 2000; Wehr and Zador, 2005). This could also explain why the neurons with the highest SSA levels (Duque et al., 2012) exhibit onset response patterns to sound stimulation. Another possibility is short-term plasticity occurring at the sites of synaptic integration in IC neurons. These possibilities are not mutually exclusive and it could be that they operate

in conjunction. It is plausible to think that the neuronal adaptation in the IC reflects high level network computations with strong participation of local inhibitory circuits (Pérez-González and Malmierca, 2012; Pérez-González et al., 2012), and with a modulatory control on SSA exerted by corticofugal projections (Anderson and Malmierca, 2013). Multidisciplinary efforts that will combine histological, electrophysiological, computational, and behavioral methods (Garagnani and Pulvermuller, 2011; Mill et al., 2011) will be necessary to unveil the basic mechanisms that generate SSA at each level along the auditory system.

CONCLUDING REMARKS AND FUTURE DIRECTIONS

In this review, we have attempted to offer an account of the current state of SSA studies in the IC because of the growing interest on the single-neuron electrophysiology of auditory deviance detection. The dependence of neuronal SSA on various stimulus features, such as deviant probability and repetition rate, and the role of AC and of inhibition in shaping SSA at this auditory stage have been addressed.

Among the questions to be resolved in the study of auditory deviance detection are whether SSA is present along the entire auditory pathway or whether it is a regionalized phenomenon to certain structures and how the deviance coding is modified by bottom-up and top-down processes that take place at each station. The localization of the most strongly adapting neurons to frequencies in the non-lemniscal portions of the subcortical nuclei opens interesting question about the neuronal circuits involved since these parts of the auditory pathway process more complex acoustic features. To address these issues, it is necessary to record neurons in the brainstem nuclei (especially those that exhibit cross-frequency integration), to track the common input sources to neurons with strong SSA, as well as, their projections, and to make simultaneous recordings at two or more connected sites. Since stimuli in a natural scene vary in multiple features, another open question is whether neurons sensitive to frequency deviants are also deviance detectors for more complex sound patterns and whether the same neurons are capable of detecting deviant stimulus immersed in more complex forms of regularity (Cornella et al., 2012; Grimm and Escera, 2012). These and other questions await future studies.

ACKNOWLEDGMENTS

We thank Dr. Nell B. Cant and Monty A. Escabí for their critical and constructive suggestions. Financial support was provided by the Spanish MEC (BFU2009-07286) and EU (EUI2009-04083, in the framework of the ERA-NET Network of European Funding for Neuroscience Research) to Manuel S. Malmierca. The funders had no role in study design, data collection and analysis, decision to publish, or preparation of the manuscript.

REFERENCES

Anderson, L. A., Christianson, G. B., and Linden, J. F. (2009). Stimulus-specific adaptation occurs in the auditory thalamus. *J. Neurosci.* 29, 7359–7363.

Anderson, L. A., and Malmierca, M. S. (2013). The effect of auditory cortical deactivation on stimulus-specific adaptation in the inferior colliculus of the rat. *Eur. J. Neurosci.* 37, 52–62.

Antunes, F. M., and Malmierca, M. S. (2011). Effect of auditory cortex deactivation on stimulus-specific adaptation in the medial geniculate body. *J. Neurosci.* 31, 17306–17316.

Antunes, F. M., Nelken, I., Covey, E., and Malmierca, M. S. (2010). Stimulus-specific adaptation in the auditory thalamus of the anesthetized rat. *PLoS ONE* 5:e14071. doi: 10.1371/journal.pone.0014071

Astikainen, P., Ruusuvirta, T., Wikgren, J., and Penttonen, M. (2006). Memory-based detection of rare sound feature combinations in anesthetized rats. *Neuroreport* 17, 1561–1564.

Astikainen, P., Stefanics, G., Nokia, M., Lipponen, A., Cong, F., Penttonen, M., et al. (2011). Memory-based mismatch response to frequency changes in rats. *PLoS ONE* 6:e24208. doi: 10.1371/journal.pone.0024208

Ayala, Y. A., Pérez-González, D., Duque, D., Nelken, I., and Malmierca, M. S. (2012). Frequency discrimination and stimulus deviance in the inferior colliculus and cochlear nucleus. *Front. Neural Circuits* 6:119. doi: 10.3389/fncir.2012.00119

Baüerle, P., Von Der Behrens, W., Kossl, M., and Gaese, B. H. (2011). Stimulus-specific adaptation in the gerbil primary auditory thalamus is the result of a fast frequency-specific habituation and is regulated by the corticofugal system. *J. Neurosci.* 31, 9708–9722.

Bibikov, N. G. (1977). 'Novelty' neurons in the frog auditory system. *Zh. Vyssh. Nerv. Deiat. Im. I P Pavlova* 27, 1075–1082.

Bibikov, N. G., and Soroka, S. K. (1979). Structure of the neurons in the midbrain auditory center in the frog, *Rana ridibunda*. *Zh. Evol. Biokhim. Fiziol.* 15, 608–616.

Binns, K. E., and Salt, T. E. (1995). Excitatory amino acid receptors modulate habituation of the response to visual stimulation in the cat superior colliculus. *Vis. Neurosci.* 12, 563–571.

Binns, K. E., and Salt, T. E. (1997). Different roles for $GABA_A$ and $GABA_B$ receptors in visual processing in the rat superior colliculus. *J. Physiol.* 504(Pt 3), 629–639.

Cant, N. B., and Benson, C. G. (2006). Organization of the inferior colliculus of the gerbil (*Meriones unguiculatus*): differences in distribution of projections from the cochlear nuclei and the superior olivary complex. *J. Comp. Neurol.* 495, 511–528.

Carral, V., Huotilainen, M., Ruusuvirta, T., Fellman, V., Naatanen, R., and Escera, C. (2005a). A kind of auditory 'primitive intelligence' already present at birth. *Eur. J. Neurosci.* 21, 3201–3204.

Carral, V., Corral, M. J., and Escera, C. (2005b). Auditory event-related potentials as a function of abstract change magnitude. *Neuroreport* 16, 301–305.

Caspary, D. M., Palombi, P. S., and Hughes, L. F. (2002). GABAergic inputs shape responses to amplitude modulated stimuli in the inferior colliculus. *Hear. Res.* 168, 163–173.

Casseday, J. H., Ehrlich, D., and Covey, E. (1994). Neural tuning for sound duration: role of inhibitory mechanisms in the inferior colliculus. *Science* 264, 847–850.

Casseday, J. H., Ehrlich, D., and Covey, E. (2000). Neural measurement of sound duration: control by excitatory-inhibitory interactions in the inferior colliculus. *J. Neurophysiol.* 84, 1475–1487.

Cornella, M., Leung, S., Grimm, S., and Escera, C. (2012). Detection of simple and pattern regularity violations occurs at different levels of the auditory hierarchy. *PLoS ONE* 7:e43604. doi:10.1371/journal.pone.0043604

Covey, E., Kauer, J. A., and Casseday, J. H. (1996). Whole-cell patch-clamp recording reveals subthreshold sound-evoked postsynaptic currents in the inferior colliculus of awake bats. *J. Neurosci.* 16, 3009–3018.

Draganova, R., Eswaran, H., Murphy, P., Huotilainen, M., Lowery, C., and Preissl, H. (2005). Sound frequency change detection in fetuses and newborns, a magnetoencephalographic study. *Neuroimage* 28, 354–361.

Duncan, C. C., Barry, R. J., Connolly, J. F., Fischer, C., Michie, P. T., Näätänen, R., et al. (2009). Event-related potentials in clinical research: guidelines for eliciting, recording, and quantifying mismatch negativity, P300, and N400. *Clin. Neurophysiol.* 120, 1883–1908.

Duque, D., Pérez-González, D., Ayala, A. Y., Palmer, A. R., and Malmierca, M. S. (2012). Topographic distribution, frequency and intensity dependence of stimulus-specific adaptation in the inferior colliculus of the rat. *J. Neurosci.* 32, 17762–17774.

Eriksson, J., and Villa, A. E. (2005). Event-related potentials in an auditory oddball situation in the rat. *Biosystems* 79, 207–212.

Escera, C., Alho, K., Schroger, E., and Winkler, I. (2000). Involuntary attention and distractibility as

evaluated with event-related brain potentials. *Audiol. Neurootol.* 5, 151–166.

Eytan, D., Brenner, N., and Marom, S. (2003). Selective adaptation in networks of cortical neurons. *J. Neurosci.* 23, 9349–9356.

Farley, B. J., Quirk, M. C., Doherty, J. J., and Christian, E. P. (2010). Stimulus-specific adaptation in auditory cortex is an NMDA-independent process distinct from the sensory novelty encoded by the mismatch negativity. *J. Neurosci.* 30, 16475–16484.

Garagnani, M., and Pulvermuller, F. (2011). From sounds to words: a neurocomputational model of adaptation, inhibition and memory processes in auditory change detection. *Neuroimage* 54, 170–181.

Grimm, S., and Escera, C. (2012). Auditory deviance detection revisited: evidence for a hierarchical novelty system. *Int. J. Psychophysiol.* 85, 88–92.

Grimm, S., Escera, C., Slabu, L., and Costa-Faidella, J. (2011). Electrophysiological evidence for the hierarchical organization of auditory change detection in the human brain. *Psychophysiology* 48, 377–384.

Gutfreund, Y. (2012). Stimulus-specific adaptation, habituation and change detection in the gaze control system. *Biol. Cybern.* 106, 657–668.

He, J., and Yu, Y. (2010). "Role of descending control in the auditory pathway," in *The Oxford Handbook of Auditory Science: The Auditory Brain*, eds A. Rees and A. R. Palmer (New York, NY: OUP), 247–268.

Hernández, O., Espinosa, N., Pérez-González, D., and Malmierca, M. S. (2005). The inferior colliculus of the rat: a quantitative analysis of monaural frequency response areas. *Neuroscience* 132, 203–217.

Huotilainen, M., Winkler, I., Alho, K., Escera, C., Virtanen, J., Ilmoniemi, R. J., et al. (1998). Combined mapping of human auditory EEG and MEG responses. *Electroencephalogr. Clin. Neurophysiol.* 108, 370–379.

Ingham, N. J., and McAlpine, D. (2005). GABAergic inhibition controls neural gain in inferior colliculus neurons sensitive to interaural time differences. *J. Neurosci.* 25, 6187–6198.

Isaacson, J. S., and Scanziani, M. (2011). How inhibition shapes cortical activity. *Neuron* 72, 231–243.

Jääskeläinen, I. P., Ahveninen, J., Belliveau, J. W., Raij, T., and Sams, M. (2007). Short-term plasticity in auditory cognition. *Trends Neurosci.* 30, 653–661.

Javitt, D. C., Steinschneider, M., Schroeder, C. E., Vaughan, H. G. Jr., and Arezzo, J. C. (1994). Detection of stimulus deviance within primate primary auditory cortex: intracortical mechanisms of mismatch negativity (MMN) generation. *Brain Res.* 667, 192–200.

Katz, Y., Heiss, J. E., and Lampl, I. (2006). Cross-whisker adaptation of neurons in the rat barrel cortex. *J. Neurosci.* 26, 13363–13372.

Kelly, J. B., and Li, L. (1997). Two sources of inhibition affecting binaural evoked responses in the rat's inferior colliculus: the dorsal nucleus of the lateral lemniscus and the superior olivary complex. *Hear. Res.* 104, 112–126.

King, C., McGee, T., Rubel, E. W., Nicol, T., and Kraus, N. (1995). Acoustic features and acoustic changes are represented by different central pathways. *Hear. Res.* 85, 45–52.

Koch, U., and Grothe, B. (1998). GABAergic and glycinergic inhibition sharpens tuning for frequency modulations in the inferior colliculus of the big brown bat. *J. Neurophysiol.* 80, 71–82.

Kraus, N., McGee, T., Littman, T., Nicol, T., and King, C. (1994). Nonprimary auditory thalamic representation of acoustic change. *J. Neurophysiol.* 72, 1270–1277.

LeBeau, F. E., Malmierca, M. S., and Rees, A. (2001). Iontophoresis *in vivo* demonstrates a key role for $GABA_A$ and glycinergic inhibition in shaping frequency response areas in the inferior colliculus of guinea pig. *J. Neurosci.* 21, 7303–7312.

LeBeau, F. E., Rees, A., and Malmierca, M. S. (1996). Contribution of GABA- and glycine-mediated inhibition to the monaural temporal response properties of neurons in the inferior colliculus. *J. Neurophysiol.* 75, 902–919.

Lee, C. C., and Sherman, S. M. (2011). On the classification of pathways in the auditory midbrain, thalamus, and cortex. *Hear. Res.* 276, 79–87.

Loftus, W. C., Bishop, D. C., and Oliver, D. L. (2010). Differential patterns of inputs create functional zones in central nucleus of inferior colliculus. *J. Neurosci.* 30, 13396–13408.

Loftus, W. C., Malmierca, M. S., Bishop, D. C., and Oliver, D. L. (2008). The cytoarchitecture of the inferior colliculus revisited: a common organization of the lateral cortex in rat and cat. *Neuroscience* 154, 196–205.

Lomber, S. G., and Malhotra, S. (2008). Double dissociation of 'what' and 'where' processing in auditory cortex. *Nat. Neurosci.* 11, 609–616.

Lomber, S. G., Payne, B. R., and Horel, J. A. (1999). The cryoloop: an adaptable reversible cooling deactivation method for behavioral or electrophysiological assessment of neural function. *J. Neurosci. Methods* 86, 179–194.

Luck, S. J., Mathalon, D. H., O'Donnell, B. F., Hamalainen, M. S., Spencer, K. M., Javitt, D. C., et al. (2011). A roadmap for the development and validation of event-related potential biomarkers in schizophrenia research. *Biol. Psychiatry* 70, 28–34.

Lumani, A., and Zhang, H. (2010). Responses of neurons in the rat's dorsal cortex of the inferior colliculus to monaural tone bursts. *Brain Res.* 1351, 115–129.

Malmierca, M. S. (2003). The structure and physiology of the rat auditory system: an overview. *Int. Rev. Neurobiol.* 56, 147–211.

Malmierca, M. S., Blackstad, T. W., and Osen, K. K. (2011). Computer-assisted 3-D reconstructions of Golgi-impregnated neurons in the cortical regions of the inferior colliculus of rat. *Hear. Res.* 274, 13–26.

Malmierca, M. S., Blackstad, T. W., Osen, K. K., Karagulle, T., and Molowny, R. L. (1993). The central nucleus of the inferior colliculus in rat: a Golgi and computer reconstruction study of neuronal and laminar structure. *J. Comp. Neurol.* 333, 1–27.

Malmierca, M. S., Cristaudo, S., Pérez-González, D., and Covey, E. (2009a). Stimulus-specific adaptation in the inferior colliculus of the anesthetized rat. *J. Neurosci.* 29, 5483–5493.

Malmierca, M. S., Hernández, O., Antunes, F. M., and Rees, A. (2009b). Divergent and point-to-point connections in the commissural pathway between the inferior colliculi. *J. Comp. Neurol.* 514, 226–239.

Malmierca, M. S., and Hackett, T. A. (2010). "Structural organization of the ascending auditory pathway," in *The Oxford Handbook of Auditory Science: The Auditory Brain,* ed D. R. Moore (New York, NY: OUP), 9–41.

Malmierca, M. S., Hernández, O., Antunes, F. M., Pérez-González, D., Izquierdo, M. A., and Covey, E. (2010). "$GABA_A$ receptors mediate stimulus-specific adaptation (SSA) in the auditory midbrain," in *33rd Midwinter Meeting of the Association for Research in Otolaryngology: ARO abstr 786*. (Anaheim, CA).

Malmierca, M. S., Hernández, O., Falconi, A., Lopez-Poveda, E. A., Merchán, M., and Rees, A. (2003). The commissure of the inferior colliculus shapes frequency response areas in rat: an *in vivo* study using reversible blockade with microinjection of kynurenic acid. *Exp. Brain Res.* 153, 522–529.

Malmierca, M. S., Hernández, O., and Rees, A. (2005a). Intercollicular commissural projections modulate neuronal responses in the inferior colliculus. *Eur. J. Neurosci.* 21, 2701–2710.

Malmierca, M. S., Saint Marie, R. L., Merchán, M. A., and Oliver, D. L. (2005b). Laminar inputs from dorsal cochlear nucleus and ventral cochlear nucleus to the central nucleus of the inferior colliculus: two patterns of convergence. *Neuroscience* 136, 883–894.

Malmierca, M. S., and Ryugo, D. K. (2011). "Descending connections of auditory cortex to the midbrain and brainstem," in *The Auditory Cortex*, eds J. A. Winer and C. E. Schreiner (New York, NY: Springer), 189–208.

Malmierca, M. S., Seip, K. L., and Osen, K. K. (1995). Morphological classification and identification of neurons in the inferior colliculus: a multivariate analysis. *Anat. Embryol. (Berl.)* 191, 343–350.

Malone, B. J., Scott, B. H., and Semple, M. N. (2002). Context-dependent adaptive coding of interaural phase disparity in the auditory cortex of awake macaques. *J. Neurosci.* 22, 4625–4638.

Merchán, M., Aguilar, L. A., Lopez-Poveda, E. A., and Malmierca, M. S. (2005). The inferior colliculus of the rat: quantitative immunocytochemical study of GABA and glycine. *Neuroscience* 136, 907–925.

Mill, R., Coath, M., Wennekers, T., and Denham, S. L. (2011). Abstract stimulus-specific adaptation models. *Neural Comput.* 23, 435–476.

Moore, D. R., Kotak, V. C., and Sanes, D. H. (1998). Commissural and lemniscal synaptic input to the gerbil inferior colliculus. *J. Neurophysiol.* 80, 2229–2236.

Moshitch, D., Las, L., Ulanovsky, N., Bar-Yosef, O., and Nelken, I. (2006). Responses of neurons in primary auditory cortex (A1) to pure tones in the halothane-anesthetized cat. *J. Neurophysiol.* 95, 3756–3769.

Movshon, J. A., and Lennie, P. (1979). Pattern-selective adaptation in visual cortical neurones. *Nature* 278, 850–852.

Müller, J. R., Metha, A. B., Krauskopf, J., and Lennie, P. (1999). Rapid adaptation in visual cortex to the

structure of images. *Science* 285, 1405–1408.

Näätänen, R. (1992). *Attention and Brain Function*. Hillsdale, NJ: Lawrence Erlbaum.

Näätänen, R., and Escera, C. (2000). Mismatch negativity: clinical and other applications. *Audiol. Neurootol.* 5, 105–110.

Näätänen, R., Gaillard, A. W., and Mantysalo, S. (1978). Early selective-attention effect on evoked potential reinterpreted. *Acta Psychol. (Amst.)* 42, 313–329.

Näätänen, R., Paavilainen, P., Rinne, T., and Alho, K. (2007). The mismatch negativity (MMN) in basic research of central auditory processing: a review. *Clin. Neurophysiol.* 118, 2544–2590.

Näätänen, R., Tervaniemi, M., Sussman, E., Paavilainen, P., and Winkler, I. (2001). "Primitive intelligence," in the auditory cortex. *Trends Neurosci.* 24, 283–288.

Nakamoto, K. T., Jones, S. J., and Palmer, A. R. (2008). Descending projections from auditory cortex modulate sensitivity in the midbrain to cues for spatial position. *J. Neurophysiol.* 99, 2347–2356.

Nakamura, T., Michie, P. T., Fulham, W. R., Todd, J., Budd, T. W., Schall, U., et al. (2011). Epidural auditory event-related potentials in the rat to frequency and duration deviants: evidence of mismatch negativity? *Front. Psychology* 2:367. doi: 10.3389/fpsyg.2011.00367

Nelken, I., and Ulanovsky, N. (2007). Mismatch negativity and stimulus-specific adaptation in animal models. *J. Psychophysiol.* 21, 214–223.

Netser, S., Zahar, Y., and Gutfreund, Y. (2011). Stimulus-specific adaptation: can it be a neural correlate of behavioral habituation? *J. Neurosci.* 31, 17811–17820.

Palombi, P. S., and Caspary, D. M. (1996). GABA inputs control discharge rate primarily within frequency receptive fields of inferior colliculus neurons. *J. Neurophysiol.* 75, 2211–2219.

Patel, C. R., Redhead, C., Cervi, A. L., and Zhang, H. (2012). Neural sensitivity to novel sounds in the rat's dorsal cortex of the inferior colliculus as revealed by evoked local field potentials. *Hear. Res.* 286, 41–54.

Pérez-González, D., Hernández, O., Covey, E., and Malmierca, M. S. (2012). $GABA_A$-mediated inhibition modulates stimulus-specific adaptation in the inferior colliculus. *PLoS ONE* 7:e34297. doi: 10.1371/journal.pone.0034297

Pérez-González, D., and Malmierca, M. S. (2012). Variability of the time course of stimulus-specific adaptation in the inferior colliculus. *Front. Neural Circuits* 6:107. doi: 10.3389/fncir.2012.00107

Pérez-González, D., Malmierca, M. S., and Covey, E. (2005). Novelty detector neurons in the mammalian auditory midbrain. *Eur. J. Neurosci.* 22, 2879–2885.

Recasens, M., Grimm, S., Capilla, A., Nowak, R., and Escera, C. (2012). Two sequential processes of change detection in hierarchically ordered areas of the human auditory cortex. *Cereb. Cortex* doi: 10.1093/cercor/bhs295. [Epub ahead of print].

Reches, A., and Gutfreund, Y. (2008). Stimulus-specific adaptations in the gaze control system of the barn owl. *J. Neurosci.* 28, 1523–1533.

Rees, A., Sarbaz, A., Malmierca, M. S., and Le Beau, F. E. (1997). Regularity of firing of neurons in the inferior colliculus. *J. Neurophysiol.* 77, 2945–2965.

Reetz, G., and Ehret, G. (1999). Inputs from three brainstem sources to identified neurons of the mouse inferior colliculus slice. *Brain Res.* 816, 527–543.

Riquelme, R., Saldana, E., Osen, K. K., Ottersen, O. P., and Merchán, M. A. (2001). Colocalization of GABA and glycine in the ventral nucleus of the lateral lemniscus in rat: an *in situ* hybridization and semiquantitative immunocytochemical study. *J. Comp. Neurol.* 432, 409–424.

Ruusuvirta, T., Penttonen, M., and Korhonen, T. (1998). Auditory cortical event-related potentials to pitch deviances in rats. *Neurosci. Lett.* 248, 45–48.

Scanziani, M. (2000). GABA spillover activates postsynaptic $GABA_B$ receptors to control rhythmic hippocampal activity. *Neuron* 25, 673–681.

Shalgi, S., and Deouell, L. Y. (2007). Direct evidence for differential roles of temporal and frontal components of auditory change detection. *Neuropsychologia* 45, 1878–1888.

Sivaramakrishnan, S., Sterbing-D'Angelo, S. J., Filipovic, B., D'Angelo, W. R., Oliver, D. L., and Kuwada, S. (2004). $GABA_A$ synapses shape neuronal responses to sound intensity in the inferior colliculus. *J. Neurosci.* 24, 5031–5043.

Slabu, L., Escera, C., Grimm, S., and Costa-Faidella, J. (2010). Early change detection in humans as revealed by auditory brainstem and middle-latency evoked potentials. *Eur. J. Neurosci.* 32, 859–865.

Slabu, L., Grimm, S., and Escera, C. (2012). Novelty detection in the human auditory brainstem. *J. Neurosci.* 32, 1447–1452.

Sobotka, S., and Ringo, J. L. (1994). Stimulus specific adaptation in excited but not in inhibited cells in inferotemporal cortex of macaque. *Brain Res.* 646, 95–99.

Sun, H., and Wu, S. H. (2009). The physiological role of pre- and postsynaptic $GABA_B$ receptors in membrane excitability and synaptic transmission of neurons in the rat's dorsal cortex of the inferior colliculus. *Neuroscience* 160, 198–211.

Syka, J., Popelar, J., Kvasnak, E., and Astl, J. (2000). Response properties of neurons in the central nucleus and external and dorsal cortices of the inferior colliculus in guinea pig. *Exp. Brain Res.* 133, 254–266.

Taaseh, N., Yaron, A., and Nelken, I. (2011). Stimulus-specific adaptation and deviance detection in the rat auditory cortex. *PLoS ONE* 6:e23369. doi: 10.1371/journal.pone.0023369

Thomas, J. M., Morse, C., Kishline, L., O'Brien-Lambert, A., Simonton, A., Miller, K. E., et al. (2012). Stimulus-specific adaptation in specialized neurons in the inferior colliculus of the big brown bat, *Eptesicus fuscus*. *Hear. Res.* 291, 34–40.

Tiitinen, H., May, P., Reinikainen, K., and Näätänen, R. (1994). Attentive novelty detection in humans is governed by pre-attentive sensory memory. *Nature* 372, 90–92.

Tikhonravov, D., Neuvonen, T., Pertovaara, A., Savioja, K., Ruusuvirta, T., Näätänen, R., et al. (2008). Effects of an NMDA-receptor antagonist MK-801 on an MMN-like response recorded in anesthetized rats. *Brain Res.* 1203, 97–102.

Ulanovsky, N., Las, L., Farkas, D., and Nelken, I. (2004). Multiple time scales of adaptation in auditory cortex neurons. *J. Neurosci.* 24, 10440–10453.

Ulanovsky, N., Las, L., and Nelken, I. (2003). Processing of low-probability sounds by cortical neurons. *Nat. Neurosci.* 6, 391–398.

Von Der Behrens, W., Bauerle, P., Kossl, M., and Gaese, B. H. (2009). Correlating stimulus-specific adaptation of cortical neurons and local field potentials in the awake rat. *J. Neurosci.* 29, 13837–13849.

Wehr, M., and Zador, A. M. (2005). Synaptic mechanisms of forward suppression in rat auditory cortex. *Neuron* 47, 437–445.

Winkler, I., Denham, S. L., and Nelken, I. (2009). Modeling the auditory scene: predictive regularity representations and perceptual objects. *Trends Cogn. Sci.* 13, 532–540.

Woods, E. J., and Frost, B. J. (1977). Adaptation and habituation characteristics of tectal neurons in the pigeon. *Exp. Brain Res.* 27, 347–354.

Yu, X. J., Xu, X. X., He, S., and He, J. (2009). Change detection by thalamic reticular neurons. *Nat. Neurosci.* 12, 1165–1170.

Zhao, L., Liu, Y., Shen, L., Feng, L., and Hong, B. (2011). Stimulus-specific adaptation and its dynamics in the inferior colliculus of rat. *Neuroscience* 181, 163–174.

Conflict of Interest Statement: The authors declare that the research was conducted in the absence of any commercial or financial relationships that could be construed as a potential conflict of interest.

Received: 19 August 2012; accepted: 02 November 2012; published online: 17 January 2013.

Citation: Ayala YA and Malmierca MS (2013) Stimulus-specific adaptation and deviance detection in the inferior colliculus. Front. Neural Circuits ***6****:89. doi: 10.3389/fncir.2012.00089*

frontiers in
NEURAL CIRCUITS

ORIGINAL RESEARCH ARTICLE
published: 14 January 2013
doi: 10.3389/fncir.2012.00119

Frequency discrimination and stimulus deviance in the inferior colliculus and cochlear nucleus

Yaneri A. Ayala[1], David Pérez-González[1], Daniel Duque[1], Israel Nelken[2] and Manuel S. Malmierca[1,3]*

[1] Auditory Neurophysiology Laboratory, Institute of Neuroscience of Castilla y León, University of Salamanca, Salamanca, Spain
[2] Department of Neurobiology, Institute of Life Sciences, The Interdisciplinary Center for Neural Computation and the Edmond and Lily Safra Center for Brain Sciences, The Hebrew University of Jerusalem, Jerusalem, Israel
[3] Department of Cell Biology and Pathology, Faculty of Medicine, University of Salamanca, Salamanca, Spain

Edited by:
Eric D. Young, Johns Hopkins University, USA

Reviewed by:
Sarah L. Pallas, Georgia State University, USA
Edward L. Bartlett, Purdue University, USA

***Correspondence:**
Manuel S. Malmierca, Laboratory for the Neurobiology of Hearing, Auditory Neurophysiology Unit (Lab 1), Institute of Neuroscience of Castilla y León, University of Salamanca, C/ Pintor Fernando Gallego 1, 37007 Salamanca, Spain.
e-mail: msm@usal.es

Auditory neurons that exhibit stimulus-specific adaptation (SSA) decrease their response to common tones while retaining responsiveness to rare ones. We recorded single-unit responses from the inferior colliculus (IC) where SSA is known to occur and we explored for the first time SSA in the cochlear nucleus (CN) of rats. We assessed an important functional outcome of SSA, the extent to which frequency discriminability depends on sensory context. For this purpose, pure tones were presented in an oddball sequence as standard (high probability of occurrence) or deviant (low probability of occurrence) stimuli. To study frequency discriminability under different probability contexts, we varied the probability of occurrence and the frequency separation between tones. The neuronal sensitivity was estimated in terms of spike-count probability using signal detection theory. We reproduced the finding that many neurons in the IC exhibited SSA, but we did not observe significant SSA in our CN sample. We concluded that strong SSA is not a ubiquitous phenomenon in the CN. As predicted, frequency discriminability was enhanced in IC when stimuli were presented in an oddball context, and this enhancement was correlated with the degree of SSA shown by the neurons. In contrast, frequency discrimination by CN neurons was independent of stimulus context. Our results demonstrated that SSA is not widespread along the entire auditory pathway, and suggest that SSA increases frequency discriminability of single neurons beyond that expected from their tuning curves.

Keywords: SSA, deviant sensitivity, change detection, mismatch negativity, non-lemniscal pathway, ROC analysis

INTRODUCTION

Auditory neurons displaying stimulus-specific adaptation (SSA) decrease their response to high probability stimuli (standards) while maintaining responsiveness to rare ones (deviants, Ulanovsky et al., 2003). SSA is correlated with behavioral habituation (Netser et al., 2011; Gutfreund, 2012) and it has been proposed to underlie sensory memory for stimulation history (Ulanovsky et al., 2004). Neurons showing SSA have been found in the mammalian auditory pathway from the inferior colliculus (IC) up to the cortex (Ulanovsky et al., 2003; Pérez-González et al., 2005; Anderson et al., 2009; Malmierca et al., 2009; von der Behrens et al., 2009; Yu et al., 2009; Antunes et al., 2010; Lumani and Zhang, 2010; Reches et al., 2010; Taaseh et al., 2011; Zhao et al., 2011; Ayala and Malmierca, 2012; Duque et al., 2012; Anderson and Malmierca, 2013) as well as in bird midbrain and forebrain (Reches and Gutfreund, 2008, 2009). Originally, SSA was suggested to emerge in the auditory cortex and to be transmitted downstream to subcortical nuclei through the corticofugal pathway (Nelken and Ulanovsky, 2007), as subcortical SSA is mostly confined to the non-lemniscal regions (Malmierca et al., 2009; Antunes et al., 2010; Duque et al., 2012), the main target of the corticofugal projections (Malmierca and Ryugo, 2011). However, it has been recently shown that cortical deactivation does not affect SSA neither in the non-lemniscal auditory thalamus (Antunes and Malmierca, 2011) nor in the IC (Anderson and Malmierca, 2013), while SSA in lemniscal regions is minimal (Malmierca et al., 2009; Antunes et al., 2010; Bäuerle et al., 2011). Thus, SSA may be computed independently in the non-lemniscal pathway and in primary auditory cortex. Thus far, the existence of SSA has not been explored in auditory nuclei below the IC, where the lemniscal and non-lemniscal divisions first emerge.

Frequency discrimination has been widely explored in psychoacoustics (Nelson and Kiester, 1978; Sinnott et al., 1985; Syka et al., 1996; Talwar and Gerstein, 1998, 1999; Shofner, 2000; Witte and Kipke, 2005; Walker et al., 2009), but few studies tested the detection of frequency deviants by single neurons (Ulanovsky et al., 2003; Malmierca et al., 2009; von der Behrens et al., 2009). SSA has already been shown to result in a change in frequency discrimination performance by single neurons (Ulanovsky et al., 2003; Malmierca et al., 2009) but this relationship has not been thoroughly explored.

The main goal of our study is to compare the relationships between frequency discrimination and SSA in two neuronal populations; one at the IC that it is already known to exhibit SSA

and the other at a lower auditory structure, the cochlear nucleus (CN) where SSA has not been explored thus far. For this purpose we assessed whether the probabilistic context affects frequency discrimination as judged by signal detection theory (Green and Swets, 1966) based on distributions of spike counts, and to what extent changes in frequency discriminability reflect the degree of SSA in these two stations. We show that SSA and the enhancement in neurometric frequency discrimination in the IC are strongly correlated and that both depend on the frequency separation and deviant probability in similar ways. Our results also demonstrated that SSA and context-dependent neuronal sensitivity are not present in CN supporting the hypothesis that SSA first emerge in non-lemniscal IC.

MATERIALS AND METHODS

SURGICAL PROCEDURES

Experiments were performed on 71 adult female rats (*Rattus norvergicus*, Rj: Long–Evans) with body weights between 160 and 270 g. All experimental procedures were carried out at the University of Salamanca with the approval of, and using methods conforming to the standards of, the University of Salamanca Animal Care Committee. Anesthesia was induced (1.5 g/kg, i.p., 20% solution) and maintained (0.5 g/kg, i.p. given as needed) with urethane. Urethane was chosen as an anesthetic because of its effects on multiple aspects of neural activity, including inhibition and spontaneous firing, are known to be less than those of barbiturates and other anesthetic drugs (Hara and Harris, 2002). The respiration was maintained artificially (SAR-830/P Ventilator) monitoring the end-tidal CO_2 level (CapStar-100). For this purpose, the trachea was cannulated and atropine sulfate (0.05 mg/kg, s.c.) was administered to reduce bronchial secretions. Body temperature was maintained at 38 ± 1°C by means of a heating blanket. Details of surgical procedures have been described previously (Hernández et al., 2005; Pérez-González et al., 2005; Malmierca et al., 2009; Antunes et al., 2010). The animal was placed inside a sound-attenuated room in a stereotaxic frame in which the ear bars were replaced by a hollow speculum that accommodated a sound delivery system.

ACOUSTIC STIMULI AND ELECTROPHYSIOLOGICAL RECORDING

Extracellular single unit responses were recorded from neurons in the IC and CN in two separate sets of experiments. For the IC recordings, a craniotomy was performed to expose the cerebral cortex overlying the IC and a tungsten electrode (1 – 2 MΩ) (Merrill and Ainsworth, 1972) was lowered through the cortex by means of a piezoelectric microdrive (Burleigh 6000 ULN). Neuron identification in the IC was based on stereotaxic coordinates, physiological criteria of tonotopicity, and response properties (Rees et al., 1997; LeBeau et al., 2001; Malmierca et al., 2003; Hernández et al., 2005; Pérez-González et al., 2005, 2006). An electrode dorsoventral penetration (with an angle of 20° from the frontal plane) through the central nucleus of the IC is identified by the stepwise progression from low to high frequencies (Malmierca et al., 2008) and by the constant presence of tonically firing units (Rees et al., 1997). Typical responses of the neurons in the cortices of the IC (i.e., dorsal, lateral, and rostral) are characterized by longer response latencies, predominantly on-phasic firing patterns and weaker tonic firing than those from the central nucleus. Cortical IC neurons commonly display broadly tuned, W-shaped, or other complex tuning curves (Lumani and Zhang, 2010; Geis et al., 2011; Duque et al., 2012) and a clear topographic organization of the frequencies along the dorsal cortex is not present (Malmierca et al., 2008; Lumani and Zhang, 2010). For the recording of CN neurons, part of the cerebellum was carefully aspirated to visually localize the dorsal cochlear nucleus (DCN). Glass micropipettes filled with 2 M NaCl (15 – 25 MΩ) or tungsten electrodes (1 – 2 MΩ) were advanced into the DCN. For some IC experiments and most of the CN recordings, an electrolytic lesion (10 – 15 μA for 10 – 15 s) was applied for subsequent histological verification of the recording site. Brains were fixed using a mixture of 1% paraformaldehyde and 1% glutaraldehyde diluted in 0.4 M phosphate buffer saline (0.5% $NaNO_3$ in PBS). After fixation, tissue was cryoprotected in 30% sucrose and sectioned in the coronal or sagital plane at a thickness of 40 μm on a freezing microtome. Slices were Nissl stained with 0.1% cresyl violet to facilitate identification of cytoarchitectural boundaries. The CN units were assigned to one of the two main divisions (dorsal or ventral) of the nucleus using as reference the standard sections from a rat brain atlas (Paxinos and Watson, 2007).

Acoustic stimuli were delivered through a sealed acoustic system (Rees, 1990; Rees et al., 1997) using two electrostatic loudspeakers (TDT-EC1) driven by two TDT-ED1 modules. Search stimuli were pure tones or noise bursts monaurally delivered under computer control using TDT System 2 hardware (Tucker-Davis Technologies) and custom software (Faure et al., 2003; Pérez-González et al., 2005, 2006; Malmierca et al., 2008). The output of the system at each ear was calibrated *in situ* using a ¼ inch condenser microphone (Brüel and Kjær 4136, Nærum, Denmark) and a DI-2200 spectrum analyzer (Diagnostic Instruments Ltd., Livingston, Scotland, UK). The maximum output of the TDT system was flat from 0.3 to 5 kHz (∼100 ± 7 dB SPL) and from 5 to 40 kHz (90 ± 5 dB SPL). The highest frequency produced by this system was limited to 40 kHz. The second and third harmonic components in the signal were 40 dB or more below the level of the fundamental at the highest output level (Hernández et al., 2005; Malmierca et al., 2009).

Action potentials were recorded with a BIOAMP amplifier (TDT), the 10× output of which was further amplified and bandpass-filtered (TDT PC1; f_c: 0.5 – 3 kHz) before passing through a spike discriminator (TDT SD1). Spike times were logged at one microsecond resolution on a computer by feeding the output of the spike discriminator into an event timer (TDT ET1) synchronized to a timing generator (TDT TG6). Stimulus generation and on-line data visualization were controlled with custom software. Spike times were displayed as dot rasters sorted by the acoustic parameter varied during testing.

Once a neuron was isolated, the monoaural frequency response area (FRA), i.e., the combination of frequencies and intensities capable of evoking a response, was obtained by an automated procedure with 5 stimulus repetitions at each frequency (from 0.5 to 40 kHz, in 20 – 30 logarithmic steps) and intensity step (steps of 10 dB) presented randomly at a repetition

rate of 4 Hz. The stimuli used to generate the tuning curves were pure tones with duration of 75 ms. The neuronal response to the combination of frequencies and intensities was plotted using MATLAB software (Mathworks, Inc.) and the best frequency (BF) and threshold for each neuron were identified.

STIMULUS PRESENTATION PARADIGMS

For all neurons, stimuli were presented in an oddball paradigm similar to that used to record mismatch negativity responses in human studies (Näätänen, 1992), and more recently in the cat auditory cortex (Ulanovsky et al., 2003, 2004), rat IC (Malmierca et al., 2009; Pérez-González et al., 2012) and auditory thalamus (Antunes et al., 2010; Antunes and Malmierca, 2011). Briefly, we presented two stimuli consisting of pure tones at two different frequencies (f_1 and f_2), that elicited a similar firing rate and response pattern at the same level of 10 – 40 dB SPL above threshold. Both frequencies were within the excitatory response area previously determined for the neuron. A train of 400 stimulus presentations containing both frequencies was delivered in three different sequences (**Figure 1**). The repetition rate of the train of stimuli for the IC neurons was 4 Hz, as it has been previously demonstrated to be suitable to elicit SSA in IC neurons of the rat (Malmierca et al., 2009). In the CN recordings, we explored repetitions rates of 4, 8, 12, and 20 Hz. Due to the different repetition rates used, the duration of the pure tones was 75 ms for the IC recordings (Hernández et al., 2005) and 25 ms for the CN recordings (in a few recordings at 4 and 8 Hz, tones lasted 75 ms as well), including a 5 ms rise/fall ramp for both cases.

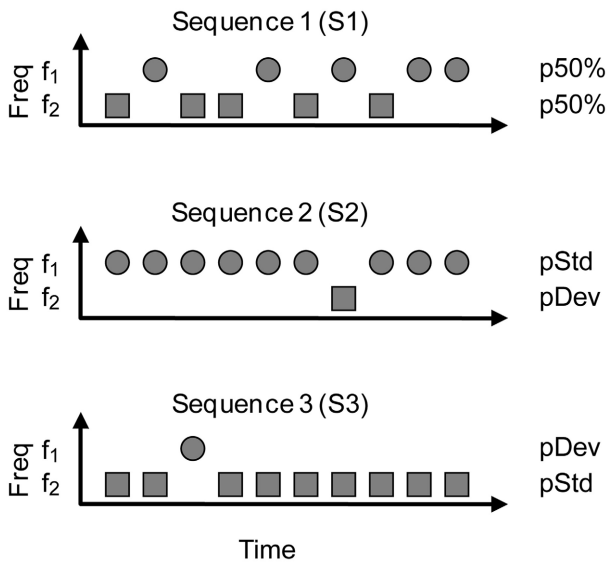

FIGURE 1 | The oddball stimulation paradigm. Two frequencies (f_1, f_2) were presented pseudo-randomly with different probabilities of occurrence. In Sequence 1 (S1), f_1, and f_2 occurred with equal probability (p50%), which served as a control condition. This condition is useful to see the neuron's tuning to the frequencies chosen. For the oddball condition, the probability of the frequencies was modified such that one frequency (f_1, circles) was the standard tone, occurring with high probability, and the other (f_2, squares) was the deviant tone, with low probability of occurrence (Sequence 2, S2). The probabilities of f_1 and f_2 were reversed in Sequence 3 (S3) in order to have each frequency presented as deviant and standard. We tested two probabilities for the deviant tone (pDev), 30 and 10%, so the corresponding probabilities for the standard (pStd) were 70 and 90%, respectively.

As shown in **Figure 1**, in Sequence 1 (S1) both frequencies were presented with the same probability of occurrence (equiprobable condition; $p(f_1) = p(f_2) = 50\%$). In Sequence 2 (S2), one frequency (f_1) was presented as the standard (i.e., high probability within the sequence: 90 or 70%); interspersed randomly among the standards were the deviant stimuli (i.e., low probability: 10 or 30%, respectively) at the second frequency (f_2). After obtaining one data set, the relative probabilities of the two stimuli were reversed, with f_2 as the standard and f_1 as the deviant (S3). Sequences 2 and 3 constitute what we refer to as an oddball condition. The responses to the standard and deviant stimuli were normalized to spikes per stimulus, to account for the different number of presentations in each condition, because of the different probabilities. We tested several frequency separations between f_1 and f_2, expressed as frequency contrast $\Delta f = (f_2 - f_1)/(f_2 \times f_1)^{1/2}$ (Ulanovsky et al., 2003). As the frequency pairs were chosen to evoke similar firing rates in responses to both tones, Δf ranged from 0.02 to 3. The Δf values were grouped into three intervals: $\Delta f \leq 0.07$, $0.07 < \Delta f \leq 0.2$ and $\Delta f > 0.2$ (≤ 0.101, $0.101 < \Delta f \leq 0.288$ and $\Delta f > 0.288$ octaves, respectively), in order to approximate to the values used in other studies, i.e., $\Delta f = 0.04$, 0.10, and 0.37 (Ulanovsky et al., 2003, 2004; Malmierca et al., 2009). The same paradigm was repeated changing the probability of the deviant tone (pDev = 10%, 30%) or the Δf. For the CN experiments, we only tested pDev = 10% and $\Delta f = 0.1$. The presentation of sequences at different deviant probabilities and at different repetition rates was randomized.

DATA ANALYSIS

We measured the sharpness of the FRA of IC neurons calculating the bandwidth (BW) and Q-values at 10 and 40 dB SPL above the threshold as in our previous work (Hernández et al., 2005; Malmierca et al., 2009). The BW at n dB expresses the difference in kHz between the lower (F_L) and upper (F_U) frequencies of the FRA ($BW_n = F_U - F_L$). The Q-value is calculated as the characteristic frequency (CF) divided by the BW at n dB above threshold ($Q_n = CF/BW$).

The amount of SSA was quantified by two indices that have been used in previous studies (Ulanovsky et al., 2003, 2004; Malmierca et al., 2009; Antunes et al., 2010; Antunes and Malmierca, 2011; Pérez-González et al., 2012). The first index was the Frequency-Specific SSA Index (SI) defined as: $SI(f_i) = [d(f_i) - s(f_i)]/[d(f_i) + s(f_i)]$, where $i = 1$ or 2 and $d(f_i)$ and $s(f_i)$ are responses (as normalized spike counts) to frequency f_i when it was deviant or standard, respectively. The second one was the Common-SSA Index (CSI) defined as $CSI = [d(f_1) + d(f_2) - s(f_1) - s(f_2)]/[d(f_1) + d(f_2) + s(f_1) + s(f_2)]$, where $d(f)$ and $s(f)$ are responses to each frequency f_1 or f_2 when they were the deviant (d) or standard (s) stimulus, respectively. These indices reflect the extent to which the neuron responds more strongly to the frequencies when they are deviant compared to when they are standard. The possible SI and CSI values range from −1 to +1,

being positive if the response to the deviant stimulus is greater and negative if the response to the standard stimulus is greater.

To estimate the neuronal sensitivity we performed a receiver operating characteristic (ROC) analysis (Tanner and Swets, 1954; Cohn et al., 1975; Fawcett, 2006; for a review of the use of ROC in psychometric and neurometric data analysis, see Stüttgen et al., 2011). This analysis has been previously used to measure the ability of CN units to signal changes in intensity (Shofner and Dye, 1989) and the sensitivity of IC units to interaural-time differences and binaural correlation (Skottun et al., 2001; Shackleton et al., 2003, 2005; Gordon et al., 2008). It is assumed that when different stimuli elicit different firing rates the response of a neuron provides the basis for discriminating between them. However, there is also a substantial variability in the responses to each stimulus, so the distributions of firing rates to similar stimuli overlap, and thus discrimination based upon firing rate will only be correct on a proportion of trials. The ROC analysis allows us to calculate the performance of the best possible discriminator between the two frequencies which is based on spike counts only. This discriminator is a function of the two probability distributions of spike counts in response to the two stimuli.

The ROC plots the probability of correct detection of f_2 against the probability of "false alarm" detection of f_2 when f_1 occurred. Since detection is assumed to be based on spike counts only, trials have to be classified to one or the other frequency based solely on the evoked spike count. Thus, any discriminator between the two frequencies consists, in practice, of a list of spike counts that are assigned to frequency f_1, with all other spike counts assigned to frequency f_2 (we do not need to consider so-called "randomized rules" here, because we are only interested in the integral of the ROC, see below). In many studies, ROCs are calculated by a threshold on spike counts: all spike counts below the threshold are assigned to one frequency, and those above the threshold to the other. However, the lemma of Neyman and Pearson (Maris, 2012) requires spike counts to be assigned to frequencies based on their likelihoods, the ratio $p(n|f_2)/p(n|f_1)$. For an optimal decision rule, a threshold is selected, and all spike counts whose likelihood is larger than that threshold are assigned to f_2 (with the others assigned to f_1). The probabilities of correct decision and false alarm for this decision rule can then be calculated in a straightforward manner. The ROC is obtained by calculating these probabilities while varying the threshold.

Then, we calculated the area under the ROC curve (AUC) as an estimate of the neural discriminability of frequency. The AUC corresponds to the probability of correct stimulus detection expected from an ideal observer in a two-alternative forced-choice psychophysical task (Green and Swets, 1966; Fawcett, 2006). Thus, sensitivity measured as AUC varies between 0.5 and 1, where 0.5 occurs when the spike count distributions for frequencies f_1 and f_2 are identical, and 1 indicates complete separation of the distributions. To compensate for sampling bias, we corrected each AUC value by performing 10,000 permutations of the original spike count distributions, assigned randomly to either f_1 or f_2, calculated the corresponding AUCs, and subtracted their mean value from the original AUC. Due to this correction some of the AUC values we report are smaller than 0.5. We also used the permutations test to estimate the probability of the AUC being significantly larger than 0.5. This way, we obtained one AUC value for the equiprobable condition (S1) and two AUC values for the oddball conditions (S2, S3). We used the mean AUC of S2 and S3 for the analyses instead of the maximum value as in previous works (Ulanovsky et al., 2003; Malmierca et al., 2009), in order to avoid an upward bias.

The CSI values were tested against zero by bootstrapping (1000 samples) in order to estimate a 95% confidence interval. Typically, CSI values smaller than 0.1 were not statistically different from zero (85% of all cases with CSI < 0.1 and 15% of the cases with CSI > 0.1). Thus, CSI values within the range of -0.1 to 0.1 were considered be due to random fluctuations in spike counts. This procedure provided a CSI cutoff comparable to other values previously set with different criteria (e.g., CSI $= 0.18$ for auditory thalamus of the rat; Antunes et al., 2010). It may be somewhat smaller than the cutoff in thalamus because of the lower variability in the responses of IC neurons (e.g., Chechik et al., 2006).

RESULTS

To investigate how frequency sensitivity is affected by the stimulation context we recorded the response of 224 well isolated single units in the IC and 51 units in the CN using an oddball paradigm. The frequency contrast ($\Delta f \leq 0.07$, $0.07 < \Delta f \leq 0.2$, $\Delta f > 0.2$) and probability of the deviant tone (pDev $= 30\%$ or 10%) were varied in IC recordings, and the repetition rate (4, 8, 12, and 20 Hz) in the CN. Additionally, an equiprobable context ($p(f_1) = p(f_2) = 50\%$) was tested as control condition in both sets of experiments.

NEURONS IN THE IC SHOW DIFFERENT DEGREES OF SSA AND STIMULUS DISCRIMINABILITY

As might be expected from our previous studies (Pérez-González et al., 2005; Malmierca et al., 2009), neurons in the IC exhibited different degrees of SSA. **Figure 2** shows the distribution of the CSI under different stimulus conditions in the current sample. The distributions of CSI are skewed toward positive values, and their medians are significantly different from zero (Signed Rank Test; $p < 0.05$) regardless of the condition tested (**Figure 2**). Positive CSI values reflect a stronger response to the deviant tone than to the standard one. The effects of frequency separation and deviant probability were tested using a Two-Way ANOVA on $\Delta f \times$ probability. There was a main effect of $\Delta f (F_{(2,\,489)} = 18$, $p = 0)$ and of probability condition $[F_{(1,\,489)} = 39,\ p = 0]$. The interaction just failed to reach significance $[F_{(2,\,489)} = 2.5$, $p = 0.08]$. *Post-hoc* comparisons showed that the most positive CSI values were observed for deviant probability of 10% at the two highest frequency contrast intervals; $0.07 < \Delta f \leq 0.2$ and $\Delta f > 0.2$. For the 10% probability condition, the CSIs increased significantly with increased frequency separation: $\mathrm{CSI}_{10\%/\Delta f > 0.2} > \mathrm{CSI}_{10\%/0.07 < \Delta f \leq 0.2} > \mathrm{CSI}_{10\%/\Delta f \leq 0.07}$. On the other hand, the *post-hoc* comparisons did not show a significant difference between the average CSIs in the 30% condition and different frequency separations. There was also a significant difference due to changes in deviant probability for the two highest frequency separation intervals: $\mathrm{CSI}_{10\%/0.07 < \Delta f \leq 0.2} > \mathrm{CSI}_{30\%/0.07 < \Delta f \leq 0.2}$; $\mathrm{CSI}_{10\%/\Delta f > 0.2} > \mathrm{CSI}_{30\%/\Delta f > 0.2}$. This trend was emphasized by

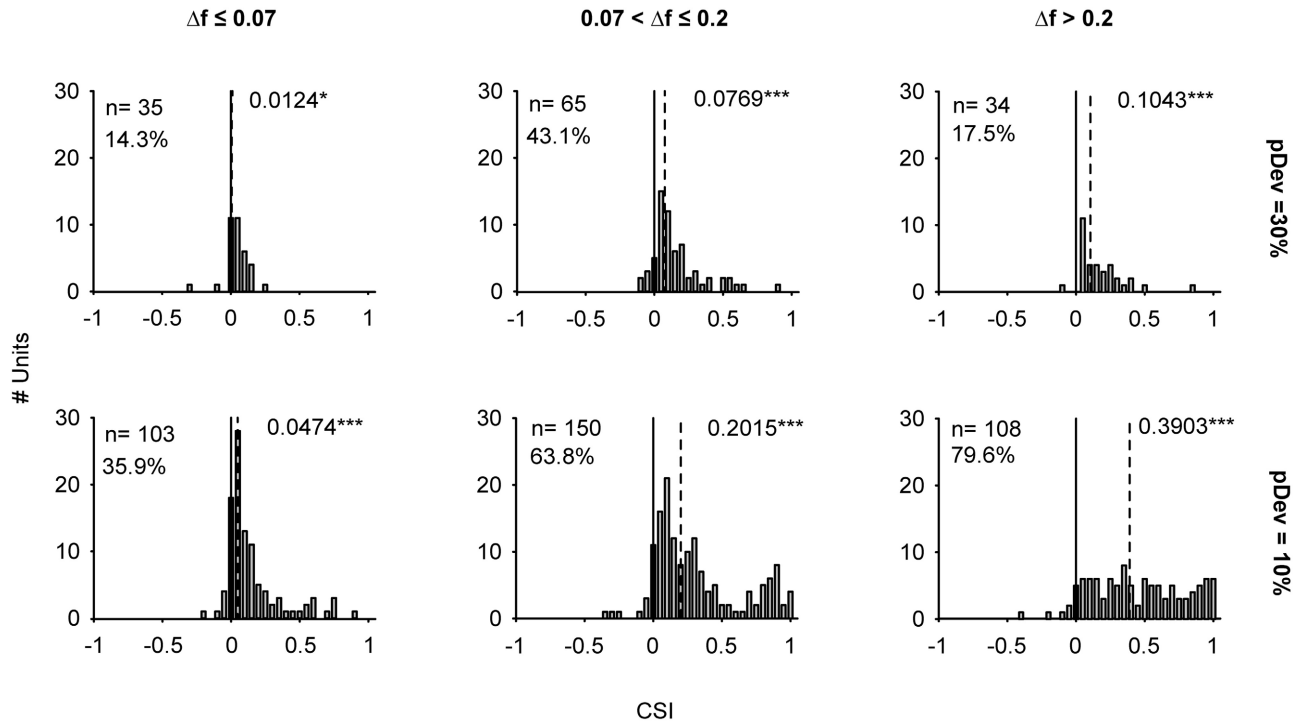

FIGURE 2 | Distribution of stimulus-specific adaptation indices of IC neurons. Histograms of the common SSA index (CSI) displayed according to the frequency separation intervals (columns: $\Delta f \leq 0.07$, $0.07 < \Delta f \leq 0.2$, $\Delta f > 0.2$) and the probability of the deviant tone (rows: pDev = 30 and 10%). The CSI was calculated from the responses recorded in S2 and S3. A CSI = 0 indicates an equal neuronal response when the tones were presented as deviant or standard, while positive and negative values represent higher firing rates when the tones were deviant or standard, respectively. For each stimulus condition the CSI values were tested against zero (solid line). The numbers next to the dashed line indicate the value of the median and the statistical significance (Signed Rank Test; $^*p < 0.05$, $^{***}p < 0.001$). The distributions moved toward positive values when Δf was larger and pDev smaller. The percentages indicate the amount of neurons with CSI > 0.1.

the higher percentage of neurons with CSI values larger than 0.1 when deviant probability was 10% compared to 30% (percentages indicated in **Figure 2**). From the six groups, only seven neurons (3.1%) showed CSI ≤ -0.1.

Examples of individual IC neurons exhibiting different CSI values are shown in **Figures 3–5**. The deviant probability for the three cases was 10% and the frequencies tested (f_1, f_2) in these examples were separated by 0.144 octaves ($\Delta f = 0.1$) around its BF at an intensity of 10 – 50 dB above threshold.

Figure 3 illustrates a neuron with a CSI not significantly different from zero (CSI = 0.04; $p > 0.05$). This neuron had a narrow FRA with a narrow bandwidth both at 10 and 40 dB SPL above its threshold (BF = 8.8 kHz, $Q_{10} = 5.62$ and $Q_{40} = 1.22$) (**Figure 3A**). It had an onset firing pattern (**Figure 3B**) and showed a mixed/complex rate-level function (**Figure 3C**). The responses elicited in the equiprobable condition (S1) and oddball condition (S2 and S3) are shown as dot rasters (**Figure 3D**) as well as the peristimulus time histograms (PSTH) (**Figure 3E**). **Figure 3F** displays the corresponding spike-count distributions and the ROC curve is shown in **Figure 3G**. This neuron displayed a very robust and reliable response across the 400 stimulus presentations. In consequence, its spike count distributions were very different from Poisson distributions: while the average spike count is about 1, the probability of having zero spike counts is much smaller than that of either frequency evoking a single spike (for a Poisson distribution, these two probabilities should be approximately equal when the mean spike count is close to 1). The spike-count distributions for f_1 and f_2 were very similar, overlapping almost completely (**Figure 3F**), although the average spike count was slightly larger for f_2 than for f_1. The large overlap between these distributions resulted in AUC values very close to 0.5, but the very low variability resulted in an AUC that was significantly larger than 0.5 in the equiprobable condition. When f_2 was the deviant, this difference was maintained, but when f_1 was the deviant, the average spike count in response to f_2 decreased slightly, enough to render the AUC not significantly different from 0.5 (AUC(S1) = 0.55, $p = 0$; AUC(S2) = 0.55, $p = 0.01$; AUC(S3) = 0.49, $p = 0.65$). Thus, the frequency discrimination capability of this neuron was poor in an equiprobable context and did not improve in an oddball stimulation context, consistent with its low CSI.

By contrast, neurons with high CSI values fired significantly differently in response to deviant and standard tones in the oddball condition. The neuron illustrated in **Figure 4** had a CSI = 0.88 ($p < 0.05$). It was tuned to a wide range of frequencies (**Figure 4A**) reflected by its low Q-values (BF = 10 kHz, $Q_{10} = 0.74$ and $Q_{40} = 0.27$). This neuron also had an onset firing pattern, although it showed a large variability of first

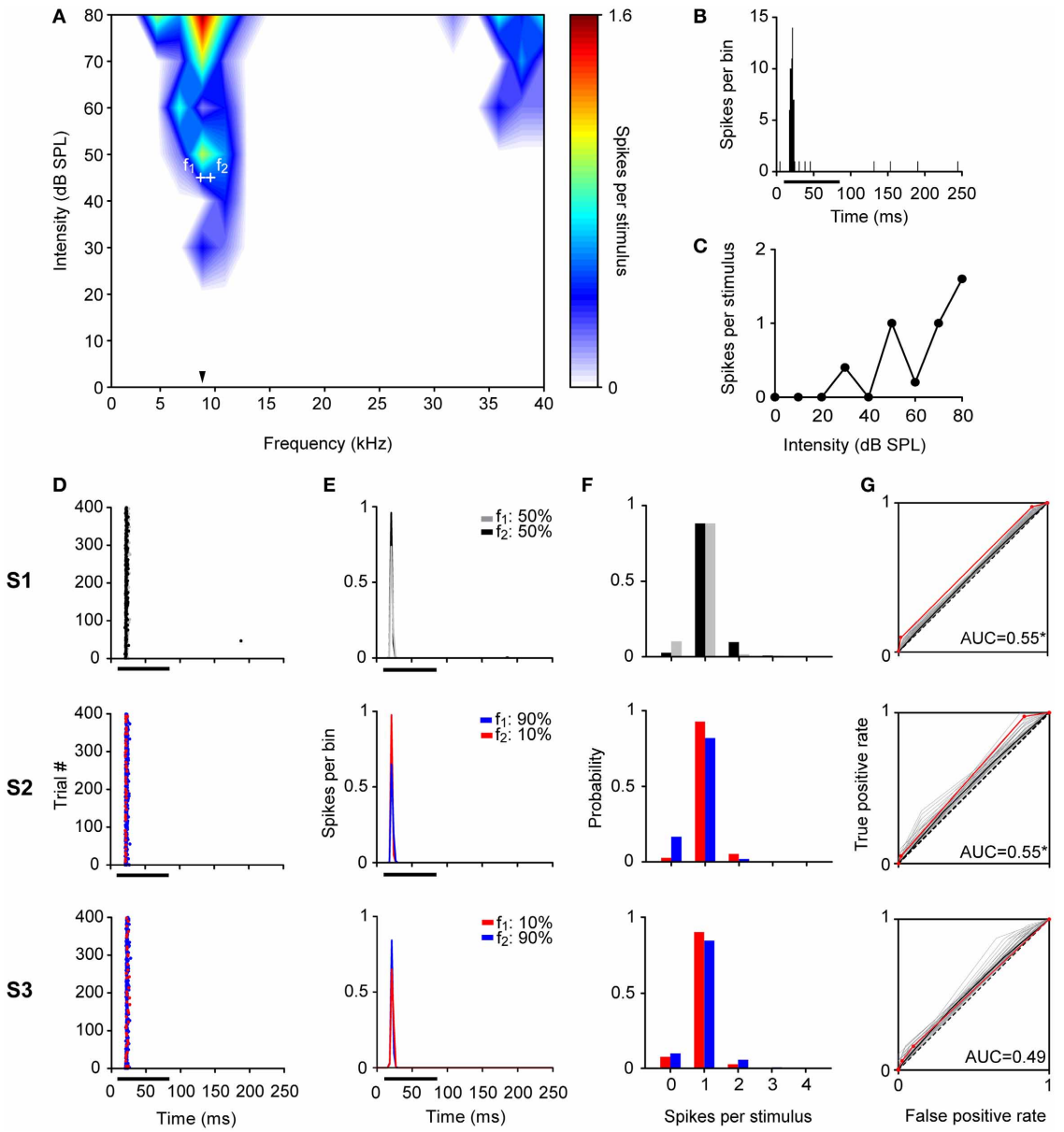

FIGURE 3 | Example of a non-adapting neuron in the IC. (A) Narrow FRA in color code for response magnitude. The tested frequencies (f_1: 8.7 kHz, f_2: 9.6 kHz, white crosses) were chosen around the BF (8.8 kHz) (arrowhead), at 45 dB SPL. **(B)** PSTH of the accumulated response to all the frequencies (0.5 – 40 kHz) and intensities (0 – 80 dB SPL) presented (1 ms bins). **(C)** Rate-level function at BF. **(D–G)** The responses of the neuron for each pair of stimuli for each of the three sequences (S1, S2, S3) are shown as dot raster plots **(D)**, PSTH (3 ms bins) **(E)**, spike probability distributions **(F)**, and ROC curves **(G)**. In the dot raster each dot represents the occurrence of a spike. The black bar under the PSTH and dot raster plots indicates the duration of the stimulus (75 ms). The probability of each frequency for each sequence is indicated on the upper left of the **(E)** panels. In the ROC curves **(G)** the dashed line corresponds to random guessing or no stimulus discrimination (AUC = 0.5), indicating complete overlap of the spike probability distributions. The red line represents the ROC curve calculated using the recorded data, the curves plotted in gray were obtained with the permutation method of the original spike count distributions, and the black line is represents the mean ROC curve of permutations. A total of 10,000 permutations were calculated, but for visual clarity only 100 curves are displayed. For each ROC curve, the area under the ROC curve (AUC) is shown corresponding to the original AUC value minus the mean AUC from permutations, as well as, the significance value for AUC > 0.5 (Permutation test; $^*p < 0.05$). The repetition rate was 4 Hz and the frequency separation was 0.141 octaves. This neuron did not show SSA (CSI = 0.04, Bootstrapping; $p > 0.05$), displaying a very similar response to f_1 and f_2 across the three sequences regardless the probability of each tone.

spike latency (FSL) (**Figure 4B**) and had a non-monotonic rate-level function (**Figure 4C**). During the equiprobable presentation of the tones (S1), this neuron adapted its response to both frequencies, and had a very low probability to respond at all ($P_{\geq 1sps} = 0.005$). In the oddball condition, responses to the standard tone remained extremely sparse, but deviant trials did evoke a few spikes with higher probability. Thus, the overlap between the spike-count distributions was reduced

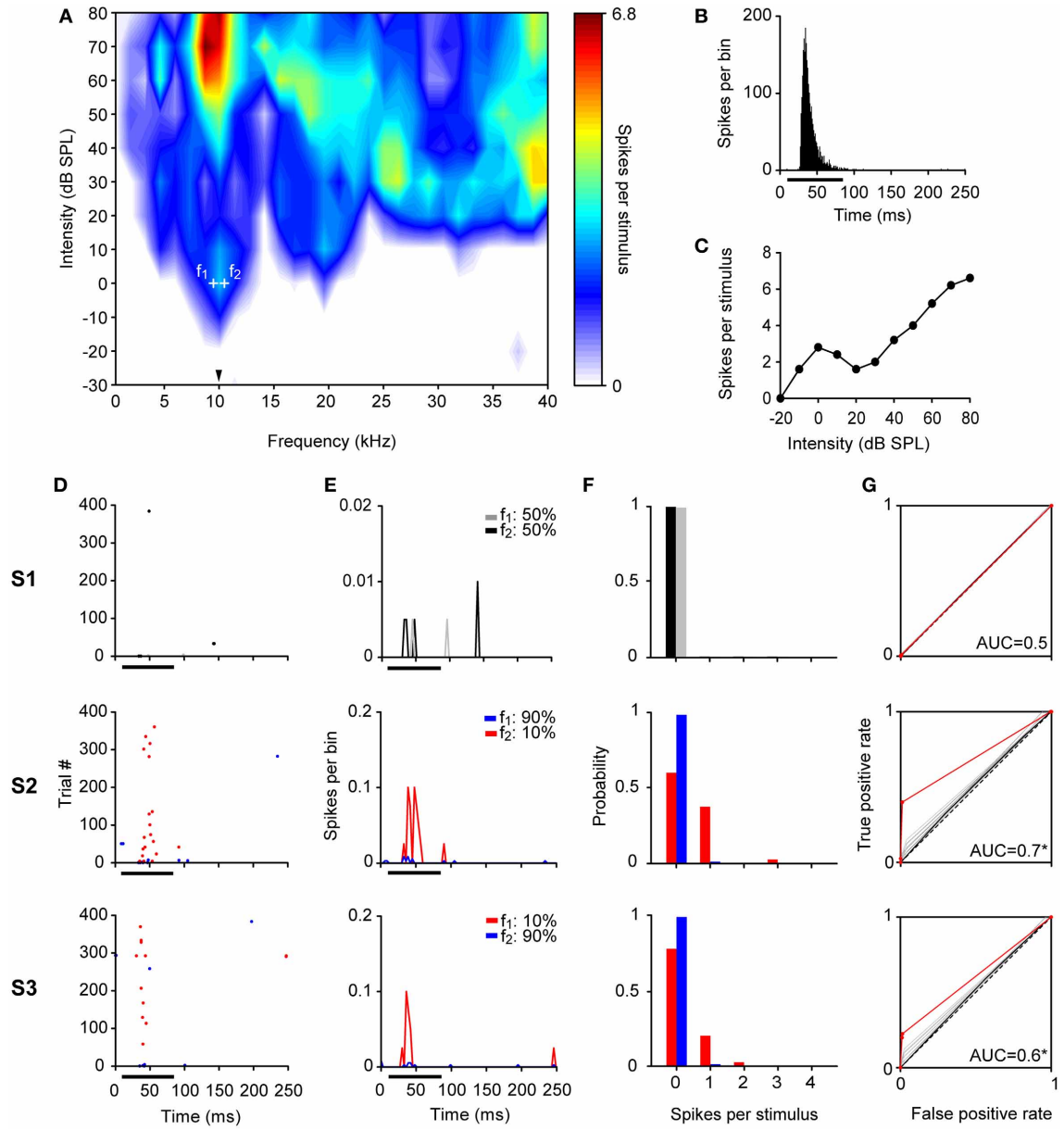

FIGURE 4 | Example of an adapting neuron in the IC. (A) FRA of a broadly tuned neuron with a BF of 10 kHz (arrowhead). The frequencies tested are indicated by the white crosses around the BF (f_1: 9.5 kHz, f_2: 9.6 kHz), at 0 dB SPL. **(B–G)** Same format as in **Figure 3**. This neuron showed strong SSA (CSI = 0.88, Bootstrapping; $p < 0.05$) reducing its firing to the high probability tone in S2 and S3 while still responding to the low probability one across most stimulus presentations. This differential firing is reflected in an AUC larger than 0.5 (Permutation test; $^*p < 0.05$) in oddball sequences (S2 and S3).

substantially (probability of firing $\geq$ 1 sps in response to the deviant/standard was 0.4/0.017 and 0.23/0.014 for S2 and S3, respectively). As a result, the AUCs for the oddball conditions were higher than for the equiprobable condition [AUC(S1) = 0.5, $p = 0.5$; AUC(S2) = 0.7, $p = 0$; AUC(S3) = 0.6, $p = 0$].

The examples shown in **Figures 3** and **4** are extreme cases, and neurons in the IC showed a continuous distribution of SSA as depicted in **Figure 2**. For example, **Figure 5** illustrates a partially-adapting neuron (CSI = 0.5; $p < 0.05$) tuned to high frequencies (**Figure 5A**) and with a non-monotonic rate-level function (**Figure 5C**). The bandwidth of the FRA increased between 10 and 40 dB above threshold, respectively (BF = 29.9 kHz, $Q_{10} = 7.81$ and $Q_{40} = 2.25$). This neuron showed a poor, although significant discrimination capability at the equiprobable condition [AUC(S1) = 0.57, $p = 0$] which improved in the oddball condition [AUC(S2) = 0.61, $p = 0$; AUC(S3) = 0.76, $p = 0$].

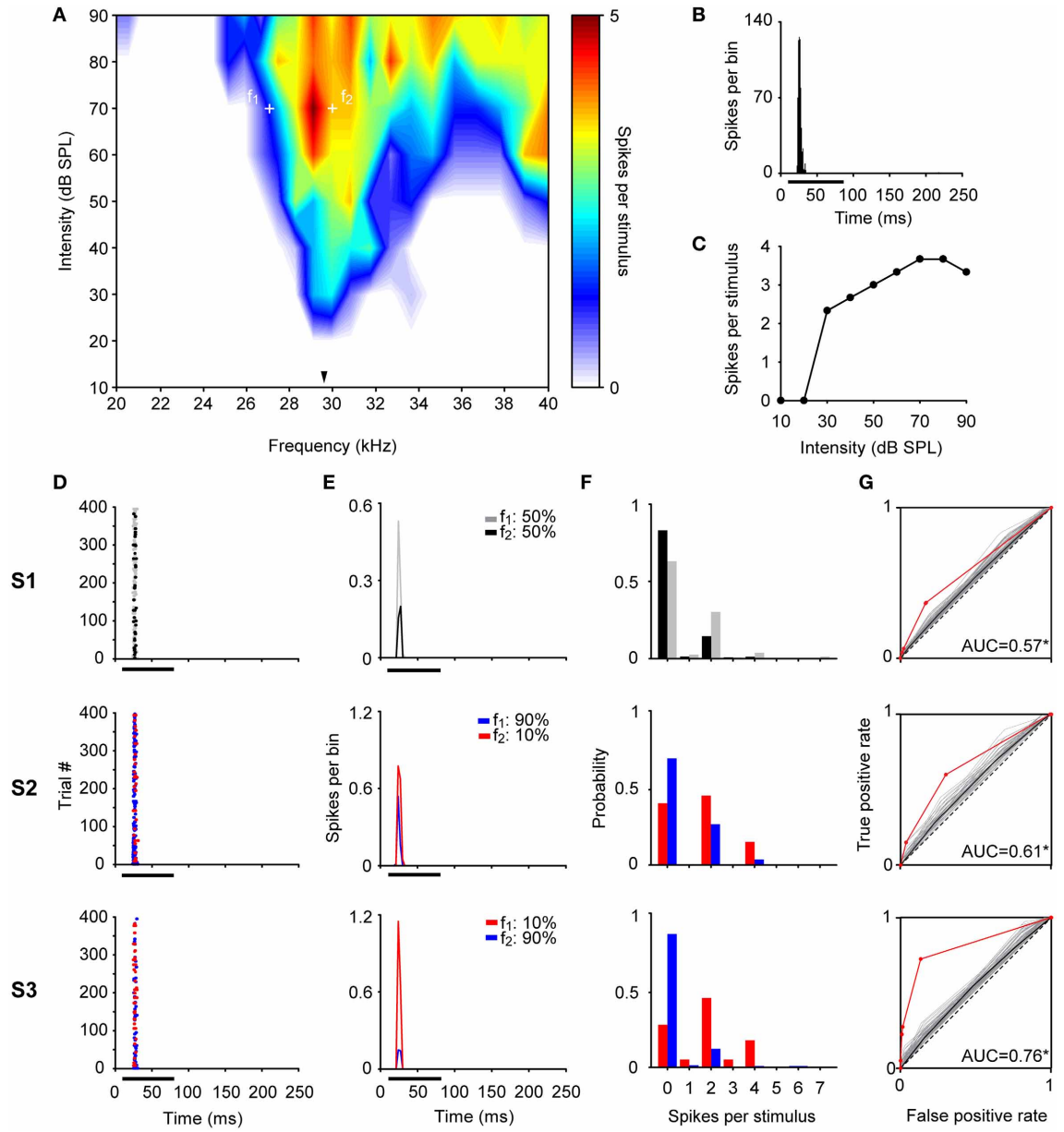

FIGURE 5 | Example of a partially-adapting neuron in the IC. (A) FRA from a neuron with a BF of 29.9 kHz (arrowhead). The frequencies tested were f_1: 27.1 kHz and f_2: 30 kHz, at 70 dB SPL. **(B–G)** Same format as in **Figure 3**. This neuron displayed a significant level of SSA (CSI = 0.5, Bootstrapping; $p < 0.05$), responding to both tones across the 400 stimulus trials. Although, the neuron displayed significant discriminability in the equiprobable condition (S1, AUC = 0.57) (Permutation test; $^*p < 0.05$), this was improved under the oddball sequences (S2, AUC = 0.61; S3, AUC = 0.76).

FREQUENCY DISCRIMINABILITY DEPENDS ON STIMULUS CONTEXT IN THE IC

IC neurons were able to discriminate very similar frequencies even when both tones had the same probability of occurrence ($p(f_1) = p(f_2) = 50\%$). The tested frequencies were selected online to evoke similar response magnitudes. Nevertheless, the noise in the estimation of response rates resulted in some imbalance between the responses to the two frequencies, leading to significant discriminability between them. The discriminability elicited under the equiprobable condition ($AUC_{50\%}$) across the three Δf intervals significantly differed from a mere random discrimination (AUC = 0.5, Signed Rank Test; $p < 0.001$) (**Figure 6A**). Furthermore, more than half of the neurons from each frequency separation group had $AUC_{50\%}$ significantly larger than 0.5 ($p < 0.05$) (**Figure 6A**, indicated in percentage). In a substantial number of cases, $AUC_{50\%}$ exceeded 0.71 (24.1, 23.2, and 41.6% for the three Δf groups), the generally accepted definition of a threshold (Green and Swets, 1966). Neurons with AUCs above this threshold for the smallest frequency contrast interval ($\Delta f \leq 0.07$) had narrower bandwidths ($Q_{10} = 6.23 \pm 5.43$)

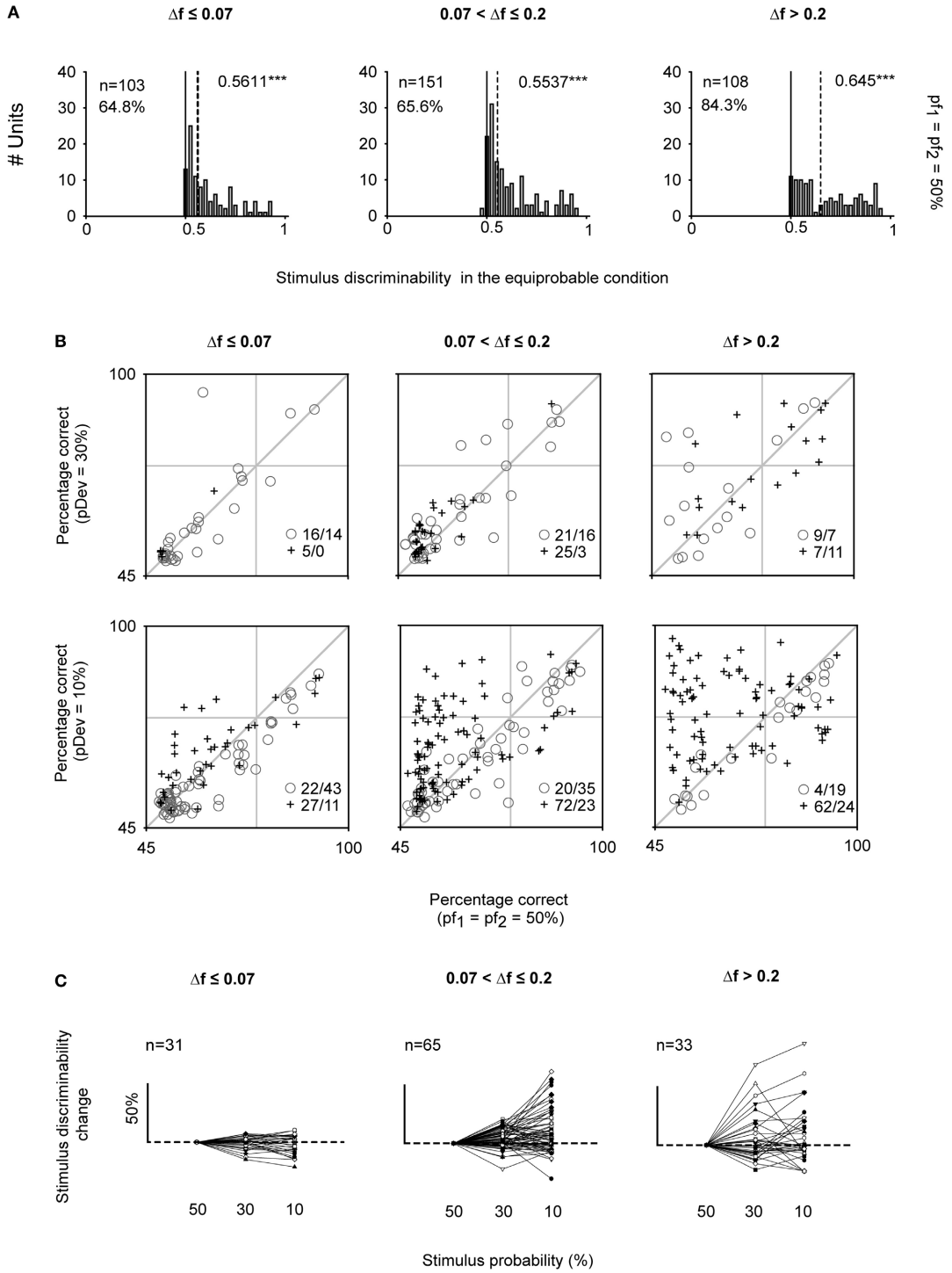

FIGURE 6 | Neurometric performance under equiprobable and oddball conditions of IC neurons. (A) Distributions of the AUC values for the equiprobable condition ($AUC_{50\%}$) indicating the median (dashed line) significantly differs from 0.5 (Signed Rank Test; $^{***}p < 0.001$). The percentage of neurons whose $AUC_{50\%}$ was higher than 0.5 is indicated for each panel (Permutation test; $p < 0.05$). **(B)** Scatter plots showing the neurometric performance for frequency discrimination expressed as percentage correct under the oddball condition (rows: pDev = 30, 10%) versus the equiprobable condition ($pf_1 = pf_2 = 50\%$), for each frequency contrast interval (columns: $\Delta f \leq 0.07$, $0.07 < \Delta f \leq 0.2$, $\Delta f > 0.2$). Separately are represented the neurons with CSI $\leq$ 0.1 (gray circles) and CSI $>$ 0.1 (dark crosses). For the oddball condition, the percentage correct corresponds to the mean AUC value obtained from S2 and S3. The number of neurons above and below the diagonal line (equal performance in both conditions) is indicated by the inset on the bottom right of each panel. **(C)** Sensitivity curves of individual neurons expressed as percentage of change elicited when pDev = 10% and 30% regarding the $pf_1 = pf_2 = 50\%$ condition.

that the rest of neurons ($Q_{10} = 3.53 \pm 5.47$) (Signed Rank Test; $p < 0.05$).

To address the central question of this paper, **Figure 6B** compares the percent correct (as estimated by AUC) in the oddball and equiprobable condition for each neuron. For the oddball condition, we used the mean discriminability ($AUC_{oddball}$) from the values elicited in the two oddball sequences since there was not significant difference in the AUC values elicited in S2 and S3 (Rank Sum Test; $p > 0.05$). Neurons whose discriminability was unaffected in the oddball condition fell along the diagonal line. Neurons under the diagonal line showed a better discriminability in the equiprobable condition. By contrast, neurons that improved their discriminability in the oddball paradigm were located above the diagonal. Neurons with CSI > 0.1 are marked by crosses, the others are marked by circles. When pDev = 10%, there was a larger proportion of neurons with CSI > 0.1 than neurons with CSI ≤ 0.1 that showed improved discriminability in the oddball condition ($\chi^2 = 58.6$, df = 1, $p < 0.001$), but these proportions did not depend on frequency separation ($\chi^2 = 5.4$, df = 2, $p = 0.07$). For this probability condition, the AUCs of neurons with CSI ≤ 0.1 were slightly, although significantly, smaller in the oddball than in the equiprobable condition ($^{46}/_{96}$, neurons above and below the bisecting line, respectively, for all frequency separation classes together). This effect was due presumably to the poorer sampling of the spike count histograms for the deviant stimuli in the oddball condition. On the other hand, $AUC_{oddball}$ increased substantially for neurons with CSI > 0.1 ($^{161}/_{59}$ neurons above and below the bissecting line, respectively). The increase resulted in many neurons whose frequency discrimination was below threshold in the equiprobable condition ($AUC_{50\%} < 0.71$) and that exceed threshold in the oddball conditions ($AUC_{oddball} > 0.71$). Within this subset of neurons, there are cases in which the neurometric performance reached values close to 100% correct in the oddball condition. Such cases were much more common at the largest frequency contrasts ($0.07 < \Delta f \leq 0.2$ and $\Delta f > 0.2$). For pDev = 30%, the discriminability did not change consistently relative to the equiprobable condition, and proportions of neurons with slight increase or decrease in discriminability were as common in the different frequency difference classes ($\chi^2 = 5.4$, df = 2, $p = 0.07$) and among CSI classes ($\chi^2 = 3.9$, df = 1, $p = 0.05$).

In order to verify whether the same trend was observed at the level of single neurons, we obtained the individual "sensitivity curves" for the neurons that were tested under all probabilities conditions (50, 30, and 10%) and for the same frequency pairs (**Figure 6C**). The discriminability increment was expressed as the percentage of change in $AUC_{oddball}$ relative to the discriminability displayed under the equiprobable condition ($AUC_{50\%}$). These sensitivity curves revealed a considerable diversity in the neuronal performance. Both neuron identity and stimulus probability had a significant effect on the discrimination capability for the intermediate Δf interval [Two-Way ANOVA on stimulus probability × neuron, significant main effect of stimulus probability: $F_{(2, 128)} = 7.7$, $p < 0.001$], but for the smallest and largest Δf the main effect of stimulus probability was not significant.

Since some neurons under the equiprobable condition showed significant discriminability values that exceeded a mere random response (**Figure 6A**), we took into account this neuron-specific tuning. We calculated the *discriminability enhancement index* (DEI) as the difference between the discriminability elicited in the oddball condition and that elicited in the equiprobable one ($DEI = AUC_{oddball} - AUC_{50\%}$). DEI ranges from −0.5 to 0.5, with positive values indicating an improvement in discriminating two stimuli under an oddball context. The comparison of the mean population values of DEI across all stimulus combinations (Two-Way ANOVA, stimulus probability × Δf) demonstrated that it was affected by the frequency separation [$F_{(2, 489)} = 5.72$, $p < 0.01$] but not by stimulus probability [$F_{(1, 489)} = 3.71$, $p = 0.055$], with no interaction between those factors [$F_{(2, 489)} = 2.1$, $p = 0.12$] (**Figure 7**).

IC NEURONS WITH HIGH SSA SHOWED A GREATER DISCRIMINABILITY ENHANCEMENT UNDER ODDBALL CONDITIONS

Finally, we analyzed the relationship between the two metrics used to quantify the neuronal responses in order to explore whether or not the change in stimulus discrimination can be predicted by their SSA index. This analysis demonstrated a strong positive correlation between the degree of adaptation (CSI) and the enhancement in the frequency discriminability (DEI) shown by neurons under the condition with the lowest deviant probability, that is, when pDev = 10% (Spearman's rho; $p < 0.001$) (**Figure 8**). The great majority of neurons with CSI < 0.1 had discrimination indices clustered around the origin (gray circles). By contrast, most neurons with CSI > 0.1 (crosses) had a positive DEI, indicating that adapting neurons had better frequency

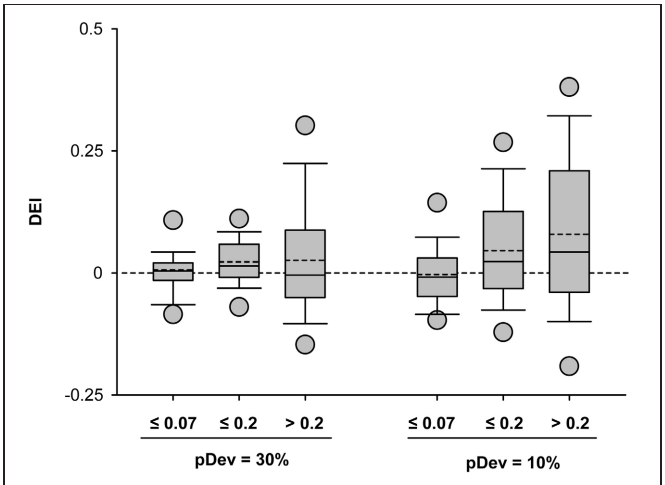

FIGURE 7 | Stimulus discriminability enhancement of IC neurons across different stimulus conditions. Box plots of the discriminability enhancement under the oddball condition (DEI) showing the mean (dashed line) and the median (solid line) values, as well as, the 5th and 95th outliers. All the mean values were positive (except for the $^{10\%}/_{\Delta f \leq 0.07}$ condition), reflecting a better stimulus discrimination when one of the frequencies is presented as a deviant tone, that is, with low probability of ocurrence (30 or 10%). The DEIs were only affected by the frequency separation [$F_{(2, 489)} = 5.72$, $p < 0.01$] (Two-Way ANOVA, deviant probability × frequency separation).

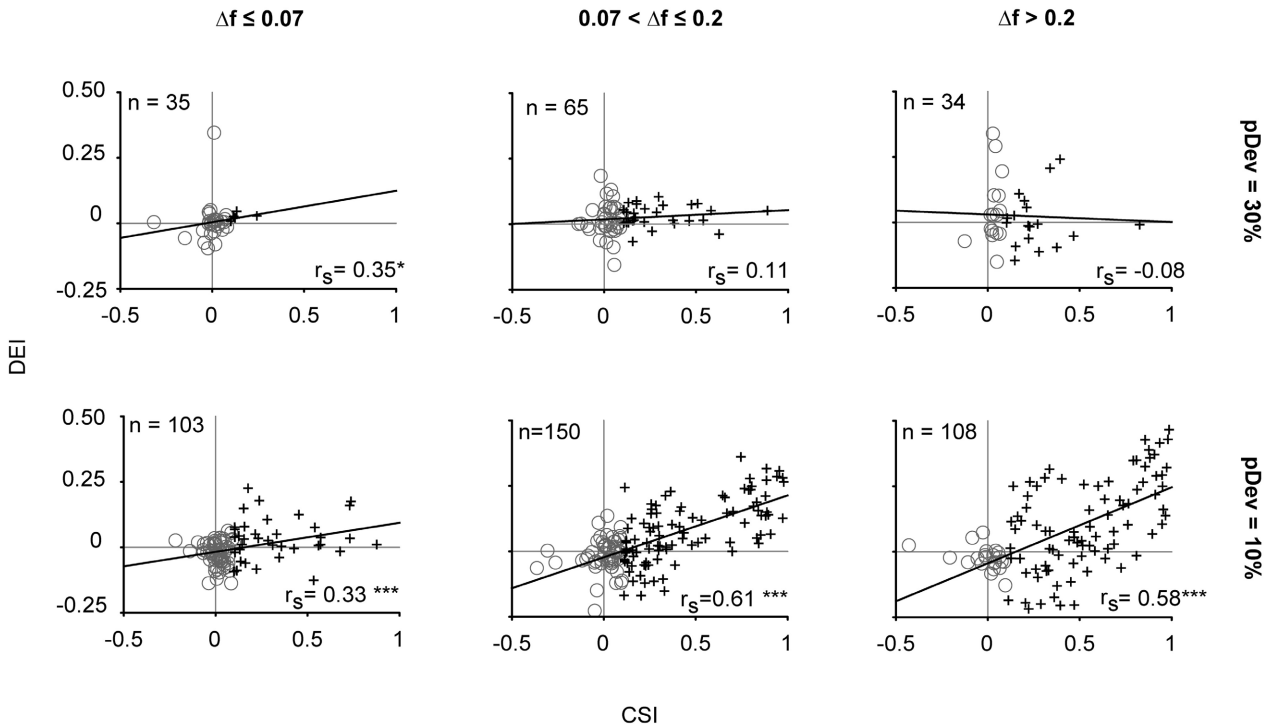

FIGURE 8 | The stimulus discriminability reflects the degree of stimulus-specific adaptation exhibited by IC neurons. Correlation of the stimulus discriminability enhancement (DEI) and the SSA index (CSI). In gray circles are represented the neurons with CSI $\leq$ 0.1 and in dark crosses those with CSI $>$ 0.1. The linear correlation was reflected by the Spearman's correlation coefficient (r_s), whose strength varied according to the frequency contrast (columns) and probability of the deviant tone (rows). $^*p < 0.05$, $^{***}p < 0.001$.

discrimination for oddball sequences, and furthermore, there was a tendency for larger CSI values to be associated with larger DEI values.

RELATION BETWEEN THE WIDTH OF FREQUENCY TUNING AND THE SSA OR DISCRIMINABILITY EXHIBITED BY IC NEURONS

Previous reports demonstrated a differential expression of SSA through the lemniscal and non-lemniscal subdivisions of the IC (Pérez-González et al., 2005; Malmierca et al., 2009; Ayala and Malmierca, 2012; Duque et al., 2012) and medial geniculate body (MGB) (Antunes et al., 2010) of the rat. Neurons in the cortical regions of the IC exhibit broader FRAs than the ones from the central nucleus and the broader the response area is, the higher the SSA levels are (Duque et al., 2012). In order to test whether or not this relationship is found in our neuronal sample, we analyzed the width of response areas as a function of the level of SSA.

Figure 9A displays the bandwidths at 10 and 40 dB SPL above threshold ($BW_{10,40}$, respectively) for the lowest deviant probability (pDev = 10%) as a function of the CSI. The group of CSI $\leq$ 0.1 included all neurons that were considered to lack SSA. The other CSI cutoffs were selected to have approximately equal-size groups. It is interesting to note that there were neurons with very broad bandwidth already at 10 dB above threshold. We performed an analysis of covariance of BW, with level above threshold (10 or 40 dB SPL) and frequency separation as qualitative factors and CSI as a continuous factor. We found a highly significant effect of CSI [$F_{(1,688)} = 37.5$, $P = 0$]. The slope of the dependence of BW on CSI indicated that BW increased on average by 6.6 kHz as CSI increased from zero to one. The main effect of frequency separation was not significant, [$F_{(2,688)} = 0.54$, $p = 0.6$], while the level above threshold had, as expected, a significant effect on BW [$F_{(1,688)} = 77.4$, $p = 0$]. There was a significant interaction between the CSI slope and level above threshold [$F_{(1,688)} = 5.8$, $p = 0.01$], and *post-hoc* comparison indicated that CSI slopes at 10 and 40 dB above threshold were significantly different ($p < 0.05$).

As expected from the positive correlation between DEI and CSI (**Figure 8**), a significant effect of DEI on BW was also found [$F_{(1,688)} = 26.7$, $p = 0$] (**Figure 9B**). In consequence, a greater neuronal discriminability in the oddball condition is associated with a wider frequency integration range. DEI also had significant interaction with level above threshold [$F_{(1,688)} = 3.9, p = 0.048$] (analysis of covariance of BW with level, frequency separation, and now with DEI as a continuous factor).

In selected cases, we made electrolytic lesions in the IC and determined that we recorded neurons from central nucleus ($n = 9$) and from cortical regions ($n = 16$). Within this very limited sample, the central nucleus neurons had a CSI of 0.11 ± 0.21 and a DEI of -0.001 ± 0.12 (median $\pm$ SD). For the cortical neurons, the CSI and DEI were of 0.34 ± 0.3 and of 0.03 ± 0.13, respectively. However, this number of histological localizations was insufficient to guarantee a reliable study to correlate SSA

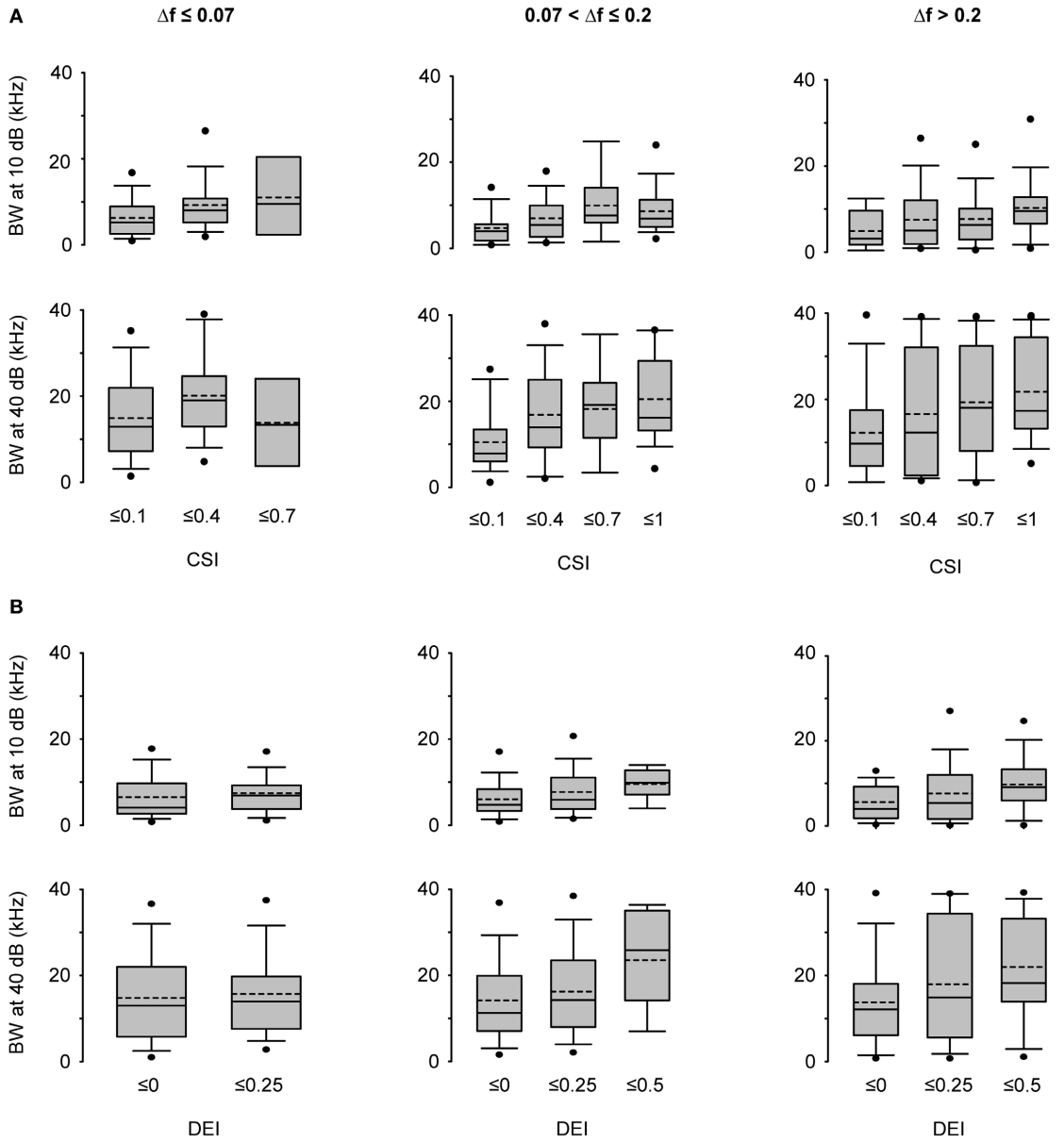

FIGURE 9 | Bandwidth of frequency response areas and SSA level of IC neurons. (A) Box plots of the bandwidth (BW) values grouped into CSI ranges for the three Δf intervals with the mean (dashed line) and median values (solid line) indicated, as well as, the 5th and 95th outliers. There is an increment in the bandwidths as neurons have higher CSI [$F_{(1,688)} = 37.5$, $P = 0$] and as the level increased [$F_{(1,688)} = 77.4$, $p = 0$] (Analysis of covariance of BW with level, Δf and CSI as factors). **(B)** Box plots of BW values grouped into DEI ranges. The BW increases for neurons that displayed higher discriminability improvement under the oddball condition [$F_{(1,688)} = 26.7$, $p = 0$]. Same format as panel **(A)**. (Analysis of covariance of BW with level, Δf and DEI as factors).

and discriminability degree across the different subdivisions of the IC. **Figure 10A** showed an example of a typical lesion located in the lateral cortex of the IC (Loftus et al., 2008; Malmierca et al., 2011).

CN NEURONS DO NOT EXHIBIT SSA AND THEIR FREQUENCY DISCRIMINABILITY IS NOT SENSITIVE TO A PROBABILITY CONTEXT

Since SSA is present in the IC, we wanted to explore whether SSA is already ubiquitously expressed earlier. We recorded 51 CN neurons to test whether SSA is exhibited by single-units and if so, whether adaptation strength correlates with neuronal sensitivity as shown for the IC neurons.

A total of 44 neurons out of 51 were localized and assigned to the ventral cochlear nucleus (VCN) ($n = 10$) or DCN ($n = 34$). The histological reconstruction for the remaining 7 neurons was not possible. **Figure 10B** shows the electrolytic lesion in a Nissl-stained section, illustrating the recording site of the neuron displayed in **Figure 11** and located in the DCN. Another example of

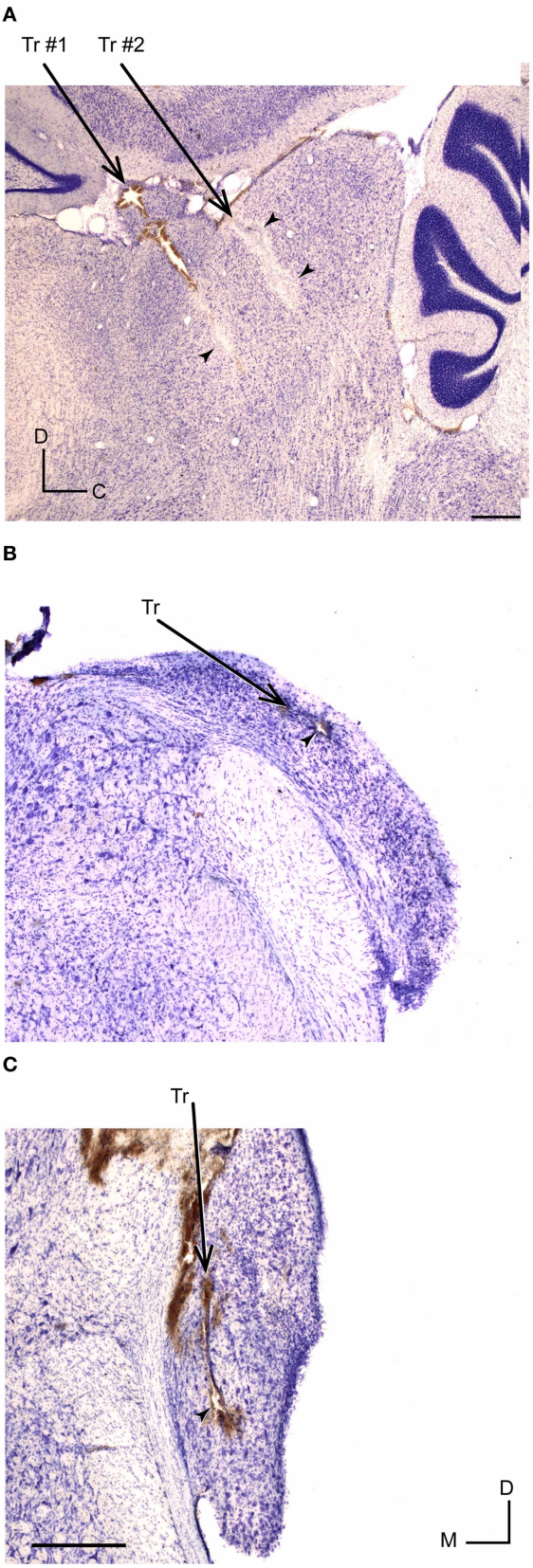

FIGURE 10 | Continued

FIGURE 10 | Histological identification of recording sites of IC and CN neurons. (A) Example of recording sites marked with an electrolytic lesion (arrowheads) in the lateral cortex of the IC at 1.9 mm lateral, according to Paxinos and Watson (2007). Two different tracts are indicated by Tr #1 and Tr #2. **(B,C)** Recording sites (arrowheads) and tracts (Tr) located in DCN (at 11.52 mm from bregma) and VCN (at 11.04 mm from bregma), respectively. The slices were Nissl stained and cut at 40 μm in a sagital **(A)** and coronal plane **(B,C)**. Scale bars of 500 μm. D, dorsal; C, caudal; M, medial.

recording site, in the VCN, is shown in **Figure 10C**. The recorded neurons had a wide variety of firing patterns and rate-level functions, as have been described in detail before (Stabler et al., 1996). More than the half of neurons in the DCN (21/34) displayed non-monotonic rate-level functions (5/10 in the VCN). Our sample of DCN neurons included chopper ($n = 13$), primary like ($n = 10$), pause/build ($n = 6$), and onset ($n = 5$) firing patterns. In the VCN, all firing patterns except the choppers were present (primary like, $n = 5$; pause/build, $n = 2$; onset, $n = 3$). **Figure 11** shows the response of a DCN neuron with a typical V-shaped FRA with a low-frequency tail. The evoked activity was robust across the 400 trials of the equiprobable (S1) and deviant sequences (S2, S3). The neuron showed significant discriminability under the equiprobable condition (AUC(S1) = 0.6, $p < 0.05$) which did not greatly improve under the oddball sequences (AUC(S2) = 0.62, AUC(S3) = 0.53, $p < 0.05$). This neuron failed to show SSA at a repetition rate of 4 Hz, as well as at faster stimuli presentation rates of 8 and 20 Hz (CSI = 0, $p > 0.05$).

SSA was not present in the neuronal population recorded in CN (**Figure 12**). We used faster repetition rates than in the IC since SSA seems to increase monotonically with stimulation rate (Malmierca et al., 2009; Antunes et al., 2010; Zhao et al., 2011; Patel et al., 2012). Regardless of the extreme repetitions rates, the strength of the neuronal response was equal for deviants and for standards stimuli (Signed Rank Test; $p > 0.05$) (**Figure 12A**) resulting in SI values clustered around zero (**Figure 12B**). There were no differences between the CSIs elicited by VCN and DCN neurons for any repetition rate tested (Rank Sum Test; $p > 0.05$). FSL is also affected by probability condition in IC, being shorter to the deviant stimulus regardless of the frequency tested (f_1 or f_2) (Malmierca et al., 2009; Pérez-González and Malmierca, 2012; Pérez-González et al., 2012). For CN neurons, the vast majority of FSL to deviant and to standard was almost equal and no differences in the median FSL between them was observed (Signed Rank Test; $p > 0.05$) (**Figure 12C**). The median of the FSLs was 9.62 ± 4.9 ms (range: 3.4 – 29.5 ms) and 9.82 ± 4.7 ms (range: 3.9 – 28.2 ms) for deviant and standard tone, respectively. These latencies are clearly shorter than the latencies of IC neurons (FSL to deviant: 26.1 ± 13.2 ms; range: 7.5 – 72 ms, FSL to standard: 29.6 ± 13.2 ms, range: 7.3 – 74.5 ms; from Malmierca et al., 2009). Although some neurons showed significant CSI > 0.1 (0.11 – 0.28) at 4 ($n = 3$), 8 ($n = 4$), 12 ($n = 2$), and 20 Hz ($n = 5$) (most of them from the DCN, $n = 5$), the average SSA indices were not significantly different from zero (Signed Rank Test; $p > 0.05$) nor they were sensitive to the rate of stimulation (Kruskal–Wallis Test; $p > 0.05$) (**Figure 12D**). Finally, CSI was not affected by increasing the frequency separation from

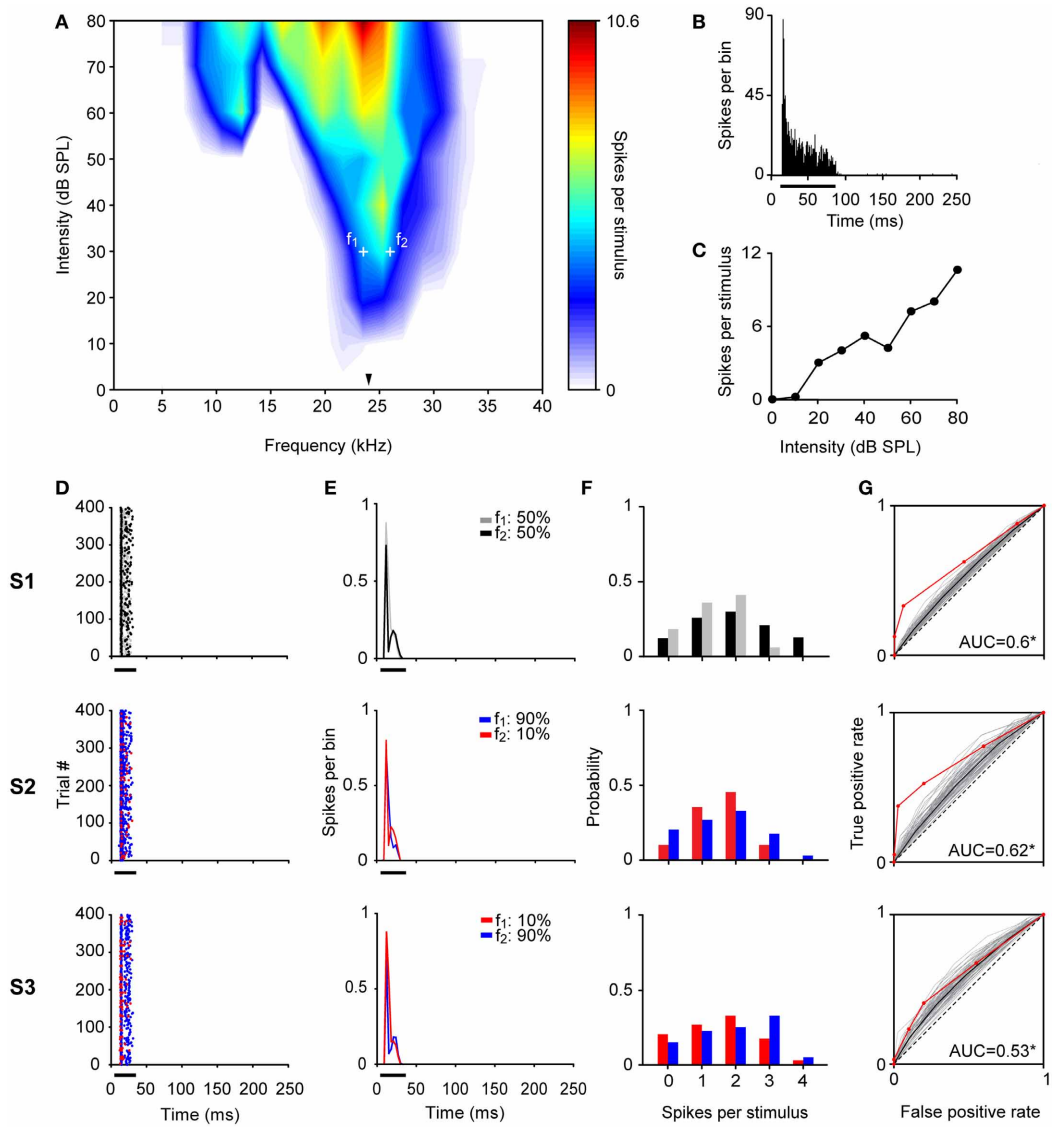

FIGURE 11 | Example of a CN neuron. The format for all panels is the same as in **Figures 3–5**. **(A)** The BF was 23.4 kHz (indicated by the arrowhead) and the tested frequencies ($f_1 = 23.4$ kHz and $f_2 = 25.9$ kHz, white crosses) differ by 0.144 octaves. The PSTH of the accumulated response to all the frequencies (0.5 – 40 KHz) and intensities (0 – 80 dB SPL) presented (1 ms bins), as well as, the rate-level function at BF are shown in **(B)** and **(C)**, respectively. The neuron exhibited a low CSI = 0.1 (Bootstrapping; $p > 0.05$) with a robust response across trials **(D,E)** and its frequency discriminability was not sensitive to the oddball condition **(F,G)**. The AUC values in all conditions were slightly higher than 0.5 (Permutation test; $^*p < 0.05$).

$\Delta f = 0.1$ to $\Delta f \geq 0.2$ $(0.2 - 0.37)$ (Signed Rank Test; $p > 0.05$) (**Figure 12E**).

In parallel with the lack of SSA, frequency discrimination was not affected by changes in tone probability in this neuronal population. The estimated correct detection in the oddball condition remained very similar to that elicited in the equiprobable one for most of the CN neurons (**Figure 13A**), and no improvement in frequency discriminability was elicited at the population level for any repetition rate group (Signed Rank Test; $p > 0.05$) (**Figure 13B**). Thus, the DEI was essentially zero and insensitive to increments in the repetition rate (Kruskal–Wallis Test; $p > 0.05$) (**Figure 13C**). As expected, it was not correlated with the SSA index (Spearman's correlation) (**Figure 13D**).

DISCUSSION

Our study demonstrates that sensitivity to frequency in IC neurons but not in CN neurons depends on probability context. Changes in frequency discriminability in IC neurons reflected the level of SSA they exhibit. Both the CSI and DEI values increased with frequency separation and DEI tended to be positive (**Figures 7** and **8**). The lack of effect of probability context in CN was related to the lack of SSA in the neuronal sample we recorded from (**Figure 12**).

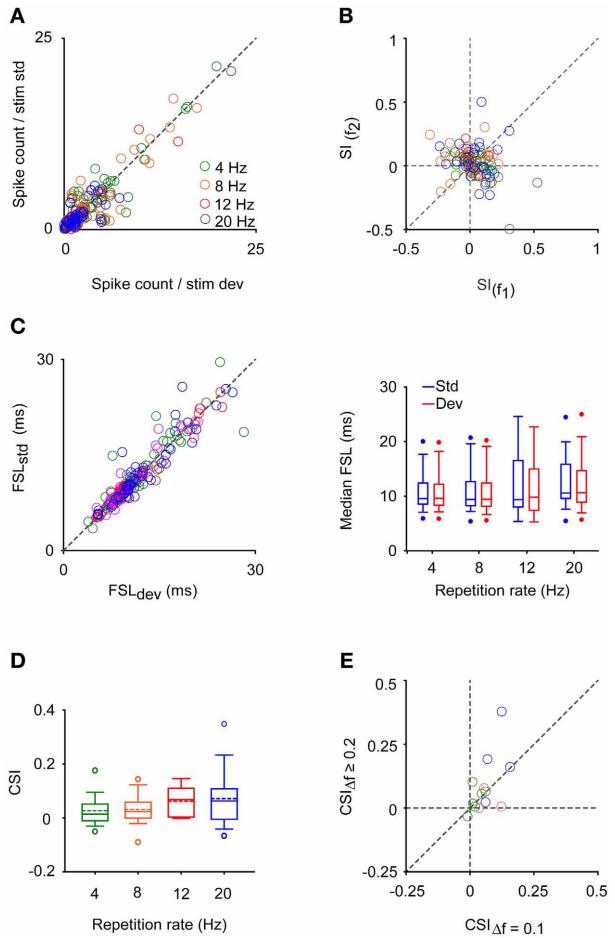

FIGURE 12 | CN neurons do not exhibit SSA. (A) Spike count to deviant (dev) and to standard (std) stimuli elicited at different repetition rates represented in a color code. This color code is the same for **(B–E)** panels. (4 Hz, $n = 47$; 8 Hz, $n = 29$; 12 Hz, $n = 9$; 20 Hz, $n = 26$) **(B)** Scattergraph of the Frequency-Specific SSA indices (SI) for f_1 and f_2 presented at different repetitions rates. This index reflects the normalized spikes counts elicited when each frequency was the deviant tone regarding the response evoked when it was the standard one. **(C)** Scattergraph of the median first spike latency (FSL) for f_1 and f_2 when they were the deviant (FSL_{dev}) or the standard (FSL_{std}) stimulus. In the right column, are displayed the box plots of the median FSL for the population of neurons to deviant (red) and to standard (blue) stimulus across repetition rates. The *n* for this panel is the double of the number of neurons tested, since two frequencies were tested as deviant and as standard stimulus for each neuron. **(D,E)** Box plots of the Common–SSA index (CSI) when increasing the rate of stimulation and scattergraph of CSI when varying the frequency separation factor (Δf), respectively.

STRONG SSA IS EXHIBITED BY IC NEURONS BUT NOT BY CN NEURONS

The strength of SSA reported here is similar to that reported previously by Malmierca et al. (2009) for IC neurons. This is not surprising, since we used a similar experimental preparation including animal model, parameters, and paradigm of stimulation (presentation rate: 4 Hz; tone duration: 75 ms; random presentation of tones). Other studies also have examined SSA in the IC, although as these studies have used different stimulation paradigms (e.g., Pérez-González et al., 2005; Lumani and Zhang, 2010), different metrics to quantify SSA (Pérez-González et al., 2005) or different stimulus repetition rates (Zhao et al., 2011), a quantitative comparison is difficult. According to the sample of histological verifications of the recording sites (**Figure 10A**) and taking into account the distribution of CSI (**Figure 2**), we recorded neurons from the central nucleus, as well as from the cortical non-lemniscal regions of IC. SSA varies as a continuum throughout the entire IC and it is strong and widespread in the non-lemniscal regions of the IC (Malmierca et al., 2009; Duque et al., 2012) and MGB (Antunes et al., 2010), being low or almost absent in the lemniscal subdivisions, the central nucleus of the IC and ventral MGB. Also, the neurons in the cortex of the IC exhibit broader response areas than those from the central nucleus (Malmierca et al., 2008, 2009; Geis et al., 2011; Duque et al., 2012). In agreement with these results, we show here that neurons with wider bandwidths (values as high as 30–40 kHz) showed the strongest SSA (**Figure 9**). Thus, the convergence of ascending, narrowly tuned frequency inputs with different frequency selectivity could be a major mechanism underlying SSA. In support to this idea, Taaseh et al. (2011) and Mill et al. (2011) showed that individual inputs showing simple fatigue could result in SSA. Beyond this mechanism, SSA could be further refined through the local inhibitory circuits and descending inputs from higher auditory centers. In this respect, a modulatory role of postsynaptic $GABA_A$ receptors in shaping SSA in the IC has already been demonstrated (Pérez-González and Malmierca, 2012; Pérez-González et al., 2012).

Considering that (1) the IC is the locus of convergence for most inputs originating at lower auditory brainstem nuclei and the locus where the lemniscal and non-lemniscal pathways appears (Malmierca et al., 2003; Lee and Sherman, 2010, 2011), and that (2) our results demonstrated the lack of widespread SSA at the CN (**Figure 12**), it is tempting to suggest that cells exhibiting strong SSA in the subcortical pathways first emerge in the non-lemniscal IC. Two possible confounds currently limit this hypothesis. First, a decrease in the responsiveness and changes in the response variability of auditory cortical neurons caused by the anesthesia (Kisley and Gerstein, 1999; Harris et al., 2011) could also result in the absence of strong SSA in CN. This would be the case, for example, if SSA in the CN were dependent on descending projections for its generation. However, this possibility seems unlikely since previous studies have demonstrated that SSA at the IC (Anderson and Malmierca, 2013) and MGB (Antunes and Malmierca, 2011) persist even if the corticofugal pathway is reversibly deactivated. Second, the CN has multiple distinct physiological response types which are well-correlated with anatomical and cellular characteristics. While neurons were recorded in both VCN and DCN, currently there is no detailed classification of CN neurons in the anesthetized rat. Therefore, we cannot rule out that we recorded from all response types in this study. Indeed, because across-frequency integration seems to be important in SSA, CN neuronal types that show frequency convergence and that project to the IC, e.g., some multipolar cells or small cells from the cap area (Winter and Palmer, 1995; Jiang et al., 1996; Palmer et al., 1996; Malmierca et al., 2002; Cant and Benson, 2003) might potentially be capable of showing high levels

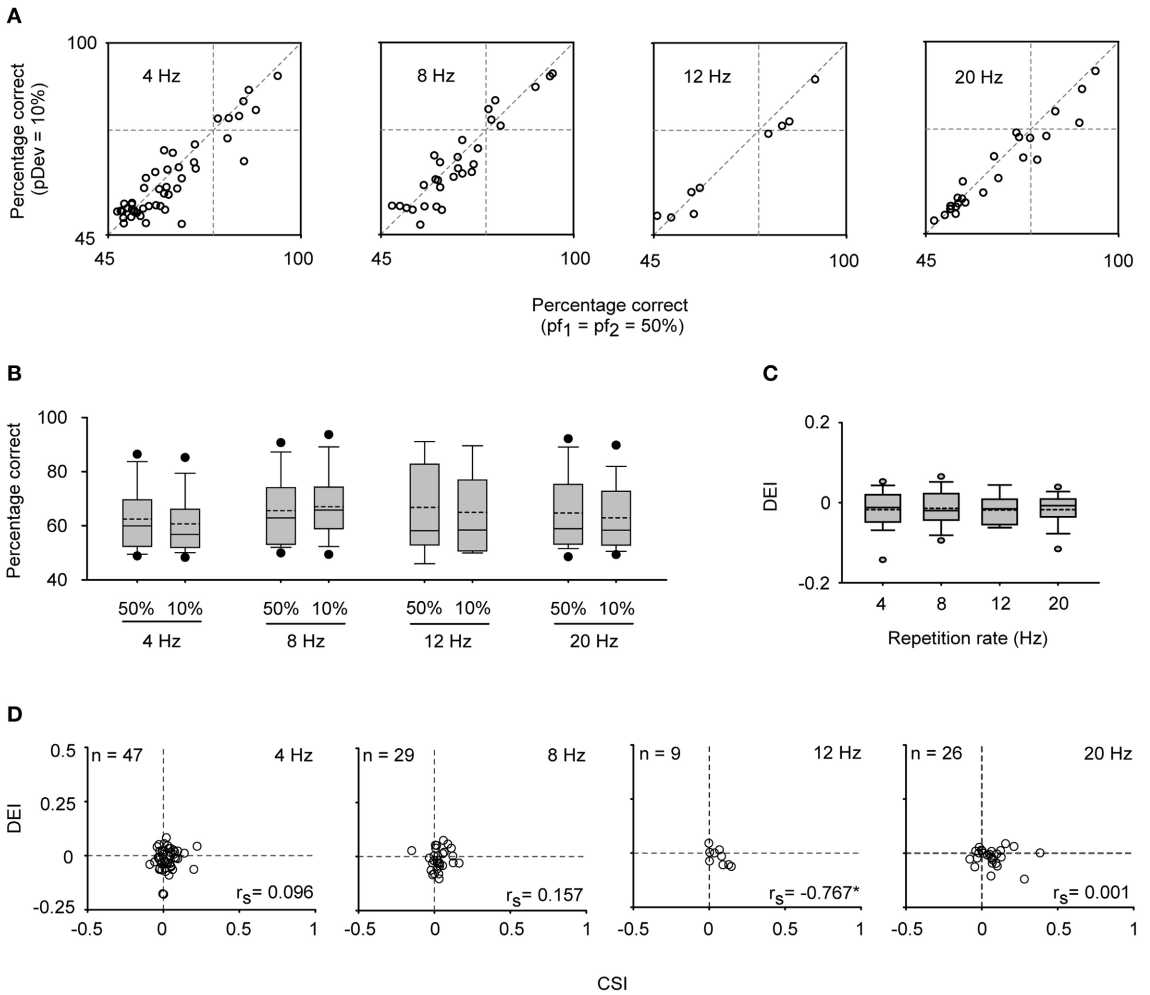

FIGURE 13 | Stimulus sensitivity in CN neurons. (A) Neurometric boxes displaying the percentage of correct identifications in the equiprobable and oddball condition (pDev = 10%) for different repetitions rates (4, 8, 12, and 20 Hz). **(B)** Box plots indicating that no improvement was elicited under the oddball condition regarding the equiprobable one (Signed Rank Test; $p > 0.05$). **(C)** Box plots that indicate that the discrimination enhancement indexes (DEI) remained at zero and did not change across repetition rate (Kruskal–Wallis Test; $p > 0.05$). **(D)** No positive correlation between the CSI and DEI was found (Spearman's correlation coefficient, r_s; $^*p < 0.05$).

of SSA as well. To rule out this possibility a detailed morphological and physiological study is necessary in the future. Finally, the presence of SSA in brainstem nuclei between the CN and IC also remains to be tested.

NEURONAL SENSITIVITY OF IC

We show here that the vast majority of IC neurons discriminate between nearby tones around BF even when they occur with equal probability (**Figures 6A,B**; upper left quadrants). While many of the AUCs were significantly larger than 0.5, they also tended to be smaller than 0.71, the standard definition of a psychophysical threshold. Note that other pairs of frequencies within the FRA with the same frequency difference could give rise to larger AUCs. Thus, our results for the equiprobable case should be seen as a lower bound on the frequency discrimination capabilities of IC neurons. Even with the biased selection of frequencies to test, a small population reached AUC > 0.71 for frequency separations as small as $\Delta f = 0.07$, very close to the psychophysical thresholds of rats (e.g., Talwar and Gerstein, 1998, 1999). Interestingly, these neurons also showed narrower bandwidths than the rest. The narrow bandwidth could result in large changes in firing rates for nearby frequencies, leading to the high AUCs (Gordon et al., 2008). Such narrowly-tuned inputs could also account for the hyperacuity of MGB and cortical neurons in oddball conditions, as previously reported (Ulanovsky et al., 2003; von der Behrens et al., 2009).

Frequency discrimination in IC depended on context, being larger when the stimuli had decreased probability (**Figures 6B,C** and **7**). Robust increases in discrimination in the oddball conditions occurred for the lower deviant probability (pDev = 10%) and the larger frequency separations ($\Delta f > 0.07$). Note that we used here the mean AUC across the two oddball sequences, rather than the maximal one as used previously (Ulanovsky et al., 2003; Malmierca et al., 2009). The mean AUC is

a more conservative estimate of frequency discriminability, and its use may explain why we did not observe extreme discrimination performance as reported previously in IC (Malmierca et al., 2009 their **Figure 7**, neurons in the upper left corner). Either way, these results emphasize the influence of context on sensory processing as early as in the IC as has been demonstrated before for the processing of interaural phase (Spitzer and Semple, 1991, 1993, 1998; McAlpine et al., 2000), level differences (Sanes et al., 1998), monaural frequency transitions (Malone and Semple, 2001) and simulated motion (Wilson and O'Neill, 1998).

FREQUENCY DISCRIMINABILITY ENHANCEMENT REFLECTS THE DEGREE OF SSA

We found a strong correlation between the discriminability enhancement and the degree of SSA, but only for the condition with the lowest deviant probability (pDev = 10%) and larger frequency separation ($\Delta f > 0.07$) (**Figure 8**). These are also the conditions that had higher CSI. This positive correlation is expected from the design of the experiment. The two frequencies were selected to evoke equivalent responses in the equiprobable condition, and in the oddball condition they were expected to evoke different responses. In consequence, we expected a substantial overlap between the spike count distributions in the equiprobable condition, but a decreasing overlap in the oddball condition. Indeed, DEI depended on deviant probability and frequency separation very similarly to CSI (**Figure 7**). Finally, the absence of SSA and null enhancement in deviant detectability by CN neurons reinforced the notion that deviant discriminability is a functional consequence of SSA (**Figures 12** and **13**).

Nevertheless, we also found that neurons with CSI ≤ 0.1 showed a significant decrease in AUC in the oddball condition (**Figure 6B**). This decrease was due to larger corrections for the AUCs obtained under the oddball condition than to the AUCs under the equiprobable one. This trend should be seen as a negative bias in the estimation of the AUC under oddball conditions. Given that as a rule AUC increased with decreasing deviant probability, our conclusions should be considered as conservative.

FUNCTIONAL SIGNIFICANCE

Neuronal responses in auditory cortex are plastic at many different time scales (Condon and Weinberger, 1991; Kilgard and Merzenich, 1998, 2002; Fritz et al., 2003; Ulanovsky et al., 2003; Froemke et al., 2007). Here we demonstrate that neurons in IC show some sort of short-term plasticity under similar conditions to neurons in MGB and A1. As previously suggested (Antunes et al., 2010), the non-lemniscal regions of the IC could transmit SSA to the non-lemniscal MGB neurons, which in turn would project to the superficial layers of AC (Cetas et al., 1999; Huang and Winer, 2000; Anderson et al., 2009). Neurons in the medial division of the MGB have large-diameter axons that are known to terminate primarily in layer I of the auditory cortex in both primary and secondary cortical fields. For example, in the somatosensory cortex Cauller and Connors (1994) observed strong excitatory effects on pyramidal cells present in layers II, III and V to be mediated by long horizontal axons located in layer I. Further experiments are required in order to check this possibility. Thus, at all levels of the auditory pathways, context-dependence of the responses could serve for adjusting the neural code to match the statistics of the input signal to produce an efficient representation of auditory scene. Similarly, the changes in responses as a function of tone probability could serve in the processes of auditory scene analysis. Indeed, auditory stream segregation is also sensitive to frequency separation and presentation rate (e.g., Fishman et al., 2004; Fishman and Steinschneider, 2010). Moreover, there is evidence suggesting the involvement of pre-attentive neural process in auditory stream segregation (Winkler et al., 2003). Thus, SSA in IC may increase the saliency of low-probability signals, helping to segregate them by reducing the ambiguity of the neuronal representations for downstream read-out mechanisms.

Interestingly, our results suggest that the initial locus for the computation of SSA is not at the very first stations of the auditory pathway, e.g., the CN. Thus, the picture of the auditory system that emerges here reinforces the idea that the initial coding of sounds is purely based on their short-term physical characteristics, and sensitivity to longer contexts that is required for higher-order processing, efficient coding, and auditory scene analysis appears only later.

AUTHOR CONTRIBUTIONS

Manuel S. Malmierca and David Pérez-González designed research; Yaneri A. Ayala performed research; Yaneri A. Ayala, Daniel Duque, David Pérez-González and Israel Nelken analyzed data; Yaneri A. Ayala, David Pérez-González, Israel Nelken and Manuel S. Malmierca wrote the paper.

ACKNOWLEDGMENTS

Financial support was provided by the Spanish MEC (BFU2009-07286), EU (EUI2009-04083, in the framework of the ERA-NET NEURON Network of European Funding for Neuroscience Research) to Manuel S. Malmierca. Israel Nelken was supported by a grant from the Israeli Ministry of Health in the framework of the ERA-NET Network. Daniel Duque held a fellowship from the Spanish MINECO (BES-2010-035649). David Pérez-González held a postdoctoral fellowship from the Botín Foundation. We thank Drs. Alan Palmer and Trevor M. Shackleton for their constructive comments on a previous version.

REFERENCES

Anderson, L. A., Christianson, G. B., and Linden, J. F. (2009). Stimulus-specific adaptation occurs in the auditory thalamus. *J. Neurosci.* 29, 7359–7363.

Anderson, L. A., Izquierdo, M. A., Antunes, F. M., and Malmierca, M. S. (2009). A monosynaptic pathway from dorsal cochlear nucleus to auditory cortex in rat. *Neuroreport* 20, 462–466.

Anderson, L. A., and Malmierca, M. S. (2013). The effect of auditory cortical deactivation on stimulus-specific adaptation in the inferior colliculus of the rat. *Eur. J. Neurosci.* 37, 52–62.

Antunes, F. M., and Malmierca, M. S. (2011). Effect of auditory cortex deactivation on stimulus-specific adaptation in the medial geniculate body. *J. Neurosci.* 31, 17306–17316.

Antunes, F. M., Nelken, I., Covey, E., and Malmierca, M. S. (2010). Stimulus-specific adaptation in the auditory thalamus of the anesthetized rat. *PLoS ONE* 5:e14071. doi: 10.1371/journal.pone.0014071

Ayala, Y. A., and Malmierca, M. S. (2012). Stimulus-specific adaptation and deviance detection in the inferior colliculus. *Front. Neural Circuits* 6:89. doi: 10.3389/fncir.2012.00089

Bäuerle, P., von der Behrens, W., Kössl, M., and Gaese, B. H. (2011). Stimulus-specific adaptation in the gerbil primary auditory thalamus is the result of a fast frequency-specific habituation and is regulated by the corticofugal system. *J. Neurosci.* 31, 9708–97022.

Cant, N. B., and Benson, C. G. (2003). Parallel auditory pathways: projection patterns of the different neuronal populations in the dorsal and ventral cochlear nuclei. *Brain Res. Bull.* 60, 457–474.

Cauller, L. J., and Connors, B. W. (1994). Synaptic physiology of horizontal afferents to layer I in slices of rat SI neocortex. *J. Neurosci.* 14, 751–762.

Cetas, J. S., de Venecia, R. K., and McMullen, N. T. (1999). Thalamocortical afferents of Lorente de Nó: medial geniculate axons that project to primary auditory cortex have collateral branches to layer I. *Brain Res.* 830, 203–208.

Chechik, G., Anderson, M. J., Bar-Yosef, O., Young, E. D., Tishby, N., and Nelken, I. (2006). Reduction of information redundancy in the ascending auditory pathway. *Neuron* 51, 359–368.

Cohn, T. E., Green, D. G., and Tanner, W. P. Jr. (1975). Receiver operating characteristic analysis. Application to the study of quantum fluctuation effects in optic nerve of Rana pipiens. *J. Gen. Physiol.* 66, 583–616.

Condon, C. D., and Weinberger, N. M. (1991). Habituation produces frequency-specific plasticity of receptive fields in the auditory cortex. *Behav. Neurosci.* 105, 416–430.

Duque, D., Pérez-González, D., Ayala, A. Y., Palmer, A. R., and Malmierca, M. S. (2012). Topographic distribution, frequency and intensity dependence of stimulus specific adaptation in the inferior colliculus of the rat. *J. Neurosci.* 32, 17762–17774.

Faure, P. A., Fremouw, T., Casseday, J. H., and Covey, E. (2003). Temporal masking reveals properties of sound-evoked inhibition in duration-tuned neurons of the inferior colliculus. *J. Neurosci.* 23, 3052–3065.

Fawcett, T. (2006). An introduction to ROC analysis. *Pattern Recognit. Lett.* 27, 861–874.

Fishman, Y. I., Arezzo, J. C., and Steinschneider, M. (2004). Auditory stream segregation in monkey auditory cortex: effects of frequency separation, presentation rate, and tone duration. *J. Acoust. Soc. Am.* 116, 1656–1670.

Fishman, Y. I., and Steinschneider, M. (2010). "Formation of auditory streams," in *The Oxford Handbook of Auditory Science: the Auditory Brain,* ed D. R. Moore (New York, NY: Oxford UP), 215–245.

Fritz, J., Shamma, S., Elhilali, M., and Klein, D. (2003). Rapid task-related plasticity of spectrotemporal receptive fields in primary auditory cortex. *Nat. Neurosci.* 6, 1216–1223.

Froemke, R. C., Merzenich, M. M., and Schreiner, C. E. (2007). A synaptic memory trace for cortical receptive field plasticity. *Nature* 450, 425–429.

Geis, H. R., van der Heijden, M., and Borst, J. G. (2011). Subcortical input heterogeneity in the mouse inferior colliculus. *J. Physiol.* 589, 3955–3967.

Gordon, N., Shackleton, T. M., Palmer, A. R., and Nelken, I. (2008). Responses of neurons in the inferior colliculus to binaural disparities: insights from the use of Fisher information and mutual information. *J. Neurosci. Methods* 169, 391–404.

Green, D. M., and Swets, J. A. (1966). *Signal Detection Theory and Psychophysics*. New York, NY: Wiley.

Gutfreund, Y. (2012). Stimulus-specific adaptation, habituation and change detection in the gaze control system. *Biol. Cybern*. 106, 657–668.

Huang, C. L., and Winer, J. A. (2000). Auditory thalamocortical projections in the cat: laminar and areal patterns of input. *J. Comp. Neurol.* 427, 302–331.

Hara, K., and Harris, R. A. (2002). The anesthetic mechanism of urethane: the effects on neurotransmitter-gated ion channels. *Anesth. Analg.* 94, 313–318.

Harris, K. D., Bartho, P., Chadderton, P., Curto, C., De La Rocha, J., Hollender, L., et al. (2011). How do neurons work together? Lessons from auditory cortex. *Hear. Res.* 271, 37–53.

Hernández, O., Espinosa, N., Pérez-González, D., and Malmierca, M. S. (2005). The inferior colliculus of the rat: a quantitative analysis of monaural frequency response areas. *Neuroscience* 132, 203–217.

Jiang, D., Palmer, A. R., and Winter, I. M. (1996). Frequency extent of two-tone facilitation in onset units in the ventral cochlear nucleus. *J. Neurophysiol.* 75, 380–395.

Kilgard, M. P., and Merzenich, M. M. (1998). Plasticity of temporal information processing in the primary auditory cortex. *Nat. Neurosci.* 1, 727–731.

Kilgard, M. P., and Merzenich, M. M. (2002). Order-sensitive plasticity in adult primary auditory cortex. *Proc. Natl. Acad. Sci. U.S.A.* 99, 3205–3209.

Kisley, M. A., and Gerstein, G. L. (1999). Trial-to-trial variability and state-dependent modulation of auditory-evoked responses in cortex. *J. Neurosci.* 19, 10451–10460.

LeBeau, F. E., Malmierca, M. S., and Rees, A. (2001). Iontophoresis *in vivo* demonstrates a key role for GABA(A) and glycinergic inhibition in shaping frequency response areas in the inferior colliculus of guinea pig. *J. Neurosci.* 21, 7303–7312.

Lee, C. C., and Sherman, S. M. (2010). Topography and physiology of ascending streams in the auditory tectothalamic pathway. *Proc. Natl. Acad. Sci. U.S.A.* 107, 372–377.

Lee, C. C., and Sherman, S. M. (2011). On the classification of pathways in the auditory midbrain, thalamus, and cortex. *Hear. Res.* 276, 79–87.

Loftus, W. C., Malmierca, M. S., Bishop, D. C., and Oliver, D. L. (2008). The cytoarchitecture of the inferior colliculus revisited: a common organization of the lateral cortex in rat and cat. *Neuroscience* 154, 196–205.

Lumani, A., and Zhang, H. (2010). Responses of neurons in the rat's dorsal cortex of the inferior colliculus to monaural tone bursts. *Brain Res.* 1351, 115–129.

Malmierca, M. S., Blackstad, T. W., and Osen, K. K. (2011). Computer-assisted 3-D reconstructions of Golgi-impregnated neurons in the cortical regions of the inferior colliculus of rat. *Hear. Res.* 274, 13–26.

Malmierca, M. S., Cristaudo, S., Pérez-González, D., and Covey, E. (2009). Stimulus-specific adaptation in the inferior colliculus of the anesthetized rat. *J. Neurosci.* 29, 5483–5493.

Malmierca, M. S., Hernández, O., Falconi, A., Lopez-Poveda, E. A., Merchan, M., and Rees, A. (2003). The commissure of the inferior colliculus shapes frequency response areas in rat: an *in vivo* study using reversible blockade with microinjection of kynurenic acid. *Exp. Brain Res.* 153, 522–529.

Malmierca, M. S., Izquierdo, M. A., Cristaudo, S., Hernández, O., Pérez-González, D., Covey, E., et al. (2008). A discontinuous tonotopic organization in the inferior colliculus of the rat. *J. Neurosci.* 28, 4767–4776.

Malmierca, M. S., Merchán, M. A., Henkel, C. K., and Oliver, D. L. (2002). Direct projections from cochlear nuclear complex to auditory thalamus in the rat. *J. Neurosci.* 22, 10891–10897.

Malmierca, M. S., and Ryugo, D. K. (2011). "Descending connections of auditory cortex to the midbrain and brainstem," in *The Auditory Cortex*, eds J. A. Winer and C. E. Schreiner (New York, NY: Springer), 189–208.

Malone, B. J., and Semple, M. N. (2001). Effects of auditory stimulus context on the representation of frequency in the gerbil inferior colliculus. *J. Neurophysiol.* 86, 1113–1130.

Maris, E. (2012). Statistical testing in electrophysiological studies. *Psychophysiology* 49, 549–565.

McAlpine, D., Jiang, D., Shackleton, T. M., and Palmer, A. R. (2000). Responses of neurons in the inferior colliculus to dynamic interaural phase cues: evidence for a mechanism of binaural adaptation. *J. Neurophysiol.* 83, 1356–1365.

Merrill, E. G., and Ainsworth, A. (1972). Glass-coated platinum-plated tungsten microelectrodes. *Med. Biol. Eng.* 10, 662–672.

Mill, R., Coath, M., Wennekers, T., and Denham, S. L. (2011). A neurocomputational model of stimulus-specific adaptation to oddball and Markov sequences. *PLoS Comput. Biol.* 7:e1002117. doi: 10.1371/journal.pcbi.1002117

Näätänen, R. (1992). *Attention and Brain Function*. Hillsdale, NJ: Lawrence Erlbaum.

Nelken, I., and Ulanovsky, N. (2007). Mismatch negativity and stimulus-specific adaptation in animal models. *J. Psychophysiol.* 21, 214–223.

Nelson, D. A., and Kiester, T. E. (1978). Frequency discrimination in the chinchilla. *J. Acoust. Soc. Am.* 64, 114–126.

Netser, S., Zahar, Y., and Gutfreund, Y. (2011). Stimulus-specific adaptation: can it be a neural correlate of behavioral habituation? *J. Neurosci.* 31, 17811–17820.

Palmer, A. R., Jiang, D., and Marshall, D. H. (1996). Responses of ventral cochlear nucleus onset and chopper units as a function of signal bandwidth. *J. Neurophysiol.* 75, 780–794.

Patel, C. R., Redhead, C., Cervi, A. L., and Zhang, H. (2012). Neural sensitivity to novel sounds in the rat's dorsal cortex of the inferior colliculus as revealed by evoked local field potentials. *Hear. Res.* 286, 41–54.

Paxinos, G., and Watson, C. (2007). *The Rat Brain in Stereotaxic Coordinates*. Burlington, VT: Elsevier-Academic.

Pérez-González, D., Hernández, O., Covey, E., and Malmierca, M. S. (2012). GABA(A)-mediated inhibition modulates stimulus-specific adaptation in the inferior

colliculus. *PLoS ONE* 7:e34297. doi: 10.1371/journal.pone.0034297

Pérez-González, D., and Malmierca, M. S. (2012). Variability of the time course of stimulus-specific adaptation in the inferior colliculus. *Front. Neural Circuits* 6:107. doi: 10.3389/fncir.2012.00107

Pérez-González, D., Malmierca, M. S., and Covey, E. (2005). Novelty detector neurons in the mammalian auditory midbrain. *Eur. J. Neurosci.* 22, 2879–2885.

Pérez-González, D., Malmierca, M. S., Moore, J. M., Hernández, O., and Covey, E. (2006). Duration selective neurons in the inferior colliculus of the rat: topographic distribution and relation of duration sensitivity to other response properties. *J. Neurophysiol.* 95, 823–836.

Reches, A., and Gutfreund, Y. (2008). Stimulus-specific adaptations in the gaze control system of the barn owl. *J. Neurosci.* 28, 1523–1533.

Reches, A., and Gutfreund, Y. (2009). Auditory and multisensory responses in the tectofugal pathway of the barn owl. *J. Neurosci.* 29, 9602–9613.

Reches, A., Netser, S., and Gutfreund, Y. (2010). Interactions between stimulus-specific adaptation and visual auditory integration in the forebrain of the barn owl. *J. Neurosci.* 30, 6991–6998.

Rees, A. (1990). A close-field sound system for auditory neurophysiology. *J. Physiol.* 430, 2.

Rees, A., Sarbaz, A., Malmierca, M. S., and Le Beau, F. E. (1997). Regularity of firing of neurons in the inferior colliculus. *J. Neurophysiol.* 77, 2945–2965.

Sanes, D. H., Malone, B. J., and Semple, M. N. (1998). Role of synaptic inhibition in processing of dynamic binaural level stimuli. *J. Neurosci.* 18, 794–803.

Shackleton, T. M., Arnott, R. H., and Palmer, A. R. (2005). Sensitivity to interaural correlation of single neurons in the inferior colliculus of guinea pigs. *J. Assoc. Res. Otolaryngol.* 6, 244–259.

Shackleton, T. M., Skottun, B. C., Arnott, R. H., and Palmer, A. R. (2003). Interaural time difference discrimination thresholds for single neurons in the inferior colliculus of guinea pigs. *J. Neurosci.* 23, 716–724.

Shofner, W. P. (2000). Comparison of frequency discrimination thresholds for complex and single tones in chinchillas. *Hear. Res.* 149, 106–114.

Shofner, W. P., and Dye, R. H. Jr. (1989). Statistical and receiver operating characteristic analysis of empirical spike-count distributions: quantifying the ability of cochlear nucleus units to signal intensity changes. *J. Acoust. Soc. Am.* 86, 2172–2184.

Sinnott, J. M., Petersen, M. R., and Hopp, S. L. (1985). Frequency and intensity discrimination in humans and monkeys. *J. Acoust. Soc. Am.* 78, 1977–1985.

Skottun, B. C., Shackleton, T. M., Arnott, R. H., and Palmer, A. R. (2001). The ability of inferior colliculus neurons to signal differences in interaural delay. *Proc. Natl. Acad. Sci. U.S.A.* 98, 14050–14054.

Spitzer, M. W., and Semple, M. N. (1991). Interaural phase coding in auditory midbrain: influence of dynamic stimulus features. *Science* 254, 721–724.

Spitzer, M. W., and Semple, M. N. (1993). Responses of inferior colliculus neurons to time-varying interaural phase disparity: effects of shifting the locus of virtual motion. *J. Neurophysiol.* 69, 1245–1263.

Spitzer, M. W., and Semple, M. N. (1998). Transformation of binaural response properties in the ascending auditory pathway: influence of time-varying interaural phase disparity. *J. Neurophysiol.* 80, 3062–3076.

Stabler, S. E., Palmer, A. R., and Winter, I. M. (1996). Temporal and mean rate discharge patterns of single units in the dorsal cochlear nucleus of the anesthetized guinea pig. *J. Neurophysiol.* 76, 1667–1688.

Stüttgen, M. C., Schwarz, C., and Jakel, F. (2011). Mapping spikes to sensations. *Front. Neurosci.* 5:125. doi: 10.3389/fnins.2011.00125

Syka, J., Rybalko, N., Brozek, G., and Jilek, M. (1996). Auditory frequency and intensity discrimination in pigmented rats. *Hear. Res.* 100, 107–113.

Taaseh, N., Yaron, A., and Nelken, I. (2011). Stimulus-specific adaptation and deviance detection in the rat auditory cortex. *PLoS ONE* 6:e23369. doi: 10.1371/journal.pone.0023369

Talwar, S. K., and Gerstein, G. L. (1998). Auditory frequency discrimination in the white rat. *Hear. Res.* 126, 135–150.

Talwar, S. K., and Gerstein, G. L. (1999). A signal detection analysis of auditory-frequency discrimination in the rat. *J. Acoust. Soc. Am.* 105, 1784–1800.

Tanner, W. P. Jr., and Swets, J. A. (1954). A decision-making theory of visual detection. *Psychol. Rev.* 61, 401–409.

Ulanovsky, N., Las, L., Farkas, D., and Nelken, I. (2004). Multiple time scales of adaptation in auditory cortex neurons. *J. Neurosci.* 24, 10440–10453.

Ulanovsky, N., Las, L., and Nelken, I. (2003). Processing of low-probability sounds by cortical neurons. *Nat. Neurosci.* 6, 391–398.

von der Behrens, W., Bäuerle, P., Kossl, M., and Gaese, B. H. (2009). Correlating stimulus-specific adaptation of cortical neurons and local field potentials in the awake rat. *J. Neurosci.* 29, 13837–13849.

Walker, K. M., Schnupp, J. W., Hart-Schnupp, S. M., King, A. J., and Bizley, J. K. (2009). Pitch discrimination by ferrets for simple and complex sounds. *J. Acoust. Soc. Am.* 126, 1321–1335.

Wilson, W. W., and O'Neill, W. E. (1998). Auditory motion induces directionally dependent receptive field shifts in inferior colliculus neurons. *J. Neurophysiol.* 79, 2040–2062.

Winkler, I., Sussman, E., Tervaniemi, M., Horvath, J., Ritter, W., and Naatanen, R. (2003). Preattentive auditory context effects. *Cogn. Affect. Behav. Neurosci.* 3, 57–77.

Winter, I. M., and Palmer, A. R. (1995). Level dependence of cochlear nucleus onset unit responses and facilitation by second tones or broadband noise. *J. Neurophysiol.* 73, 141–159.

Witte, R. S., and Kipke, D. R. (2005). Enhanced contrast sensitivity in auditory cortex as cats learn to discriminate sound frequencies. *Brain Res. Cogn. Brain Res.* 23, 171–184.

Yu, X. J., Xu, X. X., He, S., and He, J. (2009). Change detection by thalamic reticular neurons. *Nat. Neurosci.* 12, 1165–1170.

Zhao, L., Liu, Y., Shen, L., Feng, L., and Hong, B. (2011). Stimulus-specific adaptation and its dynamics in the inferior colliculus of rat. *Neuroscience* 181, 163–174.

Conflict of Interest Statement: The authors declare that the research was conducted in the absence of any commercial or financial relationships that could be construed as a potential conflict of interest.

Received: 10 September 2012; accepted: 19 December 2012; published online: 14 January 2013.

*Citation: Ayala YA, Pérez-González D, Duque D, Nelken I and Malmierca MS (2013) Frequency discrimination and stimulus deviance in the inferior colliculus and cochlear nucleus. Front. Neural Circuits **6**:119. doi: 10.3389/fncir.2012.00119*

frontiers in
NEURAL CIRCUITS

ORIGINAL RESEARCH ARTICLE
published: 18 September 2012
doi: 10.3389/fncir.2012.00067

Inhibition shapes response selectivity in the inferior colliculus by gain modulation

Joshua X. Gittelman[1]*, Le Wang[2], H. S. Colburn[2] and George D. Pollak[1]

[1] *Section of Neurobiology, Institute for Neuroscience, Center for Perceptual Systems, The University of Texas, Austin, TX, USA*
[2] *Department of Biomedical Engineering, Hearing Research Center, Boston University, Boston, MA, USA*

Edited by:
Manuel S. Malmierca, University of Salamanca, Spain

Reviewed by:
Anna Magnusson, Karolinska Institutet, Sweden
Hermann Wagner, Aachen University, Germany

****Correspondence:***
Joshua X. Gittelman, Department of Science, Washington State University, 14204 NE Salmon Creek Avenue, Vancouver, WA 98686-9600, USA.
e-mail: jx.gittelman@vancouver.wsu.edu

Pharmacological block of inhibition is often used to determine if inhibition contributes to spike selectivity, in which a preferred stimulus evokes more spikes than a null stimulus. When inhibitory block reduces spike selectivity, a common interpretation is that differences between the preferred- and null-evoked inhibitions created the selectivity from less-selective excitatory inputs. In models based on empirical properties of cells from the inferior colliculus (IC) of awake bats, we show that inhibitory differences are not required. Instead, inhibition can enhance spike selectivity by changing the gain, the ratio of output spikes to input current. Within the model, we made preferred stimuli that evoked more spikes than null stimuli using five distinct synaptic mechanisms. In two cases, synaptic selectivity (the differences between the preferred and null inputs) was entirely excitatory, and in two it was entirely inhibitory. In each case, blocking inhibition eliminated spike selectivity. Thus, observing spike rates following inhibitory block did not distinguish among the cases where synaptic selectivity was entirely excitatory or inhibitory. We then did the same modeling experiment using empirical synaptic conductances derived from responses to preferred and null sounds. In most cases, inhibition in the model enhanced spike selectivity mainly by gain modulation and firing rate reduction. Sometimes, inhibition reduced the null gain to zero, eliminating null-evoked spikes. In some cases, inhibition increased the preferred gain more than the null gain, enhancing the difference between the preferred- and null-evoked spikes. Finally, inhibition kept firing rates low. When selectivity is quantified by the selectivity index (SI, the ratio of the difference to the sum of the spikes evoked by the preferred and null stimuli), inhibitory block reduced the SI by increasing overall firing rates. These results are consistent with inhibition shaping spike selectivity by gain control.

Keywords: inhibition, spike threshold, modeling, response selectivity, gain control, directional selectivity

INTRODUCTION

To determine the role of inhibition in sensory processing, iontophoretic application of pharmacological agents during extracellular recording has been used for decades (Sillito, 1975; Moore and Caspary, 1983; Yang et al., 1992; Klug et al., 2002; Andoni et al., 2007; Kutscher and Covey, 2009). Typically, stimulus-evoked spikes are measured before and after application of the agent. Spike selectivity, a difference between the spikes evoked by a preferred stimulus compared to a less-preferred or null stimulus, is generally reduced following inhibition block.

A limitation is that extracellular electrodes only measure output spikes, and therefore the underlying mechanisms must be inferred. For example, blocking inhibition in the auditory midbrain nucleus, the inferior colliculus (IC), reduces spike selectivity for frequency, intensity, frequency modulations (FMs), duration, binaural sensitivity, and conspecific communication calls (Yang et al., 1992; Casseday et al., 1994; Fuzessery and Hall, 1996; Kautz and Wagner, 1998; Klug et al., 1999; Andoni et al., 2007). A common interpretation is that spike selectivity depends on differences between the preferred- and null-evoked inhibitions: differences in timing (temporal pattern), in size (total conductance), or both. These differences, combined with the differences between the preferred and null excitations, comprise what we term "synaptic selectivity." Synaptic selectivity is required to create input selectivity, i.e., the differences between the total input current, the summation of all of the excitation and inhibition evoked by the preferred and null stimuli. Input selectivity then underlies spike selectivity.

Additionally, inhibition might enhance spike selectivity by modulating the neuronal gain i.e., the ratio of output (spikes) to input (current) (Ingham and McAlpine, 2005; Pérez-González et al., 2012). In cases where inhibition modulates spike selectivity by setting the gain, synaptic selectivity could rely on differences between the preferred and null excitations to generate input selectivity, and inhibition does not necessarily contribute to synaptic selectivity. Instead, inhibition reduces the input current, which can reduce output spikes and also modulate the gain. For example, inhibition could enhance spike selectivity by keeping the null inputs below spike threshold, such that they evoke no spikes (gain = 0), but preferred inputs evoke spikes (Rose and Blakemore, 1974; Wehr and Zador, 2003; Gittelman et al., 2009; Katzner et al., 2011). After inhibitory block, both the preferred

and null inputs get bigger. If null signals become suprathreshold (gain > 0), spikes are evoked and spike selectivity is reduced.

Inhibition might also enhance spike selectivity by keeping firing rates well below maximum (saturation) and in a range with high gain, where small input selectivity translates into large spike selectivity (Gittelman et al., 2009; Gittelman and Li, 2011). If blocking inhibition increases the inputs enough to approach saturation, null firing will increase more than the preferred, reducing or even eliminating the difference between the preferred and null spike counts. In this scenario, inhibition enhances spike selectivity even when the preferred and null inhibitions are identical and the synaptic selectivity mechanism is entirely excitatory. We term these inhibitory mechanisms that do not contribute to synaptic selectivity as "gain control," and we note that roles for inhibition in gain control and synaptic selectivity are not mutually exclusive.

We previously reported that inhibition enhances FM selectivity in IC cells by keeping null responses below threshold (Gittelman et al., 2009; Gittelman and Pollak, 2011). This finding was independent of whether inhibition contributed to synaptic selectivity and is consistent with gain control described above. However, the conclusions were based solely on studies in one IC cell type (sustained cells with high input resistance), with a limited range of synaptic selectivity mechanisms and passive neuronal modeling (no voltage-gated channels, no spikes). In the current study, modeling was used to test a broader range of scenarios. Spiking models were designed with input/output (I/O) functions that span the range of IC cells measured *in vivo*. Selective spiking was created with a broad range of synaptic selectivity mechanisms, including two in which inhibition made no contribution to synaptic selectivity, i.e., there were no differences between the preferred and null inhibitions. We then removed inhibition from the models to determine whether the mechanisms underlying synaptic selectivity could be distinguished based on the changes in spike selectivities before and after blocking inhibition. Finally, previously reported data were analyzed using these spiking models to determine whether inhibition acting as a gain control was consistent with the effects of blocking inhibition on FM selectivity in the IC.

MATERIALS AND METHODS

In vivo

Membrane properties and FM-evoked conductance analyses from the cells presented here were reported previously (Gittelman et al., 2009). Responses to current steps and to FM sweeps were recorded using patch electrodes in whole-cell current-clamp mode from the central nucleus of the IC in awake *Tadarida brasilensis mexicana*. Input/output (I/O) functions were the number of spikes evoked in the first 50 ms during prolonged (200 ms) current step injections, as functions of current level. The eight conductance sets were derived from five sustained cells in which we recorded spikes and postsynaptic potentials (PSPs) evoked by a pair of FMs, a preferred and null FM that differed only in direction. In two cells we used a single FM pair in each cell to derive one conductance set per cell. In three cells we used two FM pairs in each cell to derive two conductance sets per cell, for a total of eight conductance sets (16 conductance pairs).

CELL MODELING

Single-compartment models comprised excitatory and inhibitory synaptic inputs, voltage-independent leak channels, and three voltage-dependent channels (Rothman and Manis, 2003): sodium (Na); a high-threshold potassium (KHT); and low-threshold potassium (KLT). Parameters were optimized to match empirically measured spiking, either average (**Figures 1**, **2**), or individual neurons (**Figures 3**, **4**). We assumed two synaptic conductances, one for excitation and one for inhibition with reversal potentials of 0 and −70 mV, respectively.

Average responses

We matched the average measured I/O functions of sustained and onset-burst cell types (Tan et al., 2007; Xie et al., 2008). The published voltage-dependent channels (Rothman and Manis, 2003) recreated the sustained responses. However, while the published KLT currents create onset responses, such as those recorded *in vitro* (Koch and Grothe, 2003), they do not generate the bursting pattern observed in the IC *in vivo* (Tan et al., 2007; Xie et al., 2008). Onset-burst cells can fire a burst of spikes at the start of a prolonged depolarization, rather than the single spike fired by onset cells recorded *in vitro*. In conjunction with KLT, a number of mechanisms could produce this burst pattern, such as hyperpolarization-activated currents (Ih) and *t*-type calcium currents (Kopp-Scheinpflug et al., 2011). However, our goal here was to match the I/O function in the simplest way possible, by extending the temporal window for spike initiation to enable bursting. To achieve the burst pattern, we changed KLT activation to a sigmoid-shaped temporal window W(t). Thus,

$$\overline{G_{KLT}}\,(t) = \overline{G_{KLT}} * W(t) = \frac{\overline{G_{KLT}}}{(1+\exp(-(t-T_{delay})))^4},$$

where $\overline{G_{KLT}}$ is the maximum conductance for KLT, T_{delay} is the relative delay, and t is time (ms). This equation simulated the effect of delayed KLT activation because $\overline{G_{KLT}}(t)$ is close to 0 for $t < T_{delay}$ and $\overline{G_{KLT}}(t)$ rapidly increases to $\overline{G_{KLT}}$ for $t > T_{delay}$. The timing and shape of W(t) determined the number of spikes in the burst before KLT activated sufficiently to curtail firing. We found a good match to the empirical data with $T_{delay} = 5$ ms. While perhaps not biophysically realistic, implementing W(t) achieved the goal of matching the measured onset-burst function. In our view, the results in this study are not affected by how the I/O function was achieved.

Individual cells

The average sustained model was adjusted to match empirical measurements from the individual sustained-type cells (**Figures 3**, **4**). First, the model membrane capacitance and leak conductance were adjusted to match measured values. Then, the maximum voltage-gated conductances (G_{Na}, G_{KHT}, and G_{KLT}) were systematically varied until the model spike counts matched the empirical spiking responses to FM sweeps and current steps. To simulate measured spike variability, we scaled the derived synaptic conductances by factors chosen randomly from a Gaussian distribution (mean = 1; SD = 0.05). Scaling the conductances would represent variation in the size of the

postsynaptic currents, possibly due, for example, to variation in the afferent firing or in vesicle release. Models were then stimulated with 25 independent pairs of scaled synaptic conductances. Model spike probability, the average spikes/trial, was calculated and compared to measured spike probability.

Conductance waveforms

In **Figure 2**, both the excitatory and inhibitory conductance waveforms [$g_E(t)$ and $g_I(t)$ respectively] were simulated as the difference of two exponentials, i.e., $g_E(t) = \frac{G_E}{g_{norm}}\left[\exp(-t/\tau_E) - \exp(-t/\tau_{E\_rise})\right]$, where G_E is the peak conductance, t is time (ms), τ_E and τ_{E_rise} are the decay and rising time constants (ms), respectively, with $\tau_E > \tau_{E\_rise}$. The constant g_{norm} was chosen so that the maximum value of the conductance was G_E. Specifically, the peak value of $g_E(t)$ occurs at time t_p, where $t_p = \frac{\tau_{E\_rise} * \tau_E}{\tau_E - \tau_{E\_rise}} \ln\frac{\tau_E}{\tau_{E\_rise}}$ and g_{norm} is the value of the difference in the exponentials at time t_p, $g_{norm} = \exp(-t_p/\tau_E) - \exp(-t_p/\tau_{E\_rise})$. The conductance parameters that we varied to generate selective responses were relative peak times, the conductance sizes (the integrated conductance functions) and the shapes (the time constants). Each conductance parameter was varied separately, once for excitation and once for inhibition. The integrated conductance was held fixed by adjusting the maximum conductance.

RESULTS

MODEL CELLS MATCH INTRINSIC FIRING PROPERTIES MEASURED *In vivo*

How synaptic selectivity, the differences between the preferred- and null-evoked synaptic inputs, translates into spike selectivity depends on the excitability of the postsynaptic cells. We therefore optimized model cells to match the spike counts evoked by prolonged current steps measured *in vivo* from 20 IC cells that were representative of the larger data set in (Xie et al., 2008) (**Figure 1**). IC cells have been categorized into three types that account for ~95% of the population in our hands: sustained, adapting, and onset (Koch and Grothe, 2003; Xie et al., 2008). We concentrated on the spike counts in the first 50 ms, since we ultimately examined responses to brief (<50 ms) signals. During this period, adapting and sustained cell spike counts are similar, and thus, we only present sustained and onset models [~85% of the cells in Xie et al. (2008)].

Examples of measured and computed spike waveforms and stimulating currents are shown for the sustained and onset cell (**Figures 1A,B**, respectively). The spike counts match well in both cell types, although the waveforms are somewhat different, especially in the sustained cell. In particular, spike heights in the sustained model decline, likely due to Na channel inactivation, and the membrane potential in between spikes is rather different. We suspect this is due to the limited implementation of voltage-gated channels and cell geometry, but we do not think that is has a major impact on our findings (see "Discussion").

Single compartment models were optimized to match the average responses of these two cell populations ("average models"), and are shown as input/output (I/O) functions (**Figure 1C**). Although, we used current steps as stimuli, the I/O curve shape would be similar if the input current were synaptic input strength.

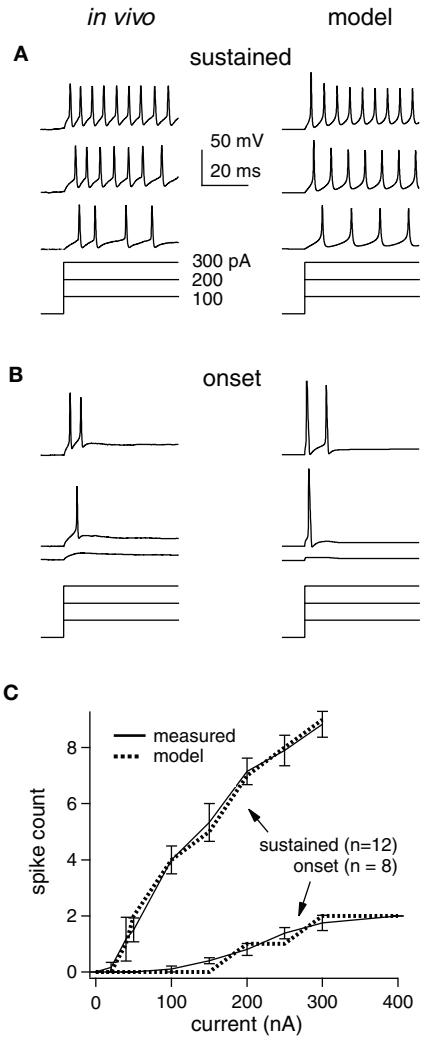

FIGURE 1 | Measured and modeled current-step responses match. **(A)** *in vivo* (left) and model cell (right) potentials (top) for a sustained cell stimulated with current steps (bottom). Scale bars and step sizes also apply to **(B)**. **(B)** Same as **(A)** for an onset cell. **(C)** Empirical and model I/O functions for average response of each cell type.

We did not inject enough current to reach saturation in the *in vivo* study, but as expected the slopes become less steep with increasing stimulus strength (Darian-Smith, 1960; Tateno et al., 2004). We used these average model cells to examine the roles of inhibition in generating spike selectivity.

CHANGES IN SPIKE COUNTS AFTER INHIBITORY BLOCK DO NOT DISTINGUISH AMONG FIVE SYNAPTIC MECHANISMS IN THE MODEL CELLS

We next created spike selectivity with five different mechanisms of synaptic selectivity (**Figure 2**) using the average sustained (top, **A–E**) and onset (bottom, **F–J**) cell models from **Figure 1**. These examples were designed to illustrate that amongst very diverse mechanisms of synaptic selectivity, the role(s) of inhibition are not always revealed by changes in spike counts following

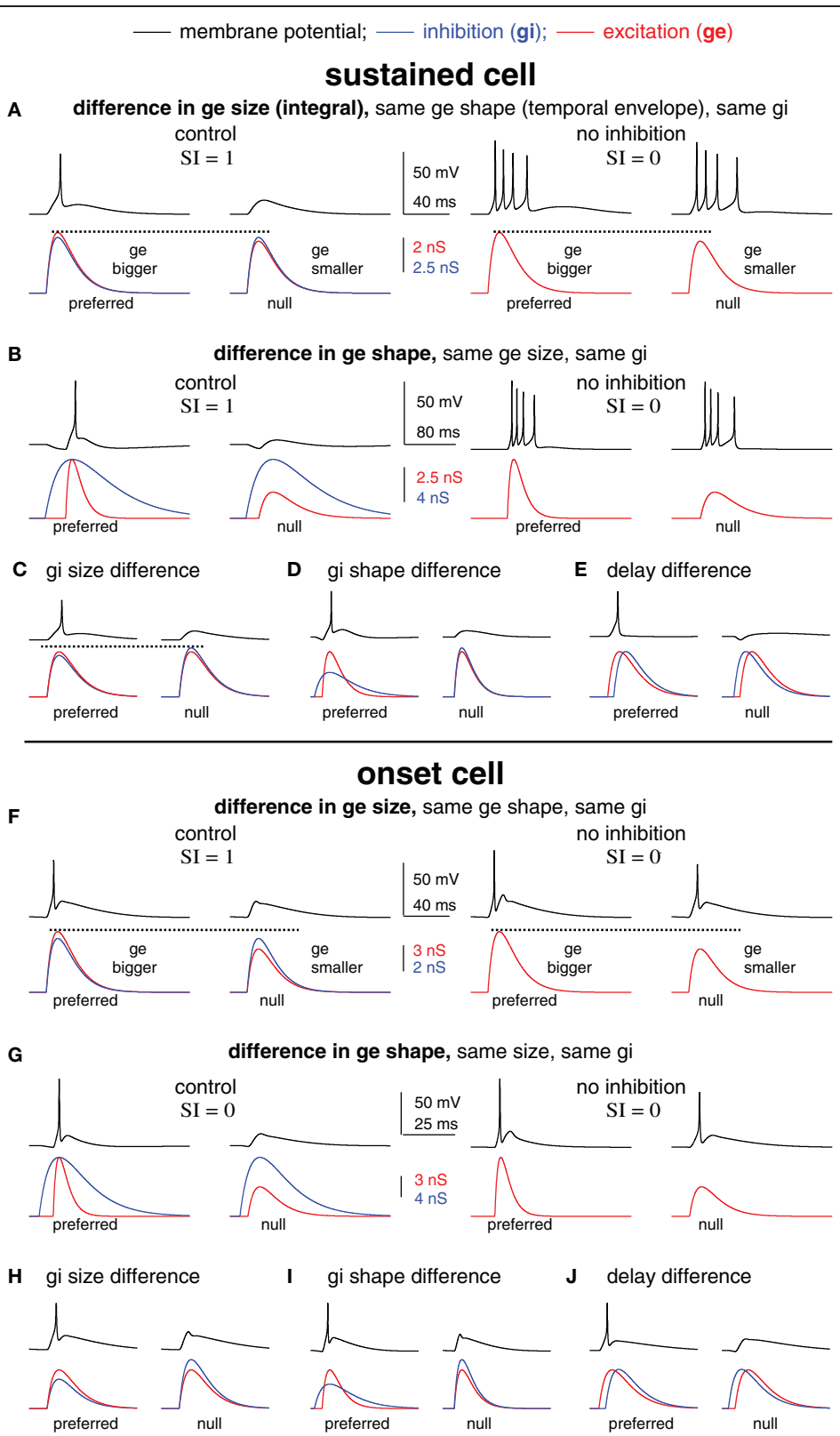

FIGURE 2 | Blocking inhibition can eliminate spike selectivity independent of the underlying mechanism of synaptic selectivity. Spike selectivity is generated by five different mechanisms of synaptic selectivity in a modeled sustained cell **(A–E)** and onset cell **(F–J)**. Each mechanism had differences in only one synaptic conductance parameter, as shown. In each case, the preferred conductance pair evoked one spike and the null-evoked no spikes (selectivity index SI = 1). Removing inhibition eliminated spike selectivity (SI = 0) in every example.

inhibitory block. In each case, synaptic selectivity was created by only a single difference between the preferred- and null synaptic inputs, as described below. Of the five cases, the mechanism underlying synaptic selectivity was entirely excitatory in two, entirely inhibitory in two, and in one case both excitation and inhibition contributed. However, inhibition reduced the current strength in all five cases, which modulated the gain, i.e., the ratio of output spikes to input current. As will be shown, spike selectivity was dependent on the relative gains of the preferred and null inputs. Consequently, eliminating inhibition from the model eliminated spike selectivity in every case.

In the first example, the mechanism underlying synaptic selectivity was entirely excitatory (sustained cell, **Figure 2A**, left; onset cell, **Figure 2F**, left). The only difference between the preferred- and null synaptic conductances was that the integral (size) of the preferred excitatory conductance was larger than the null. The preferred and null excitations were identical in temporal envelope (shape), and the preferred and null inhibitions were identical in both size and shape. Finally, there was no delay between the excitation and inhibition in either the preferred or null conductance pair. In this (and each) example, the synaptic conductances were made such that the preferred conductance pair evoked spikes but the null pair did not.

We then show what would happen if inhibition were blocked. We simulated blocking inhibition by eliminating inhibition and stimulating with excitation only (**Figures 2A,F** right). In each model cell, the preferred and null excitation presented alone evoked identical spike counts. Indeed, they were designed to do so in order to illustrate the point that blocking inhibition can eliminate spike selectivity even when inhibition makes no contribution to synaptic selectivity. Consider that the preferred and null inhibitions were identical, and therefore, inhibition could not by itself create synaptic selectivity. Instead, the difference between the preferred and null excitations created synaptic selectivity. However, in the absence of inhibition, the synaptic selectivity did not translate into spike selectivity. In order to translate into spike selectivity, synaptic selectivity must generate a difference in the inputs (input selectivity) that falls in a region of the I/O curve that is sufficiently steep to generate a difference in the spike counts (see schematic in **Figure 5**). Here, we made the excitatory inputs so that when presented without inhibition the resulting inputs were both large, and thus, fell in the upper region of the I/O function that was not sufficiently steep to generate spike count differences. With inhibition, the inputs were reduced in amplitude, shifting their position leftward on the I/O function where the slope was steep enough to generate spike differences (in this case, the null generated no spikes). By reducing the strength of both the preferred and null inputs, inhibition modulated the gain. Spike selectivity was enhanced because the gain of the null was reduced to zero, whereas the preferred gain was still positive.

The second example was similar to the first except that synaptic selectivity was due to the difference in the temporal envelopes (shapes) of the preferred and null excitation, with no differences in the size (integral) of excitation, and no differences between the preferred and null inhibitions (sustained cell, **Figure 2B**; onset cell, **Figure 2G**). Again, the inputs were designed so that in the absence of inhibition the preferred and null excitations evoked identical spike counts (right). These (extreme) examples show that inhibition can enhance spike selectivity by modulating the gain without contributing to synaptic selectivity.

In the remaining three examples, synaptic selectivity depended on inhibition; there were no differences between the preferred and null excitations. Consequently, removing inhibition eliminated synaptic selectivity entirely, and therefore eliminated both input- and spike selectivity (not shown). In two cases the synaptic selectivity was entirely inhibitory; the preferred and null inhibitions differed either in size (total conductance) (sustained cell, **Figure 2C**; onset cell, **Figure 2H**) or shape (sustained cell, **Figure 2D**; onset cell, **Figure 2I**), and the preferred and null excitations were identical. The last example shows the classic case of creating spike selectivity by a difference in the delay between excitation and inhibition (sustained cell, **Figure 2E**; onset cell, **Figure 2J**).

We note that in addition to its contribution to synaptic selectivity, inhibition was also designed to enhance spike selectivity in each of the five cases as a gain control, i.e., by keeping the null inputs below threshold and by keeping the overall input strength well below saturation. We conclude from this section that in many scenarios the elimination of spike selectivity following inhibitory block does not reveal the mechanisms underlying synaptic selectivity. Importantly, the results were similar in the two different model cells that represent the extremes of the cell types found in the IC (Xie et al., 2008; Gittelman et al., 2009), suggesting that this may be true in many cell types.

BLOCKING INHIBITION REDUCES SPIKE SELECTIVITY FOR FM DIRECTION BY ADJUSTING THE GAIN

We now examine how inhibition contributes to spike selectivity for FM direction in IC cells using the above modeling strategy with empirical data. We used this approach to assess the extent to which inhibition enhanced spike selectivity by contributing to synaptic selectivity as compared to acting as a gain control, and to determine whether the empirically derived model was consistent with the ubiquitous finding that blocking inhibition reduces spike selectivity and increases spike counts.

In this section we used previously published synaptic conductances that were derived from FMs presented in sets consisting of two identical sweeps, one that swept upward and one that swept downward. The "average" sustained model cell from **Figure 1** was adjusted to match the empirically derived I/O functions for each individual cell from which FM-evoked conductances were derived. Each FM evoked a conductance pair consisting of an excitation and an inhibition. Thus, each FM set, consisting of a downward and an upward sweep, evoked two conductance pairs, one evoked by the preferred sweep direction, and another evoked by the null direction. We refer to the preferred- and null-evoked conductance pairs together as a conductance "set." In three cells, two FM sets were presented, and in two cells only one FM set was presented. Thus, we derived two conductance sets each from three cells, and one conductance set each from two cells for a total of eight conductance sets, or 16 conductance pairs.

We show an example cell in **Figure 3**, followed by summary results in **Figure 4**. The computed and measured I/O functions of the example cell were identical (**Figure 3A**), and the FM-evoked spiking matched the spiking computed by stimulating the model with the FM-evoked conductance pairs (**Figures 3B,C**). The preferred FM reliably evoked spikes, whereas the null FM never evoked spikes (average spikes/trial of 0.9 and 0, respectively, **Figure 3B**). We calculated spike selectivity using the SI [SI = (P − N)/(P + N)], where P is the preferred spike count and N is the null spike count. The SI ranges from 0 (non-selective) to 1 (maximum selectivity). Here, SI = 1. Similar to the measured data, computed firing probability to the preferred conductance pair was 0.92, and computed firing to the null was 0 (SI = 1, **Figure 3C**).

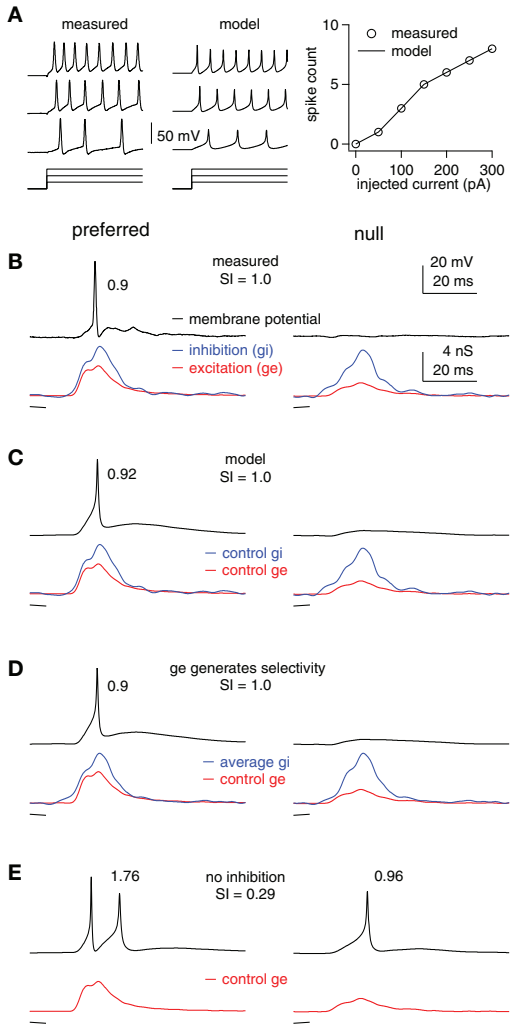

FIGURE 3 | Inhibition enhances FM selectivity by controlling the gain, example cell. (A) Measured and computed responses to 100, 200, and 300 pA current steps (50 ms shown). Right: measured and computed I/O functions. **(B)** Measured membrane potentials (top) in response to preferred (downward, single trace) and null (upward, average of 10 traces) FMs and the derived FM-evoked synaptic conductance (bottom). Spike probability and SI as shown. **(C–E)** Using the model cell from **(A)** and the control excitations shown in **(B)**, we computed membrane responses using **(C)** the control inhibitions, **(D)** the average of the preferred and null inhibitions, and **(E)** no inhibition. Model firing probabilities and SIs as shown.

Inspection of the FM-evoked synaptic conductance waveforms shows that the preferred excitation was larger than the null excitation, and they differed in shape. Additionally, the preferred inhibition was also slightly larger than the null inhibition, and they differed somewhat in shape (**Figures 3B,C**, bottom). We point this out to make it clear that both excitation and inhibition contributed to synaptic selectivity, but that it is not clear how inhibition's contribution to synaptic selectivity affected spike selectivity.

To determine the extent to which inhibition's contribution to synaptic selectivity affected spike selectivity, we eliminated the differences between the preferred and null inhibitions. We did this by averaging the preferred and null inhibitory conductance (**Figure 3D**). We then stimulated the model cell with a conductance pair comprised of the average inhibition and either the preferred or the null excitation. Under these conditions, inhibition makes no contribution to synaptic selectivity, but continues to modulate the input strength in approximately the same way as in the control condition.

In this model, the differences in excitation combined with the average inhibition generated the same firing probabilities and spike selectivity as the measured values. The firing probability computed using the conductance pair with the average inhibition and the preferred excitation was 0.9, whereas, the firing probability computed from the conductance pair with the null excitation was 0 (SI = 1). In other words, whatever contribution inhibition made to synaptic selectivity in this example, that contribution was undetectable in the spike counts.

We next assessed the extent to which inhibition's role in modulating input strength affected spike selectivity by asking how eliminating inhibition affected the difference between the preferred and null spikes. Without inhibition, the preferred excitation evoked an average of 1.76 spikes per stimulus, whereas the null firing count increased to 0.96, reducing the SI to 0.29 (**Figure 3E**). Note that inhibition enhanced spike selectivity in two ways that are consistent with gain control. First, it kept the null response below threshold, i.e., the null gain = 0. Also, the null firing increased slightly more than the preferred following inhibitory block. More importantly, because the SI is calculated as a ratio, the overall increase in firing reduced the SI. This points out that by limiting the overall firing rates, inhibition can increase the relative difference in spiking, even if it does not alter the absolute spiking difference.

We conclude that in this example, inhibition enhanced spike selectivity by controlling the gain and by limiting firing rates rather than by its contribution to synaptic selectivity. Furthermore, the effects of removing inhibition on spike rate and spike selectivity are consistent with the effects commonly observed when inhibition is blocked *in vivo*. Although, this example is representative of most of our data, there are cells in which inhibition's contribution to synaptic selectivity does affect spike selectivity, as shown in the next section.

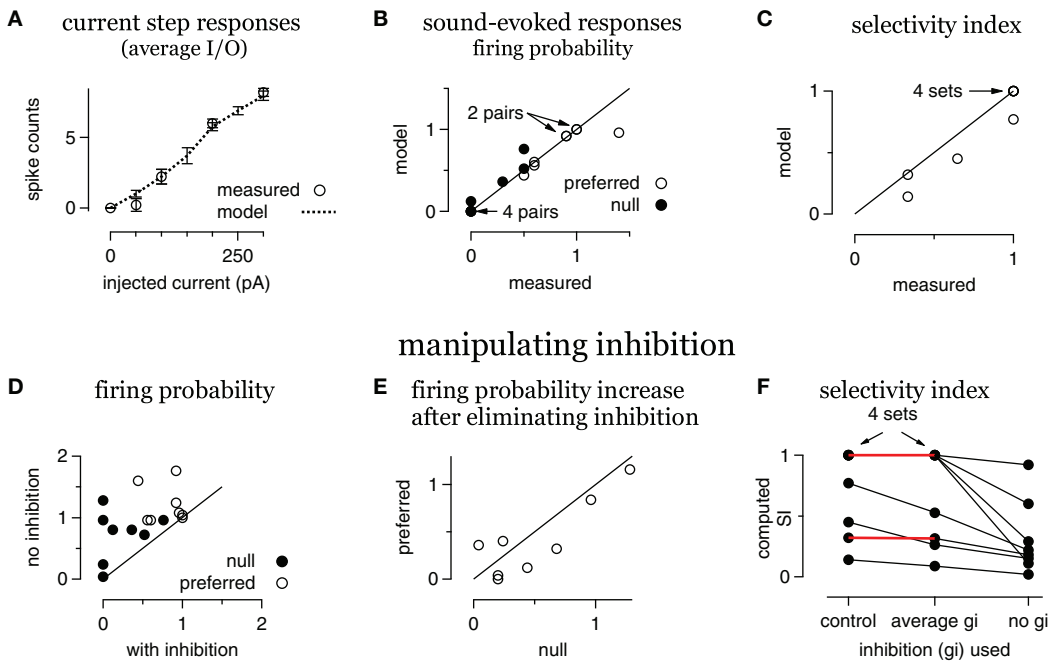

FIGURE 4 | Inhibition enhances FM selectivity by controlling gain, summary. (A) Average modeled and measured I/O curves. **(B)** Measured FM-evoked spike probability plotted against spike probability computed in the models using the derived FM-evoked conductance pairs. **(C)** Selectivity index (SI) for all eight FM sets, modeled vs. measured. **(D)** Computed spike probability, with and without inhibition. **(E)** The change in computed spikes/trial following the elimination of inhibition. The change is equal to the spikes/trial under control conditions with inhibition intact subtracted from the spikes/trial with no inhibition. **(F)** Selectivity index computed using either the control conductance sets, conductance sets with the average inhibition and the control excitations, or with the control excitations only. Red lines indicate no change in SI using the average inhibition.

SUMMARY DATA

A summary of the eight conductance sets from the five cells is shown in **Figure 4**. On average, the spike counts evoked by current steps computed from the model cells were similar to the measured spike counts (**Figure 4A**). The responses computed from the FM-evoked conductance waveforms matched the measured FM-evoked firing probability closely (**Figure 4B**). In 14/16 conductance pairs, the computed and measured firing probabilities were within 10%. In one conductance set, the computed firing probability to the preferred conductance pair was 0.96, lower than the measured probability of 1.4. In another set, the null-computed spiking probability was 0.7 compared to the measured 0.5.

In terms of directional selectivity, the model cells and measured data were also similar (**Figure 4C**). We show the computed SI plotted against the measured SI for each conductance set. In five out of eight sets, the computed and measured SIs were equal. In three sets, the computed SI was slightly lower than measured. Since blocking inhibition typically reduces the SI, a low computed SI for the control condition is a conservative error. Taken together, the models are a good representation of the individual cells.

To determine the extent to which inhibition enhanced spike selectivity by contributing to synaptic selectivity or gain control, we computed firing probabilities and SIs using either the average of the preferred and null inhibitions or by eliminating inhibition. We first show the effect of eliminating inhibition on firing probability (**Figures 4D,E**).

Eliminating inhibition increased spike probability in almost every case (**Figure 4D**), and inhibition kept the null responses below threshold (gain = 0) in four out of eight sets. Furthermore, the increase in firing probability, the difference between the firing probability with and without inhibition, was greater in the null than in the preferred in six out of eight sets (**Figure 4E**). Thus, inhibition affected firing rates and the gain in most cases.

We next assessed the effect on spike selectivity of inhibition's contribution to synaptic selectivity compared with inhibition's contribution to gain control (**Figure 4F**). For each conductance set, we show the SI computed with the control excitation combined with either the control inhibition (control), the average inhibition or with no inhibition. In five out of eight cases, using the average inhibition did not alter the SI (red horizontal lines, four cases are overlapping), indicating that any contribution that inhibition made to synaptic selectivity was undetectable in the spike counts. In these five cases, the SI was not reduced until inhibition was eliminated. In the remaining three cases, eliminating the inhibitory differences reduced the SI. However, eliminating inhibition entirely reduced the SI even more, indicating that inhibition contributed to spike selectivity by enhancing synaptic selectivity and as a gain control in these three cells. Thus, inhibition sometimes enhanced spike selectivity by enhancing

synaptic selectivity (three out of eight), but always enhanced spike selectivity as a gain control (eight out of eight).

DISCUSSION

SUMMARY

Using modeling and results from *in vivo* whole-cell recordings, we investigated the role of inhibition in shaping neuronal response selectivity in the IC. The first result is that changes in spike selectivity following inhibitory block do not necessarily distinguish amongst potential underlying mechanism(s) of spike selectivity. This was shown in two distinct cell types, sustained cells and onset cells, which represent the extremes of the cell types found in the IC in terms of input/output functions. Using empirically derived synaptic inputs and modeling, we found that when inhibitory block reduced or eliminated spike selectivity, inhibition sometimes enhanced spike selectivity by contributing to synaptic selectivity, but always by modulating the firing rates and gain. These inhibitory mechanisms are not mutually exclusive. We first discuss the simplicity of the model cells, then briefly review the terms gain and gain control in the context of enhancing spike selectivity.

SIMPLE MODEL

Although, the model cells in this study are very simple, they captured the essential empirically measured features, and we do not believe that a more complex or physiologically accurate model would change the central conclusions. For example, as noted in the methods, the low-voltage-activated potassium conductance in the onset cell model was not physiological. In order to fire a few spikes rather than a single spike at the start of prolonged depolarization, we mathematically delayed the activation of a KLT current. A more physiologically accurate approach would have been to include additional currents, such as, a Ih or a *t*-type calcium current (Sivaramakrishnan and Oliver, 2001; Koch and Grothe, 2003). However, modeling studies have shown that many different combinations of intrinsic properties can achieve the same I/O curve (Prinz et al., 2003), and suggest that similar I/O curves would be functionally similar independent of the underlying intrinsic properties. Also, we would expect that a multi-compartment model with the appropriate complement of intrinsic properties might show a greater role for synaptic selectivity in creating differences between preferred and null PSPs (PSP selectivity). For example, Ih in cortical dendrites strongly affects the temporal summation of inputs, and is not homogenously expressed (Magee, 1998). Due to space clamp issues, such dendritic processing might be undetectable in somatic recordings, even with channel blockers (Williams and Mitchell, 2008). Although, we have argued that the small size and high input resistance of most IC cells likely reduces the space clamp problem in IC cells compared to cortical neurons (Gittelman and Li, 2011), processing in the dendrites could be undetected or underestimated. However, we suggest that inhibition would function similarly in the dendrites with the exception that the output might be PSPs instead of spikes, i.e., there would be no spike threshold. Nevertheless, inhibition would keep PSP size small and away from saturation. Whatever processing occurs in the dendrites

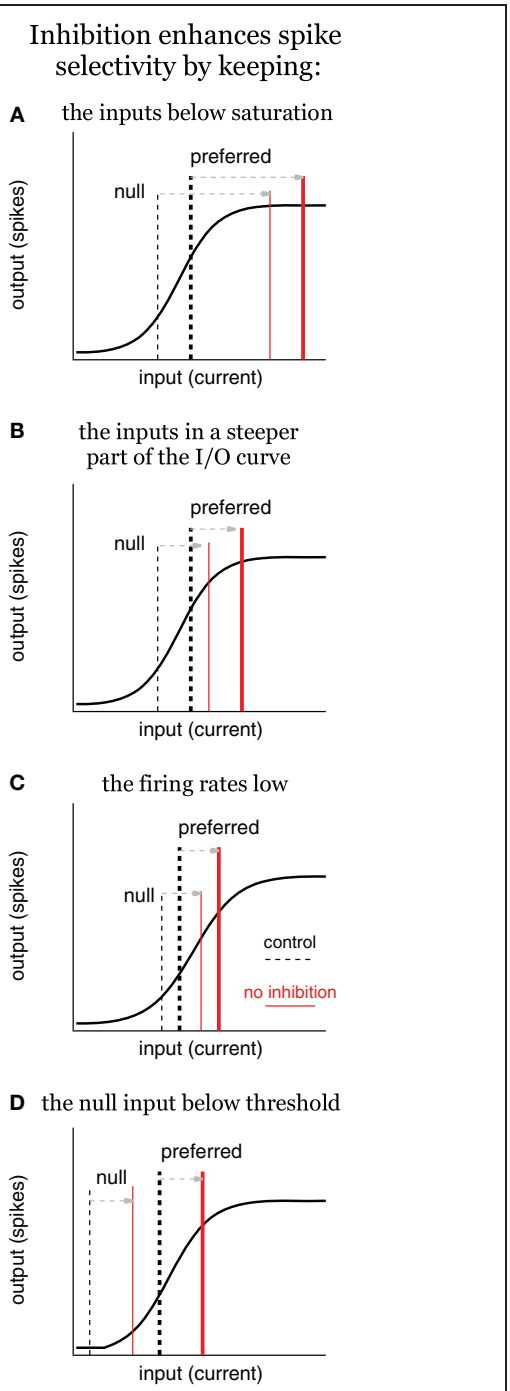

FIGURE 5 | Inhibition enhances spike selectivity by modulating gain, schematic. Input/output (I/O) schematics illustrate three scenarios in which inhibition enhances spikes selectivity by reducing spike rates and controlling gain, the ratio of output/input. In each panel, the solid black line represents the I/O curve, the dashed vertical lines represent the input current for the control condition (tall and thick for preferred; short and thin for null), and the red lines represent the input current with no inhibition. Inhibition enhances spike selectivity by: **(A)** keeping the inputs below saturation; **(B)** keeping the inputs in the steepest part of the I/O curve; **(C)** keeping the firing rates low; and **(D)** keeping the null input below threshold, where the gain is zero. In **(C)**, it is not required for inhibition to change the gain to enhance spike selectivity, although, it does in this example.

would then be passed as input to the next compartment (e.g., the soma).

GAIN AND GAIN CONTROL

Before illustrating how inhibition modulates gain and how this affects spike selectivity, we note that gain and gain control have been described in a number of different ways in the literature. In order to clarify these terms, we consider a neuronal I/O curve with current as the input and spikes as the output (**Figure 5**). Neuronal I/O curves are typically sigmoidal in that in response to small (subthreshold) inputs the output is zero. As the current strength increases, the output increases up to a point, and then eventually saturates. It is often the case that continuing to increase the current strength will eventually decrease the output (not shown).

Gain is the ratio of output/input (y/x), and therefore, the gain changes with input strength. At the far left of the curve, when the output is zero, the gain is zero. As the current strength increases, the I/O curve enters a rising phase during which output increases approximately in proportion to input. During this rising phase, the gain increases rapidly at first, but then more slowly as saturation is approached. During the saturation phase (far right), gain decreases as input strength increases, but does not return to zero.

One definition of gain control, termed additive/subtractive, is a horizontal shift of the I/O curve (Ingham and McAlpine, 2005). With only excitatory current as the input (X-axis), inhibition shifts the I/O curve rightward (see Figure 9, Ingham and McAlpine, 2005). However, the input to a cell is not just excitation, but also includes inhibition. Therefore, the input is better described as total current rather than just excitatory current. With total current as the input, inhibition does not change the I/O curve, rather it changes the input strength (Holt and Koch, 1997; Chance et al., 2002). In this mathematically equivalent view, inhibition works as an additive/subtractive gain control by shifting the input strength leftward along the X-axis (see section "How Modulating Gain Affects Spike Selectivity").

Another definition of gain that is often used in neurobiology is the slope of the I/O curve (dy/dx), i.e., the proportional change of output with respect to input (Isaacson and Scanziani, 2011). To distinguish between this definition and the preceding definition (y/x), we refer to dy/dx as the proportional gain. The proportional gain also changes with input strength, but in a different way. The proportional gain is zero at the far left of the curve when the output is zero. It increases at the start of the rising phase, peaks at the midpoint of the rising phase, and then decreases as saturation is approached, rapidly returning zero.

Also in neurobiology, it is often the case that only the rising phase of the I/O curve is considered in discussions of proportional gain (Isaacson and Scanziani, 2011). As the rising phase can be fit reasonably well with a line, the proportional gain is considered constant. Gain control is then defined as a change in the slope of that rising phase (Chance et al., 2002; Ingham and McAlpine, 2005). Termed multiplicative or divisive gain control, this is a useful definition when considering, for example, how attention changes spike selectivity with respect to an environmental stimulus rather than with respect to current (McAdams and Maunsell, 1999; Treue and Martínez Trujillo, 1999). However, without considering the entire I/O curve it is not possible to describe the multiple ways in which inhibition modulates the gain, the proportional gain, and spike selectivity. When the entire curve is considered, and input is defined as current, inhibition modulates the gain and the proportional gain by shifting the net input current leftward with no concomitant change to the slope of the I/O curve (Holt and Koch, 1997; Chance et al., 2002). As we describe next, these changes in gain can account for changes in spike selectivity. Importantly, they can also account for the multiplicative/divisive gain control observed when the input (X-axis) is an environmental stimulus rather than current (Murphy and Miller, 2003).

HOW MODULATING GAIN AFFECTS SPIKE SELECTIVITY

How inhibition alters gain and spike selectivity depends on where the inputs fall along the I/O curve, and where they move when inhibition is removed. We illustrate how inhibition can shape spike selectivity without contributing to synaptic selectivity using a schematic (**Figure 5**). In each scenario, we assume that the difference between the preferred and null input currents is due to differences between the preferred and null excitations, i.e., synaptic selectivity relies entirely on excitation to generate input selectivity. The preferred and null inhibitions are presumed identical. Although, not strictly true, we conservatively assume that identical inhibitions would shift the inputs leftward equally along the X-axis (and thus blocking inhibition would shift the inputs equally rightward). At typical resting potentials, identical inhibitions would actually shift the null slightly more along the X-axis than it would shift the preferred. In most situations, this would mean that inhibition enhances spike selectivity more than if the lateral shifts were exactly equal.

In the first scenario, inhibition enhances spike selectivity by keeping the inputs below saturation (**Figure 5A**). Under control conditions, the inputs fall within the rising phase, with high proportional gain. The preferred input (tall, thick dashed line) is larger than the null (short, thin dashed line), and therefore, evokes more spikes compared to the null. Once inhibition is removed, both inputs shift rightward equally, such that they both evoke the maximum number of spikes, i.e., the output saturates (red lines), and spike selectivity is eliminated. In other words, inhibition keeps the inputs within the rising portion of the I/O curve, where the gains are high, and the gain of the preferred is larger than the null gain. The steep slope (high proportional gain) results in even small differences between the preferred and null inputs translating into differences in the spiking. When inhibition is removed in this example, the inputs shift rightward to a region of the I/O curve where the preferred gain is less than the null gain, and the proportional gain goes to zero. Consequently, no matter how large the difference between the preferred and null inputs, they will evoke the same number of spikes. This, and each subsequent example, shows an example of inhibition enhancing spike selectivity by functioning as a subtractive gain control. By reducing input strength, inhibition changed the gains of the preferred and null inputs, and consequently increased the difference in output spikes.

There is a corollary to this example in which the inputs shift rightward to a region of gentler slope, but do not reach saturation (**Figure 5B**). It should be clear that without reaching saturation,

the preferred proportional gain decreases more than the null proportional gain. Consequently, the same difference between the preferred and null inputs would generate a smaller difference in spiking, i.e., spike selectivity would decrease even without reaching saturation.

Consistent with the above ideas, studies in the IC show that inhibition prevents spike rate from approaching saturation (Sivaramakrishnan et al., 2004; Ingham and McAlpine, 2005). This is also true in the cortex, where inhibition prevents epileptiform activity (Dudek and Sutula, 2007; Katzner et al., 2011), although, the phenomenon is not typically described as gain control.

Additionally, inhibition keeps spike rates low, which also enhances spike selectivity (**Figure 5C**). Under control conditions the preferred input is larger than the null, but both fall within the rising phase of the I/O function. When inhibition is removed, both shift equally to the right, but stay within the rising phase. In this example the proportional gain does not change (much). However, the preferred and null gains do change. With inhibition, the preferred gain is substantially larger compared to the null gain. When inhibition is removed, both the preferred and the null gain increase, but the null gain increases more compared to the preferred. In other words, the difference between the preferred and null gain is reduced. Because the SI is a ratio, it decreases when the preferred and null spikes increase equally.

Finally, inhibition enhances spike selectivity by keeping the null input below spike threshold (**Figure 5D**, Rose and Blakemore, 1974; Wehr and Zador, 2003; Gittelman et al., 2009; Katzner et al., 2011). The null evokes no spikes under control conditions, and therefore, the null gain is zero. When inhibition is removed, both the preferred and null inputs shift equally to the right, and the null exceeds threshold (null gain > 0). Although this may increase the absolute difference between the preferred and null spikes, it nevertheless reduces spike selectivity as measured by the SI [$SI = (P-N)/(P+N)$, where P is the preferred spike count and N is the null spike count]. Under control conditions the null spike count $N = 0$, and so the $SI = 1$. After inhibition is blocked, $N > 0$, so $SI < 1$.

What this suggests is that when quantified by a SI, nearly any change in firing rates will change the SI, and in most situations, increasing firing rates will reduce it. Blocking inhibition almost always increases firing rates in the IC, and therefore, almost always reduces the SI. What is important here is that this is true independent of whether or not inhibition contributes to synaptic selectivity.

SYNAPTIC SELECTIVITY vs. GAIN CONTROL

Evidence suggests that inhibition contributes to synaptic selectivity in the IC, but this contribution only enhances spike selectivity in some cells or perhaps to particular stimuli. A clear example from extracellular recordings is for non-monotonic rate level functions, in which firing rates increase initially as sound intensity increases, but the rates decrease as sound intensity continues to increase. In addition to increasing overall firing rates, blocking inhibition often converts this profile to monotonic, in which firing rates increase continuously or saturate as the sound level increases, but do not decrease (Park and Pollak, 1993; Fuzessery and Hall, 1996; Sivaramakrishnan et al., 2004). The simplest interpretation of these results is that high intensities recruit additional inhibition that suppresses the spiking response under control conditions. Consider the medium intensity sound as the preferred signal, and the high intensity sound as the null. In this case, inhibition enhances spike selectivity by contributing to the synaptic selectivity: the null stimulus evoked more inhibition compared to the preferred stimulus. However, inhibition also changes the input strength, and so likely enhances spike selectivity by subtractive gain control (see section "Gain and Gain Control").

The most direct evidence for inhibition contributing to synaptic selectivity comes from the few *in vivo* whole cell recordings in the IC in which the excitatory and inhibitory inputs are at least partially isolated. Inhibition contributes to synaptic selectivity for FM sweeps, at least in some cells (Gittelman et al., 2009; Gittelman and Li, 2011; Kuo and Wu, 2012). In one recent study, Kasai et al. (2012) found the clearest evidence for inhibition creating selective responses to the offset of tones, possibly in the absence of excitation. These cells fired selectively to the offset of a preferred tone duration, i.e., the preferred duration evoked a robust response, whereas a null duration evoked fewer or no spikes. In two of the 11 offset neurons, the selective firing was due to a (presumably) inhibition-induced hyperpolarization, combined with intrinsic properties that facilitate anode-break excitation. Although, the separation of excitation and inhibition was not perfect, no evidence of excitation was found, suggesting that it was small if present. In other words, inhibition was the major—and possibly only—contributor to synaptic selectivity in these two cells.

Interestingly, it has now been demonstrated in the mammalian auditory system that excitation is not necessary for selective spiking, at least in the superior paraolivary nucleus (SPN). Kopp-Scheinpflug et al. (2011) showed *in vitro* that offset responses can be evoked by inhibitory transmission that hyperpolarizes the cell along with Ih and low-threshold *t*-type calcium currents that facilitate rebound excitation. Although it is not clear how common this mechanism is *in vivo*, the study nicely demonstrates that under certain conditions no excitation is required to evoke spikes. Biophysically, the onset cells in the IC are similar to those in the SPN (Koch and Grothe, 2003; Xie et al., 2008). Combined with the observations of Kasai et al. (2012) in which no evidence of excitatory input was found in duration-tuned cells of the IC, there is a possibility that the same mechanism operates in the IC. This may be the most extreme case possible, in which inhibition is the only synaptic input, and therefore, is the exclusive contributor to synaptic selectivity.

Having noted that inhibition enhances spike selectivity by contributing to synaptic selectivity in some situations, several studies in which spike selectivity was measured in the IC before and after inhibitory block using extracellular electrodes have proposed that inhibition increases selectivity by gain control (Ingham and McAlpine, 2005; Pérez-González et al., 2012). Following inhibitory block, tuning for interaural phase differences (IPD) is reduced and the overall firing rates increase, without a change in the best IPD (Ingham and McAlpine, 2005). The authors

suggest one way to explain these changes is by the mechanisms in **Figure 5**, in which inhibition operates as a subtractive gain control. Similarly, the effects of blocking inhibition on stimulus specific adaptation (SSA) are consistent with inhibition functioning as a subtractive gain control (Pérez-González et al., 2012). Firing rates to the high-probability standard tone (null-like) and to the low-probability deviant tone (preferred-like) increased during inhibitory block, which reduced the SSA selectivity index (also a ratio), consistent with the model in **Figure 5C**. There were also cases in which inhibition eliminated the response to the standard tone, i.e., kept it below threshold, as in **Figure 5D**.

Evidence from whole-cell recordings in the IC suggests it is very rare for a sound to evoke excitation without evoking inhibition. As noted above, sometimes inhibition is evoked in the absence of excitation (Xie et al., 2007; Kuo and Wu, 2012), and this occasionally evokes spikes (Kasai et al., 2012). However, in general, sounds that drive spikes evoke both excitation and inhibition, consistent with a role for inhibition in enhancing spike selectivity by modulating firing rates and gain. What is most striking is that even when inhibition reduces the difference between the preferred and null PSPs, it can still enhance spike selectivity by the mechanisms shown in **Figure 5** (Gittelman et al., 2009; Gittelman and Li, 2011). As noted at the end of section "How Modulating Gain Affects Spike Selectivity," when inhibition is present with excitation, it nearly always enhances spike selectivity by reducing firing rates and/or by subtractive gain modulation.

Finally, we note that inhibition performs these same functions in the cortex (see Isaacson and Scanziani, 2011, for an excellent review). Whole-cell recordings *in vivo* have found evidence that inhibition enhances synaptic selectivity in the cortex in some cells and for some stimuli (Anderson et al., 2001; Zhang et al., 2003; Tan et al., 2004; Wu et al., 2006; Ye et al., 2010). But the majority of studies suggest that in most cells, excitation and inhibition are approximately co-tuned and approximately balanced, in that excitation and inhibition have very similar receptive fields, and that the ratio of excitation to inhibition is roughly constant (Anderson et al., 2000; Wehr and Zador, 2003; Tan et al., 2004; Priebe and Ferster, 2005; Okun and Lampl, 2008). These characteristics are consistent with inhibition reducing synaptic selectivity, but functioning as a gain control. Furthermore, inhibition enhances spike selectivity in the cortex by preventing hyperexcitability (Dudek and Sutula, 2007; Katzner et al., 2011), and often by keeping null inputs below threshold (Rose and Blakemore, 1974; Wehr and Zador, 2003). Although most cortical studies limit the definition of gain control to "multiplicative/divisive" gain control as described in section "Gain and Gain Control," and therefore do not refer to these mechanisms as gain control (Isaacson and Scanziani, 2011), functionally these are the same roles served by inhibition in the IC. Although data in the IC are limited, they suggest that inhibition enhancing spike selectivity by controlling the gain may be a general rule rather than an exception.

ACKNOWLEDGMENTS

We thank the anonymous reviewers for their insightful comments, helpful suggestions and careful editing. We also thank Carl Resler for technical support. Supported by NIH grants DC007856, DC009741, and DC00100.

REFERENCES

Anderson, J., Lampl, I., Reichova, I., Carandini, M., and Ferster, D. (2000). Stimulus dependence of two-state fluctuations of membrane potential in cat visual cortex. *Nat. Neurosci.* 3, 617–621.

Anderson, J. S., Lampl, I., Gillespie, D. C., and Ferster, D. (2001). Membrane potential and conductance changes underlying length tuning of cells in cat primary visual cortex. *J. Neurosci.* 21, 2104–2112.

Andoni, S., Li, N., and Pollak, G. D. (2007). Spectrotemporal receptive fields in the inferior colliculus revealing selectivity for spectral motion in conspecific vocalizations. *J. Neurosci.* 27, 4882–4893.

Casseday, J. H., Ehrlich, D., and Covey, E. (1994). Neural tuning for sound duration: role of inhibitory mechanisms in the inferior colliculus. *Science* 264, 847–850.

Chance, F. S., Abbott, L. F., and Reyes, A. D. (2002). Gain modulation from background synaptic input. *Neuron* 35, 773–782.

Darian-Smith, I. (1960). Neurone activity in the cat's trigeminal main sensory nucleus elicited by graded afferent stimulation. *J. Physiol.* 153, 52–73.

Dudek, F. E., and Sutula, T. P. (2007). Epileptogenesis in the dentate gyrus: a criticalbperspective. *Prog. Brain Res.*163, 755–773.

Fuzessery, Z. M., and Hall, J. C. (1996). Role of GABA in shaping frequency tuning and creating FM sweep selectivity in the inferior colliculus. *J. Neurophysiol.* 76, 1059–1073.

Gittelman, J. X., and Li, N. (2011). FM velocity selectivity in the inferior colliculus is inherited from velocity-selective inputs and enhanced by spike threshold. *J. Neurophysiol.* 106, 2399–2414.

Gittelman, J. X., Li, N., and Pollak, G. D. (2009). Mechanisms underlying directional selectivity for frequency-modulated sweeps in the inferior colliculus revealed by *in vivo* whole-cell recordings. *J. Neurosci.* 29, 13030–13041.

Gittelman, J. X., and Pollak, G. D. (2011). It's about time: how input timing is used and not used to create emergent properties in the auditory system. *J. Neurosci.* 31, 2576–2583.

Holt, G. R., and Koch, C. (1997). Shunting inhibition does not have a divisive effect on firing rates. *Neural Comput.* 9, 1001–1013.

Ingham, N. J., and McAlpine, D. (2005). GABAergic inhibition controls neural gain in inferior colliculus neurons sensitive to interaural time differences. *J. Neurosci.* 25, 6187–6198.

Isaacson, J. S., and Scanziani, M. (2011). How inhibition shapes cortical activity. *Neuron* 72, 231–243.

Kasai, M., Ono, M., and Ohmori, H. (2012). Distinct neural firing mechanisms to tonal stimuli offset in the inferior colliculus of mice *in vivo*. *Neurosci. Res.* 73, 224–237.

Katzner, S., Busse, L., and Carandini, M. (2011). GABAA inhibition controls response gain in visual cortex. *J. Neurosci.* 31, 5931–5941.

Kautz, D., and Wagner, H. (1998). GABAergic inhibition influences auditory motion-direction sensitivity in barn owls. *J. Neurophysiol.* 80, 172–185.

Klug, A., Bauer, E. E., Hanson, J. T., Hurley, L., Meitzen, J., and Pollak, G. D. (2002). Response selectivity for species-specific calls in the inferior colliculus of Mexican free-tailed bats is generated by inhibition. *J. Neurophysiol.* 88, 1941–1954.

Klug, A., Bauer, E. E., and Pollak, G. D. (1999). Multiple components of ipsilaterally evoked inhibition in the inferior colliculus. *J. Neurophysiol.* 82, 593–610.

Koch, U., and Grothe, B. (2003). Hyperpolarization-activated current (Ih) in the inferior colliculus: distribution and contribution to temporal processing. *J. Neurophysiol.* 90, 3679–3687.

Kopp-Scheinpflug, C., Tozer, A. J., Robinson, S. W., Tempel, B. L., Hennig, M. H., and Forsythe, I. D. (2011). The sound of silence: ionic mechanisms encoding sound termination. *Neuron* 71, 911–925.

Kuo, R. I., and Wu, G. K. (2012). The generation of direction selectivity in the auditory system. *Neuron* 73, 1016–1027.

Kutscher, A., and Covey, E. (2009). Functional role of GABAergic and glycinergic inhibition in the intermediate nucleus of the lateral lemniscus of the big brown bat. *J. Neurophysiol.* 101, 3135–3146.

Magee, J. C. (1998). Dendritic hyperpolarization-activated currents modify the integrative properties of hippocampal CA1

pyramidal neurons. *J. Neurosci.* 18, 7613–7624.

McAdams, C. J., and Maunsell, J. H. (1999). Effects of attention on orientation-tuning functions of single neurons in macaque cortical area V4. *J. Neurosci.* 19, 431–441.

Moore, M. J., and Caspary, D. M. (1983). Strychnine blocks binaural inhibition in lateral superior olivary neurons. *J. Neurosci.* 3, 237–242.

Murphy, B. K., and Miller, K. D. (2003). Multiplicative gain changes are induced by excitation or inhibition alone. *J. Neurosci.* 23, 10040–10051.

Okun, M., and Lampl, I. (2008). Instantaneous correlation of excitation and inhibition during ongoing and sensory-evoked activities. *Nat. Neurosci.* 11, 535–537.

Park, T. J., and Pollak, G. D. (1993). GABA shapes a topographic organization of response latency in the mustache bat's inferior colliculus. *J. Neurosci.* 13, 5172–5187.

Pérez-González, D., Hernández, O., Covey, E., and Malmierca, M. S. (2012). GABA(A)-mediated inhibition modulates stimulus-specific adaptation in the inferior colliculus. *PLoS ONE* 7:e34297. doi: 10.1371/journal.pone.0034297

Priebe, N. J., and Ferster, D. (2005). Direction selectivity of excitation and inhibition in simple cells of the cat primary visual cortex. *Neuron* 45, 133–145.

Prinz, A. A., Billimoria, C. P., and Marder, E. (2003). Alternative to hand-tuning conductance-based models: construction and analysis of databases of model neurons. *J. Neurophysiol.* 90, 3998–4015.

Rose, D., and Blakemore, C. (1974). Effects of bicuculline on functions of inhibition in visual cortex. *Nature* 249, 375–377.

Rothman, J. S., and Manis, P. B. (2003). Kinetic analyses of three distinct potassium conductances in ventral cochlear nucleus neurons. *J. Neurophysiol.* 89, 3083–3096.

Sillito, A. M. (1975). The contribution of inhibitory mechanisms to the receptive field properties of neurones in the striate cortex of the cat. *J. Physiol.* 250, 305–329.

Sivaramakrishnan, S., and Oliver, D. L. (2001). Distinct K currents result in physiologically distinct cell types in the inferior colliculus of the rat. *J. Neurosci.* 21, 2861–2877.

Sivaramakrishnan, S., Sterbing-D'Angelo, S. J., Filipovic, B., D'Angelo, W. R., Oliver, D. L., and Kuwada, S. (2004). GABA(A) synapses shape neuronal responses to sound intensity in the inferior colliculus. *J. Neurosci.* 24, 5031–5043.

Tan, A. Y., Zhang, L. I., Merzenich, M. M., and Schreiner, C. E. (2004). Tone-evoked excitatory and inhibitory synaptic conductances of primary auditory cortex neurons. *J. Neurophysiol.* 92, 630–643.

Tan, M. L., Theeuwes, H. P., Feenstra, L., and Borst, J. G. (2007). Membrane properties and firing patterns of inferior colliculus neurons: an *in vivo* patch-clamp study in rodents. *J. Neurophysiol.* 98, 443–453.

Tateno, T., Harsch, A., and Robinson, H. P. (2004). Threshold firing frequency-current relationships of neurons in rat somatosensory cortex: type 1 and type 2 dynamics. *J. Neurophysiol.* 92, 2283–2294.

Treue, S., and Martínez Trujillo, J. C. (1999). Feature-based attention influences motion processing gain in macaque visual cortex. *Nature* 399, 575–579.

Wehr, M., and Zador, A. M. (2003). Balanced inhibition underlies tuning and sharpens spike timing in auditory cortex. *Nature* 426, 442–446.

Williams, S. R., and Mitchell, S. J. (2008). Direct measurement of somatic voltage clamp errors in central neurons. *Nat. Neurosci.* 11, 790–798.

Wu, G. K., Li, P., Tao, H. W., and Zhang, L. I. (2006). Nonmonotonic synaptic excitation and imbalanced inhibition underlying cortical intensity tuning. *Neuron* 52, 705–715.

Xie, R., Gittelman, J. X., Li, N., and Pollak, G. D. (2008). Whole cell recordings of intrinsic properties and sound-evoked responses from the inferior colliculus. *Neuroscience* 154, 245–256.

Xie, R., Gittelman, J. X., and Pollak, G. D. (2007). Rethinking tuning: *in vivo* whole-cell recordings of the inferior colliculus in awake bats. *J. Neurosci.* 27, 9469–9481.

Yang, L., Pollak, G. D., and Resler, C. (1992). GABAergic circuits sharpen tuning curves and modify response properties in the mustache bat inferior colliculus. *J. Neurophysiol.* 68, 1760–1774.

Ye, C. Q., Poo, M. M., Dan, Y., and Zhang, X. H. (2010). Synaptic mechanisms of direction selectivity in primary auditory cortex. *J. Neurosci.* 30, 1861–1868.

Zhang, L. I., Tan, A. Y., Schreiner, C. E., and Merzenich, M. M. (2003). Topography and synaptic shaping of direction selectivity in primary auditory cortex. *Nature* 424, 201–205.

Conflict of Interest Statement: The authors declare that the research was conducted in the absence of any commercial or financial relationships that could be construed as a potential conflict of interest.

Received: 08 May 2012; accepted: 31 August 2012; published online: 18 September 2012.

Citation: Gittelman JX, Wang L, Colburn HS and Pollak GD (2012) Inhibition shapes response selectivity in the inferior colliculus by gain modulation. Front. Neural Circuits ***6****:67. doi: 10.3389/fncir.2012.00067*

frontiers in
NEURAL CIRCUITS

ORIGINAL RESEARCH ARTICLE
published: 11 October 2012
doi: 10.3389/fncir.2012.00073

Inhibition shapes selectivity to vocalizations in the inferior colliculus of awake mice

***Zachary M. Mayko*[1], *Patrick D. Roberts*[2] *and Christine V. Portfors*[1]*

[1] School of Biological Sciences, Washington State University, Vancouver, WA, USA
[2] Department of Biomedical Engineering, Oregon Health and Science University, Portland, OR, USA

Edited by:
Manuel S. Malmierca, University of Salamanca, Spain

Reviewed by:
Achim Klug, University of Colorado, USA
Kevin Davis, University of Rochester, USA

***Correspondence:**
Christine V. Portfors, School of Biological Sciences, Washington State University, 14204 NE Salmon Creek Avenue, Vancouver, WA 98686, USA.
e-mail: portfors@vancouver.wsu.edu

The inferior colliculus (IC) is a major center for integration of auditory information as it receives ascending projections from a variety of brainstem nuclei as well as descending projections from the thalamus and auditory cortex. The ascending projections are both excitatory and inhibitory and their convergence at the IC results in a microcircuitry that is important for shaping responses to simple, binaural, and modulated sounds in the IC. Here, we examined the role inhibition plays in shaping selectivity to vocalizations in the IC of awake, normal-hearing adult mice (CBA/CaJ strain). Neurons in the IC of mice show selectivity in their responses to vocalizations, and we hypothesized that this selectivity is created by inhibitory microcircuitry in the IC. We compared single unit responses in the IC to pure tones and a variety of ultrasonic mouse vocalizations before and after iontophoretic application of $GABA_A$ receptor ($GABA_AR$) and glycine receptor (GlyR) antagonists. The most pronounced effects of blocking $GABA_AR$ and GlyR on IC neurons were to increase spike rates and broaden excitatory frequency tuning curves in response to pure tone stimuli, and to decrease selectivity to vocalizations. Thus, inhibition plays an important role in creating selectivity to vocalizations in the IC.

Keywords: inferior, colliculus, mouse, frequency tuning, inhibition, vocalization

INTRODUCTION

Neural processing of sensory information relies on the microcircuitry and cellular properties of neurons in the sensory pathway. Identifying the microcircuitry in specific sensory nuclei is important for understanding how behaviorally relevant information is processed, and for determining how changes in cellular properties caused by neural modulators alters sensory processing. Within the auditory pathway, microcircuitry is well understood in the cochlear nucleus (Young and Oertel, 2010) and the nucleus laminaris in chick (Wang et al., 2010). The necessary characterization of microcircuitry has not yet been completed in the main auditory midbrain nucleus, the inferior colliculus (IC). This is a necessary and critical step for a full understanding of the IC's function in analyzing and identifying complex and behaviorally relevant auditory signals.

The IC is the major processing and integrating center in the auditory midbrain (Winer and Schreiner, 2005) as it receives massive ascending projections from all auditory brainstem nuclei (Adams, 1979; Brunso-Bechtold et al., 1981; Frisina et al., 1998) as well as descending projections from the auditory thalamus and cortex (Saldana et al., 1996; Winer et al., 1998). In addition, there are commissural (Aitkin and Phillips, 1984) and intrinsic (Oliver et al., 1991) projections. Ascending projections into the IC are glutamatergic, GABAergic, or glycineric (Willard and Ryugo, 1983; Saint Marie and Baker, 1990; Saint Marie, 1996; Cant, 2005; Schofield, 2005) and commissural projections are GABAergic (Reetz and Ehret, 1999). This convergence of excitatory and inhibitory inputs onto single neurons in the IC results in microcircuits that are important for regulating response properties. In particular, inhibitory inputs play an important role in shaping IC responses to simple, binaural, and modulated sounds (Faingold et al., 1989, 1991; Vater et al., 1992a; Yang et al., 1992; Park and Pollak, 1993, 1994; Casseday et al., 1994; Klug et al., 1995; Fuzessery and Hall, 1996; Le Beau et al., 1996; Palombi and Caspary, 1996; Burger and Pollak, 1998; Koch and Grothe, 1998; LeBeau et al., 2001; Caspary et al., 2002; Zhang and Kelly, 2003). There has been much less focus, however, on how inhibitory inputs to IC neurons shape responses to more complex sounds such as social vocalizations.

In the Mexican free-tailed bat, inhibition plays a role in creating selectivity to social vocalizations (Klug et al., 2002; Xie et al., 2005). Pharmacologically blocking GABAergic and glycinergic receptors in the IC decreases selectivity to social vocalizations (Klug et al., 2002; Xie et al., 2005). In contrast, blocking inhibition in the nuclei of the lateral lemniscus does not alter the selectivity of neurons to social vocalizations (Xie et al., 2005). These results indicate that inhibitory circuitry in IC is important for creating selectivity for social vocalizations in bats (Xie et al., 2005). It is not known in any other species, however, whether inhibitory microcircuits in the IC function in the same manner as in bats to create selectivity for vocalizations. Determining whether this is a general feature or one that is a specialization of bats is crucial for understanding the evolution of neural processing of communication sounds.

The purpose of this study was to examine how inhibitory microcircuitry in the IC shapes selectivity to vocalizations in awake, normal-hearing adult mice (CBA/CaJ strain). Selectivity to social vocalizations occurs in the IC of mice, and just like in bats, there is heterogeneity in the level of selectivity with some neurons being highly selective for one or two vocalizations

and other neurons responding to many vocalizations (Portfors et al., 2009; Holmstrom et al., 2010). Because mice are becoming an important model for understanding neural mechanisms of auditory processing disorders due to the benefits of genetic engineering, a thorough understanding of IC structure and function in normal hearing mice is necessary.

We locally blocked inhibitory inputs to IC neurons by iontophoretically applying antagonists to $GABA_A$ receptors ($GABA_AR$) and glycine receptors (GlyR). We compared responses to tones and vocalizations before and after application of these antagonists. We used the changes in tone responses to identify potential ways that inhibition could shape selectivity to vocalizations. We found that blocking inhibitory receptors increased evoked firing in all neurons and changed the shape of the excitatory receptive field in some neurons. Both of these effects contributed to the decreased selectivity to vocalizations. These results suggest that the complex interplay between excitation and inhibition in the IC helps create heterogeneous neural responses to behaviorally relevant sounds.

MATERIALS AND METHODS

We recorded auditory responses from single neurons in the IC of awake, restrained CBA/CaJ mice. All mice were female and between the ages of 2 and 12 months. The CBA/CaJ strain exhibits normal hearing sensitivity into its second year of life (Willott, 1986, 1991, 2005). As in our previous studies with this strain, we did not find any apparent differences in neural response properties across the ages of mice used in this study (Portfors and Felix II, 2005; Portfors et al., 2009, 2011). Animals were housed with same-sex litter mates on a reversed 12 h light/dark schedule. All mice had *ad libitum* access to food and water. All animal care and experimental procedures were in accordance with the guidelines of the National Institutes of Health, and were approved by the Washington State University Institutional Animal Care and Use Committee.

SURGICAL PROCEDURES

At least 24 hours prior to the first electrophysiological recording session, we mounted a headpost onto the skull of the mouse (Muniak et al., 2012). We placed the mouse in an induction chamber with isoflurane to induce anesthesia. We then placed it in a rodent stereotaxic frame with a mouse adaptor and maintained isoflurane inhalation via a nose mask. We made an incision in the scalp along the midline and reflected the skin laterally. We cemented a hollow metal rod (the headpost) onto the skull and a tungsten ground electrode into the right cerebral cortex using ultraviolet-cured dental cement. Using stereotaxic coordinates slightly modified from Paxinos and Franklin (2001), we made a craniotomy (usually 1×1 mm) over top of the left IC. We then covered the hole with petroleum jelly or bone wax to prevent the brain from dehydrating, applied a local anesthetic (lidocaine) and an antibiotic (Neosporin) to the exposed muscle, and returned the mouse to its home cage to recover from surgery.

ACOUSTIC STIMULATION

Acoustic stimulation was computer-controlled and included tone bursts (100 ms duration, 1 ms rise/fall time, 4/s) and a suite of mouse vocalizations used in a previous study of mouse IC (Portfors et al., 2009). All stimuli were stored in the computer and were output through a high speed, 16-bit digital-to-analog converter (Microstar Laboratories, Bellevue, WA, USA; 400,000 samples/s), fed to a programmable attenuator (Tucker Davis Technologies, Alachua, FL, USA; PA5), a power amplifier (Parasound), and to a leaf tweeter speaker (Emit) located 10 cm away from the mouse. We tested the acoustic properties of the system using a 1/4-inch calibrated microphone (Bruel and Kjaer, Denmark; model 4135) placed in the position normally occupied by the animal's ear. There was a smooth, gradual decrease in sound pressure from 6 to 100 kHz of about 3 dB per 10 kHz. Distortion components in tonal stimuli were buried in the noise floor, at least 50 dB below the signal level, as measured by custom-designed software performing a fast Fourier transform of the digitized microphone signal.

ELECTROPHYSIOLOGICAL RECORDING AND DRUG APPLICATION

We conducted electrophysiological experiments in a single-walled sound-attenuating chamber. On experimental days, we placed the animal securely into a foam body mold and attached the headpost to a custom-made stereotax apparatus (Muniak et al., 2012). If at any time during the experiment the animal showed signs of distress, the experiment was terminated. Experimental sessions lasted 4–5 h and we used each animal in 1–3 sessions.

We obtained responses of single units to pure tones and mouse vocalizations before and after the application of $GABA_AR$ and GlyR antagonists. To obtain well isolated single unit responses, we used a single micropipette electrode mounted on a five-barreled pipette for microiontophoretic application of drugs (Havey and Caspary, 1980). The tip of the single electrode extended 10–25 μm beyond the multibarrel pipette and contained 1 M NaCl. We broke the tip of the multibarrel pipette to a diameter of approximately 30 μm. We filled the center barrel of the multibarrel pipette with 1 M NaCl and connected it to a sum channel to balance all currents used to apply or retain drugs. The rest of the barrels contained the $GABA_AR$ antagonists bicuculline (10 mM, pH 3.0, vehicle 0.9% physiological saline; Sigma) and the GlyR antagonist strychnine (10 mM, pH 3.0, vehicle 0.9% physiological saline; Fluka, Milwaukee, WI). We used similar iontophoresis currents for drug retention and ejection to those used in previous studies (Wenstrup and Leroy, 2001; Ingham and McAlpine, 2005; Sanchez et al., 2008). Bicuculline and strychnine were retained with negative current (−15 nA each) and ejected with positive current (range, +10 nA to +40 nA each). As in previous studies (Razak and Fuzessery, 2009), our control experiments confirmed that current injection as high as 100 nA through pH-adjusted vehicle solutions did not have any effect on neuronal discharge properties.

We prepared all drugs and recording solutions the day of the experiment. We inserted separate silver wires into each barrel of the micropipette electrode and connected them to a microiontophoresis current generator (model 650, David Kopf Instruments, Tujunga, CA) to separately control the retention and ejection currents for each drug. We advanced the electrodes into the IC using a hydraulic micropositioner (David

Kopf Instruments, Tujunga, CA) located outside the acoustic chamber. Extracellular action potentials were amplified (Dagan Corporation, Mineapolis, MN, USA), filtered (bandpass, 500–6000 Hz; Krohn-Hite, Brockton, MA, USA) and sent through a spike enhancer (Fredrick Haer, Bowdoin, ME, USA) before being digitized (Microstar Laboratories, Bellevue, WA, USA; 10,000 samples/s). Neural waveforms were displayed and archived using custom-written C++ software. Waveforms, raster plots, peristimulus time histograms (PSTHs), and statistics were viewed on-line and stored for off-line analysis.

We used tone bursts as search stimuli (varying duration, 1 ms rise/fall time) to obtain well isolated single units. All tests were first run in the control condition. We obtained characteristic frequency (CF) and minimum threshold (MT) audiovisually. We defined CF as the frequency that evoked a response to 50% of the stimulus presentations at the lowest intensity, and MT as the lowest intensity that evoked a response 50% of the time to the CF. To obtain excitatory frequency tuning curves, we presented pure tones (100-ms duration, 1 ms rise/fall time, 4/s, 200 ms recording window) between 6 and 100 kHz in 2-kHz steps, and varied the intensity in 10- to 20-dB steps starting at threshold. We presented each frequency and intensity pair 10–20 times. We then obtained responses to vocalizations by presenting the suite of 14 vocalizations (variable duration, 1 ms rise/fall time, 4/s, 200-ms recording window) 10–40 times at multiple intensities.

Once the stimulus protocol was completed in the control condition, we applied the $GABA_AR$ and GlyR antagonists. Drug ejection times varied depending on the effect of the drug. We ejected bicuculline and strychnine together because we were interested in the general effects of inhibition on responses to vocalizations rather than the separate effects of GABAergic and glycinergic inhibition. We initially applied low ejection currents (+10 nA) and then gradually increased the current if there was no effect. Once the response reached a steady-state, we kept the ejection currents at this level. We then ran the same protocol as in the control condition. At the end of the stimulus protocol, we turned off the ejection current and re-applied the retention current. Complete or partial recovery was determined by comparing response rate to a CF tone in the no-drug, drug and recovery states.

DATA ANALYSIS

Spike counts and raw waveforms were stored in the computer during data collection. We examined raw waveforms off-line to ensure only spikes from well isolated single units were used in the data analysis. Single units had signal-to-noise ratios of at least 4:1 and an inter-spike interval of at least 2 ms. Data were exported from the data collection software and analyzed using programs written in Matlab (The MathWorks, Inc., Natick, MA, USA). We generated frequency tuning curves from the pure tone tests using statistical comparisons between evoked responses and spontaneous activity (Holmstrom et al., 2007), and determined sharpness of tuning by calculating Q10dB values. We compared the bandwidth of the tuning curve at the highest intensity before and after application of drugs to determine the extent of broadening. We defined broadening as an expansion of the frequency range of greater than 2 kHz.

We calculated a selectivity index value (SI) for each neuron that responded to at least one vocalization (criterion of at least 50% of presentations evoking a time-locked response or an increase in rate of 20% above spontaneous activity). We defined the SI as: $SI = (Ct - Ce)/Ct$, where Ct is the number of calls presented and Ce is the number of calls that evoked a response (at the highest intensity presented). Essentially, the SI value can be thought of as providing a normalized value to the number of vocalizations that fail to evoke a response. Thus, a SI value of 0 means that no vocalizations fail to evoke a response, and the neuron is defined as un-selective. A high SI value indicates that a large number of vocalizations do not evoke responses, thus defining the neuron as selective. The highest SI value that can be calculated is determined by the number of vocalizations presented. With our suite of 14 stimuli, the highest SI value (13 vocalizations failing to evoke a response) was 0.93. We used a standard student t-test (two-tailed, equal variance) to determine whether there was a significant difference between the selectivity of neurons under control and drug conditions.

To test whether changes in selectivity to vocalizations during application of $GABA_AR$ and GlyR antagonists were related to changes in the excitatory frequency tuning curve of the neuron, we applied a modeling methodology developed and utilized in our previous studies of IC (Holmstrom et al., 2007, 2010). For each neuron, a model was optimized to approximate the relationship between the pure tone input and the resulting firing rate of the neuron. The model was a discrete (in both frequency and time) linear finite impulse response filter. We used this model to predict how the neuron would respond to each vocalization by converting each vocalization into a spectrographic representation and convolving it with the filter. By comparing each predicted response to the actual response, we could determine how well each neuron's excitatory frequency tuning curve explained the neural responses to each vocalization.

RESULTS

We recorded responses of 73 single units before and after blocking $GABA_AR$ and GlyR. Characteristic frequencies (CFs) of the units ranged from 6 kHz to 65 kHz (**Figure 1**).

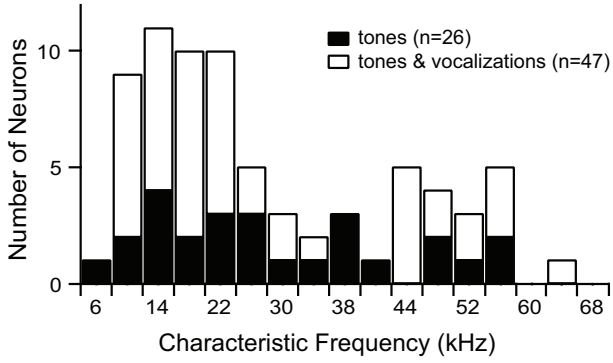

FIGURE 1 | Characteristic frequencies of single units presented with tones alone, or tones and vocalizations.

INHIBITION SHAPES RESPONSES TO SIMPLE STIMULI IN THE IC OF AWAKE MICE

We obtained frequency tuning curves before and after blocking $GABA_AR$ and GlyR in 72 single units (1 unit was presented with vocalization stimuli but not tone stimuli). As has been shown previously in anesthetized animals (Vater et al., 1992a; Palombi and Caspary, 1996; LeBeau et al., 2001), we found that the major effect of blocking $GABA_AR$ and GlyR in the IC was to increase neuronal firing rates. In 3/72 neurons, the increased rate was only in spontaneous activity; no change occurred in tone-evoked responses.

We found that 35/72 neurons increased their firing rate to tones only within the control excitatory frequency tuning curve; there was no change in shape of the excitatory frequency tuning curve. **Figure 2A** illustrates a neuron with this type of response. The evoked responses are shown as spectral-temporal histograms in which frequency is plotted vs. time for one intensity level, and the color of each 4 ms bin represents the average number of spikes per presentation. This representation allows both spectral and temporal information to be displayed in one plot (Portfors and Roberts, 2007). The first plot shows the response under control conditions, the second plot is with iontophoretic application of bicuculline and strychnine, and the third plot is the difference between the two conditions (control condition minus drug condition, where the color scale indicates which response is stronger in each spectral-temporal bin; green indicates no difference, warm colors indicate response magnitude in control condition is greater, and cool colors indicate response magnitude in drug condition is greater). The neuron in **Figure 2A** had two discrete regions of excitation and was classified as a multiply-tuned (Portfors and Felix II, 2005) or type IV (Egorova et al., 2001; Portfors et al., 2011) unit. As can be seen in the spectral-temporal histogram, the response rate increased when $GABA_AR$ and GlyR were blocked, increasing by 68% with no broadening of the excitatory tuning curve. To quantify the changes in rate between the control and drug conditions, we subtracted the area under the control frequency tuning curve from the area under the drug frequency tuning curve for each neuron. On average, the response rate increased by 114% when $GABA_AR$ and GlyR were blocked.

We found that 23/72 neurons increased their firing rate and had a broadening of their V-shaped excitatory tuning curve when inhibition was blocked. **Figure 2B** illustrates a neuron with this type of response. The first spectral-temporal histogram shows that only a narrow range of tones at low frequencies evoked a response (Q10dB value of 1.43). The second spectral-temporal histogram shows the broader range of frequencies that evoked a response when bicuculline and strychnine were applied to the neuron. The third spectral-temporal histogram shows the difference between the control and drug conditions and clearly illustrates the range of frequencies that were suppressed by the inhibitory inputs in the control condition. The Q10dB value decreased from 1.43 to 0.78. In this example, a firing pattern change from a phasic to sustained response can also be seen.

Figure 2C illustrates another way that inhibitory inputs can shape excitatory frequency tuning curves; by suppressing responses to particular frequencies at certain intensities. Neurons affected by inhibition in this way are commonly called O-type (Ramachandran et al., 1999; Davis et al., 2003) or type II (Egorova et al., 2001). Under control conditions (first spectral-temporal histogram), responses to a CF tone were suppressed at high intensities. After $GABA_AR$ and GlyR were blocked, the CF tone at high intensities evoked a strong response (drug and difference spectral-temporal histograms in **Figure 2C**). Eleven of the neurons we recorded from had O-shaped tuning curves, and all of these changed their tuning to V-shaped when inhibition was blocked. Overall, 34 neurons showed increases in rate and changes in the shape of their excitatory tuning curve (broadening of V-shape or change from O- to V-shape) when inhibition was blocked.

We also found that inhibition can affect timing of tone-evoked responses. **Figure 2D** shows an example where blocking $GABA_AR$ and GlyR caused a large shift in latency. The median first spike latency in the control condition was 115 ms, and it decreased to 10 ms when bicuculline and strychnine were applied. A shift in latency occurred in 11 of 72 neurons (five had no change in tuning curve shape, four had broadening of their tuning curve, two changed from O- to V-shaped tuning curves). The changes in latency ranged from 5 to 105 ms. Inhibition can also influence temporal firing pattern. **Figure 2E** shows one neuron in which inhibition created an onset response to a CF tone. Blocking $GABA_AR$ and GlyR converted the onset response to sustained response. This effect occurred in 10 neurons (eight had no change in tuning curve shape, one had broadening of its tuning curve, one changed from O- to V-shaped).

INHIBITION SHAPES RESPONSES TO VOCALIZATIONS IN THE IC OF AWAKE MICE

We presented vocalization stimuli to 47 single units (**Figure 1**). All of the vocalizations were ultrasonic (all energy above 20 kHz), but they had various spectral ranges, durations, and frequency modulations. We used this set of stimuli in a previous study of neural selectivity in the IC of mice (Portfors et al., 2009). Most neurons we recorded from had excitatory receptive areas that encompassed the spectral range of at least one of the vocalization stimuli. Forty neurons responded to at least one vocalization. We found that blocking $GABA_AR$ and GlyR decreased selectivity in most of these neurons (**Figure 3**).

SI values significantly decreased when $GABA_AR$ and GlyR were blocked ($p < 0.001$). The average SI value in the control condition was 0.76 and 0.58 in the drug condition. Of the 40 neurons that responded to one or more vocalizations, 31 had decreased selectivity when bicuculline and strychnine were applied (**Figure 4**). Eleven neurons did not respond to any of the vocalizations under control (no response, NR, in **Figure 4**) but did respond to at least one vocalization during drug application.

We examined whether changes in selectivity to vocalizations were related to changes in excitatory frequency tuning curves in 39 of the 40 neurons that responded to vocalizations (1 of the 40 neurons did not have a frequency tuning curve). Of those 39 neurons, 29 showed decreases in selectivity to vocalizations.

Seventeen of the neurons with decreased selectivity (59%), had increased firing rates to tones without broadening of their excitatory frequency tuning curves. **Figure 5** shows one example of a neuron with this type of response. The effects of inhibition on

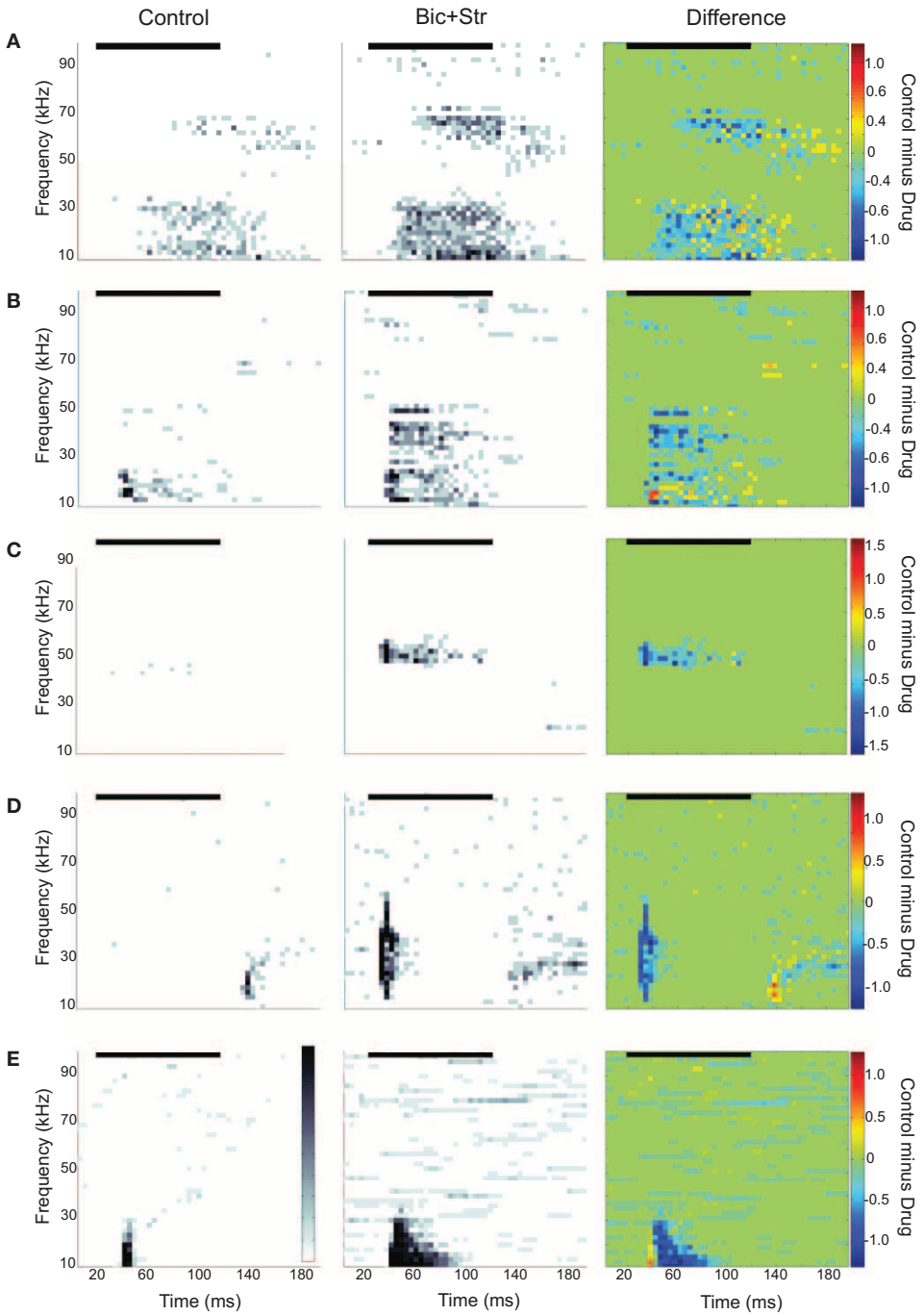

FIGURE 2 | Spectral-temporal histograms of different effects of blocking $GABA_AR$ and GlyR on IC responses to tones. Each row is a different IC neuron. The order of the panels left to right is control condition, drug condition, and control-drug (difference). In the difference plots, cool colors indicate greater firing rates under drug condition and warm colors indicate higher firing rates under control conditions. **(A)** Increased evoked firing rate to tones without a broadening of the excitatory frequency tuning curve. **(B)** Increased rate and broadening of the excitatory frequency tuning curve. **(C)** Conversion of an O-shaped to a V-shaped excitatory frequency tuning curve. **(D)** Latency shift. **(E)** Conversion of an onset to a sustained evoked firing pattern. In all plots, the black horizontal line indicates the sound stimulus. Bin width is 4 ms.

responses to pure tones for this neuron are shown in **Figure 2A**. **Figure 5A** plots the response rate predicted based on the excitatory frequency tuning curve of the neuron to each of the 14 vocalizations (each vocalization is a different symbol) vs. the actual response of the neuron under control conditions. This neuron did not respond to 8 of the 14 vocalizations in the control condition (SI = 0.57). **Figure 5B** shows the fit of the excitatory tuning curve prediction to the actual response for two of

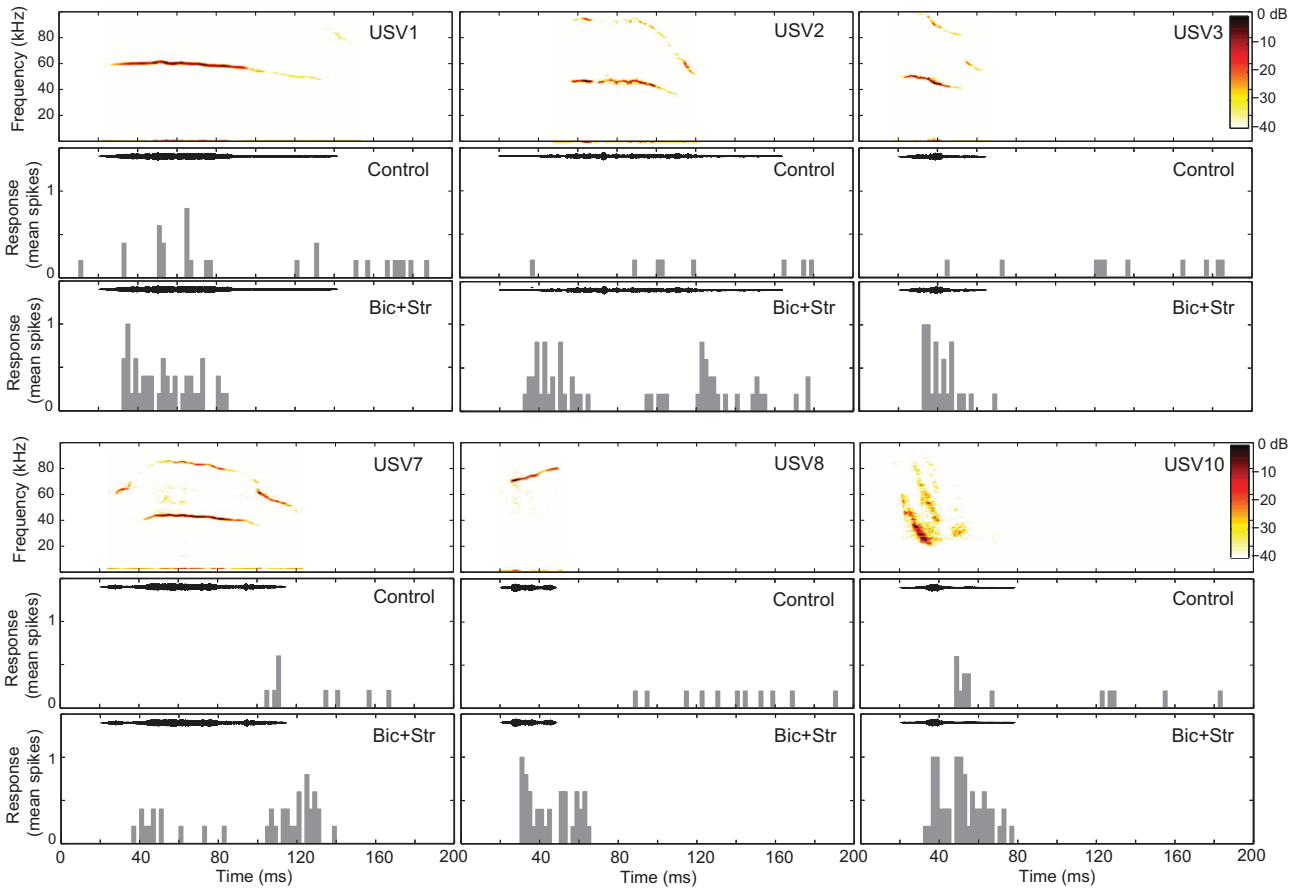

FIGURE 3 | Blocking $GABA_AR$ and GlyR decreases neuronal selectivity to vocalizations in the IC. The responses of one single unit to six vocalizations before (control) and after (Bic + Str) blocking $GABA_AR$ and GlyR. Responses to only 6 of the 14 presented vocalizations are shown for clarity. SI values were 0.57 and 0 in the control and drug conditions, respectively. Bin width is 4 ms.

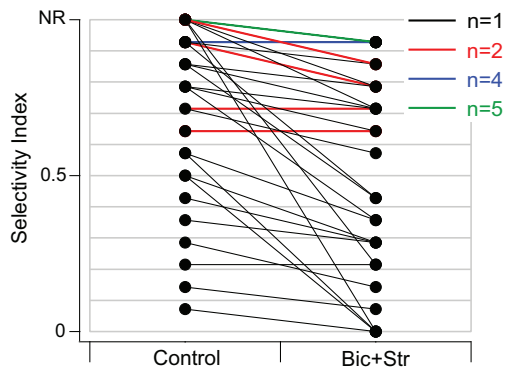

FIGURE 4 | Blocking $GABA_AR$ and GlyR significantly decreased selectivity to vocalizations in the IC of awake mice. SI values in control and drug condition for each neuron. Black lines represent one single unit, red lines represent two single units with the same values, blue lines represent four units with the same values, and green lines represent five units with the same values. Neurons in the NR (no-response) category did not respond to any vocalizations in the control condition but did respond to at least one vocalization in the drug condition. Thirty-one of forty neurons had decreased SI values.

the vocalization stimuli. The symbol that is inset in the spectrogram matches the symbol in **Figure 5A**. The neuron did not respond to the first displayed vocalization (USV10) with enough spikes to be considered a response (spikes to less than 50% of presentations). The predicted response based on the excitatory tuning curve matched the actual response reasonably well; both the predicted and actual responses were below our threshold for a response. The neuron responded to the second displayed vocalization (USV12) as was predicted based on the excitatory frequency tuning curve.

Figure 5C shows the predicted responses to vocalizations vs. the recorded responses in the drug condition. The predicted and actual response rates were higher for each of the vocalization stimuli under the drug condition compared to the control condition. Selectivity also decreased. The SI value was 0.36 in the drug condition compared to 0.57 in the control condition. The fit of the response rates predicted from the excitatory tuning curve to the actual response rates to two of the vocalizations are shown in **Figure 5D**. In each of the plots, the response rate to the vocalizations was higher than in the control condition, and the neuron responded to the USV10 vocalization. Based on the frequency tuning profile of this neuron (**Figure 2A**), it is clear that

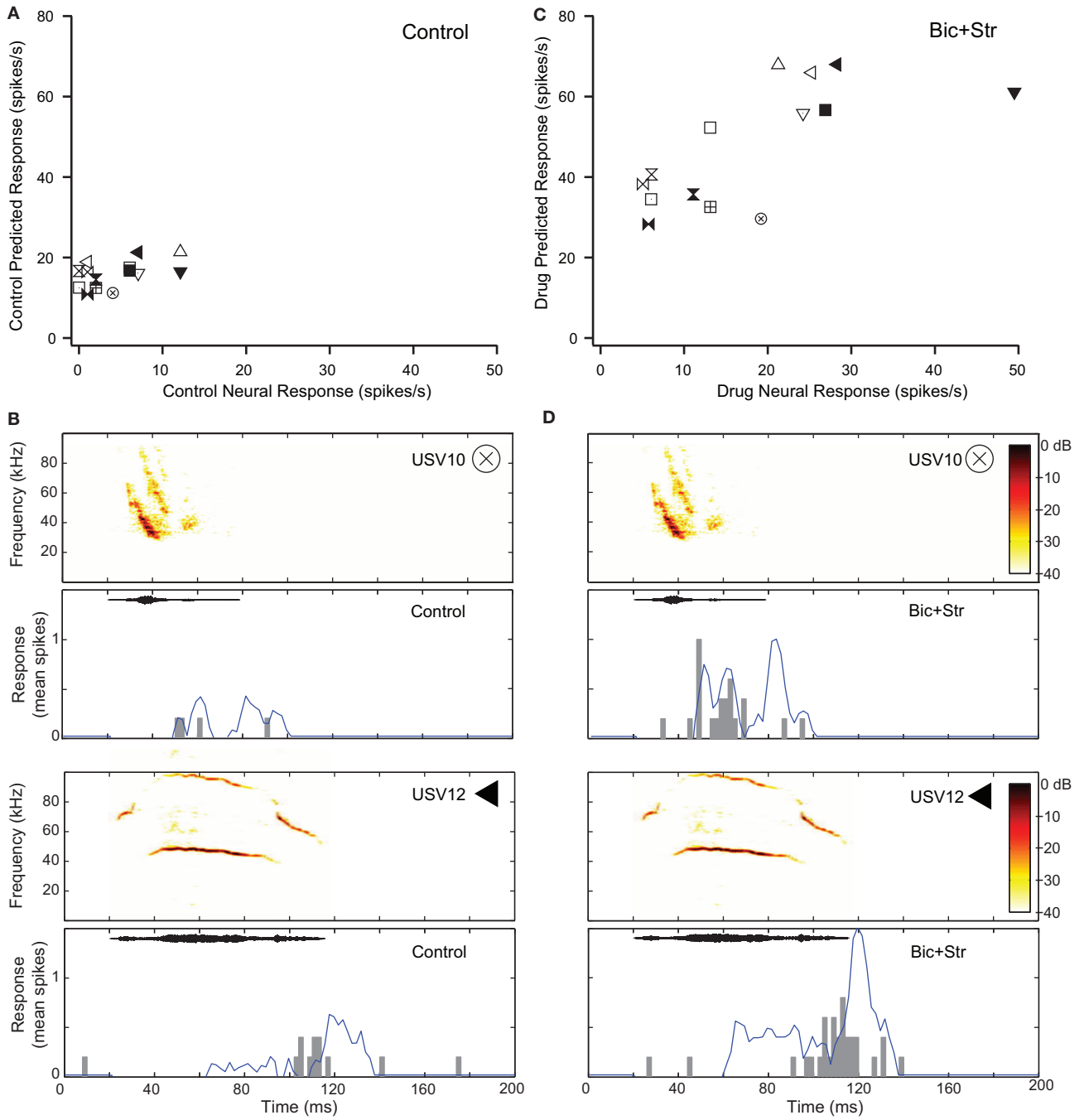

FIGURE 5 | Decreased selectivity to vocalizations can occur without a change in the shape of the excitatory tuning curve. (A) Predicted and actual response rates of one neuron (same as in **Figure 2A**) to all the vocalizations in the control condition. **(B)** Predicted (blue lines) and actual responses (gray bars) to two vocalizations in the control condition. **(C)** Predicted and actual response rates to all the vocalizations in the drug condition. **(D)** Predicted (blue lines) and actual responses (gray bars) to two vocalizations in the drug condition. Symbols inset in spectrograms match those vocalizations in the scatter plots. Each symbol denotes a different vocalization.

the change in selectivity was not due to a change in shape of the excitatory frequency tuning curve.

Blocking $GABA_AR$ and GlyR increased response rate and broadened the V-shaped, excitatory frequency tuning curves of 10 neurons that showed decreases in selectivity (34%). **Figure 6** shows this effect for the neuron whose responses to pure tones are shown in **Figure 2B**. This neuron did not respond to any of the vocalizations in the control condition (**Figure 6A**). **Figure 6B** shows the fit of the excitatory frequency tuning curve prediction and the actual response for two of the vocalizations. In both

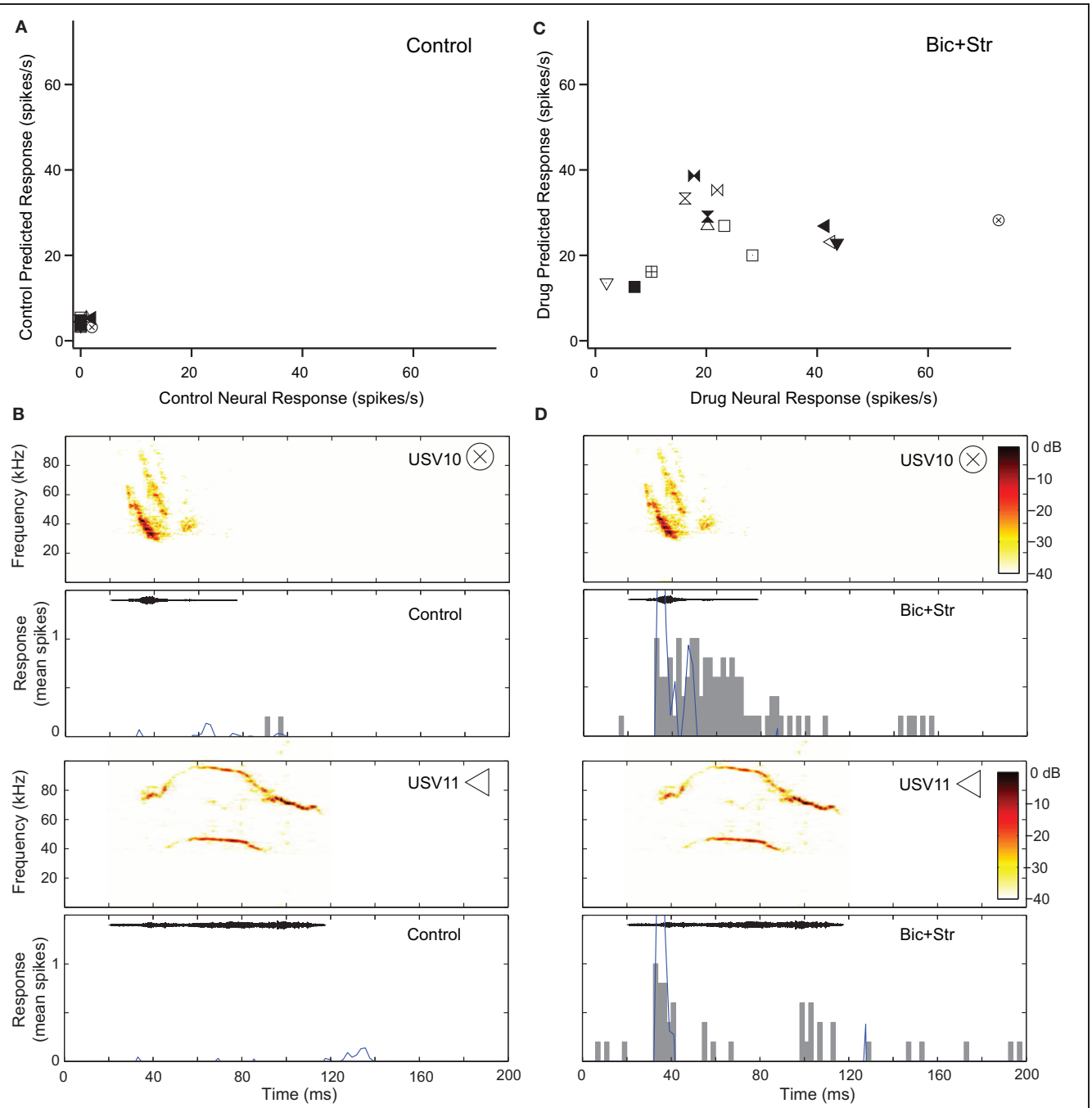

FIGURE 6 | Decreased selectivity to vocalizations can occur with a change in the shape of the excitatory frequency tuning curve. (A) Predicted and actual response rates of one neuron (same as in **Figure 2B**) to all the vocalizations in the control condition. **(B)** Predicted (blue lines) and actual responses (gray bars) to two vocalizations in the control condition. **(C)** Predicted and actual response rates to all the vocalizations in the drug condition. **(D)** Predicted (blue lines) and actual responses (gray bars) to 2 vocalizations in the drug condition. Symbols inset in spectrograms match those vocalizations in the scatter plots. Each symbol denotes a different vocalization.

cases, the neuron did not respond to the vocalization because the spectral content of the vocalization did not fall within the excitatory frequency tuning curve. As shown in **Figure 6C**, blocking $GABA_AR$ and GlyR decreased the selectivity of the neuron dramatically. The neuron responded to 11 of the vocalizations in the drug condition. Blocking inhibition broadened the excitatory frequency tuning curve (**Figure 2B**) resulting in an increased number of vocalizations that had spectral content within the excitatory frequency tuning curve. This can be seen for two of the vocalizations (**Figure 6D**) where the predicted response based on

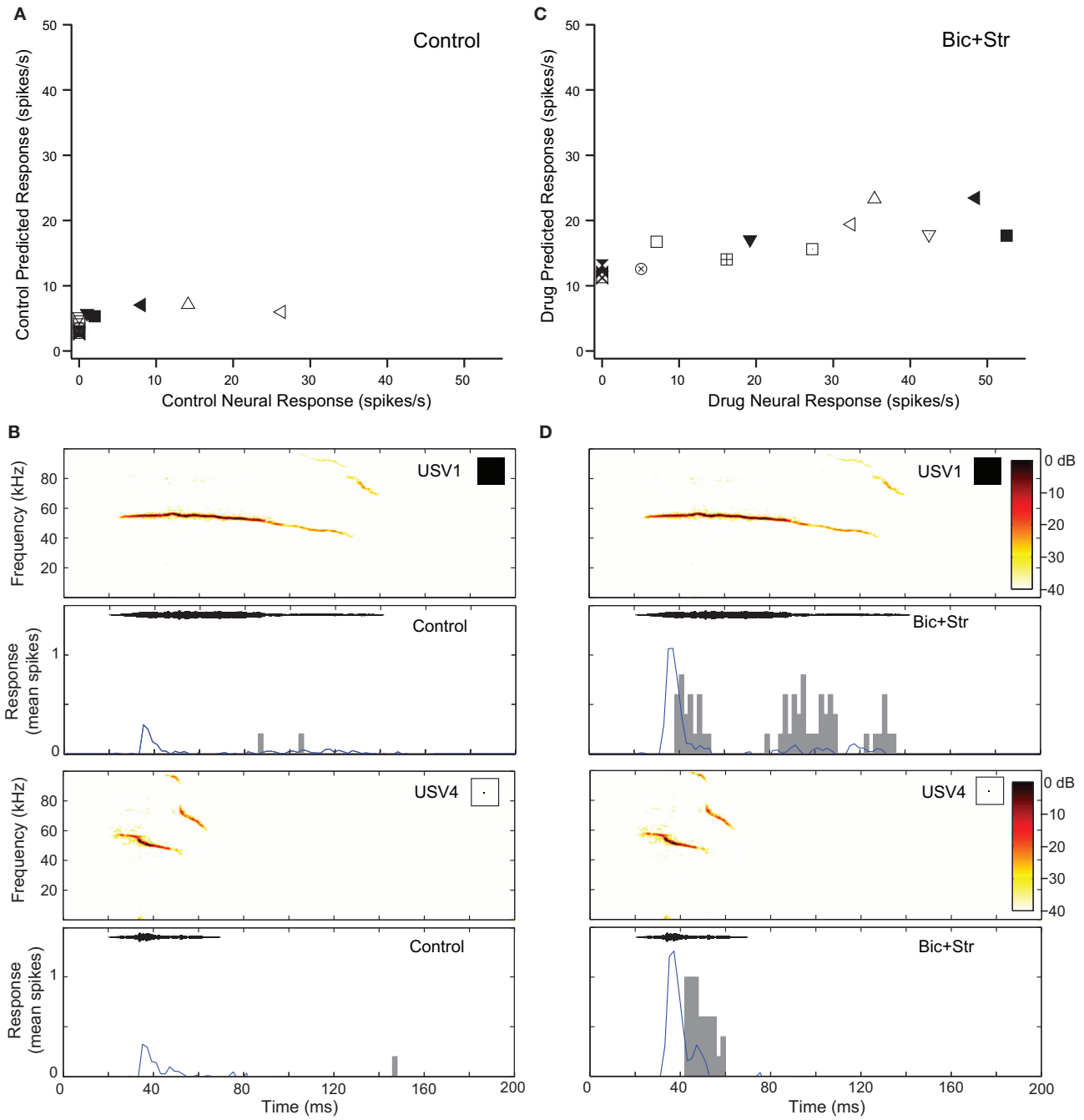

FIGURE 7 | Decreases in selectivity can occur in O-shaped neurons. **(A)** Predicted and actual response rates of one neuron (**Figure 2C**) to all the vocalizations in the control condition. **(B)** Predicted (blue lines) and actual responses (gray bars) to two vocalizations in the control condition. **(C)** Predicted and actual response rates to all the vocalizations in the drug condition. **(D)** Predicted (blue lines) and actual responses (gray bars) to two vocalizations in the drug condition. Symbols inset in spectrograms match those vocalizations in the scatter plots. Each symbol denotes a different vocalization.

the excitatory frequency tuning curve is greater than in the control condition.

Blocking $GABA_AR$ and GlyR increased response rate and changed O-shaped frequency tuning curves into V-shaped tuning curves in two of the neurons that showed decreases in selectivity (7%). **Figure 7** shows the responses of one of those O-shaped neurons (same neuron as **Figure 2C**) to vocalizations in the control and drug conditions. In the control condition, this neuron had a SI value of 0.78 (no response to 11 of the vocalizations; **Figure 7A**). **Figure 7** shows the predicted and actual responses for two vocalizations. The neuron was not predicted to respond to either of the displayed vocalizations (USV1 and USV4) with a rate

greater than the criteria for defining an evoked response, and the neuron did not respond to these stimuli. Blocking $GABA_AR$ and GlyR decreased the selectivity of the neuron (**Figure 2C**). The SI of the neuron decreased to 0.36. With a change from an O-shaped to a V-shaped tuning curve, the excitatory tuning curve predicted the neuron would respond to many more vocalizations and the recorded responses matched these predictions well (**Figure 7D**).

The modeling techniques we used here help us to understand how changes in the excitatory frequency tuning curves when inhibition was blocked were related to changes in selectivity to vocalizations in the IC. In **Figure 8** we compare how well the excitatory tuning curves predicted the actual responses in the control and drug conditions for 40 neurons (the set of neurons presented with vocalization stimuli that had tuning curve data). In the control condition, the number of vocalizations predicted to evoke responses was greater than the number of vocalizations that actually evoked responses in the majority (19/40) of neurons. For example, there were six neurons that were predicted to respond to four or more vocalizations, but either only one or none of the vocalizations evoked responses (**Figure 8A**). For 14 neurons, the predictions matched the recorded responses and for seven neurons, the number of vocalizations predicted to evoke responses was less than the actual number that evoked responses (**Figure 8A**). The correlation coefficient under control conditions was $r^2 = 0.28$. Thus, the excitatory frequency tuning curve accurately predicted responses to vocalizations in only 14/40 neurons.

When inhibition was blocked, there was a better match between the number of vocalizations predicted to evoke responses and the number that actually evoked responses, as shown by the higher correlation coefficient ($r^2 = 0.48$). In the drug condition there were 17 neurons where the predictions matched the recorded responses (**Figure 8B**). A big difference was that with inhibition blocked there was now only one neuron that did not respond to any vocalizations when it was predicted to respond to many. It is clear, however, that even when inhibition was blocked, the predictions for some neurons remained poor. In some cases, more vocalizations were predicted to evoke responses than actually did, and in other cases, the neurons responded to one or more of the vocalizations even though they were not predicted to respond.

Figure 8 also identifies the neurons that had changes in the shape of their tuning curve vs. those that only had changes in rate within the original frequency tuning curve. There was no obvious difference in the predictions for these groups of neurons. This suggests that inhibition was acting in multiple ways on these neurons to create selectivity to vocalizations.

DISCUSSION

In this study we examined how inhibition in the IC modulates responses to simple and complex sounds in awake mice. We found that inhibitory inputs modulate responses to simple stimuli by modulating firing rate, shaping frequency tuning curves in a variety of ways, and altering temporal firing patterns. We also found that inhibitory inputs increase selectivity to vocalizations, but in a diverse manner. Thus, the complex interplay between excitation and inhibition in the IC is important for creating the diversity of response properties in the IC.

INHIBITORY INPUTS MODULATE RESPONSES TO SIMPLE STIMULI IN THE IC OF AWAKE MICE

Many studies have tested the role of inhibition in regulating response properties in the IC (Faingold et al., 1989, 1991; Vater et al., 1992a; Yang et al., 1992; Park and Pollak, 1993, 1994;

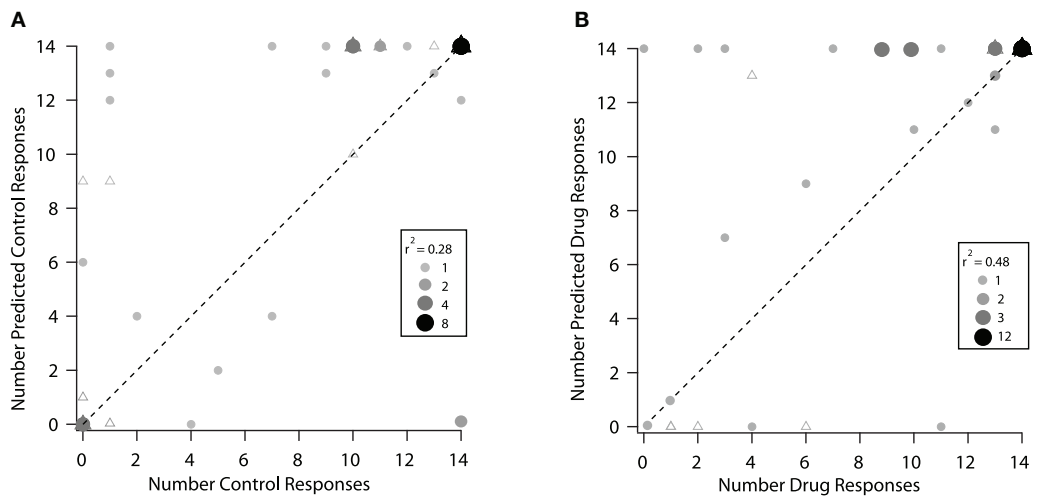

FIGURE 8 | Predicted responses to vocalizations based on the excitatory frequency tuning curves were better under drug conditions. (A) Control condition. The predicted number of vocalizations to evoke a response is plotted vs. the actual number that evoked a response for each neuron. **(B)** Same neurons are plotted under the drug condition. The triangles represent neurons that showed a change in rate and a change in the shape of their excitatory frequency tuning curve and circles represent neurons that showed a change in rate only within the original tuning curve. In some cases, the triagles are covered by the circles. The shade and size of the circle represent the number of neurons overlapping at that point (if a triangle is underneath, it is counted and represented in the size of the circle). The size of the point and the shade of gray indicates the number of neurons that are represented by the particular dot in each of the control and drug plots. The dashed line represents equality in the number of predicted and actual responses.

Casseday et al., 1994; Klug et al., 1995; Fuzessery and Hall, 1996; Le Beau et al., 1996; Palombi and Caspary, 1996; Burger and Pollak, 1998; Koch and Grothe, 1998; LeBeau et al., 2001; Caspary et al., 2002; Zhang and Kelly, 2003). To our knowledge, ours is the first study to examine the role of inhibition in modulating responses to simple and complex stimuli in the IC of awake mice. We anticipated that our results for simple stimuli would be the same as previously reported for other mammalian species under anesthesia and for awake bats, however, it was nonetheless important to determine this explicitly since mice are becoming an important model for understanding neural mechanisms of auditory processing disorders due to the benefits of genetic engineering.

In general, we found that the effects of locally blocking GABAergic and glycinergic receptors by applying receptor antagonists in the IC of mice are the same as have been reported in other species. We describe these effects here, and also propose different microcircuits that could contribute to the effects we observed. Our techniques in this study do not allow us to ascribe specific circuits to particular effects of blocking inhibition, but we can use these putative circuits for future testing of specific hypotheses to provide further insight into the mechanisms of creating heterogeneous and selective responses in the IC. Although we propose particular microcircuits to describe particular effects of blocking inhibition, it is highly likely that multiple circuits contribute to an individual neuron's responses to simple and complex sounds. In addition, it is highly likely that the microcircuitry is different in each neuron, thus contributing to the diversity of response properties in the IC.

The ubiquitous effect of blocking $GABA_AR$ and GlyR in the IC of awake mice was an increase in response rate. In three of the neurons, the firing rate increases were only in spontaneous activity, and not evoked activity. In about half of the neurons, the increase in tone-evoked response rate was not accompanied by a change in the shape of the excitatory frequency tuning curve. One interpretation of this is that the excitatory and inhibitory inputs in these neurons were co-tuned. A suggested microcircuitry to create this response is shown in **Figure 9A**, where the inhibitory inputs are aligned in frequency with the excitatory inputs (Kelly and Caspary, 2005) and arrive simultaneously. In this microcircuitry, the inhibition only decreases response rate within the frequency range of the excitatory inputs. In another potential circuit, the inhibition could be un-tuned in frequency. This circuitry could explain how spontaneous activity increases when inhibitory receptors are blocked.

In about 50% of the neurons, blocking inhibitory receptors changed the shape of their excitatory frequency tuning curve. This expansion of the tuning curve could occur on both the high and

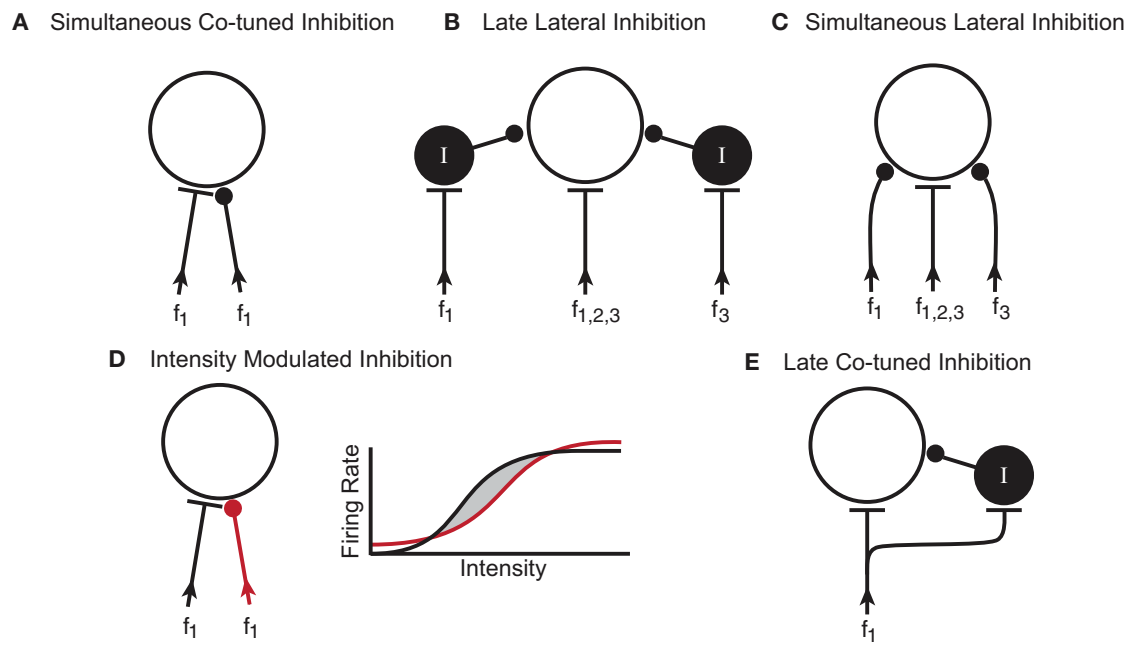

FIGURE 9 | Potential microcircuits that could shape responses to simple and complex stimuli in the IC. (A) Simultaneous co-tuned inhibition. The excitatory and inhibitory inputs have similar frequency tuning and arrival time at the IC neuron. **(B)** Late lateral inhibition. Lateral inhibition results from inhibitory interneurons (I) with frequency ranges that are lateral (f1 and f3) to the excitatory input (f1,2,3). Synapsing onto an interneuron could delay the arrival time of the inhibition relative to the excitatory input. **(C)** Simultaneous lateral inhibition. Lateral inhibition results from direct inhibitory inputs (f1 and f3). **(D)** Intensity modulated inhibition. Excitatory (black) and inhibitory (red) inputs are co-tuned in frequency but have different rate-intensity responses. The rate-intensity function shows that at low and high intensities, the inhibitory input (red line) has a greater response than the excitatory input (black line). At middle intensities, the excitatory input has a greater response than the inhibitory input and the neuron fires (shaded region between the black and red lines). **(E)** Late co-tuned inhibition. Excitatory inputs synapse directly onto the IC neuron and onto an inhibitory interneuron such that the late arrival time of the inhibitory input creates an onset response. In all diagrams f, frequency; I, inhibitory interneuron.

low frequency sides, but more often there was a large expansion on the low frequency side (Yang et al., 1992; LeBeau et al., 2001). One interpretation of these results is that GABAergic and/or glycinergic inputs onto IC neurons create lateral inhibition. The two circuit diagrams illustrated in **Figures 9B,C** are potential ways that inhibitory inputs to IC neurons could narrow excitatory frequency tuning curves. In both putative circuits, the inhibitory inputs are aligned with the excitatory input but have a broader frequency range. In one circuit (**Figure 9B**), the inputs coming into the IC are all excitatory and some of them synapse onto GABAergic interneurons. Considering that between 20–40% of the neurons in the IC are thought to be GABAergic (Caspary et al., 1990; Oliver et al., 1994; Winer et al., 1996), it is likely these interneurons play a role in shaping responses. In the second putative circuit (**Figure 9C**), the inhibitory inputs arise from lower brainstem nuclei and synapse directly on the IC neuron. In the current study, we are unable to distinguish between these two potential microcircuits but it is probable that both occur, either in the same neuron or in different neurons.

Another way that inhibition can modulate the shape of the tuning curve is to create O-shaped responses, where high intensity stimuli inhibit the neural response. The circuit diagram in **Figure 9D** illustrates one way inhibition could do this. In this case, excitatory and inhibitory inputs to the IC neuron are co-tuned in frequency and occur simultaneously, but they have different rate-intensity responses. The rate-intensity plot in **Figure 9D** shows that at low and high intensities the inhibitory input has a greater response (red line) and the neuron does not fire. At middle intensities (shaded region between the red and black lines), the excitatory input (black line) has a greater response and the neuron fires.

Besides shaping response rate and shape of the excitatory frequency tuning curve, inhibitory inputs to IC neurons can also affect temporal firing properties. Changes in latencies to monaural and binaural stimuli have been observed in both the mustached bat and guinea pig after iontophoretically blocking inhibitory receptors in IC (Park and Pollak, 1993; Le Beau et al., 1996). The changes in latency observed in our study (5–105 ms) agree with those seen in the mustached bat where the reported changes in latency spanned from 5 to 65 ms. Inhibitory inputs to IC neurons may lengthen latency by either arriving earlier or simultaneously with excitatory inputs such that an increased amount of time is required for the neuron to reach threshold (Park and Pollak, 1993).

Inhibition can also shape the temporal firing patterns of neurons. Onset responses become more sustained in some IC neurons when $GABA_AR$ and GlyR are blocked (Le Beau et al., 1996; Jen and Zhang, 1999). **Figure 9E** shows a putative circuit diagram to explain how inhibitory inputs to IC neurons could create onset responses to tonal stimuli. In this case, the excitatory input synapses directly on the recorded IC neuron as well as onto an inhibitory interneuron. The longer delay of the inhibitory input suppresses the evoked response after the onset thus creating a phasic response.

It is clear from *in vivo* studies where inhibitory receptors can be pharmacologically blocked that inhibition plays a role in shaping the frequency and temporal responses of IC neurons to simple stimuli. The sources of input to these neurons however is harder to determine in these types of studies. Inhibitory projections to the IC come from various brainstem nuclei such as the nuclei of the lateral lemniscus (Adams and Mugnaini, 1984; Gonzalez-Hernandez et al., 1996; Kelly and Li, 1997; Vater et al., 1997; Zhang et al., 1998), the superior paraolivary nucleus (Helfer et al., 1989; Kelly and Li, 1997; Kulesza et al., 2003), and the lateral superior olive (Saint Marie et al., 1989; Glendenning et al., 1992). Inhibitory inputs to IC also arise from the medial geniculate body (Vater et al., 1992b) and perhaps the auditory cortex (Adams, 1979; Jen et al., 2001). Moreover, inhibitory interneurons likely contribute to shaping IC response properties. The various sources of inhibitory inputs with their own unique response properties likely contribute to creating many different microcircuits in the IC that shape heterogeneous responses to simple stimuli.

INHIBITORY CIRCUITS INCREASE SELECTIVITY TO VOCALIZATIONS IN THE IC OF AWAKE MICE

Whereas the importance of GABAergic and glycinergic inhibition in shaping responses to simple, binaural and modulated sounds has been well documented (Faingold et al., 1991; Vater et al., 1992a; Yang et al., 1992; Park and Pollak, 1993, 1994; Casseday et al., 1994; Klug et al., 1995; Fuzessery and Hall, 1996; Le Beau et al., 1996; Burger and Pollak, 1998; Koch and Grothe, 1998; LeBeau et al., 2001; Caspary et al., 2002; Zhang and Kelly, 2003), the role of inhibitory microcircuitry in shaping responses to behaviorally relevant vocalizations has received less attention. Only two studies have examined the role of inhibition in shaping selectivity to vocalizations, both done in bats (Klug et al., 2002; Xie et al., 2005). In these studies, blocking inhibition decreased selectivity to social vocalizations in the IC but not in the nuclei of the lateral lemniscus suggesting that inhibition plays a role in creating selectivity to vocalizations in the IC of bats.

Our findings in the IC of awake mice are similar. Pharmacological blocking of GABAergic and glycinergic inputs to IC neurons significantly decreased neuronal selectivity to vocalizations. The magnitude of change varied across neurons. In the most extreme cases, a highly selective neuron (responding to 1 or 2 vocalizations) became completely un-selective and responded to all the vocalizations when $GABA_AR$ and GlyR were blocked. In addition, some neurons did not respond to any of the vocalizations under control conditions but then responded to some or all of them when $GABA_AR$ and GlyR were blocked. These results indicate that inhibition is important in shaping selectivity to vocalizations in the IC.

There are potentially multiple ways that inhibition could affect selectivity to vocalizations. In this study, we used the effects of inhibition on frequency tuning curves to predict the effects of inhibition on selectivity to vocalizations. While the underlying inhibitory circuitry that shapes selectivity to vocalizations cannot be specifically determined by our experimental methods, the effect of inhibition on response properties to tones and vocalizations can provide clues and stimulate future studies.

As described above, one effect of inhibition is to decrease firing rate to tones within the excitatory frequency tuning curve without

changing its shape. This suggests that the inhibitory inputs (at least the ones that were pharmacologically blocked) have similar frequency tuning as the excitatory inputs and possibly keep the membrane potential at subthreshold levels for some vocalizations and not others, thereby selectively shaping responses. A limitation of our study is the use of extracellular neural recordings where subthreshold excitatory and inhibitory responses cannot be measured. To better understand how inhibitory microcircuitry is operating at subthreshold levels, future work should include measuring synaptic currents in responses to vocalization stimuli with *in vivo* whole cell recordings. These sorts of future studies would help tease apart how the thresholds, latencies, durations, and strengths of multiple inhibitory inputs to each IC neuron likely create the heterogeneous responses to vocalizations that occur in the IC (Klug et al., 2002; Holmstrom et al., 2010).

Another way that inhibition could create selectivity to vocalizations is by sharpening the excitatory frequency tuning curve so that fewer vocalizations contain energy that falls within the excitatory region. Moreover, by creating neurons with inhibitory side-bands, selectivity to vocalizations can be enhanced because any vocalization that contains spectral energy within these inhibitory bands would not evoke a response. Therefore, in the case where two vocalizations share spectral content that falls within the excitatory tuning curve but one also has energy that falls within the inhibitory side-bands, the neuron will not respond to the one that stimulates the inhibition, thereby being selective. Thus, neurons with inhibitory side-bands could be more selective to vocalization stimuli compared to those neurons with just a narrow excitatory region. This is a mechanism also proposed for creating selective responses to vocalizations in the mustached bat IC (Portfors, 2004). Less than 40% of the neurons in our study that showed decreased selectivity to vocalizations had expanded tuning curves when inhibition was blocked. This could mean that only about half of the neurons in the IC of awake mice have inhibition side-bands, that the side-bands of some neurons were narrower than the 2 kHz resolution that we tested here, or that we did not completely block the inhibition in some neurons. One study in anesthetized mice suggested that the majority of neurons in IC have inhibitory side-bands (Egorova et al., 2001). It is unclear whether the differences in the two studies is due to anesthesia or methods. Regardless of the extent of inhibitory side-bands in IC neurons, it is clear that inhibitory circuitry that creates side-bands is important for creating selectivity to vocalizations in some neurons.

Inhibitory microcircuits in IC can modify the shape of excitatory frequency tuning curves in other ways that can shape responses to vocalizations. For example, neurons with O-shaped tuning curves, where responses are suppressed to stimuli at high intensities, show selectivity to vocalizations. In these neurons, a vocalization would need to have the appropriate spectral content as well as intensity profile to evoke a response. We found that 15% of neurons in awake mouse IC had O-shaped tuning curves, and that this type of tuning plays a role in creating selectivity to vocalizations. The distribution of O-shaped neurons seems to depend on the species and the recording method. In decerebrate cats, O-shaped neurons are common, comprising about 50% of neurons in the central nucleus of the IC (Ramachandran et al., 1999) but they are less common (5–10%) in non-decerebrated cats (Ehret and Merzenich, 1988) and mice (Egorova et al., 2001). Regardless, the inhibitory microcircuitry that creates these responses is likely important in shaping responses to vocalizations to, at least, a small extent in mice.

Our modeling results, using the frequency tuning curve to predict responses to vocalizations, are similar to those obtained by Klug et al. (2002) in the IC of Mexican free-tailed bats. They also found that responses to vocalizations are not well predicted from responses to tones, and that blocking inhibition pharmacologically as we did here, decreases selectivity and improves predicted responses based on tones. In both studies, however, predictions for some neurons remained poor when inhibition was blocked. In some neurons, more vocalizations were predicted to evoke responses than actually did, and in other neurons, the model failed to predict responses to vocalizations that actually evoked responses. These findings suggest the presence of other mechanisms for creating selectivity to vocalizations. It is well known that there are multiple non-linearities in the IC as well as in brainstem nuclei, and these likely are involved in creating selectivity to vocalizations. For example, combination sensitivity is important for creating selectivity to vocalizations in bats (O'Neill and Suga, 1979; Mittmann and Wenstrup, 1995; Portfors and Wenstrup, 1999; Portfors, 2004) and these types of responses have also been found in mice (Portfors and Felix II, 2005). Other non-linearities that occur in lower brainstem nuclei (Spirou et al., 1999; Portfors and Wenstrup, 2001b; Marsh et al., 2006) are also factors that likely shape selectivity to vocalizations in the IC. In addition, we have previously shown that neurons in the IC of mice that are tuned to frequencies much lower than the spectral content of the vocalization respond to these vocalizations because of cochlear distortions (Portfors et al., 2009). These neurons may be the ones that respond to particular vocalizations even though they are not predicted to based on single tone frequency tuning curves. In general, multiple mechanisms throughout the ascending auditory system contribute to creating the diversity of selective responses to vocalizations in the IC.

The results found here in mice, combined with the findings in bats (Klug et al., 2002; Xie et al., 2005), provide strong evidence that inhibitory microcircuits in IC play an important role in shaping selectivity to vocalizations. That these inhibitory microcircuits are similar in mice and bats suggests that the IC has evolved common circuitry across mammals. In addition, the finding that inhibition shapes selectivity to vocalizations in mice provides further evidence that selectivity to behaviorally relevant sounds is created at the level of the auditory midbrain (Portfors and Wenstrup, 2001a; Bauer et al., 2002; Nataraj and Wenstrup, 2005; Xie et al., 2005) rather than at the auditory cortex.

ACKNOWLEDGMENTS

This material is based upon work supported by National Science Foundation under Grant No. IOS-0920060 to Christine V. Portfors and IIS-0827722 to Patrick D. Roberts. We thank the reviewers for helpful comments.

REFERENCES

Adams, J. (1979). Ascending projections to the inferior colliculus. *J. Comp. Neurol.* 183, 519–538.

Adams, J., and Mugnaini, E. (1984). Dorsal nucleus of the lateral lemniscus: a nucleus of GABAergic projection neurons. *Brain Res. Bull.* 13, 585–590.

Aitkin, L., and Phillips, S. (1984). The interconnections of the inferior colliculi through their commissure. *J. Comp. Neurol.* 228, 210–216.

Bauer, E. E., Klug, A., and Pollak, G. D. (2002). Spectral determination of responses to species-specific calls in the dorsal nucleus of the lateral lemniscus. *J. Neurophysiol.* 88, 1955–1967.

Brunso-Bechtold, J. K., Thompson, G. C., and Masterton, R. B. (1981). HRP study of the organization of auditory afferents ascending to central nucleus of inferior colliculus in cat. *J. Comp. Neurol.* 197, 705–722.

Burger, R., and Pollak, G. (1998). Analysis of the role of inhibition in shaping responses to sinusoidally amplitude-modulated signals in the inferior colliculus. *J. Neurophysiol.* 80, 1686–1701.

Cant, N. (2005). "Projections from the cochlear nuclear complex to the inferior colliculus," in *The Inferior Colliculus*, eds J. Winer and C. Schreiner (New York, NY: Springer), 115–131.

Caspary, D., Palombi, P., and Hughes, L. (2002). GABAergic inputs shape responses to amplitude modulated stimuli in the inferior colliculus. *Hear. Res.* 168, 163–173.

Caspary, D., Raza, A., Armour, B., Pippen, J., and Arneric, S. (1990). Immunocytochemical and neurochemical evidence for age related loss of GABA in the inferior colliculus: implications for neural presbycusis. *J. Neurosci.* 10, 2363–2372.

Casseday, J. H., Ehrlich, D., and Covey, E. (1994). Neural tuning for sound duration – role of inhibitory mechanisms in the inferior colliculus. *Science* 264, 847–850.

Davis, K. A., Ramachandran, R., and May, B. J. (2003). Auditory processing of spectral cues for sound localization in the inferior colliculus. *J. Assoc. Res. Otolaryngol.* 4, 148–163.

Egorova, M., Ehret, G., Vartanian, I., and Esser, K.-H. (2001). Frequency response areas of neurons in the mouse inferior colliculus. i. Threshold and tuning characteristics. *Exp. Brain Res.* 140, 145–161.

Ehret, G., and Merzenich, M. (1988). Complex sound analysis (frequency resolution, filtering and spectral integration) by single units of the inferior colliculus of the cat. *Brain Res. Rev.* 13, 139–163.

Faingold, C., Boersma Anderson, C., and Caspary, D. (1991). Involvement of GABA in acoustically-evoked inhibition in inferior colliculus neurons. *Hear. Res.* 52, 201–216.

Faingold, C., Gehlbach, G., and Caspary, D. (1989). On the role of GABA as an inhibitory neurotransmitter in inferior colliculus neurons: iontophoretic studies. *Brain Res.* 500, 302–312.

Frisina, D., Walton, J., Lynch-Armour, M., and Klotz, D. (1998). Inputs to a physiologically characterized region of the inferior colliculus of the young adult CBA mouse. *Hear. Res.* 115, 61–81.

Fuzessery, Z. M., and Hall, J. C. (1996). Role of GABA in shaping frequency tuning and creating fm sweep selectivity in the inferior colliculus. *J. Neurophysiol.* 76, 1059–1073.

Glendenning, K., Baker, B., Hutson, K., and Masterton, R. (1992). Acoustic chiasm v: inhibition and excitation in the ipsilateral and contralateral projections of the LSO. *J. Comp. Neurol.* 319, 100–122.

Gonzalez-Hernandez, T., Mantolan-Sarmiento, B., Gonzalez-Gonzalez, B., and Perez-Gonzalez, H. (1996). Sources of GABAergic input to the inferior colliculus of the rat. *J. Comp. Neurol.* 372, 309–326.

Havey, D., and Caspary, D. (1980). A simple technique for constructing piggy-back multibarrel microelectrodes. *Electroencephalogr. Clin. Neurophysiol.* 45, 249–251.

Helfer, R., Snead, C., and Altschuler, R. (1989). GABA and glycine immunoreactivity in the guinea pig superior olivary complex. *Brain Res.* 501, 269–286.

Holmstrom, L., Eeuwes, L., Roberts, P., and Portfors, C. (2010). Efficient encoding of vocalizations in the auditory midbrain. *J. Neurosci.* 3, 802–819.

Holmstrom, L., Roberts, P. D., and Portfors, C. V. (2007). Responses to social vocalizations in the inferior colliculus of the mustached bat are influenced by secondary tuning curves. *J. Neurophysiol.* 47, 461–481.

Ingham, N., and McAlpine, D. (2005). GABAergic inhibition controls neural gain in inferior colliculus neurons sensitive to interaural time differences. *J. Neurosci.* 25, 6187–6198.

Jen, P. H. S., and Zhang, J. P. (1999). Corticofugal regulation of excitatory and inhibitory frequency tuning curves of bat inferior collicular neurons. *Brain Res.* 841, 184–188.

Jen, P. H. S., Zhou, X. M., and Wu, C. H. (2001). Temporally patterned sound pulse trains affect intensity and frequency sensitivity of inferior collicular neurons of the big brown bat, Eptesicus fuscus. *J. Comp. Physiol. A* 187, 605–616.

Kelly, J., and Caspary, D. (2005). "Pharmacology of the inferior colliculus," in *The Inferior Colliculus*, eds J. Winer and C. E. Schreiner (New York, NY: Springer-Verlag), 248–281.

Kelly, J., and Li, L. (1997). Two sources of inhibition affecting binaural evoked responses in the rat inferior colliculus: the dorsal nucleus of the lateral lemniscus and the superior olivary complex. *Hear. Res.* 104, 112–126.

Klug, A., Bauer, E. E., Hanson, J. T., Hurley, L., Meitzen, J., and Pollak, G. D. (2002). Response selectivity for species-specific calls in the inferior colliculus of Mexican free-tailed bats is generated by inhibition. *J. Neurophysiol.* 88, 1941–1954.

Klug, A., Park, T. J., and Pollak, G. D. (1995). Glycine and GABA influence binaural processing in the inferior colliculus of the moustache bat. *J. Neurophysiol.* 74, 1701–1713.

Koch, U., and Grothe, B. (1998). GABAergic and glycinergic inhibition sharpens tuning for frequency modulations in the inferior colliculus of the big brown bat. *J. Neurophysiol.* 80, 71–82.

Kulesza, R. J., Spirou, G. A., and Berrebi, A. S. (2003). Physiological response properties of neurons in the superior paraolivary nucleus of the rat. *J. Neurophysiol.* 89, 2299–2312.

Le Beau, F., Rees, A., and Malmierca, M. (1996). Contribution of GABA- and glycine-mediated inhibition to the monaural temporal response properties of neurons in the inferior colliculus. *J. Neurophysiol.* 75, 902–919.

LeBeau, F. E. N., Malmierca, M. S., and Rees, A. (2001). Iontophoresis *in vivo* demonstrates a key role for GABA(a) and glycinergic inhibition in shaping frequency response areas in the inferior colliculus of guinea pig. *J. Neurosci.* 21, 7303–7312.

Marsh, R. A., Nataraj, K., Gans, D., Portfors, C. V., and Wenstrup, J. J. (2006). Auditory responses in the cochlear nucleus of awake mustached bats: precursors to spectral integration in the auditory midbrain. *J. Neurophysiol.* 95, 88–105.

Mittmann, D. H., and Wenstrup, J. J. (1995). Combination-sensitive neurons in the inferior colliculus. *Hear. Res.* 90, 185–191.

Muniak, M., Mayko, Z., Ryugo, D., and Portfors, C. (2012). Preparation of an awake mouse for recording neural responses and injecting tracers. *J. Vis. Exp.* 64, e3755.

Nataraj, K., and Wenstrup, J. J. (2005). Roles of inhibition in creating complex auditory responses in the inferior colliculus: facilitated combination-sensitive neurons. *J. Neurophysiol.* 93, 3294–3312.

Oliver, D., Winer, J., Beckius, G., and Saint Marie, R. (1994). Morphology of GABAergic neurons in the inferior colliculus of the cat. *J. Comp. Neurol.* 340, 27–42.

Oliver, D. L., Kuwada, S., Yin, T. C. T., Haberly, L. B., and Henkel, C. K. (1991). Dendritic and axonal morphology of HRP-injected neurons in the inferior colliculus of the cat. *J. Comp. Neurol.* 303, 75–100.

O'Neill, W., and Suga, N. (1979). Target range sensitive neurons in the auditory cortex of the mustached bat. *Science* 203, 69–73.

Palombi, P., and Caspary, D. (1996). GABA inputs control discharge rate primarily within frequency receptive fields of inferior colliculus neurons. *J. Neurophysiol.* 75, 2211–2219.

Park, T. J., and Pollak, G. D. (1993). GABA shapes a topographic organization of response latency in the mustache bat inferior colliculus. *J. Neurosci.* 13, 5172–5187.

Park, T. J., and Pollak, G. D. (1994). Azimuthal receptive-fields are shaped by GABAergic inhibition in the inferior colliculus of the mustache bat. *J. Neurophysiol.* 72, 1080–1102.

Paxinos, G., and Franklin, K. (2001). *The Mouse Brain in Stereotaxic Coordinates, 2nd Edn.* San Diego, CA: Academic Press.

Portfors, C. (2004). Combination sensitivity and processing of communication calls in the inferior colliculus of the moustached bat Pteronotus parnellii. *An. Acad. Bras. Cinc.* 76, 253–257.

Portfors, C., and Felix II, R. (2005). Spectral integration in the inferior colliculus of the CBA/CaJ mouse. *Neuroscience* 136, 1159–1170.

Portfors, C. V., Mayko, Z. M., Jonson, K. G., Cha, G. F., and Roberts, P. D. (2011). Spatial organization of receptive fields in the auditory midbrain of awake mouse. *Neuroscience* 193, 429–439.

Portfors, C. V., and Roberts, P. D. (2007). Temporal and frequency characteristics of cartwheel cells in the dorsal cochlear nucleus of the awake mouse. *J. Neurophysiol.* 98, 744–756.

Portfors, C. V., Roberts, P. D., and Jonson, K. (2009). Over-representation of species-specific vocalizations in the awake mouse inferior colliculus. *Neuroscience* 162, 486–500.

Portfors, C. V., and Wenstrup, J. J. (1999). Delay-tuned neurons in the inferior colliculus of the mustached bat: implications for analyses of target distance. *J. Neurophysiol.* 82, 1326–1338.

Portfors, C. V., and Wenstrup, J. J. (2001a). Responses to combinations of tones in the nuclei of the lateral lemniscus. *J. Assoc. Res. Otolaryngol.* 2, 104–117.

Portfors, C. V., and Wenstrup, J. J. (2001b). Topographical distribution of delay-tuned responses in the mustached bat inferior colliculus. *Hear. Res.* 151, 95–105.

Ramachandran, R., Davis, K. A., and May, B. J. (1999). Single-unit responses in the inferior colliculus of decerebrate cats i. classification based on frequency response maps. *J. Neurophysiol.* 82, 152–163.

Razak, K., and Fuzessery, Z. (2009). GABA shapes selectivity for the rate and direction of frequency-modulated sweeps in the auditory cortex. *J. Neurophysiol.* 102, 1366–1378.

Reetz, G., and Ehret, G. (1999). Inputs from three brainstem sources to identified neurons of the mouse inferior colliculus slice. *Brain Res.* 816, 527–543.

Saint Marie, R. (1996). Glutamatergic connections of the auditory midbrain: selective uptake and axonal transport of D-[3H]aspartate. *J. Comp. Neurol.* 373, 255–270.

Saint Marie, R., and Baker, R. (1990). Neurotransmitter-specific uptake and retrograde transport of [3H]glycine from the inferior colliculus by ipsilateral projections of the superior olivary complex and nuclei of the lateral lemniscus. *Brain Res.* 524, 224–253.

Saint Marie, R., Ostapoff, R.-M., Morest, D., and Wenthold, R. (1989). Glycine-immunoreactive projection of the cat lateral superior olive: possible role in midbrain ear dominance. *J. Comp. Neurol.* 279, 382–396.

Saldana, E., Feliciano, M., and Merchan, M. A. (1996). Distribution of descending projections from primary auditory neocortex to inferior colliculus mimics the topography of intracollicular projections. *J. Comp. Neurol.* 371, 15–40.

Sanchez, J., Gans, D., and Wenstrup, J. (2008). Glycinergic inhibition mediates selective excitatory responses to combinations of sounds. *J. Neurosci.* 28, 80–90.

Schofield, B. (2005). "Superior olivary complex and lateral lemniscal connections of the auditory midbrain," in *The Inferior Colliculus*, eds J. Winer and C. Schreiner (New York, NY: Springer), 132–154.

Spirou, G., Davis, K. A., Nelken, I., and Young, E. D. (1999). Spectral integration by type II interneurons in dorsal cochlear nucleus. *J. Neurophysiol.* 82, 648–663.

Vater, M., Covey, E., and Casseday, J. H. (1997). The columnar region of the ventral nucleus of the lateral lemniscus in the big brown bat (*Eptesicus fuscus*): synaptic arrangements and structural correlates of feedforward inhibitory function. *Cell Tissue Res.* 289, 223–233.

Vater, M., Habbicht, H., Kossl, M., and Grothe, B. (1992a). The functional-role of GABA and glycine in monaural and binaural processing in the inferior colliculus of horseshoe bats. *J. Comp. Physiol. A* 171, 541–553.

Vater, M., Kossl, M., and Horn, A. K. E. (1992b). GAD- and GABA-immunoreactivity in the ascending auditory pathway of horseshoe and mustached bats. *J. Comp. Neurol.* 325, 183–206.

Wang, Y., Sanchez, J. T., and Rubel, E. (2010). "Nucleus laminaris," in *Handbook of Brain Microcircuits*, eds G. Shepherd and S. Grillner (New York, NY: Oxford University Press), 224–233.

Wenstrup, J. J., and Leroy, S. A. (2001). Spectral integration in the inferior colliculus: role of glycinergic inhibition in response facilitation. *J. Neurosci.* 21, 1–6.

Willard, F., and Ryugo, D. (1983). "Anatomy of the central auditory system," in *The Auditory Psychobiology of the Mouse*, ed J. Willott (Springfield, IL: Charles C. Thomas), 201–304.

Willott, J. (2005). "Hearing loss and the inferior colliculus," in *The Inferior Colliculus*, eds J. Winer and C. Schreiner (New York, NY: Springer-Verlag), 585–682.

Willott, J. F. (1986). Effects of aging, hearing loss, and anatomical location on thresholds of inferior colliculus neurons in c57bl/6 and CBA mice. *J. Neurophysiol.* 56, 391–408.

Willott, J. F. (1991). Central physiological correlates of ageing and presbycusis in mice. *Acta Otolaryngol.* 476, 153–156.

Winer, J., Larue, D., Diehl, J., and Hefti, B. (1998). Auditory cortical projections to the cat inferior colliculus. *J. Comp. Neurol.* 400, 147–174.

Winer, J., Larue, D., and Pollak, G. (1996). GABA and glycine in the central auditory system of the mustache bat: structural substrates for inhibitory neuronal organization. *J. Comp. Neurol.* 355, 317–353.

Winer, J., and Schreiner, C. (2005). *The Inferior Colliculus.* New York, NY: Springer-Verlag.

Xie, R., Meitzen, J., and Pollak, G. D. (2005). Differing roles of inhibition in hierarchical processing of species-specific calls in auditory brainstem nuclei. *J. Neurophysiol.* 94, 4019–4037.

Yang, L., Pollak, G. D., and Resler, C. (1992). GABAergic circuits sharpen tuning curves and modify response properties in the mustache bat inferior colliculus. *J. Neurophysiol.* 68, 1760–1774.

Young, E., and Oertel, D. (2010). "Cochlear nucleus," in *Handbook of Brain Microcircuits*, eds G. Shepherd and S. Grillner (New York, NY: Oxford University Press), 215–223.

Zhang, D., Li, L., Kelly, J., and Wu, S. (1998). GABAergic projections from the lateral lemniscus to the inferior colliculus of the rat. *Hear. Res.* 117, 1–12.

Zhang, H., and Kelly, J. (2003). Glutamatergic and GABAergic regulation of neural responses in inferior colliculus to amplitude modulated sounds. *J. Neurophysiol.* 90, 477–490.

Conflict of Interest Statement: The authors declare that the research was conducted in the absence of any commercial or financial relationships that could be construed as a potential conflict of interest.

Received: 24 May 2012; accepted: 25 September 2012; published online: 11 October 2012.

Citation: Mayko ZM, Roberts PD and Portfors CV (2012) Inhibition shapes selectivity to vocalizations in the inferior colliculus of awake mice. Front. Neural Circuits ***6****:73. doi: 10.3389/fncir.2012.00073*

frontiers in
NEURAL CIRCUITS

REVIEW ARTICLE
published: 23 October 2012
doi: 10.3389/fncir.2012.00075

Mechanisms of spectral and temporal integration in the mustached bat inferior colliculus

***Jeffrey James Wenstrup*[1]*, *Kiran Nataraj*[1†] *and Jason Tait Sanchez*[2]**

[1] *Department of Anatomy and Neurobiology, Northeast Ohio Medical University, Rootstown, OH, USA*
[2] *Knowles Hearing Center, Roxelyn and Richard Pepper Department of Communication Sciences and Disorders, Northwestern University, Evanston IL, USA*

Edited by:
Manuel S. Malmierca, University of Salamanca, Spain

Reviewed by:
Jagmeet S. Kanwal, Georgetown University, USA
Ellen Covey, University of Washington, USA

****Correspondence:***
Jeffrey James Wenstrup, Department of Anatomy and Neurobiology, Northeast Ohio Medical University, 4209 State Route 44, Rootstown, OH 44272-0095, USA.
e-mail: jjw@neomed.edu

†Present address:
Kiran Nataraj, 38 Crown Street, #102, New Haven, CT 06510, USA.

This review describes mechanisms and circuitry underlying combination-sensitive response properties in the auditory brainstem and midbrain. Combination-sensitive neurons, performing a type of auditory spectro-temporal integration, respond to specific, properly timed combinations of spectral elements in vocal signals and other acoustic stimuli. While these neurons are known to occur in the auditory forebrain of many vertebrate species, the work described here establishes their origin in the auditory brainstem and midbrain. Focusing on the mustached bat, we review several major findings: (1) Combination-sensitive responses involve facilitatory interactions, inhibitory interactions, or both when activated by distinct spectral elements in complex sounds. (2) Combination-sensitive responses are created in distinct stages: inhibition arises mainly in lateral lemniscal nuclei of the auditory brainstem, while facilitation arises in the inferior colliculus (IC) of the midbrain. (3) Spectral integration underlying combination-sensitive responses requires a low-frequency input tuned well below a neuron's characteristic frequency (ChF). Low-ChF neurons in the auditory brainstem project to high-ChF regions in brainstem or IC to create combination sensitivity. (4) At their sites of origin, both facilitatory and inhibitory combination-sensitive interactions depend on glycinergic inputs and are eliminated by glycine receptor blockade. Surprisingly, facilitatory interactions in IC depend almost exclusively on glycinergic inputs and are largely independent of glutamatergic and GABAergic inputs. (5) The medial nucleus of the trapezoid body (MNTB), the lateral lemniscal nuclei, and the IC play critical roles in creating combination-sensitive responses. We propose that these mechanisms, based on work in the mustached bat, apply to a broad range of mammals and other vertebrates that depend on temporally sensitive integration of information across the audible spectrum.

Keywords: combination-sensitive, combination sensitivity, biosonar, echolocation, lateral lemniscus, glycinergic, medial nucleus of trapezoid body, facilitation

INTRODUCTION

Our ability to perceive the location and identity of sound sources depends on information distributed across the frequency and time structure of complex acoustic signals. The peripheral auditory system performs an initial spectral analysis that separates acoustic information into a series of frequency channels. Subsequent analyses by the central auditory system combine information obtained from different frequency channels, including information about signal elements that have occurred at different times. The process of comparing information across frequency and time is termed here "spectro-temporal integration." Spectro-temporal integration is essential for localization of sounds (Hebrank and Wright, 1974; Knudsen and Konishi, 1979; Middlebrooks, 1992; Populin and Yin, 1998), perception of conspecific vocalizations in social interactions (Park and Dooling, 1985; Boothroyd et al., 1996; Shannon et al., 2004; Moore, 2008), and analysis of sonar echoes in bats (Simmons et al., 2004; Genzel and Wiegrebe, 2008).

This review describes mechanisms in the auditory brainstem and midbrain that contribute to spectro-temporal integration. The focus is on studies of the mustached bat (*Pteronotus parnellii*). This species displays two highly developed acoustic behaviors—echolocation and social communication—that require spectro-temporal integration for the analysis of its complex vocal signals. Spectro-temporal integration is particularly evident in the specialized responses to the mustached bat's echolocation signal (**Figure 1**), a complex vocalization with multiple acoustic elements. Work in the mustached bat provides an in-depth description of one form of spectro-temporal integration, *combination sensitivity*, which is characterized by neural interactions activated by distinct signal elements that occur in different frequency bands or at different times. Combination sensitivity creates selective responses to particular features of biosonar pulse-echo combinations in bats (Feng et al., 1978; Suga et al., 1978; O'Neill and Suga, 1979; Sullivan, 1982; Schuller et al., 1991; Fitzpatrick et al., 1993) and to social vocalizations

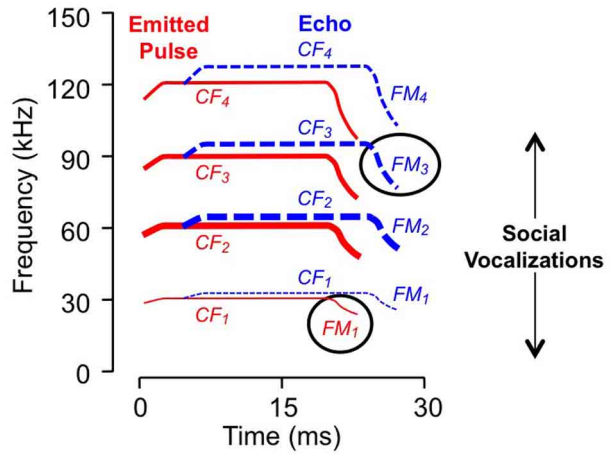

FIGURE 1 | Spectral and temporal features of vocalizations. Schematic sonogram of echolocation signal displays emitted pulse (in red) and a Doppler (frequency) shifted and time delayed echo (in blue). Each signal is composed of CF, constant frequency; FM, frequency modulated components, with several harmonic elements (e.g., FM_1, FM_2, etc.). *Line thickness* indicates relative intensity: the second harmonic of the emitted pulse, near 60 kHz, is the most intense while the fundamental is usually less intense than either the second or third harmonics. *Ovals* indicate sonar elements to which the neurons in **Figure 2** are tuned. Social vocalizations span the range from approximately 5–100 kHz.

in a broad range of vertebrates, including frogs (Fuzessery and Feng, 1983), birds (Margoliash and Fortune, 1992; Lewicki and Konishi, 1995), bats (Ohlemiller et al., 1996; Esser et al., 1997), and other mammals (Rauschecker et al., 1995; Kadia and Wang, 2003).

Although most studies have described combination sensitivity in the auditory forebrain, the work reviewed here reveals a sequence of spectro-temporal integrative events within the auditory brainstem and midbrain that results in the combination-sensitive neurons observed in the auditory forebrain. Along the way, these studies have identified several novel features of auditory brainstem and midbrain processing: (1) combination-sensitive response properties observed in midbrain and forebrain neurons depend on spectral convergence at distinct sites within the ascending auditory pathway, (2) spectral integration in combination sensitivity involves projections of low-frequency-tuned brainstem auditory neurons onto neurons tuned to much higher frequencies, and (3) glycinergic neurons are critically involved in both inhibitory and facilitatory combination-sensitive interactions. Further, the work identifies three regions that play key roles in creating combination sensitivity: the medial nucleus of the trapezoidal body, lateral lemniscal nuclei, and the inferior colliculus (IC). The integrative mechanisms described here are expected to apply broadly to vertebrates that utilize spectro-temporal integration to analyze complex vocal signals.

This review first considers the auditory response properties of combination-sensitive neurons and then describes mechanisms and circuitry underlying these properties.

COMBINATION-SENSITIVE RESPONSE PROPERTIES IN THE INFERIOR COLLICULUS

Here we describe combination-sensitive response properties in the IC, the major nucleus of the auditory midbrain. The IC appears to be the locus of many of the integrative mechanisms underlying combination sensitivity. These mechanisms involve facilitation, inhibition, or both. **Figure 2** shows spectral and temporal features of facilitatory combination sensitivity (**Figures 2A,C**) and inhibitory combination sensitivity (**Figures 2B,D**). The facilitated neuron in **Figure 2A** responds weakly to signals at its characteristic frequency (ChF) of 83 kHz, and is facilitated by low-frequency signals tuned to 27 kHz. The facilitatory effect of the low-frequency signal is strong only when it precedes the ChF signal by 0–4 ms, and it peaks at 2 ms (**Figure 2C**). The inhibited neuron in **Figure 2B** responds well to the ChF signal at 80 kHz, but that response is inhibited by a simultaneous signal near 27 kHz (**Figures 2B,D**). This inhibitory interaction is clearly distinct from the inhibition adjacent to excitatory tuning curves that is termed "sideband inhibition." In each of these neurons, the response to the complex signal depends on distinct and well-timed spectral inputs.

In the mustached bat's IC, the majority of neurons are combination-sensitive but estimates vary substantially across studies. Between 23 and 62% of tested IC neurons display facilitation, while 24–41% of tested neurons show inhibition without facilitation (Mittmann and Wenstrup, 1995; Portfors and Wenstrup, 1999; Leroy and Wenstrup, 2000; Nataraj and Wenstrup, 2005, 2006; Macías et al., 2012). The numbers reported in these studies likely vary due to different testing methods and neuronal populations sampled, and may also differ as a result of the different sub-species of mustached bats that were studied. However, each of these studies reveals that combination sensitivity is a common response feature within the mustached bat's IC. Similar findings of combination sensitivity have not been reported in the IC of other bat species. However, studies in the big brown bat have shown that a midbrain region rostral to the IC contains combination-sensitive neurons that are tuned to pulse-echo delay (Feng et al., 1978; Dear and Suga, 1995). In the mouse IC, a smaller number of combination-sensitive neurons have been reported: approximately 16% of IC neurons are facilitatory, while 12% display inhibitory combination sensitivity without facilitation (Portfors and Felix, 2005).

In the sections below, we describe the spectral and temporal properties of these neurons in greater detail because these properties are related both to the underlying mechanisms and to the functional roles in acoustically guided behavior.

FREQUENCY TUNING

Combination-sensitive neurons in the mustached bat IC are responsive to two distinct frequency bands (**Figures 2A,B**). These neurons typically display a clearly identifiable ChF that is almost always tuned to the higher of the two spectral bands. ChFs of these neurons range from 30 kHz to nearly 120 kHz, spanning most of the mustached bat's audible range (**Figures 3A,B**). Responsiveness to the lower frequency band is sometimes apparent when single tonal stimuli are presented. In many cases,

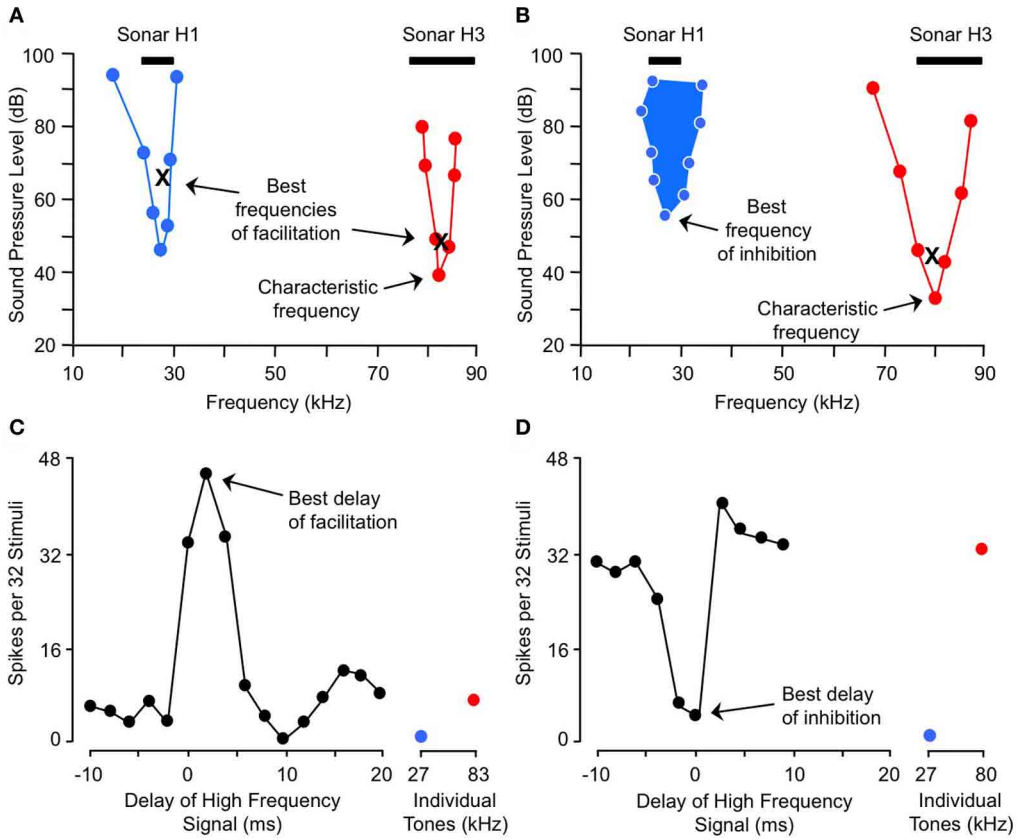

FIGURE 2 | Spectral and temporal tuning of combination sensitivity in the mustached bat's IC. Figure shows responses of a facilitated neuron **(A** and **C)** and an inhibited neuron **(B** and **D)**. **(A)** Facilitation frequency tuning curves for high-frequency (*red*) and low-frequency (*blue*) tone bursts. These curves were obtained by fixing the frequency and level of one tone burst (X) while varying the frequency and level of a second tone burst in the other frequency band, in order to obtain threshold facilitative responses. Facilitation was defined as a response to the combination stimulus that was 20% greater than the sum of responses to the two stimuli presented separately. The high-frequency tone burst was presented at a delay corresponding to the neuron's best delay of facilitation (shown in **C**). **(B)** Excitatory (*red*) and inhibitory (*filled blue*) tuning of neuron showing combination-sensitive inhibition. The low-frequency inhibitory tuning curve was obtained by presenting a characteristic frequency tone burst at a fixed level (X), then varying the frequency and level of a low-frequency tone burst to obtain threshold inhibitory responses. Inhibition was defined as a response to the combination stimulus that was 20% less than the sum of responses to the two stimuli presented separately. The two tones were presented at the neuron's best delay of inhibition (shown in **D**). Black bars at top in **(A** and **B)** indicate frequency ranges of fundamental (H1) and third (H3) harmonic elements of biosonar call. **(C)** Delay tuning of facilitation for neuron in **(A)**. Neuron responded poorly to individual tone bursts, but strongly to the combination of facilitating tones when the high-frequency signal was delayed by 0–4 ms. Note inhibition of high-frequency response by low-frequency signal at delay of 10 ms. **(D)** Delay tuning of inhibition for neuron in **(B)**. Neuron's response to the ChF tone was inhibited by low-frequency tones when the signals were presented simultaneously. Adapted from Portfors and Wenstrup (1999), with permission.

however, responsiveness to the low-frequency signal is only revealed by presenting low-frequency tones in combination with the ChF tone. These tests show that most low-frequency responsiveness, whether facilitating or inhibiting, is tuned below 30 kHz (**Figures 3A,B**).

Note: In some of the neuroethological literature, including echolocation, the term "best frequency" is used synonymously with "ChF." For this review we use "ChF" as it is used by many auditory neuroscientists to designate the sound frequency requiring the lowest intensity to evoke an excitatory response. We use the abbreviation "ChF" because we already use the abbreviation "CF" to designate the constant frequency (CF) component of bat sonar signals. For both low and high frequencies that evoke the strongest facilitation, we use the term "best facilitating frequency." The best high facilitating frequency and the ChF were always very close (Portfors and Wenstrup, 1999).

For the majority of combination-sensitive neurons, facilitatory or inhibitory interactions are based on frequency combinations that occur within pulse-echo sequences of the echolocation call (**Figures 3A,B**; Portfors and Wenstrup, 1999; Leroy and Wenstrup, 2000; Nataraj and Wenstrup, 2005, 2006). The echolocation call (**Figure 1**) is a brief but complex signal consisting of CF and frequency modulated (FM) elements present in multiple harmonics. The fundamental includes a relatively long (up to 30 ms) CF component near 30 kHz, terminated by a brief (<5 ms) FM down-sweep to about 23 kHz. The fundamental is attenuated by the vocal tract while the second harmonic, with CF near 60 kHz, is usually the most intense. Echoes of the emitted signal

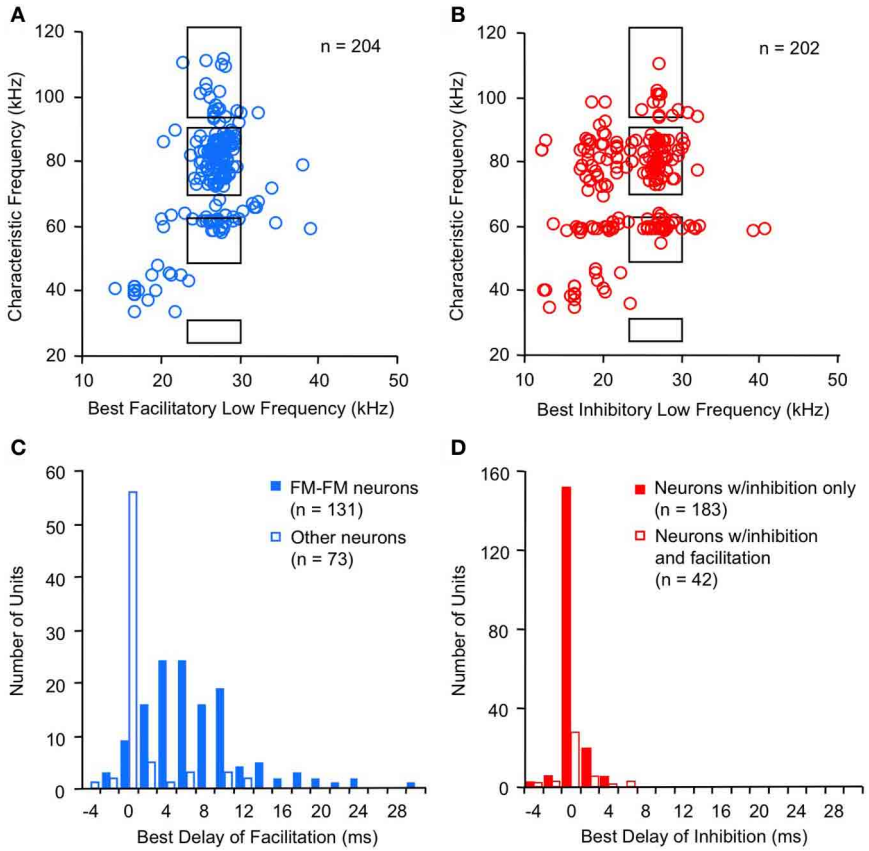

FIGURE 3 | Spectral and temporal features of combination-sensitive neurons in mustached bat IC. (A,B) Spectral tuning of facilitation **(A)** and inhibition **(B)**. *Black rectangles* indicate frequency combinations that are present in echolocation signals. **(C,D)** Delay tuning of facilitation and inhibition. Best delays of facilitation **(C)** were broadly distributed for FM–FM neurons but tightly distributed around 0 ms delay for other types of facilitated neurons. Delay tuning of combination-sensitive inhibition **(D)** was similar for neurons showing only inhibition and for those facilitated neurons showing early inhibition. Data from Portfors and Wenstrup (1999); Leroy and Wenstrup (2000); Nataraj and Wenstrup (2005, 2006).

are delayed as a function of the distance between the bat and an echo source, and they are Doppler (frequency)-shifted upward as the bat approaches the echo source. CF components carry information underlying the detection and identification of sonar targets, including the fluttering insects that are the mustached bat's prey (Goldman and Henson, 1977). FM components carry information about the distance of sonar targets (Simmons, 1971, 1973; Simmons and Stein, 1980). Many combination-sensitive neurons also respond to signal elements in the mustached bat's social vocalizations. Mustached bats are highly social animals (Bateman and Vaughan, 1974) that depend on vocal signals to communicate within the dark caves that serve as roosts. The repertoire of social vocalizations spans a broad frequency range from about 5 kHz to nearly 100 kHz (**Figure 1**) and is considerably more varied than the stereotyped echolocation signal (Kanwal et al., 1994).

The fact that most combination-sensitive neurons are tuned to frequency combinations that occur in echolocation signals suggests that the majority of these neurons operate during echolocation behavior. Further, in all combination-sensitive IC neurons tuned to echolocation frequencies, the low-frequency facilitation or inhibition is tuned to the sonar fundamental (23–30 kHz). This indicates a special role of the fundamental in biosonar signal processing. The general view of this role is that the fundamental serves as an acoustic marker for the emitted sound: the fundamental in the emitted sound is sufficiently intense to activate auditory neurons but the fundamental in echoes is too faint to evoke a response (Suga and O'Neill, 1979; Kawasaki et al., 1988; Wenstrup and Portfors, 2011).

The frequency tuning properties of combination-sensitive neurons are indicative of their analysis of CF or FM components of biosonar echoes. Analysis of CF echoes is performed by neurons with extraordinarily sharp tuning to the CF_2 (near 60 kHz) or CF_3 (near 90 kHz) echo components. These neurons may be facilitated or inhibited by signals in the CF_1 frequency range near 30 kHz or by signals in the FM_1 range (29–23 kHz). These are designated CF–CF or FM–CF neurons, respectively. Analysis of FM echoes is performed by FM–FM neurons that are less sharply tuned to the frequencies in FM_2, FM_3, or FM_4 sonar components. As described below, these differences in frequency tuning are correlated with differences in temporal properties. The neurons illustrated in **Figure 2** are of the FM_1–FM_3 type, responding

to well-timed combinations of FM_1 and FM_3 elements of sonar signals (**Figure 1**).

While the emphasis here has been on neurons tuned to biosonar frequency combinations, it is apparent from **Figures 3A** and **B** that many combination-sensitive responses are activated by frequency combinations that do not occur in sonar signals. We have speculated that these neurons play roles in the analysis of social vocalizations (Leroy and Wenstrup, 2000). Further, given the spectral overlap between sonar and social vocalizations, many combination-sensitive neurons tuned to sonar frequencies will also be activated by the multi-harmonic signals in social vocalizations (Ohlemiller et al., 1996; Esser et al., 1997).

A striking feature of the population of inhibitory neurons in **Figure 3B** is the large number of neurons that display an inhibitory effect tuned to signals below 23 kHz. This inhibitory effect, initially characterized on the basis of frequency tuning, also differs from inhibition tuned above 23 kHz in the sound levels required to evoke inhibition (Nataraj and Wenstrup, 2006) and in temporal properties (see section "Temporal features of low-frequency suppression"). Moreover, inhibition below 23 kHz is commonly associated with excitatory responses to the low-frequency stimulus. There is strong evidence that this suppression is the result of cochlear mechanisms related to the low-frequency "tails" of tuning curves that generate excitatory responses at high sound levels (Marsh et al., 2006; Nataraj and Wenstrup, 2006; Gans et al., 2009; Peterson et al., 2009). While not considered to be an example of combination sensitivity, it nonetheless contributes to the integrative features of neuronal responses to complex signals with energy in this <23 kHz band. For example, there is evidence that these high-ChF neurons respond well to low-frequency social vocalizations that occur at high sound levels. Furthermore, the suppressive feature of responses in the tail of the tuning curve "occludes," or suppresses, any response to signals near the neuron's ChF (Kiang and Moxon, 1974; Portfors et al., 2002; Sheykholeslami et al., 2004). The low-frequency excitation permits these neurons to analyze acoustic signals in multiple frequency bands.

A final point related to frequency tuning is that combination-sensitive neurons occur in the IC frequency band representations that correspond to their higher, ChF response. Thus, the neuron in **Figure 2A**, with ChF of 83 kHz, was located within the high-frequency (>62 kHz) part of the IC. The low-frequency signal that facilitates this ChF response is tuned to 27 kHz. In order for these combination-sensitive interactions to occur, low and high-frequency-tuned inputs must converge onto single neurons where combination-sensitive response properties are created.

TEMPORAL SENSITIVITY

The temporal features of spectral interactions in combination sensitivity are revealed in delay tests, in which the relative timing of the spectrally distinct signals is varied (**Figures 2C,D**). These temporal features are typically characterized by the relative timing that evokes the strongest interaction, either a peak (for facilitation) or a trough (for inhibition) in the delay function, or both (**Figure 4**). We refer to these as the best delay of facilitation or the best delay of inhibition. Positive delays are those for which the low-frequency signal leads the high-frequency signal. The delay functions, when combined with changes in signal duration, also reveal the duration of spectral interactions and their relationship to signal onset or offset.

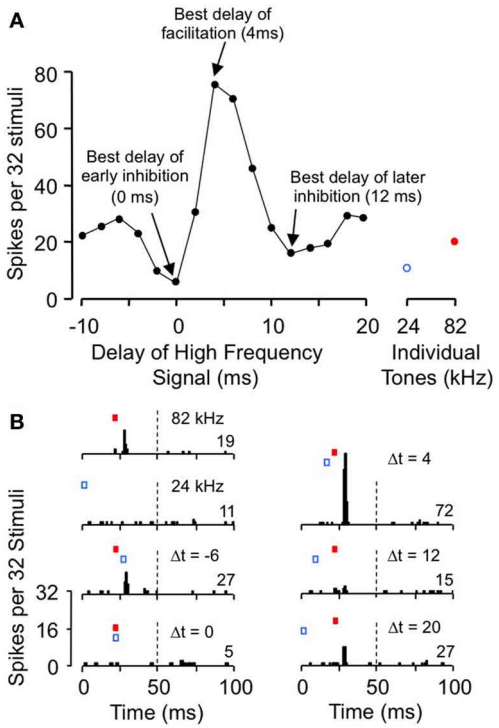

FIGURE 4 | Delay tuning of neuron showing both facilitation and inhibition. (A) This neuron's excitatory response to ChF tones (at 82 kHz) is inhibited by low frequency tones (24 kHz) at short and long delays, but is facilitated at intermediate delays. **(B)** Post-stimulus time histograms showing temporal features of the neuron's response to tone combinations. Adapted from Nataraj and Wenstrup (2005), with permission.

Temporal features of facilitation

Facilitatory interactions display a broad range of best delays, ranging from −4 ms to +30 ms (**Figure 3C**; Portfors and Wenstrup, 1999; Nataraj and Wenstrup, 2005). A large number of neurons display the strongest facilitation when the two signals occur simultaneously (0 ms delay), with a substantial population at positive delays. Neurons with positive best delays of facilitation (in which the high-frequency signal is delayed) are likely involved in coding pulse-echo delays that occur in echolocation. Only a very few neurons show best facilitation when the high-frequency signal leads the low-frequency signal.

The distribution of best delays of facilitation differs among neurons tuned to different frequency bands. Thus, FM–FM neurons are responsible for the broad distribution of best delays. This broad range of positive delays is thought to encode sonar pulse-echo delays, in which the FM_1 signal serves as a marker for the emitted pulse and the higher harmonic FM signal serves as a marker for the subsequent returning echo. A pulse-echo delay of 34 ms, the maximum best delay of facilitation observed in the mustached bat, corresponds to a bat-target distance of nearly 6 m. This corresponds roughly to the maximum distance of detection

in many bat species (Kick, 1982; Schnitzler and Kalko, 1998; Holderied and von Helversen, 2003). The range of best facilitatory delays requires mechanisms that can delay the facilitating effect of the FM_1 signal for up to 30 ms relative to the facilitating effect of the ChF signal.

For other combination-sensitive neurons, best delays of facilitation occur mostly when the different spectral elements are presented simultaneously (**Figure 3C**). This is true both for neurons that analyze the CF component of sonar signals (Portfors and Wenstrup, 1999; Nataraj and Wenstrup, 2005) as well as for neurons facilitated by frequencies that do not occur in sonar but may occur in social vocalizations (Leroy and Wenstrup, 2000; Nataraj and Wenstrup, 2005). Functionally, these neurons detect the coincidence of spectral elements in complex vocal signals. Such facilitatory interactions appear less mechanistically challenging than those in FM–FM neurons, since the facilitation only requires that the high and low-frequency excitations occur simultaneously.

Gans and co-workers (2009) investigated how the timing of facilitation was related to the duration of the low-frequency facilitating signal (**Figure 5**). They found that changes in low-frequency duration had no significant effect on delay tuning (**Figure 5A**). The rising phase of the facilitation peak (FAC_{START}) was unaffected by low-frequency duration (**Figures 5A,B**), indicating that the facilitation is locked to the onset of the low-frequency signal rather than to its offset. Further, the falling phase of the delay curve (FAC_{END}) was unrelated to changes in signal duration, indicating that the facilitation has a fixed duration unrelated to the low-frequency signal duration (**Figure 5C**). Although the duration of the facilitating effect varied for different neurons, it was on average 5.3 ms. These results suggest

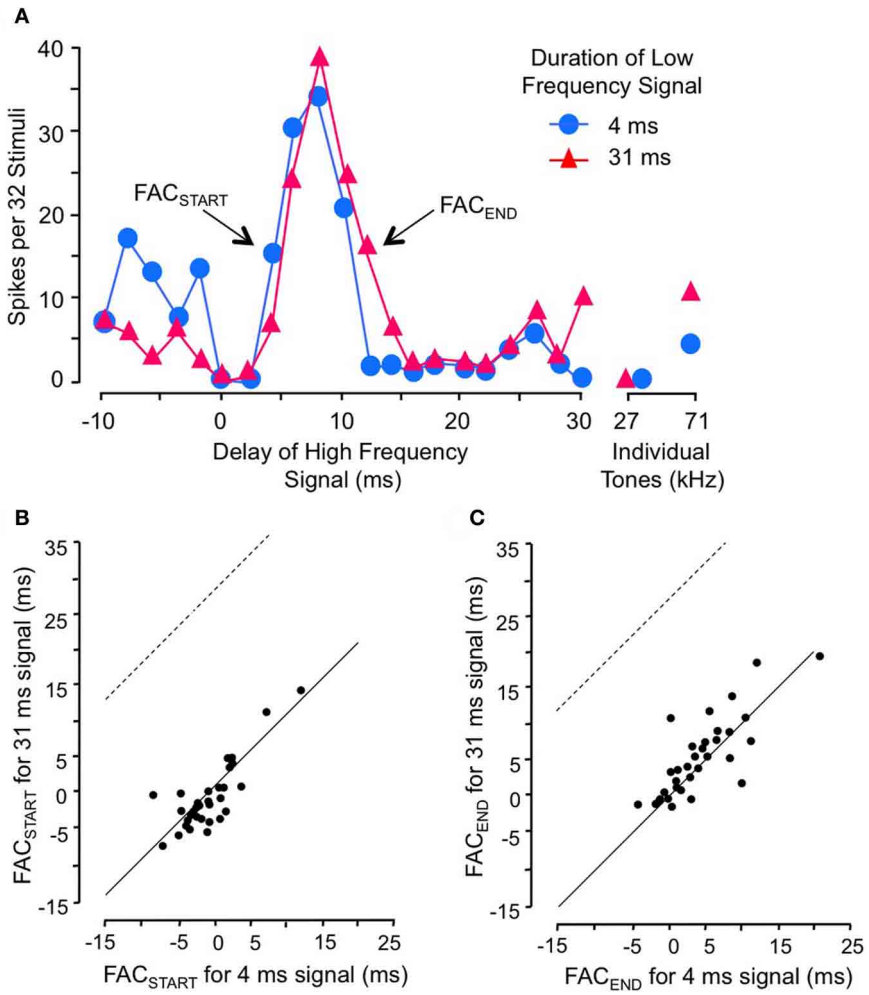

FIGURE 5 | Facilitation in combination-sensitive neurons is activated by the onset of the low-frequency signal and is phasic. (A) Delay sensitivity of neuron was tested with two durations of low-frequency signal. **(B)** FAC_{START} in scatterplot refers to the shortest delay that evokes facilitation. Data points fall along the *solid* line, indicating that the change in low-frequency duration had no effect on this measure. Thus, facilitation is locked to the onset of the low-frequency signal. If the facilitation was locked to low-frequency offset, the delay curve is expected to shift to the right and data points in this scatter plot would fall along the *dashed* line. **(C)** FAC_{END} refers to the longest delay that evokes facilitation, a measure of the duration of the facilitating effect of the low-frequency signal. FAC_{END} is invariant with changes in low-frequency duration, indicating that the facilitating effect is phasic and independent of low-frequency signal duration. Adapted from Gans et al. (2009), with permission.

that the onset of the low frequency signal activates a brief facilitating influence that generally cannot be extended by a longer stimulus. An input neuron with a phasic temporal pattern is consistent with these observations. Macías et al. (2012) showed that most IC facilitated neurons have delay tuning that is relatively invariant with level of the high-frequency signal. This suggests that inputs to delay-tuned neurons have level-invariant response latencies.

Temporal features of inhibition

For inhibitory combination-sensitive interactions, a low-frequency signal inhibits the excitatory response to the higher ChF signal (O'Neill, 1985; Mittmann and Wenstrup, 1995). Unlike facilitatory interactions, the strongest inhibition usually occurs when the two signals are presented simultaneously, i.e., having a best inhibitory delay of 0 ms (**Figure 3D**, Mittmann and Wenstrup, 1995; Portfors and Wenstrup, 1999; Leroy and Wenstrup, 2000; Nataraj and Wenstrup, 2006). No differences occur in the timing of inhibition for neurons responsive to different FM or CF sonar components or to signals that do not occur in sonar. In almost all cases, the inhibition is activated by the onset of the low-frequency signal (Gans et al., 2009). In general, the inhibition is phasic, lasting under 10 ms, but a smaller percentage of neurons show an inhibitory effect that could last as long as the stimulus. This suggests that the low-frequency inputs to neurons that create combination-sensitive inhibition are predominantly phasic. Neurons in the intermediate nucleus of the lateral lemniscus (INLL), which also show combination-sensitive inhibition, display similar temporal features of inhibition (Peterson et al., 2009). However, the width of inhibitory delay tuning curves may be larger among INLL neurons.

The majority of neurons (∼75%) that display facilitatory combination sensitivity also show inhibitory combination-sensitive interactions (Nataraj and Wenstrup, 2005). As indicated in **Figure 4**, these interactions may occur at delays shorter than or longer than the delays that evoke facilitation. "Early inhibition," generally occurring when the high and low-frequency signals are presented simultaneously, was most common, observed in 59% of facilitated neurons. The features of this early inhibition are indistinguishable from combination-sensitive neurons showing only inhibition (**Figure 3D**); there is no difference in the distribution of inhibitory delays, the strength of inhibition, or the width of inhibitory delay functions (Nataraj and Wenstrup, 2005, 2006). In general, early inhibition occurred in most facilitated neurons with best delays of 6 ms or longer, while early inhibition rarely occurred in neurons with best delays of facilitation of 4 ms or less. It was thus observed almost exclusively in FM–FM neurons, since these have the longest best delays of facilitation. "Late inhibition" (**Figures 2C**, **4**) occurred in 37% of facilitated neurons. Its properties are distinct from those of early inhibition and mechanistic studies suggest a different origin (Nataraj and Wenstrup, 2005).

In general terms, inhibitory combination-sensitive interactions suppress neural responses when two spectral elements have approximately simultaneous onsets. For neurons tuned to sonar frequencies, the FM_1 or CF_1 inhibition suppresses the response to emitted sonar pulse. However, these neurons may respond well to echoes because the intensity of echo FM_1 or CF_1 components are too weak to activate the inhibition. In sonar, these neurons function as "echo-only" neurons (Mittmann and Wenstrup, 1995). For neurons that also show delay-tuned facilitation, the early inhibition suppresses response during pulse emission while the facilitation creates a strong response over a narrow range of distances. Later inhibition enhances the contrast between the strong response at facilitated delays and the responses at other delays (Portfors and Wenstrup, 1999; Nataraj and Wenstrup, 2005).

Another function of inhibitory (and facilitatory) combinatorial interactions is in analyzing spectral content in social vocalizations. In several mustached bat social vocalizations, the energy in the frequency range below 30 kHz is variable (Kanwal et al., 1994). Neurons tuned to higher frequencies, but with low-frequency combination sensitivity, may encode the level of low-frequency formants in social vocalizations (Leroy and Wenstrup, 2000). Evidence for this appears in responses of neurons with inhibitory combination sensitivity in the IC of mustached bats (Portfors, 2004) and in the auditory cortex of monkeys (Rauschecker et al., 1995).

Temporal features of low-frequency suppression

Suppression activated by the lowest frequencies in the mustached bat audible range, below 23 kHz, has temporal features distinct from combination-sensitive inhibition described in the preceding paragraphs. For example, the <23 kHz suppressive interactions almost always extend for the duration of the suppressing signal, rather than for a brief period following signal onset (Gans et al., 2009). Further, when the <23 kHz signal evokes an excitatory response, this response suppresses spiking responses to the high-frequency signal. These temporal features are consistent with cochlear suppression (Sachs and Kiang, 1968; Arthur et al., 1971; Kiang and Moxon, 1974), and contrast with temporal features of inhibition tuned in the 23–30 kHz range. Thus, in neurons inhibited by 23–30 kHz, excitatory response to the 23–30 kHz signals can also occur, but such spikes add to spiking evoked by high-frequency signals rather than suppress the high-frequency response (Nataraj and Wenstrup, 2006). The low-frequency cochlear-type suppression blocks responses to signals near the neuron's ChF while permitting responses to sound frequencies within the tail of the tuning curve.

MECHANISMS UNDERLYING COMBINATION-SENSITIVE INHIBITION

As discussed earlier, there are several key response features of neurons that display combination-sensitive inhibition: (1) responses to ChF signals is inhibited by signals in the low (23–30 kHz) band; (2) this inhibition is usually phasic, locked to signal onset, and best when the ChF and low-frequency tones are presented simultaneously; (3) in many IC neurons, these inhibitory interactions co-occur with facilitatory interactions tuned to the same frequency bands. What mechanisms and circuitry underlie these features?

COMBINATION-SENSITIVE INHIBITION ORIGINATES IN LATERAL LEMNISCAL NUCLEI AND DEPENDS ON GLYCINERGIC INHIBITION

Although inhibitory combination-sensitive interactions have been observed in thalamic (Olsen and Suga, 1991b; Wenstrup,

1999) combination-sensitive neurons, their prominence among neurons in the mustached bat's IC suggested an origin in the IC or auditory centers below the IC. Mittmann (1997) and Portfors and Wenstrup (2001) showed that some inhibitory combination-sensitive responses occur in the INLL. Recent work in the mustached bat shows that combination-sensitive inhibition is a common response property among NLL neurons (Peterson et al., 2009). This is particularly true for INLL, but low-frequency inhibitory responses were also observed in the multipolar part of the ventral nucleus of the lateral lemniscus (VNLLm). Since previous work suggested that lower auditory brainstem structures do not display combination-sensitive inhibition (cochlear nucleus, Marsh et al., 2006), Peterson and colleagues hypothesized that these responses arise in so-called "monaural" nuclei of the lateral lemniscus, the INLL and VNLL. Collectively, these nuclei provide the largest projection to regions of the mustached bat's IC that contain combination-sensitive responses (Wenstrup et al., 1999; Yavuzoglu et al., 2011).

To test whether inhibitory interactions acting within NLL create combination-sensitive inhibition, Peterson and colleagues (2009) recorded auditory responses from NLL neurons before and after inhibitory receptor blockade. **Figure 6A** illustrates the effect of inhibitory receptor blockade on low-frequency inhibition in an INLL neuron. In control tests, this neuron's response to tone bursts at its ChF (56 kHz) was inhibited by 28 kHz tone bursts, and the inhibition was strongest with simultaneous presentation (0 ms delay). Blockade of $GABA_A$ receptors (via bicuculline) did not reduce the low-frequency inhibition, but additional blockade of glycine receptors (via strychnine) eliminated the low-frequency inhibition. Other tests (not shown here, see Peterson et al., 2009) indicated that the elimination of inhibition is entirely attributable to GlyR blockade. Across the tested sample of lateral lemniscal neurons, low-frequency inhibition was either eliminated or greatly reduced by GlyR blockade in all neurons (**Figure 6B**). In contrast, $GABA_AR$ blockade alone was ineffective in all neurons (**Figure 6B**). This asymmetric effect strongly suggests that low-frequency-tone-evoked inhibition depends on a low-frequency-tuned glycinergic input to high-ChF neurons in the lateral lemniscal nuclei.

These results are striking in their contrast to similar tests conducted on suppressive responses tuned to frequencies below 23 kHz (**Figures 6C,D**). In the same neuron as in **Figure 6A**, suppression by an 18 kHz tone was unaffected by either $GABA_AR$ or combined GlyR and $GABA_AR$ blockade (**Figure 6C**). This was true across the entire sample of NLL neurons (**Figure 6D**). This result indicates that the suppressive responses to tones <23 kHz do not originate in NLL, and it is consistent with the view that this suppression is of cochlear origin.

COMBINATION-SENSITIVE INHIBITION MAY BE MODIFIED IN IC

Studies of IC neurons support a conclusion that inhibitory combination-sensitive responses arise at levels below the IC but may be modified by interactions within the IC (Nataraj and Wenstrup, 2005, 2006). **Figures 6E** and **F** illustrate results of receptor blockade experiments. For the single neuron (**Figure 6E**), neither GlyR blockade nor combined GlyR and $GABA_AR$ blockade eliminated the 26 kHz inhibition of a high-ChF (86 kHz) response. However, note that some features of the low-frequency inhibition, especially the inhibition that occurs at delays of 2–6 ms, are reduced by GlyR blockade. Across the sample of tested neurons, inhibitory receptor blockade reduced inhibition in many neurons but eliminated it in only a few neurons (12% of tested neurons). The reduction in inhibition can occur for several reasons: it may result from blockade of low-frequency-tuned inhibitory inputs, but it may also result from the overall increase in excitation to ChF tones that occur when most inhibitory inputs are blocked.

To test whether IC neurons with high ChFs receive low-frequency inhibitory input, Peterson and colleagues (2008) used sharp electrodes to record postsynaptic potentials from combination-sensitive neurons. In the majority of neurons that showed combination-sensitive inhibition (57% of 118 neurons), they observed no low-frequency evoked inhibitory postsynaptic potentials (IPSPs) even though the high-frequency signal often evoked IPSPs. For these neurons, their inhibitory combination-sensitive response is almost certainly inherited from auditory brainstem nuclei. This is consistent with the major result of the microiontophoretic studies that inhibitory combination sensitivity in almost all IC neurons persists after local blockade of inhibitory receptors (Nataraj and Wenstrup, 2006). However, 43% of tested IC neurons show low-frequency-evoked IPSPs, indicating the presence of 23–30 kHz-tuned inhibitory inputs onto some of the high-ChF, combination-sensitive neurons. These results are consistent with the receptor blockade results showing that low-frequency inhibition is eliminated in a few neurons and is reduced in many more neurons. We believe the data support a conclusion that most IC neurons with the inhibitory combination-sensitive response property inherit that response from neurons in the lateral lemniscal nuclei, but a subset receive additional low-frequency inhibitory inputs that contribute to the IC response. In only a few IC neurons, combination-sensitive inhibition arises *de novo* through integration of high-frequency excitatory input and low-frequency inhibition.

These conclusions regarding inhibitory combination sensitivity in the IC also apply to the early inhibition observed in facilitated neurons. Nataraj and Wenstrup (2005) found that early inhibition was often reduced but rarely eliminated (8% of tested neurons) by GlyR or $GABA_AR$ blockade. This suggests a common mechanism or set of mechanisms underlying combination-sensitive inhibition for IC neurons, whether or not they also display facilitatory interactions.

CIRCUITRY UNDERLYING COMBINATION-SENSITIVE INHIBITION IN INLL AND IC

Yavuzoglu et al. (2010) investigated the circuitry underlying combination-sensitive inhibition. They placed deposits of retrograde tracer at INLL recording sites featuring high ChF, inhibitory combination-sensitive response properties. The major inputs to these INLL sites are from the anteroventral cochlear nucleus (AVCN, contralateral) and the medial nucleus of the trapezoid body (MNTB, ipsilateral) (**Figure 7A**). Glycine immunochemistry, in combination with the retrograde transport, showed that MNTB provides the vast majority of glycinergic input (84% of input neurons) and LNTB provides most of the remainder (13%).

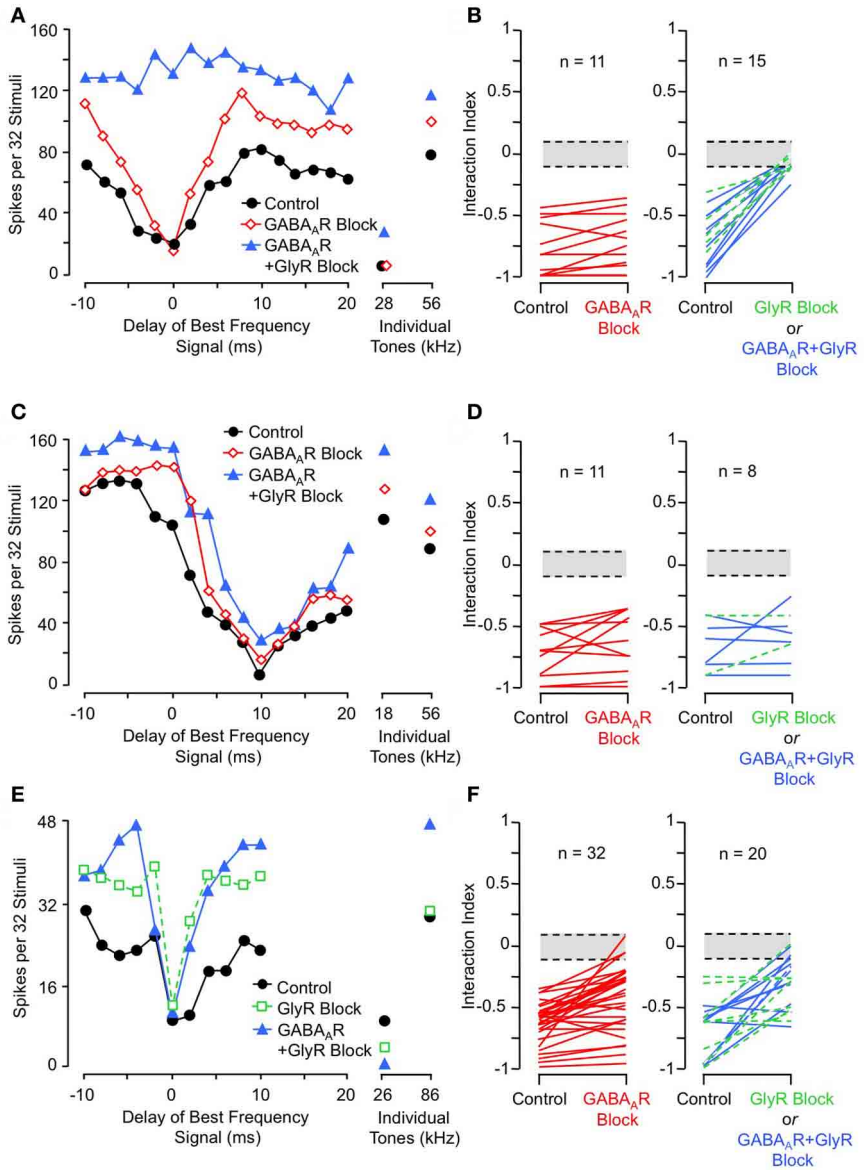

FIGURE 6 | Effects of receptor blockade on low-frequency-evoked inhibition and suppression. (A) In INLL neuron, blockade of $GABA_A$ receptor ($GABA_AR$) by bicuculline did not eliminate 28 kHz inhibition, but addition of GlyR blockade by strychnine completely eliminated this inhibition. **(B)** Effects of receptor blockade on 23–30 kHz inhibition on population of tested NLL neurons. While $GABA_AR$ blockade alone (*at left*) did not eliminate combination-sensitive inhibition in any neuron, GlyR blockade (*at right*) always eliminated or greatly reduced inhibition evoked by 23–30 kHz signal. In **(B, D,** and **F)**, *interaction index* expresses the degree of facilitation (*positive values*) or inhibition (*negative values*). The *greyed area* indicates no significant interaction. *Green dashed lines* indicate results from GlyR receptor blockade alone, compared to *black lines* that show combined $GABA_AR$ and GlyR blockade. **(C)** In same INLL neuron as in **(A)**, blockade of $GABA_AR$ or both $GABA_AR$ and GlyR failed to eliminate 18 kHz suppression. **(D)** Effects of receptor blockade on <23 kHz suppression among NLL neurons. Neither $GABA_AR$ nor GlyR blockade eliminated suppression tuned to frequencies below 23 kHz. **(E)** In an IC neuron, blockade of GlyR did not eliminate 26 kHz inhibition, although the delay function was narrowed. Combination of GlyR and $GABA_AR$ blockade failed to eliminate 26 kHz inhibition. **(F)** Effects of receptor blockade on 23–30 kHz inhibition among IC neurons. Data suggest that many IC neurons inherit combination sensitivity from auditory brainstem inputs, but that some inhibitory inputs tuned to 23–30 kHz terminate onto high-ChF neurons in IC. Adapted from Peterson et al. (2009) **(A–D)** and Nataraj and Wenstrup (2005, 2006) **(E,F)**, with permission.

It is noteworthy that input from VNLL, including the exclusively glycinergic columnar region, is very weak and inconsistent across experiments.

Most inputs to combination-sensitive INLL neurons originate from regions of the cochlear nucleus or MNTB that are associated with high frequencies (Yavuzoglu et al., 2010). Thus, labeled neurons are located in the more caudal regions of AVCN and more medial part of MNTB, regions known from physiological studies and other anatomical studies to be associated with ChFs above 60 kHz (Zook and Casseday, 1985; Zook and Leake,

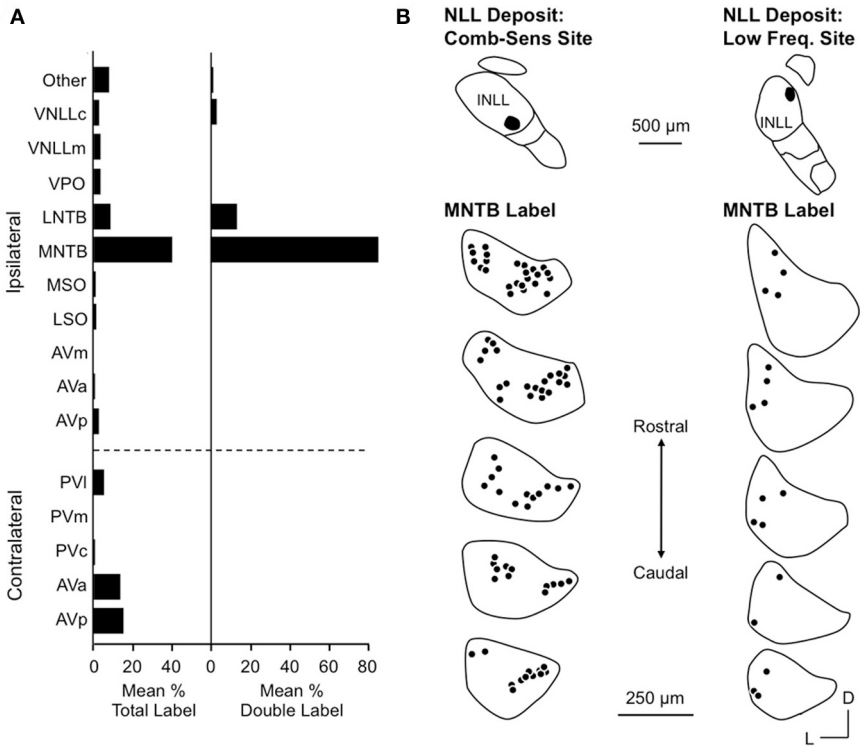

FIGURE 7 | Inputs to INLL neurons that show combination-sensitive inhibition. (A) *Left.* Distribution of retrograde labeling after INLL deposits in five animals. *Right.* Distribution of double labeled cells (glycine-immunopositive and retrogradely labeled) after INLL tracer deposits. The ipsilateral MNTB provides the strongest glycinergic input to INLL neurons. **(B)** Comparison of retrograde label in MNTB after INLL deposits at combination-sensitive site (*left*) and low-frequency tuned site (right). MNTB labeling after combination-sensitive deposits is in both medial and lateral locations, indicating input from both low and high-frequency bands. MNTB label after low-frequency tuned deposits is located laterally, i.e., in the low-frequency representation. Adapted from Yavuzoglu et al. (2010), with permission.

1989). However, Yavuzoglu and colleagues also reported retrograde labeling in the lateral part of MNTB, a region known to represent the lower frequencies in the mustached bat's audible range (**Figure 7B**). This consistent finding indicates that neurons in the lateral, low-frequency part of MNTB provide a spectrally unmatched input to high-frequency parts of INLL. This is the likely anatomical substrate for combination-sensitive inhibition in INLL (**Figure 8**).

The response properties in MNTB neurons are mostly consistent with the features of low-frequency inhibition as observed in IC combination-sensitive neurons (Gans et al., 2009). Gans and colleagues showed that low-frequency inhibition is typically but not always phasic, suggesting that low-frequency inputs to the INLL integrating neuron should be predominantly phasic. Most MNTB neurons are reported to show phasic-tonic temporal patterns that feature a tightly locked first spike and a much lower probability of subsequent spikes (Smith et al., 1998; Kopp-Scheinpflug et al., 2003; Tolnai et al., 2008). This pattern is consistent with the features of combination-sensitive inhibition in INLL neurons. Glycinergic inputs from LNTB neurons, on the other hand, do not possess the appropriate response properties, since LNTB neurons receive their primary excitation from the ipsilateral ear and project to the ipsilateral INLL. This would suggest an ipsilateral inhibitory input to INLL neurons, whereas Peterson et al. (2009) show that low-frequency inhibition is activated by the contralateral ear.

For IC neurons that display combination-sensitive inhibition, we propose that that the inhibition evoked by 23–30 kHz tones is the result of a direct excitatory projection from the inhibitory combination-sensitive neurons in INLL and perhaps VNLLm (**Figure 8**). The evidence described above establishes that the IC response property is, in most cases, inherited from its inputs, and that the combination-sensitive response is common in the INLL. INLL neurons project strongly to IC recording sites with combination-sensitive inhibition (Wenstrup et al., 1999; Yavuzoglu et al., 2011). Further, many and perhaps most of these INLL inputs are excitatory. This last point requires emphasis, since it is often presumed that the VNLL/INLL complex provides primarily inhibitory projections to IC. Thus, in the mustached bat, the majority of neurons in INLL are unlabeled by glycine or GABA immunocytochemistry, unlike VNLL and DNLL neurons observed in the same histological sections (Winer et al., 1995). Regions corresponding to INLL in rat and cat, sometimes considered to be the most dorsal part of VNLL, also show significant numbers of presumptive excitatory neurons (Saint Marie et al., 1997; Riquelme et al., 2001). It is less clear whether neurons in VNLLm are excitatory (Winer

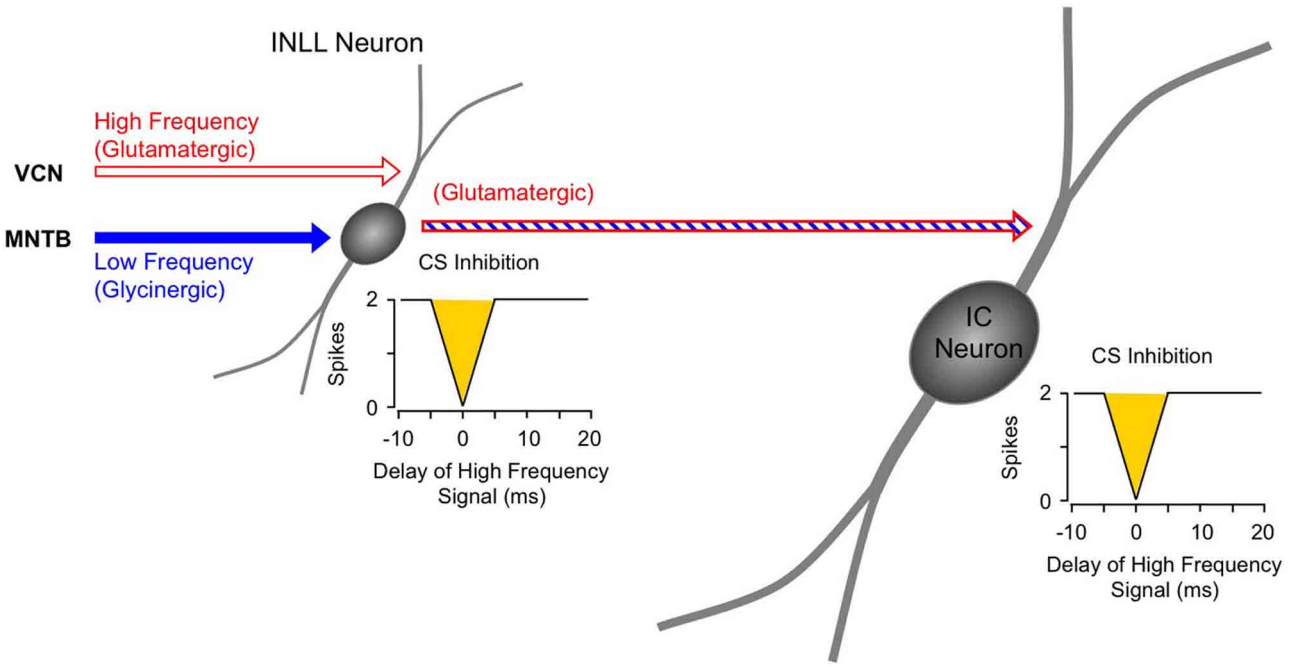

FIGURE 8 | Schematic diagram of circuitry underlying combination-sensitive inhibition in INLL and IC. The *red and blue striped arrow* indicates sensitivity to both low and high-frequency bands.

et al., 1995). While observations do not rule out other sources from which IC neurons inherit combination sensitivity, no other brainstem auditory nucleus is known to contain such response properties.

In a subset of IC neurons with combination-sensitive inhibition, pharmacological or physiological evidence suggests that low-frequency inhibition acts directly on high-frequency tuned neurons. Work by Yavuzoglu and colleagues (2011) provide evidence in support of this, showing that the high-frequency IC receives input from neurons in VNLL that are tuned to low frequencies and are glycinergic. Although these inputs were examined primarily in the context of facilitatory combination-sensitive interactions, the observed connections could also contribute to the inhibitory interactions observed in combination-sensitive neurons of the IC.

MECHANISMS UNDERLYING COMBINATION-SENSITIVE FACILITATION

Facilitated combination-sensitive neurons detect the coincidence of excitation evoked by acoustic signals in two distinct frequency bands (Olsen and Suga, 1991a,b; Portfors and Wenstrup, 1999). Mechanistic explanations must account for several response features: (1) neuronal integration of high and low-frequency tuned responses, (2) a range of best delays of facilitation, from 0 ms (simultaneous low and high-frequency elements) to more than 30 ms lag in the high-frequency signal, (3) phasic facilitation locked to signal onset; and (4) co-occurrence of facilitatory and inhibitory interactions within single IC neurons.

COMBINATION-SENSITIVE FACILITATION ORIGINATES IN IC AND DEPENDS ON GLYCINERGIC INPUT

Facilitative combination-sensitive responses are abundant in several areas of the mustached bat's auditory cortex (Suga and O'Neill, 1979; Suga et al., 1983; Suga and Horikawa, 1986; Edamatsu et al., 1989; Fitzpatrick et al., 1998) and thalamus (Olsen and Suga, 1991a,b; Wenstrup and Grose, 1995; Yan and Suga, 1996a; Wenstrup, 1999). In IC, these facilitative responses are commonly observed in frequency representations above 30 kHz (Mittmann and Wenstrup, 1995; Portfors and Wenstrup, 1999; Leroy and Wenstrup, 2000). Comparative physiological recordings across auditory brainstem and midbrain nuclei suggest that combination-sensitive facilitation originates in the IC. Thus, no facilitatory responses occur in the cochlear nuclei (Marsh et al., 2006) and very few have been recorded in the lateral lemniscal nuclei (Mittmann, 1997; Portfors and Wenstrup, 2001).

Further support comes from pharmacological studies of inhibitory receptor blockade. Several studies of IC neurons show that blockade of the glycine receptor by strychnine eliminates or greatly reduces facilitation in all combination-sensitive neurons (Wenstrup and Leroy, 2001; Nataraj and Wenstrup, 2005; Sanchez et al., 2008). **Figure 9A** shows an example of the general trend (**Figure 9B**): GlyR blockade eliminates facilitation that is strongest at 4 ms delay, even though the excitatory discharge to single tones is unaffected. In contrast, blockade of $GABA_A$Rs is usually ineffective (**Figures 9C,D**); in all such cases, addition of GlyR blockade eliminated combination-sensitive facilitation (**Figure 9D**). Further studies using the $GABA_A$R blocker gabazine suggest that $GABA_A$Rs play no role in facilitation

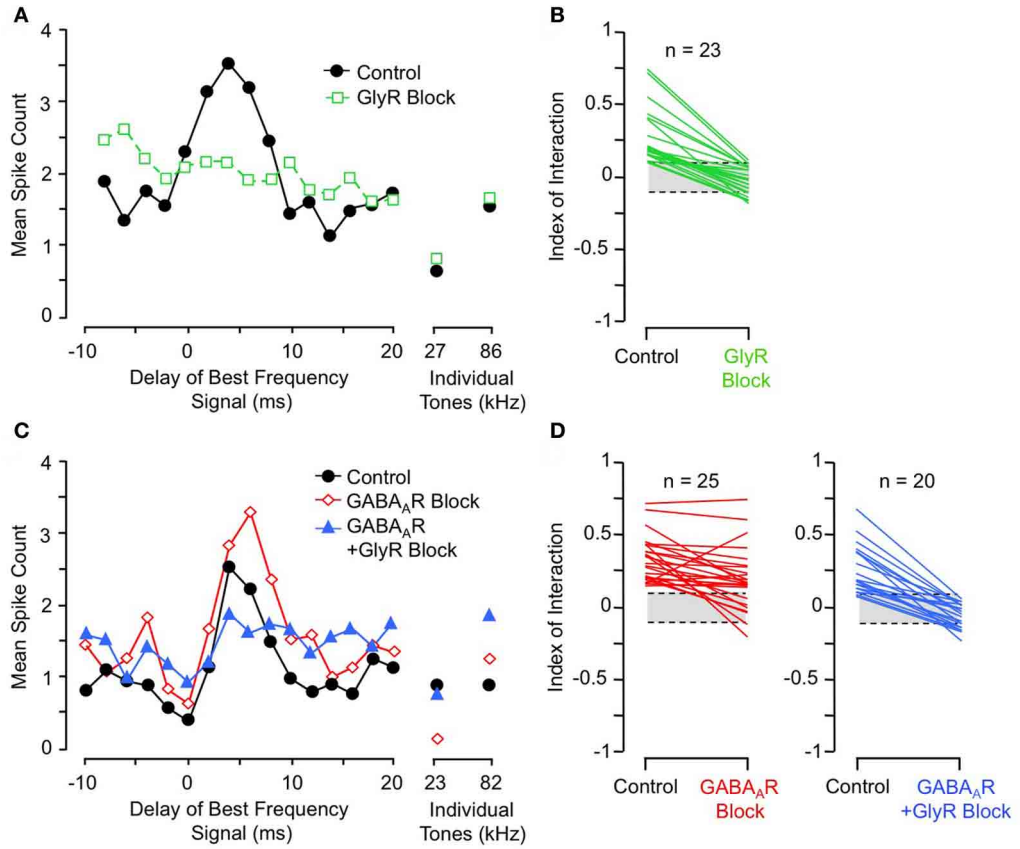

FIGURE 9 | Glycine receptor blockade eliminates combination-sensitive facilitation in IC neurons. (A) In IC neuron, blockade of GlyRs eliminates 27 kHz facilitation of 86 kHz ChF response. **(B)** Effects of GlyR blockade on low-frequency facilitation among IC neurons. In all neurons, GlyR blockade eliminated or greatly reduced combination-sensitive facilitation. **(C)** In an IC neuron, blockade of $GABA_A$Rs did not eliminate facilitation, but addition of GlyR blockade eliminated facilitation. **(D)** In most IC neurons, facilitation was not eliminated by $GABA_A$R blockade, but addition of GlyR blockade always eliminated the facilitation. Adapted from Nataraj and Wenstrup (2005), with permission.

(Sanchez et al., 2008). The robust effect of GlyR blockade, seen across three separate studies, argues strongly that facilitation originates in the IC. It also suggests an important role for glycinergic inhibition in the facilitatory mechanism. Since GlyR blockade eliminates facilitation for both sonar and non-sonar combinations of spectral elements, and for facilitation over a broad range of best delays (Nataraj and Wenstrup, 2005; Sanchez et al., 2008), glycinergic input appears to be a fundamental contributor to mechanisms underlying combination-sensitive facilitation.

MECHANISMS OF COMBINATION-SENSITIVE FACILITATION: ROLES OF EXCITATION AND INHIBITION

In general, facilitation in the central nervous system is thought to depend on excitatory inputs. Proposed mechanisms of facilitation in response to combinations of sensory inputs include the summation of subthreshold excitatory inputs (Finn et al., 2007), enhancement through postsynaptic glutamate receptors (Binns, 1999), and combinations of excitatory inputs with inhibitory inputs that generate post inhibitory rebound (Casseday et al., 1994). Studies in the mustached bat reveal a novel mechanism by which distinct inhibitory inputs create facilitation, presumably through dual post inhibitory rebound.

Sanchez and colleagues (2008) compared the contributions of excitatory and inhibitory transmission in creating combination-sensitive facilitation in the IC. Unexpectedly, excitatory neurotransmission by glutamate played no role. They found that blockade of AMPA receptors (AMPARs) and/or NMDA receptors (NMDARs) had no effect on combination-sensitive facilitation, even though glutamate receptor blockade eliminated spike discharge in response to single tonal stimuli (**Figures 10A,B**). Blockade of $GABA_A$ receptors in addition to glutamate receptor blockade generally failed to eliminate the facilitation or even change the number of spikes evoked by single tonal or combination stimuli. Only blockade of the glycine receptor was effective in eliminating response facilitation, and it was successful in all tested neurons. (**Figure 10C**).

These results rule out any contribution of ionotropic glutamate receptors to the basic mechanism for combination-sensitive facilitation in IC. Not only were single tonal responses eliminated by glutamate receptor blockade, but application of the $GABA_A$ and glycine receptor blockers did not uncover residual

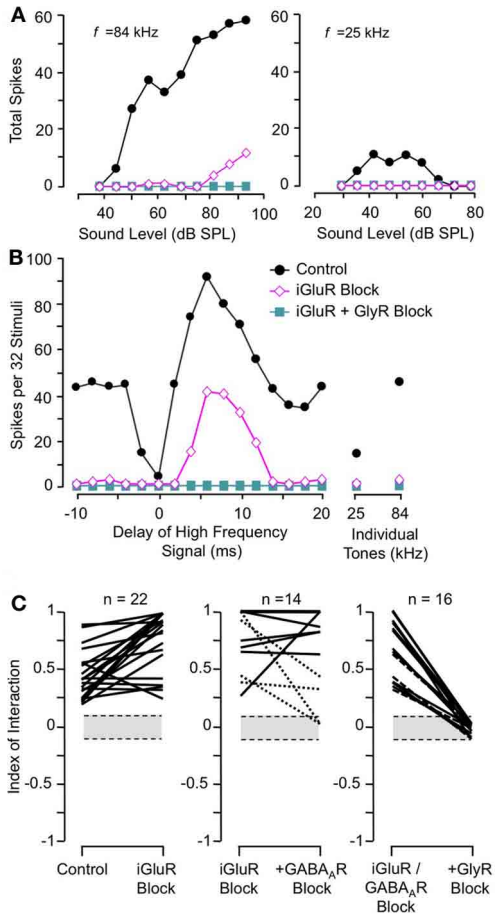

FIGURE 10 | Glutamate receptors (iGluRs) play no role in combination-sensitive facilitation. (A) Responses to ChF and low-frequency tones are eliminated by iGluR blockade. **(B)** Blockade of iGluRs eliminated excitatory responses to single tones, but facilitated combination-sensitive responses persisted. Only the application of a GlyR blocker eliminated facilitatory interactions. **(C)** Effects of receptor blockade on low-frequency facilitation among IC neurons. In all neurons, iGluR blockade failed to eliminate facilitation, but GlyR blockade always eliminated facilitation. Blockade of GABA$_A$Rs generally did not eliminate facilitation. Adapted from Sanchez et al. (2008), with permission.

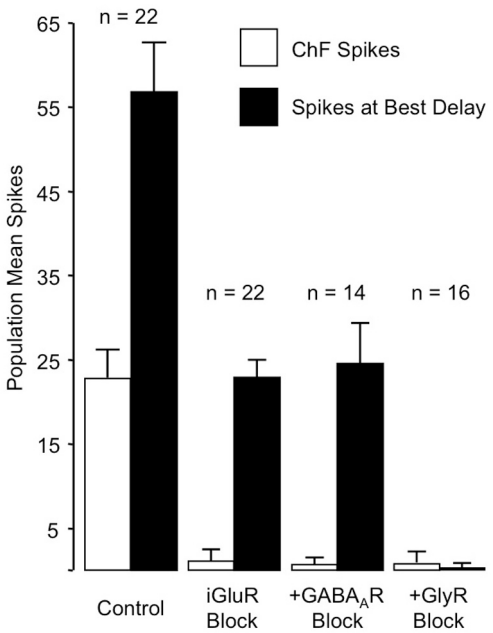

FIGURE 11 | Primary role of GlyR receptors in the facilitated response of IC neurons. Graphs show number of spikes evoked by ChF and combination stimuli at best delay, averaged across the number of neurons in the sample. iGluR blockade eliminates spikes evoked by ChF tones, but does not eliminate facilitated spikes evoked by combination stimuli. The addition of GABA$_A$R blockade to the iGluR blockade (+GABA$_A$R Block) has little additional effect on the facilitated spikes. Facilitation spikes are only eliminated by addition of the GlyR blockade (+GlyR Block). Neither + GABA$_A$R Block nor +GlyR Block revealed additional excitatory response to the ChF response, suggesting that iGluR blockade successfully eliminated glutamatergic excitation to the neurons. Adapted from Sanchez et al. (2008), with permission.

excitation that could result from incomplete glutamate receptor blockade (**Figure 11**). As a result, glycine modulation of glutamatergic transmission, as may occur in the auditory brainstem (Turecek and Trussell, 2001), or inheritance from auditory cortico-collicular inputs (Yan and Suga, 1999; Suga et al., 2000) are not viable mechanisms for combination-sensitive facilitation. Further, mechanisms that depend on a combination of glutamate excitation and glycine-evoked post-inhibitory rebound (Casseday et al., 1994; Wenstrup and Leroy, 2001) are not sufficient to account for the facilitatory interaction.

Instead, the work by Sanchez and colleagues suggests that combination sensitivity in the mustached bat's IC depends exclusively on well-timed glycinergic inputs tuned to different sound frequencies. Sanchez et al. hypothesized that the facilitatory effect of glycinergic inputs could result either from coincidence of post-inhibitory rebound excitations (**Figure 12**, *inset*) or direct glycine-evoked depolarizations as occurs in birds and developing mammals (Hyson et al., 1995; Kandler and Friauf, 1995; Lu and Trussell, 2001). To test these hypotheses and to further explore the mechanisms underlying combination sensitivity, Peterson and colleagues (2008) obtained intracellular recordings from facilitated combination-sensitive neurons in the mustached bat's IC. The surprising result was that in all but one tested neuron, there was no evidence of low-frequency-evoked transient hyperpolarization OR depolarization that could be related to the inputs that create response facilitation. In addition, the intracellular recordings showed no evidence of shunting inhibition that might conceal inhibitory inputs. Because the facilitatory interactions originate in IC neurons, the authors concluded that the glycinergic inputs underlying facilitation must be electrically segregated from the soma, isolated in specific dendritic regions.

The Peterson et al. study (2008) did not resolve the question of the mechanism underlying combination-sensitive facilitation. Any mechanism must also explain the delay tuning observed in many of these neurons, accounting for delays in low-frequency excitation that can exceed 30 ms. These delays are not present in the response latencies of auditory brainstem neurons that

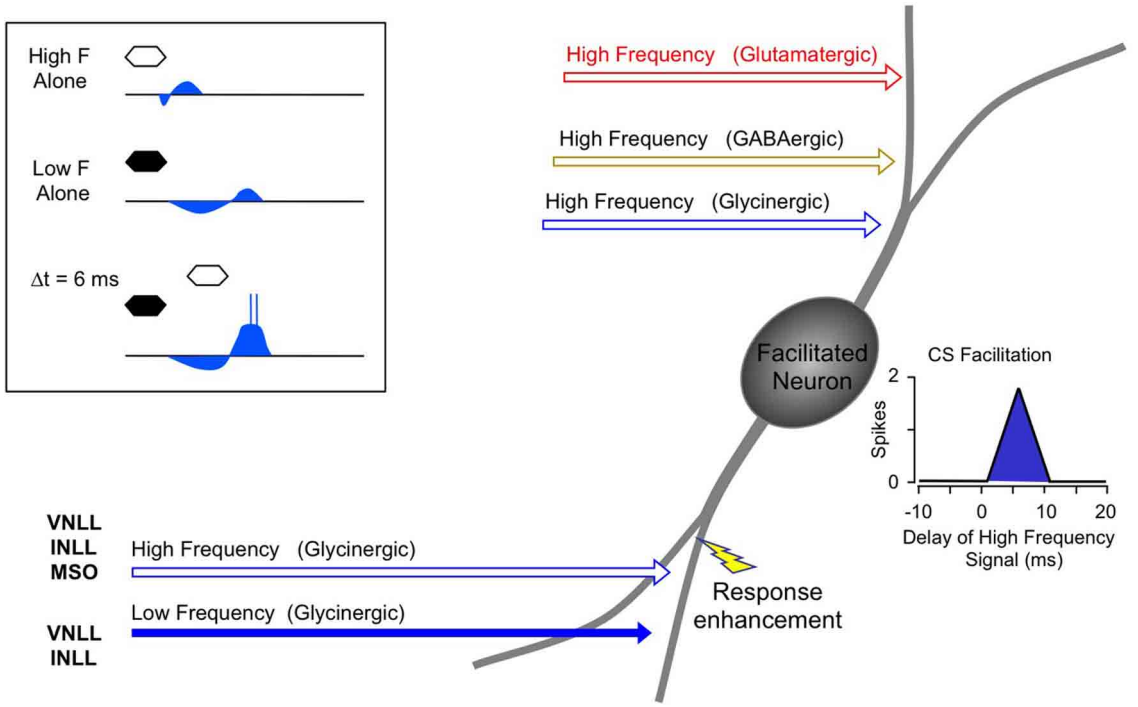

FIGURE 12 | Schematic diagram of mechanisms and circuitry underlying combination-sensitive facilitation in IC. *Inset* shows hypothesized mechanism of post-inhibitory rebound. Neuron receives a variety of high frequency inputs tuned to its ChF (*upper right*) that do not appear to interact with glycinergic inputs related to facilitation (*lower left*). *Response enhancement* refers to hypothesized boost in the glycine rebound potentials that allows the facilitation signal to reach the spike trigger zone.

provide input to the IC (Klug et al., 2000; Portfors and Wenstrup, 2001; Marsh et al., 2006). In our view, a post-inhibitory rebound mechanism is most capable of generating the delayed excitation necessary for combination-sensitive facilitation. In such a mechanism (**Figure 12**; Peterson et al., 2008), glycinergic input tuned to the lower frequency signal may create an extended period of hyperpolarization with variably timed rebound. When this excitation coincides and colocalizes with high-frequency, glycine-evoked excitation, response facilitation occurs. We further propose that an additional mechanism, such as voltage-gated sodium channels placed nearer to the soma, is necessary to generate a sufficient voltage boost to allow the facilitation signal to reach the neuron's spike trigger zone. This would explain why the low-frequency input is hidden from the "view" of somatic intracellular recording, even while the facilitation signal is clearly detectable (Peterson et al., 2008).

For whichever mechanism applies, three observations strongly support a conclusion that the site of facilitation is isolated from other inputs to IC neurons. First, facilitating interactions are unaffected by glutamatergic and GABAergic inputs (**Figures 10**, **11**; Sanchez et al., 2008). Second, glycine receptors inhibit glutamatergic responses to ChF tones while contributing to facilitation (Wenstrup and Leroy, 2001; Nataraj and Wenstrup, 2005; Sanchez et al., 2008). Third, $GABA_A$- receptors inhibit glutamatergic responses to best frequency tones in the same neurons that display facilitation dependent on glycine receptors. The presence, in the same neuron, of inhibitory and facilitatory chloride-mediated influences suggests that effects of increased chloride conductance are local within the neuron. Our interpretation of these observations is that facilitatory interactions are segregated on specific dendrites, away from other sources of input (**Figure 12**). Regardless of where the inputs are located on IC neurons, this facilitatory response—due to differently tuned glycinergic inputs—violates the segregation of differently tuned neurons within the tonotopically organized ascending auditory pathway. How does facilitation arise in the context of the auditory system's tonotopic organization?

CIRCUITRY UNDERLYING COMBINATION-SENSITIVE FACILITATION IN IC

Facilitated combination-sensitive neurons in the mustached bat's IC receive a broad range of inputs (Wenstrup et al., 1999; Yavuzoglu et al., 2011) that activate glutamatergic, GABAergic, and glycinergic mechanisms (Wenstrup and Leroy, 2001; Nataraj and Wenstrup, 2005; Sanchez et al., 2008). Of these, only a subset of the glycinergic inputs contributes to response facilitation. Further, IC facilitated neurons must receive glycinergic inputs tuned to two frequency bands: its ChF and, in most cases, the 23–30 kHz band that contributes to most combination-sensitive facilitation. Yavuzoglu et al. (2011) combined glycine immunohistochemistry with retrograde tract tracing to identify the sources of these glycinergic inputs (**Figure 13**). Tracers deposited at facilitated, combination-sensitive recording sites in IC resulted in tracer-glycine double-labeled neurons in VNLL and

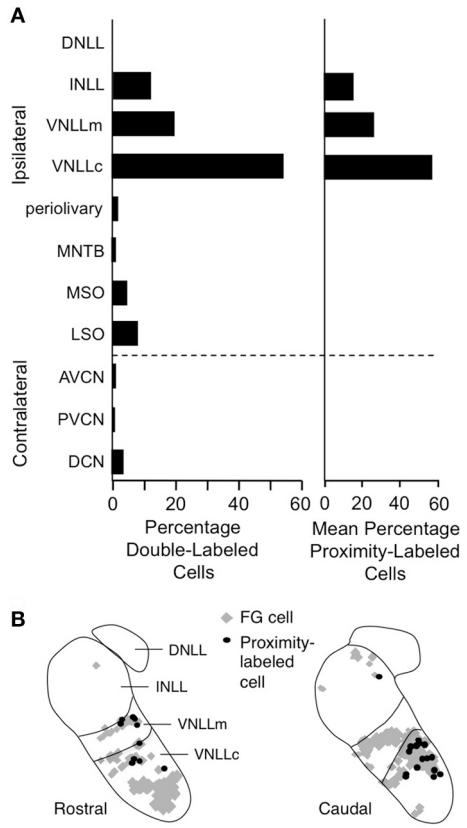

FIGURE 13 | Lateral lemniscal nuclei provide key glycinergic inputs to facilitated combination-sensitive neurons in IC. (A) *Left.* Average percentages of neurons double-labeled by tracer (FluoroGold, FG) deposited at IC combination-sensitive recording sites and by glycine immunohistochemistry. This represents the distribution of glycinergic inputs to IC regions containing facilitated combination-sensitive neurons. *Right.* Distribution of "proximity-labeled neurons"; these neurons are retrogradely labeled by the IC tracer deposits and within 50 μm of a labeled terminal resulting from deposit of a second tracer in a low frequency part of AVCN. This represents neurons that likely receive input tuned to 23–30 kHz and project to high-ChF, combination-sensitive recording sites in IC. **(B)** Locations of these "proximity labeled" cells in VNLL and INLL from one experiment. Adapted from Yavuzoglu et al. (2011), with permission.

INLL, and to a lesser extent in the lateral and medial superior olive (LSO and MSO, respectively). Together, these four auditory brainstem nuclei accounted for ∼93% of glycine-immunolabeled neurons that project to facilitate combination-sensitive neurons in the IC of the mustached bat (**Figure 13A**). Of these inputs, the source of facilitating high-frequency glycinergic input almost certainly arises from the VNLL and INLL. Because ipsilateral LSO neurons are not excited by contralateral stimuli (Covey et al., 1991), and only a small number of MSO neurons provide glycinergic inputs to IC (Winer et al., 1995; Yavuzoglu et al., 2011), it is unlikely that LSO and MSO contribute significantly to combination-sensitive responses.

To identify the source(s) of low-frequency input, Yavuzoglu et al. (2011) placed a deposit of a retrograde tracer at an IC site displaying combination-sensitive facilitation, and a second, anterograde tracer at a 23–30 kHz recording site in the AVCN. Only VNLL and INLL contained neurons retrogradely labeled by the IC in close proximity to anterogradely labeled boutons from the low-frequency AVCN deposit (**Figure 13B**). These experiments confirm that VNLL and INLL are the sources of the low-frequency, glycinergic inputs that underlie combination-sensitive facilitation. Of these, it appears that the columnar part of VNLL (VNLLc), with distinctive morphology and physiological properties, is the most likely source of these low-frequency inputs (**Figure 13B**).

Several features of neurons in VNLLc are particularly well suited to the functional properties needed for facilitated neurons in IC. First, all of these neurons are thought to be glycinergic (Winer et al., 1995; Vater et al., 1997). Second, most of these neurons in bats have onset temporal patterns (Metzner and Radtke-Schuller, 1987; Covey and Casseday, 1991; Portfors and Wenstrup, 2001) that correspond closely to the inputs required to create the transient, onset-type facilitation observed in most IC neurons (Gans et al., 2009). Third, the level-tolerant response latencies of most VNLLc neurons (Covey and Casseday, 1991) are consistent with the observation that delay tuning in most IC facilitated neurons does not change with increasing sound level (Macías et al., 2012). These features of VNLLc neurons strengthen the conclusion that they provide the critical glycinergic inputs underlying combination-sensitive facilitation in IC (**Figure 12**).

In other species, VNLL neurons are not segregated so clearly by functional properties or by transmitters, but some VNLL neurons display similar onset response properties (Batra and Fitzpatrick, 1999; Zhang and Kelly, 2006) and may be glycinergic (Saint Marie and Baker, 1990; Saint Marie et al., 1997; Riquelme et al., 2001). Given the topographically complex organization of frequency in this nucleus, it seems reasonable to propose that such neurons could play similar spectral integrative roles in their projections to the IC.

PROCESSING OF COMBINATION-SENSITIVE RESPONSES BEYOND THE MIDBRAIN

The spectro-temporal integrating mechanisms that occur in the auditory brainstem and midbrain appear to explain the basic elements of combination-sensitive responses observed in the auditory thalamus and cortex. Thus, in physiological studies of the mustached bat, auditory midbrain responses show the full range of frequency interactions, the low-frequency inhibition at 0 ms, and the range of best delays of facilitation that have been observed in auditory thalamus or cortex (Portfors and Wenstrup, 2003; Hagemann et al., 2011; Wenstrup and Portfors, 2011; Macías et al., 2012). Anatomical studies in this species show that combination-sensitive regions of the IC project to comparable regions of the medial geniculate body (MGB, Frisina et al., 1989; Wenstrup et al., 1994; Wenstrup and Grose, 1995) and that the combination-sensitive regions in MGB project to the appropriate cortical combination-sensitive areas (Pearson et al., 2007). There is thus strong but indirect support that cortical responses could be inherited from their midbrain and thalamic precursors.

Is there additional processing of combination-sensitive responses beyond the midbrain? The answer appears to be yes for some features of the combination-sensitive response. Thus,

there is a greater likelihood, compared to midbrain neurons, that combination-sensitive neurons in MGB will not respond to separate signals, but only respond to the appropriate combination of signals (Yan and Suga, 1996a; Portfors and Wenstrup, 1999, 2003; Wenstrup, 1999). FM–FM neurons in auditory cortex are more likely to respond to FM–FM combinations than to separate elements, to display preferences for FM sweeps rather than to tonal stimuli (Taniguchi et al., 1986; Hagemann et al., 2011; Macías et al., 2012), and to respond to more than one FM harmonic in the echo (Misawa and Suga, 2001). Among cortical FM–FM neurons, delay tuning is more dependent on sound level than in IC (Hagemann et al., 2011; Macías et al., 2012). Finally, cortical FM–FM neurons are more likely to show longer term changes in delay tuning as the result of conditioning or other experience (Yan and Suga, 1996b; Suga et al., 2002; Xiao and Suga, 2004).

The mechanisms underlying these transformations are not understood. A parsimonious hypothesis is that the additional features of cortical responses are layered onto the fundamental response properties established in the brainstem and midbrain. However, auditory cortical neurons receive multiple inputs that may eliminate selectivity apparent in some of the inputs. Based on their work in the pallid bat, Fuzessery and co-workers (Razak and Fuzessery, 2009; Fuzessery et al., 2011) have proposed that selectivity for the rate and direction of FM sweeps, which exists among IC neurons, may be at least partially re-created in the auditory cortex through GABAergic mechanisms. The functional implication of this re-creation is not understood. In the mustached bat, the modifications introduced beyond the auditory midbrain may create response properties that can be modified by experience. Further work is needed to clarify these issues.

OVERALL VIEW AND IMPLICATIONS

Studies in the mustached bat provide an extensive description of the mechanisms of spectro-temporal integration acting in the mammalian auditory brainstem and midbrain. Although the mechanisms of facilitation and delay tuning are not completely understood, it is possible to draw several conclusions regarding auditory brainstem mechanisms underlying spectro-temporal integration. These conclusions point to computational mechanisms operating in the auditory brainstem and midbrain that may be used for other forms of spectro-temporal integration in other species.

SEQUENTIAL COMBINATORIAL INTERACTIONS IN THE MUSTACHED BAT

The inhibitory and facilitatory interactions that create the response properties observed in IC, MGB, and auditory cortex occur as separate spectro-temporal integrative events within the auditory brainstem and midbrain (**Figure 14**). Combination-sensitive inhibition is mostly created at a lower level, primarily within the INLL, and depends on integration of high-frequency-tuned excitatory inputs and low-frequency-tuned inhibitory inputs. Combination-sensitive facilitation is created in the auditory midbrain and depends on differently tuned glycinergic inputs. Facilitatory IC neurons appear to receive inputs from different tonotopic regions of the VNLL and INLL (**Figure 14**). While they also receive other inputs, including glutamatergic inputs, only their glycinergic inputs appear to contribute to combinatorial response properties.

A subset of facilitatory neurons in IC, MGB, and auditory cortex also display inhibitory combination sensitivity. These likely

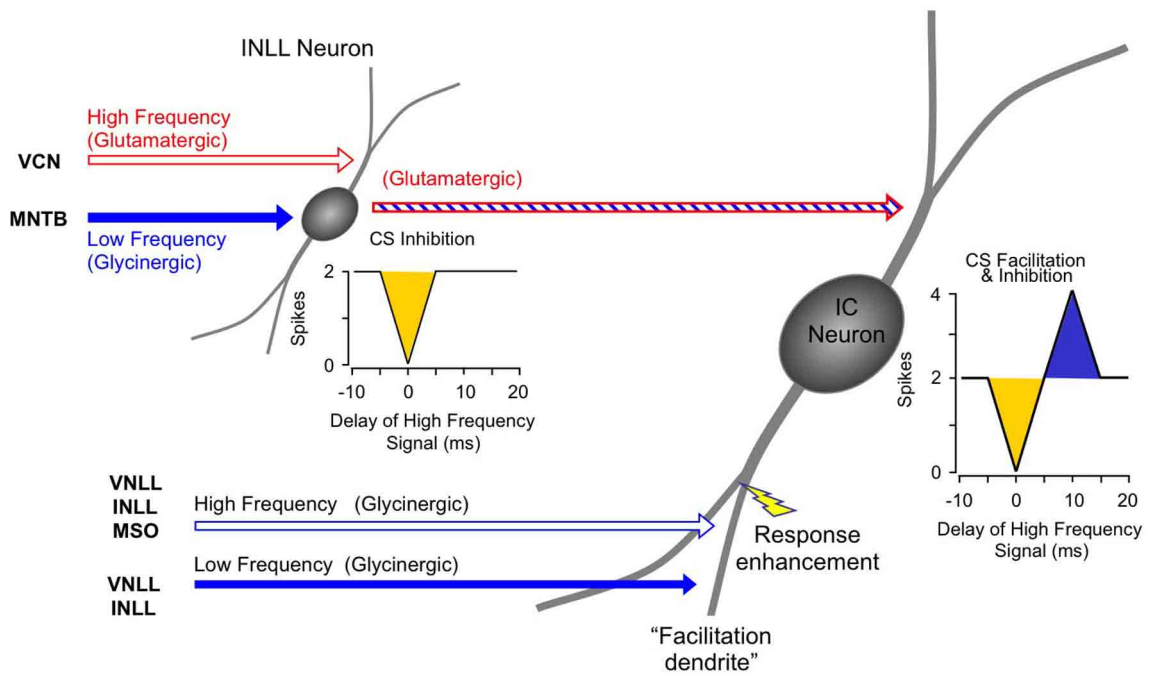

FIGURE 14 | Schematic diagram of circuitry underlying combination-sensitive facilitation and inhibition in IC neuron.

arise in IC as a result of the convergence of a glutamatergic input from inhibited combination-sensitive INLL neurons with the glycinergic inputs from VNLL and INLL that create facilitation. The irony here is that some glycinergic ("inhibitory") inputs participate in response facilitation while the glutamatergic ("excitatory") input conveys inhibitory combination-sensitive responses from INLL. This irony is a caution to circuit analyses: sources of "inhibition" and "excitation" to a particular neuron's response should be corroborated by mechanistic studies that establish whether inhibition or excitations are acting at that site.

The interactions that create combination-sensitive responses in the mustached bat appear more hierarchical and the mechanisms appear more unitary than those observed in relation to some other complex response properties observed in IC, such as binaural processing or FM sweep selectivity (Fuzessery et al., 2011; Pollak et al., 2011; Pollak, 2012). One explanation for the well-defined set of interactions underlying combination sensitivity is that the system appears to be prewired before the first experience with echolocation. Thus, tuning to pulse-echo delay occurs in the auditory cortex on the first day after birth, and many features of mature responses are evident within the first week (Vater et al., 2010; Kössl et al., 2012). It is not clear whether this tuning precedes combination sensitivity in the IC, but our hypothesis is that the brainstem and midbrain mechanisms and circuitry form during prenatal development.

NEW ROLES FOR BRAINSTEM NUCLEI UNDERLYING SPECTRAL INTEGRATION

Spectral integration depends on convergence of information from neurons that are tuned to different frequencies. For many neurons in the auditory system, these interactions may result from so-called lateral excitatory or inhibitory effects, in which the inputs are tuned to adjacent or overlapping frequency bands. However, many studies in non-echolocating species show that neurons, particularly in auditory cortex, respond to sounds in distinct frequency bands (Sutter and Schreiner, 1991; Rauschecker et al., 1995; Brosch et al., 1999; Sadagopan and Wang, 2009). These interactions are evident in physiological studies but are difficult to demonstrate anatomically.

As a form of spectral interaction, combination sensitivity in the mustached bat is noteworthy because it involves widely separated frequency bands that may be more amenable to experimental study. The work summarized here shows that most combination-sensitive interactions depend on projections from neurons tuned to a specific lower frequency band (~23–30 kHz) and that these projections occur in specific auditory brainstem nuclei. Thus, for combination-sensitive inhibition, low-frequency neurons in MNTB project to high-ChF neurons in INLL. For combination-sensitive facilitation, low-frequency-tuned neurons in VNLL project onto high ChF neurons in IC. These spectrally unmatched projections in the auditory brainstem have not been reported previously, but may underlie a variety of spectro-temporal integrative responses, from asymmetric inhibitory sidebands (Fuzessery et al., 2011), to facilitation between adjacent frequency bands within an FM sweep (Razak and Fuzessery, 2008), to inhibition that may contribute to other spectral responses (Xie et al., 2007).

The work presented in this review identifies a new role for the MNTB that involves spectro-temporal integration. The MNTB is normally associated with binaural comparisons of similarly tuned inputs (Boudreau and Tsuchitani, 1968; Guinan et al., 1972; Kuwabara and Zook, 1992; Sanes and Friauf, 2000; Thompson and Schofield, 2000; Brand et al., 2002; Kim and Kandler, 2003; Pecka et al., 2008). More recent work shows that MNTB contributes to the offset response of neurons in the superior paraolivary nucleus, a major source of GABAergic inhibition to the IC (Kadner et al., 2006; Kulesza et al., 2007). The work on mustached bats demonstrates that some MNTB neurons project to unmatched frequency representations of target nuclei, creating specific forms of cross-frequency interactions. This is a role that should be explored further in other mammalian species, due to the widespread projections of MNTB to superior olivary and lateral lemniscal nuclei.

This review also describes specific functional roles for neurons in the ventral and intermediate nuclei of the lateral lemniscus. VNLL, especially the columnar subdivision, appears to contribute to combination-sensitive facilitation through convergence of glycinergic low-frequency (23–30 kHz) and high-frequency neurons onto high-ChF neurons in IC. Projections from VNLL that are not matched to the ChF of target IC neurons may underlie the inhibition that contributes to FM sweep selectivity in other bat species (Voytenko and Galazyuk, 2007; Pollak et al., 2011; Williams and Fuzessery, 2011). INLL performs an important spectral integrative function as the initial site where combination-sensitive inhibition arises. Through its excitatory projection, the INLL appears to convey a particular response feature to IC neurons—combination-sensitive inhibition.

CRITICAL ROLES OF GLYCINERGIC NEURONS IN SPECTRAL INTEGRATION

These studies show a predominant role for brainstem glycinergic neurons in the spectral interactions that underlie combination sensitivity. Low frequency tuned glycinergic neurons from MNTB create well timed, predominantly onset inhibition of excitatory responses tuned to frequency bands 1–3 octaves higher. The MNTB low-frequency input provides fast inhibition to suppress the response to a simultaneously delivered high-frequency signal.

The role of glycinergic inputs in combination-sensitive facilitation demonstrated in these studies reveals a novel mechanism of response facilitation/excitation. While it is well known that glycinergic or GABAergic inputs can create excitation or facilitation (Casseday et al., 1994; Wenstrup and Leroy, 2001; Person and Perkel, 2005), the studies reviewed here show that facilitation depends entirely upon glycinergic inputs. We have speculated that these inputs, which appear to result from distinctly tuned glycinergic inputs, create a form of spectral integration that is transient and locked to signal onset. Further, since glycinergic VNLLc neurons respond well at high repetition rates and are phasic (Covey and Casseday, 1991), their synapses onto IC neurons may be more resistant to synaptic fatigue than glutamatergic synapses at the high stimulation rates that can occur during echolocation (Sanchez et al., 2008). The fast action of glycinergic synapses and the phasic release of glycine by VNLL neurons may be optimal for the form of combination sensitivity displayed by these neurons.

The glycinergic facilitation mechanism may also underlie the sub millisecond facilitation reported in the pallid bat IC (Razak and Fuzessery, 2008).

For many neurons, delay tuning requires a delayed excitation evoked by the low-frequency input, so that facilitation is strongest when the high-frequency signal occurs several ms later (e.g., resulting from pulse-echo delay). The mechanism underlying the timing of the facilitation is not understood, but our data suggest it does not depend on glutamatergic or GABAergic inputs to the IC facilitated neurons. We have speculated that the glycinergic rebound excitation may follow a variable period of increased chloride conductance that creates the opportunity for delayed low-frequency excitation. Further research is needed here, but it has the potential to reveal interesting postsynaptic mechanisms of information processing within IC neurons.

SEGREGATED SIGNAL PROCESSING BY IC NEURONS

The nature of facilitatory spectral integration by IC neurons in the mustached bat has led us to propose that individual neurons perform different signal processing operations in different cellular compartments, or processing domains (**Figure 14**; Peterson et al., 2008; Sanchez et al., 2008). Specifically, we propose that inputs onto IC neurons are anatomically and electrically isolated to preclude immediate interactions with other inputs. These different sites integrate information from different sets of inputs, and may operate under different conditions. For example, during roosting, bats primarily hear social vocalizations. These generally have lower repetition rates than those during echolocation in pursuit of insects. IC neurons would likely respond to these social signals through activation of their ChF-tuned glutamatergic, GABAergic, and glycinergic inputs. These inputs would also be influenced by frequencies within the very low-frequency (<23 kHz) tails of the high-ChF tuning curves, which activate excitation and/or suppression (Marsh et al., 2006; Nataraj and Wenstrup, 2006). During sonar behavior, stimulation rates that exceed 40/s may result in reduced responsiveness to the glutamatergic inputs. Under these conditions, the same neuron may be activated primarily by its glycinergic inputs related to combination sensitivity, and the delay tuning resulting from the glycinergic inputs would dictate the overall response. Our data suggest that these sets of inputs do not appear to interact, leading to largely independent processing of acoustic stimuli in a context-dependent fashion.

ACKNOWLEDGMENTS

Preparation of this manuscript was supported by research grant R01 DC00937 (Jeffrey James Wenstrup) from the National Institute on Deafness and Other Communication Disorders of the U.S. Public Health Service. We are profoundly grateful to Don Gans (deceased) for his many contributions to the study of combination-sensitive neurons in the mustached bat's inferior colliculus. We also thank Marie Gadziola, Jasmine Grimsley, and Jeff Mellott for comments on the manuscript and Carol Grose for assistance in figure preparation. We are grateful to the Wildlife Section of the Ministry of Agriculture, Land and Marine Resources of Trinidad and the Natural Resources Conservation Authority of Jamaica for permissions necessary to use mustached bats in this research.

REFERENCES

Arthur, R. M., Pfeiffer, R. R., and Suga, N. (1971). Properties of "two-tone inhibition" in primary auditory neurones. *J. Physiol.* 212, 593–609.

Bateman, G. C., and Vaughan, T. A. (1974). Nightly activities of mormoopid bats. *J. Mammal.* 55, 45–65.

Batra, R., and Fitzpatrick, D. C. (1999). Discharge patterns of neurons in the ventral nucleus of the lateral lemniscus of the unanesthetized rabbit. *J. Neurophysiol.* 82, 1097–1113.

Binns, K. E. (1999). The synaptic pharmacology underlying sensory processing in the superior colliculus. *Prog. Neurobiol.* 59, 129–159.

Boothroyd, A., Mulhearn, B., Gong, J., and Ostroff, J. (1996). Effects of spectral smearing on phoneme and word recognition. *J. Acoust. Soc. Am.* 100, 1807–1818.

Boudreau, J. C., and Tsuchitani, C. (1968). Binaural interaction in the cat superior olive S segment. *J. Neurophysiol.* 31, 442–454.

Brand, A., Behrend, O., Marquardt, T., McAlpine, D., and Grothe, B. (2002). Precise inhibition is essential for microsecond interaural time difference coding. *Nature* 417, 543–547.

Brosch, M., Schulz, A., and Scheich, H. (1999). Processing of sound sequences in macaque auditory cortex: response enhancement. *J. Neurophysiol.* 82, 1542–1559.

Casseday, J. H., Ehrlich, D., and Covey, E. (1994). Neural tuning for sound duration: role of inhibitory mechanisms in the inferior colliculus. *Science* 264, 847–850.

Covey, E., and Casseday, J. H. (1991). The monaural nuclei of the lateral lemniscus in an echolocating bat: parallel pathways for analyzing temporal features of sound. *J. Neurosci.* 11, 3456–3470.

Covey, E., Vater, M., and Casseday, J. H. (1991). Binaural properties of single units in the superior olivary complex of the mustached bat. *J. Neurophysiol.* 66, 1080–1094.

Dear, S. P., and Suga, N. (1995). Delay-tuned neurons in the midbrain of the big brown bat. *J. Neurophysiol.* 73, 1084–1100.

Edamatsu, H., Kawasaki, M., and Suga, N. (1989). Distribution of combination-sensitive neurons in the ventral fringe area of the auditory cortex of the mustached bat. *J. Neurophysiol.* 61, 202–207.

Esser, K. H., Condon, C. J., Suga, N., and Kanwal, J. S. (1997). Syntax processing by auditory cortical neurons in the FM-FM area of the mustached bat Pteronotus parnellii. *Proc. Nat. Acad. Sci. U.S.A.* 94, 14019–14024.

Feng, A. S., Simmons, J. A., and Kick, S. A. (1978). Echo detection and target-ranging neurons in the auditory system of the bat Eptesicus fuscus. *Science* 202, 645–648.

Finn, I. M., Priebe, N. J., and Ferster, D. (2007). The emergence of contrast-invariant orientation tuning in simple cells of cat visual cortex. *Neuron* 54, 137–152.

Fitzpatrick, D. C., Kanwal, J. S., Butman, J. A., and Suga, N. (1993). Combination-sensitive neurons in the primary auditory cortex of the mustached bat. *J. Neurosci.* 13, 931–940.

Fitzpatrick, D. C., Suga, N., and Olsen, J. F. (1998). Distribution of response types across entire hemispheres of the mustached bat's auditory cortex. *J. Comp. Neurol.* 391, 353–365.

Frisina, R. D., O'Neill, W. E., and Zettel, M. L. (1989). Functional organization of mustached bat inferior colliculus. II. Connections of the FM2 region. *J. Comp. Neurol.* 284, 85–107.

Fuzessery, Z. M., and Feng, A. S. (1983). Mating call selectivity in the thalamus and midbrain of the leopard frog (Rana p. pipiens): single and multiunit analyses. *J. Comp. Physiol.* 150, 333–344.

Fuzessery, Z. M., Razak, K. A., and Williams, A. J. (2011). Multiple mechanisms shape selectivity for FM sweep rate and direction in the pallid bat inferior colliculus and auditory cortex. *J. Comp. Physiol. A Neuroethol. Sens. Neural. Behav. Physiol.* 197, 615–623.

Gans, D., Sheykholeslami, K., Peterson, D. C., and Wenstrup, J. (2009). Temporal features of spectral integration in the inferior colliculus: effects of stimulus duration and rise time. *J. Neurophysiol.* 102, 167–180.

Genzel, D., and Wiegrebe, L. (2008). Time-variant spectral peak and notch detection in echolocation-call sequences in bats. *J. Exp. Biol.* 211, 9–14.

Goldman, L., and Henson, O. Jr. (1977). Prey recognition and selection by the constant frequency bat, *Pteronotus p.* parnellii. *Behav. Ecol. Sociobiol.* 2, 411–419.

Guinan, J. J. J., Guinan, S. S., and Norris, B. E. (1972). Single auditory units in the superior olivary complex I: responses to sounds and classification based on physiological properties. *Int. J. Neurosci.* 4, 101–120.

Hagemann, C., Vater, M., and Kössl, M. (2011). Comparison of properties of cortical echo delay-tuning in the short-tailed fruit bat and the mustached bat. *J. Comp. Physiol. A Neuroethol. Sens. Neural. Behav. Physiol.* 197, 605–613.

Hebrank, J., and Wright, D. (1974). Spectral cues used in the localization of sound sources on the median plane. *J. Acoust. Soc. Am.* 56, 1829–1834.

Holderied, M. W., and von Helversen, O. (2003). Echolocation range and wingbeat period match in aerial-hawking bats. *Proc. Biol. Sci.* 270, 2293–2299.

Hyson, R. L., Reyes, A. D., and Rubel, E. W. (1995). A depolarizing inhibitory response to GABA in brainstem auditory neurons of the chick. *Brain Res.* 677, 117–126.

Kadia, S. C., and Wang, X. (2003). Spectral integration in A1 of awake primates: neurons with single- and multipeaked tuning characteristics. *J. Neurophysiol.* 89, 1603–1622.

Kadner, A., Kulesza, R. J. Jr., and Berrebi, A. S. (2006). Neurons in the medial nucleus of the trapezoid body and superior paraolivary nucleus of the rat may play a role in sound duration coding. *J. Neurophysiol.* 95, 1499–1508.

Kandler, K., and Friauf, E. (1995). Development of electrical membrane properties and discharge characteristics of superior olivary complex neurons in fetal and postnatal rats. *Eur. J. Neurosci.* 7, 1773–1790.

Kanwal, J. S., Matsumura, S., Ohlemiller, K., and Suga, N. (1994). Analysis of acoustic elements and syntax in communication sounds emitted by mustached bats. *J. Acoust. Soc. Am.* 96, 1229–1254.

Kawasaki, M., Margoliash, D., and Suga, N. (1988). Delay-tuned combination-sensitive neurons in the auditory cortex of the vocalizing mustached bat. *J. Neurophysiol.* 59, 623–635.

Kiang, N. Y., and Moxon, E. C. (1974). Tails of tuning curves of auditory-nerve fibers. *J. Acoust. Soc. Am.* 55, 620–630.

Kick, S. A. (1982). Target detection by the echolocating bat, *Eptesicus fuscus*. *J. Comp. Physiol.* 145, 431–435.

Kim, G., and Kandler, K. (2003). Elimination and strengthening of glycinergic/GABAergic connections during tonotopic map formation. *Nat. Neurosci.* 6, 282–290.

Klug, A., Khan, A., Burger, R. M., Bauer, E. E., Hurley, L. M., Yang, L., et al. (2000). Latency as a function of intensity in auditory neurons: influences of central processing. *Hear. Res.* 148, 107–123.

Knudsen, E. I., and Konishi, M. (1979). Mechanisms of sound localization in the barn owl (*Tyto alba*). *J. Comp. Physiol.* 133, 13–21.

Kopp-Scheinpflug, C., Lippe, W. R., Dorrscheidt, G. J., and Rubsamen, R. (2003). The medial nucleus of the trapezoid body in the gerbil is more than a relay: comparison of pre- and postsynaptic activity. *J. Assoc. Res. Otolaryngol.* 4, 1–23.

Kössl, M., Voss, C., Mora, E. C., Macias, S., Foeller, E., and Vater, M. (2012). Auditory cortex of newborn bats is prewired for echolocation. *Nat. Commun.* 3, 773.

Kulesza, R. J. Jr., Kadner, A., and Berrebi, A. S. (2007). Distinct roles for glycine and GABA in shaping the response properties of neurons in the superior paraolivary nucleus of the rat. *J. Neurophysiol.* 97, 1610–1620.

Kuwabara, N., and Zook, J. M. (1992). Projections to the medial superior olive from the medial and lateral nuclei of the trapezoid body in rodents and bats. *J. Comp. Neurol.* 324, 522–538.

Leroy, S. A., and Wenstrup, J. J. (2000). Spectral integration in the inferior colliculus of the mustached bat. *J. Neurosci.* 20, 8533–8541.

Lewicki, M. S., and Konishi, M. (1995). Mechanisms underlying the sensitivity of songbird forebrain neurons to temporal order. *Proc. Natl. Acad. Sci. U.S.A.* 92, 5582–5586.

Lu, T., and Trussell, L. O. (2001). Mixed excitatory and inhibitory GABA-mediated transmission in chick cochlear nucleus. *J. Physiol.* 535, 125–131.

Macias, S., Mora, E. C., Hechavarria, J. C., and Kössl, M. (2012). Properties of echo delay-tuning receptive fields in the inferior colliculus of the mustached bat. *Hear. Res.* 286, 1–8.

Margoliash, D., and Fortune, E. S. (1992). Temporal and harmonic combination-sensitive neurons in the zebra finch's HVc. *J. Neurosci.* 12, 4309–4326.

Marsh, R. A., Nataraj, K., Gans, D., Portfors, C. V., and Wenstrup, J. J. (2006). Auditory responses in the cochlear nucleus of awake mustached bats: precursors to spectral integration in the auditory midbrain. *J. Neurophysiol.* 95, 88–105.

Metzner, W., and Radtke-Schuller, S. (1987). The nuclei of the lateral lemniscus in the rufous horseshoe bat, Rhinolophus rouxi. A neurophysiological approach. *J. Comp. Physiol. A* 160, 395–411.

Middlebrooks, J. C. (1992). Narrow-band sound localization related to external ear acoustics. *J. Acoust. Soc. Am.* 92, 2607–2624.

Misawa, H., and Suga, N. (2001). Multiple combination-sensitive neurons in the auditory cortex of the mustached bat. *Hear. Res.* 151, 15–29.

Mittmann, D. H. (1997). *Identification of a Neural System for Analyzing Spectral and Temporal Elements of Acoustic Signals in the Auditory Brain Stem.* Akron, OH: University of Akron.

Mittmann, D. H., and Wenstrup, J. J. (1995). Combination-sensitive neurons in the inferior colliculus. *Hear. Res.* 90, 185–191.

Moore, B. C. (2008). Basic auditory processes involved in the analysis of speech sounds. *Philos. Trans. R. Soc. Lond. B Biol. Sci.* 363, 947–963.

Nataraj, K., and Wenstrup, J. J. (2005). Roles of inhibition in creating complex auditory responses in the inferior colliculus: facilitated combination-sensitive neurons. *J. Neurophysiol.* 93, 3294–3312.

Nataraj, K., and Wenstrup, J. J. (2006). Roles of inhibition in complex auditory responses in the inferior colliculus: inhibited combination-sensitive neurons. *J. Neurophysiol.* 95, 2179–2192.

Ohlemiller, K. K., Kanwal, J. S., and Suga, N. (1996). Facilitative responses to species specific calls in cortical FM-FM neurons of the mustached bat. *Neuroreport* 7, 1749–1755.

Olsen, J. F., and Suga, N. (1991a). Combination-sensitive neurons in the medial geniculate body of the mustached bat: encoding of relative velocity information. *J. Neurophysiol.* 65, 1254–1274.

Olsen, J. F., and Suga, N. (1991b). Combination-sensitive neurons in the medial geniculate body of the mustached bat: encoding of target range information. *J. Neurophysiol.* 65, 1275–1296.

O'Neill, W. E. (1985). Responses to pure tones and linear FM components of the CF-FM biosonar signal by single units in the inferior colliculus of the mustached bat. *J. Comp. Physiol. A* 157, 797–815.

O'Neill, W. E., and Suga, N. (1979). Target range-sensitive neurons in the auditory cortex of the mustached bat. *Science* 203, 69–73.

Park, T. J., and Dooling, R. J. (1985). Perception of species-specific contact calls by budgerigars (*Melopsittacus undulatus*). *J. Comp. Psychol.* 99, 391–402.

Pearson, J. M., Crocker, W. D., and Fitzpatrick, D. C. (2007). Connections of functional areas in the mustached bat's auditory cortex with the auditory thalamus. *J. Comp. Neurol.* 500, 401–418.

Pecka, M., Brand, A., Behrend, O., and Grothe, B. (2008). Interaural time difference processing in the mammalian medial superior olive: the role of glycinergic inhibition. *J. Neurosci.* 28, 6914–6925.

Person, A. L., and Perkel, D. J. (2005). Unitary IPSPs drive precise thalamic spiking in a circuit required for learning. *Neuron* 46, 129–140.

Peterson, D. C., Nataraj, K., and Wenstrup, J. J. (2009). Glycinergic inhibition creates a form of auditory spectral Integration in nuclei of the lateral lemniscus. *J. Neurophysiol.* 102, 1004–1016.

Peterson, D. C., Voytenko, S., Gans, D., Galazyuk, A., and Wenstrup, J. (2008). Intracellular recordings from combination-sensitive neurons in the inferior colliculus. *J. Neurophysiol.* 100, 629–645.

Pollak, G. D. (2012). Circuits for processing dynamic interaural intensity disparities in the inferior colliculus. *Hear. Res.* 288, 47–57.

Pollak, G. D., Gittelman, J. X., Li, N., and Xie, R. (2011). Inhibitory projections from the ventral nucleus of the lateral lemniscus and superior paraolivary nucleus create directional selectivity of frequency modulations in the inferior colliculus: a comparison of bats with other mammals. *Hear. Res.* 273, 134–144.

Populin, L. C., and Yin, T. C. (1998). Behavioral studies of sound localization in the cat. *J. Neurosci.* 18, 2147–2160.

Portfors, C. V. (2004). Combination sensitivity and processing of communication calls in the inferior colliculus of the Moustached Bat Pteronotus parnellii. *An. Acad. Bras. Cienc.* 76, 253–257.

Portfors, C. V., and Felix, R. A. (2005). 2nd Spectral integration in the inferior colliculus of the CBA/CaJ mouse. *Neuroscience* 136, 1159–1170.

Portfors, C. V., Gans, D. P., and Wenstrup, J. J. (2002). "Responses to communication calls in the inferior colliculus of the mustached bat," in *Twenty-Fifth Midwinter Meeting of the Association for Research in Otolaryngology* (St. Petersburg Beach, FL), 37.

Portfors, C. V., and Wenstrup, J. J. (1999). Delay-tuned neurons in the inferior colliculus of the mustached bat: implications for analyses of target distance. *J. Neurophysiol.* 82, 1326–1338.

Portfors, C. V., and Wenstrup, J. J. (2001). Responses to combinations of tones in the nuclei of lateral lemniscus. *J. Assoc. Res. Otolaryngol.* 2, 104–117.

Portfors, C. V., and Wenstrup, J. J. (2003). "Neural processing of target distance: transformation of combination-sensitive responses," in *Echolocation in Bats and Dolphins*, eds J. Thomas, C. Moss, and M. Vater (Chicago: University of Chicago Press), 141–146.

Rauschecker, J. P., Tian, B., and Hauser, M. (1995). Processing of complex sounds in the macaque nonprimary auditory cortex. *Science* 268, 111–114.

Razak, K. A., and Fuzessery, Z. M. (2008). Facilitatory mechanisms underlying selectivity for the direction and rate of frequency modulated sweeps in the auditory cortex. *J. Neurosci.* 28, 9806–9816.

Razak, K. A., and Fuzessery, Z. M. (2009). GABA shapes selectivity for the rate and direction of frequency-modulated sweeps in the auditory cortex. *J. Neurophysiol.* 102, 1366–1378.

Riquelme, R., Saldana, E., Osen, K. K., Ottersen, O. P., and Merchan, M. A. (2001). Colocalization of GABA and glycine in the ventral nucleus of the lateral lemniscus in rat: an *in situ* hybridization and semiquantitative immunocytochemical study. *J. Comp. Neurol.* 432, 409–424.

Sachs, M. B., and Kiang, N. Y. (1968). Two-tone inhibition in auditory-nerve fibers. *J. Acoust. Soc. Am.* 43, 1120–1128.

Sadagopan, S., and Wang, X. (2009). Non-linear spectrotemporal interactions underlying selectivity for complex sounds in auditory cortex. *J. Neurosci.* 29, 11192–11202.

Saint Marie, R. L., and Baker, R. A. (1990). Neurotransmitter-specific uptake and retrograde transport of [3H]glycine from the inferior colliculus by ipsilateral projections of the superior olivary complex and nuclei of the lateral lemniscus. *Brain Res.* 524, 244–253.

Saint Marie, R. L., Shneiderman, A., and Stanforth, D. A. (1997). Patterns of gamma-aminobutyric acid and glycine immunoreactivities reflect structural and functional differences of the cat lateral lemniscal nuclei. *J. Comp. Neurol.* 389, 264–276.

Sanchez, J. T., Gans, D., and Wenstrup, J. J. (2008). Glycinergic "inhibition" mediates selective excitatory response to combinations of sounds. *J. Neurosci.* 28, 80–90.

Sanes, D. H., and Friauf, E. (2000). Development and influence of inhibition in the lateral superior olivary nucleus. *Hear. Res.* 147, 46–58.

Schnitzler, H. U., Kalko, E. (1998). "How echolocating bats search and find food," in *Bat Biology and Conservation*, eds T. Kunz, P. A. Racey (Washington, DC: Smithsonian Institution Press), 183–196.

Schuller, G., O'Neill, W. E., and Radtke-Schuller, S. (1991). Facilitation and delay sensitivity of auditory cortex neurons in CF-FM bats, *Rhinolophus rouxi* and *Pteronotus p.parnellii*. *Eur. J. Neurosci.* 3, 1165–1181.

Shannon, R. V., Fu, Q. J., and Galvin, J. 3rd. (2004). The number of spectral channels required for speech recognition depends on the difficulty of the listening situation. *Acta Otolaryngol. Suppl.* 552, 50–54.

Sheykholeslami, K., Gans, D., Portfors, C., and Wenstrup, J. (2004). Representation of species-specific vocalizations in the inferior colliculus of the mustached bat. *Soc. Neurosci. Abstr.* 30, 305.12.

Simmons, J. A. (1971). Echolocation in bats: signal processing of echoes for target range. *Science* 171, 925–928.

Simmons, J. A. (1973). The resolution of target range by echolocating bats. *J. Acoust. Soc. Am.* 54, 157–173.

Simmons, J. A., and Stein, R. A. (1980). Acoustic Imaging in bat sonar: echolocation signals and the evolution of echolocation. *J. Comp. Neurol.* 135, 61–84.

Simmons, J. A., Neretti, N., Intrator, N., Altes, R. A., Ferragamo, M. J., and Sanderson, M. I. (2004). Delay accuracy in bat sonar is related to the reciprocal of normalized echo bandwidth, or Q. *Proc. Natl. Acad. Sci. U.S.A.* 101, 3638–3643.

Smith, P. H., Joris, P. X., and Yin, T. C. (1998). Anatomy and physiology of principal cells of the medial nucleus of the trapezoid body (MNTB) of the cat. *J. Neurophysiol.* 79, 3127–3142.

Suga, N., Gao, E., Zhang, Y., Ma, X., and Olsen, J. F. (2000). The corticofugal system for hearing: recent progress. *Proc. Natl. Acad. Sci. U.S.A.* 97, 11807–11814.

Suga, N., and Horikawa, J. (1986). Multiple time axes for representation of echo delays in the auditory cortex of the mustached bat. *J. Neurophysiol.* 55, 776–805.

Suga, N., and O'Neill, W. E. (1979). Neural axis representing target range in the auditory cortex of the mustache bat. *Science* 206, 351–353.

Suga, N., O'Neill, W. E., Kujirai, K., and Manabe, T. (1983). Specificity of combination-sensitive neurons for processing of complex biosonar signals in auditory cortex of the mustached bat. *J. Neurophysiol.* 49, 1573–1626.

Suga, N., O'Neill, W. E., and Manabe, T. (1978). Cortical neurons sensitive to combinations of information-bearing elements of biosonar signals in the mustache bat. *Science* 200, 778–781.

Suga, N., Xiao, Z., Ma, X., and Ji, W. (2002). Plasticity and corticofugal modulation for hearing in adult animals. *Neuron* 36, 9–18.

Sullivan, W. E. 3rd. (1982). Neural representation of target distance in auditory cortex of the echolocating bat *Myotis lucifugus*. *J. Neurophysiol.* 48, 1011–1032.

Sutter, M. L., and Schreiner, C. E. (1991). Physiology and topography of neurons with multipeaked tuning curves in cat primary auditory cortex. *J. Neurophysiol.* 65, 1207–1226.

Taniguchi, I., Niwa, H., Wong, D., and Suga, N. (1986). Response properties of FM-FM combination-sensitive neurons in the auditory cortex of the mustached bat. *J. Comp. Physiol. A* 159, 331–337.

Thompson, A. M., and Schofield, B. R. (2000). Afferent projections of the superior olivary complex. *Microsc. Res. Techn.* 51, 330–354.

Tolnai, S., Hernandez, O., Englitz, B., Rubsamen, R., and Malmierca, M. S. (2008). The medial nucleus of the trapezoid body in rat: spectral and temporal properties vary with anatomical location of the units. *Eur. J. Neurosci.* 27, 2587–2598.

Turecek, R., and Trussell, L. O. (2001). Presynaptic glycine receptors enhance transmitter release at a mammalian central synapse. *Nature* 411, 587–590.

Vater, M., Covey, E., and Casseday, J. H. (1997). The columnar region of the ventral nucleus of the lateral lemniscus in the big brown bat (*Eptesicus fuscus*): synaptic arrangements and structural correlates of feedforward inhibitory function. *Cell Tissue Res.* 289, 223–233.

Vater, M., Foeller, E., Mora, E. C., Coro, F., Russell, I. J., and Kössl, M. (2010). Postnatal maturation of primary auditory cortex in the mustached bat, Pteronotus parnellii. *J. Neurophysiol.* 103, 2339–2354.

Voytenko, S. V., and Galazyuk, A. V. (2007). Intracellular recording reveals temporal integration in inferior colliculus neurons of awake bats. *J. Neurophysiol.* 97, 1368–1378.

Wenstrup, J. J. (1999). Frequency organization and responses to complex sounds in the medial geniculate body of the mustached bat. *J. Neurophysiol.* 82, 2528–2544.

Wenstrup, J. J., and Grose, C. D. (1995). Inputs to combination-sensitive neurons in the medial geniculate body of the mustached bat: the missing fundamental. *J. Neurosci.* 15, 4693–4711.

Wenstrup, J. J., and Leroy, S. A. (2001). Spectral integration in the inferior colliculus: role of glycinergic inhibition in response facilitation. *J. Neurosci.* 21, RC124.

Wenstrup, J. J., Larue, D. T., and Winer, J. A. (1994). Projections of physiologically defined subdivisions of the inferior colliculus in the mustached bat: targets in the medial geniculate body and extrathalamic nuclei. *J. Comp. Neurol.* 346, 207–236.

Wenstrup, J. J., Mittmann, D. H., and Grose, C. D. (1999). Inputs to combination-sensitive neurons of the inferior colliculus. *J. Comp. Neurol.* 409, 509–528.

Wenstrup, J. J., and Portfors, C. V. (2011). Neural processing of target distance by echolocating bats: functional roles of the auditory midbrain. *Neurosci. Biobehav. Rev.* 35, 2073–2083.

Williams, A. J., and Fuzessery, Z. M. (2011). Differential roles of GABAergic and glycinergic input on FM selectivity in the inferior colliculus of the pallid bat. *J. Neurophysiol.* 106, 2523–2535.

Winer, J. A., Larue, D. T., and Pollak, G. D. (1995). GABA and glycine in the central auditory system of the mustache bat: structural substrates for inhibitory neuronal organization. *J. Comp. Neurol.* 355, 317–353.

Xiao, Z., and Suga, N. (2004). Reorganization of the auditory cortex specialized for echo-delay processing in the mustached bat. *Proc. Natl. Acad. Sci. U.S.A.* 101, 1769–1774.

Xie, R., Gittelman, J. X., and Pollak, G. D. (2007). Rethinking tuning: *in vivo* whole-cell recordings of the inferior colliculus in awake bats. *J. Neurosci.* 27, 9469–9481.

Yan, J., and Suga, N. (1996a). The midbrain creates and the thalamus sharpens echo-delay tuning for the cortical representation of target-distance information in the mustached bat. *Hear. Res.* 93, 102–110.

Yan, J., and Suga, N. (1996b). Corticofugal modulation of time-domain processing of biosonar

information in bats. *Science* 273, 1100–1103.

Yan, J., and Suga, N. (1999). Corticofugal amplification of facilitative auditory responses of subcortical combination-sensitive neurons in the mustached bat. *J. Neurophysiol.* 81, 817–824.

Yavuzoglu, A., Schofield, B. R., and Wenstrup, J. J. (2010). Substrates of auditory frequency integration in a nucleus of the lateral lemniscus. *Neuroscience* 169, 906–919.

Yavuzoglu, A., Schofield, B. R., and Wenstrup, J. J. (2011). Circuitry underlying spectrotemporal integration in the auditory midbrain. *J. Neurosci.* 31, 14424–14435.

Zhang, H., and Kelly, J. B. (2006). Responses of neurons in the rat's ventral nucleus of the lateral lemniscus to monaural and binaural tone bursts. *J. Neurophysiol.* 95, 2501–2512.

Zook, J. M., and Casseday, J. H. (1985). Projections from the cochlear nuclei in the mustache bat, *Pteronotus parnellii*. *J. Comp. Neurol.* 237, 307–324.

Zook, J. M., and Leake, P. A. (1989). Connections and frequency representation in the auditory brainstem of the mustache bat, *Pteronotus parnellii*. *J. Comp. Neurol.* 290, 243–261.

Conflict of Interest Statement: The authors declare that the research was conducted in the absence of any commercial or financial relationships that could be construed as a potential conflict of interest.

Received: 01 June 2012; accepted: 02 October 2012; published online: 23 October 2012.

Citation: Wenstrup JJ, Nataraj K and Sanchez JT (2012) Mechanisms of spectral and temporal integration in the mustached bat inferior colliculus. Front. Neural Circuits ***6****:75. doi: 10.3389/fncir.2012.00075*

frontiers in
NEURAL CIRCUITS

ORIGINAL RESEARCH ARTICLE
published: 20 August 2012
doi: 10.3389/fncir.2012.00056

Recovery cycle times of inferior colliculus neurons in the awake bat measured with spike counts and latencies

Riziq Sayegh, Brandon Aubie, Siavosh Fazel-Pour and Paul A. Faure*

Department of Psychology, Neuroscience & Behaviour, McMaster University, Hamilton, ON, Canada

Edited by:
Manuel S. Malmierca, University of Salamanca, Spain

Reviewed by:
Zoltan M. Fuzessery, University of Wyoming, USA
Philip Jen, University of Missouri, USA

***Correspondence:**
Paul A. Faure, Department of Psychology, Neuroscience & Behaviour, McMaster University, 1280 Main Street West, Hamilton, ON L8S 4K1, Canada.
e-mail: paul4@mcmaster.ca

Neural responses in the mammalian auditory midbrain (inferior colliculus; IC) arise from complex interactions of synaptic excitation, inhibition, and intrinsic properties of the cell. Temporally selective duration-tuned neurons (DTNs) in the IC are hypothesized to arise through the convergence of excitatory and inhibitory synaptic inputs offset in time. Synaptic inhibition can be inferred from extracellular recordings by presenting pairs of pulses (paired tone stimulation) and comparing the evoked responses of the cell to each pulse. We obtained single unit recordings from the IC of the awake big brown bat (*Eptesicus fuscus*) and used paired tone stimulation to measure the recovery cycle times of DTNs and non-temporally selective auditory neurons. By systematically varying the interpulse interval (IPI) of the paired tone stimulus, we determined the minimum IPI required for a neuron's spike count or its spike latency (first- or last-spike latency) in response to the second tone to recover to within ≥50% of the cell's baseline count or to within 1 SD of it's baseline latency in response to the first tone. Recovery times of shortpass DTNs were significantly shorter than those of bandpass DTNs, and recovery times of bandpass DTNs were longer than allpass neurons not selective for stimulus duration. Recovery times measured with spike counts were positively correlated with those measured with spike latencies. Recovery times were also correlated with first-spike latency (FSL). These findings, combined with previous studies on duration tuning in the IC, suggest that persistent inhibition is a defining characteristic of DTNs. Herein, we discuss measuring recovery times of neurons with spike counts and latencies. We also highlight how persistent inhibition could determine neural recovery times and serve as a potential mechanism underlying the precedence effect in humans. Finally, we explore implications of recovery times for DTNs in the context of bat hearing and echolocation.

Keywords: auditory neurophysiology, big brown bat (*Eptesicus fuscus*), duration-tuned neurons, echolocation, neuroethology, paired tone stimulation

1. INTRODUCTION

The ability to extract temporal information from an acoustic signal is important for processing human speech (Denes, 1955), discriminating species-specific communication calls (Pollack and Hoy, 1979), localizing sounds (Knudsen and Konishi, 1979; Carr and Konishi, 1990), and echolocation by bats (Simmons, 1971, 1979; Suga and O'Neill, 1979; O'Neill and Suga, 1982). Neurons with spiking responses selective for signal duration, known as duration-tuned neurons (DTNs), provide one neural mechanism for encoding temporal information. DTNs have been observed across a variety of vertebrate species and taxa including frogs (Potter, 1965; Gooler and Feng, 1992; Leary et al., 2008), chinchillas (Chen, 1998), guinea pigs (Wang et al., 2006), mice (Brand et al., 2000; Xia et al., 2000; Tan and Borst, 2007), rats (Pérez-González et al., 2006), cats (He et al., 1997), and bats (Jen and Schlegel, 1982; Pinheiro et al., 1991; Casseday et al., 1994; Ehrlich et al., 1997; Fuzessery and Hall, 1999; Faure et al., 2003; Mora and Kössl, 2004; Luo et al., 2008). Because DTNs have also been found in the visual cortex of cats (Duysens et al., 1996), this suggests that neural mechanisms of duration selectivity may be similar across sensory modalities. The physiological response properties and underlying neural mechanisms of auditory DTNs have been studied most extensively in echolocating bats. The biological function(s) of DTNs to hearing is(are) unknown; however, the range of neural best durations (BD) within a species (BD = stimulus duration that causes maximum spiking) correlates with the range of vocalization durations of species-specific communication sounds in non-echolocating vertebrates and with biosonar pulse durations in echolocating bats (for reviews, see Sayegh et al., 2011; Jen et al., 2012).

Duration tuning in the mammalian inferior colliculus (IC) is hypothesized to arise from the convergence and temporal interaction of excitatory and inhibitory synaptic inputs arriving at the neuron (Casseday et al., 1994, 2000; Covey et al., 1996; Faure et al., 2003; Aubie et al., 2009). Biologically plausible computational models of DTNs support the hypothesis that neural mechanisms of duration selectivity may be shared across vertebrates (Aubie et al., 2012). A number of studies have demonstrated that neural inhibition is necessary for creating DTNs in the IC. For example, focal application of $GABA_A$ and/or glycine receptor antagonists have been shown to greatly diminish and/or eliminate the spiking responses of DTNs (Fuzessery and Hall, 1999; Jen and Feng,

1999), with the blocking of $GABA_A$ receptors having the greatest effect on temporal tuning and duration selectivity (Casseday et al., 2000). Whole-cell intracellular patch clamp recordings (Covey et al., 1996; Tan and Borst, 2007; Leary et al., 2008) and/or single-unit extracellular recordings combined with paired tone stimulation (Faure et al., 2003) have revealed that inhibitory inputs to DTNs usually precede excitatory inputs, and that the inhibition lasts from 5 to 150 ms after stimulus offset. Hence, DTNs receive inhibition that leads excitation. This inhibition also persists for as long or longer than the duration of the stimulus that evoked it. We know that inhibition occurs in some types of IC neurons that are not tuned to stimulus duration (Faingold et al., 1991; Pollak and Park, 1993; Torterolo et al., 1995; Kuwada et al., 1997; Pedemonte et al., 1997; Klug et al., 1999), and in these cells inhibition can persist for as long as 100 ms after stimulus offset (Yin, 1994; Covey et al., 1996; Litovsky and Delgutte, 2002). Owing to the importance of inhibition in creating the temporal tuning profile and response properties of DTNs, we hypothesized that the leading and persistent inhibition evoked by each signal in a paired tone stimulus could temporally interact and sum, resulting in DTNs exhibiting longer recovery cycle times than non-DTNs. Herein we test this hypothesis.

The recovery time of an evoked neural response can be measured with paired pulse stimulation (Grinnell, 1963). Often the stimulus is a pair of equal amplitude pure tones set to the cell's characteristic or best excitatory frequency (BEF) and presented at varying interpulse intervals (IPIs). Some studies have used pairs of acoustic clicks presented at varying interstimulus delays (Fitzpatrick et al., 1995; Litovsky and Yin, 1998a; Litovsky and Delgutte, 2002), while others have used pairs of frequency modulated (FM) sweeps or variable amplitude tones to mimic the loud outgoing vocalizations and faint returning echoes used for echolocation by bats (Grinnell, 1963; Suga, 1964; Friend et al., 1966; Pollak et al., 1977a,b; Lu et al., 1997; Wang et al., 2010). A cell's recovery time is measured by determining the minimum IPI required for the spiking response evoked by the second stimulus (R2) to recover within a specified level of the spiking response evoked by the first stimulus (R1). The most common and unbiased criterion for measuring recovery time is to report the IPI where the R2/R1 ratio is $\geq$0.5. Note that this measure is normally based enitrely on spike counts. To the best of our knowledge, no previous study has measured neural recovery times with a spike latency criterion.

Previous studies in bats reported that spike count recovery cycle times of IC neurons are highly variable, ranging anywhere from 4 to 200 ms (Suga, 1964; Friend et al., 1966; Suga and Schlegel, 1973; Pollak et al., 1977a; Lu et al., 1997; Tang et al., 2011). The recovery cycle times of many DTNs are shortest when the pulse and echo durations are set to the cell's BD and presented at biologically relevant pulse-echo amplitude differences (Wang et al., 2008, 2010). The frequency selectivity of DTNs has also been reported to sharpen when the pulse and echo are presented at BD (Wu and Jen, 2008b). These findings suggest that the responses of DTNs may be specialized for processing loud outgoing echolocation pulses and fainter returning echos. Because DTNs are found in both echolocating and non-echolocating mammals, the ability to echolocate cannot be a prerequisite for the evolution of auditory duration selectivity (Sayegh et al., 2011). Nevertheless, this does not preclude a more specialized functional role for DTNs in hearing and echolocation by bats.

Recovery cycle times also provide a way to observe the effects of synaptic inhibition to a neuron. Application of bicucculine, a $GABA_A$ receptor antagonist, has been shown to shorten the recovery times of IC neurons (Lu et al., 1997; Zhou and Jen, 2003), suggesting that inhibitory inputs control the minimum time needed for response recovery. In this study, we measured and compared the recovery cycle times of DTNs and non-DTNs using both spike count and spike latency measures as a way to further our understanding about the strength and time course of the leading and persistent inhibition that is responsible for the creation of auditory midbrain microcircuits sensitive to temporal acoustic features.

2. METHODS

2.1. SURGICAL PROCEDURES

Electrophysiological data were obtained from 33 adult big brown bats (*Eptesicus fuscus*) of both sexes that were housed in a husbandry facility where colony temperature and lighting varied according to ambient conditions (Faure et al., 2009). To facilitate multiple recordings and to precisely replicate the position of the bat's head between sessions, a stainless steel post was glued to the skull. Prior to the head-posting surgery, bats were given a subcutaneous injection of buprenorphine (0.03 mL; 1:9 mixture of 0.3 mg/mL Temgesic and sterile water; 0.045 mg/kg). For the surgery, bats were first placed in an anesthesia induction chamber ($12 \times 10 \times 10$ cm) where they inhaled a 1–5% isofluorane:oxygen gaseous mixture (flow rate: 1 L/min). Anesthetized bats were then placed in a foam-lined body restraint within a stereotaxic alignment system (David Kopf Instruments Model 1900) fitted with a custom mask for gas inhalation. The hair covering the skull was shaved and the underlying skin was swabbed with Betadine® disinfectant. Local anesthetic (0.2 mL bupivicaine; 5 mg/mL) was injected subcutaneously prior to making a midline incision in the scalp. The temporal muscles were reflected, the skull was scraped clean and swabbed with 70% ethanol, and a post was glued to the skull overlying the cortex with cyanoacrylate adhesive (Henkel Loctite Corporation) cured with liquid acrylic hardener (Zipkicker; Pacer Technology®). A chlorided silver wire, attached to the head post, was placed under the temporal muscles and served as the reference electrode. Recordings began 1–4 days after surgery. Each bat was used in 1–8 sessions lasting ca. 4–8 h each on separate days. Recordings were terminated if a bat showed signs of discomfort (e.g., struggling body movements). Between sessions, the electrode penetration site was covered with a piece of contact lens and Gelfoam® coated in Polysporin®. Bats were housed individually in a temperature- and humidity-controlled room and were given *ad libitum* access to food and water. All procedures were approved by the McMaster University Animal Research Ethics Board and were in accordance with the Canadian Council on Animal Care.

2.2. ELECTROPHYSIOLOGICAL RECORDINGS

Recordings were conducted inside a double-walled, sound attenuating booth with electrical shielding (Industrial Acoustics

Co., Inc.). Prior to recording, each bat was given a subcutaneous injection of a neuroleptic (0.3 mL; 1:1 mixture of 0.05 mg/mL fentanyl citrate and 2.5 mg/mL Inapsine [droperidol]; 19.1 mg/kg). Bats were then placed in a foam-lined body restraint that was suspended by springs within a small animal stereotaxic frame that was customized for bats (ASI Instruments) and mounted atop of an air vibration table (TMC Micro-G). The bat's head was immobilized by securing the headpost to a stainless steel rod attached to a manipulator (ASI Instruments) mounted on the stereotaxic frame. The dorsal surface of the IC was exposed for recording by making a small hole in the skull and dura mater with a scalpel. Single-unit extracellular recordings were made with thin-wall borosilicate glass microelectrodes with a capillary filament (o.d. = 1.2 mm; A-M Systems, Inc.) and filled with 3 M NaCl. Typical electrode resistances ranged from 10 to 30 MΩ. Electrodes were positioned over the dorsal surface of the IC with manual manipulators (ASI Instruments), and advanced into the brain with a stepping hydraulic micropositioner (David Kopf Instruments Model 2650). Action potentials were recorded with a Neuroprobe amplifier (A-M Systems Model 1600) whose 10× output was bandpass filtered and further amplified (500–1000×) by a Tucker Davis Technologies spike pre-conditioner (TDT PC1; lowpass $f_c = 7$ kHz; high-pass $f_c = 300$ Hz). Spike times were logged on a computer by passing the PC1 output to a spike discriminator (TDT SD1) and then an event timer (TDT ET1) synchronized to a timing generator (TDT TG6). Electrodes were visually aimed at the dorsal surface of the IC and all recordings are assumed to be from the central nucleus of the IC (ICc).

2.3. STIMULUS GENERATION AND DATA COLLECTION

Stimulus generation and on-line data collection were controlled with custom software that displayed spike times as dot raster displays ordered by the acoustic parameter that was randomized during unit testing (see Faure et al., 2003). Briefly, pure tone pulses were digitally generated with a two-channel array processor (TDT Apos II; 357 kHz sampling rate) optically interfaced to two digital-to-analog (D/A) converters (TDT DA3-2) whose individual outputs were fed to a low-pass anti-aliasing filter (TDT FT6-2; $f_c = 120$ kHz), two programmable attenuators (TDT PA5) and two signal mixers (TDT SM5) with equal weighting. The output of each mixer was fed to a manual attenuator (Leader LAT-45) before final amplification (Krohn-Hite Model 7500). All stimuli were presented monaurally, contralateral to the IC being recorded, using a Brüel & Kjær (B&K) $\frac{1}{4}$ inch condenser microphone (Type 4939; protective grid on) modified for use as a loudspeaker with a transmitting adaptor (B&K Type UA-9020) to correct for non-linearities in the transfer function (Frederiksen, 1977). The loudspeaker was positioned ca. 1 mm in front of the external auditory meatus. The output of each speaker, measured with a B&K Type 4138 $\frac{1}{8}$ inch condenser microphone (90° incidence; grid off) connected to a measuring amplifier (B&K Type 2606) and bandpass filter (K-H Model 3500), was quantified with a sound calibrator (B&K Type 4231) and expressed in decibels sound pressure level (dB SPL re 20 μPa) equivalent to the peak amplitude of continuous tones of the same frequency (Stapells et al., 1982). The loudspeaker transfer functions were flat ±6 dB from 28–118 kHz, and there was at least 30 dB attenuation at the ear opposite the source (Ehrlich et al., 1997). All stimuli had rise/fall times of 0.4 or 0.5 ms shaped with a square cosine function and were presented at a trial stimulation rate of 3 Hz.

Single units were found by searching with short duration pure tones and/or downward FM sweeps. Upon unit isolation, we determined the cell's BEF, acoustic threshold, first-spike latency (FSL) and last-spike latency (LSL) re signal onset, and for DTNs we also determined the BD and duration-selective response class (i.e., shortpass, bandpass or longpass DTNs; see Faure et al., 2003; Fremouw et al., 2005). In all cases, neural response parameters were determined by systematically varying the frequency, attenuation, or duration of the stimulus in blocks, with 10–20 stimulus repetitions per randomized step in each block. Following the paired tone stimulation paradigm of Faure et al. (2003), we presented cells with pairs of BEF tone pulses. The onset of the first pulse (P1) was fixed in time relative to the onset of recording; the onset of the second pulse (P2) was systematically varied. The stimulus IPI was defined as the time between the onset of P1 and the onset of P2. For DTNs the durations of P1 and P2 were set to the cell's BD, whereas for non-DTNs the paired tone duration was randomly chosen from 1–9 ms. Because P1 and P2 were matched in stimulus frequency, duration, amplitude, and phase at all IPIs presented, whenever the two tones temporally overlapped they summed to form a single composite tone with a +6 dB amplitude pedestal, the duration of which was determined by the amount of overlap.

2.4. MEASURING RECOVERY TIMES

We tested 73 IC neurons with paired tone stimulation and generated 132 data files: 59 cells were tested at both +10 dB and +20 dB above threshold (118 files), and 14 cells were tested at only +10 dB above threshold. The IPI between P1 and P2 was randomly varied, typically in 2 ms steps (115 of 132 files; 87%); however, two files used 1 ms steps, 1 file used 2.5 ms steps, 1 file used 4 ms steps, and 13 files used 5 ms steps.

2.4.1. Baseline data and windowing responses

For each file, we measured the baseline FSL and baseline LSL in response to tone P1 for the 10 trials with the longest IPIs. We did this to minimize the influence of tone P2 on the measurement of the Baseline Response R1 re P1 (see **Figure 1A**). We used 20 stimulus repetitions at each IPI to calculate a mean ± standard deviation (SD) FSL and LSL (re P1). We then averaged the 10 means and 10 SDs to calculate a grand mean ± average SD baseline FSL and baseline LSL (re P1) for each file. The baseline FSL and baseline LSL were used to define the P1 and P2 analysis windows. The P1 analysis window started at the onset of P1 + baseline FSL −2 SDs and ended at the onset of P1 + baseline LSL +2 SDs. The P2 analysis window started at the onset of P2 + baseline FSL −2 SDs and ended at the onset of P2 + baseline LSL +2 SDs. Spikes were assumed to be evoked by P1 if they fell into the P1 analysis window, and spikes were assumed to be evoked by P2 if they fell into the P2 analysis window. For trials where the IPI was small and the P1 and P2 analysis windows overlapped—when the onset of P1 + baseline LSL +2 SDs was > the onset of P2 + baseline FSL −2 SDs, thus making it difficult to confidently assign spikes as being evoked by either P1

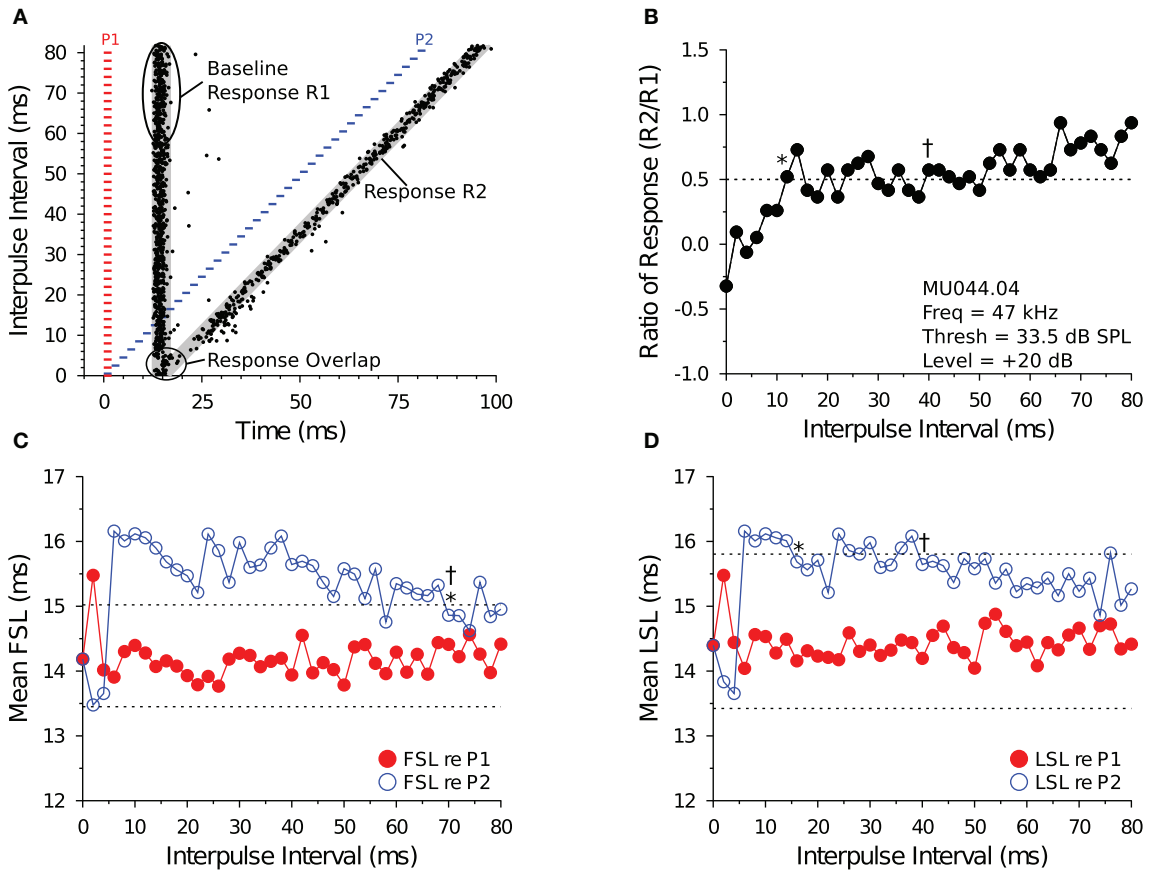

FIGURE 1 | Measuring recovery cycle times of IC neurons. (A) Dot raster display of an *in vivo* shortpass DTN in response to paired tone stimulation at varying IPIs. The *red bars* represent the onset, duration, and offset of the first tone pulse (P1), and the *blue bars* represent the onset, duration, and offset of the second tone pulse (P2). Stimuli P1 and P2 were set to the cell's BEF and, if duration-tuned, BD. The timing of action potentials are illustrated as *black dots*. We calculated the mean ± SD baseline FSL and baseline LSL in response to P1 over the 10 longest IPIs from the onset of P1 to the onset of P2. Baseline latencies were used to define the P1 and P2 analysis windows (*gray regions*) used for assigning spikes as being evoked by stimulus P1 or P2, and for calculating the Baseline Response R1. The P1 analysis window began at the onset of P1 + baseline FSL − 2 SDs and ended at the onset of P1 + mean LSL + 2 SDs (re P1). The P2 analysis window began at the onset of P2 + baseline FSL − 2 SDs and ended at the onset of P2 + mean LSL + 2 SDs (re P2), and was used to measure the responses evoked by P2 (Response R2). For trials where the P1 and P2 analysis windows overlapped, a single analysis window was defined starting from the onset of P1 + baseline FSL − 2 SDs and ending at the onset of P2 + baseline LSL + 2 SDs. **(B)** Recovery times measured with spike count. The ordinate shows the spike count ratio of response (R2/Baseline R1) as a function of stimulus IPI. The *dotted line* at 0.5 represents the 50% spike count recovery threshold. The asterisk (*) at 12 ms illustrates the recovery time of the cell determined with the short-to-long method, and the dagger (†) at 40 ms represents the recovery time of the same cell determined with the long-to-short method. **(C,D)** Recovery times measured with spike latency. The *red line with closed symbols* represents spike latency (re P1), and the *blue line with open symbols* represents spike latency (re P2). The *dotted lines* represent ± 1 SD relative to the mean baseline FSL or baseline LSL (see **A**). **(C)** Mean FSL (re P1 and P2) as a function of IPI. The asterisk (*) at 70 ms illustrates the FSL recovery time measured with the short-to-long method, and the dagger (†) at 70 ms represents the FSL recovery time of the same cell determined with the long-to-short method. **(D)** Mean LSL (re P1 and P2) as a function of IPI. The asterisk (*) at 16 ms illustrates the LSL recovery time of the cell measured with the short-to-long method, and the dagger (†) at 40 ms represents the LSL recovery time of the same cell determined with the long-to-short method. In this example, FSL took longer to recover than LSL. MU044.04.09: BEF, 47 kHz; BD, 2 ms; threshold, 33.5 dB SPL; amplitude +20 dB re threshold; 20 repetitions per IPI step.

or P2—we used a single, combined analysis window to measure the evoked response. The combined analysis window started from the onset of P1 + baseline FSL −2 SDs and ended at the onset of P2 + baseline LSL +2 SDs.

2.4.2. Spike count recovery

We used the P1 and P2 analysis windows (described above) to count spikes and measure spike latencies evoked by tones P1 and P2, respectively, and to calculate the response criteria for measuring recovery cycle times. We did this so that evoked responses were compared with equal duration analysis windows. Assuming spike latencies are normally distributed, then at 2 SDs wide the P1 and P2 analysis windows should capture ≥95% of evoked responses. The P1 analysis window was used to measure the Baseline spiking Response R1 evoked by tone P1. The P2 analysis window was used to measure the spiking Response R2 evoked by tone P2 (**Figure 1A**). At each IPI, we calculated a R2/Baseline R1 ratio of response (**Figure 1B**). The R2 spike count was defined as having "recovered" when this ratio was ≥0.5—that is, when the spike count evoked by P2 recovered to within 50% of the baseline spike

count evoked by P1. For trials where the IPI was small and the P1 and P2 analysis windows overlapped, the spike count ratio of response was calculated by first counting the number of spikes that fell into the combined P1 + P2 analysis window and then subtracting the Baseline Response R1 spike count before dividing this value by the Baseline Response R1 spike count, which is similar to the method used by Suga (1964) to deal with response overlap.

Some cells showed variation (ringing) in their spike count ratio of response function, so we developed two algorithms to measure recovery times from the functions. The algorithms assess response recovery starting from different ends of the function (**Figure 1B**). The *short-to-long method* assesses the function starting from the shortest IPIs on the left and moving toward the longest IPIs on the right. Using this technique, the recovery time of a cell was defined as the smallest IPI where the ratio of response function crossed and remained $\geq$0.5 for at least two consecutive IPIs (see * in **Figure 1B**). In a small subset of files (9/132, 6.8%), we observed a brief facilitation in the ratio of response function at short IPIs, followed by a decrease below 0.5 at intermediate IPIs, and then an increase above 0.5 at longer IPIs (e.g., **Figures 6C,D**). For these files, the recovery time was defined as the smallest IPI where the spike count ratio of response function remained $\geq$0.5 for most of the remaining points at longer IPIs (based on visual inspection by 2 observers), which is similar to the method used by Fitzpatrick et al. (1995). The *long-to-short method* assesses the spike count recovery function starting from the longest IPIs on the right and moving toward the shortest IPIs on the left. With this technique the recovery time of a cell was defined as the largest IPI where the spike count ratio of response function was $\geq$0.5 if at least two consecutive data points at smaller IPIs were $<$0.5 (see † in **Figure 1B**), or if most data points at shorter IPIs remained below 0.5 (based on visual inspection by 2 observers).

2.4.3. Spike latency recovery

In most data files we noticed an increase in the FSL or LSL (or both) of the evoked response (re P2) at short IPIs, and then a return to baseline R1 latencies at longer IPIs (e.g., **Figures 1C,D**). We used this latency change as an alternative method for determining the recovery times of IC neurons. Using the Baseline Response R1 FSL and LSL data (re P1) for each file, we measured response recovery with spike latencies using a $\pm$1 SD criterion. We then employed similar short-to-long and long-to-short analysis algorithms to measure spike latency recovery times. The *short-to-long method* starts with the shortest IPI on the left where the R2 latency had increased to $>$1 SD above the Baseline Response R1 latency, and moving right it selects the shortest subsequent IPI where the R2 latency returns and remains within 1 SD of baseline for at least two consecutive IPIs (see * in **Figures 1C,D**). The *long-to-short method* starts from the longest IPI on the right and moving left it determines the shortest subsequent IPI where the R2 latency falls within 1 SD of baseline if at least two consecutive points at shorter IPIs were $>$1 SD of baseline (see † in **Figures 1C,D**). A number of data files did not show a $\pm$1 SD change in FSL (8/132, 6.1%) or LSL (56/132, 42.4%), and for these cases it was not possible to measure a spike latency recovery time.

2.5. DATA ANALYSIS

Unless stated otherwise, all data are reported as the mean $\pm$ standard error (SE). Parameter correlations were calculated with linear regression in Python (SciPy module) and relationships are reported as the coefficient of determination (R^2 and p-values). Unless explicitly testing for factor effects, we grouped recovery time values across cell types (bandpass, shortpass, allpass) at both +10 dB and +20 dB (re threshold). We used the linear and non-linear mixed-effects models analysis-of-variance (ANOVA) package written in R to test for effects of cell type, analysis method, and relative amplitude on recovery cycle times, FSLs, and LSLs, with cell type and relative amplitude as fixed factors and cell ID as a random factor (Pinheiro and Bates, 2000).

3. RESULTS

3.1. RESPONSE PROPERTIES

DTNs can be categorized into one of three response classes based on the shape of the duration tuning function (Sayegh et al., 2011). Bandpass DTNs respond maximally at BD, with spike counts that eventually fall to $\leq$50% of the maximum at durations both longer and shorter than BD. Shortpass DTNs also respond maximally at BD, with spike counts that eventually fall to $\leq$50% of the maximum at durations longer than BD but not shorter. The spiking responses of shortpass and bandpass DTNs are typically transient and offset-evoked, with FSL (re stimulus onset) increasing with stimulus duration (Faure et al., 2003). Longpass DTNs do not have a BD; instead, they respond only when the stimulus duration exceeds some minimum duration (Faure et al., 2003; Aubie et al., 2009; Sayegh et al., 2011). Longpass DTNs differ from typical sensory neurons in that they do not show a decrease in FSL with increasing stimulus amplitude that is typical of neurons that integrate stimulus energy (Brand et al., 2000; Faure et al., 2003; Pérez-González et al., 2006). Longpass DTNs were not used in this report. By definition, allpass neurons are not duration-selective and therefore do not have a BD. Allpass neurons spike in response to all signal durations that contain sufficient stimulus energy. The response pattern of allpass neurons can be transient or sustained, with spikes typically occurring at a constant (onset-evoked) FSL re stimulus onset.

We obtained single unit extracellular recordings from 73 IC neurons. Of these, 16 (22%) were shortpass DTNs, 18 (25%) were bandpass DTNs, and 39 (53%) were not duration-selective (i.e., allpass neurons). Recovery times were determined at +10 dB for all cells and at +20 dB re threshold for 59 cells (14 shortpass, 13 bandpass, and 32 allpass).

Traveling dorsal to ventral in direction, the BEF of cells systematically increased as the depth of the recording electrode was advanced into the IC ($R^2 = 0.57$, $p \ll 0.001$; data not shown). This tonotopic relationship held true within all cell types and response classes (allpass $R^2 = 0.65$, $p \ll 0.001$; shortpass $R^2 = 0.56$, $p \ll 0.001$; and bandpass $R^2 = 0.41$, $p < 0.001$). There was no correlation between neuronal BD and electrode depth (**Figure 2A**), but there was a significant negative correlation between BD and BEF (**Figure 2B**). There was also no correlation between BEF and the mean baseline spike count at +10 dB ($R^2 = 0.030$, $p = 0.15$), but at +20 dB (re

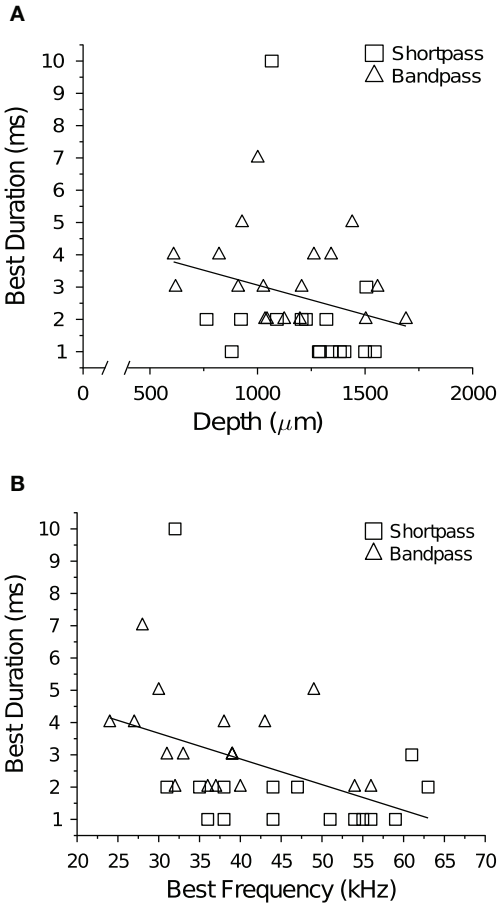

FIGURE 2 | Temporal tuning and spatial topography or tonotopy in the IC. (A) There was no correlation between neuronal BD and the depth of the recording electrode ($R^2 = 0.070$, $p = 0.13$). Note the broken abscissa. **(B)** There was a negative correlation between neuronal BD and BEF ($R^2 = 0.20$, $p = 0.0081$).

threshold) there was a weak, positive correlation ($R^2 = 0.068$, $p = 0.046$).

We measured the average spike latency (re stimulus onset) at each level above threshold (**Table 1**) and found that FSL ($F = 2.12$, $p = 0.13$) and LSL ($F = 0.17$, $p = 0.84$) did not vary as a function of response class. Mean FSLs decreased with a +10 dB increase in stimulus amplitude ($F = 7.46$, $p = 0.0084$), but there was no change in LSL ($F = 0.0016$, $p = 0.97$). Neurons with higher BEFs had shorter FSLs (**Figures 3A,B**). There was also a negative correlation between BEF and LSL (**Figures 3C,D**). Neurons with longer FSLs (but not LSLs) were distributed more dorsally in the IC at shallower electrode depths (data not shown).

3.2. RECOVERY CYCLE TIMES

Figure 4 illustrates the response characteristics of a bandpass DTN to presentations of variable duration BEF tones (**Figures 4A,B**) and to pairs of BEF and BD tones varied in IPI (**Figures 4C,D**). This cell responded to 24 kHz tone durations between 1 and 8 ms, with a maximum of ca. 2 spikes per stimulus

Table 1 | Mean ± SE first- and last-spike latency as a function of cell type and level above threshold.

Cell type	*n*	Spike latency (ms) +10 dB	*n*	Spike latency (ms) +20 dB
FIRST-SPIKE LATENCY				
Allpass	39	15.42 ± 0.98	32	13.20 ± 0.96
Bandpass	18	18.33 ± 1.30	13	16.86 ± 1.28
Shortpass	16	14.32 ± 1.57	14	12.76 ± 1.24
LAST-SPIKE LATENCY				
Allpass	39	20.37 ± 1.43	32	18.42 ± 1.58
Bandpass	18	21.34 ± 1.75	13	20.71 ± 1.79
Shortpass	16	19.57 ± 2.49	14	16.00 ± 2.08

The average baseline R1 latency at +10 and +20 dB (re threshold) was used as the input for each cell.

at a BD of 4 ms. Because the cell's FSL increased with stimulus duration it was characterized as offset responding. When stimulated with pairs of BD tones that were randomly varied in IPI, spike counts in response to tone P2 became suppressed (**Figure 4D**) and the spike latency (both FSL and LSL) was delayed at short IPIs (**Figures 4E,F**). Evidence that neural inhibition alters the responses can be seen in **Figure 4C** during and following the period of response overlap. At an IPI of 2 ms, the leading inhibition evoked by each stimulus sums and this appears to lengthen the cell's FSL without drastically altering its spike count. At IPIs from 4 to ca. 36 ms, the persistent inhibition evoked by P1 appears to interact with the leading inhibition evoked by P2 and this suppresses the spike count and delays the FSL of the response evoked by P2. Eventually, the spike count and latencies recover to within baseline values, although subtle effects of persistent inhibition can still be observed at long IPIs because the mean FSL (re P2) does not begin to overlap the mean FSL (re P1) until an IPI of 76 ms. Indeed, for this cell it is clear that FSL takes longer to recover than LSL. The recovery time of the cell, as determined from the spike count ratio of response function, was similar for the short-to-long (42 ms) and long-to-short (38 ms) analysis methods. The recovery time of the cell, as determined from the FSL function (re P2), returned to within 1 SD of baseline at 56 ms using both the short-to-long and long-to-short methods (**Figure 4E**). The recovery time of the cell, as determined from LSL function (re P2), returned to within 1 SD of baseline at 20 ms using both methods (**Figure 4F**).

Figure 5 illustrates the response characteristics of a shortpass DTN to presentations of variable duration BEF tones (**Figures 5A,B**) and to pairs of BEF and BD tones varied in IPI (**Figures 5C,D**). This cell responded to 38 kHz tone durations between 1 and 4 ms, with a maximum of ca. 1.9 spikes per stimulus at a BD of 2 ms. The FSL of the cell also increased with stimulus duration and followed stimulus offset. When stimulated with pairs of BD tones that were randomly varied in IPI, the spike count in response to tone P2 became suppressed (**Figure 5D**) and both the FSL and LSL were delayed at short IPIs (**Figures 5E,F**). Eventually, the spike count and latencies recovered to within baseline values. The effect of neural inhibition can be seen in **Figure 5C** during and following the period of response overlap.

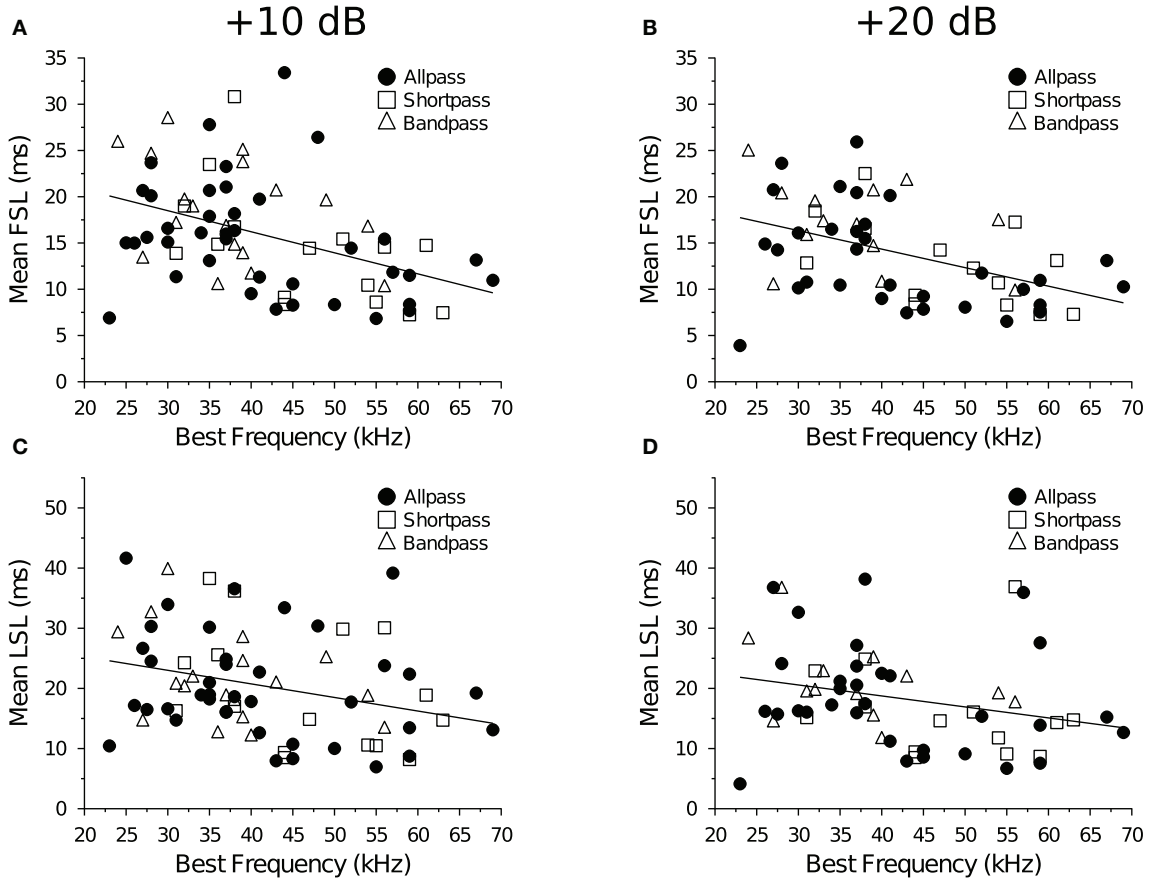

FIGURE 3 | Spike latency and tonotopy in the IC. (A,B) First-spike latency as a function of BEF. Neurons with lower BEFs had longer average FSLs at both **(A)** +10 dB ($R^2 = 0.18$, $p = 0.00019$) and **(B)** +20 dB ($R^2 = 0.21$, $p = 0.00031$) re threshold. **(C,D)** Last-spike Latency as a function of BEF. Neurons with lower BEFs had longer average LSLs at both **(C)** +10 dB ($R^2 = 0.087$, $p = 0.011$) and **(D)** +20 dB ($R^2 = 0.070$, $p = 0.044$) re threshold.

At an IPI of 2 ms, when the paired BD stimulus was effectively a single 4 ms tone with a brief amplitude modulation at its midpoint (caused by the fall-and-rise times of each stimulus), the leading inhibition evoked by each stimulus sums and this appears to decrease the spike count and lengthen the FSL (re P2). At IPIs from 4 to ca. 40 ms, the persistent inhibition evoked by P1 appears to interact with the leading inhibition evoked by P2 and this suppresses the spike count and delays the FSL of the response evoked by P2. The recovery time of the cell, as determined from the spike count ratio of response function, was 46 ms for both the short-to-long and long-to-short analysis methods. The recovery time of the cell, as determined from the FSL function (re P2), returned to within 1 SD of baseline at an IPI of 20 ms for both analysis methods (**Figure 5E**). The recovery time of the cell, as determined from the LSL function (re P2), returned to within 1 SD of baseline at an IPI of 14 ms with the short-to-long method, and we were unable to measure a recovery time with the long-to-short method because LSL did not deviate by >1 SD for two consecutive IPIs (**Figure 5F**). Notice again that subtle effects of persistent inhibition can be observed in the paired tone responses because the mean FSL and mean LSL (re P2) do not begin to overlap the mean FSL and mean LSL (re P1) until IPIs longer than the measured recovery times. Again, FSL takes longer to recover than LSL.

Figure 6 illustrates the response characteristics of an allpass neuron to presentations of 28 kHz BEF tones that were randomly varied in duration (**Figures 6A,B**) and to pairs of BEF tones varied in IPI (**Figures 6C,D**). For this cell, spike counts remained within 50% of the maximum response at all durations tested. Because FSL did not change with stimulus duration, the cell was characterized as onset responding. When the cell was stimulated with 3 ms tone pairs that were randomly varied in IPI (**Figure 6C**), a brief facilitatory response was observed at IPIs from 2 to 10 ms before the spike count (re P2) became suppressed at intermediate IPIs (**Figure 6D**). Paired tone stimulation only slightly delayed FSLs re P2 (**Figure 6E**), and LSLs re P2 were unaffected (**Figure 6F**). The recovery time of the cell, as determined from the spike count ratio of response function, was 54 ms using both the short-to-long and long-to-short analysis methods. The recovery time of the cell, as determined from the FSL function (re P2), returned to within 1 SD of baseline at an IPI of 14 ms using the short-to-long method, and at 22 ms using the long-to-short method (**Figure 6E**). We were unable to measure a recovery time with LSL because it did not deviate by >1 SD at any IPI tested (**Figure 6F**).

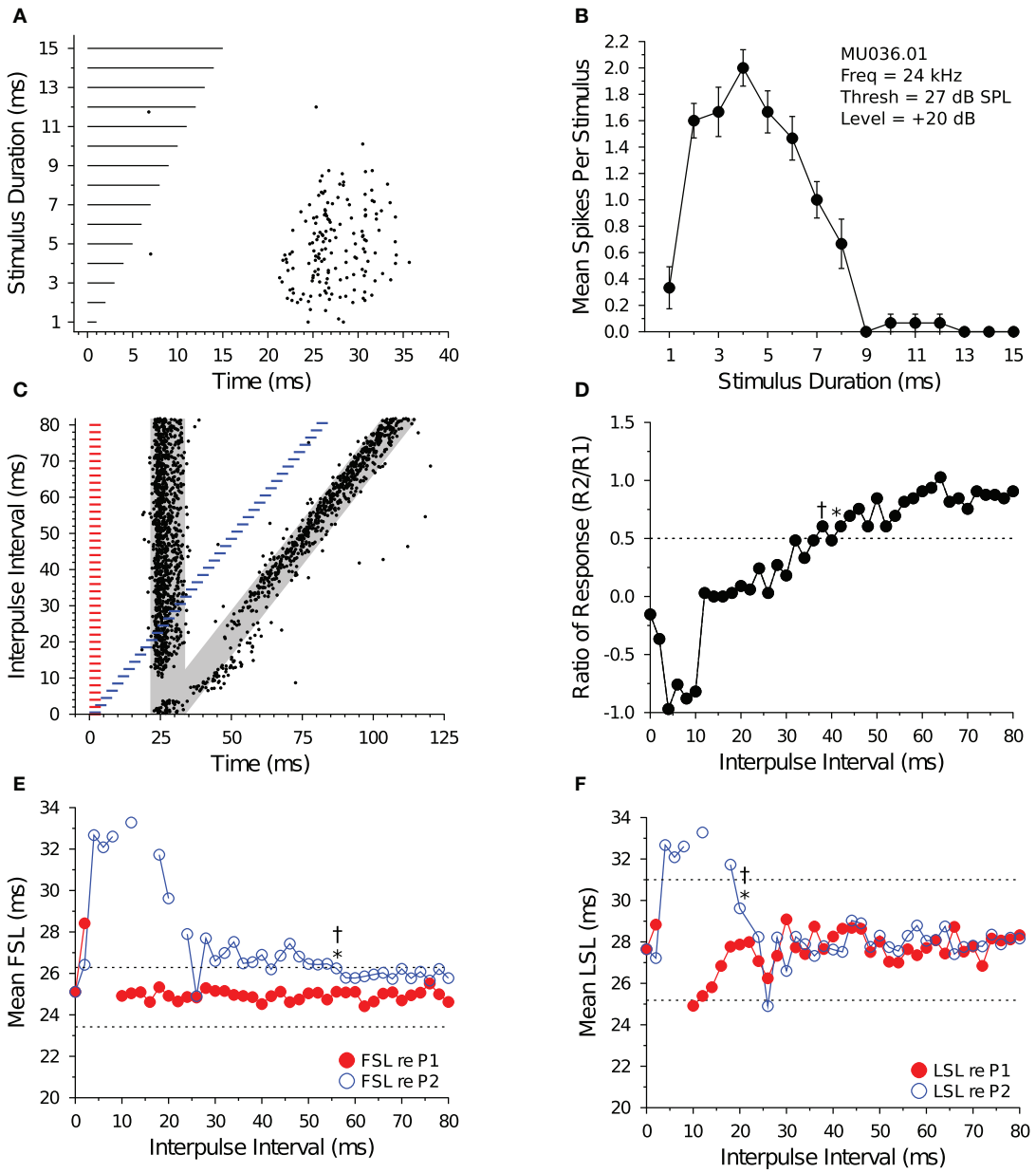

FIGURE 4 | Response and recovery in a bandpass DTN. (A) Dot raster display of spiking in a bandpass DTN in response to variable duration BEF tones. **(B)** Mean ± SE spikes per stimulus as a function of stimulus duration. This cell had a BD of 4 ms. **(C)** Dot raster display illustrating spiking in response to pairs of BD tones presented at variable IPIs. The *shaded gray regions* illustrate the customized P1 and P2 analysis windows bounded by ±2 SDs from the baseline FSL and baseline LSL of the cell (see **Figure 1**). **(D)** Spike count ratio of response as a function of IPI. Evoked spiking in response to P2 recovers to within 50% of baseline (*dotted line*) in response to P1 at 42 ms using the short-to-long method (*), and at 38 ms using the long-to-short method (†). **(E)** Mean FSL and **(F)** mean LSL as a function of IPI for responses evoked by P1 (red closed symbols) and P2 (blue open symbols). **(E)** The cell's FSL (re P2) returns to within 1 SD of baseline at 56 ms using both the short-to-long and long-to-short methods, whereas **(F)** the LSL (re P2) returns to within 1 SD of baseline at 20 ms using both the short-to-long and long-to-short methods. Latencies determined after windowing responses with the cell-specific P1 and P2 analysis windows. *Dotted lines* represent ±1 SD relative to baseline latency (re P1). Missing values represent IPIs where no spikes fell into the analysis window. **(A,B)** MU036.01.06: BEF, 24 kHz; threshold, 27 dB SPL; amplitude +20 dB re threshold; 15 repetitions per stimulus. **(C–F)** MU036.01.31: BEF, 24 kHz; threshold, 27 dB SPL; amplitude +20 dB re threshold; 20 repetitions per IPI step.

3.3. RECOVERY CYCLES MEASURED WITH SPIKE COUNTS AND LATENCIES

For the majority of cells and data files (92 of 132 files; 70%), recovery cycle times measured with the short-to-long and long-to-short analysis algorithms yielded identical values. Indeed, recovery times determined with the two algorithms were highly correlated at both +10 dB (**Figure 7**) and +20 dB (data not shown) above threshold for spike counts

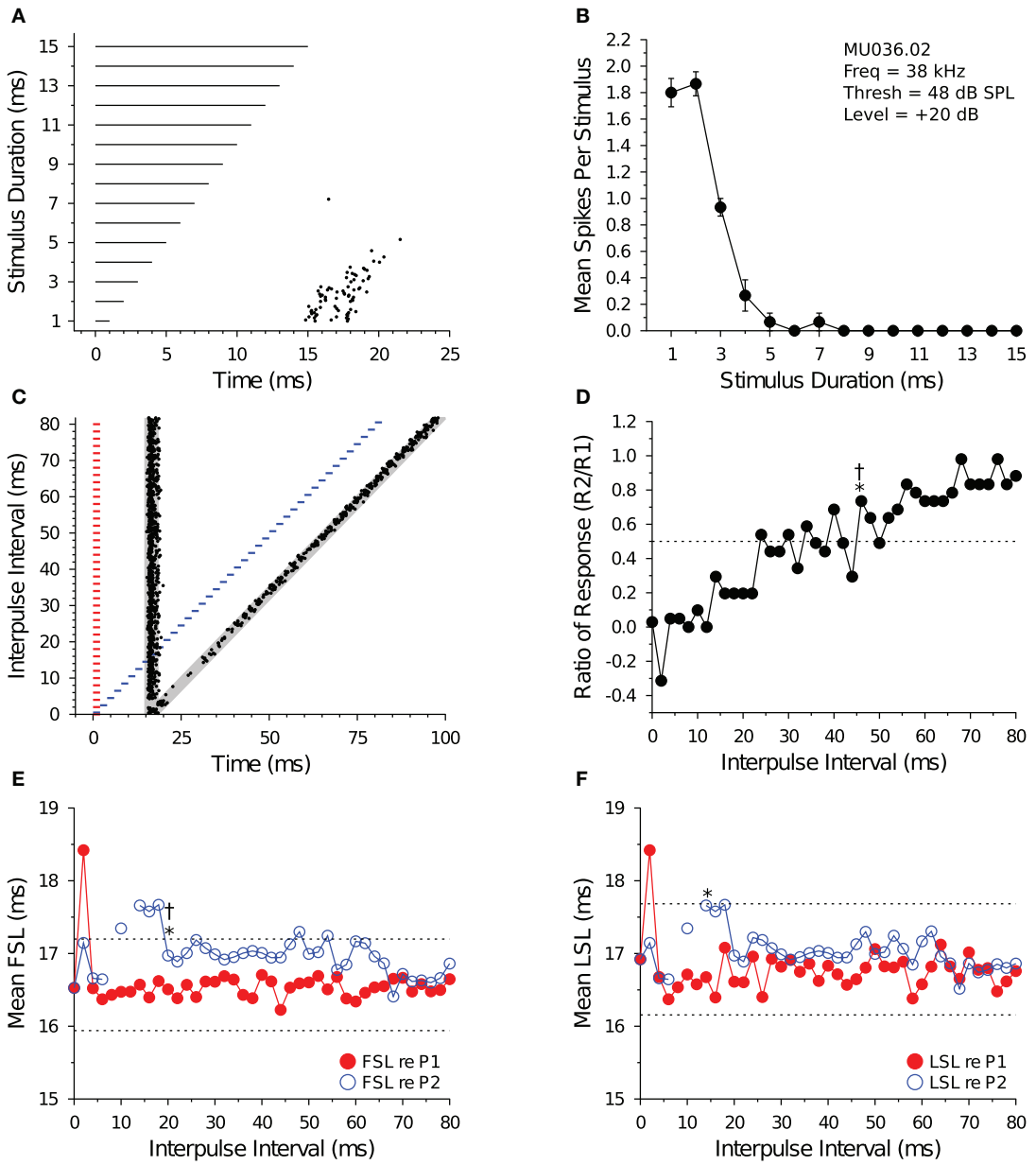

FIGURE 5 | Response and recovery in a shortpass DTN. (A) Dot raster display of spiking in a shortpass DTN in response to variable duration BEF tones. **(B)** Mean ± SE spikes per stimulus as a function of stimulus duration. This cell had a BD of 2 ms. **(C)** Dot raster display illustrating spiking in response to pairs of BD tones presented at variable IPIs. The *shaded gray regions* illustrate the customized P1 and P2 analysis windows bounded by ±2 SDs from the baseline FSL and baseline LSL of the cell (see **Figure 1**). **(D)** Spike count ratio of response as a function of IPI. Spiking in response to tone P2 recovers to within 50% of baseline (*dotted line*) in response to P1 at 46 ms using both the short-to-long (*) and long-to-short (†) method. **(E)** Mean FSL and **(F)** mean LSL as a function of IPI for responses evoked by tone P1 (red closed symbols) and tone P2 (blue open symbols). **(E)** The cell's FSL (re P2) returns to within 1 SD of baseline at 20 ms using both the short-to-long and long-to-short methods, whereas **(F)** the LSL (re P2) returns to within 1 SD of baseline at 14 ms using the short-to-long method. No recovery time value was obtained with the long-to-short method because there was not two consecutive IPIs where the function deviated by >1 SD from the baseline LSL. Latencies determined after windowing spikes with the cell-specific P1 and P2 analysis windows. *Dotted lines* represent ±1 SD relative to baseline latency (re P1). Missing values represent IPIs where no spikes fell into the analysis window. **(A,B)** MU036.02.06: BEF, 38 kHz; threshold, 48 dB SPL; amplitude +20 dB re threshold; 15 repetitions per stimulus. **(C–F)** MU036.02.12: BEF, 38 kHz; threshold, 48 dB SPL; amplitude +20 dB re threshold; 20 repetitions per IPI step.

(**Figure 7A**), FSL (**Figure 7B**) and LSL measures (**Figure 7C**). Of the remaining 40 files that were not in agreement, 15 had recovery times that differed by ≤4 ms (absolute value). When the two methods for determining recovery times did not agree, the long-to-short method generally yielded longer values than the short-to-long method, as evidenced by the number of points falling above the unity lines in **Figure 7**.

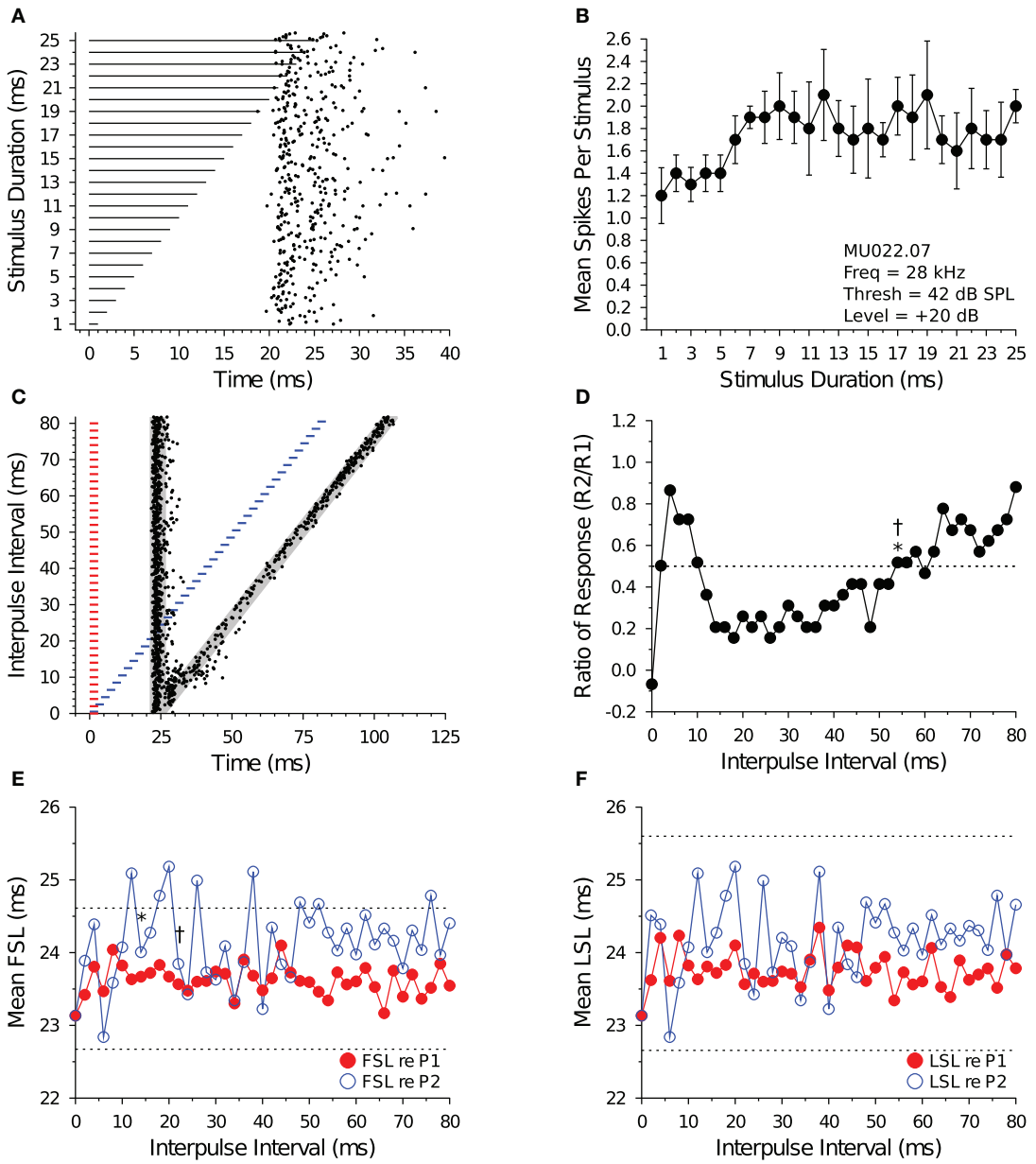

FIGURE 6 | Response and recovery in a non-DTN. (A) Dot raster display of spiking in an allpass neuron in response to variable duration BEF tones. **(B)** Mean ± SE spikes per stimulus as a function of stimulus duration. By definition, allpass neurons do not have a BD. **(C)** Dot raster display illustrating spiking in response to pairs of 3 ms tones presented at variable IPIs. The *shaded gray regions* illustrate the customized P1 and P2 analysis windows bounded by ±2 SDs from the baseline FSL and baseline LSL of the cell (see **Figure 1**). **(D)** Spike count ratio of response as a function of IPI. Spiking in response to tone P2 recovers to within 50% of baseline (*dotted line*) in response to P1 at 54 ms using both the short-to-long (*) and long-to-short (†) method. **(E)** Mean FSL and **(F)** mean LSL as a function of IPI for responses evoked by tone P1 (red closed symbols) and tone P2 (blue open symbols). **(E)** The cell's FSL (re P2) returns to within 1 SD of baseline at 14 ms using the short-to-long method and at 22 ms using the long-to-short method, whereas **(F)** the LSL (re P2) function did not deviate by >1 SD from baseline at any IPI, hence no recovery time value was obtained. Latencies determined after windowing spikes with the cell-specific P1 and P2 analysis windows. *Dotted lines* represent ±1 SD relative to baseline latency (re P1). **(A,B)** MU036.02.06: BEF, 38 kHz; threshold, 48 dB SPL; amplitude +20 dB re threshold; 15 repetitions per stimulus. **(C–F)** MU036.02.12: BEF, 38 kHz; threshold, 48 dB SPL; amplitude +20 dB re threshold; 20 repetitions per IPI step.

Table 2 lists the mean ± SE 50% spike count recovery times determined with both analysis algorithms as a function of neural response class and level above threshold. Using the short-to-long method, non-duration-selective neurons and shortpass DTNs had the shortest recovery times, and bandpass DTNs had significantly longer recovery times (short-to-long spike recovery time: $F = 4.31$, $p = 0.017$). When we analyzed the data measured with the long-to-short technique, the differences in recovery cycle

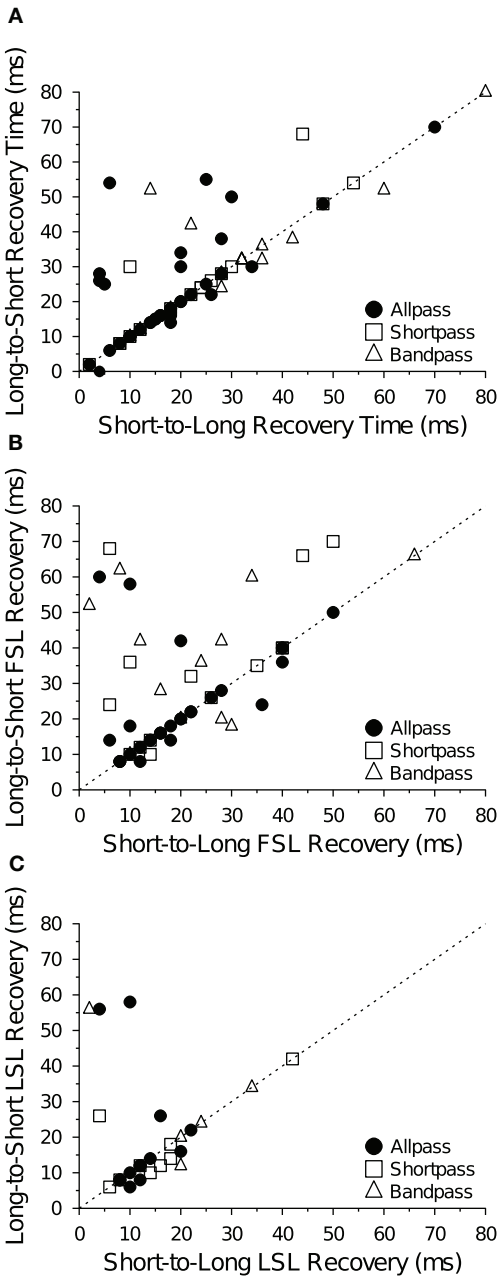

FIGURE 7 | Comparison of recovery time measures. Each panel shows recovery times of IC neurons at +10 dB (re threshold) measured with the short-to-long (abscissa) and long-to-short (ordinate) analysis methods based on **(A)** spike count, **(B)** FSL and **(C)** LSL criteria. The two methods are in agreement when points fall along the *dotted unity line* $y = x$. Recovery times were positively correlated at +10 dB (A: $R^2 = 0.77$, $p \ll 0.001$; B: $R^2 = 0.30$, $p \ll 0.001$; C: $R^2 = 0.22$, $p = 0.0089$) and at +20 dB (data not shown) above threshold. The sample size (n) and number of points that fall above, below (but not on) the unity line are: **(A)** $n = 73$, 14 above, 9 below; **(B)** $n = 57$, 19 above, 7 below; and **(C)** $n = 30$, 6 above, 7 below.

Table 2 | Mean ± SE spike count recovery time (and range) as a function of cell type and level above threshold measured with the short-to-long and long-to-short analysis methods.

Cell type	*n*	Recovery time (ms) +10 dB	*n*	Recovery time (ms) +20 dB
SHORT-TO-LONG METHOD				
Allpass	39	20.13 ± 2.93 (2–100)	32	17.50 ± 2.14 (0–54)
Bandpass	18	34.83 ± 5.82 (10–105)	13	23.54 ± 3.23 (6–42)
Shortpass	16	23.00 ± 3.81 (2–54)	14	18.79 ± 3.87 (2–54)
LONG-TO-SHORT METHOD				
Allpass	39	25.97 ± 4.05 (0–148)	32	20.91 ± 3.17 (0–76)
Bandpass	18	36.94 ± 5.64 (10–105)	13	26.15 ± 3.70 (6–44)
Shortpass	16	25.75 ± 4.49 (2–68)	14	20.21 ± 4.00 (2–50)

Recovery measured as the IPI where the spike count in response to P2 was ≥50% of the baseline spike count (re P1).

Table 3 | Mean ± SE first-spike latency (FSL) recovery time (and range) as a function of cell type and level above threshold, measured with the short-to-long and long-to-short analysis methods.

Cell type	*n*	Recovery time (ms) +10 dB	*n*	Recovery time (ms) +20 dB
SHORT-TO-LONG METHOD				
Allpass	36	20.64 ± 2.35 (4–58)	28	17.50 ± 2.05 (5–42)
Bandpass	17	23.65 ± 4.26 (2–66)	13	23.08 ± 5.36 (4–68)
Shortpass	16	21.56 ± 3.85 (4–50)	14	26.71 ± 6.40 (4–80)
LONG-TO-SHORT METHOD				
Allpass	29	23.52 ± 2.76 (8–60)	21	23.48 ± 2.52 (8–52)
Bandpass	14	41.14 ± 7.35 (10–110)	11	26.00 ± 5.67 (8–64)
Shortpass	14	34.50 ± 5.62 (10–70)	12	33.83 ± 6.76 (6–72)

Recovery time measured as the IPI where the FSL in response to P2 returned to within 1 SD of the baseline FSL (re P1).

Table 4 | Mean ± SE last-spike latency (LSL) recovery time (and range) as a function of cell type and level above threshold, measured with the short-to-long and long-to-short analysis methods.

Cell type	*n*	Recovery time (ms) +10 dB	*n*	Recovery time (ms) +20 dB
SHORT-TO-LONG METHOD				
Allpass	20	13.65 ± 1.90 (4–45)	15	11.33 ± 2.09 (2–34)
Bandpass	13	18.08 ± 3.29 (2–45)	9	17.33 ± 3.46 (4–40)
Shortpass	9	15.33 ± 3.74 (4–42)	9	13.11 ± 1.74 (6–20)
LONG-TO-SHORT METHOD				
Allpass	15	18.40 ± 4.29 (6–58)	7	21.29 ± 5.45 (10–52)
Bandpass	6	42.67 ± 14.82 (12–110)	7	20.57 ± 4.31 (4–40)
Shortpass	9	16.44 ± 3.75 (6–42)	7	14.29 ± 4.52 (6–40)

Recovery time measured as the IPI where the LSL in response to P2 returned to within 1 SD of the baseline LSL (re P1).

times across neural response classes were no longer significant (long-to-short spike recovery time: $F = 1.68$, $p = 0.1942$); however, a statistically significant difference in recovery cycle times between neural response classes re-emerged when the data were re-analyzed using the average recovery cycle time of the short-to-long and long-to-short algorithms (average spike recovery time: $F = 3.23$, $p = 0.046$). There was no effect of tone amplitude (level above threshold) on recovery times measured with

either spike count algorithm (short-to-long: $F = 0.063$, $p = 0.80$; long-to-short: $F = 0.20$ $p = 0.65$).

Tables 3 and **4** list the mean ± SE spike latency recovery times as a function of neural response class and level above threshold using the short-to-long and the long-to-short analysis methods. Overall, there was no main effect of response class or tone amplitude on FSL (**Table 3**) or LSL (**Table 4**) recovery times. Bandpass DTNs had significantly longer FSL recovery times with the long-to-short method (long-to-short FSL recovery: $F = 3.90$ $p = 0.026$). For the remainder of this paper, we present recovery times as the average of the short-to-long and long-to-short analysis algorithms for both spike counts and spike latencies unless we were unable to obtain an average, in which case the algorithm that provided a value was used.

Previous studies on the recovery cycle times of auditory neurons have used only spike counts as the dependent measure (Suga, 1964; Friend et al., 1966; Suga and Schlegel, 1973; Pollak et al., 1977b; Lu et al., 1997). In our dataset, we were able to measure recovery times with a 50% change in spike count for all 132 data files at +10 dB and +20 dB (re threshold). And for a majority of cells we were able to measure recovery time with a 1 SD change in FSL ($n = 124$ files) and LSL ($n = 75$ files). Recovery times measured with a spike count criterion were positively correlated with recovery times measured with a FSL (**Figures 8A,B**) and LSL (**Figures 8C,D**) criterion at both +10 dB and +20 dB (re threshold). There was also a positive correlation between recovery times measured with a FSL and LSL criterion at +10 dB (**Figure 8E**) and +20 dB above threshold (**Figure 8F**). Upon closer inspection, we found no obvious bias for recovery times measured with spike counts and FSLs because similar numbers of points fell above and below the unity lines at both levels above threshold (**Figures 8A,B**); however, recovery times measured with spike counts and FSLs tended to be longer than those measured with LSLs, as evidenced by a greater number of points falling below the unity lines in the scatterplots (**Figures 8C–E**).

In a further analysis we compared recovery times measured with spike counts, FSLs and LSLs but only in cells that provided values for all three measures (**Table 5**). Using this subset of data, the positive correlation between spike count and FSL recovery times remained and became stronger ($R^2 = 0.27$, $p < 0.001$, $n = 42$). Measuring recovery times with a LSL criterion was a limiting factor for inclusion in this restricted subset of data, hence the correlations between spike count and LSL recovery times and between LSL and FSL recovery times were identical to those in **Figures 8C–F**. Using a repeated measures ANOVA, we found a significant main effect of the response parameter used to measure neural recovery (spike count, FSL, LSL: $F = 15.02$, $p \ll 0.001$). Recovery times determined with a 1 SD change in LSL were significantly shorter than recovery times measured with a 50% change in spike count or with a 1 SD change in FSL (**Table 5**). Moreover, there was now a significant main effect of stimulus amplitude, with recovery times decreasing at the higher stimulus level above threshold (+10 dB and +20 dB: $F = 5.28$, $p = 0.024$). There was no significant interaction between any main effects (analyses not shown).

3.4. RECOVERY CYCLES AND RESPONSE PROPERTIES

At +10 dB (re threshold), stimulus duration was not correlated with recovery cycle time, regardless of cell type (data not shown), but at +20 dB there was a positive correlation between stimulus duration and the spike count recovery time (**Figure 9A**). There was no correlation between stimulus duration and FSL recovery time (**Figure 9B**) or LSL recovery time (**Figure 9C**) at either level above threshold. When allpass neurons were removed from the analysis there was still no correlation between BD and the spike count recovery cycle time at +10 dB ($R^2 = 0.023$, $p = 0.39$, $n = 34$), and the positive correlation at +20 dB became stronger ($R^2 = 0.16$, $p = 0.044$, $n = 26$). Neural BEFs did not correlate with spike count recovery times at either +10 dB ($R^2 = 0.0019$, $p = 0.72$) or +20 dB ($R^2 = 0.0095$, $p = 0.46$) above threshold (data not shown). There was also no correlation between the spike count recovery time of a cell and its baseline spike count at both +10 dB ($R^2 = 0.019$, $p = 0.25$) and +20 dB ($R^2 = 0.00024$, $p = 0.91$) above threshold (data not shown).

Neurons with short FSLs typically had short spike count recovery times, and this result held true at both +10 dB (**Figure 10A**) and +20 dB above threshold (data not shown). At +10 dB (re threshold), neurons with short FSLs also had short FSL (**Figure 10B**) and LSL recovery times (**Figure 10C**), but at +20 dB (re threshold) the correlations were no longer significant (data not shown).

4. DISCUSSION

4.1. RECOVERY CYCLES AND SPIKE LATENCIES

Spike counts and latencies are basic response properties commonly reported in electrophysiological papers. And while changes in both can be used to assess response features, such as the onset and duration of synaptic inhibition in DTNs (Faure et al., 2003) or the presence of neuromodulators in midbrain microcircuits (Hurley and Pollak, 2005), often studies report only a change in spike count even though numerous electrophysiological and computational papers have shown that spike latency is as (if not more) important at encoding stimulus specific and related information at all levels of the central auditory system (Middlebrooks et al., 1994; Klug et al., 2000; Brugge et al., 2001; Furukawa and Middlebrooks, 2002; Heil, 2004; Nelken et al., 2005). Fontaine and Peremans (2009) argue that a spike-timing code (as opposed to a spike rate or count code) is more appropriate for processing the short duration echolocation signals emitted by bats. Neural FSLs may also be used as an alternative to spike counts/rates when rapid responses are required (Grothe and Klump, 2000; VanRullen et al., 2005), and are critical to mechanisms underlying sound localization (Joris et al., 1998).

In this study, we compared recovery cycle times measured with spike counts and spike latencies. We do not know which measures are more pertinent for assessing neural response recovery and/or its relevance to perception because both spike count and timing codes can be used independently to represent stimulus features (VanRullen et al., 2005). The relative importance, if any, will depend on which parameter(s) is(are) most important for encoding and transmitting stimulus specific information in the central nervous system. Because our analyses employed

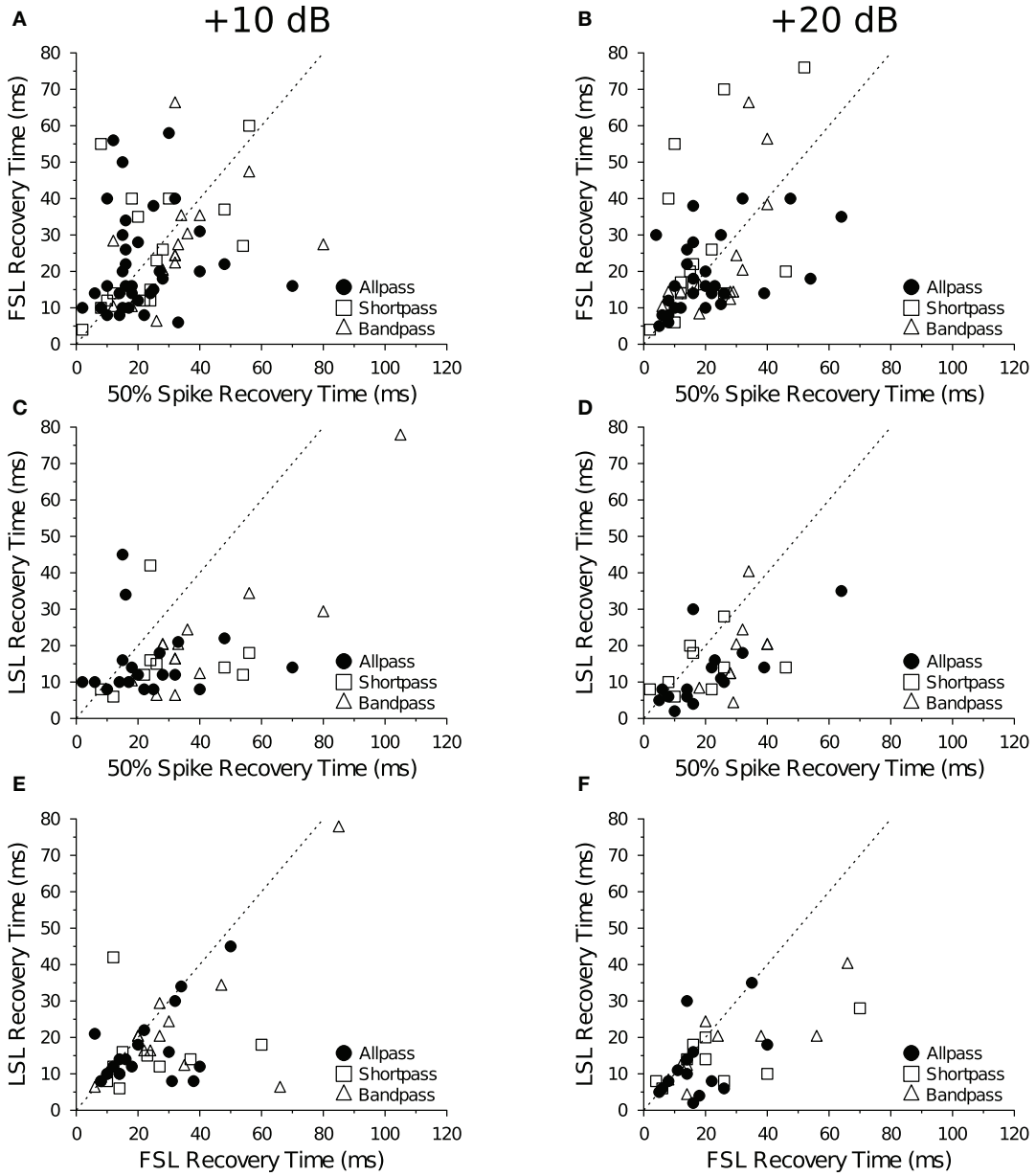

FIGURE 8 | Comparison of mean recovery times measured with spike counts and spike latencies. Each panel shows the average recovery times of IC neurons at +10 dB (left) and +20 dB (right) re threshold. Recovery times are in agreement when points fall along the *dotted unity line* $y = x$. **(A,B)** There was a positive correlation between the mean 50% spike count and mean FSL recovery time in DTNs and non-DTNs at **(A)** +10 dB ($R^2 = 0.17$, $p < 0.001$) and **(B)** +20 dB ($R^2 = 0.21$, $p < 0.001$) re threshold. **(C,D)** There was a positive correlation between the mean spike count and mean LSL recovery time at **(C)** +10 dB ($R^2 = 0.28$, $p < 0.001$) and **(D)** +20 dB ($R^2 = 0.35$, $p < 0.001$) re threshold. **(E,F)** There was a positive correlation between FSL and LSL recovery times at **(E)** +10 dB ($R^2 = 0.32$, $p \ll 0.001$) and **(F)** +20 dB ($R^2 = 0.41$, $p \ll 0.001$) re threshold. The sample size (n) and number of points that fall above, below (but not on) the unity line are: **(A)** $n = 69$, 28 above, 39 below; **(B)** $n = 55$, 26 above, 24 below; **(C)** $n = 42$, 6 above, 35 below; **(D)** $n = 34$, 8 above, 25 below; **(E)** $n = 42$, 4 above, 25 below; and **(F)** $n = 34$, 4 above, 17 below.

dissimilar criteria for assessing response recovery (50% spike count *versus* 1 SD latency change), the sets of results may not be directly comparable. Despite this caveat, recovery times measured with spike counts were reasonably well correlated with those measured with spike latencies (**Figure 8**). Nevertheless, some neurons with small spike count recovery times had large spike latency recovery times (and vice versa), suggesting that some factors governing spike count recovery differ from those governing spike latency recovery. When we restricted our analysis and examined only those cells that provided recovery times with spike count, FSL and LSL, the correlations between the recovery times remained (or strengthened). Recovery times measured with LSL were significantly shorter than those measured with spike counts and FSL in the same cells (**Table 5**). Altogether, the

Table 5 | Mean ± SE recovery times as a function of the measured recovery parameter and level above threshold.

Recovery parameter	Recovery time (ms) +10 dB	Recovery time (ms) +20 dB
Spike count	33.38 ± 3.83	22.88 ± 2.30
FSL	25.14 ± 2.64	21.74 ± 2.82
LSL	17.99 ± 2.05	13.91 ± 1.61

Only cells with recovery times measured with all three parameters were included (n = 42: +10 dB; n = 34: +20 dB).

results suggest that spike latencies can be employed as an alternative measure of response recovery. We encourage researchers to continue developing additional analyses that exploit changes in spike latency.

Inhibition is thought to play a role in determining FSL and the duration of recovery times of central auditory neurons. Bicucculine ($GABA_A$ receptor antagonist) application shortens the recovery times of most IC neurons (Lu et al., 1997; Zhou and Jen, 2003) and also shorten FSLs (Park and Pollak, 1993; Lu et al., 1997). The effect of inhibition on FSL has been disputed. It has been suggested that a reduction in FSL can be attributed to offset responding neurons changing to onset responding neurons when inhibition is removed or its effects are blocked because this causes FSL to shorten by the duration of the stimulus (Fuzessery et al., 2003). Intracellular recordings from the IC of the big brown bat reveal the presence of an onset-evoked hyperpolarization in the majority of units studied (Covey et al., 1996; Voytenko and Galazyuk, 2008), suggesting that onset-evoked inhibition plays a role in governing first-spike timing. In this study we found that neurons with shorter FSLs had shorter recovery times, a relationship that also exists for sound localizing neurons in the IC of the awake rabbit (Fitzpatrick et al., 1995). Together, these findings support the hypothesis that factors influencing the duration of recovery cycles and the timing of FSLs are related.

4.2. EFFECT OF STIMULUS AMPLITUDE AND BEF ON FSL AND RECOVERY TIMES

As in previous studies, we found that FSLs of DTNs and non-DTNs in the IC of the bat decreased with increasing electrode depth (Park and Pollak, 1993; Fuzessery et al., 2003) and increasing BEFs (Haplea et al., 1994; Fuzessery et al., 2003). Neural FSLs also decreased with increasing stimulus amplitude (**Table 3**; Heil, 2004; Tan et al., 2008). We found no correlation between neuronal BEFs and spike count recovery times at either +10 dB or +20 dB (re threshold). This result differs from a previous study that found a strong negative correlation between these variables in the IC of the bat (Zhou and Jen, 2003). Gross electrode recordings from the bat's auditory brainstem revealed that stimulation with higher acoustic frequencies resulted in faster response recovery (Grinnell, 1963). Given that FSL is also negatively correlated with BEF (**Figure 3**; Haplea et al., 1994; Fuzessery et al., 2003), if a negative correlation exists between BEF and spike count recovery time then we might expect a similar correlation between FSL and spike count recovery time. In the present study, we were unable to detect a correlation between BEF and the spike count recovery time at either level above threshold. Therefore, the positive relationship that we observed between spike count recovery time and FSL cannot be explained by a covariance with BEF.

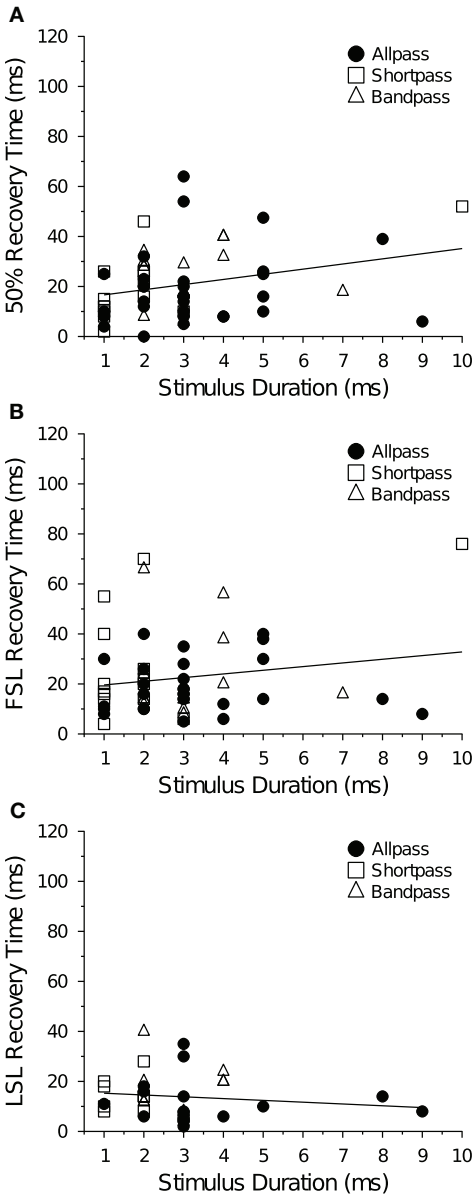

FIGURE 9 | Mean recovery time as a function of stimulus duration at +20 dB above threshold. (A) Average 50% spike count recovery times as a function of paired tone stimulus duration. Spike count recovery times were positively correlated with stimulus duration ($R^2 = 0.081$, $p = 0.029$). **(B)** Average FSL and **(C)** average LSL recovery times as a function of paired tone stimulus duration. Stimulus duration was not correlated with FSL ($R^2 = 0.030$, $p = 0.20$) or LSL recovery times ($R^2 = 0.012$, $p = 0.54$). Spike count, FSL and LSL recovery times were also not correlated with stimulus duration at +10 dB (re threshold). For DTNs stimulus duration was set to BD, whereas for allpass neurons stimulus duration was randomly chosen between 1 and 9 ms.

Some studies have used pairs of unequal amplitude tones to determine the recovery cycle characteristics of IC neurons. For

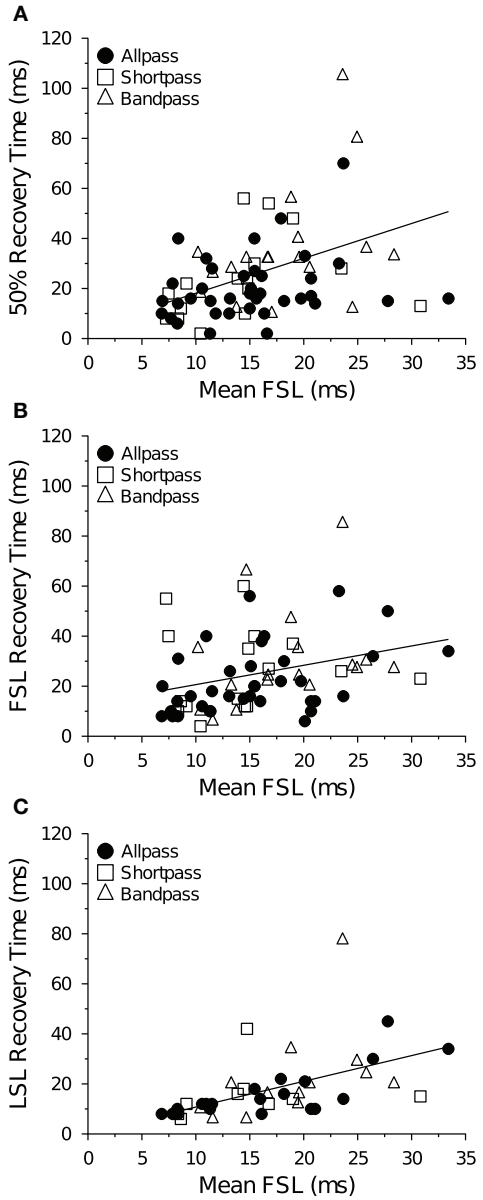

FIGURE 10 | Mean recovery time as a function of FSL at +10 dB above threshold. (A) Average 50% spike count recovery times as a function of FSL. Neurons with longer FSLs had longer spike count recovery times ($R^2 = 0.16$, $p < 0.001$, $n = 73$). **(B)** Average FSL and **(C)** average LSL recovery times as a function of FSL. Neurons with longer FSLs had longer FSL ($R^2 = 0.089$, $p = 0.013$, $n = 69$) and LSL recovery times ($R^2 = 0.28$, $p < 0.001$, $n = 42$). Spike count recovery times were also correlated with mean FSL at +20 dB (re threshold), but there was no correlation with FSL or LSL recovery times and mean FSL at +20 dB (re threhsold).

example, Friend et al. (1966) found that recovery times shortened as the intensity of stimulus P1 was decreased relative to P2. This result is consistent with the hypothesis that inhibition evoked by P1 was easier to overcome by increased excitation evoked by the relatively higher intensity P2 stimulus. Moreover, the effect of stimulus amplitude on spike count recovery times co-varies with stimulus duration (Wang et al., 2008, 2010). Using gross electrode recordings in the bat brainstem in response to equal amplitude tones, Grinnell (1963) reported more rapid neural recovery for stimuli of reduced intensity—a finding that is opposite to our results. In the present study, recovery times in the population of DTNs and non-DTNs remained stable over a 10 dB change in SPL in response to pairs of equal amplitude tones (**Tables 2–4**); however, when we restricted our analysis to look only at those cells with recovery times measured with spike count and latency criteria, recovery times shortened from +10 to +20 dB (re threshold) regardless of the recovery parameter examined (**Table 5**). This suggests that neural excitation may have increased relative to inhibition at higher levels above threshold. Additional studies employing a wider range of stimulus amplitudes are needed to determine if the recovery times of DTNs are tolerant over the same dynamic range (40–50 dB) as the amplitude tolerance of duration tuning (Zhou and Jen, 2001; Fremouw et al., 2005).

4.3. SPATIAL MAPPING OF BEST DURATION

We found no correlation between neuronal BD and the depth of the recording electrode in the population of DTNs tested (**Figure 2**). This result agrees with a number of previous studies that found no spatial organization of DTNs in the ICc of the bat (Pinheiro et al., 1991; Ehrlich et al., 1997; Faure et al., 2003; Luo et al., 2008). In contrast, other studies have reported a significant positive correlation between BD and BEF (Jen and Wu, 2006; Wu and Jen, 2006, 2008b), suggesting the possibility that the ICc of the bat contains a spatial map of duration tuning. In the present study, we found a significant negative correlation between BD and BEF (**Figure 2**)—a relationship in the opposite direction of three previous reports. Given the inconsistency of the result within and across laboratories, we conclude there is no strong evidence to support the hypothesis that a spatial map of duration tuning exists in the IC of the bat.

4.4. BIOLOGICAL SIGNIFICANCE OF RECOVERY TIMES

Recovery cycle times of IC neurons in the cat (Yin, 1994; Litovsky and Yin, 1998a,b), rabbit (Fitzpatrick et al., 1995, 1999) and barn owl (Keller and Takahashi, 1996) have been suggested as a potential neural mechanism underlying the precedence effect for humans listening in reverberant environments (for review, see Litovsky et al., 1999). The precedence effect is a binaural psychoacoustical phenomenon that describes the sound localization performance of participants listening to pairs of sounds separated by an interval (e.g., pulse and reflected echo). When two sounds have a brief IPI (<1 ms; Wallach et al., 1949), participants detect a single sound located in a position midway between the sources (i.e., summing localization). When two sounds are presented with a longer delay (1–5 ms IPI for single clicks; ≤35–70 ms IPI for other complex sounds; Wallach et al., 1949), participants localize the source in the direction of the first sound. Because the first arriving wavefront takes precedence in sound localization, the precedence effect is also known as the law of the first wavefront. Recovery cycle times measured from auditory neurons in the ICc of the bat (**Tables 2–4**) broadly correlate with the range of IPIs over which the precedence effect occurs in

humans. A behavioural correlate of the precedence effect has been studied in cats (3–16 ms; Cranford and Oberholtzer, 1976), rats (0.25–16 ms; Kelly, 1974), and crickets (4–75 ms; Wyttenbach and Hoy, 1993). While it seems reasonable to assume that echolocating bats also experience a precedence effect during acoustic orientation and prey detection, psychoacoustical experiments on two species of gleaning bats suggest they may not (Schuchmann et al., 2006).

Our results demonstrate that recovery cycle times of midbrain auditory neurons in the bat, which have been explored mainly in the context of echolocation (for review, see Jen et al., 2012), are quite similar to those measured from the IC of other vertebrates (Yin, 1994; Fitzpatrick et al., 1995; Keller and Takahashi, 1996). This suggests that factors governing the recovery cycle times of central auditory neurons are similar in echolocating and non-echolocating species. It also reinforces the utility of bats as an animal model for understanding general principles of mammalian hearing and auditory physiology despite the fact that bats echolocate and are "hearing specialists." The function(s) of DTNs to hearing and echolocation is(are) still unknown; however, the range of neural BDs and the temporal bandwidth of duration tuning are generally matched to the range of vocalization durations in echolocating bats (Sayegh et al., 2011). If DTNs play a direct role in echolocation, then one might predict they should exhibit short recovery times so that the same neuron could respond to both loud outgoing vocalizations and later returning echoes. Alternatively, owing to the importance of leading and persistent inhibition in creating temporally selective neural responses, one could also predict that the inhibition evoked by each pulse in a paired tone stimulus would temporally interact and sum, resulting in DTNs exhibiting longer recovery cycle times than non-DTNs. Our results support the latter prediction: bandpass DTNs had significantly longer recovery times than shortpass DTNs and allpass neurons. In contrast, a recent study examining auditory neurons in the IC of the echolocating bat *Pipistrellus abramus* found no significant difference in the recovery times of DTNs and allpass neurons (Wang et al., 2010).

If DTNs function in echo ranging, then the recovery cycle time would play an important role in determining the minimum target distance over which a neuron could respond. The recovery time can be viewed as equivalent to the two-way travel time of the bat's outgoing sound and returning echo. Assuming a recovery cycle time for a DTN of 36 ms, this would be equivalent to a one-way travel time of 18 ms (speed of sound in air = 344 mm/ms) and would correspond to a target distance of 6.19 m (344 mm/ms*18 ms). Neurons with shorter (longer) recovery cycles would have shorter (longer) minimum target detection distances because these cells could respond more rapidly (slowly) to successive sound presentations such as pulse-echo pairs. For example, a neuron with a recovery time of 2 ms could fire action potentials in response to both the pulse and echo at a minimum distance of 34.4 cm (344 mm/ms*1 ms), whereas a neuron with a recovery time of 100 ms could encode a minimum target distance of 17.2 m (344 mm/ms*50 ms).

In theory, the recovery time of a DTN, in combination with BD, could determine perceptual integration time and cause a cell to be tuned to detect small pulse-echo delays and short target distances. For example, assume a bandpass DTN with a BD of 5 ms is stimulated with pulse and echo biosonar sounds lasting 2 ms each. Although the cell may not spike in response to either the pulse (P1) or the echo (P2) when presented alone, simply because the durations of both signals are shorter than the cell's BD, the neuron might respond to the stimulus pair if presented at a short gap of 1 ms representing a target at 17.2 cm (344 mm/ms*0.5 ms). In this case, the DTN may respond to the pulse-echo pair as a single, unified (i.e., fused) stimulus because the combined 2 ms pulse + 1 ms gap + 2 ms echo duration is close to the neuronal BD (Sayegh et al., 2011). By extending this line of reasoning we would predict that neurons with short BDs would be tuned to short target distances, and neurons with longer BDs would be tuned to longer target distances. This is because cells with long BDs may be able to tolerate a wider range of silence between pulse-echo pairs at sub-optimal durations. In support of this novel hypothesis, which is distinct but not mutually exclusive from the idea that DTNs are tuned to the duration of single relevant sounds, we found a weak but positive correlation between stimulus duration and spike count recovery time at +20 dB above threshold (**Figure 9B**), but there was no correlation between stimulus duration and spike latency recovery times. Grinnell (1963) observed an increase in recovery time as the duration of the P1 (but not P2) stimulus increased. Jen et al. (2012) reported that spike count recovery times of DTNs increased with the duration of the pulse-echo stimulus; however, this effect does not hold for equal amplitude stimulus pairs and occurs only in some neurons at specific pulse-echo amplitude differences (Wang et al., 2008). In contrast, Pollak et al. (1977a) found recovery times of IC auditory neurons increased at short (<2 ms) stimulus durations. These conflicting reports point to the need for future studies to test the hypothesis that DTNs can respond to pairs of tones presented at sub-optimal durations (i.e., not at BD) and separated by relatively short gaps of silence.

In a small subset of cells we observed a brief facilitation in the spike count ratio of recovery function at short IPIs (**Figures 6C,D**). These neurons could be delay-tuned combination-sensitive cells that respond best at short echo delays (O'Neill and Suga, 1982; Portfors and Wenstrup, 1999). The range of recovery times that we observed for both DTNs and non-DTNs in the ICc of *E. fuscus* nicely corresponds to the range of pulse-to-pulse intervals (repetition rates) used by foraging bats during the search (50–100 ms), approach (10–50 ms) and terminal feeding buzz (4–7 ms) phases of hunting (Griffin et al., 1960). The subset of DTNs with facilitatory responses at short IPIs may be especially well-suited for echolocation at short target distances.

4.5. RECOVERY CYCLES AND NEURAL INHIBITION

Faure et al. (2003) used paired tone stimulation to measure the onset and duration of the leading and persistent inhibition that creates DTNs in the IC of the bat. In that study, P1 was set to the neuron's BD and P2 was set to a longer, non-excitatory duration. In the present study, we used pairs of excitatory tones to measure and compare the recovery cycle times of DTNs with non-DTNs, and found that bandpass DTNs

had significantly longer recovery times than non-DTNs using spike count recovery and one measure of spike latency recovery. These results also highlight the importance of neural inhibition to duration tuning. Previous studies have suggested that the strength and time course of GABAergic inhibition can account for some variation in the recovery cycles of DTNs. Blocking GABAergic inhibition with bicucculine shortened recovery times in a majority of IC cells (Lu et al., 1997; Zhou and Jen, 2003). Presenting stimuli that mimicked pulse-echo pairs at short IPIs also sharpened duration-selectivity (Wu and Jen, 2006; Jen and Wu, 2008) and frequency-selectivity (Wu and Jen, 2008a,b); in the latter two examples, the sharpening of the response evoked by the "echo" was thought to have arisen from the recruitment and persistence of inhibition evoked by the "pulse."

During paired tone stimulation, if the inhibition evoked by stimulus P1 encroaches upon the excitation evoked by stimulus P2 then recovery times of cells with persistent inhibition are expected to be longer than in cells with less or no persistent inhibition. We might also expect FSLs (re signal onset) to increase because spikes evoked by P2 could be delayed by persistent inhibition evoked by P1. Meanwhile, neuronal LSLs (re P2) may largely be unaffected. In general, our results support the hypothesis that recovery cycle times are determined, at least in part, by the inhibition evoked by tone P1 that persists and influences the spiking responses evoked by tone P2. We also found that FSLs (re P2) were more likely to deviate by >1 SD from baseline than LSLs (re P2), a finding that is consistent with the effects of persistent inhibition.

Recovery times measured in IC neurons are on the order of tens of milliseconds and therefore cannot be due to a neuron's absolute and/or relative refractory periods caused by post-spiking increases in potassium permeability and inactivation of sodium channels because these effects typically last only a few milliseconds (Hodgkin, 1951; Hodgkin and Huxley, 1952). Stimulus repetition rate can also affect the measurement of recovery times. In the ICc of the bat, increasing stimulus repetition rate increases the observed FSL and minimum threshold (Jen and Chen, 1998), increases directional selectivity (Zhou and Jen, 2004), and alters duration selectivity (Jen and Feng, 1999; Jen and Wu, 2005; Zhou and Jen, 2006). In theory, increasing the stimulus repetition rate increases the recovery cycle time of a neuron because persistent inhibition evoked by one stimulus trial influences responses evoked on the subsequent trial. In our study, stimulus repetition rate cannot explain differences in the recovery cycle times between DTNs and non-DTNs because all of the data were collected at the same rate (3 Hz). We believe that differences in the recovery times between DTNs and non-DTNs were caused, in part, by inhibition lasting longer than the duration of the P1 tone that evoked it. This persistent inhibition would sum with the leading inhibition evoked by tone P2, resulting in DTNs exhibiting longer recovery times than a random selection of other types of IC neurons not tuned to stimulus duration. Other factors can also affect neural recovery times, including the length of the axons that provide synaptic input (axonal delay; Smith et al., 1993), the time course of temporal facilitation and depression of excitatory and inhibitory synapses (e.g., neurotransmitter depletion; Zucker and Regehr, 2002), receptor desensitization (Raman and Trussell, 1992; Raman et al., 1994), presynaptic modulation of inhibition via intracellular calcium accumulation (Lu and Trussell, 2000) and/or $GABA_B$ receptors (Ma et al., 2002), and intrinsic cellular properties such as subthreshold sound-evoked oscillations (Hechavarra et al., 2011). Additional studies are needed to shed light on the mechanisms that shape and govern the recovery cycle times of mammalian central auditory neurons.

5. SUMMARY

1. Spike counts are traditionally used to measure the recovery cycle times of neurons. Herein we demonstrate that spike latencies may also be used to measure response recovery. In general, recovery times measured with spike counts were positively correlated with recovery times measured with spike latencies, although recovery times measured with a 1 SD change in LSL (re baseline latency) were significantly shorter than recovery times measured with a 50% change in spike count (re baseline count) or with a 1 SD change in FSL (re baseline latency).
2. Previous studies have shown that neural inhibition is necessary for creating DTNs in the IC of the bat. Because DTNs are known to have inhibition that persists for as long or longer than the duration of the stimulus evoking the inhibition, we predicted that DTNs would have longer recovery times than non-DTNs. Recovery times of bandpass DTNs obtained with spike counts and one measure of FSL recovery were longer than recovery times of shortpass DTNs and non-DTNs.
3. Increasing the amplitude of the paired tone stimulus from +10 to +20 dB (re threshold) did not shorten recovery times in the population of cells tested, indicating that recovery kinetics of IC neurons in the bat are tolerant to a +10 dB change in stimulus amplitude. When we restricted our analysis to the subset of neurons that provided recovery time values measured with spike counts, FSLs, and LSLs, we found that increasing stimulus amplitude shortened recovery times in the same cells. Additional studies employing a wider range of stimulus levels are needed to fully characterize the effect of stimulus amplitude on the recovery times of IC neurons.
4. Neurons with short FSLs had shorter recovery times than cells with longer FSLs. Inhibition is an important determinant of the recovery cycle time and FSL of DTNs and non-DTNs. Our results demonstrate that the neural mechanisms controlling FSL and recovery cycle kinetics may be related.

ACKNOWLEDGMENTS

Research supported by a Discovery Grant from the Natural Sciences and Engineering Research Council (NSERC) of Canada to Paul A. Faure. Riziq Sayegh supported by an Ontario Graduate Scholarship and Brandon Aubie supported by a NSERC Canada Graduate Scholarship. The McMaster Bat Lab is also supported by infrastructure grants from the Canada Foundation for Innovation and the Ontario Innovation Trust.

REFERENCES

Aubie, B., Becker, S., and Faure, P. A. (2009). Computational models of millisecond level duration tuning in neural circuits. *J. Neurosci.* 29, 9255–9270.

Aubie, B., Sayegh, R., and Faure, P. A. (2012). Duration tuning across vertebrates. *J. Neurosci.* 32, 6373–6390.

Brand, A., Urban, A., and Grothe, B. (2000). Duration tuning in the mouse auditory midbrain. *J. Neurophysiol.* 84, 1790–1799.

Brugge, J. F., Reale, R. A., Jenison, R. L., and Schnupp, J. (2001). Auditory cortical spatial receptive fields. *Audiol. Neurootol.* 6, 173–177.

Carr, C. E., and Konishi, M. (1990). A circuit for detection of interaural time differences in the brain stem of the barn owl. *J. Neurosci.* 10, 3227–3246.

Casseday, J. H., Ehrlich, D., and Covey, E. (1994). Neural tuning for sound duration: role of inhibitory mechanisms in the inferior colliculus. *Science* 264, 847–850.

Casseday, J. H., Ehrlich, D., and Covey, E. (2000). Neural measurement of sound duration: control by excitatory-inhibitory interactions in the inferior colliculus. *J. Neurophysiol.* 84, 1475–1487.

Chen, G.-D. (1998). Effects of stimulus duration on responses of neurons in the chinchilla inferior colliculus. *Hear. Res.* 112, 142–150.

Covey, E., Kauer, J. A., and Casseday, J. H. (1996). Whole-cell patch-clamp recording reveals subthreshold sound-evoked postsynaptic currents in the inferior colliculus of awake bats. *J. Neurosci.* 16, 3009–3018.

Cranford, J. L., and Oberholtzer, M. (1976). Role of neocortex in binaural hearing in the cat. II. The 'precedence effect' in sound localization. *Brain Res.* 111, 225–239.

Denes, P. (1955). Effect of duration on the perception of voicing. *J. Acoust. Soc. Am.* 27, 761–764.

Duysens, J., Schaafsma, S. J., and Orban, G. A. (1996). Cortical off response tuning for stimulus duration. *Vision Res.* 36, 3243–3251.

Ehrlich, D., Casseday, J. H., and Covey, E. (1997). Neural tuning to sound duration in the inferior colliculus of the big brown bat, *Eptesicus fuscus*. *J. Neurophysiol.* 77, 2360–2372.

Faingold, C. L., Boersma Anderson, C. A., and Caspary, D. M. (1991). Involvement of GABA in acoustically-evoked inhibition in inferior colliculus neurons. *Hear. Res.* 52, 201–216.

Faure, P. A., Fremouw, T., Casseday, J. H., and Covey, E. (2003). Temporal masking reveals properties of sound-evoked inhibition in duration-tuned neurons of the inferior colliculus. *J. Neurosci.* 23, 3052–3065.

Faure, P. A., Re, D. E., and Clare, E. L. (2009). Wound healing in the flight membranes of big brown bats. *J. Mammal.* 90, 1148–1156.

Fitzpatrick, D. C., Kuwada, S., Batra, R., and Trahiotis, C. (1995). Neural responses to simple simulated echoes in the auditory brain stem of the unanesthetized rabbit. *J. Neurophysiol.* 74, 2469–2486.

Fitzpatrick, D. C., Kuwada, S., Kim, D. O., Parham, K., and Batra, R. (1999). Responses of neurons to click-pairs as simulated echoes: auditory nerve to auditory cortex. *J. Acoust. Soc. Am.* 106, 3460–3472.

Fontaine, B., and Peremans, H. (2009). Bat echolocation processing using first-spike latency coding. *Neural Netw.* 22, 1372–1382.

Frederiksen, E. (1977). Condenser microphones used as sound sources. *Brüel and Kjær Tech. Rev.* 3, 3–23.

Fremouw, T., Faure, P. A., Casseday, J. H., and Covey, E. (2005). Duration selectivity of neurons in the inferior colliculus of the big brown bat: tolerance to changes in sound level. *J. Neurophysiol.* 94, 1869–1878.

Friend, J. H., Suga, N., and Suthers, R. A. (1966). Neural responses in the inferior colliculus of echolocating bats to artificial orientation sounds and echoes. *J. Cell. Physiol.* 67, 319–332.

Furukawa, S., and Middlebrooks, J. C. (2002). Cortical representation of auditory space: information-bearing features of spike patterns. *J. Neurophysiol.* 87, 1749–1762.

Fuzessery, Z. M., and Hall, J. C. (1999). Sound duration selectivity in the pallid bat inferior colliculus. *Hear. Res.* 137, 137–154.

Fuzessery, Z. M., Wenstrup, J. J., Hall, J. C., and Leroy, S. (2003). Inhibition has little effect on response latencies in the inferior colliculus. *JARO* 4, 60–73.

Gooler, D. M., and Feng, A. S. (1992). Temporal coding in the frog auditory midbrain: the influence of duration and rise-fall time on the processing of complex amplitude-modulated stimuli. *J. Neurophysiol.* 67, 1–22.

Griffin, D. R., Webster, F. A., and Michael, C. R. (1960). The echolocation of flying insects by bats. *Anim. Behav.* 8, 141–154.

Grinnell, A. D. (1963). The neurophysiology of audition in bats: temporal parameters. *J. Physiol.* 167, 67–96.

Grothe, B., and Klump, G. M. (2000). Temporal processing in sensory systems. *Curr. Opin. Neurobiol.* 10, 467–473.

Haplea, S., Covey, E., and Casseday, J. H. (1994). Frequency tuning and response latencies at three levels in the brainstem of the echolocating bat, *Eptesicus fuscus*. *J. Comp. Physiol. A* 174, 671–683.

He, J., Hashikawa, T., Ojima, H., and Kinouchi, Y. (1997). Temporal integration and duration tuning in the dorsal zone of cat auditory cortex. *J. Neurosci.* 17, 2615–2625.

Hechavarra, J. C., Cobo, A. T., Fernández, Y., Macas, S., Kössl, M., and Mora, E. C. (2011). Sound-evoked oscillation and paradoxical latency shift in the inferior colliculus of the big fruit-eating bat, *Artibeus jamaicensis*. *J. Comp. Physiol. A* 197, 1159–1172.

Heil, P. (2004). First-spike latency of auditory neurons revisited. *Curr. Opin. Neurobiol.* 14, 461–467.

Hodgkin, A. L. (1951). The ionic basis of electrical activity in nerve and muscle. *Biol. Rev.* 26, 339–409.

Hodgkin, A. L., and Huxley, A. F. (1952). A quantitative description of membrane current and its application to conduction and excitation in nerve. *J. Physiol.* 117, 500–544.

Hurley, L. M., and Pollak, G. D. (2005). Serotonin shifts first-spike latencies of inferior colliculus neurons. *J. Neurosci.* 25, 7876–7886.

Jen, P. H.-S., and Chen, Q.-C. (1998). The effect of pulse repetition rate, pulse intensity, and bicuculline on the minimum threshold and latency of bat inferior collicular neurons. *J. Comp. Physiol. A* 182, 455–465.

Jen, P. H.-S., and Feng, R. B. (1999). Bicuculline application affects discharge pattern and pulse-duration tuning characteristics of bat inferior collicular neurons. *J. Comp. Physiol. A* 184, 185–194.

Jen, P. H.-S., and Schlegel, P. A. (1982). Auditory physiological properties of the neurones in the inferior colliculus of the big brown bat, *Eptesicus fuscus*. *J. Comp. Physiol. A* 147, 351–363.

Jen, P. H.-S., and Wu, C. H. (2005). The role of GABAergic inhibition in shaping the response size and duration selectivity of bat inferior collicular neurons to sound pulses in rapid sequences. *Hear. Res.* 202, 222–234.

Jen, P. H.-S., and Wu, C. H. (2006). Duration selectivity organization in the inferior colliculus of the big brown bat, *Eptesicus fuscus*. *Brain Res.* 1108, 76–87.

Jen, P. H.-S., and Wu, C. H. (2008). Echo duration selectivity of the bat varies with pulse-echo amplitude difference. *Neuroreport* 19, 373–377.

Jen, P. H.-S., Wu, C. H., and Wang, X. (2012). Dynamic temporal signal processing in the inferior colliculus of echolocating bats. *Front. Neural Circuits* 6:27. doi: 10.3389/fncir.2012.00027

Jen, P. H.-S., and Zhou, X. M. (1999). Temporally patterned pulse trains affect duration tuning characteristics of bat inferior collicular neurons. *J. Comp. Physiol. A* 185, 471–478.

Joris, P. X., Smith, P. H., and Yin, T. C. T. (1998). Coincidence detection in the auditory system: 50 years after Jeffress. *Neuron* 21, 1235–1238.

Keller, C. H., and Takahashi, T. T. (1996). Responses to simulated echoes by neurons in the barn owl's auditory space map. *J. Comp. Physiol. A* 178, 499–512.

Kelly, J. B. (1974). Localization of paired sound sources in the rat: small time differences. *J. Acoust. Soc. Am.* 55, 1277–1284.

Klug, A., Bauer, E. E., and Pollak, G. D. (1999). Multiple components of ipsilaterally evoked inhibition in the inferior colliculus. *J. Neurophysiol.* 82, 593–610.

Klug, A., Khan, A., Burger, R. M., Bauer, E. E., Hurley, L. M., Yang, L., Grothe, B., Halvorsen, M. B., and Park, T. J. (2000). Latency as a function of intensity in auditory neurons: influences of central processing. *Hear. Res.* 148, 107–123.

Knudsen, E. I., and Konishi, M. (1979). Mechanisms of sound localization in the barn owl (*Tyto alba*). *J. Comp. Physiol. A* 133, 13–21.

Kuwada, S., Batra, R., Yin, T. C. T., Oliver, D. L., Haberly, L. B., and Stanford, T. R. (1997). Intracellular recordings in response to monaural and binaural stimulation of neurons in the inferior colliculus of the cat. *J. Neurosci.* 17, 7565–7581.

Leary, C. J., Edwards, C. J., and Rose, G. J. (2008). Midbrain auditory neurons integrate excitation and inhibition to generate duration selectivity: an *in vivo* whole-cell patch study in anurans. *J. Neurosci.* 28, 5481–5493.

Litovsky, R. Y., Colburn, H. S., Yost, W. A., and Guzman, S. J. (1999). The precedence effect. *J. Acoust. Soc. Am.* 106, 1633–1654.

Litovsky, R. Y., and Delgutte, B. (2002). Neural correlates of the precedence effect in the inferior colliculus: effect of localization cues. *J. Neurophysiol.* 87, 976–994.

Litovsky, R. Y., and Yin, T. C. T. (1998a). Physiological studies of the precedence effect in the inferior colliculus of the cat. I. Correlates of psychophysics. *J. Neurophysiol.* 80, 1285–1301.

Litovsky, R. Y., and Yin, T. C. T. (1998b). Physiological studies of the precedence effect in the inferior colliculus of the cat. II. Neural mechanisms. *J. Neurophysiol.* 80, 1302–1316.

Lu, T., and Trussell, L. O. (2000). Inhibitory transmission mediated by asynchronous transmitter release. *Neuron* 26, 683–694.

Lu, Y., Jen, P. H.-S., and Zheng, Q.-Y. (1997). GABAergic disinhibition changes the recovery cycle of bat inferior collicular neurons. *J. Comp. Physiol. A* 181, 331–341.

Luo, F., Metzner, W., Wu, F. J., Zhang, S. Y., and Chen, Q. C. (2008). Duration-sensitive neurons in the inferior colliculus of horseshoe bats: adaptations for using CF-FM echolocation pulses. *J. Neurophysiol.* 99, 284–296.

Ma, C. L., Kelly, J. B., and Wu, S. H. (2002). Presynaptic modulation of GABAergic inhibition by $GABA_B$ receptors in the rat's inferior colliculus. *Neuroscience* 114, 207–215.

Middlebrooks, J. C., Clock, A. E., Xu, L., and Green, D. M. (1994). A panoramic code for sound location by cortical neurons. *Science* 264, 842–844.

Mora, E. C., and Kössl, M. (2004). Ambiguities in sound duration selectivity by neurons in the inferior colliculus of the bat *Molossus molossus* from Cuba. *J. Neurophysiol.* 91, 2215–2226.

Nelken, I., Chechik, G., Mrsic-Flogel, T. D., King, A. J., and Schnupp, J. W. H. (2005). Encoding stimulus information by spike numbers and mean response time in primary auditory cortex. *J. Comput. Neurosci.* 19, 199–221.

O'Neill, W. E., and Suga, N. (1982). Encoding of target range and its representation in the auditory cortex of the mustached bat. *J. Neurosci.* 2, 17–31.

Park, T. J., and Pollak, G. D. (1993). GABA shapes a topographic organization of response latency in the mustache bat's inferior colliculus. *J. Neurosci.* 13, 5172–5187.

Pedemonte, M., Torterolo, P., and Velluti, R. A. (1997). *In vivo* intracellular characteristics of inferior colliculus neurons in guinea pigs. *Brain Res.* 759, 24–31.

Pérez-González, D., Malmierca, M. S., Moore, J. M., Hernández, O., and Covey, E. (2006). Duration selective neurons in the inferior colliculus of the rat: topographic distribution and relation of duration sensitivity to other response properties. *J. Neurophysiol.* 95, 823–836.

Pinheiro, A. D., Wu, M., and Jen, P. H.-S. (1991). Encoding repetition rate and duration in the inferior colliculus of the big brown bat, *Eptesicus fuscus*. *J. Comp. Physiol. A* 169, 69–85.

Pinheiro, J. C., and Bates, D. M. (2000). *Mixed-Effects Models in S and S-PLUS*. (New York, NY: Springer-Verlag).

Pollack, G. S., and Hoy, R. R. (1979). Temporal pattern as a cue for species-specific calling song recognition in crickets. *Science* 204, 429–432.

Pollak, G. D., Bodenhamer, R., Marsh, D. S., and Souther, A. (1977a). Recovery cycles of single neurons in the inferior colliculus of unanesthetized bats obtained with frequency-modulated and constant-frequency sounds. *J. Comp. Physiol. A* 120, 215–250.

Pollak, G. D., Marsh, D. S., Bodenhamer, R., and Souther, A. (1977b). Characteristics of phasic on neurons in inferior colliculus of unanesthetized bats with observations relating to mechanisms for echo ranging. *J. Neurophysiol.* 40, 926–942.

Pollak, G. D., and Park, T. J. (1993). The effects of GABAergic inhibition on monaural response properties of neurons in the mustache bat's inferior colliculus. *Hear. Res.* 65, 99–117.

Portfors, C. V., and Wenstrup, J. J. (1999). Delay-tuned neurons in the inferior colliculus of the mustached bat: implications for analyses of target distance. *J. Neurophysiol.* 82, 1326–1338.

Potter, H. D. (1965). Patterns of acoustically evoked discharges of neurons in the mesencephalon of the bullfrog. *J. Neurophysiol.* 28, 1155–1184.

Raman, I. M., and Trussell, L. O. (1992). The kinetics of the response to glutamate and kainate in neurons of the avian cochlear nucleus. *Neuron* 9, 173–186.

Raman, I. M., Zhang, S., and Trussell, L. O. (1994). Pathway-specific variants of AMPA receptors and their contribution to neuronal signaling. *J. Neurosci.* 14, 4998–5010.

Sayegh, R., Aubie, B., and Faure, P. A. (2011). Duration tuning in the auditory midbrain of echolocating and non-echolocating vertebrates. *J. Comp. Physiol. A* 197, 571–583.

Schuchmann, M., Hübner, M., and Wiegrebe, L. (2006). The absence of spatial echo suppression in the echolocating bats *Megaderma lyra* and *Phyllostomus discolor*. *J. Exp. Biol.* 209, 152–157.

Simmons, J. A. (1971). Echolocation in bats: signal processing of echoes for target range. *Science* 171, 925–928.

Simmons, J. A. (1979). Perception of echo phase information in bat sonar. *Science* 204, 1336–1338.

Smith, P. H., Joris, P. X., and Yin, T. C. T. (1993). Projections of physiologically characterized spherical bushy cell axons from the cochlear nucleus of the cat: evidence for delay lines to the medial superior olive. *J. Comp. Neurol.* 331, 245–260.

Stapells, D. R., Picton, T. W., and Smith, A. D. (1982). Normal hearing thresholds for clicks. *J. Acoust. Soc. Am.* 72, 74–79.

Suga, N. (1964). Recovery cycles and responses to frequency modulated tone pulses in auditory neurones of echo-locating bats. *J. Physiol.* 175, 50–80.

Suga, N., and O'Neill, W. E. (1979). Neural axis representing target range in the auditory cortex of the mustache bat. *Science* 206, 351–353.

Suga, N., and Schlegel, P. (1973). Coding and processing in the auditory systems of FM-signal-producing bats. *J. Acoust. Soc. Am.* 54, 174–190.

Tan, M. L., and Borst, J. G. G. (2007). Comparison of responses of neurons in the mouse inferior colliculus to current injections, tones of different durations, and sinusoidal amplitude-modulated tones. *J. Neurophysiol.* 98, 454–466.

Tan, X., Wang, X., Yang, W., and Xiao, Z. (2008). First spike latency and spike count as functions of tone amplitude and frequency in the inferior colliculus of mice. *Hear. Res.* 235, 90–104.

Tang, J., Fu, Z.-Y., Jen, P. H.-S., and Chen, Q.-C. (2011). Recovery cycles of single-on and double-on neurons in the inferior colliculus of the leaf-nosed bat, *Hipposideros armiger*. *Brain Res.* 1385, 114–126.

Torterolo, P., Pedemonte, M., and Velluti, R. A. (1995). Intracellular *in vivo* recording of inferior colliculus auditory neurons from awake guinea-pigs. *Arch. Ital. Biol.* 134, 57–64.

VanRullen, R., Guyonneau, R., and Thorpe, S. J. (2005). Spike times make sense. *Trends Neurosci.* 28, 1–4.

Voytenko, S. V., and Galazyuk, A. V. (2008). Timing of sound-evoked potentials and spike responses in the inferior colliculus of awake bats. *Neuroscience* 155, 923–936.

Wallach, H., Newman, E. B., and Rosenzweig, M. R. (1949). The precedence effect in sound localization. *Am. J. Psychol.* 62, 315–336.

Wang, J., van Wijhe, R., Chen, Z., and Yin, S. (2006). Is duration tuning a transient process in the inferior colliculus of guinea pigs? *Brain Res.* 1114, 63–74.

Wang, X., Luo, F., Jen, P. H.-S., and Chen, Q.-C. (2010). Recovery cycle of neurons in the inferior colliculus of the FM bat determined with varied pulse-echo duration and amplitude. *Chinese J. Physiol.* 53, 119–129.

Wang, X., Luo, F., Wu, F.-J., Chen, Q.-C., and Jen, P. H. S. (2008). The recovery cycle of bat duration-selective collicular neurons varies with hunting phase. *Neuroreport* 19, 861–865.

Wu, C. H., and Jen, P. H.-S. (2006). GABA-mediated echo duration selectivity of inferior collicular neurons of *Eptesicus fuscus*, determined with single pulses and pulse-echo pairs. *J. Comp. Physiol. A* 192, 985–1002.

Wu, C. H., and Jen, P. H.-S. (2008a). Auditory frequency selectivity is better for expected than for unexpected sound duration. *Neuroreport* 19, 127–131.

Wu, C. H., and Jen, P. H.-S. (2008b). Echo frequency selectivity of duration-tuned inferior collicular neurons of the big brown bat, *Eptesicus fuscus*, determined with pulse-echo pairs. *Neuroscience* 156, 1028–1038.

Wyttenbach, R. A., and Hoy, R. R. (1993). Demonstration of the precedence effect in an insect. *J. Acoust. Soc. Am.* 94, 777–784.

Xia, Y.-F., Qi, Z.-H., and Shen, J.-X. (2000). Neural representation of sound duration in the inferior colliculus of the mouse. *Acta Otolaryngol.* 120, 638–643.

Yin, T. C. T. (1994). Physiological correlates of the precedence effect and summing localization in the inferior colliculus of the cat. *J. Neurosci.* 14, 5170–5186.

Zhou, X., and Jen, P. H.-S. (2001). The effect of sound intensity on duration-tuning characteristics of bat inferior collicular neurons. *J. Comp. Physiol. A* 187, 63–73.

Zhou, X., and Jen, P. H.-S. (2003). The effect of bicuculline application on azimuth-dependent recovery cycle of inferior collicular neurons of the big brown bat, *Eptesicus fuscus*. *Brain Res.* 973, 131–141.

Zhou, X., and Jen, P. H.-S. (2004). Azimuth-dependent recovery cycle affects directional selectivity of bat inferior collicular neurons determined with sound pulses within a pulse train. *Brain Res.* 1019, 281–288.

Zhou, X., and Jen, P. H.-S. (2006). Duration selectivity of bat inferior collicular neurons improves with increasing pulse repetition rate. *Chinese J. Physiol.* 49, 46–55.

Zucker, R. S., and Regehr, W. G. (2002). Short-term synaptic plasticity. *Annu. Rev. Physiol.* 64, 355–405.

Conflict of Interest Statement: The authors declare that the research was conducted in the absence of any commercial or financial relationships that could be construed as a potential conflict of interest.

Received: 08 May 2012; accepted: 30 July 2012; published online: 20 August 2012.
Citation: Sayegh R, Aubie B, Fazel-Pour S and Faure PA (2012) Recovery cycle times of inferior colliculus neurons in the awake bat measured with spike counts and latencies. Front. Neural Circuits ***6****:56. doi: 10.3389/fncir.2012.00056*

frontiers in
NEURAL CIRCUITS

REVIEW ARTICLE
published: 08 May 2012
doi: 10.3389/fncir.2012.00027

Dynamic temporal signal processing in the inferior colliculus of echolocating bats

Philip H.-S. Jen[1]*, Chung Hsin Wu[2] and Xin Wang[3]

[1] *Division of Biological Sciences and Interdisciplinary Neurobiology Program, University of Missouri, Columbia, MO, USA*
[2] *Department of Life Science, National Taiwan Normal University, Taipei, Taiwan, ROC*
[3] *College of Life Science, Central China Normal University, Wuhan, Hubei, PRC*

Edited by:
Manuel S. Malmierca, University of Salamanca, Spain

Reviewed by:
Zoltan M. Fuzessery, University of Wyoming, USA
Donal G. Sinex, Utah State University, USA

****Correspondence:***
Philip H.-S. Jen, Division of Biological Sciences, University of Missouri, Columbia, MO, USA.
e-mail: jenp@missouri.edu

In nature, communication sounds among animal species including humans are typical complex sounds that occur in sequence and vary with time in several parameters including amplitude, frequency, duration as well as separation, and order of individual sounds. Among these multiple parameters, sound duration is a simple but important one that contributes to the distinct spectral and temporal attributes of individual biological sounds. Likewise, the separation of individual sounds is an important temporal attribute that determines an animal's ability in distinguishing individual sounds. Whereas duration selectivity of auditory neurons underlies an animal's ability in recognition of sound duration, the recovery cycle of auditory neurons determines a neuron's ability in responding to closely spaced sound pulses and therefore, it underlies the animal's ability in analyzing the order of individual sounds. Since the multiple parameters of naturally occurring communication sounds vary with time, the analysis of a specific sound parameter by an animal would be inevitably affected by other co-varying sound parameters. This is particularly obvious in insectivorous bats, which rely on analysis of returning echoes for prey capture when they systematically vary the multiple pulse parameters throughout a target approach sequence. In this review article, we present our studies of dynamic variation of duration selectivity and recovery cycle of neurons in the central nucleus of the inferior colliculus of the frequency-modulated bats to highlight the dynamic temporal signal processing of central auditory neurons. These studies use single pulses and three biologically relevant pulse-echo (P-E) pairs with varied duration, gap, and amplitude difference similar to that occurring during search, approach, and terminal phases of hunting by bats. These studies show that most collicular neurons respond maximally to a best tuned sound duration (BD). The sound duration to which these neurons are tuned correspond closely to the behaviorally relevant sounds occurring at different phases of hunting. The duration selectivity of these collicular neurons progressively increases with decrease in the duration of pulse and echo, P-E gap, and P-E amplitude difference. GABAergic inhibition plays an important role in shaping the duration selectivity of these collicular neurons. The duration selectivity of these neurons is systematically organized along the tonotopic axis of the inferior colliculus and is closely correlated with the graded spatial distribution of $GABA_A$ receptors. Duration-selective collicular neurons have a wide range of recovery cycle covering the P-E intervals occurring throughout the entire target approaching sequences. Collicular neurons with low best frequency and short BD recover rapidly when stimulated with P-E pairs with short duration and small P-E amplitude difference, whereas neurons with high best frequency and long BD recover rapidly when stimulated with P-E pairs with long duration and large P-E amplitude difference. This dynamic variation of echo duration selectivity and recovery cycle of collicular neurons may serve as the neural basis underlying successful hunting by bats. Conceivably, high best frequency neurons with long BD would be suitable for echo recognition during search and approach phases of hunting when the returning echoes are high in frequency, large in P-E amplitude difference, long in duration but low in repetition rate. Conversely, low best frequency neurons with shorter BD and sharper duration selectivity would be suitable for echo recognition during the terminal phase of hunting when the highly repetitive echoes are low in frequency, small in P-E amplitude difference, and short in duration. Furthermore,

the tonotopically organized duration selectivity would make it possible to facilitate the recruitment of different groups of collicular neurons along the tonotopic axis for effective processing of the returning echoes throughout the entire course of hunting.

Keywords: duration selectivity, echolocation, inferior colliculus, pulse-echo pairs, recovery cycle, temporal signal processing

INTRODUCTION

In nature, communication sounds among animal species including humans are typical complex sounds that vary with time in several parameters including amplitude, frequency, duration as well as separation, and order of individual sounds (Popper and Fay, 1995; Shannon et al., 1995). Among these parameters, sound duration is a simple but important one that contributes to the distinct spectral and temporal attributes of individual biological sounds. Previous studies of selectivity of auditory neurons to sound duration show that most auditory neurons respond maximally to a specific duration or a range of durations (frogs, Narins and Capranica, 1980; Feng et al., 1990; Gooler and Feng, 1992), (bats, Jen and Schlegel, 1982; Pinheiro et al., 1991; Casseday et al., 1994, 2000; Ehrlich et al., 1997; Galazyuk and Feng, 1997; Fuzessery and Hall, 1999; Jen and Feng, 1999; Jen and Zhou, 1999; Zhou and Jen, 2001, 2006; Faure et al., 2003; Fremouw et al., 2005; Jen and Wu, 2005, 2006, 2008; Wu and Jen, 2006, 2010), (cats, He et al., 1997), (chinchillas, Chen, 1998), (mice, Brand et al., 2000) and (rats, Perez-Gonzalez et al., 2006). The sound duration to which these neurons are tuned correspond closely to the behaviorally relevant sounds in these animal species. As such, duration-selective auditory neurons play an important role for sound recognition particularly in human speech, animal communication, and bat echolocation (Popper and Fay, 1995; Shannon et al., 1995; Covey and Casseday, 1999).

On the other hand, natural sounds such as vocal communication sounds of many animal species typically occur as temporally patterned trains of sound pulses. When stimulated with these sound pulses, the response of auditory neurons to an individual sound pulse is inevitably affected by the preceding and succeeding sounds (i.e., forward and backward masking). For example, the inferior collicular neurons show larger responses to single pulses presented in temporal isolation than to the same pulse presented in temporally patterned trains of sound pulses (Moriyama et al., 1994). Furthermore, the response size of collicular neurons progressively decreases with sequentially presented sound pulses (Pinheiro et al., 1991; Moriyama et al., 1994; Brosch and Schreiner, 1997; Lu et al., 1997, 1998; Litovsky and Yin, 1998; Jen and Zhou, 1999; Jen et al., 2001; Zhou and Jen, 2002a,b; Jen and Wu, 2005). These neurophysiological findings have been corroborated by behavioral studies, which show a human subject or an animal only perceives the leading source when two spatially separated clicks are presented with a brief delay within 5 ms (Wallach et al., 1949; Zurek, 1980; Freyman et al., 1991). When the delay between the two sounds is larger than 8–10 ms range, both the leading and lagging sounds are perceived as individual one (Freyman et al., 1991). However, longer delay of several milliseconds is required for perception of individual sounds when tested with trains of paired sounds or when each leading sound is succeeded by several echoes of various time delays (Yost and Soderquist, 1984; Yost and Guzman, 1996). All these studies indicate that when encountered with temporally patterned trains of sequential sound pulses, the separation of individual sounds is an important temporal attribute that determines an animal's ability in perceiving individual sounds.

The neural basis underlying an animal's ability in perception of individual sounds is the recovery cycle of auditory neurons, which determines a neuron's ability in responding to closely spaced sound pulses. Many studies have shown that neurons in the inferior colliculus of various animal species have a wide range of recovery cycle (cats, Litovsky and Yin, 1998; rabbits, Fitzpatrick et al., 1995; barn owls, Keller and Takahashi, 1996; bats, Grinnell, 1963; Suga, 1964, 1970; Friend et al., 1966; Suga and Schlegel, 1973; Pollak et al., 1977; Lu et al., 1997; Zhou and Jen, 2003; Wang et al., 2008, 2010). The recovery cycle of auditory neurons is particularly important for bats, which rely on this neuronal property to determine the target distance.

During hunting, insectivorous bats emit intense ultrasonic pulses and analyse multiple parameters of the returning echoes to extract information about their prey (Griffn, 1958). They progressively shorten the duration, decrease the amplitude, lower the frequency, and increase the repetition rate of emitted pulses as they search, approach, and finally intercept insects or negotiate obstacles (Griffn, 1958; Simmons et al., 1979; Jen and Kamada, 1982; Surlykke and Moss, 2000). Because bats typically hunt together with conspecifics, a bat has to be able to differentiate the echoes of its own emitted pulses from the echoes of pulses emitted by other bats for successful prey capture. Therefore, in the real world the bat's ear is bombarded by the pulse-echo (P-E) pairs not only produced by the bat itself but also by others during hunting. Since the gap, duration, amplitude of the P-E pairs vary throughout the entire course of hunting, analysis of an echo parameter by the bat would be inevitably affected by other co-varying echo parameters produced by the bat itself and conspecifics. For example, previous studies have shown that increasing pulse repetition rate improves multiple-parametric selectivity of inferior collicular neurons (Pinheiro et al., 1991; Wu and Jen, 1996; Galazyuk et al., 2000; Jen et al., 2001; Zhou and Jen, 2002a). The increase in pulse repetition rate also elevates the minimum threshold and lengthens the response latency of most collicular and cortical neurons (Phillips et al., 1989; Chen and Jen, 1994; Jen and Chen, 1998). Furthermore, pulse duration and repetition rate profoundly influence the best delay of auditory cortical neurons of the bat in which delay tuning typically narrows and eventually disappears at higher pulse repetition rate and shorter pulse duration (Tanaka et al., 1992; Wong et al., 1992; Tanaka and Wong, 1993). For all these reasons, the important temporal attributes of sound duration and separation of individual sounds are even more obvious for bats which rely on duration selectivity for recognition of echo duration and recovery cycle for echo ranging.

In this review article, we present our studies of duration selectivity and recovery cycle of inferior collicular neurons of the frequency-modulated (FM) bat, *Eptesicus fuscus* and *Pipistrellus abramus*, to highlight the dynamic variation of temporal signal processing of central auditory neurons. These studies use single pulses and three biologically relevant P-E pairs of combinations of three pulse durations (1.5, 4, and 10 ms) at varied P-E gaps that are comparable to that occurring during the search, approach and terminal phases of hunting by bats (Griffn, 1958; Simmons et al., 1979; Jen and Kamada, 1982; Surlykke and Moss, 2000). A detailed description of materials and methods can be found in these studies (Jen and Wu, 2006, 2008; Wu and Jen, 2006; Wang et al., 2008, 2010).

DYNAMIC VARIATION OF ECHO DURATION SELECTIVITY OF COLLICULAR NEURONS WITH OTHER CO-VARYING PARAMETERS

The echo duration selectivity of a collicular neuron is studied by plotting its duration tuning curves using the number of impulses in response to eight durations (1, 1.5, 2, 4, 6, 8, 10, and 20 ms) of the echo pulses of three P-E pairs. The echo duration tuning curves of collicular neurons can be described as band-, short-, long-, and all-pass using the same criterion adopted in previous studies (**Figure 1**, Jen and Feng, 1999; Jen and Zhou, 1999; Wu and Jen, 2006). The collicular neurons with band-, short-, and long-pass echo duration tuning curves show a maximal number of impulses to the best duration (BD) and are, therefore, duration-selective neurons (**Figures 1A–C**). Neurons with all-pass echo duration tuning curves are non-duration-selective neurons because their number of impulses never varies more than 50% with sound duration (**Figure 1D**).

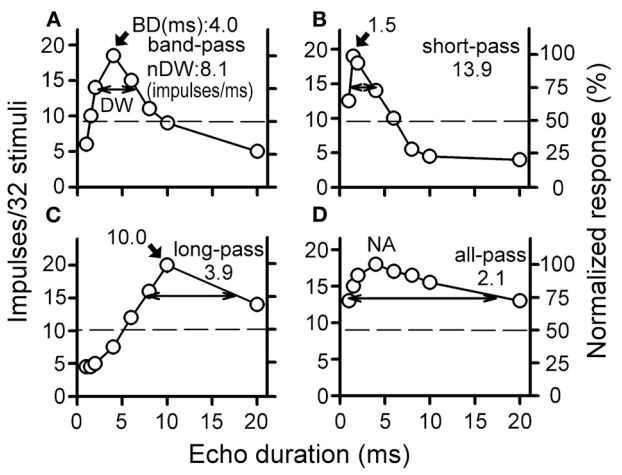

FIGURE 1 | (A) band-pass, **(B)** short-pass, **(C)** long-pass, and **(D)** all-pass duration tuning curves of collicular neurons of the FM bat, *Eptesicus fuscus*. Each horizontal dashed line indicates the 50% maximal response. The selectivity of each echo duration curve is expressed with a best duration (BD, indicated with an arrowhead) and a normalized duration width (nDW indicated with a double-arrowheads). NA: a BD is not available [Adapted from Wu and Jen (2006)].

Because the maximal number of impulses in response to the BD varied greatly among individual collicular neurons, a normalized duration-width (nDW) is used to express the broadness of a duration tuning curve for consistent comparison of duration selectivity of collicular neurons obtained under different stimulation conditions. An nDW is obtained by dividing the maximum by the width of a duration tuning curve at 75% of the maximum (**Figure 1**, DW indicated by a double-head arrow). Thus, neurons with a large nDW have narrower duration tuning curve than neurons with a small nDW.

Collicular neurons have sharper duration tuning curves when determined with the echo pulses of P-E pairs than with single pulses (**Figure 2**). The duration tuning curves of collicular neurons becomes progressively broader with lengthening of pulse duration and P-E gap (progressive decrease in the nDW). Collicular neurons have the broadest duration tuning curves when measured with single pulses (the smallest nDW). Also, a neuron's duration tuning curves may change from one type into another when measured with different P-E pairs and single pulses (**Figures 2D,G,H**). These observations indicate that a bat's echo duration selectivity in the real world is sharper than what is shown by earlier studies using single pulses (Jen and Schlegel, 1982; Pinheiro et al., 1991; Casseday et al., 1994, 2000; Ehrlich et al., 1997; Galazyuk and Feng, 1997; Fuzessery and Hall, 1999; Jen and Feng, 1999; Zhou and Jen, 2001).

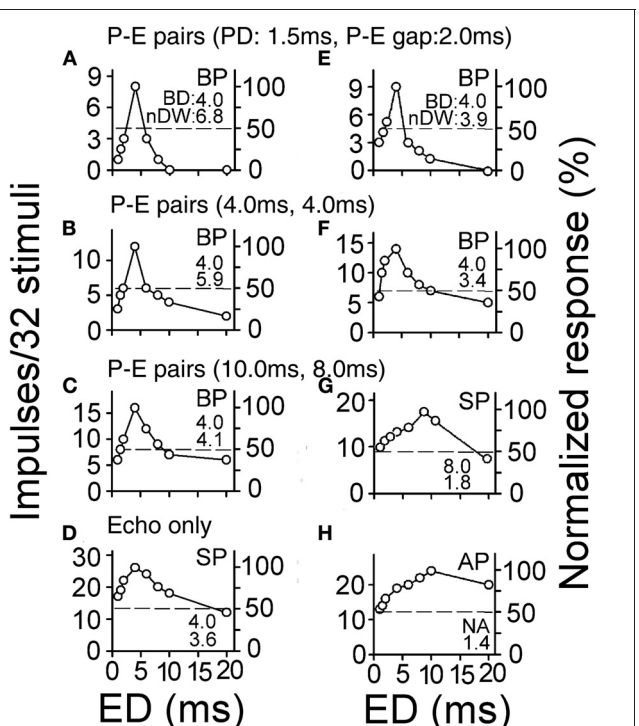

FIGURE 2 | (A–H) The echo duration tuning curves of two collicular neurons determined with the echo pulses of three pulse-echo (P-E) pairs and with single pulses. The type of duration tuning curve, the BD and the nDW are shown within each plot. Note that the nDW progressively decreases with lengthening of PD and P-E gap of three P-E pairs [Adapted from Wu and Jen (2006)].

Echo duration selectivity of collicular neurons also varies with P-E amplitude difference. When studied with three biologically relevant P-E pairs at two different P-E amplitude differences, the echo duration selectivity is greater (larger nDW) when determined with 4 ms or 10 ms pulse duration at 4 ms or 8 ms P-E gap at 20-dB than at 10-dB amplitude difference (**Figures 3Ab, Ac** vs. **Bb, Bc**). However, the echo duration selectivity is greater when determined with 1.5 ms pulse duration and 2 ms P-E gap at 10-dB than at 20-dB amplitude difference (**Figures 3Ba** vs. **Aa**). These data indicate that echo duration selectivity of collicular neurons becomes sharper when echo duration progressively shortens and P-E amplitude difference decreases throughout a target approach sequence.

Collicular neurons are tonotopically organized along the dorso-ventral axis of the inferior colliculus. Their BDs are between 1.5 and 10 ms covering the duration of pulses emitted by the FM bat during three phases of hunting. The BD and nDW of collicular neurons, respectively, increases and decreases with BF and recording depth. As such, collicular neurons at upper inferior colliculus with low BF have short BD and large nDW while those at deeper inferior colliculus with high BF have long BD and small nDW (Jen and Wu, 2006; Wu and Jen, 2006).

ECHO DURATION SELECTIVITY IS SHAPED BY GABA-MEDIATED INHIBITION

One of the major inhibitory inputs in the inferior colliculus is mediated by GABA (Roberts and Ribak, 1987; Fubara et al., 1996). By means of application of GABA or bicuculline, which is an antagonist for $GABA_A$ receptors (Cooper et al., 1982; Bormann, 1988), many studies have shown that interaction of excitation and GABAergic inhibition contributes to auditory temporal processing and shapes multiple-parametric selectivity (e.g., duration, frequency, amplitude, direction, etc.) of collicular neurons using single repetitive sound pulses or temporally patterned trains of sound pulses (Faingold et al., 1991; Vater et al., 1992; Yang et al., 1992; Park and Pollak, 1993; Casseday et al., 1994, 2000; Klug et al., 1995; LeBeau et al., 1996; Lu et al., 1997, 1998; Koch and Grothe, 1998; Jen and Feng, 1999; Jen and Zhang, 2000; Lu and Jen, 2001; Jen et al., 2002; Zhou and Jen, 2002a,b). To study the contribution of GABAergic inhibition to echo duration selectivity of collicular neurons, echo duration tuning curves are measured before and during bicuculline and GABA application.

In agreement with previous studies (Casseday et al., 1994, 2000; Jen and Feng, 1999), bicuculline application broadens the echo duration tuning curves of collicular neurons obtained with three P-E pairs by producing a greater increase in the number of impulses for shorter and longer non-BD echo pulses than for the BD echo pulse (**Figures 4A** vs. **B**). As a result, bicuculline application changes a neuron's band-pass echo duration tuning curve into all-pass echo duration tuning curve with greatly decreased nDW (**Figures 4A** vs. **B**). Conversely, GABA application narrows the echo duration tuning curves of collicular neurons by producing a greater decrease in the number of impulses for non-BD echo pulses than for BD echo pulse (**Figures 4C** vs. **D**).

Although bicuculline and GABA application, respectively, broadens and narrows the duration tuning curves of collicular neurons, drug application does not change the depth-dependent duration selectivity of these neurons. The nDW of these neurons

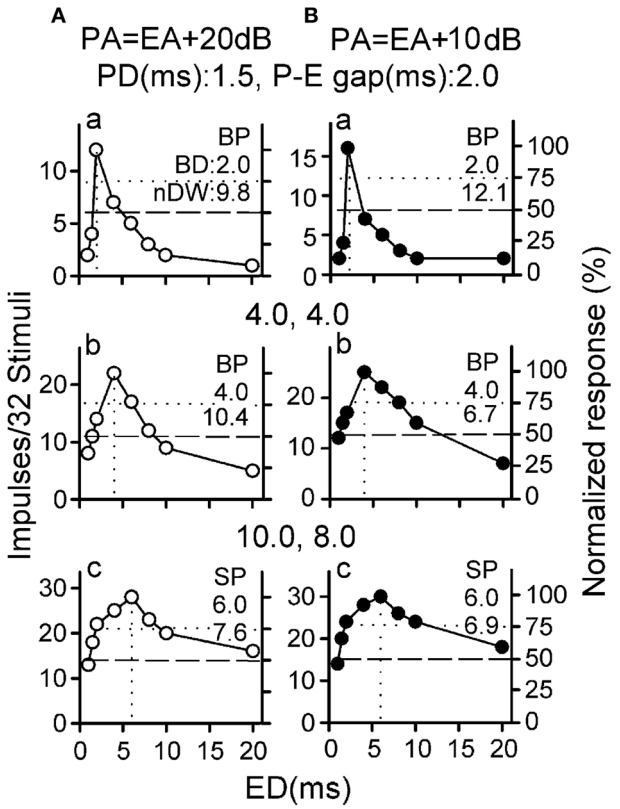

FIGURE 3 | (A,B) The echo duration tuning curves of a collicular neuron determined with three P-E pairs with varied pulse duration and P-E gap at 20-dB (unfilled) and 10-dB (filled) P-E amplitude differences [Adapted from Jen and Wu (2008)].

significantly decreases with recording depth both before and during drug application (**Figures 5Aa,Ba**). The change in nDW is significantly larger for neurons at upper than at deeper inferior colliculus during bicuculline application but the opposite is observed during GABA application (**Figures 5Ab** vs. **Bb**). These observations are likely due to the fact that neurons with $GABA_A$ receptors are mostly distributed in the dorso-medial region but are sparsely distributed in the ventro-lateral region of the inferior colliculus (Fubara et al., 1996). As such, high BF neurons at deeper inferior colliculus would conceivably receive fewer GABAergic inhibitory inputs than low BF neurons at upper inferior colliculus. For this reason, bicuculline application would produce greater change and GABA application would produce lesser change in nDW of duration tuning curves of low BF neurons at upper inferior colliculus than high BF neurons at deeper inferior colliculus. In sum, these data suggest that echo duration selectivity of collicular neurons shaped by GABAergic inhibition is systematically organized along the dorso-ventral axis of the inferior colliculus.

Previous studies show that glycine-mediated inhibition also shapes the duration selectivity of collicular neurons and neurons with glycine receptors are mostly distributed at the ventro-lateral region of the inferior colliculus but are sparsely distributed at dorso-medial region (Fubara et al., 1996; Ehrlich et al., 1997).

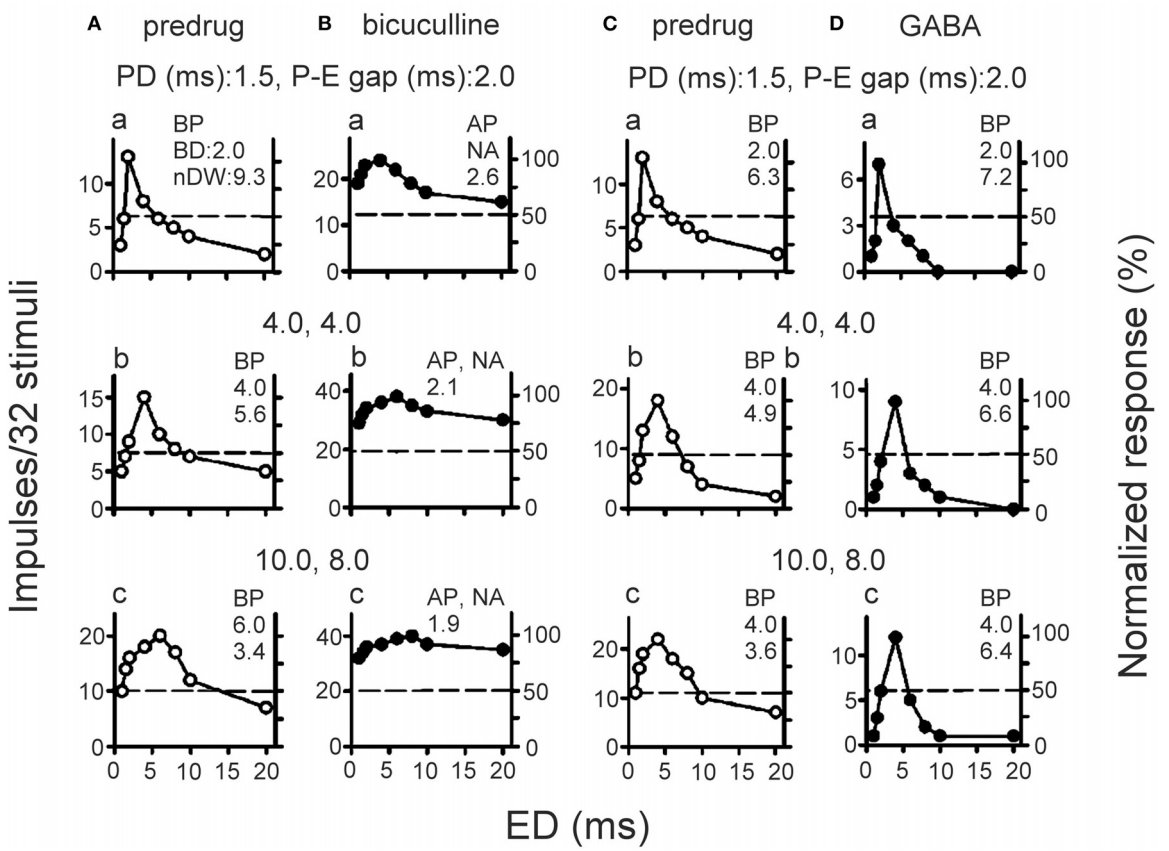

FIGURE 4 | (A,B) Echo duration tuning curves of two collicular neurons determined with three P-E pairs of varied pulse duration and P-E gap before (predrug, **A,C**) and during bicuculline **(B)** or GABA **(D)** application [Adapted from Wu and Jen (2006)].

Therefore, it is conceivable that glycine-mediated duration selectivity of collicular neurons may also be systematically organized along the dorso-ventral axis of the inferior colliculus. Future work is needed to determine whether GABA- and glycine-mediated duration selectivity of collicular neurons is organized systematically but oppositely along the distribution gradients of $GABA_A$ and glycine receptors.

DYNAMIC VARIATION OF THE RECOVERY CYCLE OF DURATION-SELECTIVE COLLICULAR NEURONS WITH P-E AMPLITUDE DIFFERENCE

A neuron's recovery cycle is measured by calculating the percent ratio of the neuron's number of impulses in response to the echo relative to the pulse at different P-E intervals and amplitude difference. The bat's collicular neurons have a wide range of recovery cycle covering the P-E intervals occurring throughout the entire sequence of hunting (Suga, 1964; Friend et al., 1966; Suga and Schlegel, 1973; Pollak et al., 1977; Lu et al., 1997; Wang et al., 2008, 2010). In general, a neuron's recovery cycle increases with P-E duration and P-E amplitude difference.

To study the dynamic temporal processing of sound duration and separation of individual sounds, the dynamic variation of the recovery cycle of 30 duration-selective collicular neurons has been studied using biologically relevant P-E pairs. While the recovery cycle of 10 neurons varies unpredictably with three P-E pairs, the recovery cycle of 20 neurons varies predictably with P-E pairs in relation to the BD and P-E amplitude difference (**Figures 6A,B**). Specifically, neurons with 1–2 ms BD recover rapidly when stimulated with P-E pairs at 10 dB amplitude difference and the duration of both P and E matches the BD (i.e., P-E pairs in the terminal phase, **Figure 6A-2**, filled arrow, solid circles). Conversely, neurons with 8–20 ms BD recover rapidly when stimulated with P-E pairs at 20 dB amplitude difference and the duration of both P and E matches the BD (i.e., P-E pairs at the search phase, **Figure 6B-3**, filled arrow, unfilled circles). However, neurons with 4–6 ms BD recover rapidly when stimulated with 4 ms of P and E at both 10 and 20 dB amplitude differences (i.e., P-E pairs at the approach phase). These observations indicate that duration selectivity and recovery cycle of most collicular neurons of the bat co-vary when the echo duration and P-E amplitude difference progressively decrease throughout the entire course of hunting.

POSSIBLE NEURAL MECHANISM UNDERLYING DYNAMIC TEMPORAL SIGNAL PROCESSING

A previous study examines the interaction of excitation and inhibition in collicular neurons using a probe (excitatory pulse) and a masker (inhibitory pulse) (Lu and Jen, 2002). This study shows

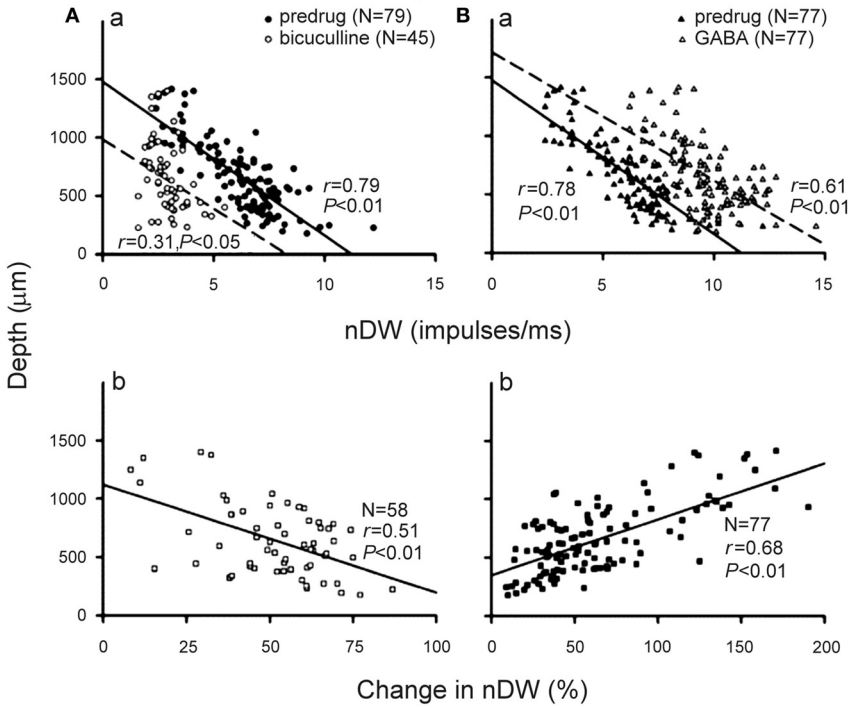

FIGURE 5 | (Aa,Ba) The distribution of nDW of collicular neurons obtained before (filled circles and triangles) and during (unfilled circles and triangles) bicuculline **(Aa)** and GABA **(Ba)** application in relation to the recording depth. (**Ab**,**Bb**) The distribution of percent change in nDW in relation to the recording depth. The linear regression line and correlation coefficient for each plot are shown by a solid line and *r* [From Jen and Wu (2006)].

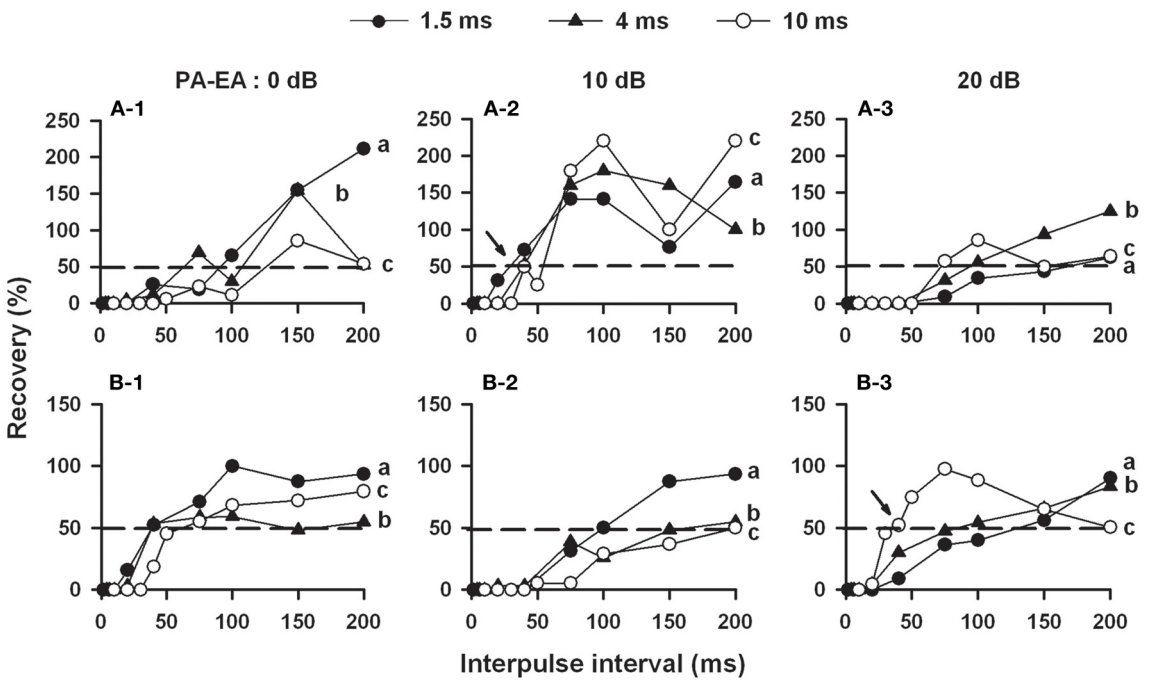

FIGURE 6 | (A) The recovery cycle of two duration-selective collicular neurons measured with P-E pairs that vary in P-E gap, duration, and amplitude differences (PA-EA = 0, 10, and 20 dB). The BDs of these two neurons are 1.5 ms **(A)** and 10 ms **(B)**. Note that neuron A has the shortest 50% recovery time (dashed line) when stimulated with 1.5 ms of P and E at 10-dB P-E amplitude difference (**A-2**, arrow) while neuron B recovers rapidly when stimulated with 10 ms of P and E at 20-dB P-E amplitude difference (**B-3**, arrow) [Adapted from Wang et al. (2008)].

that masking of probe-elicited responses of collicular neurons occurs when a masker is presented within a certain inter-pulse intervals (the temporal window) in relation to the probe. Within the temporal window, the strength of this forward masking increases with shortening of inter-pulse interval. Other studies have also shown that temporal interaction of excitation and GABAergic inhibition shapes the duration selectivity and recovery cycle of collicular neurons (Casseday et al., 1994; Ehrlich et al., 1997; Lu et al., 1997; Wu and Jen, 1998, 2006; Lu and Jen, 2002; Faure et al., 2003; Zhou and Jen, 2003; Jen and Wu, 2005, 2006, 2008).

It is conceivable that when stimulated with P-E pairs, a neuron's recovery cycle is shaped by the GABA-mediated forward masking, in which the P serves as the masker and the E serves as the probe. As such, the probe-elicited response is dependent on the duration of P and E, the gap and amplitude difference between P and E. The forward masking and the recovery cycle may be the two predominant factors to shape a neuron's echo duration selectivity. Conceivably, when stimulated with the BD and P-E amplitude difference, integration of excitation and inhibition must result in an optimal time window within which neurons respond maximally and recover rapidly. This forward masking may also account for the sharper echo duration selectivity of collicular neurons obtained with echo pulses of P-E pairs than with single echo pulses.

BIOLOGICAL RELEVANCE OF DYNAMIC TEMPORAL SIGNAL PROCESSING

Insectivorous bats emit ultrasonic signals and analyse the returning echoes to extract information about the target range, shape, and location (Griffin, 1958). The highly successful hunting suggests that the bat's auditory system must be able to encode the changes in echo parameters produced by the bat and its conspecifics during a target approaching sequence. Whereas duration selectivity of auditory neurons underlies a bat's ability in recognition of sound duration, the recovery cycle of auditory neurons determines a neuron's ability in responding to closely spaced sound pulses. Therefore, the recovery cycle of neurons underlies the bat's ability in encoding the pulse repetition rate so as to analyse the order of individual sound pulses.

To perform effective recognition of echo duration and echo ranging, a bat must be able to encode progressive variation of duration and repetition rate of emitted pulses and returning echoes throughout the entire course of hunting. Our studies show that the bat's collicular neurons have a wide range of BD and recovery cycle covering pulse durations and P-E intervals occurring during different phases of hunting. In addition, a neuron's duration selectivity is closely correlated with its recovery cycle such that the recovery cycle of most duration-selective neurons varies predictably with biologically relevant P-E duration, interval and amplitude difference. Conceivably, high best frequency neurons with long BD would be suitable for echo recognition during search and approach phases of hunting when the returning echoes are high in frequency, large in P-E amplitude difference, long in duration but low in repetition rate. Conversely, low best frequency neurons with shorter BD and sharper duration selectivity would be suitable for echo recognition during the terminal phase of hunting when the highly repetitive echoes are low in frequency, small in P-E amplitude difference and short in duration. This dynamic variation of echo duration selectivity and recovery cycle of collicular neurons may serve as the neural basis underlying successful prey capture by bats. Since these duration-selective collicular neurons are tonotopically organized, this organization would conceivably facilitate the recruitment of different groups of collicular neurons for effective processing of the returning echoes throughout a target approaching sequence.

In our studies we use insectivorous bats as the mammalian model to examine the dynamic temporal processing in the inferior colliculus. Because the layout of the auditory pathway of a bat is fundamentally similar to that of other mammals, the dynamic variation of duration selectivity and recovery cycle of collicular neurons observed in these studies conceivably also occurs in other mammalian species. Future work is necessary to test this contention.

ACKNOWLEDGMENTS

We thank two anonymous reviewers for reading an earlier version of this article. The research works described in and the preparation of this review article have been supported by the Research Board, Research Council, College of Arts and Sciences, and Division of Biological Sciences of University of Missouri-Columbia, USA to Jen, the National Research Council of ROC to Wu (NSC 100-2311-B-003-002, NSC 100NPP001-1) and from the National Science Foundation of PRC to Wang (#31000493).

REFERENCES

Bormann, J. (1988). Electrophysiology of $GABA_A$ and $GABA_B$ receptor subtypes. *Trends Neurosci.* 11, 112–116.

Brand, A., Urban, A., and Grothe, B. (2000). Duration tuning in mouse auditory midbrain. *J. Neurophysiol.* 84, 1790–1799.

Brosch, M., and Schreiner, C. E. (1997). Time course of forward masking tuning curves in cat primary auditory cortex. *J. Neurophysiol.* 77, 923–943.

Casseday, J. H., Ehrlich, D., and Covey, E. (1994). Neural tuning for sound duration: role of inhibitory mechanisms in the inferior colliculus. *Science* 264, 847–850.

Casseday, J. H., Ehrlich, D., and Covey, E. (2000). Neural measurement of sound duration: control by excitatory–inhibitory interaction in the inferior colliculus. *J. Neurophysiol.* 84, 1475–1487.

Chen, G. D. (1998). Effects of stimulus duration on responses of neurons in the chinchilla inferior colliculus. *Hear. Res.* 122, 142–150.

Chen, Q. C., and Jen, P. H. S. (1994). Pulse repetition rate increases the minimum threshold and latency of auditory neurons. *Brain Res.* 654, 155–158.

Cooper, J. R., Bloom, F. E., and Roth, R. H. (1982). *The Biomedical Basis of Neuropharmacology*. Oxford, New York, NY: Oxford University Press.

Covey, E., and Casseday, J. H. (1999). Timing in the auditory system of the bats. *Annu. Rev. Physiol.* 61, 457–476.

Ehrlich, D., Casseday, J. H., and Covey, E. (1997). Neural tuning to sound duration in the inferior colliculus of the big brown bat, *Eptesicus fuscus*. *J. Neurophysiol.* 77, 2360–2372.

Faingold, C. L., Anderson, C. A. B., and Caspary, D. M. (1991). Involvement of GABA in acoustically-evoked inhibition in inferior colliculus neurons. *Hear. Res.* 52, 201–216.

Faure, P. A., Fremouw, T., Casseday, J. H., and Covey, E. (2003). Temporal masking reveals properties of sound-evoked inhibition in duration-tuned neurons of the inferior colliculus. *J. Neurosci.* 23, 3052–3065.

Feng, A. S., Hall, J. C., and Gooler, D. M. (1990). Neural basis of sound pattern recognition in anurans. *Prog. Neurobiol.* 34, 313–329.

Fitzpatrick, D. C., Kuwada, S., Batra, R., and Trahiotis, C. (1995). Neural responses to simple, simulated echoes in the auditory brainstem of the unanesthetized rabbit. *J. Neurophysiol.* 74, 2469–2486.

Fremouw, T., Faure, P. A., Casseday, J. H., and Covey, E. (2005). Duration selectivity of neurons in the inferior colliculus of the big brown bat: tolerance to changes in sound level. *J. Neurophysiol.* 94, 1869–1878.

Freyman, R. L., Clifton, R. K., and Litovsky, R. Y. (1991). Dynamic processes in the precedence effect. *J. Acoust. Soc. Am.* 90, 874–884.

Friend, J. H., Suga, N., and Suthers, R. A. (1966). Neural responses in the inferior colliculus of echolocating bats to artificial orientation sounds and echoes. *J. Cell. Physiol.* 67, 319–332.

Fubara, B. M., Casseday, J. H., Covey, E., and Schwartz-Bloom, R. D. (1996). Distribution of $GABA_A$, $GABA_B$, and glycine receptors in the central auditory system of the big brown bat, *Eptesicus fuscus*. *J. Comp. Neurol.* 369, 83–92.

Fuzessery, Z. M., and Hall, J. C. (1999). Sound duration selectivity in the pallid bat inferior colliculus. *Hear. Res.* 137, 137–154.

Galazyuk, A. V., and Feng, A. S. (1997). Encoding of sound duration by neurons in the auditory cortex of the little brown bat, *Myotis lucifugus*. *J. Comp. Physiol. A* 180, 301–311.

Galazyuk, A. V., Liano, D., and Feng, A. S. (2000). Temporal dynamics of acoustic stimuli enhance amplitude tuning of inferior colliculus neurons. *J. Neurophysiol.* 83, 128–138.

Gooler, D. M., and Feng, A. S. (1992). Temporal coding in frog auditory midbrain: the influence of duration and rise-fall time on processing of complex amplitude-modulated stimuli. *J. Neurophysiol.* 67, 1–22.

Griffn, D. R. (1958). *Listening in the Dark*. New Haven, CT: Yale University Press. (Reprinted by Dover Publications, New York, NY, 1974).

Grinnell, A. D. (1963). The neurophysiology of audition in bats: temporal parameters. *J. Physiol.* 167, 67–96.

He, J. F., Hashikawa, T., Ojima, H., and Kinouchi, Y. (1997). Temporal integration and duration tuning in the dorsal zone of cat auditory cortex. *J. Neurosci.* 17, 2615–2625.

Jen, P. H. S., and Chen, Q. C. (1998). The effect of pulse repetition rate, pulse intensity, and bicuculline on the minimum threshold and latency of bat inferior collicular neurons. *J. Comp. Physiol. A* 182, 455–465.

Jen, P. H. S., and Feng, R. B. (1999). Bicuculline application affects discharge pattern and pulse-duration tuning characteristics of bat inferior collicular neurons. *J. Comp. Physiol. A* 184, 185–194.

Jen, P. H. S., and Kamada, T. (1982). Analysis of orientation signals emitted by the CF-FM bat, *Pteronotus parnellii parnellii* and the FM bat, *Eptesicus fuscus* during avoidance of moving and stationary obstacles. *J. Comp. Physiol. A* 148, 389–398.

Jen, P. H. S., and Schlegel, P. (1982). Auditory physiological properties of the neurons in the inferior colliculus of the big brown bat, *Eptesicus fuscus*. *J. Comp. Physiol. A* 147, 351–363.

Jen, P. H. S., and Wu, C. H. (2005). The role of GABAergic inhibition in shaping the response size and duration selectivity of bat inferior collicular neurons to sound pulses in rapid sequences. *Hear. Res.* 202, 222–234.

Jen, P. H. S., and Wu, C. H. (2006). Duration selectivity organization in the inferior colliculus of the big brown bat, *Eptesicus fuscus*. *Brain Res.* 1108, 76–87.

Jen, P. H. S., and Wu, C. H. (2008). Echo duration selectivity of the bat varies with pulse-echo amplitude difference. *Neuroreport* 19, 373–377.

Jen, P. H. S., and Zhang, J. P. (2000). The role of GABAergic inhibition on direction dependent sharpening of frequency tuning in bat inferior collicular neurons. *Brain Res.* 862, 127–137.

Jen, P. H. S., and Zhou, X. M. (1999). Temporally patterned sound trains affect duration tuning characteristics of bat inferior collicular neurons. *J. Comp. Physiol. A* 185, 471–478.

Jen, P. H. S., Wu, F. J., and Chen, Q. C. (2002). The effect of two-tone stimulation on responses of two simultaneously recorded neurons in the inferior colliculus of the big brown bat, *Eptesicus fuscus*. *Hear. Res.* 168, 139–149.

Jen, P. H. S., Zhou, X. M., and Wu, C. H. (2001). Temporally patterned pulse trains affect frequency tuning and intensity coding of inferior collicular neurons of the big brown bat, *Eptesicus fuscus*. *J. Comp. Physiol. A* 187, 605–616.

Jen, P. H.-S., Wu, C. H., Luan, R. H., and Zhou, X. M. (2002). GABAergic inhibition contributes to pulse repetition rate-dependent frequency selectivity in inferior colliculus of the big brown bat, *Eptesicus fuscus*. *Brain Res.* 948, 159–164.

Keller, C. H., and Takahashi, T. T. (1996). Response to simulated echoes by neurons in the barn owl's auditory space map. *J. Comp. Physiol. A* 178, 499–512.

Klug, A., Park, T. J., and Pollak, G. D. (1995). Glycine and GABA influence binaural processing in the inferior colliculus of the mustache bat. *J. Neurophysiol.* 74, 1701–1713.

Koch, U., and Grothe, B. (1998). GABAergic and glycinergic inhibition sharpens tuning for frequency modulations in the inferior colliculus of the big brown bat. *J. Neurophysiol.* 80, 71–82.

LeBeau, F. E., Malmierca, M. S., and Rees, A. (2001). Iontophoresis *in vivo* demonstrates a key role for GABAA and glycinergic inhibition in shaping frequency response areas in the inferior colliculus of guinea pig. *J. Neurosci.* 21, 7303–7312.

LeBeau, F. E., Rees, A., and Malmierca, M. S. (1996). Contribution of GABA- and glycine-mediated inhibition to the monaural temporal response properties of neurons in the inferior colliculus. *J. Neurophysiol.* 75, 902–919.

Litovsky, R. Y., and Yin, T. C. (1998). Physiological studies of the precedence effect in the inferior colliculus of the cat. I. Correlates of psychophysics. *J. Neurophysiol.* 80, 1285–1301.

Lu, Y., Jen, P. H. S., and Wu, M. (1998). GABAergic disinhibition affects the responses of bat inferior collicular neurons to temporally patterned sound pulses. *J. Neurophysiol.* 79, 2303–2315.

Lu, Y., Jen, P. H. S., and Zheng, Q. Y. (1997). GABAergic disinhibition changes the recovery cycle of bat inferior colliculus neurons. *J. Comp. Physiol. A* 181, 331–341.

Lu, Y., and Jen, P. H. S. (2001). GABAergic and glycinergic neural inhibition in excitatory frequency tuning of bat inferior collicular neurons. *Exp. Brain Res.* 14, 331–339.

Lu, Y., and Jen, P. H. S. (2002). Interaction of excitation and inhibition in inferior collicular neurons of the big brown bat, *Eptesicus fuscus*. *Hear. Res.* 169, 140–150.

Moriyama, T., Hou, T.-Z., Wu, M., and Jen, P. H. S. (1994). Responses of inferior collicular neurons of the FM bat, *Eptesicus fuscus* to pulse trains with varied pulse amplitudes. *Hear. Res.* 79, 105–114.

Narins, P. M., and Capranica, R. R. (1980). Neural adaptation for processing the two-note call of the Puerto Rican treefrog, *Eleutherodactylus coqui*. *Brain Behav. Evol.* 17, 48–66.

Park, T. J., and Pollak, G. D. (1993). GABA shapes sensitivity to interaural intensity disparities in the mustache bat's inferior colliculus: implications for encoding sound location. *J. Neurosci.* 13, 2050–2067.

Perez-Gonzalez, D., Malmierca, M. S., Moore, J. M., Hernandez, O., and Covey, E. (2006). Duration selective neurons in the inferior colliculus of the rat: topographic distribution and relation of duration sensitivity to other response properties. *J. Neurophysiol.* 95, 823–836.

Phillips, D. P., Hall, S. E., and Hollett, J. L. (1989). Pulse repetition rate and signal level effects on neuronal responses to brief pulses in cat auditory cortex. *J. Acoust. Soc. Am.* 85, 2537–2549.

Pinheiro, A. D., Wu, M., and Jen, P. H. S. (1991). Encoding repetition rate and duration in the inferior colliculus of the big brown bat, *Eptesicus fuscus*. *J. Comp. Physiol. A* 169, 69–85.

Pollak, G. D., Bodenhamer, R., Marsh, D. S., and Souther, A. (1977). Recovery cycles of single neurons in the inferior colliculus of unanesthetized bats obtained with frequency-modulated and constant-frequency sounds. *J. Comp. Physiol. A* 120, 215–250.

Popper, A. N., and Fay, R. R. (eds). (1995). *Hearing by Bats*. Berlin, Heidelberg, New York: Springer.

Roberts, R. C., and Ribak, C. E. (1987). An electron microscopic study of GABAergic neurons and terminals in the central nucleus of the inferior colliculus of the cat. *J. Neurocytol.* 16, 333–345.

Shannon, R. V., Zeng, F. G., Kamath, V., Wygonski, J., and Ekelid, M. (1995). Speech recognition with primary temporal cues. *Science* 270, 303–304.

Simmons, J. A., Fenton, M. B., and O'Farrell, M. J. (1979). Echolocation and pursuit of prey by bats. *Science* 203, 16–21.

Suga, N. (1964). Recovery cycles and responses to frequency modulated tone pulses in auditory neurons of echolocating bats. *J. Physiol.* 175, 50–80.

Suga, N. (1970). Echo-ranging neurons in the inferior colliculus of bats. *Science* 170, 449–452.

Suga, N., and Schlegel, P. (1973). Coding and processing in the auditory system of FM signal producing bats. *J. Acoust. Soc. Am.* 54, 174–190.

Surlykke, A., and Moss, C. F. (2000). Echolocation behavior of big brown bat, *Eptesicus fuscus*, in the field and

the laboratory. *J. Acoust. Soc. Am.* 108, 2419–2429.

Tanaka, H., Wong, D., and Taniguchi, I. (1992). The influence of stimulus duration on the delay tuning of crotical neurons in the FM bat, *Myotis lucifugus*. *J. Comp. Physiol. A* 171, 29–40.

Tanaka, H., and Wong, D. (1993). The influence of temporal pattern of stimulation on delay tuning of neurons in the auditory cortex of the FM bat, *Myotis lucifugus*. *Hear. Res.* 66, 58–66.

Vater, M., Habbicht, H., Kossl, M., and Grothe, B. (1992). The functional role of GABA and glycine in monaural and binaural processing in the inferior colliculus of horseshoe bats. *J. Comp. Physiol. A* 171, 541–553.

Wallach, H., Newman, E. B., and Rosenzweig, M. R. (1949). The precedence effect in sound localization. *J. Am. Psychol.* 57, 315–336.

Wang, X., Luo, F., Wu, F. J., Chen, Q. C., and Jen, P. H. S. (2008). The recovery cycle of bat duration-selective collicular neurons varies with hunting phase. *Neuroreport* 19, 861–865.

Wang, X., Luo, F., Wu, F. J., Jen, P. H. S., and Chen, Q. C. (2010). The recovery cycle of neurons in the inferior colliculus of the FM bat determined with varied pulse-echo duration and amplitude. *Chin. J. Physiol.* 53, 119–129.

Wong, D., Maekawa, M., and Tanaka, H. (1992). The effect of pulse repetition rate on the delay sensitivity of neurons in the auditory cortex of the FM bat, *Myotis lucifugus*. *J. Comp. Physiol. A* 170, 393–402.

Wu, C. H., and Jen, P. H. S. (2006). GABA-mediated echo duration selectivity of inferior collicular neurons of *Eptesicus fuscus*, determined with single pulses and pulse-echo pairs. *J. Comp. Physiol. A* 192, 985–1002.

Wu, C. H., and Jen, P. H. S. (2010). A duration coding mechanism underlying bat echo recognition. *Adapt. Med.* 2, 71–77.

Wu, M., and Jen, P. H. S. (1996). Temporally patterned sound pulses affect directional sensitivity of inferior collicular neurons of the big brown bat, *Eptesicus fuscus*. *J. Comp. Physiol. A* 179, 385–393.

Wu, M., and Jen, P. H.-S. (1998). The recovery properties of neurons in the inferior colliculus, auditory cortex and the pontine nuclei of the big brown bat, *Eptesicus fuscus*. *Chin. J. Physiol.* 41, 1–8.

Yang, L., Pollak, G. D., and Resler, C. (1992). GABAergic circuits sharpen tuning curves and modify response properties in the mustache bat inferior colliculus. *J. Neurophysiol.* 68, 1760–1774.

Yost, W. A., and Guzman, S. J. (1996). Auditory processing of sound sources: is there an echo in here? *Curr. Dir. Psychol. Sci.* 5, 125–131.

Yost, W. A., and Soderquist, D. R. (1984). The precedence effect: revisited. *J. Acoust. Soc. Am.* 76, 1377–1383.

Zhou, X. M., and Jen, P. H. S. (2001). The effect of sound intensity on duration-tuning characteristics on bat inferior collicular neurons. *J. Comp. Physiol. A* 187, 63–73.

Zhou, X. M., and Jen, P. H. S. (2002a). The role of GABAergic inhibition in shaping directional selectivity of bat inferior collicular neurons determined with temporally patterned pulse trains. *J. Comp. Physiol. A* 188, 815–826.

Zhou, X. M., and Jen, P. H. S. (2002b). The effect of sound duration on rate-intensity functions of inferior collicular neurons of the big brown bat, *Eptesicus fuscus*. *Hear. Res.* 166, 124–135.

Zhou, X. M., and Jen, P. H. S. (2003). The effect of bicuculline application on azimuth dependent recovery cycle of inferior collicular neurons of the big brown bat, *Eptesicus fuscus*. *Brain Res.* 973, 131–141.

Zhou, X. M., and Jen, P. H. S. (2006). Duration selectivity of bat inferior collicular neurons improves with increasing repetition rate. *Chin. J. Physiol.* 49, 46–55.

Zurek, P. M. (1980). The precedence effect and its possible role in the avoidance of interaural ambiguities. *J. Acoust. Soc. Am.* 67, 952–964.

Conflict of Interest Statement: The authors declare that the research was conducted in the absence of any commercial or financial relationships that could be construed as a potential conflict of interest.

Received: 25 February 2012; accepted: 20 April 2012; published online: 08 May 2012.

Citation: Jen PH-S, Wu CH and Wang X (2012) Dynamic temporal signal processing in the inferior colliculus of echolocating bats. Front. Neural Circuits ***6****:27. doi: 10.3389/fncir.2012.00027*

frontiers in
NEURAL CIRCUITS

ORIGINAL RESEARCH ARTICLE
published: 17 August 2012
doi: 10.3389/fncir.2012.00054

Multiple mechanisms shape FM sweep rate selectivity: complementary or redundant?

Anthony J. Williams and Zoltan M. Fuzessery*

Department of Zoology and Physiology, University of Wyoming, Laramie, WY, USA

Edited by:
Manuel S. Malmierca, University of Salamanca, Spain

Reviewed by:
Christine Portfors, Washington State University, USA
George D. Pollak, The University of Texas at Austin, USA

****Correspondence:***
Zoltan M. Fuzessery, Department of Zoology and Physiology, 3166, University of Wyoming, 1000 East University Avenue, Laramie, WY 82071, USA.
e-mail: zmf@uwyo.edu

Auditory neurons in the inferior colliculus (IC) of the pallid bat have highly rate selective responses to downward frequency modulated (FM) sweeps attributable to the spectrotemporal pattern of their echolocation call (a brief FM pulse). Several mechanisms are known to shape FM rate selectivity within the pallid bat IC. Here we explore how two mechanisms, stimulus duration and high-frequency inhibition (HFI), can interact to shape FM rate selectivity within the same neuron. Results from extracellular recordings indicated that a derived duration-rate function (based on tonal response) was highly predictive of the shape of the FM rate response. Longpass duration selectivity for tones was predictive of slowpass rate selectivity for FM sweeps, both of which required long stimulus durations and remained intact following iontophoretic blockade of inhibitory input. Bandpass duration selectivity for tones, sensitive to only a narrow range of tone durations, was predictive of bandpass rate selectivity for FM sweeps. Conversion of the tone duration response from bandpass to longpass after blocking inhibition was coincident with a change in FM rate selectivity from bandpass to slowpass indicating an active inhibitory component to the formation of bandpass selectivity. Independent of the effect of duration tuning on FM rate selectivity, the presence of HFI acted as a fastpass FM rate filter by suppressing slow FM sweep rates. In cases where both mechanisms were present, both had to be eliminated, by removing inhibition, before bandpass FM rate selectivity was affected. It is unknown why the auditory system utilizes multiple mechanisms capable of shaping identical forms of FM rate selectivity though it may represent distinct but convergent modes of neural signaling directed at shaping response selectivity for important biologically relevant sounds.

Keywords: duration tuning, sideband inhibition, inferior colliculus

INTRODUCTION

The breakdown of complex sensory input into simpler components for extraction of specific cues that guide behavior is a common strategy utilized across sensory modalities. For the auditory system, this involves a reduction of complex sounds into their individual spectrotemporal components (Brugge, 1992). Many species exhibit a strong selectivity for the rate and direction of frequency modulations (FMs), which are common components of complex sounds (Pollak and Park, 1995; Andoni and Pollak, 2011). Several underlying mechanisms have been identified that shape FM selectivity involving the spectrotemporal integration of excitatory and inhibitory inputs across the receptive field of an auditory neuron (Suga, 1968; Britt and Starr, 1976; Heil et al., 1992; Shannon-Hartman et al., 1992; Gordon and O'Neill, 1998; Gittelman et al., 2009; Fuzessery et al., 2010). In the current study, we focus on how more than one mechanism can interact to shape the selectivity for FM sweep rate. The high-frequency region of the pallid bat inferior colliculus (IC) is ideal for this type of analysis due to a high degree of rate selectivity for the downward FM sweeps of their echolocation call (Brown, 1976; Bell, 1982; Fuzessery et al., 1993) and because the mechanisms driving FM rate selectivity have been identified (Fuzessery et al., 2010). Specifically, we focus on how duration tuning and sidebands of high-frequency inhibition (HFI) interact to shape rate selectivity for downward FM sweeps, and the neural circuitry that might shape these underlying mechanisms.

The IC is a highly integrative midbrain region of the auditory system that combines excitatory and inhibitory input from at least a dozen lower level nuclei (Pollak and Park, 1995; Oliver, 2005) and is also the first level of the auditory system where duration tuned neurons appear (Sayegh et al., 2011). The mechanisms driving duration tuning have typically been studied using simple stimuli such as pure tones (Ehrlich et al., 1997; Galazyuk and Feng, 1997; Chen, 1998; Fuzessery and Hall, 1999; Brand et al., 2000; Mora and Kossl, 2004; Jen and Wu, 2006; Perez-Gonzalez et al., 2006; Luo et al., 2008; Macias et al., 2011). Tone duration selectivity can be used to predict a neuron's best FM sweep rate, and it is likely that both forms of selectivity share the same underlying mechanisms (Fuzessery et al., 2006). Duration tuning has been described as the temporal integration of excitatory and inhibitory input using a variety of models, based on the results of both extra- and intracellular recording (Casseday et al., 1994; Fuzessery and Hall, 1999; Leary et al., 2008; Aubie et al., 2009; Sayegh et al., 2011).

Auditory neurons within the IC typically have a narrow excitatory receptive field bounded by sideband inhibition (Covey and Casseday, 1995; Ramachandran et al., 1999) that is responsible for much of the observed FM selectivity (Britt and Starr, 1976; Shannon-Hartman et al., 1992; Gordon and O'Neill, 1998; Koch and Grothe, 1998; Brimijoin and O'Neill, 2005; Williams and Fuzessery, 2011). In the pallid bat, many neurons exhibit an early-arriving (relative to excitation) band of low-frequency inhibition (LFI) that can shut down the response to an upward FM sweep and create selectivity for downward FM sweeps (Fuzessery et al., 2006; Razak and Fuzessery, 2006). The presence of a late-arriving band of HFI acts to suppress responses to slower sweep rates (Fuzessery et al., 2006; Razak and Fuzessery, 2006). It has also been shown that elimination of HFI, either through removing the high-frequency region from the FM sweep or by pharmacological blockade of inhibitory input, is associated with a subsequent loss of FM rate selectivity (Razak and Fuzessery, 2009; Williams and Fuzessery, 2011). However, given the complex integrative nature of the IC, many neurons exhibit more than one mechanism that can shape FM rate selectivity (Gordon and O'Neill, 1998; Fuzessery et al., 2010; Gittelman and Li, 2011). The focus of the current study was to evaluate the predictive value of duration tuning and HFI on FM rate selectivity, and how the two mechanisms interact to shape a neuron's selectivity for FM sweep rate.

MATERIALS AND METHODS

Extracellular single-unit recordings were obtained from the IC of 44 adult pallid bats. Bats were captured in New Mexico and housed in a free-flight environmental chamber (85–90°F) maintained on a reverse 12:12 h light:dark cycle at the University of Wyoming Biological Sciences animal facility. The bats were fed mealworms raised on ground Purina rat chow. All surgical procedures, animal welfare assurances, and experimental manipulations were approved by an Institutional Animal Care and Use Committee based on guidelines required by the National Institutes of Health for animal research.

SURGICAL PROCEDURES

Each bat was isolated from the main colony room and allowed 2–3 days to acclimate to their home cage prior to surgery. All surgical procedures were performed as previously described (Fuzessery et al., 2006) in a designated surgical suite. In brief, bats were initially sedated with an inhalation anesthetic (Isoflurane, USP) followed by an intraperitoneal injection of pentobarbital sodium (30 mg/kg of body weight) and acepromazine (2 mg/kg of body weight). Upon loss of reflexive responses to a toe pinch, animals were placed in a bite bar and a midline incision made in the scalp. The superficial muscles over the dorsal surface of the skull were carefully separated and reflected by blunt dissection. The anterior region of the skull was gently scraped clean and a thin layer of glass microbeads was applied and secured with cyanoacrylate for placement of a head pin. A 1 mm^2 exposure was made over the left or right IC by carefully excising the skull with a microscalpel. Exposed muscle was covered with petroleum jelly (Vaseline®) and the skull was kept moist with periodic applications of physiological saline throughout the course of the recording session. Following surgery, the animals were taken to the recording chamber (see below) and secured in a Plexiglas restraining device. A cylindrical aluminum head pin was mounted to a cross bar and secured to the anterior skull using dental cement to prevent movement of the head.

RECORDING AND DATA ACQUISITION PROCEDURES

Bats were isolated in a heated (85–90°F), sound-proofed chamber lined with anechoic foam during the 6–8 h recording session. Auditory stimuli were generated by digital hardware (Modular Instruments and Tucker Davis Technologies) controlled by a custom-written software program (Fuzessery et al., 1991). Modulated waveforms were amplified with a stereo amplifier and presented as monaural closed-field stimuli through Infinity emit-K ribbon tweeters fitted with funnels attached for insertion into the pinnae. Speaker output was calibrated with a Bruel and Kjaer 1/8 inch microphone placed at the tip of funnel (±15 dB response from 20 to 70 kHz).

In vivo single-unit recordings of extracellular neuronal activity were obtained with glass microelectrodes (1 M NaCl, 2–5 MΩ resistance) mounted diagonally in a "piggy-back" configuration (Havey and Caspary, 1980) to a five-barrel glass pipette (WPI) used for iontophoresis of inhibitory receptor antagonists (see below). All data were recorded from the high-frequency region of the pallid bat IC (best frequency = 30–60 kHz) at penetration depths of 1000–2000 μm from the surface of the brain using a similar recording protocol as described previously (Razak and Fuzessery, 2009; Williams and Fuzessery, 2011).

The best frequency and excitatory tuning curve were determined with single tones over a range of intensity levels. Rise/fall times were 1 ms unless signals were shorter than 1 ms, in which case they were each one half of the signal. All subsequent recordings were performed at a single intensity level 5–10 dB above the intensity threshold for the best frequency. Pairs of tones, offset in time, from within and outside the excitatory bandwidth, were used to determine the extent of sideband inhibition, using the two-tone inhibition protocol described below. FM sweeps (30 kHz bandwidth) and best frequency tones were then presented over a range of durations (0.1–100 ms) to establish, respectively, selectivity for FM rate and tone duration. Response magnitudes for stimuli are defined as the total number of spikes in response to 30 stimulus presentations presented at an interpulse interval of 400 ms. Single-unit output was identified audiovisually, and based on the consistency of the action potential waveform, and on high signal-to-noise ratio.

PREDICTED RATE FUNCTIONS

The predicted rate function of a neuron was derived from its response to a single tone presented over a range of tone durations (**Figure 2**). We have previously (Fuzessery et al., 2006) predicted the best sweep rate of neurons with bandpass duration selectivity by dividing the bandwidth (kHz) of the excitatory tuning curve by the best duration (ms). This is the sweep rate at which an FM sweep will traverse the excitatory tuning curve in a time equal to the neuron's best duration. In the present study, we predict the entire rate function of a neuron using the responses to a single excitatory tone over a range of durations to predict the response

at a given sweep rate. Sweep rate selectivity was predicted from the tone by dividing the bandwidth of the tuning curve by the duration of the tone. The response to that tone duration was then used to construct the sweep rate function. For example, the neuron in **Figure 2** had an excitatory bandwidth of 13 kHz. Therefore, a 15 ms tone duration (**Figure 2A**, arrow) would correspond to a 0.87 kHz/ms sweep rate. The response at this duration was 35 spikes, and was used to predicted the response at 0.87 kHz/ms (**Figure 2B**, arrow). This process was repeated for each data point in the duration function (**Figure 2A**) to construct the entire predicted sweep rate function, which was then compared with the actual rate function (**Figure 2B**).

TWO-TONE INHIBITION

The spectral width and relative arrival time of inhibitory sidebands were determined using a two-tone inhibition over time protocol as previously described (Fuzessery et al., 2006). The focus of the present study is HFI, which if present in this population of neurons, always arrives later than excitation, and serves to determine the slowest sweep rate to which a neuron will respond.

In brief, inhibitory tones from the high-frequency region (if present) were paired with an excitatory tone of the same intensity level to audiovisually map out the frequency range of sideband inhibition. Excitatory tones were always shorter than inhibitory tones, with excitatory tones of 1–2 ms duration, and inhibitory tones of 5–10 ms duration. The delay between an excitatory and inhibitory tone was then varied to determine the relative arrival time of inhibition for each sideband region. Specifically, the delay between the onsets of the two tones was varied to determine the delay-frequency combination resulting in at least a 90% reduction in the response. If the inhibitory tone had to be presented before the excitatory tone for suppression to occur (i.e., positive delay) then excitatory input was assumed to arrive before inhibition. If the inhibitory tone could suppress the excitatory tone even when presented after the excitatory tone (i.e., negative delay) then inhibitory input was assumed to arrive before excitation. A predicted FM cutoff rate (i.e., the slowest rate to which the neuron would respond) was calculated from the bandwidth and arrival time of HFI as previously described (Fuzessery et al., 2006) using the following formula: predicted FM cutoff rate (kHz/ms) = HFI bandwidth (kHz)/HFI arrival time (ms). FM sweeps presented at a rate slower than the predicted FM cutoff rate would cause HFI to arrive before excitation, and the response would be suppressed.

MICROIONTOPHORESIS

Microiontophoretic applications of inhibitory receptor blockers were delivered using a previously described protocol (Razak and Fuzessery, 2009; Williams and Fuzessery, 2011). Immediately before a recording session, individual iontophoresis barrels were loaded with gabazine (GBZ, 10 mM, pH 4.0, Sigma) or strychnine (STRYCH, 3 mM, pH 4.0, Sigma) dissolved in physiological saline. The center barrel was used as a balance electrode (1 M sodium chloride). A retaining current (−15 nA) was used to retain the drugs during the search phase and pre-drug (control) recording phase. Escalating iontophoretic ejection currents of +10 to +60 nA were used to apply the drug. Three types of tests were performed following drug application to confirm the effectiveness of inhibitory receptor blockade, as previously described (Razak and Fuzessery, 2009; Williams and Fuzessery, 2011) (1) Recovery data, quantified as number of spikes, were obtained in 25 neurons at 5 min intervals after the ejection current was turned off to monitor the return to pre-drug response levels, which took 10–30 min. (2) Current was passed through the balance barrel in 18 neurons to verify that the ejection current did not affect the response. (3) In all neurons, ejection currents were gradually increased from +10 to +60 nA, with responses monitored at each interval, to avoid possible response saturation. When both drugs were tested on a neuron, the response of the neuron returned to pre-drug levels before the second drug was tested.

DATA ANALYSIS

A Pearson correlation test was used to compare predicted versus actual FM rate responses. A Fisher Exact Test was used to evaluate the proportion of neurons affected by the application of GBZ or STRYCH on duration tuning or FM rate selectivity. All data are presented as the mean ± S.D. P-values <0.05 were considered significant.

RESULTS

Selectivity for downward FM sweep rates between 0.3–300 kHz/ms (30 kHz bandwidth, 0.1–100 ms duration) were measured in 79 IC neurons, and the roles of duration tuning and HFI in shaping their selectivity were evaluated (**Table 1**). The majority of neurons evaluated (72%, 57/79) were tuned to a limited range of FM sweep rates, and exhibited bandpass rate selectivity (**Figure 1A**). The remaining neurons (28%, 22/79) were not tuned to sweep rates, and instead exhibited slowpass rate selectivity (**Figure 1B**). This percentage of rate-tuned neurons is similar to that reported in previous studies of the pallid bat IC (Fuzessery et al., 2010). We have previously reported the presence of fastpass rate selectivity (Fuzessery et al., 2006), but because, in the present study, we extended the range of sweep rates to include faster rates (300 kHz/ms), all neurons eventually ceased to respond as sweep rates were increased.

Table 1 summarizes the four possible conditions in terms of the mechanisms shaping sweep rate selectivity. If neither duration tuning or HFI was present, the neurons all had slowpass rate functions (**Figure 1B**). If either or both duration tuning were present, the neurons had bandpass rate

Table 1 | Comparison of FM and tonal stimulus selectivity to presence or absence of HFI.

FM rate	Bandpass duration	HFI	Percent
Slowpass ($n = 22$)	No	No	100% (22/22)
Bandpass ($n = 57$)	No	Yes	62% (35/57)
	Yes	No	14% (8/57)
	Yes	Yes	24% (14/57)

Numbers in parentheses indicate the number of neurons in each group/total number of either slowpass or bandpass FM selective neurons.

functions (**Figure 1A**). When both mechanisms were present, their relative contributions to shaping rate selectivity were determined by either eliminating HFI by starting the downward FM sweep at a frequency just lower than the high-frequency inhibitory sideband, or by eliminating duration selectivity or HFI through the iontophoresis of inhibitory receptor blockade (**Table 2**).

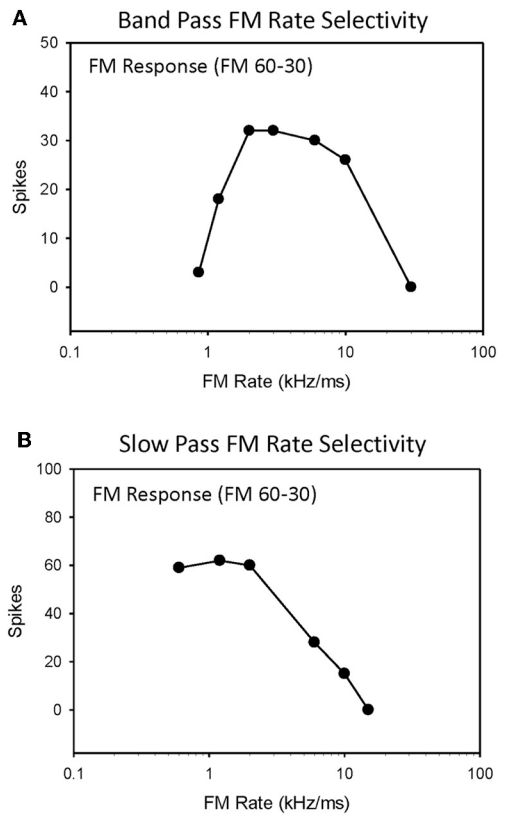

FIGURE 1 | Single-unit responses from the high-frequency region of the pallid bat IC were recorded for downward FM sweep rates ranging from 0.3 to 300 kHz/ms and classified as either bandpass (A) or slowpass (B).

PREDICTING SWEEP RATE SELECTIVITY FROM DURATION TUNING

We have previously (Fuzessery et al., 2006) predicted only the best sweep rates of neurons with bandpass rate selectivity from their duration functions, by dividing the bandwidth of their excitatory tuning curves (kHz) by their best durations (ms). This gives the sweep rate at which an FM sweep will pass through the excitatory tuning curve in a time equal to the best duration. Here we construct the entire predicted rate function for each neuron from its duration function. **Figure 2** demonstrates how the duration function was used to predict the FM rate response. This neuron exhibited a longpass duration selectivity, responding to tones longer than 3 ms (**Figure 2A**). It lacked HFI, so, as expected, it exhibited a slowpass rate selectivity, responding to sweep rates slower than 6 kHz/ms (**Figure 2B**). Its predicted rate function was constructed from the duration function by dividing the width of the excitatory tuning curve by the tone duration, and using the response magnitude at that calculated rate to create a predicted sweep rate function. This neuron had a tuning curve width of 13 kHz. To illustrate the construction of one point in the predicted function (arrows, **Figures 2A,B**), a 15 ms tone duration is equivalent to the time taken for a sweep rate of 0.87 kHz/ms (13 kHz/15 ms) to traverse the tuning curve. The response at this tone duration was 36 spikes (**Figure 2A**), and when normalized in the predicted rate function, was 100% maximum response (**Figure 2B**). The predicted rate function (**Figure 2B**) of this neuron was strongly predictive of the actual FM rate function (**Figure 2C**). Overall, there was a positive correlation observed between predicted and actual FM rates of all slowpass neurons evaluated (mean $r^2 = 0.936 \pm 0.065$, $n = 22$).

An example of a predicted rate function for a neuron with a bandpass duration function, and lacking HFI, is shown in **Figure 3**. This neuron had an excitatory tuning curve bandwidth of 5 kHz, so the maximum response to a 2 ms tone (**Figure 3A**, arrow) predicts the response to a 2.5 kHz/ms sweep rate (**Figure 3B**, arrow), with a high correlation between predicted and actual FM rates (**Figure 3C**, $r^2 = 0.952$, $p < 0.05$). Overall, a positive correlation between predicted and actual rate functions was observed for all 8 bandpass FM rate selective neurons tested that did not exhibit HFI (**Table 1**, mean $r^2 = 0.878 \pm 0.178$, $n = 8$).

Table 2 | Effect of eliminating the underlying mechanisms (duration tuning/HFI) on bandpass FM rate selectivity.

Bandpass duration tuning	HFI	Bandpass FM rate selectivity	*n*	Test
Eliminated	Absent	Eliminated	2	Iontophoresis (2 STRYCH)
Intact	Absent	Intact	3	Iontophoresis (2 STRYCH, 1 GBZ)
Eliminated	Intact	Intact	4	Iontophoresis (2 STRYCH, 2 GBZ)
Eliminated	Eliminated	Eliminated	1	Iontophoresis (1 STRYCH)
Intact	Intact	Intact	5	Iontophoresis (1 STRYCH, 4 GBZ)
Intact	Eliminated	Intact	5	Removal of HFI from FM Sweep

Two types of tests were used (right column) to evaluate the removal of duration tuning and HFI: (1) iontophoresis of GBZ or STRYCH to block inhibitory input or (2) directly removing HFI by excluding the high-frequency region from the FM sweep. "Absent" indicates that HFI was not present. "Eliminated" responses indicate a conversion of duration tuning from bandpass to longpass or conversion of FM rate tuning from bandpass to slowpass. "Intact" responses indicate that bandpass selectivity did not change.

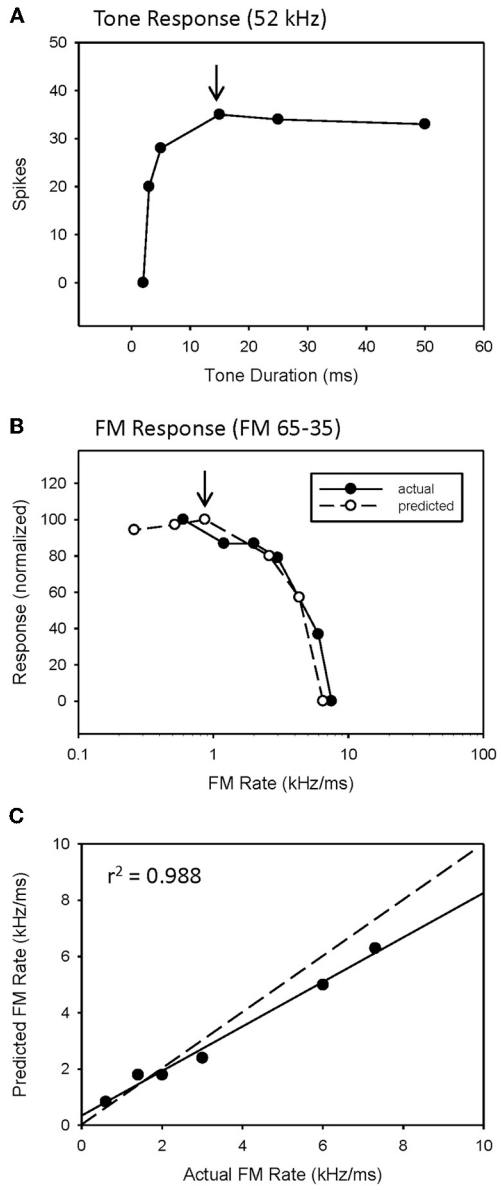

FIGURE 2 | A slowpass FM rate selective neuron (B) exhibiting longpass duration tuning for tones (A). The duration function, based on longpass duration tuning (see Methods), predicted the slowpass FM rate response **(B)** with a significant correlation between predicted and actual FM rates **(C)**. The dashed line indicates perfect predictions, and the solid line indicates the actual correlation.

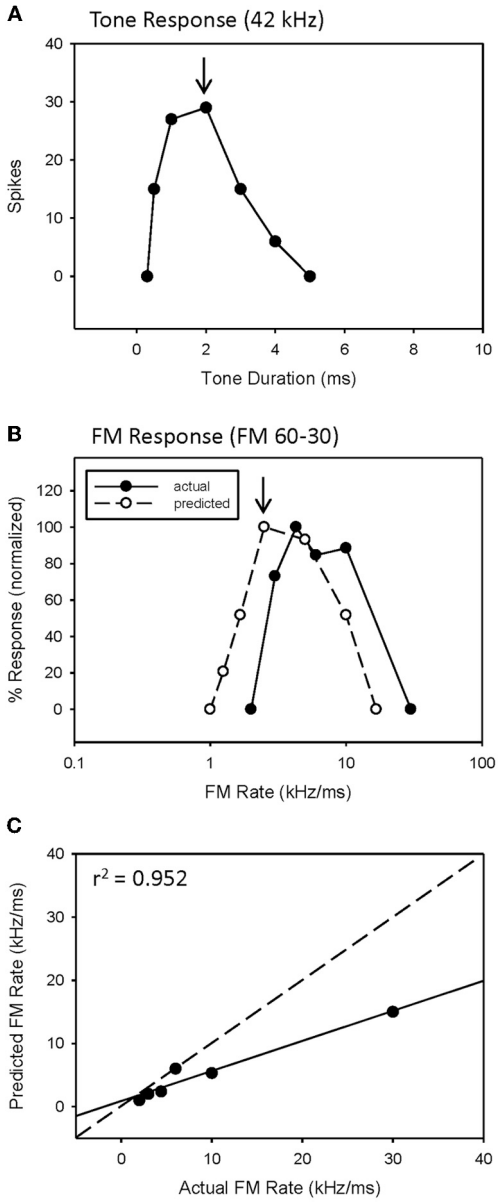

FIGURE 3 | The duration function of a bandpass duration-tuned neuron (A) that was predictive of a bandpass FM rate response (B) with a significant correlation (C) between predicted and actual FM rates (B).

However, while the correlations were high, the absolute values for actual and predicted functions were off in a consistent manner. Note the shift in the predicted function toward slower sweep rates, relative to the actual FM rate response (**Figure 3B**). This is reflected in the shallower slope of the prediction line (**Figure 3C**, slope = 0.476). This was a typical pattern observed between the predicted and actual rate functions across the entire population of neurons tested, both slowpass and bandpass. Although some neurons did exhibit both high correlation and slope values (e.g., **Figure 2C**), the average difference in slopes between predicted and actual FM rates = 0.617 ± 0.373 ($n = 48$), indicating a 1.6 fold (1/slope) underestimation of actual FM responses on average. As will be discussed, this shift in the predicted rate function toward slower rates is likely due to an underestimation of the excitatory bandwidth, which is broader when measured with FM sweeps as opposed to tones.

INTERACTION OF DURATION TUNING AND HFI ON FM RATE SELECTIVITY

While the entire sweep rate function of a neuron can be predicted from its tone duration function, HFI can be used to predict only

the slowest sweep to which a neuron will respond, which is the bandwidth of HFI (kHz) divided by the arrival time (ms) of HFI relative to the arrival of excitation (Fuzessery et al., 2006). This is the cutoff rate, i.e., the sweep rate at which the delayed HFI will arrive at the same time as the excitatory input, and suppress the response.

The majority of bandpass FM rate-selective neurons exhibited HFI (86%) and either longpass (62%) or bandpass (38%) duration tuning for tones (**Table 1**). It is predicted that those with longpass duration functions will have bandpass rate selectivity shaped entirely by HFI, while those with bandpass duration functions will have bandpass rate selectivity shaped by either mechanism, or a combination of the two.

The majority of bandpass FM rate selective neurons exhibited longpass duration tuning and HFI (**Table 1**). It would be expected that the removal of HFI, by starting a downward sweep at a frequency just below this inhibitory domain, would eliminate their bandpass selectivity. This was tested in 13 of these neurons. An example is shown in **Figure 4**. This neuron exhibited longpass duration tuning for tones with a strong response to tone durations >1 ms (**Figure 4A**). A tone (35 kHz) from within high-frequency inhibitory sideband (**Figure 4C**) completely suppressed the response to a best-frequency tone (33 kHz) when the higher frequency tone was presented 5 ms before the excitatory tone (**Figure 4B**). Elimination of HFI in the downward 33–20 kHz sweep (**Figure 4C**) sweep converted the FM rate response from bandpass to slowpass (**Figure 4D**) demonstrating that HFI acts as a fastpass filter for FM rate selectivity by suppressing slow FM sweep rates. In this neuron, the predicted FM cutoff rate was 0.8 kHz/ms (4 kHz/5 ms), which was close to the actual FM cutoff rate of 0.67 kHz/ms (**Figure 4D**).

Overall, there was a positive correlation between predicted and actual FM cutoff rates (**Figure 4E**, $r^2 = 0.781$, $n = 17$, $P < 0.05$). Moreover, the predicted slowpass rate functions from duration tuning were accurate when the HFI was removed from the sweep, as demonstrated in **Figure 4F** ($r^2 = 0.975$ between actual and predicted rates, $p < 0.05$). Thus, when bandpass rate selective neurons had longpass duration functions and HFI, their rate selectivity was shaped entirely by HFI.

Fourteen neurons (24%) expressed both bandpass duration tuning for tones and HFI. The effect of removing HFI from a downward FM sweep was tested in five of these neurons. Effects ranged from a minimal change in FM selectivity (**Figure 5A**) to a broadening of the bandpass rate selectivity to include slower FM sweep rates (**Figure 5C**). In the first case (**Figure 5A**), this can be interpreted as HFI setting a cutoff rate that was the same or lower than that shaped by the bandpass duration function; hence eliminating HFI had little effect on the rate function. Moreover, the predicted rate function accurately predicted the actual rate function, with or without HFI in the FM sweep. In contrast, in the second case (**Figure 5C**), the cutoff rate shaped by HFI occurred at a faster rate than that shaped by bandpass duration tuning. Therefore, the bandpass rate function broadened when HFI was removed, and was then accurately predicted by the duration function. In all cases, bandpass FM rate selectivity remained intact and a high correlation was observed between predicted and actual FM rate responses, when HFI was excluded from the FM sweep (**Figures 5B,D**, mean $r^2 = 0.948 \pm 0.068$, $n = 5$). Thus, when both HFI and bandpass duration tuning were present, duration tuning could either shape the entire rate function, or HFI could determine the cutoff rate, and duration tuning determine the reminder of the rate function.

Despite the fact that FM sweep rates were tested over a broad range of 0.3–300 kHz/ms, three neurons were responsive to even slower rates, and their bandpass duration functions predicted that, if slower rates had been tested, these neurons would have exhibited bandpass rate selectivity. Because it was not clear whether their predicted and actual rate functions were similar, these neurons were excluded from the study.

INHIBITORY MECHANISMS SHAPING FM RATE SELECTIVITY

A previous study demonstrated that, in the majority of neurons tested, bandpass duration tuning is created at the level of the IC in the pallid bat by an on-best frequency inhibition and can be eliminated by blocking GABAergic input with bicuculline (Fuzessery and Hall, 1999). In the present study, bandpass duration tuning was eliminated following application of either STRYCH (**Figure 6A**, 5/7 neurons) or GBZ (**Figure 7A**, 3/8 neurons), indicating that either inhibitory pathway (glycinergic or GABAergic) is involved in sculpting this form of selectivity.

The iontophoretic blockade of inhibitory inputs was used as a second test of the roles of duration tuning and HFI in shaping rate selectivity. **Table 2** summarizes the effects of inhibitory receptor blockade on 15 bandpass duration tuned neurons, some of which also had HFI, and its subsequent effect on bandpass rate tuning. In the first two rows, the neurons lacked HFI. If receptor blockade eliminated duration tuning, rate tuning was also eliminated. In the next three rows, neurons possessed both HFI and duration tuning. Both mechanisms had to be eliminated by receptor blockade to eliminate rate tuning. If one mechanism was not eliminated, rate tuning remained intact. For neurons in the bottom row, HFI was eliminated not by iontophoresis, but rather by eliminating HFI by starting the downward sweep at a frequency lower than the inhibitory sideband (e.g., **Figure 4C**). Since duration tuning remained intact, so did the rate tuning.

Overall, when both underlying mechanisms were absent or eliminated, bandpass rate selectivity was lost (3/20 neurons), but if either of the mechanisms remained intact, bandpass FM rate selectivity also remained intact (17/20 neurons) ($P < 0.05$ between groups, Fisher's Exact Test).

An example of a bandpass rate-selective neuron expressing only bandpass duration tuning is shown in **Figure 6**. Blocking GABAergic input had only a minor effect on its bandpass duration tuning (**Figure 6A**) and consequently a minor effect on rate selectivity, which remained bandpass (**Figure 6B**). In contrast, blocking glycinergic input changed its duration function from bandpass to longpass (**Figure 6A**), and its rate function from bandpass to slowpass (**Figure 6B**).

An example of bandpass rate-selective neuron expressing both duration tuning and HFI is show in **Figure 7**. As in the previous neuron, blocking inhibition, in this case GABAergic inhibition, eliminated bandpass duration tuning (**Figure 7A**). This neuron's HFI inhibition was examined by delaying an excitatory tone (42 kHz) with respect to a high-frequency inhibitory tone

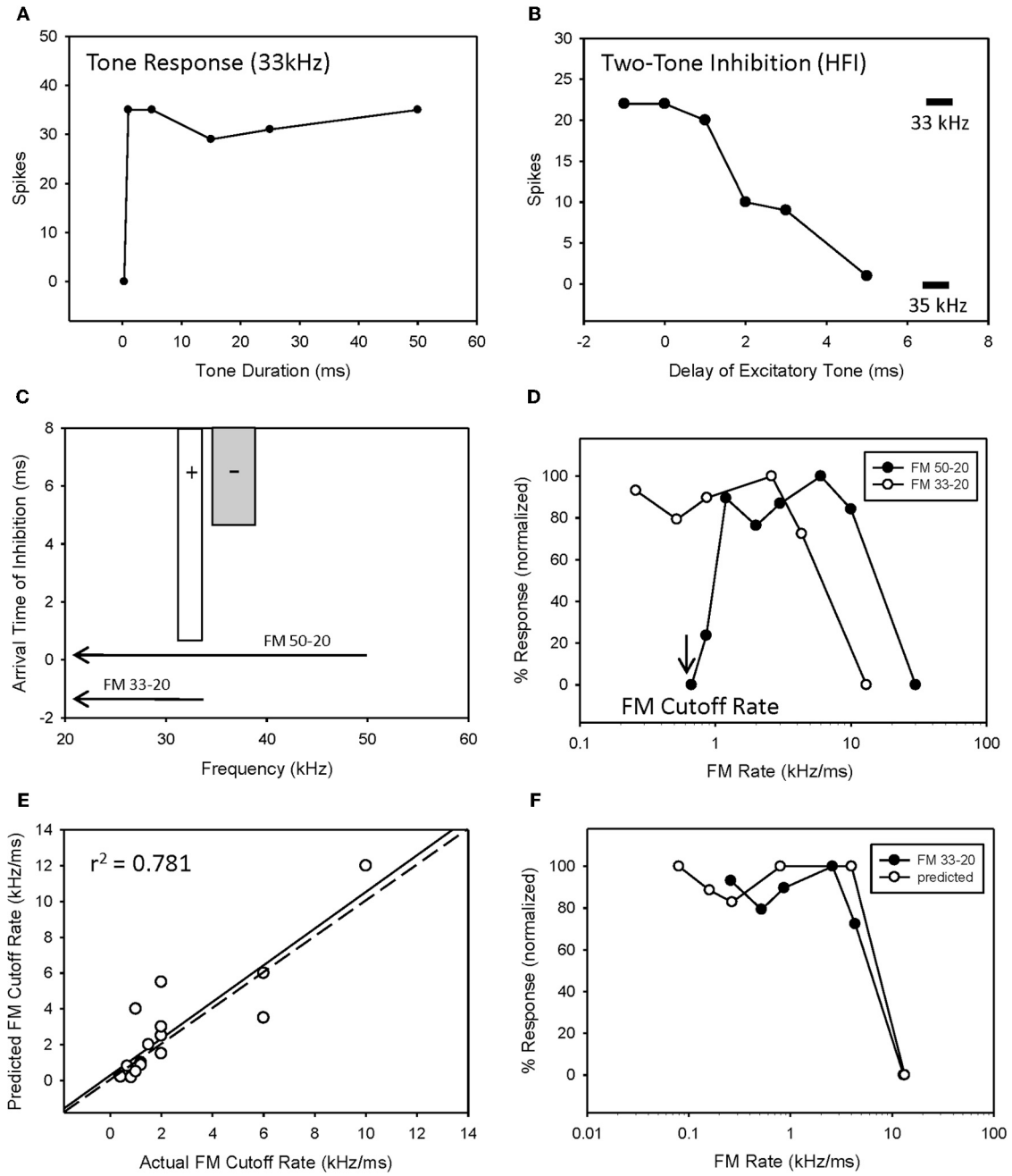

FIGURE 4 | HFI acts as a fastpass FM rate filter. Neuron exhibiting longpass duration tuning for tones **(A)** and a delayed HFI **(B)**. FM sweep responses were compared both with and without the contribution of HFI **(C)**. Removal of HFI converted the FM rate response from bandpass to slowpass **(D)**. A positive correlation was observed between predicted and actual FM cutoff rates **(E)** as derived from the bandwidth and arrival time of HFI (see Methods). The duration function was only predictive of the FM rate response when HFI was removed from the sweep **(F)**.

(46 kHz), and showed that the arrival of inhibition was delayed by about 3 ms (**Figure 7B**). Blocking inhibition had little effect on the two-tone inhibition function. Since HFI remained intact after blocking GABAergic inhibition, the neuron's bandpass rate selectivity also showed little change before and during receptor blockade (**Figure 7C**).

A third example shows the result of eliminating both underlying mechanisms (**Figure 8**). Blocking glycinergic input eliminated both bandpass duration tuning (**Figures 8A,D**) and HFI (**Figures 8B,E**). Following the elimination of HFI, the bandwidth of the excitatory tuning curve expands to well beyond the frequencies in the inhibitory sideband (**Figure 8E**). Prior to blocking

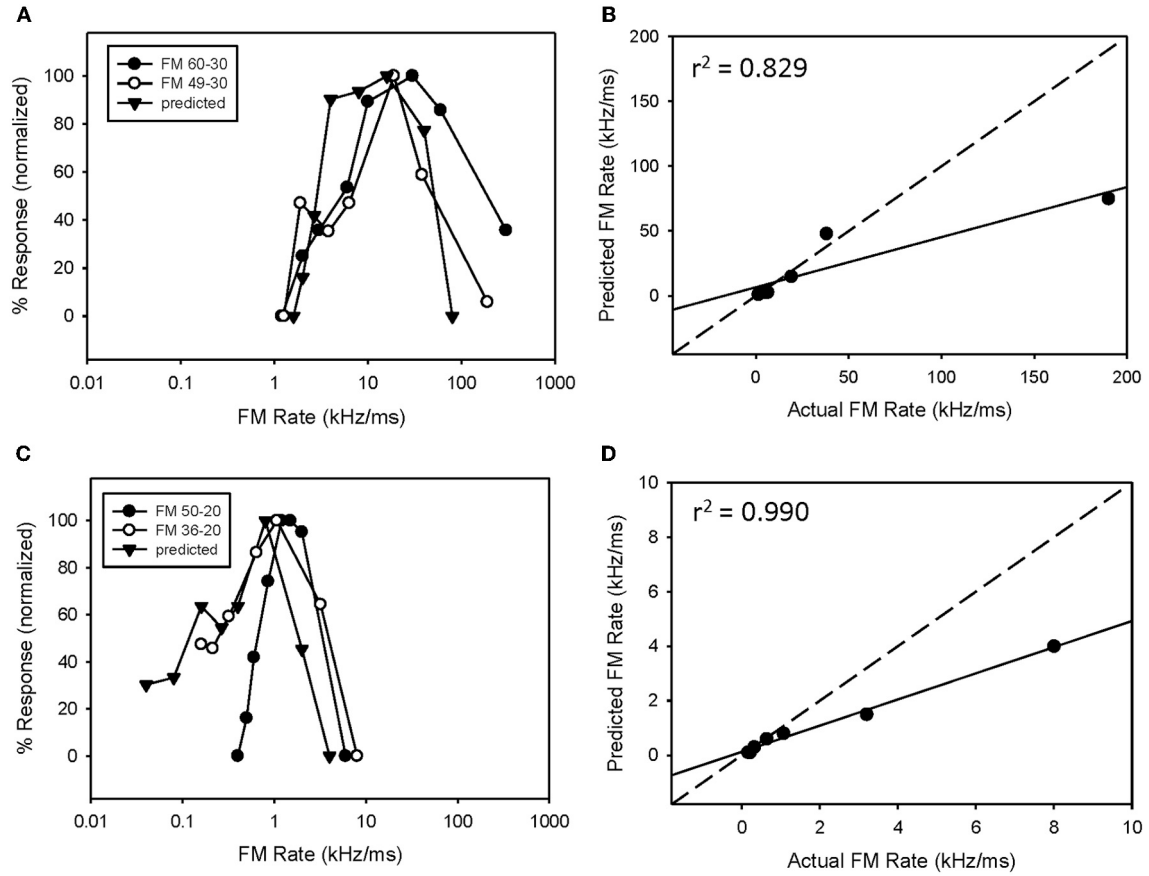

FIGURE 5 | In neurons expressing HFI, predicted responses were compared to FM sweeps both in the presence and absence of HFI by eliminating the high-frequency region from the sweep. The effect of removing HFI ranged from a minimal change in the FM rate response **(A)**, a broadening of the FM rate response to include slower FM sweep rates **(C)**. In each case, predicted and actual FM rates were significantly correlated but only in the absence of HFI **(B,D)**.

inhibition (**Figure 8C**), the elimination of HFI with a downward sweep (49–30 kHz) had no effect on the rate function, indicating that the neuron's duration tuning played the dominant role in shaping rate tuning. When STRYCH was applied, this bandpass duration tuning was eliminated, and, as expected, so was the bandpass rate selectivity. Moreover, the duration function during disinhibition predicted the rate selectivity (**Figure 8F**).

In 5 of 15 bandpass rate-selective neurons tested, blocking inhibition had little effect on duration tuning. The example in **Figure 10** shows that blocking GABAergic inhibition elevated response magnitude but did not eliminate bandpass duration tuning (**Figure 9A**). Similarly, it had little effect on the arrival time of HFI (**Figure 9B**). Consequently, blocking inhibition did not eliminate bandpass rate selectivity in this neuron (**Figure 9C**).

Finally, we have emphasized the mechanisms that shape bandpass selectivity and the slowest sweep rates to which a neuron will respond. Regarding the fastest sweeps to which these neurons respond, it is important to note that blocking inhibition had little or no effect on this response property. All neurons stopped responding at increasingly short tone durations, or increasingly fast sweep rates, and this is likely due to the intrinsic properties of neurons in the circuits projecting to these IC neurons, rather than the inhibitory inputs they receive.

DISCUSSION

Present results demonstrate that similar expressions of bandpass FM sweep rate selectivity can be created by either bandpass duration tuning, or a delayed HFI that determines the slowest sweep rate to which a neuron will respond. The elimination of HFI by starting an FM sweep at a frequency lower than the HFI will eliminate bandpass rate selectivity. The elimination of duration tuning or HFI in these neurons through the blockade of inhibitory receptors will also eliminate rate selectivity. If a neuron possessed both duration tuning and HFI, both mechanisms had to be eliminated in order to eliminate a neuron's bandpass rate selectivity.

COMPLEMENTARY OR REDUNDANT?

That two mechanisms can create the same sweep rate selectivity begs the question of whether these mechanisms are redundant or complementary. Both are true in that both mechanisms can contribute to the rate selectivity of a given neuron, or either can act alone. As shown in the hypothetical neuron in

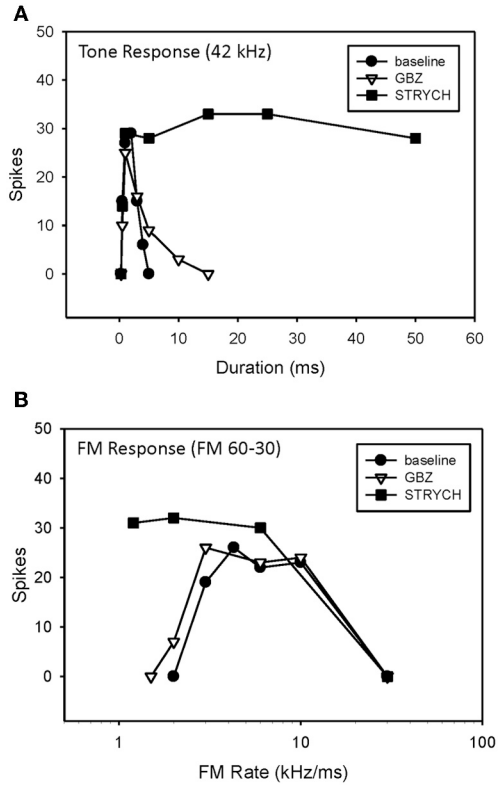

FIGURE 6 | Conversion of duration tuning (A) and FM rate selectivity (B) from bandpass to slowpass following application of STRYCH. GBZ had no effect on either parameter.

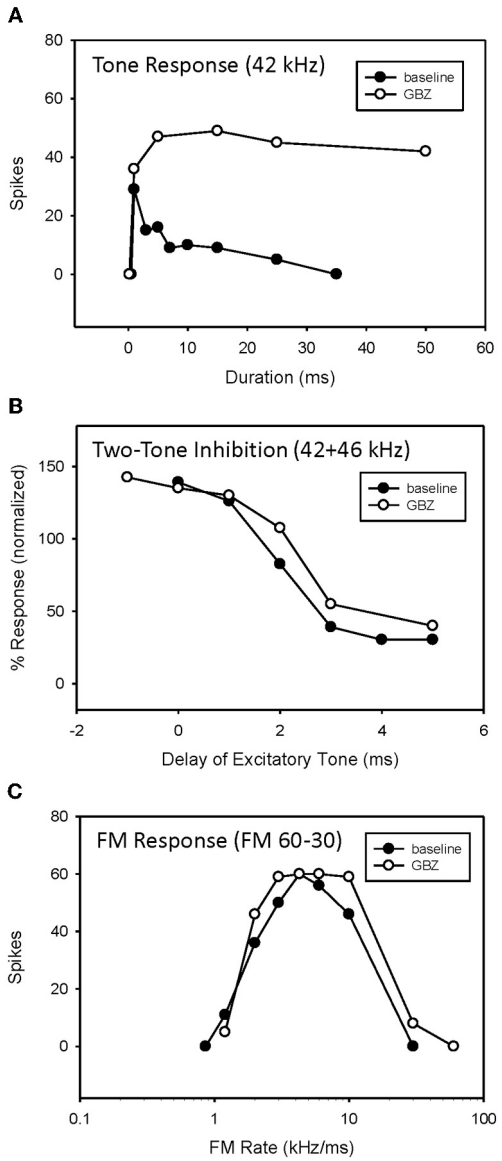

FIGURE 7 | Application of GBZ converted duration tuning from bandpass to longpass (A) but did not eliminate HFI (B) or bandpass FM rate selectivity (C) in this neuron.

Figure 10, duration tuning alone can create bandpass rate tuning (**Figure 10A**, solid line). This type of duration tuning has been modeled as a coincidence mechanism in which an excitatory rebound from the IPSP combined with the excitatory input to drive the neuron (Casseday et al., 1994; Covey et al., 1996; review, Sayegh et al., 2011). Alternatively, we have modeled the mechanism underlying duration tuning as an early inhibition that persists the duration of a tone, and a delayed excitatory input that has a fixed latency (**Figure 10B**). The neuron will respond to a tone of increasing duration until the inhibition overlaps with the delayed excitation, and suppresses the response, and has thus been termed an anti-coincidence model (Fuzessery and Hall, 1999). The best duration, and the range of excitatory durations, of a neuron will be determined by the arrival time of the excitatory input (**Figure 10B**). If the excitatory input is delayed further, the neuron will respond to longer tone durations. Conversely, if it arrives earlier, the neuron can respond only to shorter durations before it is inhibited. It is not clear what determines the arrival time of the excitatory input; we have previously reported (Fuzessery et al., 2002) that blocking inhibitory inputs to IC neurons in the pallid bat have little effect on their response latency.

If HFI is also present, it can directly or indirectly contribute to the sculpting of rate selectivity. The arrival time of HFI is influenced by two factors. The cutoff sweep rate can be predicted by the inhibitory bandwidth (kHz) divided by the arrival time (ms). The broader the bandwidth of the inhibitory sideband (**Figure 10C**,**1**), the sooner a downward sweep will encounter the sideband and trigger inhibitory input. Also, if HFI simply arrives sooner relative to excitation (**Figure 10C**,**3**), the cutoff rate will be faster. If the cutoff rate shaped by HFI is faster than that shaped by the duration function (**Figure 10A**,**3**), it will directly contribute to shaping the slow-rate flank of the bandpass rate function (e.g., **Figure 5C**). If it is not faster (**Figure 10A**,**1**), it will not contribute, and the rate function will be shaped entirely by the duration function.

Even if HFI does not directly shape rate selectivity, it can have an indirect influence. If a neuron's rate selectivity is shaped by duration tuning, its best rate can be predicted by the bandwidth

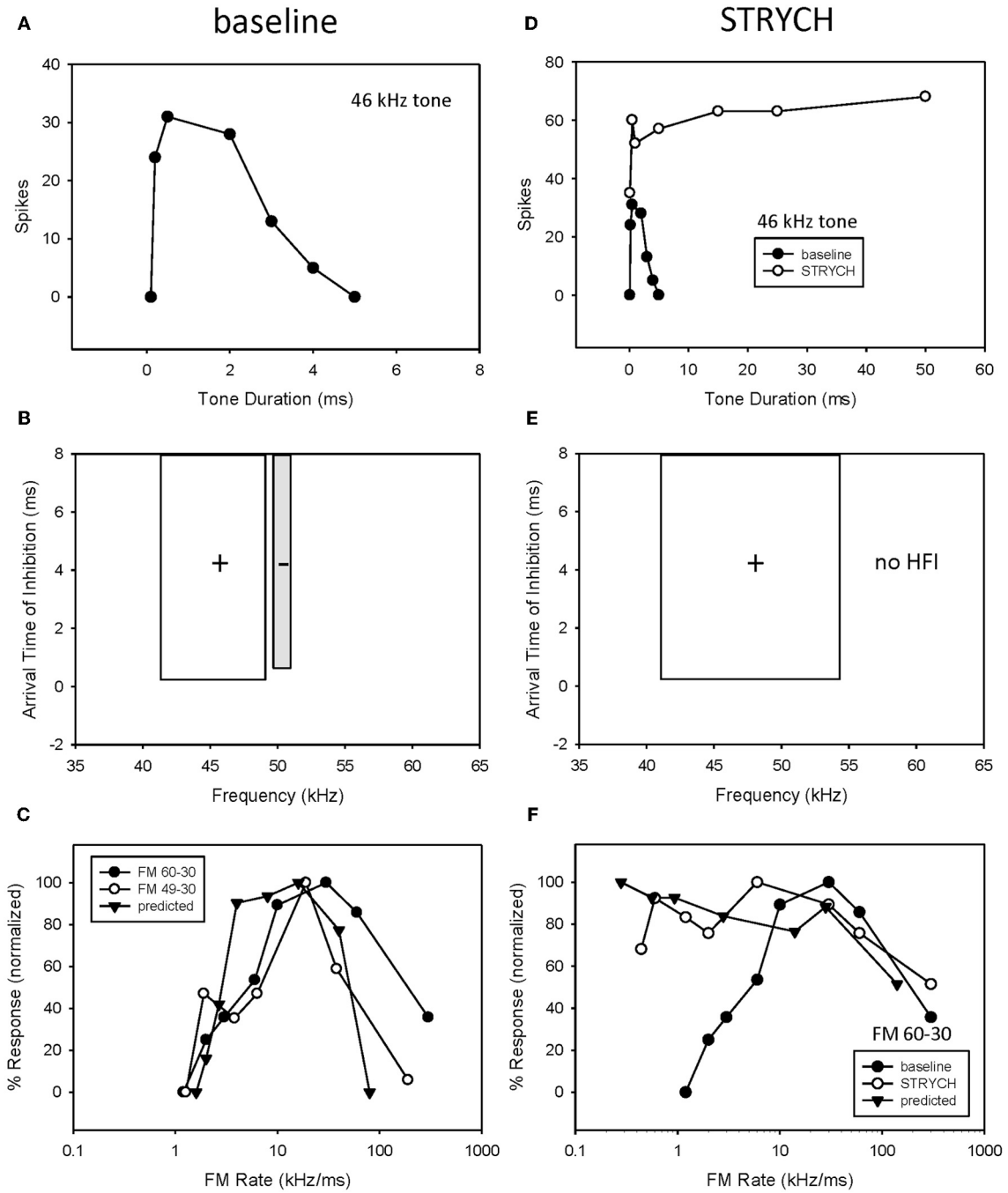

FIGURE 8 | If more than one mechanism was present both had to be eliminated before FM rate selectivity was affected. In this neuron, exhibiting both bandpass duration tuning **(A)** and HFI **(B)**, the elimination of HFI from the FM sweep did not eliminate bandpass FM rate selectivity **(C)**. In comparison, application of STRYCH eliminated bandpass duration tuning **(D)**, HFI **(E)**, and bandpass FM rate selectivity **(F)**.

of its excitatory tuning curve (kHz) divided by its best duration (ms). Inhibitory sidebands can shape this excitatory bandwidth (Yang et al., 1992; Fuzessery and Hall, 1996; LeBeau et al., 2001), as shown in **Figures 8B,E**, where disinhibition eliminates inhibitory sidebands and expands the excitatory tuning curve. If strong inhibitory flanks narrow the excitatory bandwidth (e.g., **Figure 10C,2,4**), the best rate will decrease, assuming that the best duration remains constant. Conversely, if the excitatory bandwidth increases (**Figure 10C,5**), the best rate will increase because an FM sweep now has to traverse the broader excitatory tuning curve more rapidly. For example, if a neuron's best duration is 1 ms, and the excitatory bandwidth was to increase from 3

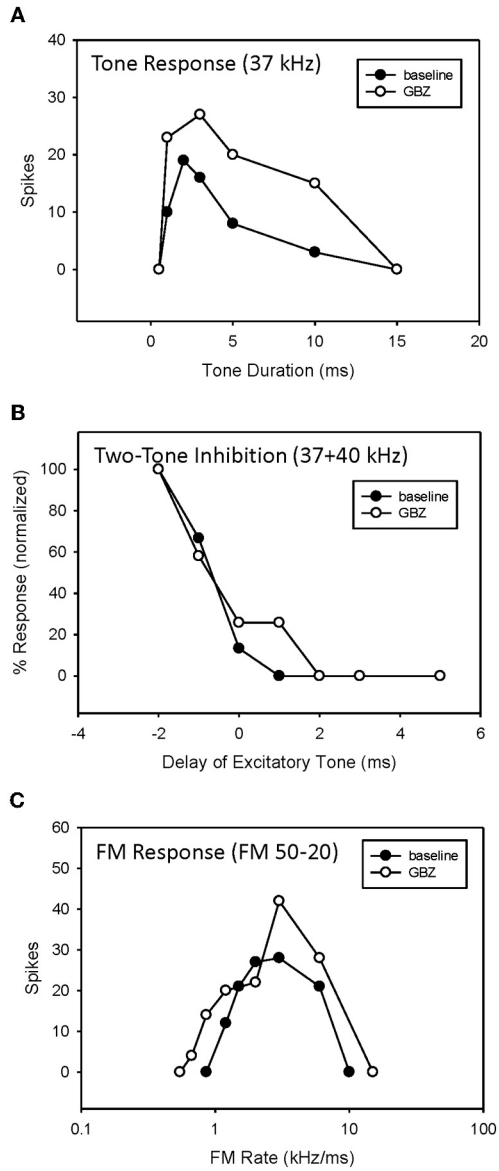

FIGURE 9 | Application of GBZ was ineffective at eliminating bandpass duration tuning (A), HFI (B), or band-pass FM rate selectivity (C) in this neuron.

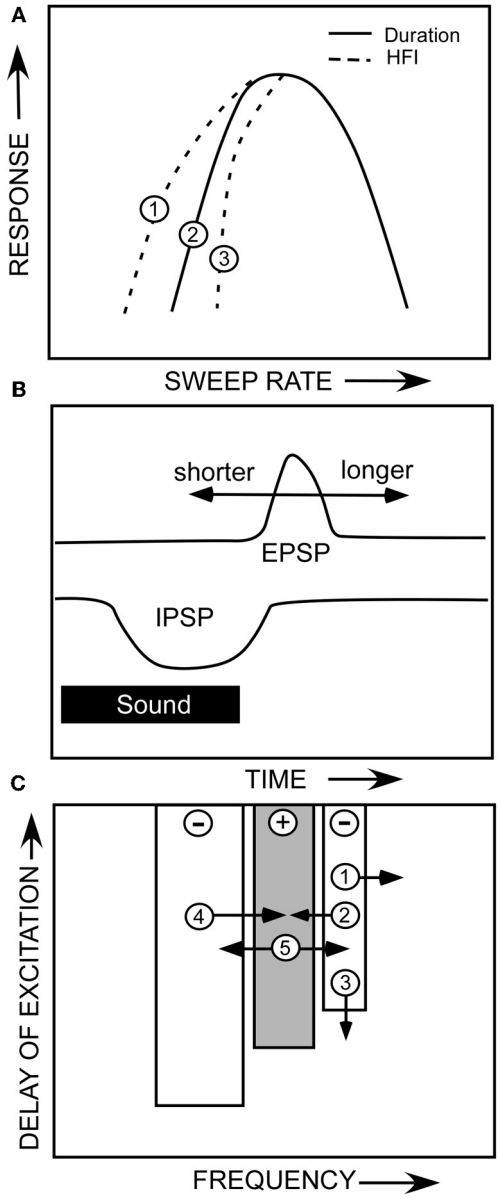

FIGURE 10 | (A) A hypothetical neuron showing how duration tuning and HFI could potentially affect sweep rate selectivity. **(B)** The anti-coincidence mechanism thought to underlie bandpass duration tuning. **(C)** A diagram of the multiple ways that changes in the properties of a neuron's inhibitory and excitatory frequency domains could influence sweep rate selectivity. See text.

to 6 kHz, the best rate would increase from 3 to 6 kHz. There are thus multiple ways in which duration tuning and HFI can interact directly and indirectly, in a redundant or complementary fashion, to shape selectivity for FM sweep rate.

Asymmetrical facilitation is a third mechanism that is known to shape sweep rate selectivity in the pallid bat IC (Williams and Fuzessery, 2010). It has been most thoroughly documented in the FM specialists because the weak response to single tones makes the two-tone facilitation readily apparent. FM specialists were not included in the present study because strong responses to tones were required to predict sweep rate functions. The extent to which asymmetrical facilitation contributed to rate selectivity in this study is not clear, but our ability to predict rate selectivity, and to also eliminate it by eliminating duration tuning or HFI, suggests that this third mechanism did not play a major role in shaping the selectivity of the neurons tested in the present study.

CIRCUITRY UNDERLYING THE CREATION OF SWEEP RATE SELECTIVITY

Inhibitory circuits play a significant role in shaping duration tuning, HFI, and FM sweep selectivity in the pallid bat IC (Fuzessery and Hall, 1996, 1999), so the present finding (**Table 2**) that

duration tuning persists in 8 of 15 neurons, and HFI persists in 12 of 15 neurons in which inhibitory inputs were blocked suggests that the pallid bat IC may be inheriting some of this response selectivity from lower levels of the system, rather than creating it within the IC. There was not a significant difference in the percentage neurons in which duration tuning was eliminated by GBZ or STRYCH, suggesting that both inhibitory circuits play a similar role in shaping this form of selectivity. HFI was eliminated in only 3 of 15 neurons, suggesting that this response property is largely inherited from lower levels. The issue of where this selectivity is created was more thoroughly addressed in a recent study of the pallid bat IC (Williams and Fuzessery, 2011) that focused on the creation of HFI and LFI, the latter shaping sweep direction selectivity. The application of GBZ or STRYCH eliminated LFI in the majority of neurons, suggesting that both inhibitory circuits can shape LFI. When both drugs were applied, LFI was eliminated in 86% of neurons, suggesting that much of the LFI, and therefore sweep direction selectivity, is created through intrinsic IC processing. In contrast, only STRYCH application eliminated HFI, and this occurred in only 33% of neurons. Even when both GBZ and STRYCH were applied, HFI was lost in only 38% of neurons. These results, along with those of the present study, are consistent in that they both suggest that the HFI inhibition shaping rate selectivity is largely inherited from lower levels of the system. These results also suggest that GABA- and glycinergic circuits may play differential roles in shaping various forms of response properties in the auditory system.

UNDERESTIMATION OF SWEEP RATE SELECTIVITY

When predicting a neuron's sweep rate function from its duration function, there was an overall underestimation of rate selectivity by a factor of 1.6. In other words, although the shape of the predicted rate function closely approximated the actual function, it was shifted toward lower sweep rates. This is likely due to an underestimation of the bandwidth of the excitatory frequency domains. Auditory neurons have been found to respond to frequencies outside of the excitatory tuning curve, which is typically described using tones, if those frequencies are presented as part of a spectrotemporally more complex sound. This has been referred to as their "extraclassical" tuning curve (Xie et al., 2007; Schneider and Woolley, 2011). The pallid bat IC contains neurons termed FM specialists that respond preferentially or exclusively to downward FM sweeps that mimic its biosonar signal (Fuzessery, 1994). A large percentage of these exhibit an asymmetrical facilitation when presented with two tones delayed in time, as they would occur within a downward (but not upward) FM sweep (Williams and Fuzessery, 2010). When the excitatory domains of these FM specialists were measured with a series of narrowband downward FM sweeps, the bandwidths of the excitatory domains were broader than when measured with tones. We therefore suggest that some predicted rate functions were underestimated because we used tones to measure the excitatory tuning curve, but obtained sweep rate functions using FM sweeps. The FM sweeps excited the broader extraclassical tuning curve, but the tones did not. Since the predicted rates equal the excitatory bandwidth divided by the best duration, this would result in a lower predicted sweep rate.

BEHAVIORAL RELEVANCE OF DURATION AND RATE TUNING

Duration selectivity has been found in both echolocating mammals (Ehrlich et al., 1997; Galazyuk and Feng, 1997; Fuzessery and Hall, 1999; Casseday et al., 2000; Faure et al., 2003; Mora and Kossl, 2004; Fremouw et al., 2005; Jen and Wu, 2006; Luo et al., 2008; Macias et al., 2011) and non-echolocating mammals (Chen, 1998; Brand et al., 2000; Xia et al., 2000; He, 2002; Perez-Gonzalez et al., 2006; Wang et al., 2006), and in anurans (Potter, 1965; Narins and Capranica, 1980; Gooler and Feng, 1992; Leary et al., 2008; Xia et al., unpublished data). These neurons likely play important roles in the selective detection and analysis of communication signals and biosonar echoes (review, Sayegh et al., 2011). Several forms of duration tuning have been reported in the IC, including allpass, shortpass, longpass, bandpass, and even band-reject. In the present study, we reported only bandpass and longpass because we sampled responses over a broad range of durations, including the microsecond range. This eliminated the allpass and shortpass categories, since there is a minimum sound duration required by all neurons to elicit a response.

To our knowledge, it is only in the pallid bat where the idea has been suggested that bandpass duration tuning serves to create FM sweep selectivity, and not to detect signal duration *per se* (Fuzessery et al., 2006; review, Sayegh et al., 2011). Indeed, such neurons are sweep-rate selective, because even when an FM sweep's bandwidth or duration is changed, these neurons continue to maintain the same best sweep rate (Fuzessery et al., 2006). It is axiomatic that a neuron that has bandpass duration tuning will also have bandpass sweep-rate selectivity. In other words, what is a purely temporal filter when presented with a tone becomes a spectrotemporal filter when presented with a spectrotemporally dynamic sound.

Although we initially reported (Fuzessery and Hall, 1999) that the durations of echolocation pulses (1.5–6 ms) roughly matched the range of best durations (0.5–7 ms), the match between the best sweep rates and echolocation pulse sweep rates is closer. Pallid bat echolocation pulses have bandwidths of 20–30 kHz (Brown, 1976; Fuzessery et al., 1993), which over the range of pulse durations would yield sweep rates of 3–20 kHz/ms. The best sweep rates of IC neurons range from 1 to 10 kHz, with a mean of 4 kHz/ms (Fuzessery et al., 2006). Although the distributions do not overlap perfectly, most rate-tuned neurons will respond to the range of sweep rates. If durations are considered, the mean best duration of IC neurons is 1.6 ms, which means almost half of the population is tuned to durations shorter than the minimum 1.5 ms pulse duration. We therefore suggest that, during development, the system tunes itself to the sweep rate of the echolocation pulse (and not its duration), since this is the primary signal that it is responsible for processing. This may also apply to other bat species, but interestingly, most of the other bat species that have been studied have constant-frequency (CF) or quasi-CF biosonar pulses (Casseday et al., 1994; Luo et al., 2008; Macias et al., 2011). Since these signals are essentially tones or shallow FM sweeps, a neuronal tuning to duration rather than sweep rate has greater behavior relevance. Perhaps the common denominator among these bat species is the need for the selective detection of echoes. In the pallid bat, we have suggested (Fuzessery, 1994) that neuronal selectivity for sweep rate is one of several filters,

along with sweep direction and spectrum selectivity, that serve the selective detection of biosonar echoes by eliminating responses to other sounds in the environment. This function may be particularly important in a gleaner like the pallid bat, which uses echolocation primarily for general orientation, while passively listening for prey-generated sounds. Strong spectrotemporal filters may facilitate the segregation of these two auditory streams while the bat is hunting (Fuzessery, 1994; Barber et al., 2003).

Similar bandpass selectivity for short signal durations is also present in the lateral IC of the pallid bat (Fuzessery, 1997; Fuzessery and Hall, 1999). This region is tuned to frequencies below the echolocation pulse, and its neurons respond preferentially to noise transients used in the passive sound localization of prey (Bell, 1982; Fuzessery et al., 1993). This raises the interesting possibility that, while the duration tuning in the two neuronal populations is similar, one population may be tuned to the sweep rate of biosonar echoes, while the other is selective for the duration of short noise bursts.

To conclude, the ecological niche ocuppied by the pallid bat appears to necessitate the participation of neurons that respond selectively to biologically relevant signals, one of them being biosonar echoes. Selective pressure has apparently acted to produce multiple mechanisms that act separately or in concert to create the required degree of selectivity. Within this context, it is of interest that the two mechanisms discussed here appear to be the result of different inhibitory circuits within the auditory brainstem. The on-best frequency inhibition shaping duration tuning is either GABA- or glycinergic, while HFI is primarily the result of only glycinergic input (Williams and Fuzessery, 2011), suggesting that selective pressure has acted upon the two inhibitory pathways in a differential manner.

ACKNOWLEDGMENTS

We thank Terri Zumsteg for comments of this manuscript. Research funded by NIDCD grant DC5202.

REFERENCES

Andoni, S., and Pollak, G. D. (2011). Selectivity for spectral motion as a neural computation for encoding natural communication signals in bat inferior colliculus. *J. Neurosci.* 31, 16529–16540.

Aubie, B., Becker, S., and Faure, P. A. (2009). Computational models of millisecond level duration tuning in neural circuits. *J. Neurosci.* 29, 9255–9270.

Barber, J. R., Razak, K. A., and Fuzessery, Z. M. (2003). Can two streams of auditory information be processed simultaneously? Evidence from the gleaning bat *Antrozous pallidus*. *J. Comp. Physiol. A Neuroethol. Sens. Neural Behav. Physiol.* 189, 843–855.

Bell, G. (1982). Behavioral and ecological aspects of gleaning by the desert insectivorous bat, *Antrozous pallidus* (Chiroptera: Vestpertilionidae). *Behav. Ecol. Sociobiol.* 10, 217–223.

Brand, A., Urban, R., and Grothe, B. (2000). Duration tuning in the mouse auditory midbrain. *J. Neurophysiol.* 84, 1790–1799.

Brimijoin, W. O., and O'Neill, W. E. (2005). On the prediction of sweep rate and directional selectivity for FM sounds from two-tone interactions in the inferior colliculus. *Hear. Res.* 210, 63–79.

Britt, R., and Starr, A. (1976). Synaptic events and discharge patterns of cochlear nucleus cells. II. Frequency-modulated tones. *J. Neurophysiol.* 39, 179–194.

Brown, P. (1976). Vocal communication in the pallid bat, *Antrozous pallidus*. *Z. Tierpsychol.* 41, 34–54.

Brugge, J. F. (1992). "An overview of central auditory processing," in *The Mammalian Auditory Pathway: Neurophysiology*, eds R. Fay and A. Popper (New York, NY: Springer-Verlag), 1–33.

Casseday, J. H., Ehrlich, D., and Covey, E. (1994). Neural tuning for sound duration: role of inhibitory mechanisms in the inferior colliculus. *Science* 264, 847–850.

Casseday, J. H., Ehrlich, D., and Covey, E. (2000). Neural measurement of sound duration: control by excitatory-inhibitory interactions in the inferior colliculus. *J. Neurophysiol.* 84, 1475–1487.

Chen, G. D. (1998). Effects of stimulus duration on responses of neurons in the chinchilla inferior colliculus. *Hear. Res.* 122, 142–150.

Covey, E., and Casseday, J. H. (1995). "The lower brainstem auditory pathways," in *Hearing by Bats*, eds A. Popper and R. Fay (New York, NY: Springer-Verlag), 235–295.

Covey, E., Kauer, J. A., and Casseday, J. H. (1996). Whole-cell patch-clamp recording reveals subthreshold sound-evoked postsynaptic currents in the inferior colliculus of awake bats. *J. Neurosci.* 16, 3009–3018.

Ehrlich, D., Casseday, J. H., and Covey, E. (1997). Neural tuning to sound duration in the inferior colliculus of the big brown bat, *Eptesicus fuscus*. *J. Neurophysiol.* 77, 2360–2372.

Faure, P. A., Fremouw, T., Casseday, J. H., and Covey, E. (2003). Temporal masking reveals properties of sound-evoked inhibition in duration-tuned neurons of the inferior colliculus. *J. Neurosci.* 23, 3052–3065.

Fremouw, T., Faure, P. A., Casseday, J. H., and Covey, E. (2005). Duration selectivity of neurons in the inferior colliculus of the big brown bat: tolerance to changes in sound level. *J. Neurophysiol.* 94, 1869–1878.

Fuzessery, Z. M. (1994). Response selectivity for multiple dimensions of frequency sweeps in the pallid bat inferior colliculus. *J. Neurophysiol.* 72, 1061–1079.

Fuzessery, Z. M. (1997). Acute sensitivity to interaural time differences in the inferior colliculus of a bat that relies on passive sound localization. *Hear. Res.* 109, 46–62.

Fuzessery, Z. M., Buttenhoff, P., Andrews, B., and Kennedy, J. M. (1993). Passive sound localization of prey by the pallid bat (*Antrozous p. pallidus*). *J. Comp. Physiol. A* 171, 767–777.

Fuzessery, Z. M., Gumtow, R. G., and Lane, R. (1991). A microcomputer-controlled system for use in auditory physiology. *J. Neurosci. Methods* 36, 45–52.

Fuzessery, Z. M., and Hall, J. C. (1996). Role of GABA in shaping frequency tuning and creating FM sweep selectivity in the inferior colliculus. *J. Neurophysiol.* 76, 1059–1073.

Fuzessery, Z. M., and Hall, J. C. (1999). Sound duration selectivity in the pallid bat inferior colliculus. *Hear. Res.* 137, 137–154.

Fuzessery, Z. M., Razak, K. A., and Williams, A. J. (2010). Multiple mechanisms shape selectivity for FM sweep rate and direction in the pallid bat inferior colliculus and auditory cortex. *J. Comp. Physiol. A Neuroethol. Sens. Neural Behav. Physiol.* 197, 615–623.

Fuzessery, Z. M., Richardson, M. D., and Coburn, M. S. (2006). Neural mechanisms underlying selectivity for the rate and direction of frequency-modulated sweeps in the inferior colliculus of the pallid bat. *J. Neurophysiol.* 96, 1320–1336.

Fuzessery, Z. M., Wenstrup, J. J., Hall, J. C., and Leroy, S. (2002). Inhibition has little effect on response latencies in the inferior colliculus. *J. Assoc. Res. Otolaryngol.* 4, 60–73.

Galazyuk, A. V., and Feng, A. S. (1997). Encoding of sound duration by neurons in the auditory cortex of the little brown bat, *Myotis lucifugus*. *J. Comp. Physiol. A* 180, 301–311.

Gittelman, J. X., and Li, N. (2011). FM velocity selectivity in the inferior colliculus is inherited from velocity-selective inputs and enhanced by spike threshold. *J. Neurophysiol.* 106, 2399–2414.

Gittelman, J. X., Li, N., and Pollak, G. D. (2009). Mechanisms underlying directional selectivity for frequency-modulated sweeps in the inferior colliculus revealed by *in vivo* whole-cell recordings. *J. Neurosci.* 29, 13030–13041.

Gooler, D. M., and Feng, A. S. (1992). Temporal coding the frog auditory midbrain: the influence of duration and rise-fall time on the processing of complex amplitude-modulated stimuli. *J. Neurophysiol.* 67, 1–22.

Gordon, M., and O'Neill, W. E. (1998). Temporal processing across frequency channels by FM selective auditory neurons can account for FM rate selectivity. *Hear. Res.* 122, 97–108.

Hall, J. C. (1999). GABAergic inhibition shapes frequency tuning and modifies response properties in the auditory midbrain of the leopard frog. *J. Comp. Physiol. A* 185, 479–491.

Havey, D. C., and Caspary, D. M. (1980). A simple technique for constructing 'piggy-back' multibarrel microelectrodes. *Electroencephalogr. Clin. Neurophysiol.* 48, 249–251.

He, J. (2002). OFF responses in the auditory thalamus of the guinea pig. *J. Neurophysiol.* 88, 2377–2386.

Heil, P., Langner, G., and Scheich, H. (1992). Processing of frequency-modulated stimuli in the chick auditory cortex analogue: evidence for topographic representations and possible mechanisms of rate and directional sensitivity. *J. Comp. Physiol. A* 171, 583–600.

Jen, P. H., and Wu, C. H. (2006). Duration selectivity organization in the inferior colliculus of the big brown bat, *Eptesicus fuscus*. *Brain Res.* 1108, 76–87.

Koch, U., and Grothe, B. (1998). GABAergic and glycinergic inhibition sharpens tuning for frequency modulations in the inferior colliculus of the big brown bat. *J. Neurophysiol.* 80, 71–82.

Leary, C. J., Edwards, C. J., and Rose, G. J. (2008). Midbrain auditory neurons integrate excitation and inhibition to generate duration selectivity: an *in vivo* whole-cell patch study in anurans. *J. Neurosci.* 28, 5481–5493.

LeBeau, F. E., Malmierca, M. S., and Rees, A. (2001). Iontophoresis *in vivo* demonstrates a key role for GABA(A) and glycinergic inhibition in shaping frequency response areas in the inferior colliculus of guinea pig. *J. Neurosci.* 21, 7303–7312.

Luo, F., Metzner, W., Wu, F., Zhang, S., and Chen, Q. (2008). Duration-sensitive neurons in the inferior colliculus of horseshoe bats: adaptations for using CF-FM echolocation pulses. *J. Neurophysiol.* 99, 284–296.

Macias, S., Mora, E. C., Hechavarria, J. C., and Kossl, M. (2011). Duration tuning in the inferior colliculus of the mustached bat. *J. Neurophysiol.* 106, 3119–3128.

Mora, E. C., and Kossl, M. (2004). Ambiguities in sound-duration selectivity by neurons in the inferior colliculus of the bat *Molossus molossus* from Cuba. *J. Neurophysiol.* 91, 2215–2226.

Narins, P. M., and Capranica, R. R. (1980). Neural adaptations for processing the two-note call of the Puerto Rican treefrog, *Eleutherodactylus coqui*. *Brain Behav. Evol.* 17, 48–66.

Oliver, D. L. (2005). "Neuronal organization in the inferior colliculus," in *The Inferior Colliculus*, eds J. A. Winer and C. E. Schreiner (New York, NY: Springer Science+Business Media, Inc.), 69–114.

Perez-Gonzalez, D., Malmierca, M. S., Moore, J. M., Hernandez, O., and Covey, E. (2006). Duration selective neurons in the inferior colliculus of the rat: topographic distribution and relation of duration sensitivity to other response properties. *J. Neurophysiol.* 95, 823–836.

Pollak, G., and Park, T. (1995). "The inferior colliculus," in *Hearing by Bats,* eds A. Popper and R. Fay (New York, NY: Springer-Verlag), 296–367.

Potter, H. D. (1965). Patterns of acoustically evoked discharges of neurons in the mesencephalon of the bullfrog. *J. Neurophysiol.* 28, 1155–1184.

Ramachandran, R., Davis, K. A., and May, B. J. (1999). Single-unit responses in the inferior colliculus of decerebrate cats. I. Classification based on frequency response maps. *J. Neurophysiol.* 82, 152–163.

Razak, K. A., and Fuzessery, Z. M. (2006). Neural mechanisms underlying selectivity for the rate and direction of frequency-modulated sweeps in the auditory cortex of the pallid bat. *J. Neurophysiol.* 96, 1303–1319.

Razak, K. A., and Fuzessery, Z. M. (2009). GABA shapes selectivity for the rate and direction of frequency-modulated sweeps in the auditory cortex. *J. Neurophysiol.* 102, 1366–1378.

Sayegh, R., Aubie, B., and Faure, P. A. (2011). Duration tuning in the auditory midbrain of echolocating and non-echolocating vertebrates. *J. Comp. Physiol. A Neuroethol. Sens. Neural Behav. Physiol.* 197, 571–583.

Schneider, D. M., and Woolley, S. M. (2011). Extra-classical tuning predicts stimulus-dependent receptive fields in auditory neurons. *J. Neurosci.* 31, 11867–11878.

Shannon-Hartman, S., Wong, D., and Maekawa, M. (1992). Processing of pure-tone and FM stimuli in the auditory cortex of the FM bat, *Myotis lucifugus*. *Hear. Res.* 61, 179–188.

Suga, N. (1968). Analysis of frequency-modulated and complex sounds by single auditory neurones of bats. *J. Physiol.* 198, 51–80.

Wang, J., van Wijhe, R., Chen, Z., and Yin, S. (2006) Is duration tuning a trnsient process in the inferior colliculus of guinea pigs? *Brain Res.* 1114, 63–74.

Williams, A. J., and Fuzessery, Z. M. (2010). Facilitatory mechanisms shape selectivity for the rate and direction of FM sweeps in the inferior colliculus of the pallid bat. *J. Neurophysiol.* 104, 1456–1471.

Williams, A. J., and Fuzessery, Z. M. (2011). Differential roles of GABAergic and glycinergic input on FM selectivity in the inferior colliculus of the pallid bat. *J. Neurophysiol.* 106, 2523–2535.

Xia, Y. F., Qi, Z. H., and Shen, J. X. (2000). Neural representation of sound duration in the inferior colliculus of the mouse. *Acta Otolaryngol.* 120, 638–643.

Xie, R., Gittelman, J. X., and Pollak, G. D. (2007). Rethinking tuning: *in vivo* whole-cell recordings of the inferior colliculus in awake bats. *J. Neurosci.* 27, 9469–9481.

Yang, L., Pollak, G. D., and Resler, C. (1992). GABAergic circuits sharpen tuning curves and modify response properties in the mustache bat inferior colliculus. *J. Neurophysiol.* 68, 1760–1774.

Conflict of Interest Statement: The authors declare that the research was conducted in the absence of any commercial or financial relationships that could be construed as a potential conflict of interest.

Received: 04 June 2012; accepted: 30 July 2012; published online: 17 August 2012. Citation: Williams AJ and Fuzessery ZM (2012) Multiple mechanisms shape FM sweep rate selectivity: complementary or redundant? Front. Neural Circuits ***6****:54. doi: 10.3389/fncir.2012.00054*